Exploring Complex Problems in Fluid Dynamics: from CFD to Experiments Leveraging ML

by

Jose del Aguila Ferrandis
B.S., Technical University of Madrid (2016)
S.M., Technical University of Madrid (2018)

Submitted to the Department of Mechanical Engineering
and Center for Computational Science & Engineering

in partial fulfillment of the requirements for the degree of
Doctor of Philosophy in Mechanical Engineering and Computation at the
MASSACHUSETTS INSTITUTE OF TECHNOLOGY
May 2024

Authored by: Jose del Aguila Ferrandis

Department of Mechanical Engineering
and Center for Computational Science & Engineering
May 3, 2024

Certified by: Michael Triantafyllou Ph.D.

Henry L. and Grace Doherty Professor in Ocean Science and Engineering;
Professor of Mechanical and Ocean Engineering; Director, MIT Sea Grant
Thesis Supervisor

Accepted by: Nicolas Hadjiconstantinou, Ph.D.

Nicolas Hadjiconstantinou, Ph.D.
Professor of Mechanical Engineering;
Mechanical Engineering Department Committee on Graduate Theses

Accepted by: Youssef M. Marzouk, Ph.D.

Youssef M. Marzouk, Ph.D.
Professor of Aeronautics and Astronautics;
Co-Director Center for Computational Science and Engineering; Center for Computational Science & Engineering Committee on Graduate Theses

Exploring Complex Problems in Fluid Dynamics: from CFD to Experiments Leveraging ML

by

José del Águila Ferrandis

Submitted to the Department of Mechanical Engineering
and Center for Computational Science & Engineering
on May 3rd, 2024, in partial fulfillment of the
requirements for the degree of
Doctor of Philosophy in Mechanical Engineering and Computation

Abstract

Structures operating in the marine environment are subject to large steady and unsteady forces, typically at high Reynolds number. Given the current limitations on CFD at high Reynolds number, and the high expense to conduct experiments at relevant scales, design is constrained by the limited available data, incomplete knowledge of the principal physical mechanisms, and restricted parametric searches, ML offers opportunities to overcome these limitations.

In this thesis we demonstrate we apply ML methods to three engineering problems of high importance to theory and applications:

1. *Optimizing Vortex Generators to Reduce Ship Form Drag: In the quest for reducing ship emissions, it is imperative that the fluid mechanics of ship resistance be explored for improving propulsive efficiency. Form drag is a significant part of the resistance of high block coefficient ships and remains a last frontier for hull ship optimization. We explore the optimization of vortex generators (VG) as a powerful tool for reducing flow separation.*

2. *Mapping the Properties of Fluid Forces in Vortex Induced Vibrations of SCR Risers: Vortices form in the wake of bluff bodies as a result of flow instabilities that are hard to study parametrically, especially for complex structures such as steel catenary risers (SCR). The resulting vibrations are of theoretical and practical importance. By using experimental and field data we can extract hydrodynamic databases the incorporate known physics, fill the parametric space, and provide new knowledge. By focusing on the SCR vibratiosn,w we demonstrate that we not only extract physics, but can provide accurate predictions as well.*

3. *Causal Learning of Large Amplitude Ship Motions with Emphasis on Parametric Rolling: Predicting ship motions in severe sea states is complex due to the nonlinear wave-body interactions involved. This section introduces a simulation approach utilizing neural networks trained on stochastic wave elevations from multiple sea states.*

The trained networks can predict core vessel motions, including the challenging phenomenon of parametric rolling. Once trained using detailed CFD simulations, these networks provide swift and efficient vessel dynamics predictions. The research also explores the statistics of non-linear motions, aiming for consistent and accurate predictions across different wave conditions. This methodology, influenced by the universal approximation theorem for functionals, represents a significant advancement in addressing engineering challenges.

In summary, these studies emphasize the role of ML a instrumental tool in advancing marine systems, driving them toward increased efficiency and adaptability.

Thesis Supervisor: Michael Triantafyllou Ph.D.
Title: Henry L. and Grace Doherty Professor in Ocean Science and Engineering; Professor of Mechanical and Ocean Engineering; Director, MIT Sea Grant

Acknowledgments

As I reflect on the profound journey that has been my PhD, I am filled with immense gratitude for those who have guided, inspired, and supported me along this transformative path.

Firstly, I extend my deepest thanks to my advisor, Prof. Michael Triantfyllou. His expert guidance in nonlinear fluid mechanics has not only shaped my academic pursuits but also inspired my entire PhD work. His dedication and mentorship have been a beacon of knowledge and inspiration throughout this journey.

I am immensely grateful to Prof. George Karniadakis for constantly challenging me and encouraging me to step outside my comfort zone. His innovative approach in applying machine learning techniques and his ability to imbue advanced mathematical concepts into my thought process have enriched my academic experience immeasurably.

Special thanks to Prof. Themis Sapsis for advancing my statistical understanding of nonlinear systems. His rigorous approach and insightful suggestions have equipped me with the right tools to analyze and interpret complex data effectively.

I owe a great deal of my understanding in Computational Fluid Dynamics to my discussions with Prof. Wim van Rees. His deep insights into complex techniques have helped me grasp the intricate implications of various assumptions and decisions throughout my research.

A profound acknowledgment goes to Prof. Chrys Chryssostomidis, and by extension to Marge Chryssostomidis, who was the first to believe in my potential at MIT. His unwavering support during my initial visiting periods helped lay a solid foundation for my PhD endeavors. His exemplary values and kindness have profoundly influenced me both personally and professionally, setting me on a path that I am eager and optimistic to follow.

From the onset of my time at MIT, I have been fortunate to collaborate with Stefano Brizzolara, Luca Bonfiglio, and Joao Seixas de Medeiros. Our engaging discussions and collaborative work in hydrodynamics have significantly fueled my imagination and strengthened my resolve to dedicate the necessary time and energy to pursue my PhD.

I must also acknowledge my project teammates Andreas, Edvard, Igor, Alfonso, Jill, and Jack. Our collective efforts in the VIV, VG, and artificial reef projects have not only challenged us but also bonded us in unique ways. Thank you for your steadfast support and camaraderie through all these years.

Participating in Spain@MIT, where we shared Spanish culture with the broader MIT community, has been a highlight of my journey. I thank Alvaro, Dani, Junkal, Ximo, Marc, Juanjo, and Jorge for their friendship and shared cultural experiences. Serving as president alongside Carmen, I am proud of the events and initiatives we spearheaded, which have enriched our community. The financial support from La Caixa during my first two years, along with meeting exceptional scholars like Fer, Joaquin, and Gonzalo, has left unforgettable experiences in my life.

The pandemic years brought unexpected challenges, yet I found a resilient community among friends like Alvaro, Agni, Carlos, Marga, Ximo, Ari, Alexa Ferran, Maria, Hele, Jon, Edu, Marta, Marc and Judit. Your support during these tough times, coupled with shared moments running, playing tennis, and skiing, provided the strength needed to persevere.

My academic discussions with Jose and Lucia on programming and IT automation, and my spirited exchanges with Theo about mountain adventures during gym sessions at the Z-center, have been both refreshing and enlightening. At SidPac, the companionship of Abhishek ensured I never felt isolated.

To Genaro, Javi, and Amanda, thank you for embracing our Latin culture and for the deep dives into mathematical concepts on differential equations and quantum computations that enriched our time together.

I am also grateful to Cristina, Jorge, Michael, Rodrigo, and Ane for the joyful times spent dancing salsa/bachata, skiing, or simply relaxing, which have been vital for my well-being.

To my incredible family—my parents, brothers, and sister—thank you for providing a sanctuary of optimism and love at crucial crossroads throughout this journey.

And to all those I have not explicitly mentioned but who have touched my life during my PhD journey, know that your contributions to my life and work are deeply appreciated.

Indeed, it is fortunate that my head is physically attached to my body, for I would surely lose it otherwise.

Contents

List of Figures

List of Tables

Chapter 1

Introduction

1.1 A Brief Overview of Scientific Machine Learning

1.1.1 Definition and Distinction

Scientific Machine Learning (SciML) represents a paradigm shift in computational science, merging traditional machine learning (ML) techniques with the rich domain knowledge of physical laws and scientific principles. Unlike conventional ML approaches that predominantly rely on large datasets for model training, SciML emphasizes the integration of physical laws to guide the learning process, particularly beneficial in scenarios characterized by sparse or complex data.

At the heart of SciML's divergence from mainstream ML is its focus on incorporating domain-specific knowledge directly into the model architecture. This approach is exemplified by Physics-Informed Neural Networks (PINNs) [216], which embed physical constraints (e.g., conservation laws) into the training process, enhancing the model's ability to generalize from limited data while ensuring physically plausible outcomes. Such integration not only improves the accuracy and interpretability of the models but also significantly reduces the dependency on extensive data collections, a common bottleneck in traditional ML applications.

Furthermore, SciML introduces innovative frameworks for modeling complex systems, as demonstrated by Deep Operator Networks (DeepONets, [156]). These networks learn mappings between function spaces, enabling the prediction of complex, nonlinear oper-

ators with applications ranging from fluid dynamics to material science. This ability to handle high-dimensional, nonlinear systems with fewer assumptions about the underlying phenomena marks a significant advancement over conventional approaches.

By leveraging scientific principles, SciML models achieve a balance between computational efficiency and predictive accuracy, making them particularly suited for solving intricate scientific problems where data may be limited or expensive to obtain. The flexibility and generalizability of SciML techniques, such as DeepONets, highlight their potential to transcend disciplinary boundaries, offering powerful tools for tackling a wide array of challenges in science and engineering.

Incorporating real-world applications and outcomes, such as the prediction of vortex-induced vibrations in marine structures or the modeling of climate change impacts, further illustrates the practical significance and transformative potential of SciML. Through its unique blend of machine learning and domain-specific knowledge, SciML is well prepared to revolutionize our approach to scientific discovery and technological innovation, providing insights and solutions that were previously beyond reach.

1.1.2 Importance of Data and Computational Resources

In the realm of scientific machine learning (SciML), the relationship of data availability against computational resources emerges as a critical consideration, particularly when contrasted with the development of large language models (LLMs) like GPT-based systems. LLMs capitalize on the vast expanse of online data, equivalent to millennia of human cognitive processing, coupled with relatively modest computational demands. This abundant data reservoir empowers LLMs to execute complex tasks by essentially mining the web for information, a feat less computationally intensive than often perceived.

However, transitioning to the domain of scientific challenges, such as complex fluid dynamics, reveals a stark contrast. Many scenarios of interest in this field are uncharted, lacking prior analysis. The pursuit of insights into these scenarios necessitates costly time consuming experiments or numerical models that demand substantial computational resources, akin to piecing together a 20-million-word puzzle for a coherent understanding. This analogy highlights the intricate balance between data scarcity and the high compu-

tational cost required for generating and processing scientific data effectively.

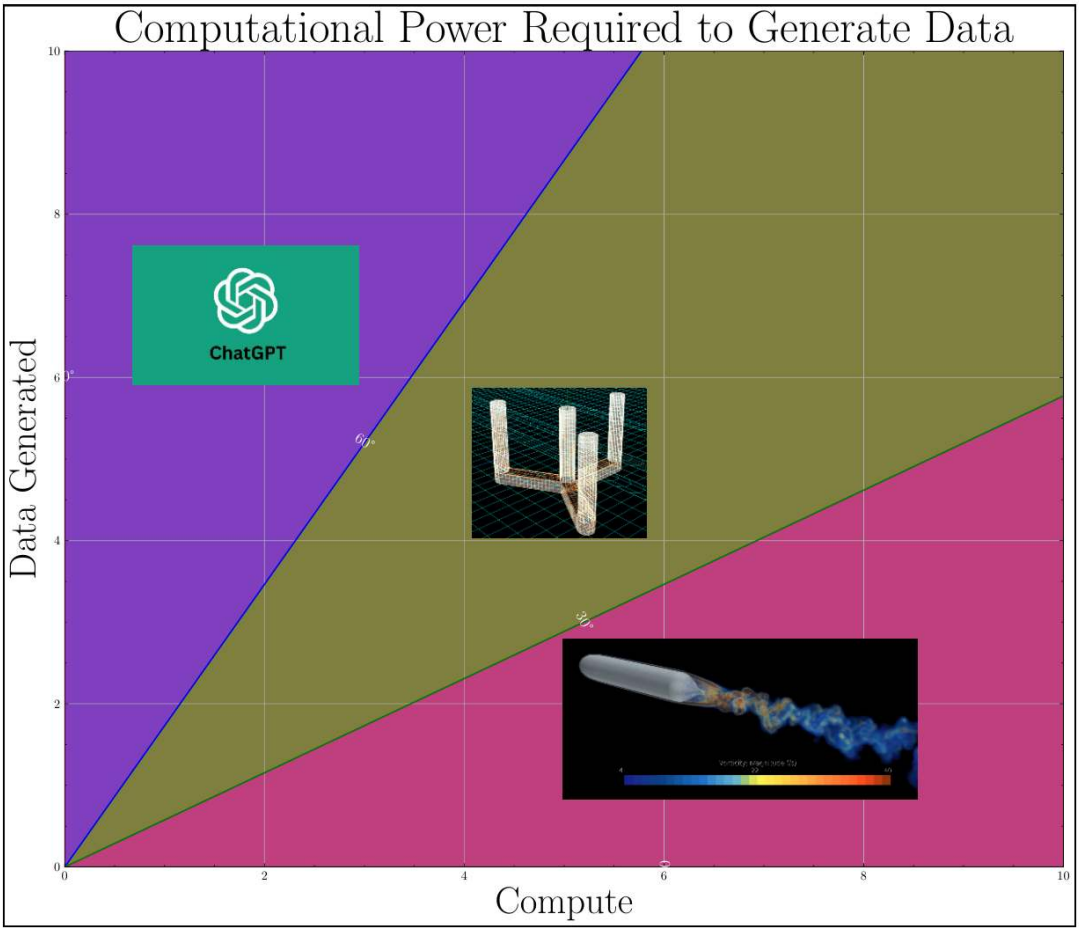

Figure 1-1: Obtaining more datapoints can be orders of magnitude more cost depending on the learning problem. For qualitative analysis, consider the vertical axis a log scale.

In fig. 1-1 a graphical representation of this balance is provided, illustrating the computational power required to generate data across different scientific domains. This graph serves as a compelling visual aid, emphasizing the exponential increase in computational resources needed as the complexity of the problem escalates.

Such insights emphasize the critical need for efficient SciML approaches that can navigate the delicate interplay between available data and computational constraints. By integrating physical laws and leveraging domain-specific knowledge, SciML aims to optimize this balance, enabling the advancement of scientific discovery even in areas where data is sparse or computational resources are limited.

1.2 Challenges in Scientific Machine Learning

1.2.1 Scenarios in Physics Learning with ML

The landscape of scientific machine learning (SciML) presents a spectrum of scenarios dictated by the availability of data, each necessitating a distinct approach to integrate physics with machine learning. This spectrum can be broadly categorized into three scenarios, illustrating the varying degrees of reliance on physics knowledge and data analysis techniques.

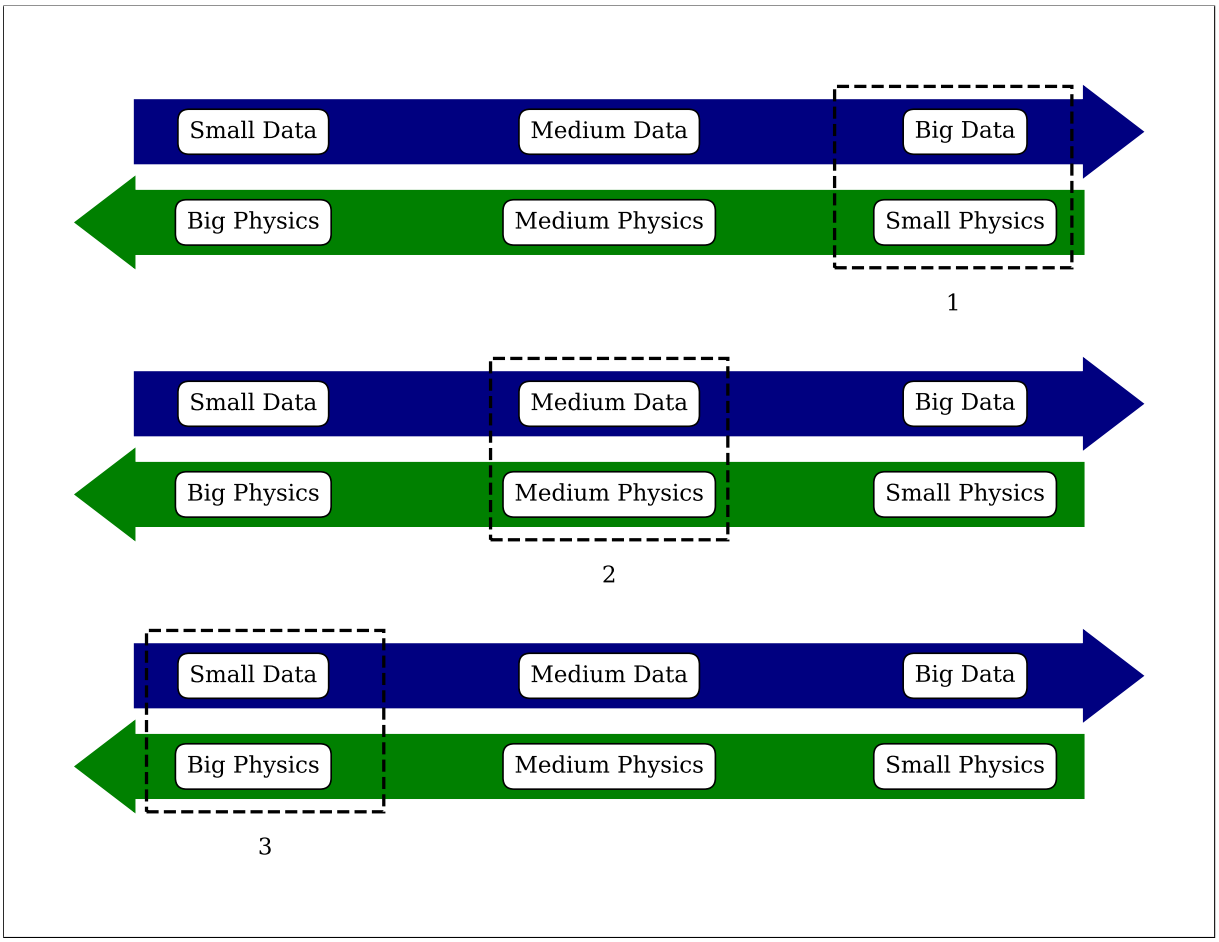

Figure 1-2: The relationship between available data and analytical knowledge on a given problem will determine the most effective way of exploring solutions to it.

Scenario 1: Seas of Data – Minimal Reliance on Physics In the first scenario, researchers find themselves with an abundance of data that covers virtually every conceiv-

able situation relevant to their domain of inquiry. This "seas of data" scenario represents an idealized condition where the sheer volume of data can compensate for gaps in explicit physics understanding. Under these circumstances, conventional big data analysis techniques take precedence, leveraging statistical patterns and correlations within the data to derive insights. The underlying assumption is that the data itself contains enough information to model the phenomena of interest accurately, thereby minimizing the need for injecting explicit physical laws or principles into the learning algorithms.

Scenario 2: Abundant but Incomplete Data – Inductive Biases Based on Physics The second scenario emerges when the available data, while plentiful and informative, falls short of covering the entire spectrum of possible situations. This scenario is characterized by "good and abundant data" that nonetheless leaves uncharted territories within the problem space. Here, the role of physics becomes more pronounced, necessitating the introduction of inductive biases to bridge the gaps. Inductive biases, informed by the underlying physical laws, help in extrapolating beyond the directly observed data, enabling the model to make informed predictions about unobserved scenarios. The integration of these physics-based biases allows for a more nuanced understanding and characterization of the entire space, enhancing the model's generalizability and robustness.

Scenario 3: Sparse Data – Heavy Reliance on Physics The third and most challenging scenario occurs when data is scarce or barely sufficient to cover the domain of interest. This "sparse data" scenario demands a profound understanding of physics to inform the learning process. Researchers must rely heavily on theoretical knowledge and physical principles to guide the design and implementation of their models. In such cases, the model's ability to make accurate predictions hinges on incorporating sophisticated representations of the underlying physics, compensating for the lack of empirical data. This approach often involves leveraging physics-informed neural networks (PINNs) or other methodologies that explicitly encode physical laws into the learning process, enabling the model to extrapolate from minimal data by adhering to known physical behaviors.

These scenarios encapsulate the adaptive nature of SciML, highlighting how the interplay between data availability and physics knowledge shapes the approach to learning and prediction. As we traverse from seas of data to sparse data landscapes, the reliance shifts from purely data-driven methods to increasingly physics-informed strategies, highlighting the versatility and potential of SciML to tackle a broad spectrum of scientific challenges.

1.3 Tools and Techniques in Scientific ML

1.3.1 Overview of Scientific ML Tools

The realm of Scientific Machine Learning (SciML) is characterized by its diverse toolkit, designed to address the wide range of complex challenges of integrating physical laws with machine learning techniques. At its core, SciML is about leveraging the right tools for specific scientific inquiries and, for now, there is no silver bullet in this interdisciplinary field.

Among these tools, Physics-Informed Neural Networks (PINNs) stand out for embedding physical laws into neural network architectures, ensuring predictions are both data-driven and physically plausible. Deep Operator Networks (DeepONets) take a different approach, focusing on learning mappings between function spaces to predict complex physical phenomena accurately. Gaussian Processes (GPs) offer a probabilistic perspective, providing not just predictions but also crucial estimates of uncertainty, which is invaluable in scenarios where data is noisy or sparse.

Moreover, the domain utilizes machine learning models like recurrent neural networks (RNNs) and Long Short-Term Memory (LSTM) networks for capturing temporal dynamics, making them ideal for modeling time-evolving systems such as fluid dynamics. Hybrid models represent a synthesis of traditional numerical simulations and machine learning, combining the interpretability and reliability of physics-based models with the efficiency and adaptability of ML techniques. This blend not only achieves high accuracy but also significantly reduces computational demands.

In summary, SciML's toolkit is vast and varied, offering specialized approaches for different scientific challenges. This variety emphasizes the adaptability of SciML to various

domains, from predicting complex fluid dynamics to uncovering unknown physical laws, showcasing its potential to transform scientific research and discovery.

1.3.2 Physics-Informed Neural Networks (PINNs)

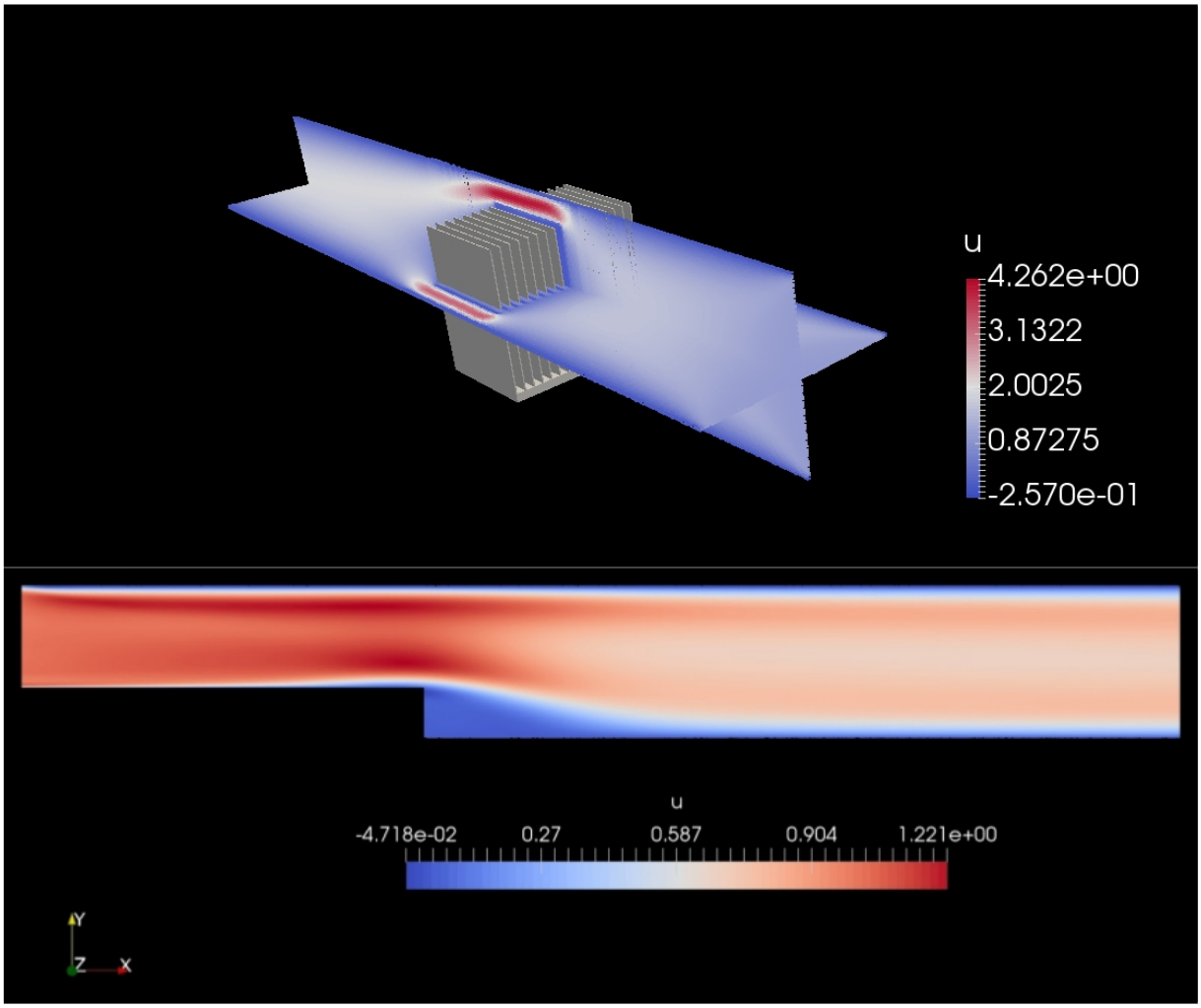

Figure 1-3: Examples of simulations with SimNet. Above, flow over an FPGA heat sink using mass conservation schemes to improve flow field prediction. Below, flow over a step using $k - \omega$ turbulence model.

Physics-Informed Neural Networks (PINNs) (fig. 1-3) along with evolutions such as Variational Physics-Informed Neural Networks (VPINNs) have (fig. 1-4) emerged as powerful frameworks in Scientific Machine Learning (SciML), each embedding physical laws into deep learning models to enhance prediction accuracy and reduce data dependency. While both approaches aim to integrate domain-specific knowledge, they differ signifi-

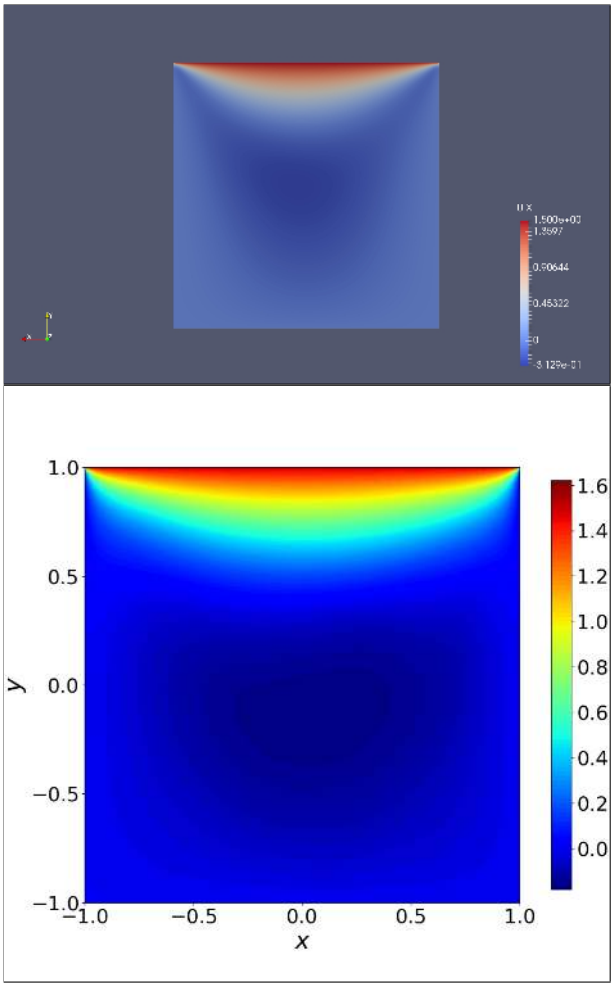

Figure 1-4: Top to Bottom: OpenFoam and hp-VPINNs.

cantly in their methodology and application.

Methodological Differences PINNs incorporate physical laws through differential equations directly into the loss function, which is a blend of data fidelity and physics compliance. The generic loss function for PINNs is given by:

$$\mathcal{L}_{PINN} = \mathcal{L}_{data} + \lambda \mathcal{L}_{physics}, \tag{1.1}$$

where $\mathcal{L}_{data}$ measures prediction errors against observational data, $\mathcal{L}_{physics}$ ensures adherence to physical laws, and λ is a balance parameter.

Conversely, VPINNs adopt a variational approach, minimizing a loss function derived from the variational principle of the governing equations. This results in an integral-based

formulation:

$$\mathcal{L}_{VPINN} = \int_{\Omega} \left(\mathcal{F}(\mathbf{u}, \nabla\mathbf{u}, \ldots)\right)^2 d\Omega, \tag{1.2}$$

where $\mathcal{F}$ denotes the variational formulation, $\mathbf{u}$ represents the solution field, and Ω is the domain of interest.

Choices Between Methods The choice between PINNs and VPINNs hinges on problem specifics, with VPINNs offering enhanced stability and accuracy in scenarios where the variational principle naturally complements the physical problem. These differences highlight the adaptability of SciML tools in addressing diverse scientific challenges.

The delineation between PINNs and VPINNs highlights the evolution of SciML in embedding physical knowledge within neural networks. By selecting the appropriate framework based on problem characteristics, researchers can achieve significant advancements in understanding and solving complex scientific problems.

1.3.3 Learning Functionals and Advanced Techniques

Functionals and operators represent foundational concepts in the realm of scientific machine learning, enabling higher layers of abstraction in the modeling and prediction of complex systems. Functionals, in essence, are mappings from a space of functions to the real numbers, offering a framework for understanding how entire functions can influence outcomes. Operators extend this notion by facilitating transformations between functions, serving as critical tools for describing physical phenomena, such as the evolution of fluid dynamics.

The transition towards learning functionals [54] and operators marks a significant shift in computational modeling, addressing the limitations of classical numerical simulations. Traditional approaches, which often rely on discretization and approximation techniques, can struggle with the high-dimensional and nonlinear nature of many scientific problems. Learning functionals and operators through neural networks, however, provides a pathway to directly approximate these mathematical constructs without the need for explicit discretization, enabling more efficient and accurate predictions of complex systems.

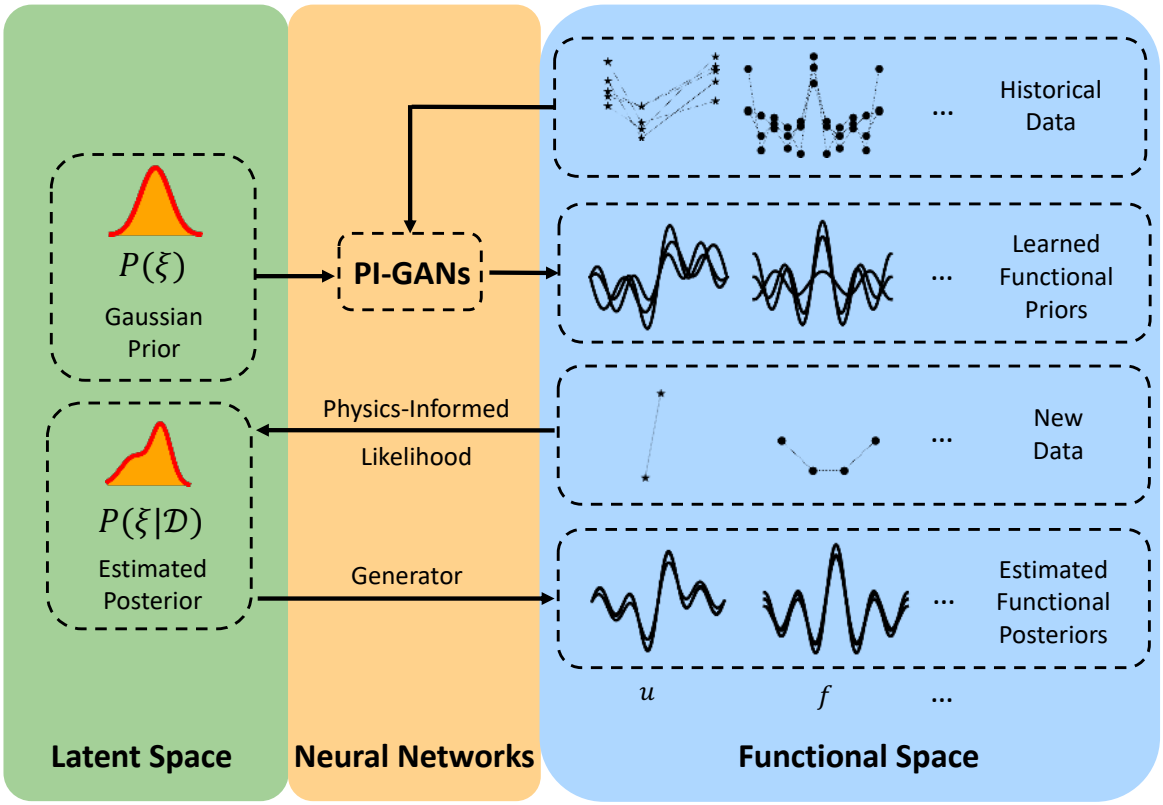

Figure 1-5: Schematic of learning functional priors and posteriors from data and physics. The "PI" part is based on either physics-informed neural networks with automatic differentiation or operator approximation in the form of DeepONet. $P(\mathbf{m}\xi)$ is the prior distribution for input noise $\mathbf{m}\xi$, i.e., $\mathcal{N}(0, \mathbf{m}I)$, $P(\mathbf{m}\xi|\mathcal{D})$ represents the posterior distribution of $\mathbf{m}\xi$, where $\mathcal{D}$ is new data.

Recent advancements in deep learning have ushered in innovative methodologies for learning functionals and operators. Deep Operator Networks (DeepONet), [156] as one example, propose a framework for learning mappings between function spaces, effectively predicting the outcome of complex operators applied to unseen functions. This capability is paramount in scenarios where the underlying physics are known, but analytical solutions are intractable or computationally prohibitive.

Similarly, the concept of functional priors [168] introduces a novel perspective on incorporating domain knowledge into the learning process (fig. 1-6). By embedding physical laws or empirical observations as priors within the neural network architecture, researchers can guide the learning process, ensuring that the models adhere to fundamental principles and improving generalization to unseen data.

The implications of being able to learn functionals and operators extend across numer-

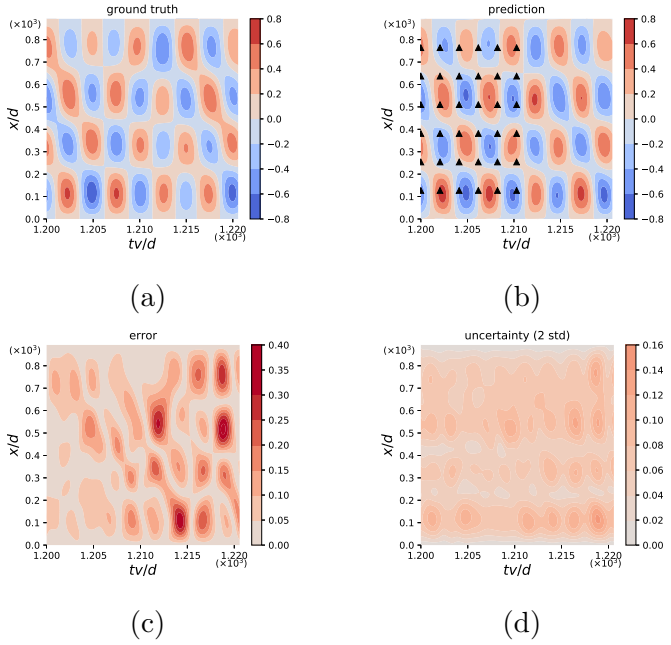

Figure 1-6: Predicted displacements in a window, using the learned functional prior. (a) The ground truth of the dimensionless displacement in a time window. (b-d) The corresponding prediction (mean of posterior), the error of the prediction, and the uncertainty (2 standard deviations of posterior), with 6 sensors.

ous domains of science and engineering. From predicting the behavior of fluid flows under varying conditions to understanding the impact of material properties on structural dynamics, these approaches open new avenues for discovery and innovation. Moreover, they hold the promise of revolutionizing the way we approach simulation and modeling, moving towards a paradigm where data-driven insights and physical understanding coalesce.

1.4 Application to Marine Hydrodynamics and Beyond

1.4.1 Marine Hydrodynamics Challenges

The fusion of Scientific Machine Learning (SciML) with marine hydrodynamics heralds a transformative potential for navigating through the complex, dynamic, and uncertain seas that define marine systems. This endeavor sails through the turbulent flows of high Reynolds numbers, ventures into the unpredictable storms of weather conditions, and confronts the critical mission applications demanding unwavering reliability and sustainability. While the journey is fraught with formidable challenges, it is precisely these challenges that sow the seeds for groundbreaking advancements, potentially redefining

our engagement with the marine environment.

At the forefront of these challenges is the intricate maze of complex fluid dynamics, distinguished by high Reynolds numbers. Traditional computational fluid dynamics (CFD) methods face a Herculean task in capturing the chaotic dance of turbulent flows, often constrained by computational limits and the need for simplification. Yet, SciML emerges as a beacon of hope, offering a route to transcend these barriers by efficiently encapsulating knowledge and leveraging data-driven insights. The potential to harness deep learning for illuminating the nuances of fluid dynamics represents a significant leap towards models that adeptly handle the vast spectrum of marine conditions, enabling real-time decision-making capabilities by anti-amortization of the information they have seen during their training processes.

Navigating the unpredictable seas of marine environments, with their uncertain weather patterns and long-term forces, presents a monumental challenge to modeling and simulation efforts. The sea's capricious nature demands models capable of anticipating and predicting rare but catastrophic events. This challenge opens doors to refine SciML approaches, utilizing models adept at processing sequential data to enhance our understanding and prediction of environmental impacts. A concerted effort in data collection and the adoption of algorithms designed for uncertainty quantification could dramatically improve prediction accuracy, serving as a guiding light through the fog of uncertainty.

The imperative for effective and reliable mission-critical applications and environmental stewardship casts a significant challenge over the advancement of marine systems. The marine industry, critical to global trade and a significant contributor to CO_2 emissions, faces an urgent need for efficiency, reliability, and sustainability. SciML holds the promise of driving innovations that could lead to more sustainable and adaptable marine systems. However, realizing this promise necessitates not only technological advancements in machine learning and computational resources but also a deep integration of domain-specific knowledge into the SciML framework. The vision of hybrid models, blending the precision of physics-based simulations with the adaptability of machine learning, emerges as a solution that aligns accuracy with environmental considerations.

The ultimate goal of integrating SciML in marine hydrodynamics is an advanced level

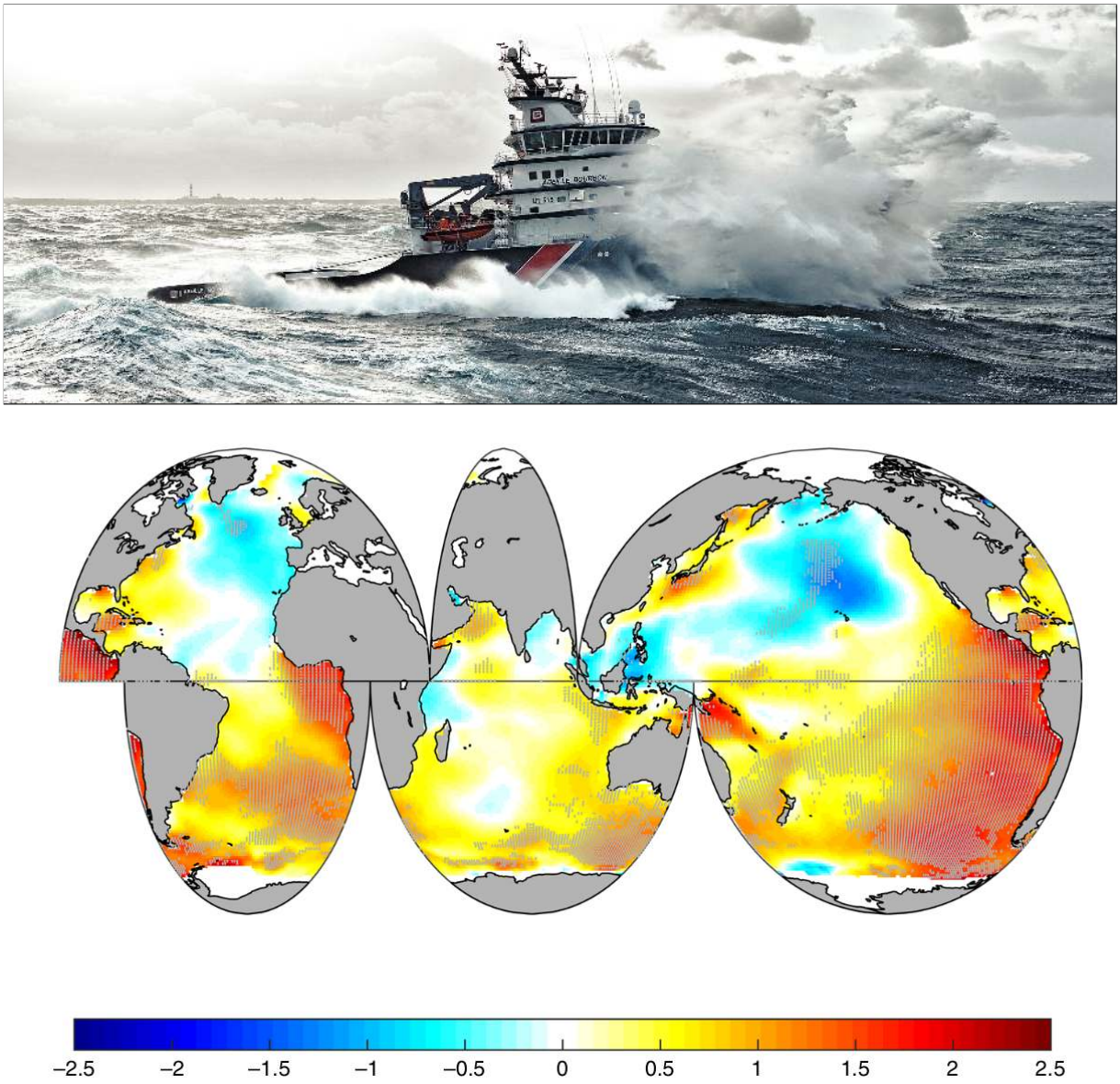

Figure 1-7: Mean Wave Power annual change from 1985 to 2008, [222]. Global wave power has been on the rise since 1948, increasing by as much as 2.5% annually in certain regions, leading to greater uncertainties in ocean operations.

of understanding and predictive capability, facilitating proactive and informed decision-making in complex scenarios. Addressing challenges such as boundary layer control problems through SciML is an example of this goal, highlighting the potential to unlock insights into fluid behaviors far beyond the capabilities of traditional methods. This approach, however, is contingent upon overcoming the integration challenges of seamlessly blending machine learning with existing simulation frameworks, a task both daunting and critical.

In conclusion, the path to integrating SciML into marine hydrodynamics is strewn with

challenges as deep and vast as the oceans themselves. Yet, the promise of deep learning, enhanced data strategies, and the amalgamation of domain expertise illuminates a way forward. This path leads to a new horizon where marine systems are not only more efficient and reliable but also capable of gracefully navigating the uncertain and changing waters of our planet.

1.4.2 Interdisciplinary Relevance of Boundary Layer Control

The interdisciplinary relevance of research into incompressible flows, especially at high Reynolds numbers, serves as a bridge between a long number of scientific fields of study. Prominent amongst these are marine and aerospace engineering. This shared focus not only highlights common challenges and complexities but also points to the universal impact and application of fluid dynamics research. Central to both disciplines is the study of boundary layer control, where techniques and insights from one field can significantly inform and enhance the other.

In aerospace engineering, controlling the boundary layer and using vortex generators are crucial for maintaining aerodynamic wing performance. The main challenge is to prevent loss of lift, which can occur due to flow separation under certain conditions. High Reynolds number flows in aerospace typically reflect the operational environments of aircraft at cruising speeds, where managing the boundary layer is essential for improving lift and, secondly, reducing drag, thereby boosting flight efficiency and safety.

Marine engineering faces a parallel challenge, though with a focus on minimizing pressure drag on hydrodynamic bodies like ship hulls and underwater vehicles. In these applications, even though reducing pressure drag is the goal, frictional forces still make up the largest drag component. This reality highlights the importance of designing vortex generators that introduce minimal parasitic drag to achieve a net reduction in total drag. Effective boundary layer control in marine contexts, therefore, requires a delicate balance, underscoring the need for vortex generators that are efficient yet minimally intrusive.

Although the end goals differ—preventing lift loss in aerodynamics versus minimizing pressure drag in hydrodynamics—the foundational fluid dynamics principles remain consistent across both domains. This cross-disciplinary connection emphasizes the im-

portance of understanding high Reynolds number flows and boundary layer control techniques. Innovations in one field can offer valuable methodologies for the other, encouraging a beneficial exchange of knowledge that advances both areas.

The work presented in this Thesis on boundary layer control has a broader significance that extends beyond linking marine and aerospace engineering; it enhances our overall understanding of fluid behaviors across various applications. By exploring boundary layer control's impact on different engineering challenges, the research sheds light on fluid dynamics' fundamental role in designing more efficient and effective systems. It showcases how targeted knowledge in one specialty area can lead to significant advancements across multiple fields, driven by the shared principles of fluid dynamics.

Chapter 2

Inferring Functionals in Vessel Dynamics in Extreme Sea States With Machine Learning

Dynamical systems play a crucial role in fields like engineering and physics. Their theoretical and computational characterization is often a complex task. This chapter focuses on inferring functionals that characterize the dynamics of vessels in response to their interaction with the marine environment, notably stochastic marine waves (see fig. 2-17).

The last few years have seen increased research into the efficient combination of machine learning techniques to unravel complex physics. Notable among such techniques are Gaussian Processes, which efficiently handle multiple information streams to create surrogate models of parametric systems interacting with complex physics. Their combination with neural networks, however, has been successful only recently, as seen in [167].

A rise in the application of deep learning techniques in fluid dynamics has been evident recently, with [149] standing as a notable example. However, the method introduced here is unique in its use of deterministic system characterization and stochastic forcing terms introduced by marine waves. Essentially, the approach presented learns a non-linear mapping to reconstruct dynamics from stochastic marine wave realizations in a data-driven manner.

Other research attempts at data-driven reconstruction of dynamical systems exist.

For example, [295] and [213] deal with noisy dynamical systems and aircraft dynamics identification, respectively. These systems are arguably simpler as they don't require complex spatial discretization.

One significant question not addressed in this chapter is the system's stability over the entire state space. Knowing this could enhance the learning of dynamical systems, as shown in [127]. This chapter does not venture into that territory, due to the computational burden of the process. The current research partially addresses this issue by studying the statistics of linear potential models, which do not consider non-linear phenomena, which we resolve here.

2.1 Navigation and its Centric Role in the Development of Human Society

Initially, navigation was predominantly coastal, with vessels covering short distances, either by rowing or using sails, limited to periods when sea conditions were anticipated to be good. However, unforeseen storms would sometimes surprise these mariners, resulting in a significant number of references to both actual and fictional shipwrecks caused by severe weather in historical records [33].

Navigation has been a critical element in human history, facilitating exploration, trade, cultural exchange, and conquest. For instance, the tales of Ulysses (Odysseus) in Homer's epic, The Odyssey, highlight the significance of navigation in the ancient world [179]. Ulysses' complex journey back to Ithaca after the Trojan War not only serve as an example of the perilous nature of seafaring but also underlines the vital role of navigation in connecting distant lands and civilizations.

In subsequent history, the epoch-making voyage of Ferdinand Magellan stands as a testament to the evolving sophistication and importance of navigation [265]. Magellan's expedition in the 16th century marked the first circumnavigation of the earth, demonstrating the extent to which improved navigational techniques and understanding could expand horizons and reshape our perception of the world [205]. Despite the perils and challenges, the success of this voyage ushered in an era of global exploration and connec-

tivity, largely driven by advances in navigation.

In essence, the history of navigation is not merely a tale of developing technology or increasing knowledge of the world's waterways. It is an integral part of our shared human story, intertwining with our deepest desires for exploration, understanding, and connection [227].

The significance of navigation continues to be paramount in our current age, just as it was during the times of Ulysses and Magellan. While the means and methods have evolved due to technological advancements, navigation remains at the core of many sectors, primarily maritime trade, national defense, and scientific research [27].

Global commerce is heavily reliant on maritime trade, where sophisticated navigation ensures the efficient and safe transport of goods across the world's oceans [262, 95]. Accurate and reliable navigation is also of utmost importance in the realm of national defense [270]. Naval operations, whether for patrolling, humanitarian assistance, or conflict situations, require precision in navigation to guarantee effectiveness and safety.

Meanwhile, scientific research, especially in areas such as climate studies, marine biology, and oceanography, depends on precise navigation to reach remote and often unexplored regions of our oceans [206]. Exploratory missions, data collection expeditions, and environmental monitoring activities all hinge on the ability to accurately navigate the vast and often challenging marine environments.

Seakeeping techniques are crucial in the design of vessels intended for challenging navigations, significantly contributing to their safety, efficiency, and overall performance [66, 160]. A ship's seakeeping abilities determine how well it can withstand and perform in adverse sea conditions. For instance, the design must consider factors such as ship stability, resistance to capsizing, wave resistance, and the vessel's overall structural integrity [15].

A vessel that has been meticulously designed with seakeeping in mind can effectively counteract the harsh conditions often encountered in open seas, such as high waves, strong winds, and powerful currents. These considerations are essential not only for ambitious navigations like polar expeditions or deep-sea research but also in offshore operations such as the construction and maintenance of offshore wind farms [97].

In these offshore endeavors, assessing operability windows, which are periods when sea conditions are suitable for operations, is a critical aspect that heavily relies on seakeeping principles[51]. Ships equipped with advanced seakeeping features can safely operate within a broader range of conditions, thus increasing the potential operability windows.

Furthermore, seakeeping also has a direct impact on the comfort and wellbeing of the crew and passengers. Good seakeeping design minimizes the impact of motion sickness and fatigue, thereby ensuring safety and boosting crew performance.

2.2 Motion Prediction of Vessels at Sea and Their Role in Assessing Operability Windows

Seakeeping is the study of a vessel's behavior in marine environments1. It is a methodology that focuses on examining the movements and the stresses experienced by marine systems [66].

Waves cause movements and oscillations to ships according to its six degrees of freedom [160]. These movements lead to accelerations that induce discomfort to the people on board and dynamic loads on the ship's structure as well as other elements such as sensors, equipment, cargo and masts, among many other elements [221].

2.2.1 Influence of Motions in the Operability of Vessels at Sea

It's undeniable that marine vessels systems frequently operate in environments that are as challenging as they are formidable [61]. Given the continuous, immense power of the sea, it becomes vital for ships to be designed and built with the goal of maintaining functionality, ensuring habitability, and minimizing potential damage, particularly in the face of severe storms. The relentless action of waves can induce significant motions in a ship, which in turn can affect its operability and the comfort and safety of those on board. Therefore, a ship's design must take into consideration these wave-induced motions to ensure it can operate effectively and remain habitable, even in adverse conditions, thereby ensuring its ability to weather storms with minimal damage.

WAVE	ORIGIN	MECHANISM	PERIOD	VELOCITY
Planetary	Earth's Rotation	Gravity	∼100 days	1-100 km/h
Tides	Atr. Moon Sun	Gravity	12-24 horas	1700 km/h
Tsunami	Earthquakes	Gravity	10 min-2 horas	¡800 km/h
Wind Waves	Wind	Gravity	1-25 s	2-40 m/s
Capilar	Wind	Surf. Tension	$< 10^{-1}$ s	25-50 m/s

Table 2.1: Types of ocean waves, their origins, and their main characteristics.

2.2.2 Classical Wave Theory, an Overview

The main meteorological and oceanographic effects considered for assessing a ships operability and seakeeping properties are in order of importance:

1. Wind-generated waves (wind sea) [145, 170].

2. Waves generated by distant storms, swell.

3. Local surface wind.

4. Surface currents due to local storms.

5. Deep currents.

6. Ocean currents (e.g., the Gulf of Mexico current).

The first phenomenon mentioned in the previous list, ocean waves, is a physical phenomenon whose restoring mechanism is gravity.

The waves that are most influential in the design of ocean going vessels are the waves originating from the wind, as they have characteristic periods closer to the natural periods of the Ship. The simplest theory that can be used to describe ocean waves is the *Linear Wave Theory*. This theory, along with non-linear theories, depends on a series of parameters:

1. *Period (T)*: defined as the time that elapses between two successive crests traveling through the same stationary point.

2. *Wave height (H)*: defined as the vertical distance between consecutive crest and trough. It is important to note that in linear theories, the amplitude between crests will be the same as between troughs, unlike higher-order Stokes waves, for example.

3. *Depth (d)*: defined as the vertical distance between the seafloor and the mean water level.

4. *Wave length (λ)*: represents the distance between two consecutive wave crests.

5. *Frequency (f)*: mathematically defined as the inverse of the period.

6. *Wave elevation (η)*: the elevation at a given moment at a point above or below the mean water level.

7. *Horizontal velocity of water particle (u)*: the change over time in the horizontal position of a fluid particle.

8. *Vertical velocity of water particle (v)*: the change over time in the vertical position of a fluid particle.

9. *Horizontal acceleration of water particle ($\dot{u}$)*: the change over time in the horizontal velocity of a fluid particle.

10. *Vertical acceleration of water particle ($\dot{v}$)*: the change over time in the vertical velocity of a fluid particle.

In the *Linear Wave Theory*, the problem is reduced, through simplifications not discussed here, to solving the Laplace's equation (2.1):

$$\nabla^2 \phi = 0 \tag{2.1}$$

Under the boundary conditions on the free surface:

$$g\eta + \frac{\partial \phi}{\partial t} = 0 \quad \text{at} \quad z = 0 \tag{2.2}$$

$$\frac{\partial \eta}{\partial t} - \frac{\partial \phi}{\partial z} = 0 \quad \text{at} \quad z = 0 \tag{2.3}$$

which are reduced to:

$$\frac{\partial^2 \phi}{\partial t^2} + g\frac{\partial \phi}{\partial z} = 0 \quad \text{at} \quad z = 0 \tag{2.4}$$

and the bottom condition:

$$\frac{\partial \phi}{\partial z} = 0 \quad \text{at} \quad z = 0 \tag{2.5}$$

resulting in the final velocity potential:

$$\phi = \frac{Hg}{2\omega}\frac{\cosh(k(h+z))}{\cosh(kh)}\sin(kx - \omega t) \tag{2.6}$$

To the parameters mentioned above, the following should be added:

1. *Oscillation frequency (ω)*: $\omega = \frac{2\pi}{T}$.
2. *Wave number (k)*: $k = \frac{2\pi}{\lambda}$.
3. *Wave propagation velocity (c)*: $c = \frac{\lambda}{T}$.

In the *Linear Theory*, depending on the depth, simplifications can be made in the theory. The limits of these simplifications are determined by the relationships between depth (h) and wavelength (λ).

The made simplification allows for the calculation of forces on ocean-going vessels in irregular seas. This is possible thanks to the principle of superposition, which only applies to linear waves [135, 52].

If the Linear Wave Theory is not sufficient, the next step is to use second-order Stokes waves. The steps to obtain the wave formulation are the same for all higher-order methods. The solution can be obtained using the Stokes perturbation method [52, 261]. In this method, the velocity potential and the free surface elevation are expanded in power series with respect to the small parameter $\varepsilon = ka$ [261].

$$\phi = \sum_{i=1}^{n} \varepsilon^i \phi_i \qquad \eta = \sum_{i=1}^{n} \varepsilon^i \eta_i \tag{2.7}$$

Since the ∇^2 operator is linear, all the functions ϕ^i satisfy the Laplace's equation:

Variable	Finite Depth	Infinite Depth
Velocity Potential	$\phi = \frac{Hg}{2\omega} \frac{\cosh(k(h+z))}{\cosh(kh)} \sin(kx - \omega t)$	$\phi = \frac{Hg}{2\omega} e^{kz} \sin(kx - \omega t)$
Free Surface Elevation	$\eta = \frac{H}{2} \cos(kx - \omega t)$	$\eta = \frac{H}{2} \cos(kx - \omega t)$
Dispersion Relation	$\omega^2 = gk \cdot \tanh(kh)$	$\omega^2 = gk$
Horizontal Particle Velocity	$u = \frac{H\omega}{2} \frac{\cosh(k(z+h))}{\sinh(kh)} \cos(kx - \omega t)$	$u = \frac{H\omega}{2} e^{kz} \cos(kx - \omega t)$
Horizontal Particle Acceleration	$a_x = \omega^2 \frac{H}{2} \frac{\cosh(k(z+h))}{\sinh(kh)} \sin(kx - \omega t)$	$a_z = \omega^2 \frac{H}{2} e^{kz} \sin(kx - \omega t)$
Vertical Particle Velocity	$w = \frac{H\omega}{2} \frac{\sinh(k(z+h))}{\sinh(kh)} \sin(kx - \omega t)$	$w = \frac{H\omega}{2} e^{kz} \sin(kx - \omega t)$
Vertical Particle Acceleration	$a_z = -\omega^2 \frac{H}{2} \frac{\sinh(k(z+h))}{\sinh(kh)} \cos(kx - \omega t)$	$a_z = \omega^2 \frac{H}{2} e^{kz} \cos(kx - \omega t)$
Dynamic Pressure	$p_{dyn} = \rho g \frac{H}{2} \frac{\cosh(k(z+h))}{\cosh(kh)} \cos(kx - \omega t)$	$p_{dyn} = \rho g \frac{H}{2} e^{kz} \cos(kx - \omega t)$

Table 2.2: Formulation of the Airy Wave Theory.

Classification	Criterion	Approximation of $tanh(kh)$	λ
Deep Water	$h/\lambda \geq 0.5$	1	$\lambda = \frac{gT^2}{2\pi}$
Shallow Water	$h/\lambda \leq 0.05$	kh	$\lambda = T\sqrt{gh}$
Intermediate Water	$0.05 < h/\lambda < 0.5$		$\lambda = \frac{gT^2}{2\pi} tanh(kh)$

Table 2.3: Simplifications of the *Linear Theory* based on the depth.

$$\nabla^2(\phi) = \varepsilon\nabla^2(\phi_1) + \varepsilon^2\nabla^2(\phi_2) + ... + \varepsilon^i\nabla^2(\phi_i) + ... + \varepsilon^n\nabla^2(\phi_n) = 0 \tag{2.8}$$

This condition must hold for any value of ε, so $\nabla^2(\phi_i) = 0$ for all i. To satisfy the kinematic and dynamic boundary conditions at the free surface, Taylor expansions of these conditions around $z = 0$ are performed. Thus, the kinematic condition can be expressed as:

$$\left[\frac{\partial\phi}{\partial z} - \frac{\partial\eta}{\partial t} - \frac{\partial\phi}{\partial x}\frac{\partial\eta}{\partial x}\right]_{z=\eta} = \left[\frac{\partial\phi}{\partial z} - \frac{\partial\eta}{\partial t} - \frac{\partial\phi}{\partial x}\frac{\partial\eta}{\partial x}\right]_{z=0} + \eta\frac{\partial}{\partial z}\left[\frac{\partial\phi}{\partial z} - \frac{\partial\eta}{\partial t} - \frac{\partial\phi}{\partial x}\frac{\partial\eta}{\partial x}\right]_{z=0} +$$

$$+ \frac{\eta^2}{2}\frac{\partial^2}{\partial z^2}\left[\frac{\partial\phi}{\partial z} - \frac{\partial\eta}{\partial t} - \frac{\partial\phi}{\partial x}\frac{\partial\eta}{\partial x}\right]_{z=0} + ... + \frac{\eta^n}{n!}\frac{\partial^n}{\partial z^n}\left[\frac{\partial\phi}{\partial z} - \frac{\partial\eta}{\partial t} - \frac{\partial\phi}{\partial x}\frac{\partial\eta}{\partial x}\right]_{z=0} \tag{2.9}$$

To solve these equations, the perturbation series expansions of η and ϕ need to be substituted, truncating the terms of order higher than i, the order being solved for. The results obtained, taken from reference [226], for the second-order theory are as follows:

The perturbation series to solve for the velocity potential is:

$$\phi = \varepsilon^1\phi_1 + \varepsilon^2\phi_2 \tag{2.10}$$

And the resulting potential, applying the boundary conditions, is:

$$\phi = \frac{\omega}{k^2}\left[(ka)\frac{cosh(k(h+z))}{sinh(kh)}\sin(kx-\omega t) + \frac{3}{8}(ka)^2\frac{cosh(2k(h+z))}{sinh^4(kh)}\sin(2(kx-\omega t))\right] \tag{2.11}$$

The perturbation series to solve for the free surface elevation is:

$$\eta = \varepsilon^1\eta_1 + \varepsilon^2\eta_2 \tag{2.12}$$

And the resulting expression, applying the boundary conditions, is:

$$\eta = \frac{1}{k}\left[(ka)\cos(kx-\omega t) + \frac{1}{4}(ka)^2\frac{cosh(kh)}{sinh^3(kh)}(2+cosh(2kh))\cos(2(kx-\omega t))\right] \tag{2.13}$$

From the velocity potential, the particle velocities and accelerations can be obtained, resulting in the following expressions:

$$\begin{aligned} u = \frac{\partial\phi}{\partial x} = c\Big[&(ka)\tfrac{cosh(k(h+z))}{sinh(kh)}\cos(kx-\omega t) + \\ &+\tfrac{3}{4}(ka)^2\tfrac{cosh(2k(h+z))}{sinh^4(kh)}\cos(2(kx-\omega t))\Big] \end{aligned} \tag{2.14}$$

$$\begin{aligned} w = \frac{\partial\phi}{\partial z} = c\Big[&(ka)\tfrac{cosh(k(h+z))}{sinh(kh)}\sin(kx-\omega t) + \\ &+\tfrac{3}{4}(ka)^2\tfrac{cosh(2k(h+z))}{sinh^4(kh)}\sin(2(kx-\omega t))\Big] \end{aligned} \tag{2.15}$$

The accelerations, neglecting convective terms, are:

$$\begin{aligned} \dot{u} \cong \frac{\partial u}{\partial t} = c\omega\Big[&(ka)\tfrac{cosh(k(h+z))}{sinh(kh)}\sin(kx-\omega t) + \\ &+\tfrac{3}{2}(ka)^2\tfrac{cosh(2k(h+z))}{sinh^4(kh)}\sin(2(kx-\omega t))\Big] \end{aligned} \tag{2.16}$$

$$\dot{w} \cong \frac{\partial \phi}{\partial t} = -c\omega\Big[(ka)\frac{sinh(k(h+z))}{sinh(kh)}\cos(kx-\omega t)+ \\ +\frac{3}{2}(ka)^2\frac{sinh(2k(h+z))}{sinh^4(kh)}\cos(2(kx-\omega t))\Big] \tag{2.17}$$

In these equations, c is given by the dispersion equation, which is the same as in the first-order theory:

$$c^2 = \frac{g}{k}tanh(kh) \tag{2.18}$$

Finally, the expression for the pressure is:

$$p = \frac{\rho g}{k}\Big[-kz + (ka)\frac{cosh(k(h+z))}{cosh(kh)}\cos(kx-\omega t)+ \\ +\frac{(ka)^2}{2sinh(2kh)}\Big(\frac{3cosh(2k(h+z))}{sinh^2(kh)}-1\Big)\cos(2(kx-\omega t))+ \\ (ka)^2\frac{1-cosh(2k(h+z))}{2sinh(2kh)}\Big] \tag{2.19}$$

Derived from:

$$p = -\rho g z - \rho\frac{\partial \phi}{\partial t} \tag{2.20}$$

The difference in shape between the second-order Stokes wave and the Airy wave is found in the crests and troughs of the wave. The crests are more pronounced, and the troughs are less pronounced, as can be seen in the lower figure:

Regarding the *Fifth-Order Stokes Theory*, it is not extensively developed in this chapter due to the required length. This type of theory is usually applied to waves in deep water with a steep slope [261, 70]. The expressions have a similar form to the second-order Stokes waves, but now they consist of five elements that are ordered in series [52].

2.2.3 Dynamic Fetch and Other Non-linear Wave Phenomena

Dynamic fetch occurs when wind blows over a moving storm system, allowing waves to grow larger and travel farther than they would under a stationary wind field. Multiple weather systems can generate different sets of waves: local storms create short, frequent

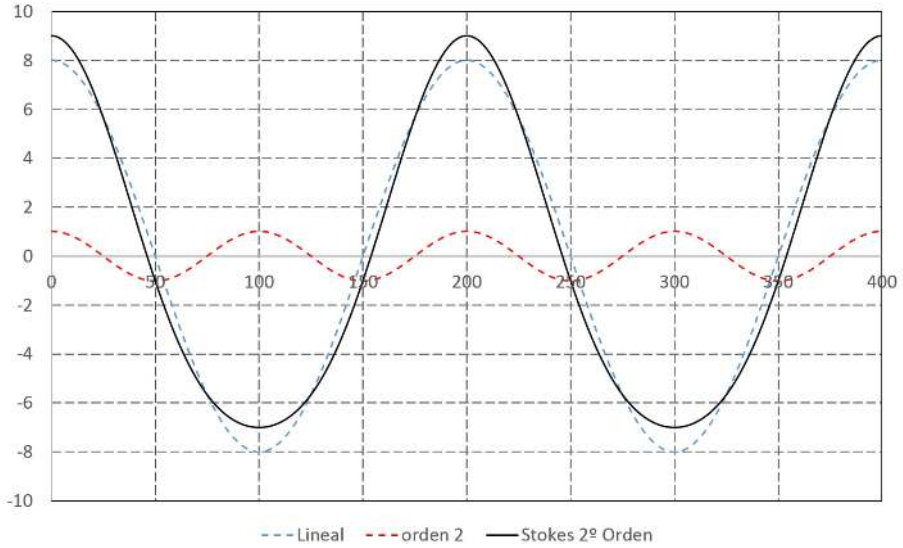

Figure 2-1: Comparison of the Airy wave and second-order Stokes wave [226].

waves, while distant storms produce long-period swells. When these wave trains interact, they can either amplify or diminish each other. Constructive interference happens when wave crests align, forming larger waves and potentially leading to rogue waves. Conversely, destructive interference occurs when a wave crest meets a trough, canceling each other out and resulting in smaller waves. Several factors influence where these wave trains combine and amplify. Ocean currents can bend wave paths, causing them to converge, while underwater topography (bathymetry) can focus wave energy, increasing wave height in certain areas. Changing wind directions and intensities also affect wave direction and energy.

Traditional linear wave theory, which assumes small amplitude waves and linear superposition, often fails to adequately analyze these complex scenarios. This theory does not account for the nonlinear interactions between wave trains or the energy transfer in dynamic fetch conditions. Nonlinear effects, such as wave-wave interactions and energy focusing, play a crucial role in wave amplification and the formation of extreme waves [121, 191]. Research has shown that the linear approach is insufficient for understanding and predicting rogue waves, which are better described by models incorporating nonlinear Schrödinger equations and modulation instability [192].

Real-world examples include the North Atlantic, where swells from distant storms and local winds combine to create significant wave heights [128], and the Southern Ocean,

where continuous strong winds generate multiple overlapping wave systems, leading to very high seas [298]. Understanding these interactions is crucial for maritime safety and navigation, as it helps predict areas where wave amplification might occur. Advanced models that incorporate nonlinear dynamics and real-time data are essential for accurately predicting wave behavior in these complex environments. For instance, the use of spectral wave models, which include the effects of wave-wave interactions, has significantly improved wave forecasting accuracy [272].

2.2.4 Traditional Experimental Methods for Motion Prediction of Vessels at Sea

Traditionally, the problem of understanding the motions of a vessel, when sailing at a constant speed and heading, can be simplified to obtaining the response of that vessel when, at that speed, it is excited by a train of regular waves of a specific frequency that encounter the vessel with a given relative heading [183, 1]. This simplification is only possible assuming linearity in the vessel's response. Under this assumption, when considering individual frequencies, it is possible to analyze each of the components separately because the total response is simply the sum of the response to each individual frequency [66].

If one wishes to calculate the behavior of the vessel in an irregular sea with short crests, it is necessary to determine the responses by considering an adequate number of relative headings between the vessel and the sea. This is essential to accurately capture the directional characteristics of the specific sea conditions. Consequently, the number of test runs or simulations would significantly increase, as it would be required to test for various relative headings for each case. For a given speed and all frequencies of interest, it is essential to test for all relevant relative headings with respect to the waves.

In other words, each test with a regular wave of a specific frequency provides a value of $H(\omega)$, which represents an ordinate of the transfer function and, consequently, the Response Amplitude Operator (RAO) ($H(w)^2$) for the tested speed and heading conditions. This means that for each navigation condition, it will be necessary to test with as many regular waves as the desired number of RAO ordinates.

Clearly, each of these tests also provides the phase difference between the measured response and the excitation, which is of utmost importance [190]. Accurately quantifying the phase is crucial for various systems that rely on precise timing and synchronization. For example, actioning systems like cranes and applying systems like balance tanks heavily depend on knowing the phase with respect to the exciting wave. The phase information enables precise coordination and control, ensuring optimal performance and safety in these systems. Therefore, accurately determining the phase is essential for their effective operation in dynamic marine environments.

Using complex a complex representation [166] in the problem above, one can fully capture all variables in one single expression. Under linear conditions, tank waves can be simply represented as $\zeta = \zeta_0 \cdot \cos(\omega \cdot t)$ and the response of the ship to the wave excitation will also be a sinusoidal function with different amplitude and phase $\mathrm{R} = \mathrm{R}_0 \cdot \cos(\omega \cdot \mathrm{t} + \delta)$. The transfer function for this specific frequency would then be:

$$H(\omega) = \frac{\mathrm{R}_0 \cdot \cos(\omega \cdot \mathrm{t} + \delta)}{\zeta_0 \cdot \cos(\omega \cdot \mathrm{t})} = \frac{\mathrm{Re}\left\{\mathrm{R}_0 \cdot \exp[\mathrm{i} \cdot (\omega \cdot \mathrm{t} + \delta)]\right\}}{\mathrm{Re}\left\{\zeta_0 \cdot \exp[\mathrm{i} \cdot \omega \cdot \mathrm{t}]\right\}} = \frac{\mathrm{R}_0}{\zeta_0} \cdot \exp[\mathrm{i} \cdot \delta] \tag{2.21}$$

The RAO is then given by:

$$\mathrm{RAO} \equiv |\mathrm{H}(\omega)|^2 = \left(\frac{\mathrm{R}_0}{\zeta_0}\right)^2 \tag{2.22}$$

Following the principle of superposition, an irregular sea can be described by a spectrum of elevations $\phi_{\zeta\zeta}(\omega)$ or a spectrum of wave slopes $\phi_{\zeta'\zeta'}(\omega)$. With this information, with linear theory, it is very simple to calculate the amplitude spectrum of a ship in its six degrees of freedom as:

$$\begin{aligned} \phi_{\mathrm{ttj}}(\omega) &= \phi_{\zeta\zeta}(\omega) \cdot \left[\mathrm{H}_{\mathrm{ttj}}(\omega)\right]^2 = \phi_{\zeta\zeta}(\omega) \cdot \mathrm{RAO}_{\mathrm{ttj}}(\omega) \quad \mathrm{j} = 1, 2, 3 \\ \phi_{\mathrm{rrj}}(\omega) &= \phi_{\zeta'\zeta'}(\omega) \cdot \left[\mathrm{H}_{\mathrm{rrj}}(\omega)\right]^2 = \phi_{\zeta'\zeta'}(\omega) \cdot \mathrm{RAO}_{\mathrm{rrj}}(\omega) \quad \mathrm{j} = 4, 5, 6 \end{aligned} \tag{2.23}$$

It is crucial to emphasize that the transfer function encompasses more than just response amplitudes [142]. It is equally essential to accurately determine the phase difference between each motion of the vessel with respect to a reference position of the exciting wave

[65]. This phase information is vital for reconstructing the precise absolute motion of any point on the rigid vessel. By considering both translations of the vessel's center of gravity and rotations around that center, the complete picture of the vessel's motion can be effectively captured [75]. Hence, a comprehensive understanding of both the amplitude and phase is indispensable for accurately characterizing the absolute motion of any point on the vessel.

With this information at hand, linear theory can approximate the movement of any point of the vessel as:

$$\overline{\mathrm{D}} = \bar{\eta} + \bar{\xi} \wedge \overline{\mathrm{P}} \tag{2.24}$$

Where:

$$\overline{\mathrm{D}} = \eta_{1\mathrm{p}}\bar{\mathrm{i}} + \eta_{2\mathrm{p}}\bar{\mathrm{j}} + \eta_{3\mathrm{p}}\overline{\mathrm{k}} \tag{2.25}$$

$$\bar{\eta} = \eta_1\bar{\mathrm{i}} + \eta_2\bar{\mathrm{j}} + \eta_3\overline{\mathrm{k}} \tag{2.26}$$

$$\bar{\xi} = \eta_4\bar{\mathrm{i}} + \eta_5\bar{\mathrm{j}} + \eta_6\overline{\mathrm{k}} \tag{2.27}$$

$$\overline{\mathrm{P}} = \mathrm{x}\bar{\mathrm{i}} + \mathrm{y}\bar{\mathrm{j}} + \mathrm{z}\overline{\mathrm{k}} \tag{2.28}$$

In the above expressions $\overline{\mathrm{D}}$ is the vector that describes displacement of a point on the ship, $\bar{\eta}$ is the translation vector of the center of gravity of the ship, $\bar{\xi}$ is the vector of rotation of around the center of gravity of the ship and $\overline{\mathrm{P}}$ is the position vector of a point on the ship. With this information at hand the displacement coordinates can be obtained as:

$$\begin{aligned} \eta_{1p} &= \eta_1 + \eta_5 \cdot z - \eta_6 \cdot y \\ \eta_{2p} &= \eta_2 + \eta_6 \cdot x - \eta_4 \cdot z \\ \eta_{3\mathrm{p}} &= \eta_3 + \eta_4 \cdot y - \eta_5 \cdot x \end{aligned} \tag{2.29}$$

Which can be differentiated numerically in a straight forward way to obtain velocities

and accelerations on any point of the ship, if needed.

It is essential to recognize that recent developments in numerical simulations have paved the way for higher fidelity predictions [72, 99]. Advanced computational fluid dynamics (CFD) models, for instance, can now capture intricate flow patterns and accurately simulate the behavior of vessels in adverse sea conditions. These techniques have the potential to provide valuable information on phenomena like vessel motions, slamming, and water on deck, which were previously challenging to consider in traditional methods.

However, it is important to acknowledge that even advanced numerical methods also have their limitations. Assumptions and simplifications made in the models can affect the accuracy of predictions, especially when dealing with complex fluid-structure interactions or highly nonlinear behaviors. Validation and calibration against experimental data remain crucial to ensure the reliability of numerical simulations.

To achieve the most robust and comprehensive understanding, a synergistic approach is recommended. Integrating state-of-the-art numerical simulations with well-designed towing tank experiments can offer the best of both worlds. By leveraging the strengths of each method, designers and engineers can gain valuable insights into vessel behavior and validate numerical predictions with real-world data.

Therefore, when considering the use of towing tank experiments or novel numerical techniques [258], a thorough assessment of the specific project requirements, technical risks, available resources, and time constraints is crucial. While experiments still play a vital role [20], the adoption of novel numerical techniques should be considered as a complementary tool to enhance the understanding of complex phenomena and guide the design process.

2.2.4.1 Similarity Laws in Towing Tank Testing

To emphasize the fact that there is no one analysis method that is able to solve the seakeeping problem, it is necessary to perform dimensional analysis [31] on the quantities of interest that define the seakeeping problem. The oscillations of a ship that sails at constant velocity and bearing over regular waves is defined by:

$$z_0 = f_1 \left[\{U\}; \{\zeta_0, \omega_0, \alpha\}; \{\mu, g, \rho\}; \{L, (X_i), (I_i)\} \right] \tag{2.30}$$

Where:

1. U: Ship velocity.
2. ζ_0: Amplitude of the incident wave.
3. ω_0: Absolute frequency of the incident wave.
4. α: Relative heading between the ship and the waves.
5. μ: Dynamic viscosity of the water in which the ship is sailing.
6. g: Acceleration due to gravity.
7. ρ: Density of the water in which the ship is sailing.
8. L: Characteristic linear dimension of the ship, typically its length at the waterline.
9. (X_i): Exterior geometry of the ship, i.e., its hull form.
10. (I_i): Mass and inertia distribution of the ship in the desired loading condition.

Each term in eq. (2.30) groups parameters of different nature. The first group includes only the ship velocity, the second describes the incident wave, the third represents the characteristics of the fluid in which the ship is sailing, and the fourth encompasses the geometric and mass properties of the ship. If eq. (2.30) is adimensionalized we obtain:

$$\frac{z_0}{\varsigma_0} = f_2 \left[\left\{ \frac{U}{\sqrt{g \cdot L}}; \frac{U \cdot L}{\mu/\rho} \right\}; \left\{ \frac{\varsigma_0}{L}; \omega_0 \cdot \sqrt{\frac{L}{g}}; \alpha \right\}; \left\{ \frac{(X_i)}{L}; \frac{I_i}{\rho \cdot L^5} \right\} \right] \tag{2.31}$$

Obtaining the well know Reynolds [223] and Froude [79] numbers in the first bracket. In experimental testing it is desirable to have similarity between the model and the full sized ship. This implies that three types of forces have to remain proportional. These forces can qualitatively be expressed as:

1. Gravity Forces:

$$\mathrm{GF} = \mathrm{m} \cdot \mathrm{g} \propto \rho \cdot \mathrm{L}^3 \cdot \mathrm{g} \tag{2.32}$$

2. Inertial Forces:

$$\mathrm{IF} = \mathrm{m} \cdot \frac{\mathrm{dU}}{\mathrm{dt}} = \mathrm{m} \cdot \frac{\mathrm{dU}}{\mathrm{dx}} \cdot \frac{\mathrm{dx}}{\mathrm{dt}} \propto \cdot \rho \cdot \mathrm{L}^3 \cdot \frac{\mathrm{U}}{\mathrm{L}} \cdot \mathrm{U} \tag{2.33}$$

3. Viscous forces, which depend on the wetted area, dynamic viscosity and the boundary layer properties close the ship hull:

$$\mathrm{VF} \propto \cdot \mathrm{L}^2 \cdot \mu \cdot \frac{U}{\mathrm{L}} = \mathrm{L} \cdot \mu \cdot \mathrm{U} \tag{2.34}$$

From the above analysis the relationship between the different forces follow:

$$\begin{aligned} \tfrac{\mathrm{FI}}{\mathrm{FG}} &\propto \mathrm{Fn}^2 \\ \tfrac{\mathrm{FI}}{\mathrm{FV}} &\propto \mathrm{Rn} \end{aligned} \tag{2.35}$$

Implying that, to obtain total similarity between model scale and full scale, Froude and Reynolds numbers must be equal in both scales [80]. Considering the scale factor $R = L/L'$, where (') denotes a magnitude associated with the model scale, equal Froude numbers lead to $U' = U/\sqrt{R}$ and equal Reynolds numbers to $U' = U \cdot R$ [108]. The above assumes that water properties don't change between the sea and the experimental basin. Although it is true that fluid properties can be changed to allow simultaneous Froude and Reynolds similarity, there is no practical fluid that allows for this [236].

As priority must be given to one of the two similarity laws governing model experiments, Froude's law is preferred. This choice is based on the understanding that inertia and gravity forces play a dominant role in most phenomena related to ship dynamics, compared to the effects of viscosity. The Froude's law is universally accepted and widely applied in calm water tests, and it can be confidently employed for experiments conducted in wave conditions as well. It is important to note that while this preference aligns with general practice, it is essential to consider specific factors and potential limitations that may arise in different experimental scenarios.

If deemed necessary, adjustments can be made to experimental results to consider po-

tential scale effects resulting from variations in Reynolds numbers between the model and the ship. While such corrections are not commonly employed in ship testing, it is essential to ensure that the models used are adequately sized to minimize the influence of scale effects. Generally, it is widely accepted that beyond a certain critical Reynolds number, discrepancies in flow characteristics between the model and the ship have a negligible impact on test outcomes [112]. However, it is important to recognize the complexities and challenges associated with implementing scale corrections, as factors beyond Reynolds number, such as turbulence and boundary layer effects, may also contribute to disparities between the model and the ship. Thoughtful examination and further research are necessary to comprehensively comprehend and address these potential sources of discrepancy in experimental results. The typical factors to go from model scale to real scale are:

MAGNITUDE	FACTOR
Linear dimension	R
Rotation	1
Angular frequency	$1/\sqrt{R}$
Forces, masses	$(\rho/\rho') \cdot R^3$
Pressures	$(\rho/\rho') \cdot R$
Accelerations	1
Time	$\sqrt{R}$
Velocity	$\sqrt{R}$

Table 2.4: Conversion factors to from model scale to full scale.

To conclude this section I would like to highlight another limitation of experimental testing. Although results over the years have demonstrated to provide very accurate predictions, iteration in designs is costly and slow compared to a well optimized numerical codes [126] and/or surrogate models [73]. This draws interest in optimized numerical simulation and development of efficient surrogate models that can be coupled with optimization methods to explore design spaces [248]. Further discussion this will be presented in the following chapters.

2.3 Computational Hydrodynamics for Vessel Motion Prediction

One of the major challenges in the design of vessels is predicting their seakeeping behavior in adverse marine environments [141]. Similar to offshore wind farms and platforms, motion predictions of floating vessels in waves have traditionally relied on potential flow-based numerical models [183]. However, these models are often limited by their small amplitude assumption, which restricts their applicability in practical scenarios [141]. Despite these limitations, conventional linear seakeeping methods formulated in the frequency domain remain the most widely used models.

State-of-the-art numerical methods for wave-induced response of ships and other large-volume marine structures involve consistent second-order potential-flow solvers, although they do not account for current and forward speed. Empirical formulas are used to capture important viscous damping effects such as rolling of ships and slow-drift motions of moored structures [162, 163, 164]. Nonlinear wave effects on ships are typically simplified by considering only Froude-Krylov and hydrostatic restoring terms, while slamming is analyzed using strip theory with a high-frequency free surface condition based on either von Karman or generalized Wagner methods. These simplifications are necessary to ensure computational efficiency.

In addition, it is important to consider the stochastic response of vessels in representative sea states, each with a duration of 3-5 hours [187]. Overall, the seakeeping prediction for vessels presents similar challenges as those encountered in the design of offshore wind farms and platforms.

2.3.1 Computational Hydrodynamics for Vessel Motion Prediction as a Field: Advantages & Disadvantages Over Traditional Experiments

Computational Hydrodynamics for vessel motion prediction is a field that utilizes numerical methods and simulations to predict the behavior of ships and other floating structures

in various marine environments [137, 19]. It offers several advantages over traditional experimental methods, but also has some disadvantages.

One of the key advantages of computational hydrodynamics is cost-effectiveness. Numerical simulations can be conducted at a lower cost compared to physical experiments, which often require significant resources such as model fabrication, towing tanks, or wave basins [137, 19]. Additionally, simulations are time-efficient, allowing for rapid analysis and evaluation of different design scenarios or operational conditions [259].

Flexibility is another advantage offered by computational methods. Numerical models can be easily modified and adjusted to investigate various parameters and scenarios [194, 267], providing more flexibility in the design and optimization process. Furthermore, computational hydrodynamics enables the study of vessel behavior on a larger scale, such as in extreme weather conditions [110, 98] or complex seaways [11], which may be challenging to replicate in physical experiments.

The availability of detailed and extensive data is another benefit of computational hydrodynamics. Simulations can provide information on various aspects of vessel motions, including accelerations, velocities, and loads [84], which may be difficult to measure accurately in experiments.

However, there are some disadvantages to consider. The accuracy of numerical predictions relies on the quality of mathematical models, assumptions, and input data [21]. Errors or uncertainties in these factors can affect the reliability of the results. Additionally, validating numerical models can be complex and time-consuming, requiring comparison with real-world measurements from physical experiments or full-scale trials [21].

Conducting accurate and reliable computational hydrodynamics simulations requires a high level of expertise in numerical methods, hydrodynamics, and computational tools [260]. Skilled personnel are needed to develop, run, and interpret the simulations effectively. Moreover, high-fidelity simulations with complex geometries and detailed physics require significant computational resources, including powerful computers and specific expertise [109], which can increase the computational costs and limit accessibility for some organizations.

It's important to acknowledge that numerical simulations involve simplifications and

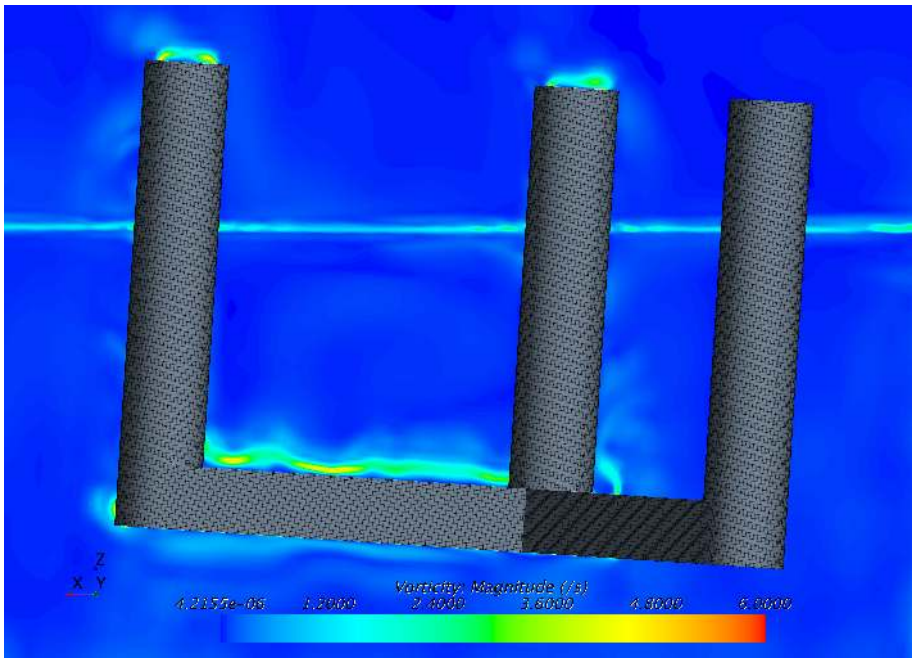

Figure 2-2: Example of high-fidelity simulation using Unsteady Average Navier-Stokes (URANS) to accurately quantify viscous damping in a semisubmersible offshore platform for wind energy.

assumptions about the physical phenomena being modeled [208, 224]. These simplifications can introduce uncertainties and limitations that may affect the accuracy of the predictions.

In summary, computational hydrodynamics offers numerous advantages, including cost and time savings, flexibility, and the ability to conduct large-scale simulations. However, it also has challenges related to model accuracy, validation, complexity, resource requirements, and assumptions. A comprehensive approach that combines computational methods with experimental validation can provide more reliable results for vessel motion prediction [259].

2.3.2 Evolution of Complexity and Fidelity of Computational Hydrondynamic Codes Enabled by recent Developments in Computing Hardware

The evolution of computing hardware has played a crucial role in advancing the complexity and fidelity of Computational Hydrodynamic Codes, enabling the use of new numerical

techniques for vessel design [30, 193, 217]. With the availability of more powerful computers and advanced computational algorithms [158, 36], designers now have access to sophisticated tools that can accurately simulate and analyze the behavior of ships and floating structures in complex marine environments.

One significant development is the utilization of high-performance computing (HPC) systems [157]. These systems consist of clusters of interconnected processors capable of performing massive parallel computations. HPC enables the handling of large-scale simulations with higher levels of detail and complexity [254, 42, 117]. It allows for the incorporation of more refined mathematical models and the inclusion of additional physical phenomena, such as fluid-structure interactions, wave breaking, or multiphase flows. This enhanced fidelity enables more accurate predictions of vessel performance and response.

Furthermore, recent advancements in numerical methods and algorithms have also contributed to the improvement of Computational Hydrodynamic Codes [57, 89]. For example, the adoption of advanced turbulence models, such as Large Eddy Simulation (LES), Detached Eddy Simulation (DES), or Unsteady Navier-Stokes (URANS) enables the accurate prediction of turbulent flow [203] behavior around ships [172]. These models capture the small-scale turbulent structures that were previously challenging to simulate, resulting in more realistic and reliable predictions of drag, maneuverability, and seakeeping performance.

However, the aforementioned methods have to deal with modelling limitation due to the assumptions they introduce to simplify and model more efficiently fluids. Large Eddy Simulation (LES), Detached Eddy Simulation (DES), and Unsteady Reynolds-Averaged Navier-Stokes (URANS) are commonly used in fluid dynamics but have limitations due to their reliance on empirically tuned closure models. LES's limitations include high computational cost, model uncertainty from the need for subgrid-scale (SGS) models, and difficulty handling near-wall regions [172]. DES, a hybrid method, faces issues with mode switching, grid dependence, and delayed transition from RANS to LES. URANS simplifies the Navier-Stokes equations by time-averaging and relies on turbulence models, introducing modeling uncertainty. It also assumes isotropic, time-averaged turbulence, limiting its ability to accurately predict complex, unsteady flows. All these methods,

despite their advancements in fluid dynamics, face significant constraints due to their empirical nature, modeling uncertainty, and computational challenges [292].

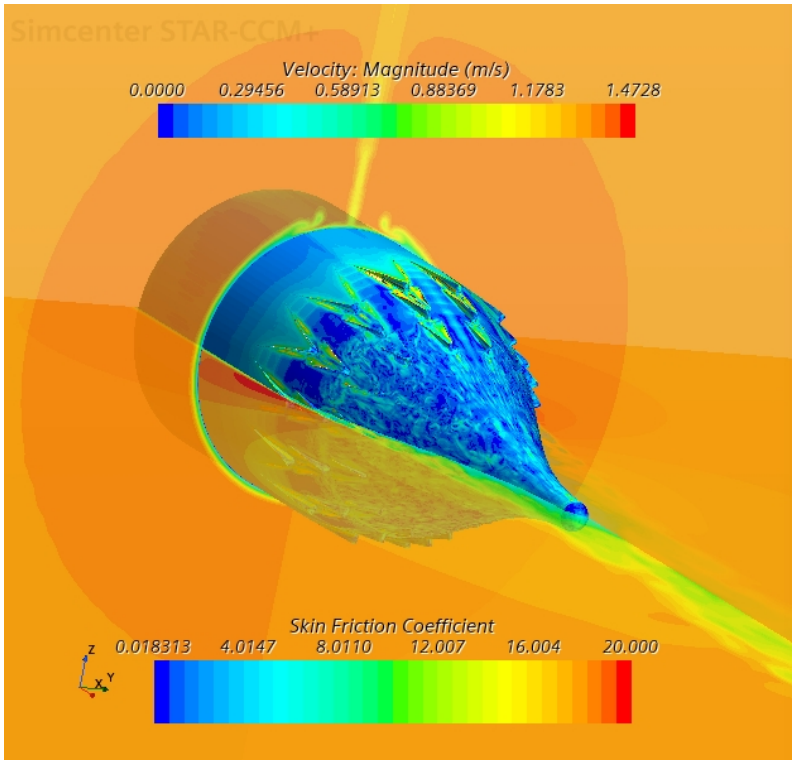

Figure 2-3: Example of DES simulation used to analyze boundary layer detachment.

In addition, developments in mesh generation techniques have allowed for the creation of more detailed and complex computational grids [269]. Adaptive mesh refinement [18] and unstructured meshing methods [152] rovide higher resolution in areas of interest, such as the ship hull or areas with complex flow patterns. This enables more accurate representation of the geometry and flow features, resulting in improved simulation accuracy.

Furthermore, the coupling of Computational Fluid Dynamics (CFD) codes with other simulation tools, such as structural analysis or control systems, allows for a more comprehensive and integrated approach to ship design [249, 138]. These coupled simulations enable the investigation of coupled phenomena, such as the dynamic response of the vessel under various loading conditions or the optimization of control strategies for improved performance and safety.

Overall, the recent developments in computing hardware have empowered the use of more advanced numerical techniques in Computational Hydrodynamics [99, 72]. These

advancements have led to increased complexity and fidelity in the simulations, providing designers with powerful tools to analyze and optimize ship designs with higher accuracy and reliability.

Another emerging technique is Smooth Particle Hydrodynamics (SPH) [174], which is a mesh-free Lagrangian method. SPH models fluid as a collection of particles, and it is particularly well-suited for simulating free surface flows and fluid-structure interactions [36]. SPH has gained popularity in various fields [150], including naval architecture and offshore engineering [243], as it can handle large deformations and complex geometries more efficiently than traditional mesh-based methods. While LES, DES & URANS techniques are widely used in vessel design and optimization, the adoption of SPH is still relatively limited. SPH has shown promise in specific applications, such as sloshing analysis [139], wave-structure interactions, and fluid sloshing [253, 159] in partially filled tanks. However, its use in general vessel design is not as common compared to other numerical methods like potential flow solvers or RANS-based CFD simulations. The choice of numerical technique depends on the specific requirements of the design problem and the expertise of the engineering team.

2.4 Generating Input to Train the ML Algorithm

The unavailability of a comprehensive dataset encompassing both vessel motions and the corresponding ocean sea states has necessitated the use of simulations. These simulations aim to recreate the specific conditions under which the proposed tool would be utilized. However, conducting these simulations is a challenging technical task in itself. The reliability and meaningfulness of the resulting algorithm heavily rely on the accurate representation of complex physics within these high-fidelity simulations. Therefore, a detailed overview of the simulation method employed is provided in the following pages.

2.4.1 Overview of the Simulation Method.

This section presents a description of the STAR-CCM+ code, a Volume of Fluid URANS solver that incorporates viscous effects. The code assumes turbulent flow and considers a

smooth surface for the body. It solves the averaged continuity and momentum equations for incompressible fluids, accounting for the absence of body forces acting on the floating object.

$$\frac{\partial(\rho\overline{u}_i)}{\partial x_i} = 0 \tag{2.36}$$

$$\frac{\partial(\rho\overline{u}_i)}{\partial t} + \frac{\partial}{\partial x_j}(\rho\overline{u}_i\overline{u}_j + \rho\overline{u_i'u_j'}) = -\frac{\partial\overline{p}}{\partial x_i} + \frac{\partial\overline{\tau}_{ij}}{\partial x_j} \tag{2.37}$$

$$\overline{\tau}_{ij} = \mu\left(\frac{\partial\overline{u}_i}{\partial x_j} + \frac{\partial\overline{u}_j}{\partial x_i}\right) \tag{2.38}$$

Where $\overline{\tau}_{ij}$ in Equation 2.37 represents the components of the averaged viscous force tensor, $\overline{p}$ denotes the averaged pressure, and $\overline{u}$ corresponds to the Cartesian components of the averaged velocity. In Equation 2.37, $\overline{u_i'u_j'}$ refers to the Reynolds stresses, ρ represents the fluid density, and μ denotes the dynamic viscosity.

To ensure the desired mesh resolution in the boundary layer, it is important to keep the $y+$ values near the ship surface below a certain threshold (fig. 2-4). In [230], it was found that $y+$ values around 50 provide a good approximation. Here, $y+$ is defined as $y+ = y \cdot v^*/\nu$, where y is a coordinate perpendicular to the body surface with $y = 0$ at the body surface. v^* denotes the friction velocity, which is the square root of the ratio between the absolute value of the wall shear stress and the fluid density. Additionally, $\nu = \mu/\rho$. The viscous sublayer is assumed to be below the given $y+$ values. Since the simulations have an average $y+$ value of around 60 (Tab. 2.5), the discretization of the integral formulation of the Navier-Stokes equations requires a turbulence model. The two commonly used turbulence models are k-ϵ and k-ω. For these simulations, a combination of the two models, namely the SST k-ω Menter turbulence model [169], has been employed. This model incorporates the k-ϵ model away from the walls and switches to the k-ω model when calculating near the walls, where the boundary layer develops."

To model the free surface, the time-domain viscous model uses a Volume of Fluid method (VOF) [169]. This model assumes that the same equations governing the physics of one of the phases can be solved for all phases present in the computational domain (each cell or finite volume). A good reference for the theory behind this type of numerical

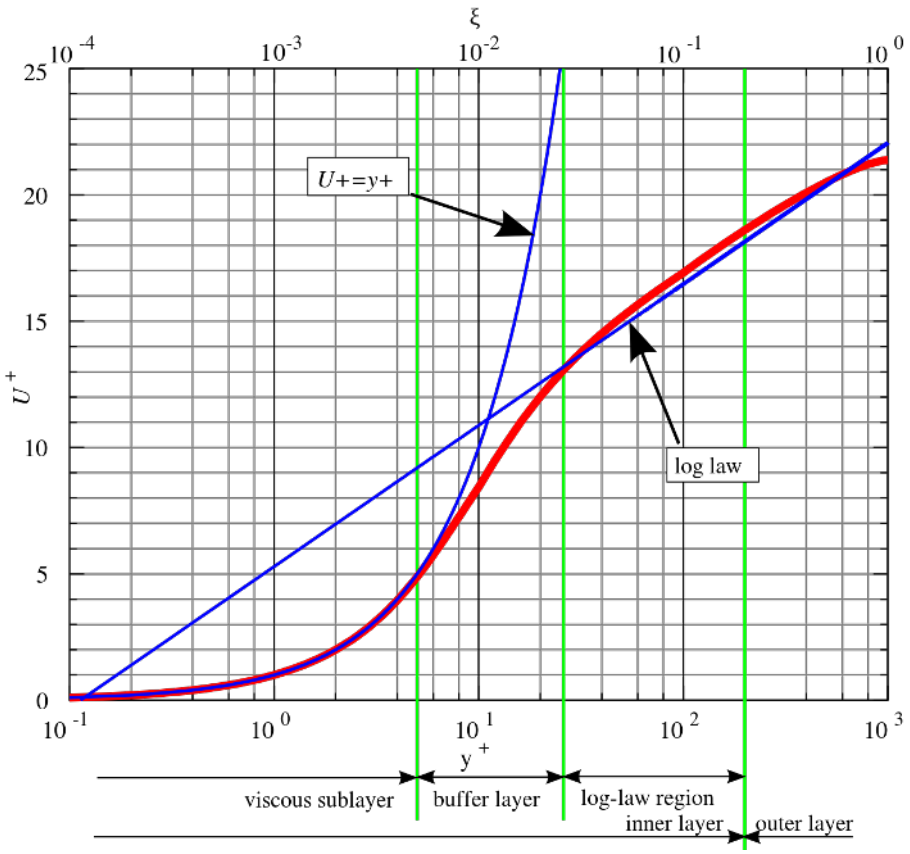

Figure 2-4: Law of the wall for the different regions of the boundary layer. It is valid for high reynolds numbers and when shear stresses are constant and the pressure field has zero gradient.

method can also be found in [72].

In order to simulate the behavior and to obtain realistic ship motions, a Dynamic Fluid Body Interaction (DFBI) model is used. The ship is allowed to move in three degrees of freedom, to translate in the longitudinal and vertical directions (surge & heave) and to rotate around the transversal direction (pitch).

It is necessary to identify constraints to define the time step. These constraints depend on the physics that have to be simulated. The objective is to record the following physical phenomena:

1. Heave, pitch and surge ship motions.

2. The waves that travel on the free surface throughout time.

For the heave, pitch and surge movements, the ITTC recommends at least 100 time steps per period of encounter with the waves [266, 201, 9]. The period of encounter, considering

the spectral peak period, ranges from $\sim 6 - 12s$, so $0.06 - 0.12s$ is the minimum time step regarding the motions. Furthermore, the Courant Number (CNN) on the free surface must stay below 0.1. Following best practices from previous work, the CNN criteria on the free surface is found to be the most stringent condition when choosing the time step, see [71] for more details.

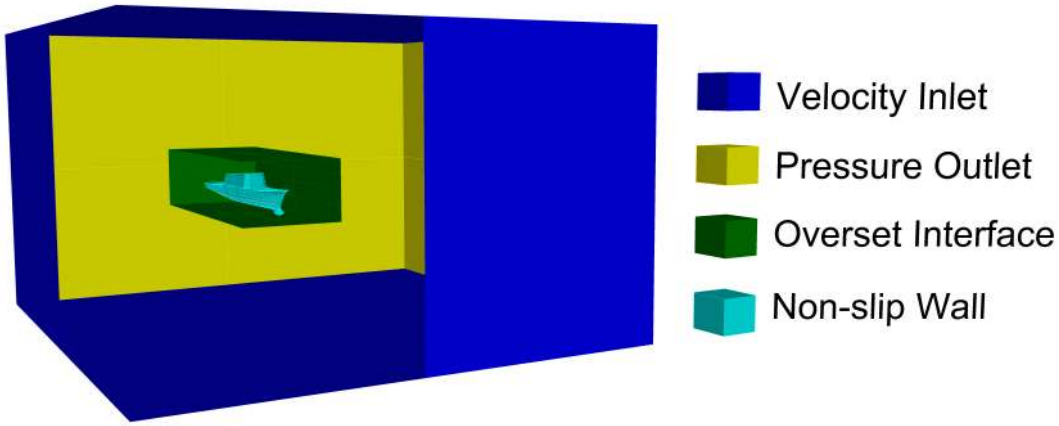

Figure 2-5: Representation of the boundary conditions using a color code. Relative dimensions between the floating body and the computational domain have been modified to allow for better visualization. (here and in Fig. 2-6).

The ship, as it can be seen in Fig. 2-5, is positioned $1 \cdot \lambda_p$ from the velocity inlet.

An hexahedral volume mesh is used for the *Background* and *Overset* regions which are overlapped (Chimera grid). Additionally, prism layers are introduced in the *Overset Region*, around the ships hull surface boundary. No prism layers are used on the ship's superstructure, the force contribution from it is negligible compared to the wetted area of the Hull.

The sizes of the domains *Block Region* and *Overset Region* are chosen using best practices derived from previous seakeeping studies. Good examples are references [189] and [266]. The dimensions of the ship and waves are used to perform the necessary proportions. The water depth is 1.2 of the largest wave length, which should give negligible finite water depth errors. The final measures for this particular case, here $L_p = 140$ is the

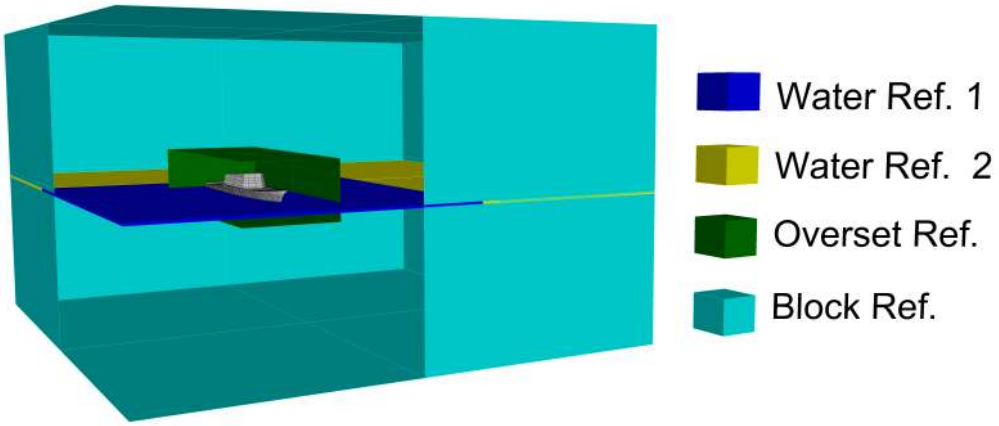

Figure 2-6: Representation of the mesh volume controls using a color code.

length of the ship, are the following:

1. Length: $3.7 \cdot \lambda_p$.

2. Width: $8.4 \cdot L$.

3. Depth: $3.6 \cdot L$.

A series of volume controls have been applied to generate an unstructured grid with the necessary refinements to capture the different physical scales that characterize the problem studied. These volume controls are described in the Fig. 2-6. The mesh refinements in the volume controls have been defined in relation to the wave dimensions and the estimated boundary layer size. These dimensions are presented in Table 2.5. The volume refinements used are:

1. *Water Ref 1*: the main purpose of this refinement is to establish continuity in the vertical dimension of the mesh while providing an expansion of the mesh in the horizontal plane. The expansion is done with the objective of creating numerical dissipation at the end of the domain before the *Pressure Outlet*. The objective is to

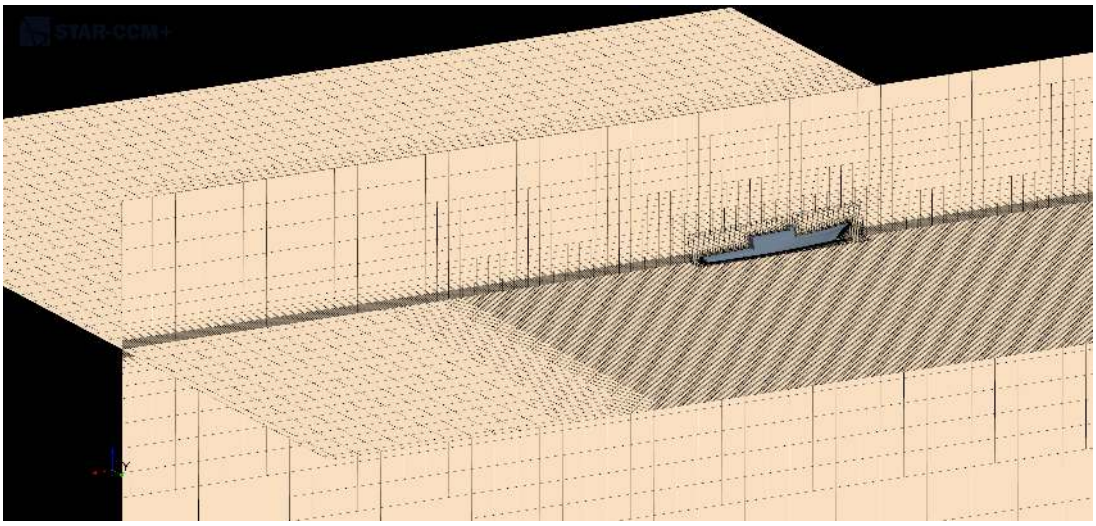

Figure 2-7: Example of the computational domain used to simulate the second sea spectra ($T_p = 12.7s,\ \ H_s = 5.09m$). The mesh expands when reaching the pressure outlets. This creates a numerical beach $1.5 \cdot \lambda_p$ long. Further mesh refinements are done near the ship, the results of these refinements can be seen in Fig. 2-8.

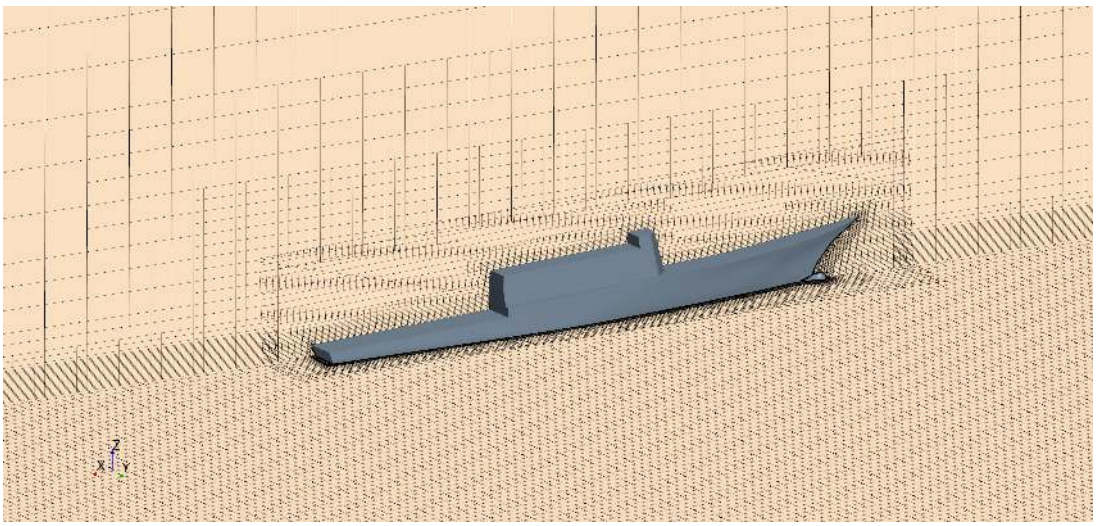

Figure 2-8: Second example of a mesh near the ship at a time instant during the simulation.

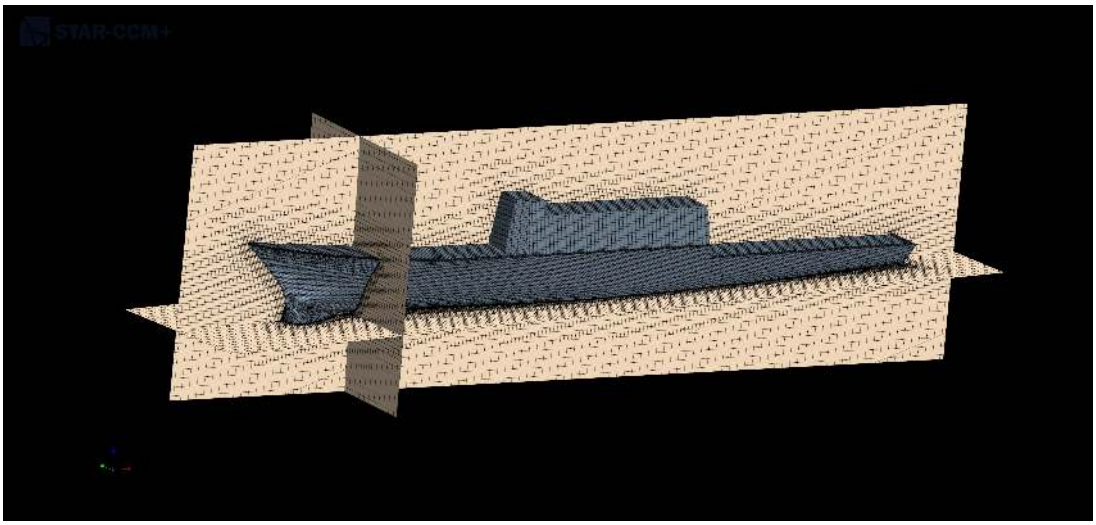

Figure 2-9: Example of a mesh near the ship at a time instant during the simulation. The overset domain is $1.35 \cdot L_p$ long, $2.0 \cdot B_p$ wide and $4.0 \cdot D_p$ deep. The ship is centered within the overset domain.

damp out the waves that enter the domain to eliminate any possible reflections in the *Pressure Outlet* that introduce perturbations in the solution.

2. *Water Ref 2*: this volume control intends to provide an adequate continuum for the wave to propagate uniformly, with minimal numerical dissipation. Regarding the length of *Water Ref 2* refinement ($2.4 \cdot \lambda_p$), it is advised that this length is at least equal to twice the length of the wave simulated (Fig. 2-6).

3. *Ship refinement*: the purpose of this volume control is to provide higher grid resolution in the area near the platform.

The surface control used is the following:

1. *Hull*: the surface size control has been created to represent the ship's geometry accurately. Moreover, this enables a good quality prism layer expansion.

The mesh and time convergence has been divided into three steps:

1. *Convergence of the Block Region mesh*, for the long crested irregular wave. This has proven the most important in the convergence of the results. Best practices from previous validations have been taken to define the mesh refinements, such as those

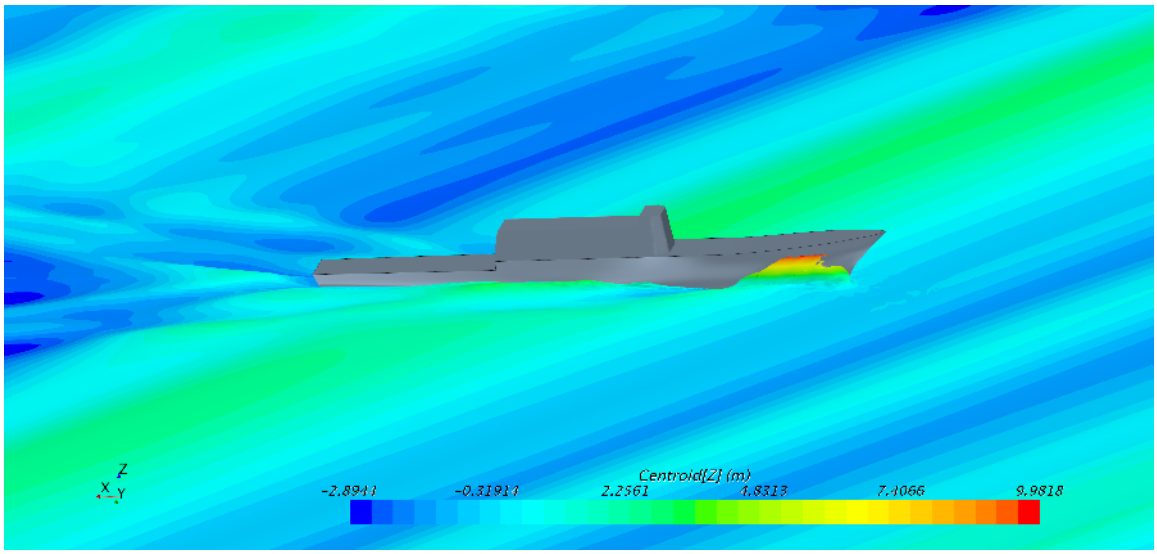

(a) Wave elevation.

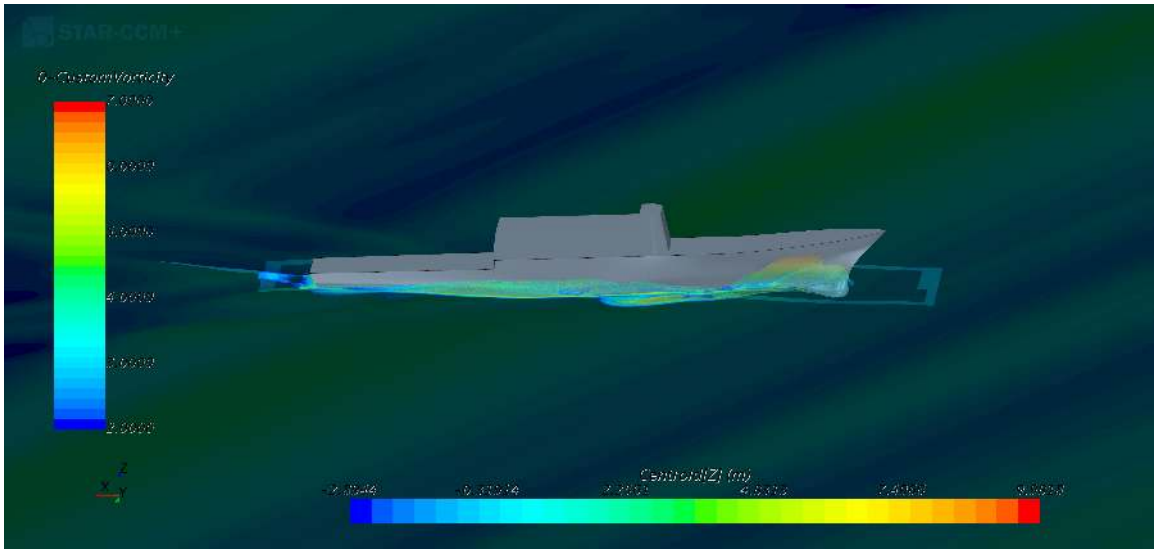

(b) Magnitude of the vorticity field.

Figure 2-10: In Fig. 2-10a, the wave elevation is plotted and, in Fig. 2-10b, non-linear phenomena at the vessel's natural period ($T_p = 12.7s$, $H_s = 5.09$) can be seen. In Fig. 2-10b, the color map represents the module of the vorticity field. As it can be observed in the image, the vorticity is mainly generated by the ship's bow underwater instrumentation dome.

Table 2.5: Mesh characteristics for each of the 11 URANS simulations. The mesh sizes range between 10 and 13 million cells and average y+ values remain below 60, limiting the viscous sublayer along the body surface. The mesh refinements are defined in relation to the wave length (λ_p) and wave height (H_w). The number of cells per wave height and wavelength remains constant through the different cases. Within some control volumes, the mesh is allowed to expand until otherwise specified, so as to create a numerical beach. There are a minimum of eight equal sized cell layers per transition

				Overset			Platform Ref 1			Water Ref 1			Water Ref 2		
	# of cells total	# of cells Overset	y+	X	Y	Z	X	Y	Z	X	Y	Z	X	Y	Z
M1($T_w = 9.7s$)	9549703	3290648	55	$\frac{\lambda_p}{93}$	$\frac{\lambda_p}{93}$	$\frac{H_p}{14}$	$\frac{\lambda_p}{93}$	$\frac{\lambda_p}{93}$	$\frac{H_p}{14}$	Expand	Expand	$\frac{H_p}{14}$	$\frac{\lambda_p}{93}$	$\frac{\lambda_p}{93}$	$\frac{H_p}{14}$
M1($T_w = 12.4s$)	6541834	3102192	55	$\frac{\lambda_p}{93}$	$\frac{\lambda_p}{93}$	$\frac{H_p}{14}$	$\frac{\lambda_p}{93}$	$\frac{\lambda_p}{93}$	$\frac{H_p}{14}$	Expand	Expand	$\frac{H_p}{14}$	$\frac{\lambda_p}{93}$	$\frac{\lambda_p}{93}$	$\frac{H_p}{14}$
M1($T_w = 13.7s$)	7357841	3053689	55	$\frac{\lambda_p}{93}$	$\frac{\lambda_p}{93}$	$\frac{H_p}{14}$	$\frac{\lambda_p}{93}$	$\frac{\lambda_p}{93}$	$\frac{H_p}{14}$	Expand	Expand	$\frac{H_p}{14}$	$\frac{\lambda_p}{93}$	$\frac{\lambda_p}{93}$	$\frac{H_p}{14}$

found in Ref. [189]. According to this publication, good results can be obtained with approximately 20 cells per wave height and 100 cells per wavelength. The peak period values are taken as reference to compare against monocromatic wave studies, with the intention to give preferential attention to the wave components that contain the largest amount of energy. The final mesh dimensions, relative to the wave dimensions in the simulations, are presented in Tab. 2.5. The sharpening factor is left at 0.0, so there is no term for numerical diffusion in the volume fraction transport equation.

Table 2.6: Principal dimensions and mass properties of the ship.

Length (L)	140 m
Beam (B)	40 m
Depth (D)	12 m
Displacement (Δ)	8621275.0kg
Radius of gyration (r_{xx})	3.61 m
Radius of gyration (r_{yy})	37.5 m
Center of gravity z-coordinate	0.0 m
Center of gravity x-coordinate	-74.23 m

2. *Convergence of the remaining volume refinements.* Additional volume refinements are created to provide the right domain dimensions and appropriate refinement for the *Overset Region*, and a long enough numerical beach at the end of the domain.

3. *Convergence of the ship's surface size and boundary layer mesh (prism layer).* As in the first point, recommendations from Ref. [189] have again been followed. Ten prism layers have been used, with a growth rate factor of 1.3 and $y+$ values are 55 on average (Tab. 2.5). Consequently wall functions are necessary to perform the simulations.

2.4.1.1 Boundary Conditions

Given the unique characteristics of the problem at hand, we've precisely defined specific boundary conditions. It's important to note that there can be multiple appropriate boundary conditions for this same problem. The ones we've employed are graphically depicted in Fig. 2-5, with varying conditions represented using a color-coding system.

To prevent numerical wave reflections from the outlet, we've designed a numerical beach in the region preceding the Pressure Outlet. This area extends over a range equal to twice the wavelength ($2 \cdot \lambda_w$) used in the study. The function of this numerical beach is to diminish the vertical velocity of fluid particles by damping motion in the vertical direction.

Our process of inducing damping aligns with the guidelines stated in reference [202]. This damping setup allows for more accurate simulation results by minimizing the potential interference caused by wave reflections.

2.4.1.2 Coordinate Systems

In our computations, we make use of two distinct reference frames. Initially, the fo-

cus is on the global reference frame, where we analyze the flow problem and calculate the magnitude of the resultant force acting on the body. Upon obtaining these forces, we then transition to the local reference frame specific to the ship.

This ship-centric reference system has its origin located at the ship's center of gravity. The x-axis in this frame follows the fore-aft direction of the ship. Using this local frame of reference, the previously calculated forces and moments are translated and adapted accordingly.

With these newly adapted force values in hand, we then proceed to calculate the resulting movement of the ship. This comprehensive two-step approach ensures accurate and reliable calculations of the ship's reaction to external forces.

2.4.1.3 Simulation of Irregular Long Crested Seas

Dynamics of waves developing at the sea surface can be described in a probabilistic manner, assuming the process is stationary, homogeneous, and ergodic. A finite sum of individual components is then utilized to represent the wave elevation, approximating a Stieltjes integral, as identified in [240, 244].

The stochastic process characterizing sea surface elevations is represented by experimental sea spectra, which are employed to induce vessel motions (refer to fig. 2-11). For a specific spatial location, we consider $\zeta(t)$ as the sea surface elevation over time. This time signal is defined as the sum of sinusoidal waves with random phases ε_i, ranging between $-\pi$ and π and sampled from a uniform distribution, with incommensurate frequencies ω_i covering the spectrum's frequency range:

$$\zeta(t) = \sum_{i=1}^{n} a_i \cos\left(\omega_i t + \varepsilon_i\right), \tag{2.39}$$

The modified Pierson-Moskowitz spectrum [5], denoted as $S(\omega)$, is used, with T_1 representing the mean wave period:

$$\frac{S(\omega)}{H_s^2 T_1} = \frac{0.11}{2\pi}\left(\frac{\omega T_1}{2\pi}\right)^{-5} \exp\left[-0.44\left(\frac{\omega T_1}{2\pi}\right)^{-4}\right], \tag{2.40}$$

The domain's initial conditions are imposed by computing the velocity and pressure

Variable	Formula
Wave Profile	$\zeta(x_1,t) = \sum_{n=1}^{N} a_n cos[k_n(x_1 - c_n t) + \varepsilon_n]$
Horizontal Velocity	$u(x_1,x_2,t) = \sum_{n=1}^{N} \frac{a_n \omega_n}{sinh(k_n h)} cosh[k_n(x_2+h)] cos[k_n(x_1 - c_n t) + \varepsilon_n]$
Vertical Velocity	$v(x_1,x_2,t) = \sum_{n=1}^{N} \frac{a_n \omega_n}{sinh(k_n h)} sinh[k_n(x_2+h)] sin[k_n(x_1 - c_n t) + \varepsilon_n]$
Horizontal Acceleration	$\dot{u}(x_1,x_2,t) = \sum_{n=1}^{N} \frac{a_n \omega_n}{cosh(k_n h)} cosh[k_n(x_2+h)] sin[k_n(x_1 - c_n t) + \varepsilon_n]$
Vertical Acceleration	$\dot{v}(x_1,x_2,t) = \sum_{n=1}^{N} \frac{a_n \omega_n}{sinh(k_n h)} cosh[k_n(x_2+h)] cos[k_n(x_1 - c_n t) + \varepsilon_n]$
Dynamic Pressure	$p(x_1,x_2,t) = \sum_{n=1}^{N} \frac{a_n \rho g}{sinh(k_n h)} cosh[k_n(x_2+h)] cos[k_n(x_1 - c_n t) + \varepsilon_n]$

Table 2.7: Formulation for irregular long crested seas, with (x_1, x_2) spatial location in the mean plane of the surface elevations.

fields as a superposition of individual regular waves. The general formulation for long crested irregular seas, where both space (x_1, x_2) and time (t) are independent variables [96], is presented in table 2.7. These variables are numerically integrated over time, also accounting for nonlinear interactions with the vessels.

The sea states modeled differ for each of the two vessels under consideration. For both, we use the Pierson-Moskowitz spectrum to generate fully developed irregular long crested seas [204]. The catamaran's sea state is defined by: $H_s = 0.3m$ and $T_p = 1.48s$, where H_s represents the significant wave height and T_p is the peak wave period [101]. Conversely, the DTBM's vessel sea state is composed of oblique waves advancing at a 30 angle relative to the longitudinal direction, with $H_s = 10.66m$ and $T_p = 13.4s$. This corresponds to a World Meteorological Organization (WMO) sea state code 8 [293].

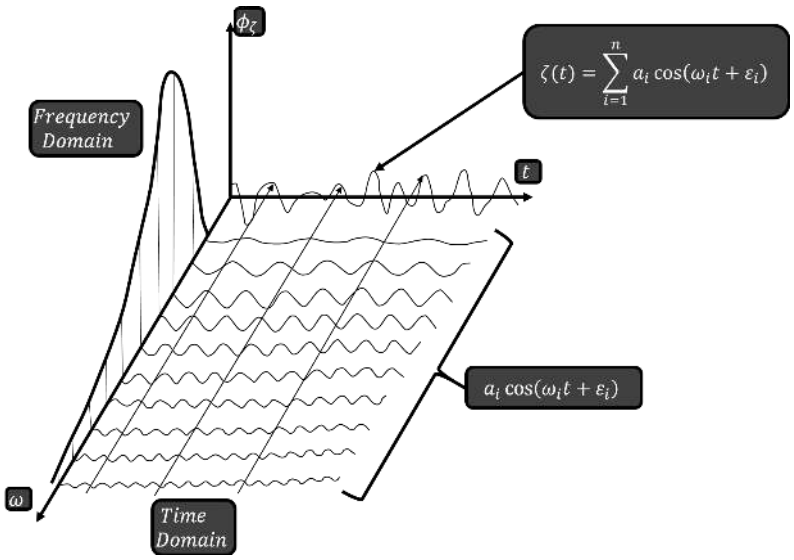

Figure 2-11: *Graphical description of the spectral analysis performed to characterize sea states.* Given an energy spectrum specific to a particular ocean region, we can decompose the waves into different frequencies. The amplitudes corresponding to each frequency are given by the energy contained in each frequency in the wave spectra. Also, ϵ_i are random phases sampled from a uniform distribution.

2.4.2 Description of the Compiled Simulation Data

Having outlined the simulation setup in previous sections, we proceeded with the data set sampling. We embarked on this comprehensive simulation campaign due to the following reasons:

1. A lack of existing data sets that compile both full-sized vessel motions and corresponding exciting waves.

2. The significant cost and risk associated with subjecting a vessel to the extremely severe sea states under consideration [94]. While such sea states might exceed the operational capabilities of these vessels, our primary focus lies on the hydrodynamic aspects of the problem [37].

3. The ability to record data at high resolution and concurrently inspect several variables and fields, which aids in determining the most optimal configuration and observing the effects of individual variables.

With these considerations in mind, our final data set comprises 49 seeds of 3 different sea states sampled from the Pierson Moskowitz spectrum, yielding a total of 147 seeds. The computations spanned over three years, leveraging an automated sampling and post-processing system to establish an efficient workflow. The simulated sea states, listed in order of increasing severity, are: ($H_s = 3.53m, T_p = 9.7s$, $H_s = 5.09m, T_p = 12.4s$, $H_s = 10.66m, T_p = 13.4s$). Detailed graphs depicting wave elevation and motion data for each of these seeds are available in figs. A-1 to A-9, and are further discussed in appendix A.

2.5 From Hypothesis to Formulation of the ML Problem

In essence, our primary objective is to establish a functional mapping that derives vessel motions from ocean wave data [219]. This mapping, which exists between two spaces of functions, can be deemed a functional correspondence. The efficiency and accuracy of this mapping hinge on two factors: the comprehensiveness of the information provided and the efficacy of the algorithm that encapsulates the relationship between these functional spaces [237, 22].

Given these prerequisites, we prefer representations with fewer parameters as they not only enhance computational efficiency but also curb overfitting. Numerous machine

learning models were examined before we settled on our final configuration. It's worth noting that the specific model applied in the context of this thesis is not set in stone; it may undergo modifications as our understanding of the dynamics improves and more representative data becomes available in the future.

2.5.1 Overview ML Methods for Time/Sequence Series Prediction

Time series forecasting methods span from the simplest, such as Linear Regression, to more advanced ones like LSTM, GRUs and Transformer models. Linear Regression is straightforward to implement and understand, but may oversimplify complex problems due to its assumptions about the data. ARIMA, a well-established method, excels with univariate time series data with trends or seasonality but struggles with multiple complex seasonality patterns.

Neural network-based models have been effective at capturing the complexity of time series data. Recurrent Neural Networks (RNNs) are good for sequence prediction where context from the recent past is important, but have difficulties with long-term dependencies. Long Short-Term Memory (LSTM) and Gated Recurrent Units (GRUs) were developed to handle such dependencies. LSTMs are effective but computationally intensive, while GRUs are a simpler and more efficient alternative.

Convolutional Neural Networks (CNNs), traditionally used for image data, can also be applied to sequence prediction tasks, especially when spatial/temporal dependencies exist. However, they're not inherently suited to temporal data.

For more complex tasks where input and output sequences are of different lengths, Sequence-to-sequence (Seq2Seq) models are a great fit. Finally, Transformer Models, which capture global dependencies in the data, are state-of-the-art for many tasks, but require large amounts of data and computing resources.

Choosing the right model depends heavily on the specific problem, the nature of the data, and the available computational resources. Often, a combination of methods and experimentation is needed to find the most effective solution.

2.5.2 Choice of ML Method

Accurately replicating the movements of vessels through computer simulation is already a remarkable achievement and serves as a critical alternative to using real vessels to investigate their operational limits. Such real-world investigations are typically cost-prohibitive and fraught with risk, due to the extreme environmental conditions under which these operations occur. Simulation, therefore, holds a distinct advantage in this regard, although still severely limited by computational cost.

The challenges posed by these conditions significantly limit the availability of meaningful data and create obstacles in generating novel, useful datasets that present interesting scenarios for training Machine Learning methods. Given this scarcity of data, LSTM RNNs [100] were selected for their economy in terms of parameter space. They are particularly suited to situations where data is limited, which is the case here. The ultimate objective is to create an algorithm that can draw from a variety of data sources, both simulated and real, to accurately learn the mappings between complex functional spaces, even under challenging operational conditions. The future goal of extending this work to cover all operating conditions largely depends on data availability. Nevertheless, the foundational structure of the algorithm can largely be maintained.

RNNs, representing an evolution of feedforward neural networks [263], are specially crafted to capture sequence-related features. They offer a dynamic state that evolves as the network processes more of the sequence, making them particularly adept at integrating newly available information over lengthy sequences. A unique attribute of RNNs is their parameter sharing mechanism, using the same function to transform the preceding state. This is efficient and conducive for capturing sequence dynamics. However, traditional RNNs face challenges, like the vanishing gradient problem, which prompted the turn towards gated units, specifically LSTM and GRU cells, for the lengthy time series utilized in this study [46].

LSTMs, among gated cells, possess gates that control the information flow within the cell's state, mitigating the vanishing gradient problem. After an extensive convergence study of network properties, LSTMs emerged as more expressive, catering effectively to the complexities of the data in question. While alternative architectures such as NARX

were considered, their inability to 'forget' was a significant limitation. This flaw could lead to the accumulation of residual errors, compromising the performance in predicting extended sequences.

Among gated cells, the LSTM emerges as the choice for its well-established reputation, its expressiveness, and its innate ability to handle long sequences without accumulating errors [263]. Although LSTMs have seen widespread applications in areas like language modeling, the focus in this work diverges from those traditional uses, instead harnessing its strengths for the unique challenges presented by vessel movement simulations.

While Transformers have achieved state-of-the-art results in many sequence modeling tasks, especially in NLP [281, 120], they require a significant amount of data for training. Their architecture, designed around self-attention mechanisms, allows them to capture long-range dependencies in the data, potentially even more effectively than LSTMs in certain contexts. However, given the limited availability of data in our scenario and the computational resources required to train such models, LSTMs were deemed more suitable. The future, with the availability of more data and increased computational capacity, might see a turn towards experimenting with transformer architectures for vessel movement simulations.

The formulation of LSTM cells follows established guidelines [100, 87]. Here, the internal memory c_t and visible state h_t constitute the evolving pair $[c_t, h_t]$. The forget gate f_t, aptly named, regulates memory cell pruning. The input gate i_t governs memory cell readouts into the visible state h_t, facilitated by the output gate o_t. The memory cell c_t evolves via contributions from both forget and input gates.

$$
\begin{aligned}
f_t &= \sigma_g\left(W_f x_t + U_f c_{t-1} + b_f\right) \\
i_t &= \sigma_g\left(W_i x_t + U_i c_{t-1} + b_i\right) \\
o_t &= \sigma_g\left(W_o x_t + U_o c_{t-1} + b_o\right) \\
c_t &= f_t \odot c_{t-1} + i_t \odot \sigma_c\left(W_c x_t + b_c\right) \\
h_t &= o_t \odot \sigma_h\left(c_t\right)
\end{aligned}
\tag{2.41}
$$

By revisiting and refining these foundational elements, we establish a robust framework for modeling complex sequences, as demonstrated in our study.

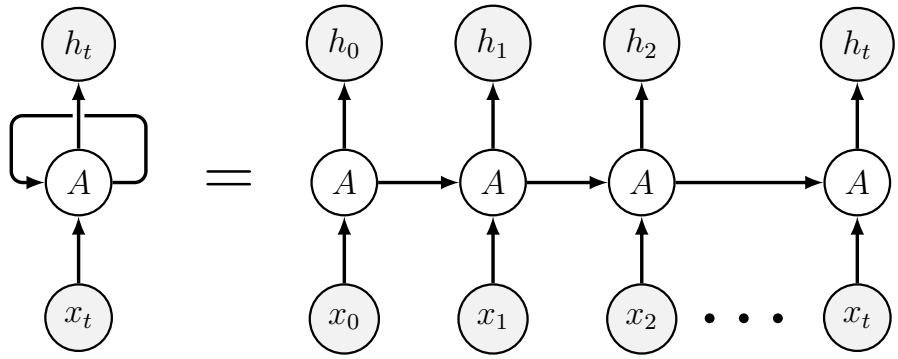

Figure 2-12: Unfolding a RNN.

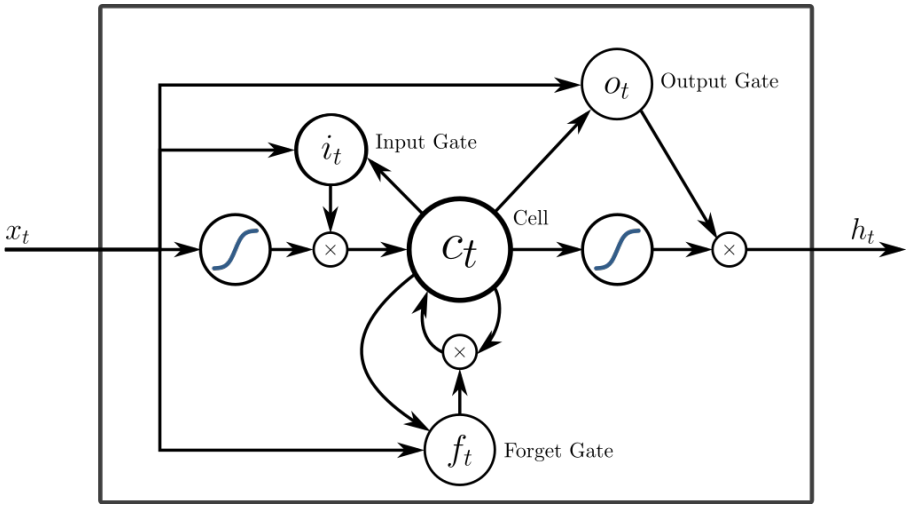

Figure 2-13: Peephole LSTM cell.

2.5.3 Neural Network Architecture Convergence

Neural network architecture analysis plays an essential role in optimizing the performance and predictive capabilities of LSTM recurrent neural networks. It serves as a systematic exploration of different network configurations to identify the most effective setup for a specific task. This process involves fine-tuning hyperparameters, which are variable settings that define the network architecture's and thus its behavior during the learning process.

In the context of LSTM networks, several key hyperparameters can be tuned to enhance their performance. The number of LSTM units or neurons in each layer is a crucial consideration. A higher number of neurons can potentially capture more intricate patterns in the data, but it also increases computational complexity. On the other hand,

too few neurons might lead to underfitting. The number of hidden layers in the network also affects its depth and capacity to learn hierarchical features. Deeper networks can model complex relationships but might be prone to overfitting. Batch size, which determines the number of training samples used in each iteration, influences training speed and convergence stability.

Additionally, hyperparameters like the learning rate and optimization algorithm influence the rate of convergence during training. Learning rate determines the step size in updating network weights, and the choice of optimizer affects how these updates are performed. Regularization techniques, such as dropout [256] and recurrent dropout [12], can be employed to prevent overfitting by randomly disabling certain neurons during training, however they did not improve substantially the performance of the LSTM networks trained for vessel motion modeling. However, in the context of sparse data, the application of dropout can present specific challenges. One significant concern is the risk of excessive regularization. Since the model might already find it challenging to fit the sparse data, introducing dropout could further impede this process, potentially leading to underfitting. Additionally, the already intricate task of learning meaningful representations from limited data can be further hampered by the random dropout of neurons during training [111].

This randomness introduced by dropout can manifest in another concerning way—increased variance in model predictions. Such unpredictability in outcomes can be detrimental, especially when the objective is to achieve consistent and reliable results [82]. Moreover, the stochastic nature of dropout can introduce noise into the optimization landscape, making it harder for the model to find a suitable minimum, thereby posing optimization challenges[119] .

It's worth noting that while dropout is a valuable tool, its effects in the realm of limited data haven't been as extensively researched as its broader applications [92]. However, practitioners should be aware of several practical considerations. Firstly, simplicity is crucial when dealing with small datasets [56]. Networks with fewer parameters are more apt for such scenarios, as their smaller size inherently regularizes them, potentially rendering additional dropout unnecessary or even counterproductive. Secondly, regard-

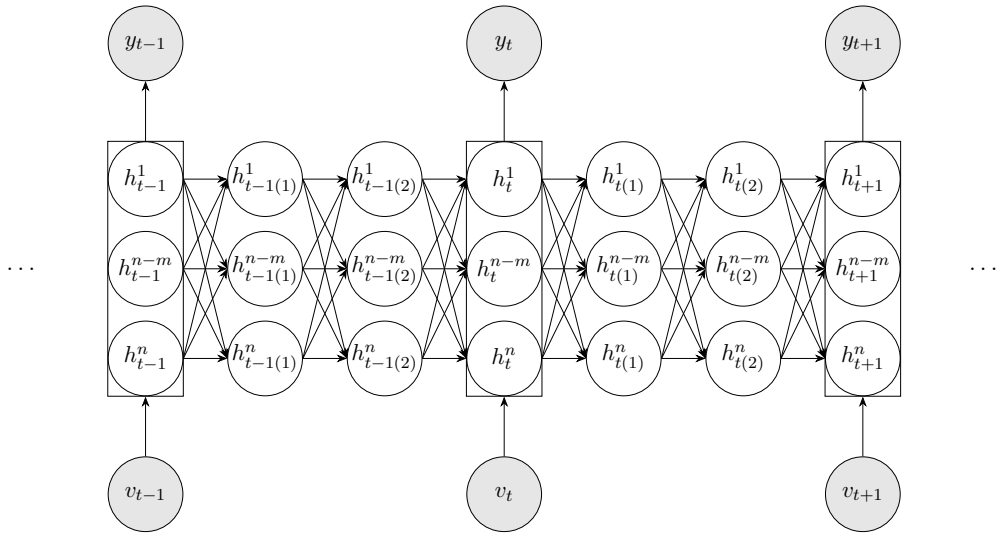

Figure 2-14: Neural network architecture convergence.

less of the size of the dataset, careful validation remains essential [211]. A validation set, albeit small, can provide crucial insights into the model's performance, helping identify potential issues of underfitting or overfitting. Lastly, one might consider other forms of regularization, like L1 or L2 regularization, which could offer a more controlled approach than dropout when data is limited [184]. As with many techniques in deep learning, the specific effects of dropout can vary depending on the problem at hand, making empirical testing and ongoing validation indispensable [148].

Furthermore, the selection of loss functions and evaluation metrics is critical in guiding the network's learning process and assessing its performance [289]. These choices depend on the specific nature of the task, whether it's classification, regression, or sequence generation. We experiment with three different loss functions to explore the effect of highlighting different features of the data during the training process. These loss functions were: Mean Square Error, Amplitude Magnified Mean Square Error [125] and Relative Entropy [132].

In summary, neural network architecture analysis involves the strategic adjustment of hyperparameters to strike a balance between model complexity and generalization capacity [161]. By iteratively fine-tuning these parameters and evaluating the network's behavior on validation data, researchers and practitioners can optimize LSTM networks for specific tasks, ensuring they achieve the desired accuracy and predictive power.

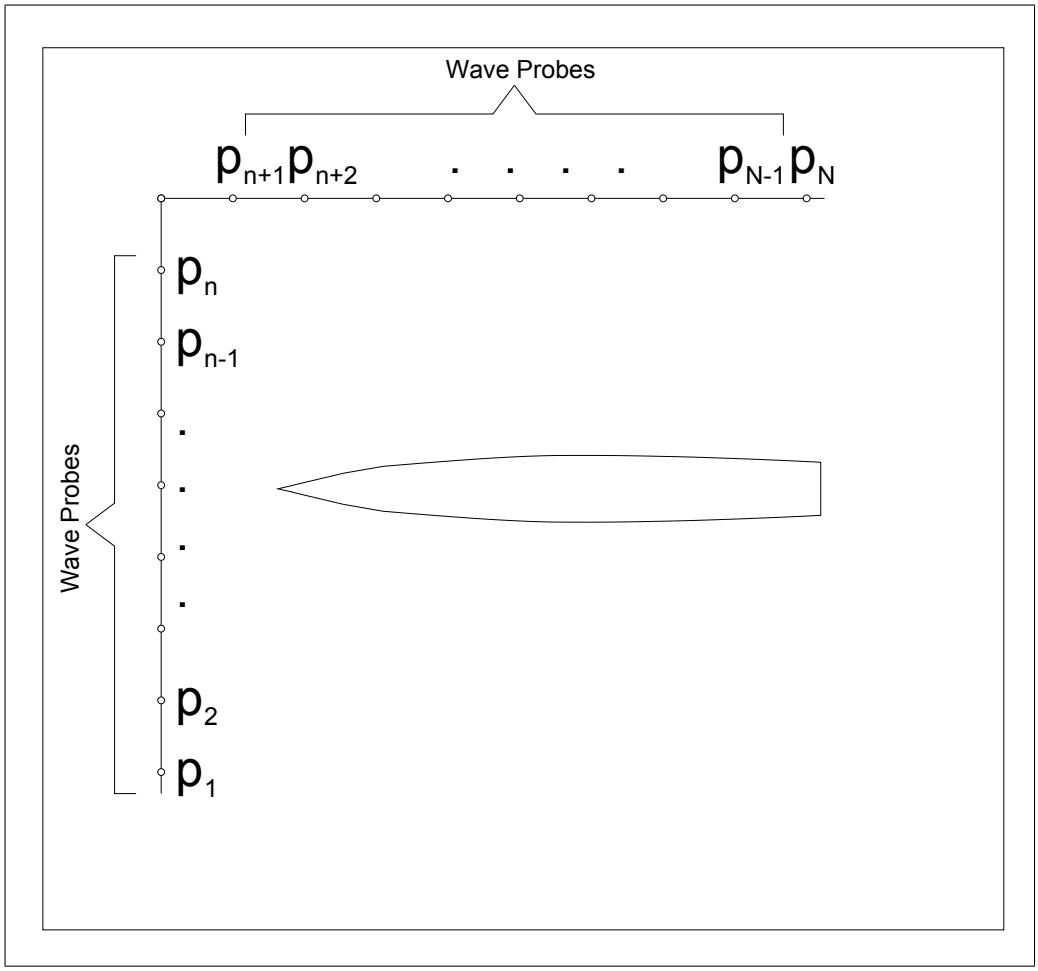

Figure 2-15: Schematic of wave probes in the computational domain.

2.5.4 Engineering the Data to Obtain Maximum Accuracy in the Predictions

Much like in numerical methods, the format in which data is feed into ML algorithms may emphasize or hide certain features in the data. In numerical methods this is controlled with the numerical stencil [140] (upwind, centered, forward backwards differences...) each type having particular advantages and disadvantages. Centered difference stencils generally provide higher accuracy due to their second-order accuracy. Upwind stencils can provide better stability for problems [91] with a dominant transport direction. Therefore, the type and size of the numerical stencil can significantly influence the accuracy, stability, and computational cost of the numerical solution. Generally, larger stencils involve more grid points, leading to more accurate solutions but at a higher computational cost.

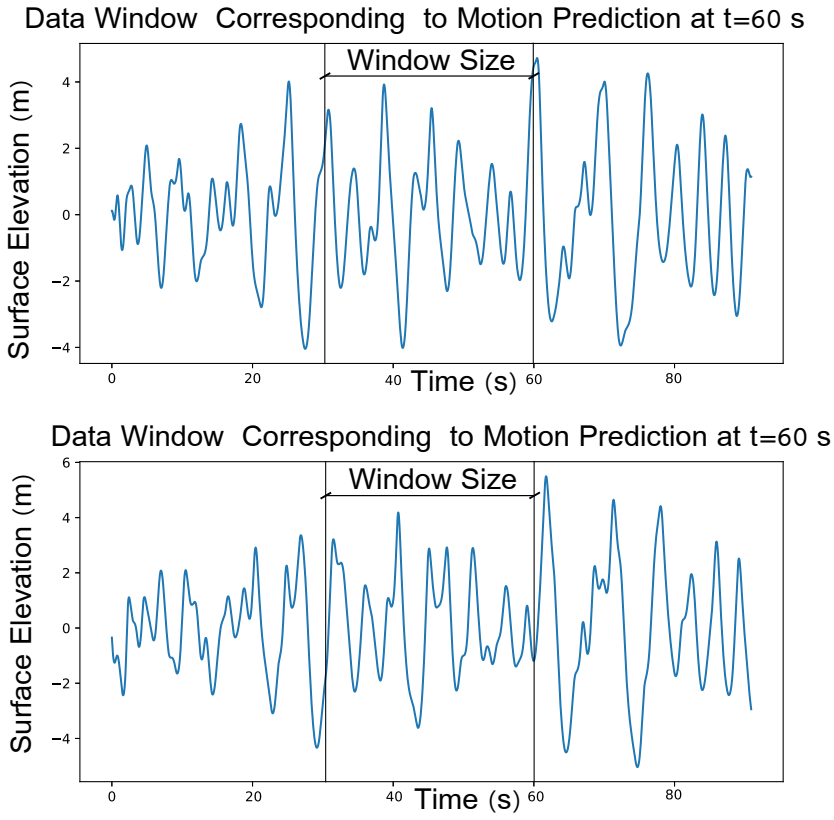

Figure 2-16: Profile of the wave in the longitudinal & transversal direction, respectively corresponding to test case one.

However, larger stencils can introduce noise into the solution for several reasons [40]. Firstly, round-off errors, which are inherent in the storage and manipulation of floating-point numbers, can accumulate in larger stencils due to the increased number of calculations [273]. This accumulation can appear as noise in the solution. Additionally, small errors, including round-off errors, can amplify over time, introducing significant noise into the solution. Stability is crucial, and careful selection of stencils is necessary to ensure it.

Nevertheless, larger stencils are capable of resolving higher frequency components in the solution. These components, if not physically meaningful or if they're artifacts of the initial or boundary conditions or the discretization, might manifest as noise. Lastly, if the stencil doesn't accurately represent the derivatives in the PDE, it can introduce errors that may appear as noise, particularly if they are not smoothly distributed.

To address these issues, careful stencil selection, taking into account the PDE, the domain, and the specifics of the problem is essential. Additionally, techniques such as filtering or smoothing, error control, and adaptive meshing can help manage potential

noise introduced by larger stencils.

The insights gained from numerical analysis [32] remain profoundly applicable when devising Machine Learning algorithms. If the data lacks sufficient information to accurately represent the physical process, attempts to learn complex interrelationships between quantities of interest are destined to falter from the outset. Conversely, inundating the algorithm with irrelevant information during training can be akin to introducing noise [129, 56]. This noise must subsequently be filtered, complicating the learning task. Thus, a well-invested effort in discerning relevant input and crafting an apt data processing framework to generate it can yield significant benefits throughout all stages of the process.

With the previous in mind, I design a stencil that feeds information into the neural network in a efficient and representative way (See fig. 2-15). Let $\theta(t) = (\theta_1(t), \theta_2(t), \theta_3(t))$ be a vector function that outputs *Heave*, *Pitch* and *Roll* of a vessel. We attempt to approximate:

$$\theta(t) = f_{NN}(P_1^k(t), P_2^k(t), ..., P_N^k(t))$$

where, $P_N^k(t)$ are N *wave probes* along the intersection of two vertical planes with the free surface. Where:

$$P_N^k(t) = (p_N(t), p_N(t - \Delta t)), p_N(t - 2\Delta t)), p_N(t - k\Delta t)) \tag{2.42}$$

Given that the process has a certain amount of memory it is of interest to have available for the predictions at time t information on wave elevations during a window of time before time t (See fig. 2-16). This window is designed in such a way that it provides additional useful information without going so far as to provided information that is so far into the past that has no effect in the current prediction. Training in this condition, as explained earlier, would add an additional task of filtering this irrelevant information. With this in mind, we feed to the neural network at any given instance $P_N^k(t)$, the wave elevation at time t and the k previous time steps. This window size k is one of the hyperparameters of the network that is tunned during the network architecture convergence.

2.5.5 Approximation of Continuous Functionals by Neural Networks and Application to Dynamical Systems

The methodology I put forward in this thesis draws inspiration from the theoretical foundations presented in [43], which demonstrates that Neural Networks (NNs) can approximate continuous functionals with high precision. Extending beyond nonlinear functional mapping (i.e., mapping from a space of functions into real numbers), we consider nonlinear operator mapping, which navigates from a space of functions to another function space. The theoretical foundations for this are provided in [44], with DeepONet [156] serving as a prime example. Several related studies support these findings [103, 102, 49, 231, 130]. LSTM networks are acknowledged for their robust modelling of complex dynamic physical systems. However, the examined data in this thesis may not strictly adhere to all the assumptions on which the theorems outlined in [43] are based. Specifically, we highlight the continuity of functions inputted into the functional modeling the physical system and the compactness of the sets where they are defined. This observation hints at a potential for further generalization of these results.

The critical findings from [43] can be paraphrased as follows: Under minimal conditions, a functional delineated on a compact set within $C[a,b]$ or $L^p[a,b]$ (infinite-dimensional spaces) can be approximated to an arbitrary degree of accuracy using a single-hidden-layer neural network. Specifically, for a compact set U in $C[a,b]$, σ (a bounded sigmoidal function), and $\mathcal{F}$, a continuous functional defined on U, the functional $\mathcal{F}(u)$ can be approximated for all $u \in U$ by:

$$\mathcal{F}(u) = \sum_{i=1}^{N} c_i \sigma \left(\sum_{j=0}^{m} \xi_{i,j} u\left(x_j\right) + \theta_i \right). \tag{2.43}$$

In the above equation, c_i, ξ_{ij}, θ_i represent real numbers, while $u(x_j)$ denotes the value of u at x_j.

The theorem and its corresponding explicit expression hold the potential to exert a broad influence on the foreseeable applications of neural networks in dynamical systems modeling [197, 199]. In this thesis, we have embraced this framework and executed its implementation for practical applications, marking the first instance in the realm of naval

hydrodynamics.

Throughout the case studies explored in this thesis, the output of the dynamical system - characterized here as vessels undergoing unsteady motions - is perceived as a functional response to a forcing term, in this case, ocean waves. Among other significant findings in this thesis, we underline the computational advantages brought about by the synergistic application of dynamic physical models and Recurrent Neural Networks (RNNs). This advantage becomes even more pronounced in the context of complex physical simulations. The simulations performed for this research indicate substantial computational savings in generating the motion dataset characterizing the vessel's behavior, all while upholding the desired accuracy levels. Moreover, the surrogate model developed in this process holds the potential to facilitate the creation of a 'digital twin' of the actual vessel. This development is especially relevant in ensuring secure and efficient operations, particularly when navigating under extreme weather conditions. This technology empowers sailors by providing high-quality information that supports them in managing these demanding situations over extended durations.

The initial focus involves modeling the two degrees-of-freedom (2DOF) motions (heave pitch) of a catamaran vessel under the influence of nonlinear 5th-order regular waves, and certain outcomes are depicted in fig. 2-19. We then transition to irregular stochastic waves that mimic real-life sea states, showcasing outcomes in figs. 2-21 to 2-25. Ultimately, we delve into approximating the three degrees-of-freedom (heave, pitch roll) motion of a conceptual DTMB battleship, as illustrated in fig. 2-27. Through these stages, we believe we have attained a state-of-the-art generalization of motions primarily governed by the Navier-Stokes equations. A succinct exploration of the underlying physics is provided in section 2.4.1, and for more in-depth information, refer to [53].

2.5.5.1 Representation of Dynamical Systems with Functionals

This section provides a summary of the extension of eq. (2.43) to dynamical systems, as described in [43]. This summary focuses on the crucial aspects that ensure the learnability of a dynamical system.

The *first* assumption grounding this approach is that the dynamical system can be

modelled as a continuous functional defined on a compact set. This is a non-trivial assertion, and its validity might not be easy to establish for the vessels analyzed in this study, even though the results obtained so far have been very promising.

The *second* assumption rests on the idea that the representation of functionals for the dynamical system can be achieved through a windowing operator. To articulate this more formally, suppose X_1 and X_2 are sets in $\mathbf{R}^{q_1}$ and $\mathbf{R}^{q_2}$, respectively, and these sets correspond to functions defined in $\mathbf{R}^n$. We perceive the dynamical system under consideration as a map from X_1 to X_2, such that for every $u \in X_1$, we have $Gu = v \in X_2$. With this in mind, an n-dimensional windowing operator W can be defined for $x \in X$, which is centered at α and has a width of $2a$:

$$\left(W_{\alpha,a}x\right)(\beta) = \begin{cases} x(\beta) & \text{if } \beta \in \Gamma_{\alpha,a} \\ 0 & \text{if } \beta \notin \Gamma_{\alpha,a} \end{cases}.$$

Using this window operator, we can restrict a non-empty set U of X_1, $U_{\alpha,a} = \left\{ u|_{\Gamma_{\alpha,a}}, u \in U \right\}$. This reads as, $u|_{\Gamma_{\alpha,a}}$ is the restriction of u to $\Gamma_{\alpha,a}$.

We consider that a map G from X_1 to X_2 has *approximately finite memory* if $\forall \epsilon > 0$ there is $a > 0$ such that:

$$\left| (Gu)_j(\alpha) - \left(GW_{\alpha,a}u\right)_j(\alpha) \right| < \epsilon, \quad j = 1, \ldots, q_2 \quad \forall \alpha \in \mathbf{R}^n, u \in U.$$

The aforementioned considerations profoundly influence the learnability of the dynamical process. They restrict the application of the functional approximation proof to those dynamical systems for which it's not necessary to have a complete historical record of states for their approximation. Moreover, to yield an explicit expression of the functional, the subsequent assumptions are essential:

1. If $u \in U$, then $u|_{\Gamma_{\alpha,a}} \in U$, $\forall \alpha \in \mathbf{R}^n, a > 0$.

2. $\forall\ \alpha \in \mathbf{R}^n, a > 0, U_{\alpha,a}$ is a compact set in $C_V\left(\prod_{k=1}^n [\alpha_k - a_k, \alpha_k + a_k]\right)$ or a compact set in $L_V^p\left(\prod_{k=1}^n [\alpha_k - a_k, \alpha_k + a_k]\right)$, where V stands for $\mathbf{R}^{q_1}$.

3. Then, if we let $(Gu)(\alpha) = ((Gu)_1(\alpha), \ldots, (Gu)_{q_2}(\alpha))$, consequently each $(Gu)_j(\alpha)$ will be a continuous functional defined over $U_{\alpha,a}$, with the corresponding topology

in $C_V\left(\prod_{k=1}^{n}[\alpha_k - a_k, \alpha_k + a_k]\right.$ or $\left. L_V^p\left(\prod_{k=1}^{n}[\alpha_k - a_k, \alpha_k + a_k]\right)\right.$.

Given the above results and following the process given in reference [43], we can find the extension of eq. (2.43) to dynamical systems in the following theorem:

Theorem: If U and G satisfy all the assumptions (1-3) made previously, and G is of *approximately finite memory*, then $\forall \epsilon > 0$, $\exists a > 0$, m a positive integer, $(m+1)^n$ points in $\prod_{k=1}^{n}[\alpha_k - a_k, \alpha_k + a_k]$, N a positive integer, constants $c_i(G, \alpha, a)$ that only depend on G, α, a, and $q_2 \times (m+1)^n$ - vectors ξ_i, $i = 1, \ldots, N$, such that:

$$\left| (Gu)_j(\alpha) - \sum_{i=1}^{N} c_i(G, \alpha, a)\sigma\left(\overline{\xi}_i \cdot \overline{u}_{q_1,n,m} + \theta_i\right) \right| < \epsilon, \quad j = 1, 2, \ldots, q_2.$$

In conclusion, it is important to highlight the *approximately finite memory* assumption. This forms the foundation for building the functional approximation as a sum of functionals defined in the subsets identified by the previously defined window operator. In our empirical analysis, we set a benchmark against a case which, we anticipate, will allow for a highly accurate representation of the functional from the subsets provided by the window operator, under the *approximately finite memory* assumption.

2.5.6 Cost functions and How they Allow to Weight Differently Multiple Data Properties

During the course of the thesis several cost functions have been explored to train the LSTM networks. This efford has had the objective of quantifying the effect of highlighting some features more than others in the training data. Overall, it has been observed that Mean Square Error (MSE) provides the best accuracy when training. However, given a low tolerance to having underpredictions in particular scenarios, it may be worth it to train the network to slightly over-predict on average. With this in mind I have been experimenting with cost functions such as Relative Entropy (RE) and Amplitude Weighted Mean Square Error (AWMSE).

2.5.6.1 Mean Square Error

The Mean Square Error (MSE) is an extensively employed statistical metric, often favored for evaluating the accuracy of a machine learning model or comparing the fits of different models.

MSE calculates the average of the squares of differences between predicted and actual values, offering a comprehensive measure of prediction error. This essentially allows for quantification of the discrepancy between the estimator (the dataset used to derive predictions) and the true values.

However, while the MSE is a powerful tool, it is not without limitations. For instance, its heavy penalty on larger errors due to the squaring operation can sometimes lead to a misleading representation of the model's performance, especially when dealing with outliers.

$$\text{MSE} = \frac{1}{n}\sum_{i=1}^{n}\left(Y_i - \hat{Y}_i\right)^2, \tag{2.44}$$

2.5.6.2 Relative Entropy

Inspired by [229] in the application of Relative Entropy to improve predictions of extreme events in dynamical systems, we explore in this Thesis the advantages of using Relative Entropy when predicting dynamics of ocean going vessels in extreme weather conditions.

In the study conducted by Qi and Majda [214], the application of Relative Entropy (or Kullback-Leibler divergence) as a loss function for training neural networks was examined. They utilized Relative Entropy to measure the divergence between the actual and predicted outcomes, after the application of the softmax function.

For a given $y \in \mathbb{R}^s$, the loss function they propose for a single datapoint is defined as follows:

$$\begin{aligned} L_{QM}(\mathbf{x}) &= KL\left(\sigma(f(\mathbf{x}))\left\|\sigma(\hat{f}(\mathbf{x}))\right.\right) + \alpha KL\left(\sigma(-f(\mathbf{x}))\left\|\sigma(-\hat{f}(\mathbf{x}))\right.\right) \\ &= \sum\left(\sigma(f(\mathbf{x}))\log\left(\frac{\sigma(f(\mathbf{x}))}{\sigma(\hat{f}(\mathbf{x}))}\right) + \alpha\sigma(-f(\mathbf{x}))\log\left(\frac{\sigma(-f(\mathbf{x}))}{\sigma(-\hat{f}(\mathbf{x}))}\right)\right) \end{aligned} \tag{2.45}$$

In the equation above, log is applied element-wise and the sum is taken over s dimensions. The softmax function, σ, is defined as:

$$\sigma(\vec{y})_i = \frac{e^{y_i}}{\sum_{j=1}^{K} e^{y_j}} \tag{2.46}$$

The softmax function ensures that outputs are weighted by the exponent of their magnitude, hence concentrating the learning on large magnitude features. This approach showed considerable effectiveness in the context of [214], where y was the high-dimensional solution to a partial differential equation (PDE).

However, this method can't be directly applied for scalar output y. This limitation arises because for any $y \in \mathbb{R}^1$, $\sigma(y) = 1$. Furthermore, Eq. (2.45) only emphasizes extreme values within a single output sample, but lacks the capacity to compare multiple y values.

However, it's feasible to develop analogous loss functions where an operator similar to soft-max is applied across multiple samples, instead of the indices within a single sample.

Suppose that f and $\hat{f}$ are such that the expectation of the exponential of $f(\mathbf{x})$, denoted as $\mathbb{E}_x[exp(f(\mathbf{x}))]$, and the expectation of the exponential of $\hat{f}(\mathbf{x})$, denoted as $\mathbb{E}_x[exp(\hat{f}(\mathbf{x}))]$, are finite and non-zero. This is a reasonable assumption that holds in the set containing $L^{\infty}(X)$. We can then define an operator $G(f)$ using the following formula,

$$\begin{aligned} G(f)(\mathbf{x}) &= e^{f(\mathbf{x})} p_x(\mathbf{x}) \left(\int_X e^{f(\mathbf{x})} p_x(\mathbf{x}), d\mathbf{x} \right)^{-1} \\ &= e^{f(\mathbf{x})} p_x(\mathbf{x}), \mathbb{E}_x \left[e^{f(\mathbf{x})} \right]^{-1}. \end{aligned} \tag{2.47}$$

This operator can be seen as a continuous equivalent of the soft-max function. The functions that result from applying G to an input are probability density functions on the set X. The value of $G(f)(\mathbf{x})$ is proportional to both the sample density $p_x(\mathbf{x})$ and $e^{f(\mathbf{x})}$.

$G(f)$ concentrates mass on those values of $\mathbf{x}$ that have non-vanishing likelihood under p_x and whose image under f is large, meaning it focuses on extreme values. Importantly, when f is linear, the operator defined in Eq. (2.47) is known as exponential tilting, a concept introduced by Efron in 1981, and has been used in importance sampling [62, 245].

We define the relative entropy loss L_{RE} as the Kullback-Leibler (KL) divergence between $G(f)$ and $G(\hat{f})$, represented mathematically as:

$$L_{RE}(\hat{f}) = KL\left(G(f)|\, G(\hat{f})\right). \tag{2.48}$$

In this equation, f denotes the true function we wish to approximate, and $\hat{f}$ is our approximation of this function. The operator $G(\cdot)$ represents a transformation applied to these functions.

In contrast to the formulation in [214], where normalization of $G(f)$ is applied across dimensions of y, we normalize across the input space X. This alternative approach enables exponential weighting of outputs by their magnitude, even when y is scalar.

We aim to minimize the relative entropy loss with respect to $\hat{f}$. Expanding equation (2.48) and discarding terms not dependent on $\hat{f}$, we arrive at:

$$\begin{aligned} L_{RE}(\hat{f}) &= \mathbb{E}_{\mathbf{x}}\left[\frac{e^{f(\mathbf{x})}}{\mathbb{E}_{\mathbf{x}}\left[e^{f(\mathbf{x})}\right]}\log\left(\frac{e^{f(\mathbf{x})}p_x(\mathbf{x}), \mathbb{E}_{\mathbf{x}}\left[e^{\hat{f}(\mathbf{x})}\right]}{e^{\hat{f}(\mathbf{x})}p_x(\mathbf{x}), \mathbb{E}_{\mathbf{x}}\left[e^{f(\mathbf{x})}\right]}\right)\right] \\ &\propto \mathbb{E}_{\mathbf{x}}\left[e^{f(\mathbf{x})}\log\left(e^{f(\mathbf{x})-\hat{f}(\mathbf{x})}, \mathbb{E}_{\mathbf{x}}\left[e^{\hat{f}(\mathbf{x})}\right]\right)\right] \\ &= \mathbb{E}_{\mathbf{x}}\left[e^{f(\mathbf{x})}(f(\mathbf{x}) - \hat{f}(\mathbf{x})) + e^{f(\mathbf{x})}\log\left(\mathbb{E}_{\mathbf{x}}\left[e^{\hat{f}(\mathbf{x})}\right]\right)\right]. \end{aligned} \tag{2.49}$$

In this final form, the relative entropy loss is the expectation over X of a term related to the difference between $f(\mathbf{x})$ and $\hat{f}(\mathbf{x})$, plus a term representing the logarithm of the expected value of $e^{\hat{f}(\mathbf{x})}$.

We encounter an issue with the term inside the log when trying to estimate the individual expectations in the Relative Entropy (RE) loss function using sums over the dataset. This problem is addressed using Jensen's inequality:

$$\log\left(\mathbb{E}_{\mathbf{x}}\left[e^{\hat{f}(\mathbf{x})}\right]\right) \geq \mathbb{E}_{\mathcal{D}}\left[\log\left(\frac{1}{m}\sum_{i=1}^{m} e^{\hat{f}(\mathbf{x}_i)}\right)\right] \log\left(\mathbb{E}_{\mathbf{x}}\left[e^{\hat{f}(\mathbf{x})}\right]\right) \geq \mathbb{E}_{\mathcal{D}}\left[\log\left(\frac{1}{m}\sum_{i=1}^{m} e^{\hat{f}(\mathbf{x}_i)}\right)\right] \tag{2.50}$$

In this inequality, the second and third expectations are taken over the random samples $\mathcal{D}$. The term on the left side, the expected log of the empirical average of $exp(\hat{f}(\mathbf{x}))$, is an underestimate of the term on the right. We therefore aim to find an upper bound for the left-hand side term that can be accurately approximated and minimized.

We use a Taylor expansion around α to find this upper bound, since the logarithm

can be bounded above by its first-order Taylor expansion at any α. This results in:

$$\log\left(\mathbb{E}_{\mathbf{x}}\left[e^{\hat{f}(\mathbf{x})}\right]\right) \leq \log(\alpha) + \frac{\mathbb{E}_{\mathbf{x}}\left[e^{\hat{f}(\mathbf{x})}\right] - \alpha}{\alpha}. \tag{2.51}$$

Here, α is a parameter that we choose to minimize the error in the Taylor approximation and make the bound as tight as possible. For α close to $\mathbb{E}_{\mathbf{x}}\exp(\hat{f}(\mathbf{x}))$, we select $\alpha = \mathbb{E}_{\mathbf{x}}\exp(f(\mathbf{x}))$ assuming that $f \approx \hat{f}$. This simplifies the upper bound of L_{RE} considerably, and terms not depending on $\hat{f}$ can be ignored. This upper bound can be easily approximated from the dataset $\mathcal{D}$ using:

$$L_{RE}(\hat{f}) = \mathbb{E}_{\mathbf{x}}\left[e^{\hat{f}(\mathbf{x})} - e^{f(\mathbf{x})}\hat{f}(\mathbf{x})\right] = \mathbb{E}_{\mathcal{D}}\left[\frac{1}{m}\sum_{\mathcal{D}}\left(e^{\hat{f}(\mathbf{x}_i)} - e^{f(\mathbf{x}_i)}\hat{f}(\mathbf{x}_i)\right)\right]. \tag{2.52}$$

Following [214], we note that the relative entropy loss only emphasizes the error on large positive values of $f(\mathbf{x})$. Therefore, we introduce a generalization to focus the loss function on predicting positive outliers, using the parameter λ to control this emphasis. This generalized loss function is:

$$L_{RE,\lambda}(\hat{f}) = L_{RE}(\hat{f}) + \lambda L_{RE}^{(-)}(\hat{f}), \tag{2.53}$$

where $L_{RE}^{(-)}(\hat{f})$ is defined by replacing f and $\hat{f}$ in Eq. (2.52) with $-f$ and $-\hat{f}$, respectively. The skew of the dataset determines the value of λ. In our case, since the data contains extremes that skew positive, we set $\lambda = 0.1$ to focus on predicting positive outliers.

2.5.6.3 Amplitude Weighted Mean Square Error

Amplitude Weighted Mean Square Error (AWMSE) is a variation of the Mean Square Error (MSE) that assigns different weights to the errors based on the amplitude of the quantity of interest. This is designed to place greater emphasis on deviations from the peak values of the variable that we are trying to approximate.

$$\text{AMMSE} = \frac{1}{n}\sum_{i=1}^{n}\left(Y_i - \hat{Y}_i\right)^2\left(\epsilon_1 - \epsilon_2 Y_i^2\right) \tag{2.54}$$

This approach can be especially beneficial in certain applications where errors of peak values are particularly undesirable or costly. However, like MSE, AWMSE can be influenced heavily by outliers, due to the added emphasis on large errors.

2.6 Nonlinear Functional Approximation for Modeling Nonlinear Motions

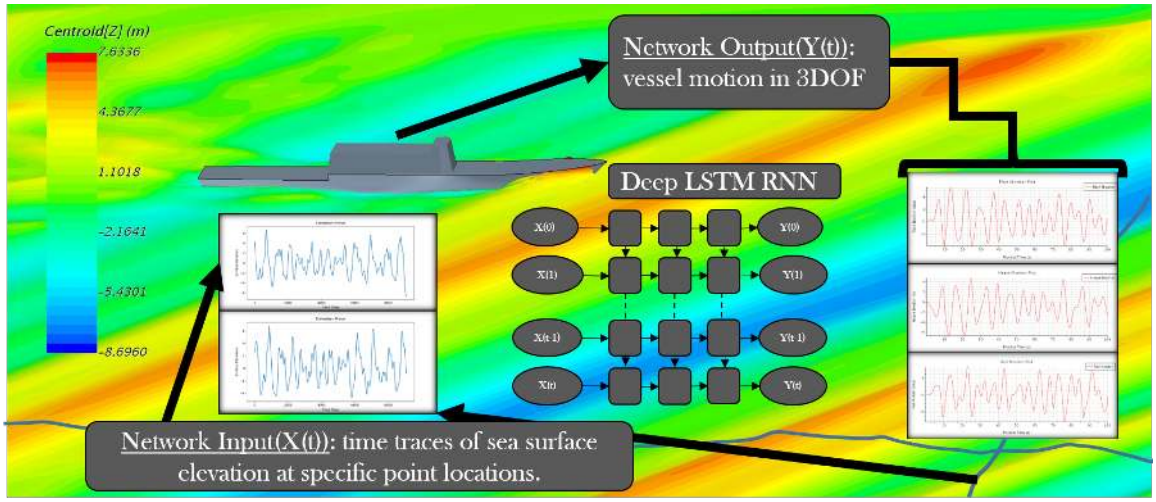

Figure 2-17: *Schematic of the physical problem simulated and inputs and outputs of the deep LSTM RNN.* The inputs for training are sea surface elevations in the form of time series, while the corresponding outputs are the vessel motions. Sea surface elevations are recorded at specific point locations that can be chosen from lines over the free surface. Vessel motions in the training cases are obtained from an URANS solver. Shown here as inputs ($X(t)$) are two unseen surface elevations, which serve as test cases in our simulation example for the DTMB vessel.

In order to formulate a nonlinear functional approximation for predicting motion dynamics, we have designed LSTM networks aimed at approximating the 2DOF or 3DOF motions of vessels traversing irregular waves in both head-on and oblique seas. We first demonstrate results related to a catamaran vessel navigating under the mild conditions of a WMO sea state 1. Subsequently, we showcase results of the DTBM vessel sailing through the extreme conditions found in a WMO sea state 8.

2.6.1 Catamaran Vessel

We commence our exploration with simple Stokes 5th-order waves, as shown in fig. 2-19. To distinguish between the two most frequently used gated RNN cells, we initially set up benchmark cases. This involves comparing two distinct regular waves and evaluating network sizes of 5 and 20 neurons for a single hidden layer, for both GRU and LSTM networks. The results, featured in fig. 2-19, indicate that for this specific application, LSTM networks exhibit greater expressiveness, a trend that becomes more apparent when the neuron count is increased from 5 to 20. As we progress, we will employ an LSTM network with a single hidden layer for regular waves, while for irregular waves, more complex networks will be adopted.

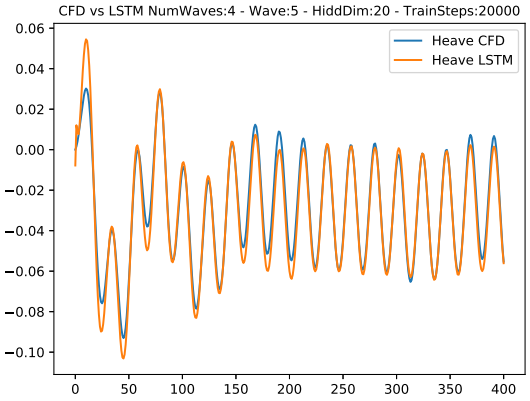

(a) LSTM test: 20 neurons, 1 hidden layer.

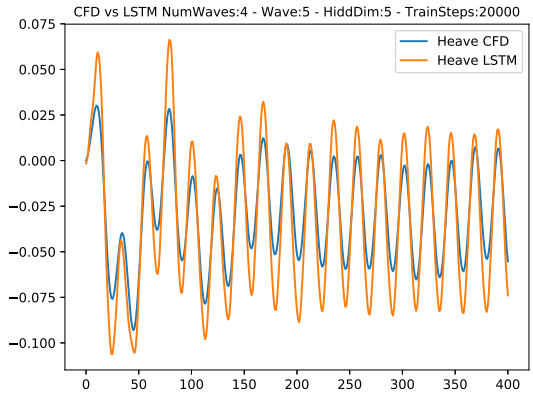

(b) LSTM test: 5 neurons, 1 hidden layer.

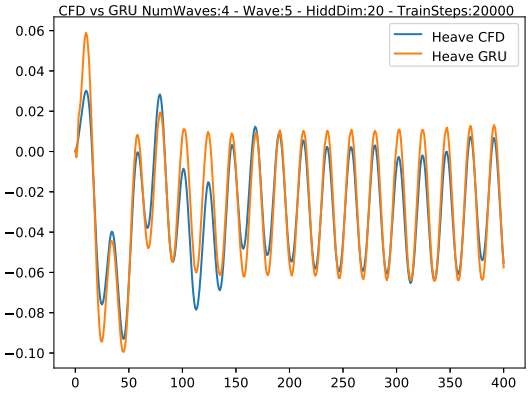

(c) GRU test: 20 neurons, 1 hidden layer.

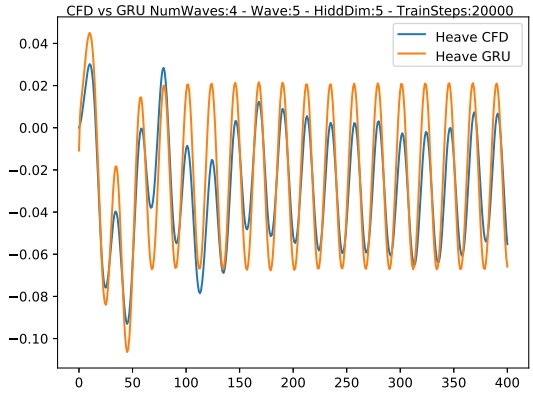

(d) GRU test: 5 neurons, 1 hidden layer.

Figure 2-18: *Comparison of LSTM and GRU for a 5th-order Stokes regular wave (wave amplitude is* $0.15m$*) for the catamaran vessel.* The data-set is composed of 5 waves of varying amplitude. The first 4 waves are used as training cases (for 20000 steps) while the last wave (shown here) is used for testing. Each time step corresponds to $\Delta t = 0.0625s$.

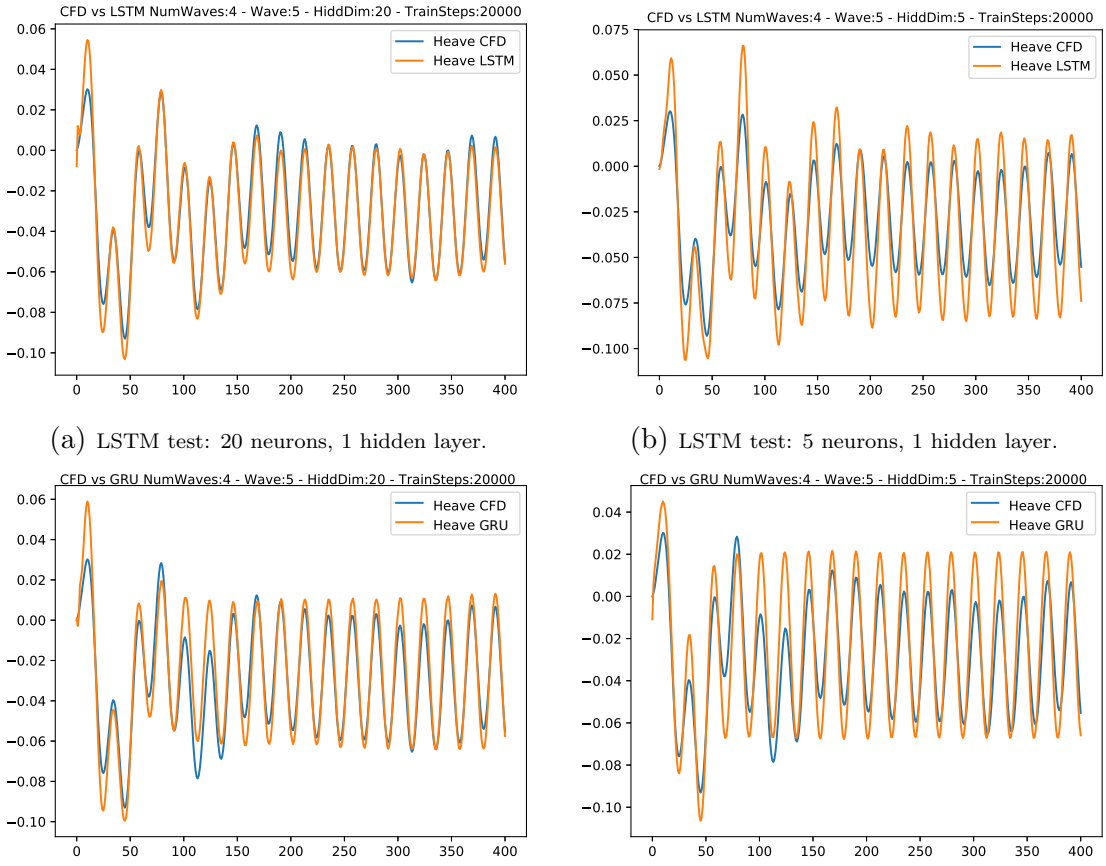

(a) LSTM test: 20 neurons, 1 hidden layer.

(b) LSTM test: 5 neurons, 1 hidden layer.

(c) GRU test: 20 neurons, 1 hidden layer.

(d) GRU test: 5 neurons, 1 hidden layer.

Figure 2-19: *Comparison of LSTM and GRU for a 5th-order Stokes regular wave (wave amplitude is* $0.15m$*) for the catamaran vessel.* The data-set is composed of 5 waves of varying amplitude. The first 4 waves are used as training cases (for 20000 steps) while the last wave (shown here) is used for testing. Each time step corresponds to $\Delta t = 0.0625s$.

Upon selecting the type of neural network, we conducted tests with stochastic waves designed to emulate the typical sea states a catamaran vessel might encounter. It was observed that the pitch angular motion was modeled with greater accuracy compared to the vertical motion. Subsequently, we proceeded to enhance the network's architecture, increasing its expressiveness while avoiding overfitting issues.

The data used for training and testing the networks is illustrated in fig. 2-20. The outcomes of this study are presented in figs. 2-21 to 2-25. Specifically, fig. 2-21 illustrates the heave and pitch motions predicted by an LSTM network featuring 20 neurons and 1 layer. The left column showcases predictions based on the training data, while the right column presents predictions for unseen data. The training dataset consists of three

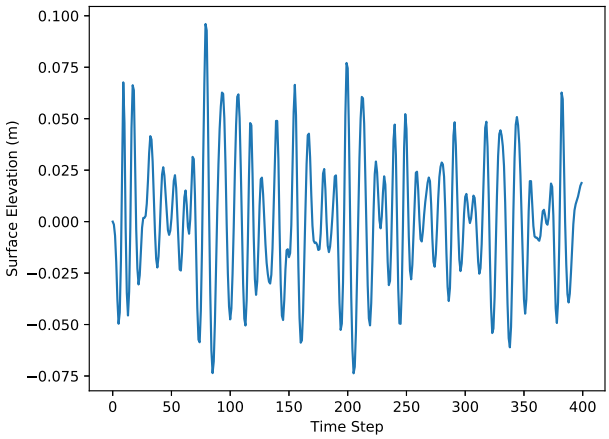

(a) Network input figs. 2-21a and 2-21c.

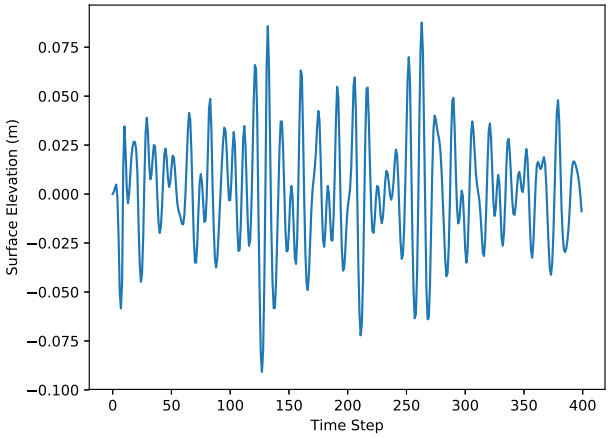

(b) Network input figs. 2-21b and 2-21d.

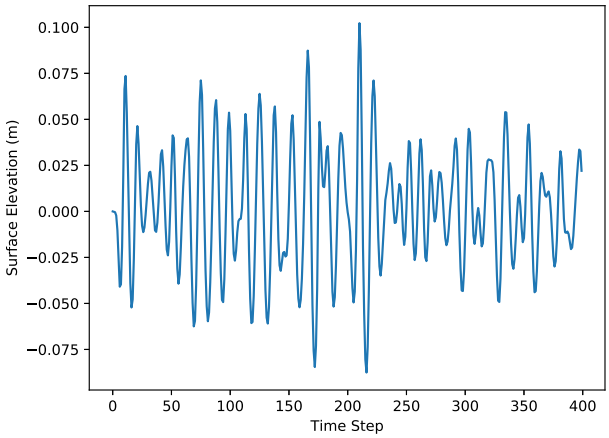

(c) Network input fig. 2-22.

Figure 2-20: *LSTM network inputs for 2DOF catamaran vessel in irregular head seas.* Each time step corresponds to $\Delta t = 0.0625s$.

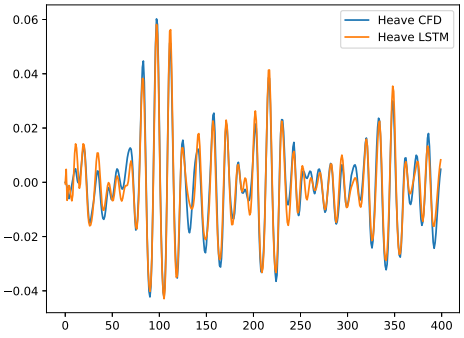

(a) Vertical vessel motion. Training based on three different sequences.

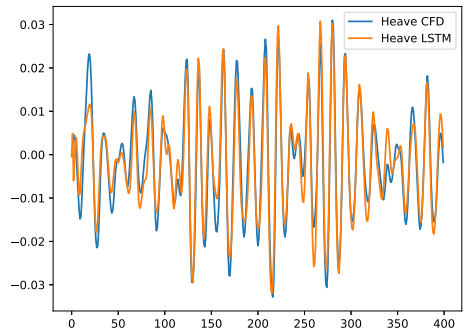

(b) Vertical vessel motion. Testing based on the training of (a).

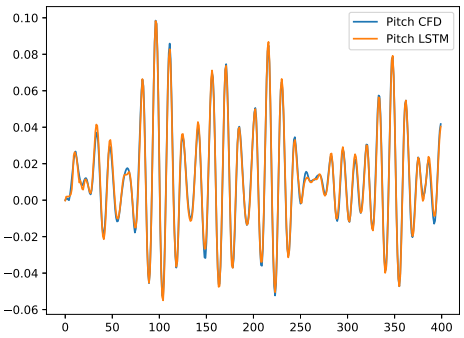

(c) Angular vessel motion. Training based on three different sequences.

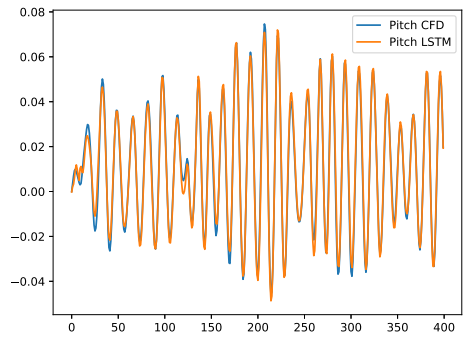

(d) Angular vessel motion. Testing based on the training of (c).

Figure 2-21: *LSTM network (20 neurons, 1 layer) for the catamaran vessel subject to irregular waves.* The left column (a, c) shows the vertical and angular vessel motions after training with three different sea state realizations; one such realization is shown in fig. 2-21a. The right column (b, d) shows the vertical and angular vessel motions for testing given the inputs indicated in fig. 2-21b. Each time step corresponds to $\Delta t = 0.0625s$.

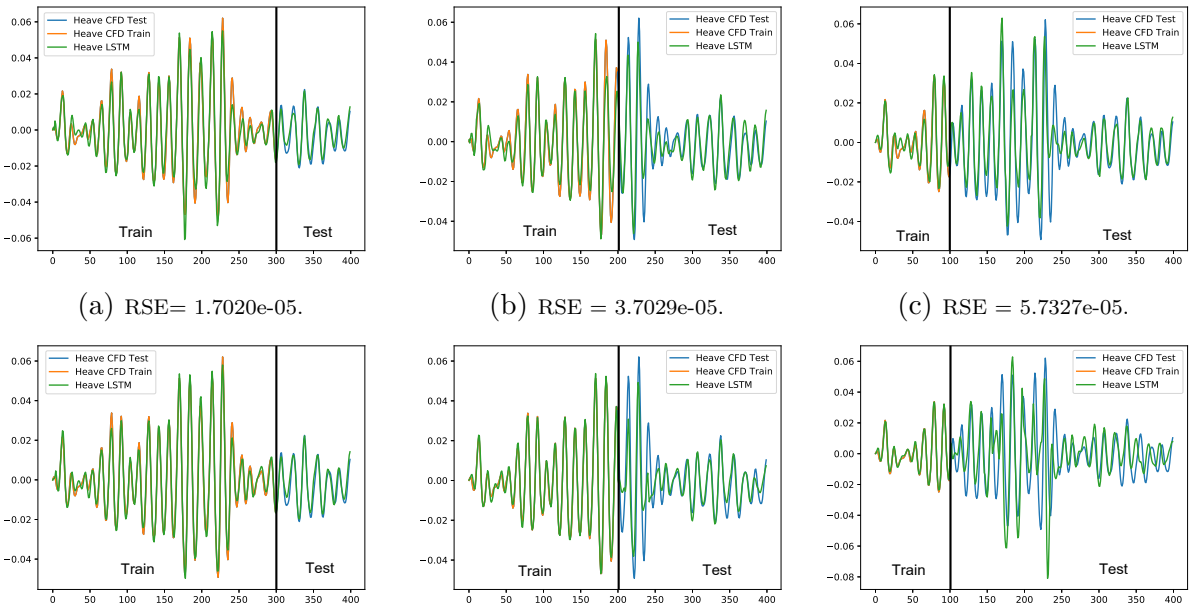

(a) RSE= 1.7020e-05. (b) RSE = 3.7029e-05. (c) RSE = 5.7327e-05.

(d) RSE = 8.4781e-06. (e) RSE = 4.5099e-05. (f) RSE = 2.5656e-04.

Figure 2-22: *Vertical motion of the catamaran vessel using two LSTM networks with 1 layer and 15 neurons (upper row) and 3 layers and 15 neurons (lower row).* The left column corresponds to 2/3 training data from fig. 2-20c, the middle column corresponds to 1/2 of the training data, and the right column corresponds to 1/4 of the training data. Each time step corresponds to $\Delta t = 0.0625s$.

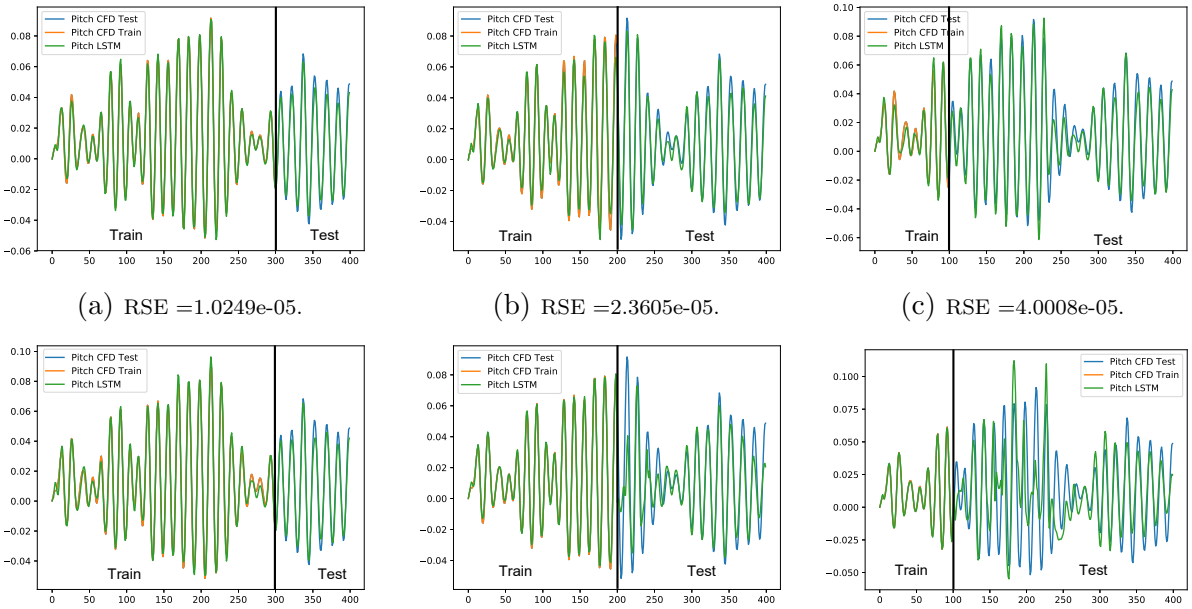

(a) RSE =1.0249e-05. (b) RSE =2.3605e-05. (c) RSE =4.0008e-05.

(d) RSE = 1.2446e-05. (e) RSE = 1.1840e-04. (f) RSE = 4.3936e-04.

Figure 2-23: *Angular motion of the catamaran vessel using two LSTM networks with 1 layer and 15 neurons (upper row) and 3 layers and 15 neurons (lower row).* The left column corresponds to 2/3 training data from fig. 2-20c, the middle column corresponds to 1/2 of the training data, and the right column corresponds to 1/4 of the training data. Each time step corresponds to $\Delta t = 0.0625s$.

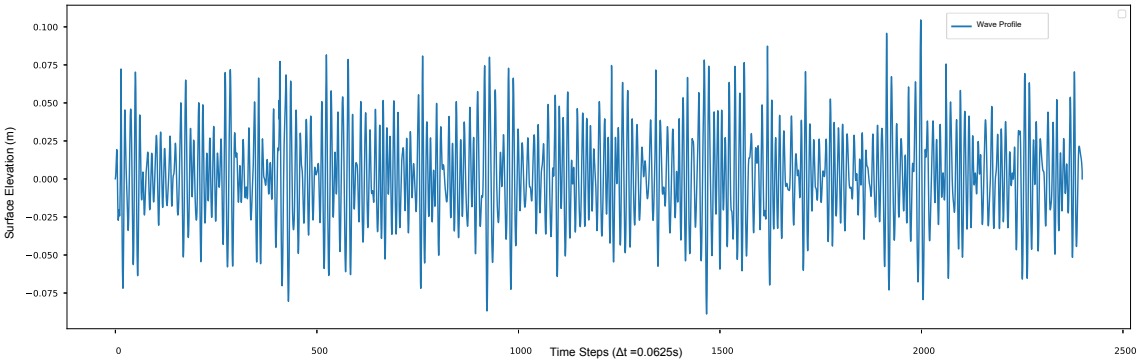

(a)

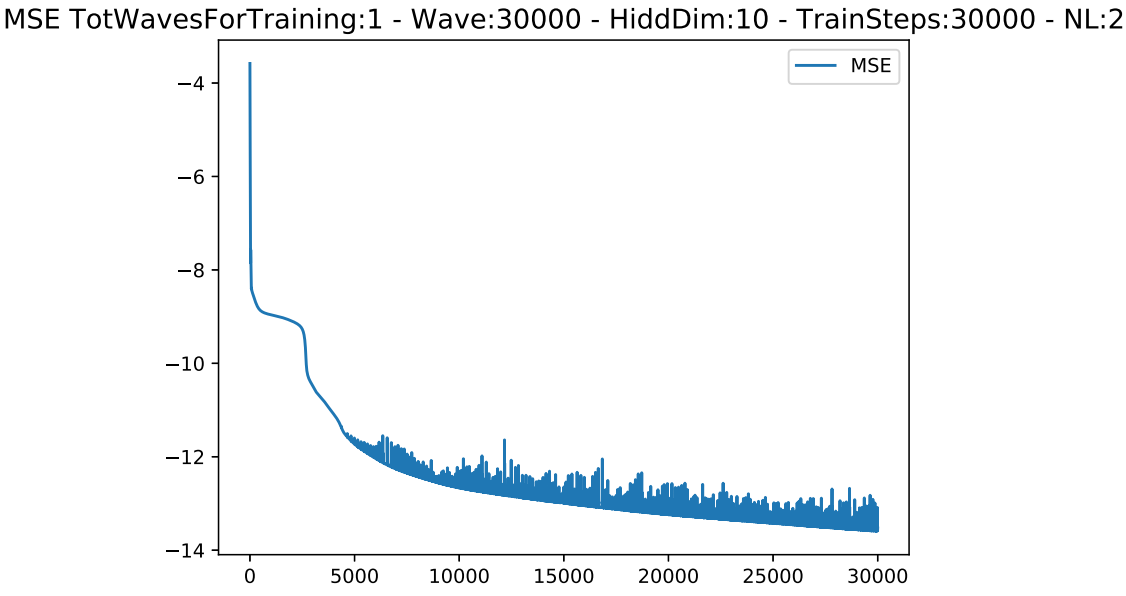

(b)

Figure 2-24: Figure (a) shows the surface elevation input to the network. Each time step corresponds to $\Delta t = 0.0625s$. Mean squared error (MSE) ploted in (d), early training stop performed to prevent over-fitting.

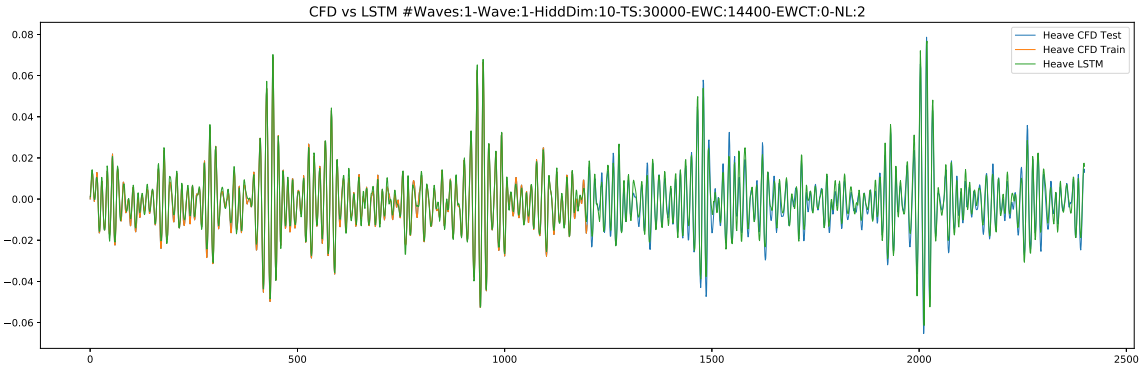

(a)

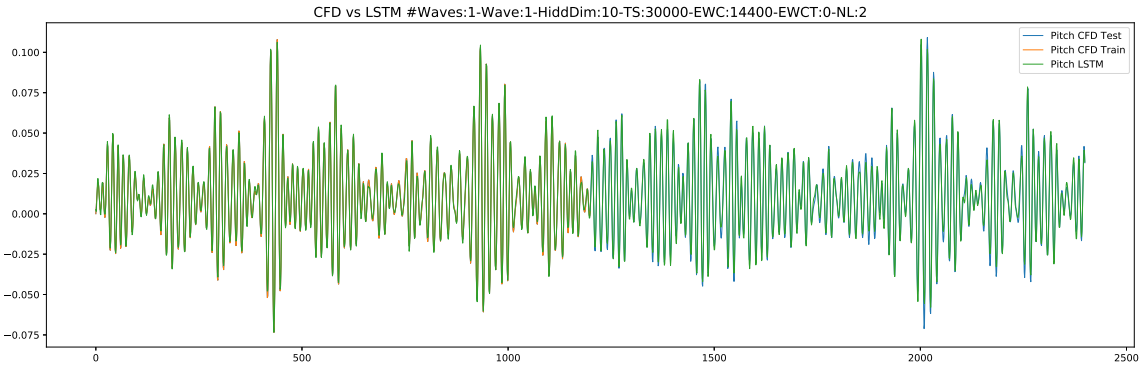

(b)

Figure 2-25: *Long-time predictions of vertical (a) and angular (b) motions of the catamaran vessel using a LSTM network with 2 layers and 10 neurons.* The vertical line in (a),(b) denotes the beginning of testing. Each time step corresponds to $\Delta t = 0.0625s$.

distinct sequences for surface elevation, akin to the one demonstrated in fig. 2-20a. The testing predictions, displayed in the right column of figure 6, are generated from surface elevation inputs depicted in fig. 2-20b. It is evident that this shallow network effectively approximates the two degrees of freedom (DOF) catamaran vessel subjected to irregular waves.

A more systematic exploration of network architectures and training extents is depicted in figures 7 and 8. These figures demonstrate outcomes from a set of 64 parametric variations involving five network architecture parameters: neurons, hidden layers, training steps, the number of sequences in the training process, and the fraction of a sequence utilized in training. In the initial six plots, sub-figures 2-22a - 2-22f, we analyze the evolution of motion predictions as the fraction of sequence used in the training process (2-22a $\rightarrow$ 2-22c or 2-22d $\rightarrow$ 2-22f) or the number of hidden layers (2-22a $\rightarrow$ 2-22d or 2-22b $\rightarrow$ 2-22e or 2-22c $\rightarrow$ 2-22f) is varied. The second set of subplots in fig. 2-23 (2-23a - 2-23f) mirrors the first set, with the only difference being that instead of vertical motion (heave), angular motion (pitch) is plotted. Importantly, accurate predictions for both heave and pitch are achievable even with a small training dataset, as long as the LSTM architecture is adjusted to mitigate overfitting concerns.

The accuracy of long-term LSTM predictions is examined in fig. 2-25a-b. Additionally, fig. 2-24b displays the convergence history of the loss function. The inputs for the LSTM network are presented in fig. 2-24a. The network, comprising 2 layers and 10 neurons, is trained on the first half of the sea surface elevation time series and generates predictions for vertical and angular motions in the second half. As evident, the motion dynamics are predicted with remarkable accuracy and stability over the long term, corroborating the findings from unused data obtained via the CFD solver.

To summarize, we have noted the following primary trends:

1. As the quantity of information provided to the network decreases (compare column 2-22a $\downarrow$ 2-23d to 2-22c $\downarrow$ 2-23f), it becomes evident that the network's accuracy diminishes, and it becomes more susceptible to overfitting.

2. Overfitting is accentuated in subplots 2-22f and 2-23f. This is to be expected as they have the highest number of parameters due to their three hidden layers. Thus,

as we enhance the expressive power of the network, it becomes necessary to also increase the volume of information provided for training.

3. LSTM networks function as stable long-term predictors concerning the amplitude, frequency, and phase of vessel motions.

We have drawn the following conclusions from our studies concerning the network architecture convergence:

1. Given the available data, a hidden layer with 15 neurons accurately approximates the functional aspect of the catamaran motions for a mild sea state.

2. With ample data, these predictions can be improved with more expressive networks. However, such networks are considerably prone to overfitting. This is apparent as accuracy in figs. 2-22d and 2-23d is better or equal to that in figs. 2-22a and 2-23a. However, it noticeably deteriorates when we reduce the amount of information in the training cases. To illustrate this, it can be observed that the accuracy in figs. 2-22f and 2-23f is inferior to that in figs. 2-22c and 2-23c.

3. The data modeling framework is both feasible and practical, and additionally, it's incredibly fast. In particular, it took around 120 hours (on a 20-processor computer) to run the CFD solver to obtain the training labeled data. In contrast, training the LSTM takes approximately half an hour on a GPU, and obtaining predictions in our testing experiments takes only a fraction of a second. For instance, in figs. 2-22c and 2-23c, we can train the network on the first quarter of the sequence and reproduce the remaining three-quarters, at a negligible cost compared to using CFD for the entire sequence.

2.6.2 DTBM Vessel - Single Spectra Predictions

We extend our investigation to a more challenging scenario by introducing a third degree of freedom (DOF) to model the motions of a second vessel in an extreme sea state (see fig. 2-17). This 3DOF captures the vessel's rolling motion around its longitudinal axis.

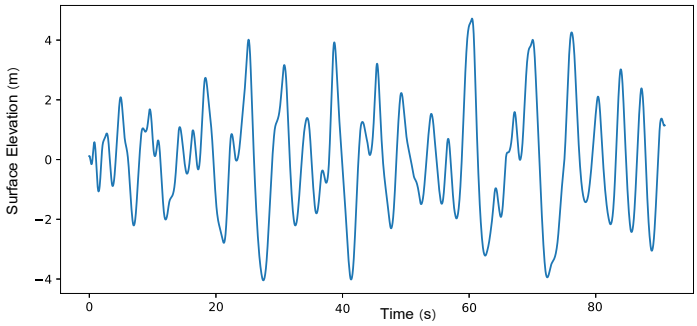

(a) Profile of the wave in the longitudinal direction corresponding to test case one.

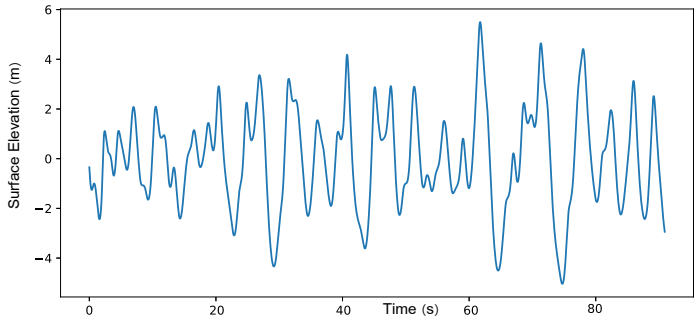

(b) Profile of the wave in the transversal direction corresponding to test case one.

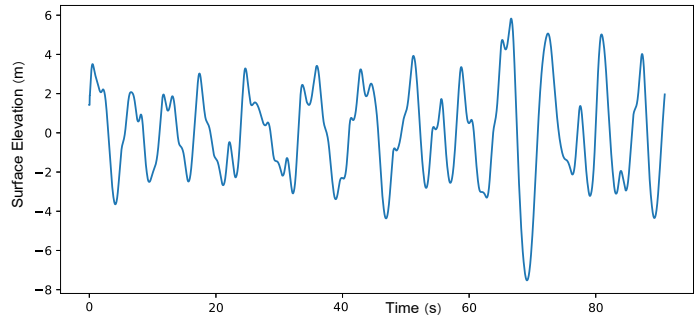

(c) Profile of the wave in the longitudinal direction corresponding to test case two.

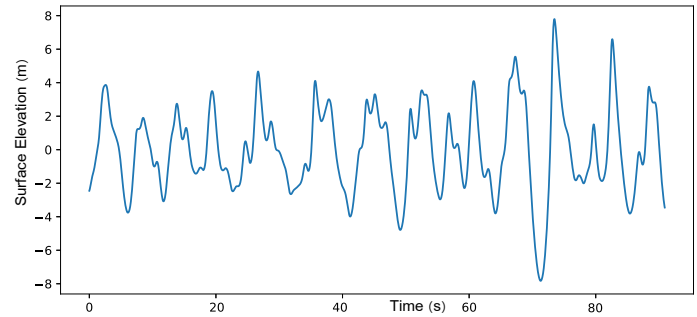

(d) Profile of the wave in the transversal direction corresponding to test case two.

Figure 2-26: *Network surface elevation inputs for the DTMB vessel.* They are two-dimensional and represent a long crested irregular oblique waves. Each time step is $\Delta t = 0.2s$.

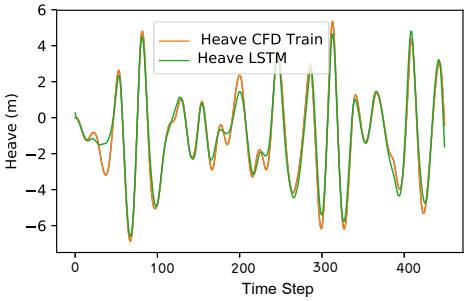

(a) RSE = 0.0380

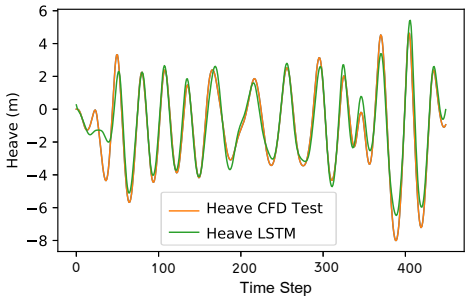

(b) RSE = 0.0773

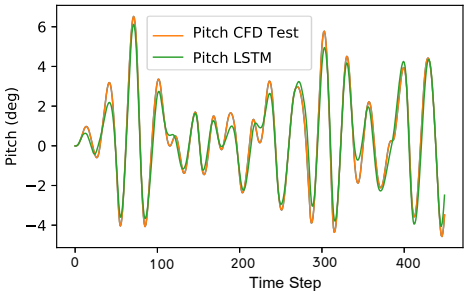

(c) RSE = 0.0444

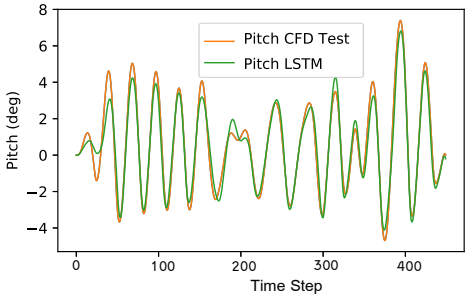

(d) RSE = 0.0463

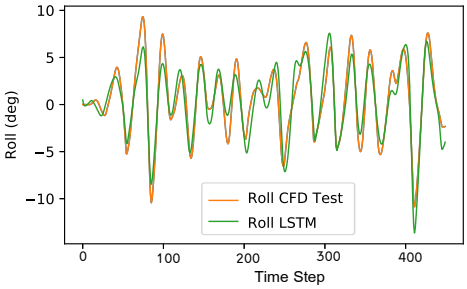

(e) RSE = 0.1490

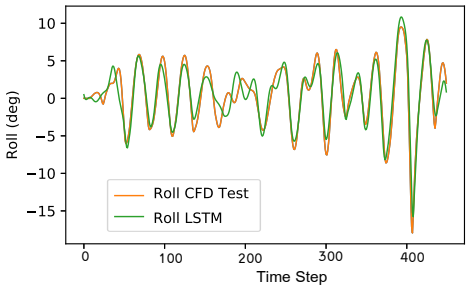

(f) RSE = 0.1215

Network	Case	Heave RSE	Pitch RSE	Roll RSE	Overall RSE	Layers	Neurons	Train Steps
1	Test 1	0.0770	0.0734	0.1595	0.192	8	90	5000
	Test 2	0.0910	0.0747	0.1257				
2	Test 1	0.0674	0.0685	0.1910	0.220	8	70	5000
	Test 2	0.1245	0.0962	0.1210				
3	Test 1	0.0380	0.0444	0.1490	0.165	4	90	5000
	Test 2	0.0773	0.0463	0.1215				
4	Test 1	0.0731	0.0658	0.1919	0.230	16	70	5000
	Test 2	0.0547	0.0399	0.1634				

(g) Testing errors of four different LSTM networks for DTBM vessel in WMO sea state 8 at Froude number 0.4.

Figure 2-27: *LSTM test results (4 hidden layers, 90 neurons) network architecture 3, RSE=0.165.* Heave, Pitch and Roll motion dynamics of a notional DTBM battleship sailing in WMO sea state 8 at Froude number 0.4. The inputs provided to the network are shown in fig. 2-26 (a),(b) (left column) and fig. 2-26 (c),(d) (right column) corresponding to 5000 train steps. Each time step is $\Delta t = 0.2s$.

Unlike heave and pitch, rolling is significantly swayed by the liquid's viscous properties, which play a crucial role in marine dynamics.

While heave and pitch motions can be approximated well using stiffness and mass matrices, the nonlinearity of roll motion, especially under the influence of viscous effects, necessitates a more tailored approach. In more challenging conditions like the extreme sea state 8 — a state which tests the bounds of many marine models — the foundational linear assumptions of conventional marine modeling become less reliable.

Traditional methods, such as the Boundary Element Methods (BEMs), while invaluable in simpler scenarios, have inherent limitations when it comes to more complex marine dynamics. BEMs are largely based on linear potential flow theory, making them less equipped to handle viscous effects, turbulent flow, or advanced non-linear wave interactions. Additionally, the Green's function employed in BEMs may present singularity issues, especially in proximity to boundaries. As wave frequencies climb, BEMs can become particularly computationally intensive, due to the increased discretization of the boundary. This also poses challenges when trying to handle non-linear wave-structure interactions [74, 153], dynamic free surface interactions, especially those intersecting with the body, and very thin structures. This limitation in handling viscous effects is crucial, especially when predicting wave loads, motion response, and wave-structure interactions near the sea surface [37] further explores these limitations, emphasizing the challenges BEMs face in such intricate scenarios.

Contrastingly, the Unsteady Reynolds average Navier-Stokes (URANS) approach offers a more refined model [290], though it is computationally taxing and may not always be broadly applicable. As a solution, to approximate the 3DOF (heave, pitch, and roll) for the DTBM vessel in these treacherous sea conditions, our focus shifted towards the development of a surrogate model via functional learning. This approach leans heavily on the capabilities of deep recurrent neural networks, especially those furnished with LSTM (Long Short-Term Memory) cells, celebrated for their efficiency in managing sequential data, akin to sea surface time series.

Just as with the methodology presented in section 2.6.1, deep recurrent neural networks featuring LSTM cells are harnessed to approximate the functionals that provide

precise vessel motion estimations based on sea surface time series. Four examples of architecture convergence are shown in fig. 2-27, each delineating 3DOF motions. Test sequences are curated from unseen sea state realizations illustrated in fig. 2-26. The LSTM-predicted motions (heave, pitch, and roll) are contrasted against CFD code predictions (using previously unused data) to calculate the relative squared error (RSE)

$$RSE = \frac{\sum_{j=i}^{n} \left(Y_i - \hat{Y}_i\right)^2}{\sum_{j=1}^{n} \left(\hat{Y}_i - mean(\hat{Y}_i)\right)^2} \tag{2.55}$$

The architecture convergence exhibits consistent and accurate approximations of vessel motions in extreme sea states, although roll motion performance is slightly inferior due to its inherent complexity. The best-performing network architecture is depicted in Fig. 2-27, showcasing accurate predictions for roll motions with significant amplitudes (around 20 degrees), as well as heave and pitch motions. Refer to the table in fig. 2-27 for a summary of all tested LSTM architectures.

Overall, the architecture convergence findings align with those in section 2.6.1. More extensive data would allow for training more sophisticated networks, enhancing motion prediction accuracy. Such data could potentially be sourced from various channels, including real vessels operating under harsh weather conditions, such as military, coastguard, or rescue vessels. To mitigate the computational load of training, we can adopt multifidelity training, as demonstrated in [167]. This approach combines low-fidelity data from tools like CAT-5D with high-fidelity URANS data, improving efficiency while maintaining accuracy.

2.6.3 DTBM vessel - Multiple Spectra Predictions

So far, our exploration has been centered around evaluating the potential of recurrent neural networks to approximate ship motions using sea elevation data. However, our investigations have been constrained to a somewhat limited scenario where the predictions stem from a static statistical environment. This limited perspective arises from our exclusive focus on individual sea states, which, although instructive, don't encapsulate the diverse conditions vessels might encounter. Real-world maritime scenarios see ves-

sels navigating a spectrum of conditions, shaped by myriad factors like seasonal shifts, meteorological variations, and geographical nuances [65].

It's essential to recognize that as ships traverse vast oceanic expanses, they often encounter a blend of different sea states, each with unique spectra. This maritime tapestry makes multispectra predictions particularly invaluable. They offer a richer, more composite understanding of ship behavior, factoring in the nuanced interplay of multiple sea states that a vessel might grapple with during its journey.

However, an even more intricate challenge lies in the realm of short-crested seas [257], though our current modeling hasn't ventured into predicting their behavior yet. Unlike their long-crested counterparts that largely feature unidirectional wave propagation, short-crested seas are characterized by waves traveling in multiple directions. This multidirectional propagation is largely a result of intricate interactions between various weather systems. As multiple weather fronts converge, interact, and sometimes conflict, they give rise to these complex wave patterns. Such interactions can be due to temperature gradients causing atmospheric instabilities, converging wind patterns, or the influence of underlying oceanic currents and topographies. The resultant wave patterns are less predictable and manifest a more tangled relationship between the encountered wave spectra and the resultant ship motions. This makes predicting the most optimal vessel heading in such seas a formidable task [106], given the heightened risk of rolling [198], yawing, or even more severe reactions [195] like broaching.

Recognizing these intricacies and the ambiguity around encountered sea states, our study now pivots towards predicting vessel motions for unlabeled sea states [207]. Drawing from 147 random seeds across three distinct sea states (49 seeds for each), we embrace a heightened modeling challenge. Not only must the model predict vessel motions, but it must also discern the specific sea state from the sea elevation data. This nuance is of particular import in severe sea states. Here, standard assumptions of linearity fall short, with Response Amplitude Operators (RAOs) subject to fluctuations due to myriad factors — wave slope, ship hull design intricacies, and a host of nonlinear events, from wave breaking to slamming [122].

To offer a more granular understanding of these nonlinear dynamics on vessel motions,

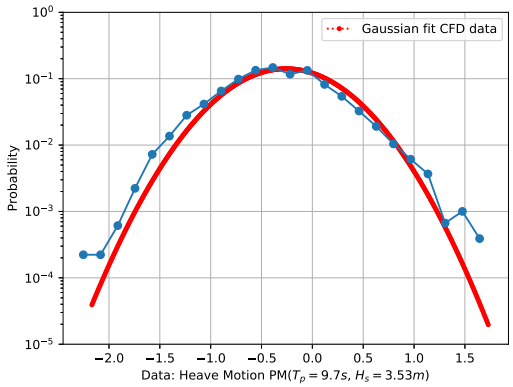

(a) Heave motions PDF.

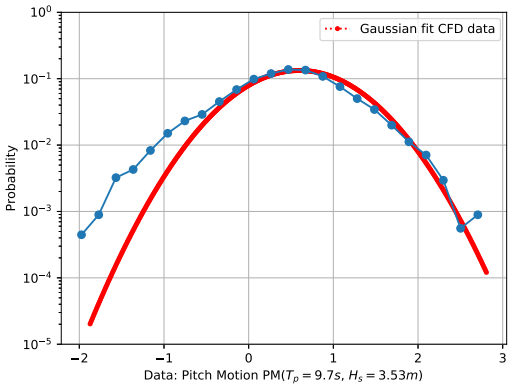

(b) Pitch motions PDF.

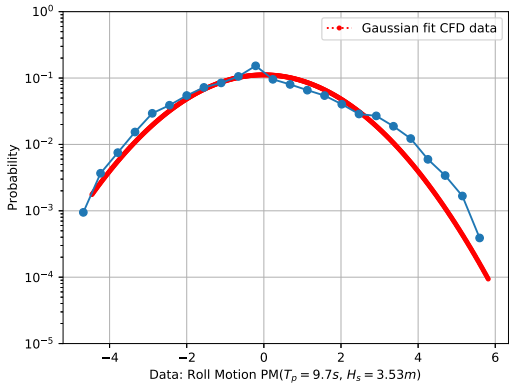

(c) Roll motions PDF.

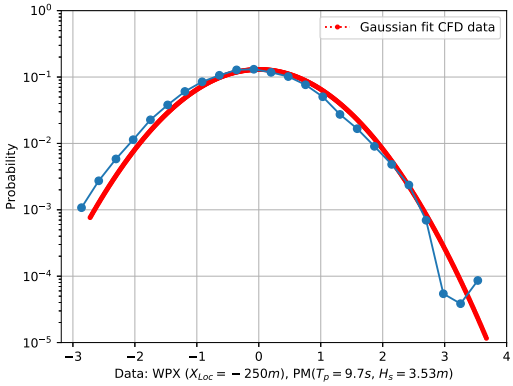

(d) Wave probe PDF.

Figure 2-28: Probability density functions (PDFs) of vessel motions and sea state. Deviations from typical Gaussian motions can be seen comparing to a least squares Gaussian fit. Froude number 0.4, time step $\Delta t = 0.2s$, $T_p = 9.7s$, $H_s = 3.53m$, $v = 30kt$.

we meticulously scrutinize both the simulated motion statistics (our benchmark) and those interpreted by the Machine Learning algorithm. This exercise lets us gauge the neural network's efficacy in tracking and parsing these complex statistics across the sea states in our study. Our empirical findings, captured in figs. 2-28 to 2-30, present probability density functions for vessel movements and point-wise sea elevations across each examined sea state.

With this setup, our aim is to present an initial step towards leveraging neural network-based algorithms to encapsulate information vital for predicting vessel motions, in regular and extreme weather conditions. Non-linearity of the sea state and resulting vessel motions can be quantified by measuring deviation from the best fitting Gaussian distribution.

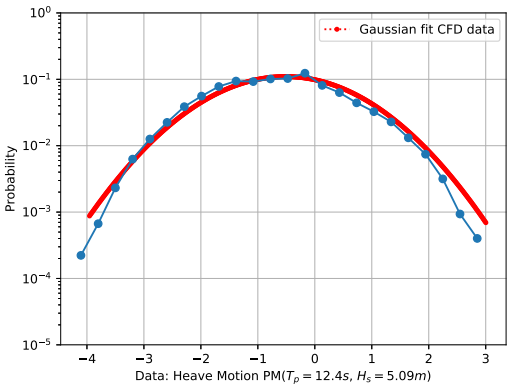

(a) Heave motions PDF.

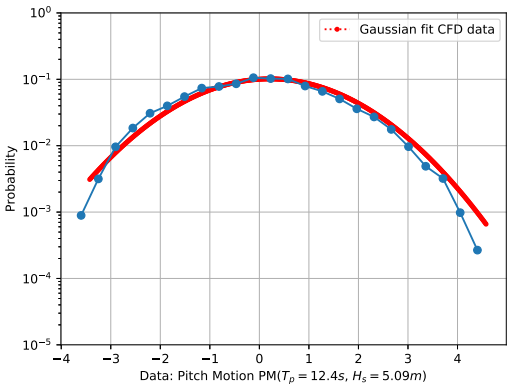

(b) Pitch motions PDF.

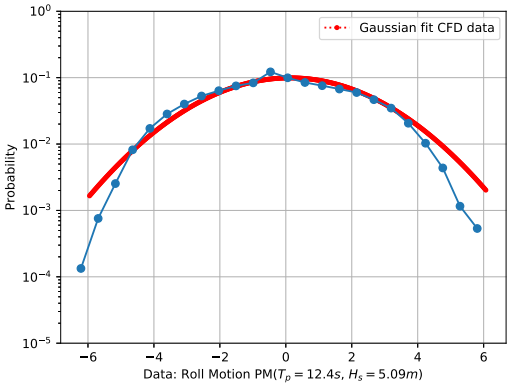

(c) Roll motions PDF.

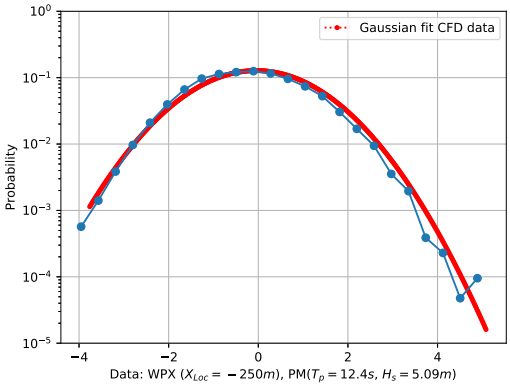

(d) Wave probe PDF.

Figure 2-29: Probability density functions (PDFs) of vessel motions and sea state. Deviations from typical Gaussian motions can be seen comparing to a least squares Gaussian fit. Froude number 0.4, time step $\Delta t = 0.2s$, $T_p = 12.4s$, $H_s = 5.09m$, $v = 30kt$.

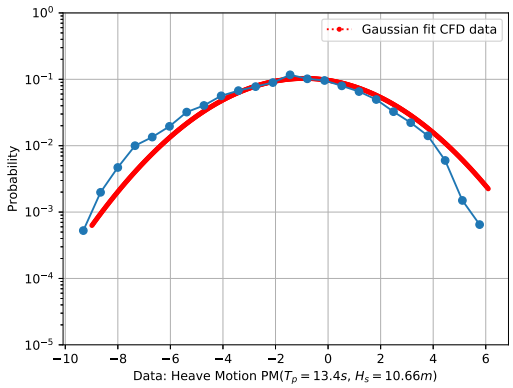

(a) Heave motions PDF.

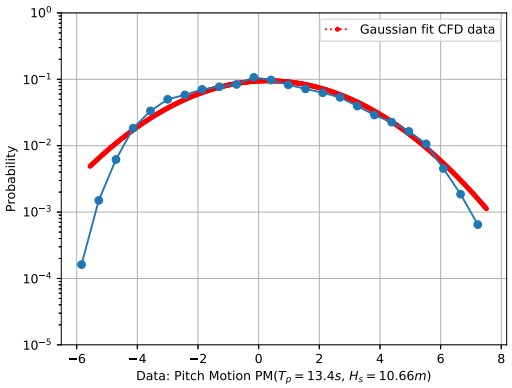

(b) Pitch motions PDF.

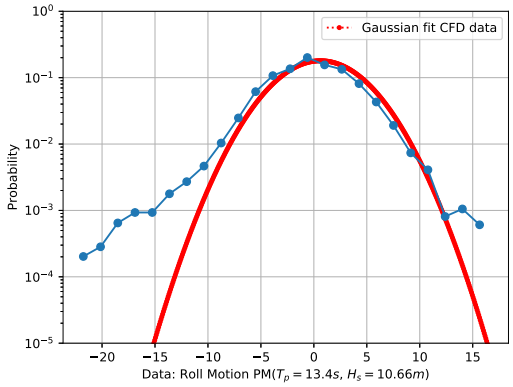

(c) Roll motions PDF.

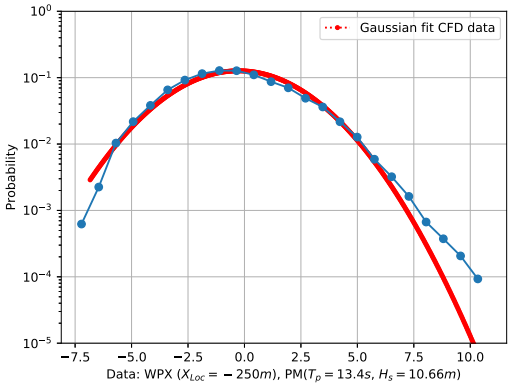

(d) Wave probe PDF.

Figure 2-30: Probability density functions (PDFs) of vessel motions and sea state. Deviations from typical Gaussian motions can be seen comparing to a least squares Gaussian fit. Froude number 0.4, time step $\Delta t = 0.2s$, $T_p = 13.4s$, $H_s = 10.66m$, $v = 30kt$.

These comparisons are presented for the three considered Sea States in figs. 2-28 to 2-30. The deviations from the fitted Gaussian distributions increase with wave steepness in the following order: PM($T_p = 13.4s$, $H_s = 10.66m$) > PM($T_p = 9.7s$, $H_s = 3.53m$) > PM($T_p = 12.4s$, $H_s = 5.09m$), given that the approximate wave steepness H_s/λ_p is: $0.037 > 0.024 > 0.021$, respectively. Wave non-linearity in the compiled data results from imposing steep linear waves with a Pierson–Moskowitz spectrum that evolves non-linearly thanks to second order spatio-temporal numerical solvers in the finite volume computational mesh, given that they are too steep to exist in reality.

2.6.3.1 Network Architecture Convergence

The dataset used in this section can be inspected in great detail in appendix A. In figs. A-1 to A-3, the network wave probes along the longitudinal direction of the vessel are presented. In figs. A-4 to A-6, the network wave probes along the transversal direction of the vessel can be consulted. The resulting motions to those sea elevation inputs are presented in figs. A-7 to A-9. The amplitude spectrum of network wave probes along the longitudinal and transversal direction of the vessel can be inspected in figs. A-10 to A-12 & figs. A-13 to A-14 respectively. The amplitude spectrum corresponding to the vessel motions can be compared to the inputs and are presented in figs. A-16 to A-18. Lastly, to understand overall trends of over-predicting or under-predicting we calculate the average difference of the absolute values of the predictions to the reference predictions provided by the CFD and plot them in bar charts in figs. A-19 to A-21.

The most significant part of the network architecture convergence is presented in fig. 2-37. In this table, the inverse of error values expressed as relative square error is provided for two cases where we train using mean square error and relative entropy, respectively. By calculating the inverse, bigger values indicate better performance of the neural network. The parameters that we vary here are the depth of the LSTM recurrent neural network and the size of the window of past sea elevation values that we feed into the neural network. Each of the sea states is color coded in the first column of fig. 2-37, green being the mildest ($H_s = 3.53m$, $T_p = 9.7s$), yellow being medium intensity ($H_s = 5.09m$, $T_p = 12.4s$), and red the most severe sea state ($H_s = 10.66m$,

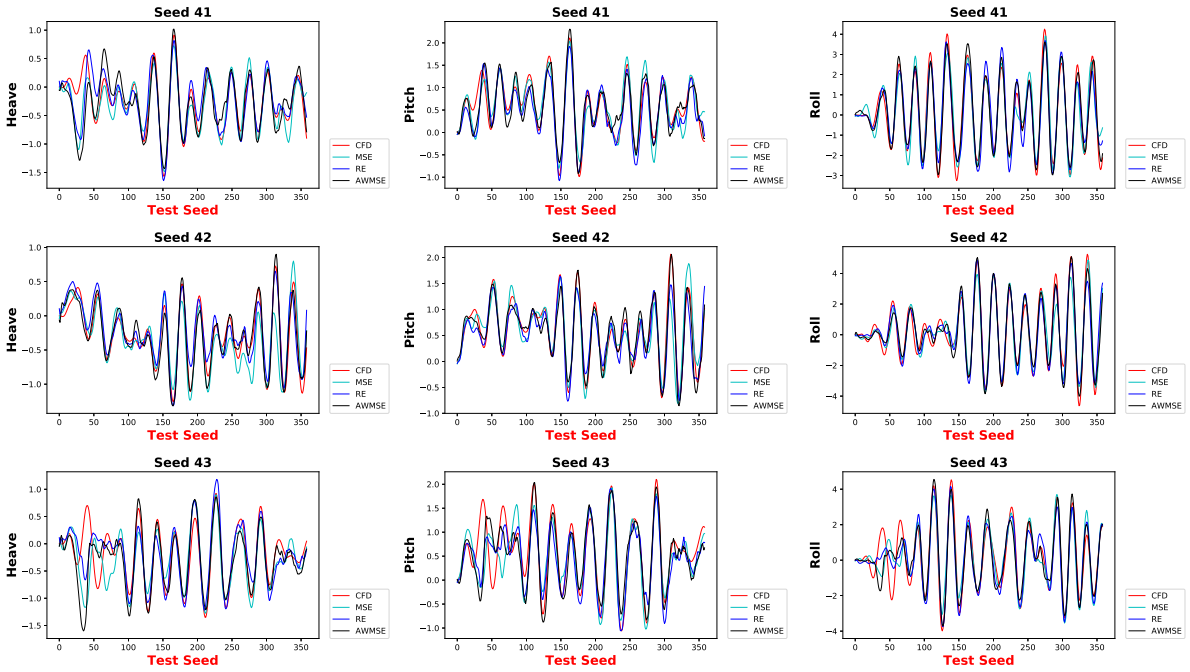

Figure 2-31: *LSTM test results (6 hidden layers, 250 neurons).* Heave, Pitch and Roll motion dynamics of a notional DTBM battleship at Froude number 0.4, time step $\Delta t = 0.2s$, $T_p = 9.7s$, $H_s = 3.53m$, $v = 30kt$.

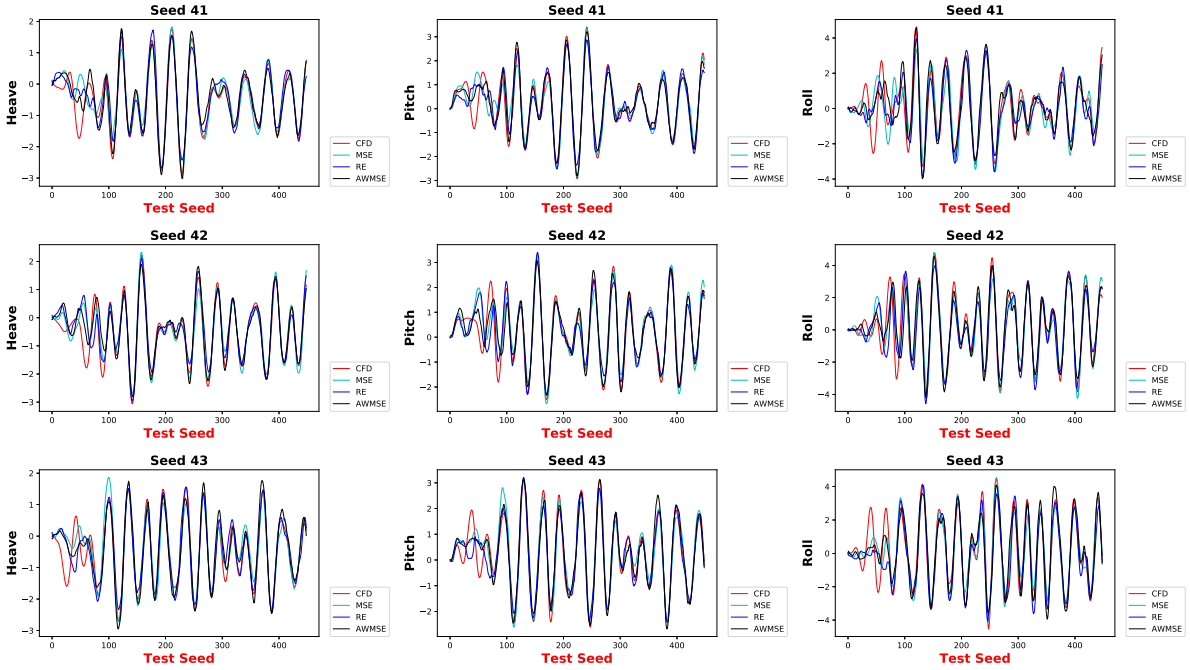

Figure 2-32: *LSTM test results (6 hidden layers, 250 neurons).* Heave, Pitch and Roll motion dynamics of a notional DTBM battleship at Froude number 0.4, time step $\Delta t = 0.2s$, $T_p = 12.4s$, $H_s = 5.09$, $v = 30kt$.

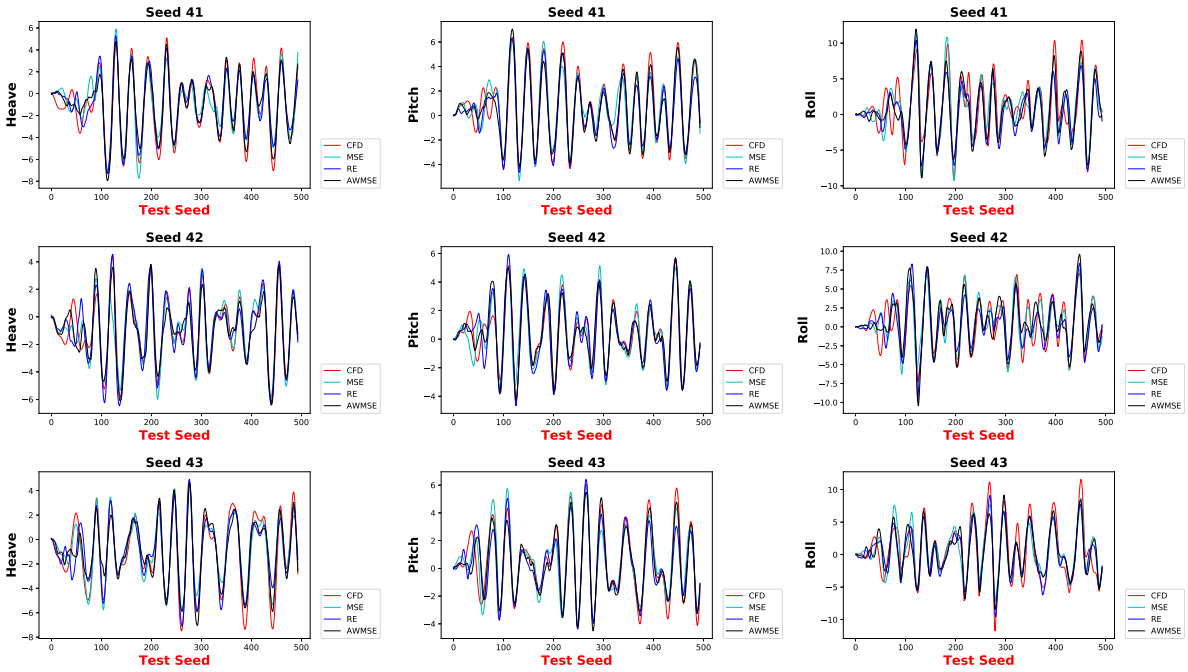

Figure 2-33: *LSTM test results (6 hidden layers, 250 neurons).* Heave, Pitch and Roll motion dynamics of a notional DTBM battleship at Froude number 0.4, time step $\Delta t = 0.2s$, $T_p = 13.4s$, $H_s = 10.66m$, $v = 30kt$.

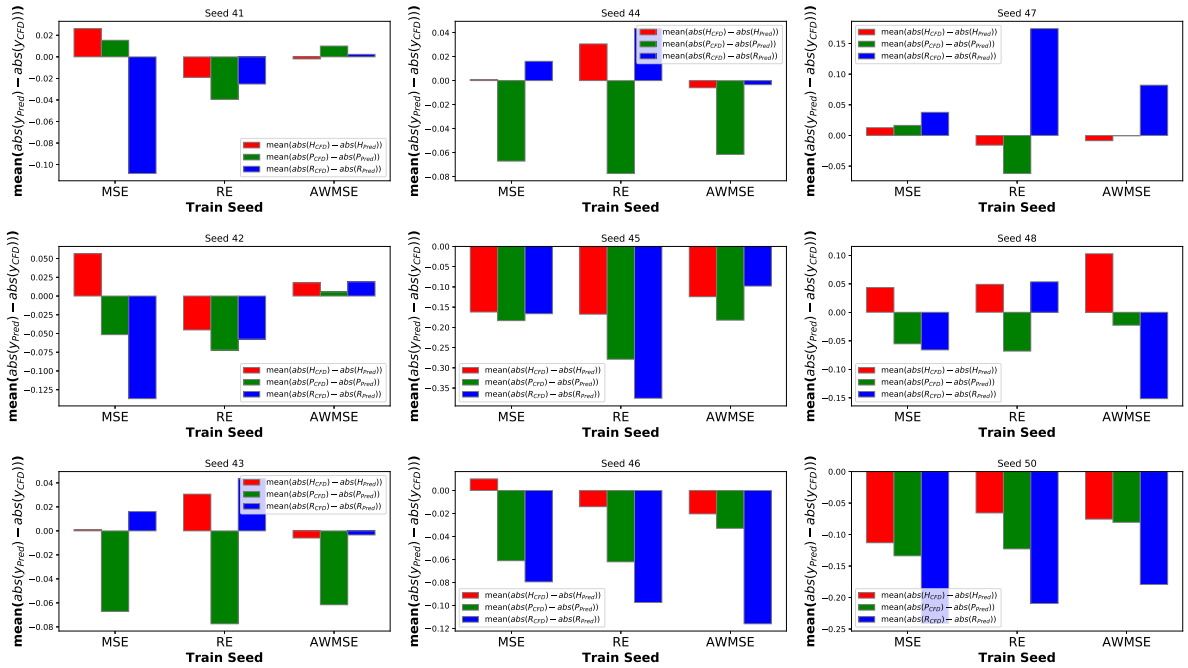

Figure 2-34: *LSTM test results (6 hidden layers, 250 neurons).* Heave, Pitch and Roll motion dynamics of a notional DTBM battleship at Froude number 0.4, time step $\Delta t = 0.2s$, $T_p = 9.7s$, $H_s = 3.53m$, $v = 30kt$.

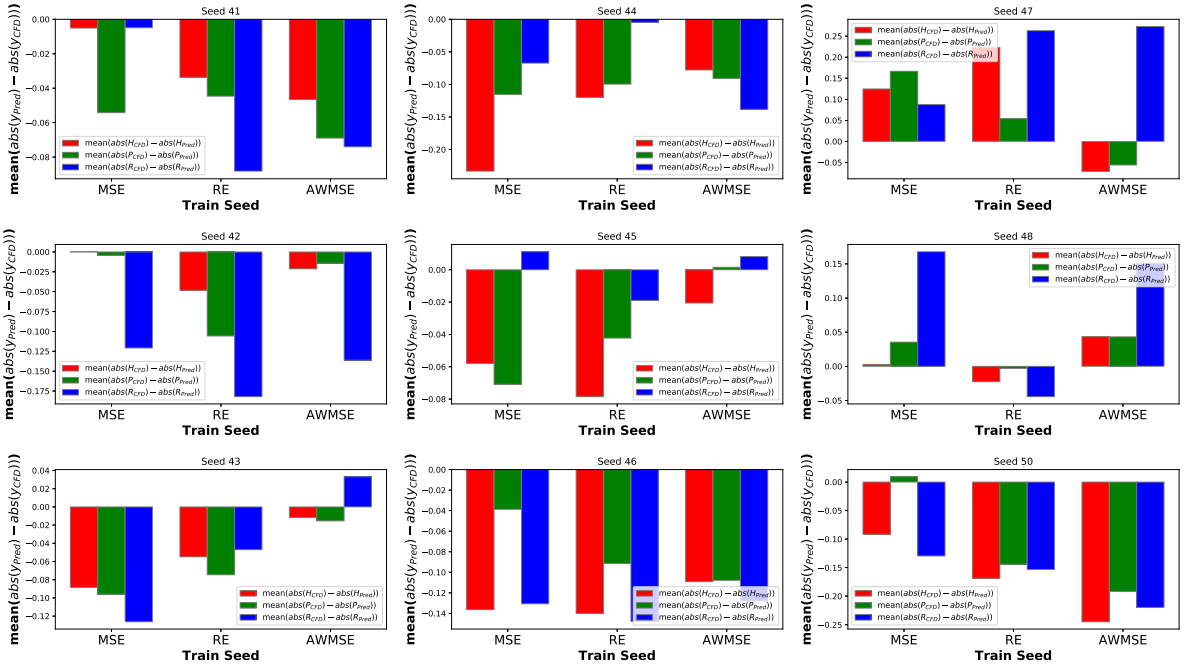

Figure 2-35: *LSTM test results (6 hidden layers, 250 neurons).* Heave, Pitch and Roll motion dynamics of a notional DTBM battleship at Froude number 0.4, time step $\Delta t = 0.2s$, $T_p = 12.4s$, $H_s = 5.09m$, $v = 30kt$.

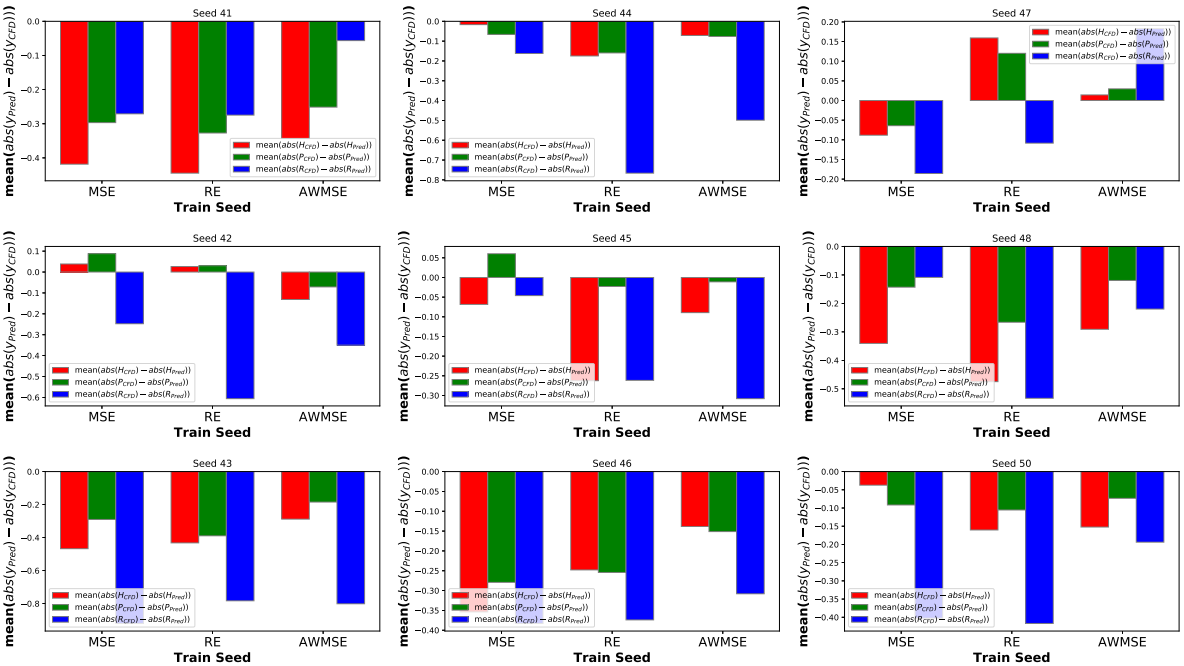

Figure 2-36: *LSTM test results (6 hidden layers, 250 neurons).* Heave, Pitch and Roll motion dynamics of a notional DTBM battleship at Froude number 0.4, time step $\Delta t = 0.2s$, $T_p = 13.4s$, $H_s = 10.66m$, $v = 30kt$.

$T_p = 13.4s$). Not so evidently in the mildest sea state, but it can be seen that the deeper networks provide a significant improvement of performance both in terms of MSE and RE. However, this comes at the cost of a significant increase of training time and as we double the depth of the networks and diminishes the ability to parallelize the training process, and we increase the number of trainable parameters. For this reason it is this trade-off between training time and overall network performance that is used to provide a recommendation for the best architecture. The effect of the second parameter studied, window size for past sea elevation values, has a smaller observable effect in the performance of the network. Looking at fig. 2-37, particularly at the harshest sea state and the deeper network configuration, a very consistent improvement of the performance of the network can be observed when increasing the window size, although not as large as changing the depth of the network.

	Mean RSE Heave		Mean RSE Pitch		Mean RSE Roll	
HD_250_TS_10000_WT_40_MP_97_Nts_70_NL_3	12.176	8.982	12.163	10.630	17.337	19.680
HD_250_TS_10000_WT_40_MP_97_Nts_140_NL_3	2.244	6.380	10.504	9.140	18.385	19.823
HD_250_TS_10000_WT_40_MP_97_Nts_70_NL_6	8.586	8.003	9.322	10.016	19.044	19.630
HD_250_TS_10000_WT_40_MP_97_Nts_140_NL_6	13.780	9.525	19.981	10.558	33.654	21.751
Cost Function	MSE	RE	MSE	RE	MSE	RE
	Mean RSE Heave		Mean RSE Pitch		Mean RSE Roll	
HD_250_TS_10000_WT_40_MP_124_Nts_70_NL_3	7.407	6.814	14.746	14.140	10.222	9.851
HD_250_TS_10000_WT_40_MP_124_Nts_140_NL_3	4.030	3.753	9.439	7.761	7.876	7.209
HD_250_TS_10000_WT_40_MP_124_Nts_70_NL_6	8.293	11.376	16.854	20.635	12.066	13.349
HD_250_TS_10000_WT_40_MP_124_Nts_140_NL_6	6.762	9.252	14.385	17.632	11.757	13.991
Cost Function	MSE	RE	MSE	RE	MSE	RE
	Mean RSE Heave		Mean RSE Pitch		Mean RSE Roll	
HD_250_TS_10000_WT_40_MP_134_Nts_70_NL_3	19.658	18.345	23.819	21.077	9.399	9.014
HD_250_TS_10000_WT_40_MP_134_Nts_140_NL_3	12.591	12.582	17.869	17.561	10.736	10.293
HD_250_TS_10000_WT_40_MP_134_Nts_70_NL_6	23.380	21.586	25.004	25.315	9.365	9.177
HD_250_TS_10000_WT_40_MP_134_Nts_140_NL_6	28.609	22.849	32.327	24.783	13.364	11.880
Cost Function	MSE	RE	MSE	RE	MSE	RE
	Mean RSE Heave		Mean RSE Pitch		Mean RSE Roll	

Figure 2-37: *Inverse of RSE for each architecture and cost function combination.*The network architectures are encoded using labels. The label HD_250_TS_10000_WT_40_MP_97_Nts_70_NL_3 encodes the network design as: 250 cells in the hidden dimension and 3 layers of depth (withing the RNN cell), 10000 training steps, training on 40 seeds of a sea state with a modal period of 9.7s, feeding residual wave information from 70 previous time steps. Two cost functions are tested in the training process: Mean Squared Error (MSE) and Relative Entropy (RE).

Although not presented here, tests experimenting with the dimension of the hidden state as well as the number of training steps have been performed. The hidden state had a dimension of 250 as it was easily parallelized to train across a wide network. Regarding the training steps, in the particular configuration of the problem of predicting across three

different spectra, training for more than 10000 steps (given a sequence length of about 500, is equivalent to 20 epochs) was seen to cause over-fitting. Adam optimizer was used to train the networks.

2.6.3.2 Test Results and Conclusions

Although the full results are presented in appendix A, in the following section we look in detail into a small sample of the test seeds to extract insights from the comparison of the network predictions under three different cost functions. The resulting predictions of roll motions for all three cost functions can be consulted in figs. A-28 to A-30; the same can be said for pitch in figs. A-25 to A-27 and heave in figs. A-22 to A-24.

Within figs. 2-31 to 2-33 we can have a close look at the time series of the predictions that result from the training on MSE, RE & AWMSE; and compare them to the reference prediction provided by the high fidelity CFD. We can clearly see that there is good agreement both in amplitude a well in phase prediction of the motion signal. As remarked in section 2.2.4, It is crucial to underline that successful motion prediction involves more than mere response amplitudes; it also necessitates precise determination of the phase differences between each of the vessel's motions and a reference position of the exciting wave. This phase information is indispensable for reconstructing the exact absolute motion of any point on the rigid vessel. By accounting for both the translations of the vessel's center of gravity and the rotations around that center, a comprehensive picture of the vessel's motion is captured. Therefore, a thorough understanding of both amplitude and phase is essential for accurate characterization of the vessel's motion.

To have a better metric for comparison we utilize bar charts that represent the average of the difference of absolute value of motion predictions to the absolute value of the reference motions, provided by the CFD. These bar charts are presented in figs. 2-34 to 2-36. The first impression is that no training function has a dominating performance over the remaining two, although it can be said that AWMSE provides, on average, the smallest under-prediction errors and this can be seen most clearly, during the worst sea state, when looking at the bar charts during training and during testing in fig. A-21, in terms of mean amplitude error comparisons. In this last figure, a clear trend of under-

prediction while training on RE can be seen, although this does not translate so clearly to the testing set, where AWMSE is the one that under-predicts responses the least.

2.7 Global Analysis and Discussion

An inherent challenge in understanding the probability of observing particular magnitudes of motions for specific sea states lies in the formulation of meaningful probability density functions (PDFs). These PDFs are especially crucial in the context of non-Gaussian motions such as roll. To effectively address this and derive a meaningful PDF, we conducted experiments by varying the size of the test and training portions of the sampled CFD data. This variation ensures that the sampled PDFs capture the true essence of the data and are not merely artifacts of a specific data split.

By contrasting the sampled PDFs against the CFD data, as depicted in fig. 2-44, we make some critical observations. Specifically, the PDFs resulting from training the machine learning algorithm on Mean Squared Error and Relative entropy appear nearly indistinguishable. Conversely, training on Amplitude Weighted Mean Square Error produces a PDF with a slightly more pronounced tail. This observation aligns with findings presented in the bar charts in figs. A-19 to A-21. With this enriched understanding, decision-makers are better positioned to strike a balance — they could opt for slightly reduced accuracy in neural network predictions in exchange for a diminished risk of under-predicting vessel motions.

An important factor that needs to be identified is the source of non-linearity that leads to non-Gaussian distributions of the vessel movements. These can be many, namely:

1. *Geometrical*: The shape and mass distribution of a vessel play an critical role in its stability [160]. Initially, the righting moment of a vessel behaves linearly but, due to geometrical constraints, it can reach a point where it disappears. Particularly in the longitudinal direction, any non-symmetry—unless the vessel has a canoe shape—amplifies this effect. The calculated righting arms at large angles of stability, both longitudinally and transversely, confirm these behaviors. By examining fig. 2-38, especially $GZ_{Longitudinal}$ within pitch angles of $-10°$ to $10°$, the non-linear and

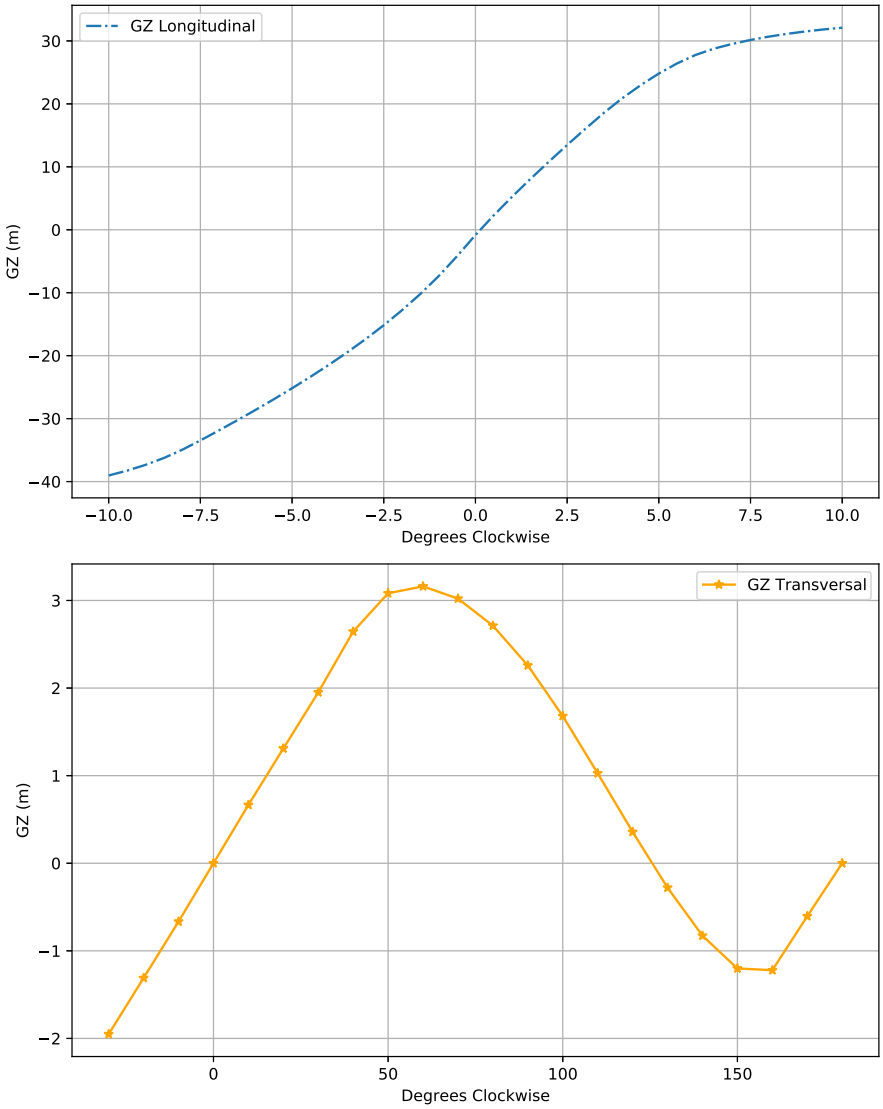

Figure 2-38: From top to bottom, GZ values for longitudinal and transversal large angle stability.

Figure 2-39: Differences when experiencing a breaking and a non-breaking waves are very large. Picture source is SAFEHAVEN MARINE and found in [268].

non-symmetrical nature becomes evident. However, angles greater than 6° remain rare in simulations, indicating minimal sources of non-linearity in most operational conditions.

2. *Wave steepness*: In deep ocean waters, as waves grow in amplitude due to external forces such as wind or through wave-wave interactions, nonlinear effects begin to surface [188]. A prominent result of this non-linearity is the steepening of the wave's face. Here, the forward-facing side of the wave becomes steeper compared to its trailing side. Wind forcing on waves can exacerbate this asymmetry, particularly when wind speeds approach or exceed the wave speeds.

3. *Wave breaking*: The continuation of wave steepening can culminate in the wave reaching a threshold where it breaks [59]. Before the actual break, the asymmetry between the forward and trailing wave faces becomes particularly pronounced. Waves can break onto the ship, either on its deck or sides fig. 2-39. Such wave breaking events lead to highly localized and impulsive forces [58]. These forces, in turn, can exert enormous pressures, potent enough to inflict structural damage or even deformations at the point of impact.

4. *Non-linear coupling of motions*: Motions in the marine environment seldom occur in isolation. For instance, significant roll motions can couple with heave, resulting in intricate movement patterns. The resulting motion is more complex than a mere linear combination of the two original motions. Understanding these coupled dynamics is essential for accurate marine simulations [106].

5. *Parametric rolling*: A phenomenon that has been well-researched in naval architecture, parametric rolling arises due to periodic variations in a ship's buoyancy when confronted with longitudinal waves [76]. The danger arises when a ship encounters waves with lengths similar to its own. The alternating lifting of its bow and stern can then interact with the ship's natural pitching frequency. If this interaction's frequency is nearly twice the ship's roll frequency, it can lead to large amplitude rolls. Such motions not only endanger the ship's stability but also pose a range of other challenges, including the potential for capsizing, cargo or equipment damage,

safety hazards for the crew, and increased structural stress.

2.7.1 Parametric Rolling

Parametric rolling is a resonant phenomenon that ships can experience under specific conditions [181, 300]. One of the primary triggers for this kind of rolling is when the roll period of the ship is roughly twice the wave encounter frequency. This means that if a ship has a roll period of about 12 seconds, it's particularly susceptible to parametric rolling when encountering waves with a frequency close to every 6 seconds. Moreover, the positioning of the waves plays a crucial role [77]. When waves are aligned close to the ship's bow or stern, the risk for parametric rolling is enhanced due to the periodic submersion and emergence of the vessel's bow or stern, which varies the ship's buoyancy in sync with its rolling frequency.

Inspection of simulation visualizations has allowed us to determine the frequency of encounter with waves. These visual insights were corroborated in fig. 2-40, where the Short-Time Fourier Transforms (STFTs) visually reinforce this phenomenon. The plots distinctly highlight the instances when the vessel's largest roll motions (with a period close to 12 seconds) coincide with an encounter frequency of about 6 seconds with the seas. This synchronization between the roll motions and wave encounter frequency is a clear manifestation of parametric rolling. Recognizing and understanding these patterns is vital for ensuring the safety of the vessel and its crew, as the onset of parametric rolling can lead to dangerous scenarios if not properly managed.

Upon closely examining the phase state diagrams fig. 2-41 of our vessel's motions in seas of the harshest states, a pronounced coupling between the roll and pitch motions was evident. This coupling, starkly visible in the phase state diagrams, is a distinctive feature of parametric rolling, indicating that the ship is interacting with waves of a length close to its own. Further confirmation came from our calculations of encounter periods, which highlighted that the ship frequently encountered waves with lengths and periodicities conducive to the onset of parametric rolling. In essence, these findings corroborate that our ship's motion, particularly in the roll and pitch directions, is not just influenced by regular wave interactions but is also severely affected by parametric rolling. Such violent

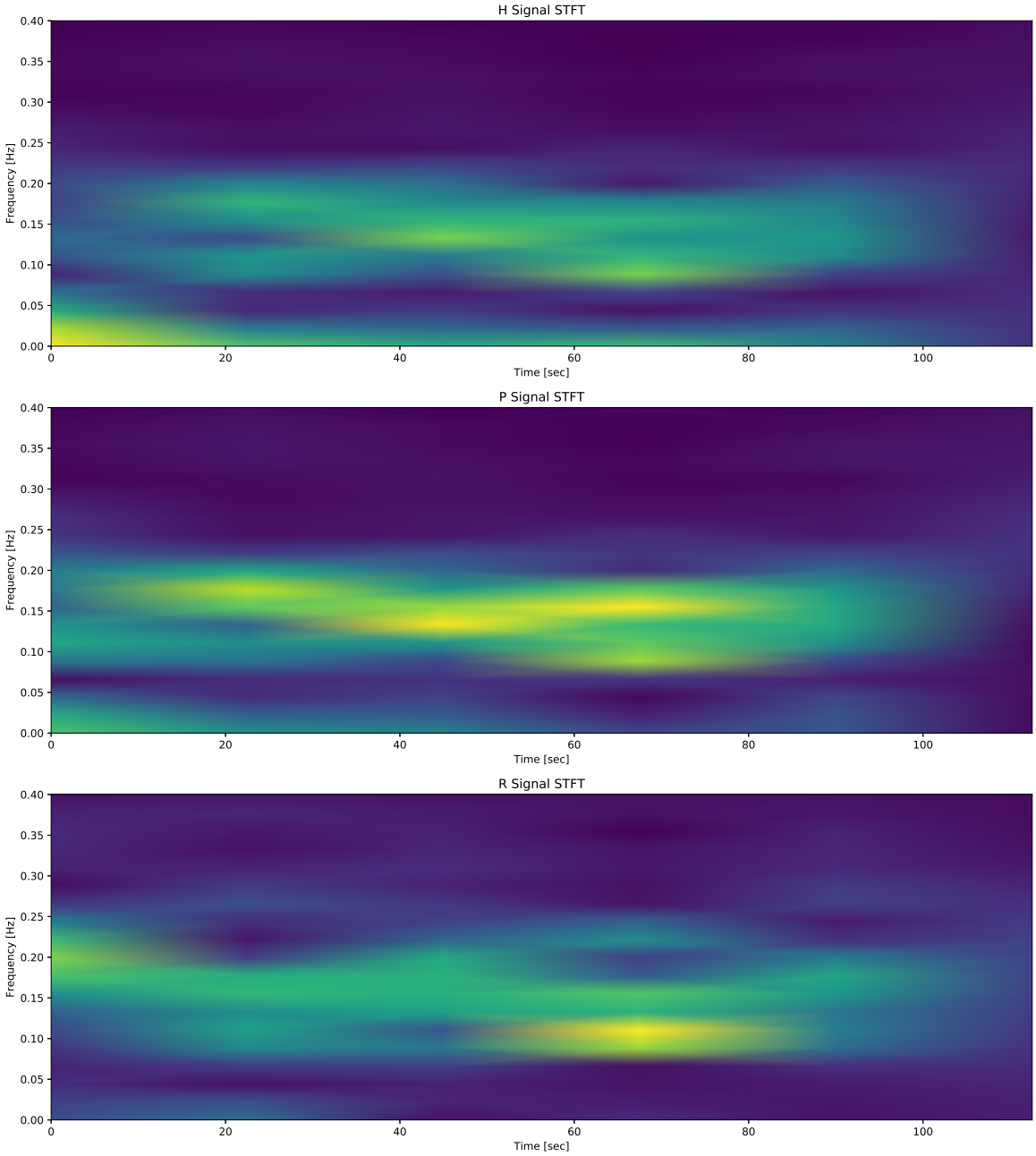

Figure 2-40: Short-Time Fourier Transforms (STFTs) for Heave, Pitch, and Roll respectively of the battleship under the load configuration considered in this thesis.

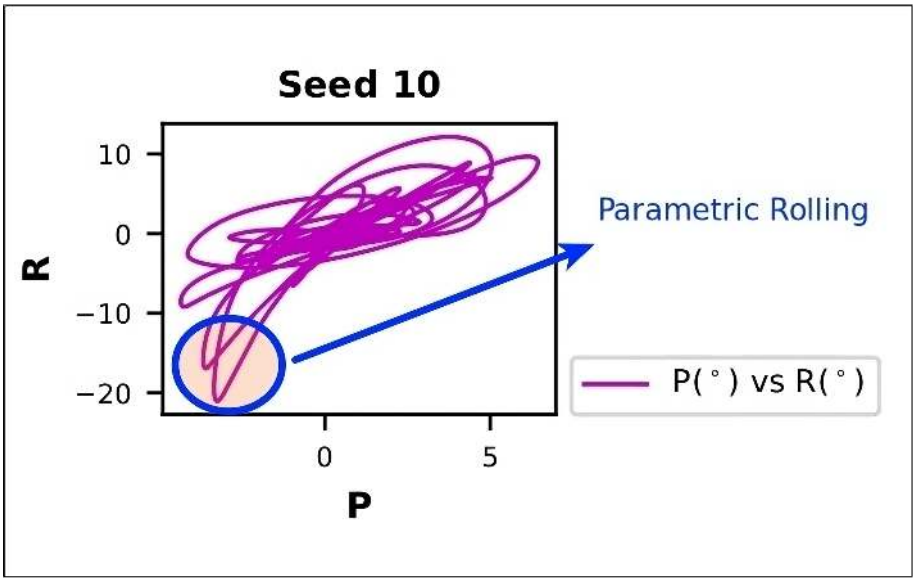

Figure 2-41: Characteristic coupling of roll and pitch during parametric rolling motions are evidenced in this phase state diagram.

couplings between roll and pitch reiterate the criticality of understanding this phenomenon to ensure the safety and operational efficiency of the vessel.

2.7.2 Breaking Waves

Breaking seas have a transformative effect on the sea surface elevation and, by extension, on the probability density functions (PDFs) of those elevations [13]. The process of wave breaking, at its core, involves the transfer of energy from higher frequency components to lower ones, causing the dissipation of wave energy [154].

When a wave breaks, it often results in a sharp and pronounced crest [277], leading to an elevation of the sea surface. This elevation shift caused by wave breaking can result in a noticeable shift in the PDF of sea surface elevation towards positive values, indicating an increased likelihood of wave crests compared to troughs [264]. The action of wave breaking essentially skews the PDF towards these crests, see fig. 2-30d.

Furthermore, the steepening effect of breaking waves means that the amplitude of crests becomes more pronounced than troughs. In statistical terms, this will make the sea surface elevation distribution positively skewed, indicating a dominance of crests over troughs. This skewness stands in contrast to non-breaking seas, where the distribution might be more symmetric, showing roughly equal probabilities for crests and troughs.

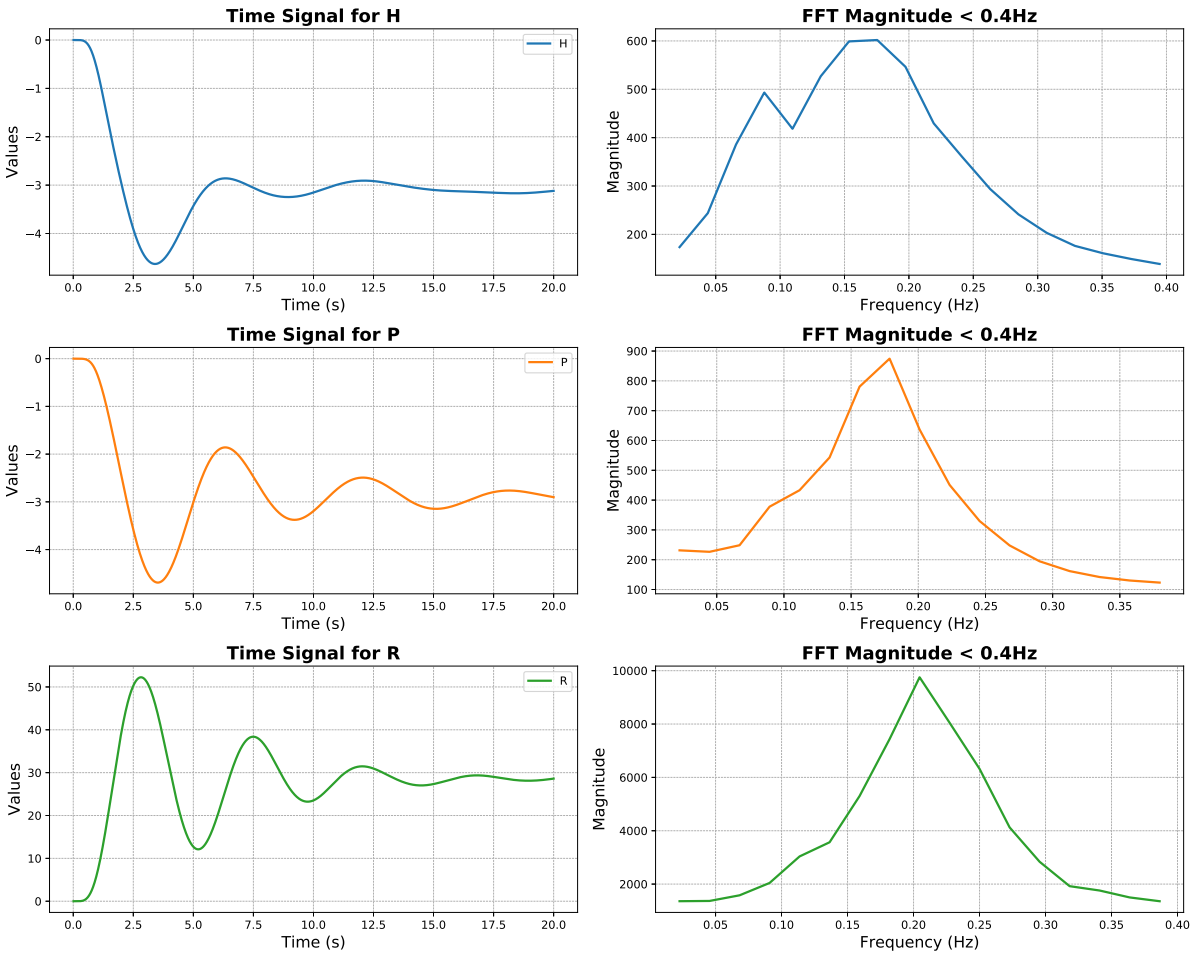

Figure 2-42: Decay tests for Heave, Pitch, and Roll respectively of the battleship under the load configuration considered in this thesis.

This shift and skewness in the PDF due to breaking seas is not just a statistical curiosity. It has tangible implications in marine and offshore engineering, as the asymmetry in wave elevations can influence the dynamic response of structures, the loading on ships, and even the safety of marine operations [118], see fig. 2-39. Recognizing and understanding the shift in the PDF due to breaking is crucial for accurate wave modeling and prediction [35], especially in extreme sea conditions where wave breaking is more prevalent.

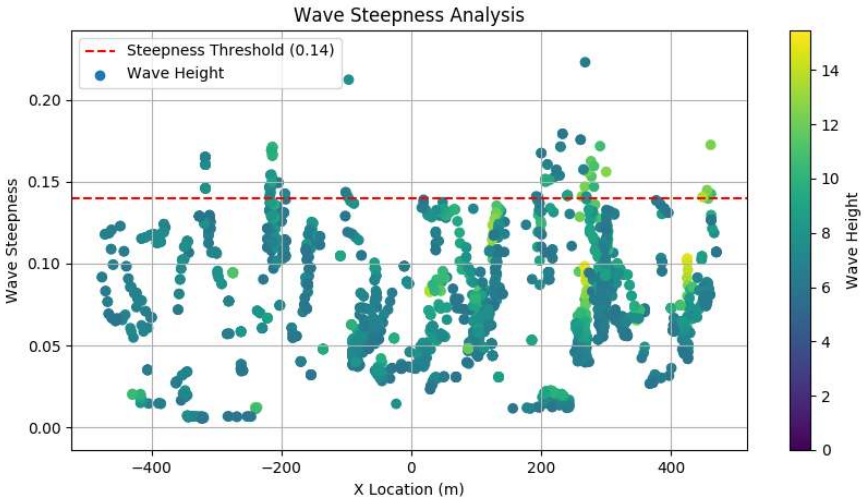

Figure 2-43: Visualization of wave steepness across the fluid domain, with data points color-coded by wave height. The gradient in color intensity reflects variations in wave amplitude, offering insights into regions of increased steepness and potential breaking zones. The horizontal dashed line demarcates the wave breaking limit.

2.8 Cost Function Tradeoff

In numerical optimization and machine learning, the selection of an appropriate cost function is paramount. This choice essentially dictates the priorities of the model during its training phase. Let's delve into three particular cost functions that we've used for our analysis:

1. Mean Squared Error (MSE): This is perhaps one of the most widely-used cost functions. It computes the average of squared differences between the predicted and actual values. Given its sensitivity to larger deviations, it's an excellent choice when larger errors are deemed undesirable.

2. Relative Entropy: Often referred to in the context of information theory, this function quantifies the divergence between two probability distributions. It becomes particularly relevant when the primary objective is to reproduce a specific distribution in the predictions.

3. Amplitude Weighted Mean Squared Error (AWMSE): This is a nuanced version of MSE. By weighing errors in accordance with the true signal's amplitude, it places a premium on accuracy specifically in high-amplitude regions. This predisposes it to predict extreme events with a heightened probability.

A comparative analysis of the probabilistic density functions (pdfs) of roll motion, as modeled by these cost functions, is showcased in fig. 2-44. When assessing which cost function to employ, the decision should stem from the overarching objectives. If the goal is broad accuracy across the spectrum, MSE might be suitable. If replicating a specific distribution is the target, Relative Entropy might be the best fit. However, if the focus leans heavily towards accurately capturing and predicting extreme events, AWMSE becomes a compelling choice. As with many aspects in data science and engineering, the choice is often a trade-off, influenced by both the specific problem constraints and the larger goals of the project.

2.8.1 Conclusions

As reliable data streams become accessible, we can consider incorporating additional variables of interest, such as wave added resistance or engine fuel consumption. This information could originate from ship sensors or computer simulations. Notably, our research endeavors lead us to realize that these tools hold the potential to yield real-time predictions for tasks that were previously computationally impractical, since they involve solving non-linear partial differential equations withing very large unstructured meshes. These predictions could encompass a range of critical quantities such as propeller torque, ship resistance, and ship motions, opening doors to operability studies and, particularly in the context of carbon emissions reduction, weather routing [282, 302] strategies to minimize fuel consumption and subsequently reduce carbon dioxide emissions.

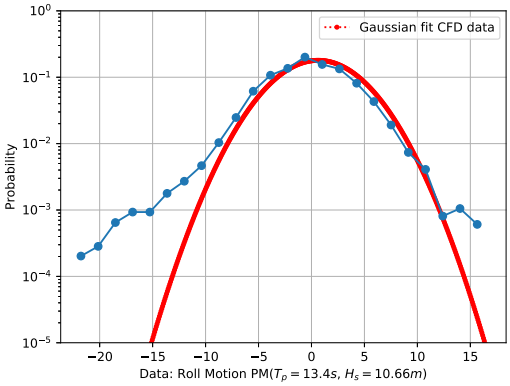

(a) CFD Roll motions PDF.

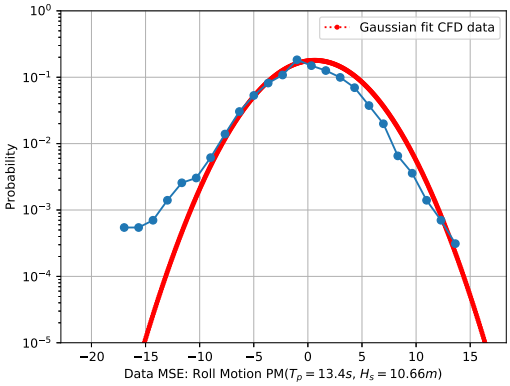

(b) MSE Roll motions PDF.

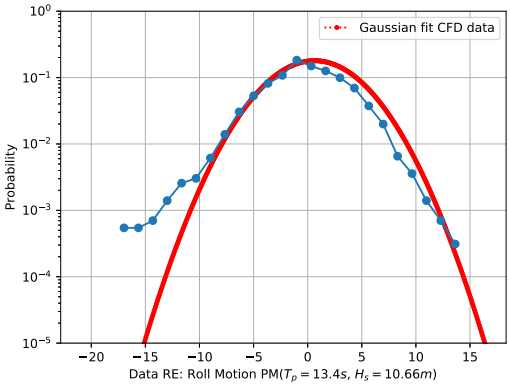

(c) RE Roll motions PDF.

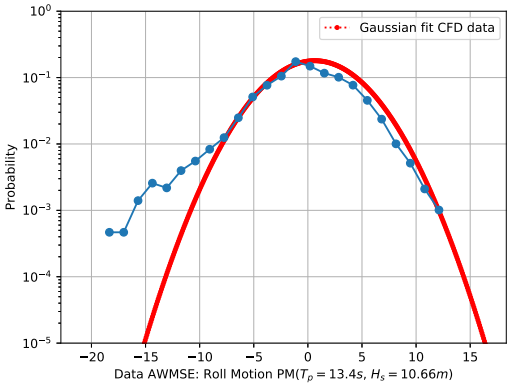

(d) AWMSE probe PDF.

Figure 2-44: Probability density functions (PDFs) of roll vessel motions for different training cost functions. Deviations from typical Gaussian motions can be seen comparing to a least squares Gaussian fit. Froude number 0.4, time step $\Delta t = 0.2s$, $T_p = 13.4s$, $H_s = 10.66m$, $v = 30kt$.

In the comprehensive examination of the phase state diagrams pertaining to our vessel's motion within challenging marine environments, we identified a marked coupling between the roll and pitch motions fig. 2-41. This observed coupling, distinctly manifested within the phase state diagrams, is characteristic of the phenomenon termed as 'parametric rolling.' This phenomenon arises when the ship's interaction is dominantly with waves whose length is commensurate to the ship's own [77]. Our analysis extended to the ship's encounter periods. The outcomes showed that our vessel recurrently interacts with waves, the properties of which — specifically length and periodicity — are predisposing factors for the emergence of parametric rolling. Contrary to merely enhancing the oscillations observed during typical wave interactions, parametric rolling can precipitate substantially augmented amplitudes in the vessel's roll and pitch.

Related to these insights, data from container shipping incidents reveal a significant correlation between parametric rolling and lost cargo. According to the World Shipping Council, an average of 1,382 containers were lost at sea annually between 2008 and 2019 [115]. A subset of these incidents, particularly in routes exposed to long swells and adverse weather, were attributed directly to parametric rolling. The consequent loss not only pertains to tangible cargo but also encompasses considerable economic ramifications and potential environmental hazards.

Given the palpable influence of standard wave interactions, the contribution of parametric rolling to a vessel's motion dynamics is profound and warrants rigorous academic scrutiny [255]. Instances of abrupt, amplified motions underscore the exigency of comprehending this phenomenon in the broader context of maritime safety and vessel operability [246].

The implications of these findings are several. For the academic community, it beckons further research into predictive modeling and real-time monitoring methodologies. For maritime stakeholders, the insights emphasize the importance of informed navigation, especially in seas known for conditions conducive to parametric rolling [198]. This knowledge is essential not only for the preservation of marine assets but also to ensure the well-being of maritime personnel and the safeguarding of marine ecosystems.

Chapter 3

Predicting Vortex Induced Vibrations of Marine Risers

Vortex-induced vibrations (VIVs) persist as one of the paramount challenges in the marine industry. At a glance, these vibrations, brought on by seemingly simple cylindrical structures experiencing cross-flows, might appear straightforward. However, the reality is starkly different. The interaction results in exceptionally intricate hydrodynamic behaviors which, even today, remain not fully deciphered. These phenomena, often oscillating between structured patterns and chaotic turbulences, have immense implications, especially when it comes to the Offshore Oil & Gas sector—one of the linchpins of global economic progress.

Marine risers, which play an instrumental role in safe oil extraction, operate in these demanding environments. The stability and integrity of these risers are critically tested by VIVs. An unmitigated exposure to these forces not only jeopardizes the equipment but poses potential hazards to the environment and the safety of personnel. As we strive for sustainable and safe methods of extracting resources from the ocean's depths, a profound understanding of VIVs becomes indispensable. Only by looking deeper into the complex interplay between fluid and structural dynamics can we engineer solutions that ensure our marine infrastructures stand resilient against the relentless forces of the sea.

In this chapter, we introduce a comprehensive methodology designed to assimilate vast quantities of data into empirical models. Our primary aim is to highlight the immense

potential that sensors, along with the data they capture, possess in refining the predictions associated with Vortex-induced Vibration (VIV) phenomena.

While our approach prominently utilizes a semi-empirical VIV prediction tool known as VIVA, it is essential to note that the optimization techniques employed for extracting resilient hydrodynamic databases tailored for a Steel Catenary Riser (SCR) are by no means restricted solely to this tool.

To ensure the integrity and reliability of the information sourced from these databases, we have subjected them to meticulous cross-validation. Remarkably, based on our extensive literature survey, there appears to be a lacuna in existing research where such an in-depth cross-validation of this specific methodology is conspicuously absent.

3.1 Introduction

Riser systems have a wide range of configuration solutions that have been used in the oil and gas industry. These systems are most commonly used for the safe transportation of material between the seabed to an offshore platform or from the platform to the seabed. Riser configurations can be divided into:

1. *Free-standing risers*: Free-standing marine risers are vertical pipelines used to transport produced hydrocarbons from a subsea reservoir to surface facilities, or vice versa for water injection or drilling mud. Unlike traditional risers that are supported along their length by the platform or vessel, free-standing risers are not physically connected to a structure over their entire length. They primarily rely on their weight, buoyancy modules, and anchors or bases on the seabed to maintain their upright position. This design allows them to move laterally, accommodating the motion of floating platforms due to waves, currents, and wind. These risers are often used in deepwater drilling and production scenarios where traditional risers would be impractical or too costly. Their design requires careful analysis to ensure stability and to manage potential issues like vortex-induced vibrations.

2. *Top-tensioned risers (TTRs)*: Top-tensioned marine risers are vertical pipelines utilized in offshore drilling and production operations to connect the subsea infras-

tructure to surface facilities on floating platforms. These risers are maintained in an upright position by applying tension at the top, typically using tensioners located on the platform. This tension ensures that the riser remains straight and taut, even in deep water, allowing it to accommodate the platform's vertical motions caused by waves, tides, and other oceanic forces. The riser itself is made up of a series of interconnected pipe sections, often reinforced to withstand internal and external pressures. The top-tensioned design is particularly beneficial for deep-water applications where traditional fixed or gravity-based structures might be impractical. The ability to counteract bending stresses from ocean currents, waves, and platform movements is vital for maintaining the riser's integrity and ensuring the safe transfer of oil, gas, or drilling fluids between the seabed and the platform.

3. *Catenary risers*: Steel catenary risers (SCRs) are a type of offshore pipeline used to transport production or injection fluids between the seabed and production platforms. As the name suggests, they hang in a catenary shape, which is the curve that a hanging chain or cable assumes under its own weight when supported only at its ends. SCRs are predominantly made of steel, offering strength and durability under challenging marine conditions. They are anchored to the seabed and rise to the water's surface, where they connect to floating production systems. Their flexible, free-hanging design allows them to accommodate the movements of floating platforms due to waves, currents, and tides. However, their exposure to oceanic conditions demands meticulous engineering to counter challenges like vortex-induced vibrations and corrosion. As a critical component in offshore oil and gas production, SCRs are designed to operate reliably for several decades.

4. *Hybrid risers*: Hybrid marine risers combine the features of both the traditional steel catenary risers (SCRs) and the top-tensioned risers (TTRs), aiming to capitalize on the strengths of both while minimizing their weaknesses. They usually consist of a free-hanging catenary section near the seabed, which is linked to a buoyant section near the surface. This buoyant section provides upward tension, ensuring the lower catenary part remains clear of the seafloor, thus reducing seabed interference. This design offers flexibility, making them suitable for deep and ultra-deepwater

applications. Furthermore, the hybrid nature of these risers provides effective load distribution, reducing the impact of environmental factors like ocean currents and waves. The use of buoyant modules can also lead to cost savings in terms of installation and materials compared to traditional riser systems. However, their design and installation require careful considerations to ensure optimal performance and safety.

Each of the riser configurations have scenarios where they are best suited to operate. Particularly, steel catenary risers compared to top-tensioned risers offer a simpler arrangement. Usually, the riser base and tensioner can be eliminated and the deck space required is reduced. However, installation of SCRs in areas where the harshness of weather conditions is exceedingly high may not be a practical task. In these areas, where larger waves and currents appear, a significant increase of extreme loading on the riser will be experienced. This issues could be addressed with similar systems used in top tensioned risers but [297], in this cases, it's competitive advantage over these would be lost.

Historically, VIV research predominantly centered around vibrations of rigid cylinders, with seminal works by [69, 235, 16] illuminating vital mechanisms such as hysteretic behaviour [64] and lock-in phenomena [50]. However, in the oil and gas sector, there's a pressing need to understand and reliably design long flexible cylinders, particularly SCR risers.

Most investigations on flexible risers have employed physical experiments [185, 83, 294, 38, 276, 107, 85, 86] and numerical computations [182, 63, 24, 26, 25]. The majority of these primarily address scenarios wherein risers retain a straight alignment and don't experience substantial tension or length variations. Such studies have been instrumental for the evolution and validation of numerical codes tailored for deep-water riser fatigue predictions offshore.

Nevertheless, a deeper understanding is required for riser and umbilical configurations exhibiting pronounced curvature, tension variations, or diverse flow inclinations. For instance, [39] revealed that untensioned catenary risers display a broader response bandwidth compared to their tensioned counterparts in perpendicular flow. Research efforts to grasp non-linear riser geometries have encompassed yawed cylinders [124, 218],

spring-mounted rigid/flexible cylinders in yawed/sheared flow [113, 301], and rigid cylinders featuring a curved axis [171]. Emphasizing the significance of fatigue quantification at the touch down point, studies by [123] and [286] considered both hard and soft seabeds. Further, the minimal pretension in steel catenary risers can amplify vessel motions, possibly synergizing with riser dynamics, as indicated by [41, 200, 284, 283, 285].

In summary, while considerable progress has been made in understanding VIVs of marine risers, there remains a vast expanse of research territories that warrant exploration for optimized riser designs in the oil and gas industry.

In the domain of predicting VIV for elongated flexible structures, semi-empirical methods have gained considerable traction. Unlike traditional approaches that compute hydrodynamic forces by resolving the Navier-Stokes equations, semi-empirical methods are anchored in rigid cylinder experiments. Broadly, these methods fall into two categories: those that directly employ experimental data for modeling hydrodynamic forces [274, 136, 280, 2], and those that conceptualize hydrodynamic forces using non-linear oscillators [64, 68].

The implications of VIV are not confined to a particular riser configuration but span across the spectrum. Overlooking VIV during the riser design phase can have dire consequences. A failure to account for it can culminate in severe fatigue [10], jeopardizing the riser's structural integrity. Such oversights can lead not only to significant economic setbacks but also, and perhaps more critically, to devastating environmental repercussions.

Building on the foundations laid in [228], we present a significant enhancement of the methodology to characterize the VIV vibrations of an SCR riser, both under interpolated and extrapolated unseen conditions. Our approach hinges on data from controlled lab experiments [28]. Before the extraction of hydrodynamic databases, the raw experimental data was meticulously preprocessed to reconstruct the deformed shapes of the SCR riser. Using this refined data, we then applied a semi-empirical method, specifically VIVA [2], to extract the hydrodynamic databases.

To evaluate our methodology's robustness, we subject these databases to rigorous tests, aiming to predict VIV responses in sets of unseen cases encountered during the extraction phase. While assessing the methodology, we consciously chose to overlook certain features,

most notably the influence of curvature [104, 155, 296] on the riser's vibrational modes. Nonetheless, given our primary focus on gauging the methodology's robustness, we assert that these omissions do not undermine the validity of our assessment.

3.2 Description of the Experiments

The experimental program, as detailed in the report [28], involved an extensive model test to gather experimental data on the Vortex-Induced Vibration (VIV) response of a Steel Catenary Riser (SCR), see 3-2. The key characteristics of these experiments are summarized as follows:

- **Riser Model**: The tests utilized a catenary riser model with a length-to-diameter ratio of approximately 900. The model was constructed from brass pipe and equipped with accelerometers for vibration measurement.

- **Test Setup**: The riser model was towed in a towing tank, allowing for systematic variation of both current velocity and inclination angle between the current and the riser.

- **Measurement Techniques**: The VIV response was primarily measured using 10 pairs of accelerometers strategically placed along the riser. These instruments captured detailed data on riser motion in response to varying current conditions.

- **Test Conditions**: A range of tests were conducted to simulate different scenarios, including varying current velocities and directions relative to the riser (see table 3.1). This approach provided a comprehensive set of data to analyze VIV behavior under diverse conditions.

This rigorous experimental setup and the resultant data were crucial in developing and validating the predictive model for VIV in SCRs, particularly under varying flow conditions. The detailed experimental approach provided a robust foundation for the predictive methodologies discussed in our manuscript.

3.3 Riser Motion Reconstruction Methodology

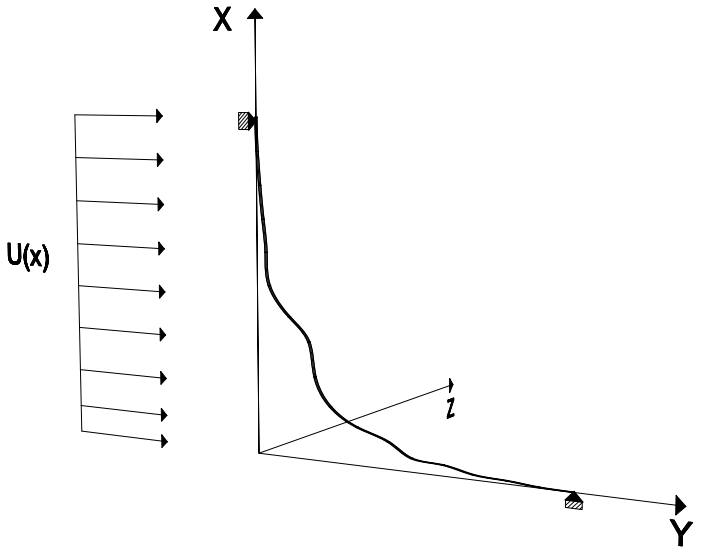

Figure 3-1: Flexible SCR riser within a uniform flow profile.

Experimental data sourced from the Norwegian Deepwater Programme (NDP) [29] serve as the foundation for testing the optimization algorithms elaborated upon in this chapter. Conducted at the MARINTEK Offshore Basin, the NDP experiments focused on a steel catenary riser (SCR) characterized by a high length-to-diameter (L/D) ratio. Accelerometer sensors, meticulously positioned along the riser, were instrumental in capturing data in both the In-Line (IL) and Cross-Flow (CF) directions. The SCR used for the experiments boasted dimensions of $L_{\text{Riser}} = 12.5\text{m}$ in length and an outer diameter $D_{\text{Riser}} = 14\text{mm}$. Notably, the count of transducers recording accelerations remained consistent across both IL and CF directions:

Type	Cross-flow	In-line
Accelerations	10	10

In this chapter, we show the result of our proposed reconstruction algorithms using a representative example. This case features a 0° angle between the catenary plane and the flow velocity, and the flow velocity is set at $0.12\,m/s$. Vibrations in this scenario predominantly exhibit the 3rd structural mode, evident in both CF and IL vibrations, as

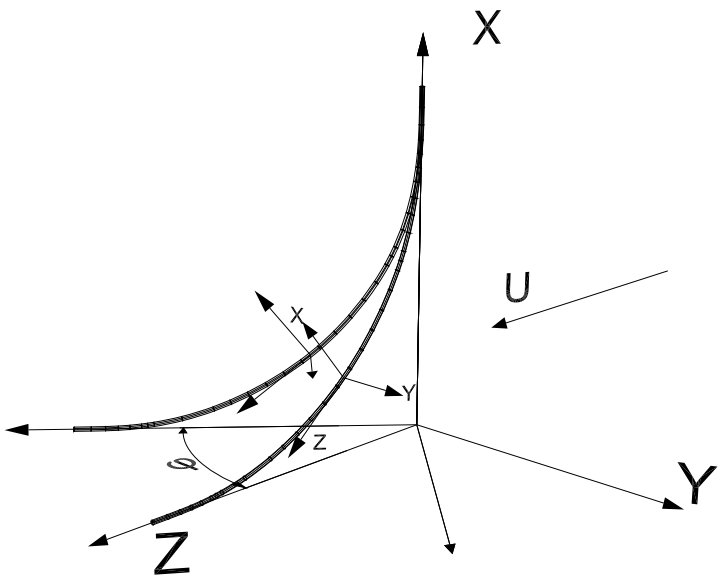

Figure 3-2: Reference frame used to reconstruct riser deformed shape from sensor readings. The angle with respect to the flow is controlled by ϕ.

depicted in fig. 3-3 and fig. 3-4. Further scrutiny of the time-resolved animations of the deformed shape confirms the absence of travelling waves.

Reconstructing the time-varying deformed shape of the riser demands a sophisticated post-processing framework. The inherent challenge lies in relying solely on strain and acceleration measurements at discrete locations along the riser [178]. While our description focuses primarily on Cross-Flow (CF) displacements, it's worth noting that In-Line (IL) displacements are addressed using a parallel approach. Leveraging the fact that the riser's ends remain fixed, the deformed shape can be aptly represented through a Fourier expansion, detailed below:

$$y(z,t) = \sum_{n=0}^{\infty} w_n(t)\varphi_n(z) \tag{3.1}$$

$$\varphi_n(z) = \sin(n\pi z/L) \tag{3.2}$$

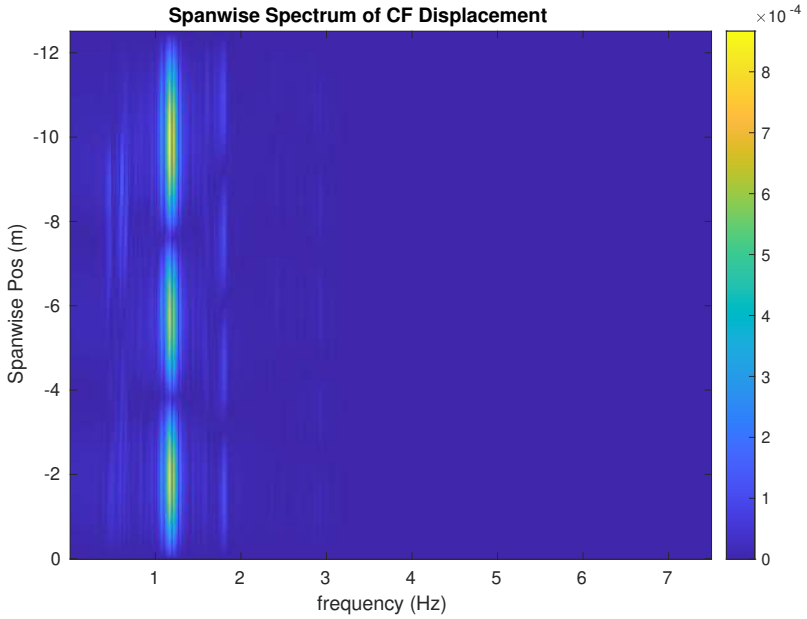

Figure 3-3: Spanwise spectrum of cross-flow displacements.

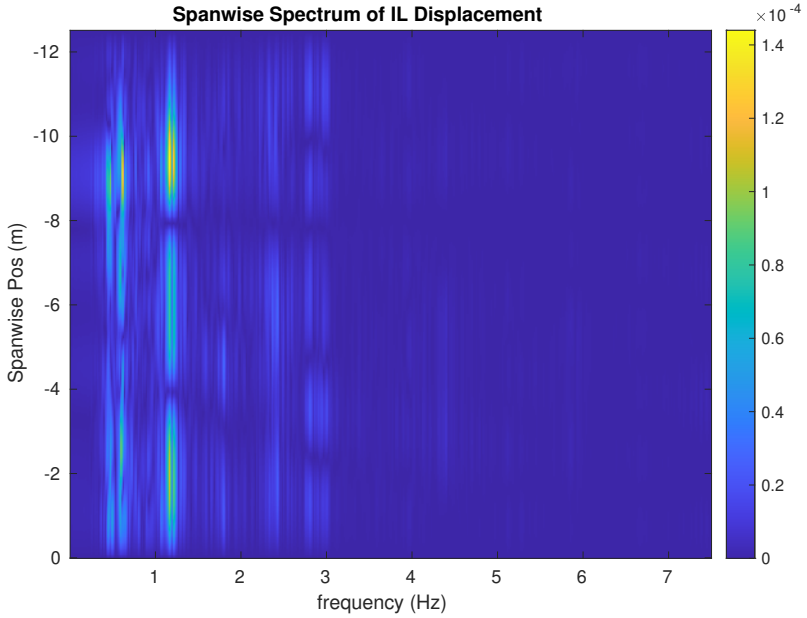

Figure 3-4: Spanwise spectrum of in-line displacements.

Truncating at an appropriate number of modes N:

$$a(z,t) = \sum_{n=1}^{N} w_{n_{tt}}(t)\varphi_n(z) \tag{3.3}$$

$$\varphi_n(z) = \sin(n\pi z/L) \Rightarrow \varphi''(z) = -(n\pi/L)^2 \sin(n\pi z/L) \tag{3.4}$$

We exploit the fact that the measurements are sampled at high frequency in time by using the following Fourier transforms:

$$\mathcal{F}\{w_n(t)\} = \hat{w}_n(\omega) \tag{3.5}$$

$$\mathcal{F}\{y(z,t)\} = \hat{y}(z,\omega) \tag{3.6}$$

$$\mathcal{F}\{a(z,t)\} = \hat{a}(z,\omega) \tag{3.7}$$

From which we can obtain:

$$\hat{y}(z,\omega) = \sum_{n=1}^{N} \hat{w}_n(\omega)\phi_n(z) \tag{3.8}$$

$$\hat{a}(z,\omega) = -\omega^2 \hat{y}(z,\omega) = -\omega^2 \sum_{n=1}^{N} \hat{w}_n(\omega)\phi_n(z) \tag{3.9}$$

Expressing the problem in the frequency domain allows expressing the previous three equations in matrix form as shown bellow:

$$\underbrace{\begin{bmatrix} y(z_1,t_1) & y(z_1,t_2) & \dots & y(z_1,t_{N_t}) \\ y(z_2,t_1) & y(z_2,t_2) & \dots & y(z_2,t_{N_t}) \\ y(z_3,t_1) & y(z_3,t_2) & \dots & y(z_3,t_{N_t}) \\ \vdots & \vdots & \ddots & \vdots \\ y(z_s,t_1) & y(z_s,t_2) & \dots & y(z_s,t_{N_t}) \\ \vdots & \vdots & \ddots & \vdots \\ y(z_{N_s},t_1) & y(z_{N_s},t_2) & \dots & y(z_{N_s},t_{N_t}) \end{bmatrix}}_{\mathbf{Y}} = \Phi \begin{bmatrix} a_0(t_1) & a_0(t_2) & \dots & a_0(t_{N_t}) \\ a_1(t_1) & a_1(t_2) & \dots & a_1(t_{N_t}) \\ a_2(t_1) & a_2(t_2) & \dots & a_2(t_{N_t}) \\ \vdots & \vdots & \ddots & \vdots \\ a_{N_m}(t_1) & a_{N_m}(t_2) & \dots & a_{N_m}(N_t) \\ b_1(t_1) & b_1(t_2) & \dots & b_1(t_{N_t}) \\ b_2(t_1) & b_2(t_2) & \dots & b_2(t_{N_t}) \\ \vdots & \vdots & \ddots & \vdots \\ b_{N_m}(t_1) & b_{N_m}(t_2) & \dots & b_{N_m}(N_t) \end{bmatrix} \tag{3.10}$$

$$\Phi\hat{W} = \hat{Y}, \tag{3.11}$$

where,

$$\hat{W} = \begin{bmatrix} \hat{w_1}(\omega_1) & \hat{w_1}(\omega_2) & \dots & \hat{w_1}(\omega_\Lambda) \\ \hat{w_2}(\omega_1) & \hat{w_2}(\omega_2) & \dots & \hat{w_2}(\omega_\Lambda) \\ \hat{w_3}(\omega_1) & \hat{w_3}(\omega_2) & \dots & \hat{w_3}(\omega_\Lambda) \\ \vdots & \vdots & \ddots & \vdots \\ \hat{w_N}(\omega_1) & \hat{w_N}(\omega_2) & \dots & \hat{w_N}(\omega_\Lambda) \end{bmatrix}, \tag{3.12}$$

$$\Phi = \begin{bmatrix} \Phi_1(z_1) & \Phi_2(z_1) & \dots & \Phi_N(z_1) \\ \Phi_1(z_2) & \Phi_2(z_2) & \dots & \Phi_N(z_2) \\ \Phi_1(z_3) & \Phi_2(z_3) & \dots & \Phi_N(z_3) \\ \vdots & \vdots & \ddots & \vdots \\ \Phi_1(z_{M_y}) & \Phi_2(z_{M_y}) & \dots & \Phi_N(z_{M_y}) \\ \Phi_1(z_1) & \Phi_2(z_1) & \dots & \Phi_N(z_1) \\ \Phi_1(z_2) & \Phi_2(z_2) & \dots & \Phi_N(z_2) \\ \Phi_1(z_3) & \Phi_2(z_3) & \dots & \Phi_N(z_3) \\ \vdots & \vdots & \ddots & \vdots \\ \Phi_1(z_{M_a}) & \Phi_2(z_{M_a}) & \dots & \Phi_N(z_{M_a}) \end{bmatrix}, \tag{3.13}$$

$$\hat{Y} = \begin{bmatrix} \hat{y}(z_1, \omega_1) & \hat{y}(z_1, \omega_2) & \dots & \hat{y}(z_1, \omega_\Lambda) \\ \hat{y}(z_2, \omega_1) & \hat{y}(z_2, \omega_2) & \cdots & \hat{y}(z_2, \omega_\Lambda) \\ \hat{y}(z_3, \omega_1) & \hat{y}(z_3, \omega_2) & \cdots & \hat{y}(z_3, \omega_\Lambda) \\ \vdots & \vdots & \ddots & \vdots \\ \hat{y}(z_{M_y}, \omega_1) & \hat{y}(z_{M_y}, \omega_2) & \cdots & \hat{y}(z_{M_y}, \omega_\Lambda) \\ \frac{-\hat{a}(z_1,\omega_1)}{\omega_1^2} & \frac{-\hat{a}(z_1,\omega_2)}{\omega_2^2} & \dots & \frac{-\hat{a}(z_1,\omega_\Lambda)}{\omega_\Lambda^2} \\ \frac{-\hat{a}(z_2,\omega_1)}{\omega_1^2} & \frac{-\hat{a}(z_2,\omega_2)}{\omega_2^2} & \dots & \frac{-\hat{a}(z_2,\omega_\Lambda)}{\omega_\Lambda^2} \\ \frac{-\hat{a}(z_3,\omega_1)}{\omega_1^2} & \frac{-\hat{a}(z_3,\omega_2)}{\omega_2^2} & \dots & \frac{-\hat{a}(z_3,\omega_\Lambda)}{\omega_\Lambda^2} \\ \vdots & \vdots & \ddots & \vdots \\ \frac{-\hat{a}(z_{M_a},\omega_1)}{\omega_1^2} & \frac{-\hat{a}(z_{M_a},\omega_2)}{\omega_2^2} & \dots & \frac{-\hat{a}(z_{M_a},\omega_\Lambda)}{\omega_\Lambda^2} \end{bmatrix}. \tag{3.14}$$

We solve for each value of ω using the pseudo-inverse Φ^+.

$$\hat{w} = \Phi^+ \hat{Y} \tag{3.15}$$

Taking the a inverse Fourier transform of $\hat{w}$, we find the coefficient matrix in the time domain, and the riser CF displacement is found:

$$y(z,t) = \sum_{n=0}^{N} w_n(t)\varphi_n(z) \tag{3.16}$$

Finding high order modes in eq. (3.11) requires a minimum number of sensors . Furthermore the use of the pseudo-inverse Φ^+ is equivalent to a least-squares fit in the frequency domain. Therefore the number of sensors available will limit the number of modes N we can use.

To improve the quality of reconstruction, we employed band-pass filtering to remove low and high frequency noise. used different weighting for the strain and acceleration measurements. The analysis of these recontructions in addition to others are presented for reference in appendices B and C.

3.4 Methodology Robustness Through Cross-Validation

Current velocity (m/s)	Dir. 0 deg.	Dir. 30 deg.	Dir. 60 deg.	Dir. 90 deg.
0.12	1000 & 5001	2004	3000	4000
0.14	1002	2001	3002	4002
0.16	1004	2002	3004	-
0.18	1006	2006	3006	4006
0.20	1008	2008	3008	4008
0.22	1010	2010	3010	-
0.24	1012 & 5012	2012	3012	4012
0.26	1015	2015	3015	-
0.28	1016	2016	3016	-
0.30	1018 & 5018	2018	3018	4018
0.32	1020	2020	3020	4020
0.34	1022 & 5022	2022	3022	4022

Table 3.1: *Experiment labels and cells colored in red for test and blue for train.* The table above corresponds to training on current directions (ϕ) 30^{o}, 60^{o} & 90^{o} and testing on 0^{o}.

To evaluate the robustness of the hydrodynamic databases derived through the methodology presented in section 3.5, we employ a cross-validation approach across four distinct current directions. Details of the training and test cases for the initial set are provided in table 3.1.

We opted for this specific cross-validation format to examine the model's ability to predict flow conditions both within and outside the range observed during training, termed as interpolation and extrapolation, respectively. A commendable performance under these conditions indicates the superior generalization capabilities of the extracted databases, as evidenced by fig. 3-6 and fig. 3-9.

3.5 Methodology

VIV amplitude and frequency predictions are approached by approximating the SCR riser to a straight riser. In this assimilation, the tension of the riser is taken as the mean tension across the SCR riser. The CF and IL components are derived from the component of water velocity perpendicular to the riser's longitudinal direction. Notably, the tangential component is disregarded in VIV computations.

This approach inherently simplifies the model by not accounting for variations in tension along the riser and the different current profiles arising from changing flow incidence angles. Unlike straight risers, the system lacks pre-tension, which means ballooning effects can significantly alter the riser's shape. This, in turn, modifies the flow incidence angle and introduces additional complexities.

Such assumptions, while simplifying, have significant implications. Past research indicates that the axial flow velocity component can influence riser tension. Additionally, ballooning effects, which can substantially alter the riser's geometry, are essential for accurate VIV predictions. However, under the specific flow conditions examined in this study, these assumptions yield satisfactory results. They notably outperform standardized databases which tend to overpredict VIV responses of marine risers by about 40%. This overprediction is often attributed to the reliance on databases derived from rigid cylinder experiments.

Consequently, we propose a methodology to harness sensor data for crafting hydro-

dynamic databases. These databases aim to enhance VIV predictions across various methods, ensuring better adaptability and accuracy.

3.5.1 Vortex-Induced Vibrations of a Vertical Flexible Cylinder

Utilizing a strip theory approach [67], the free vibrations of a vertical flexible cylinder within a current profile can be determined by employing rigid cylinder experimental data. This cylinder, oriented along the vertical axis denoted as z, extends between $z = 0$ and $z = L$.

For our model, the following parameters are introduced:

- μ - mass per unit length,
- c - structural damping per unit length,
- EI - bending stiffness,
- T - tension at the top,
- $f_l(z,t)$ - time-varying fluid lift force per unit length in the Cross Flow (CF) direction at span-wise location z.

Assuming small amplitude vibrations, the structural model of the cylinder is given by:

$$\mu\frac{\partial^2 y}{\partial t^2} + c\frac{\partial y}{\partial t} - \frac{\partial}{\partial z}(T\frac{\partial y}{\partial z}) + \frac{\partial^2}{\partial z^2}(EI\frac{\partial^2 y}{\partial z^2}) = f_l(z,t) \tag{3.17}$$

Considering the cylinder's monochromatic steady oscillation as $y(z,t) = Re\{Y(z)e^{i\omega t}\}$, where $Y(z)$ represents the complex space-dependent amplitude of oscillation at frequency ω, the lift force $f_l(z,t)$ can be defined as:

$$f_l(z,t) = Re\{[C_{my}\rho_f \forall Y(z)\omega^2 + iC_{lv}\frac{\rho_f U^2}{2}D\frac{Y(z)}{|Y(z)|}]e^{i\omega t}\} \tag{3.18}$$

On incorporating eq. (3.18) into eq. (3.17), a nonlinear eigenvalue problem emerges:

$$[-\omega^2(m + C_{my}\forall) + i\omega b]Y - \frac{\partial}{\partial z}(T\frac{\partial Y}{\partial z}) + \frac{\partial^2}{\partial z^2}(EI\frac{\partial^2 Y}{\partial z^2}) = iC_{lv}\frac{\rho_f U^2}{2}D\frac{Y}{|Y|} \tag{3.19}$$

It's noteworthy that C_{my} and C_{lv}, both dependent on A^*, V_r, and Re, can be sourced from the hydrodynamic databases related to rigid-cylinder, CF-only forced vibrations. To resolve eq. (3.19), semi-empirical tools like VIVA [275] are employed.

3.5.2 Parametric Hydrodynamic Databases

Hydrodynamic databases play a critical role in understanding and modeling Vortex-Induced Vibrations (VIV). Accurate determination of the hydrodynamic coefficients C_m and C_{lv} demands capturing the dependencies on numerous independent variables, which encompass both structural and flow parameters. Gathering such comprehensive data traditionally requires extensive experimental setups, often costly, especially when examining full-scale Reynolds numbers. Additionally, the introduction of variables like surface roughness and other properties that might change over time further complicates the task, making the pursuit of a universal database daunting, if not outright unfeasible.

In our research, we take a novel approach by evaluating the extrapolation and interpolation capabilities of databases constructed using the methodology from [228]. Our goal is to determine the accuracy of predictions under unseen flow conditions, serving as a testament to the method's robustness.

We employ parametric forms for both C_m and C_{lv}, enabling the capture of essential dynamic features. When combined with governing equations for VIV and appropriate numerical solvers, these parametric databases provide a robust predictive model framework. Drawing inspiration from experimental results for distinct structures, we tackle the optimization challenge initially introduced by [178]. The databases guiding this work owe their insights to results from the Norwegian Deep Water Program (NDP).

Our proposed hydrodynamic model comprises 14 variables, a mix of parameters governing reduced frequency transitions and slopes of hydrodynamic coefficients. The five reduced frequency values delineate the transition zones for the different regimes, which are common across C_{my}, $C_{lv,0}$, and A_c^*. For each of C_{my}, $C_{lv,0}$, and A_c^*, two additional parameters define the slopes of C_{lv} as a function of the amplitude.

Diving deeper into the model specifics, the coefficient C_{my} is modeled as primarily dependent on f_r. As illustrated in fig. 3-5, this is achieved using three regimes of constant

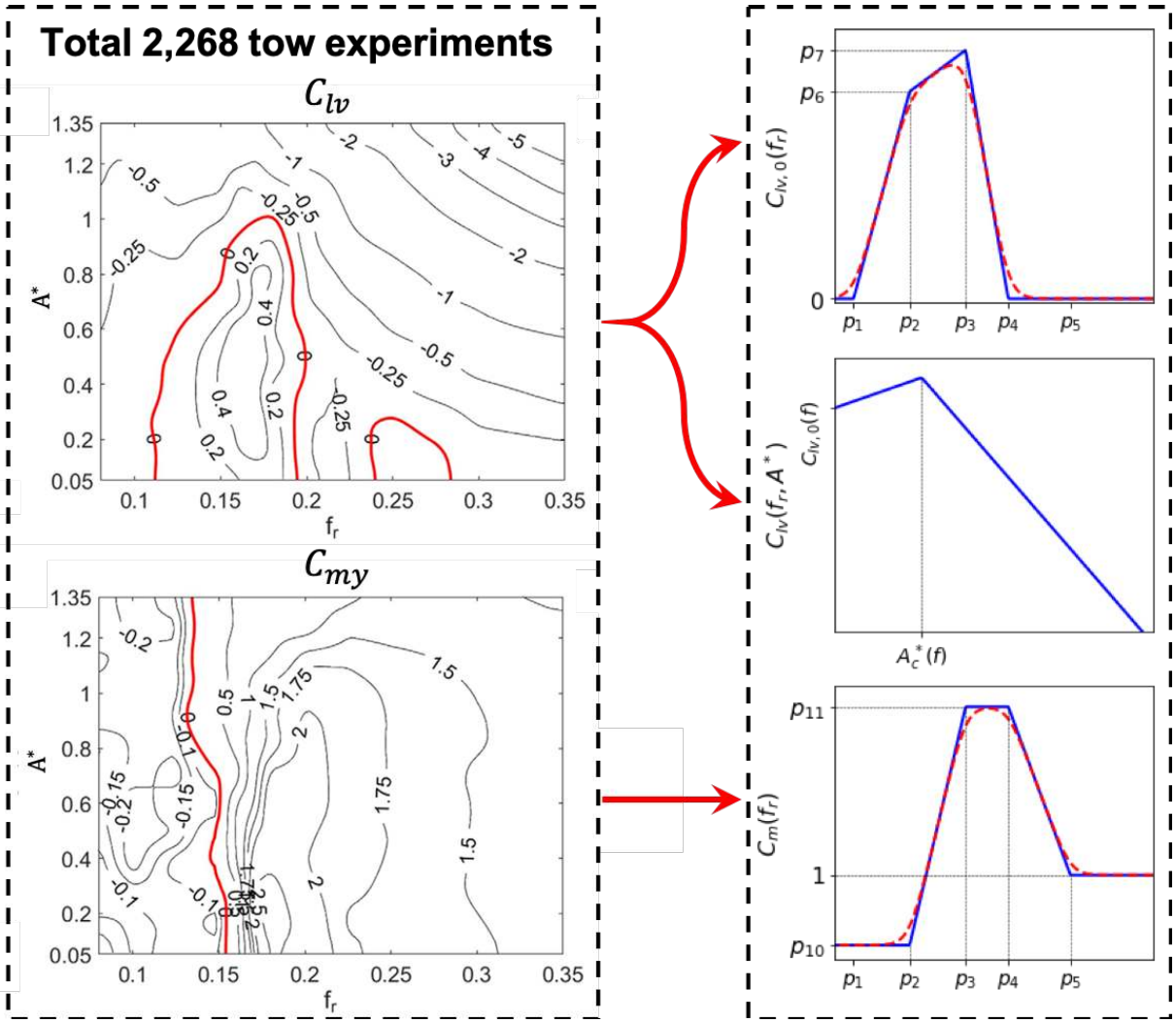

Figure 3-5: Left: A hydrodynamic coefficient database reconstructed from numerous tow experiments [228]. From this database, we derive parametric representations to approximate C_{lv} and C_m using field or experimental data (right).

C_{my} with linear transitions in between. These transitions are made smoother through the use of soft-plus functions. In parallel, C_{lv} is approximated using a piece-wise linear function, dependent on the oscillation amplitude. Its starting point, $C_{lv,0}(f_r)$, is also modeled piece-wise linearly with transitions smoothed using soft-plus functions.

The decision to model C_{my} in this specific manner stems from careful analysis of experimental evidence. The piece-wise linear approximations and soft transitions aim to ensure that the model closely adheres to observed behaviors while maintaining mathematical tractability.

3.5.3 Predicting the Structural Response

The goal of this subsection is to elucidate the methodology and approach behind predicting the structural response of flexible cylinders in the context of vortex-induced vibrations (VIV). We focus on database optimization techniques and the use of semi-empirical codes, leading to an optimization problem.

3.5.3.1 Database Optimization for Risers

Considering flexible cylinders and harmonic motion, we arrive at the non-linear eigenvalue problem detailed in eq. (3.19). This problem is fundamentally dependent on the hydrodynamic databases for C_{lv} and C_{my}. Taking inspiration from the method proposed by [178], we utilize the semi-empirical code VIVA [275] to solve eq. (3.19).

This procedure offers a mapping from given flow parameters to the predicted multi-modal amplitude $\hat{A}^*(z;\mathbf{p})$ and peak frequency $\hat{f}_{peak}(\mathbf{z})$. These parameters are deduced from experimental data, following the steps discussed in section 3.3. The objective function, aiming to minimize the discrepancy between predictions and experiments, is given by:

$$J(\mathbf{p}) = \sum_{(A^*(z),f_{peak})\in\mathcal{D}} \left(\frac{1}{L}\int_0^L |A^*(z) - \hat{A}^*(z;\mathbf{p})|^2\, dz\right)^{\frac{1}{2}} + \lambda|f_{peak} - \hat{f}_{peak}(\mathbf{z})|, \tag{3.20}$$

where $A^*(z)$ and $f_{peak}(\mathbf{z})$ represent the experimentally determined values from a dataset $\mathcal{D}$ evaluated at varying flow velocities. The optimization problem is then represented as:

$$\hat{\mathbf{p}} = \underset{\mathbf{p}}{argmin}\, J(\mathbf{p}) + \mathcal{R}(\mathbf{p}), \tag{3.21}$$

$\mathcal{R}(\mathbf{p})$ stands for regularization terms introduced to ensure the stability and plausibility of the model. Specifically, these terms penalize:

- The size of the range of reduced frequencies, $\hat{f}_r$, where C_{lv} holds positive values. This range is given by $(p_4 - p_1)$.
- The range in which C_{my} deviates from constant values, captured by $(p_5 - p_2)$.

- The maximum value of A^* on the zero contour of C_{lv}.

Such regularization terms were employed by [228], leading to results that, while subtly affected, appear more plausible.

Moving to the practical application and testing of our model, we make use of a dataset from the Norwegian Deepwater Program (NDP). This dataset is a result of large-scale laboratory experiments involving a 12.5m uniform SCR riser subjected to a uniform current. The incoming velocity during these experiments ranged between 0.12 m/s and 0.34 m/s. A comprehensive breakdown of the NDP experiment and the specifics of the dataset can be found in section 3.3.

3.5.4 Optimization Routine

Our research encountered challenges in optimization due to the complex landscape of the loss function, which presented multiple plateaus. These plateaus complicated the selection of both the descent direction and the step size, especially when relying on line search techniques. As a solution, we adopted a strategy of evaluating the cost function through random perturbations. To elaborate, during each iterative step, we updated the parameters $\mathbf{p}$ as $\mathbf{p} = \mathbf{p} + \delta_i \mathbf{v}_i$, where the perturbation factor δ_i is defined as:

$$\delta_i = \arg\min_{\delta \in \Delta} J(\mathbf{p} + \delta \mathbf{v}_i) + \mathcal{R}(\mathbf{p} + \delta \mathbf{v}_i), \tag{3.22}$$

Here, $\Delta = \{0, \delta_1, \ldots, \delta_{n_{samp}}\}$ is a set that includes zero and n_{samp} samples, all distributed according to the probability distribution p_δ. Meanwhile, $\mathbf{v}_i$ denotes a chosen search direction.

Notably, prior studies, such as that by [228], highlighted the efficacy of coordinate descent in addressing optimization problems like eq. (3.21). While the same research also acknowledged the merits of other methods—like the Nelder-Mead algorithm and simulated annealing—coordinate descent emerged as the most promising. Specifically, in this algorithm, each iteration navigates through every dimension of $\mathbf{p}$, aiming to resolve a one-dimensional optimization challenge.

$$p_i = \underset{y}{argmin}\ J(p_1, \ldots, p_{i-1}, y, p_{i+1}, \ldots) + \mathcal{R}(p_1, \ldots, p_{i-1}, y, p_{i+1}, \ldots). \tag{3.23}$$

eq. (3.21) is more easily solved after multiple trials of the optimization scheme if computational resources allow, as it is non-convex.

3.6 Optimized Databases - Results and Discussion

The cross-validation study's conclusive results are displayed in Figures figs. 3-6 to 3-9 and figs. 3-10 and 3-11. Each of the Figures figs. 3-6 to 3-9 displays four vertically stacked graphs.

In these graphs, a blue dashed line represents the span-wise RMS of CF Amplitude as predicted by VIVA. In contrast, a solid black line indicates the corresponding experimental data. The top graph showcases the hydrodynamic database's initial state, achieved after fifty random draws from the parametric database. While our proposed method aims at refining existing databases, these random draws serve to evaluate the optimization's effects from various starting points. This exercise provides a gauge on the robustness of our approach.

Below this top graph are three subsequent graphs, each capturing the same data but at distinct stages in the training process. It's important to note that these graphs offer insights into the VIV predictions for test cases (cases left out during the training phase) as training progresses.

The overall training and testing errors across different scenarios are depicted in Figures fig. 3-10 and fig. 3-11. A notable observation from these figures is that as the training error diminishes, the test error also decreases in almost all scenarios. This trend suggests a robust generalization capability of the parametric databases, validating our primary research hypothesis.

However, discrepancies emerge when examining specific catenary plane orientations. For instance, the orientation with $\phi = 90°$ exhibits both higher training and testing errors compared to other angles. This particular orientation is unique since it lacks a tangential

component of the water velocity relative to the SCR riser. This absence results in the worst-case scenario concerning the current drag on the SCR riser, leading to significant deviations from its hydrostatic shape.

Such significant shape deviations suggest that certain assumptions, as discussed at the outset in section 3.5, may no longer be valid. This discrepancy can adversely affect the accuracy of our VIV model predictions. Additionally, this condition might induce a wide-band VIV response due to the pronounced variability in the added mass and the wake capture phenomenon, as documented by [291, 176, 173].

Overall, the obtained optimized databases that perform best after random initializations, can be described as having characteristic C_{lv} contours that predict more accurate and overall smaller VIV amplitudes than when using databases extracted from rigid cylinders. To clearly observe this compare fig. 3-13 to fig. 3-14, this last one leans on the conservative side of predictions to be able to ensure that risers vibrations are not underpredicted for a wide range of situations.

In this thesis, we also undertake a comprehensive comparison with predictions derived from databases based on rigid cylinder experiments. These databases have historically been a standard reference in the field, primarily due to their conservative nature in predicting Vortex-Induced Vibrations (VIV) amplitudes. It's important to understand that these traditional databases, while reliable, often provide overestimated predictions, leading to more conservative designs and assessments in marine engineering applications. By contrasting our optimized databases against these established models, we aim to highlight not only the differences in predictive accuracy but also the potential for more refined and less conservative designs. This comparative analysis allows us to demonstrate the efficacy of our approach in yielding more precise predictions, thereby offering a pathway towards optimizing design parameters in the marine engineering sector. The critical insight gained from this comparison is instrumental in advancing our understanding of hydrodynamic forces and their impact on offshore structures, leading to a more nuanced and effective approach to design and safety assessments.

3.7 Conclusions

This chapter has systematically validated our methodology across four different current incidence angles, elucidating the generalization capabilities of the learned hydrodynamic databases essential for predicting Vortex Induced Vibrations (VIV) in marine risers. By deliberately excluding training data for specific current directions during the validation phase, we gained valuable insights into the influence of directional variance on the dynamics of riser behavior. This approach not only confirmed the robustness of our databases but also their ability to accurately predict VIV under extrapolated conditions, particularly when training data from angles $\phi = 0, 90^{\circ}$ were omitted.

Our findings are supported by a strong positive correlation observed between the training and testing errors, demonstrating commendable predictive accuracy. These results are vividly illustrated in the spanwise Root Mean Square (RMS) of the Cross-Flow (CF) Amplitudes across various figures, which document how our models adaptively refine themselves to align closely with the actual VIV dynamics encountered in operational environments (see Figures 3-6, 3-7, 3-8, 3-9).

A significant advancement brought forward by this research is the application of a method initially introduced by Rudy et al. [228], tailored to enhance the generalization of hydrodynamic databases significantly. These databases, traditionally constrained by the limitations inherent in models derived from rigid cylinder experiments, have been adeptly modified to encapsulate the complex physics of vortex-induced vibrations. Such refinements address the critical nuances of alternating sign vortices and the rapid variation in the added mass coefficient, which are crucial for accurate VIV prediction across a broad parametric range.

Despite the innovative advancements, it is recognized that existing hydrodynamic databases predominantly cater to cross-flow vibrations and often assume perfect correlation along the riser's length, derived from scenarios presenting low Reynolds numbers. Our research mitigates these gaps by integrating data from flexible riser configurations, thus broadening the applicability and relevance of the databases.

Looking forward, the potential applications of these enhanced databases are manifold.

They promise substantial improvements in wake oscillator models, offering a solution to the often impractical task of modeling exhaustive Navier-Stokes equations. As the field progresses, we anticipate that the methodologies developed here will catalyze further advancements in the complexity and scope of hydrodynamic databases, capturing more intricate behaviors and extending beyond the traditional confines of rigid cylinder observations.

This study not only reaffirms the robustness of our methodological approach but also sets a precedent for future research aimed at refining VIV predictive tools, ensuring their applicability in enhancing the operational efficiency and safety of marine infrastructure.

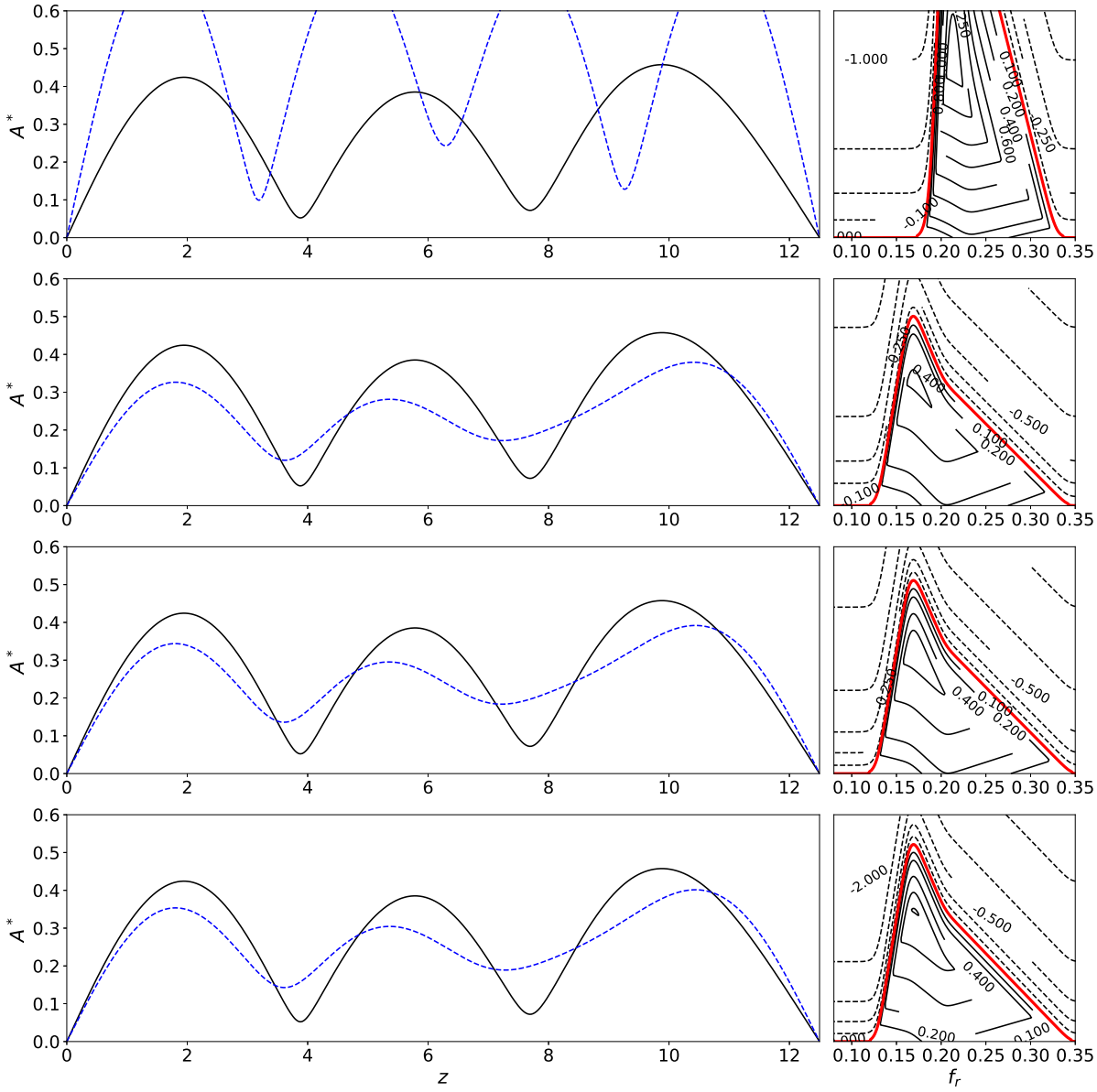

Figure 3-6: **Test case 1000**. *Cross flow RMS predictions, testing catenary plane angle with velocity* $\phi = 0°$. Solid black curve are reconstructed displacements and blue-dashed line are optimized VIVA predictions. A single hydrodynamic database is used. In this figure we represent the change in spanwise RMS response as the training is performed in the 3 catenary plane orientations to which this specific case does not belong to, in this particular case $\phi = 30°, 60°, 90°$. For the relation between experiment labels and catenary plane orientations & towing velocities table 3.1 can be consulted.

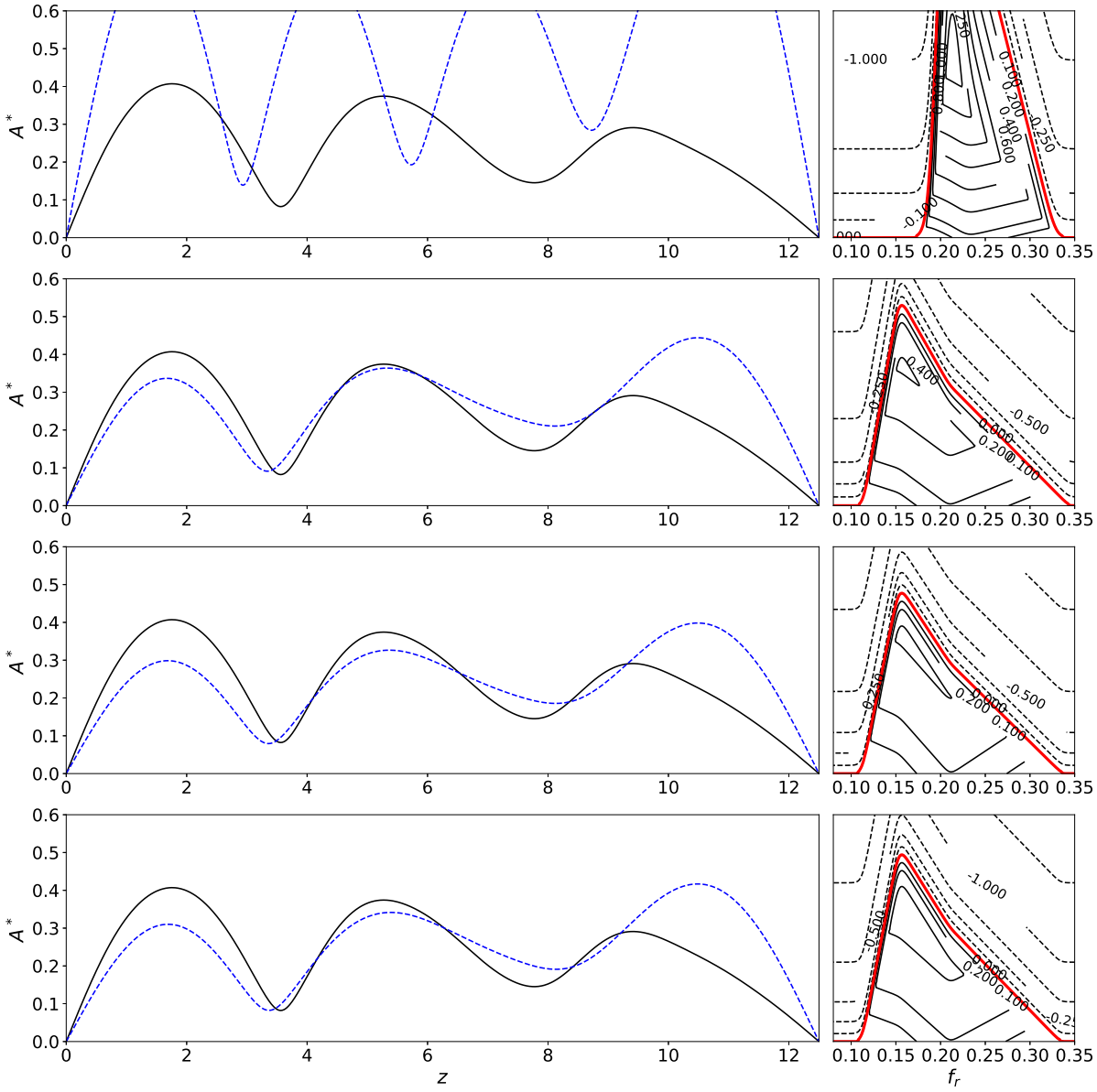

Figure 3-7: **Test case 2001**. *Cross flow RMS predictions, testing catenary plane angle with velocity* $\phi = 30°$. Solid black curve are reconstructed displacements and blue-dashed line are optimized VIVA predictions. A single hydrodynamic database is used. In this figure we represent the change in spanwise RMS response as the training is performed in the 3 catenary plane orientations to which this specific case does not belong to, in this particular case $\phi = 0°, 60°, 90°$. For the relation between experiment labels and catenary plane orientations & towing velocities table 3.1 can be consulted.

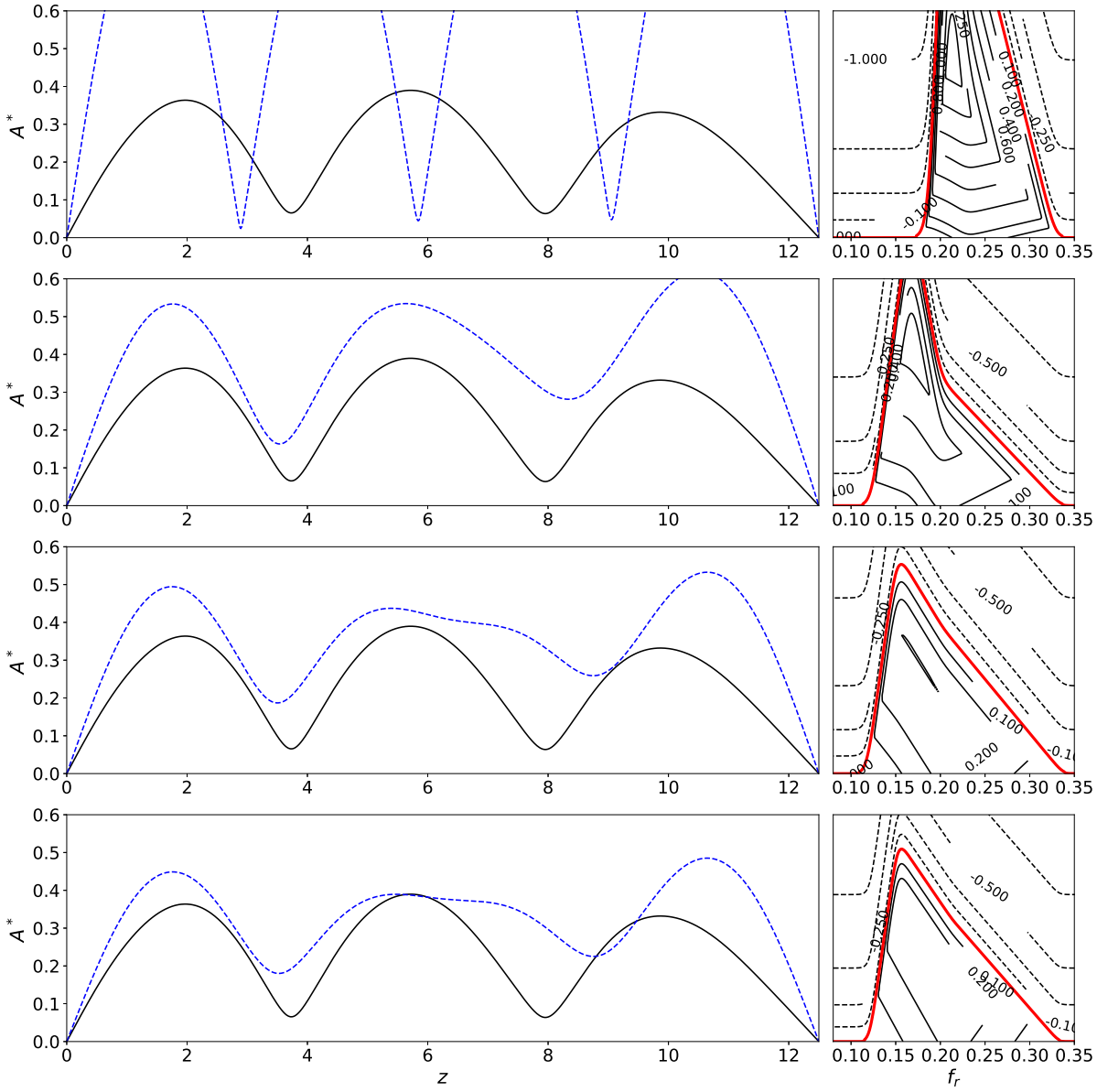

Figure 3-8: **Test case 3000**. *Cross flow RMS predictions, testing catenary plane angle with velocity* $\phi = 60°$. Solid black curve are reconstructed displacements and blue-dashed line are optimized VIVA predictions. A single hydrodynamic database is used. In this figure we represent the change in spanwise RMS response as the training is performed in the 3 catenary plane orientations to which this specific case does not belong to, in this particular case $\phi = 0°, 30°, 90°$. For the relation between experiment labels and catenary plane orientations & towing velocities table 3.1 can be consulted.

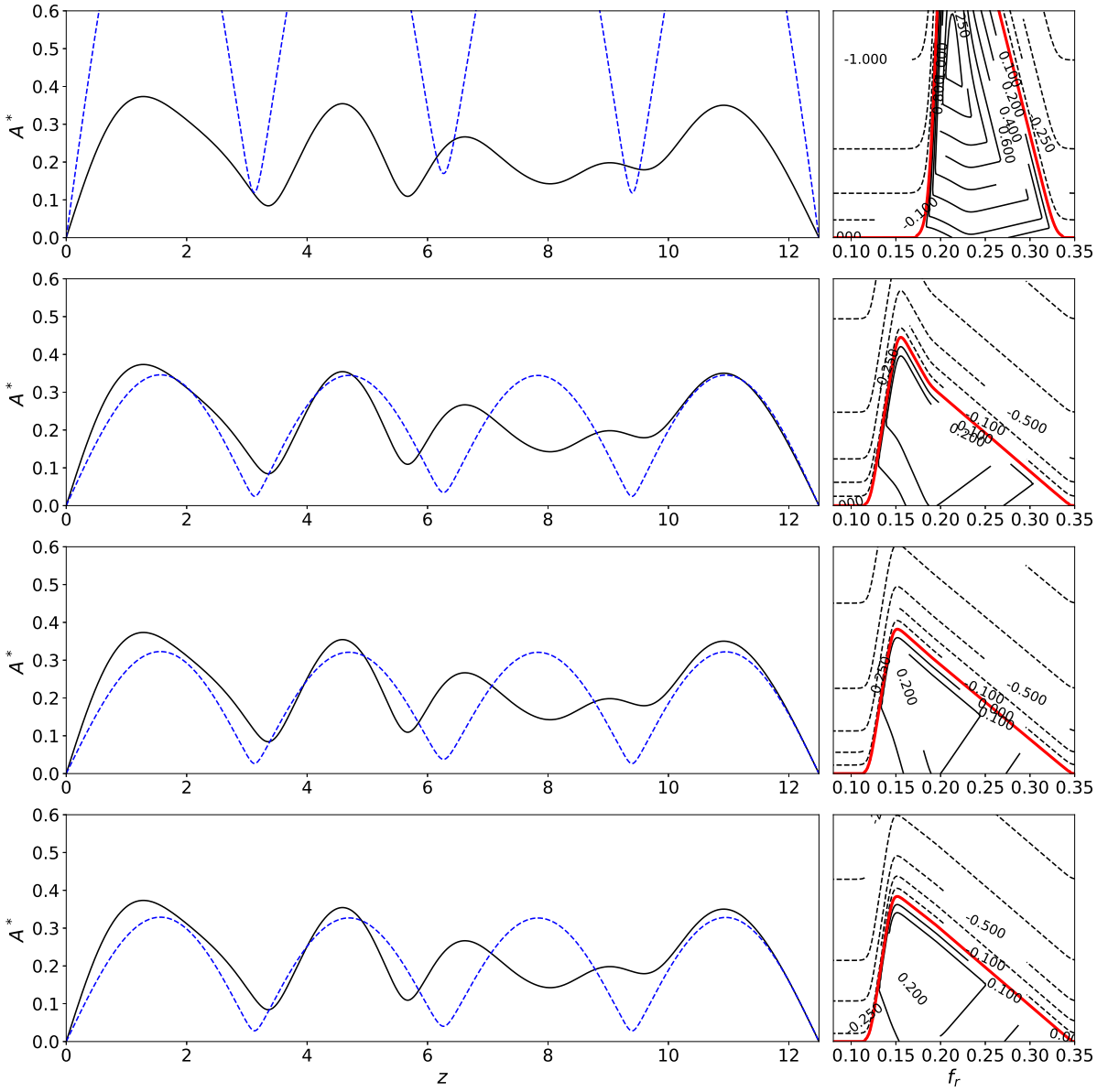

Figure 3-9: **Test case 4000**. *Cross flow RMS predictions, testing catenary plane angle with velocity* $\phi = 90°$. Solid black curve are reconstructed displacements and blue-dashed line are optimized VIVA predictions. A single hydrodynamic database is used. In this figure we represent the change in spanwise RMS response as the training is performed in the 3 catenary plane orientations to which this specific case does not belong to, in this particular case $\phi = 0°, 30°, 60°$. For the relation between experiment labels and catenary plane orientations & towing velocities table 3.1 can be consulted.

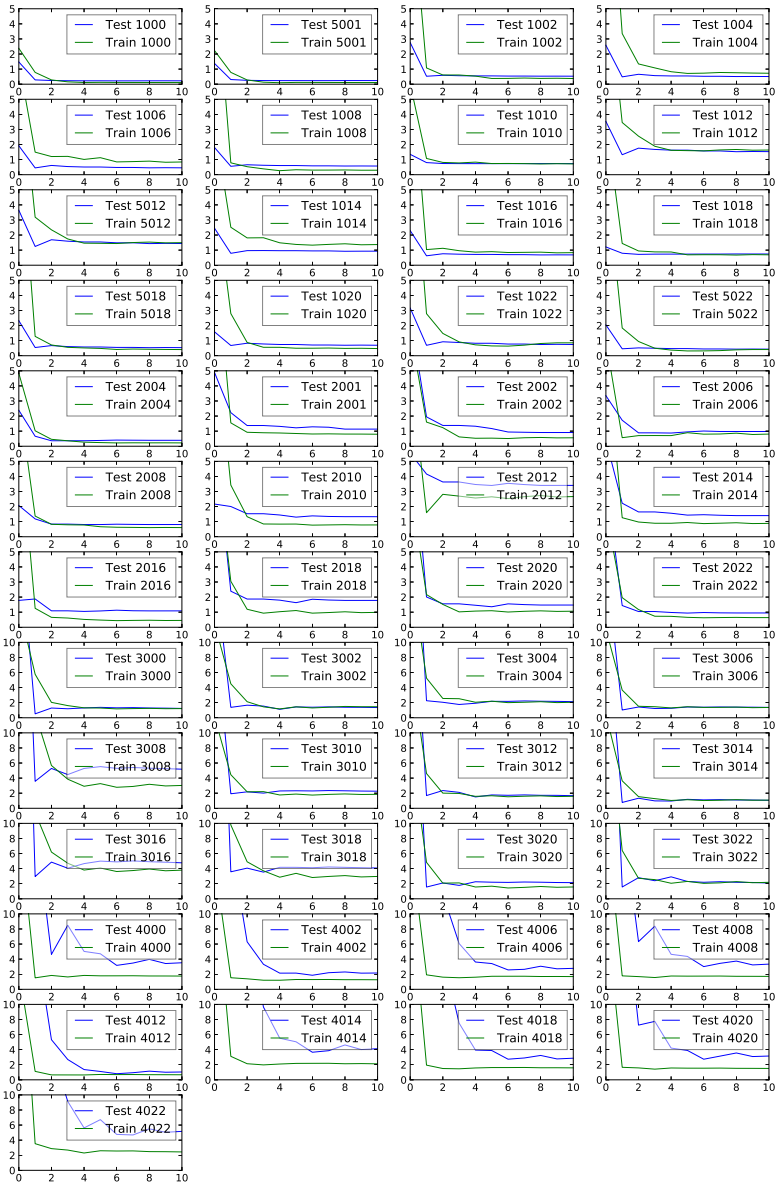

Figure 3-10: Test and train *amplitude* RSE Learning Curves. For any one plot the *test learning curve* represents the loss function when the experiment is left out of the training. This is when its current direction is left out of the training process in the cross-validation. On the other hand, the *train learning curve* is the average of the 3 scenarios when its current direction is part of the training process. Three out of four times any one case is considered in the training, when performing cross-validation across 4 different catenary plane orientations with the flow. The catenary plane orientation of any case can be consulted in table 3.1.

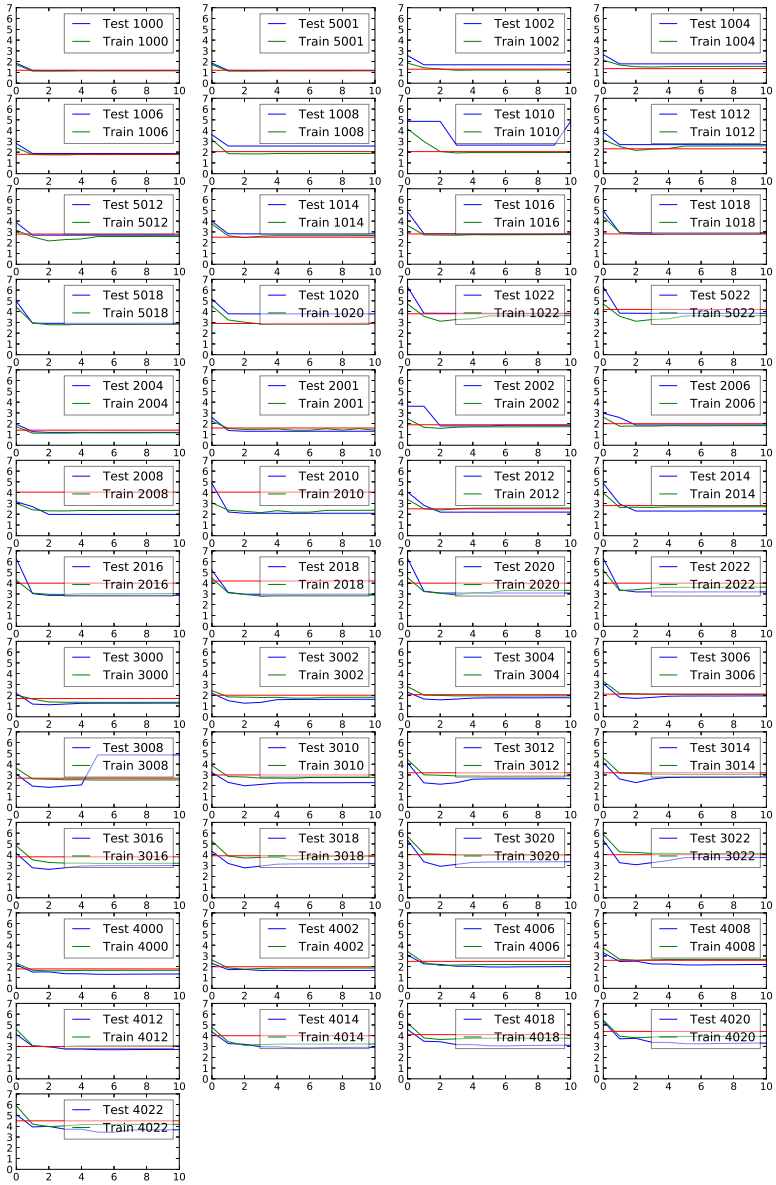

Figure 3-11: Test and train *frequency* Learning Curves. For any one plot the *test learning curve* represents the loss function when the experiment is left out of the training. This is when its current direction is left out of the training process in the cross-validation. On the other hand, the *train learning curve* is the average of the 3 scenarios when its current direction is part of the training process. Three out of four times any one case is considered in the training, when performing cross-validation across 4 different catenary plane orientations with the flow. The catenary plane orientation of any case can be consulted in table 3.1.

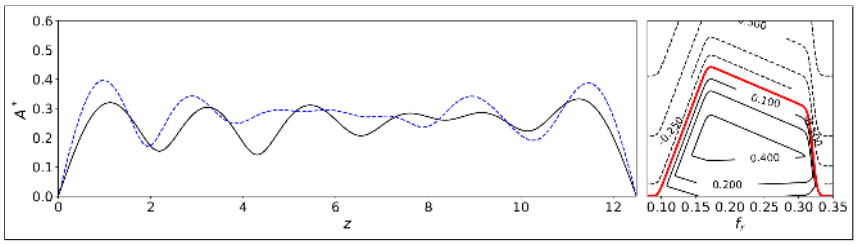

(a) Experiment 1022 at 0.34 m/s and Direction 0°.

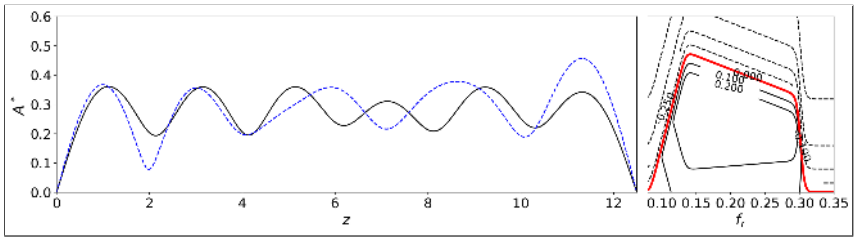

(b) Experiment 2022 at 0.34 m/s and Direction 30°.

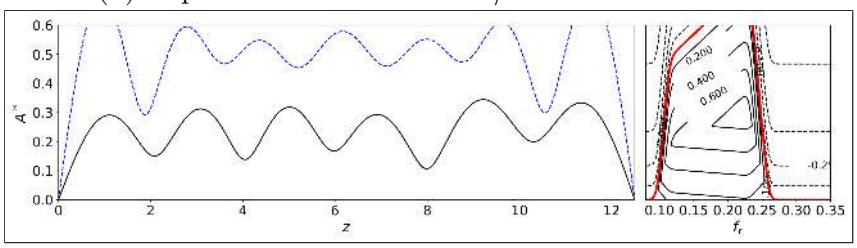

(c) Experiment 3022 at 0.34 m/s and Direction 60°.

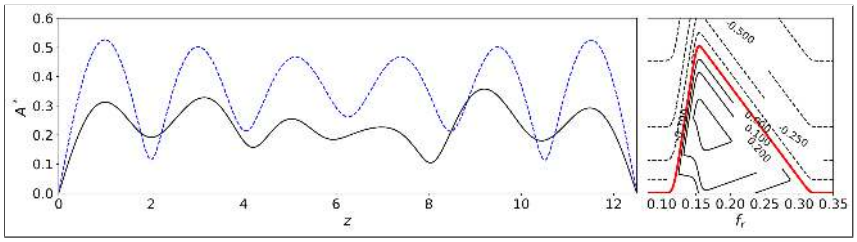

(d) Experiment 4022 at 0.34 m/s and Direction 90°.

Figure 3-12: Comparative Analysis of Experiments at a Uniform Current Velocity of 0.34 m/s. This figure showcases the results from experiments 1022, 2022, 3022, and 4022, each conducted at the same current velocity but varying current directions: 0°, 30°, 60°, and 90°, respectively. The comparison of these experiments highlights the influence of current direction on hydrodynamic responses.

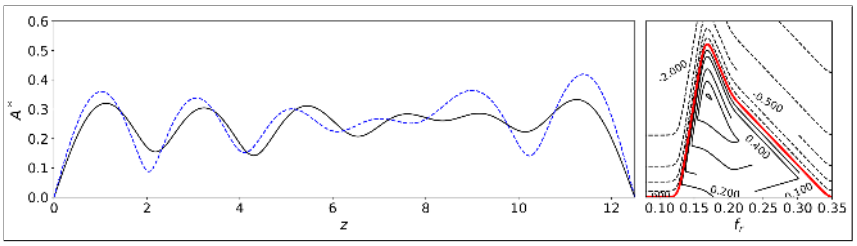

(a) Experiment 1022 at 0.34 m/s and Direction 0°.

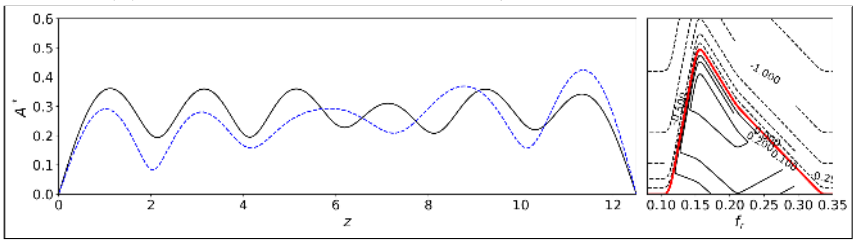

(b) Experiment 2022 at 0.34 m/s and Direction 30°.

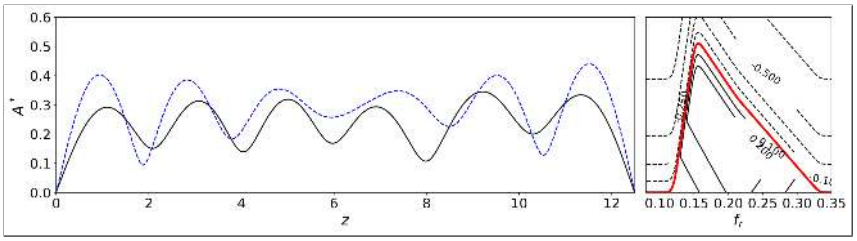

(c) Experiment 3022 at 0.34 m/s and Direction 60°.

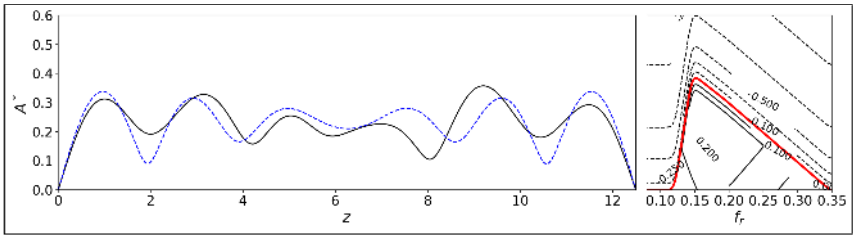

(d) Experiment 4022 at 0.34 m/s and Direction 90°.

Figure 3-13: Enhanced Optimization with Parameter Constraints in Hydrodynamic Database Training. Displayed are results from experiments 1022, 2022, 3022, and 4022, each at a uniform current velocity of 0.34 m/s but different current directions (0°, 30°, 60°, and 90°). For these experiments, parameter constraints were applied during training whenever existing experimental data were available. This approach facilitates easier optimization problems and better generalization, resulting in more consistent hydrodynamic databases when learning from diverse sets of angles.

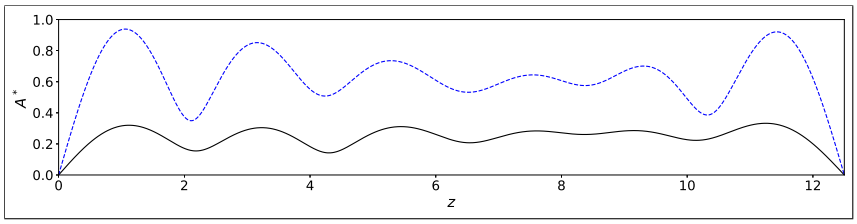

(a) Experiment 1022 at 0.34 m/s and Direction 0°.

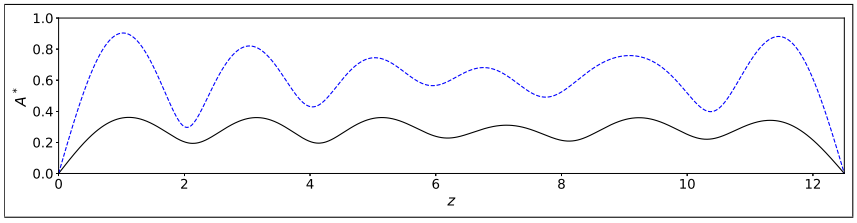

(b) Experiment 2022 at 0.34 m/s and Direction 30°.

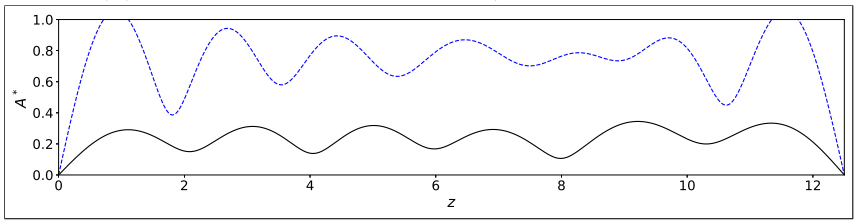

(c) Experiment 3022 at 0.34 m/s and Direction 60°.

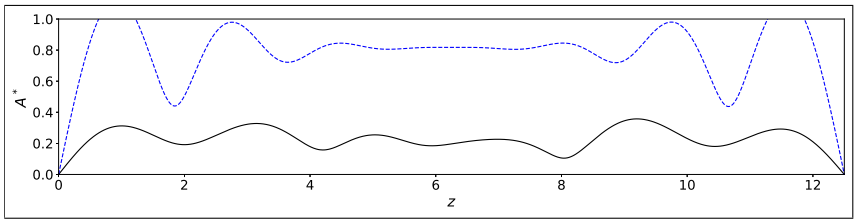

(d) Experiment 4022 at 0.34 m/s and Direction 90°.

Figure 3-14: Predictions provided by standard VIVA database. Displayed are results from experiments 1022, 2022, 3022, and 4022, each at a uniform current velocity of 0.34 m/s but different current directions (0°, 30°, 60°, and 90°). For these experiments, parameter constraints were applied during training whenever existing experimental data were available. This approach facilitates easier optimization problems and better generalization, resulting in more consistent hydrodynamic databases when learning from diverse sets of angles.

Chapter 4

Boundary Layer Control Using Vortex Generators

4.1 Introduction

Both in the air and in the water, the efficiency of moving objects is fundamentally influenced by the flow of the surrounding fluid, be it air or water. This efficiency is deeply rooted in the behavior of the boundary layer – that thin layer of fluid that clings to the surface of objects and governs a multitude of flow-related phenomena, including drag and lift [288].

Boundary layers, whether in aerodynamic or hydrodynamic contexts, are susceptible to external conditions and can undergo separation when faced with adverse pressure gradients [116]. Such separation can result in augmented drag, diminished lift or thrust, and can even lead to undesirable flow-induced vibrations or noise [225]. Therefore, the control of the boundary layer is crucial, not only for optimizing performance but also for ensuring safety across a range of engineering applications [6].

Vortex generators emerge as an effective solution to improve flow in this context. These strategically placed devices introduce controlled disturbances into the flow to delay or prevent separation, enhance fluid mixing, and achieve various other desired flow modifications [234]. By leveraging the power of vortex generation, these devices offer a nuanced approach to flow control in both aerodynamics and hydrodynamics [114].

This chapter looks into the science and application of vortex generators as tools for boundary layer control in bodies with pressure and friction drag rations similar to bulk-carrier ships. By bridging the principles that ground their operation with their wide-ranging applications, we aim to provide a thorough overview of their transformative impact on the design and optimization landscapes of both aerodynamics and hydrodynamics, described by the incompressible Navier-Stokes equations:

$$\rho\left(\frac{\partial \mathbf{u}}{\partial t} + \mathbf{u}\cdot\nabla\mathbf{u}\right) = -\nabla p + \mu\nabla^2\mathbf{u} + \mathbf{f} \tag{4.1}$$

$$\nabla\cdot\mathbf{u} = 0 \tag{4.2}$$

Where:

- ρ is the fluid density (assumed to be constant for incompressible flow).
- $\mathbf{u}$ is the velocity vector.
- t is time.
- p is pressure.
- μ is dynamic viscosity.
- $\mathbf{f}$ represents body forces (e.g., gravity).
- ∇ denotes the gradient operator.

4.1.1 Background

The story of boundary layer control is as old as the study of fluid mechanics itself. Ever since the early days of aerodynamic and hydrodynamic research, the behavior of the thin layer of fluid adjacent to surfaces has been of significant interest. Recognizing its profound impact on the performance of objects moving through fluids dates back to foundational works such as Schlichting's exploration on boundary layer theory [236].

Ludwig Prandtl's groundbreaking introduction of the boundary layer theory in the early 20th century [210] provided a framework that reshaped our understanding of fluid

flow over surfaces. With this, the importance of managing and manipulating the boundary layer became clear, especially given its implications on drag reduction and flow stability.

As the challenges of boundary layer separation became more evident, especially under adverse pressure gradients, various strategies emerged to address them. Seminal works by Van Driest [279] and others highlighted the complexity of boundary layer separation and its profound effects on flow characteristics.

The advent of vortex generators as a boundary layer control solution in the mid-20th century can be traced to early experimental studies by Taylor [93]. Their primary purpose was clear: introduce small-scale vortices to energize the boundary layer, delay separation, and foster reattachment. The success of vortex generators in various applications, from aircraft wings to ship hulls, is well-documented in numerous studies [17, 147].

Today, as research by Lin [146] and others have shown, vortex generators represent a sophisticated blend of fundamental fluid mechanics and innovative engineering, offering versatile solutions for myriad flow scenarios.

4.1.2 Objectives

4.1.3 Boundary Layer Fundamentals

The boundary layer is a fundamental concept in fluid dynamics, describing a thin layer of fluid adjacent to the surface of an object moving through a fluid or when an object is placed in a flowing fluid. Within this layer, due to the no-slip condition, the flow velocity starts from zero at the surface and increases gradually to the free-stream velocity as one moves away from the surface.

The pioneering work of Ludwig Prandtl in 1904 introduced the idea of the boundary layer. Prandtl's insight was that in many flow scenarios, the viscous effects are localized close to the surface of the object, which gives rise to the formation of this boundary layer. As the flow develops along the surface, it can manifest in several ways. Initially, fluid particles might move smoothly in parallel layers, characterizing a laminar boundary layer. This behavior is common at low Reynolds numbers or at the starting stages of flow over a surface. However, as conditions change, particularly at higher Reynolds numbers, the flow can become turbulent, exhibiting chaotic and irregular motion. Between these two

regimes, there can be a transitional phase, where intermittent turbulent "patches" are seen amidst a primarily laminar flow.

One of the critical phenomena associated with boundary layers is flow separation. This occurs when the flow slows down significantly due to an adverse pressure gradient—essentially, when the pressure increases in the flow direction. When separation occurs, it can lead to the formation of a recirculation zone, often resulting in augmented drag and undesirable flow behaviors. This connection between the boundary layer and drag is paramount in many engineering applications. Proper management and understanding of the boundary layer can be key to reducing frictional drag, often referred to as skin friction.

A crucial parameter influencing the nature of the boundary layer is the Reynolds number. This dimensionless quantity signifies the ratio of inertial forces to viscous forces in the flow. Defined as $Re = \frac{\rho u L}{\mu}$, where ρ is the fluid density, u is flow velocity, L is a characteristic length, and μ is the fluid's dynamic viscosity, the Reynolds number often dictates whether the flow is laminar, transitional, or turbulent.

Lastly, in scenarios where heat transfer is vital, the concept extends to the thermal boundary layer. Analogous to how velocity changes across the boundary layer, temperature gradients exist within the thermal boundary layer, determining the rates of heat transfer between the fluid and the object's surface.

4.1.4 Definition and Basic Concepts

4.1.4.1 Boundary Layer Definition

The region of the flow close to the wall in which viscous effects are significant and the velocity varies from zero at the wall due to the no-slip condition to the free stream value away from the wall.

4.1.4.2 Reynolds Number

$$Re = \frac{\rho u L}{\mu}$$

A dimensionless parameter characterizing the relative importance of inertial to viscous forces in a flow.

4.1.4.3 Boundary Layer Thickness

The distance from the wall to a point in the flow where the velocity is approximately the free-stream velocity.

4.1.4.4 Skin Friction Coefficient

$$C_f = \frac{2\tau_w}{\rho U^2}$$

Where τ_w is the wall shear stress. This coefficient describes the wall shear as a fraction of the dynamic pressure.

4.1.4.5 Laminar and Turbulent Boundary Layers

Different flow regimes within the boundary layer, often distinguished by the Reynolds number.

4.1.4.6 Flow Separation

Occurs when the boundary layer detaches from the surface leading to a recirculation zone.

4.1.5 Types of Boundary Layers

4.1.5.1 Based on Flow Characteristics

- **Laminar Boundary Layer**: In this type, fluid flows in smooth, orderly layers with minimal mixing between them. This type of flow is characterized by a linear velocity profile from the surface to the free stream and occurs at lower Reynolds numbers, where viscous forces are more dominant than inertial forces. The laminar flow results in lower skin friction drag and reduced rates of heat and mass transfer due to the orderly movement of fluid particles. Its predictability makes it easier to model mathematically, but it's more susceptible to becoming unstable and transitioning to turbulence under certain conditions like increased speed or surface roughness.

- **Transitional Boundary Layer**: This is the intermediate stage between laminar and turbulent flows. Intermittent "bursts" of turbulence appear amidst a primarily laminar flow, making it neither fully laminar nor fully turbulent.

- **Turbulent Boundary Layer**: Conversely, a turbulent boundary layer exhibits a chaotic flow with a complex mixture of eddies and vortices. This regime occurs at higher Reynolds numbers, where inertial forces outweigh viscous forces. The turbulent flow leads to a thicker boundary layer with a non-linear velocity profile, featuring a thin viscous sublayer near the wall. Turbulent boundary layers are associated with higher skin friction drag but offer significantly enhanced rates of heat and mass transfer due to the increased mixing. Though turbulent flows are more challenging to predict and require empirical or numerical modeling methods, they tend to remain turbulent unless there's a substantial decrease in flow velocity or Reynolds number.

4.1.5.2 Based on Thermal Effects

- **Isothermal Boundary Layer**: In scenarios where the wall temperature remains constant and there's no heat transfer between the surface and the fluid, the boundary layer remains isothermal.

- **Thermal Boundary Layer**: When there's heat transfer between the surface and the fluid, a temperature gradient develops. In this case, besides the velocity profile, there's also a temperature profile within the boundary layer. This is especially important in convective heat transfer studies.

- **Combined Thermal and Hydrodynamic Boundary Layer**: Often in real-world situations, both the velocity and temperature fields are of concern, leading to a combined boundary layer analysis.

4.1.5.3 Based on Pressure Gradient

- **Zero Pressure Gradient Boundary Layer**: This occurs on a flat plate with uniform flow, where the pressure remains constant in the streamwise direction.

- **Favorable Pressure Gradient Boundary Layer**: When the external pressure decreases in the flow direction, it's termed favorable since it can prevent or delay separation.

- **Adverse Pressure Gradient Boundary Layer**: Conversely, when the external pressure increases in the flow direction, the boundary layer faces an uphill task. This situation can induce flow separation more readily.

4.1.5.4 Based on the Geometry of the Object

- **Bluff Body Boundary Layer**: Developed over bodies with a blunt shape, such as cylinders or spheres, often leading to separated flows and wake regions.

- **Streamlined Body Boundary Layer**: Developed over bodies designed to minimize separation, like airfoils or streamlined vehicles.

In this chapter, our primary focus is on the hydrodynamic aspects of boundary layers and the use of vortex generators for flow control. While thermal effects and heat transfer are crucial considerations in many real-world applications, they fall outside the scope of our current research. However, it is worth noting that the principles and designs of vortex generators explored herein could potentially be adapted or employed to optimize heat transfer in thermal boundary layer scenarios.

4.1.6 Boundary Layer Detachment: An Energy Perspective

When fluid flows over a solid surface, energy interactions play a essential role in determining the nature and behavior of the boundary layer.

4.1.6.1 Energy Loss due to Friction

As fluid particles traverse the boundary's surface, frictional forces come into play. These forces, acting between the fluid particles and the solid boundary, sap energy from the boundary layer. Mathematically, this is seen as the viscous drag exerted on the body. Within the boundary layer, the consequence of this energy loss is a velocity gradient: fluid

particles closest to the surface move slower than those farther away, due to the no-slip condition.

$$\tau = \mu \left(\frac{\partial u}{\partial y} \right) \tag{4.3}$$

Here, τ represents the wall shear stress, μ is the dynamic viscosity, and $\frac{\partial u}{\partial y}$ is the velocity gradient perpendicular to the wall.

4.1.6.2 Adverse Pressure Gradient and Energy

As these energy-depleted particles progress downstream along the body, they may encounter regions of increasing external pressure—a phenomenon termed as an adverse pressure gradient.

To frame this in terms of energy, consider Bernoulli's principle:

$$P + \frac{1}{2}\rho u^2 + \rho g h = \text{constant} \tag{4.4}$$

Where:

- P is the pressure energy,
- ρ is the fluid density,
- u is the fluid velocity (kinetic energy),
- g is the acceleration due to gravity, and
- h is the height (potential energy).

An adverse pressure gradient implies an increase in P, and for fluid particles away from the boundary, this increase can be counteracted with a decrease in $\frac{1}{2}\rho u^2$. However, for the energy-depleted particles near the wall, this balance is disrupted, causing a substantial reduction in their kinetic energy, eventually leading to flow reversal.

4.1.6.3 Trailing Ends: The Ultimate Challenge

Many aerodynamic and hydrodynamic designs taper towards the trailing end, promoting a more pronounced adverse pressure gradient in this region. The boundary layer particles,

already sapped of energy due to friction, find it even more challenging to overcome this gradient, making detachment almost inevitable. Interventions, such as vortex generators, may be employed to delay or prevent this detachment, emphasizing their importance in engineering applications.

4.2 Vortex Generators: An Overview

4.2.1 Historical Development

The aeronautics industry's evolution during the 20th century was significantly shaped by advancements in understanding boundary layer dynamics. As aircraft designs became increasingly intricate, addressing boundary layer separation grew in importance, particularly when targeting higher speeds and varying flight envelopes.

The decades of the 1940s and 1950s witnessed intensive efforts to combat boundary layer separation challenges. In this context, vortex generators (VGs) emerged as a promising solution. Their ability to manage boundary layer separation without the need for external power was a standout feature.

A very important research point in the early history of VGs was Schubauer and Skramstad's work in 1947, laying the groundwork for future VG research [238, 239]. Fast forwarding to the dawn of the 21st century, Lin's comprehensive study in 2002 provided a nuanced examination of VG design parameters, highlighting their potential adaptability across diverse aero/hydrodynamic scenarios [147].

Into the 2000s, the study of VGs and their applications broadened. Bechert et al.'s research in 2000 presented insights into the drag reduction capabilities of riblet surfaces, suggesting potential collaborative effects with VGs [17]. Building on this, Godard and Stanislas in 2006 further explored the intricacies of how VGs influence boundary layer dynamics under various conditions [90].

Beyond the skies, VGs found applicability on the ground. By 2018, their potential in automotive applications became evident, with research by Zhang et al. highlighting this versatility [242].

4.2.2 Principle of Operation

When a flow encounters a vortex generator, due to the shape and orientation of the VG, it creates a localized disturbance, which leads to the formation of a vortex. This vortex, once formed, has a distinct core and circulation pattern, with fluid particles moving in a spiral motion around the core.

The core of the vortex is an area of low pressure. As the fluid spirals around this low-pressure core, it creates a suction effect. This suction effect is critical because it pulls or draws fluid from its surroundings towards the vortex core. As VGs are typically positioned with their tips protruding into the freestream, this means the vortices have access to the higher-energy, faster-moving fluid found outside the boundary layer [90].

Now, the boundary layer, by definition, is characterized by a velocity gradient where the fluid velocity decreases from the freestream value to almost zero at the wall. As a result, the fluid near the wall has much lower kinetic energy compared to the fluid in the freestream.

When the vortex creates suction, it actively draws this high-energy fluid from the freestream, transferring it closer to the wall or body. This process is referred to as "boundary layer energization" because the transferred high-energy fluid revitalizes or energizes the near-wall region of the boundary layer [147].

This addition of high-energy fluid helps in several ways:

- Resilience to Adverse Pressure Gradient: By introducing more energy to the boundary layer, it becomes better equipped to handle adverse pressure gradients, thereby delaying or preventing flow separation.

- Enhanced Turbulence and Mixing: The high-energy fluid introduced by the vortex can lead to increased turbulence levels. This turbulence promotes better mixing within the boundary layer, ensuring a more uniform velocity profile and suppressing the formation of flow separation regions [299].

- Redistribution of Shear Stress: With the introduction of higher-energy fluid, the shear stresses within the boundary layer are also redistributed, which can lead to enhanced wall shear and better attachment of the flow.

In summary, the vortices generated by VGs play a dual role: they not only create disturbances that delay separation but also actively draw high-energy fluid from the freestream into the boundary layer. This influx of high-energy fluid bolsters the boundary layer's resilience against adverse conditions, ensuring improved flow characteristics and performance.

4.2.3 Types of Vortex Generators

Vortex Generators (VGs) have evolved into various forms and types over the years. Each type possesses distinct characteristics tailored for specific applications or flow conditions. Below, we detail some of the common types of VGs:

4.2.3.1 Vane-Type VGs

These traditional and widely-recognized VGs resemble small fins. They are generally aligned with the flow direction and protrude from the surface into the boundary layer. When the flow collides with these fins, it gets deflected, inducing a series of vortices in the wake of each fin. These vortices help in energizing the low-momentum fluid near the surface, thereby delaying flow separation and enhancing mixing [147].

4.2.3.2 Ramp-Type VGs

Essentially miniature ramps or wedges, these VGs have an inclined profile which forces the oncoming flow to elevate as it goes over the ramp. This action disrupts the flow's laminar structure and generates vortices, which like the vane-type, serve to invigorate the boundary layer, ensuring it remains attached for longer [252].

4.2.3.3 Sub-Boundary Layer VGs (or Micro-VGs)

Much smaller than the traditional VGs, these are designed to function primarily within the boundary layer without excessively disturbing the external flow. Due to their minute size, they introduce milder perturbations, leading to vortices that are of smaller scale but still effective in terms of flow control, making them ideal for applications that demand a subtler approach [8].

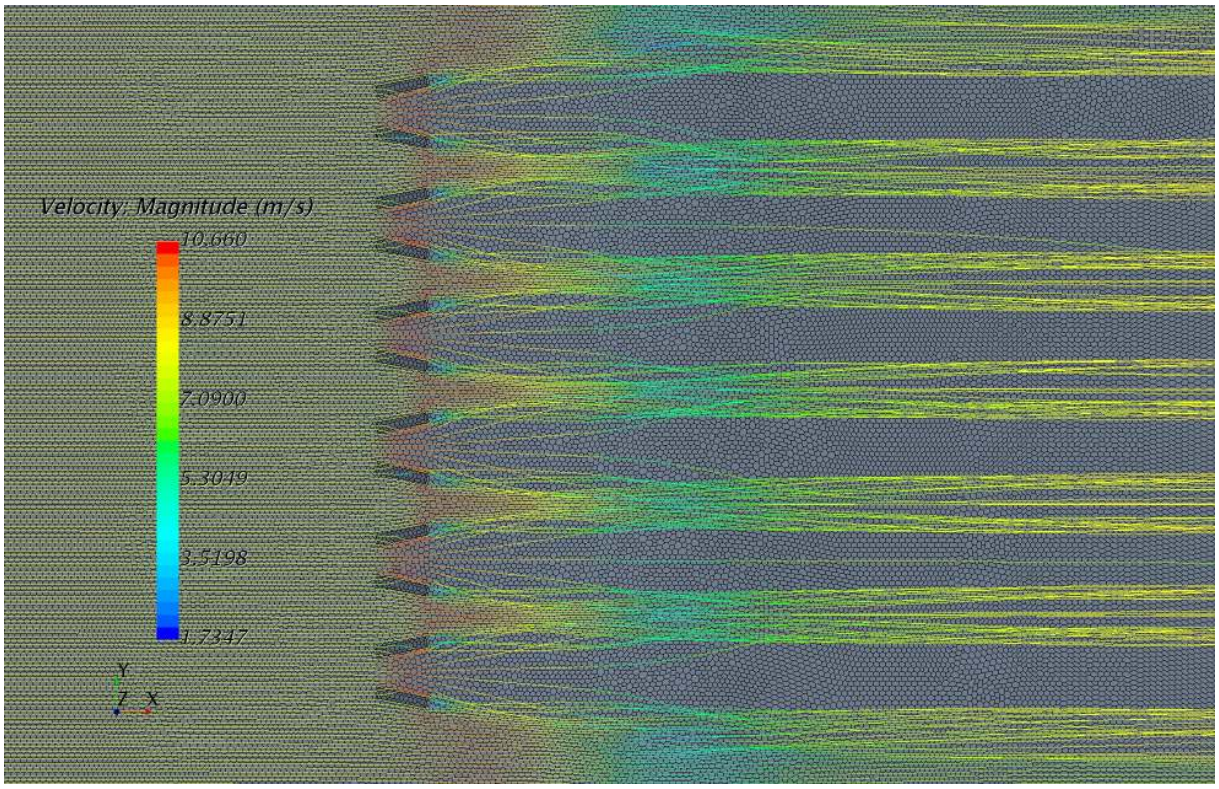

Figure 4-1: Delta wing vortex generators over a ramp. By inspecting the streamlines one can see how the VGs rotate the flow generating helical vortices that such higher energy fluid from outside the boundary layer.

4.2.3.4 Delta-Wing VGs

Resembling the shape of a delta wing from an aircraft, these VGs have a triangular design, often with a bit of a twist. The shape and orientation give rise to strong leading-edge vortices, which then spiral around the leeward side of the VG. The vortices produced by delta-wing VGs tend to be more robust and resistant to external disturbances, making them effective for a variety of aero/hydrodynamic applications [131].

4.2.3.5 Blowing/Suction VGs

These VGs differ fundamentally from the passive ones mentioned before. They involve active manipulation of the boundary layer by either introducing high momentum fluid into the boundary layer (blowing) or by drawing fluid out of it (suction). This action has the potential to drastically modify the boundary layer's velocity profile, preventing or

delaying separation. The effectiveness of this method, however, can be contingent upon the precise positioning, intensity, and pulsing frequency of the blowing/suction mechanism [90].

4.2.3.6 Co-Flow Jet VGs

Another form of active VGs, co-flow jet VGs introduce small jets of fluid that align with the main flow direction. By doing so, they not only energize the boundary layer but also enhance mixing within it. This technique proves especially beneficial in delaying flow separation by re-energizing regions of the boundary layer that are on the brink of detachment [48].

4.3 Design and Optimization of Vortex Generators

Vortex generators, small aero/hydrodynamic devices strategically placed on surfaces to influence the flow of air or other fluids, play a very important role in enhancing the performance of various aero/hydrodynamic systems. Their primary function is to delay flow separation by re-energizing the boundary layer, thereby improving lift and reducing drag [147]. The effectiveness of vortex generators is significantly influenced by their design and optimization [144, 8]. As technological advancements continue to expand the horizons of fluid dynamics, there is an ever-increasing need to understand the nuances of vortex generator designs and the methodologies to optimize them, [81]. This section looks into the critical geometric parameters that define the shape and orientation of these devices, the material considerations that impact their durability and efficiency, and the state-of-the-art optimization techniques that ensure they are tailored for specific applications. By understanding these intricacies, engineers and researchers can make informed decisions when implementing vortex generators in various applications.

4.3.1 Geometric Parameters

Vortex generators play an instrumental role in boundary layer control, with their effectiveness significantly influenced by their geometric parameters. These parameters determine

the size, strength, and location of the vortices produced. The major geometric considerations include:

1. **Height (h)**: The height of the vortex generator determines the penetration of the vortex into the free stream. A taller vortex generator influences a larger portion of the boundary layer.

2. **Base Width (b)**: The width at the base dictates the overall size of the vortex. A broader base results in a larger vortex.

3. **Spanwise Spacing (s)**: The distance between consecutive vortex generators affects the interaction of individual vortices. Proper spacing is crucial to prevent merging of vortices or leaving areas of flow uninfluenced.

4. **Chordwise Location**: The position relative to the leading or trailing edge of a surface can impact flow control effectiveness. In hydrodynamics this could be resembled to what part of the curved section it is placed.

5. **Angle of Attack (α)**: The orientation angle relative to the oncoming flow is crucial. A higher angle produces a stronger vortex, but excessive angles might cause flow separation on the generator.

6. **Shape and Profile**: Various shapes, from simple prisms to complex designs, can influence the vortex initiation and evolution.

7. **Aspect Ratio (AR)**: Defined as the ratio of height to base width, the aspect ratio affects the vortex's coherence and longevity.

8. **Leading Edge Design**: Different leading edge designs, be it rounded, sharp, or serrated, produce vortices with unique characteristics.

Optimizing these parameters requires comprehensive knowledge of the flow conditions and the desired outcomes, whether it's delaying flow separation, reducing noise, or achieving other specific goals. In this thesis we consider just three parameters: angle of attach with respect to the incomming flow, VG height and longitudinal possition along the considered axisymmetric body.

4.3.2 Material Considerations

The longevity, functionality, and effectiveness of vortex generators depend significantly on the materials used in their construction [7]. Several factors come into play when choosing the appropriate material for VGs:

1. **Mechanical Durability**: VGs often encounter mechanical stresses due to turbulent flows, impacts (e.g., from debris), and vibrational loads. The chosen material must exhibit high tensile strength and fatigue resistance.

2. **Environmental Resistance**: VGs are often exposed to various environmental conditions like UV radiation, moisture, temperature fluctuations, and corrosion. Materials should be resistant to corrosion, UV degradation, and other environmental effects.

3. **Thermal Stability**: In applications such as aerospace, VGs might experience elevated temperatures. It's essential for the material to maintain its properties and shape in varying temperature conditions.

4. **Weight Concerns**: Especially in aerospace applications, the weight of the VGs can influence the overall efficiency of the system. Lightweight materials like composites or specific grades of aluminum might be preferred.

5. **Manufacturability**: The ease of manufacturing, including shaping, cutting, and joining, plays a role in material selection. Some complex VG shapes might require materials that can be easily molded or machined.

6. **Cost-effectiveness**: While performance is paramount, the economic feasibility of material choices shouldn't be ignored. Balancing performance with cost is crucial, especially for large-scale or commercial applications.

7. **Adhesion and Integration**: If VGs are to be adhered to surfaces (as with adhesive-backed VGs), the material should support strong bonding. Moreover, integration with existing structures might require compatibility checks with other materials.

8. **Electromagnetic Properties**: For applications sensitive to electromagnetic interference, materials that don't disrupt or degrade the electromagnetic performance might be necessary.

Careful evaluation of these considerations ensures the selection of materials that optimize the performance and longevity of vortex generators across various applications.

4.4 Optimization Methods

4.4.1 Overview of Optimization Methods

Optimization methods [186] play a crucial role in the efficient design and placement of vortex generators. The choice of method depends on the complexity of the design space and the nature of the objective function.

- **Gradient-Based Optimization**: Utilizes derivatives of the objective function for optimization. It is efficient but may struggle with non-linear functions.
- **Genetic Algorithms (GAs)**: Inspired by natural selection, GAs use a population of solutions that evolve over generations. They are effective for complex problems but computationally demanding.
- **Particle Swarm Optimization (PSO)**: Simulates social behaviors of birds or fish. PSO is good for global optimization but can be resource-intensive.
- **Simulated Annealing**: Based on metallurgy annealing, it allows moves to worse solutions to escape local optima. Useful for rugged search landscapes.
- **Response Surface Methodology (RSM)**: Creates an approximate model of the objective function. Efficient when each function evaluation is expensive.

Each method has its strengths and limitations, making them suitable for specific aspects of vortex generator optimization.

4.4.2 Gaussian Processes in Optimization

Gaussian Processes (GPs) are a cornerstone of Bayesian machine learning and are particularly valuable in optimization problems [241] where the function of interest is uncertain or computationally expensive to evaluate. In the realm of engineering, GPs serve as powerful tools for surrogate modeling, assisting in the optimization of complex systems by providing a probabilistic measure of prediction uncertainty.

GPs are employed in engineering optimization for:

- Surrogate modeling of expensive-to-evaluate functions.
- Sequential decision making in algorithms like Bayesian Optimization.
- Quantifying uncertainty in optimization, crucial for risk-averse decision making.

Basic Formulation A GP is fully specified by its mean function $m(x)$ and covariance function $k(x, x')$:

- **Mean Function** $m(x)$: This function represents the average or expected value of the function $f(x)$ at each point x. Often, for simplicity, the mean function is taken to be zero, $m(x) = 0$, especially when no prior information about the data is available.
- **Covariance Function** $k(x, x')$: Also known as the kernel function, it defines the covariance (or the degree of dependency) between the function values at two points x and x' in the input space. The choice of the kernel function reflects assumptions about the function, such as smoothness, periodicity, or linearity. Common kernels include the squared exponential kernel, the Matérn kernel, and the rational quadratic kernel.

Before observing any data, a GP starts with a prior distribution over functions. This prior reflects beliefs about the properties of the function before data is taken into account. Mathematically, it is expressed as:

$$f(x) \sim \mathcal{GP}(m(x), k(x, x'))$$

This states that the function $f(x)$ follows a Gaussian Process with the specified mean and covariance.

When data $D = \{(x_i, y_i)\}_{i=1}^n$ is observed, where y_i are values (possibly noisy) of the function f at points x_i, the prior is updated to a posterior distribution over functions. This update takes into account the noise in the observations, typically modeled as Gaussian noise. The posterior distribution of the function values at new points x^* can be calculated using:

- **Posterior Mean**: $\mu(x^*)$
- **Posterior Covariance**: $\Sigma(x^*)$

These are derived from the GP prior and the likelihood of the observed data under a Gaussian noise model.

Gaussian Processes predict the function value at new test points x^* with both an expected value (mean) and a measure of uncertainty (variance). The predictive distribution of $f(x^*)$ given the observed data and the GP prior is also Gaussian:

$$f(x^*)|X, y, x^* \sim \mathcal{N}(\mu(x^*), \Sigma(x^*))$$

where X represents the matrix of training inputs, and y is the vector of observed outputs.

The strength of Gaussian Processes lies in their ability to provide uncertainty measurements along with predictions, making them particularly useful for tasks where estimating uncertainty is crucial, such as in optimization and sequential decision-making processes.

Application in Optimization In optimization, a GP models the objective function. An acquisition function then guides the sampling of new points, balancing exploitation and exploration. This iterative process continues until convergence or resource exhaustion.

Advantages:

- **Predictive Precision with Limited Data**: GPs excel in scenarios with sparse data [220]. Their Bayesian nature allows them to make the most out of every data point, providing precise predictions even in data-scarce environments.

- **Incorporation of Prior Knowledge**: GPs allow the integration of prior knowledge through the kernel choice. This flexibility can significantly enhance model accuracy [60], especially when prior physical insights about the problem are available.

- **Robustness to Overfitting**: Due to their probabilistic foundation, GPs are less prone to overfitting compared to many other machine learning models [180], making them reliable for complex optimization tasks.

- **Natural Handling of Noise**: GPs can inherently account for observational noise in the data [215], making them suitable for real-world applications where measurements are often imperfect.

Disadvantages:

- **Scalability Challenges**: The computational demand of GPs grows cubically with the number of data points, making them less practical for very large datasets [250]. This limitation can be particularly challenging in simulations or experiments with extensive data.

- **Kernel Selection and Hyperparameter Tuning**: The effectiveness of a GP is highly dependent on the kernel function and its hyperparameters. Selecting and tuning these can be non-trivial [251], requiring domain expertise and computational resources.

- **High-Dimensional Spaces**: GPs may struggle with high-dimensional optimization problems [287]. As the number of dimensions grows, the volume of the space increases exponentially, which can dilute the effectiveness of the model.

- **Interpretability**: While GPs provide uncertainty estimates, interpreting these results and the model's structure can be complex compared to more transparent models [22].

In the specific context of optimizing the proposed vortex generators, where the parameter space is limited to three dimensions (Angle, Height, Pos), Gaussian Processes (GPs)

emerge as an ideal choice. The complexity involved in aero/hydrodynamic simulations and experimental evaluations is significant, often involving intricate computational fluid dynamics models or expensive wind/water tunnel testing. GPs are adept at navigating through such complex, computationally demanding landscapes with a limited number of parameters [78, 233]. They efficiently utilize available data to make accurate predictions, thereby reducing the need for extensive and costly experiments or simulations. This capability makes GPs not only a practical but a highly effective tool for the optimization task at hand, balancing the need for precision with the constraints of experimental or computational resources.

4.5 Applications of Vortex Generators

4.5.1 Aerospace

In the aerospace sector, vortex generators play a crucial role in enhancing aircraft performance, particularly in managing boundary layer dynamics [134]. These small devices, when strategically positioned on aircraft surfaces such as wings and tail sections, effectively manipulate airflow to prevent premature flow separation. This capability is crucial during critical phases like takeoff and landing, where maintaining lift is paramount, [14]. By ensuring smoother airflow over the wing, vortex generators contribute to increased lift, thereby significantly reducing stall risks.

Furthermore, their application extends to cruising phases, where they aid in reducing aerodynamic drag, a key factor in fuel consumption, [55]. By optimizing the airflow, vortex generators contribute to more efficient fuel usage, leading to cost savings and reduced environmental impact. Their impact on stability and control is also noteworthy, as they contribute to smoother flight experience and enhanced control, particularly under challenging aerodynamic conditions.

The strategic use of vortex generators in the aerospace industry shows the intricate balance between aerodynamic efficiency and flight safety. It highlights the continual evolution of aerospace technology, where even small components can lead to significant improvements in overall aircraft performance and operational efficiency [165].

4.5.2 Wind Turbines

In the context of wind turbines, [232], the application of vortex generators is a sophisticated approach to augmenting aero/hydrodynamic performance. These devices, when attached to turbine blades, play a essential role in managing airflow. Their primary function is to create vortices that energize the boundary layer, thereby maintaining a more attached flow over the blade surface. This mechanism is critical in reducing flow separation which can lead to efficiency losses, especially under off-design wind conditions.

The result of employing vortex generators is a noticeable enhancement in the overall efficiency of wind turbines, [45, 177]. They enable the turbine blades to extract more energy from the wind by ensuring a smoother, more stable airflow, leading to consistent and increased rotational speeds. This translates into a higher electricity generation capacity, optimizing the energy output from each turbine.

Moreover, vortex generators contribute to noise reduction, an essential factor in minimizing the environmental impact of wind turbines. By smoothing the airflow and reducing turbulence, they mitigate the generation of aeroacoustic noise, which is a significant concern for wind farms located near residential areas, [143].

Another crucial benefit of vortex generators is their contribution to the longevity of turbine blades. They play a significant role in reducing mechanical stresses on the blades, which are often caused by turbulent flows and flow separation. This stress reduction is key to decreasing fatigue loads, thereby prolonging the service life of the blades and reducing maintenance costs.

In summary, vortex generators offer a multi-faceted enhancement to wind turbine performance, from improving energy efficiency and reducing noise to prolonging blade life. Their integration into turbine design is a testament to the ongoing advancements in renewable energy technologies, aiming for more efficient, sustainable, and environmentally friendly power generation.

4.5.3 Other Applications

Vortex generators, beyond their conventional use in aerospace and wind turbines, have found innovative applications in various engineering sectors. In automotive engineering [278], their strategic placement on vehicle surfaces significantly contributes to drag reduction, thereby enhancing fuel efficiency and vehicular stability, especially at high speeds. This drag reduction is crucial for performance vehicles and has implications for reducing emissions in commercial automobiles.

In the realm of thermal management, vortex generators play a very important role in heat exchangers. By promoting turbulent flow, they enhance the heat transfer coefficients, leading to more efficient cooling or heating processes [175]. This application is particularly beneficial in industries where precise temperature control is essential, such as in chemical processing plants and refrigeration systems.

Moreover, their utility extends to architectural aerodynamics [151], where vortex generators are used to mitigate wind loads on high-rise buildings, enhancing structural stability and safety. In maritime engineering, they can improve hydrodynamic efficiency for vessels, reducing fuel consumption and increasing operational range.

The potential application of vortex generators (VGs) on large marine vessels offers an intriguing area for exploration[105]. Theoretically, VGs could reduce hydrodynamic drag on these bulkier ships by energizing the boundary layer, leading to more attached flow and potentially improved fuel efficiency. However, the actual extent of these benefits could vary, depending on vessel design and operational conditions. This variability invites further research to optimize VG placement and design for different ship types.

Additionally, VGs may play a role in reducing mechanical stresses on vessels, potentially enhancing structural integrity and reducing onboard vibrations and noise. However, the effectiveness of VGs in this regard is not universally established and would most definitively depend on their precise implementation.

The impact of VGs on improving maneuverability and stability, especially at lower speeds, also presents a promising avenue, but this requires empirical validation to determine how VGs can be best adapted to specific vessel characteristics.

Lastly, while VGs could contribute to reducing emissions and enhancing environmental

sustainability, quantifying these benefits is complex and necessitates a deeper understanding of the interactions between VGs, vessel design, and operational practices.

The application of vortex generators is a testament to their versatility in fluid dynamics control, demonstrating their significant impact across a broad spectrum of industries. This versatility not only underlines their technical value but also highlights their contribution to energy efficiency and environmental sustainability across diverse sectors.

4.6 Advancements and Innovations in Vortex Generators

4.6.1 Emerging Designs and Concepts

In the realm of aero/hydrodynamics, the development of vortex generators (VGs) has evolved to meet the challenges of modern applications [4]. For instance, the emergence of bio-inspired VGs [196], drawing inspiration from nature like the tubercles on whale fins [23, 3], has shown promise in improving aero/hydrodynamic efficiency. Researchers at institutions like MIT have explored these designs, finding them effective in delaying stall and reducing drag. Similarly, the automotive industry has seen VGs applied to reduce vehicle drag, as seen in studies by Ford Motor Company. In wind energy, advancements in VGs have been directed towards increasing turbine blade efficiency [177], with companies like Vestas implementing VGs to enhance power output and reduce noise. These examples illustrate the ongoing evolution in VG design, driven by the need for efficiency, environmental sustainability, and adaptability to diverse operational conditions.

4.6.2 Integration with Other Boundary Layer Control Techniques

In the quest to enhance aero/hydrodynamic performance, the integration of vortex generators (VGs) with other boundary layer control techniques has emerged as a cutting-edge research area. This section explores the innovative combinations of VGs with methods like boundary layer suction and active flow control strategies. These hybrid systems are

designed to synergistically capitalize on the strengths of each method, leading to superior control over flow separation, drag reduction, and overall aero/hydrodynamic efficiency. The following subsections detail the state-of-the-art developments in this domain, highlighting their applications in aviation, wind energy, and other aero/hydrodynamically sensitive fields.

4.6.2.1 VGs and Boundary Layer Suction

The integration of vortex generators with boundary layer suction represents a significant advancement in aero/hydrodynamic control. This hybrid technique combines the energy-inducing capability of VGs with the stabilizing effect of suction to address flow separation challenges in high-lift configurations. VGs create vortices that energize the boundary layer, delaying flow separation. When coupled with suction, which actively removes low-energy fluid near the surface, the combined effect is a more attached flow, leading to enhanced lift and reduced drag.

This approach is particularly beneficial for aircraft wings and control surfaces, where maintaining lift at high angles of attack is crucial. The implications of this technology extend to improved aircraft performance, including better takeoff and landing capabilities, and enhanced maneuverability. Additionally, there is potential for fuel efficiency improvements, as more efficient lift generation can lead to reduced engine thrust requirements, [81].

4.6.2.2 VGs with Active Flow Control (AFC)

The integration of Vortex Generators (VGs) with Active Flow Control (AFC) methods, such as synthetic jet actuators, represents a significant advancement in aero/hydrodynamic design. This synergy provides a dynamic approach to controlling airflow, particularly over airfoils and wings. VGs, known for their ability to manipulate the boundary layer and delay flow separation, when combined with AFC, lead to an adaptable system capable of responding to varying flight conditions.

This integration allows for more precise control over drag reduction and flow separation, crucial for improving the aero/hydrodynamic efficiency of aircraft. The adaptive na-

ture of AFC systems, which can modify the flow characteristics in real-time, complements the static control provided by VGs. This results in a more versatile aero/hydrodynamic control system that can optimize performance under a broader range of conditions.

Such advancements have significant implications for aircraft design, potentially leading to designs that are more fuel-efficient and have better handling characteristics. The adaptability of these systems also opens up new possibilities in flight dynamics, allowing aircraft to maintain optimal aerodynamic performance across a wider range of speeds and maneuvers.

The reference [34] provides a comprehensive understanding of the principles behind AFC and its various applications, highlighting its potential when integrated with VGs.

4.6.2.3 Hybrid Systems in Aviation and Wind Turbines

The integration of VGs with other control strategies in aviation and wind turbines is aimed at enhancing aero/hydrodynamic performance. This approach helps in optimizing the efficiency of aircraft and wind turbines by mitigating issues such as flow separation, which can occur at high angles of attack or in varied wind conditions. In aviation, this translates to improved lift-to-drag ratios, potentially leading to better fuel efficiency and reduced emissions. In wind turbines, the improved flow control can lead to higher energy capture efficiency and reduced mechanical stress. The adaptability of these hybrid systems allows for fine-tuning based on specific operational conditions, marking a significant step forward in aero/hydrodynamic design and control. For more in-depth insights, the reference [209] can be consulted.

4.6.3 Challenges and Limitations

Despite the significant advancements in vortex generator (VG) technology, several challenges and limitations still persist [271, 88], affecting their broader applicability and efficiency. This section looks into these aspects, providing insights based on recent scientific research.

4.6.3.1 Manufacturing Complexities

The manufacturing of VGs, especially those with complex geometries or made from advanced materials, presents considerable challenges. The precision required in fabricating VGs to exact specifications often leads to increased costs and production times.

4.6.3.2 Integration Difficulties

Integrating VGs onto complex aero/hydrodynamic surfaces poses another challenge. There are difficulties in ensuring structural integrity and aero/hydrodynamic efficiency, particularly in unconventional vehicle designs or in areas with high curvature.

4.6.3.3 Weight and Fuel Efficiency Impacts

The addition of VGs can inadvertently increase the weight of the vehicle, potentially impacting fuel efficiency. There is a delicate balance between improved aero/hydrodynamic performance and the weight penalty incurred by VG installation.

4.6.3.4 Performance Limitations in Varied Flow Conditions

VGs may not perform uniformly across all flow conditions. There are limitations in the performance of VGs at varying speeds and angles of attack, and how environmental factors such as temperature and humidity can affect their effectiveness.

4.6.3.5 Future Research Directions

In addressing these challenges, ongoing research is essential. Recent developments in computational fluid dynamics and materials science are promising, as they aim to create more efficient, adaptable, and durable VGs.

4.7 Novel Vortex Generator Concepts to Reduce Drag separation in Bluff Bodies

4.7.1 Introduction - Marine Vessels with Large Form Drag

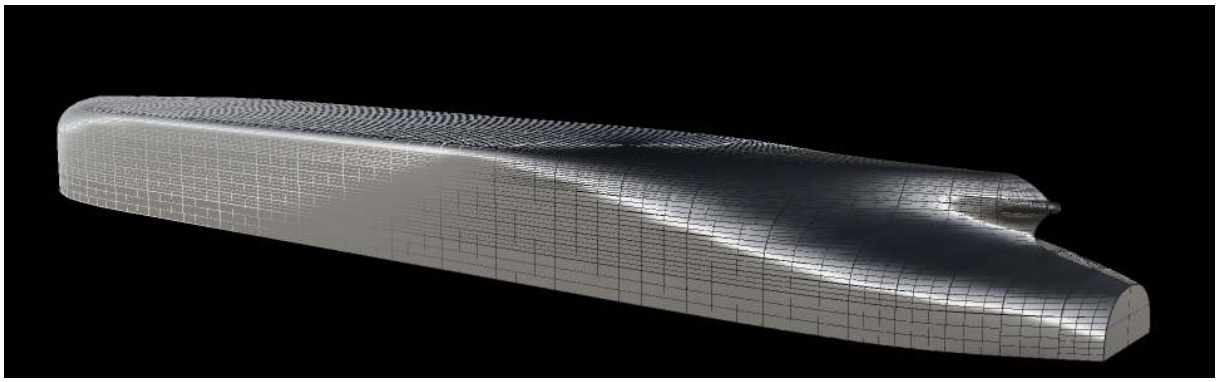

Figure 4-2: Lifted surface from lines plan of the Hedwid Oldendorff, the reference vessel that has been candidate for intervention with the novel vortex generator concepts.

In the context of bulk carriers, boundary layer detachment [133, 93] because of bluff hull shapes (due to heavy tonnage) significantly exacerbates form drag, impacting fuel efficiency and navigational performance. Vortex generators offer a solution by introducing small-scale vortices into the boundary layer. These vortices mix the slower-moving fluid near the hull with faster-moving outer flow, re-energizing the boundary layer, thus reducing the likelihood of flow separation. This process not only decreases drag but also stabilizes flow around the hull, enhancing overall efficiency. The strategic placement of vortex generators is key, and their design must be optimized to suit the specific flow characteristics of large vessels. This optimization can lead to substantial fuel savings and lower operational costs, making vortex generators an essential component in modern naval design for heavy-tonnage ships [212].

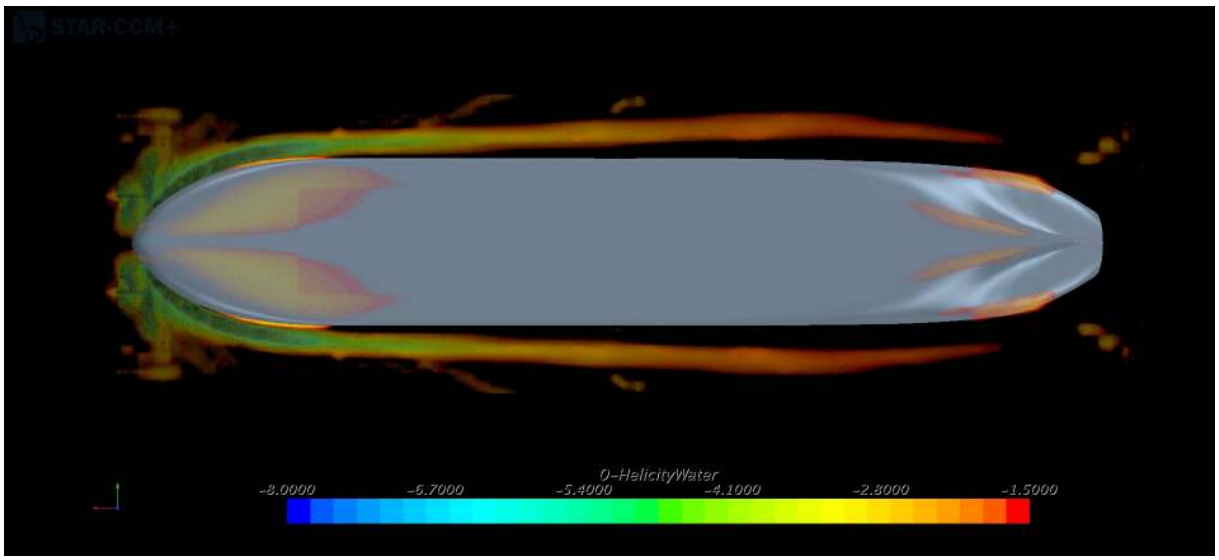

Figure 4-3: A necklace vortex at the bow of the vessel, and boundary layer detachment at the aft body is presented via a volumentric render of the vorticity in the water, through which the vessel is travelling.

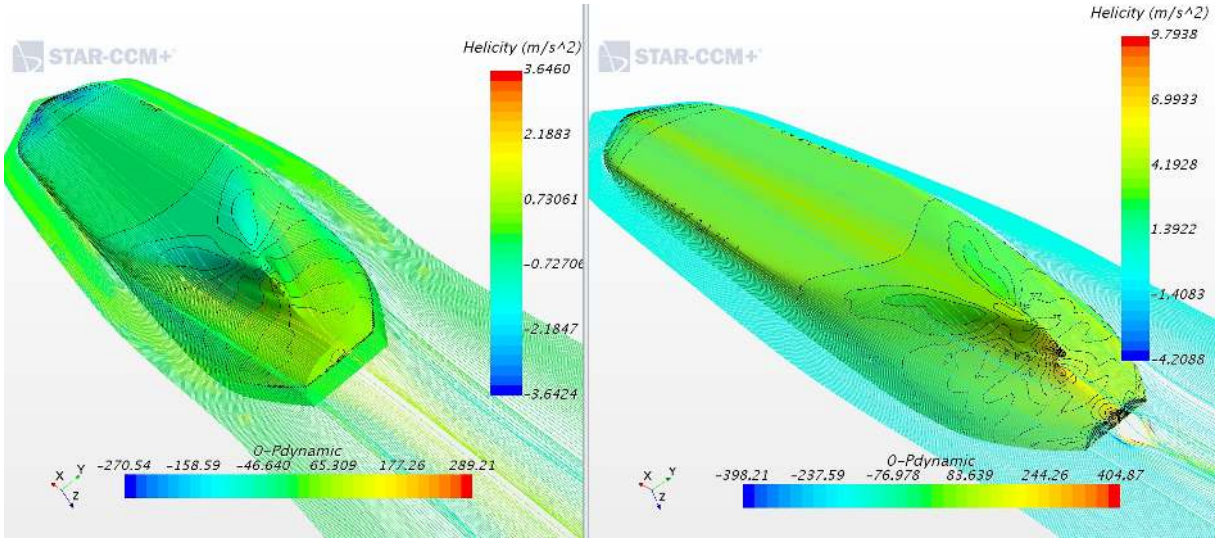

Figure 4-4: Comparison of streamlines of viscous flow on the left and of potential flow on the right. Close inspection of the streamlines show how they open up towards the aft body of the hull as the boundary thinkens detaches at certain points.

4.7.2 Methodology and Design Approach

This research initiates with a comprehensive exploration of state-of-the-art vortex generators, predominantly utilized in aerospace applications, specifically focusing on delta wing vortex generators. Recognizing the distinct aero/hydrodynamic challenges posed by bluff-shaped marine vessels, such as bulk carriers, we opted to optimize VG designs over a more analytically tractable model – an axisymmetric body with the same friction to pressure drag ratio. This approach offers a simplified yet effective platform to analyze and optimize the hydrodynamic performance of VGs.

Hydrodynamic bodies, including bulk carriers, experience significant pressure drag. However, unlike stalled wings where pressure drag is dominant, the main component of drag for these vessels remains frictional. When implementing devices such as vortex generators (VGs) to achieve net drag reduction, it is essential that these devices introduce minimal parasitic drag. Our studies demonstrate that the sharp edges characteristic of NACA ducts can effectively generate vortices, re-energizing the boundary layer with exceptional efficiency and reducing overall drag.

To evaluate candidate designs, we examine an axisymmetric body with a pressure-to-friction drag ratio akin to that of a bulk carrier. The test body, measuring $L = 1.4\,\mathrm{m}$ in length and $D = 0.2\,\mathrm{m}$ in diameter, is tested at a velocity of $v = 1.3\,\mathrm{m/s}$ in water, resulting in fully turbulent flow.

Due to the curvature of the hydrodynamic body's tail, a detached boundary layer develops downstream. This detachment is inherently unstable [247], leading to a significant pressure drop that contributes to pressure drag and generates unsteady fluid structures. These structures cause perturbations in the wake, impacting the performance of ship propellers and causing other undesirable phenomena.

The goal of this research is to correct boundary layer detachment in the axisymmetric body and reduce overall hydrodynamic drag by utilizing VGs. We leverage the sharp edges used in NACA ducts. These edges are designed to generate minimal parasitic drag while drawing in higher-energy fluid particles from outside the boundary layer, creating vortices that recirculate these particles away from the body surface. When multiple adjacent devices are employed, they form wedge-like shapes, as shown in Figure 4-13.

A crucial aspect of our methodology was the implementation of Gaussian Process Optimization. This technique enabled us to systematically evaluate the efficacy of conventional delta wing VGs in a marine context. Our preliminary findings indicated that while these VGs are effective in aerospace applications, they introduce excessive drag when applied to axisymmetric hulls, negating potential benefits in reducing overall hull resistance.

Subsequent stages of the research involved refining the VG designs to balance the trade-off between drag reduction and the additional drag introduced by VGs themselves. The goal was to evolve beyond traditional designs, leveraging the insights gained from the Gaussian Process Optimization to innovate VG configurations that are tailored for the unique hydrodynamic environment of bluff-shaped ships.

4.7.3 Computational Fluid Dynamics (CFD) Analysis

In the realm of numerical modeling, the interplay between numerical uncertainty, feasible time to results, and accurate physics simulation forms a triad where adjustments in one element invariably impact the others. This interdependence often defines the strategy and effectiveness of the simulation process.

At the core of this relationship is a fundamental trade-off: striving for reduced numerical uncertainty and heightened accuracy in physics simulation typically necessitates more refined computational models, which in turn demand greater computational resources and time. For instance, capturing complex physical phenomena like turbulent flow behavior or intricate material responses often requires employing sophisticated models such as Large Eddy Simulation (LES) in fluid dynamics or nonlinear material models in structural analysis. While these approaches enhance accuracy and reduce numerical uncertainty, they significantly extend the time to obtain results due to their computational intensity. This extension can be a critical factor in project timelines, especially in industries where rapid development and iterative design are integral, such as automotive or aerospace engineering.

Conversely, when project constraints prioritize quicker turnaround times, simpler models or coarser discretization may be employed. This expediency, however, comes with its

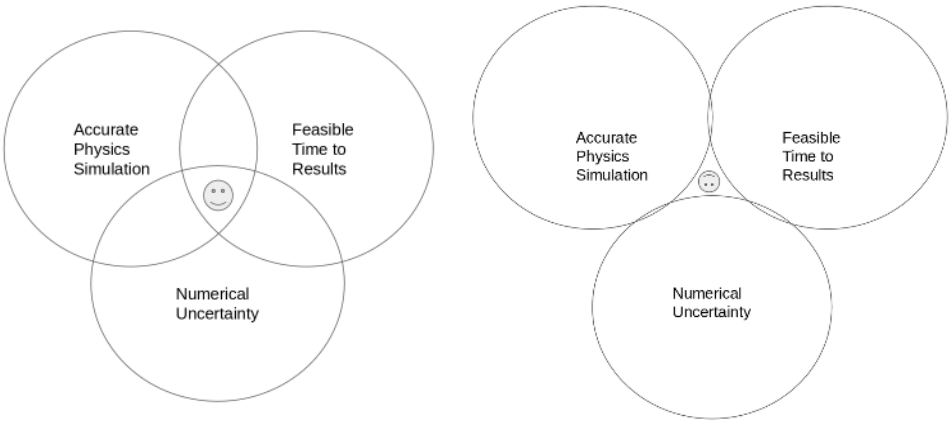

Figure 4-5: Trade-offs to consider when choosing a numerical model.

own ramifications - an increase in numerical uncertainty and potential oversimplification of physics. Such compromises might be tolerable in preliminary design stages or less critical applications, but they could lead to inadequate or misleading results in scenarios where precise modeling of physical phenomena is crucial. For example, in safety-critical systems like aircraft design or nuclear reactor analysis, underestimating physical complexities or tolerating high numerical uncertainty can lead to significant design flaws or safety risks.

Therefore, the challenge in numerical modeling lies in balancing these elements - reducing numerical uncertainty and capturing accurate physics while adhering to practical time constraints. This balancing act necessitates not only a deep understanding of the underlying physics and numerical methods but also a keen awareness of the project's specific needs and constraints. The implications of these trade-offs extend beyond mere computational concerns, influencing project costs, design efficacy, safety, and overall project success.

4.7.3.1 Detached Eddy Simulation (DES)

Detached Eddy Simulation (DES) is a computational fluid dynamics technique that combines the Unsteady Reynolds-Averaged Navier-Stokes (URANS) approach with Large Eddy Simulation (LES). DES is used for simulating turbulent flows, especially in scenarios involving both attached and detached eddies.

4.7.3.2 Governing Equations

The governing equations of DES are based on the Navier-Stokes equations, adapted according to the URANS or LES approach.

4.7.3.3 URANS Mode

In regions of attached flow, DES employs the URANS equations alongside the SST-Menter k-omega turbulence model as a closure model:

$$\frac{\partial \bar{u}_i}{\partial t} + \bar{u}_j \frac{\partial \bar{u}_i}{\partial x_j} = -\frac{1}{\rho}\frac{\partial \bar{p}}{\partial x_i} + \nu \frac{\partial^2 \bar{u}_i}{\partial x_j^2} - \frac{\partial \overline{u_i' u_j'}}{\partial x_j} \tag{4.5}$$

where $\bar{u}_i$ is the time-averaged velocity, $\bar{p}$ is the time-averaged pressure, ρ is the density, ν is the kinematic viscosity, and $\overline{u_i' u_j'}$ represents the Reynolds stress terms. The SST-Menter k-omega model is utilized here for its enhanced ability to accurately predict flow separation and adverse pressure gradients in complex boundary layers. This hybrid model combines the strengths of the k-omega model in the inner boundary layer and the k-epsilon model in free shear flows, making it highly suitable for engineering applications requiring precise boundary layer predictions.

The SST (Shear Stress Transport) Menter k-omega model is a hybrid turbulence model widely used in computational fluid dynamics. It combines the strengths of the standard k-omega model and the k-epsilon model, providing accurate predictions across a range of flows, particularly in the boundary layer.

k-Omega Model in SST

The k-omega model, used in the inner part of the boundary layer in the SST formulation, is described by two transport equations:

$$\frac{\partial k}{\partial t} + u_j \frac{\partial k}{\partial x_j} = P_k - \beta^* k\omega + \frac{\partial}{\partial x_j}\left[(\nu + \sigma_k \frac{k}{\omega})\frac{\partial k}{\partial x_j}\right] \tag{4.6}$$

$$\frac{\partial \omega}{\partial t} + u_j \frac{\partial \omega}{\partial x_j} = \frac{\gamma}{\nu_t} P_k - \beta \omega^2 + \frac{\partial}{\partial x_j}\left[(\nu + \sigma_\omega \frac{k}{\omega})\frac{\partial \omega}{\partial x_j}\right] + 2(1 - F_1)\rho\sigma_{\omega 2}\frac{1}{\omega}\frac{\partial k}{\partial x_j}\frac{\partial \omega}{\partial x_j} \tag{4.7}$$

where P_k is the production of turbulent kinetic energy, ν_t is the turbulent viscosity, and F_1 is a blending function.

k-Epsilon Model in SST

In the outer part of the boundary layer, the SST model transitions to a modified k-epsilon formulation, ensuring a smooth blend with the k-omega model.

Blending Functions

The SST model employs blending functions to transition between the k-omega model in the inner boundary layer and the k-epsilon model in the outer region or free stream.

Turbulent Viscosity

The turbulent viscosity, ν_t, is calculated differently in the inner and outer regions of the boundary layer, consistent with the k-omega and k-epsilon models, respectively.

4.7.3.4 LES Mode

In regions of detached eddies, DES adopts an LES-like approach:

$$\frac{\partial u_i}{\partial t} + u_j \frac{\partial u_i}{\partial x_j} = -\frac{1}{\rho}\frac{\partial p}{\partial x_i} + \nu \frac{\partial^2 u_i}{\partial x_j^2} + \frac{\partial \tau_{ij}}{\partial x_j} \tag{4.8}$$

where u_i and p are the instantaneous velocity and pressure fields, respectively, and τ_{ij} is the subgrid-scale stress term modeled by the LES model.

In the Improved Delayed Detached Eddy Simulation (IDDES) using the SST $k-\omega$ model, several key terms are modeled to capture the dynamics of turbulent flows. These include the subgrid-scale stress term τ_{ij}, turbulence kinetic energy k, turbulence frequency ω, and eddy viscosity ν_t.

Subgrid-Scale Stress Term τ_{ij}

The subgrid-scale stress term in LES, represented as τ_{ij}, accounts for the effects of the smaller, unresolved eddies:

$$\tau_{ij} = \overline{u_i u_j} - \overline{u}_i \, \overline{u}_j \tag{4.9}$$

This term is the difference between the resolved Reynolds stress and the product of the resolved velocities.

Turbulence Kinetic Energy k

The turbulence kinetic energy k in the SST $k-\omega$ model is defined as:

$$k = \frac{1}{2}(u'^2 + v'^2 + w'^2) \tag{4.10}$$

where u', v', w' are the fluctuating components of the velocity field.

In the Shear Stress Transport (SST) $k-\omega$ turbulence model, the behavior of turbulent flows is described by two transport equations: one for the turbulence kinetic energy k and another for the specific dissipation rate ω.

Turbulence Kinetic Energy k Equation

The transport equation for k is:

$$\frac{\partial k}{\partial t} + u_j \frac{\partial k}{\partial x_j} = P_k - \beta^* \omega k + \frac{\partial}{\partial x_j}\left[(\nu + \sigma_k \nu_t)\frac{\partial k}{\partial x_j}\right] \tag{4.11}$$

where:

- P_k is the production of turbulence kinetic energy, given by $P_k = \nu_t S^2$.
- β^* is a model constant.
- σ_k is a model constant for the diffusion term.
- ν is the molecular viscosity, and ν_t is the eddy viscosity.
- u_j is the velocity field.

Specific Dissipation Rate ω Equation

The transport equation for ω is:

$$\frac{\partial \omega}{\partial t} + u_j \frac{\partial \omega}{\partial x_j} = \frac{\gamma}{\nu_t} S^2 - \beta \omega^2 + \frac{\partial}{\partial x_j}\left[(\nu + \sigma_\omega \nu_t)\frac{\partial \omega}{\partial x_j}\right] + 2\,(1 - F_1)\,\frac{\sigma_{\omega 2}}{\omega}\frac{\partial k}{\partial x_j}\frac{\partial \omega}{\partial x_j} \tag{4.12}$$

where:

- γ, β, σ_ω, $\sigma_{\omega 2}$ are model constants.
- F_1 is a blending function.
- ν_t is the eddy viscosity, and S is the strain rate magnitude.

Eddy Viscosity ν_t

The eddy viscosity ν_t in the SST $k-\omega$ model is calculated using both k and ω:

$$\nu_t = \frac{a_1 k}{\max(a_1 \omega, S F_2)} \tag{4.13}$$

where a_1 is a model constant, S is the strain rate magnitude, and F_2 is a blending function.

4.7.3.5 Transition Between URANS and LES Modes

Improved Delayed Detached Eddy Simulation (IDDES) is a hybrid approach that blends URANS and LES methodologies. When employing the SST $k-\omega$ model in IDDES, the formulation for subgrid-scale stress modeling is adjusted to suit the nature of the flow in different regions.

URANS Mode with SST $k-\omega$ Model

In the near-wall URANS regions, the SST $k-\omega$ model is used in its standard form to model the entire range of turbulence scales:

$$\nu_t = \frac{a_1 k}{\max(a_1 \omega, S F_2)}$$

where ν_t is the eddy viscosity, k is the turbulence kinetic energy, ω is the specific rate of dissipation, S is the strain rate, F_2 is a blending function, and a_1 is a model constant.

Transition to LES Mode in IDDES

As the flow moves away from the wall and the grid resolution becomes suitable for LES, the SST $k-\omega$ model is adapted:

$$\nu_t^{LES} = f_d \cdot \nu_t$$

where ν_t^{LES} is the modified eddy viscosity for LES regions, and f_d is a damping function that reduces the turbulence model's contribution in regions where larger turbulent eddies are resolved by the grid.

Damping Function in LES Regions

The damping function f_d is crucial for the LES regions. It ensures that the model's influence diminishes as the grid resolution increases, allowing for a direct resolution of the larger turbulent eddies:

$$f_d = \text{Function of local grid size and flow parameters}$$

4.7.3.6 Utilizing DES in Preliminary Design of Vortex Generators

In the preliminary design phase of Vortex Generators (VGs), a critical aspect is understanding and predicting the characteristics of flow separation. Given the complex nature of these flows, especially around aero/hydrodynamic surfaces where VGs are employed, Detached Eddy Simulation (DES) with fully resolved boundary layers presents as an advantageous tool for several reasons.

Firstly, DES's Hybrid Approach offers a more nuanced simulation of turbulent flows compared to traditional URANS models. By combining the strengths of both URANS and LES, DES can capture the larger unsteady turbulent structures associated with flow separation more accurately. This hybrid modeling is particularly useful in predicting the behavior of flow over VGs, where the interaction between the vortex structures generated by VGs and the boundary layer can be complex.

Secondly, DES's ability to Adaptively Transition between URANS and LES modes based on the local grid resolution makes it an ideal choice for preliminary design. This adaptability is crucial in areas where flow separation occurs. VGs often influence the boundary layer and separation characteristics significantly, and DES allows for a detailed analysis of these effects, capturing both the mean flow and the larger-scale unsteadied phenomena.

Moreover, employing DES in the initial stages provides an opportunity to Predict and Monitor Flow Separation characteristics with a higher degree of fidelity. By simulating

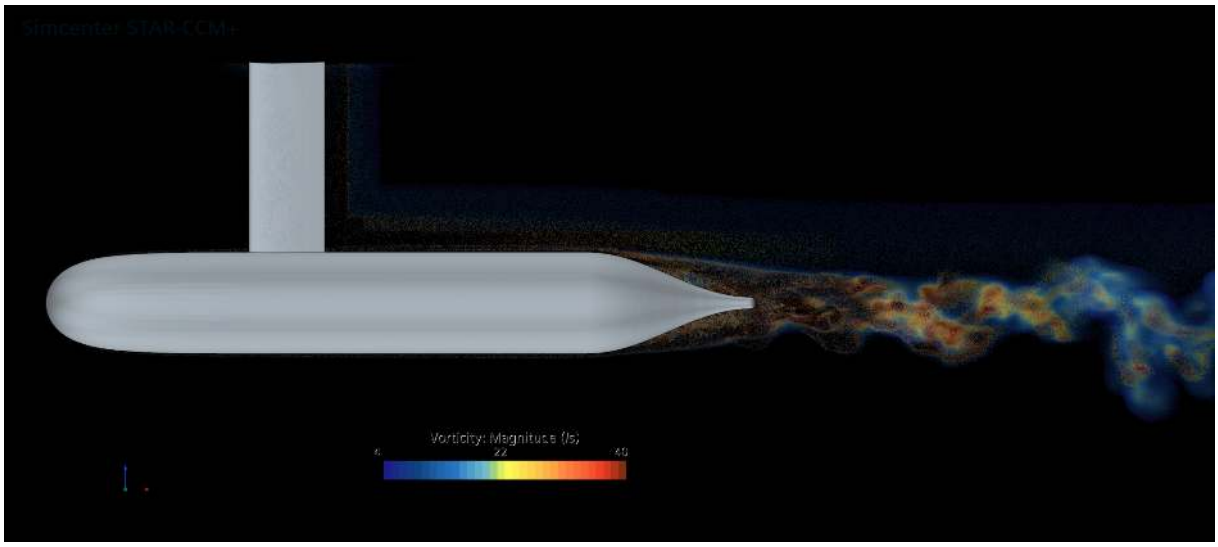

Figure 4-6: Detachment as captured by DES

different configurations of VGs and their placements, we can gain insights into the separation behavior, such as the size and strength of the vortices generated, the extent of the separated region, and the reattachment points. These insights are valuable in optimizing the VG design to achieve desired aero/hydrodynamic goals.

However, it's important to recognize the Limitations of DES in this context. DES's sensitivity to grid resolution and the need for accurate modeling of the URANS-LES transition region mean that careful consideration must be given to the meshing strategy and turbulence modeling parameters. Furthermore, DES simulations, while more efficient than full LES, still demand significant computational resources, especially when simulating complex geometries like those with VGs.

Finally, the decision to use DES acknowledges that there will likely be Differences in Flow Separation Characteristics between the simulations and real-world experiments. The nature of turbulent flows and the limitations inherent in any turbulence modeling approach mean that simulations can only approximate the actual flow behavior. Therefore, the results from DES will be used as a guide to adjust the experimental setup, allowing for iterative refinement of both the VG design and the experimental conditions. This approach ensures a more integrated and adaptive design process, leveraging the strengths of computational simulations to enhance experimental outcomes.

DES is utilized in various engineering applications, such as flows around airfoils, auto-

mobiles, and offshore platforms. It efficiently captures large-scale unsteady flow features while being more computationally efficient than a full LES in near-wall regions.

4.7.4 Design Space Exploration and Optimization

The initial phase of optimizing vortex generator (VG) configurations for an axisymmetric body involves an extensive design exploration of conventional delta wing VGs. This exploration is critical for evaluating the performance of state-of-the-art technology and determining the necessity for innovation.

Design Exploration: Figure 4-7 showcases examples of the conventional delta wing VG configurations. The design space exploration includes double-stacked counter-rotated VGs, which are visualized in the first image. This configuration is very useful in evaluating the interaction effects between VGs, which can significantly influence the overall aero/hydrodynamic performance.

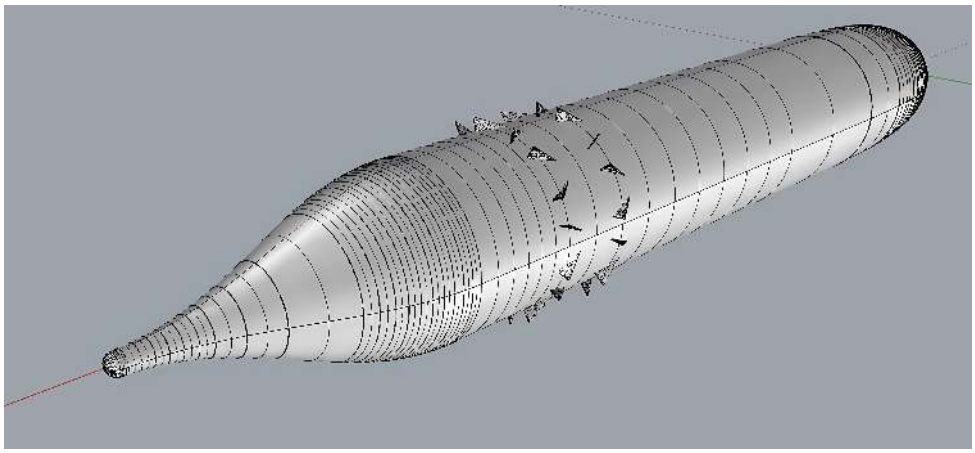

Figure 4-7: Double-stacked counter-rotated VGs on an axisymmetric body.

The second image presents a visualization of 196 single-row VGs that form the basis of the design space exploration. This visualization is not only a testament to the comprehensive scope of the study but also highlights the complexity involved in optimizing such a large number of variables.

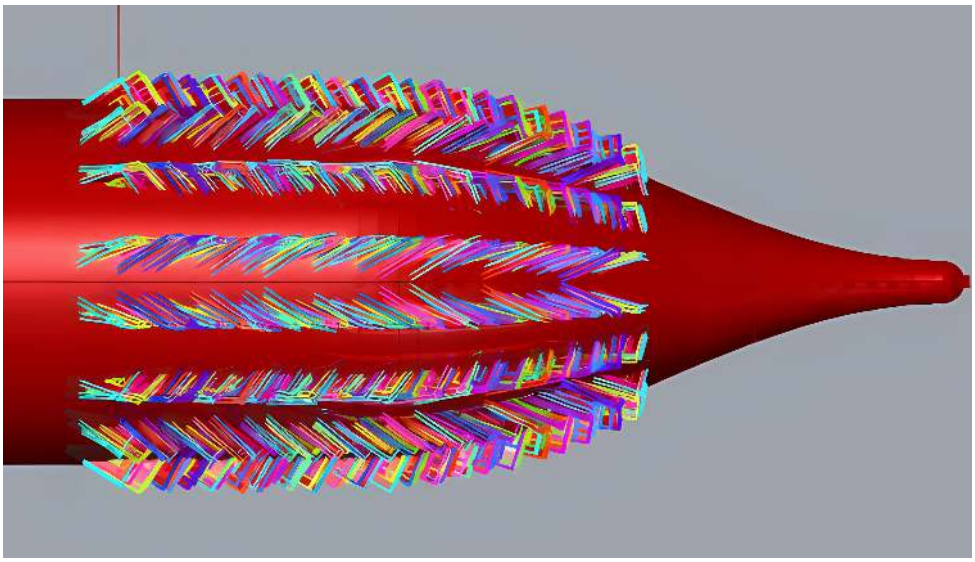

Figure 4-8: Visualization of 196 single-row VGs for design space exploration.

The third image depicts the parametric definition of the VG placement along the hull. This parametric approach allows for systematic adjustments in VG configurations, thereby facilitating an efficient exploration of the design space.

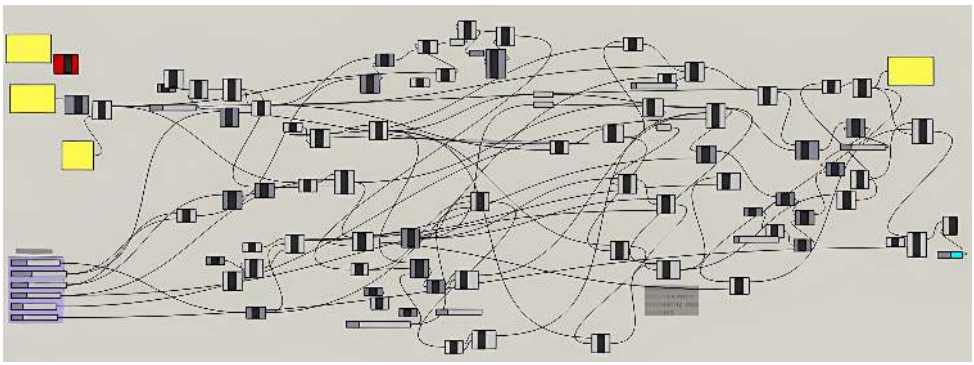

Figure 4-9: Parametric definition of VG placement along the hull.

Preliminary Exploration and Need for Innovation: This preliminary effort lays the groundwork for analyzing the aero/hydrodynamic performance of VGs. By employing a parametric study, the exploration aims to identify configurations that could potentially reduce drag and delay flow separation. The findings from this initial phase will be crucial in determining whether the existing VG technology suffices or if there is a pressing need for innovative designs.

The current state-of-the-art VGs may not achieve the desired effect, particularly in complex flow conditions such as those experienced in high Reynolds. Should the exploration reveal limitations in the performance of conventional VGs, it will highlight the necessity for novel solutions. Innovative VG designs could offer enhanced control over the flow field, leading to significant improvements in drag reduction and flow management.

In conclusion, the design exploration serves as a vital step in the optimization process. It assesses the efficacy of current VG technology and sets the stage for potential advancements. The use of advanced visualization and parametric modeling tools ground this systematic exploration, ensuring a thorough and effective approach to VG optimization.

The design exploration performed through computational studies has yielded a multidimensional dataset that captures the aero/hydrodynamic performance influenced by vortex generator (VG) configurations, see fig. 4-10. This dataset has been visualized through three-dimensional plots representing Hull Resistance, VG Resistance, and Total Resistance, color-coded to indicate corresponding resistance values. Each plot maps a parametric space defined by VG angle, VG height, and longitudinal position – the latter being the vertical axis.

The provided design exploration plots, encapsulating Hull Resistance, VG Resistance, and Total Resistance, offer valuable insights into the aero/hydrodynamic performance across a spectrum of VG configurations. Through the analysis of these plots, several conclusions can be drawn regarding the interplay of VG parameters and their impact on aero/hydrodynamic resistance.

The Hull Resistance plot suggests a discernible relationship between VG placement parameters and the hull's resistance. It highlights that the resistance varies with changes in VG angle and height, which indicates potential for optimizing these parameters to reduce hull resistance.

In the VG Resistance plot, it is apparent that the resistance attributed to the VGs themselves is somewhat less sensitive to longitudinal position. This observation points

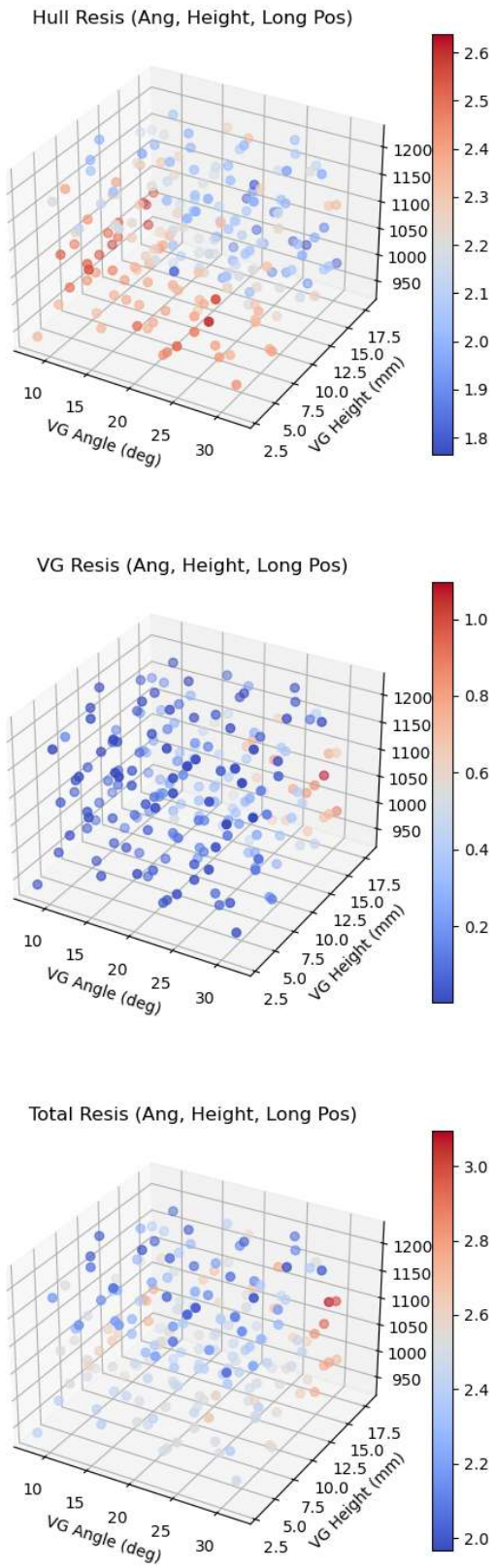

Figure 4-10: From top to bottom, graphical representations of the hull, VG, and total (hull+VG) hydrodynamic resitance, as a function of VG angle, height and logitudinal possition.

towards a possibility of mitigating the inherent resistance caused by VGs through strategic placement, particularly within specific ranges of angles and heights.

The Total Resistance plot, which amalgamates the effects of hull and VG resistance, clearly demonstrates that the overall aero/hydrodynamic performance is contingent on a delicate balance of VG angles, heights, and longitudinal positions. Cooler colors in certain regions point towards more aero/hydrodynamically favorable VG configurations. These areas represent a harmonious balance where the flow control benefits of VGs are maximized while their drag is minimized.

Collectively, the plots highlight the significance of longitudinal placement in optimizing VGs, suggesting an optimal positional range for VGs that capitalizes on their flow control advantages prior to flow detachment. The lowest resistance values in the Total Resistance plot could signify the most effective VG configurations, potentially informing further computational fluid dynamics (CFD) studies or experimental trials.

In an effort to better understand the interplay of these parameters, we have decided to plot isocontours at different percentile values within the parametric space. This approach allows for a focused analysis of how individual parameters affect the performance, isolating the influence of each by holding it constant at specific percentile benchmarks.

These isocontours are instrumental in identifying sweet spots within the design space where VGs contribute positively to the aero/hydrodynamic performance. By holding one parameter constant and observing the resistance changes with the other two, we can discern patterns that would otherwise be lost in the multi-dimensional complexity of the dataset.

To ensure a thorough examination of the parametric space, further computational modeling and analysis will be conducted. The findings will direct future experimental validations, leading to an optimized VG configuration that enhances the aero/hydrodynamic efficiency of the vehicle.

The contour plots of Vortex Generator (VG) resistance, denoted in Figure 4-11, offer nuanced insights into the hydrodynamic performance of VGs. The isosurfaces—contours of equal resistance—reveal the intricate relationship between VG configuration and its resistance characteristics. Observations suggest that VG performance is a complex function

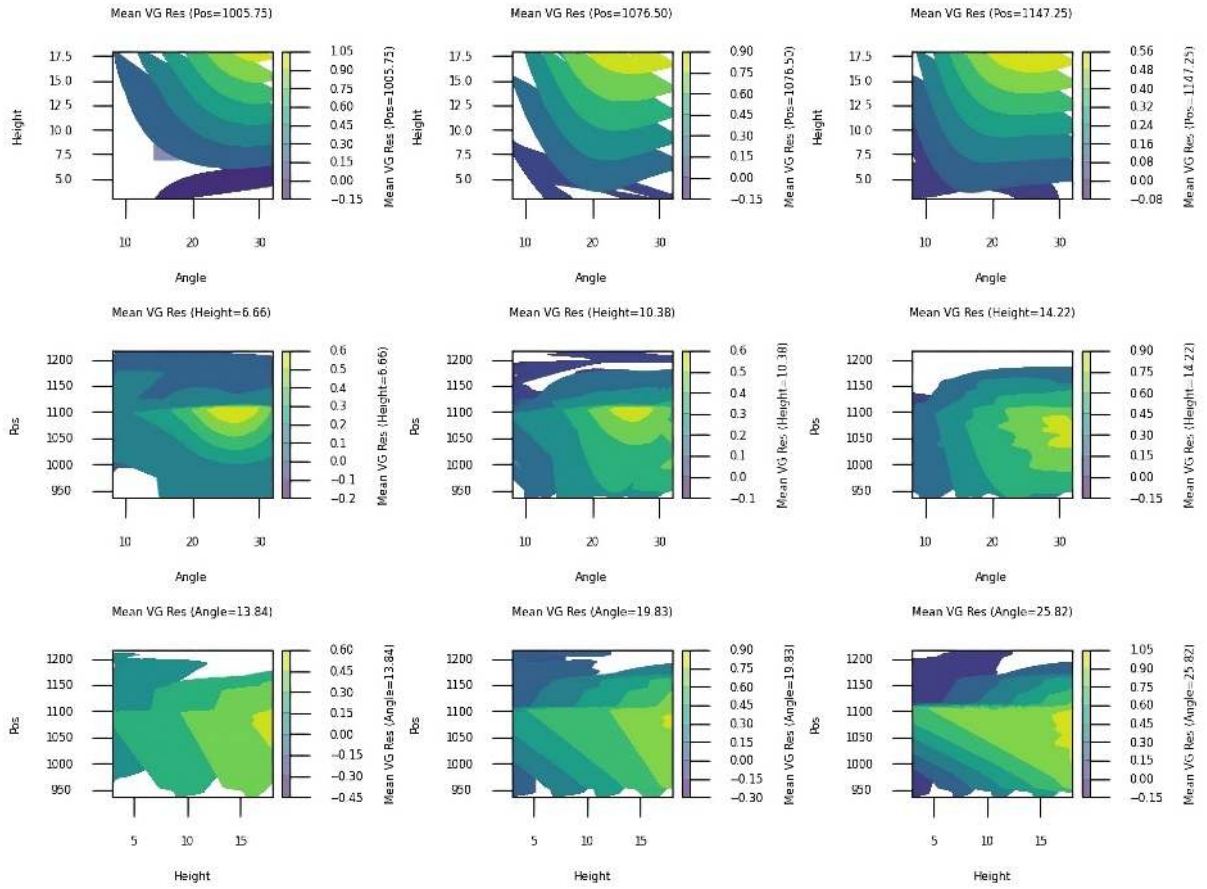

Figure 4-11: VG Drag isosurfaces. Given 3 parameters 2 are changed and the third is kept constant at the 25%, 50%, 75% percentiles, from left to right. Values correspond to half and axi-symetric body, double to obtain full body values.

of their geometric positioning and orientation with respect to the flow.

For a given longitudinal position, the isosurfaces exhibit variations in resistance across different VG angles and heights. The shape and spread of these isosurfaces indicate the existence of optimal angles and heights that minimize resistance, which is crucial for the aero/hydrodynamic efficiency of the VGs. A tightly packed contour pattern implies areas of sensitivity, where small adjustments in VG dimensions can lead to significant changes in resistance.

When height is held constant, the isosurfaces shift noticeably across various angles and positions. This shift in the contours underlines the importance of the VG's longitudinal positioning in relation to its angle of attack. The spatial gradient of the isosurfaces indicates the regions where VG adjustments are most likely to enhance hydrodynamic

performance.

Furthermore, constant-angle isosurfaces demonstrate the impact of VG height and position on resistance. The observed spread of these isosurfaces suggests that VG performance is considerably influenced by the interaction between its height and its placement along the body. The angle at which the VG is set plays a very important role in dictating this interaction, as evidenced by the changing contour patterns.

In summary, the insights derived from these isosurfaces are instrumental in understanding the hydrodynamic behavior of VGs. The data illustrated by the contours can inform the strategic placement and sizing of VGs to manipulate flow patterns beneficially. Optimizing the VG configuration based on these insights could lead to significant reductions in drag, thereby enhancing the overall efficiency of the system they are designed to improve.

Observations on Independence: In each contour plot, areas with horizontal bands of constant color indicate that variations in the horizontal parameter do not significantly affect the drag. For instance, in the middle row of plots where Height is held constant, the uniform color bands across certain angle ranges suggest that within these bands, the hull drag is relatively insensitive to changes in VG longitudinal position.

Implications for Design: Such observations are critical for hull design optimization. If a particular range of angles shows consistent drag values across a spectrum of heights, designers might prioritize the angle adjustment over height modifications for drag reduction. Conversely, if the drag values vary significantly with height within a narrow angle range, it implies that height adjustments could be more influential for aero/hydrodynamic performance.

The contour plots in Figure 4-12 provide a visualization of hull drag variation across different configurations of Angle, Height, and Longitudinal Position. These plots are invaluable in identifying how drag is influenced by changing two parameters while keeping the third at a constant percentile. The analysis shows the sensitivity of hull drag to these parameters, which is critical for the optimization of hull design.

At the 25th percentile of position, a broad high-drag region is observable, indicating

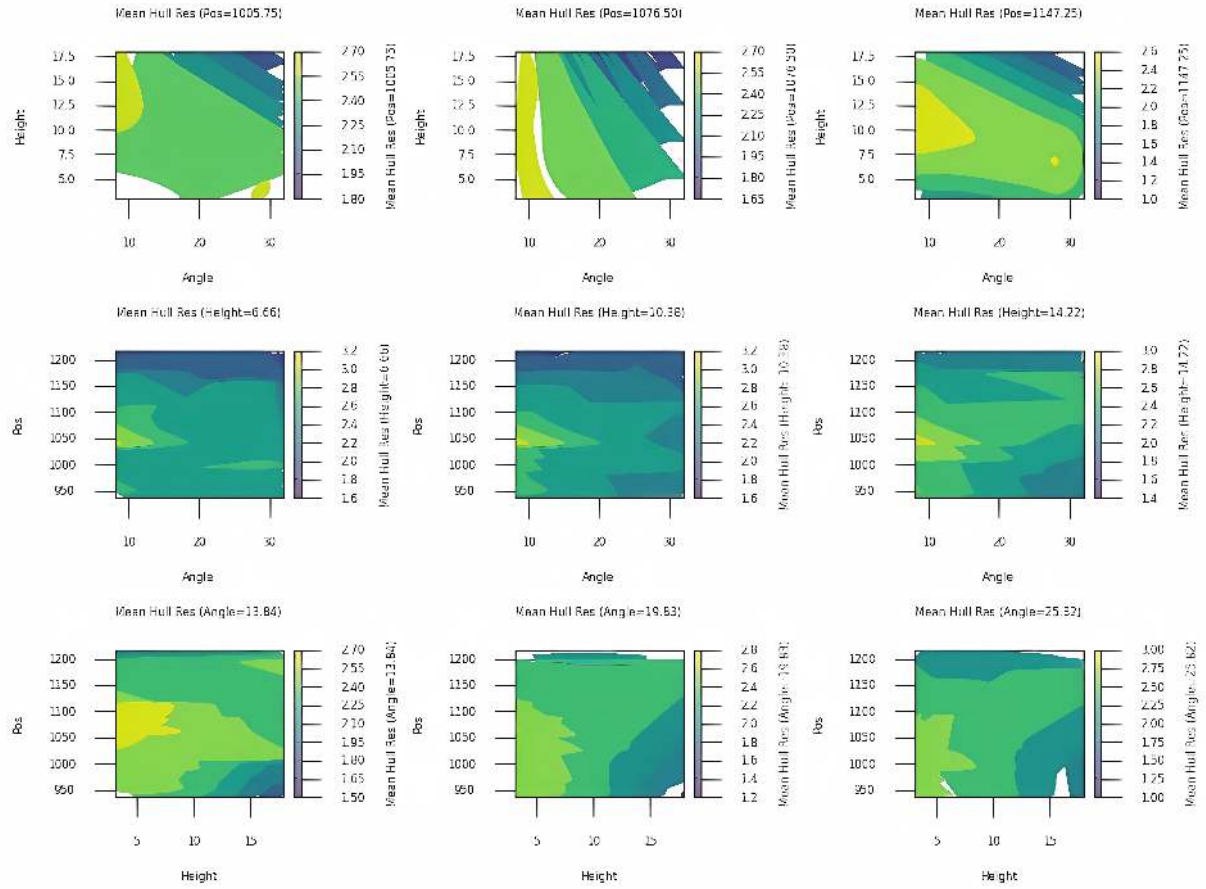

Figure 4-12: Hull drag isosurfaces. Given 3 parameters 2 are changed and the third is kept constant at the 25%, 50%, 75% percentiles, from left to right. Values correspond to half and axi-symetric body, double to obtain full body values.

potential areas of increased drag at certain angles and heights. This region becomes more focused at the 50th and 75th percentiles, suggesting that specific combinations of angle and height could minimize drag at particular longitudinal positions.

With height held constant, the drag's responsiveness to angle and position is evident; the distribution of drag values changes with increasing height percentiles. This implies that the height of the VGs affects how angle and longitudinal position influence the drag, underlining the importance of considering these interactions when shaping and positioning the VGs.

Furthermore, at different angle percentiles, the variation in drag with height and longitudinal position suggests that the angle has a pronounced impact on the drag profile. The shifting of high-drag regions across the plots emphasizes the need to take into account

the combined effects of these parameters when designing the hull to reduce drag and improve vessel performance.

In conclusion, the analysis of Figure 4-12 demonstrates that hull drag results from complex interactions between VG angle, height, and position. Optimizing VG design for reduced drag requires a careful consideration of these interdependent parameters. Experimental validation is advised to confirm the simulation findings and to adjust the VG design parameters for practical applications.

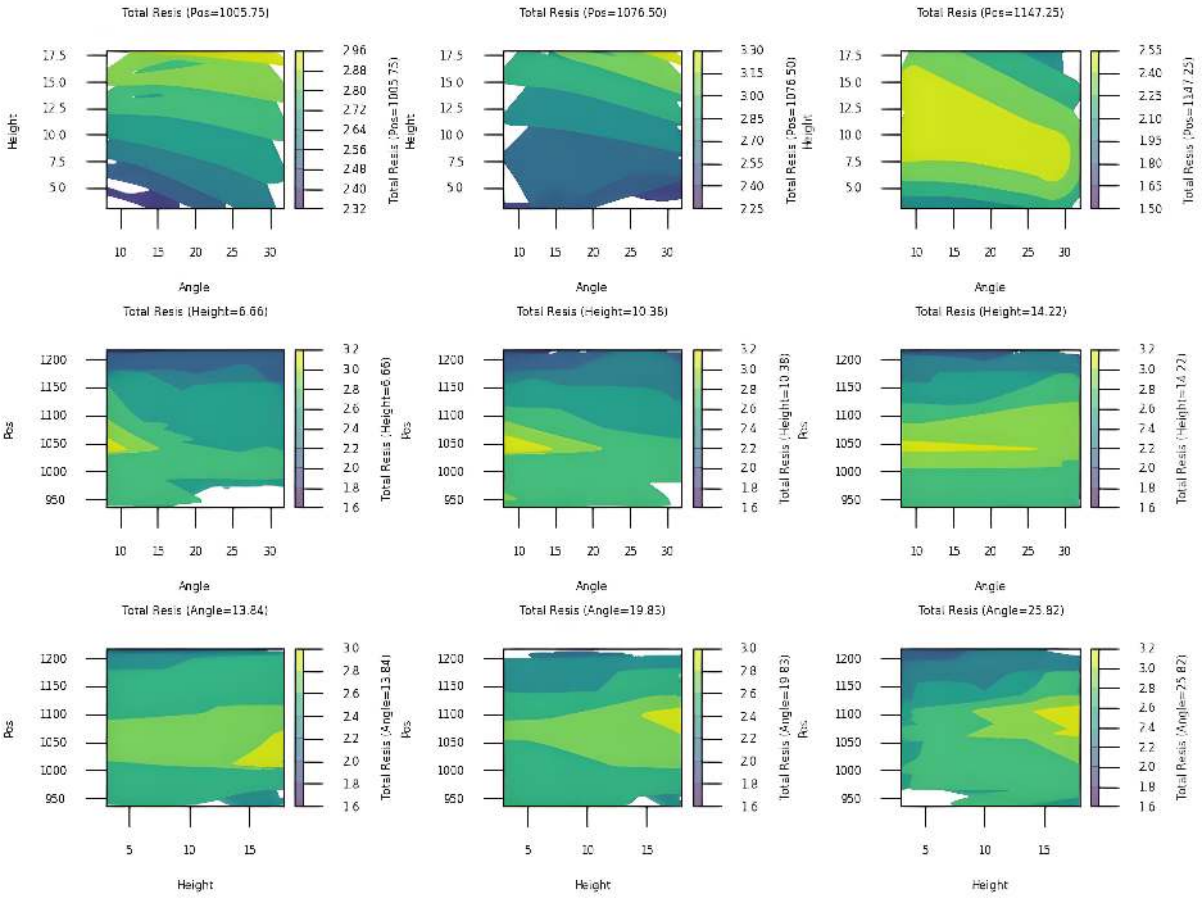

Figure 4-13: Total drag isosurfaces. Given 3 parameters 2 are changed and the third is kept constant at the 25%, 50%, 75% percentiles, from left to right. Values correspond to half and axi-symetric body, double to obtain full body values.

To conclude the parametric analysis, we present in Figure 4-13 contour plots that delineate total drag (VG + Hull Drag) isosurfaces which combine the influences of hull and Vortex Generator (VG) drag across a matrix of varying parameters: Angle, Height, and Longitudinal Position. Each row presents a snapshot of how two parameters affect

total drag while the third is held constant at predetermined percentile values.

Composing overall conclusions from the VG drag isosurface plots requires a focus on regions where the VGs are positioned upstream of the boundary layer detachment point. This is essential because VGs are primarily intended to influence the flow within the boundary layer before it detaches from the surface. In the region before detachment, VGs can introduce streamwise vortices that enhance momentum transfer and potentially delay the separation, thereby reducing drag. Any drag reduction observed by placing VGs downstream of the detachment point should be approached with skepticism as the VGs would not be functioning as designed in a detached flow.

The isosurface plots must be interpreted with a consideration of this functional range of VGs. Therefore, the integral conclusions of the preliminary delta VG analysis are:

1. VG placements should be focused on areas where the flow is still attached. The VG drag reduction in these regions is more likely to be an actual physical effect rather than a numerical artifact.

2. The contour plots should be carefully analyzed to ensure that the observed drag reductions correspond to VG placements upstream of the detachment point. Drag values that suggest reductions in areas beyond detachment should be critically evaluated or possibly disregarded if they cannot be physically justified.

3. Regions displaying drag values below the baseline of a bare hull in areas well before the detachment point would be of particular interest. These areas might indicate configurations where VGs have a pronounced effect on maintaining an attached flow and thus reducing the total drag effectively.

The logic behind focusing solely on areas upstream of the detachment point is grounded in the physics of boundary layer control. VGs are tools for flow management within the boundary layer, and their ability to reduce drag is contingent upon their interaction with the flow before it separates. Looking only at these areas aligns with the intended operational principle of VGs and ensures that any conclusions drawn from the isosurfaces are physically plausible and not a result of computational artifacts.

In light of the information that flow detachment occurs at longitudinal positions of 1100 and greater, our analysis of the contour plots for total drag reduction by Vortex Generators (VGs) is refined. The focus is directed towards the portions of the plots representing regions upstream of the detachment point.

Considering the functional range of VGs and the provided context, the overarching conclusions are as follows:

1. The plots suggest that VGs can only be effective in reducing total drag when positioned before the longitudinal detachment point of 1100. This effect is attributed to the VGs' ability to energize the boundary layer, delaying flow separation and thus minimizing drag.

2. Optimal VG configurations that lead to drag reduction are those that maintain drag values below the baseline of a half bare hull's 2.0 N drag and are located at longitudinal positions less than 1100. These configurations warrant further exploration for potential application, however there are none to be found for the delta shaped VGs. This motivated the search of innovative shaped vortex generators in the following chapters.

3. Total drag's sensitivity to VG height and angle adjustments appears to be significant in areas well before the flow detachment point. This insight points towards the strategic placement of VGs as a critical factor in their effectiveness for drag reduction. We also see successful reattachment, although because of large parasitic drag, there are no overall performance gains.

It is through this lens that the contour plots must be interpreted. The regions of interest, which are upstream of the detachment point, provide valuable data on the characteristics of behaviour of VGs and their potential effect on in aero and hydrodynamic optimization. These conclusions serve as a guide for future design iterations, emphasizing the necessity of aligning VG placement with regions where their influence on the flow is maximized, thereby ensuring meaningful drag reduction.

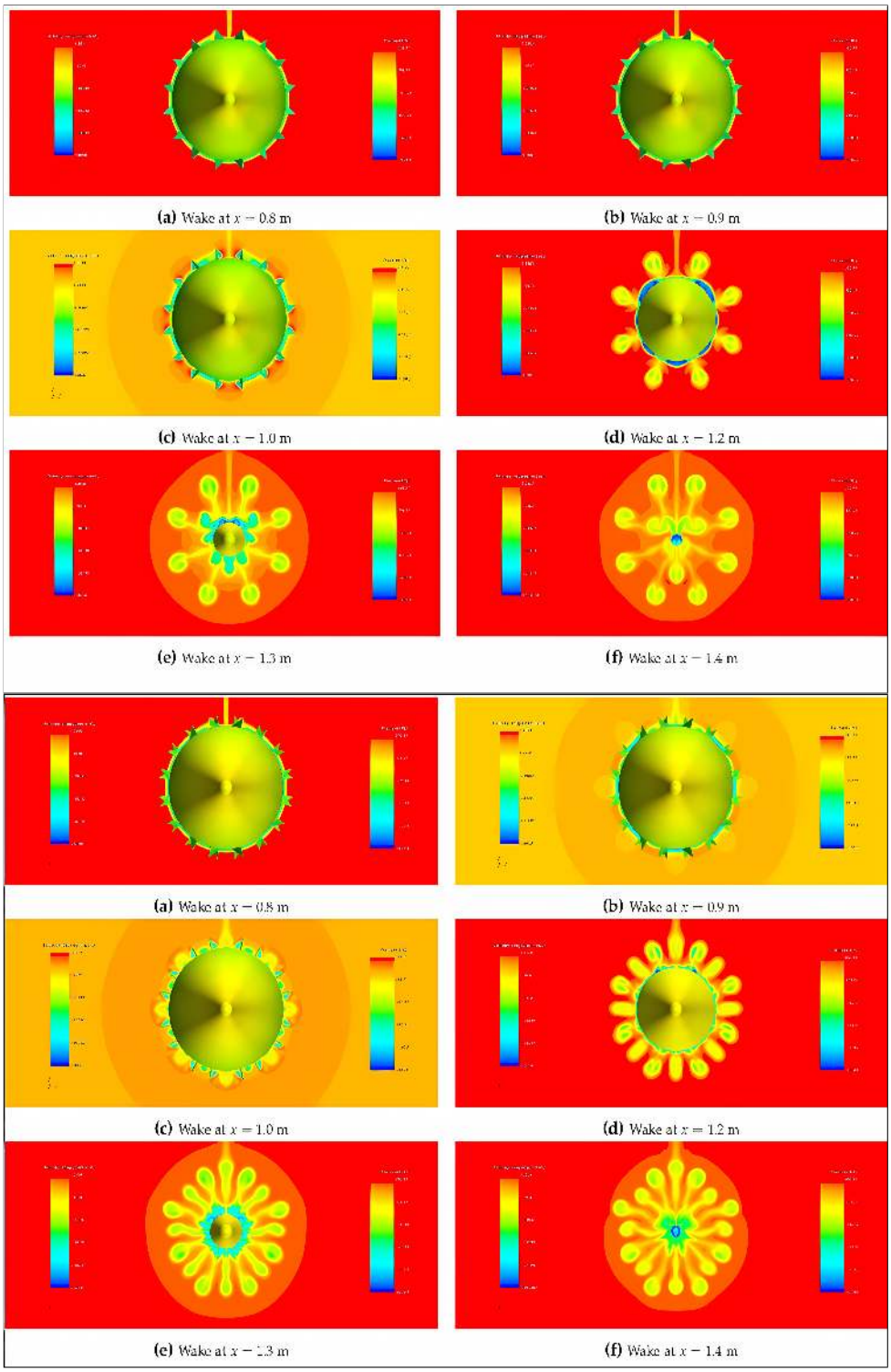

Figure 4-14: Comparison of single row of delta VGs (above) with double rows of delta VGs (below). These visualizations correspond to design number 188 (Ang: 24.9 degrees, H: 17.77 mm, L: 1002mm). The measured resistance in CFD on half a hull (including the strut) is 1.78 N for a single row, 1.72N for a double row and 2.00 N for the bare hull. However there is no total drag reduction because the hull resistance reduction is offset by the VGs parametric drag.

4.7.5 Innovative Vortex Generator Designs

The first step in considering novel VG configurations is exploring configurations with multiple rows of vortex generators (VGs) to reflect a nuanced approach to enhancing aero/hydrodynamic performance. The wake visualizations for single and double rows of VGs provide a comparative perspective on the flow control capabilities of these configurations, see fig. 4-14.

The rationale for employing multiple rows of VGs over conventional single-row setups includes several aero/hydrodynamic benefits:

- Enhanced mixing of the boundary layer due to the increased interaction between the high- and low-momentum flows.
- Improved control over the location and extent of flow separation, which is critical for maintaining lift and reducing drag.
- The ability to achieve a more significant aero/hydrodynamic effect where a stronger influence on the flow is necessary.
- Greater design flexibility and redundancy, ensuring that the flow control objectives are met even if one row of VGs is suboptimal.
- Tailored customization to manage complex flow conditions that require a more sophisticated approach.

These images, see fig. 4-14, show the wake patterns created by two effective configurations of double stacked counter-rotated vortex generators (VGs) on an axisymmetric body. These images are results of Computational Fluid Dynamics (CFD) simulations, which are valuable for understanding the flow characteristics influenced by VGs.

From the first set of images, we can observe the wake flow pattern at various distances (0.8m to 1.4m) behind the body. As the distance from the body increases, the wake pattern changes, indicating how the flow evolves and diffuses over distance. Specifically, the wake at 0.8m is relatively undisturbed, but as we move further back to 1.4m, the wake expands and displays more complex patterns. This evolution is indicative of the vortex

shedding and mixing caused by the VGs, which can influence the aero/hydrodynamic performance by delaying flow separation and potentially reducing drag.

The second set of images show the wakes of double-layered VG configurations. The wake for the double-layered VGs shows more intricate patterns (twice the number of vortices) and a more diffused wake, suggesting increased mixing and potentially more effective flow control. The single-layer VGs show a less complex wake, which may indicate a less aggressive interaction with the flow.

Using multiple rows of VGs might be advantageous because they can introduce more control points into the flow, allowing for finer adjustment of the boundary layer properties. This can lead to a more tailored aero/hydrodynamic performance, where the flow can be kept attached over a larger surface area, reducing drag and possibly improving drag reduction.

The insights from these images could suggest that while single-layer VGs may be effective in certain scenarios, double-layered VGs might offer enhanced control over the flow, especially in high Reynolds number flows where separation is more challenging to manage. This could be particularly relevant when looking to optimize performance for different operational conditions or when attempting to achieve specific aero/hydrodynamic characteristics.

In the context of innovation and design, these images suggest that while conventional VGs have a clear impact on flow behavior, there may be substantial gains from exploring more complex, multi-layer configurations. The differences in wake patterns between single and double-layer VGs highlight the potential benefits of such configurations in enhancing flow control and reducing aero/hydrodynamic drag, which is vital for high-performance designs in aerospace and automotive industries.

In the quest to optimize aero/hydrodynamic efficiency, the deployment of double rows of vortex generators (VGs) was embarked upon with the objective of enhancing boundary layer reattachment. The computational simulations and subsequent analyses indeed revealed a marked improvement in this regard. The double-row VG configurations showed a pronounced ability to energize the boundary layer, promoting reattachment even in areas susceptible to flow separation. This reattachment is crucial as it can potentially

delay stall and maintain lift at higher angles of attack or during low-speed maneuvers, if considering aeronautic applications.

However, the dual VG arrangement introduced a significant amount of parasitic drag. This type of drag is a byproduct of the additional surface area and complex flow patterns generated by the VGs themselves. Although the double rows of VGs were effective in manipulating the boundary layer, the resulting increase in drag outweighed the aero/hydrodynamic benefits of delayed flow separation. Consequently, instead of a net reduction in drag, the overall resistance to the flow increased, negating the beneficial effects of boundary layer control.

This obsereved phenomenon suggests a complex trade-off between maintaining attached flow and minimizing drag. While the double-row VGs improved flow attachment, the penalty in terms of parasitic drag led to an overall increase in total drag, emphasizing the need for a more nuanced approach to VG design and placement. Future research may need to focus on optimizing the size, shape, and distribution of VGs to harness their full potential without incurring excessive parasitic drag. This could involve exploring alternative shapes or configurations that strike a better balance between flow control and drag reduction.

This exploration underlines the importance of CFD in the design process, providing detailed insights that guide the development of new solutions and innovations in VG technology. It also emphasizes the need for experimental validation to confirm CFD predictions and ensure that new VG designs deliver the desired effects in real-world conditions.

Given our findings regarfing conventional delta wing vortex generators, in particular in regard to their large parasitic drag, we turn to the concept of utilizing wedge-shaped vortex generators inspired by NACA ducts is an innovative approach to boundary layer control on axisymmetric bodies. The NACA duct, originally designed for low-drag air intake, has a smoothly contoured entrance that minimizes flow separation and drag. This feature can be adapted to the design of vortex generators to enhance their efficiency, see fig. 4-15.

The reasoning behind this design strategy is twofold:

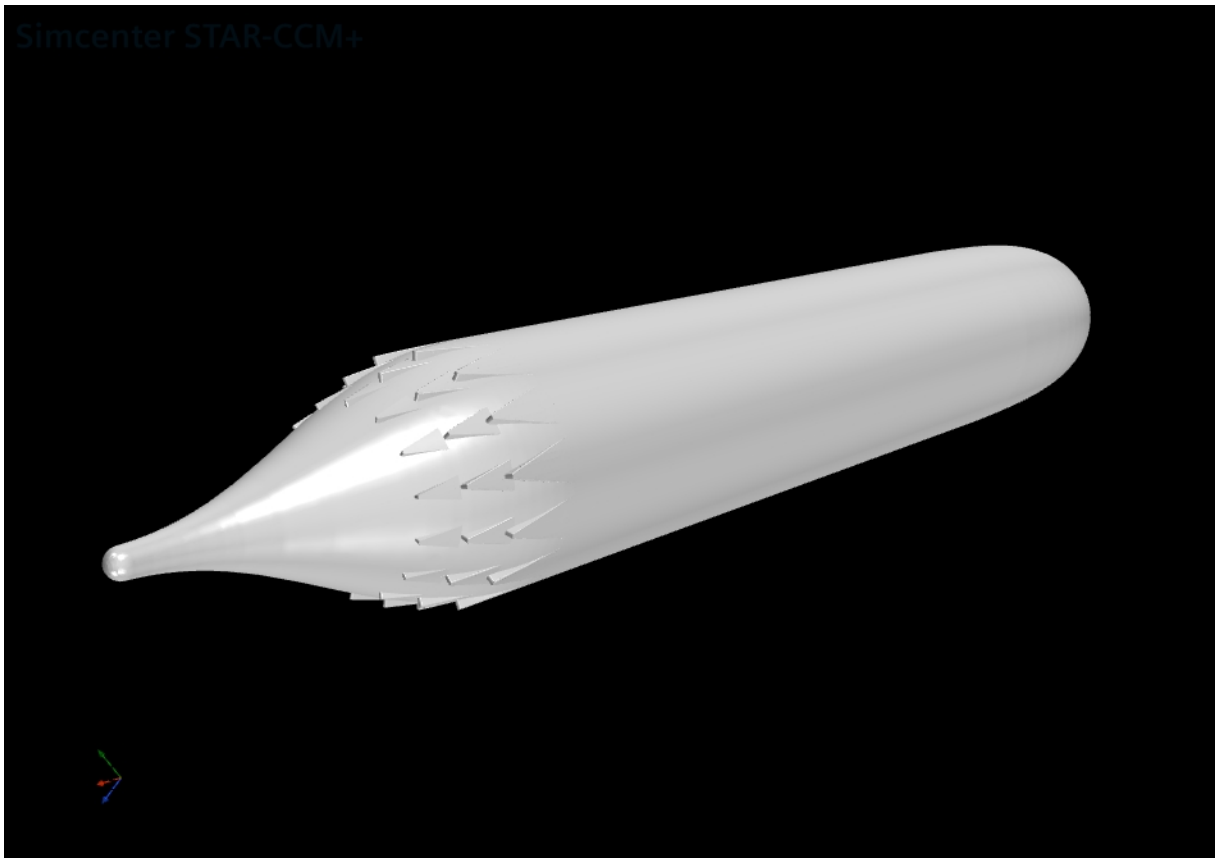

Figure 4-15: Visualization of the axisymmetric hull with wedge VGs.

1. *Flow Reattachment*: By shaping the vortex generators like an open-ended NACA duct, the intention is to harness the duct's characteristic of guiding air smoothly. The wedge shape can create a controlled vortex that helps re-energize the boundary layer, which is particularly beneficial in delaying or preventing flow separation along the body's tail.

2. *Minimized Parasitic Drag*: NACA ducts are renowned for their ability to minimize parasitic drag, which arises from form drag and skin friction. By borrowing edge shapes from NACA ducts, the wedge-shaped vortex generators can be optimized to generate vortices without the excessive drag usually associated with protruding aero/hydrodynamic devices. The goal is to create a low-profile design that induces the desired aero/hydrodynamic effect (i.e., boundary layer energy enhancement) with a minimal drag penalty.

The aero/hydrodynamic advantage of this design lies in its ability to generate a stream-

wise vortex that can mix the outer flow with the slower-moving boundary layer. By doing so, it can inject higher momentum into the boundary layer, thus making it more resistant to separation. The key to success in this design is to ensure that the vortices are strong enough to have the desired effect (changing the flow so that it becomes attached) on the boundary layer without creating excessive turbulence that would increase the drag beyond a beneficial amount.

The wedge-shaped vortex generators act, theoretically, as open-ended NACA ducts, accelerating the flow over the tail of the axisymmetric body, thus reducing the wake size and the associated pressure drag. This concept leverages the efficient design principles of NACA ducts and adapts them to serve the dual purpose of managing airflow while minimizing additional drag sources.

Furthermore there is also the possibility of utilizing multiple rows of NACA-inspired wedge-shaped vortex generators (VGs), which embodies a sophisticated strategy in aero/hydrodynamic design. Such an arrangement aims to extend the benefits of individual VGs across a larger surface area, enhancing the overall flow control across the axisymmetric body.

Multiple rows of these VGs, as depicted in fig. 4-15, function in a collaborative manner, with each row serving to progressively stabilize and re-energize the boundary layer. The first row of VGs initiates the process of boundary layer energization, while the downstream rows build on this effect. This staged interaction can maintain a healthier boundary layer, delaying flow separation and possibly mitigating the formation of turbulent wakes, even under high-lift or high-angle-of-attack flight conditions.

The advantages of employing such a multi-row VG system include the potential for increased boundary layer stabilization, the ability to tailor the VGs to specific flow conditions, and a redundancy feature where subsequent rows can continue to manage the boundary layer if upstream rows are rendered less effective due to changes in the flow regime.

However, the introduction of multiple VG rows does not come without its challenges. The complexity of the design increases, demanding more exhaustive computational fluid dynamics (CFD) studies or experimental work to fine-tune the configuration. Moreover,

each additional row potentially adds to the parasitic drag, counteracting the very issue it seeks to correct. Manufacturing and maintenance considerations also become more pronounced, impacting the overall cost and upkeep of the system.

When put alongside with traditional delta-shaped VGs, the NACA-inspired wedge VGs may offer improved aero/hydrodynamic efficiency due to their streamlined design, which inherently focuses on minimizing drag. They generate a different type of vortex that can be tailored for more subtle and precise flow control, potentially offering a superior efficiency over the more aggressive vortices produced by delta-shaped VGs.

In conclusion, the deployment of NACA-inspired VGs represents an evolution in VG technology, striving for a balance between effective flow control and drag reduction. While promising in theory, the practical application of this technology requires careful optimization to realize the potential benefits while mitigating the drawbacks. For this reason we have decided to start with a single row of these NACA inspired vortex generators.

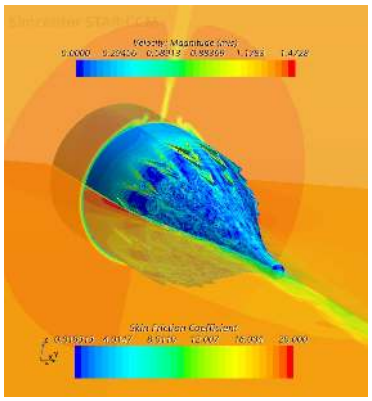

Figure 4-16: Wedge VGs. Skin friction coefficient is low and friction drag remains low, increasing performance.

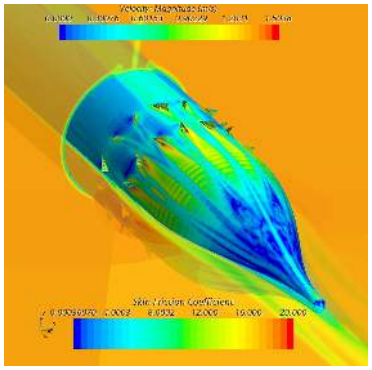

Figure 4-17: Delta Wing VGs. Noticeable increase in skin friction coefficient. High local velocity downstream of the VGs.

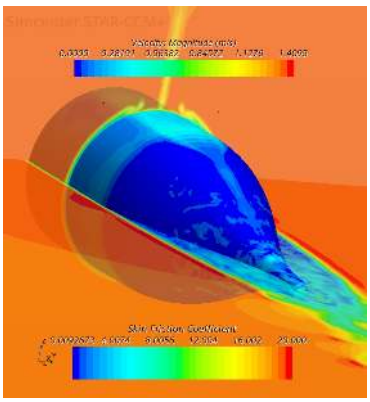

Figure 4-18: Bare Hull. Skin friction coefficient is minimal because of the low local velocity.

The computational fluid dynamics simulations depicted in figs. 4-16 to 4-18 present a informative comparative analysis of the aero/hydrodynamic performance influenced by different vortex generator configurations on an axisymmetric body. Herein, we discuss qualitative differences observed in the velocity fields and skin friction coefficients.

In fig. 4-18, representing the bare tail, exhibits several notable features:

1. A low skin friction coefficient in on the tail suggests smoothly stagnated flow con-

ditions.

2. The rear body shows a significant amount of stagnated flow, indicative of flow separation.

3. The velocity field portrays a pronounced low-velocity wake, which is characteristic of higher pressure drag due to flow detachment.

In fig. 4-17, where double rows of counter-rotated delta wing VGs are employed, we observe:

1. An increased skin friction coefficient around the VGs' location, pointing to a more turbulent flow regime.

2. Although the turbulent flow may aid in reattaching the boundary layer, it could concurrently raise the skin friction drag.

3. The velocity profile suggests a disturbed wake with reduced stagnation areas, potentially diminishing the pressure drag.

In fig. 4-16, showcasing three rows of NACA-inspired wedge VGs, reveals:

1. A more uniform skin friction distribution with less intense high-friction zones, implying a less intrusive drag increase from these VGs.

2. A more structured wake flow, implying effective re-energization of the boundary layer with a minimized drag footprint.

Insights and Conclusions: From the analysis of these images, we can deduce that:

1. The use of delta wing VGs, despite their effectiveness in wake reduction, may lead to an undesirable increment in skin friction drag.

2. The NACA-inspired wedge VGs demonstrate a capability for maintaining a healthier boundary layer with minimized parasitic drag, presenting an improved aero/hydrodynamic performance.

3. The comparison highlights the importance of VG design, where the goal is to achieve an optimal balance between drag reduction and effective flow control.

In summary, the images serve as evidence to the intricate fluid mechanics and dynamics of flow around aero/hydrodynamic bodies and the critical role of VG design in optimizing performance. The insights derived from this study are fundamental in guiding future aero/hydrodynamic enhancements with a focus on reducing drag while ensuring adequate flow control.

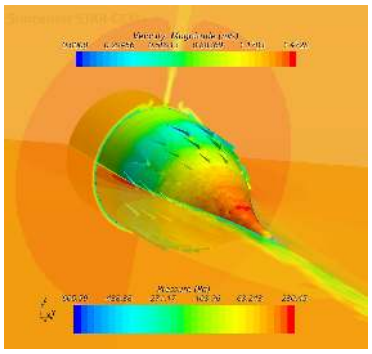

Figure 4-19: Wedge VGs. Flow remains attached to body surface.

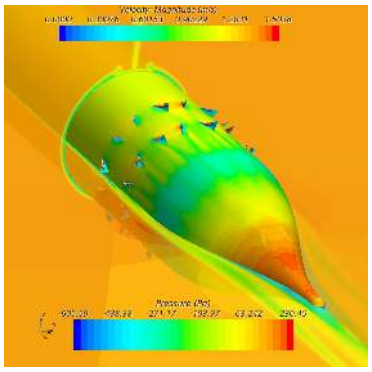

Figure 4-20: Delta Wing VGs. Flow remains attached to body surface.

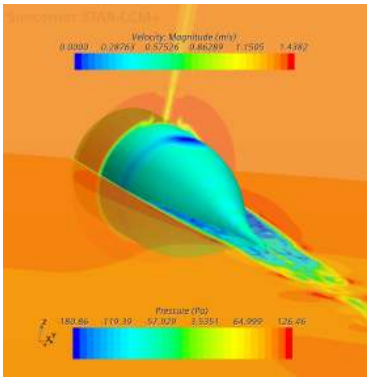

Figure 4-21: Bare Hull. Cavity with stagnated low velocity flow is fully developed.

The second series of images provided in figs. 4-19 to 4-21 depicts an axisymmetric body in various configurations, allowing us to qualitatively assess the aero/hydrodynamic performance in terms of pressure distribution and velocity magnitude. Herein, we delineate the observed differences and extract insightful conclusions.

The image in fig. 4-21, exhibits the bare tail configuration and presents the following characteristics:

1. A very substantial low-pressure region at the aft end of the body, which is indicative of flow separation.

2. A corresponding low-velocity wake directly behind the tail, signifying stagnated fluid indicative of a larger pressure drag.

Upon introducing double rows of counter-rotated delta wing VGs, as seen in fig. 4-20, we observe:

1. Higher surface pressure values on the tail, suggesting a reduction in flow separation due to the VGs.

2. An increased and more uniform velocity field around the tail, pointing towards a more attached flow and reduced wake size.

In fig. 4-19, which includes three rows of NACA-inspired wedge VGs, reveals:

1. A more energized flow pattern, indicating a high degree of mixing and an energized boundary layer with higher pressure values on the tail indicating a reattached boundary layer.

2. Less extreme variations in pressure coefficient, implying a more efficient boundary layer control with potentially reduced parasitic drag.

Insights: From the comparative analysis, several insights are obtained:

1. The presence of VGs significantly modifies the aero/hydrodynamic characteristics, enhancing flow attachment and reducing the detrimental effects of boundary layer separation.

2. While both types of VGs improve the pressure and velocity profiles, NACA-inspired VGs may offer a superior balance between flow control and parasitic drag, leading to more efficient aero/hydrodynamic performance.

3. The design and placement of VGs is critical, highlighting the need for a careful aero/hydrodynamic consideration to optimize performance for specific applications.

In conclusion, as visualized in the first set of images depicting skin friction, the visualized data suggest that NACA-inspired VGs might be advantageous over conventional delta wing VGs, potentially leading to performance benefits in various aero/hydrodynamic applications.

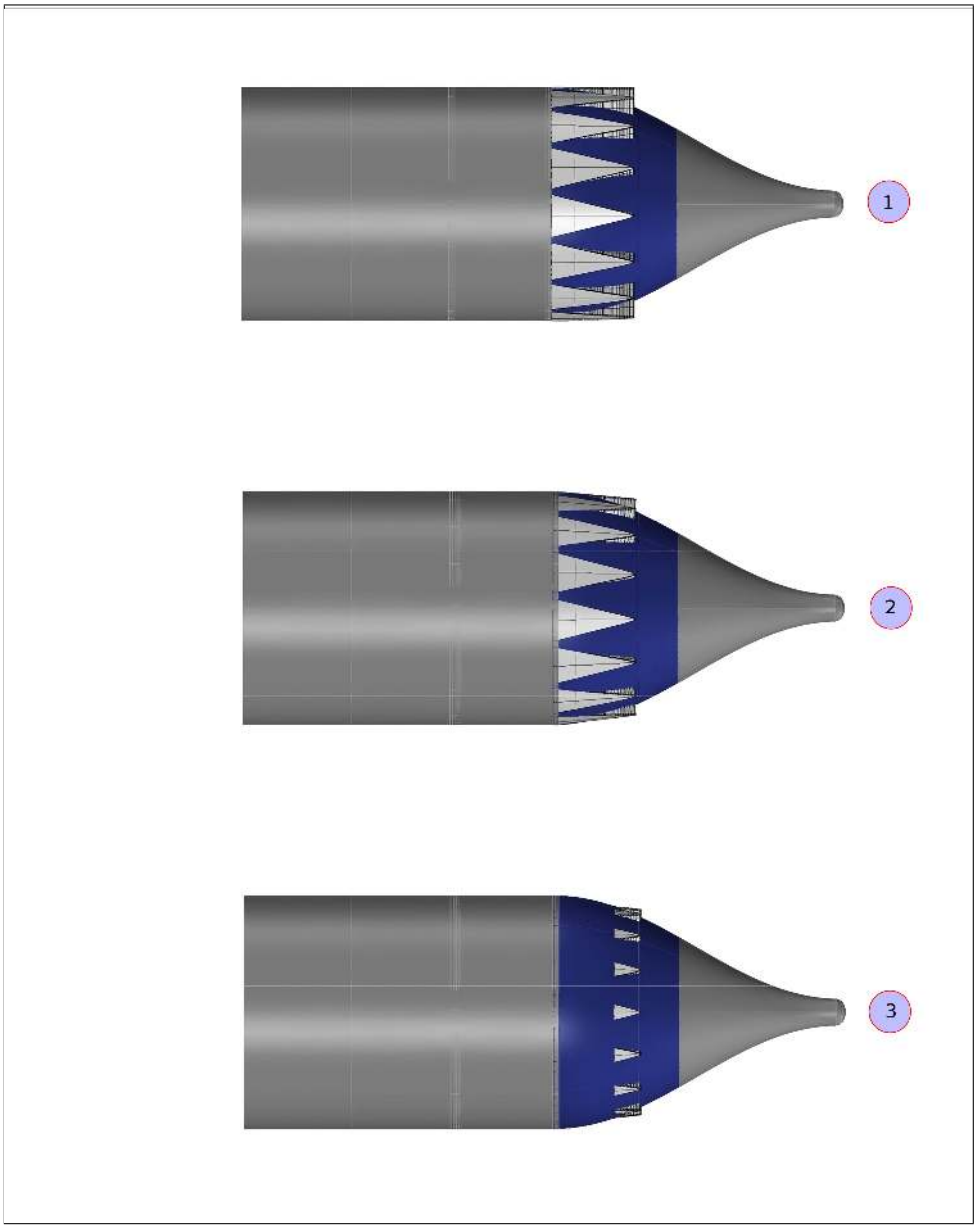

Figure 4-22: *Axisymmetric body tail geometries used to design low drag VGs.* from top to bottom are concepts that achieve increasing drag reduction, mainly due to diminishing parasitic drag in the VG concepts. The VGs in the first concept are a continuation of de cylindrical body, whereas the second concept has VGs that are tilted 5 deg into the body surface. This effectively reduces how much they protrude into the boundary layer and reduces their parasitic drag. Given that they still manage to reattach the boundary layer, they manage to further decrease drag of the axisymmetric body. The VG configuration with the largest drag reduction is the one at the bottom. In conclusion, overall, it's a trade-off between managing to change the flow regime (attachment vs detachment) with minimal intervention.

In fig. 4-22 showcases three experimental tail sections with different configurations of vortex generators (VGs) aimed at boundary layer control on marine vessels. These tail sections are part of a study to optimize flow reattachment and minimize drag by adjusting the protrusion of VGs into the boundary layer.

Tank Tested Tails: these are three tails tested in the MIT towing tank. Despite the reduction in the VGs' protrusion, the boundary layer reattachment was consistently observed in the tank tests. This suggests that even with less intrusive VGs, effective flow control can be attained.

1. *First Tail*: This tail shows VGs that are parallel to the cylindrical body, to explore the impact of VG orientation on flow reattachment.

2. *Second Tail*: The VGs here are angled 5 degrees downward relative to the cylindrical surface, indicating that slight alterations in VG angle can influence the effectiveness of flow control.

3. *Third Tail*: The last tail section displays the smallest VGs, which have been successful in reattaching the flow with minimal parasitic drag. This represents the balance between minimal VG intervention and the benefits of a fluid regime with reduced drag.

The two images provided in the bottom row of fig. 4-23 depict during towing tank experiments tail sections with and without NACA-inspired wedge vortex generators (VGs), using tell tails as indicators of the flow direction across the surface. Tell tails are simple devices that align with the local air/waterflow, and they're commonly used in aerodynamics and hydrodynamics to visually indicate the direction of the flow over a surface.

In the first image, the tail section equipped with VGs shows the tell tails aligned in the direction of the longitudinal flow, suggesting that the VGs are effectively influencing the boundary layer. This alignment indicates that the flow is attached to the surface, which is a desired outcome for reducing drag and maintaining effective propulsion and maneuverability.

The second image, showing the bare tail without VGs, presents a different scenario. The last two rows of tell tails are not aligned with the main flow direction, which indicates

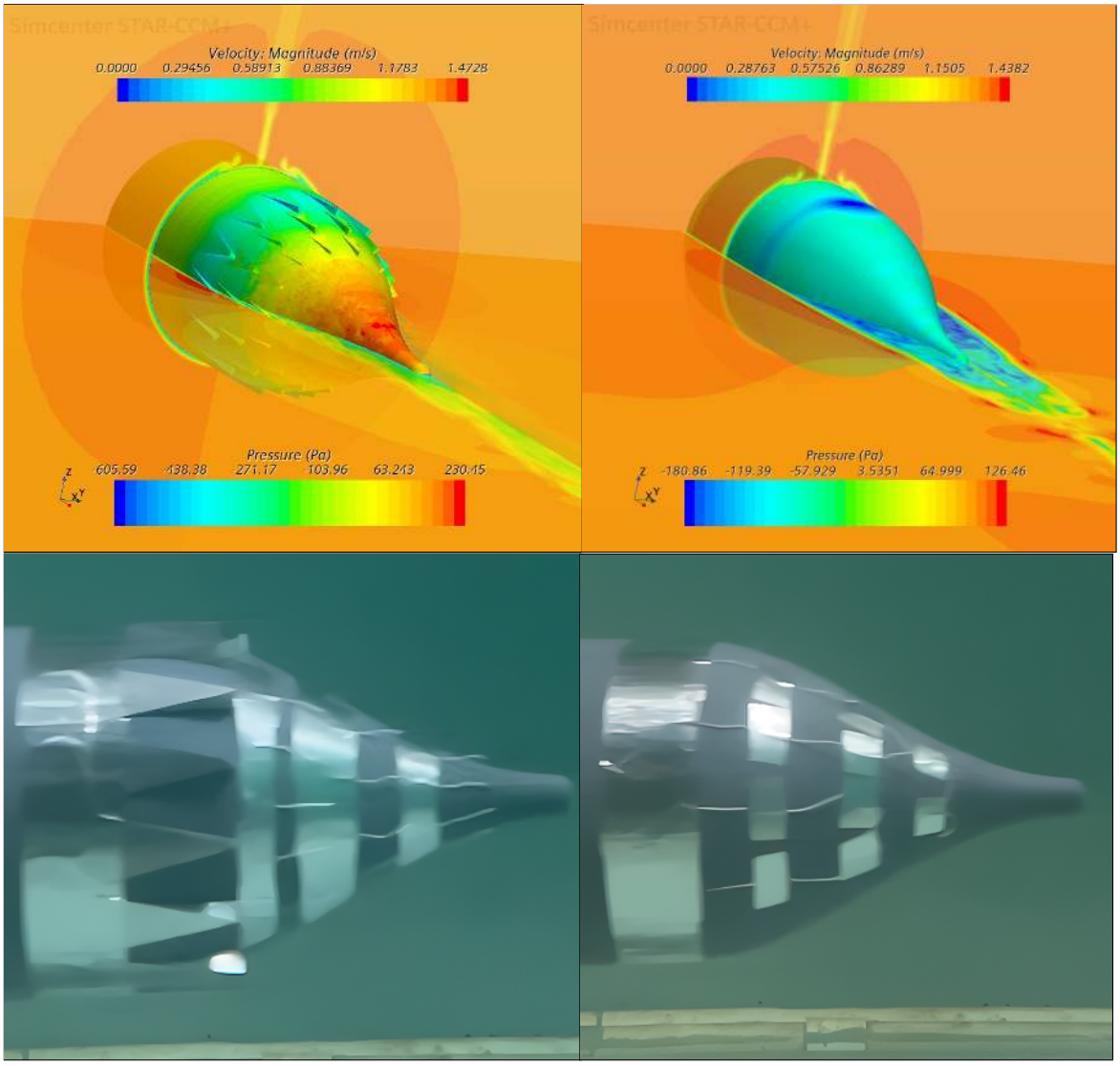

Figure 4-23: Boundary layer reattachment using innovative Wedge VGs.

flow separation. When the boundary layer separates from the surface, it can lead to increased drag, a turbulent wake, and potential performance inefficiencies.

The insights from the tell tails are quite valuable:

1. *Flow Attachment*: The aligned tell tails in the presence of VGs confirm that these devices can successfully reattach the flow. This demonstrates the effectiveness of the VGs in manipulating the boundary layer to remain close to the tail surface.

2. Flow Separation: The misaligned tell tails on the bare tail indicate areas of flow separation. This condition can lead to increased pressure drag and might adversely affect the propeller's performance by introducing unsteady flows into the propeller blades.

3. *Effectiveness of VGs*: Comparing the two sets of tell tails allows us to evaluate the effectiveness of the VGs. The contrast between the aligned and misaligned tell tails provides a clear visual representation of the flow behavior modification due to the VGs.

4. *Optimization*: The data from these experiments can be used to optimize the size, shape, and placement of VGs for different vessel designs and operating conditions.

5. *Energy Efficiency*: By ensuring that the flow remains attached, the efficiency of the vessel can be improved as the propeller operates in a more uniform flow field, reducing fuel consumption and emissions.

These findings can be integrated into the design and operational strategies of marine vessels to enhance performance and efficiency. Additionally, understanding the behavior of the boundary layer in different conditions, areas of large curvature and with various VG configurations can lead to the development of adaptive VG systems that can adjust in real-time to changing flow conditions, potentially offering even greater performance benefits.

The last set of VGs (see fig. 4-22) tested on the tail section provided significant enhancements in flow dynamics. Most notably, an overall drag reduction of 7.56% at model scale was observed (see table 4.1). This finding highlights the potential of optimized VGs

Model Scale	
CF_{ITTC}	0.00413
$CF_{Measured}$	0.00550
Fx_{Bare} (N)	4.444
$Fx_{WithVGs}$ (N)	4.108
Fxf_{Bare} (N)	3.558
k_{Bare}	1.249
$k_{WithVGs}$	1.154
CD_{Bare}	0.00683
$CD_{WithVGs}$	0.00631
N_{VGs}	14.00
R_{Body} (m)	0.100

Table 4.1: 7.5% net drag reduction measured in the MIT towing tank.

to improve marine vessel efficiency and performance by reducing energy loss due to drag at a full-scale operational level.

4.7.6 Conclusion

This chapter has demonstrated significant advancements in the application of Vortex Generators (VGs) in marine environments, driven by a critical analysis and optimization using Gaussian Processes. The initial design exploration highlighted a key limitation of conventional VG shapes; namely, their tendency to generate excessive drag when deployed in hydrodynamic settings. This insight led to a critical reevaluation of VG designs, highlighting the necessity for shapes specifically optimized for water applications and low parasitic drag to create subtle interventions and correct boundary layer detachments in hydrodynamic bodies, whose frictional drag is still much larger than the pressure component of the drag.

Inspired by the aerodynamically efficient NACA duct shapes, we developed innovative VG concepts aimed at minimizing hydrodynamic drag. These new designs represent a significant leap forward, promising not only to enhance operational efficiency but also to reduce fuel consumption dramatically. The effectiveness of these designs was empirically confirmed in rigorous testing environments such as the MIT Tow Tank, where a notable 7.5% reduction in drag was observed. This achievement not only sets a new standard in VG technology but also offers substantial improvements in fuel efficiency and operational

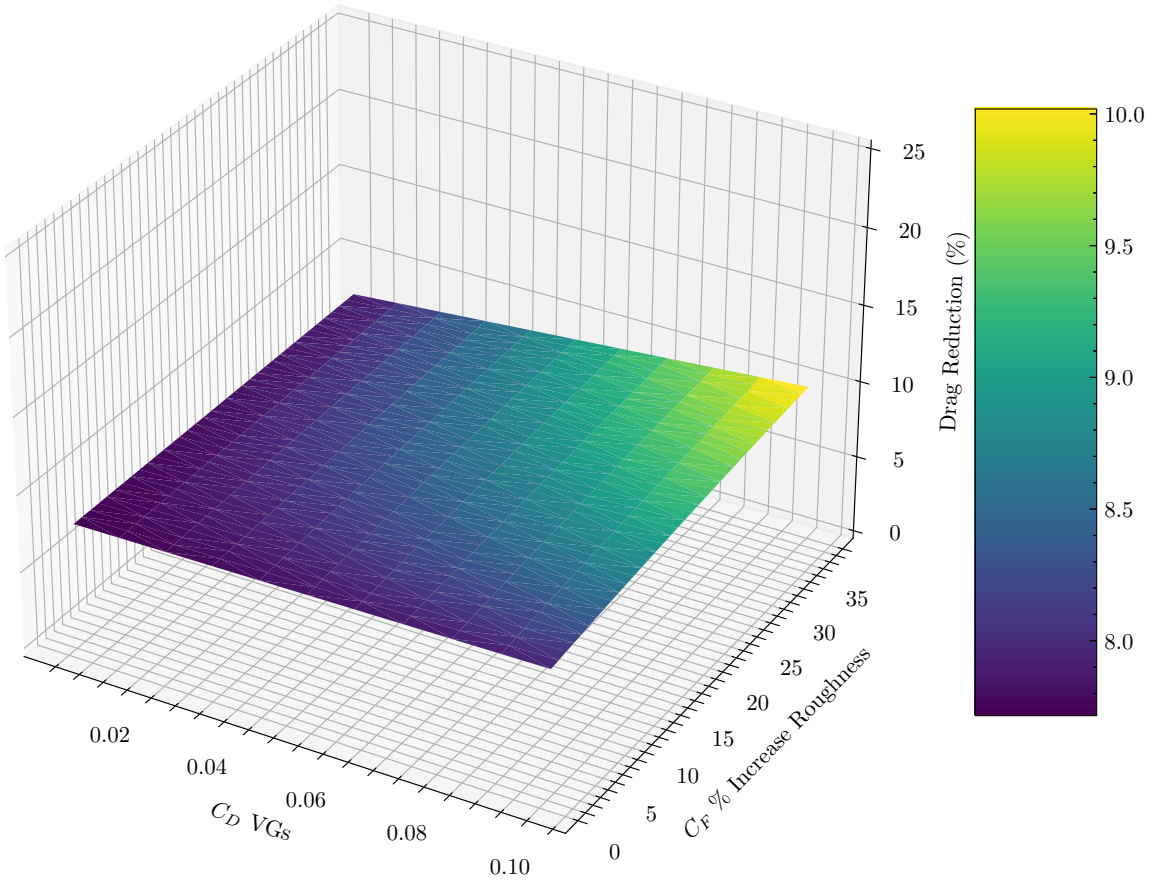

Figure 4-24: Drag reduction extrapolation to full scale considering several VG drag coefficients and full scale surface roughness [47], assuming form factor remains constant. Given that it is impractical to measure form drag reduction and the subsequent specific drag of the VGs during experiments, we start by assuming a given form factor reduction (and subsequent VG drag coefficient) and studying the projected drag reduction under this hypothesis. We can show that the response surface of the projected drag reduction is mostly flat with small changes. From this response surface we can project conservatively an 8% drag reduction if we extrapolate the tested model to typical conditions of the reference bulk carrier ($L = 300m$ and $v = 12kn$). A high efficiency delta arrow VG would have $C_D \sim 0.17$ for similar angles of attack.

cost savings for the marine industry.

However, while Computational Fluid Dynamics (CFD) analysis, more specifically Detached Eddy Simulation (DES), provided valuable insights into the flow dynamics around these new VG designs, the approach was constrained by significant uncertainties. These primarily stemmed from modeling assumptions and limitations in grid resolution. To advance our understanding and improve the reliability of our simulations, future research should focus on refining these CFD models. Integrating advanced machine learning algorithms could potentially enhance the predictive accuracy of complex flow phenomena and provide a more robust validation of experimental results.

In conclusion, the research presented in this thesis lays a solid foundation for the next generation of VG designs in marine applications. By addressing both the design flaws of traditional VGs and pioneering new, low-drag configurations, this work not only contributes to the academic field but also holds tangible promise for real-world maritime operations. Moving forward, continued innovation and rigorous validation will be key to realizing the full potential of these developments, ultimately leading to more efficient and environmentally friendly marine transport solutions.

4.7.7 Future Work

The potential applications of these NACA-inspired wedge VGs are significant for marine vessels and offshore platforms, where efficient flow control can lead to substantial improvements in seakeeping, and overall energy efficiency. In this VG shape exploration we calculate an 8% drag reduction at full scale (see fig. 4-24). Moreover, the path followed by the changes in shape throughout the VG optimization sets a natural transition to the exploration of concepts of morphable wedges that can adjust their angle and could introduce a dynamic boundary layer control mechanism, potentially optimizing performance across varying operational conditions.

By exploring different VG configurations and their impact on boundary layer behavior, this research contributes valuable insights into the design of more efficient marine vessels. The results indicate that there's a threshold of VG size and orientation that can achieve the desired flow control with small amounts of induced parasitic drag, which is crucial for

the optimization of the overall performance of marine vessels. Moreover by correcting the flow upstream and before it detaches we can improve the propeller efficiency. Through wake homogenization, which is the process of making the velocity distribution in the wake of a ship as uniform as possible, VGs also can increase the efficiency of marine propellers. The wake is the region of disturbed flow (usually turbulent) downstream of the ship, which directly impacts the propeller as it operates in this flow. The effects include:

1. *Uniform Load Distribution*: A homogenized wake ensures that the propeller blades experience a more uniform load distribution, reducing the likelihood of cavitation and blade fatigue.

2. *Consistent Propeller Performance*: With a uniform wake, the propeller can operate at optimal conditions, providing consistent performance and reducing the risk of vibrations and noise.

3. *Improved Fuel Efficiency*: A homogenized wake allows for better alignment of the propeller's angle of attack with the flow, minimizing energy losses due to misalignment and thus improving fuel efficiency.

Both flow reattachment and wake homogenization are crucial for the performance of the propeller and the ship as a whole. Vortex generators, like the ones studied in the tails configurations, can play a significant role in achieving these conditions. By carefully designing the hull's aft section and knuckles, where the flow tends to separate, engineers can control the flow to ensure that it remains attached and that the wake is as homogenized as possible when it reaches the propeller. This optimization leads to a more efficient vessel with reduced fuel consumption and emissions, better seakeeping abilities, and potentially increased operational speed or payload capacity. These improvements can mean significant cost savings and a reduced environmental footprint, which are key objectives in the marine industry.

Chapter 5

Global Conclusions

5.1 Conclusions

The exploration into the dynamics of ship motion under the influence of complex sea states has shed light on the phenomenon of parametric rolling, often exacerbated by specific wave interactions. The insights gained from the phase state diagrams and the coupling between roll and pitch motions (see Figure 2-41) underline the critical and singularly complex nature of this dynamic phenomena, which significantly impacts maritime safety and operational efficiency. These complex dynamics, with statistical shifts in their properties across three different sea states, are predicted with unparalleled speed (a fraction of a second) by the neural networks we put forward.

Through the rigorous application of SciML to high Reynolds number flows, we have advanced the field of marine engineering and provided a blueprint for addressing similar challenges across various engineering disciplines. The development and validation of hydrodynamic databases, particularly for predicting Vortex Induced Vibrations (VIV), represent a novel contribution of this research. The robustness of these databases has been systematically validated across different current incidence angles, highlighting their capability to accurately predict VIV under varied and extrapolated conditions (see Figures 3-6, 3-7, 3-8, 3-9). This methodology, grounded by a machine learning approach introduced by Rudy et al. [228], offers a novel perspective on the generalization capabilities of hydrodynamic databases and greatly improves predictions of traditional databases

extracted from rigid cylinder experiments (compare fig. 3-14, predictions of the standard VIVA database, and fig. 3-13).

In the realm of boundary layer control, the implementation of wedge-shaped vortex generators has led to a notable reduction in hydrodynamic drag (8%), empirically validated in environments such as the MIT Tow Tank. This work not only contributes to the academic field but also promises considerable practical applications in designing more efficient marine vessels and potentially other vehicles where fluid dynamics play a critical role. The design of our wedge-shaped vortex generators incorporates a natural feature that allows for the adjustment of their protrusion into the boundary layer. This dynamic adjustment capability can be informed by machine learning algorithms that encapsulate information from prior experiments or real-time data acquisition. By leveraging this technology, we can achieve real-time active control of the boundary layer, optimizing flow characteristics dynamically to adapt to changing environmental conditions or operational requirements.

5.2 Implications and Future Directions

The interdisciplinary impact of this thesis extends beyond marine engineering. The methodologies and insights have the potential to revolutionize practices in aerospace by optimizing airflow around aerodynamic bodies, in automotive by reducing vehicle drag, and in renewable energy by enhancing the aerodynamic efficiency of wind turbines. Moreover, the application of these findings to civil engineering could improve structural designs to withstand extreme weather conditions.

As we look to the future, the integration of increasingly sophisticated machine learning models with enhanced sensor technologies and simulations will likely transform engineering practices. This integration promises not only to refine our predictive capabilities but also to enable more effective control over complex physical phenomena. The continuous evolution of SciML, coupled with robust data collection and analysis, will pave the way for developing AI systems capable of proactive decision-making in real-time engineering applications.

However, the reliance on sensor data and AI also introduces new challenges, partic-

ularly related to cybersecurity in engineering systems. It is crucial to develop secure, reliable, and robust AI-based systems to ensure they deliver their intended benefits without introducing new vulnerabilities.

5.3 Concluding Remarks

This thesis marks a significant step forward in our understanding and application of fluid dynamics in engineering. The use of SciML to bridge the gap between theoretical models and empirical data has not only enhanced our analytical capabilities but also set the stage for the next generation of engineering innovations. The continued exploration of these methodologies will undoubtedly yield further insights and advancements, driving efficiency and safety in marine and other engineering fields.

Appendix A

Wave Proves & Corresponding Ship Motions

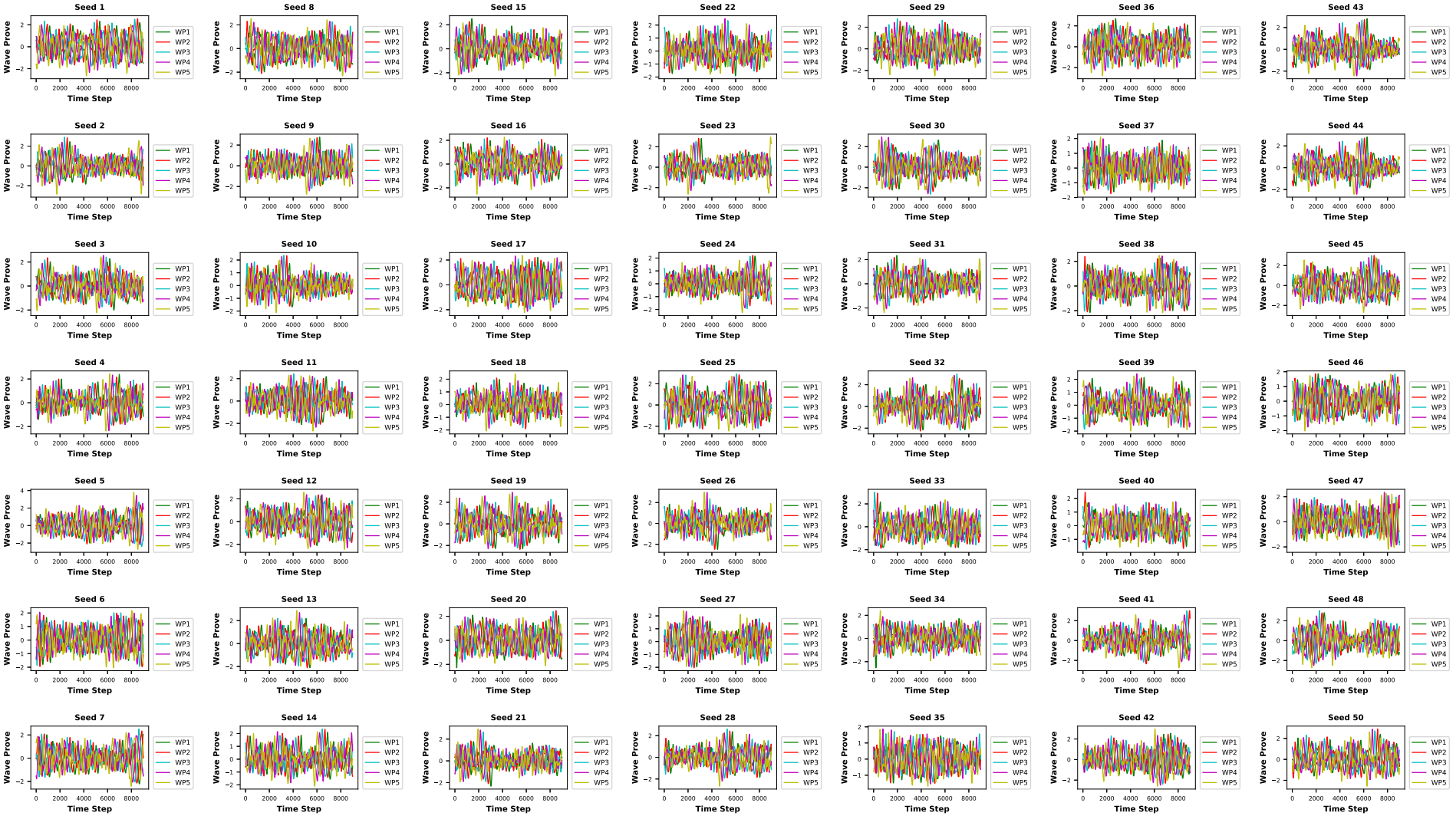

Figure A-1: *Network wave probes along the longitudinal direction of the DTMB vessel.* They are two-dimensional and represent a long crested irregular oblique waves. Each time step is $\Delta t = 0.008s$, $H_s = 3.53m$, $T_p = 9.7s$, $v = 30kt$.

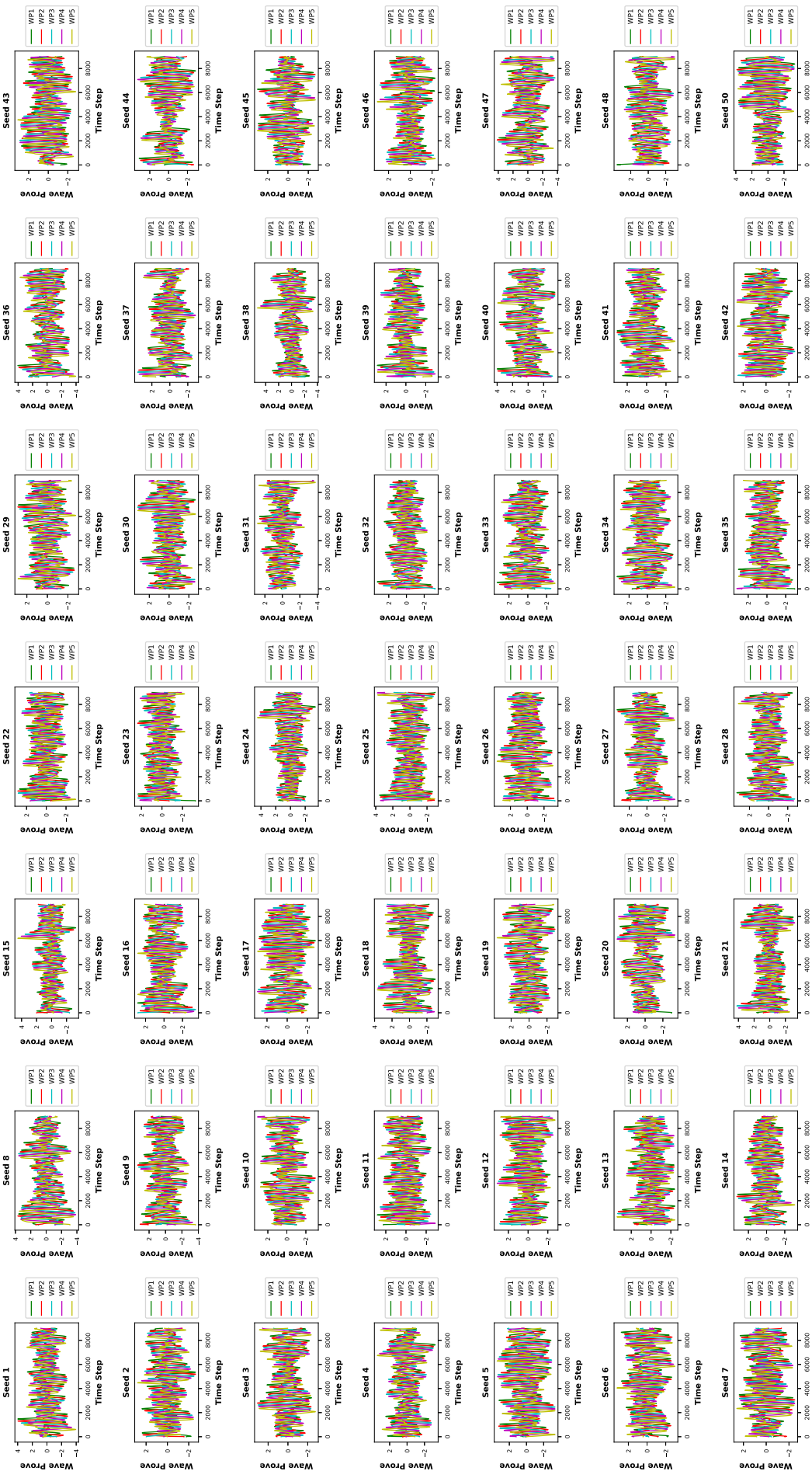

Figure A-2: *Network wave probes along the longitudinal direction of the DTMB vessel.* They are two-dimensional and represent a long crested irregular oblique waves. Each time step is $\Delta t = 0.01s$, $H_s = 5.09m$, $T_p = 12.4s$, $v = 30kt$.

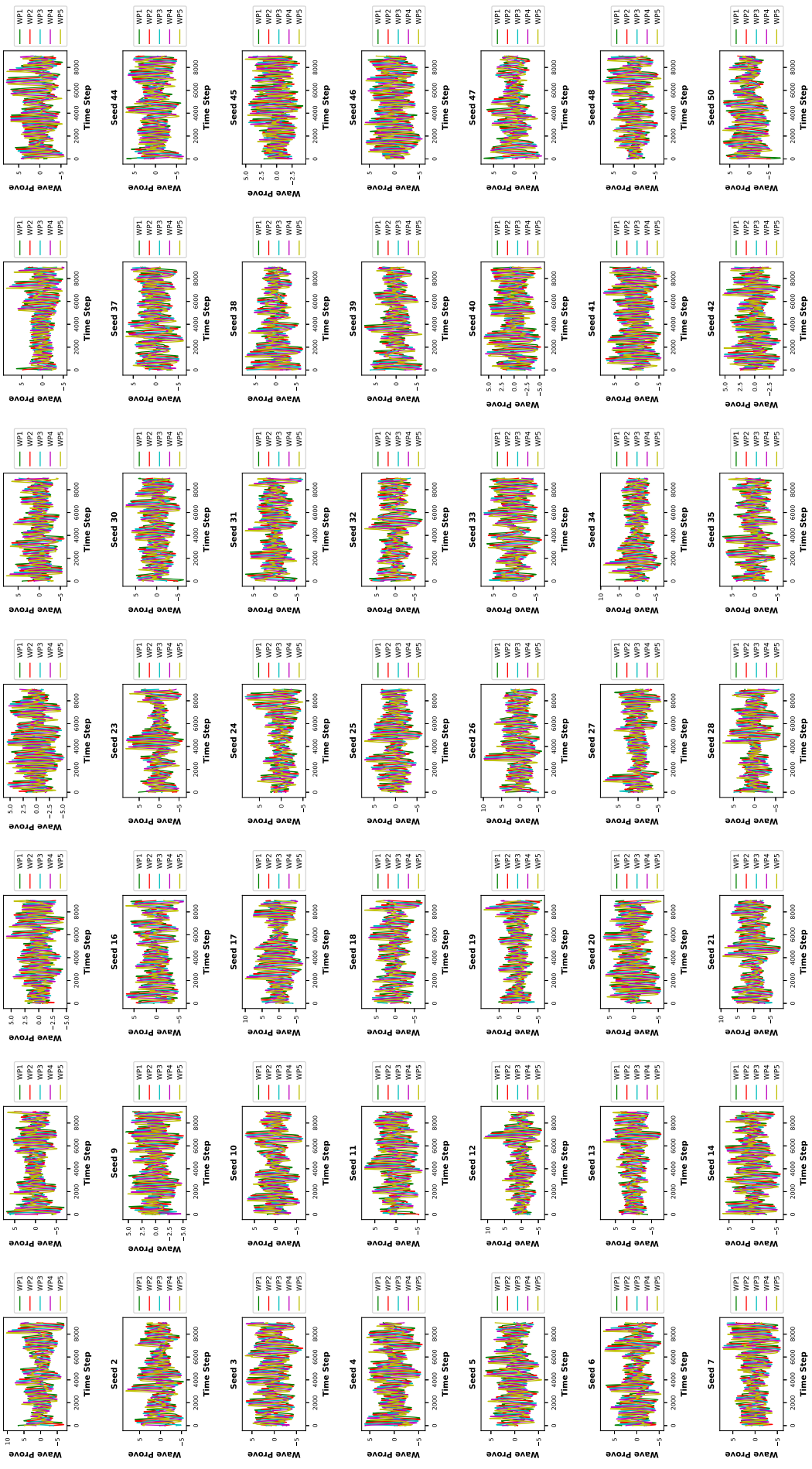

Figure A-3: *Network wave probes along the longitudinal direction of the DTMB vessel.* They are two-dimensional and represent a long crested irregular oblique waves. Each time step is $\Delta t = 0.011s$, $H_s = 10.66m$, $T_p = 13.4s$, $v = 30kt$.

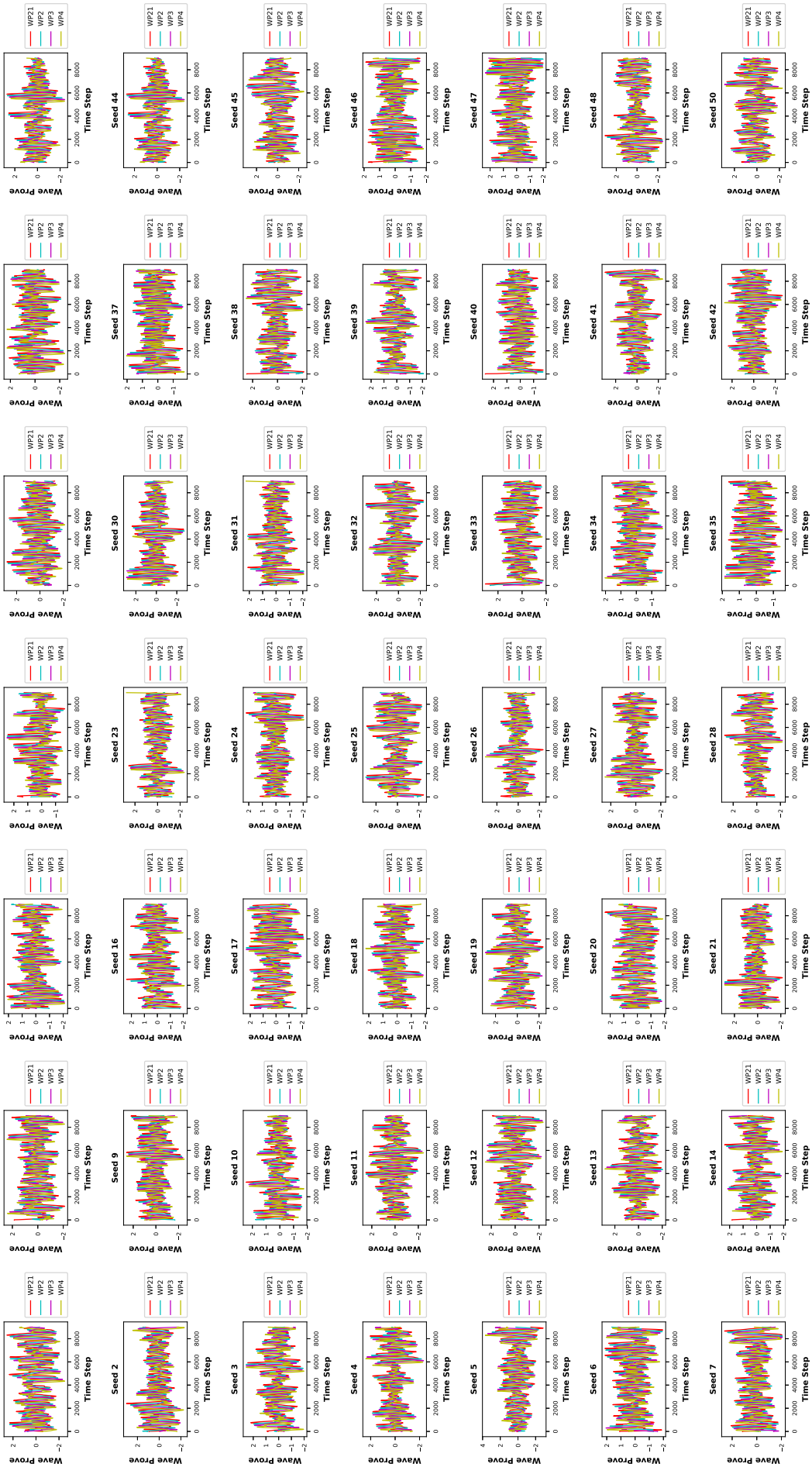

Figure A-4: *Network wave probes along the transversal direction of the DTMB vessel.* They are two-dimensional and represent a long crested irregular oblique waves. Each time step is $\Delta t = 0.008s$, $H_s = 3.53m$, $T_p = 9.7s$, $v = 30kt$.

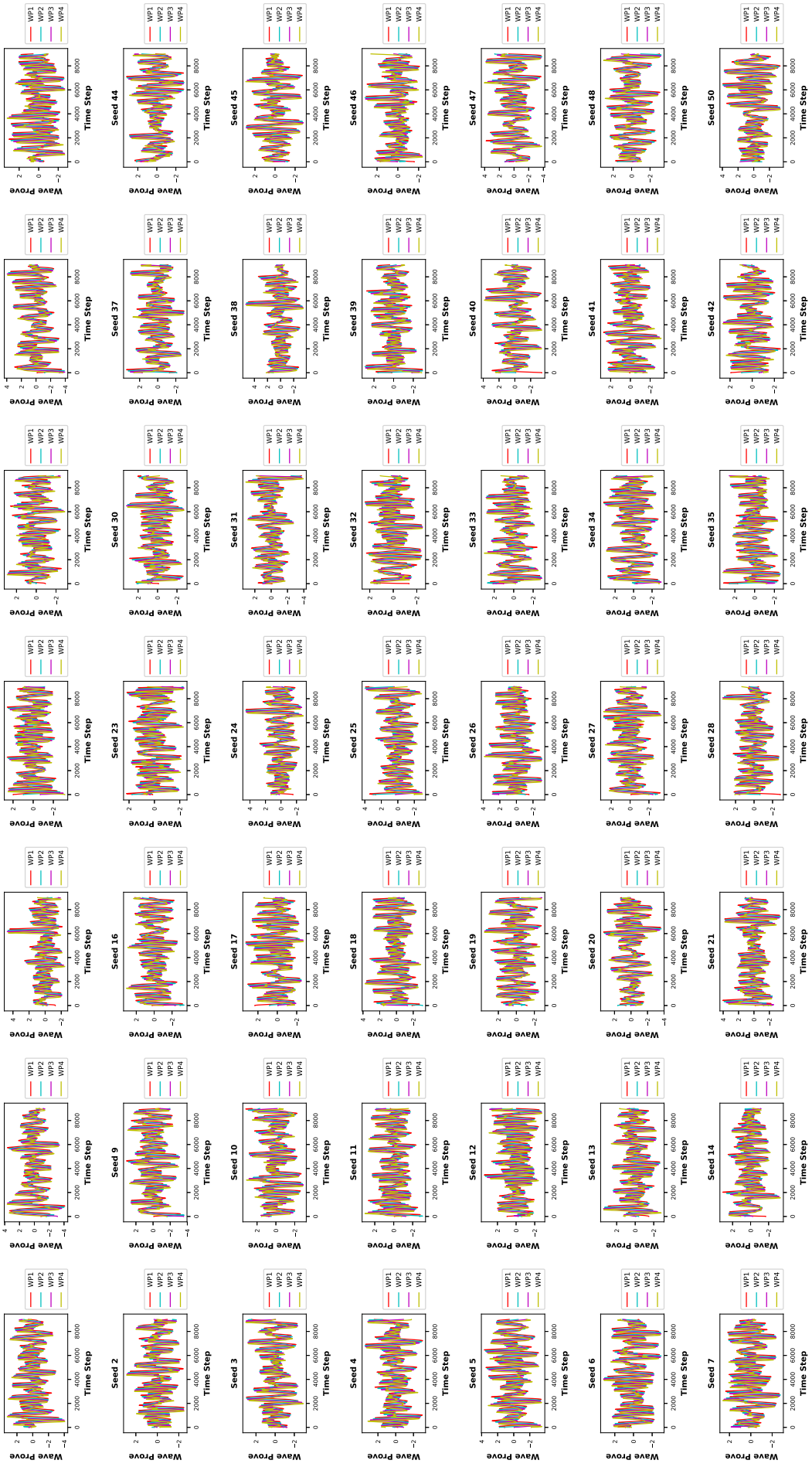

Figure A-5: *Network wave probes along the transversal direction of the DTMB vessel.* They are two-dimensional and represent a long crested irregular oblique waves. Each time step is $\Delta t = 0.01s$, $H_s = 5.09m$, $T_p = 12.4s$, $v = 30kt$.

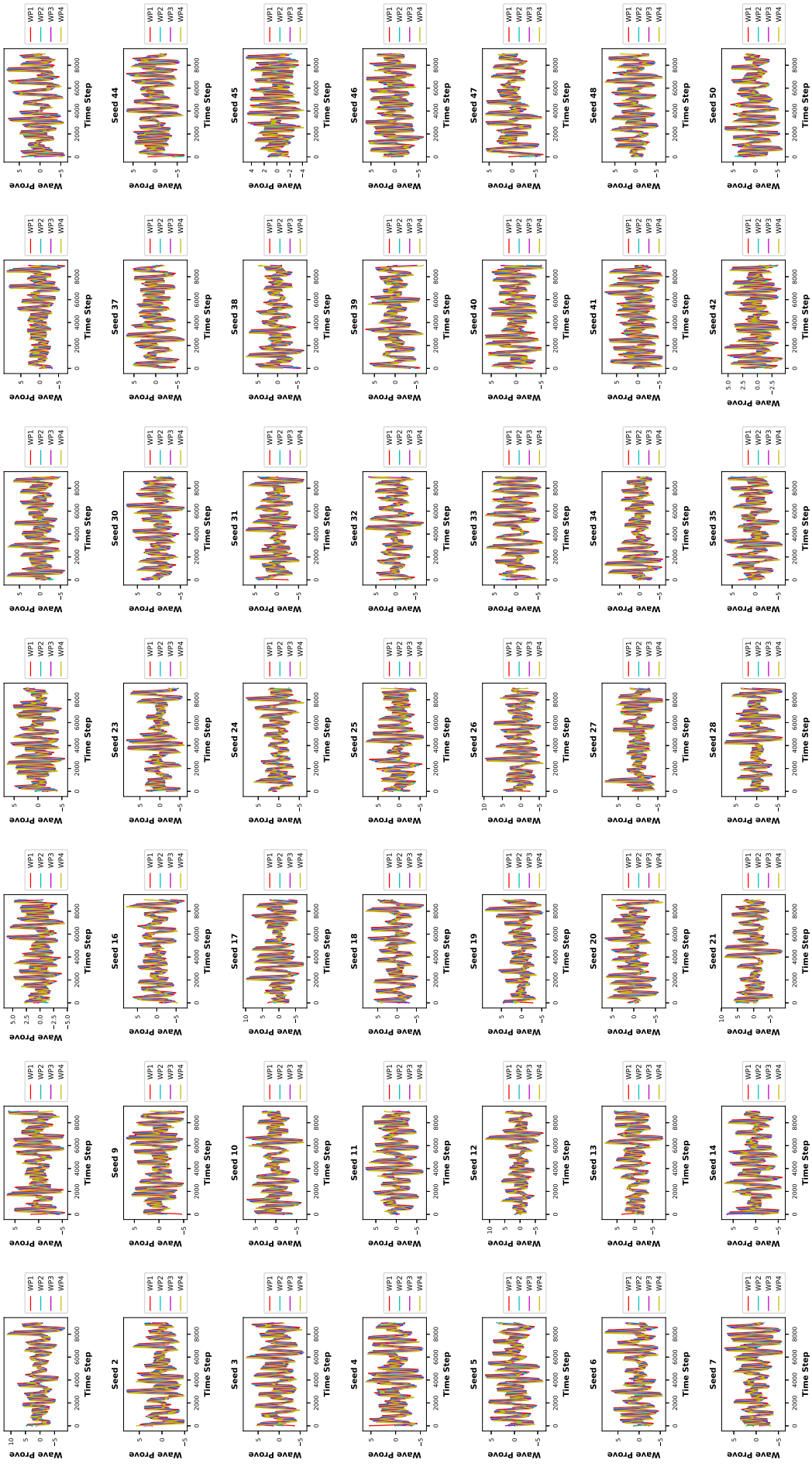

Figure A-6: *Network wave probes along the transversal direction of the DTMB vessel.* They are two-dimensional and represent a long crested irregular oblique waves. Each time step is $\Delta t = 0.011s$, $H_s = 10.66m$, $T_p = 13.4s$, $v = 30kt$.

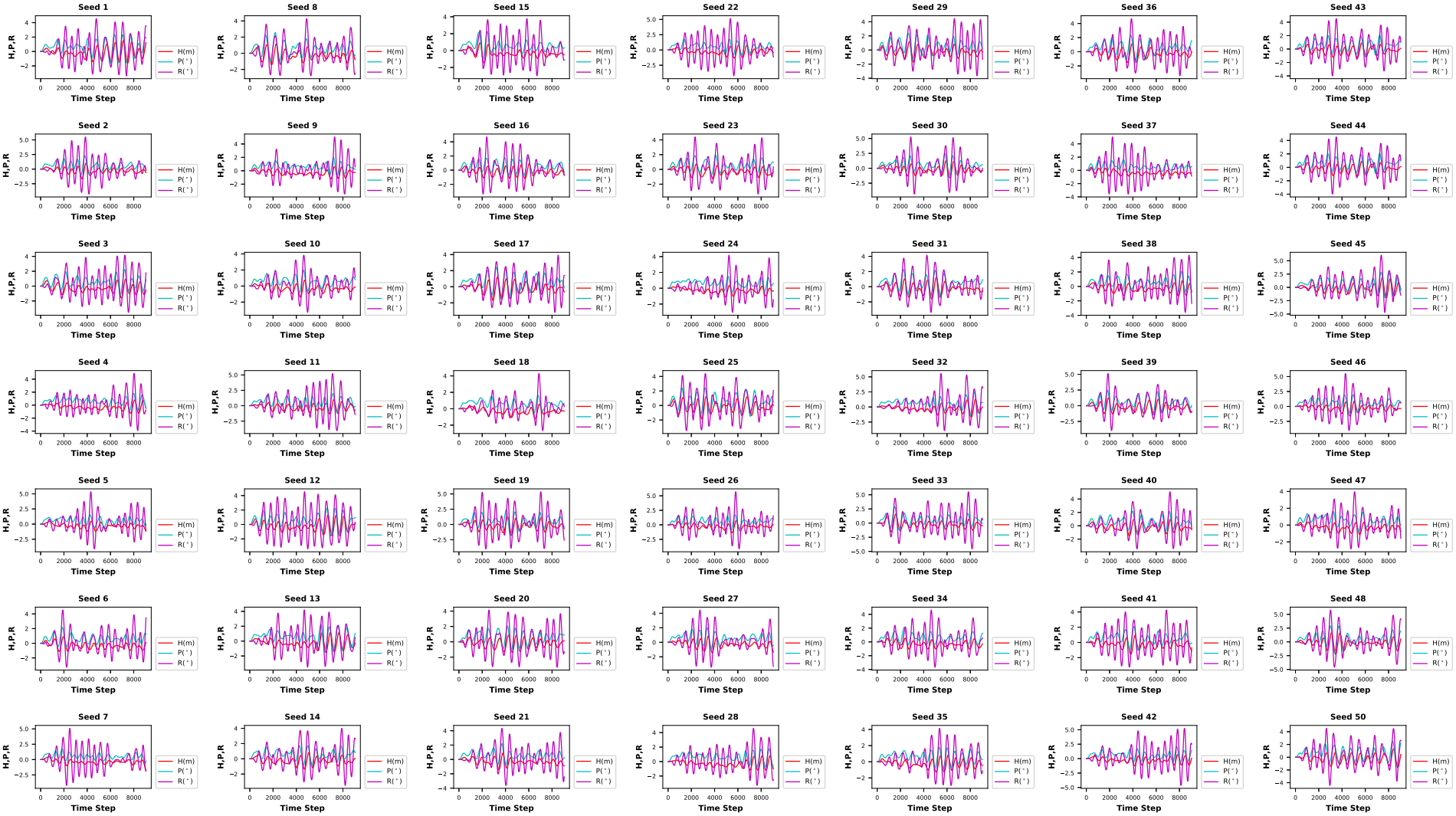

Figure A-7: *Motion time histories of the DTMB vessel.* Heave, pitch and roll motions are provided for each sea state seed. Each time step is $\Delta t = 0.008s$, $H_s = 3.53m$, $T_p = 9.7s$, $v = 30kt$.

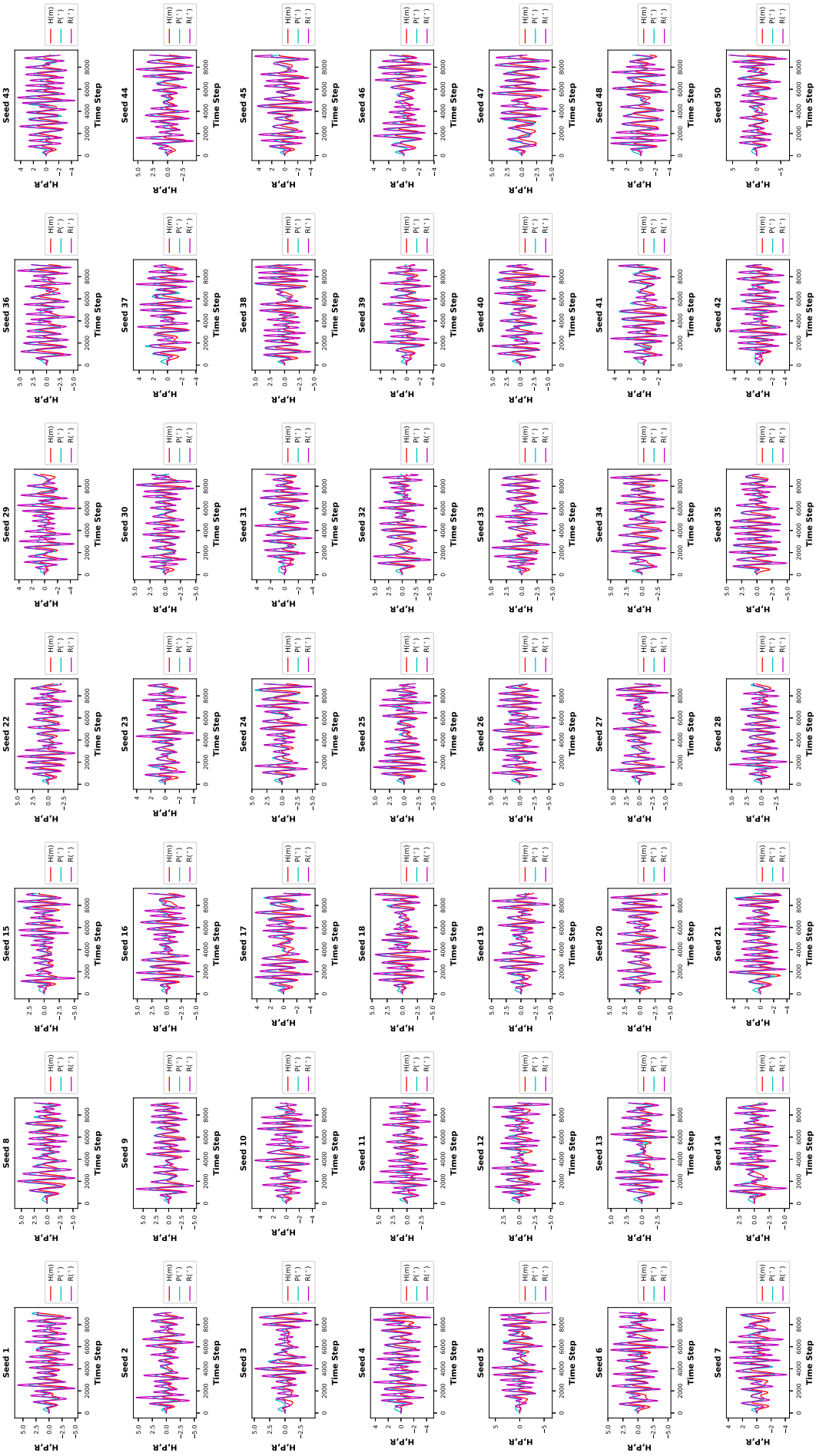

Figure A-8: *Motion time histories of the DTMB vessel.* Heave, pitch and roll motions are provided for each sea state seed. Each time step is $\Delta t = 0.01s$, $H_s = 5.09m$, $T_p = 12.4s$, $v = 30kt$.

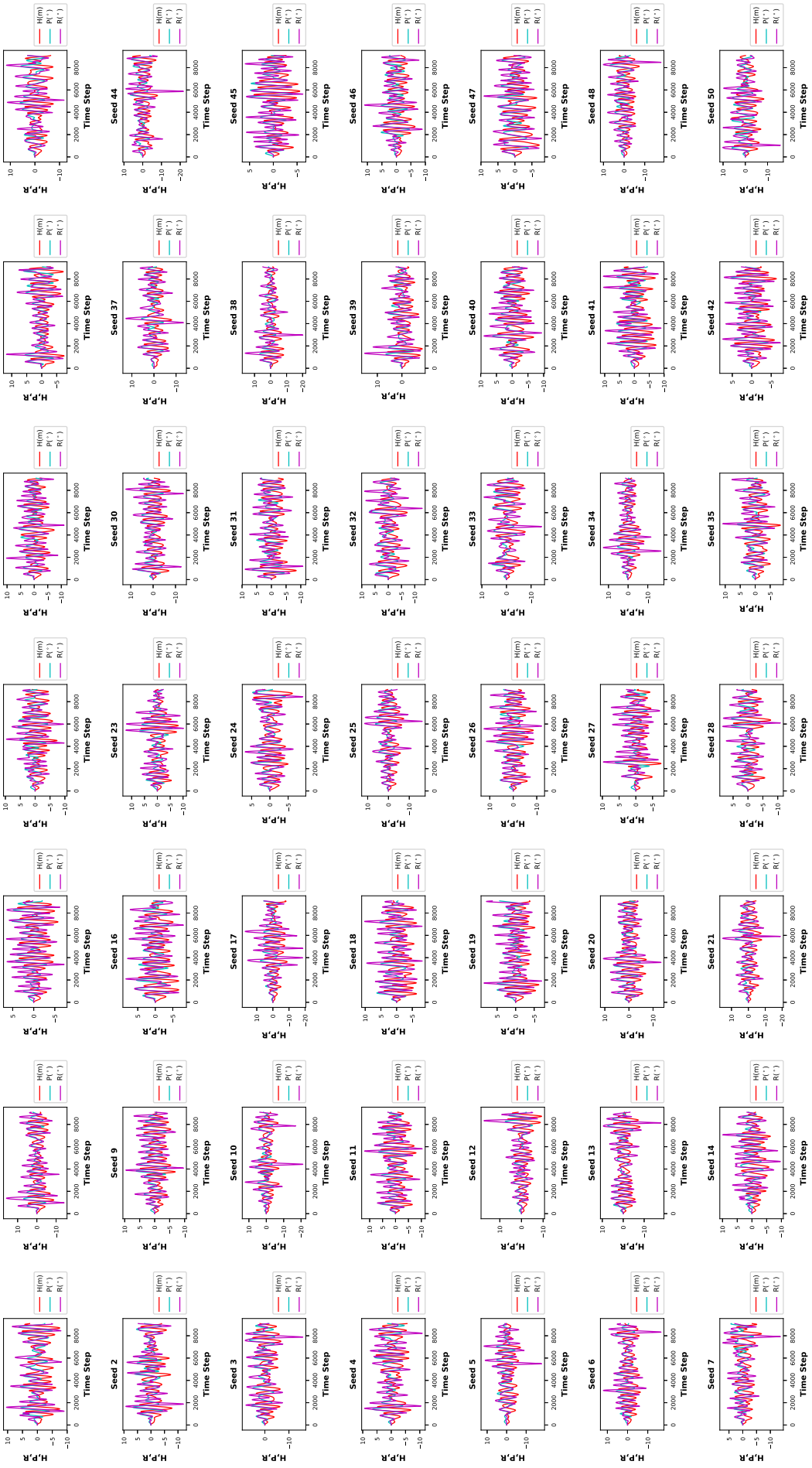

Figure A-9: *Motion time histories of the DTMB vessel.* Heave, pitch and roll motions are provided for each sea state seed. Each time step is $\Delta t = 0.011s$, $H_s = 10.66m$, $T_p = 13.4s$, $v = 30kt$.

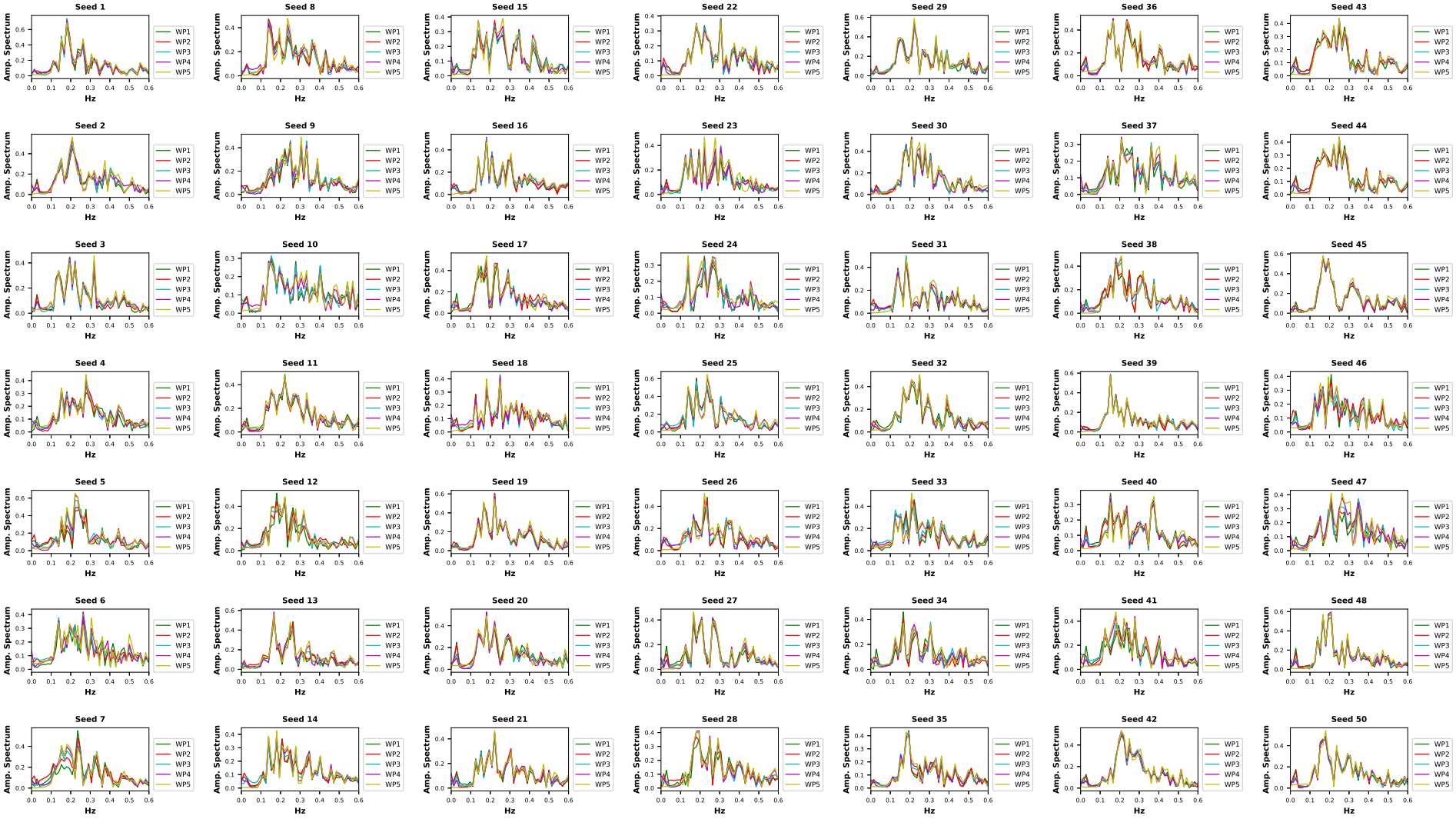

Figure A-10: *Amplitude spectrum of network wave probes along the longitudinal direction of the DTMB vessel.* They are two-dimensional and represent a long crested irregular oblique waves. Each time step is $\Delta t = 0.008s$, $H_s = 3.53m$, $T_p = 9.7s$, $v = 30kt$.

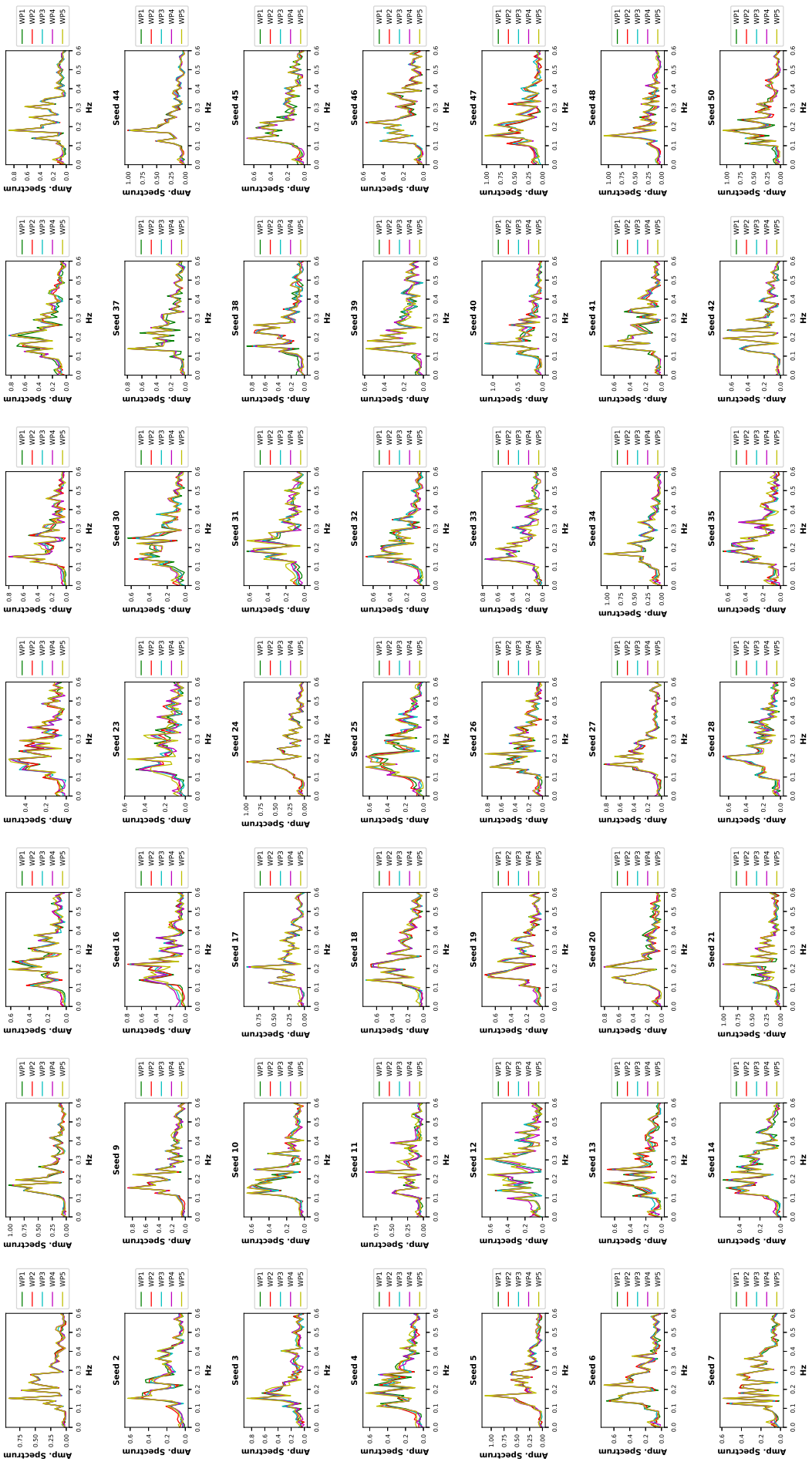

Figure A-11: *Amplitude spectrum of network wave probes along the longitudinal direction of the DTMB vessel.* They are two-dimensional and represent a long crested irregular oblique waves. Each time step is $\Delta t = 0.01s$, $H_s = 5.09m$, $T_p = 12.4s$, $v = 30kt$.

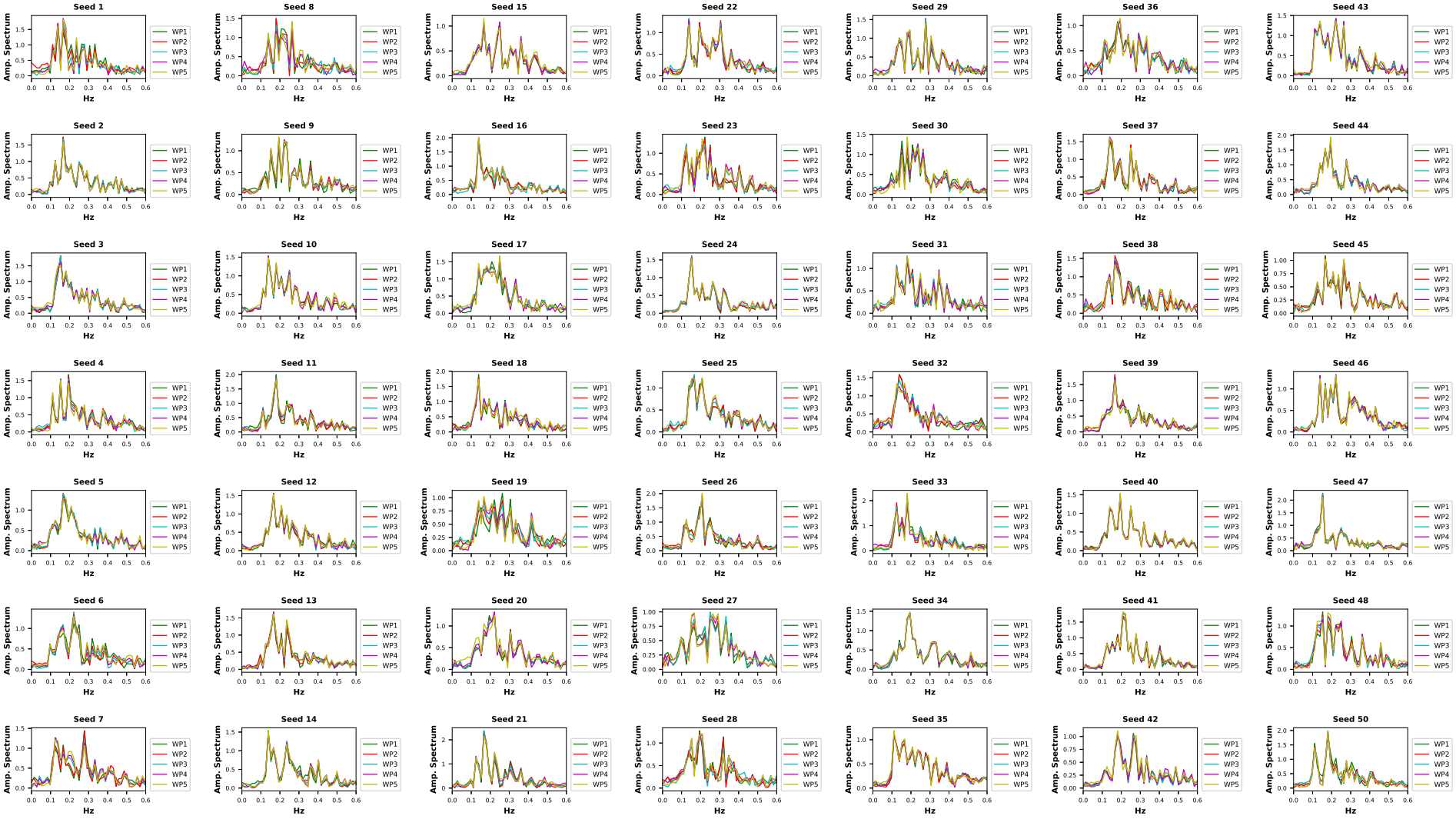

Figure A-12: *Amplitude spectrum of network wave probes along the longitudinal direction of the DTMB vessel.* They are two-dimensional and represent a long crested irregular oblique waves. Each time step is $\Delta t = 0.011s$, $H_s = 10.66m$, $T_p = 13.4s$, $v = 30kt$.

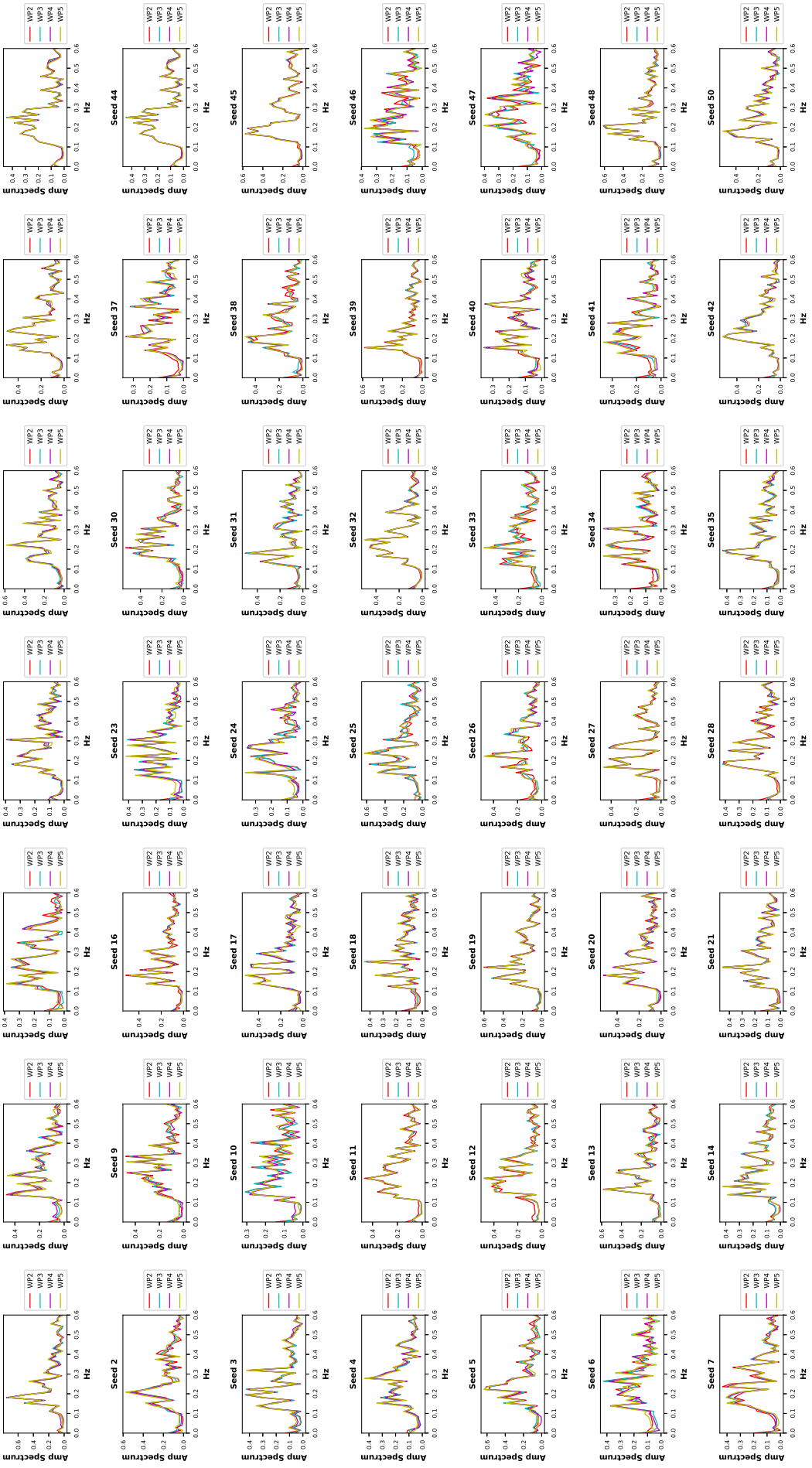

Figure A-13: *Amplitude spectrum of network wave probes along the transversal direction of the DTMB vessel.* They are two-dimensional and represent a long crested irregular oblique waves. Each time step is $\Delta t = 0.008s$, $H_s = 3.53m$, $T_p = 9.7s$, $v = 30kt$.

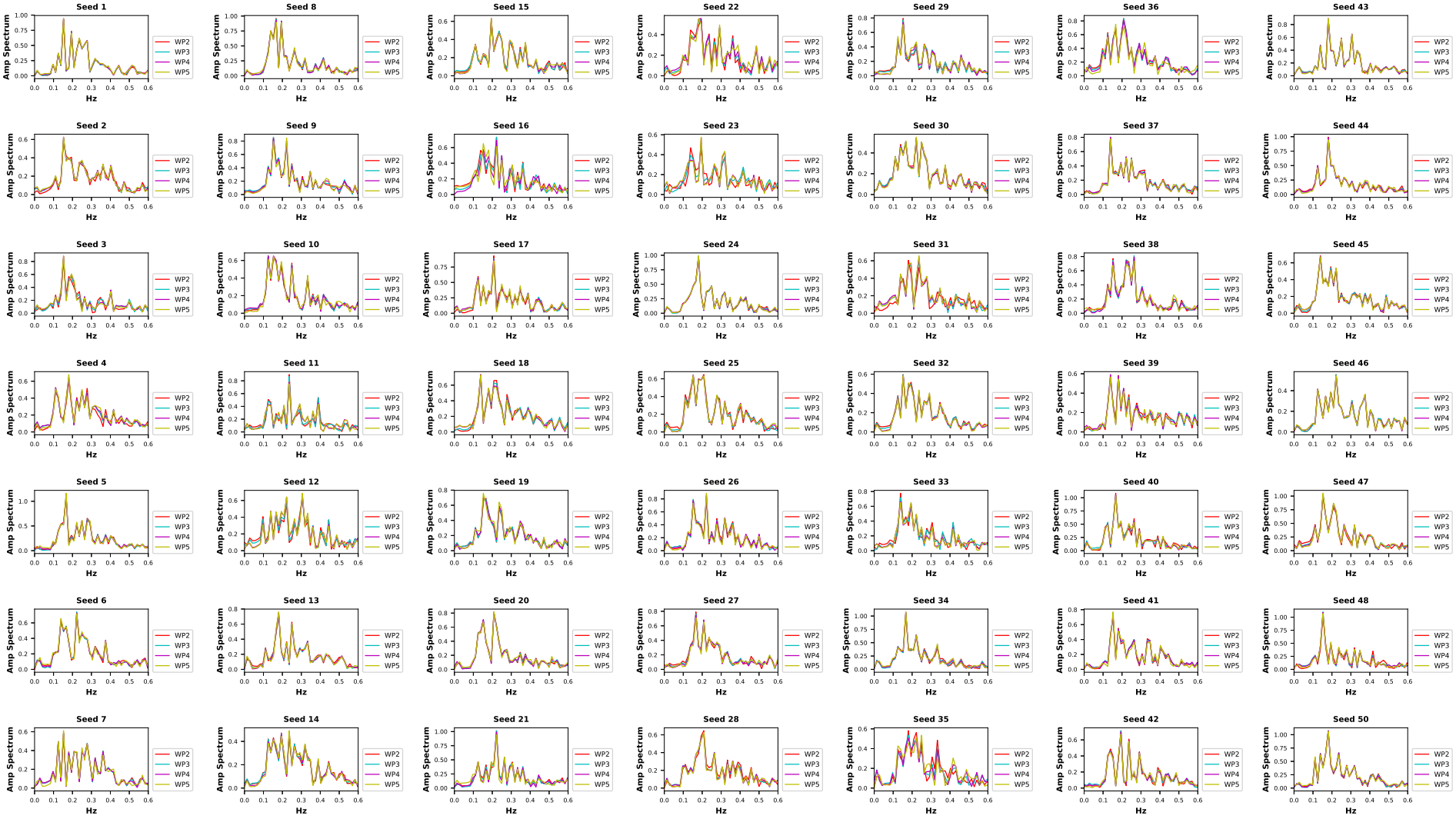

Figure A-14: *Amplitude spectrum of network wave probes along the transversal direction of the DTMB vessel.* They are two-dimensional and represent a long crested irregular oblique waves. Each time step is $\Delta t = 0.01s$, $H_s = 5.09m$, $T_p = 12.4s$, $v = 30kt$.

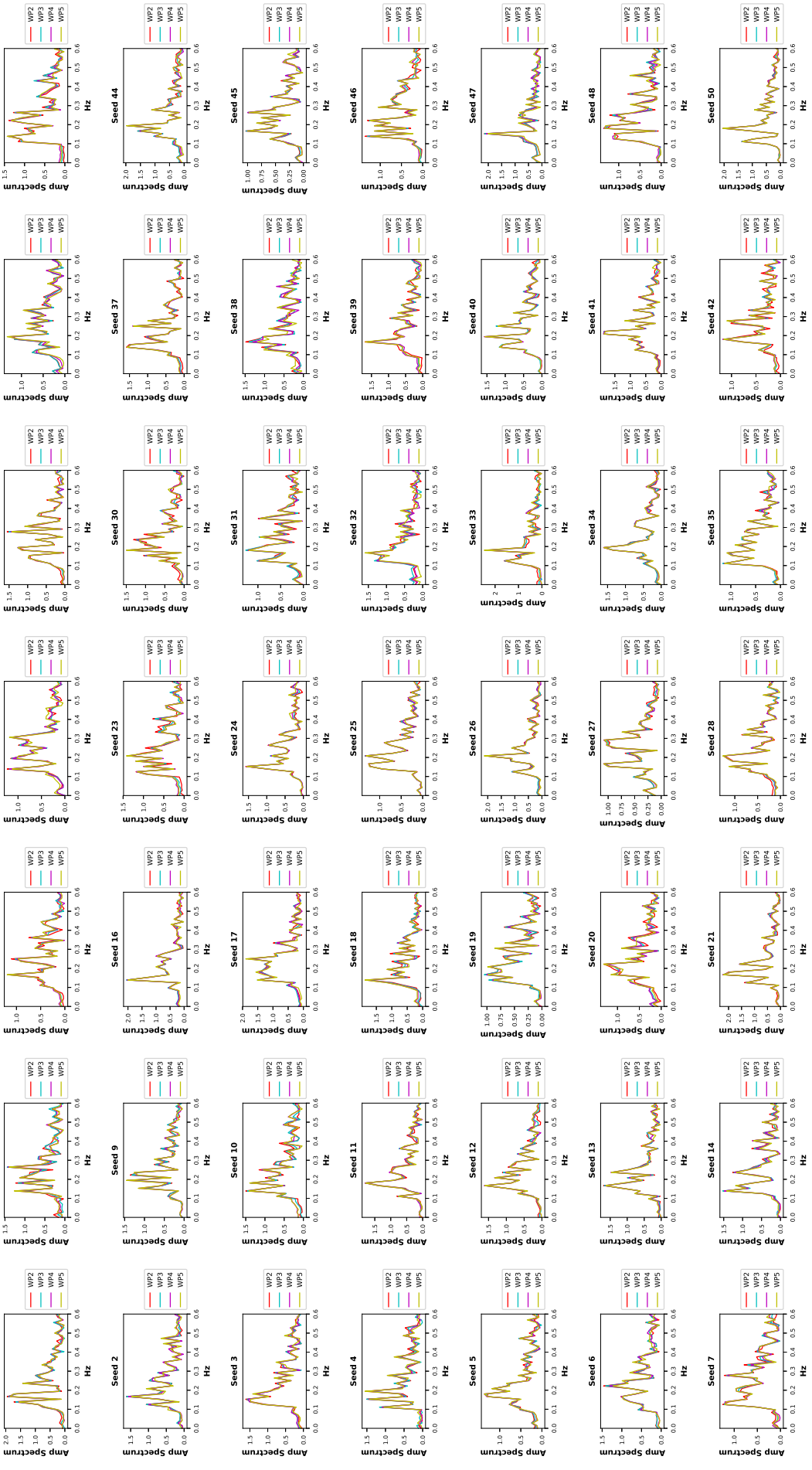

Figure A-15: *Amplitude spectrum of network wave probes along the transversal direction of the DTMB vessel.* They are two-dimensional and represent a long crested irregular oblique waves. Each time step is $\Delta t = 0.011s$, $H_s = 10.66m$, $T_p = 13.4s$, $v = 30kt$.

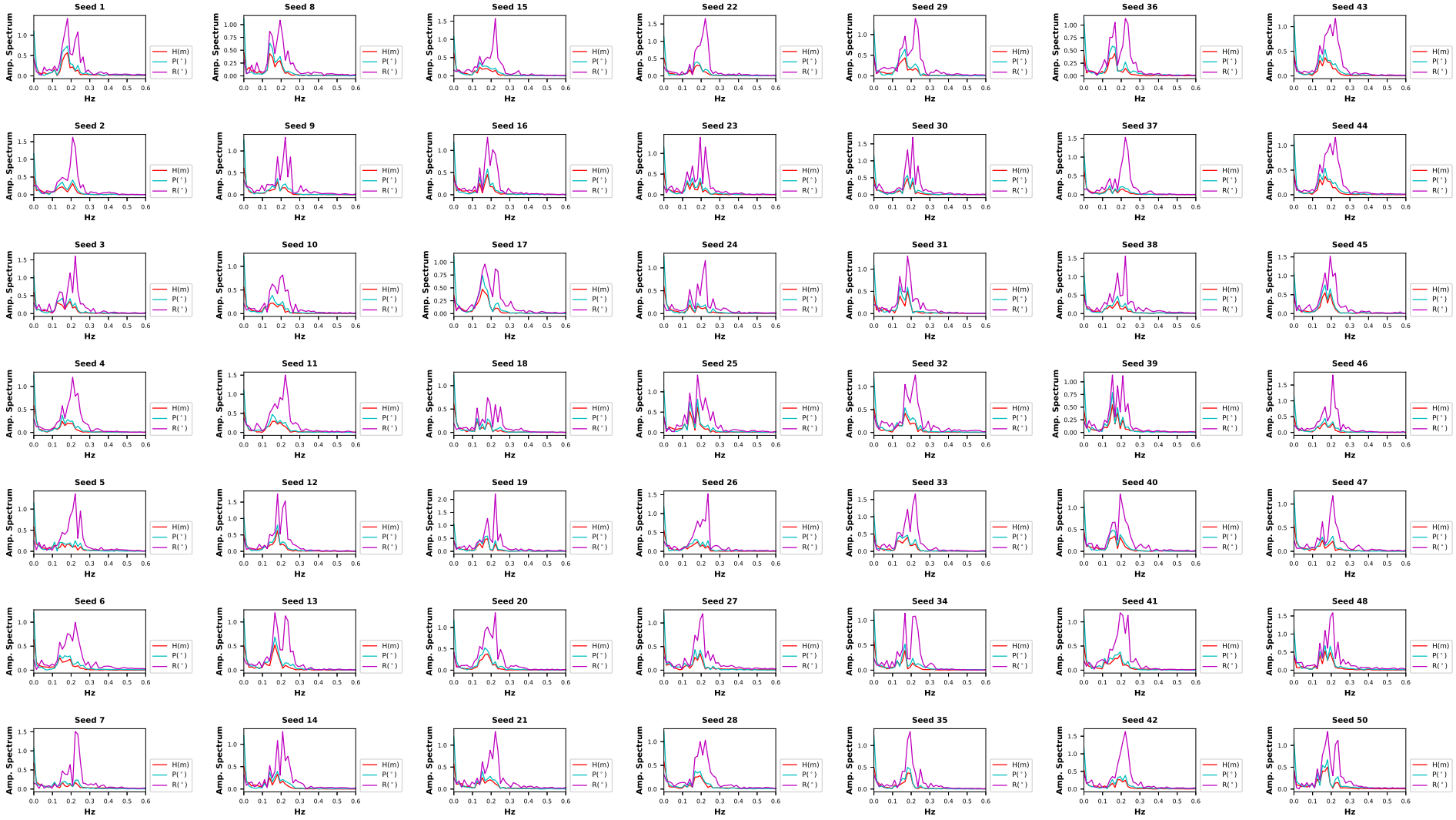

Figure A-16: *Amplitude spectrum of motion time histories of the DTMB vessel.* Heave, pitch and roll motions are provided for each sea state seed. Each time step is $\Delta t = 0.008s$, $H_s = 3.53m$, $T_p = 9.7s$, $v = 30kt$.

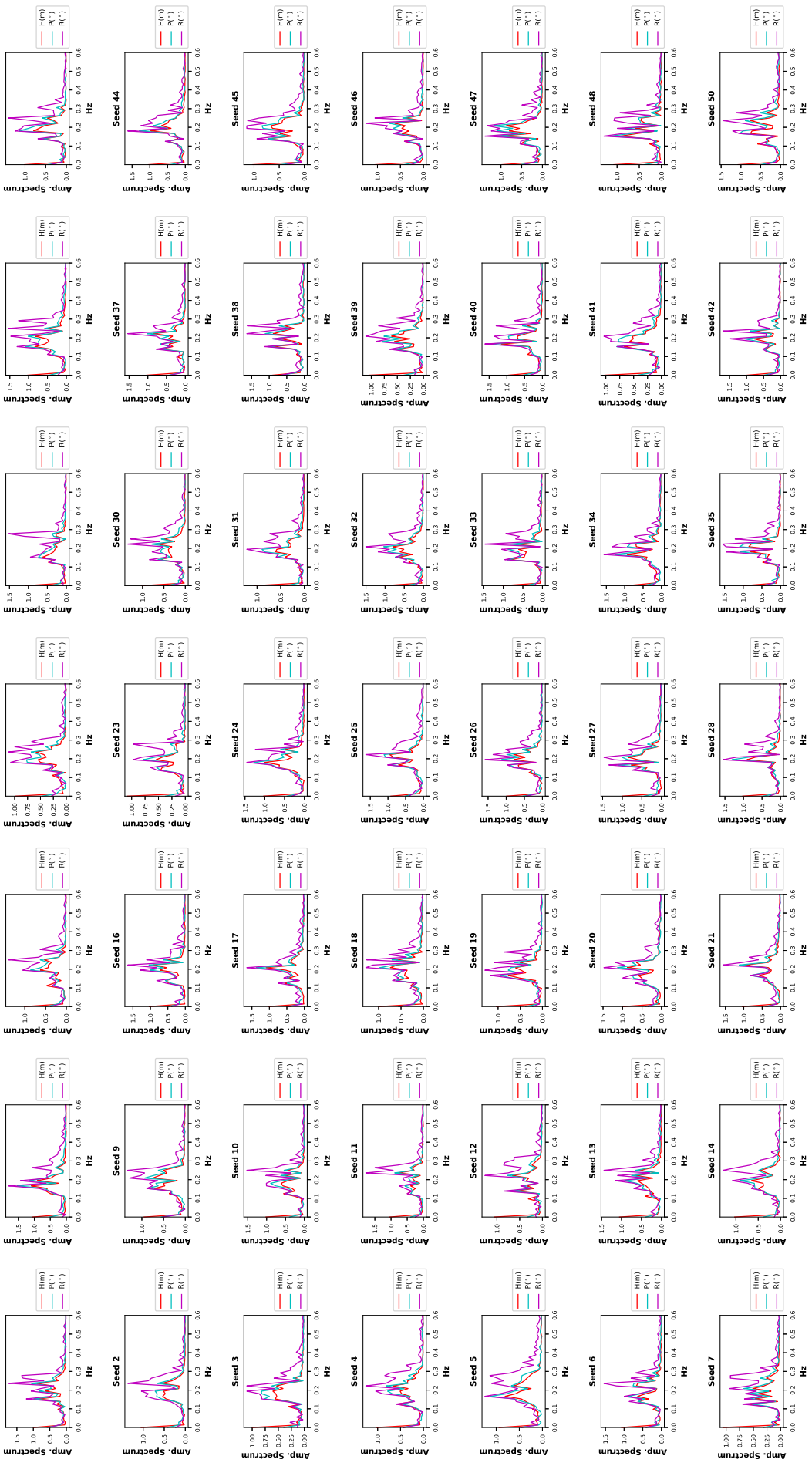

Figure A-17: *Amplitude spectrum of motion time histories of the DTMB vessel.* Heave, pitch and roll motions are provided for each sea state seed. Each time step is $\Delta t = 0.01s$, $H_s = 5.09m$, $T_p = 12.4s$, $v = 30kt$.

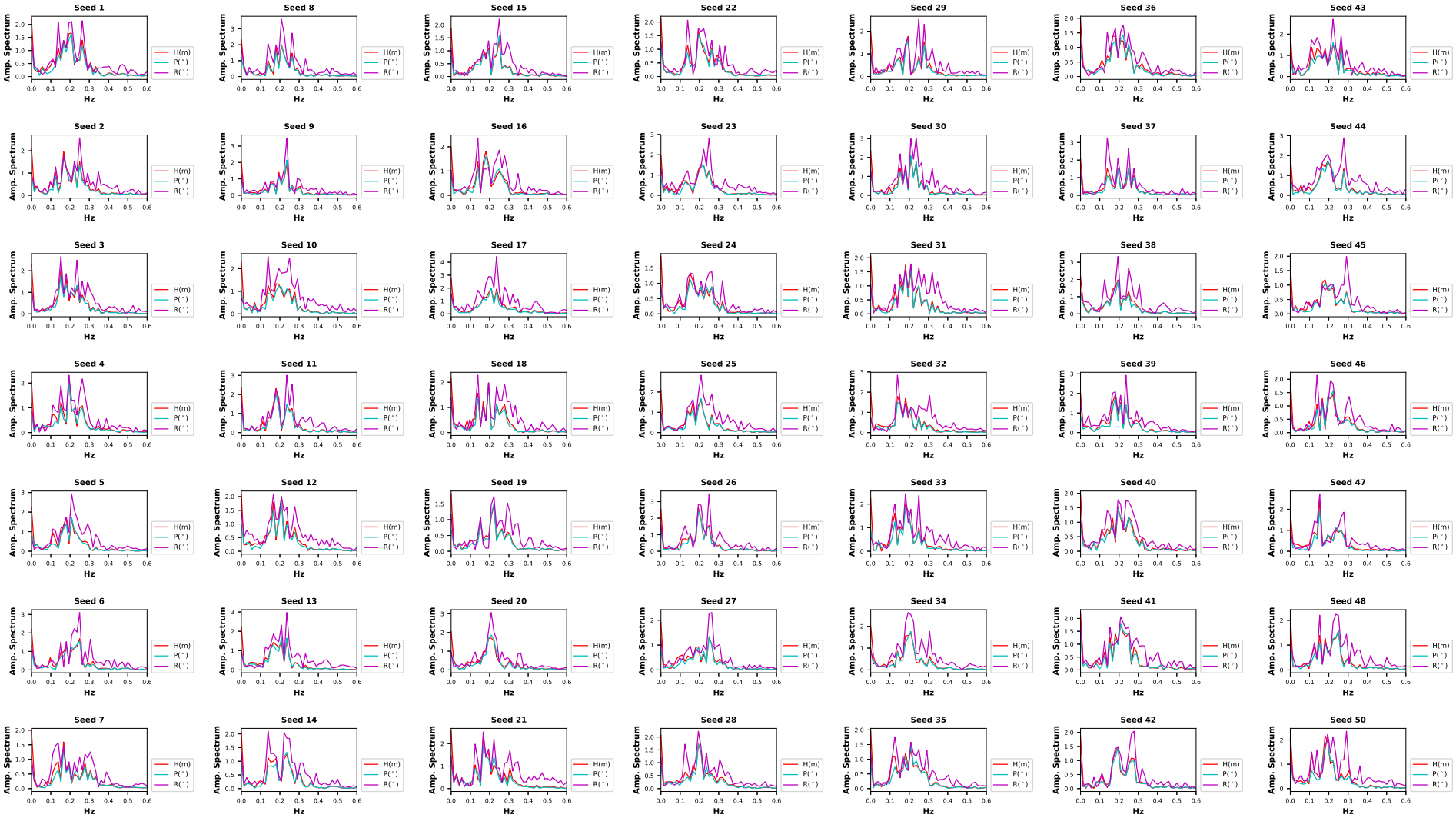

Figure A-18: *Amplitude spectrum of motion time histories of the DTMB vessel.* Heave, pitch and roll motions are provided for each sea state seed. Each time step is $\Delta t = 0.011s$, $H_s = 10.66m$, $T_p = 13.4s$, $v = 30kt$.

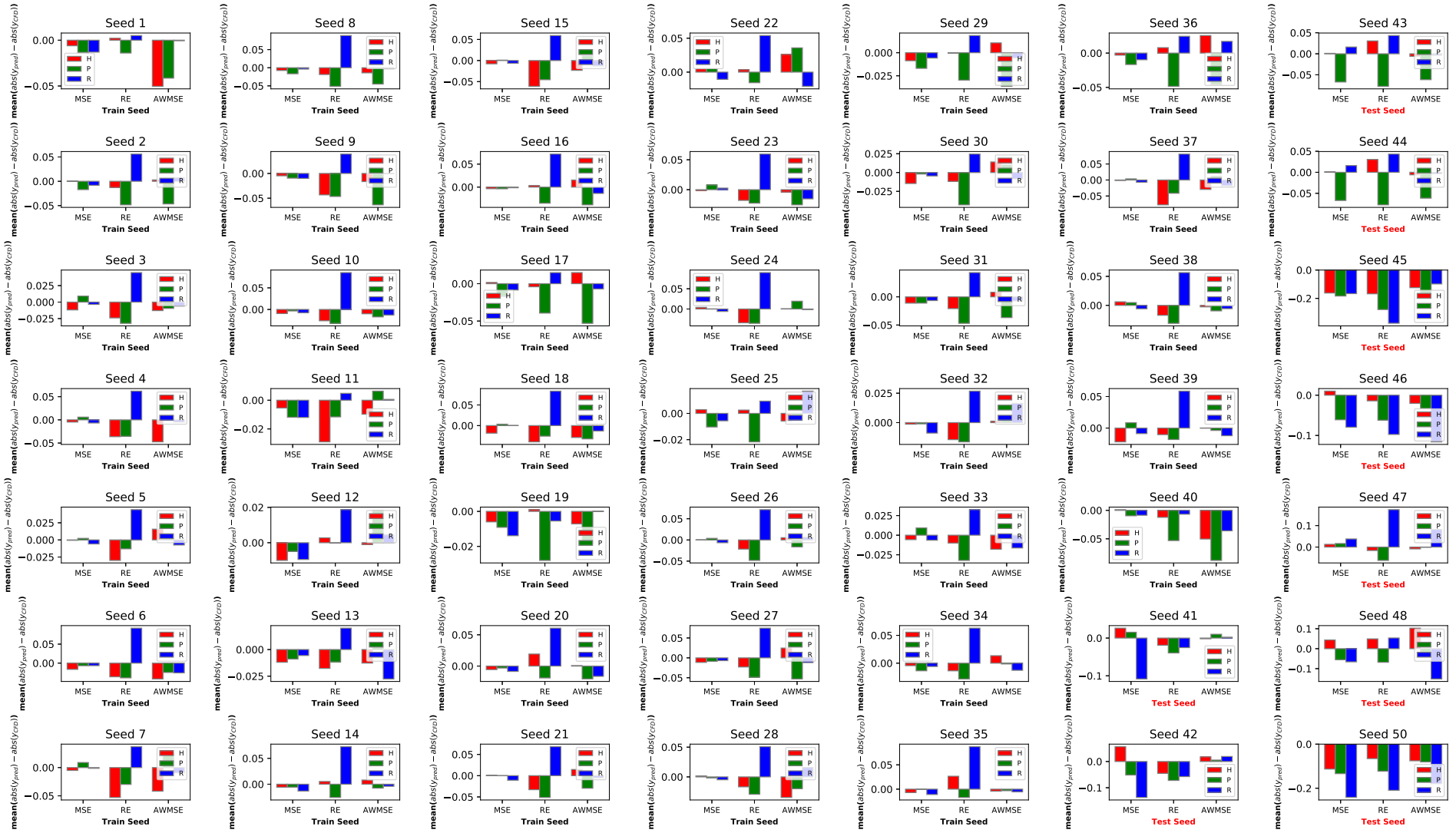

Figure A-19: *Mean amplitude error comparison between error functions for each degree of freedom:* $(mean(abs(y_{Pred}) - abs(y_{CFD})))$. Heave, pitch and roll motions are provided for each sea state seed. Each time step is $\Delta t = 0.008s$, $H_s = 3.53m$, $T_p = 9.7s$, $v = 30kt$.

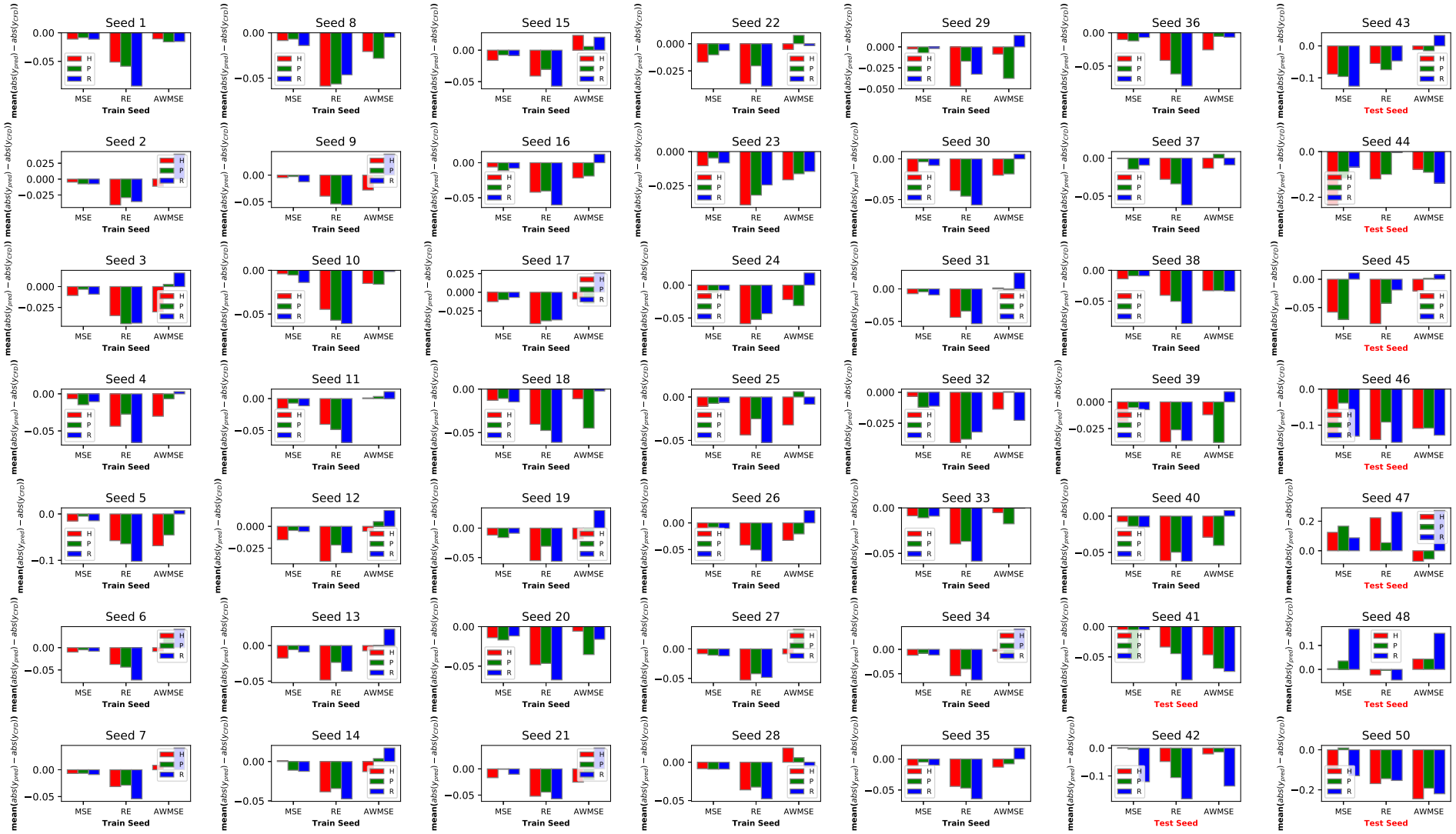

Figure A-20: *Mean amplitude error comparison between error functions for each degree of freedom: mean(abs(y_{Pred}) − abs(y_{CFD})))*.Heave, pitch and roll motions are provided for each sea state seed. Each time step is $\Delta t = 0.01s$, $H_s = 5.09m$, $T_p = 12.4s$, $v = 30kt$.

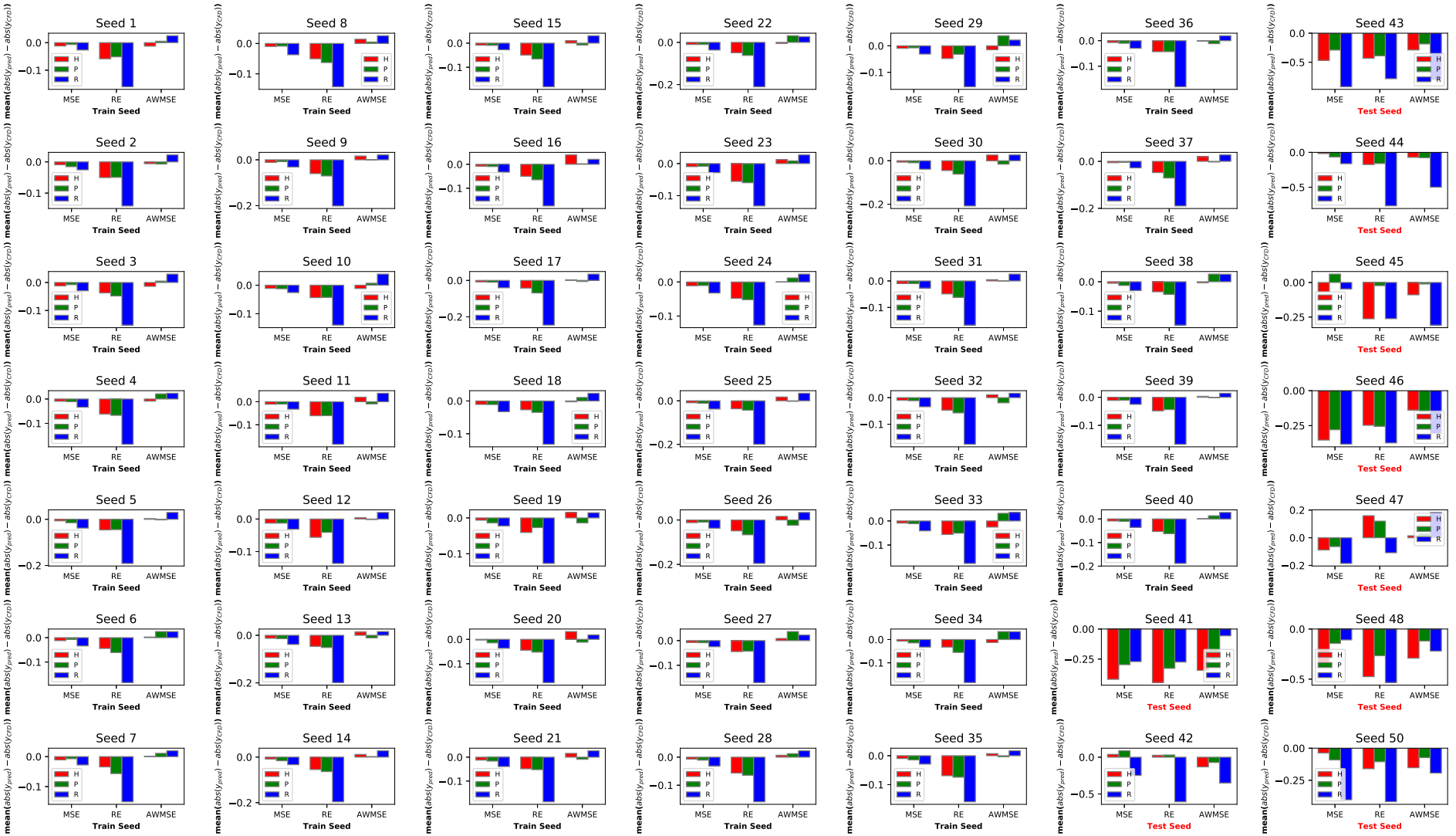

Figure A-21: *Mean amplitude error comparison between error functions for each degree of freedom: mean(abs(y_{Pred}) − abs(y_{CFD}))).* Heave, pitch and roll motions are provided for each sea state seed. Each time step is $\Delta t = 0.011s$, $H_s = 10.66m$, $T_p = 13.4s$, $v = 30kt$.

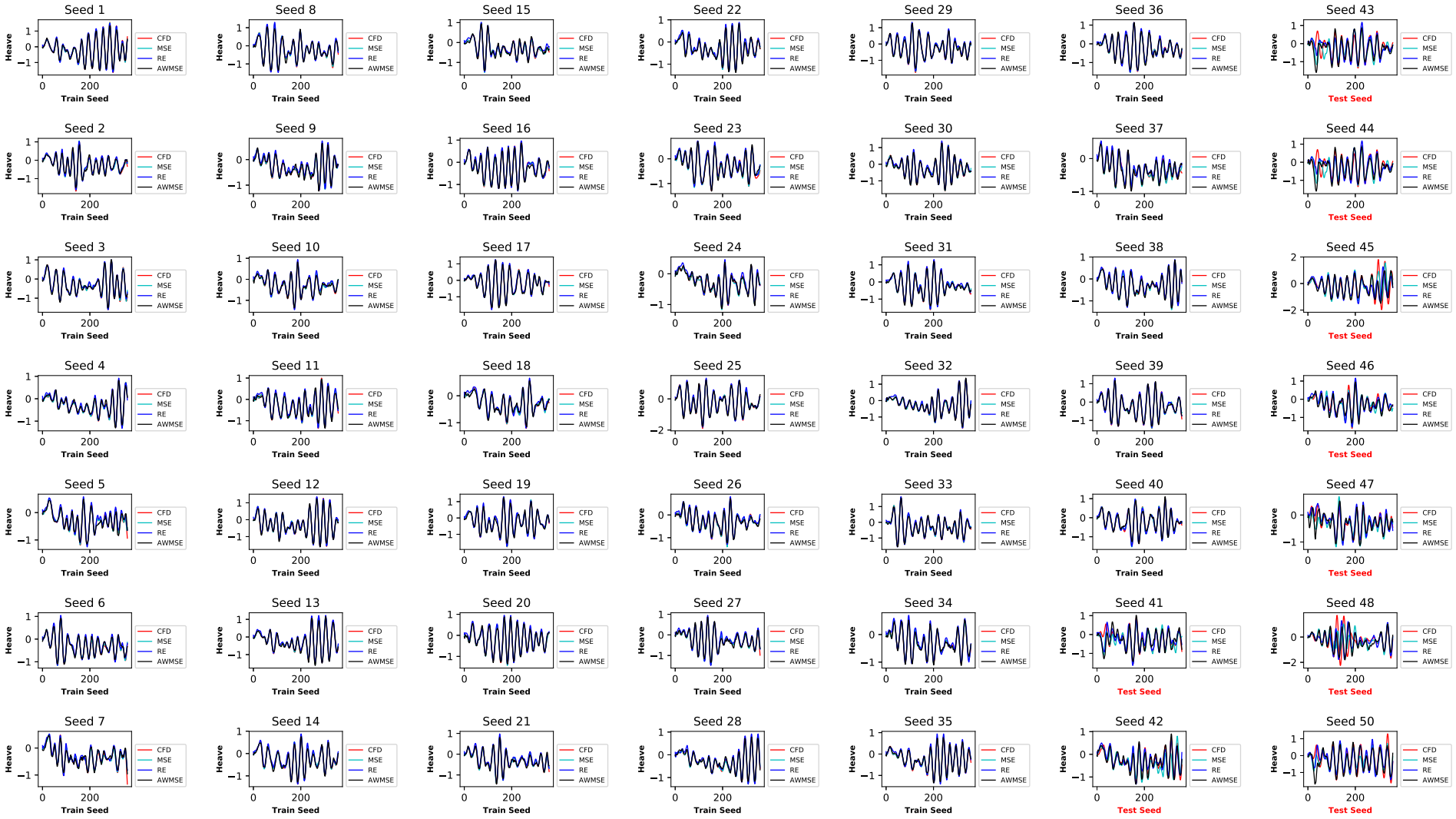

Figure A-22: *Amplitude error comparison between error functions for heave motion.* Heave motions are provided for each sea state seed. Each time step is $\Delta t = 0.008s$, $H_s = 3.53m$, $T_p = 9.7s$, $v = 30kt$.

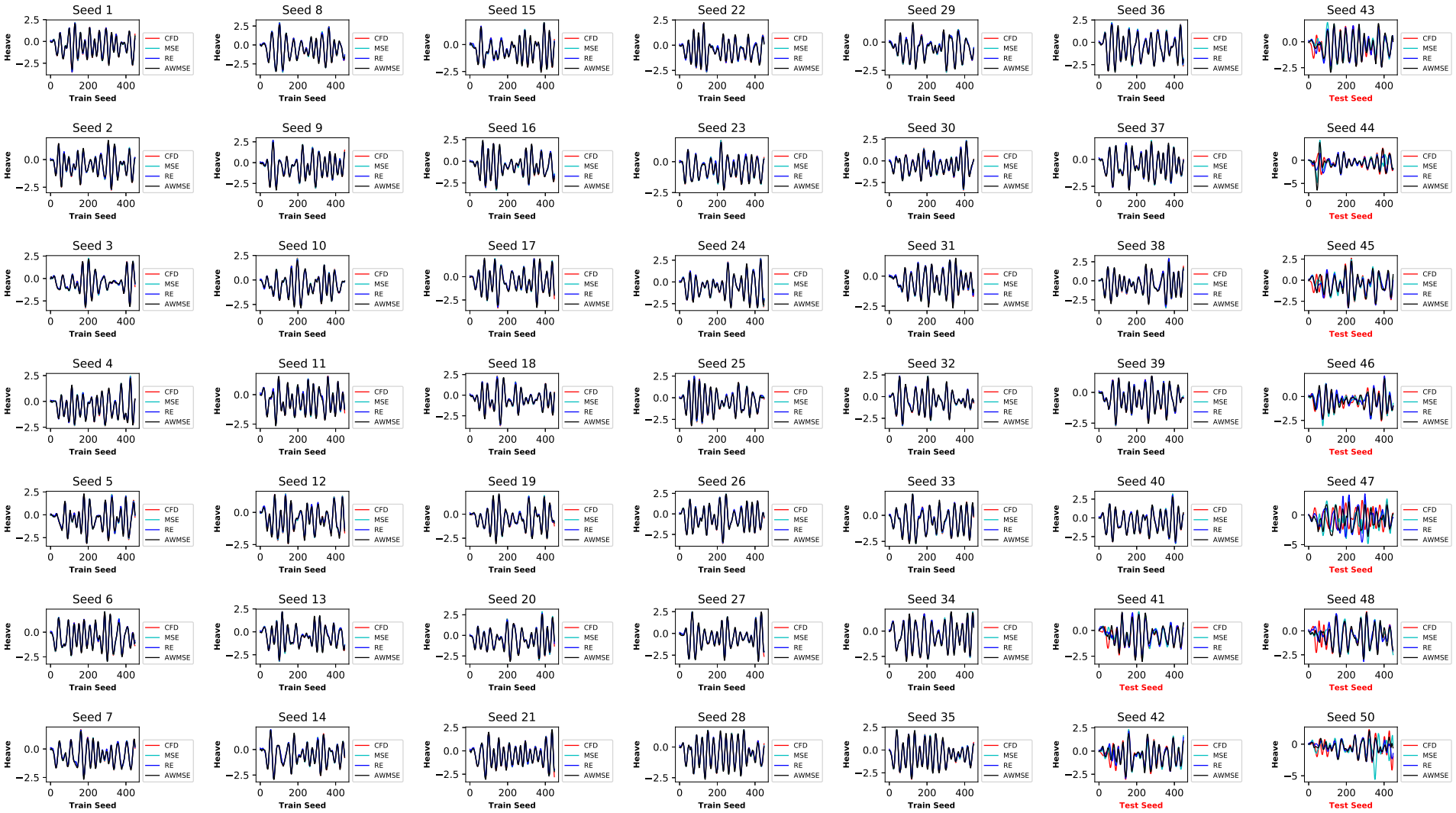

Figure A-23: *Amplitude error comparison between error functions for heave motion.* Heave motions are provided for each sea state seed. Each time step is $\Delta t = 0.01s$, $H_s = 5.09m$, $T_p = 12.4s$, $v = 30kt$.

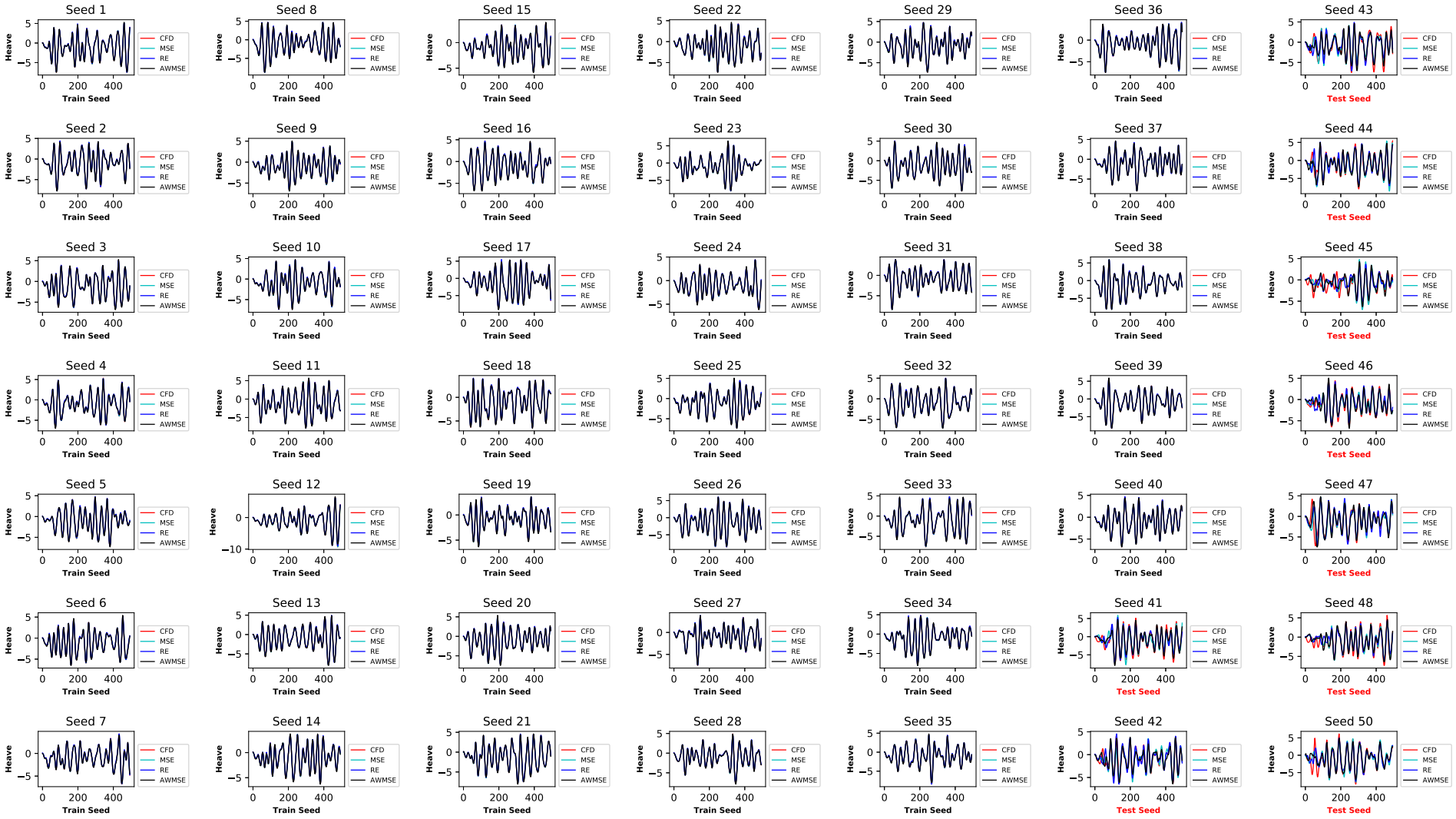

Figure A-24: *Amplitude error comparison between error functions for heave motion.* Heave motions are provided for each sea state seed. Each time step is $\Delta t = 0.011s$, $H_s = 10.66m$, $T_p = 13.4s$, $v = 30kt$.

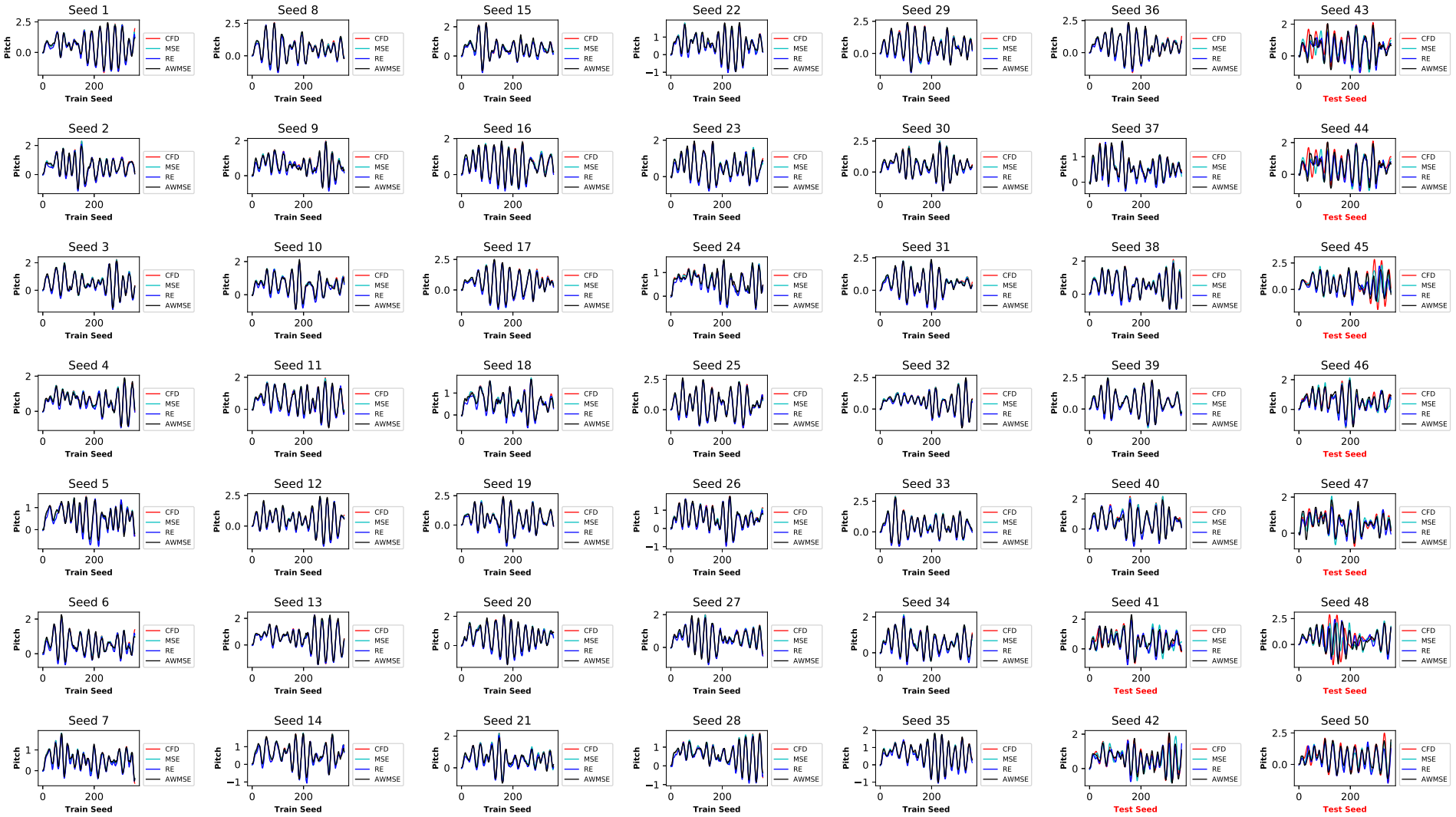

Figure A-25: *Amplitude error comparison between error functions for pitch motion.* Pitch motions are provided for each sea state seed. Each time step is $\Delta t = 0.008s$, $H_s = 3.53m$, $T_p = 9.7s$, $v = 30kt$.

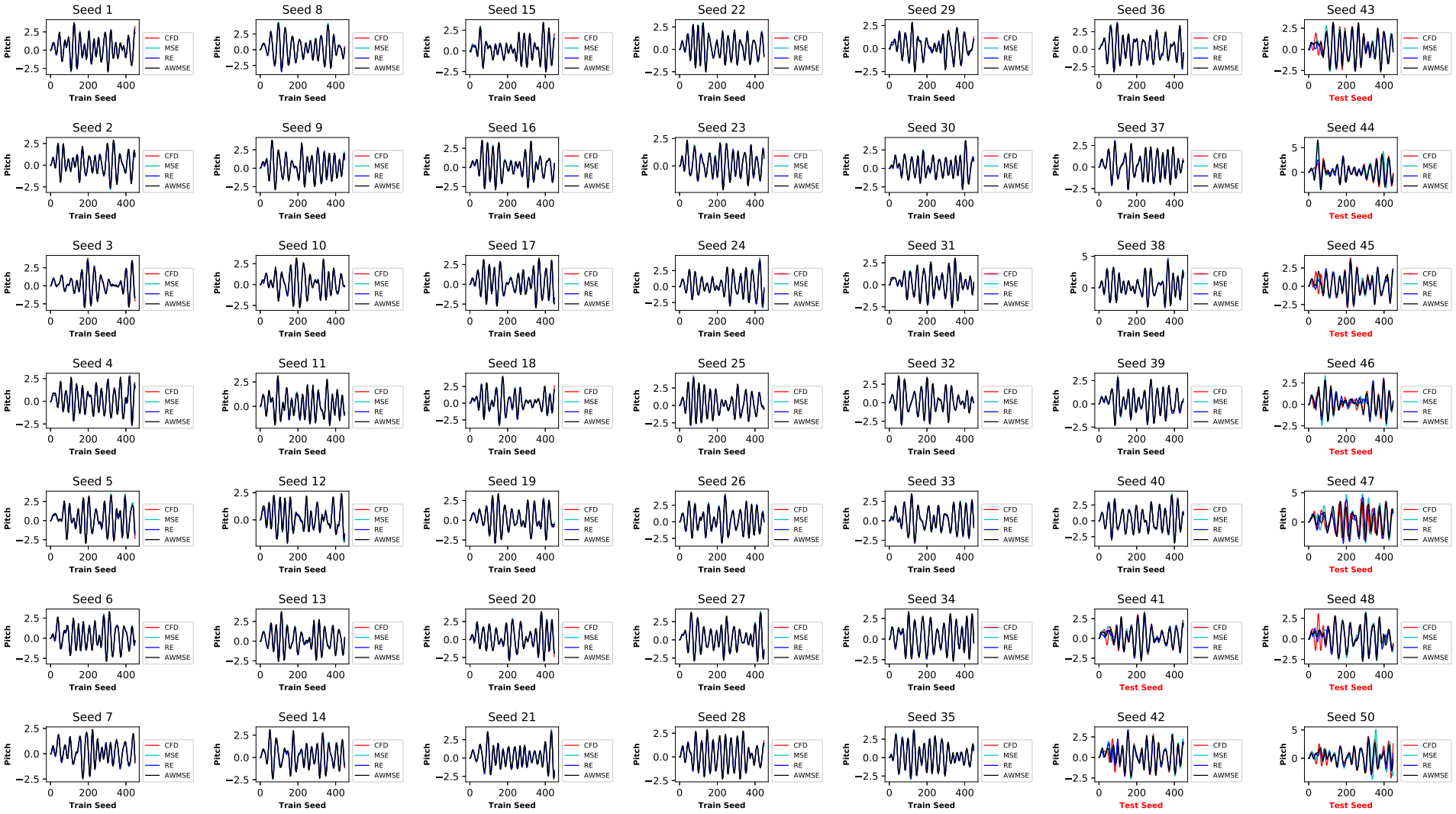

Figure A-26: *Amplitude error comparison between error functions for pitch motion.* Pitch motions are provided for each sea state seed. Each time step is $\Delta t = 0.01s$, $H_s = 5.09m$, $T_p = 12.4s$, $v = 30kt$.

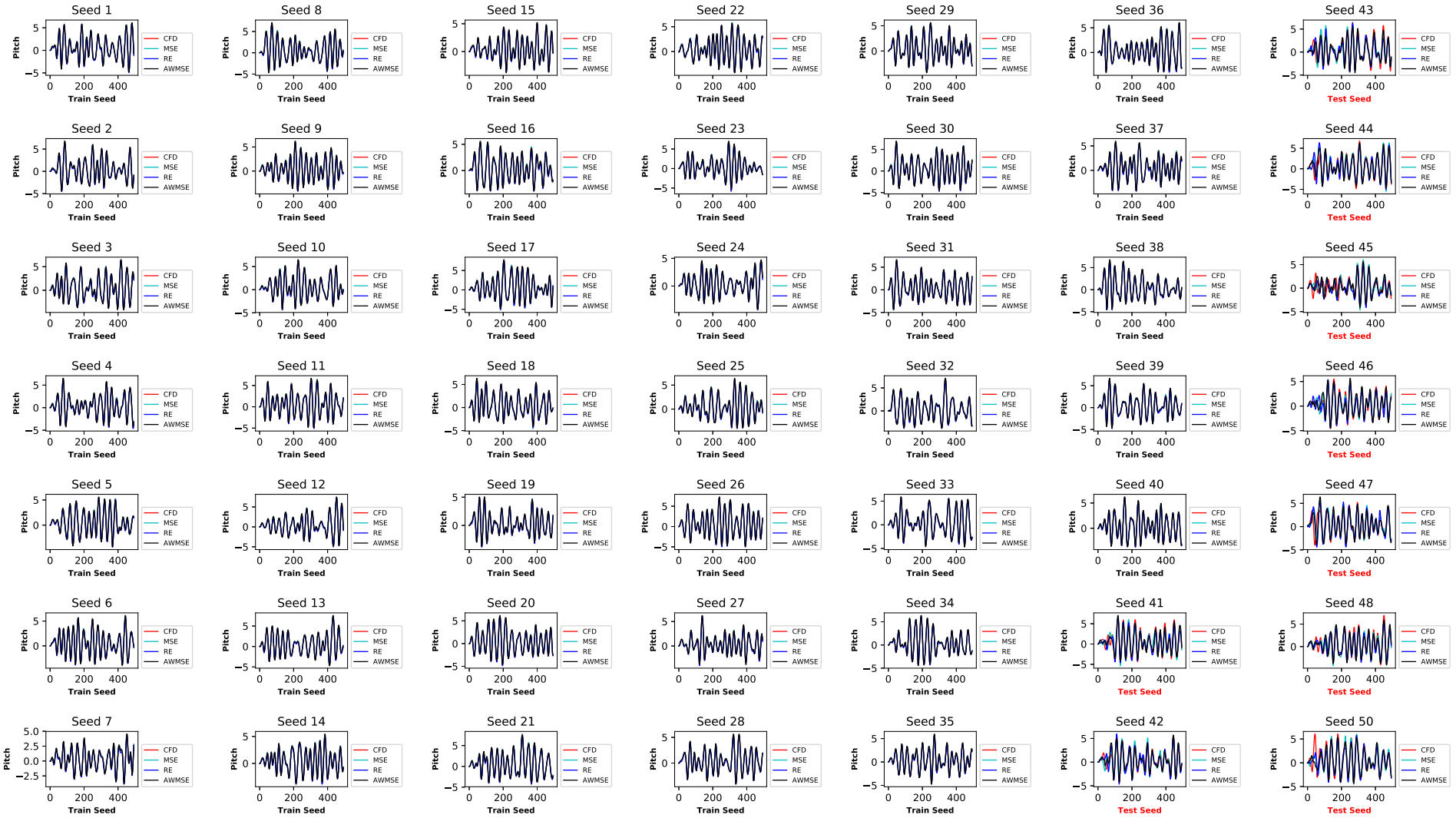

Figure A-27: *Amplitude error comparison between error functions for pitch motion.* Pitch motions are provided for each sea state seed. Each time step is $\Delta t = 0.011s$, $H_s = 10.66m$, $T_p = 13.4s$, $v = 30kt$.

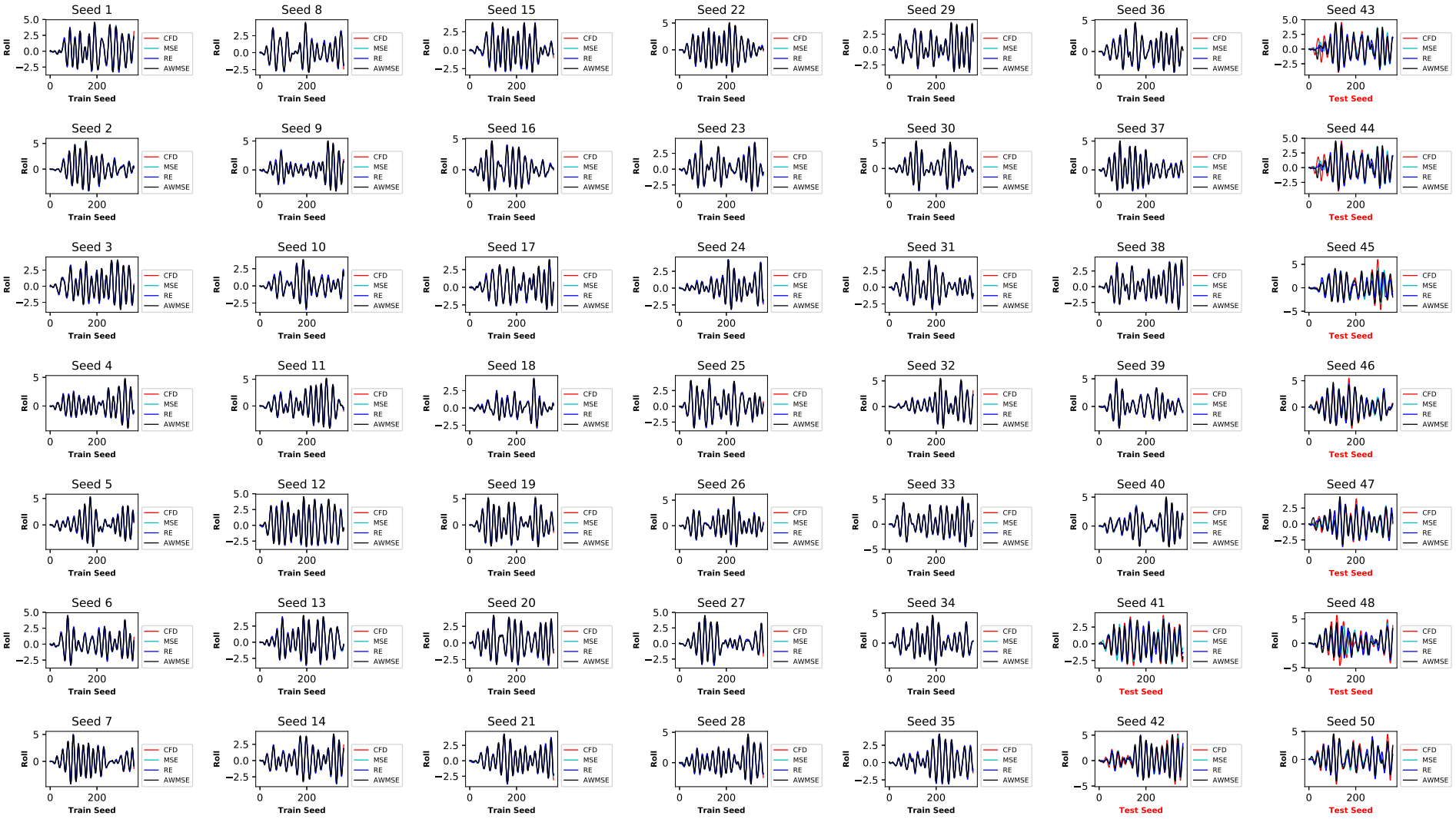

Figure A-28: *Amplitude error comparison between error functions for roll motion.* Roll motions are provided for each sea state seed. Each time step is $\Delta t = 0.008s$, $H_s = 3.53m$, $T_p = 9.7s$, $v = 30kt$.

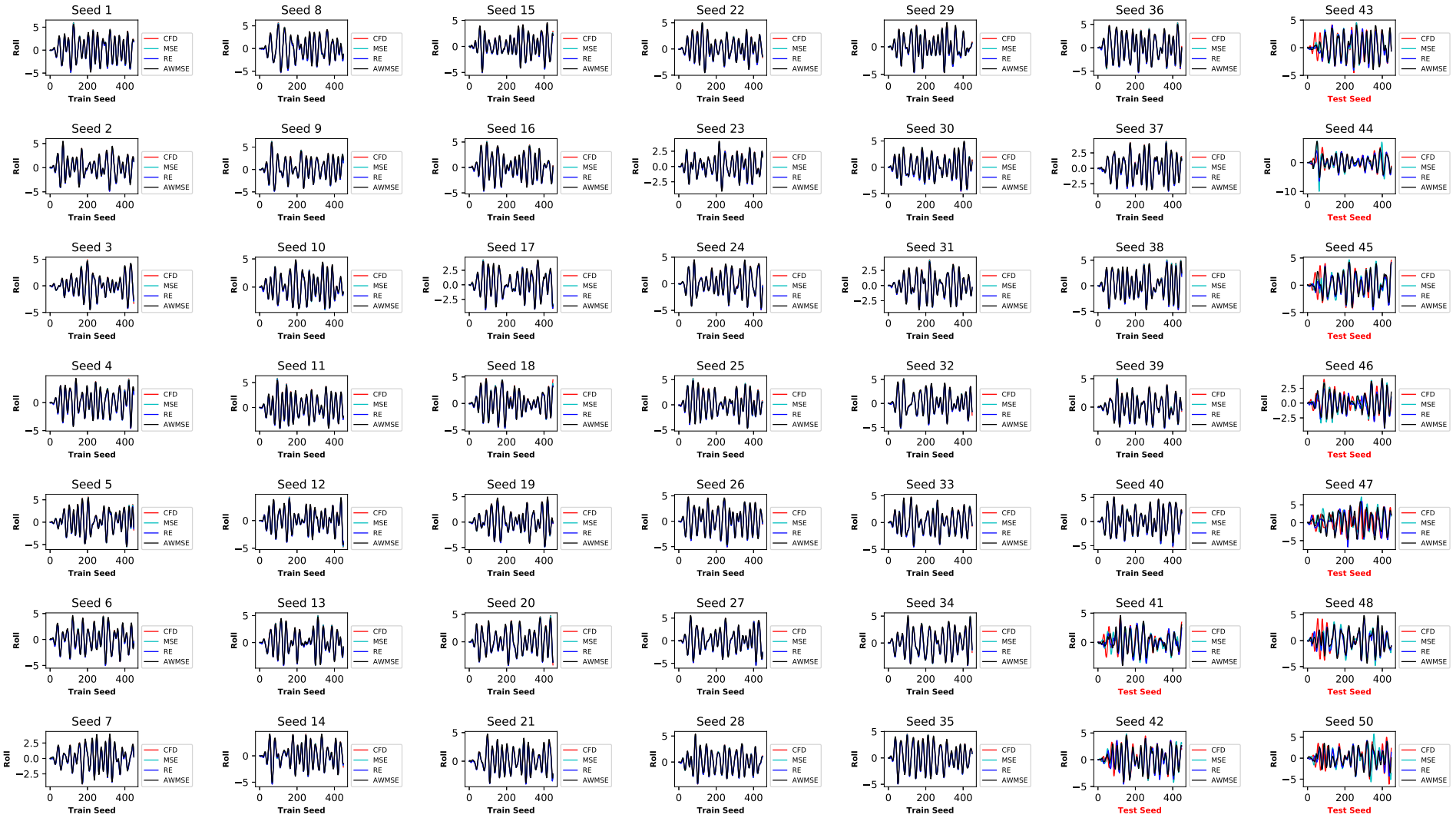

Figure A-29: *Amplitude error comparison between error functions for roll motion.* Roll motions are provided for each sea state seed. Each time step is $\Delta t = 0.01s$, $H_s = 5.09m$, $T_p = 12.4s$, $v = 30kt$.

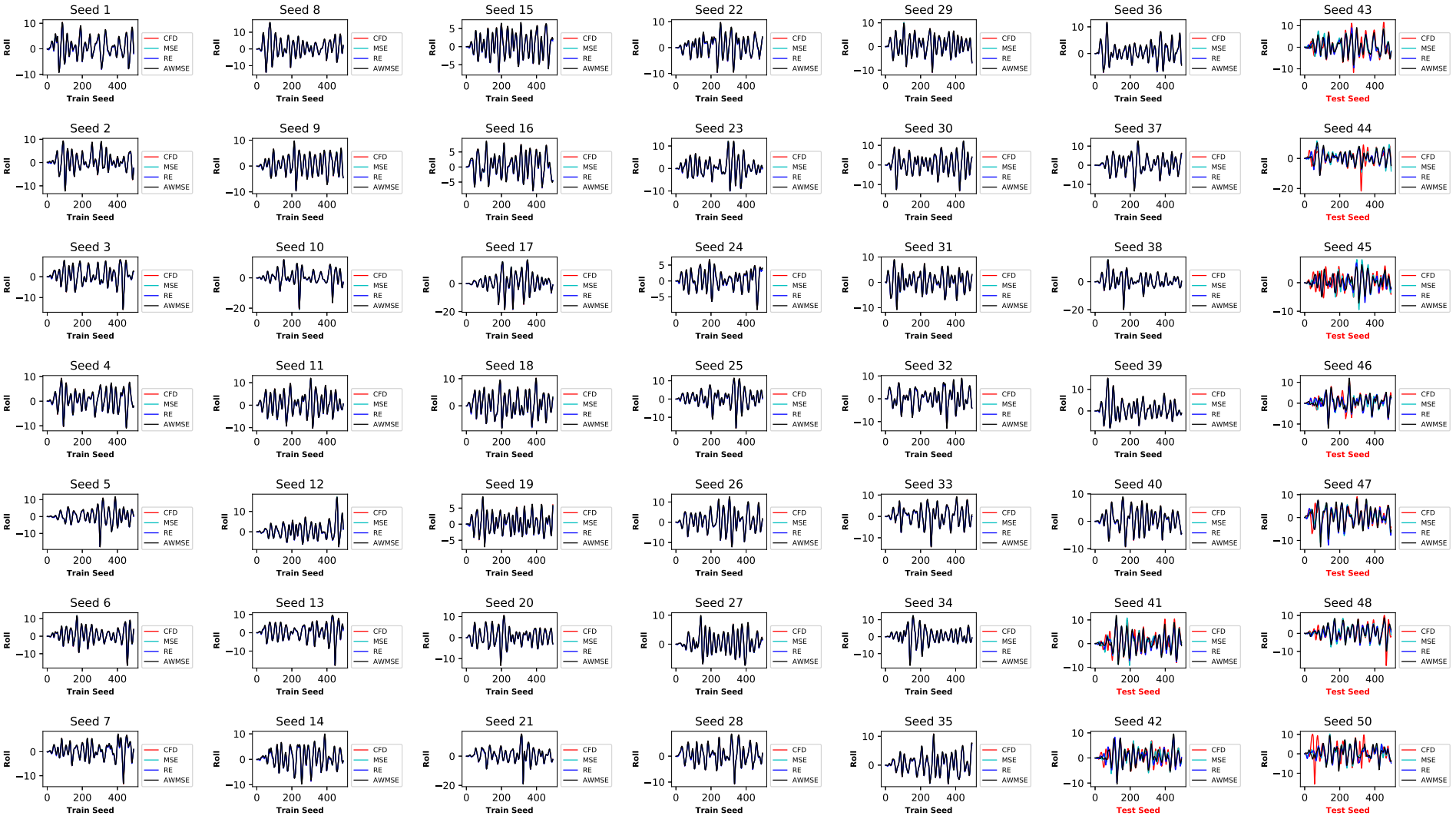

Figure A-30: *Amplitude error comparison between error functions for roll motion.* Roll motions are provided for each sea state seed. Each time step is $\Delta t = 0.011s$, $H_s = 10.66m$, $T_p = 13.4s$, $v = 30kt$.

Appendix B

SCR Riser Motion Reconstruction & Analysis

Case	$\mathrm{n}_C F$	$\mathrm{n}_I L$
1001	1 through 6	1 through 6
5002	1 through 6	1 through 6
1003	1 through 6	1 through 6
1005	1 through 6	1 through 9
1007	1 through 6	1 through 9
1009	1 through 6	1 through 9
1011	1 through 6	1 through 9
1013	1 through 6	1 through 9
5013	1 through 6	1 through 9
1015	1 through 6	1 through 9
1017	1 through 9	1 through 9
1019	1 through 9	1 through 9
5019	1 through 9	1 through 9
1021	1 through 9	1 through 9
1023	1 through 9	1 through 9
5023	1 through 9	1 through 9
2005	1 through 9	1 through 9
2000	1 through 9	1 through 9
2003	1 through 9	1 through 9
2007	1 through 9	1 through 9
2009	1 through 9	1 through 9
2011	1 through 9	1 through 9
2013	1 through 9	1 through 9
2015	1 through 9	1 through 9
2017	1 through 9	1 through 9
2019	1 through 9	1 through 9
2021	1 through 9	1 through 9
2023	1 through 9	1 through 9
3001	1 through 9	1 through 9

3003	1 through 9	1 through 9
3005	1 through 9	1 through 9
3007	1 through 9	1 through 9
3009	1 through 9	1 through 9
3011	1 through 9	1 through 9
3013	1 through 9	1 through 9
3015	1 through 9	1 through 9
3017	1 through 9	1 through 9
3019	1 through 9	1 through 9
3021	1 through 9	1 through 9
3023	1 through 9	1 through 9
4001	1 through 9	1 through 9
4005	1 through 9	1 through 9
4007	1 through 9	1 through 9
4011	1 through 9	1 through 9
4013	1 through 9	1 through 9
4017	1 through 9	1 through 9
4019	1 through 9	1 through 9
4021	1 through 9	1 through 9
4023	1 through 9	1 through 9
1000	1 through 9	1 through 9
5001	1 through 9	1 through 9
1002	1 through 9	1 through 9
1004	1 through 9	1 through 9
1006	1 through 9	1 through 9
1008	1 through 9	1 through 9
1010	1 through 9	1 through 9
1012	1 through 9	1 through 9
5012	1 through 9	1 through 9
1014	1 through 9	1 through 9

1016 1 through 9 1 through 9

1018 1 through 9 1 through 9

5018 1 through 9 1 through 9

1020 1 through 9 1 through 9

1022 1 through 9 1 through 9

5022 1 through 9 1 through 9

2004 1 through 9 1 through 9

2001 1 through 9 1 through 9

2002 1 through 9 1 through 9

2006 1 through 9 1 through 9

2008 1 through 9 1 through 9

2010 1 through 9 1 through 9

2012 1 through 9 1 through 9

2014 1 through 9 1 through 9

2016 1 through 9 1 through 9

2018 1 through 9 1 through 9

2020 1 through 9 1 through 9

2022 1 through 9 1 through 9

3000 1 through 9 1 through 9

3002 1 through 9 1 through 9

3004 1 through 9 1 through 9

3006 1 through 9 1 through 9

3008 1 through 9 1 through 9

3010 1 through 9 1 through 9

3012 1 through 9 1 through 9

3014 1 through 9 1 through 9

3016 1 through 9 1 through 9

3018 1 through 9 1 through 9

3020 1 through 9 1 through 9

3022 1 through 9 1 through 9

4000	1 through 9	1 through 9
4002	1 through 9	1 through 9
4006	1 through 9	1 through 9
4008	1 through 9	1 through 9
4012	1 through 9	1 through 9
4014	1 through 9	1 through 9
4018	1 through 9	1 through 9
4020	1 through 9	1 through 9
4022	1 through 9	1 through 9

Current velocity (m/s)	Dir. 0 deg.	Dir. 30 deg.	Dir. 60 deg.	Dir. 90 deg.
-0.12	1000 5001	2004	3000	4000
-0.14	1002	2001	3002	4002
-0.16	1004	2002	3004	-
-0.18	1006	2006	3006	4006
-0.20	1008	2008	3008	4008
-0.22	1010	2010	3010	-
-0.24	1012 5012	2012	3012	4012
-0.26	1014	2014	3014	4014
-0.28	1016	2016	3016	-
-0.30	1018	5018	2018	3018
-0.32	1020	2020	3020	4020
-0.34	1022 5022	2022	3022	4022

Current velocity (m/s)	Dir. 0 deg.	Dir. 30 deg.	Dir. 60 deg.	Dir. 90 deg.
0.12	1001 5002	2005	3001	4001
0.14	1003	2000	3003	-
0.16	1005	2003	3005	4005
0.18	1007	2007	3007	4007
0.20	1009	2009	3009	-
0.22	1011	2011	3011	4011
0.24	1013 5013	2013	3013	4013
0.26	1015	2015	3015	-
0.28	1017	2017	3017	4017
0.30	1019 5019	2019	3019	4019
0.32	1021	2021	3021	4021
0.34	1023 5023	2023	3023	4023

Table B.2: Current speed and direction with respect to the catenary plane for each experiment label. Carriage going Forwards and backwards respectively.

NDP SCR test case 1001

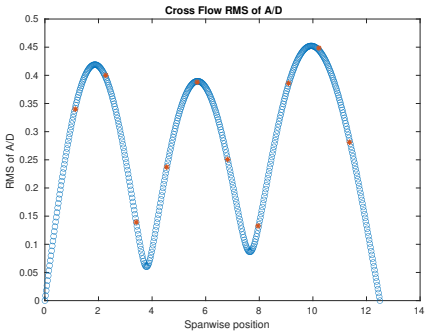

(a) Cross-flow RMS profile case 1001.

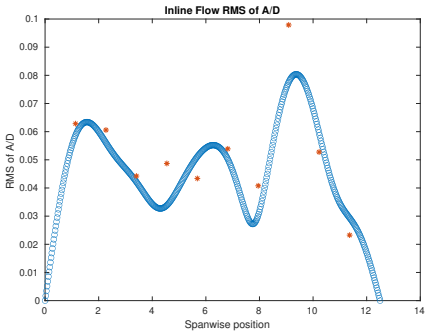

(b) Inline flow RMS profile case 1001.

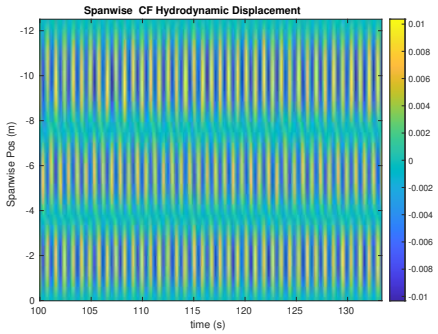

(c) Spanwise cross-flow hydrodynamic displacement case 1001.

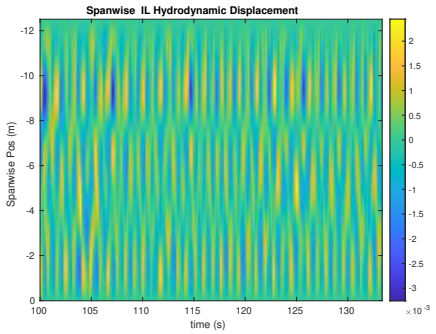

(d) Spanwise inline spectrum of hydrodynamic displacement case 1001.

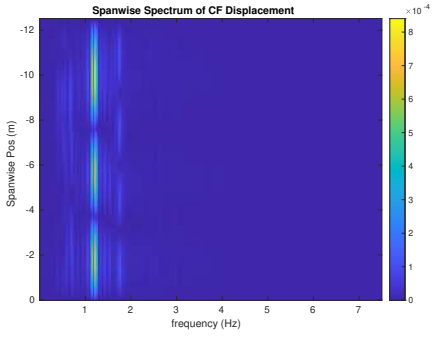

(e) Spanwise cross-flow spectrum of hydrodynamic displacement case 1001.

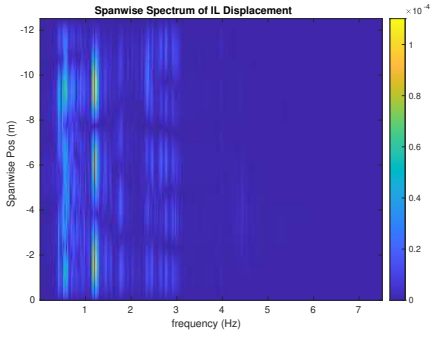

(f) Spanwise inline spectrum of hydrodynamic displacement case 1001.

Figure B-1: *Motion Analysis.* SCR case 1001.

NDP SCR test case 5002

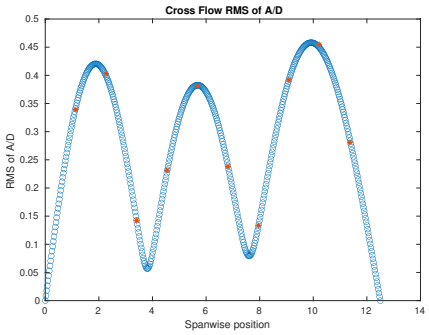

(a) Cross-flow RMS profile case 5002.

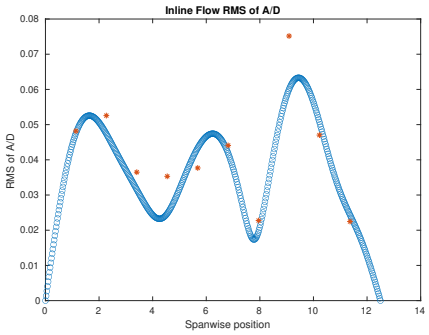

(b) Inline flow RMS profile case 5002.

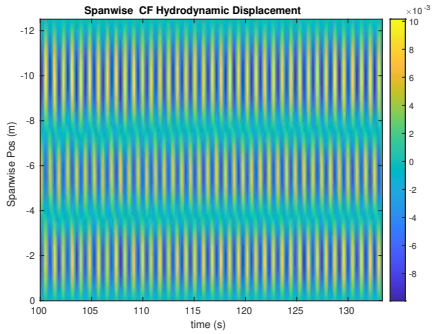

(c) Spanwise cross-flow hydrodynamic displacement case 5002.

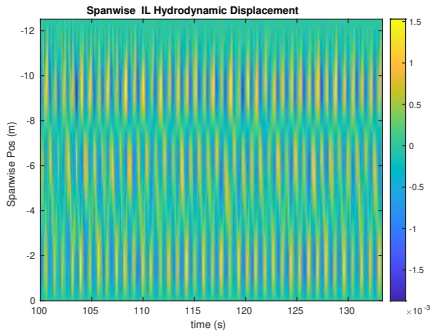

(d) Spanwise inline spectrum of hydrodynamic displacement case 5002.

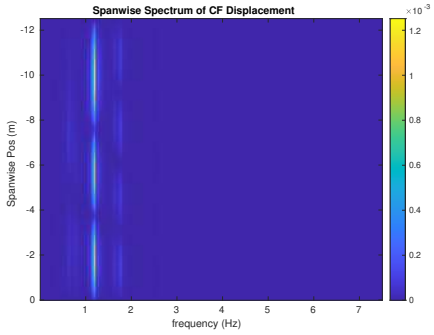

(e) Spanwise cross-flow spectrum of hydrodynamic displacement case 5002.

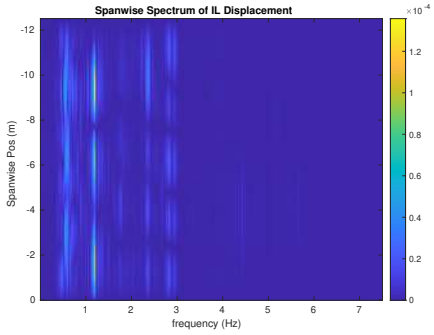

(f) Spanwise inline spectrum of hydrodynamic displacement case 5002.

Figure B-2: *Motion Analysis.* SCR case 5002.

NDP SCR test case 1003

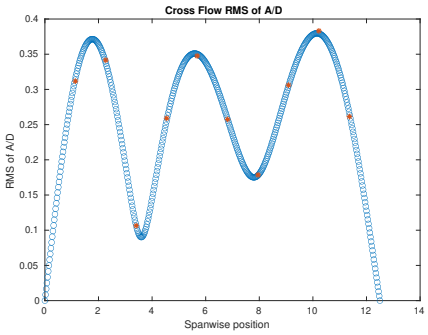

(a) Cross-flow RMS profile case 1003.

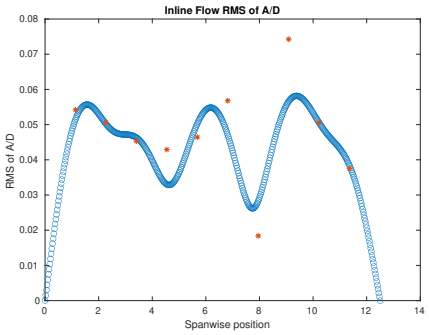

(b) Inline flow RMS profile case 1003.

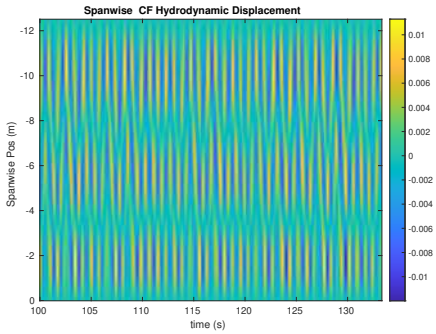

(c) Spanwise cross-flow hydrodynamic displacement case 1003.

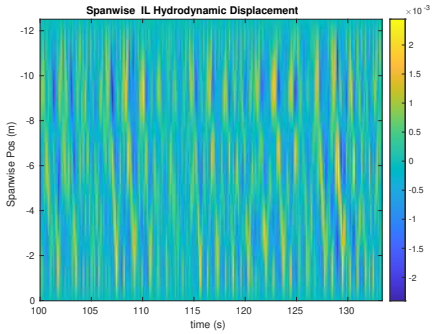

(d) Spanwise inline spectrum of hydrodynamic displacement case 1003.

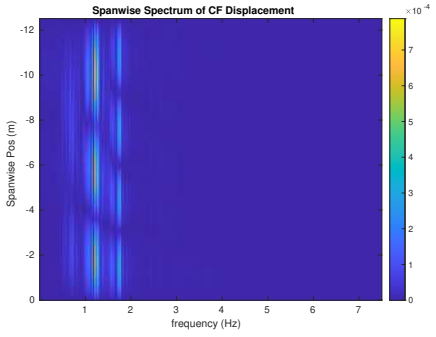

(e) Spanwise cross-flow spectrum of hydrodynamic displacement case 1003.

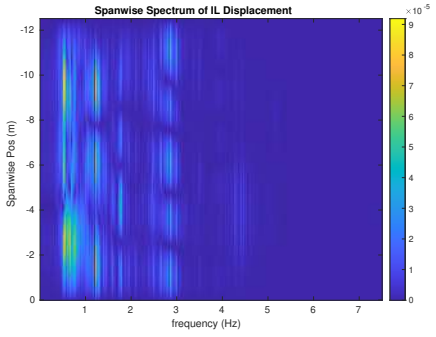

(f) Spanwise inline spectrum of hydrodynamic displacement case 1003.

Figure B-3: *Motion Analysis.* SCR case 1003.

NDP SCR test case 1005

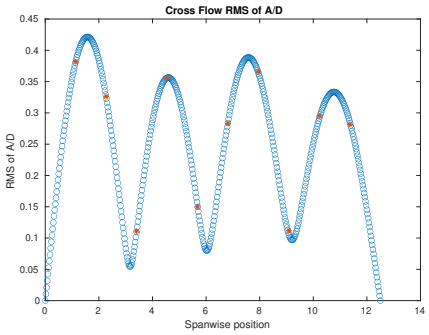

(a) Cross-flow RMS profile case 1005.

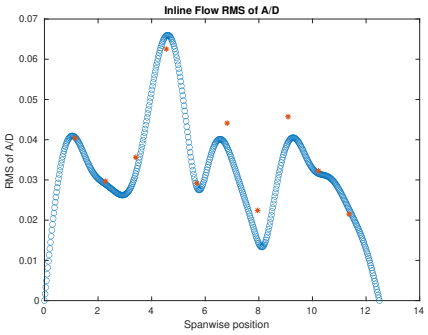

(b) Inline flow RMS profile case 1005.

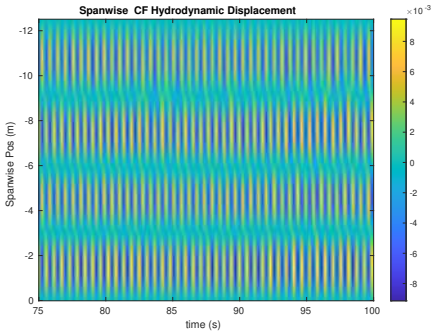

(c) Spanwise cross-flow hydrodynamic displacement case 1005.

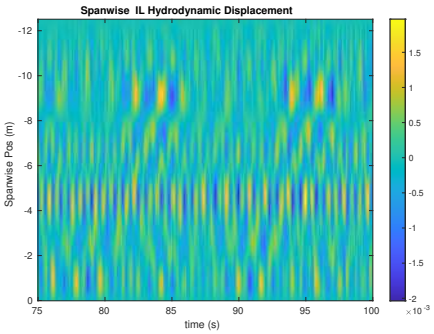

(d) Spanwise inline spectrum of hydrodynamic displacement case 1005.

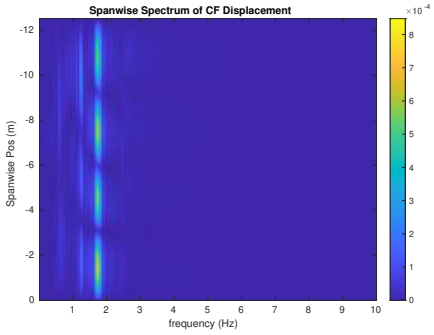

(e) Spanwise cross-flow spectrum of hydrodynamic displacement case 1005.

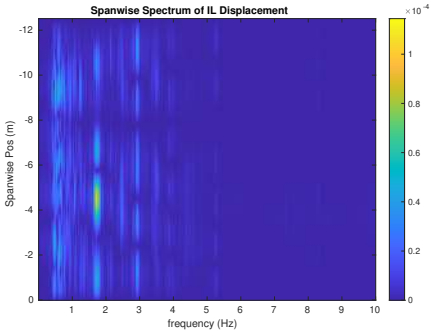

(f) Spanwise inline spectrum of hydrodynamic displacement case 1005.

Figure B-4: *Motion Analysis.* SCR case 1005.

NDP SCR test case 1007

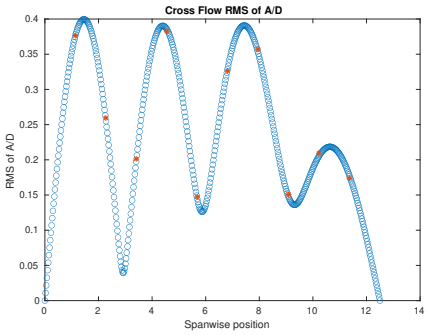

(a) Cross-flow RMS profile case 1007.

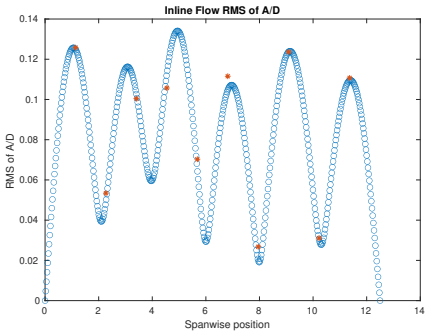

(b) Inline flow RMS profile case 1007.

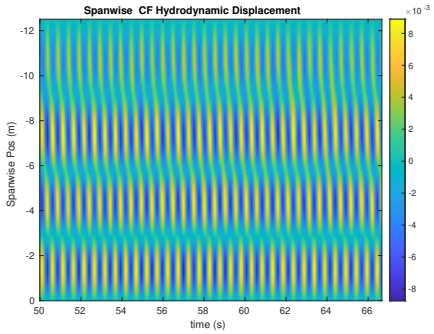

(c) Spanwise cross-flow hydrodynamic displacement case 1007.

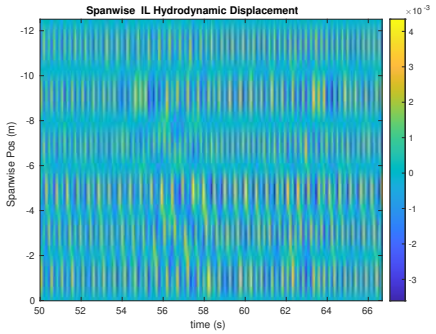

(d) Spanwise inline spectrum of hydrodynamic displacement case 1007.

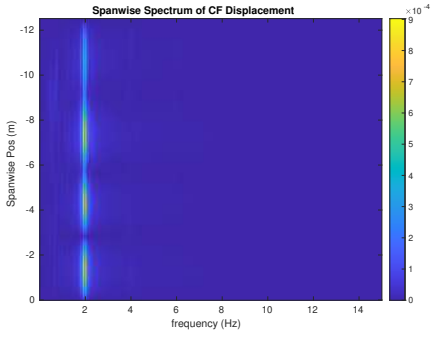

(e) Spanwise cross-flow spectrum of hydrodynamic displacement case 1007.

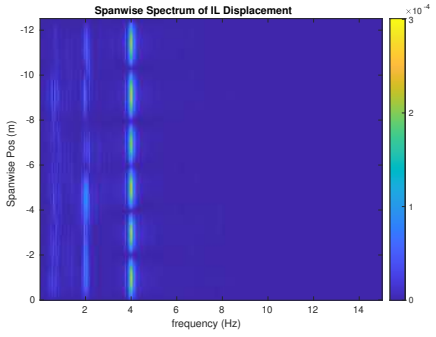

(f) Spanwise inline spectrum of hydrodynamic displacement case 1007.

Figure B-5: *Motion Analysis.* SCR case 1007.

NDP SCR test case 1009

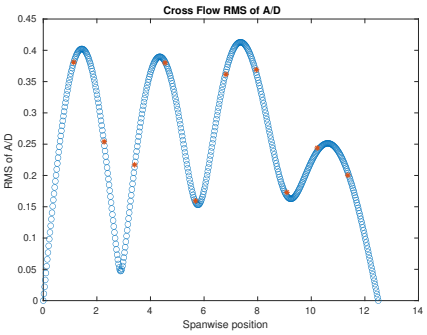

(a) Cross-flow RMS profile case 1009.

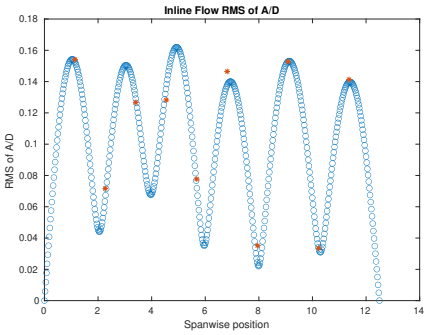

(b) Inline flow RMS profile case 1009.

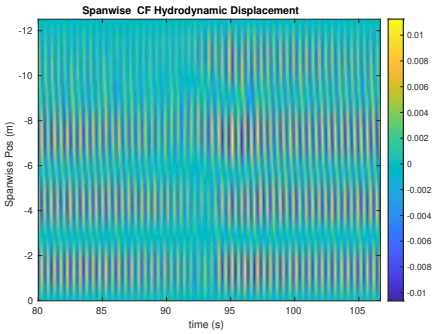

(c) Spanwise cross-flow hydrodynamic displacement case 1009.

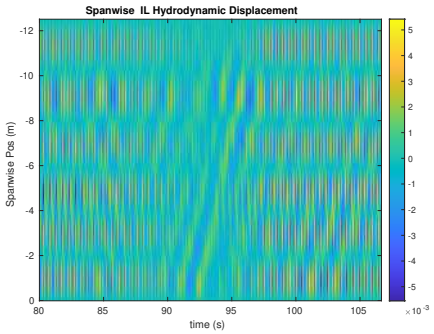

(d) Spanwise inline spectrum of hydrodynamic displacement case 1009.

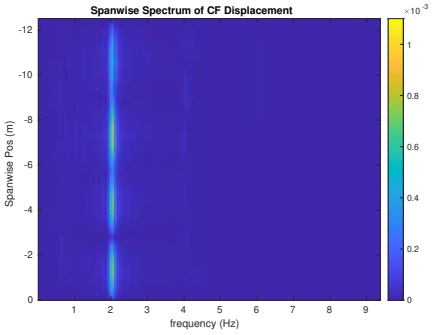

(e) Spanwise cross-flow spectrum of hydrodynamic displacement case 1009.

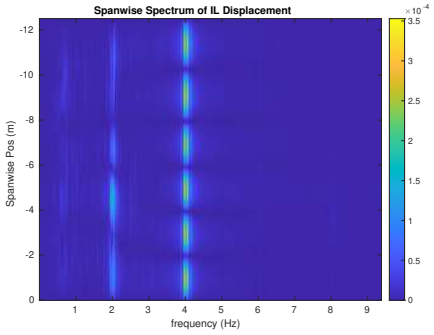

(f) Spanwise inline spectrum of hydrodynamic displacement case 1009.

Figure B-6: *Motion Analysis.* SCR case 1009.

NDP SCR test case 1011

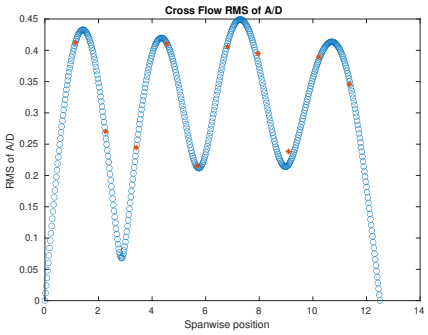

(a) Cross-flow RMS profile case 1011.

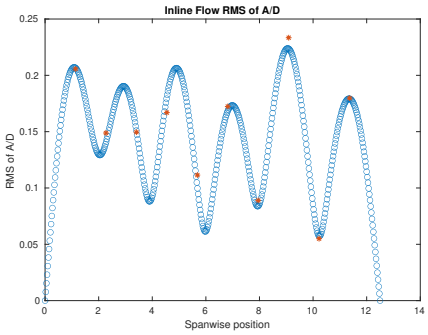

(b) Inline flow RMS profile case 1011.

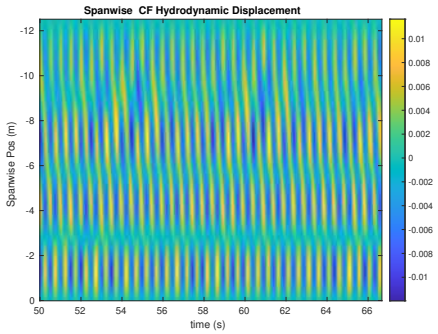

(c) Spanwise cross-flow hydrodynamic displacement case 1011.

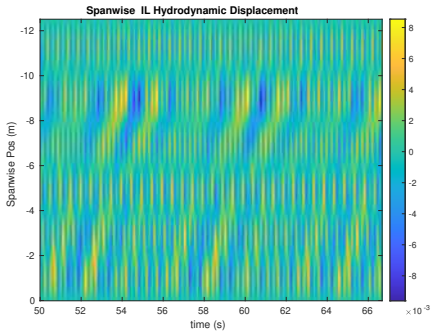

(d) Spanwise inline spectrum of hydrodynamic displacement case 1011.

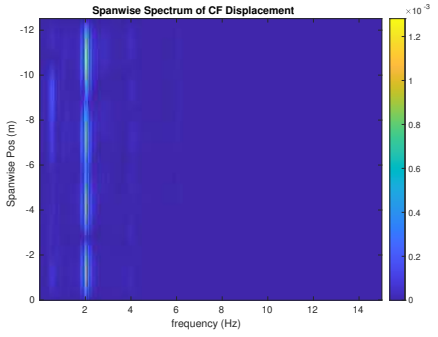

(e) Spanwise cross-flow spectrum of hydrodynamic displacement case 1011.

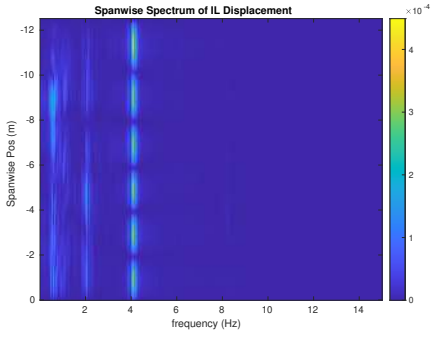

(f) Spanwise inline spectrum of hydrodynamic displacement case 1011.

Figure B-7: *Motion Analysis.* SCR case 1011.

NDP SCR test case 1013

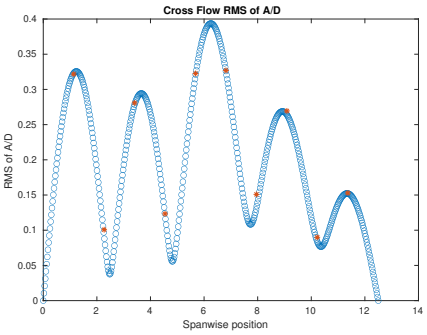

(a) Cross-flow RMS profile case 1013.

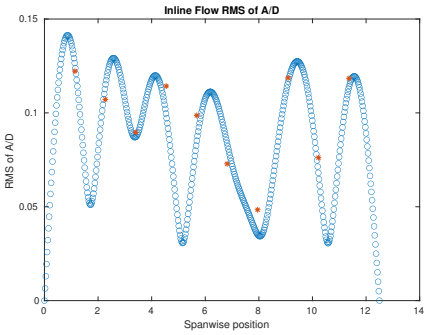

(b) Inline flow RMS profile case 1013.

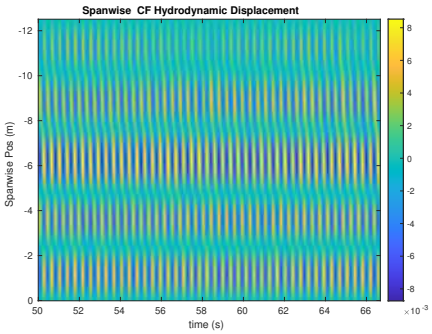

(c) Spanwise cross-flow hydrodynamic displacement case 1013.

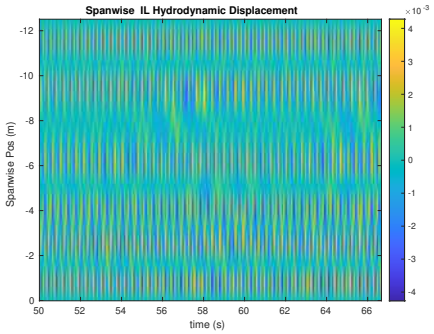

(d) Spanwise inline spectrum of hydrodynamic displacement case 1013.

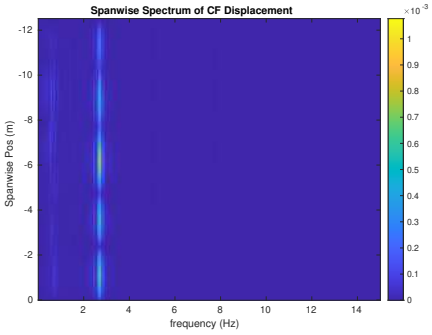

(e) Spanwise cross-flow spectrum of hydrodynamic displacement case 1013.

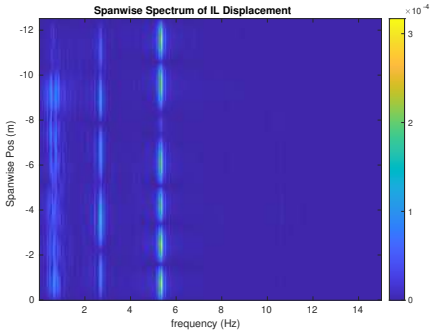

(f) Spanwise inline spectrum of hydrodynamic displacement case 1013.

Figure B-8: *Motion Analysis.* SCR case 1013.

NDP SCR test case 5013

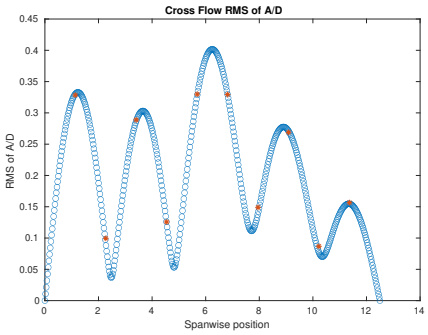

(a) Cross-flow RMS profile case 5013.

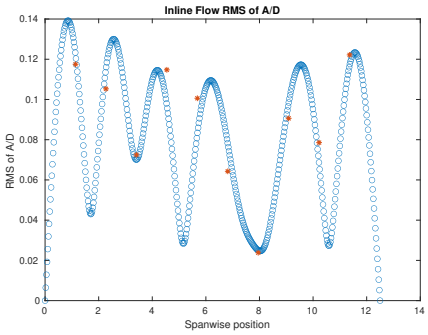

(b) Inline flow RMS profile case 5013.

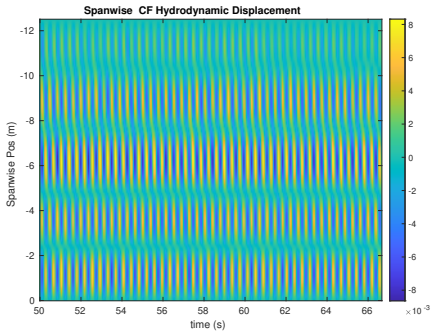

(c) Spanwise cross-flow hydrodynamic displacement case 5013.

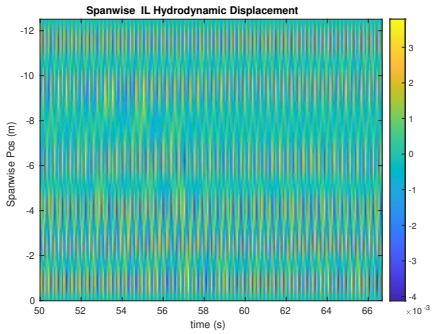

(d) Spanwise inline spectrum of hydrodynamic displacement case 5013.

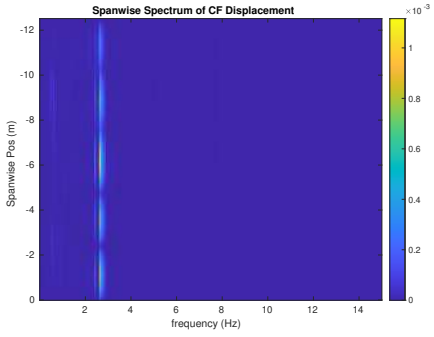

(e) Spanwise cross-flow spectrum of hydrodynamic displacement case 5013.

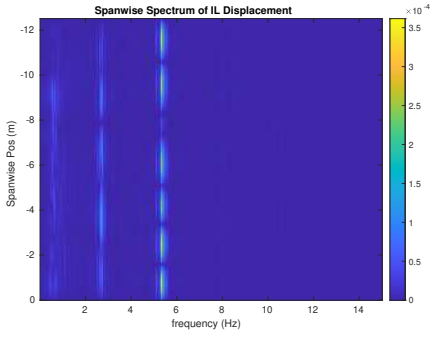

(f) Spanwise inline spectrum of hydrodynamic displacement case 5013.

Figure B-9: *Motion Analysis.* SCR case 5013.

NDP SCR test case 1015

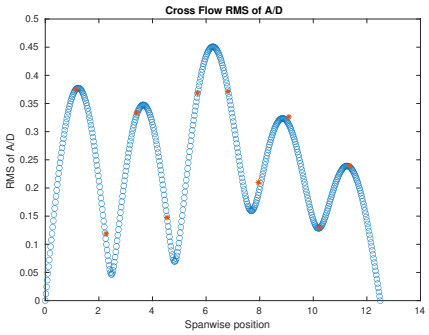

(a) Cross-flow RMS profile case 1015.

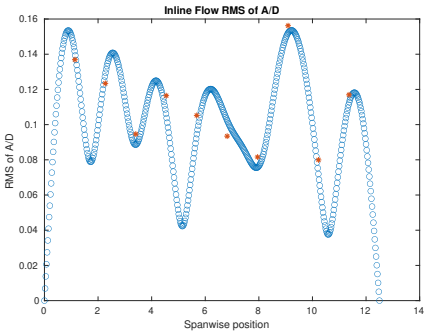

(b) Inline flow RMS profile case 1015.

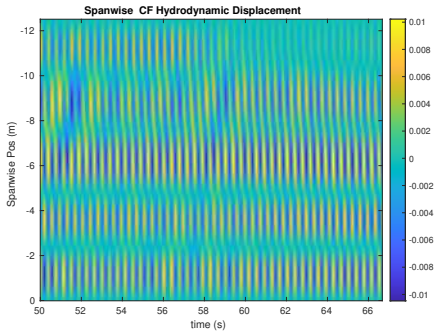

(c) Spanwise cross-flow hydrodynamic displacement case 1015.

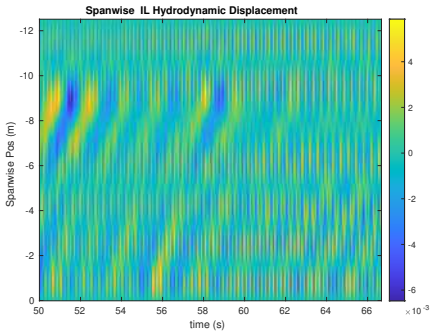

(d) Spanwise inline spectrum of hydrodynamic displacement case 1015.

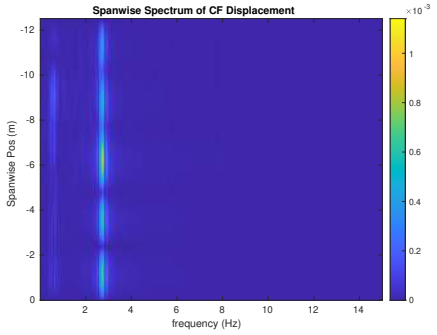

(e) Spanwise cross-flow spectrum of hydrodynamic displacement case 1015.

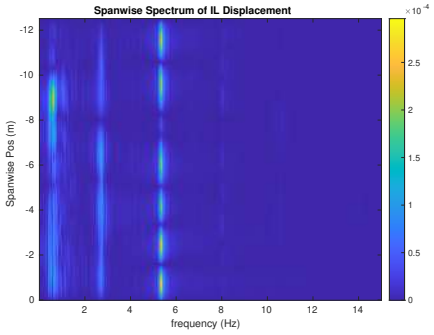

(f) Spanwise inline spectrum of hydrodynamic displacement case 1015.

Figure B-10: *Motion Analysis.* SCR case 1015.

NDP SCR test case 1017

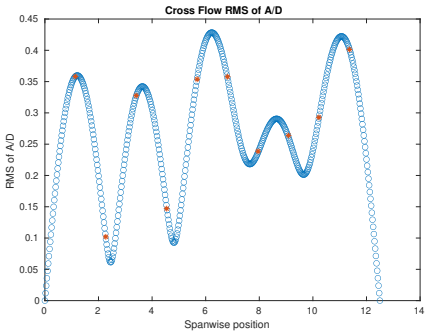

(a) Cross-flow RMS profile case 1017.

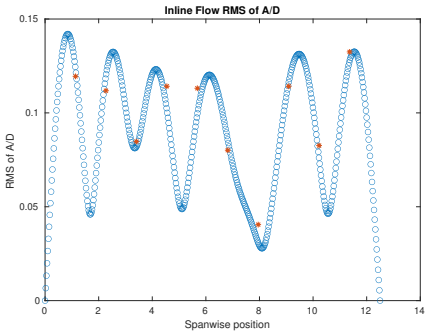

(b) Inline flow RMS profile case 1017.

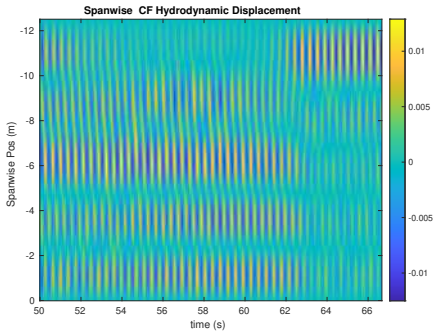

(c) Spanwise cross-flow hydrodynamic displacement case 1017.

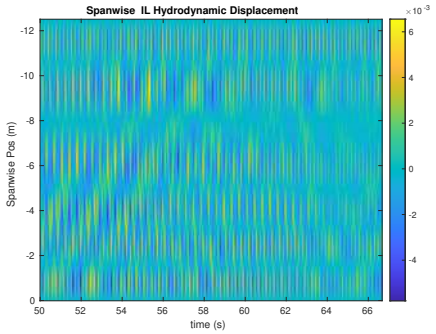

(d) Spanwise inline spectrum of hydrodynamic displacement case 1017.

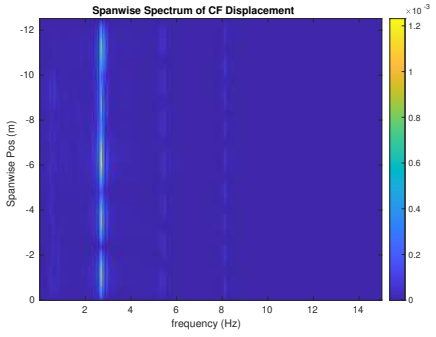

(e) Spanwise cross-flow spectrum of hydrodynamic displacement case 1017.

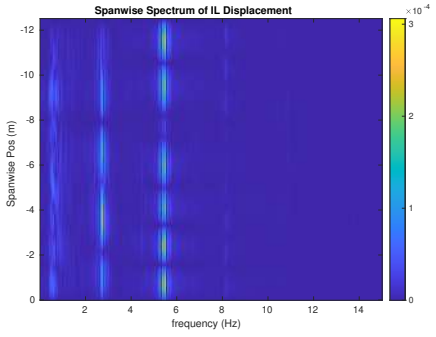

(f) Spanwise inline spectrum of hydrodynamic displacement case 1017.

Figure B-11: *Motion Analysis.* SCR case 1017.

NDP SCR test case 1019

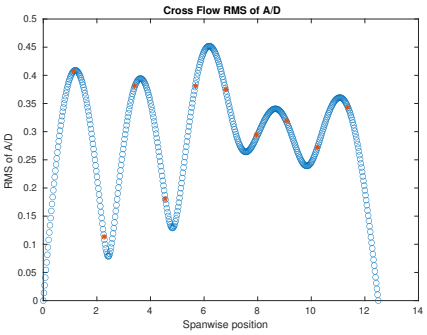

(a) Cross-flow RMS profile case 1019.

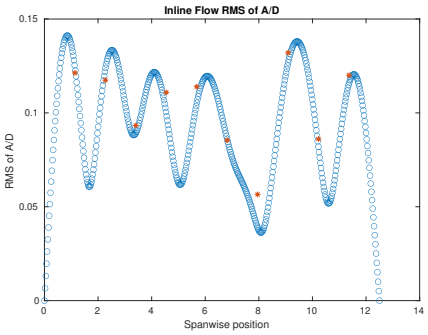

(b) Inline flow RMS profile case 1019.

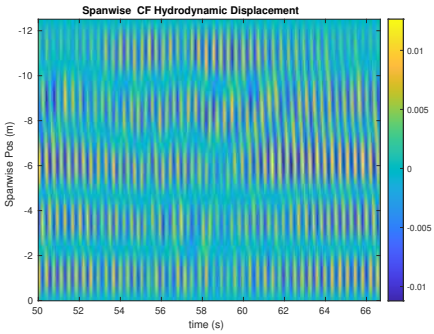

(c) Spanwise cross-flow hydrodynamic displacement case 1019.

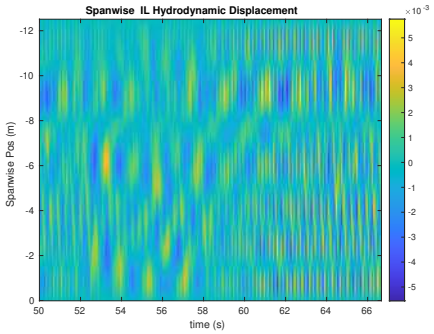

(d) Spanwise inline spectrum of hydrodynamic displacement case 1019.

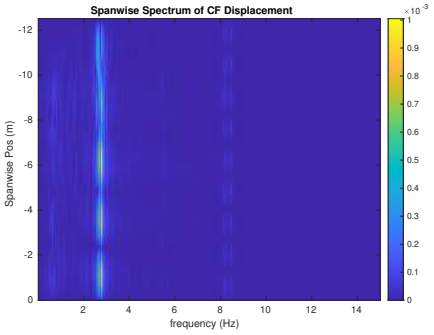

(e) Spanwise cross-flow spectrum of hydrodynamic displacement case 1019.

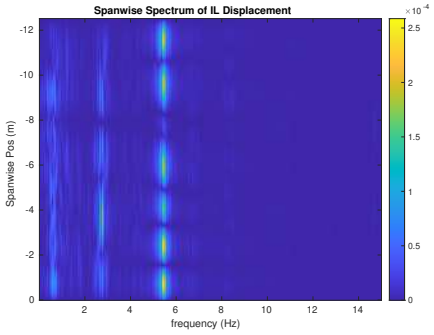

(f) Spanwise inline spectrum of hydrodynamic displacement case 1019.

Figure B-12: *Motion Analysis.* SCR case 1019.

NDP SCR test case 5019

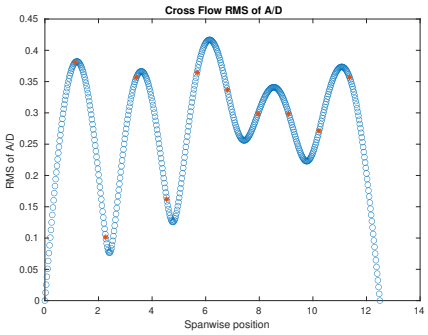

(a) Cross-flow RMS profile case 5019.

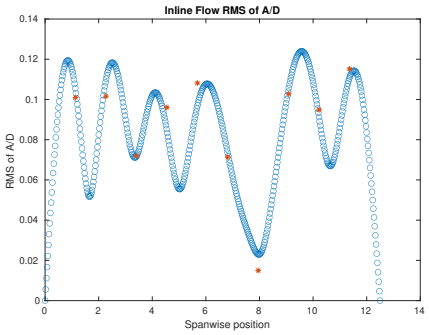

(b) Inline flow RMS profile case 5019.

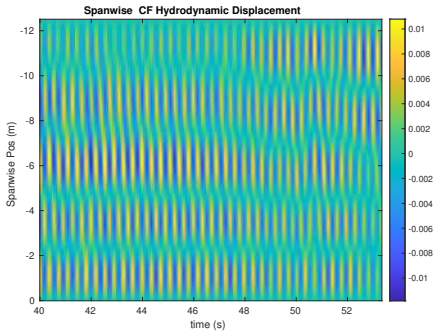

(c) Spanwise cross-flow hydrodynamic displacement case 5019.

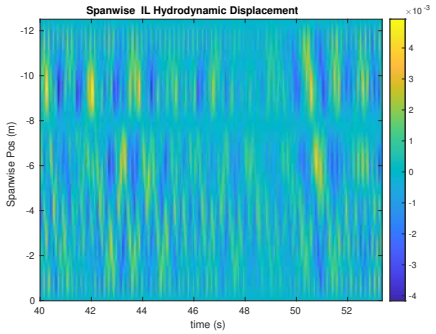

(d) Spanwise inline spectrum of hydrodynamic displacement case 5019.

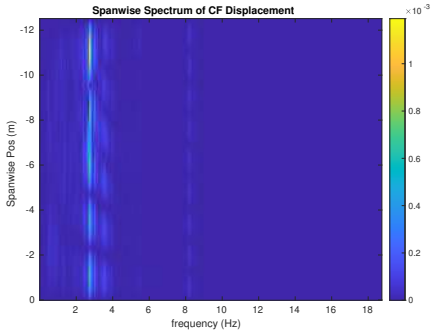

(e) Spanwise cross-flow spectrum of hydrodynamic displacement case 5019.

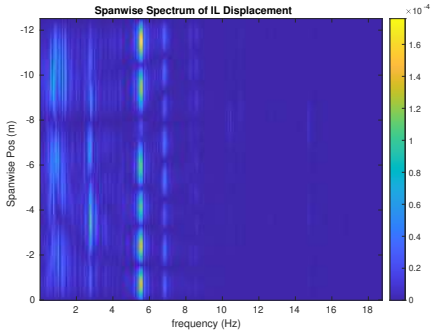

(f) Spanwise inline spectrum of hydrodynamic displacement case 5019.

Figure B-13: *Motion Analysis.* SCR case 5019.

NDP SCR test case 1021

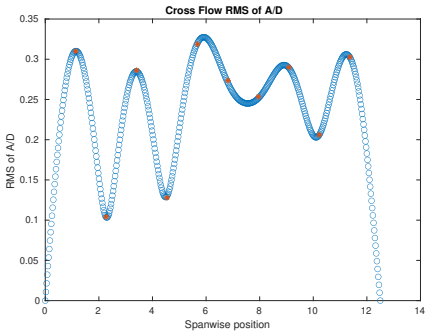

(a) Cross-flow RMS profile case 1021.

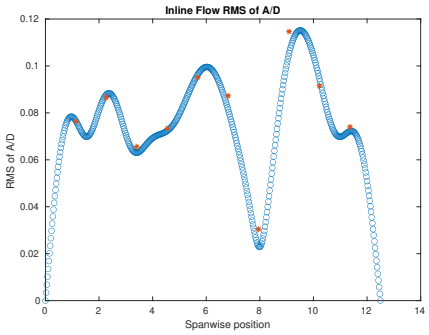

(b) Inline flow RMS profile case 1021.

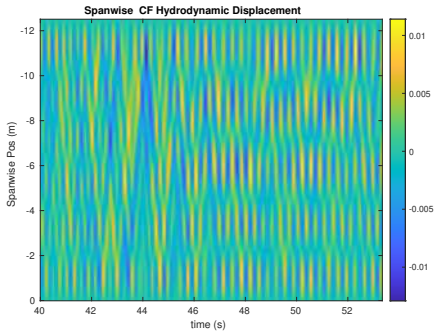

(c) Spanwise cross-flow hydrodynamic displacement case 1021.

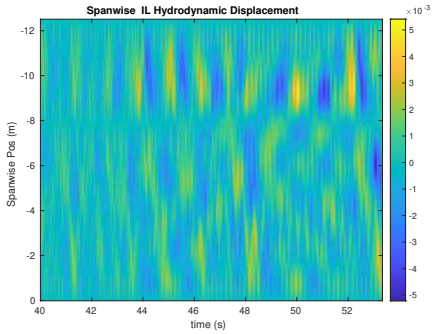

(d) Spanwise inline spectrum of hydrodynamic displacement case 1021.

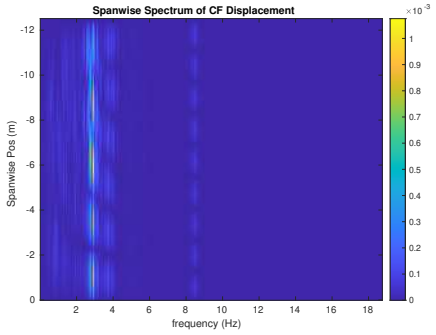

(e) Spanwise cross-flow spectrum of hydrodynamic displacement case 1021.

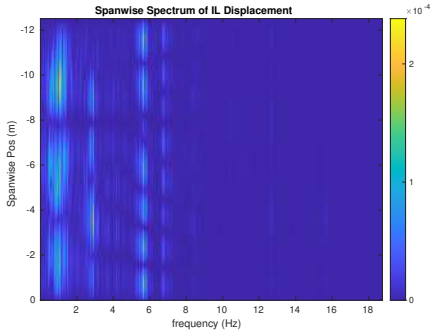

(f) Spanwise inline spectrum of hydrodynamic displacement case 1021.

Figure B-14: *Motion Analysis.* SCR case 1021.

NDP SCR test case 1023

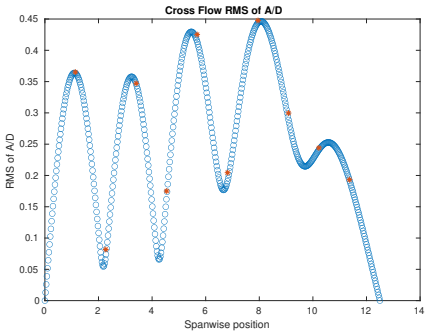

(a) Cross-flow RMS profile case 1023.

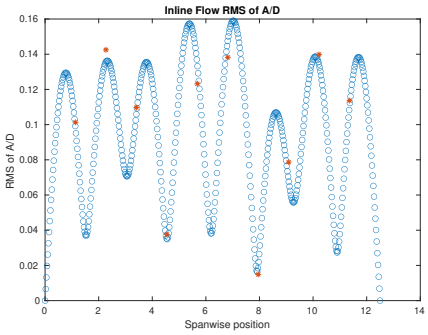

(b) Inline flow RMS profile case 1023.

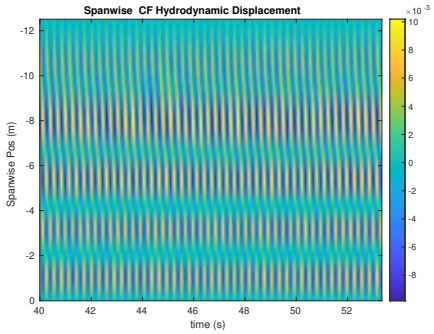

(c) Spanwise cross-flow hydrodynamic displacement case 1023.

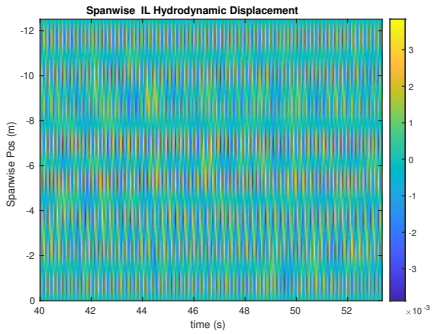

(d) Spanwise inline spectrum of hydrodynamic displacement case 1023.

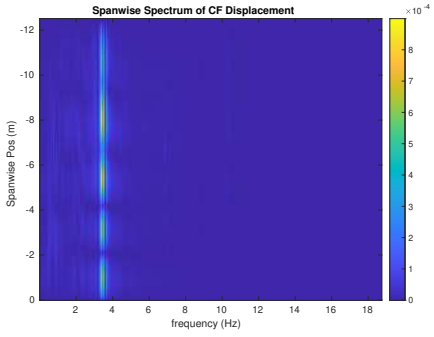

(e) Spanwise cross-flow spectrum of hydrodynamic displacement case 1023.

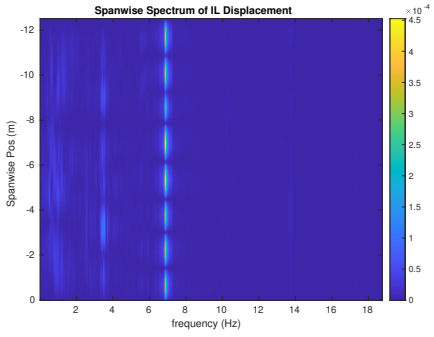

(f) Spanwise inline spectrum of hydrodynamic displacement case 1023.

Figure B-15: *Motion Analysis.* SCR case 1023.

NDP SCR test case 5023

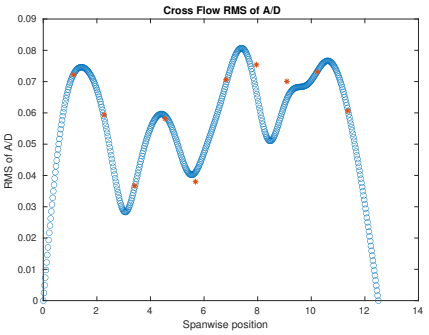

(a) Cross-flow RMS profile case 5023.

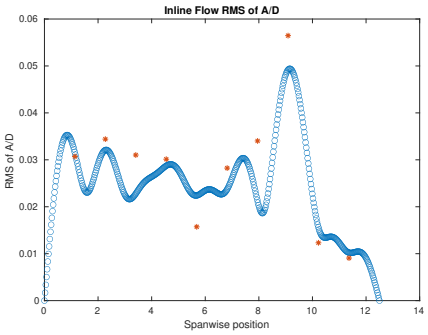

(b) Inline flow RMS profile case 5023.

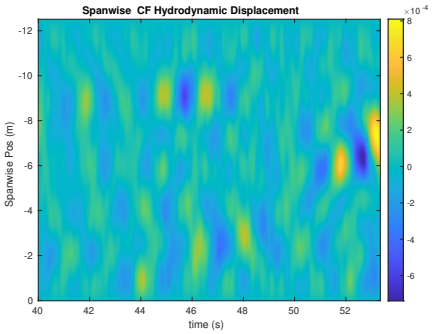

(c) Spanwise cross-flow hydrodynamic displacement case 5023.

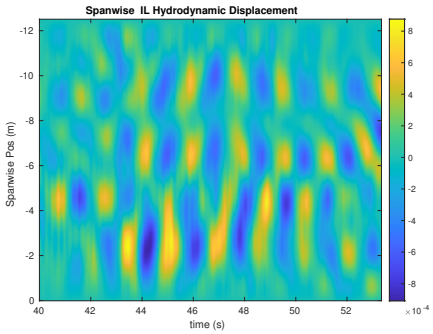

(d) Spanwise inline spectrum of hydrodynamic displacement case 5023.

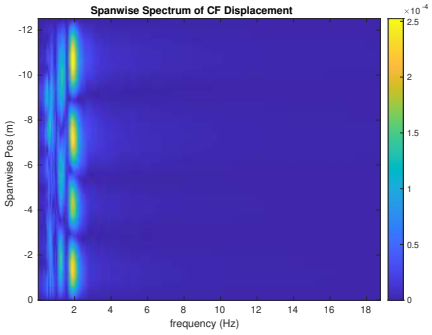

(e) Spanwise cross-flow spectrum of hydrodynamic displacement case 5023.

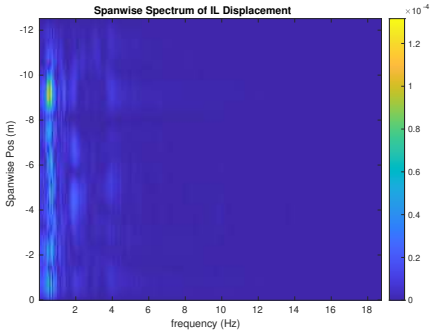

(f) Spanwise inline spectrum of hydrodynamic displacement case 5023.

Figure B-16: *Motion Analysis.* SCR case 5023.

NDP SCR test case 2005

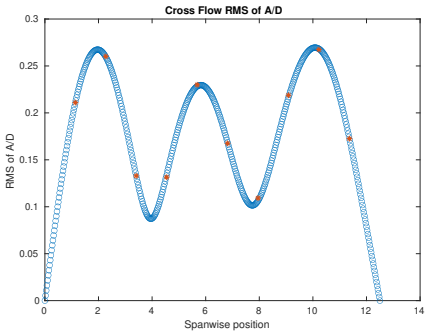

(a) Cross-flow RMS profile case 2005.

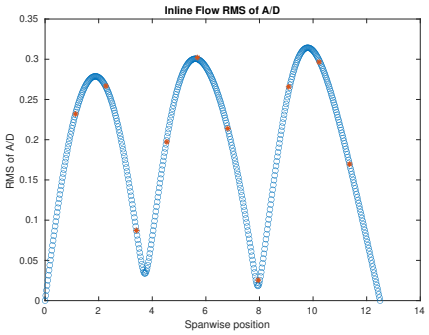

(b) Inline flow RMS profile case 2005.

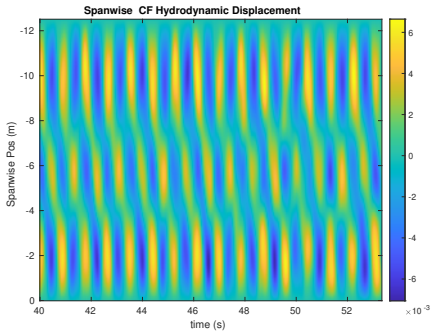

(c) Spanwise cross-flow hydrodynamic displacement case 2005.

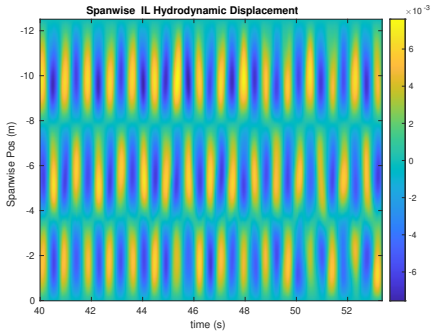

(d) Spanwise inline spectrum of hydrodynamic displacement case 2005.

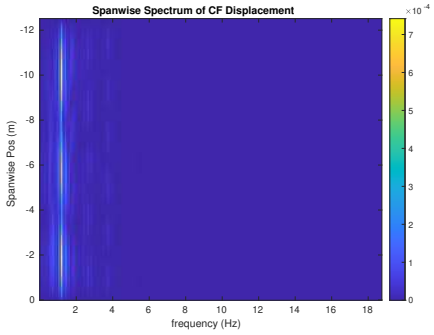

(e) Spanwise cross-flow spectrum of hydrodynamic displacement case 2005.

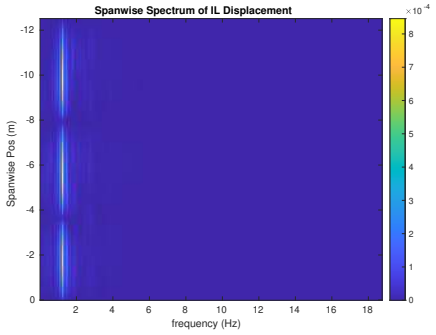

(f) Spanwise inline spectrum of hydrodynamic displacement case 2005.

Figure B-17: *Motion Analysis.* SCR case 2005.

NDP SCR test case 2000

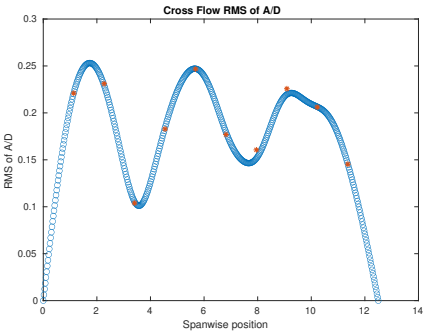

(a) Cross-flow RMS profile case 2000.

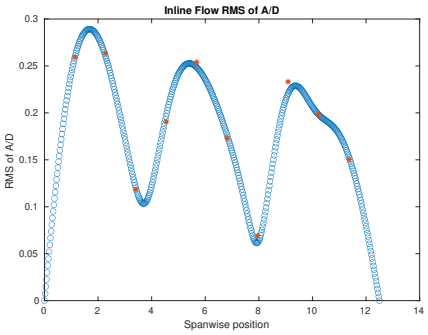

(b) Inline flow RMS profile case 2000.

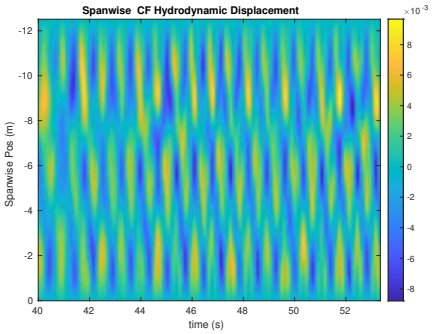

(c) Spanwise cross-flow hydrodynamic displacement case 2000.

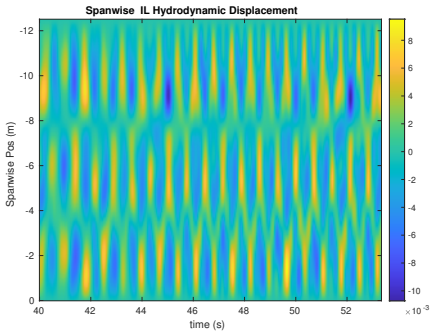

(d) Spanwise inline spectrum of hydrodynamic displacement case 2000.

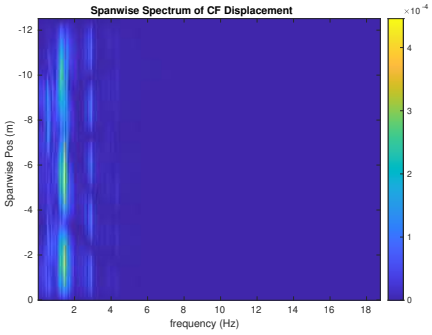

(e) Spanwise cross-flow spectrum of hydrodynamic displacement case 2000.

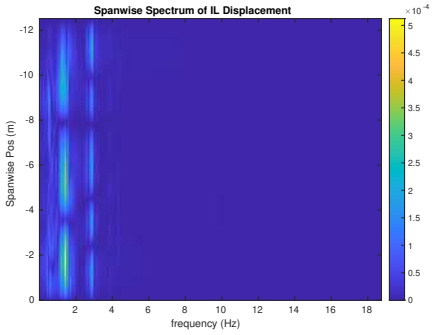

(f) Spanwise inline spectrum of hydrodynamic displacement case 2000.

Figure B-18: *Motion Analysis.* SCR case 2000.

NDP SCR test case 2003

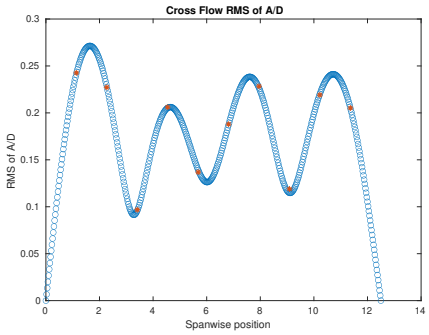

(a) Cross-flow RMS profile case 2003.

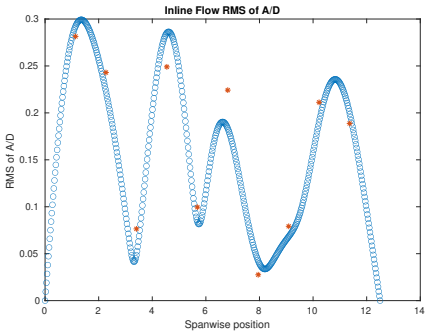

(b) Inline flow RMS profile case 2003.

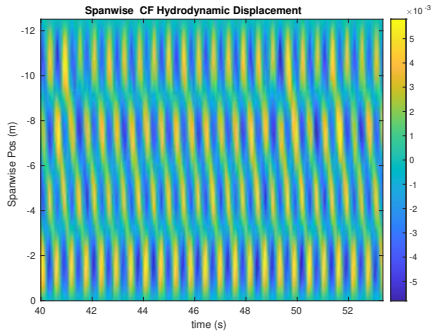

(c) Spanwise cross-flow hydrodynamic displacement case 2003.

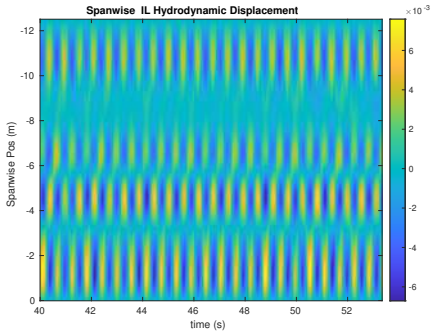

(d) Spanwise inline spectrum of hydrodynamic displacement case 2003.

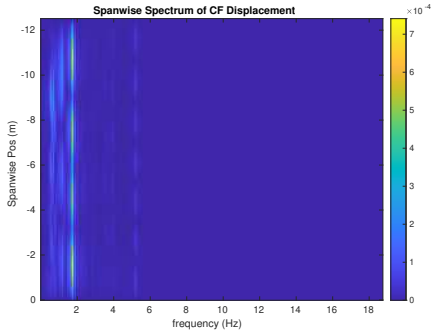

(e) Spanwise cross-flow spectrum of hydrodynamic displacement case 2003.

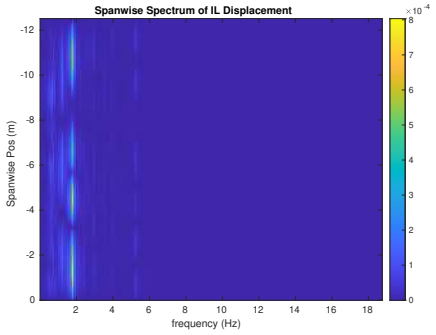

(f) Spanwise inline spectrum of hydrodynamic displacement case 2003.

Figure B-19: *Motion Analysis.* SCR case 2003.

NDP SCR test case 2007

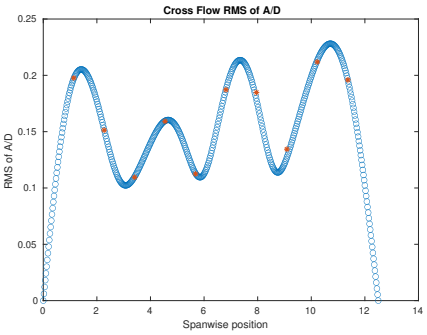

(a) Cross-flow RMS profile case 2007.

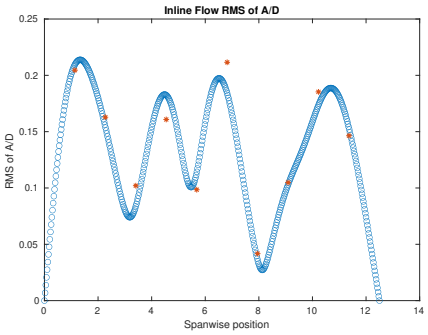

(b) Inline flow RMS profile case 2007.

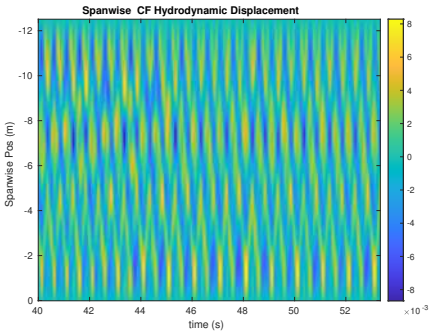

(c) Spanwise cross-flow hydrodynamic displacement case 2007.

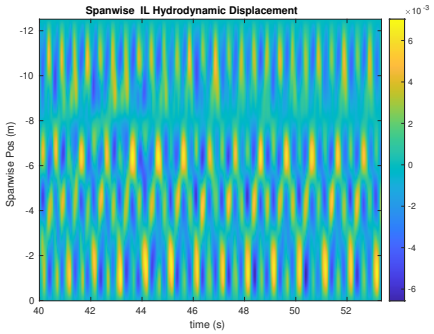

(d) Spanwise inline spectrum of hydrodynamic displacement case 2007.

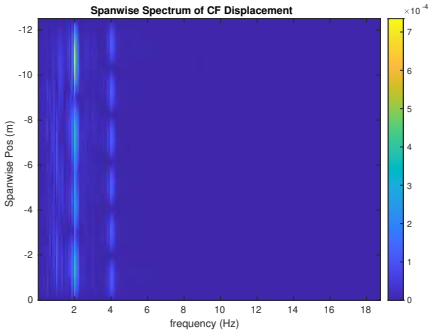

(e) Spanwise cross-flow spectrum of hydrodynamic displacement case 2007.

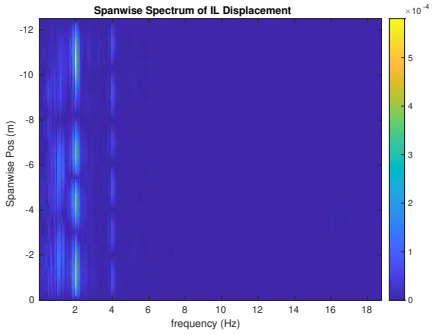

(f) Spanwise inline spectrum of hydrodynamic displacement case 2007.

Figure B-20: *Motion Analysis.* SCR case 2007.

NDP SCR test case 2009

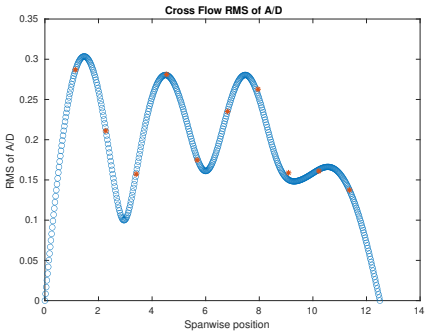

(a) Cross-flow RMS profile case 2009.

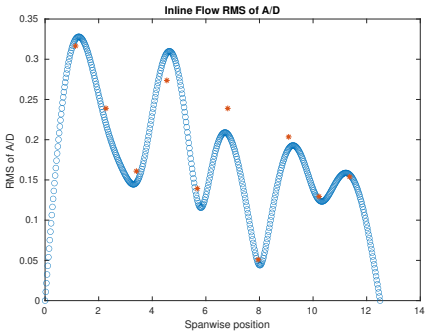

(b) Inline flow RMS profile case 2009.

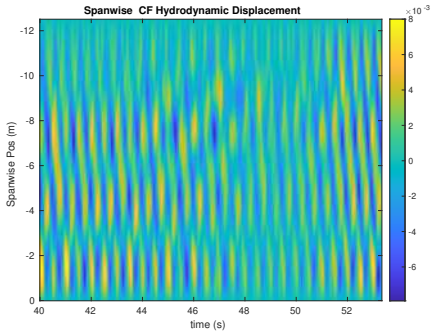

(c) Spanwise cross-flow hydrodynamic displacement case 2009.

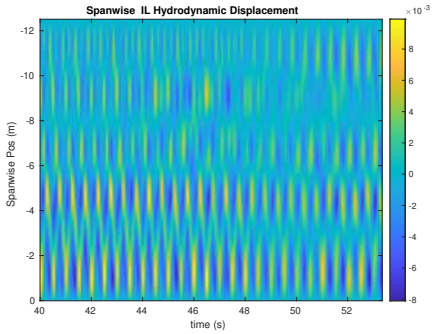

(d) Spanwise inline spectrum of hydrodynamic displacement case 2009.

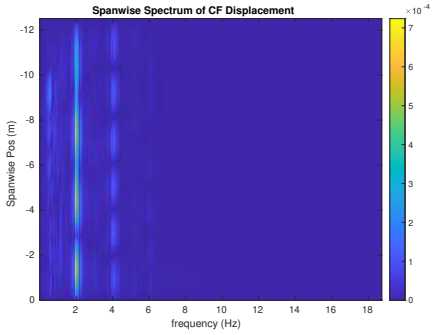

(e) Spanwise cross-flow spectrum of hydrodynamic displacement case 2009.

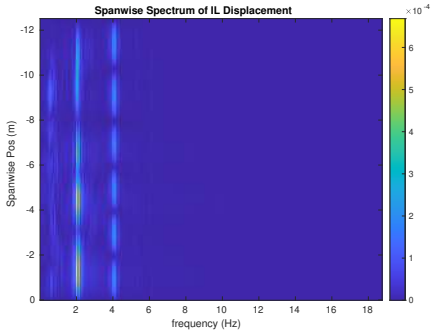

(f) Spanwise inline spectrum of hydrodynamic displacement case 2009.

Figure B-21: *Motion Analysis.* SCR case 2009.

NDP SCR test case 2011

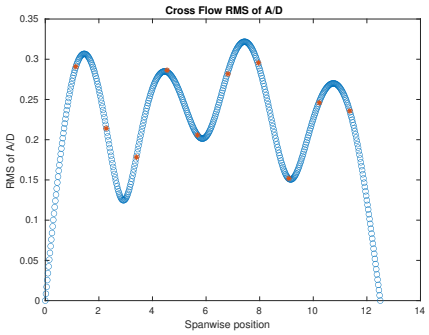

(a) Cross-flow RMS profile case 2011.

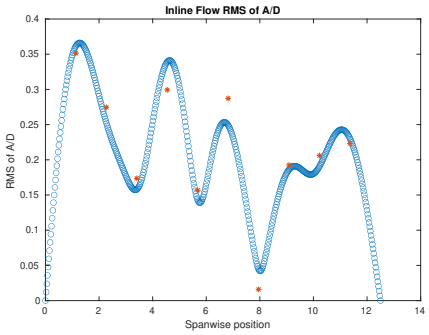

(b) Inline flow RMS profile case 2011.

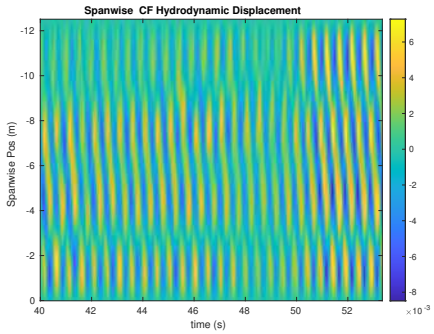

(c) Spanwise cross-flow hydrodynamic displacement case 2011.

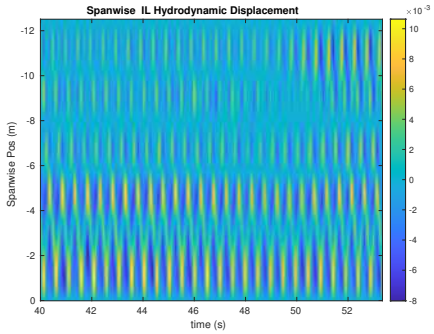

(d) Spanwise inline spectrum of hydrodynamic displacement case 2011.

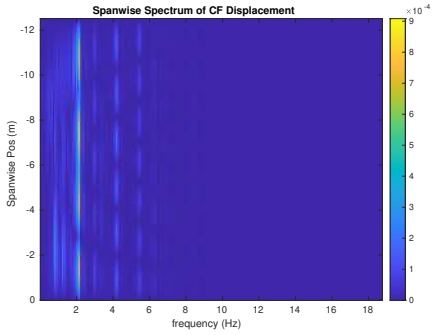

(e) Spanwise cross-flow spectrum of hydrodynamic displacement case 2011.

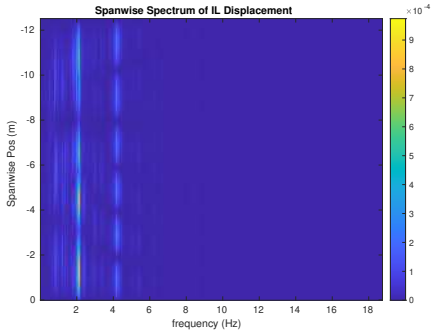

(f) Spanwise inline spectrum of hydrodynamic displacement case 2011.

Figure B-22: *Motion Analysis.* SCR case 2011.

NDP SCR test case 2013

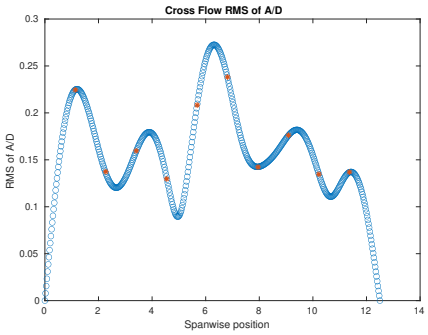

(a) Cross-flow RMS profile case 2013.

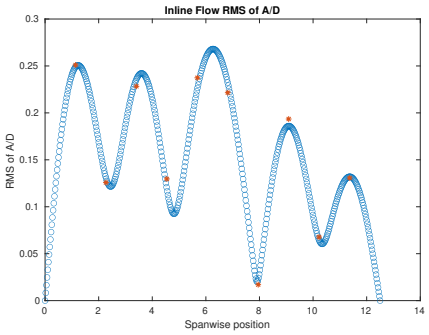

(b) Inline flow RMS profile case 2013.

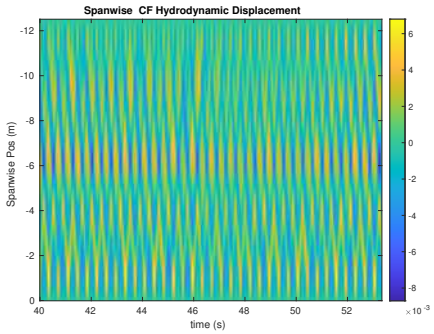

(c) Spanwise cross-flow hydrodynamic displacement case 2013.

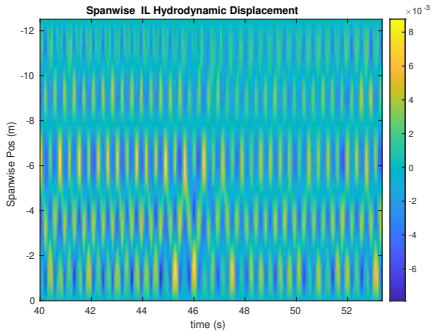

(d) Spanwise inline spectrum of hydrodynamic displacement case 2013.

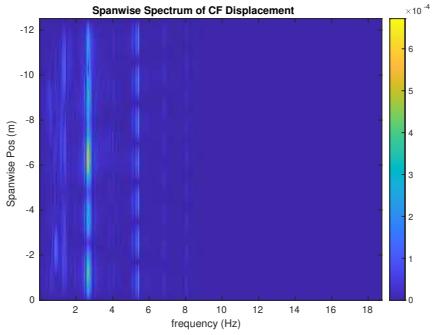

(e) Spanwise cross-flow spectrum of hydrodynamic displacement case 2013.

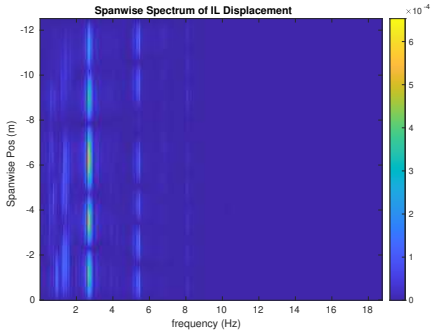

(f) Spanwise inline spectrum of hydrodynamic displacement case 2013.

Figure B-23: *Motion Analysis.* SCR case 2013.

NDP SCR test case 2015

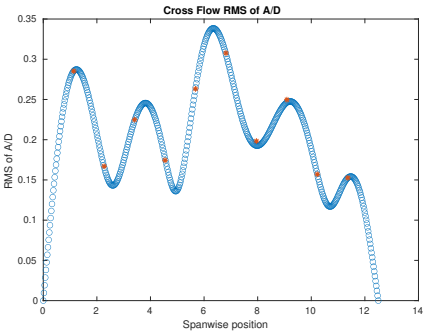

(a) Cross-flow RMS profile case 2015.

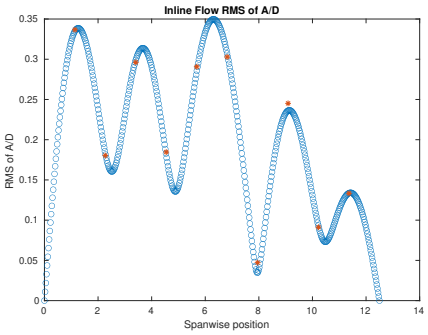

(b) Inline flow RMS profile case 2015.

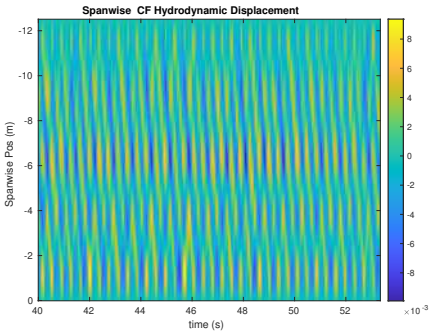

(c) Spanwise cross-flow hydrodynamic displacement case 2015.

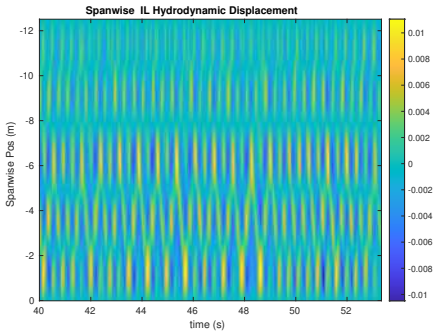

(d) Spanwise inline spectrum of hydrodynamic displacement case 2015.

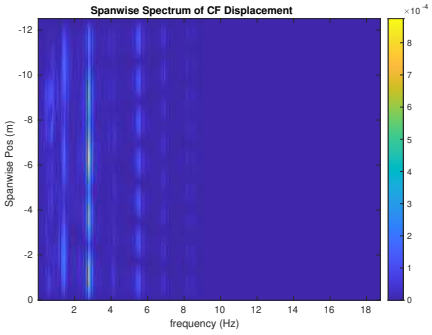

(e) Spanwise cross-flow spectrum of hydrodynamic displacement case 2015.

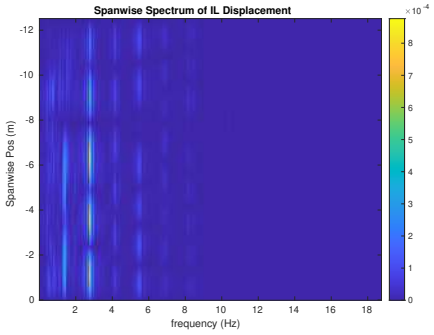

(f) Spanwise inline spectrum of hydrodynamic displacement case 2015.

Figure B-24: *Motion Analysis.* SCR case 2015.

NDP SCR test case 2017

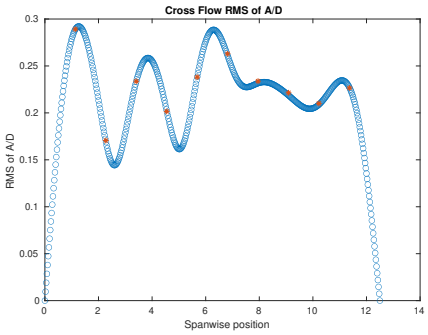

(a) Cross-flow RMS profile case 2017.

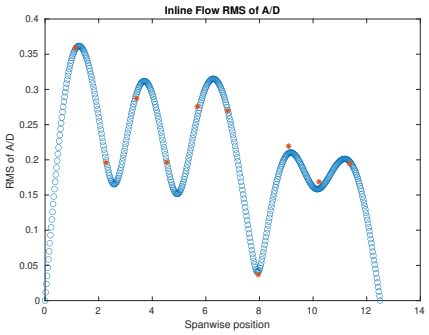

(b) Inline flow RMS profile case 2017.

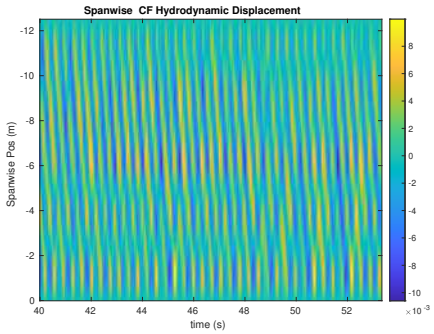

(c) Spanwise cross-flow hydrodynamic displacement case 2017.

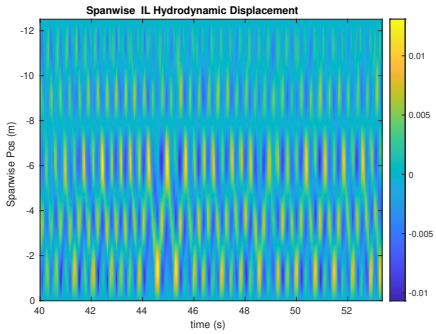

(d) Spanwise inline spectrum of hydrodynamic displacement case 2017.

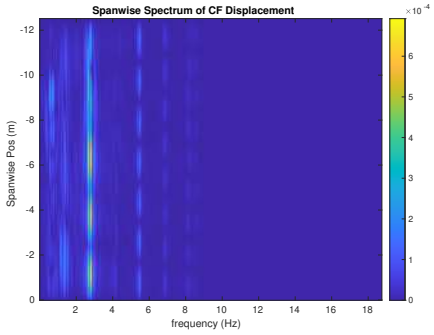

(e) Spanwise cross-flow spectrum of hydrodynamic displacement case 2017.

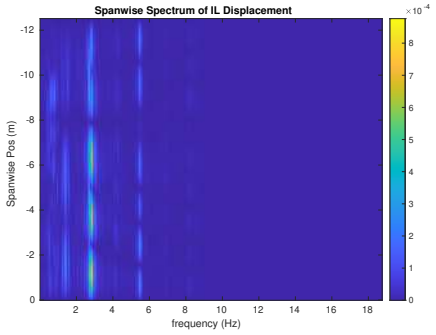

(f) Spanwise inline spectrum of hydrodynamic displacement case 2017.

Figure B-25: *Motion Analysis.* SCR case 2017.

NDP SCR test case 2019

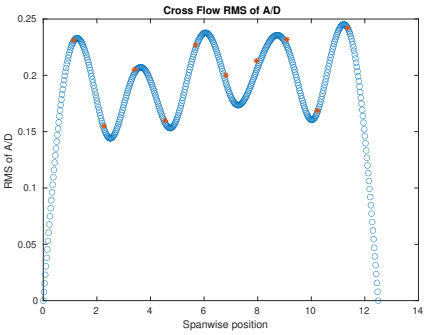

(a) Cross-flow RMS profile case 2019.

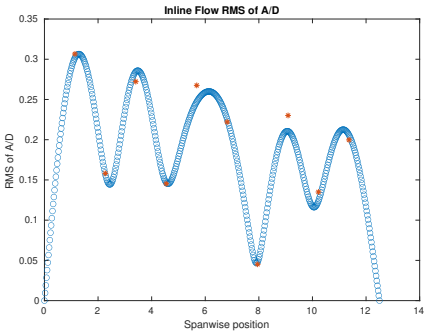

(b) Inline flow RMS profile case 2019.

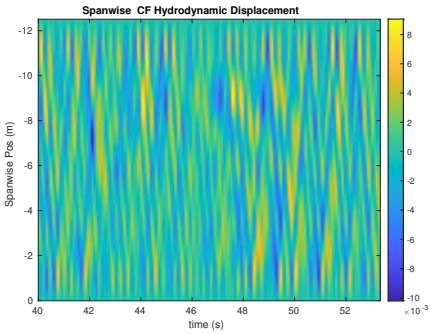

(c) Spanwise cross-flow hydrodynamic displacement case 2019.

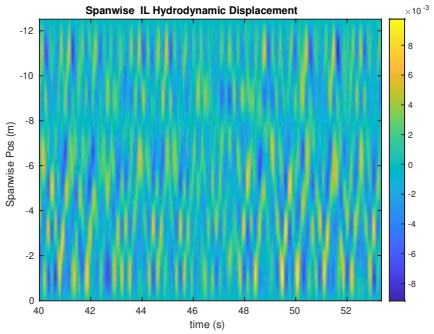

(d) Spanwise inline spectrum of hydrodynamic displacement case 2019.

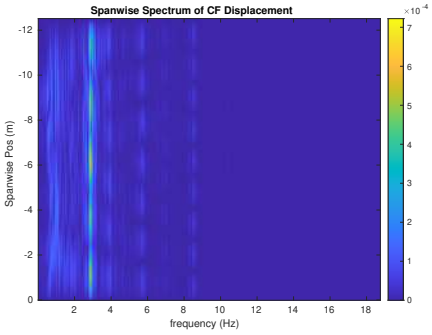

(e) Spanwise cross-flow spectrum of hydrodynamic displacement case 2019.

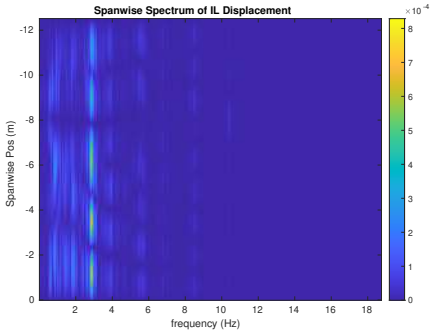

(f) Spanwise inline spectrum of hydrodynamic displacement case 2019.

Figure B-26: *Motion Analysis.* SCR case 2019.

NDP SCR test case 2021

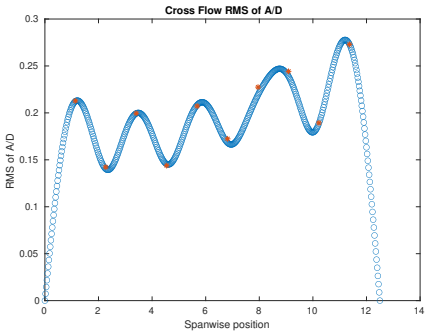

(a) Cross-flow RMS profile case 2021.

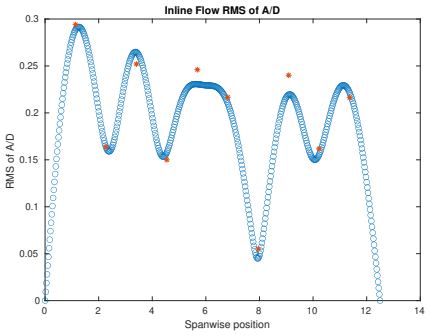

(b) Inline flow RMS profile case 2021.

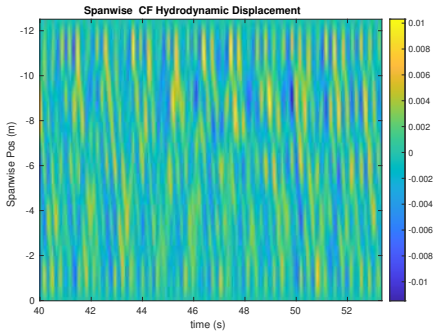

(c) Spanwise cross-flow hydrodynamic displacement case 2021.

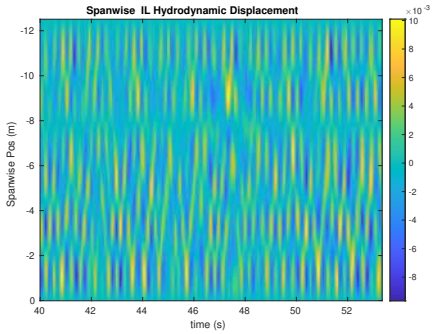

(d) Spanwise inline spectrum of hydrodynamic displacement case 2021.

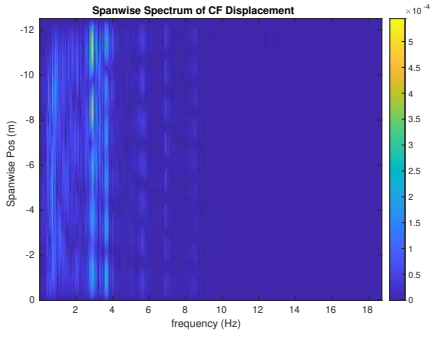

(e) Spanwise cross-flow spectrum of hydrodynamic displacement case 2021.

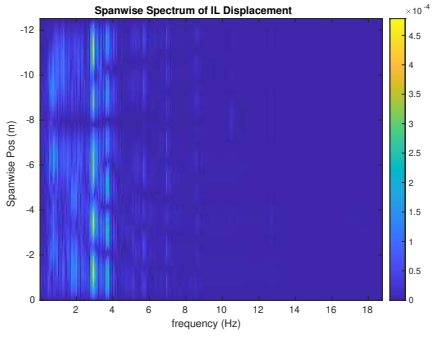

(f) Spanwise inline spectrum of hydrodynamic displacement case 2021.

Figure B-27: *Motion Analysis.* SCR case 2021.

NDP SCR test case 2023

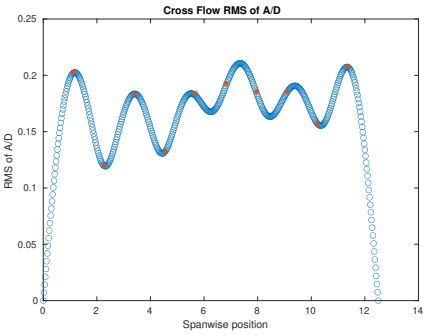

(a) Cross-flow RMS profile case 2023.

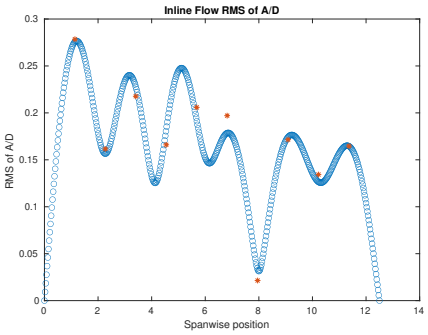

(b) Inline flow RMS profile case 2023.

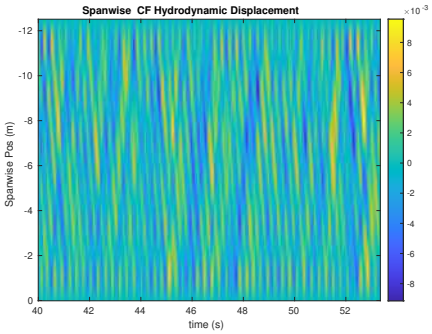

(c) Spanwise cross-flow hydrodynamic displacement case 2023.

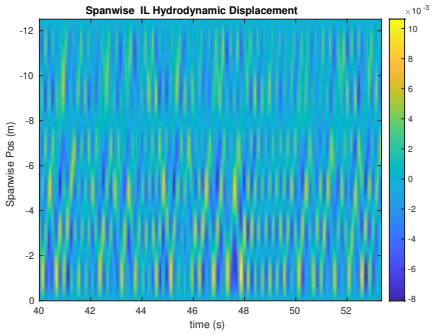

(d) Spanwise inline spectrum of hydrodynamic displacement case 2023.

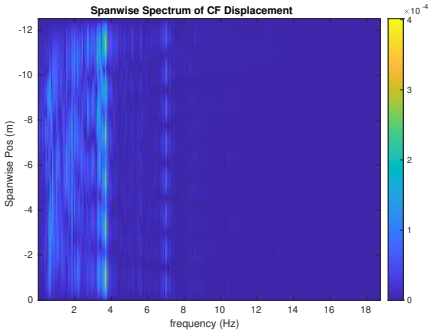

(e) Spanwise cross-flow spectrum of hydrodynamic displacement case 2023.

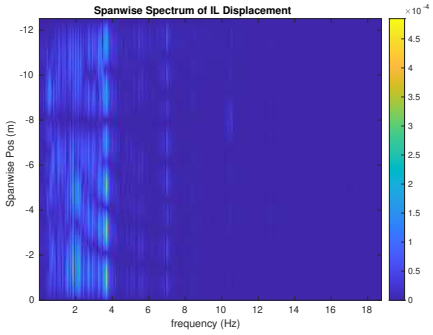

(f) Spanwise inline spectrum of hydrodynamic displacement case 2023.

Figure B-28: *Motion Analysis.* SCR case 2023.

NDP SCR test case 3001

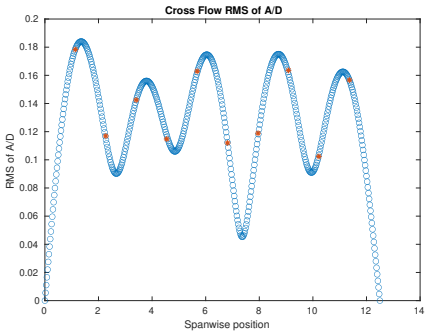

(a) Cross-flow RMS profile case 3001.

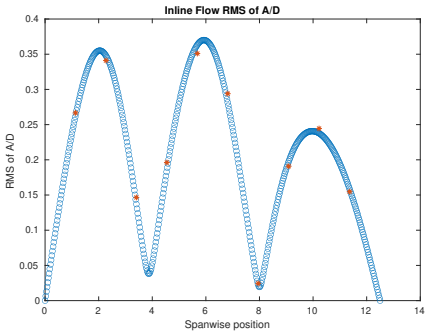

(b) Inline flow RMS profile case 3001.

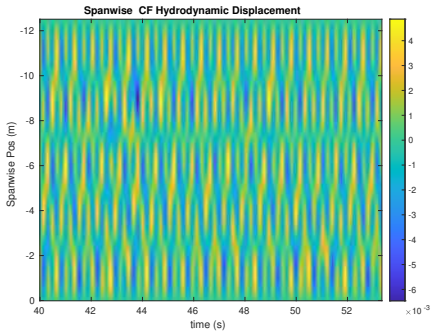

(c) Spanwise cross-flow hydrodynamic displacement case 3001.

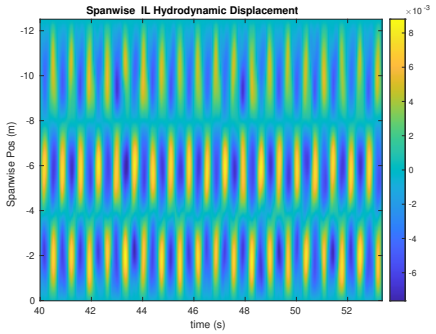

(d) Spanwise inline spectrum of hydrodynamic displacement case 3001.

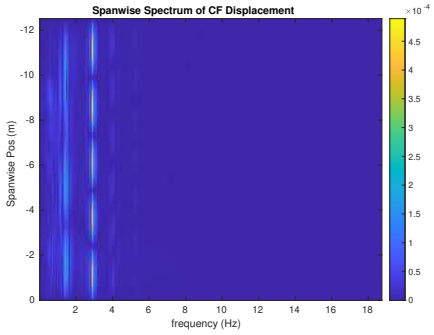

(e) Spanwise cross-flow spectrum of hydrodynamic displacement case 3001.

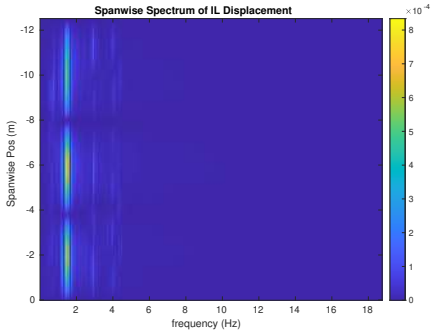

(f) Spanwise inline spectrum of hydrodynamic displacement case 3001.

Figure B-29: *Motion Analysis.* SCR case 3001.

NDP SCR test case 3003

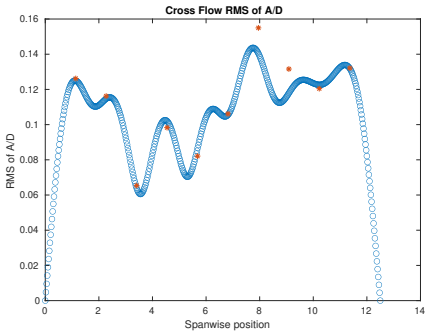

(a) Cross-flow RMS profile case 3003.

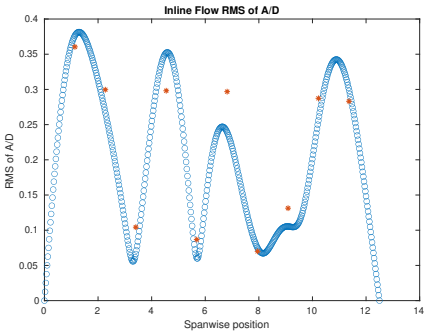

(b) Inline flow RMS profile case 3003.

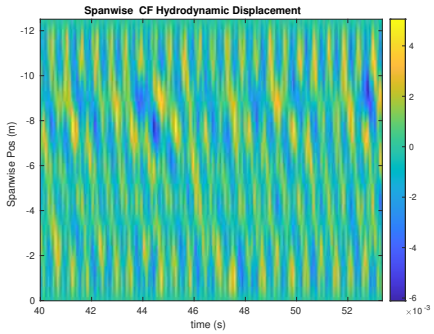

(c) Spanwise cross-flow hydrodynamic displacement case 3003.

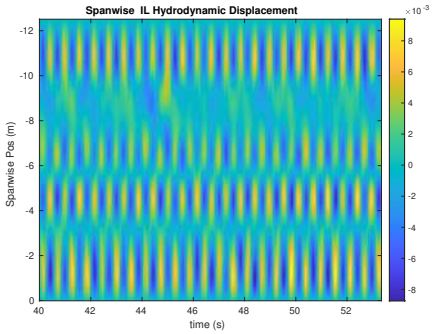

(d) Spanwise inline spectrum of hydrodynamic displacement case 3003.

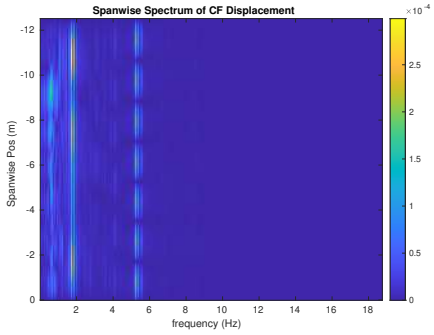

(e) Spanwise cross-flow spectrum of hydrodynamic displacement case 3003.

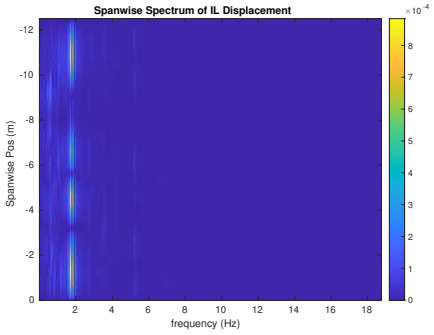

(f) Spanwise inline spectrum of hydrodynamic displacement case 3003.

Figure B-30: *Motion Analysis.* SCR case 3003.

NDP SCR test case 3005

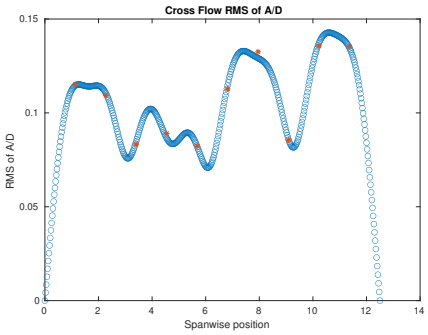

(a) Cross-flow RMS profile case 3005.

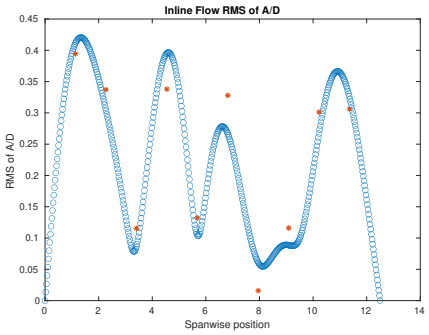

(b) Inline flow RMS profile case 3005.

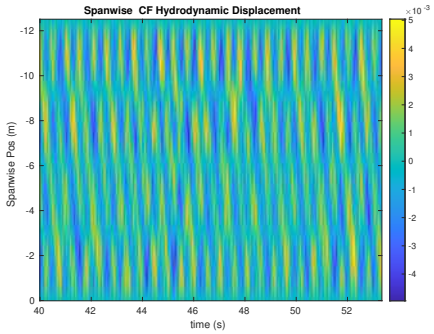

(c) Spanwise cross-flow hydrodynamic displacement case 3005.

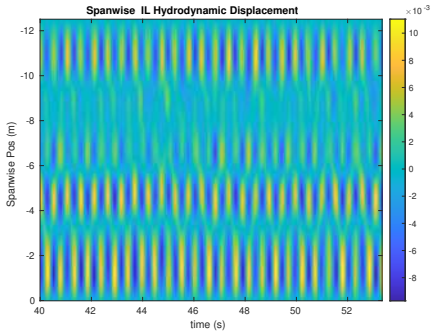

(d) Spanwise inline spectrum of hydrodynamic displacement case 3005.

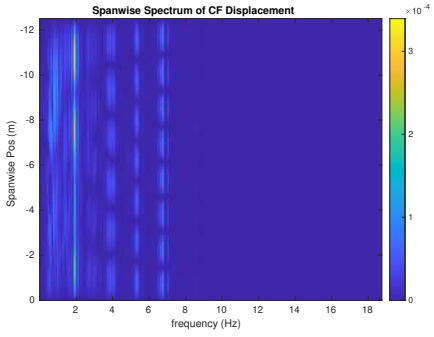

(e) Spanwise cross-flow spectrum of hydrodynamic displacement case 3005.

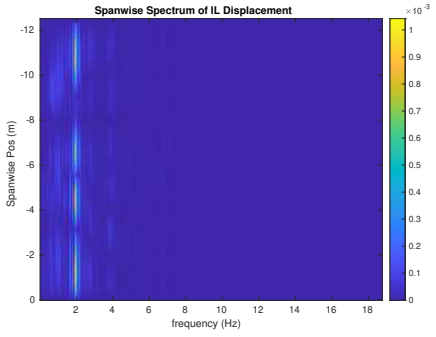

(f) Spanwise inline spectrum of hydrodynamic displacement case 3005.

Figure B-31: *Motion Analysis.* SCR case 3005.

NDP SCR test case 3007

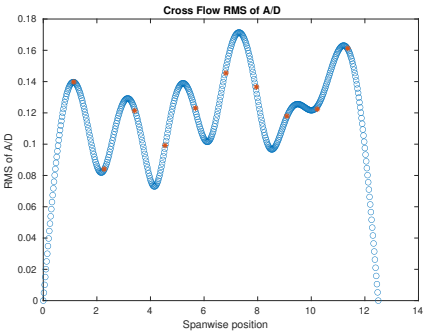

(a) Cross-flow RMS profile case 3007.

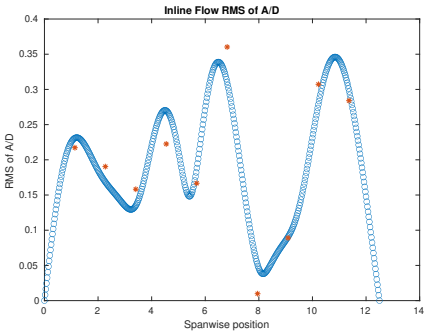

(b) Inline flow RMS profile case 3007.

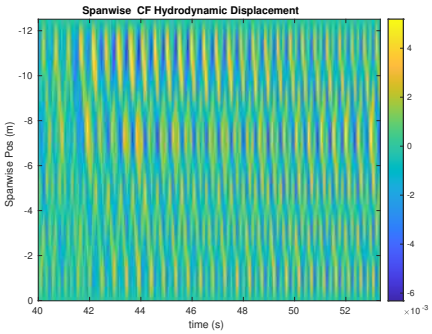

(c) Spanwise cross-flow hydrodynamic displacement case 3007.

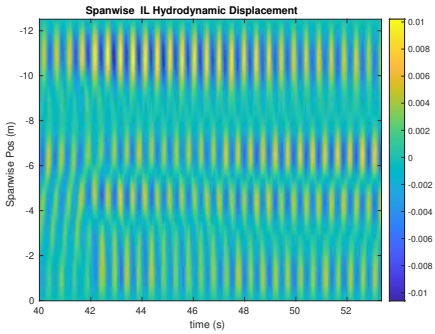

(d) Spanwise inline spectrum of hydrodynamic displacement case 3007.

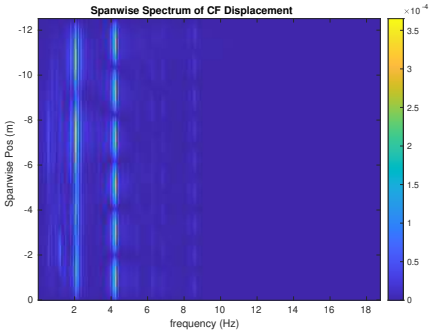

(e) Spanwise cross-flow spectrum of hydrodynamic displacement case 3007.

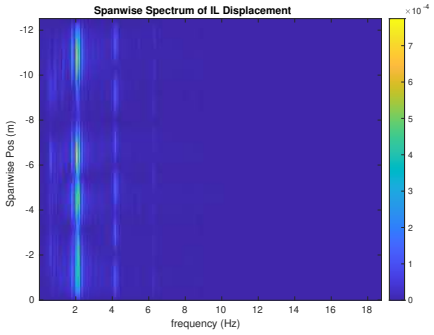

(f) Spanwise inline spectrum of hydrodynamic displacement case 3007.

Figure B-32: *Motion Analysis.* SCR case 3007.

NDP SCR test case 3009

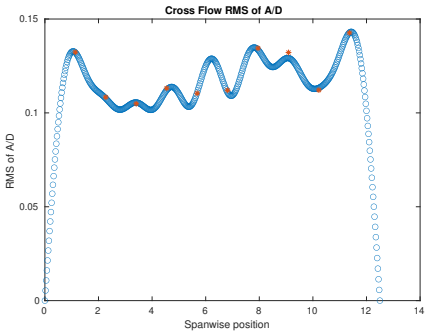

(a) Cross-flow RMS profile case 3009.

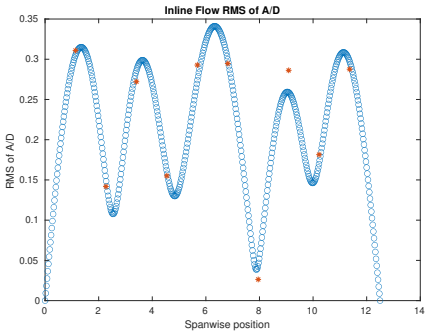

(b) Inline flow RMS profile case 3009.

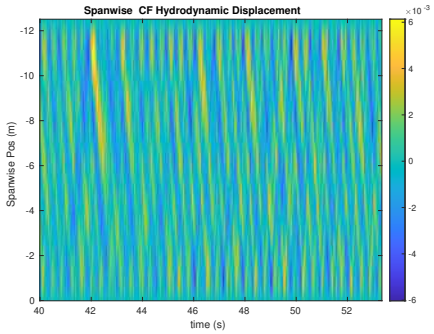

(c) Spanwise cross-flow hydrodynamic displacement case 3009.

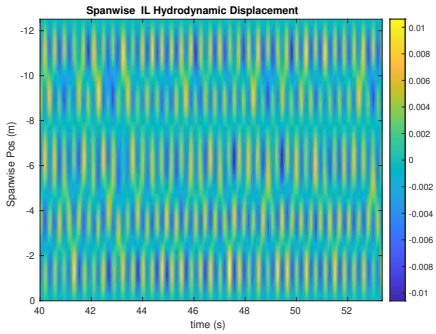

(d) Spanwise inline spectrum of hydrodynamic displacement case 3009.

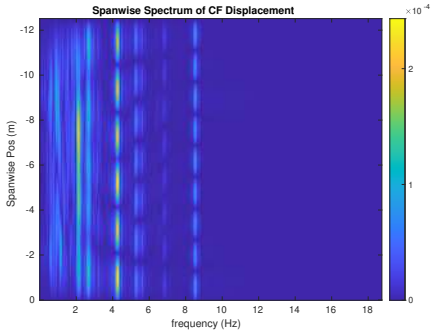

(e) Spanwise cross-flow spectrum of hydrodynamic displacement case 3009.

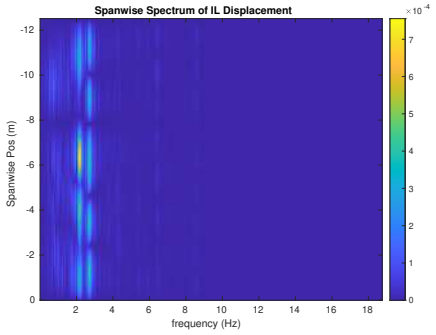

(f) Spanwise inline spectrum of hydrodynamic displacement case 3009.

Figure B-33: *Motion Analysis.* SCR case 3009.

NDP SCR test case 3011

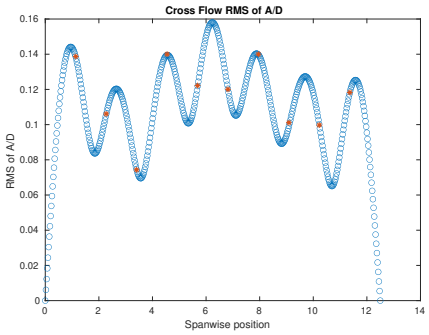

(a) Cross-flow RMS profile case 3011.

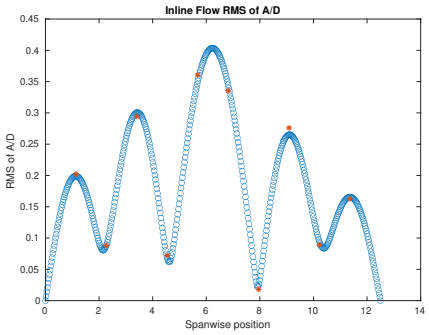

(b) Inline flow RMS profile case 3011.

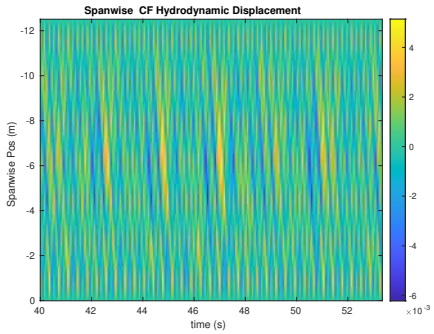

(c) Spanwise cross-flow hydrodynamic displacement case 3011.

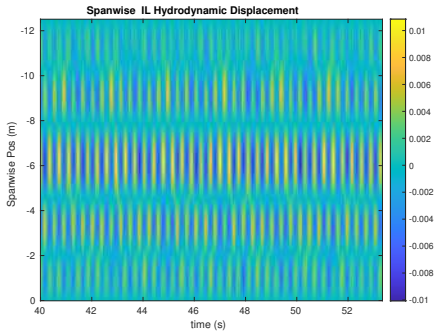

(d) Spanwise inline spectrum of hydrodynamic displacement case 3011.

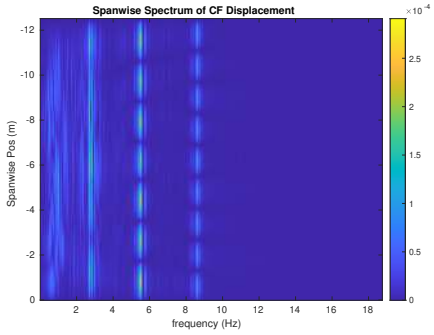

(e) Spanwise cross-flow spectrum of hydrodynamic displacement case 3011.

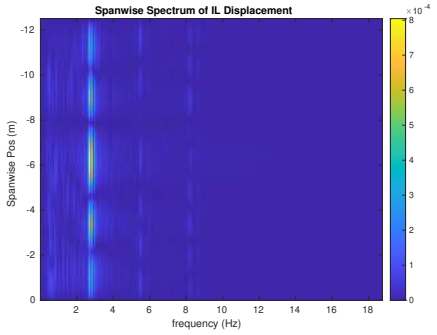

(f) Spanwise inline spectrum of hydrodynamic displacement case 3011.

Figure B-34: *Motion Analysis.* SCR case 3011.

NDP SCR test case 3013

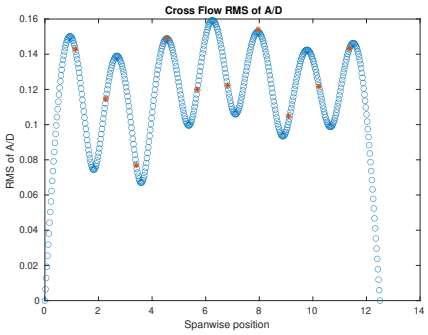

(a) Cross-flow RMS profile case 3013.

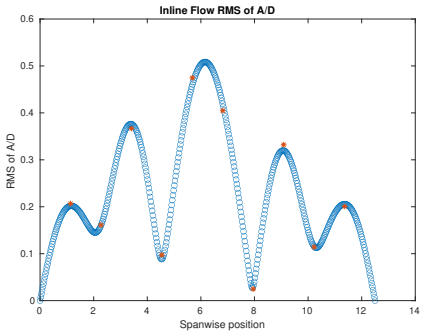

(b) Inline flow RMS profile case 3013.

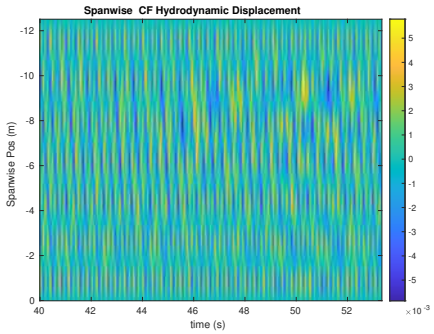

(c) Spanwise cross-flow hydrodynamic displacement case 3013.

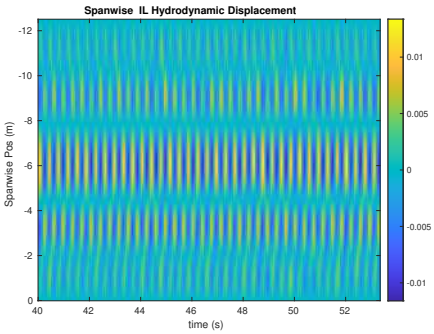

(d) Spanwise inline spectrum of hydrodynamic displacement case 3013.

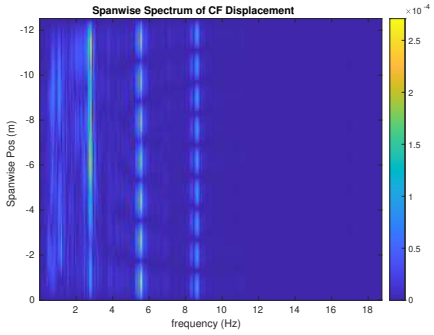

(e) Spanwise cross-flow spectrum of hydrodynamic displacement case 3013.

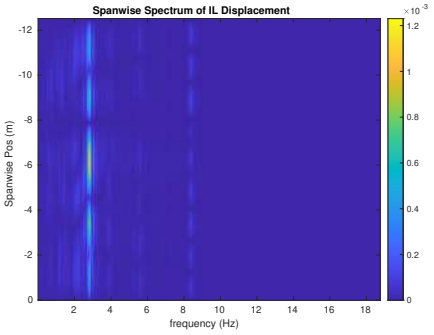

(f) Spanwise inline spectrum of hydrodynamic displacement case 3013.

Figure B-35: *Motion Analysis.* SCR case 3013.

NDP SCR test case 3015

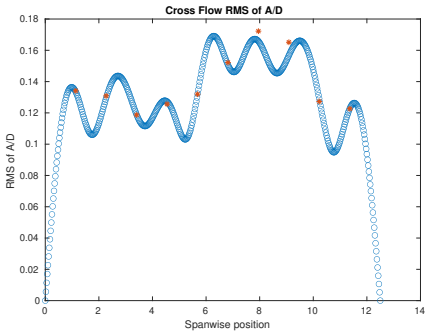

(a) Cross-flow RMS profile case 3015.

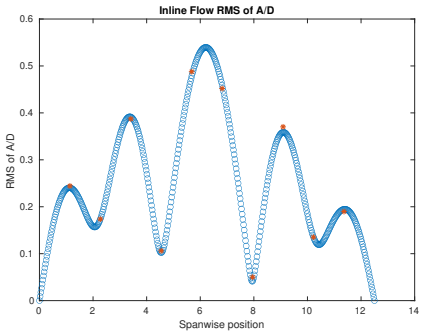

(b) Inline flow RMS profile case 3015.

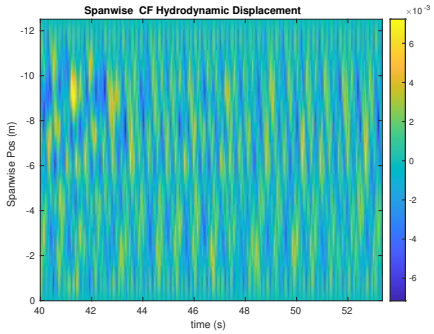

(c) Spanwise cross-flow hydrodynamic displacement case 3015.

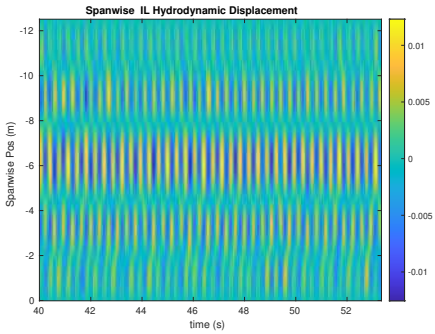

(d) Spanwise inline spectrum of hydrodynamic displacement case 3015.

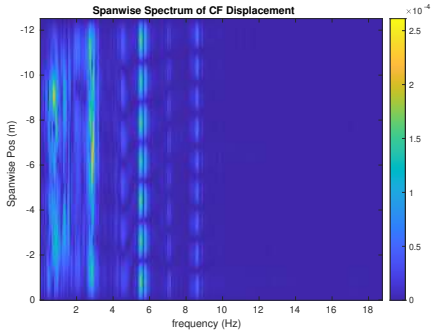

(e) Spanwise cross-flow spectrum of hydrodynamic displacement case 3015.

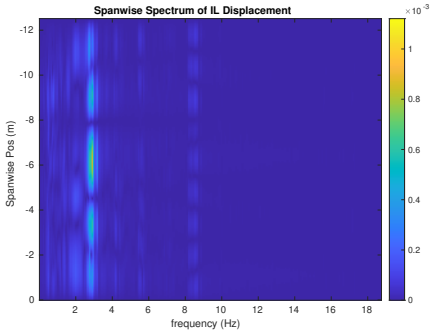

(f) Spanwise inline spectrum of hydrodynamic displacement case 3015.

Figure B-36: *Motion Analysis.* SCR case 3015.

NDP SCR test case 3017

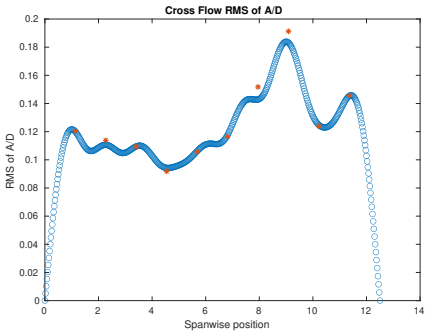

(a) Cross-flow RMS profile case 3017.

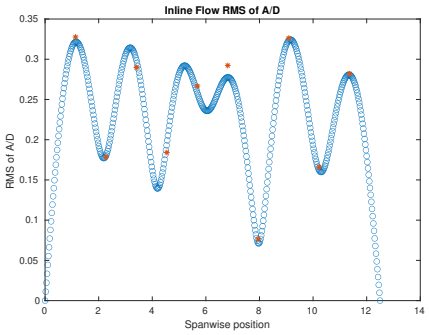

(b) Inline flow RMS profile case 3017.

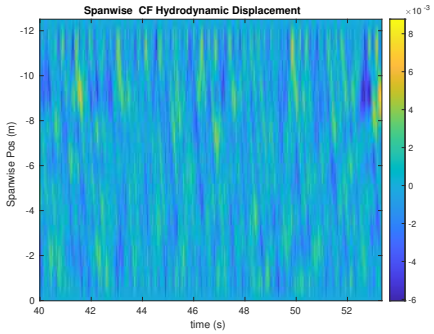

(c) Spanwise cross-flow hydrodynamic displacement case 3017.

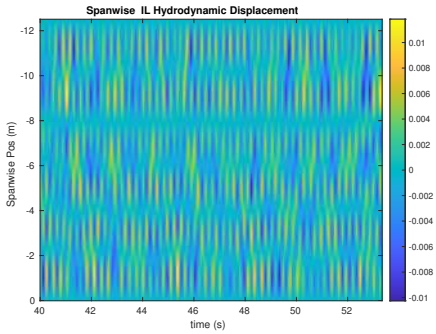

(d) Spanwise inline spectrum of hydrodynamic displacement case 3017.

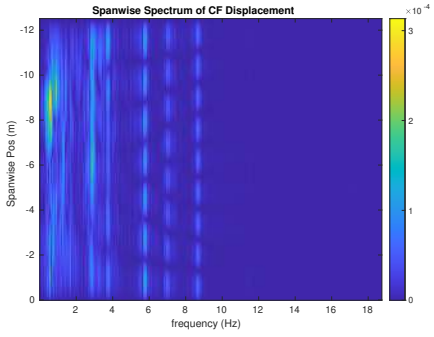

(e) Spanwise cross-flow spectrum of hydrodynamic displacement case 3017.

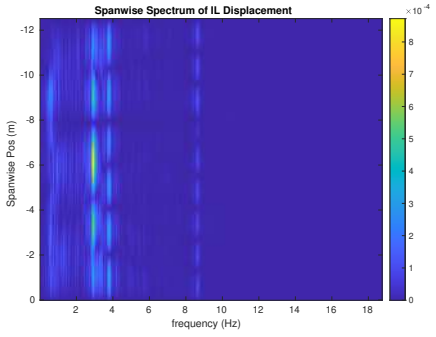

(f) Spanwise inline spectrum of hydrodynamic displacement case 3017.

Figure B-37: *Motion Analysis.* SCR case 3017.

NDP SCR test case 3019

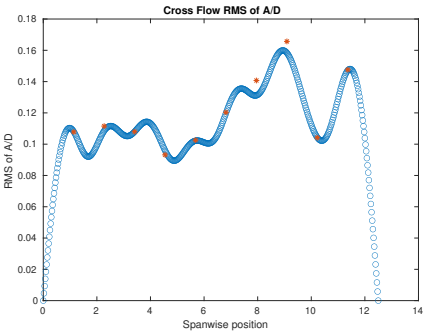

(a) Cross-flow RMS profile case 3019.

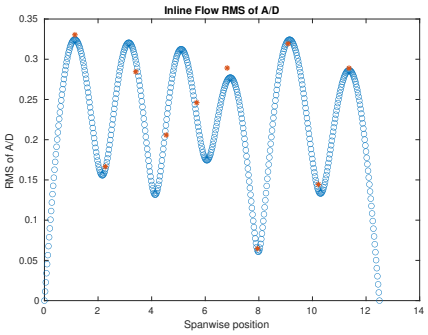

(b) Inline flow RMS profile case 3019.

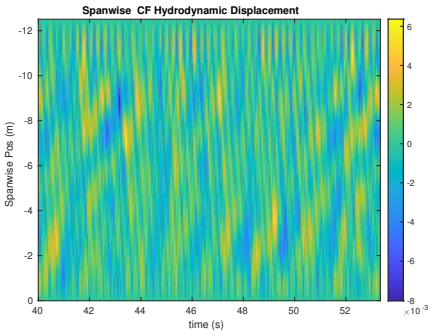

(c) Spanwise cross-flow hydrodynamic displacement case 3019.

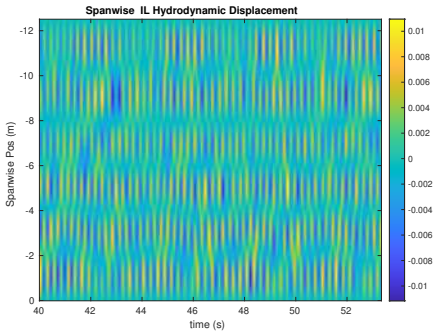

(d) Spanwise inline spectrum of hydrodynamic displacement case 3019.

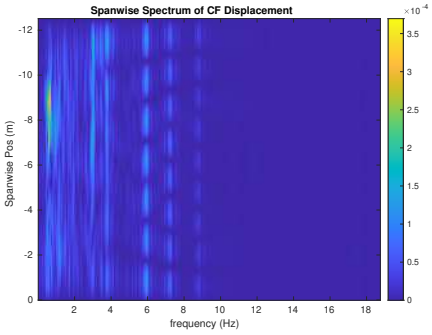

(e) Spanwise cross-flow spectrum of hydrodynamic displacement case 3019.

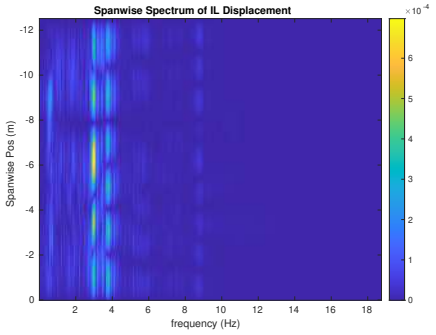

(f) Spanwise inline spectrum of hydrodynamic displacement case 3019.

Figure B-38: *Motion Analysis.* SCR case 3019.

NDP SCR test case 3021

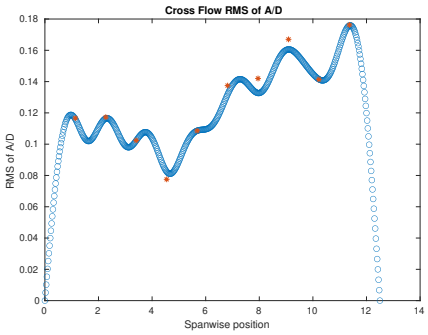

(a) Cross-flow RMS profile case 3021.

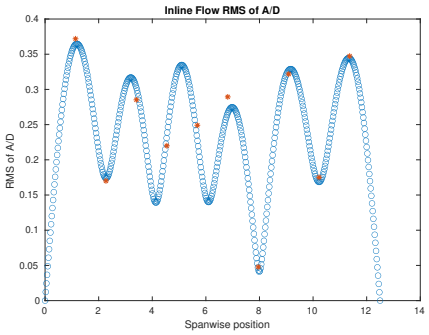

(b) Inline flow RMS profile case 3021.

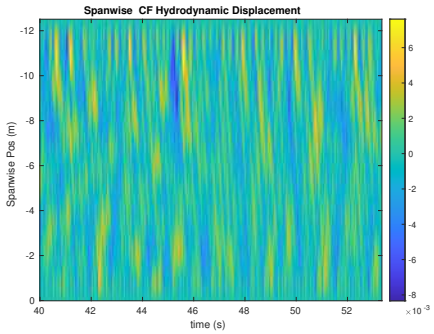

(c) Spanwise cross-flow hydrodynamic displacement case 3021.

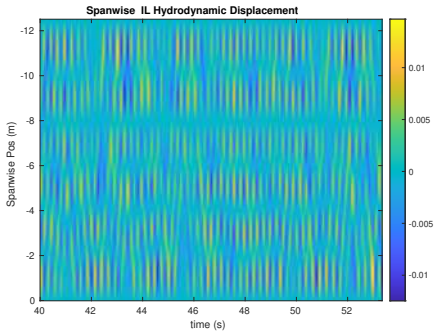

(d) Spanwise inline spectrum of hydrodynamic displacement case 3021.

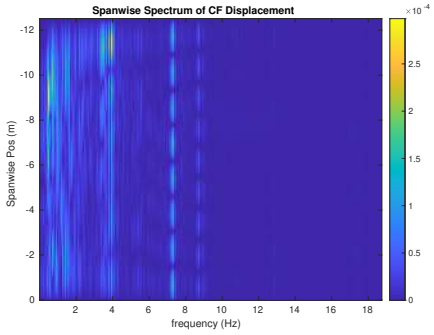

(e) Spanwise cross-flow spectrum of hydrodynamic displacement case 3021.

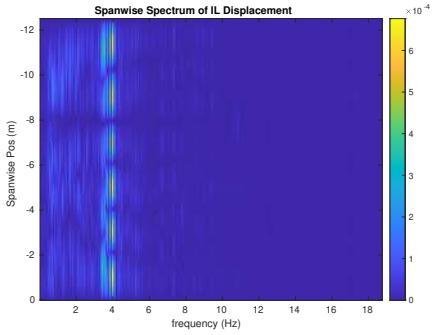

(f) Spanwise inline spectrum of hydrodynamic displacement case 3021.

Figure B-39: *Motion Analysis.* SCR case 3021.

NDP SCR test case 3023

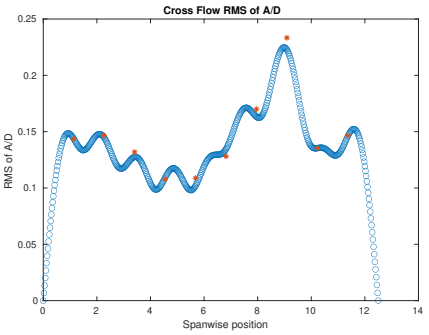

(a) Cross-flow RMS profile case 3023.

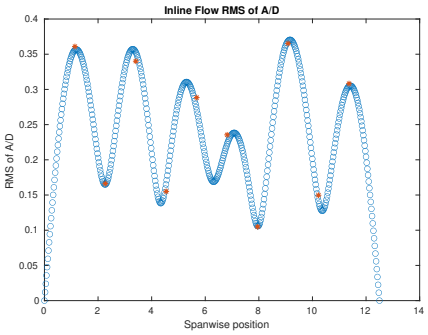

(b) Inline flow RMS profile case 3023.

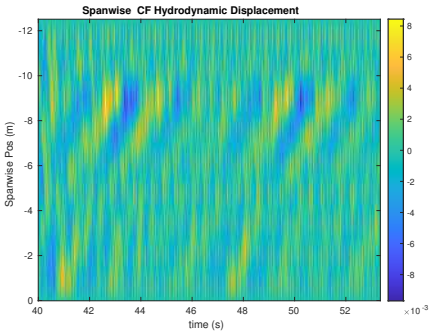

(c) Spanwise cross-flow hydrodynamic displacement case 3023.

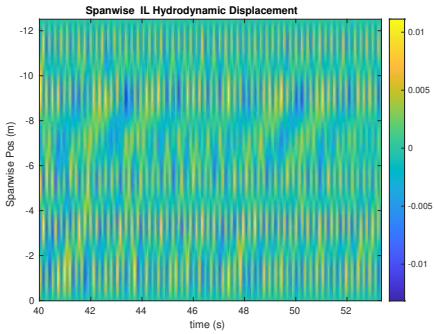

(d) Spanwise inline spectrum of hydrodynamic displacement case 3023.

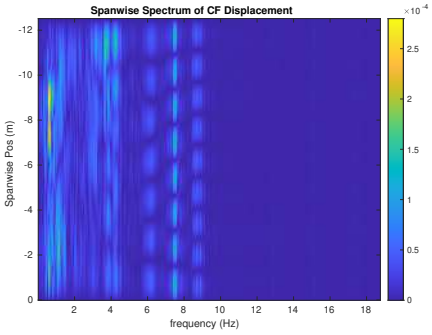

(e) Spanwise cross-flow spectrum of hydrodynamic displacement case 3023.

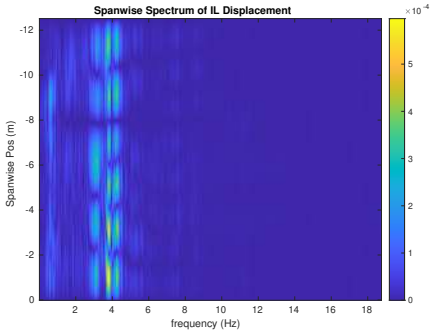

(f) Spanwise inline spectrum of hydrodynamic displacement case 3023.

Figure B-40: *Motion Analysis.* SCR case 3023.

NDP SCR test case 4001

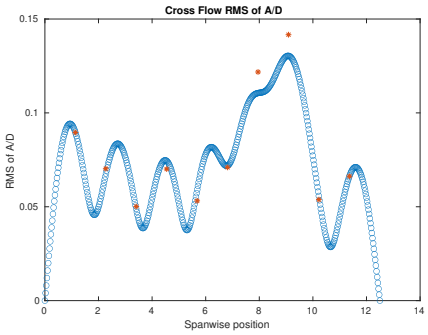

(a) Cross-flow RMS profile case 4001.

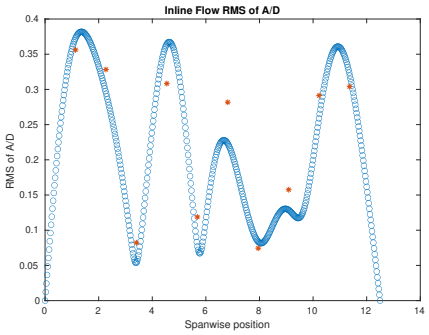

(b) Inline flow RMS profile case 4001.

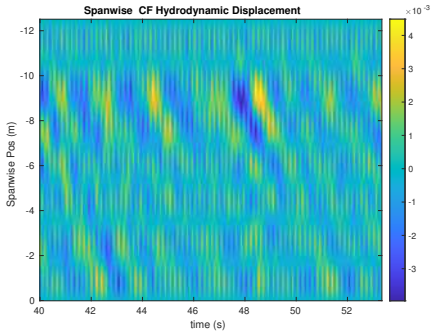

(c) Spanwise cross-flow hydrodynamic displacement case 4001.

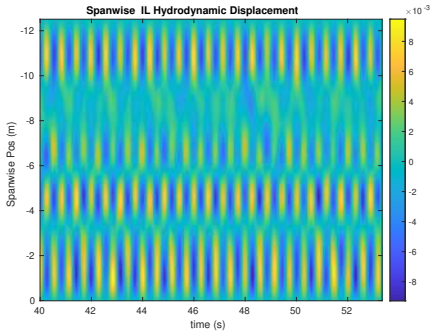

(d) Spanwise inline spectrum of hydrodynamic displacement case 4001.

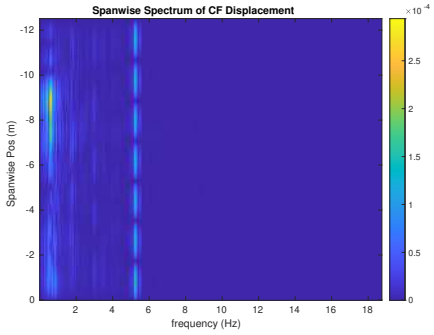

(e) Spanwise cross-flow spectrum of hydrodynamic displacement case 4001.

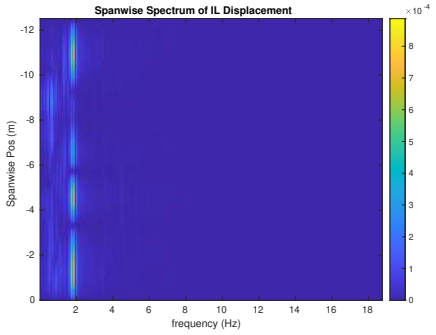

(f) Spanwise inline spectrum of hydrodynamic displacement case 4001.

Figure B-41: *Motion Analysis.* SCR case 4001.

NDP SCR test case 4005

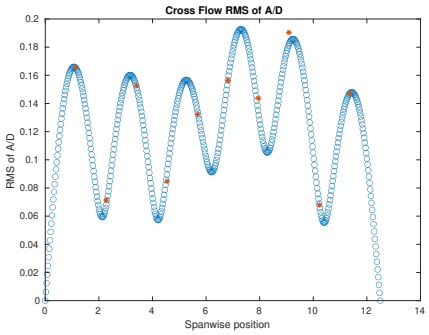

(a) Cross-flow RMS profile case 4005.

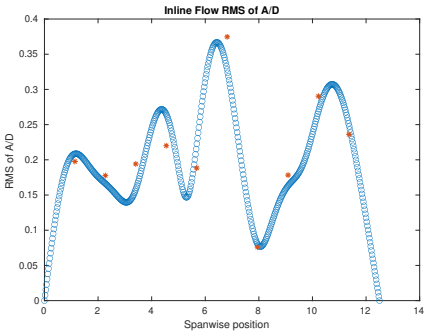

(b) Inline flow RMS profile case 4005.

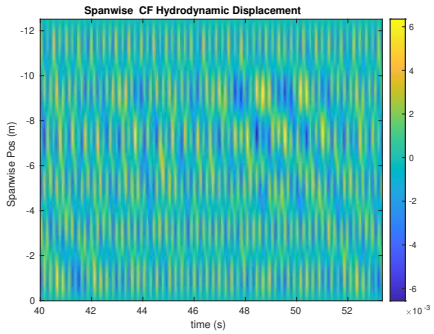

(c) Spanwise cross-flow hydrodynamic displacement case 4005.

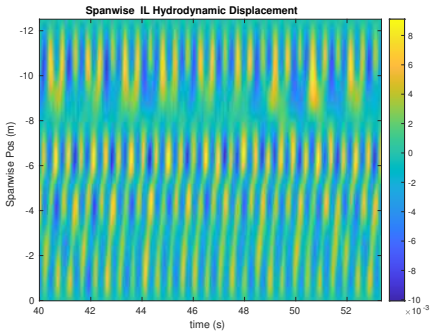

(d) Spanwise inline spectrum of hydrodynamic displacement case 4005.

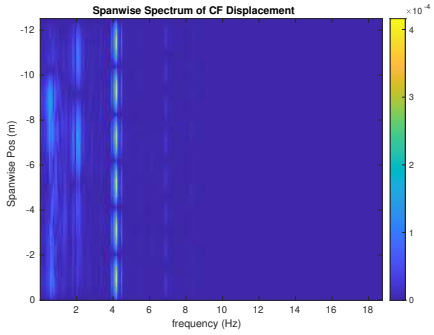

(e) Spanwise cross-flow spectrum of hydrodynamic displacement case 4005.

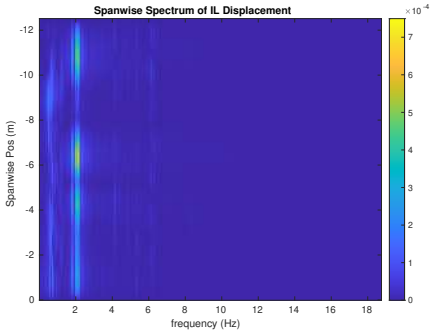

(f) Spanwise inline spectrum of hydrodynamic displacement case 4005.

Figure B-42: *Motion Analysis.* SCR case 4005.

NDP SCR test case 4007

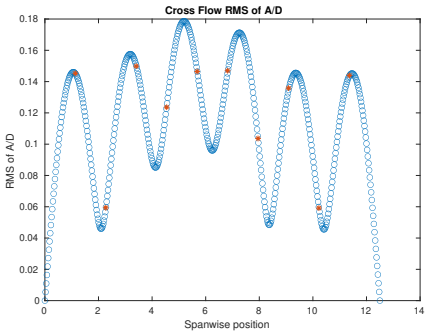

(a) Cross-flow RMS profile case 4007.

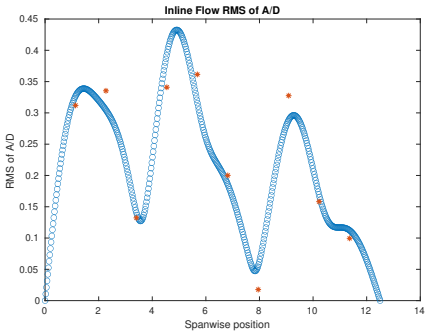

(b) Inline flow RMS profile case 4007.

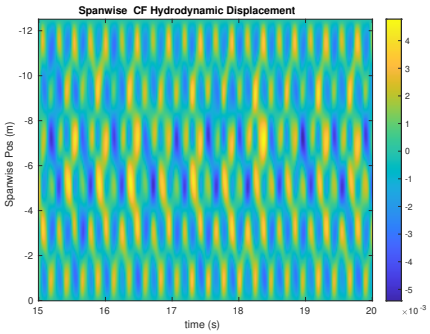

(c) Spanwise cross-flow hydrodynamic displacement case 4007.

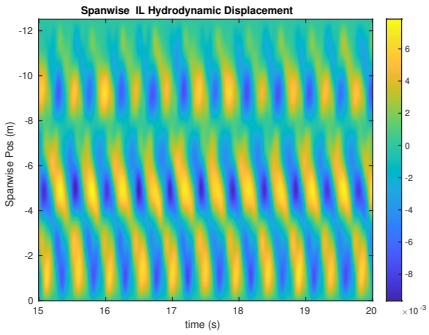

(d) Spanwise inline spectrum of hydrodynamic displacement case 4007.

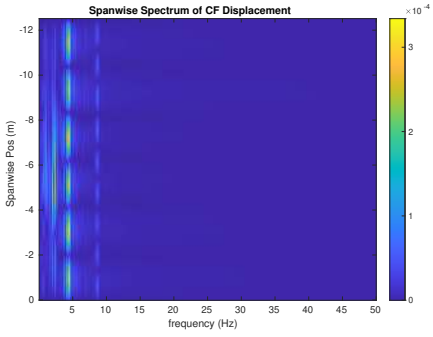

(e) Spanwise cross-flow spectrum of hydrodynamic displacement case 4007.

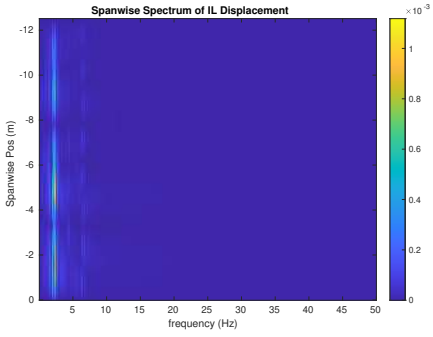

(f) Spanwise inline spectrum of hydrodynamic displacement case 4007.

Figure B-43: *Motion Analysis.* SCR case 4007.

NDP SCR test case 4011

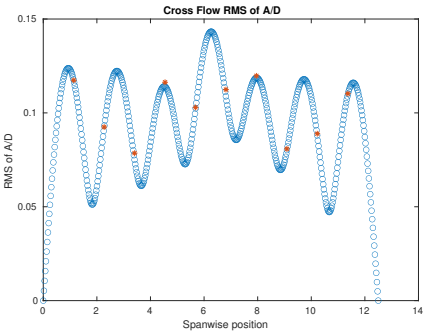

(a) Cross-flow RMS profile case 4011.

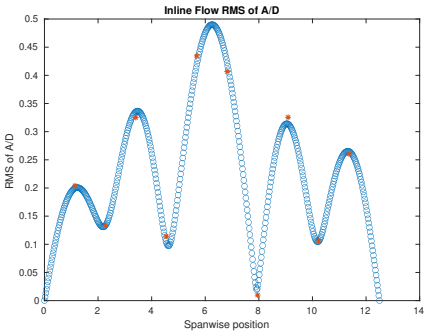

(b) Inline flow RMS profile case 4011.

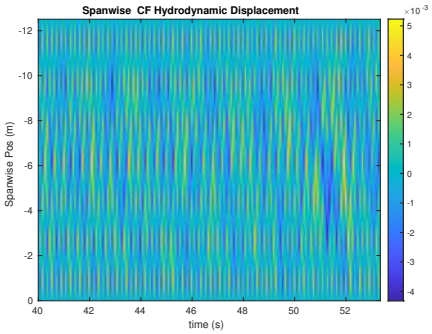

(c) Spanwise cross-flow hydrodynamic displacement case 4011.

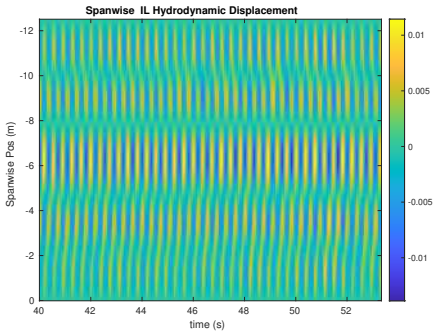

(d) Spanwise inline spectrum of hydrodynamic displacement case 4011.

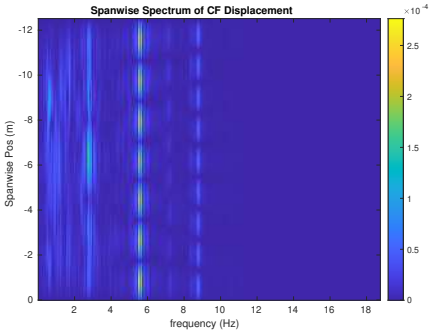

(e) Spanwise cross-flow spectrum of hydrodynamic displacement case 4011.

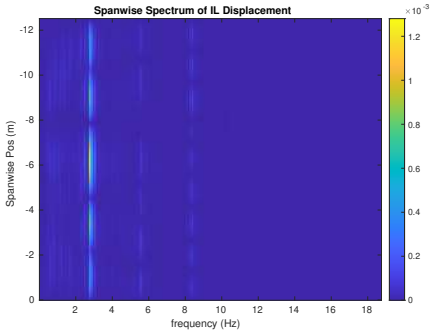

(f) Spanwise inline spectrum of hydrodynamic displacement case 4011.

Figure B-44: *Motion Analysis.* SCR case 4011.

NDP SCR test case 4013

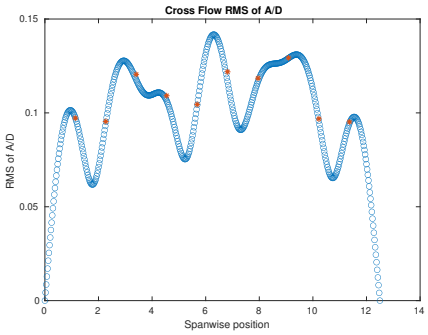

(a) Cross-flow RMS profile case 4013.

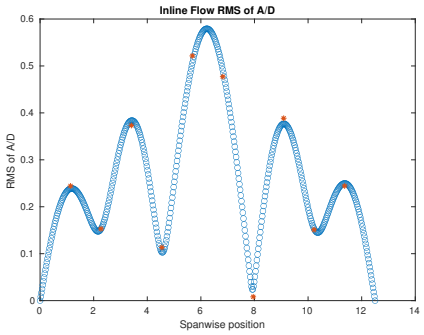

(b) Inline flow RMS profile case 4013.

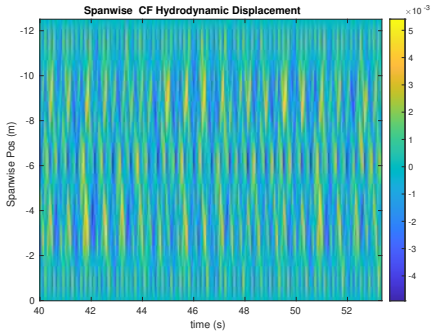

(c) Spanwise cross-flow hydrodynamic displacement case 4013.

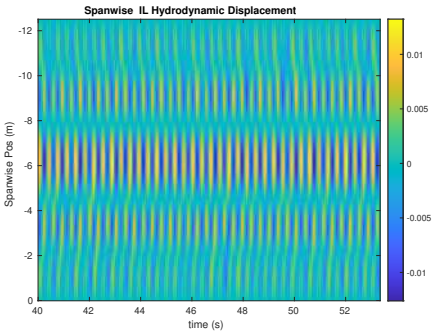

(d) Spanwise inline spectrum of hydrodynamic displacement case 4013.

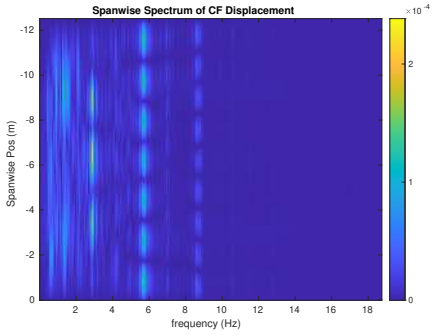

(e) Spanwise cross-flow spectrum of hydrodynamic displacement case 4013.

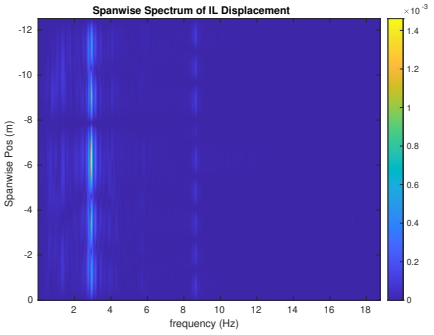

(f) Spanwise inline spectrum of hydrodynamic displacement case 4013.

Figure B-45: *Motion Analysis.* SCR case 4013.

NDP SCR test case 4017

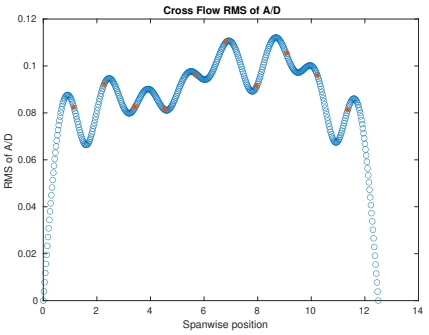

(a) Cross-flow RMS profile case 4017.

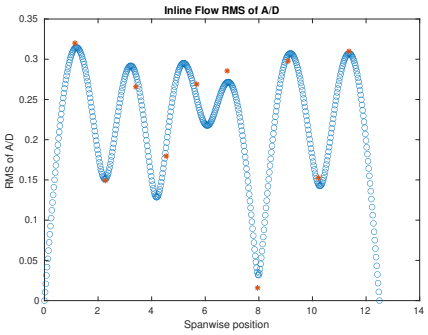

(b) Inline flow RMS profile case 4017.

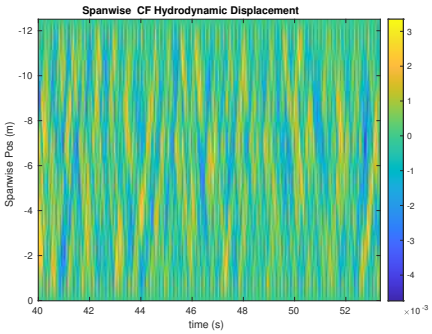

(c) Spanwise cross-flow hydrodynamic displacement case 4017.

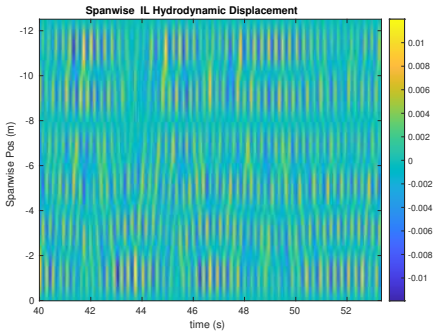

(d) Spanwise inline spectrum of hydrodynamic displacement case 4017.

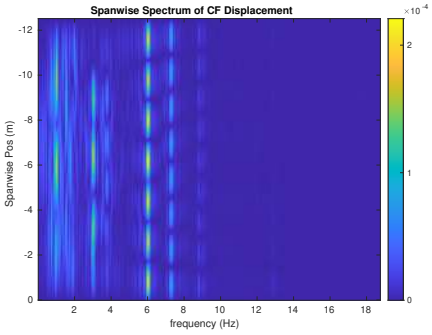

(e) Spanwise cross-flow spectrum of hydrodynamic displacement case 4017.

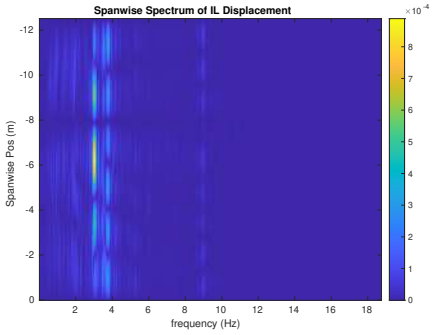

(f) Spanwise inline spectrum of hydrodynamic displacement case 4017.

Figure B-46: *Motion Analysis.* SCR case 4017.

NDP SCR test case 4019

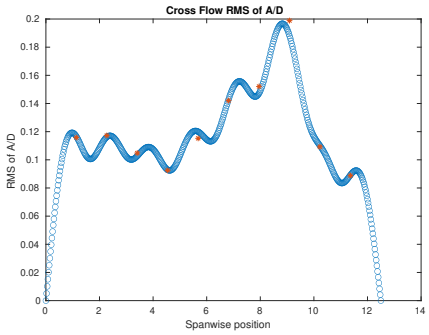

(a) Cross-flow RMS profile case 4019.

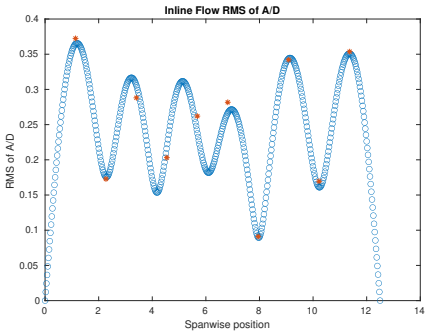

(b) Inline flow RMS profile case 4019.

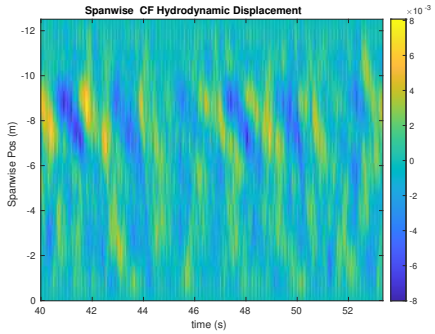

(c) Spanwise cross-flow hydrodynamic displacement case 4019.

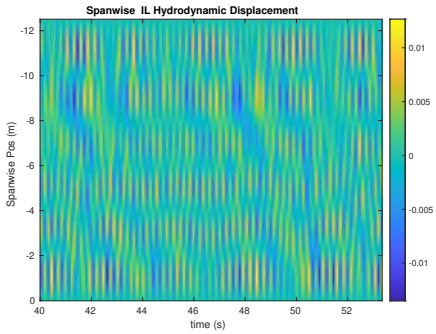

(d) Spanwise inline spectrum of hydrodynamic displacement case 4019.

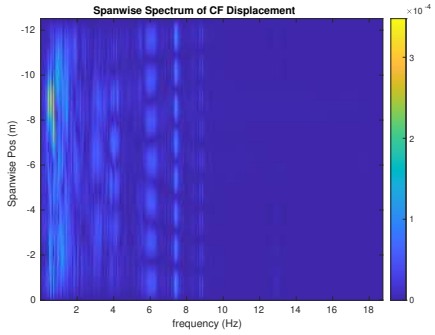

(e) Spanwise cross-flow spectrum of hydrodynamic displacement case 4019.

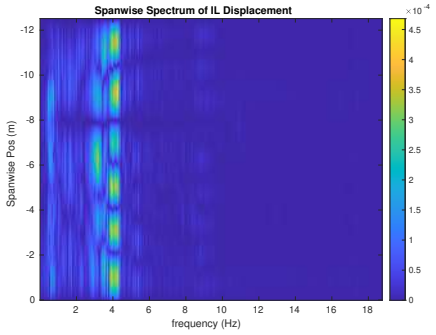

(f) Spanwise inline spectrum of hydrodynamic displacement case 4019.

Figure B-47: *Motion Analysis.* SCR case 4019.

NDP SCR test case 4021

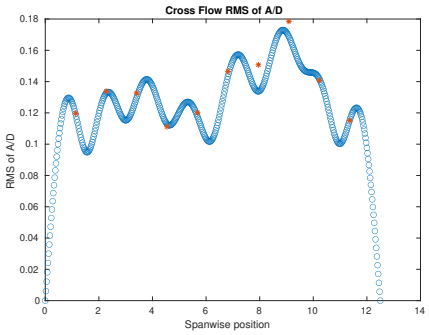

(a) Cross-flow RMS profile case 4021.

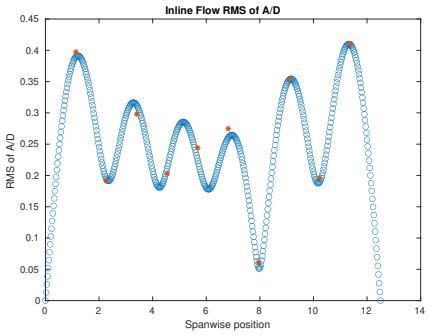

(b) Inline flow RMS profile case 4021.

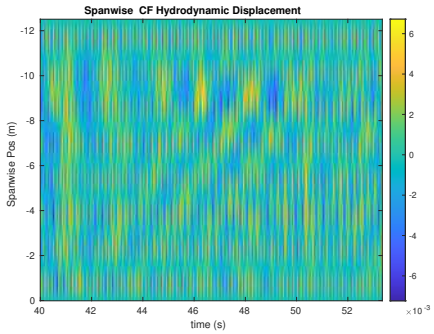

(c) Spanwise cross-flow hydrodynamic displacement case 4021.

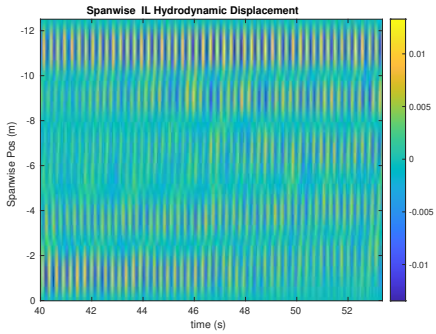

(d) Spanwise inline spectrum of hydrodynamic displacement case 4021.

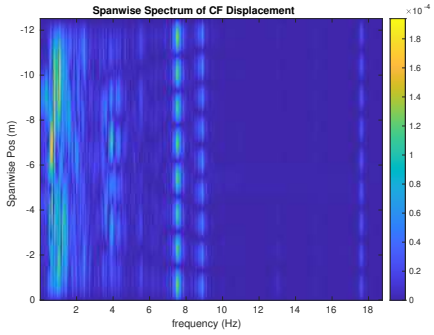

(e) Spanwise cross-flow spectrum of hydrodynamic displacement case 4021.

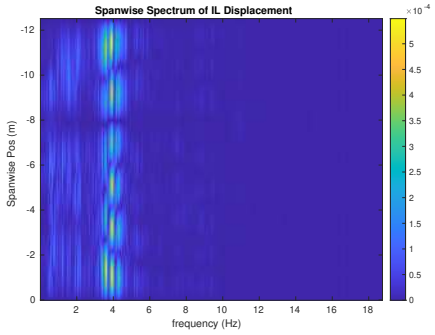

(f) Spanwise inline spectrum of hydrodynamic displacement case 4021.

Figure B-48: *Motion Analysis.* SCR case 4021.

NDP SCR test case 4023

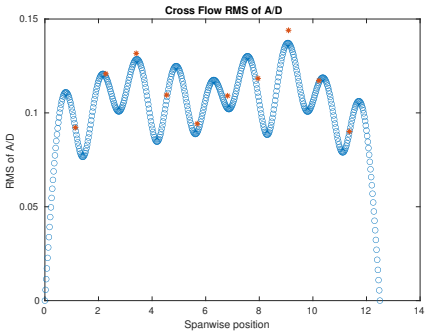

(a) Cross-flow RMS profile case 4023.

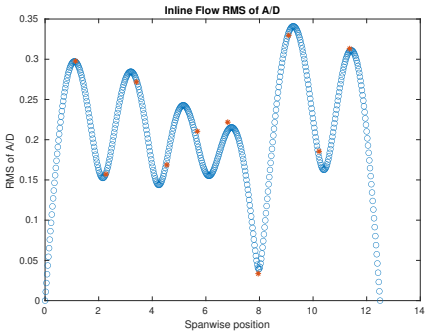

(b) Inline flow RMS profile case 4023.

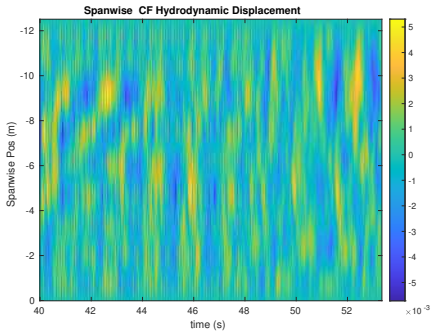

(c) Spanwise cross-flow hydrodynamic displacement case 4023.

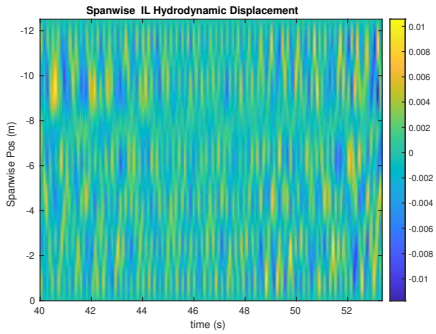

(d) Spanwise inline spectrum of hydrodynamic displacement case 4023.

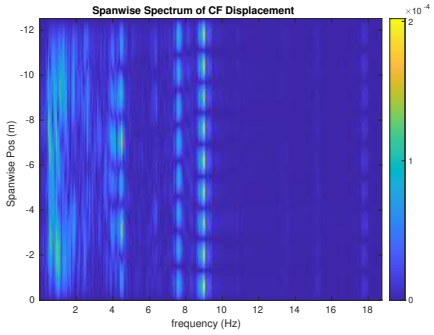

(e) Spanwise cross-flow spectrum of hydrodynamic displacement case 4023.

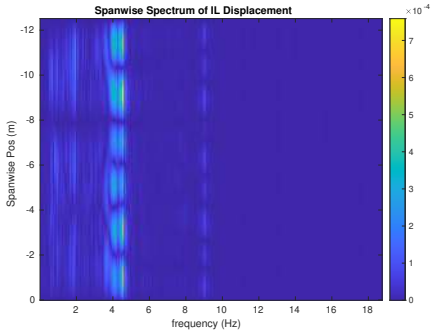

(f) Spanwise inline spectrum of hydrodynamic displacement case 4023.

Figure B-49: *Motion Analysis.* SCR case 4023.

NDP SCR test case 1000

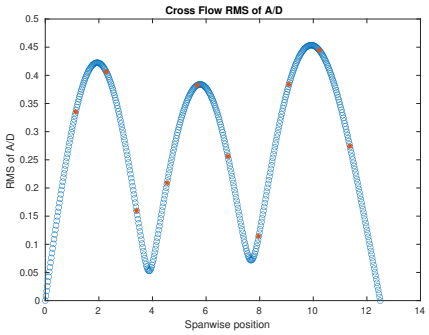

(a) Cross-flow RMS profile case 1000.

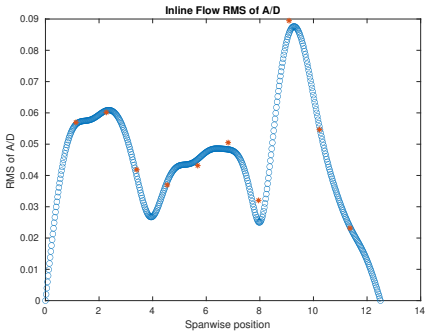

(b) Inline flow RMS profile case 1000.

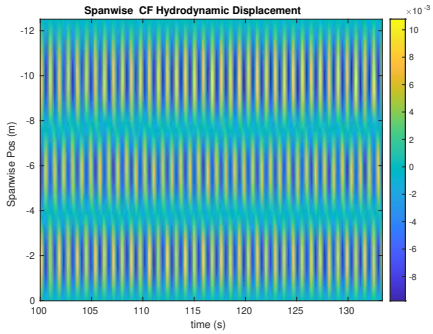

(c) Spanwise cross-flow hydrodynamic displacement case 1000.

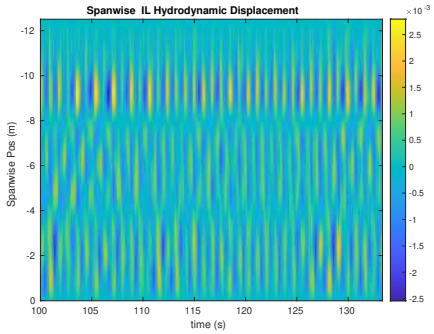

(d) Spanwise inline spectrum of hydrodynamic displacement case 1000.

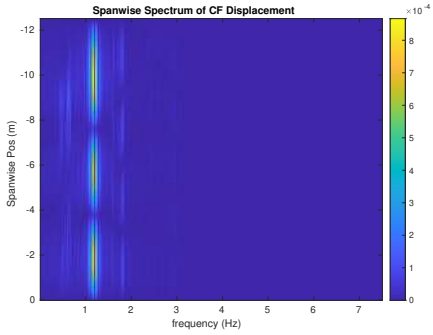

(e) Spanwise cross-flow spectrum of hydrodynamic displacement case 1000.

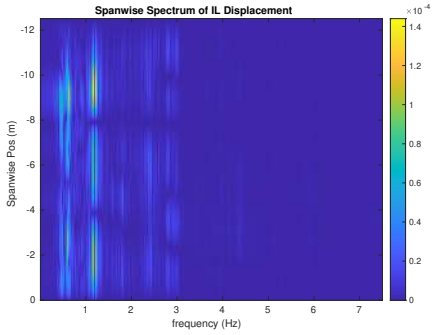

(f) Spanwise inline spectrum of hydrodynamic displacement case 1000.

Figure B-50: *Motion Analysis.* SCR case 1000.

NDP SCR test case 5001

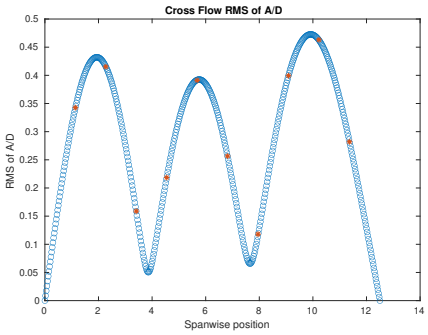

(a) Cross-flow RMS profile case 5001.

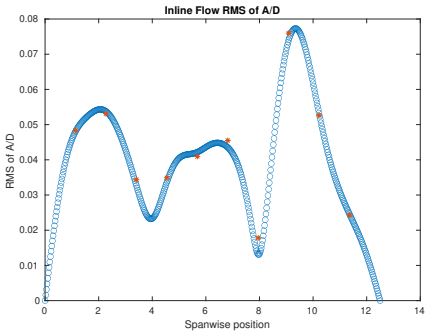

(b) Inline flow RMS profile case 5001.

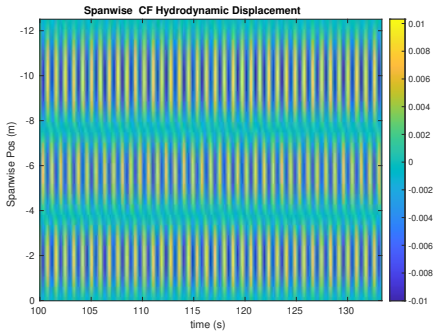

(c) Spanwise cross-flow hydrodynamic displacement case 5001.

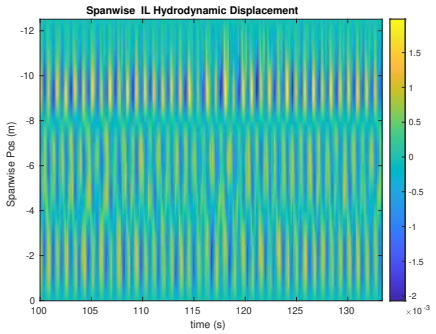

(d) Spanwise inline spectrum of hydrodynamic displacement case 5001.

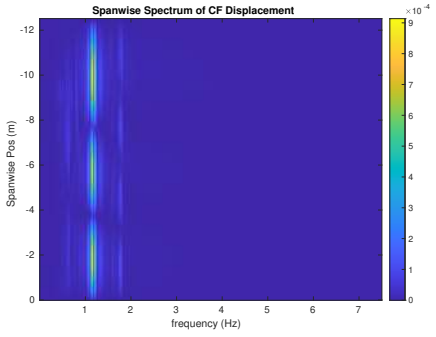

(e) Spanwise cross-flow spectrum of hydrodynamic displacement case 5001.

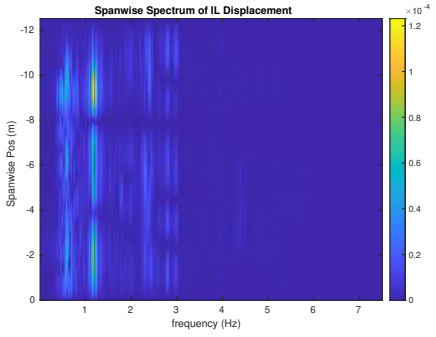

(f) Spanwise inline spectrum of hydrodynamic displacement case 5001.

Figure B-51: *Motion Analysis.* SCR case 5001.

NDP SCR test case 1002

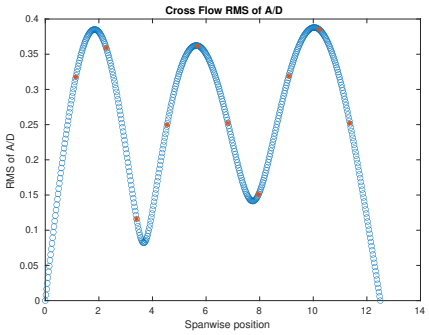

(a) Cross-flow RMS profile case 1002.

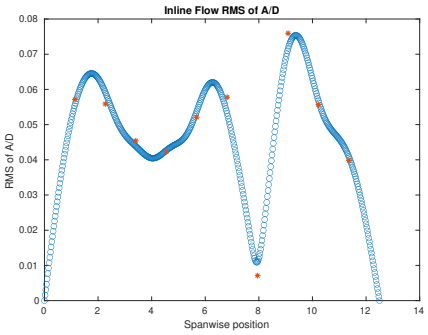

(b) Inline flow RMS profile case 1002.

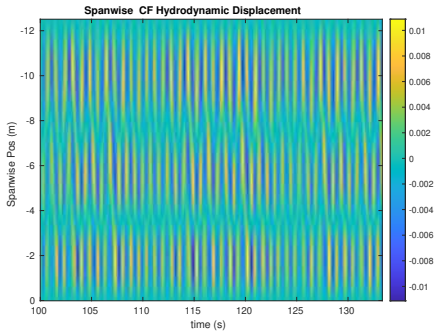

(c) Spanwise cross-flow hydrodynamic displacement case 1002.

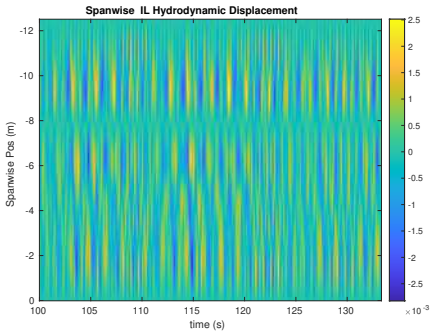

(d) Spanwise inline spectrum of hydrodynamic displacement case 1002.

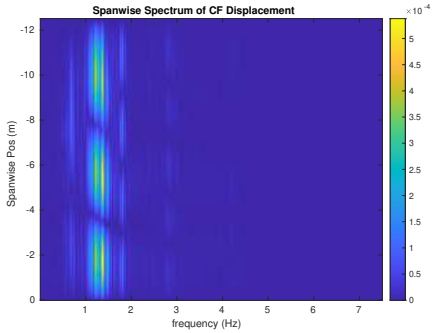

(e) Spanwise cross-flow spectrum of hydrodynamic displacement case 1002.

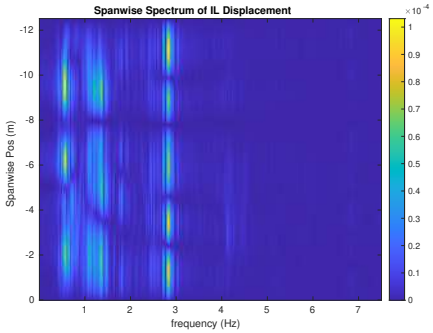

(f) Spanwise inline spectrum of hydrodynamic displacement case 1002.

Figure B-52: *Motion Analysis.* SCR case 1002.

NDP SCR test case 1004

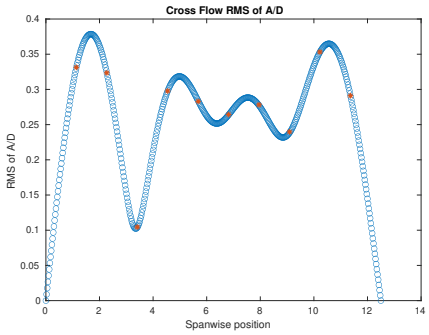

(a) Cross-flow RMS profile case 1004.

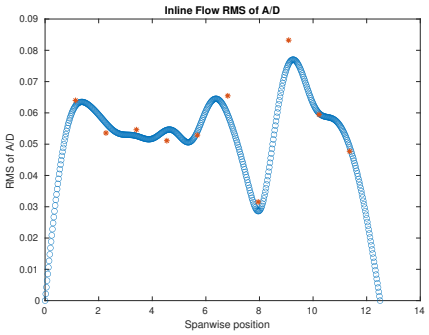

(b) Inline flow RMS profile case 1004.

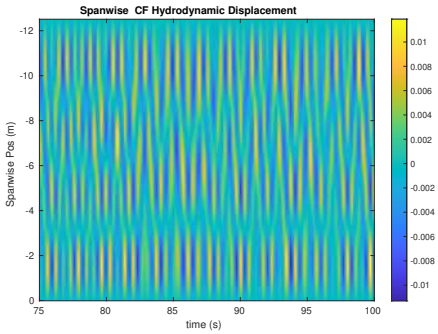

(c) Spanwise cross-flow hydrodynamic displacement case 1004.

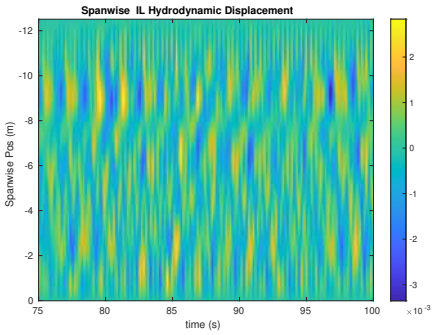

(d) Spanwise inline spectrum of hydrodynamic displacement case 1004.

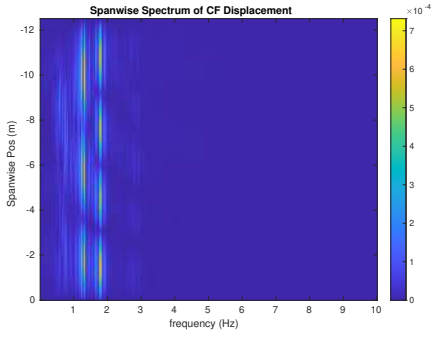

(e) Spanwise cross-flow spectrum of hydrodynamic displacement case 1004.

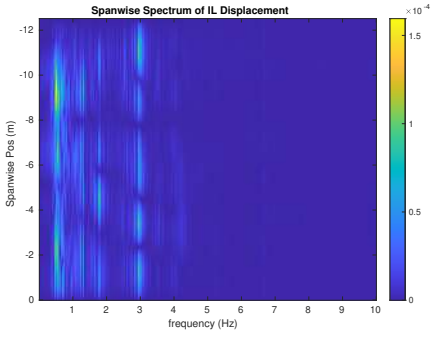

(f) Spanwise inline spectrum of hydrodynamic displacement case 1004.

Figure B-53: *Motion Analysis.* SCR case 1004.

NDP SCR test case 1006

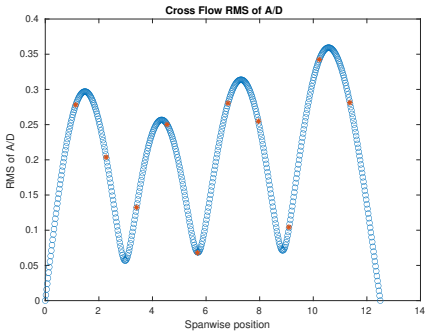

(a) Cross-flow RMS profile case 1006.

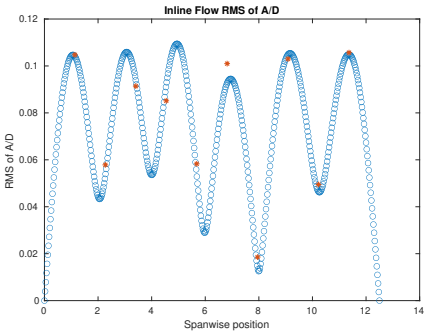

(b) Inline flow RMS profile case 1006.

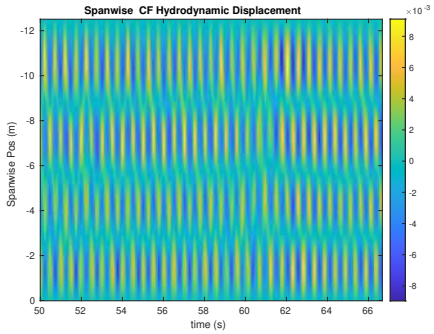

(c) Spanwise cross-flow hydrodynamic displacement case 1006.

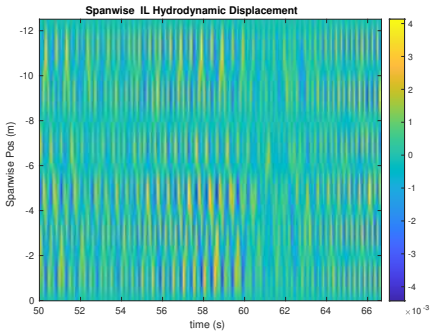

(d) Spanwise inline spectrum of hydrodynamic displacement case 1006.

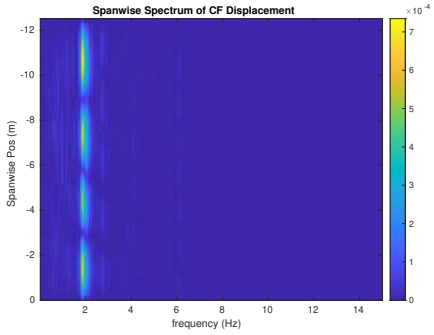

(e) Spanwise cross-flow spectrum of hydrodynamic displacement case 1006.

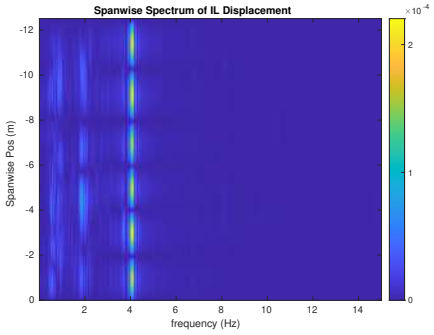

(f) Spanwise inline spectrum of hydrodynamic displacement case 1006.

Figure B-54: *Motion Analysis.* SCR case 1006.

NDP SCR test case 1008

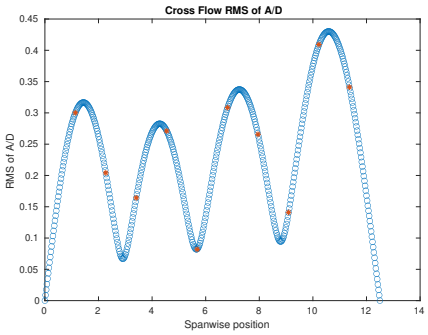

(a) Cross-flow RMS profile case 1008.

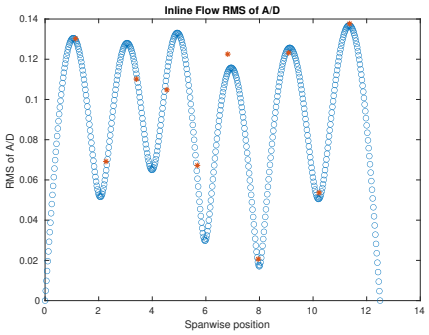

(b) Inline flow RMS profile case 1008.

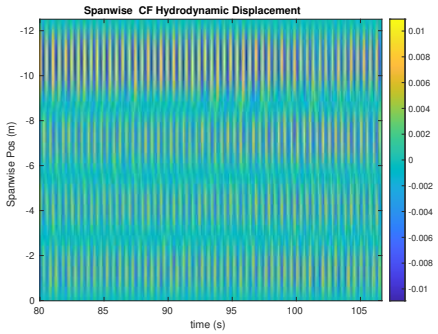

(c) Spanwise cross-flow hydrodynamic displacement case 1008.

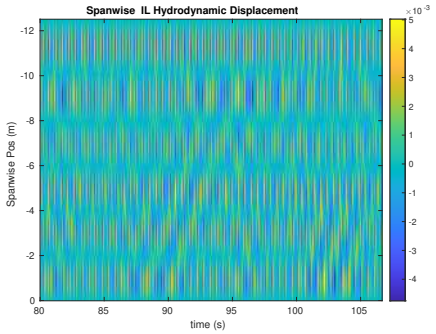

(d) Spanwise inline spectrum of hydrodynamic displacement case 1008.

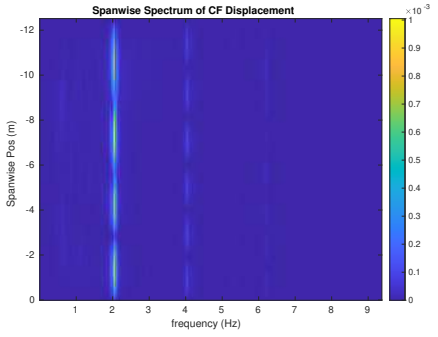

(e) Spanwise cross-flow spectrum of hydrodynamic displacement case 1008.

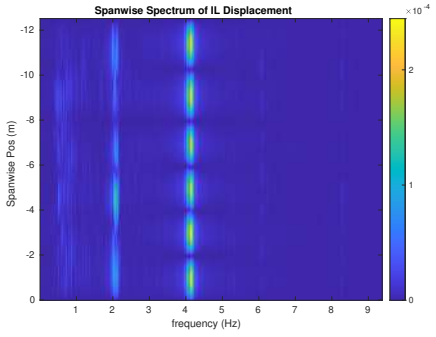

(f) Spanwise inline spectrum of hydrodynamic displacement case 1008.

Figure B-55: *Motion Analysis.* SCR case 1008.

NDP SCR test case 1010

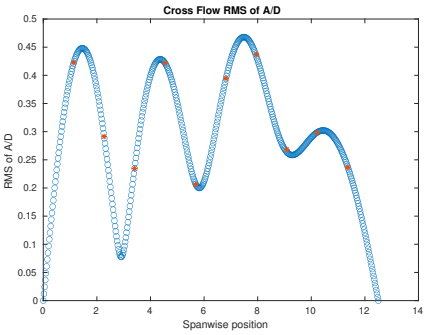

(a) Cross-flow RMS profile case 1010.

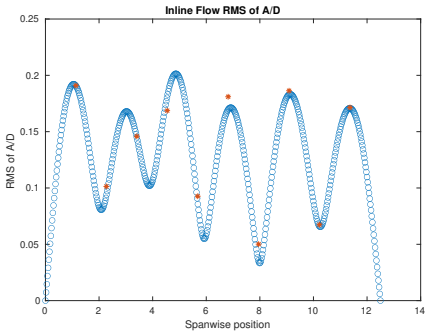

(b) Inline flow RMS profile case 1010.

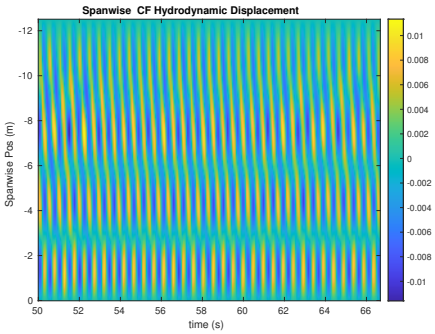

(c) Spanwise cross-flow hydrodynamic displacement case 1010.

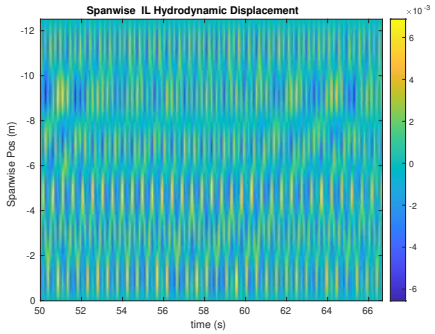

(d) Spanwise inline spectrum of hydrodynamic displacement case 1010.

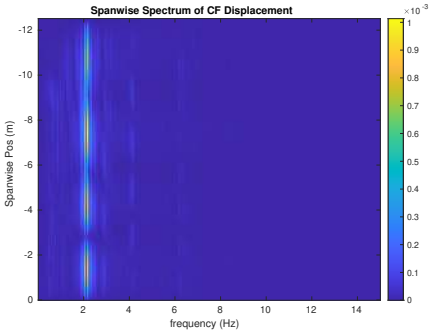

(e) Spanwise cross-flow spectrum of hydrodynamic displacement case 1010.

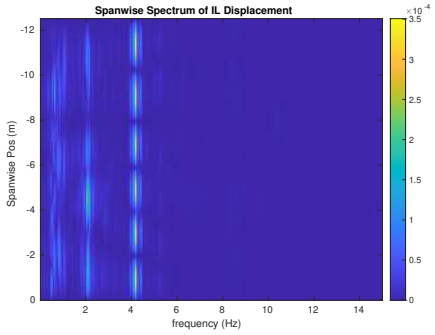

(f) Spanwise inline spectrum of hydrodynamic displacement case 1010.

Figure B-56: *Motion Analysis.* SCR case 1010.

NDP SCR test case 1012

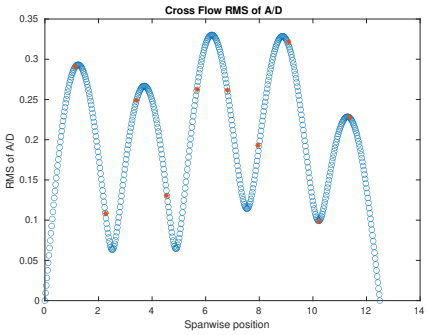

(a) Cross-flow RMS profile case 1012.

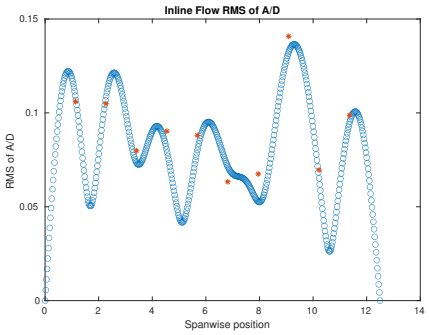

(b) Inline flow RMS profile case 1012.

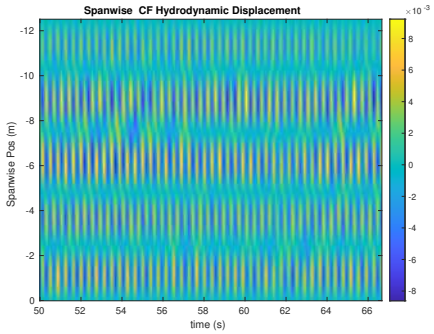

(c) Spanwise cross-flow hydrodynamic displacement case 1012.

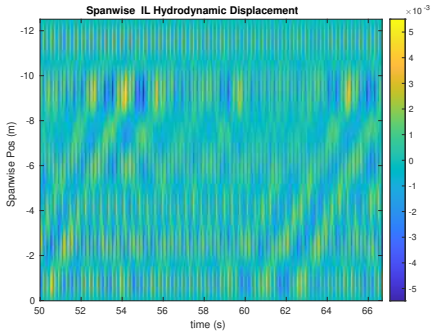

(d) Spanwise inline spectrum of hydrodynamic displacement case 1012.

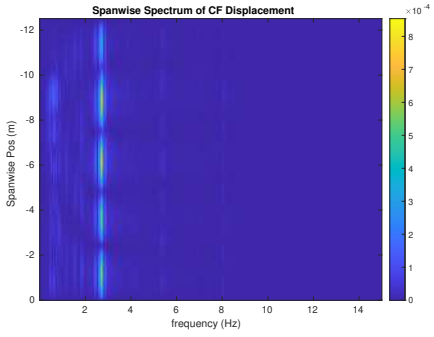

(e) Spanwise cross-flow spectrum of hydrodynamic displacement case 1012.

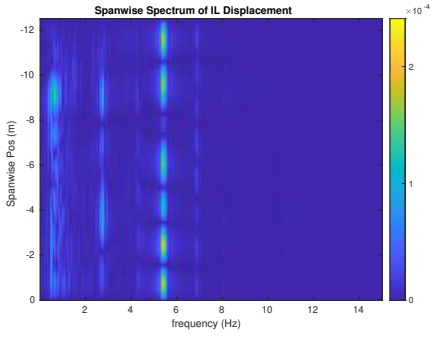

(f) Spanwise inline spectrum of hydrodynamic displacement case 1012.

Figure B-57: *Motion Analysis.* SCR case 1012.

NDP SCR test case 5012

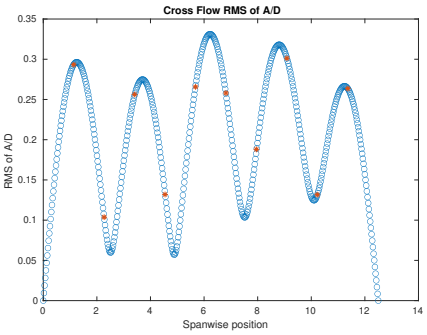

(a) Cross-flow RMS profile case 5012.

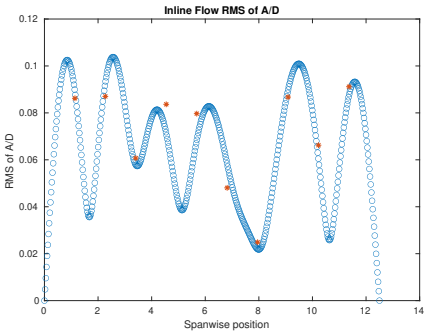

(b) Inline flow RMS profile case 5012.

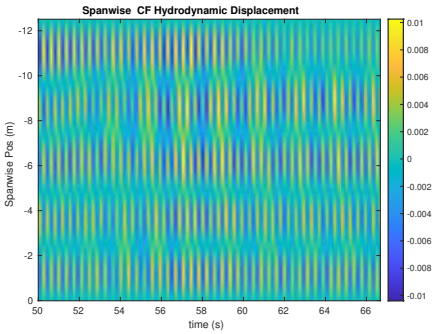

(c) Spanwise cross-flow hydrodynamic displacement case 5012.

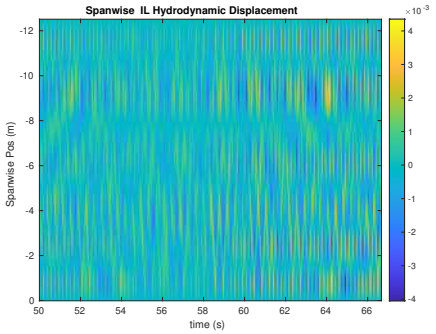

(d) Spanwise inline spectrum of hydrodynamic displacement case 5012.

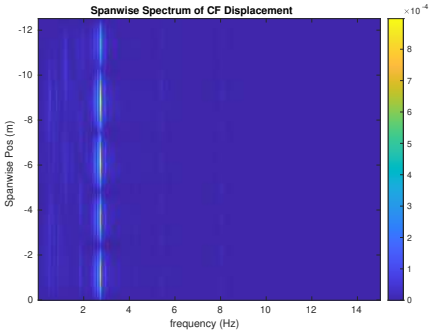

(e) Spanwise cross-flow spectrum of hydrodynamic displacement case 5012.

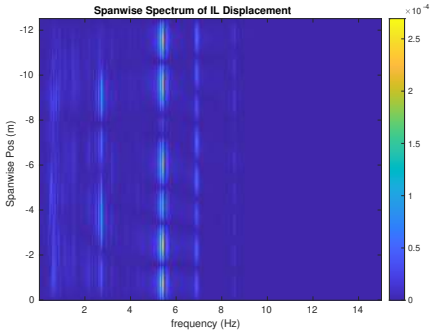

(f) Spanwise inline spectrum of hydrodynamic displacement case 5012.

Figure B-58: *Motion Analysis.* SCR case 5012.

NDP SCR test case 1014

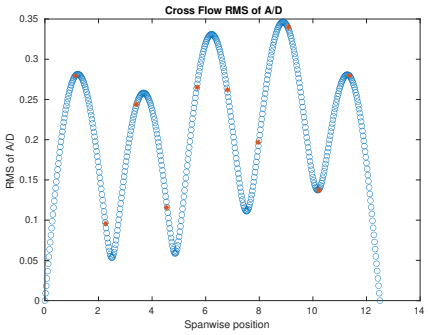

(a) Cross-flow RMS profile case 1014.

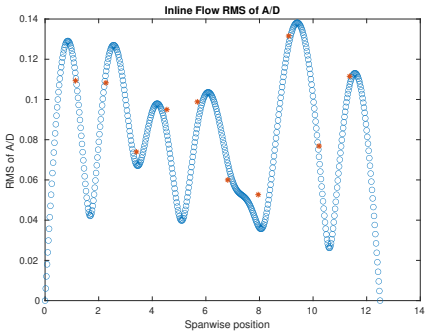

(b) Inline flow RMS profile case 1014.

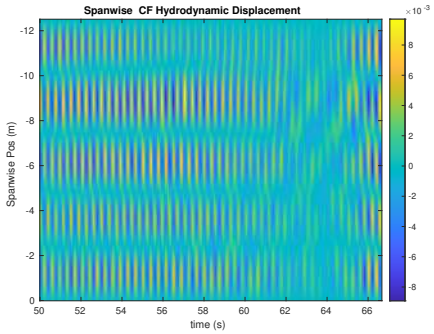

(c) Spanwise cross-flow hydrodynamic displacement case 1014.

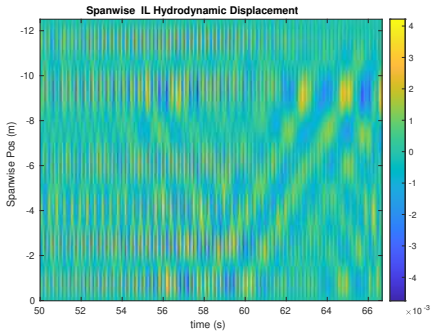

(d) Spanwise inline spectrum of hydrodynamic displacement case 1014.

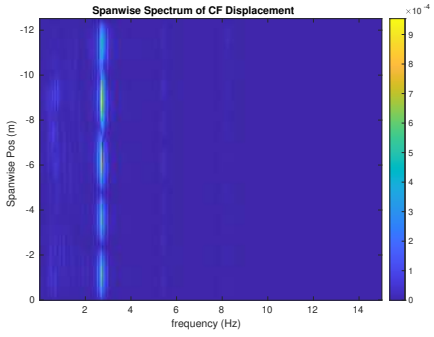

(e) Spanwise cross-flow spectrum of hydrodynamic displacement case 1014.

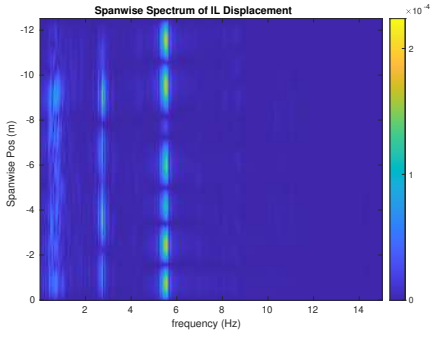

(f) Spanwise inline spectrum of hydrodynamic displacement case 1014.

Figure B-59: *Motion Analysis.* SCR case 1014.

NDP SCR test case 1016

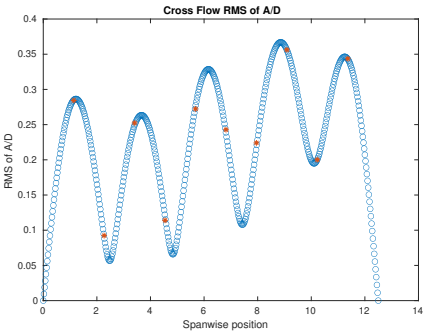

(a) Cross-flow RMS profile case 1016.

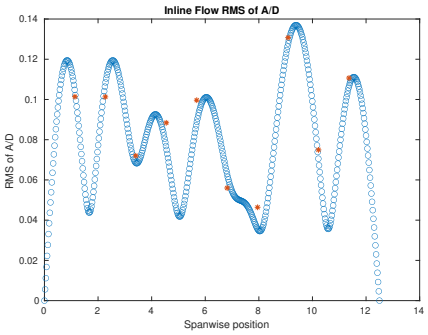

(b) Inline flow RMS profile case 1016.

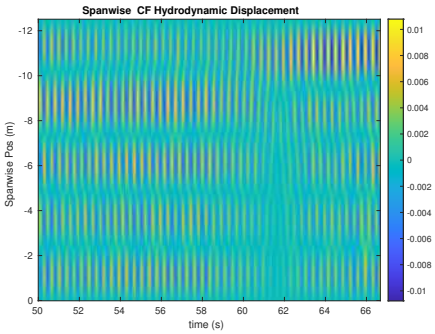

(c) Spanwise cross-flow hydrodynamic displacement case 1016.

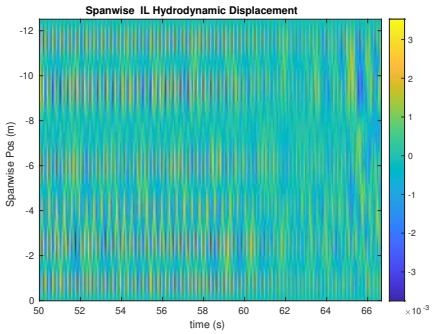

(d) Spanwise inline spectrum of hydrodynamic displacement case 1016.

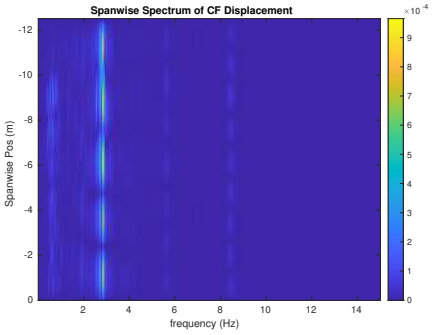

(e) Spanwise cross-flow spectrum of hydrodynamic displacement case 1016.

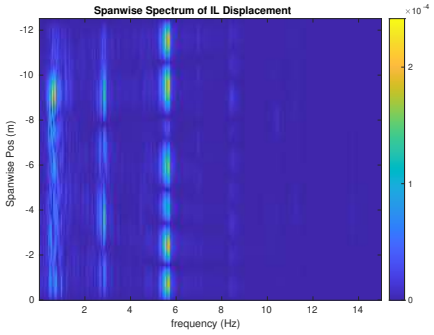

(f) Spanwise inline spectrum of hydrodynamic displacement case 1016.

Figure B-60: *Motion Analysis.* SCR case 1016.

NDP SCR test case 1018

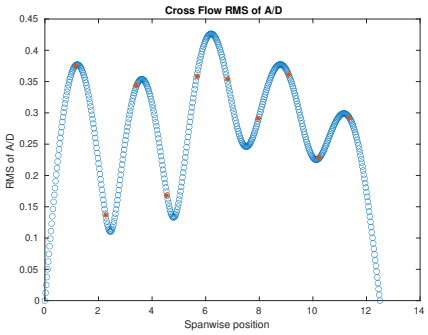

(a) Cross-flow RMS profile case 1018.

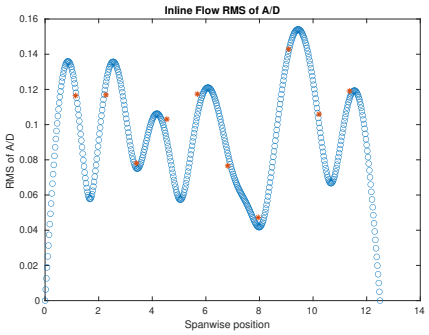

(b) Inline flow RMS profile case 1018.

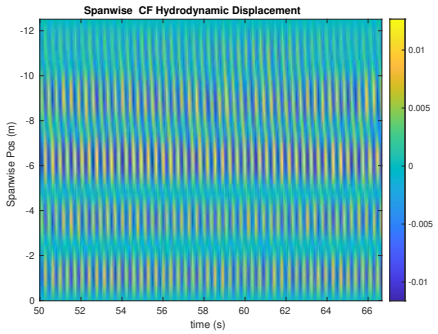

(c) Spanwise cross-flow hydrodynamic displacement case 1018.

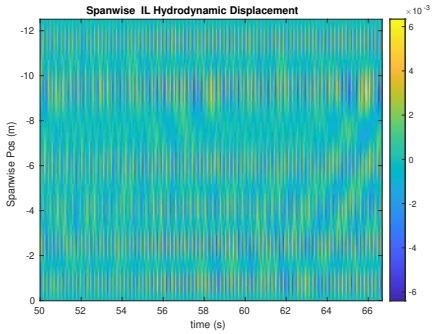

(d) Spanwise inline spectrum of hydrodynamic displacement case 1018.

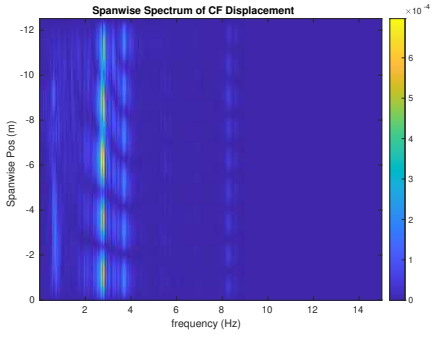

(e) Spanwise cross-flow spectrum of hydrodynamic displacement case 1018.

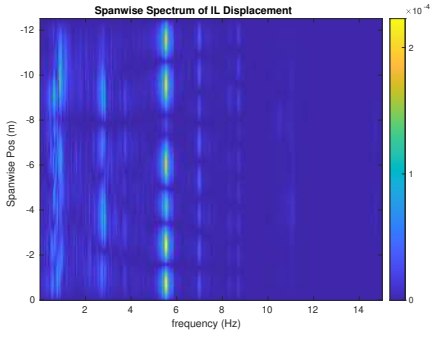

(f) Spanwise inline spectrum of hydrodynamic displacement case 1018.

Figure B-61: *Motion Analysis.* SCR case 1018.

NDP SCR test case 5018

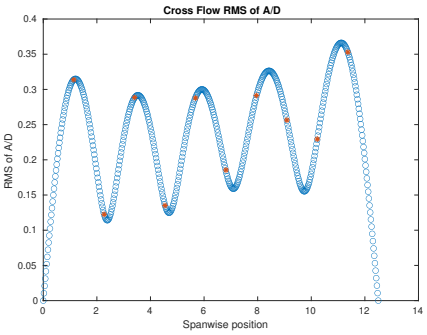

(a) Cross-flow RMS profile case 5018.

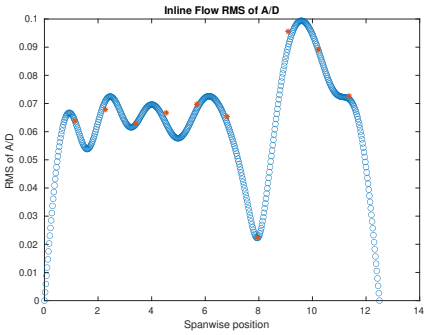

(b) Inline flow RMS profile case 5018.

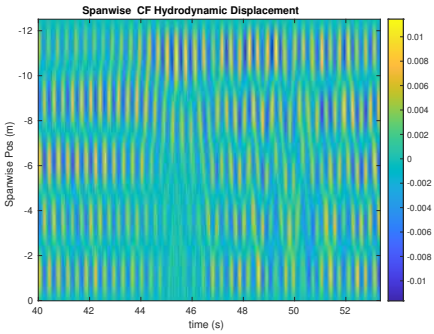

(c) Spanwise cross-flow hydrodynamic displacement case 5018.

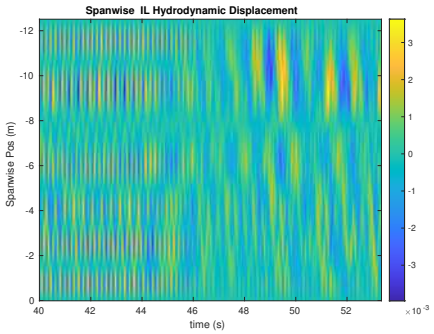

(d) Spanwise inline spectrum of hydrodynamic displacement case 5018.

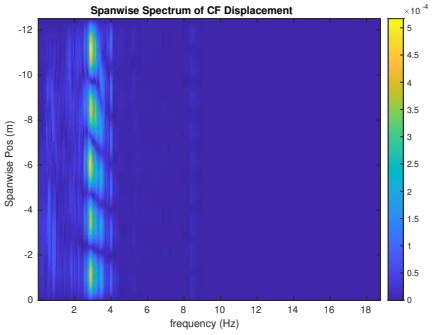

(e) Spanwise cross-flow spectrum of hydrodynamic displacement case 5018.

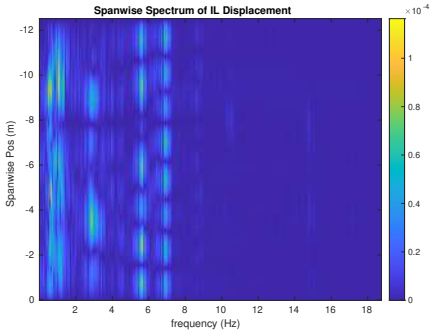

(f) Spanwise inline spectrum of hydrodynamic displacement case 5018.

Figure B-62: *Motion Analysis.* SCR case 5018.

NDP SCR test case 1020

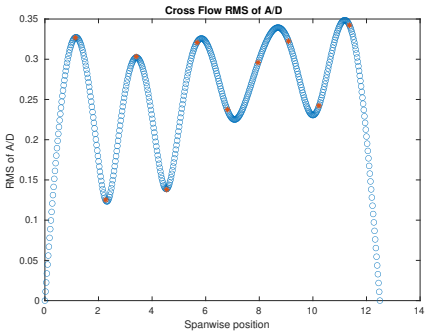

(a) Cross-flow RMS profile case 1020.

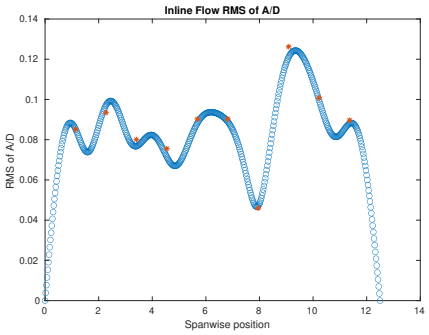

(b) Inline flow RMS profile case 1020.

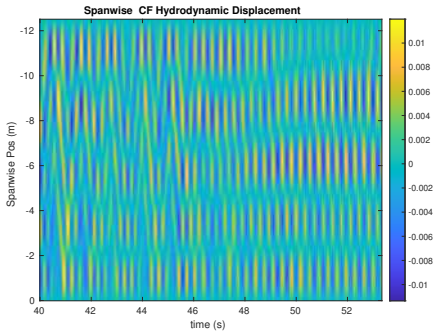

(c) Spanwise cross-flow hydrodynamic displacement case 1020.

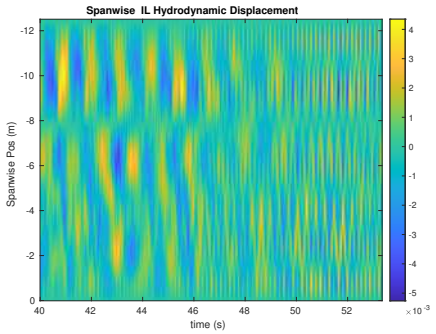

(d) Spanwise inline spectrum of hydrodynamic displacement case 1020.

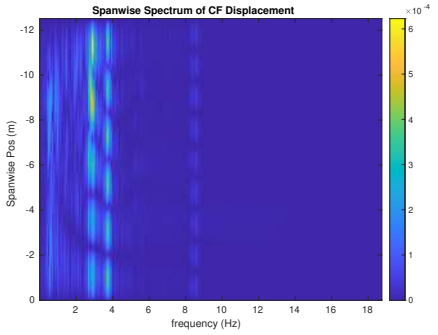

(e) Spanwise cross-flow spectrum of hydrodynamic displacement case 1020.

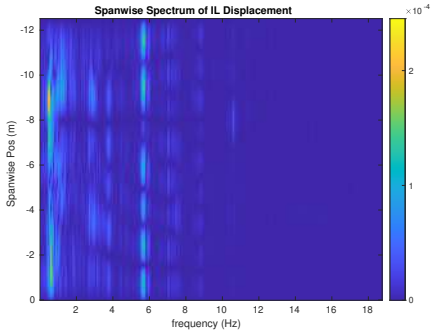

(f) Spanwise inline spectrum of hydrodynamic displacement case 1020.

Figure B-63: *Motion Analysis.* SCR case 1020.

NDP SCR test case 1022

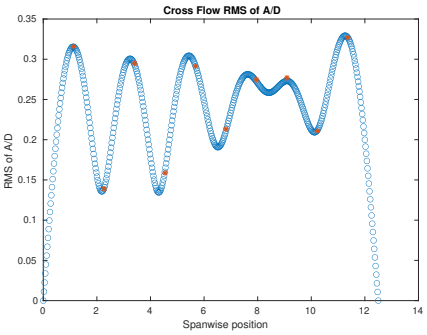

(a) Cross-flow RMS profile case 1022.

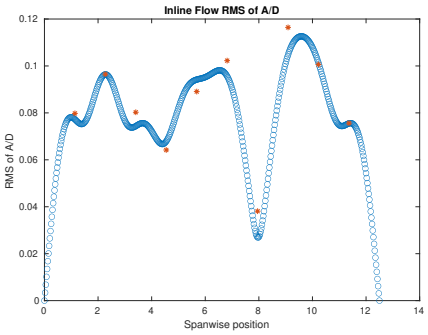

(b) Inline flow RMS profile case 1022.

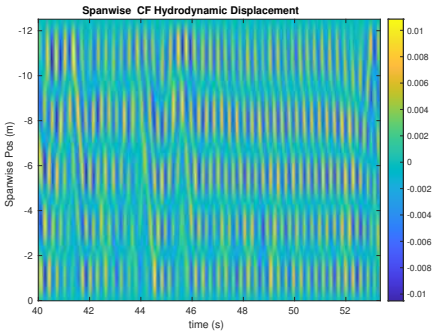

(c) Spanwise cross-flow hydrodynamic displacement case 1022.

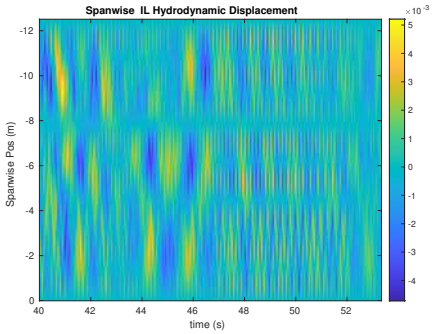

(d) Spanwise inline spectrum of hydrodynamic displacement case 1022.

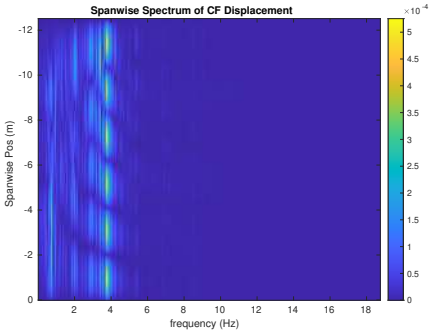

(e) Spanwise cross-flow spectrum of hydrodynamic displacement case 1022.

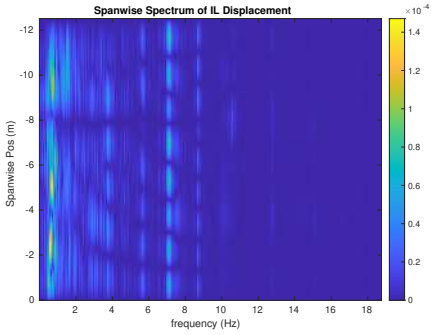

(f) Spanwise inline spectrum of hydrodynamic displacement case 1022.

Figure B-64: *Motion Analysis.* SCR case 1022.

NDP SCR test case 5022

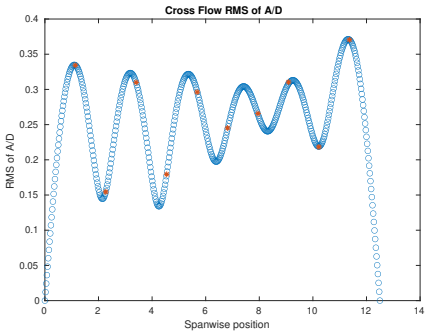

(a) Cross-flow RMS profile case 5022.

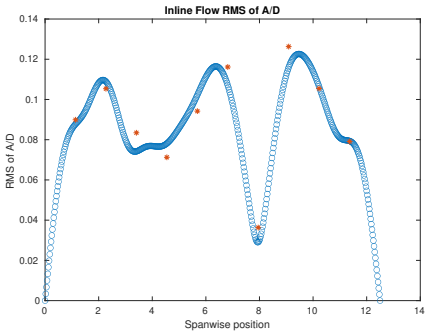

(b) Inline flow RMS profile case 5022.

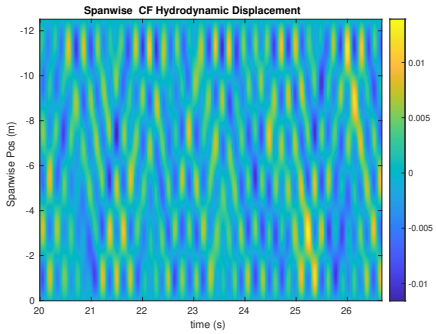

(c) Spanwise cross-flow hydrodynamic displacement case 5022.

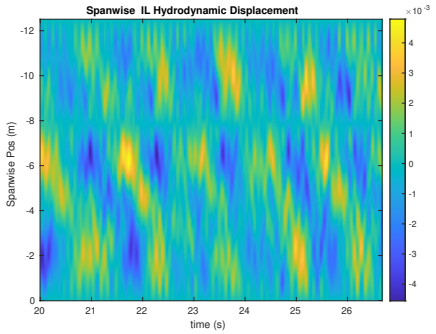

(d) Spanwise inline spectrum of hydrodynamic displacement case 5022.

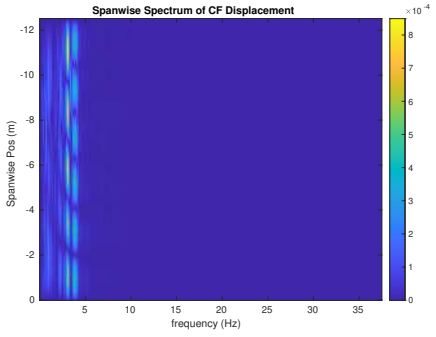

(e) Spanwise cross-flow spectrum of hydrodynamic displacement case 5022.

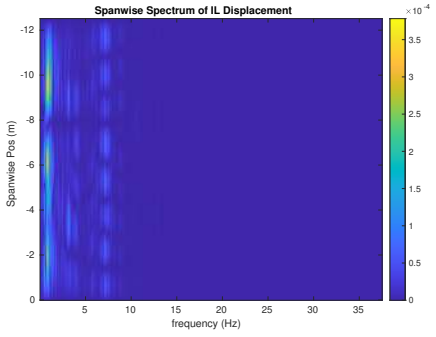

(f) Spanwise inline spectrum of hydrodynamic displacement case 5022.

Figure B-65: *Motion Analysis.* SCR case 5022.

NDP SCR test case 2004

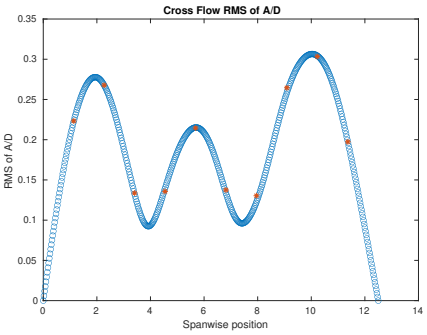

(a) Cross-flow RMS profile case 2004.

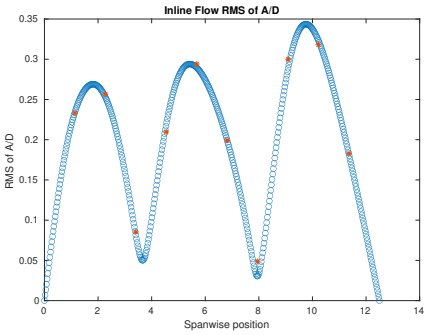

(b) Inline flow RMS profile case 2004.

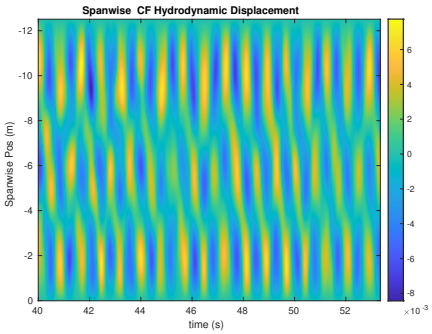

(c) Spanwise cross-flow hydrodynamic displacement case 2004.

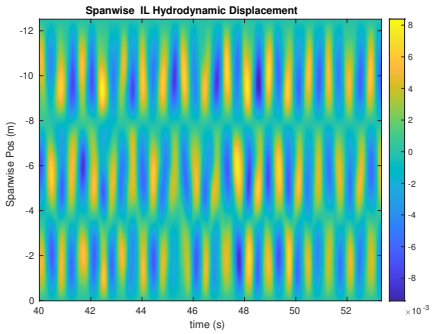

(d) Spanwise inline spectrum of hydrodynamic displacement case 2004.

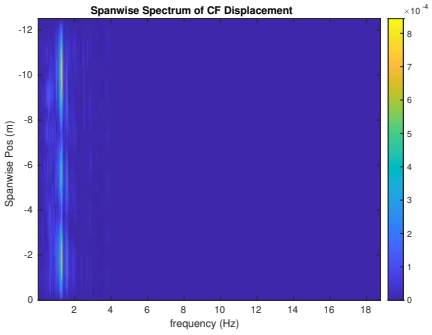

(e) Spanwise cross-flow spectrum of hydrodynamic displacement case 2004.

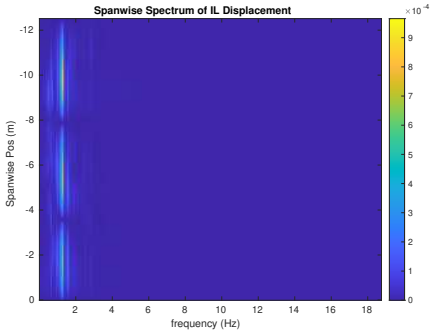

(f) Spanwise inline spectrum of hydrodynamic displacement case 2004.

Figure B-66: *Motion Analysis.* SCR case 2004.

NDP SCR test case 2001

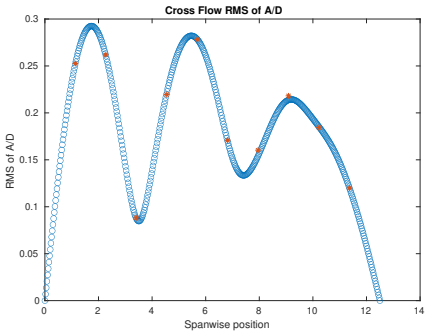

(a) Cross-flow RMS profile case 2001.

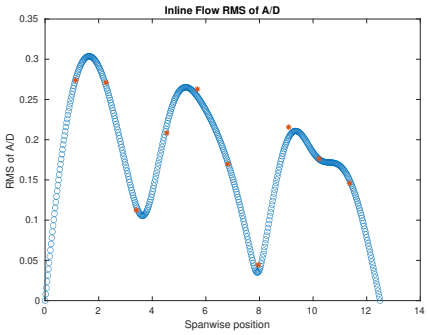

(b) Inline flow RMS profile case 2001.

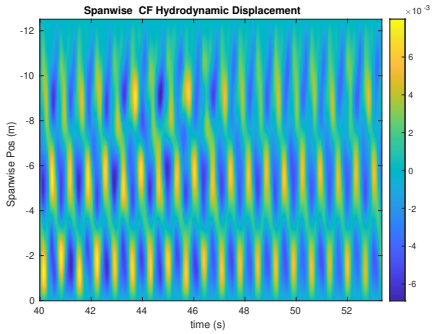

(c) Spanwise cross-flow hydrodynamic displacement case 2001.

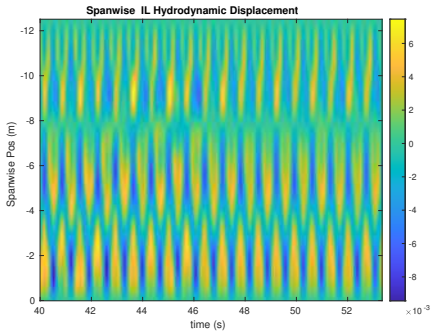

(d) Spanwise inline spectrum of hydrodynamic displacement case 2001.

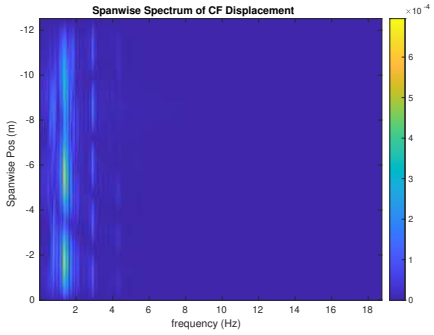

(e) Spanwise cross-flow spectrum of hydrodynamic displacement case 2001.

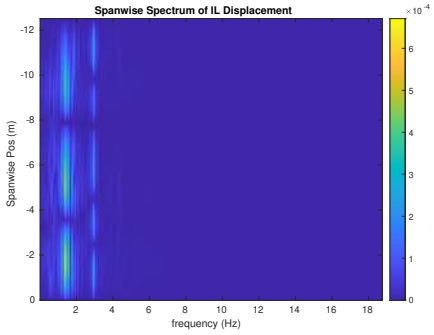

(f) Spanwise inline spectrum of hydrodynamic displacement case 2001.

Figure B-67: *Motion Analysis.* SCR case 2001.

NDP SCR test case 2002

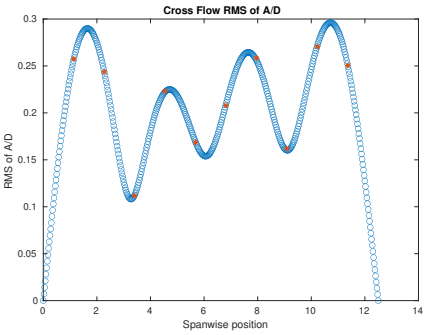

(a) Cross-flow RMS profile case 2002.

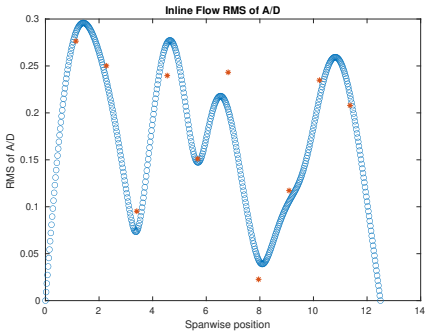

(b) Inline flow RMS profile case 2002.

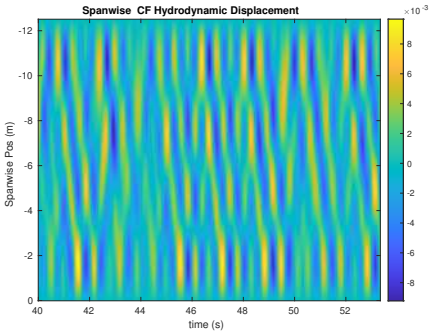

(c) Spanwise cross-flow hydrodynamic displacement case 2002.

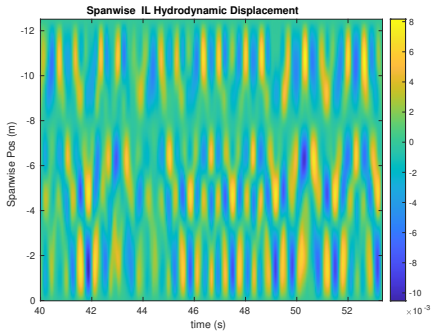

(d) Spanwise inline spectrum of hydrodynamic displacement case 2002.

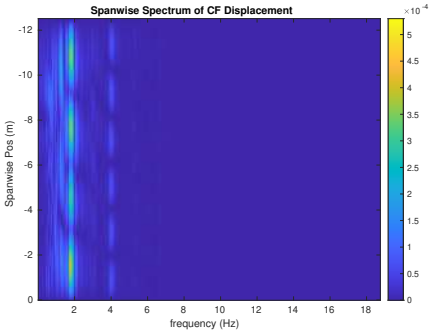

(e) Spanwise cross-flow spectrum of hydrodynamic displacement case 2002.

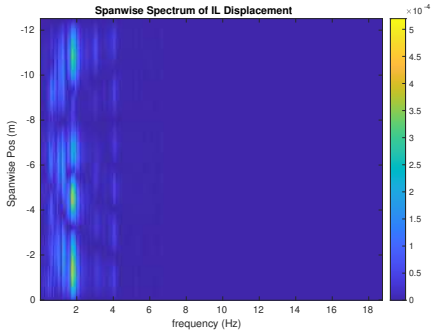

(f) Spanwise inline spectrum of hydrodynamic displacement case 2002.

Figure B-68: *Motion Analysis.* SCR case 2002.

NDP SCR test case 2006

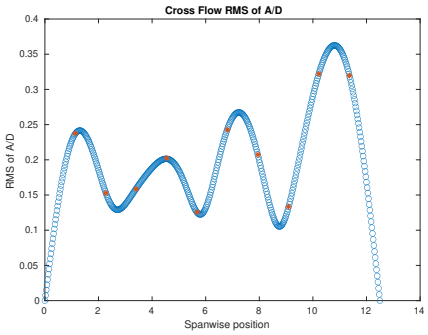

(a) Cross-flow RMS profile case 2006.

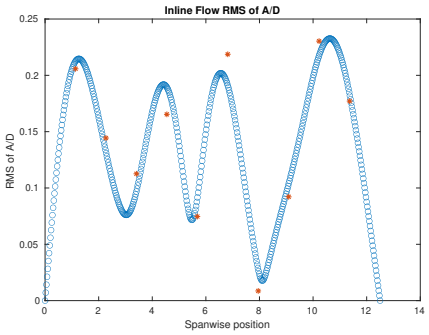

(b) Inline flow RMS profile case 2006.

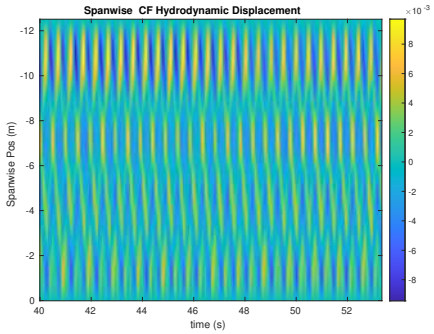

(c) Spanwise cross-flow hydrodynamic displacement case 2006.

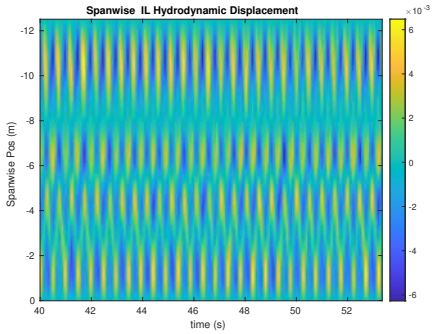

(d) Spanwise inline spectrum of hydrodynamic displacement case 2006.

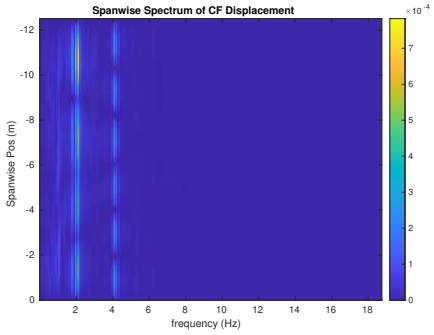

(e) Spanwise cross-flow spectrum of hydrodynamic displacement case 2006.

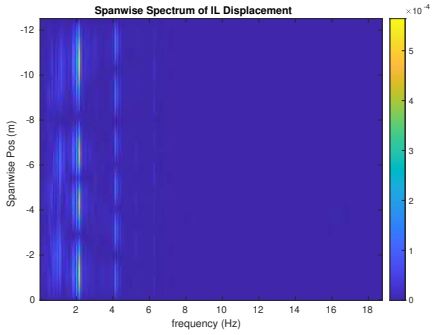

(f) Spanwise inline spectrum of hydrodynamic displacement case 2006.

Figure B-69: *Motion Analysis.* SCR case 2006.

NDP SCR test case 2008

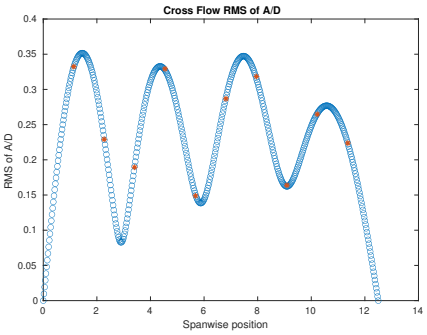

(a) Cross-flow RMS profile case 2008.

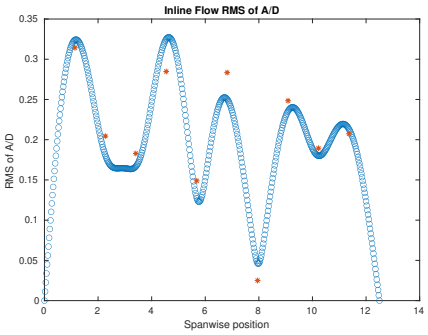

(b) Inline flow RMS profile case 2008.

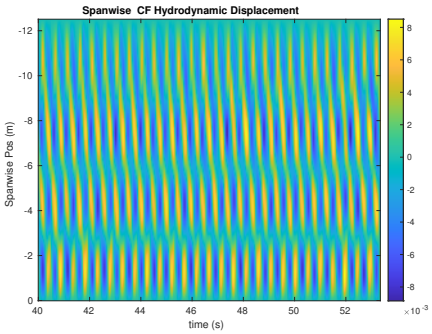

(c) Spanwise cross-flow hydrodynamic displacement case 2008.

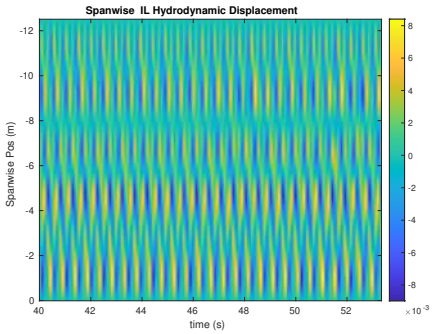

(d) Spanwise inline spectrum of hydrodynamic displacement case 2008.

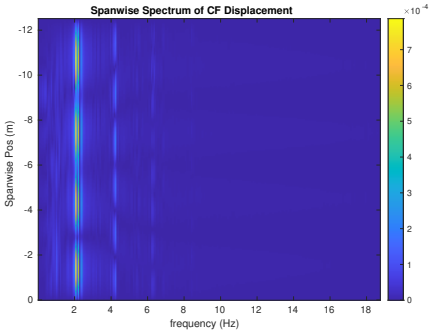

(e) Spanwise cross-flow spectrum of hydrodynamic displacement case 2008.

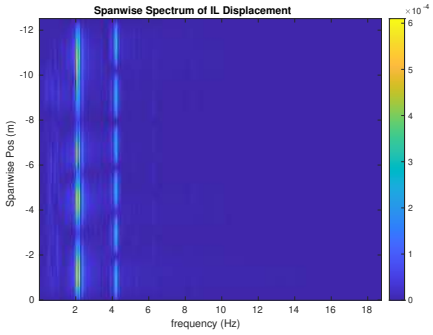

(f) Spanwise inline spectrum of hydrodynamic displacement case 2008.

Figure B-70: *Motion Analysis.* SCR case 2008.

NDP SCR test case 2010

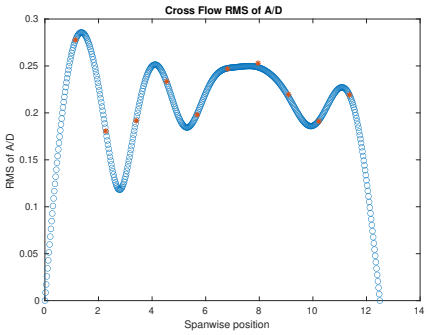

(a) Cross-flow RMS profile case 2010.

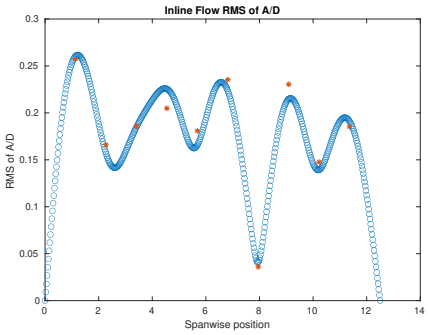

(b) Inline flow RMS profile case 2010.

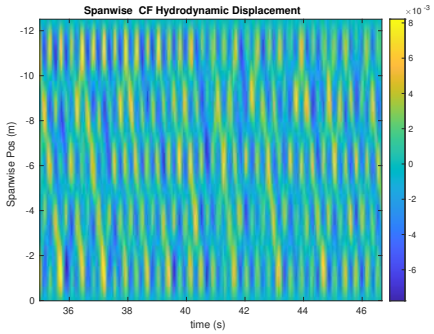

(c) Spanwise cross-flow hydrodynamic displacement case 2010.

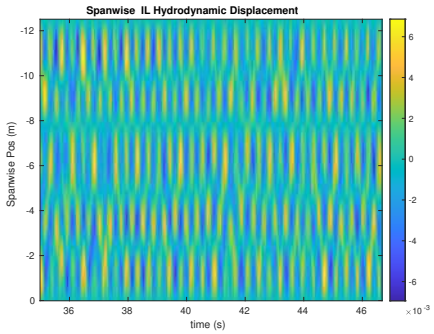

(d) Spanwise inline spectrum of hydrodynamic displacement case 2010.

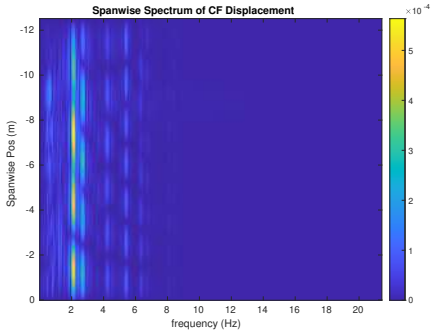

(e) Spanwise cross-flow spectrum of hydrodynamic displacement case 2010.

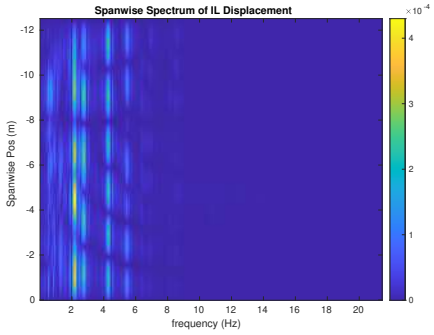

(f) Spanwise inline spectrum of hydrodynamic displacement case 2010.

Figure B-71: *Motion Analysis.* SCR case 2010.

NDP SCR test case 2012

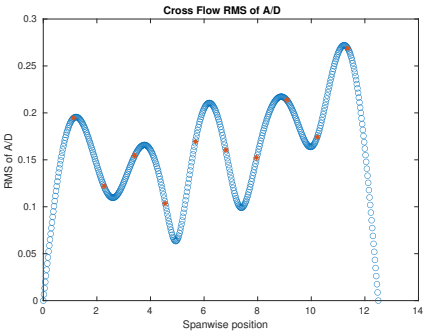

(a) Cross-flow RMS profile case 2012.

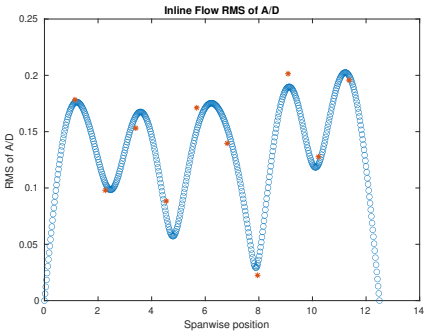

(b) Inline flow RMS profile case 2012.

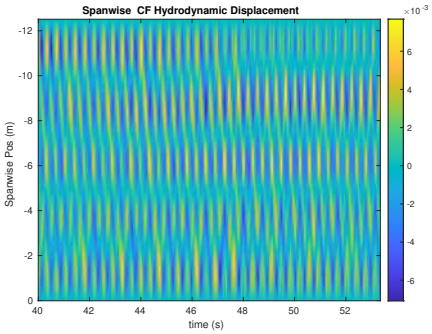

(c) Spanwise cross-flow hydrodynamic displacement case 2012.

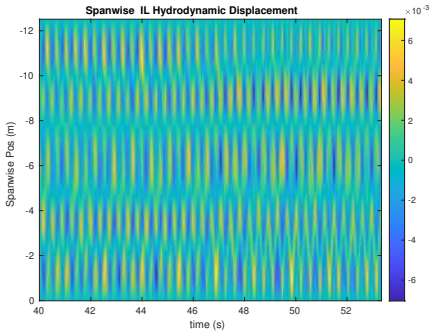

(d) Spanwise inline spectrum of hydrodynamic displacement case 2012.

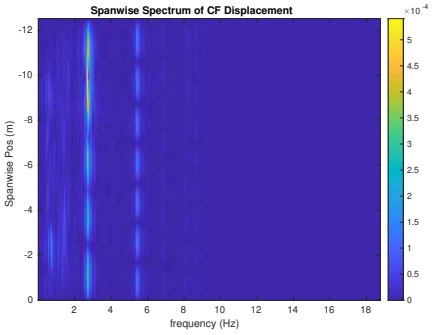

(e) Spanwise cross-flow spectrum of hydrodynamic displacement case 2012.

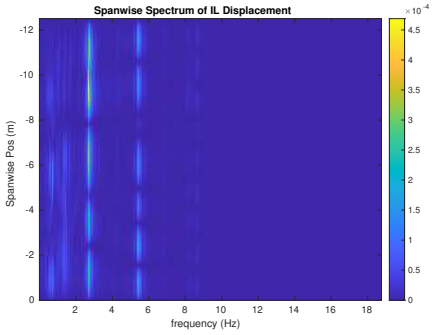

(f) Spanwise inline spectrum of hydrodynamic displacement case 2012.

Figure B-72: *Motion Analysis.* SCR case 2012.

NDP SCR test case 2014

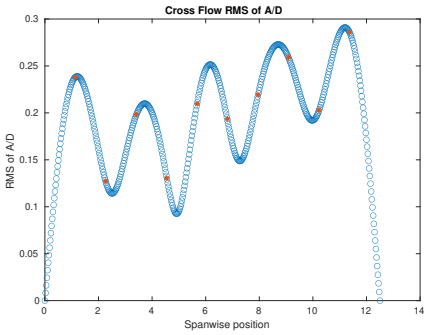

(a) Cross-flow RMS profile case 2014.

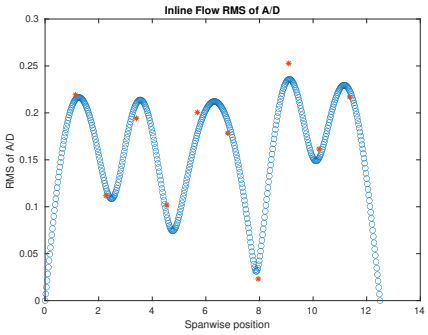

(b) Inline flow RMS profile case 2014.

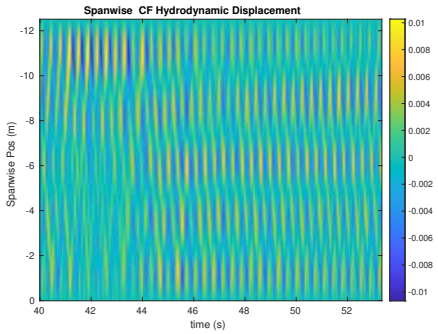

(c) Spanwise cross-flow hydrodynamic displacement case 2014.

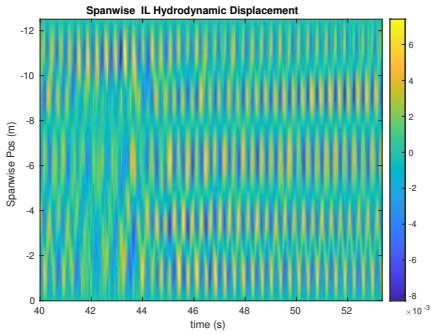

(d) Spanwise inline spectrum of hydrodynamic displacement case 2014.

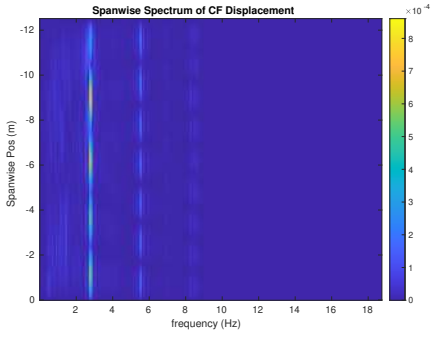

(e) Spanwise cross-flow spectrum of hydrodynamic displacement case 2014.

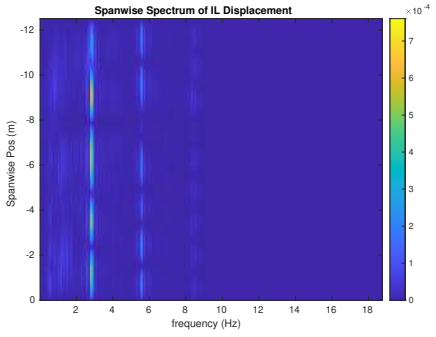

(f) Spanwise inline spectrum of hydrodynamic displacement case 2014.

Figure B-73: *Motion Analysis.* SCR case 2014.

NDP SCR test case 2016

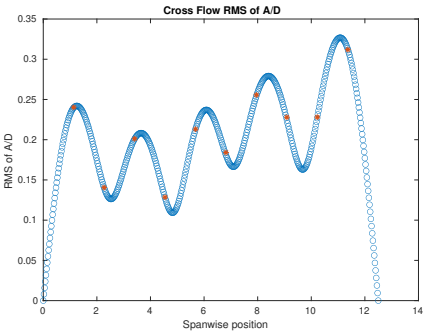

(a) Cross-flow RMS profile case 2016.

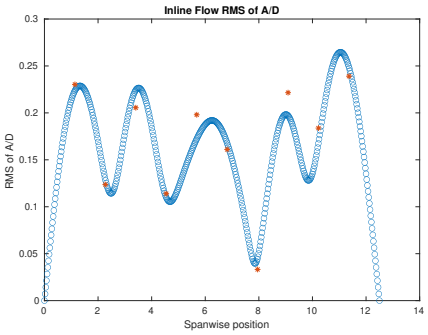

(b) Inline flow RMS profile case 2016.

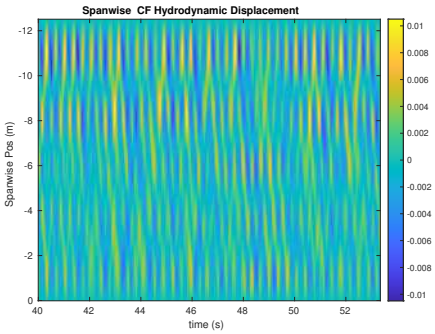

(c) Spanwise cross-flow hydrodynamic displacement case 2016.

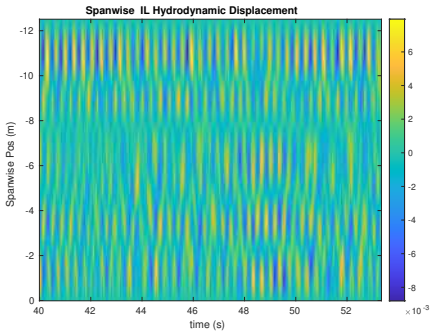

(d) Spanwise inline spectrum of hydrodynamic displacement case 2016.

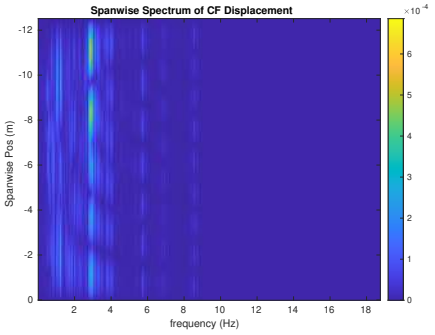

(e) Spanwise cross-flow spectrum of hydrodynamic displacement case 2016.

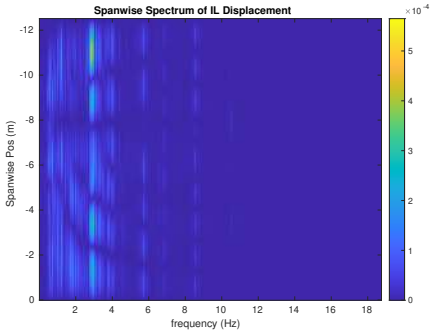

(f) Spanwise inline spectrum of hydrodynamic displacement case 2016.

Figure B-74: *Motion Analysis.* SCR case 2016.

NDP SCR test case 2018

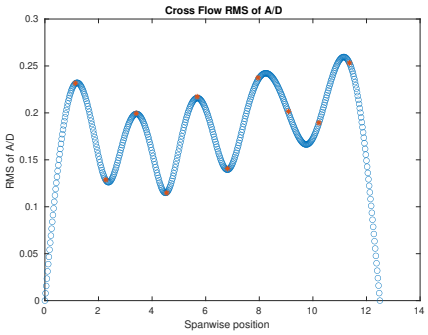

(a) Cross-flow RMS profile case 2018.

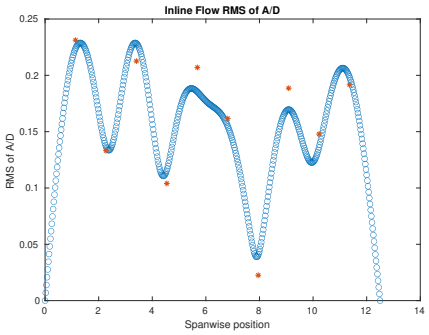

(b) Inline flow RMS profile case 2018.

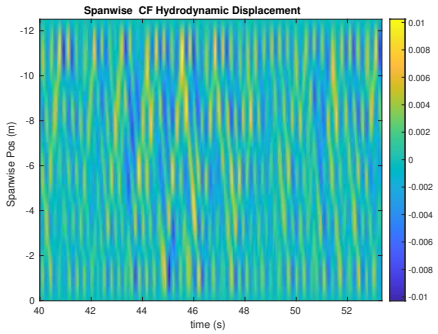

(c) Spanwise cross-flow hydrodynamic displacement case 2018.

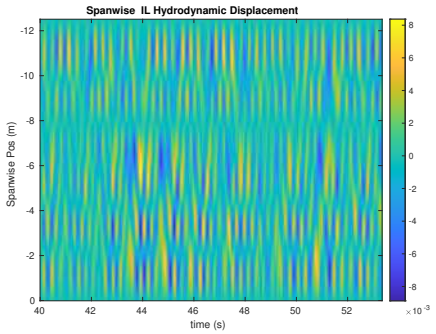

(d) Spanwise inline spectrum of hydrodynamic displacement case 2018.

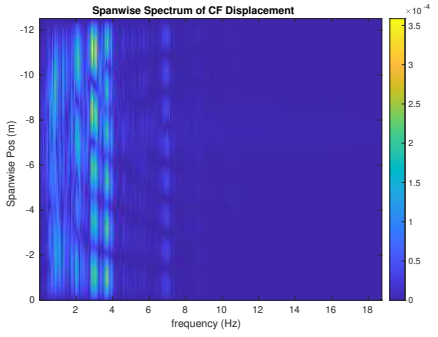

(e) Spanwise cross-flow spectrum of hydrodynamic displacement case 2018.

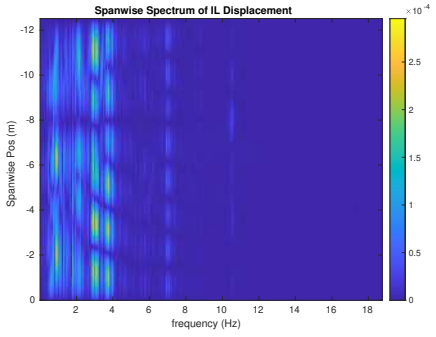

(f) Spanwise inline spectrum of hydrodynamic displacement case 2018.

Figure B-75: *Motion Analysis.* SCR case 2018.

NDP SCR test case 2020

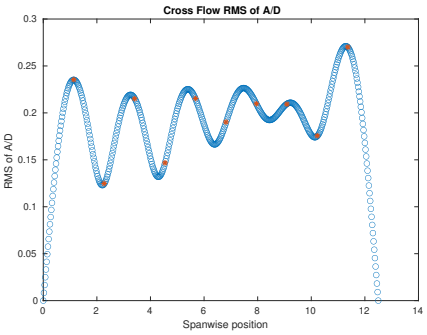

(a) Cross-flow RMS profile case 2020.

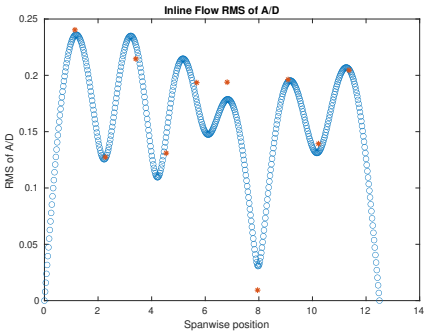

(b) Inline flow RMS profile case 2020.

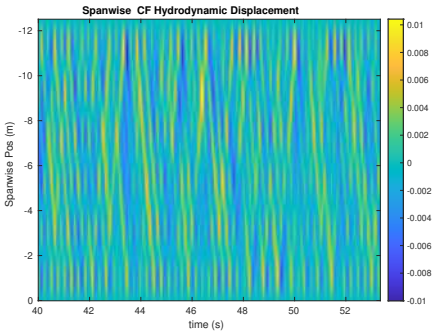

(c) Spanwise cross-flow hydrodynamic displacement case 2020.

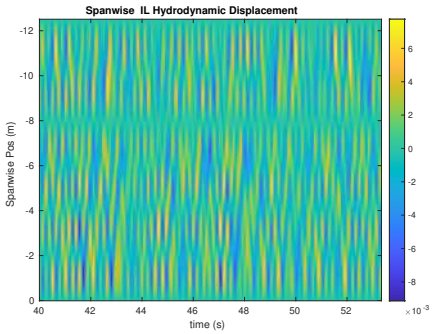

(d) Spanwise inline spectrum of hydrodynamic displacement case 2020.

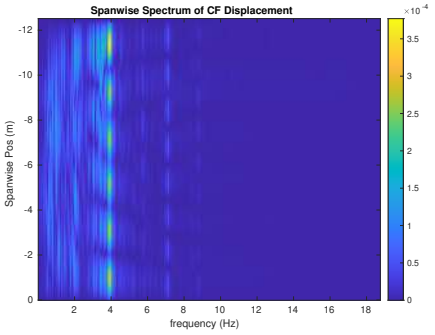

(e) Spanwise cross-flow spectrum of hydrodynamic displacement case 2020.

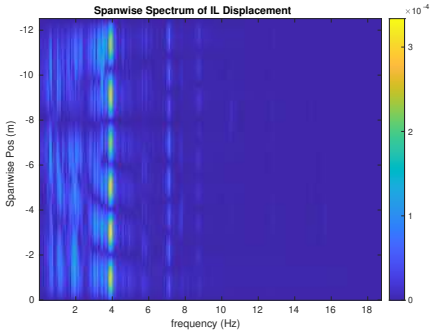

(f) Spanwise inline spectrum of hydrodynamic displacement case 2020.

Figure B-76: *Motion Analysis.* SCR case 2020.

NDP SCR test case 2022

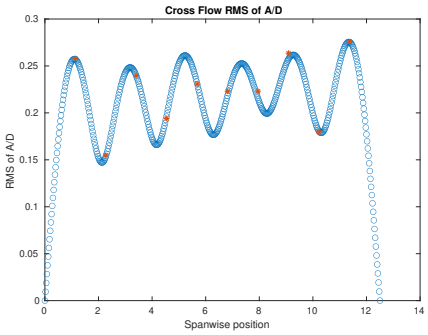

(a) Cross-flow RMS profile case 2022.

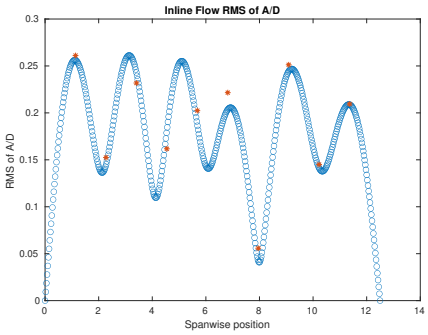

(b) Inline flow RMS profile case 2022.

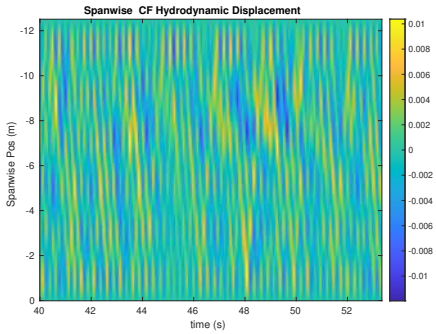

(c) Spanwise cross-flow hydrodynamic displacement case 2022.

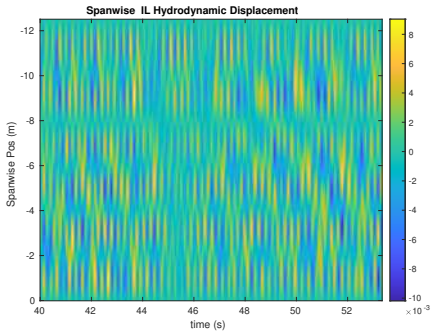

(d) Spanwise inline spectrum of hydrodynamic displacement case 2022.

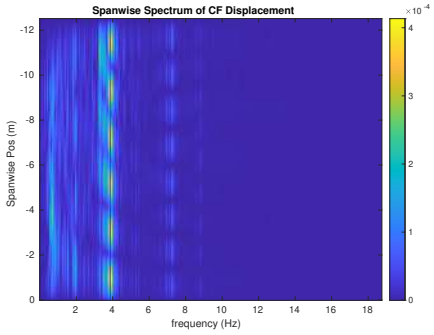

(e) Spanwise cross-flow spectrum of hydrodynamic displacement case 2022.

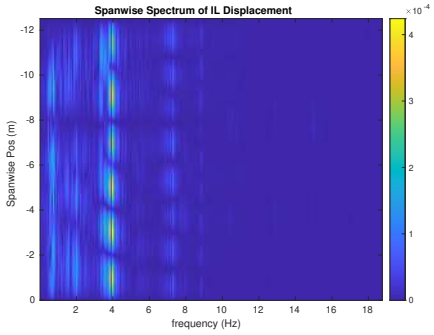

(f) Spanwise inline spectrum of hydrodynamic displacement case 2022.

Figure B-77: *Motion Analysis.* SCR case 2022.

NDP SCR test case 3000

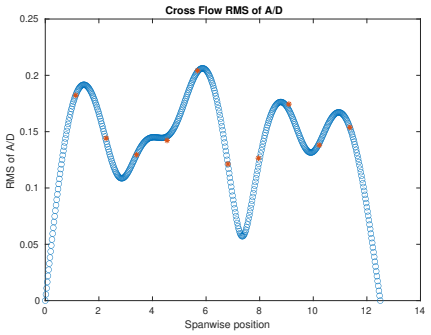

(a) Cross-flow RMS profile case 3000.

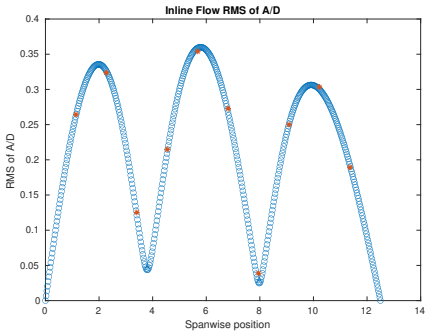

(b) Inline flow RMS profile case 3000.

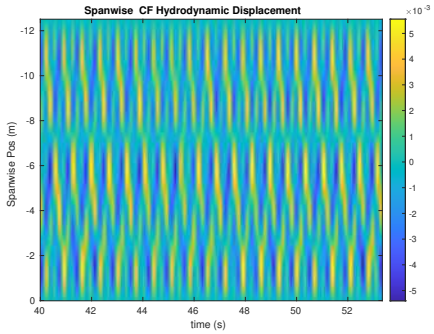

(c) Spanwise cross-flow hydrodynamic displacement case 3000.

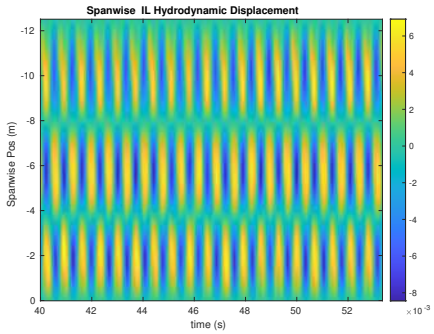

(d) Spanwise inline spectrum of hydrodynamic displacement case 3000.

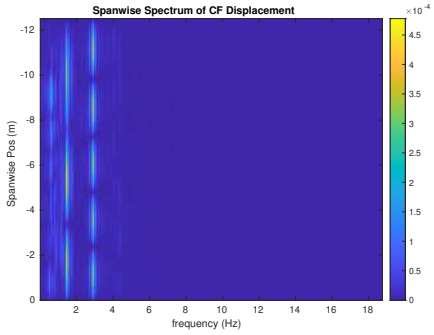

(e) Spanwise cross-flow spectrum of hydrodynamic displacement case 3000.

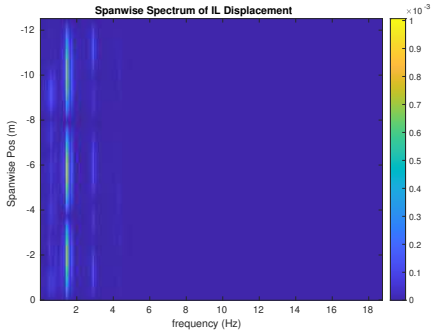

(f) Spanwise inline spectrum of hydrodynamic displacement case 3000.

Figure B-78: *Motion Analysis.* SCR case 3000.

NDP SCR test case 3002

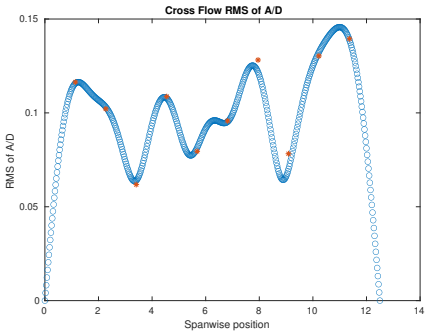

(a) Cross-flow RMS profile case 3002.

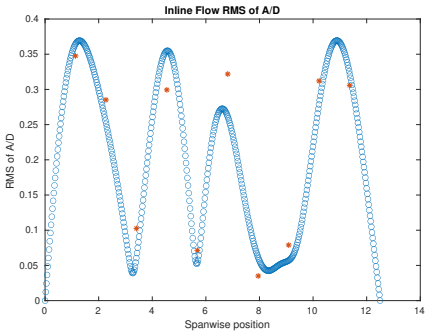

(b) Inline flow RMS profile case 3002.

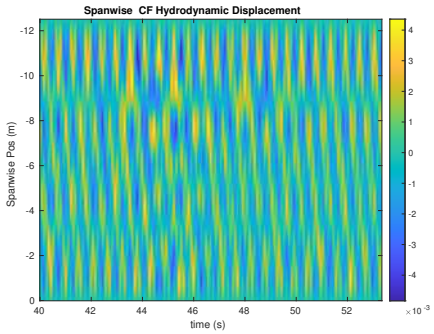

(c) Spanwise cross-flow hydrodynamic displacement case 3002.

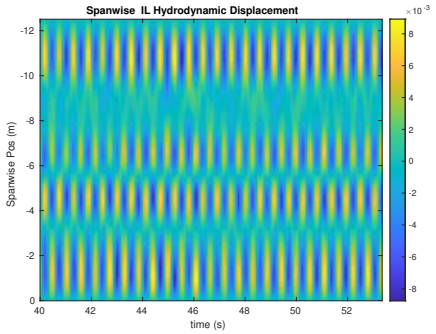

(d) Spanwise inline spectrum of hydrodynamic displacement case 3002.

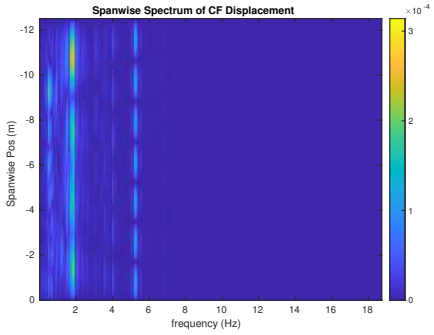

(e) Spanwise cross-flow spectrum of hydrodynamic displacement case 3002.

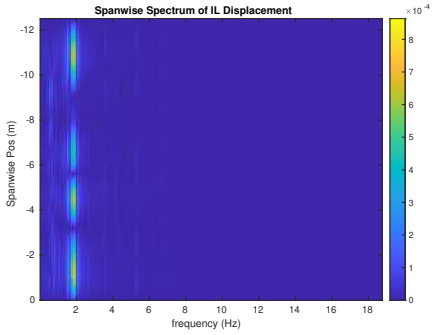

(f) Spanwise inline spectrum of hydrodynamic displacement case 3002.

Figure B-79: *Motion Analysis.* SCR case 3002.

NDP SCR test case 3004

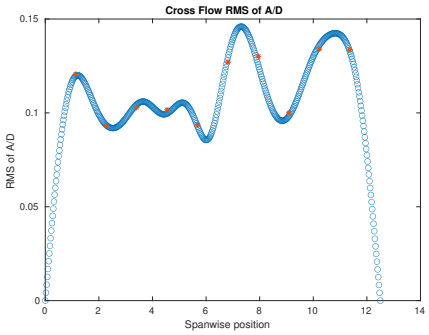

(a) Cross-flow RMS profile case 3004.

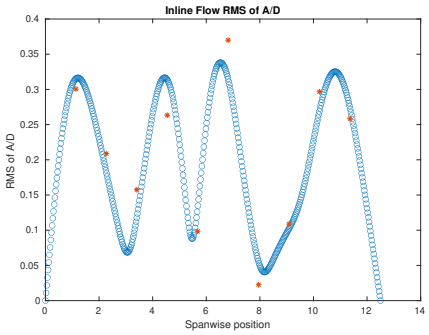

(b) Inline flow RMS profile case 3004.

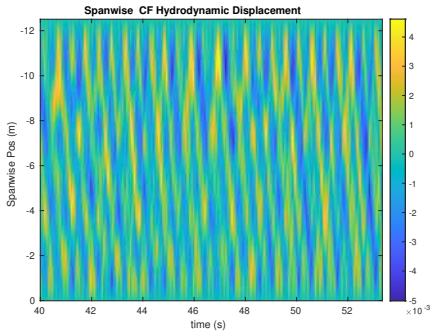

(c) Spanwise cross-flow hydrodynamic displacement case 3004.

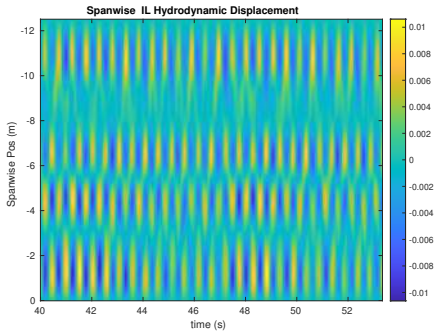

(d) Spanwise inline spectrum of hydrodynamic displacement case 3004.

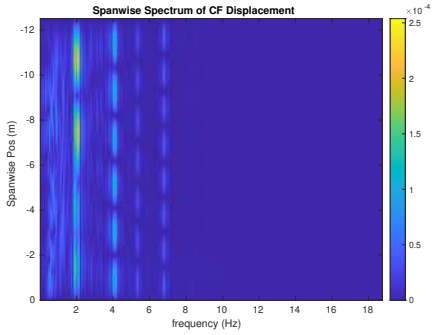

(e) Spanwise cross-flow spectrum of hydrodynamic displacement case 3004.

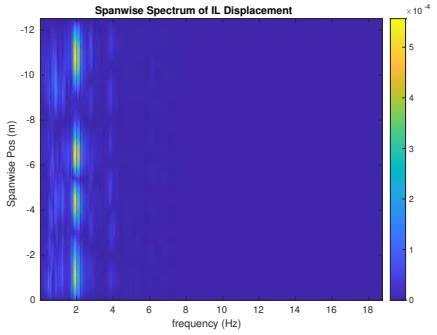

(f) Spanwise inline spectrum of hydrodynamic displacement case 3004.

Figure B-80: *Motion Analysis.* SCR case 3004.

NDP SCR test case 3006

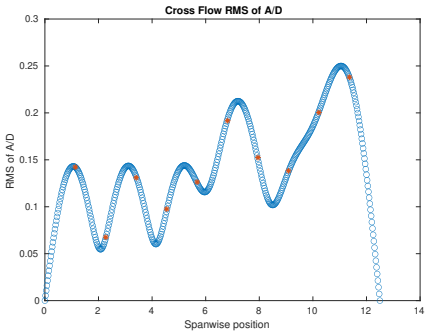

(a) Cross-flow RMS profile case 3006.

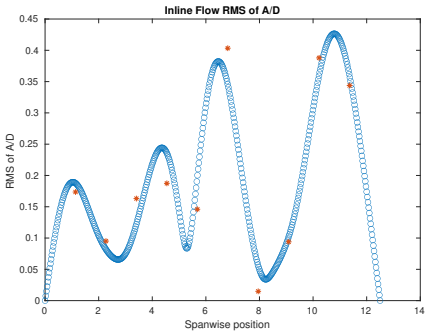

(b) Inline flow RMS profile case 3006.

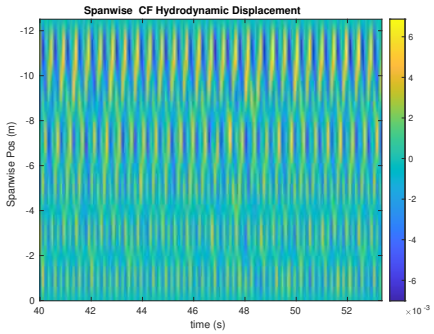

(c) Spanwise cross-flow hydrodynamic displacement case 3006.

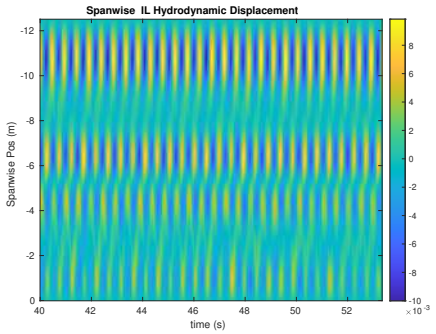

(d) Spanwise inline spectrum of hydrodynamic displacement case 3006.

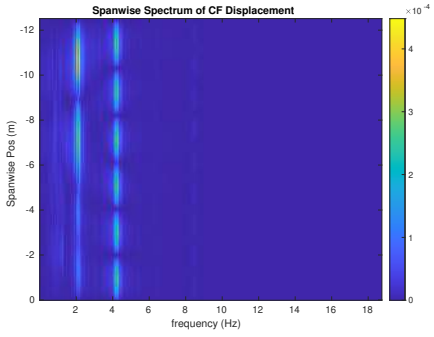

(e) Spanwise cross-flow spectrum of hydrodynamic displacement case 3006.

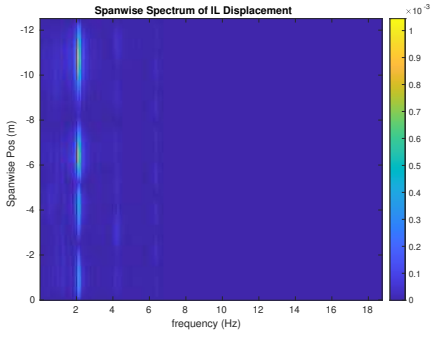

(f) Spanwise inline spectrum of hydrodynamic displacement case 3006.

Figure B-81: *Motion Analysis.* SCR case 3006.

NDP SCR test case 3008

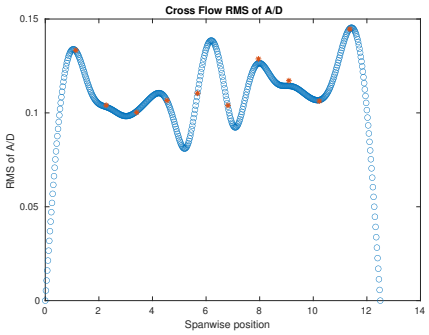

(a) Cross-flow RMS profile case 3008.

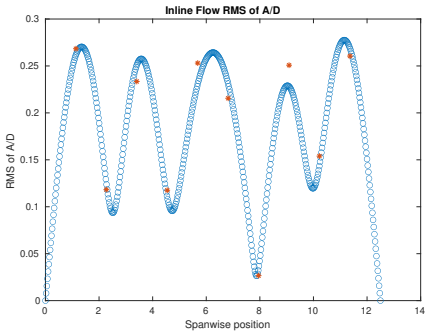

(b) Inline flow RMS profile case 3008.

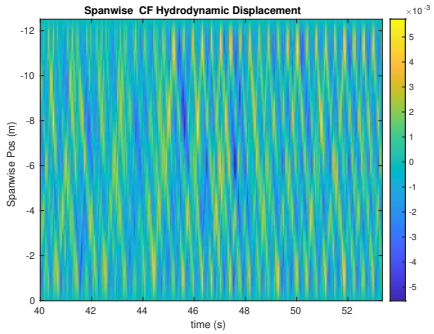

(c) Spanwise cross-flow hydrodynamic displacement case 3008.

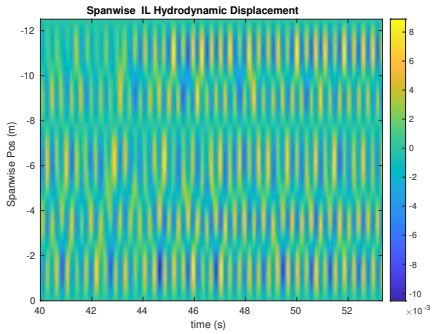

(d) Spanwise inline spectrum of hydrodynamic displacement case 3008.

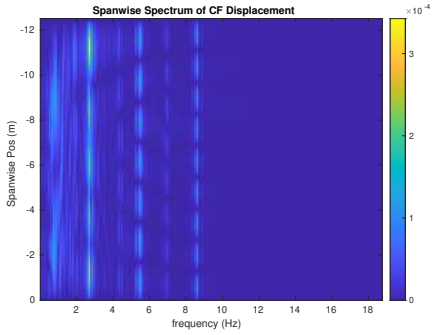

(e) Spanwise cross-flow spectrum of hydrodynamic displacement case 3008.

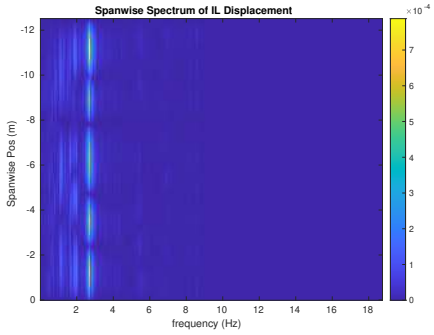

(f) Spanwise inline spectrum of hydrodynamic displacement case 3008.

Figure B-82: *Motion Analysis.* SCR case 3008.

NDP SCR test case 3010

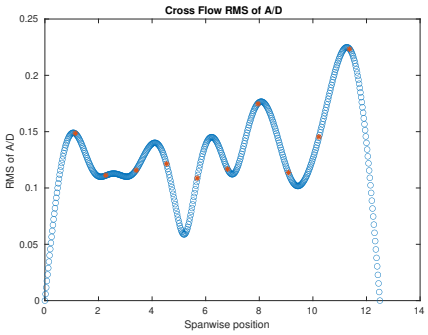

(a) Cross-flow RMS profile case 3010.

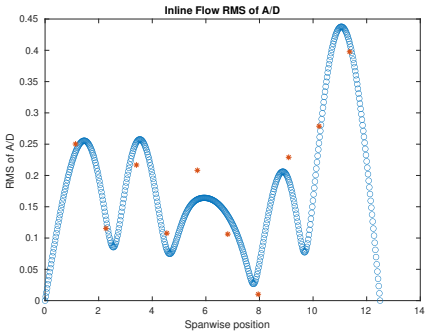

(b) Inline flow RMS profile case 3010.

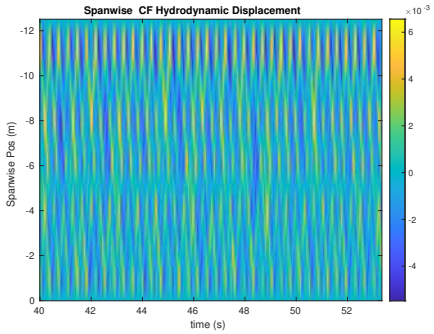

(c) Spanwise cross-flow hydrodynamic displacement case 3010.

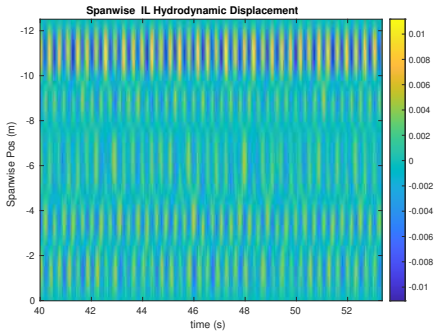

(d) Spanwise inline spectrum of hydrodynamic displacement case 3010.

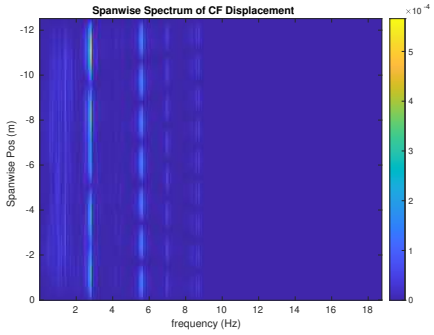

(e) Spanwise cross-flow spectrum of hydrodynamic displacement case 3010.

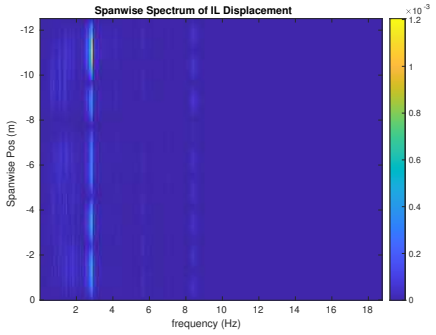

(f) Spanwise inline spectrum of hydrodynamic displacement case 3010.

Figure B-83: *Motion Analysis.* SCR case 3010.

NDP SCR test case 3012

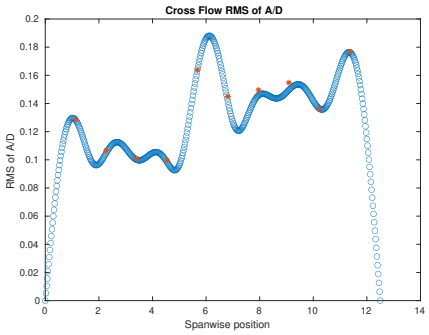

(a) Cross-flow RMS profile case 3012.

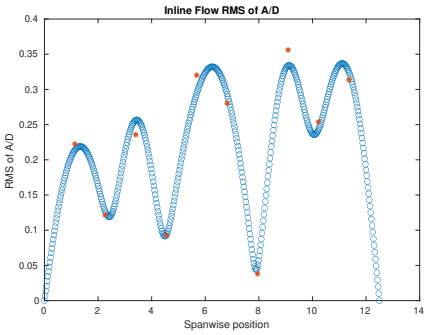

(b) Inline flow RMS profile case 3012.

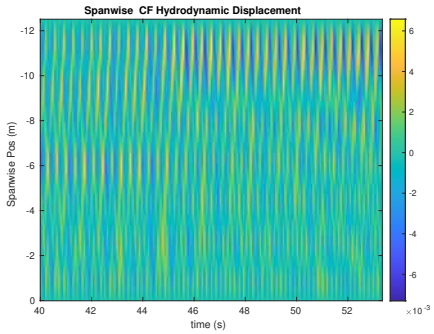

(c) Spanwise cross-flow hydrodynamic displacement case 3012.

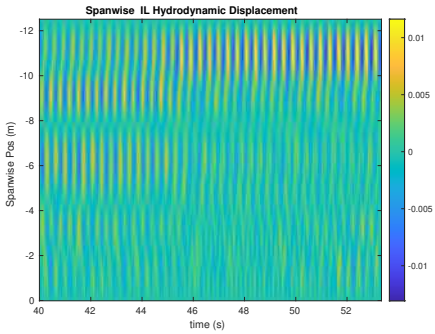

(d) Spanwise inline spectrum of hydrodynamic displacement case 3012.

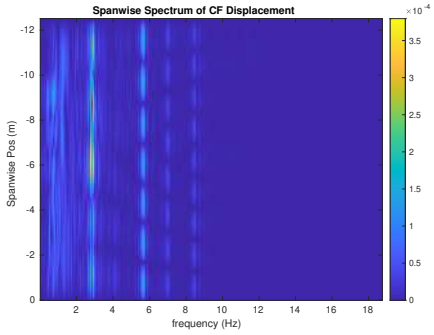

(e) Spanwise cross-flow spectrum of hydrodynamic displacement case 3012.

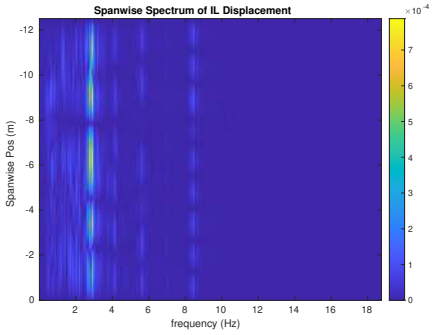

(f) Spanwise inline spectrum of hydrodynamic displacement case 3012.

Figure B-84: *Motion Analysis.* SCR case 3012.

NDP SCR test case 3014

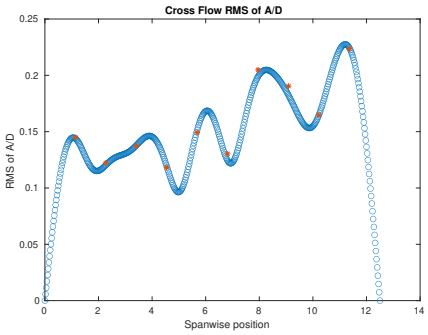

(a) Cross-flow RMS profile case 3014.

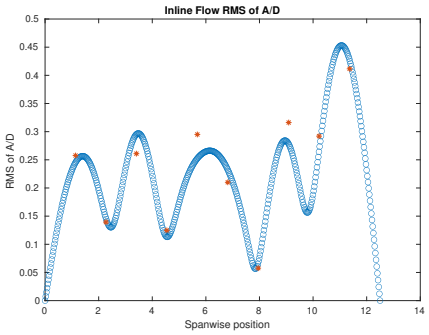

(b) Inline flow RMS profile case 3014.

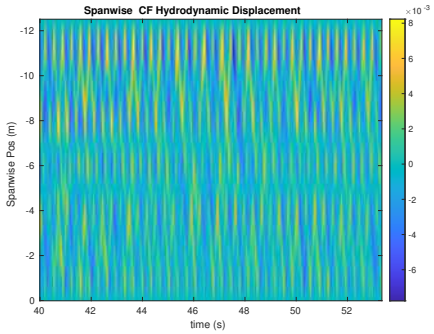

(c) Spanwise cross-flow hydrodynamic displacement case 3014.

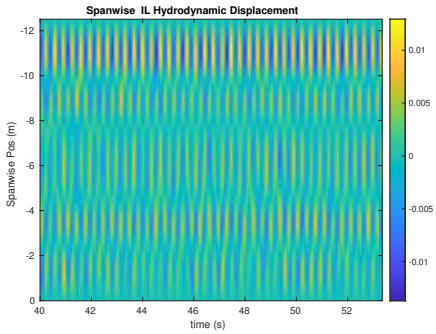

(d) Spanwise inline spectrum of hydrodynamic displacement case 3014.

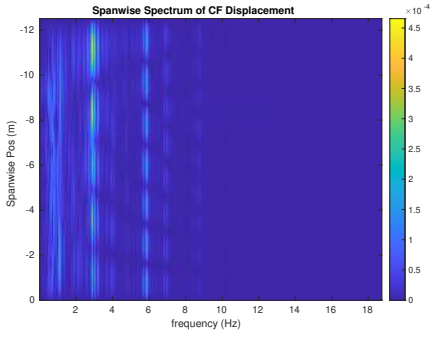

(e) Spanwise cross-flow spectrum of hydrodynamic displacement case 3014.

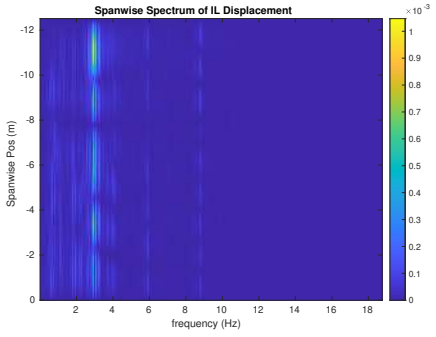

(f) Spanwise inline spectrum of hydrodynamic displacement case 3014.

Figure B-85: *Motion Analysis.* SCR case 3014.

NDP SCR test case 3016

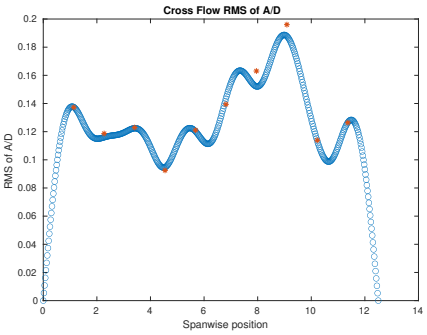

(a) Cross-flow RMS profile case 3016.

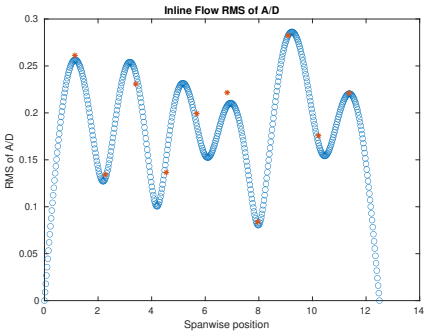

(b) Inline flow RMS profile case 3016.

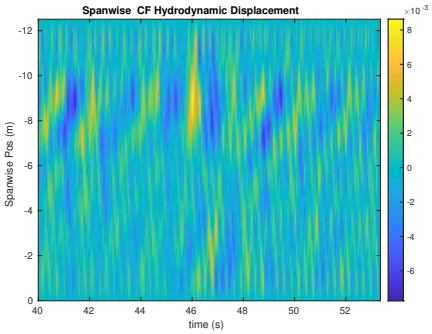

(c) Spanwise cross-flow hydrodynamic displacement case 3016.

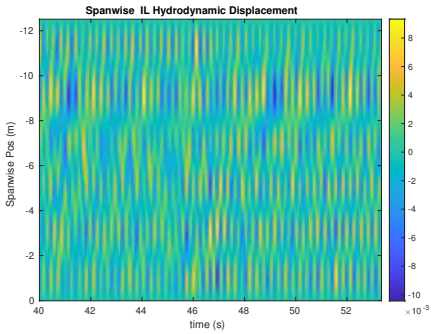

(d) Spanwise inline spectrum of hydrodynamic displacement case 3016.

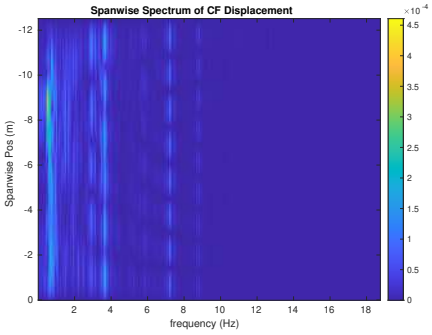

(e) Spanwise cross-flow spectrum of hydrodynamic displacement case 3016.

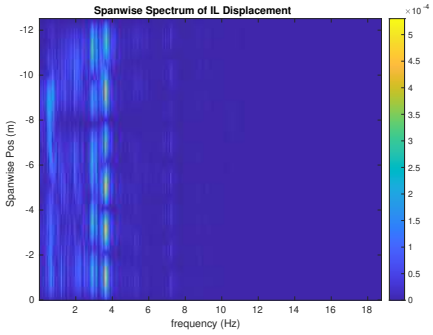

(f) Spanwise inline spectrum of hydrodynamic displacement case 3016.

Figure B-86: *Motion Analysis.* SCR case 3016.

NDP SCR test case 3018

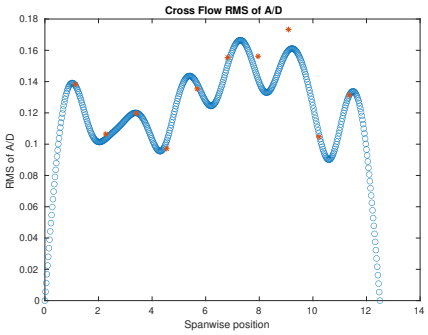

(a) Cross-flow RMS profile case 3018.

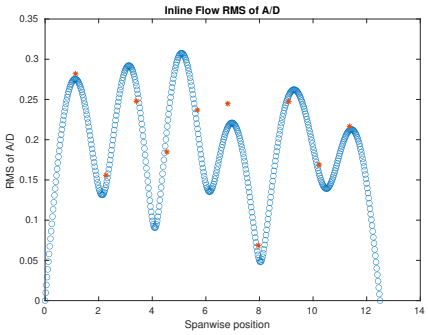

(b) Inline flow RMS profile case 3018.

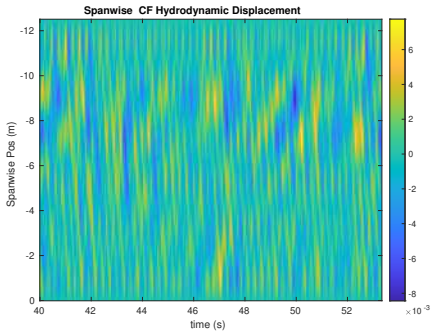

(c) Spanwise cross-flow hydrodynamic displacement case 3018.

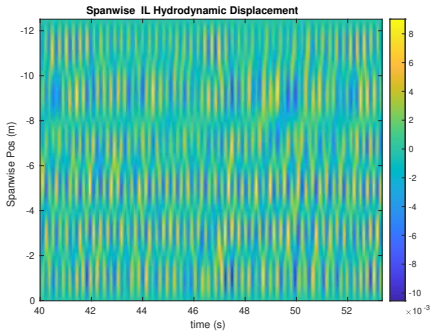

(d) Spanwise inline spectrum of hydrodynamic displacement case 3018.

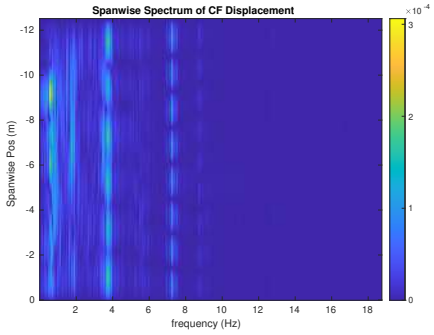

(e) Spanwise cross-flow spectrum of hydrodynamic displacement case 3018.

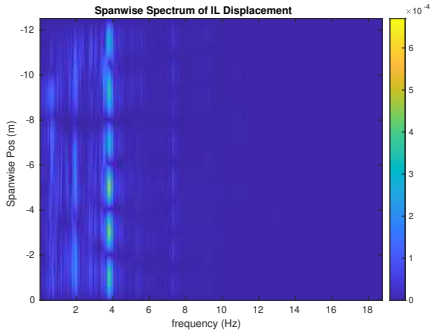

(f) Spanwise inline spectrum of hydrodynamic displacement case 3018.

Figure B-87: *Motion Analysis.* SCR case 3018.

NDP SCR test case 3020

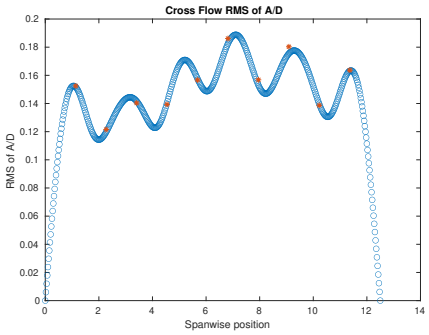

(a) Cross-flow RMS profile case 3020.

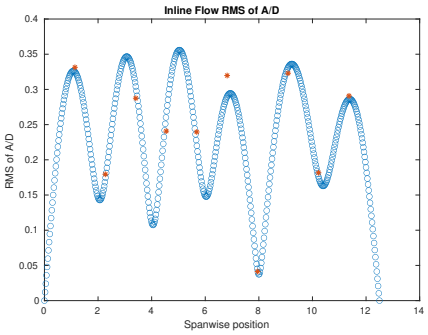

(b) Inline flow RMS profile case 3020.

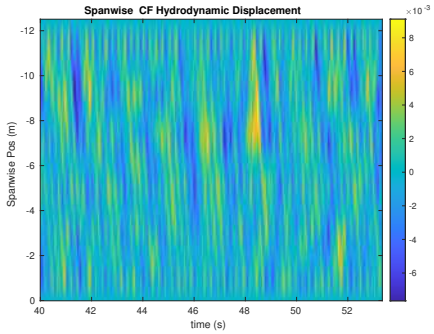

(c) Spanwise cross-flow hydrodynamic displacement case 3020.

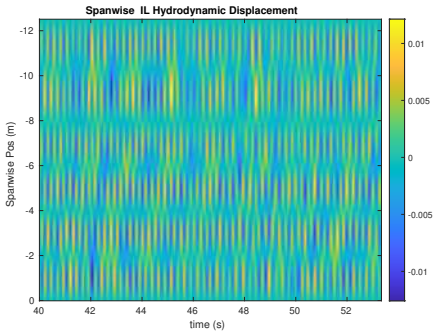

(d) Spanwise inline spectrum of hydrodynamic displacement case 3020.

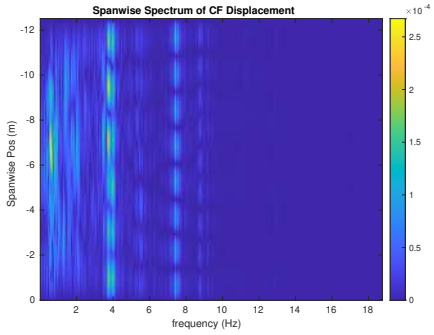

(e) Spanwise cross-flow spectrum of hydrodynamic displacement case 3020.

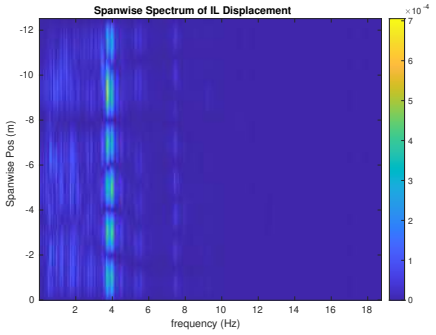

(f) Spanwise inline spectrum of hydrodynamic displacement case 3020.

Figure B-88: *Motion Analysis.* SCR case 3020.

NDP SCR test case 3022

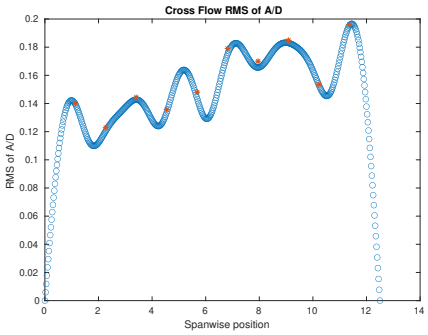

(a) Cross-flow RMS profile case 3022.

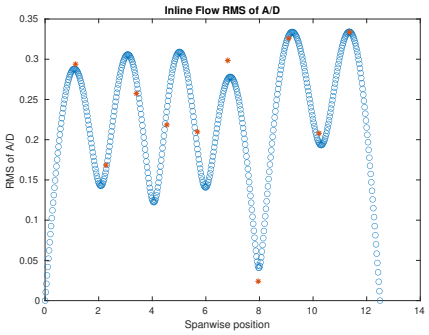

(b) Inline flow RMS profile case 3022.

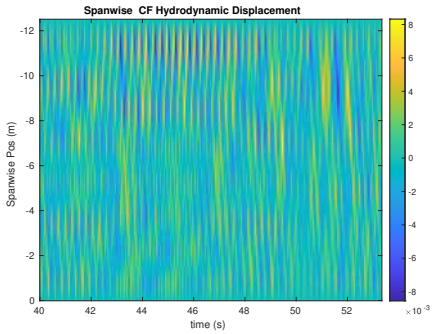

(c) Spanwise cross-flow hydrodynamic displacement case 3022.

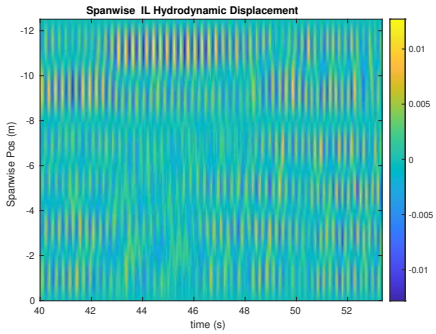

(d) Spanwise inline spectrum of hydrodynamic displacement case 3022.

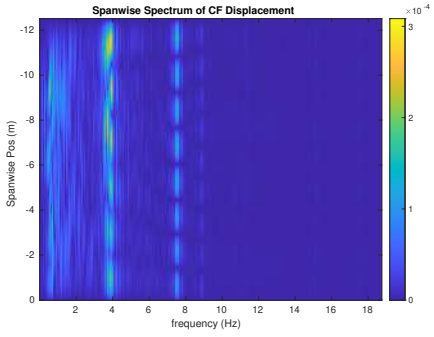

(e) Spanwise cross-flow spectrum of hydrodynamic displacement case 3022.

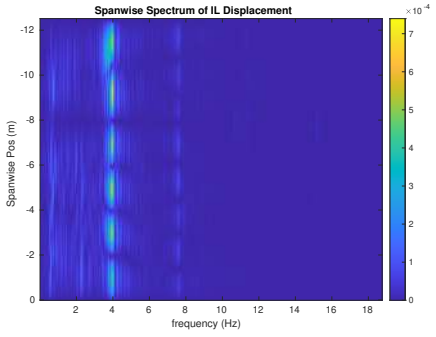

(f) Spanwise inline spectrum of hydrodynamic displacement case 3022.

Figure B-89: *Motion Analysis.* SCR case 3022.

NDP SCR test case 4000

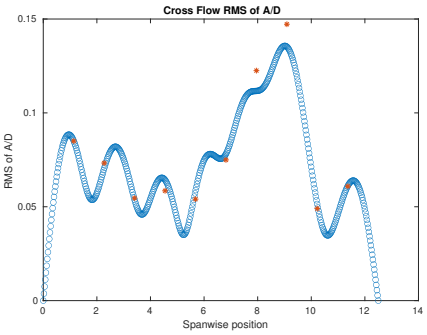

(a) Cross-flow RMS profile case 4000.

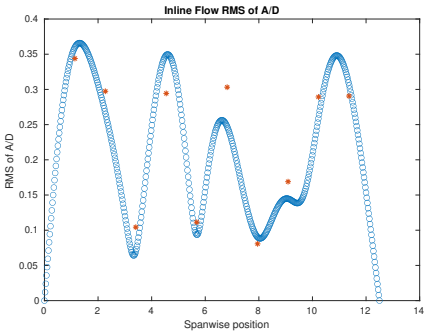

(b) Inline flow RMS profile case 4000.

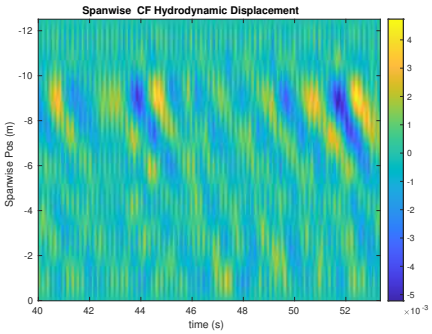

(c) Spanwise cross-flow hydrodynamic displacement case 4000.

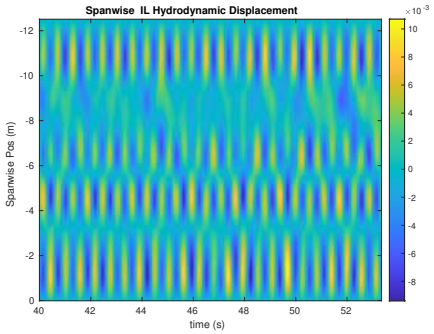

(d) Spanwise inline spectrum of hydrodynamic displacement case 4000.

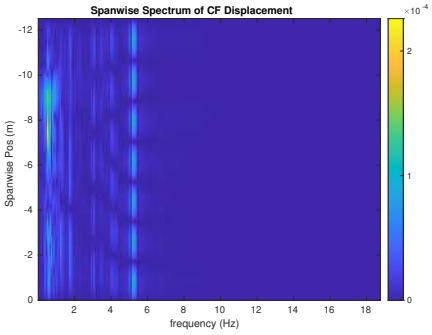

(e) Spanwise cross-flow spectrum of hydrodynamic displacement case 4000.

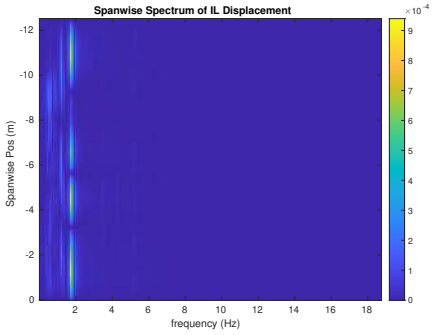

(f) Spanwise inline spectrum of hydrodynamic displacement case 4000.

Figure B-90: *Motion Analysis.* SCR case 4000.

NDP SCR test case 4002

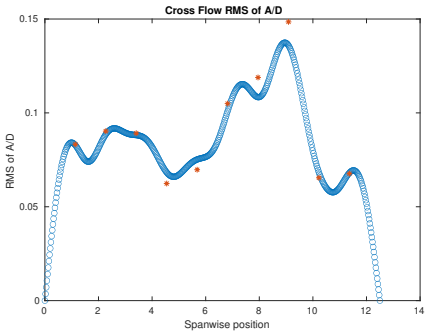

(a) Cross-flow RMS profile case 4002.

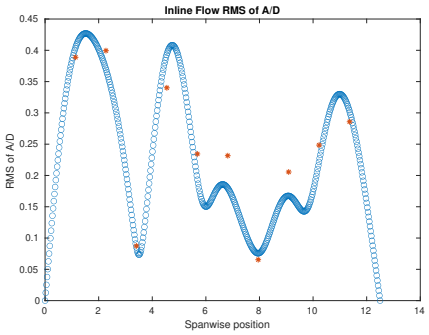

(b) Inline flow RMS profile case 4002.

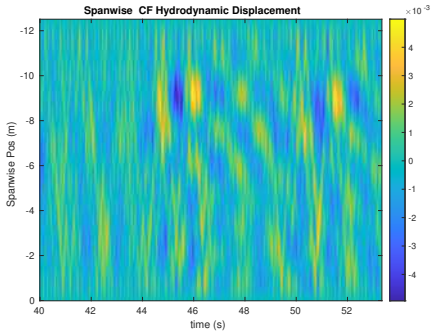

(c) Spanwise cross-flow hydrodynamic displacement case 4002.

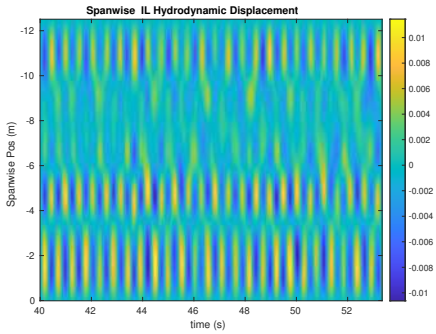

(d) Spanwise inline spectrum of hydrodynamic displacement case 4002.

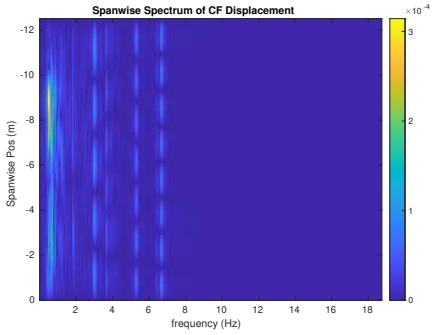

(e) Spanwise cross-flow spectrum of hydrodynamic displacement case 4002.

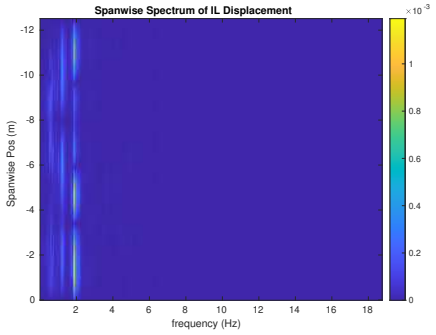

(f) Spanwise inline spectrum of hydrodynamic displacement case 4002.

Figure B-91: *Motion Analysis.* SCR case 4002.

NDP SCR test case 4006

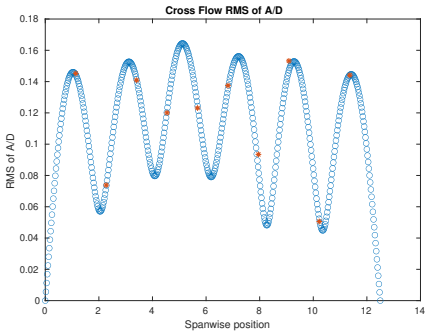

(a) Cross-flow RMS profile case 4006.

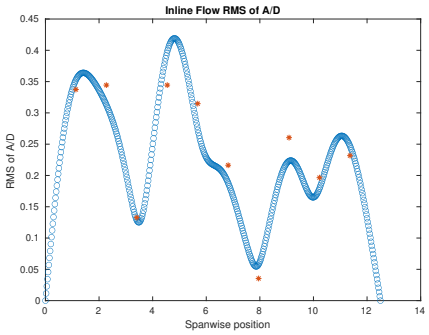

(b) Inline flow RMS profile case 4006.

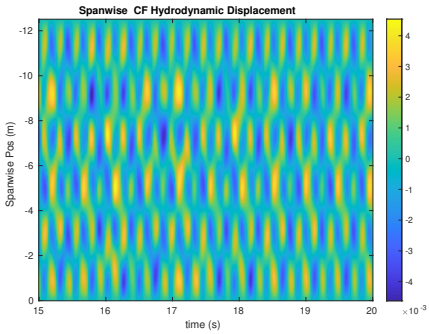

(c) Spanwise cross-flow hydrodynamic displacement case 4006.

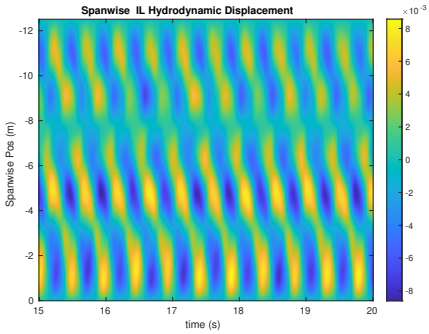

(d) Spanwise inline spectrum of hydrodynamic displacement case 4006.

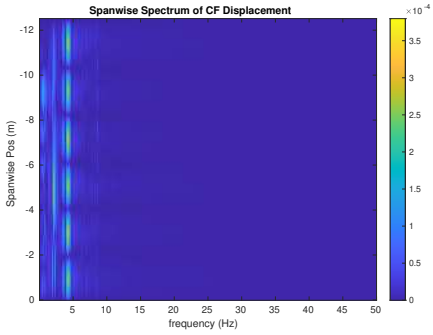

(e) Spanwise cross-flow spectrum of hydrodynamic displacement case 4006.

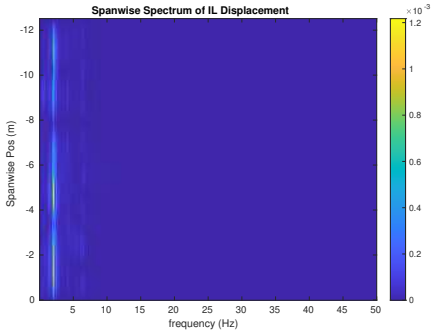

(f) Spanwise inline spectrum of hydrodynamic displacement case 4006.

Figure B-92: *Motion Analysis.* SCR case 4006.

NDP SCR test case 4008

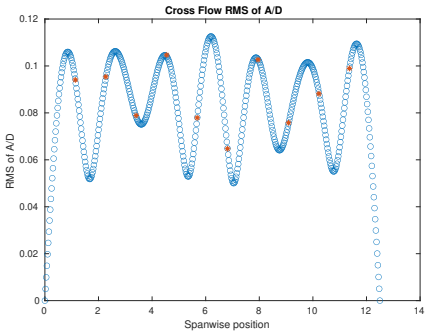

(a) Cross-flow RMS profile case 4008.

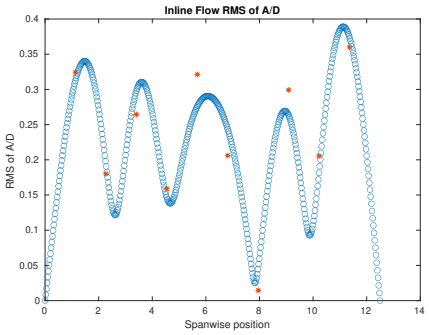

(b) Inline flow RMS profile case 4008.

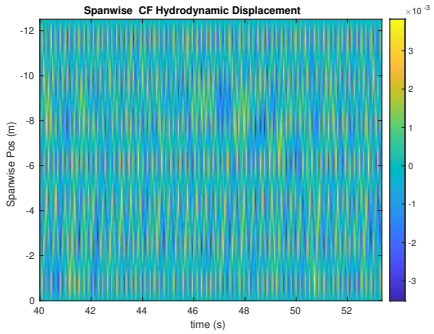

(c) Spanwise cross-flow hydrodynamic displacement case 4008.

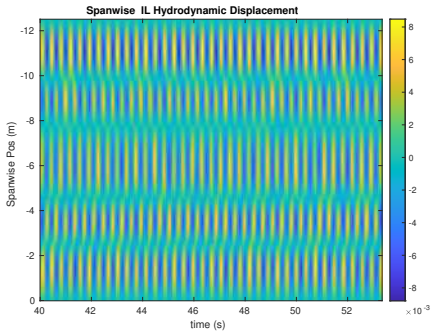

(d) Spanwise inline spectrum of hydrodynamic displacement case 4008.

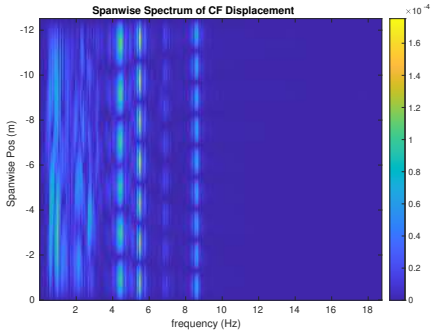

(e) Spanwise cross-flow spectrum of hydrodynamic displacement case 4008.

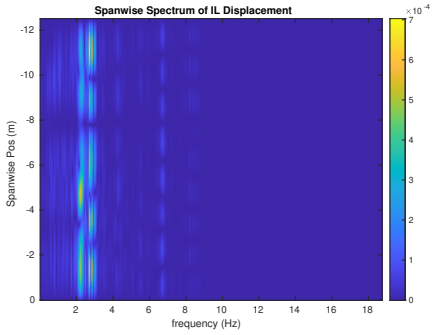

(f) Spanwise inline spectrum of hydrodynamic displacement case 4008.

Figure B-93: *Motion Analysis.* SCR case 4008.

NDP SCR test case 4012

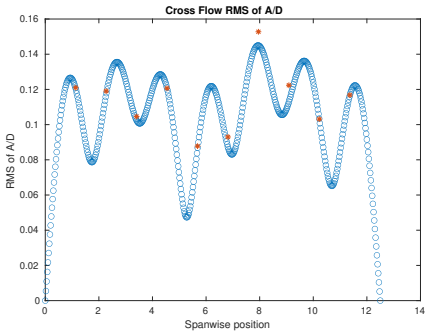

(a) Cross-flow RMS profile case 4012.

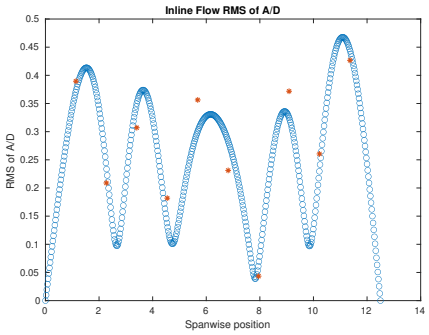

(b) Inline flow RMS profile case 4012.

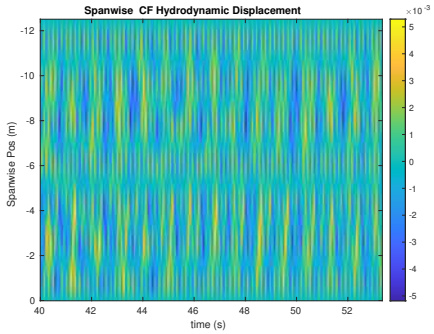

(c) Spanwise cross-flow hydrodynamic displacement case 4012.

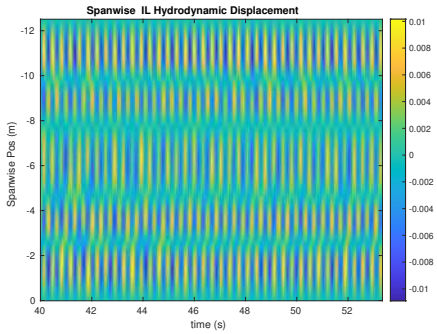

(d) Spanwise inline spectrum of hydrodynamic displacement case 4012.

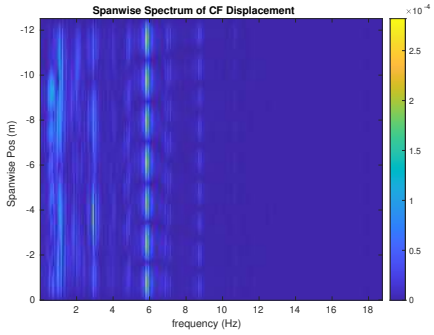

(e) Spanwise cross-flow spectrum of hydrodynamic displacement case 4012.

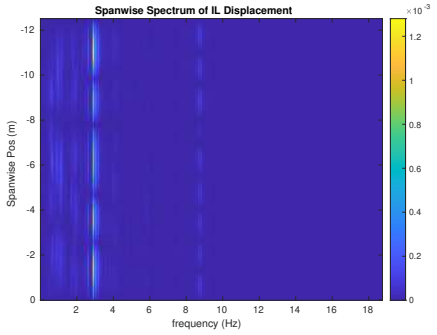

(f) Spanwise inline spectrum of hydrodynamic displacement case 4012.

Figure B-94: *Motion Analysis.* SCR case 4012.

NDP SCR test case 4014

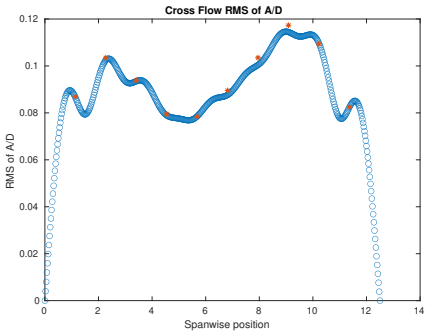

(a) Cross-flow RMS profile case 4014.

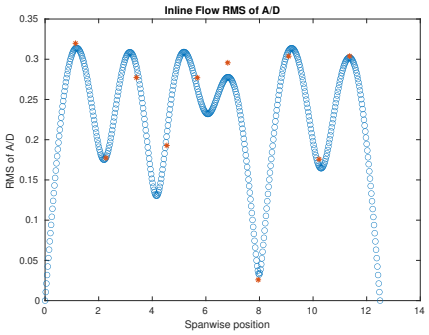

(b) Inline flow RMS profile case 4014.

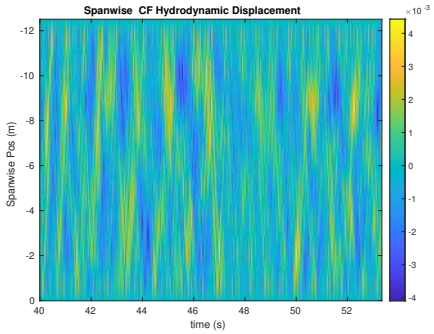

(c) Spanwise cross-flow hydrodynamic displacement case 4014.

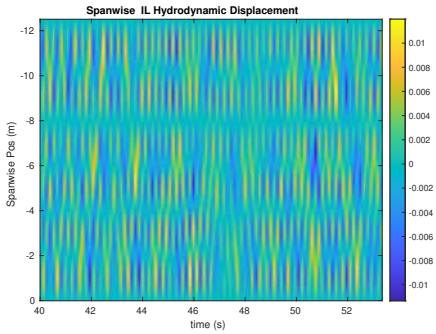

(d) Spanwise inline spectrum of hydrodynamic displacement case 4014.

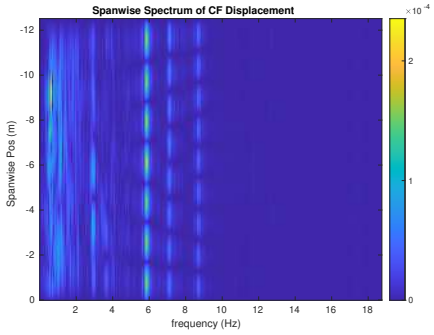

(e) Spanwise cross-flow spectrum of hydrodynamic displacement case 4014.

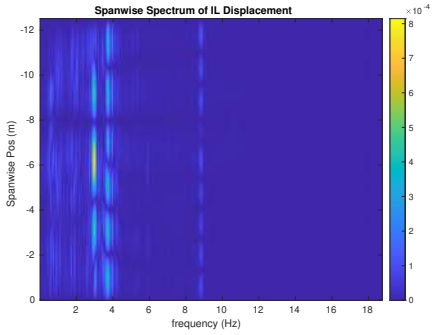

(f) Spanwise inline spectrum of hydrodynamic displacement case 4014.

Figure B-95: *Motion Analysis.* SCR case 4014.

NDP SCR test case 4018

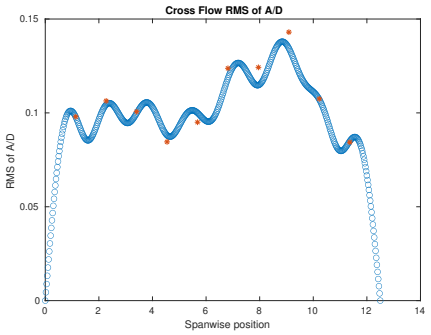

(a) Cross-flow RMS profile case 4018.

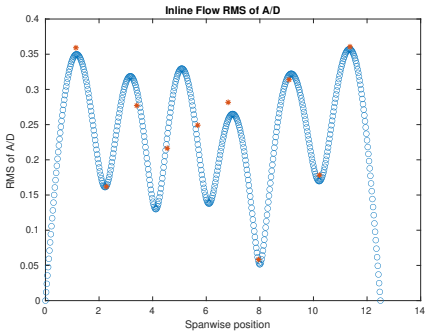

(b) Inline flow RMS profile case 4018.

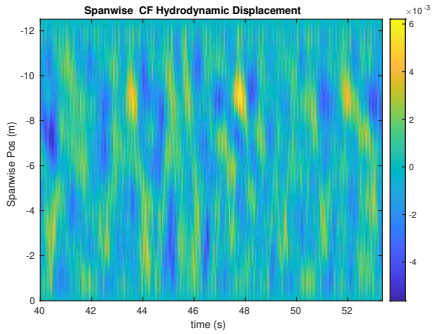

(c) Spanwise cross-flow hydrodynamic displacement case 4018.

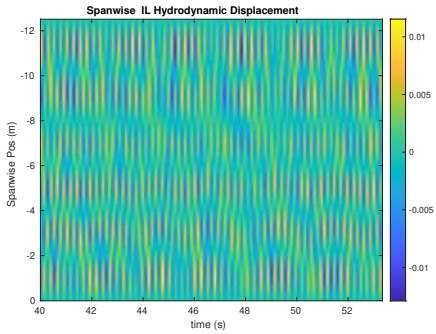

(d) Spanwise inline spectrum of hydrodynamic displacement case 4018.

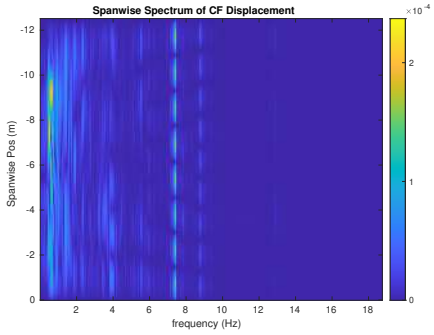

(e) Spanwise cross-flow spectrum of hydrodynamic displacement case 4018.

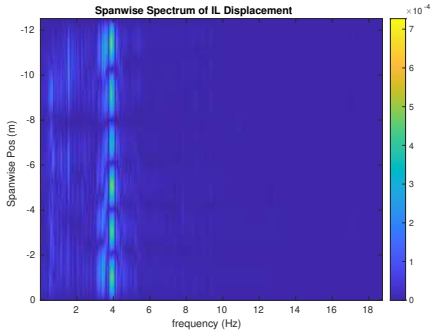

(f) Spanwise inline spectrum of hydrodynamic displacement case 4018.

Figure B-96: *Motion Analysis.* SCR case 4018.

NDP SCR test case 4020

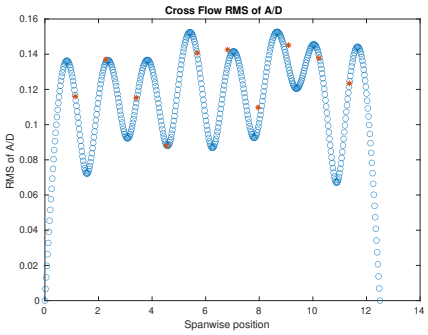

(a) Cross-flow RMS profile case 4020.

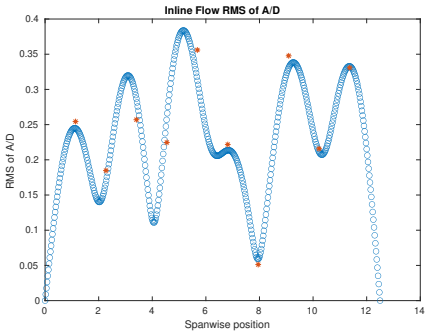

(b) Inline flow RMS profile case 4020.

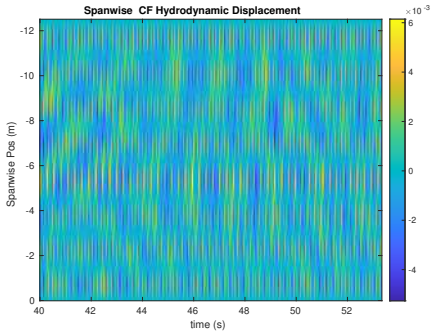

(c) Spanwise cross-flow hydrodynamic displacement case 4020.

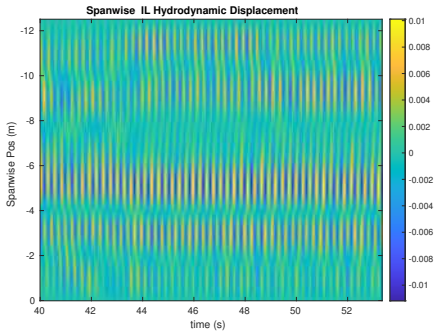

(d) Spanwise inline spectrum of hydrodynamic displacement case 4020.

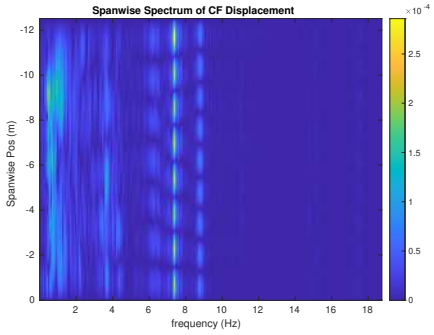

(e) Spanwise cross-flow spectrum of hydrodynamic displacement case 4020.

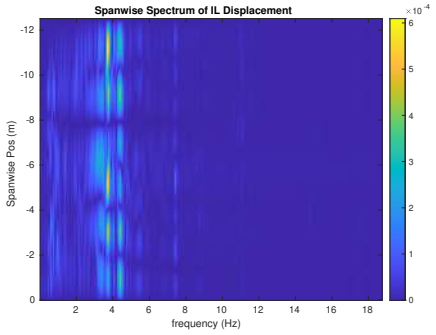

(f) Spanwise inline spectrum of hydrodynamic displacement case 4020.

Figure B-97: *Motion Analysis.* SCR case 4020.

NDP SCR test case 4022

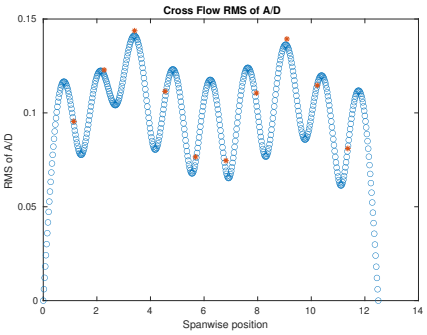

(a) Cross-flow RMS profile case 4022.

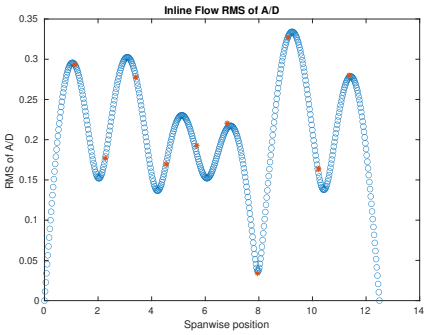

(b) Inline flow RMS profile case 4022.

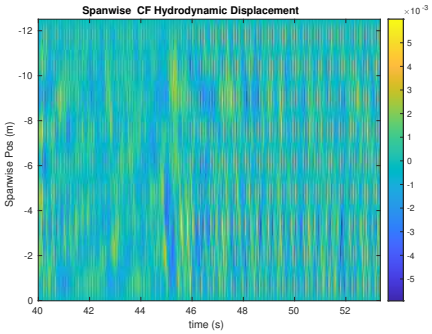

(c) Spanwise cross-flow hydrodynamic displacement case 4022.

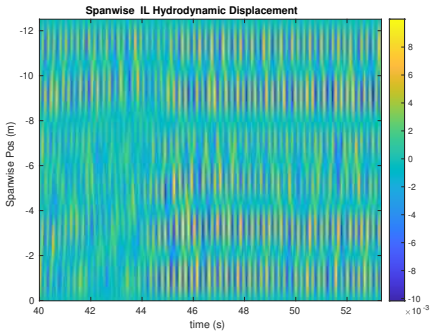

(d) Spanwise inline spectrum of hydrodynamic displacement case 4022.

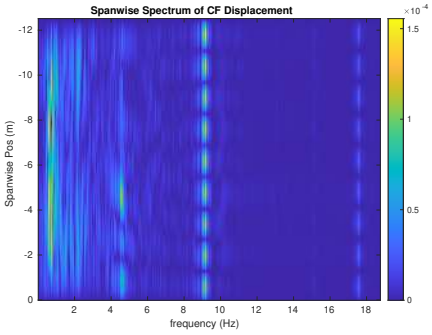

(e) Spanwise cross-flow spectrum of hydrodynamic displacement case 4022.

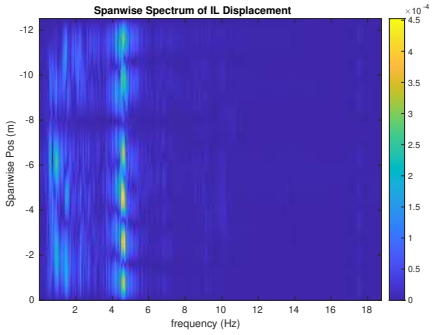

(f) Spanwise inline spectrum of hydrodynamic displacement case 4022.

Figure B-98: *Motion Analysis.* SCR case 4022.

Appendix C

SCR Straight Riser Motion Reconstruction & Analysis

Table C.1: Experiments with case number starting with 2 are naked riser experiments, the remaining are straked riser experiments. Details of the experiments should be consulted in the official NDP reports.

Case	$n_C F$	$n_I L$	Vel Profile
2010	[1:10]	[1:15]	[0.3,0.3]
2020	[1:10]	[1:15]	[0.4,0.4]
2030	[1:10]	[1:15]	[0.5,0.5]
2040	[2:11]	[3:15]	[0.6,0.6]
2050	[2:13]	[2:21]	[0.7,0.7]
2060	[1:10]	[9:15]	[0.8,0.8]
2070	[2:13]	[9:15]	[0.9,0.9]
2080	[4:15]	[13:21]	[1,1]
2090	[4:15]	[10:29]	[1.1,1.1]
2100	[4:15]	[10:29]	[1.2,1.2]
2110	[6:14]	[10:29]	[1.3,1.3]
2120	[8:19]	[10:29]	[1.4,1.4]
2130	[9:20]	[10:29]	[1.5,1.5]
2141	[9:20]	[10:29]	[1.6,1.6]
2150	[9:20]	[19:26]	[1.7,1.7]
2160	[9:20]	[19:26]	[1.8,1.8]
2170	[9:20]	[19:26]	[1.9,1.9]
2182	[9:20]	[19:26]	[2,2]
2191	[9:20]	[19:26]	[2.1,2.1]
2201	[9:20]	[19:26]	[2.2,2.2]
2210	[9:20]	[19:26]	[2.3,2.3]
2220	[9:20]	[19:26]	[2.4,2.4]
2230	[4:15]	[13:21]	[1,1]
2240	[9:20]	[19:29]	[2,2]
2310	[1:10]	[1:15]	[0.3,0]
2320	[1:10]	[1:15]	[0.4,0]
2330	[1:10]	[1:15]	[0.5,0]

2340	[2:11]	[1:15]	[0.6,0]
2350	[2:13]	[2:21]	[0.7,0]
2360	[2:13]	[2:21]	[0.8,0]
2370	[2:13]	[2:21]	[0.9,0]
2380	[4:15]	[4:23]	[1,0]
2390	[4:15]	[7:26]	[1.1,0]
2400	[4:15]	[10:29]	[1.2,0]
2410	[5:16]	[10:29]	[1.3,0]
2420	[5:16]	[10:29]	[1.4,0]
2430	[5:16]	[10:29]	[1.5,0]
2440	[10:21]	[10:29]	[1.6,0]
2450	[10:21]	[15,18,17,19,20,21,22,21,23,24,26,29]	[1.7,0]
2460	[10:21]	[15,18,17,19,20,21,22,21,23,24,26,29]	[1.8,0]
2470	[9:20]	[15,18,17,19,20,21,22,21,23,24,26,29]	[1.9,0]
2480	[9:20]	[15,18,17,19,20,21,22,21,23,24,26,29]	[2,0]
2490	[9:15]	[15,18,17,19,20,21,22,21,23,24,26,29]	[2.1,0]
2500	[9:20]	[15,18,17,19,20,21,22,21,23,24,26,29]	[2.2,0]
2510	[9:20]	[19,20,21,22,21,23,24,26,29]	[2.3,0]
2520	[9:20]	[16,18,20,23,26,29]	[2.4,0]
2530	[4:15]	[5,9,10,12,15,16,18,20]	[1,0]
2540	[5,9,10,15,18,21,24]	[10,15,18,20,23,26,29]	[2,0]
3010	[1:12]	[15:20]	[0.3,0.3]
3020	[1:12]	[15:20]	[0.4,0.4]
3030	[1:12]	[15:20]	[0.5,0.5]
3040	[1:12]	[15:20]	[0.6,0.6]
3050	[1:12]	[15:20]	[0.7,0.7]
3060	[1:12]	[15:20]	[0.8,0.8]
3070	[1:12]	[15:20]	[0.9,0.9]
3081	[1:12]	[15:20]	[1,1]
3090	[1:12]	[15:20]	[1.1,1.1]

3100	[1:12]	[15:20]	[1.2,1.2]
3110	[1:12]	[15:20]	[1.3,1.3]
3120	[1:12]	[15:20]	[1.4,1.4]
3130	[1:12]	[15:20]	[1.5,1.5]
3140	[1:12]	[15:20]	[1.6,1.6]
3150	[1:12]	[15:20]	[1.7,1.7]
3160	[1:12]	[15:20]	[1.8,1.8]
3170	[1:12]	[15:20]	[1.9,1.9]
3180	[1:12]	[15:20]	[2,2]
3190	[1:12]	[15:20]	[2.1,2.1]
3200	[1:12]	[15:20]	[2.2,2.2]
3210	[1:12]	[15:20]	[2.3,2.3]
3220	[1:12]	[15:20]	[2.4,2.4]
3320	[1:12]	[10:15]	[0.4,0]
3340	[1:12]	[10:15]	[0.6,0]
3360	[1:12]	[10:15]	[0.8,0]
3380	[1:12]	[10:15]	[1,0]
3400	[1:12]	[10:15]	[1.2,0]
3420	[1:12]	[10:15]	[1.4,0]
3440	[1:12]	[10:15]	[1.6,0]
3460	[1:12]	[10:15]	[1.8,0]
3481	[1:12]	[10:15]	[2,0]
3500	[1:12]	[10:15]	[2.2,0]
3520	[1:12]	[10:15]	[2.4,0]
3530	[1:12]	[10:15]	[1,0]
3540	[1:12]	[10:15]	[2,0]
3610	[1:12]	[5:15]	[0.3,0.3]
3620	[1:12]	[5:15]	[0.4,0.4]
3630	[1:12]	[5:15]	[0.5,0.5]
3640	[1:12]	[1:10]	[0.6,0.6]

3650	[1:12]	[1:10]	[0.7,0.7]
3660	[1:12]	[1:10]	[0.8,0.8]
3670	[1:12]	[1:10]	[0.9,0.9]
3680	[1:12]	[1:10]	[1,1]
3690	[1:12]	[1:10]	[1.1,1.1]
3700	[1:12]	[1:10]	[1.2,1.2]
3710	[1:12]	[1:10]	[1.3,1.3]
3720	[1:12]	[1:10]	[1.4,1.4]
3730	[1:12]	[1:10]	[1.5,1.5]
3740	[1:12]	[1:10]	[1.6,1.6]
3750	[1:12]	[1:10]	[1.7,1.7]
3760	[1:12]	[1:10]	[1.8,1.8]
3770	[1:12]	[1:10]	[1.9,1.9]
3780	[1:12]	[1:10]	[2,2]
3790	[1:12]	[1:10]	[2.1,2.1]
3800	[1:12]	[1:10]	[2.2,2.2]
3810	[1:12]	[1:10]	[2.3,2.3]
3820	[1:12]	[1:10]	[2.4,2.4]
3830	[1:12]	[1:10]	[1,1]
3910	[1:12]	[5:15]	[0.3,0]
3920	[1:12]	[5:15]	[0.4,0]
3930	[1:12]	[5:15]	[0.5,0]
3940	[1:12]	[1:10]	[0.6,0]
3950	[1:12]	[1:10]	[0.7,0]
3960	[1:12]	[1:10]	[0.8,0]
3970	[1:12]	[1:10]	[0.9,0]
3980	[1:12]	[1:10]	[1,0]
3990	[1:12]	[1:10]	[1.1,0]
4000	[1:12]	[1:10]	[1.2,0]
4010	[1:12]	[1:10]	[1.3,0]

4020	[1:12]	[1:10]	[1.4,0]
4030	[1:12]	[1:10]	[1.5,0]
4040	[1:12]	[1:10]	[1.6,0]
4050	[1:12]	[1:10]	[1.7,0]
4060	[1:12]	[1:10]	[1.8,0]
4070	[1:12]	[1:10]	[1.9,0]
4080	[1:12]	[1:10]	[2,0]
4090	[1:12]	[1:10]	[2.1,0]
4100	[1:12]	[1:10]	[2.2,0]
4110	[1:12]	[1:10]	[2.3,0]
4120	[1:12]	[1:10]	[2.4,0]
4130	[1:12]	[1:10]	[1,0]
4220	[1:12]	[1:15]	[0.4,0.4]
4240	[1:12]	[1:15]	[0.6,0.6]
4260	[10:14]	[2:21]	[0.8,0.8]
4280	[2:18]	[4:23]	[1,1]
4300	[5,7,8,9,10,11,12,13,14,15,17,19]	[4:23]	[1.2,1.2]
4320	[3,9,10,11,12,13,14,15]	[4:23]	[1.4,1.4]
4340	[3,9,10,11,12,13,14,15]	[4:23]	[1.6,1.6]
4360	[3,9,10,11,12,13,14,15]	[4:23]	[1.8,1.8]
4380	[3,9,10,11,12,13,14,15]	[4:23]	[2,2]
4400	[3,9,10,11,13,14,15]	[4:23]	[2.2,2.2]
4420	[5,9,10,12,11,13,14,15]	[4:23]	[2.4,2.4]
4430	[6,7,8,9,10,12,11,13,14,15]	[4:23]	[1,1]
4520	[1:17]	[4:21]	[0.4,0]
4540	[1:17]	[4:21]	[0.6,0]
4560	[1:17]	[4:21]	[0.8,0]
4580	[1:17]	[4:21]	[1,0]
4600	[1:17]	[4:21]	[1.2,0]
4620	[1:17]	[4:21]	[1.4,0]

4640	[1:17]	[4:21]	[1.6,0]
4660	[1:17]	[4:21]	[1.8,0]
4680	[1:17]	[4:21]	[2,0]
4700	[1:17]	[4:21]	[2.2,0]
4720	[1:17]	[4:21]	[2.4,0]
4730	[1:17]	[4:21]	[1,0]
4811	[1:12]	[4:21]	[0.3,0.3]
4820	[1:12]	[4:21]	[0.4,0.4]
4830	[1:12]	[4:21]	[0.5,0.5]
4840	[2:13]	[4:21]	[0.6,0.6]
4850	[3:19]	[4:21]	[0.7,0.7]
4860	[3:15]	[4:21]	[0.8,0.8]
4870	[5:13]	[4:21]	[0.9,0.9]
4880	[6,7,8,9,10,12,11,13,14,15]	[4:21]	[1,1]
4890	[3,4,5,6,7,16,17,18,19]	[4:21]	[1.1,1.1]
4900	[3,4,5,6,7,13,14,15,16,17,18,19,20,21]	[4:21]	[1.2,1.2]
4910	[3,4,5,6,7,8,14,15,16,17,18,19]	[4:21]	[1.3,1.3]
4920	[3,4,5,6,7,8,12,13,14,15,16,17,18,19]	[4:21]	[1.4,1.4]
4930	[3,4,5,6,7,8,14,15,16,17,18,19]	[4:21]	[1.5,1.5]
4940	[3,4,5,6,7,8,14,15,16,17,18,19]	[4:21]	[1.6,1.6]
4950	[3,4,5,6,7,8,15,16,17,18,19]	[4:21]	[1.7,1.7]
4960	[3,4,5,6,7,8,15,16,17,18,19]	[4:21]	[1.8,1.8]
4970	[3,4,5,6,7,8,15,16,17,18,19]	[4:21]	[1.9,1.9]
4980	[3,4,5,6,7,8,15,16,17,18,19]	[4:21]	[2,2]
4990	[3,4,5,6,7,8,15,16,17,18,19]	[4:21]	[2.1,2.1]
5000	[3,4,5,6,7,8,15,16,17,18,19]	[4:21]	[2.2,2.2]
5010	[3,4,5,6,7,8,15,16,17,18,19]	[4:21]	[2.3,2.3]
5020	[3,4,5,6,7,8,15,16,17,18,19]	[4:21]	[2.4,2.4]
5020	[3,4,5,6,7,8,15,16,17,18,19]	[4:21]	[1,1]
5110	[1:12]	[1:15]	[0.3,0]

5120	[1:12]	[1:15]	[0.4,0]
5130	[1:12]	[1:15]	[0.5,0]
5140	[1:12]	[1:15]	[0.6,0]
5150	[1:12]	[1:15]	[0.7,0]
5160	[1:12]	[1:15]	[0.8,0]
5170	[1:12]	[1:15]	[0.9,0]
5180	[1:12]	[1:15]	[1,0]
5190	[1:12]	[1:15]	[1.1,0]
5200	[1:12]	[1:15]	[1.2,0]
5210	[1:12]	[1:15]	[1.3,0]
5220	[1:12]	[1:15]	[1.4,0]
5230	[1:12]	[1:15]	[1.5,0]
5240	[1:13]	[1:15]	[1.6,0]
5250	[1:13]	[1:15]	[1.7,0]
5260	[3,4,5,6,7,12,13,14,15,16,17,18,19]	[1:15]	[1.8,0]
5270	[3,4,5,6,7,12,13,14,15,16,17,18,19]	[1:15]	[1.9,0]
5280	[3,4,5,6,7,12,13,14,15,16,17,18,19]	[1:15]	[2.0,0]
5290	[3,4,5,6,7,12,13,14,15,16,17,18,19]	[1:15]	[2.1,0]
5300	[3,4,5,6,7,12,13,14,15,16,17,18,19]	[1:15]	[2.2,0]
5310	[3,4,5,6,7,12,13,14,15,16,17,18,19]	[1:15]	[2.3,0]
5320	[3,4,5,6,7,12,13,14,15,16,17,18,19]	[1:15]	[2.4,0]
5330	[1:12]	[1:15]	[1,0]
6010	[1:12]	[1:15]	[0.3,0.3]
6020	[1:12]	[1:15]	[0.4,0.4]
6030	[1:12]	[1:15]	[0.5,0.5]
6040	[1:12]	[1:15]	[0.6,0.6]
6050	[1:12]	[1:15]	[0.7,0.7]
6060	[1:12]	[1:15]	[0.8,0.8]
6070	[1:12]	[4:23]	[0.9,0.9]
6080	[1:14]	[4:23]	[1,1]

6090	[1:14]	[4:23]	[1.1,1.1]
6100	[1:14]	[4:23]	[1.2,1.2]
6110	[9:19]	[4:23]	[1.3,1.3]
6120	[9:19]	[4:23]	[1.4,1.4]
6130	[9:19]	[4:23]	[1.5,1.5]
6140	[10:19]	[4:23]	[1.6,1.6]
6150	[10:19]	[4:23]	[1.7,1.7]
6160	[10:19]	[4:23]	[1.8,1.8]
6170	[10:19]	[4:23]	[1.9,1.9]
6180	[10:19]	[4:23]	[2,2]
6190	[10:19]	[4:23]	[2.1,2.1]
6200	[10:19]	[4:23]	[2.2,2.2]
6210	[10:19]	[4:23]	[2.3,2.3]
6220	[10:18]	[4:23]	[2.4,2.4]
6230	[10:19]	[4:23]	[1,1]
6240	[10:19]	[4:23]	[2,2]
6310	[1:12]	[1:15]	[0.3,0]
6320	[1:12]	[1:15]	[0.4,0]
6330	[1:12]	[1:15]	[0.5,0]
6340	[1:12]	[1:15]	[0.6,0]
6350	[1:12]	[1:15]	[0.7,0]
6360	[1:12]	[1:15]	[0.8,0]
6370	[1:12]	[1:15]	[0.9,0]
6380	[1:12]	[1:15]	[1,0]
6391	[1:12]	[1:15]	[1.1,0]
6400	[1:12]	[1:15]	[1.2,0]
6410	[1:12]	[1:15]	[1.3,0]
6420	[1:12]	[1:15]	[1.4,0]
6430	[1:12]	[1:15]	[1.5,0]
6440	[1:12]	[1:15]	[1.6,0]

6450	[1:12]	[1:15]	[1.7,0]
6460	[1:12]	[1:15]	[1.8,0]
6470	[1:12]	[1:15]	[1.9,0]
6480	[1:12]	[1:15]	[2,0]
6490	[1:12]	[1:15]	[2.1,0]
6500	[1:12]	[1:15]	[2.2,0]
6510	[1:12]	[1:15]	[2.3,0]
6520	[1:12]	[1:15]	[2.4,0]
6530	[1:12]	[1:15]	[1,0]
6610	[1:12]	[1:15]	[0.3,0.3]
6620	[1:12]	[1:15]	[0.4,0.4]
6630	[1:12]	[1:15]	[0.5,0.5]
6640	[1:12]	[1:15]	[0.6,0.6]
6650	[1:12]	[1:15]	[0.7,0.7]
6660	[1:12]	[1:15]	[0.8,0.8]
6670	[1:12]	[1:15]	[0.9,0.9]
6680	[1:12]	[1:15]	[1,1]
6690	[1:12]	[1:15]	[1.1,1.1]
6700	[9:16]	[1:15]	[1.2,1.2]
6710	[9:16]	[1:15]	[1.3,1.3]
6720	[9:16]	[1:15]	[1.4,1.4]
6730	[9:16]	[1:15]	[1.5,1.5]
6740	[9:16]	[1:15]	[1.6,1.6]
6750	[9:16]	[1:15]	[1.7,1.7]
6760	[9:16]	[1:15]	[1.8,1.8]
6770	[9:16]	[1:15]	[1.9,1.9]
6780	[9:16]	[1:15]	[2,2]
6790	[9:16]	[1:15]	[2.1,2.1]
6800	[9:16]	[1:15]	[2.2,2.2]
6810	[15:21]	[1:15]	[2.3,2.3]

6820	[15:21]	[1:15]	[2.4,2.4]
6830	[1:12]	[1:15]	[1,1]
6910	[1:12]	[1:15]	[0.3,0]
6920	[1:12]	[1:15]	[0.4,0]
6930	[1:12]	[1:15]	[0.5,0]
6940	[1:12]	[1:15]	[0.6,0]
6950	[1:12]	[1:15]	[0.7,0]
6960	[1:12]	[1:15]	[0.8,0]
6970	[1:12]	[1:15]	[0.9,0]
6980	[1:12]	[1:15]	[1,0]
6990	[1:12]	[1:15]	[1.1,0]
7000	[1:12]	[1:15]	[1.2,0]
7010	[1:12]	[1:15]	[1.3,0]
7020	[1:12]	[1:15]	[1.4,0]
7030	[1:12]	[1:15]	[1.5,0]
7040	[1:12]	[1:15]	[1.6,0]
7050	[1:12]	[1:15]	[1.7,0]
7060	[1:12]	[1:15]	[1.8,0]
7070	[1:12]	[1:15]	[1.9,0]
7080	[1:12]	[1:15]	[2,0]
7090	[1:12]	[1:15]	[2.1,0]
7100	[1:12]	[1:15]	[2.2,0]
7110	[1:12]	[1:15]	[2.3,0]
7120	[1:12]	[1:15]	[2.4,0]
7130	[1:12]	[1:15]	[1,0]
7140	[1:12]	[1:15]	[2,0]
7210	[1:12]	[1:15]	[0.3,0.3]
7220	[1:12]	[1:15]	[0.4,0.4]
7230	[1:12]	[1:15]	[0.5,0.5]
7240	[1:12]	[1:15]	[0.6,0.6]

7250	[1:12]	[1:15]	[0.7,0.7]
7260	[6:13]	[1:15]	[0.8,0.8]
7270	[8:15]	[1:15]	[0.9,0.9]
7280	[8:15]	[1:15]	[1,1]
7290	[9:16]	[1:15]	[1.1,1.1]
7300	[9:16]	[1:15]	[1.2,1.2]
7310	[9:16]	[8:27]	[1.3,1.3]
7320	[9:16]	[8:27]	[1.4,1.4]
7330	[9:16]	[8:27]	[1.5,1.5]
7340	[9:16]	[8:27]	[1.6,1.6]
7350	[9:16]	[8:27]	[1.7,1.7]
7360	[12:19]	[8:27]	[1.8,1.8]
7370	[12:19]	[8:27]	[1.9,1.9]
7380	[12:19]	[8:27]	[2,2]
7390	[12:19]	[8:27]	[2.1,2.1]
7400	[12:19]	[8:27]	[2.2,2.2]
7410	[12:19]	[8:27]	[2.3,2.3]
7420	[12:19]	[8:27]	[2.4,2.4]
7430	[8:15]	[1:15]	[1,1]
7810	[1:12]	[1:15]	[0.3,0.3]
7820	[1:12]	[1:15]	[0.3,0.3]
7830	[1:12]	[1:15]	[0.5,0.5]
7840	[1:12]	[1:15]	[0.6,0.6]
7850	[1:12]	[1:15]	[0.7,0.7]
7860	[1:12]	[1:15]	[0.8,0.8]
7870	[8:15]	[1:15]	[0.9,0.9]
7880	[3,9,10,11,12,13,14,15]	[1:15]	[1,1]
7890	[3,9,10,11,12,13,14,15]	[1:15]	[1.1,1.1]
7900	[3,9,10,11,12,13,14,15]	[1:15]	[1.2,1.2]
7910	[3,9,10,11,12,13,14,15]	[1:15]	[1.3,1.3]

7920	[9,10,11,12,13,14,15]	[1:15]	[1.4,1.4]
7930	[9,10,11,12,13,14,15]	[1:15]	[1.5,1.5]
7940	[9,10,11,12,13,14,15]	[9,10,11,12,13,14,15]	[1.6,1.6]
7950	[9,10,11,12,13,14,15]	[9,10,11,12,13,14,15]	[1.7,1.7]
7960	[9,10,11,12,13,14,15]	[9,10,11,12,13,14,15]	[1.8,1.8]
7970	[9,10,11,12,13,14,15]	[9,10,11,12,13,14,15]	[1.9,1.9]
7980	[9,10,11,12,13,14,15]	[13,14,15,18,17,19,20,22,21,23,26,28,29]	[2,2]
7990	[9,10,11,12,13,14,15]	[13,14,15,18,17,19,20,22,21,23,26,28,29]	[2.1,2.1]
8000	[9,10,11,12,13,14,15]	[13,14,15,18,17,19,20,22,21,23,26,28,29]	[2.2,2.2]
8010	[9,10,11,12,13,14,15]	[13,14,15,18,17,19,20,22,21,23,26,28,29]	[2.3,2.3]
8020	[9,10,11,12,13,14,15]	[13,14,15,18,17,19,20,22,21,23,26,28,29]	[2.4,2.4]
8030	[3,9,10,11,12,13,14,15]	[1:15]	[1,1]
8040	[9,10,11,12,13,14,15]	[13,14,15,18,17,19,20,22,21,23,26,28,29]	[2.2,2.2]

NDP Straight Riser ($L = 38m$) test case 2010

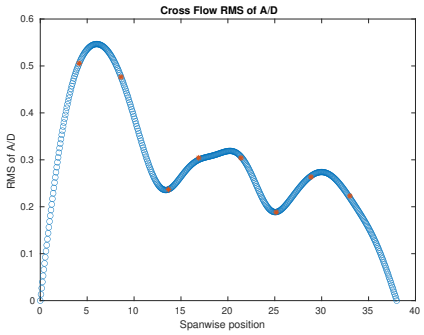

(a) Cross-flow RMS profile case 2010.

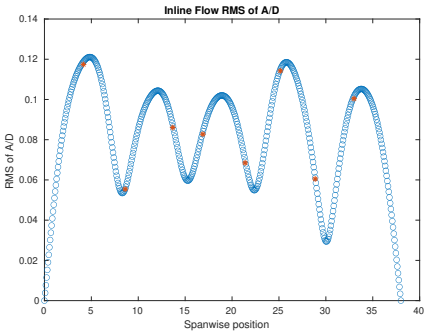

(b) Inline flow RMS profile case 2010.

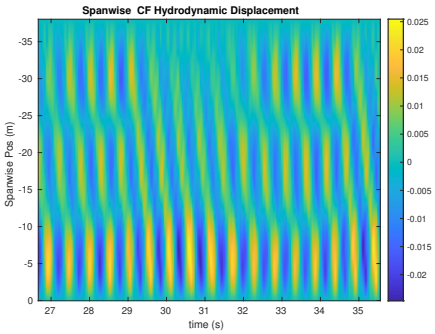

(c) Spanwise cross-flow hydrodynamic displacement case 2010.

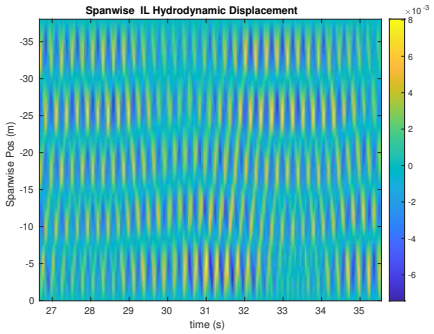

(d) Spanwise inline hydrodynamic displacement case 2010.

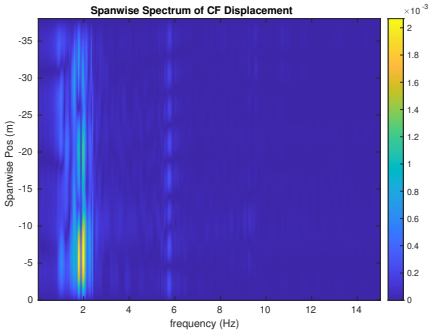

(e) Spanwise cross-flow spectrum of hydrodynamic displacement case 2010.

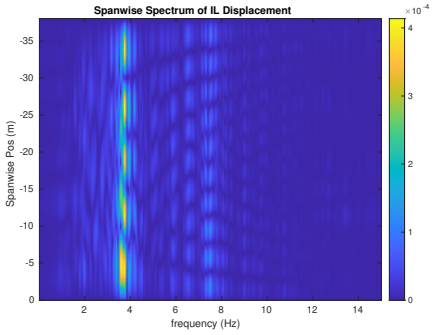

(f) Spanwise inline spectrum of hydrodynamic displacement case 2010.

Figure C-1: *Motion Analysis.* NDP Straight Riser ($L = 38m$) test case 2010.

NDP Straight Riser ($L = 38m$) test case 2020

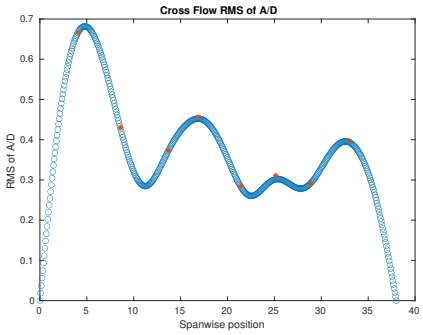

(a) Cross-flow RMS profile case 2020.

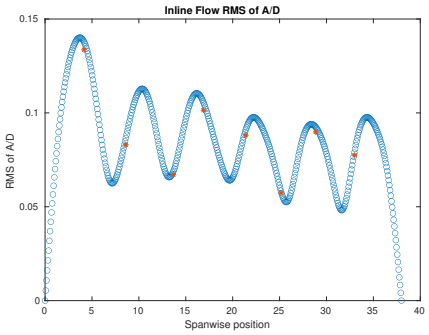

(b) Inline flow RMS profile case 2020.

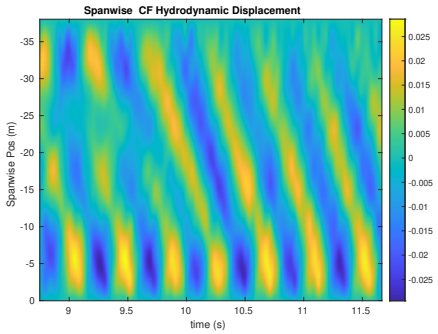

(c) Spanwise cross-flow hydrodynamic displacement case 2020.

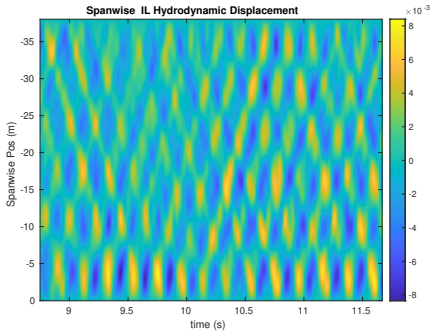

(d) Spanwise inline hydrodynamic displacement case 2020.

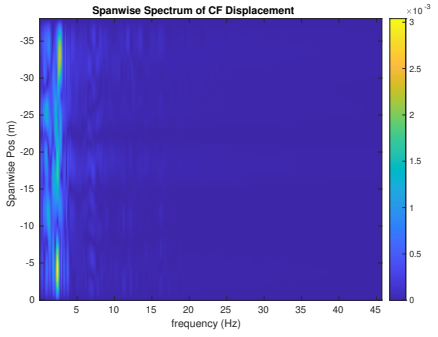

(e) Spanwise cross-flow spectrum of hydrodynamic displacement case 2020.

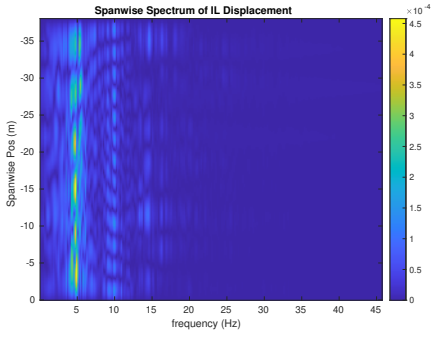

(f) Spanwise inline spectrum of hydrodynamic displacement case 2020.

Figure C-2: *Motion Analysis.* NDP Straight Riser ($L = 38m$) test case 2020.

NDP Straight Riser ($L = 38m$) test case 2030

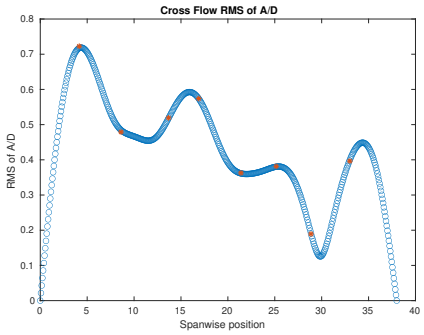

(a) Cross-flow RMS profile case 2030.

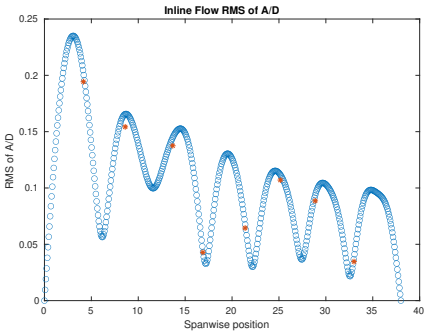

(b) Inline flow RMS profile case 2030.

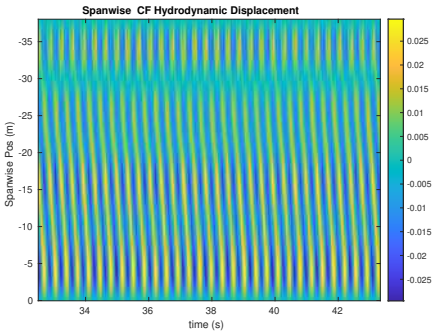

(c) Spanwise cross-flow hydrodynamic displacement case 2030.

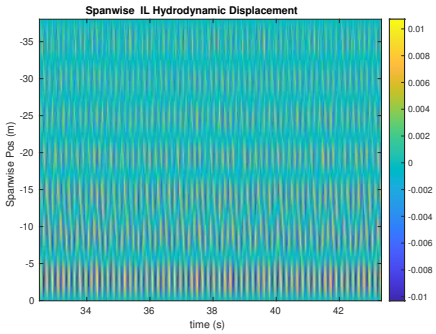

(d) Spanwise inline hydrodynamic displacement case 2030.

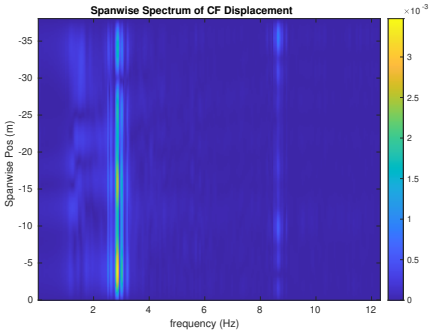

(e) Spanwise cross-flow spectrum of hydrodynamic displacement case 2030.

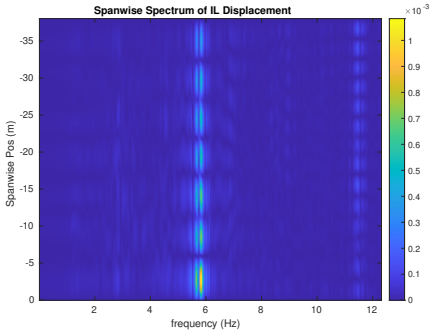

(f) Spanwise inline spectrum of hydrodynamic displacement case 2030.

Figure C-3: *Motion Analysis.* NDP Straight Riser ($L = 38m$) test case 2030.

NDP Straight Riser ($L = 38m$) test case 2040

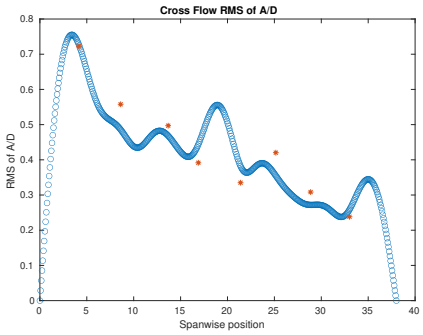

(a) Cross-flow RMS profile case 2040.

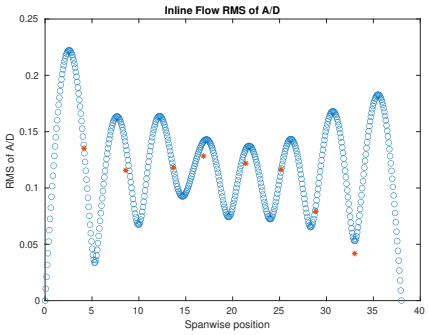

(b) Inline flow RMS profile case 2040.

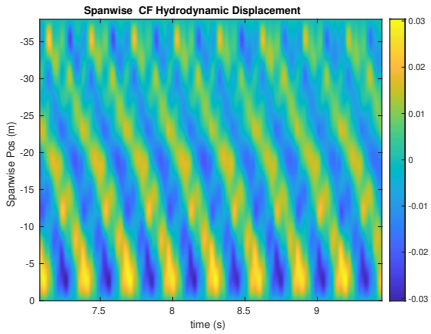

(c) Spanwise cross-flow hydrodynamic displacement case 2040.

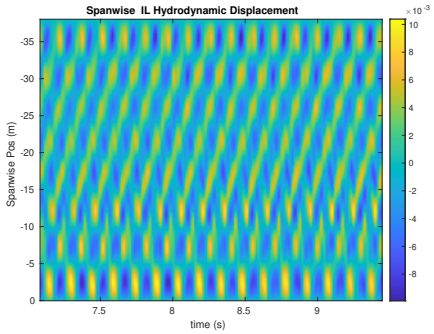

(d) Spanwise inline hydrodynamic displacement case 2040.

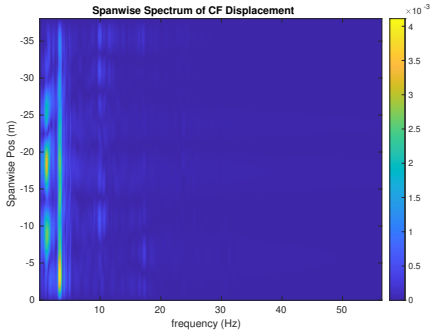

(e) Spanwise cross-flow spectrum of hydrodynamic displacement case 2040.

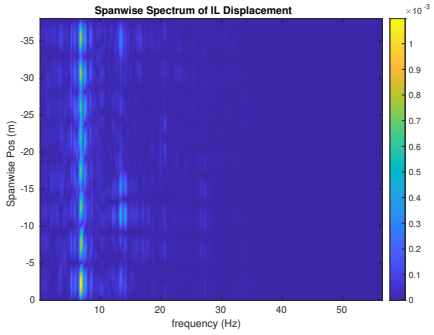

(f) Spanwise inline spectrum of hydrodynamic displacement case 2040.

Figure C-4: *Motion Analysis.* NDP Straight Riser ($L = 38m$) test case 2040.

NDP Straight Riser ($L = 38m$) test case 2050

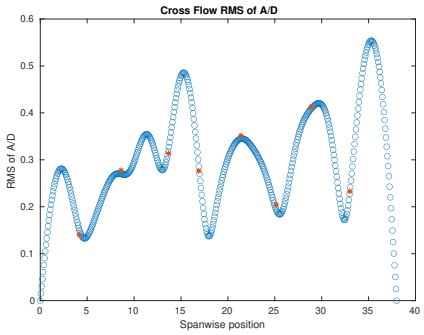

(a) Cross-flow RMS profile case 2050.

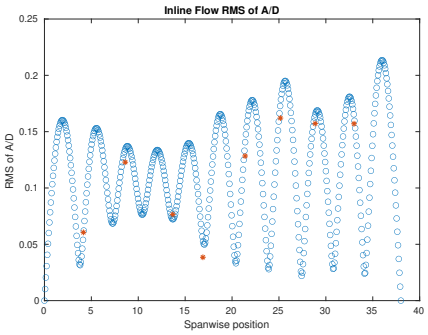

(b) Inline flow RMS profile case 2050.

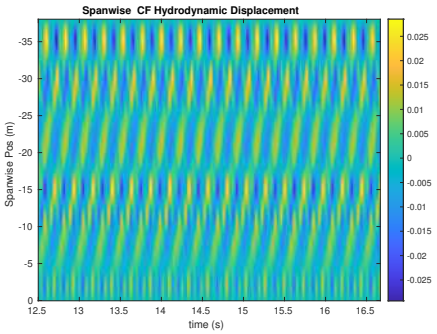

(c) Spanwise cross-flow hydrodynamic displacement case 2050.

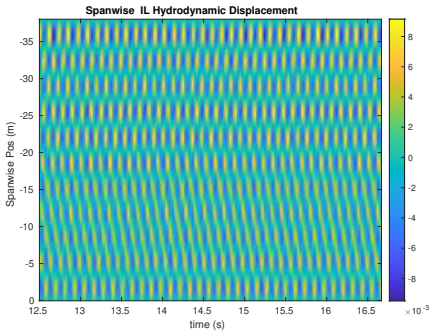

(d) Spanwise inline hydrodynamic displacement case 2050.

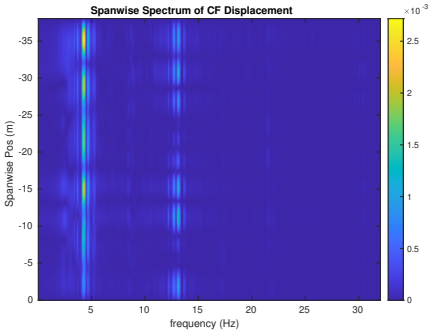

(e) Spanwise cross-flow spectrum of hydrodynamic displacement case 2050.

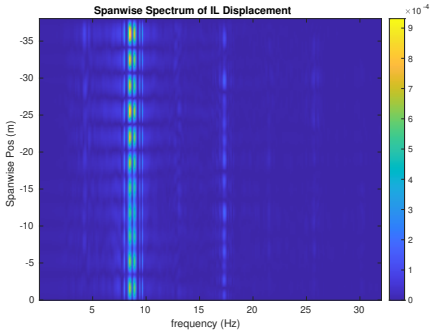

(f) Spanwise inline spectrum of hydrodynamic displacement case 2050.

Figure C-5: *Motion Analysis.* NDP Straight Riser ($L = 38m$) test case 2050.

NDP Straight Riser ($L = 38m$) test case 2060

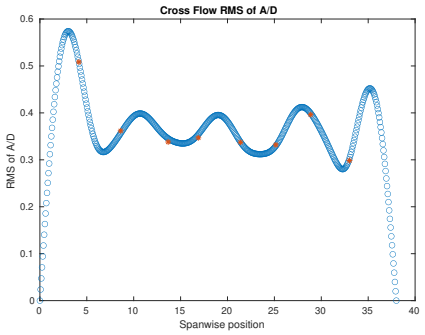

(a) Cross-flow RMS profile case 2060.

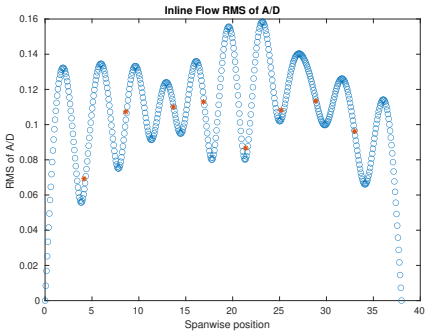

(b) Inline flow RMS profile case 2060.

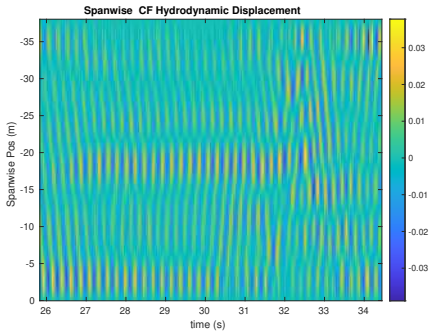

(c) Spanwise cross-flow hydrodynamic displacement case 2060.

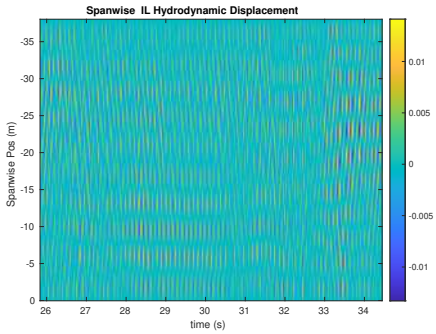

(d) Spanwise inline hydrodynamic displacement case 2060.

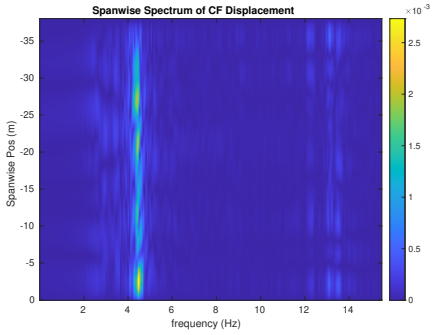

(e) Spanwise cross-flow spectrum of hydrodynamic displacement case 2060.

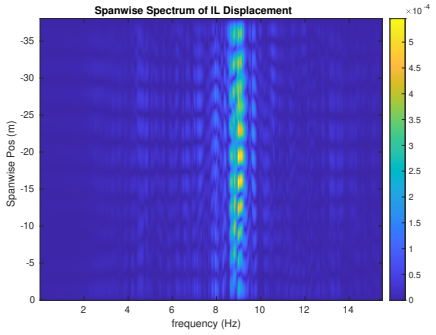

(f) Spanwise inline spectrum of hydrodynamic displacement case 2060.

Figure C-6: *Motion Analysis.* NDP Straight Riser ($L = 38m$) test case 2060.

NDP Straight Riser ($L = 38m$) test case 2070

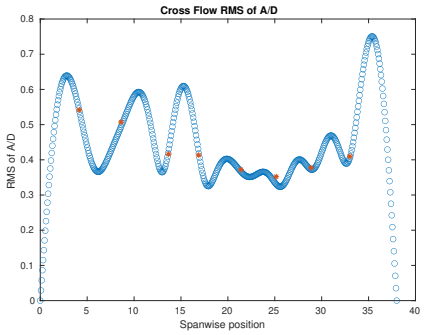

(a) Cross-flow RMS profile case 2070.

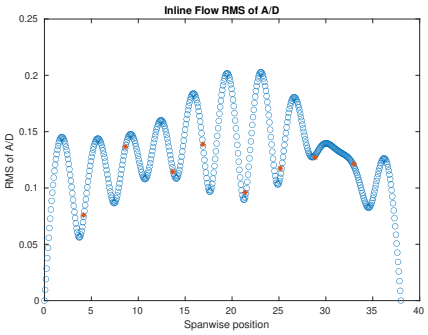

(b) Inline flow RMS profile case 2070.

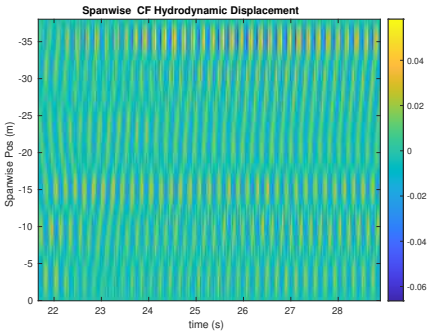

(c) Spanwise cross-flow hydrodynamic displacement case 2070.

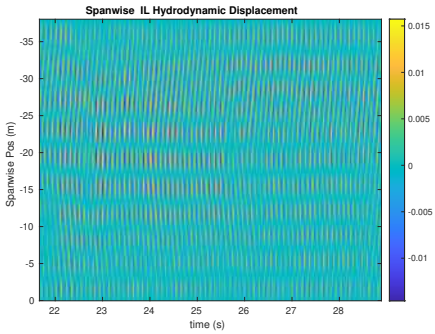

(d) Spanwise inline hydrodynamic displacement case 2070.

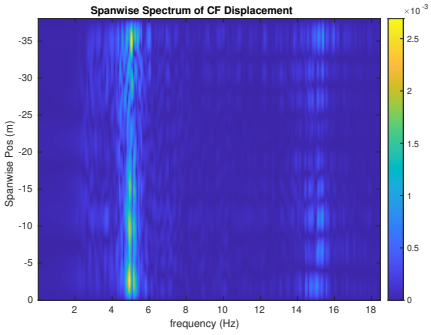

(e) Spanwise cross-flow spectrum of hydrodynamic displacement case 2070.

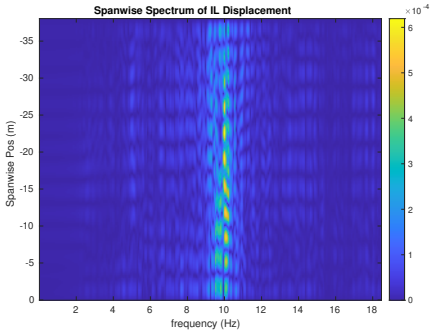

(f) Spanwise inline spectrum of hydrodynamic displacement case 2070.

Figure C-7: *Motion Analysis.* NDP Straight Riser ($L = 38m$) test case 2070.

NDP Straight Riser ($L = 38m$) test case 2080

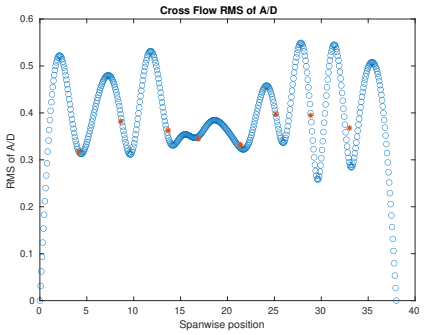

(a) Cross-flow RMS profile case 2080.

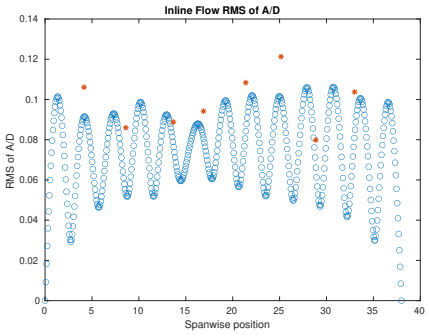

(b) Inline flow RMS profile case 2080.

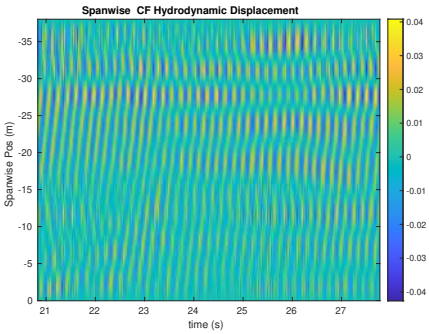

(c) Spanwise cross-flow hydrodynamic displacement case 2080.

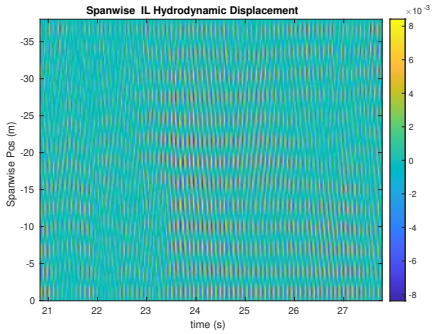

(d) Spanwise inline hydrodynamic displacement case 2080.

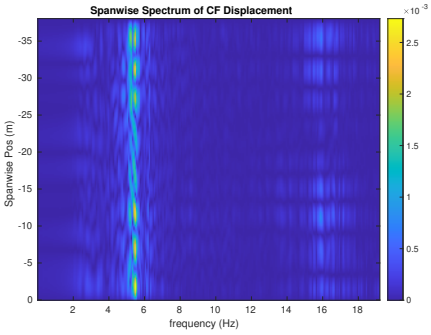

(e) Spanwise cross-flow spectrum of hydrodynamic displacement case 2080.

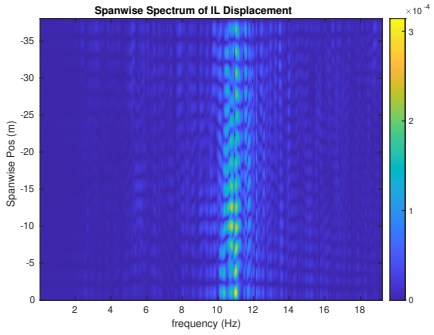

(f) Spanwise inline spectrum of hydrodynamic displacement case 2080.

Figure C-8: *Motion Analysis.* NDP Straight Riser ($L = 38m$) test case 2080.

NDP Straight Riser ($L = 38m$) test case 2090

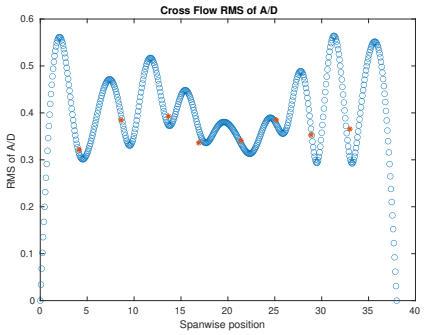

(a) Cross-flow RMS profile case 2090.

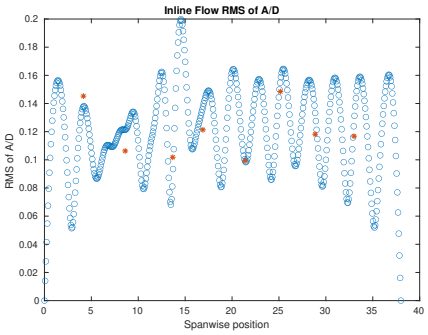

(b) Inline flow RMS profile case 2090.

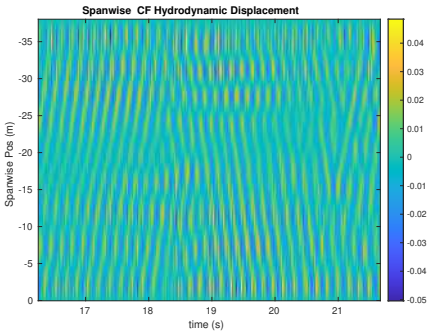

(c) Spanwise cross-flow hydrodynamic displacement case 2090.

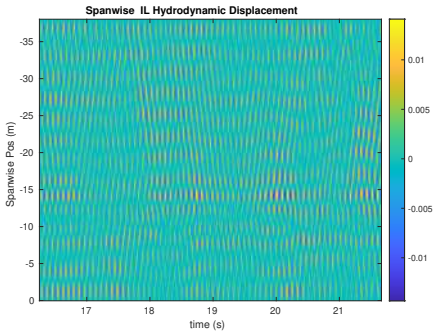

(d) Spanwise inline hydrodynamic displacement case 2090.

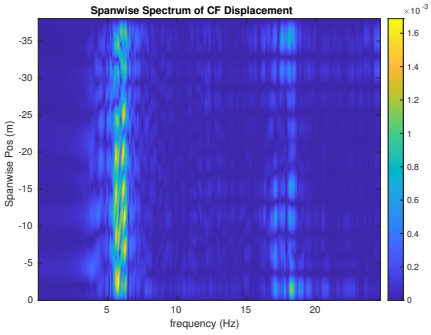

(e) Spanwise cross-flow spectrum of hydrodynamic displacement case 2090.

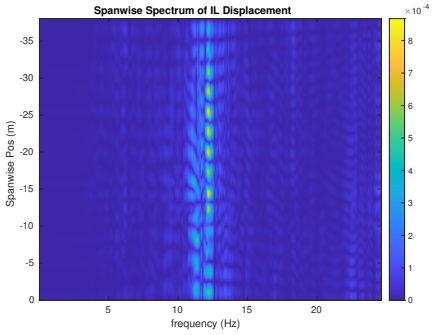

(f) Spanwise inline spectrum of hydrodynamic displacement case 2090.

Figure C-9: *Motion Analysis.* NDP Straight Riser ($L = 38m$) test case 2090.

NDP Straight Riser ($L = 38m$) test case 2100

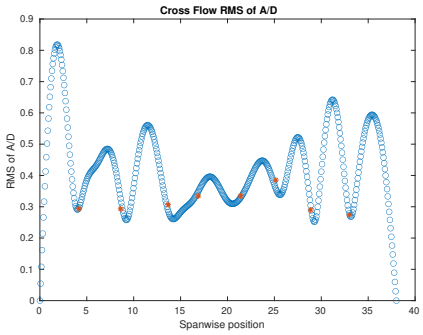

(a) Cross-flow RMS profile case 2100.

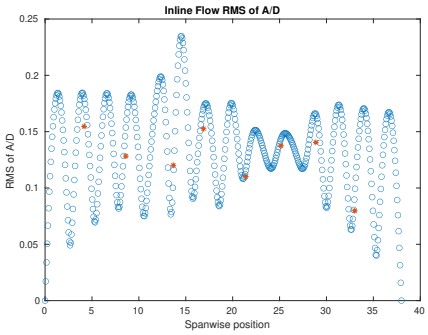

(b) Inline flow RMS profile case 2100.

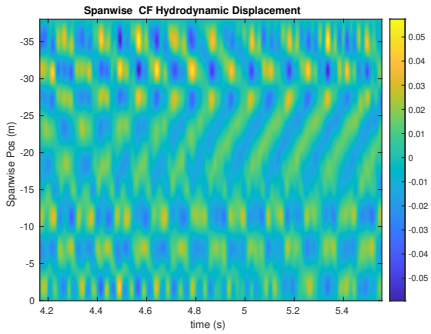

(c) Spanwise cross-flow hydrodynamic displacement case 2100.

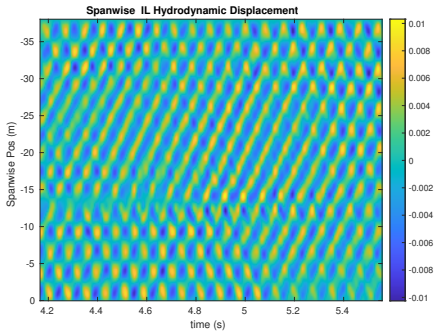

(d) Spanwise inline hydrodynamic displacement case 2100.

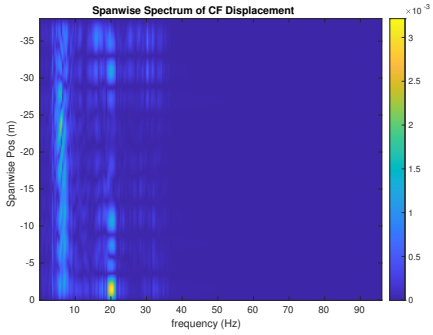

(e) Spanwise cross-flow spectrum of hydrodynamic displacement case 2100.

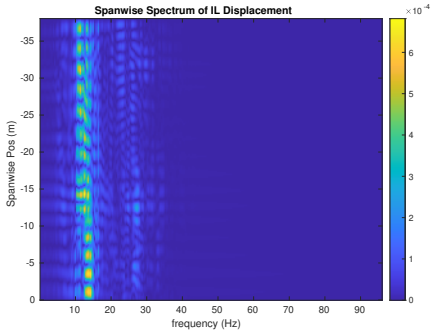

(f) Spanwise inline spectrum of hydrodynamic displacement case 2100.

Figure C-10: *Motion Analysis.* NDP Straight Riser ($L = 38m$) test case 2100.

NDP Straight Riser ($L = 38m$) test case 2110

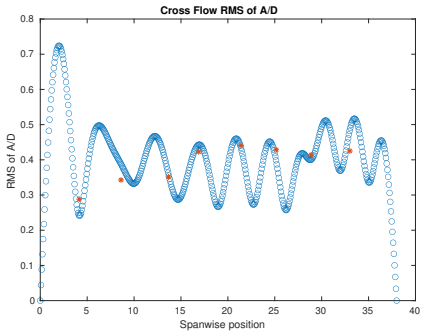

(a) Cross-flow RMS profile case 2110.

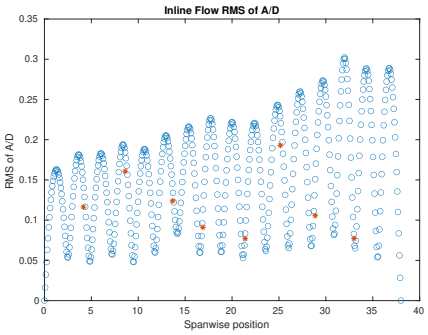

(b) Inline flow RMS profile case 2110.

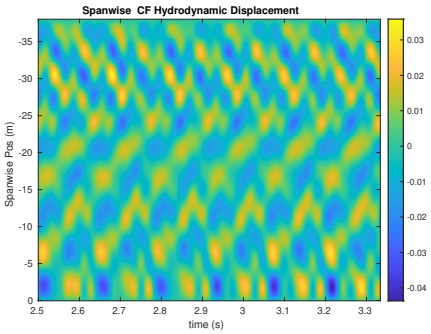

(c) Spanwise cross-flow hydrodynamic displacement case 2110.

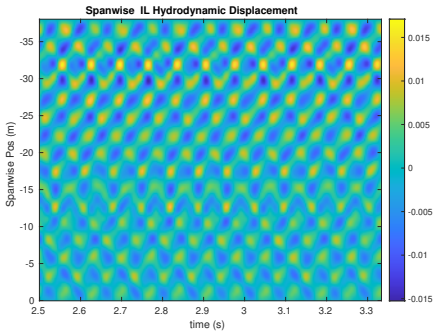

(d) Spanwise inline hydrodynamic displacement case 2110.

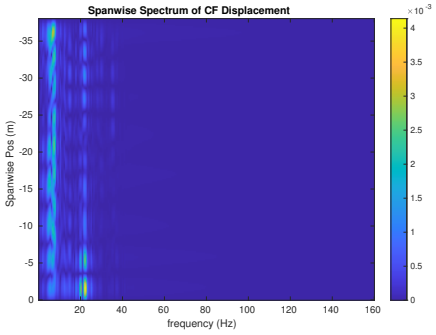

(e) Spanwise cross-flow spectrum of hydrodynamic displacement case 2110.

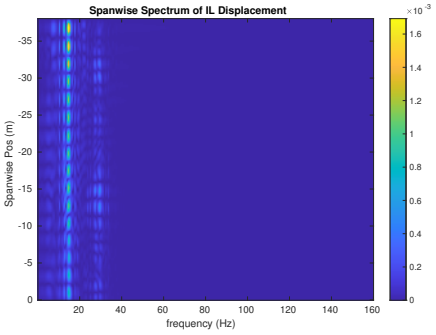

(f) Spanwise inline spectrum of hydrodynamic displacement case 2110.

Figure C-11: *Motion Analysis.* NDP Straight Riser ($L = 38m$) test case 2110.

NDP Straight Riser ($L = 38m$) test case 2120

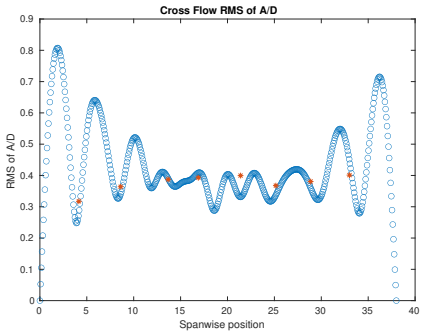

(a) Cross-flow RMS profile case 2120.

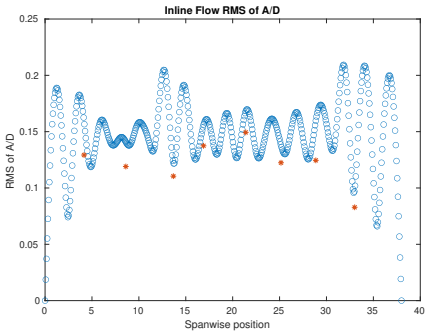

(b) Inline flow RMS profile case 2120.

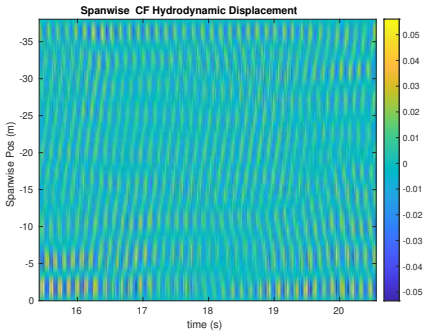

(c) Spanwise cross-flow hydrodynamic displacement case 2120.

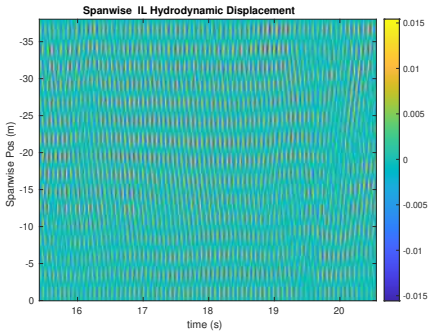

(d) Spanwise inline hydrodynamic displacement case 2120.

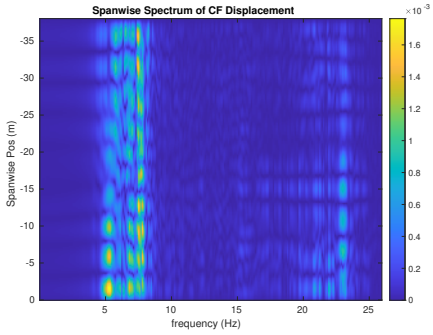

(e) Spanwise cross-flow spectrum of hydrodynamic displacement case 2120.

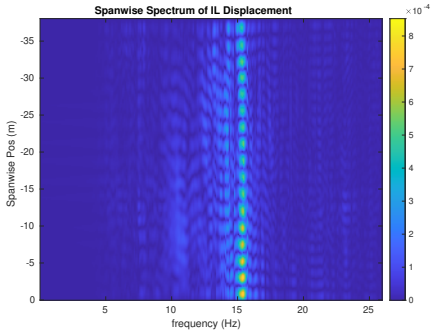

(f) Spanwise inline spectrum of hydrodynamic displacement case 2120.

Figure C-12: *Motion Analysis.* NDP Straight Riser ($L = 38m$) test case 2120.

NDP Straight Riser ($L = 38m$) test case 2130

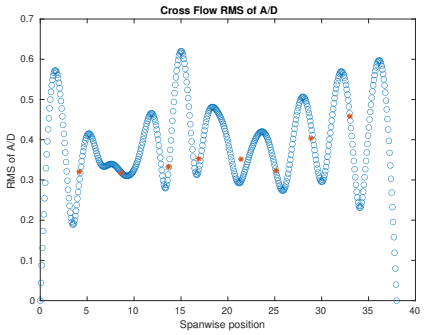

(a) Cross-flow RMS profile case 2130.

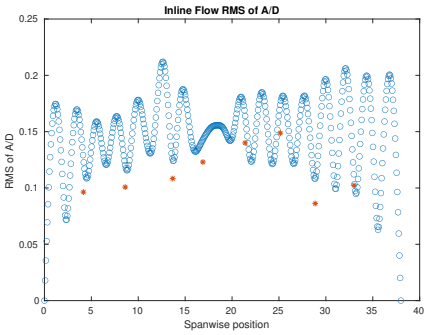

(b) Inline flow RMS profile case 2130.

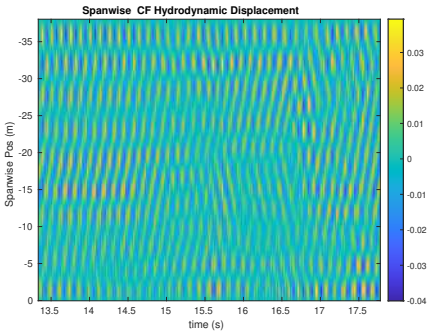

(c) Spanwise cross-flow hydrodynamic displacement case 2130.

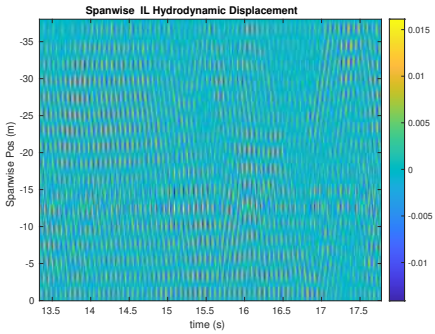

(d) Spanwise inline hydrodynamic displacement case 2130.

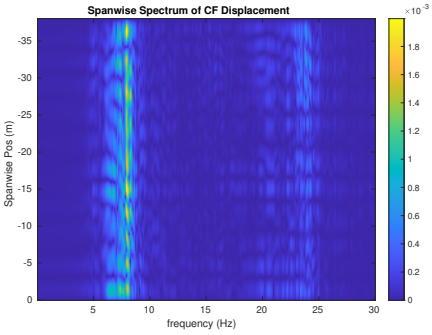

(e) Spanwise cross-flow spectrum of hydrodynamic displacement case 2130.

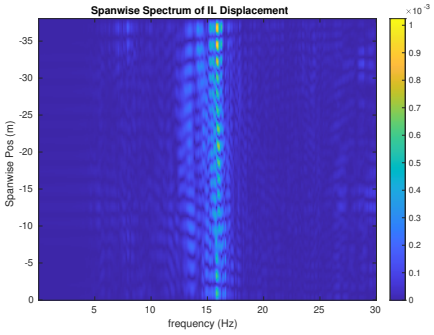

(f) Spanwise inline spectrum of hydrodynamic displacement case 2130.

Figure C-13: *Motion Analysis.* NDP Straight Riser ($L = 38m$) test case 2130.

NDP Straight Riser ($L = 38m$) test case 2141

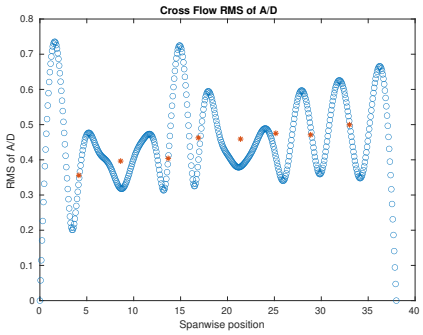

(a) Cross-flow RMS profile case 2141.

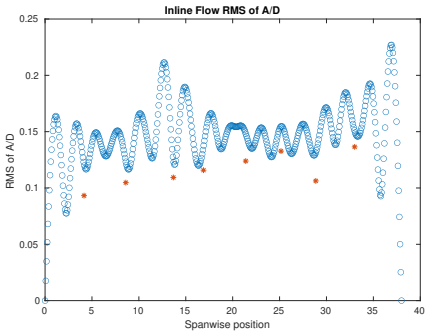

(b) Inline flow RMS profile case 2141.

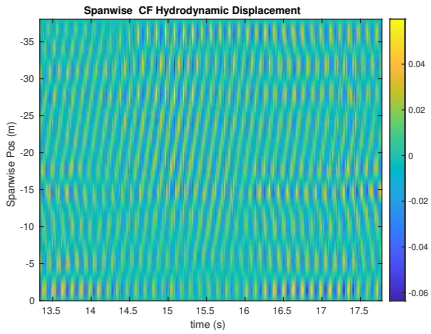

(c) Spanwise cross-flow hydrodynamic displacement case 2141.

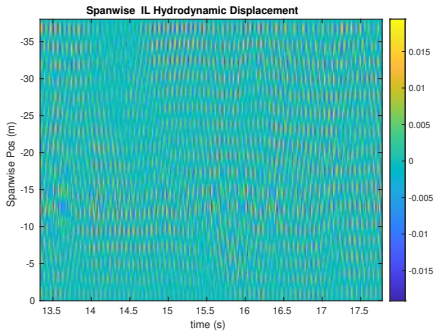

(d) Spanwise inline hydrodynamic displacement case 2141.

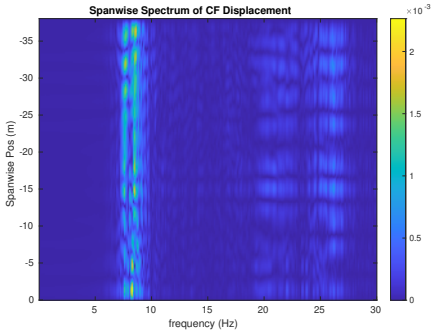

(e) Spanwise cross-flow spectrum of hydrodynamic displacement case 2141.

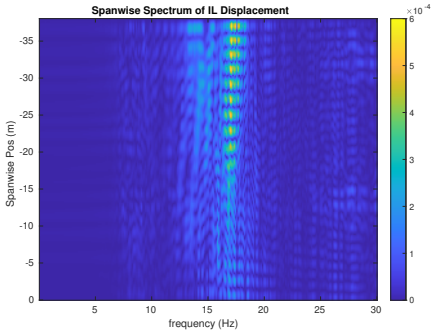

(f) Spanwise inline spectrum of hydrodynamic displacement case 2141.

Figure C-14: *Motion Analysis.* NDP Straight Riser ($L = 38m$) test case 2141.

NDP Straight Riser ($L = 38m$) test case 2150

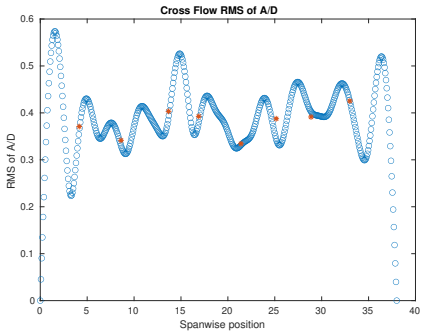

(a) Cross-flow RMS profile case 2150.

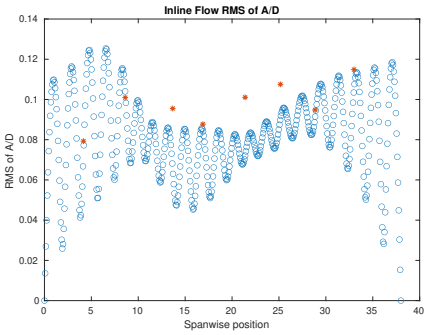

(b) Inline flow RMS profile case 2150.

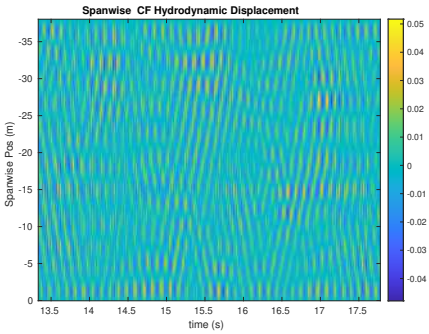

(c) Spanwise cross-flow hydrodynamic displacement case 2150.

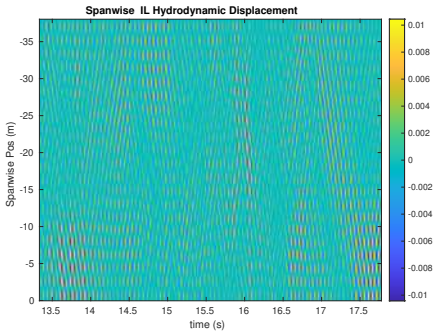

(d) Spanwise inline hydrodynamic displacement case 2150.

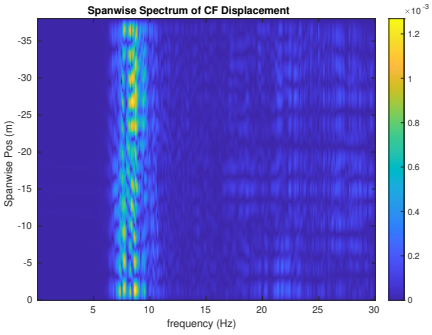

(e) Spanwise cross-flow spectrum of hydrodynamic displacement case 2150.

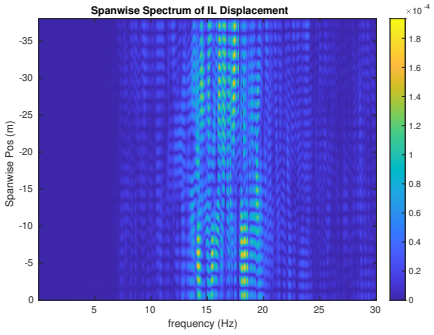

(f) Spanwise inline spectrum of hydrodynamic displacement case 2150.

Figure C-15: *Motion Analysis.* NDP Straight Riser ($L = 38m$) test case 2150.

NDP Straight Riser ($L = 38m$) test case 2160

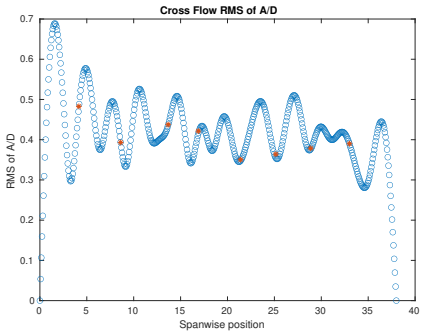

(a) Cross-flow RMS profile case 2160.

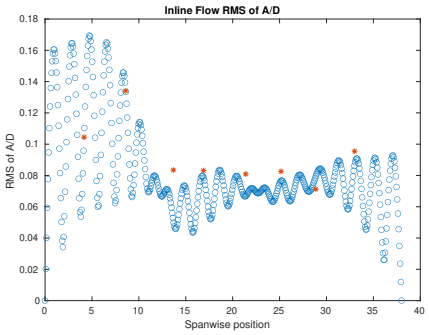

(b) Inline flow RMS profile case 2160.

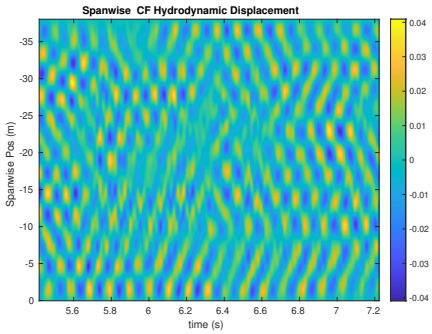

(c) Spanwise cross-flow hydrodynamic displacement case 2160.

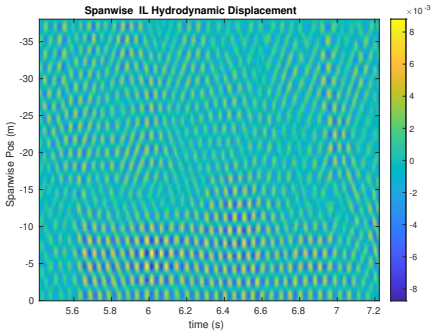

(d) Spanwise inline hydrodynamic displacement case 2160.

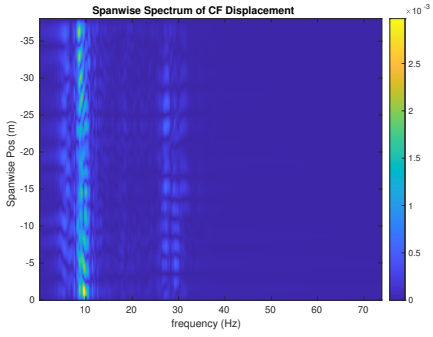

(e) Spanwise cross-flow spectrum of hydrodynamic displacement case 2160.

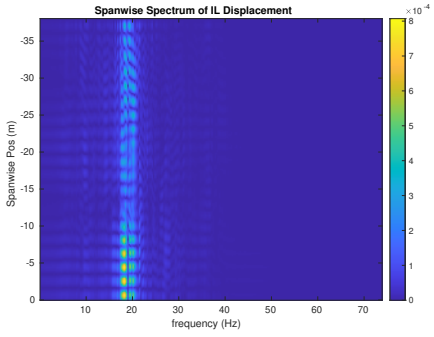

(f) Spanwise inline spectrum of hydrodynamic displacement case 2160.

Figure C-16: *Motion Analysis.* NDP Straight Riser ($L = 38m$) test case 2160.

NDP Straight Riser ($L = 38m$) test case 2170

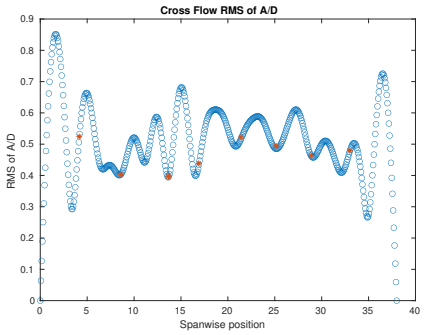

(a) Cross-flow RMS profile case 2170.

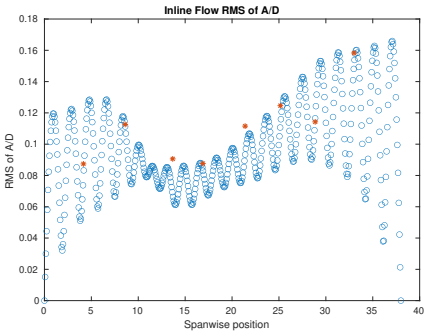

(b) Inline flow RMS profile case 2170.

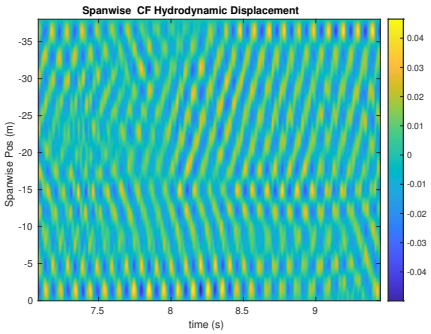

(c) Spanwise cross-flow hydrodynamic displacement case 2170.

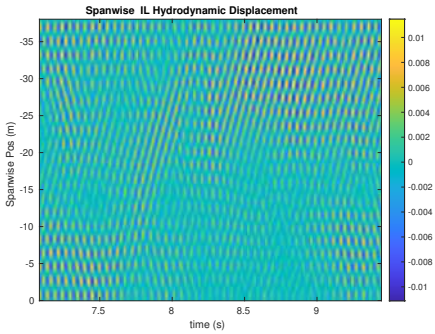

(d) Spanwise inline hydrodynamic displacement case 2170.

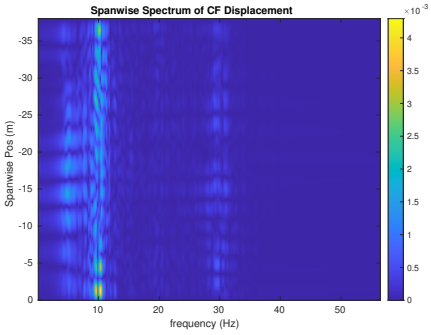

(e) Spanwise cross-flow spectrum of hydrodynamic displacement case 2170.

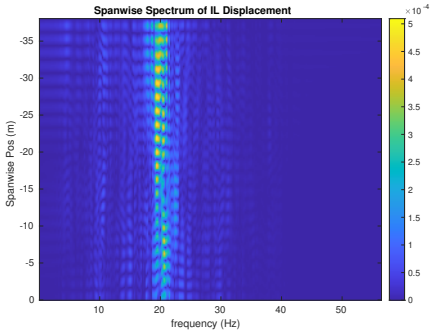

(f) Spanwise inline spectrum of hydrodynamic displacement case 2170.

Figure C-17: *Motion Analysis.* NDP Straight Riser ($L = 38m$) test case 2170.

NDP Straight Riser ($L = 38m$) test case 2182

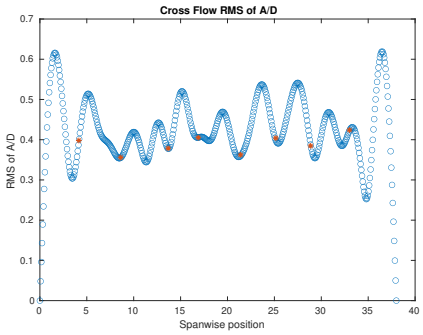

(a) Cross-flow RMS profile case 2182.

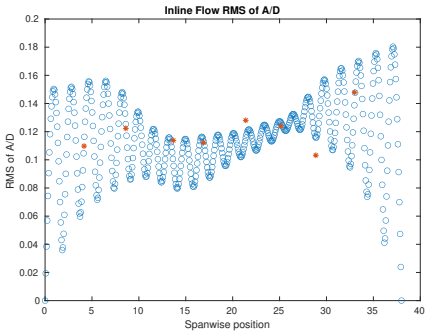

(b) Inline flow RMS profile case 2182.

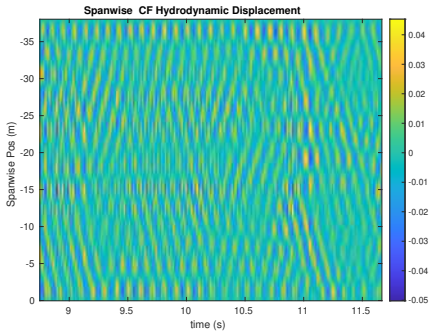

(c) Spanwise cross-flow hydrodynamic displacement case 2182.

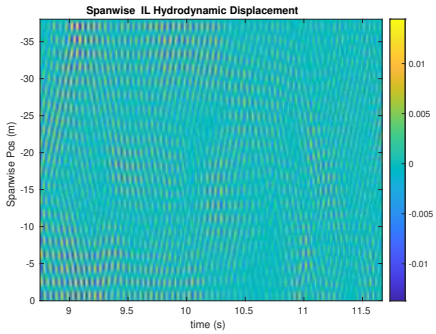

(d) Spanwise inline hydrodynamic displacement case 2182.

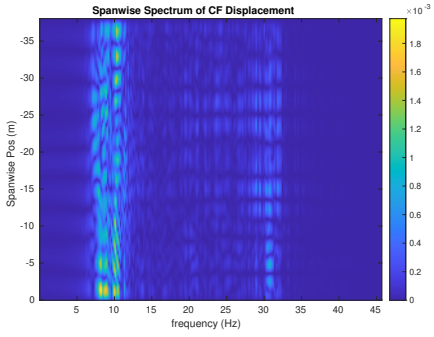

(e) Spanwise cross-flow spectrum of hydrodynamic displacement case 2182.

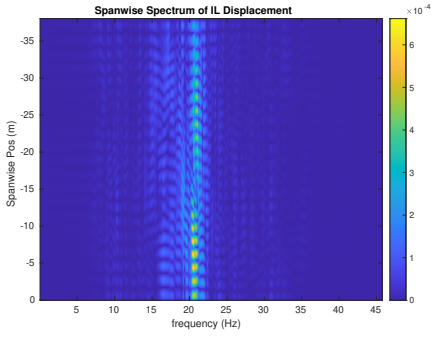

(f) Spanwise inline spectrum of hydrodynamic displacement case 2182.

Figure C-18: *Motion Analysis.* NDP Straight Riser ($L = 38m$) test case 2182.

NDP Straight Riser ($L = 38m$) test case 2191

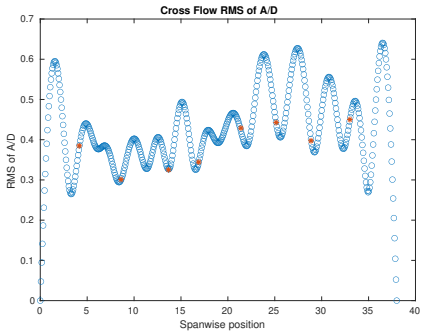

(a) Cross-flow RMS profile case 2191.

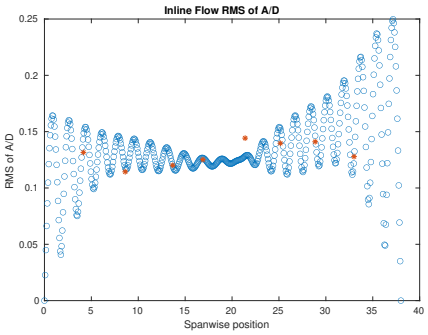

(b) Inline flow RMS profile case 2191.

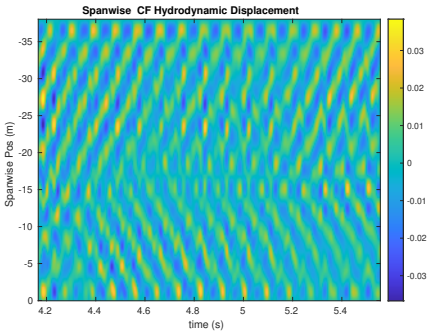

(c) Spanwise cross-flow hydrodynamic displacement case 2191.

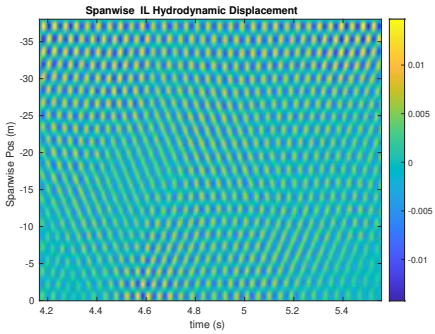

(d) Spanwise inline hydrodynamic displacement case 2191.

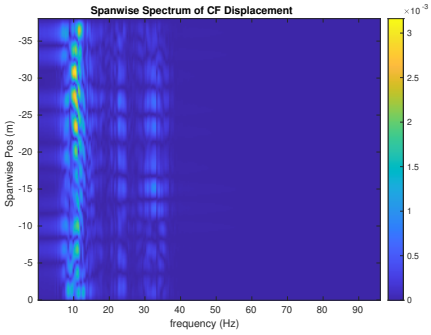

(e) Spanwise cross-flow spectrum of hydrodynamic displacement case 2191.

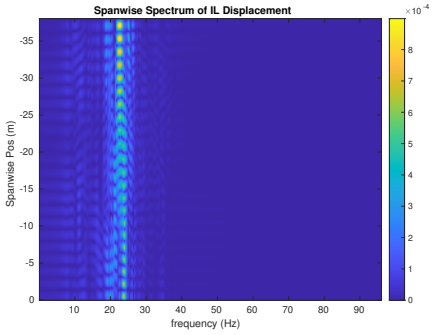

(f) Spanwise inline spectrum of hydrodynamic displacement case 2191.

Figure C-19: *Motion Analysis.* NDP Straight Riser ($L = 38m$) test case 2191.

NDP Straight Riser ($L = 38m$) test case 2201

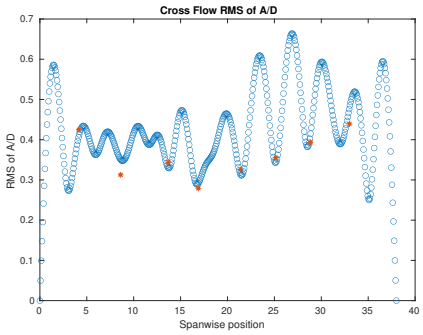

(a) Cross-flow RMS profile case 2201.

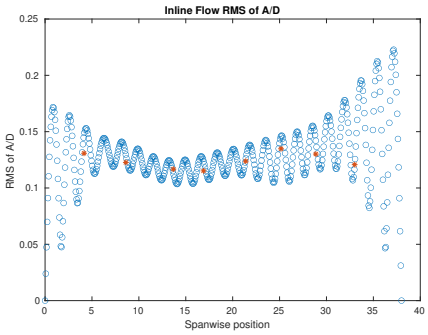

(b) Inline flow RMS profile case 2201.

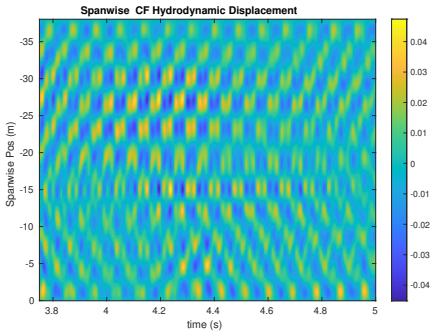

(c) Spanwise cross-flow hydrodynamic displacement case 2201.

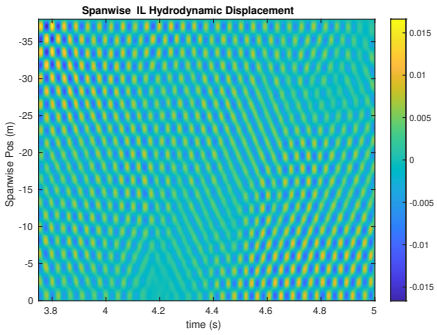

(d) Spanwise inline hydrodynamic displacement case 2201.

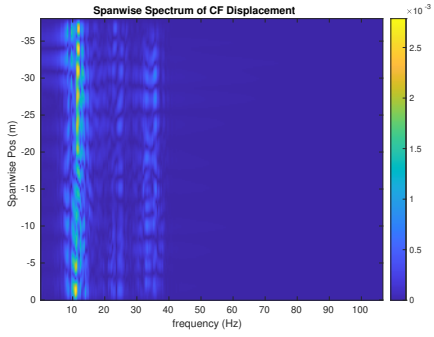

(e) Spanwise cross-flow spectrum of hydrodynamic displacement case 2201.

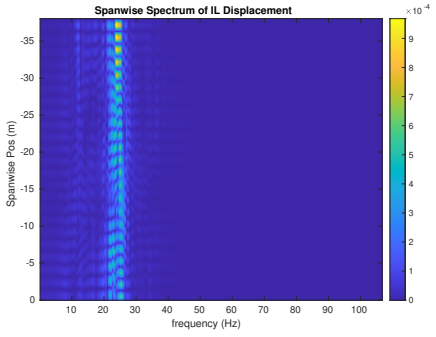

(f) Spanwise inline spectrum of hydrodynamic displacement case 2201.

Figure C-20: *Motion Analysis.* NDP Straight Riser ($L = 38m$) test case 2201.

NDP Straight Riser ($L = 38m$) test case 2210

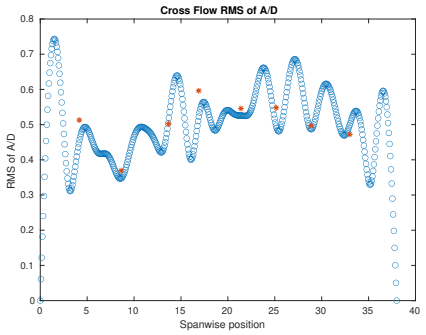

(a) Cross-flow RMS profile case 2210.

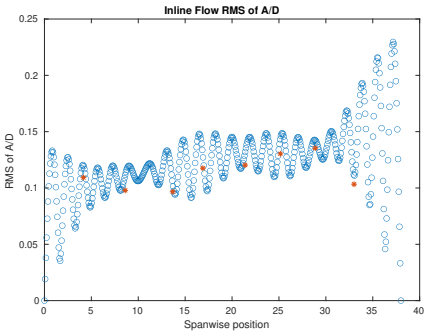

(b) Inline flow RMS profile case 2210.

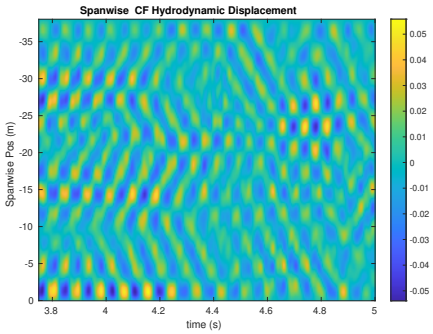

(c) Spanwise cross-flow hydrodynamic displacement case 2210.

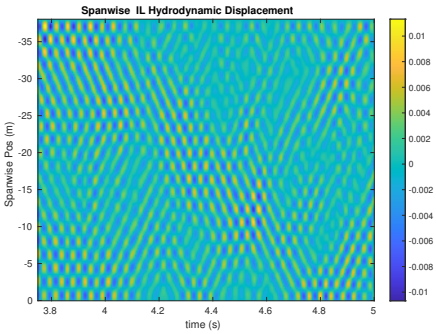

(d) Spanwise inline hydrodynamic displacement case 2210.

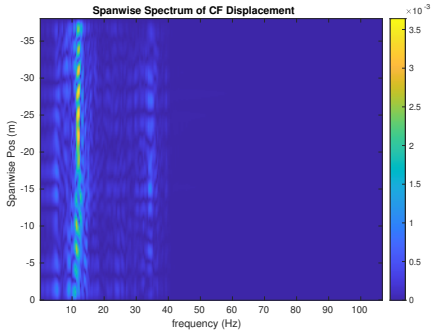

(e) Spanwise cross-flow spectrum of hydrodynamic displacement case 2210.

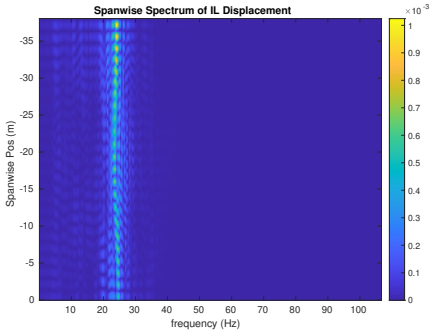

(f) Spanwise inline spectrum of hydrodynamic displacement case 2210.

Figure C-21: *Motion Analysis.* NDP Straight Riser ($L = 38m$) test case 2210.

NDP Straight Riser ($L = 38m$) test case 2220

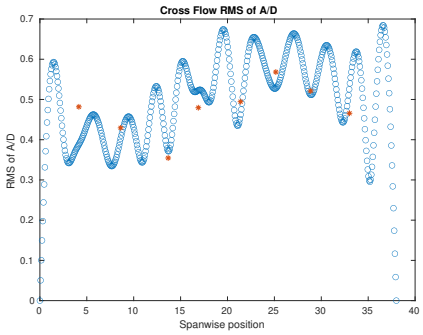

(a) Cross-flow RMS profile case 2220.

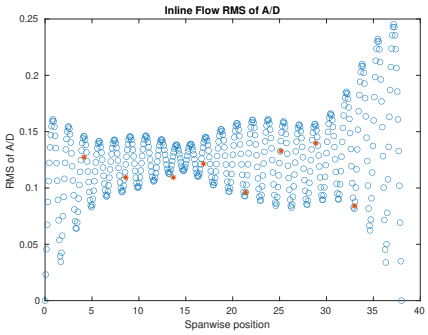

(b) Inline flow RMS profile case 2220.

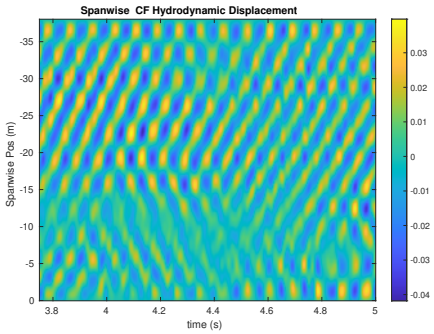

(c) Spanwise cross-flow hydrodynamic displacement case 2220.

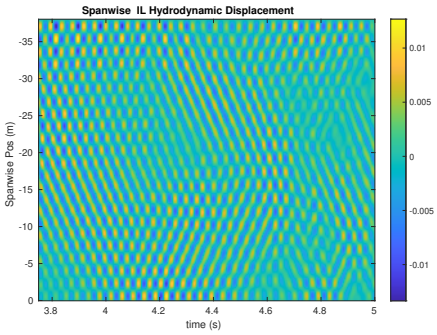

(d) Spanwise inline hydrodynamic displacement case 2220.

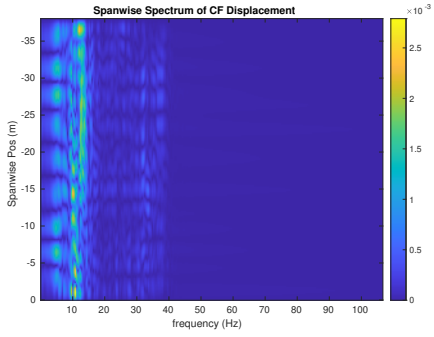

(e) Spanwise cross-flow spectrum of hydrodynamic displacement case 2220.

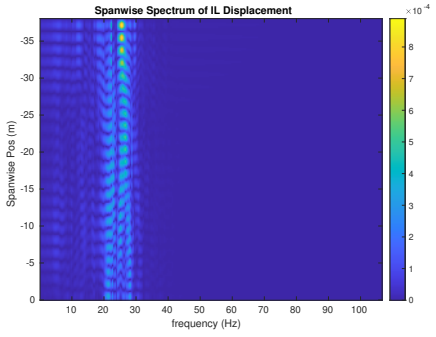

(f) Spanwise inline spectrum of hydrodynamic displacement case 2220.

Figure C-22: *Motion Analysis.* NDP Straight Riser ($L = 38m$) test case 2220.

NDP Straight Riser ($L = 38m$) test case 2230

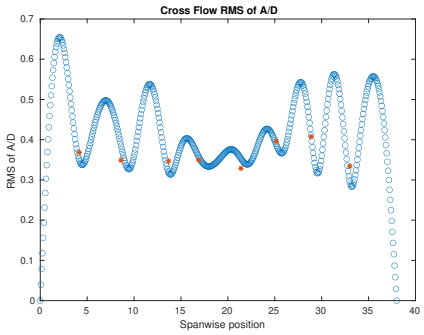

(a) Cross-flow RMS profile case 2230.

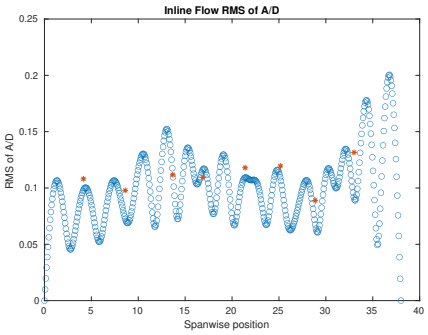

(b) Inline flow RMS profile case 2230.

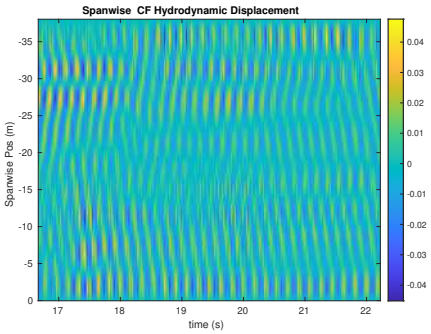

(c) Spanwise cross-flow hydrodynamic displacement case 2230.

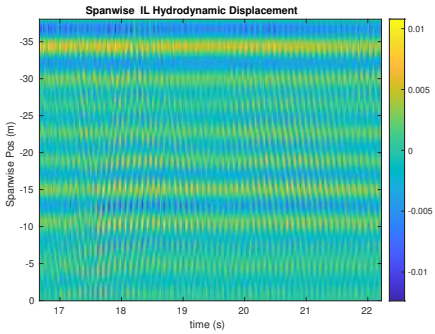

(d) Spanwise inline hydrodynamic displacement case 2230.

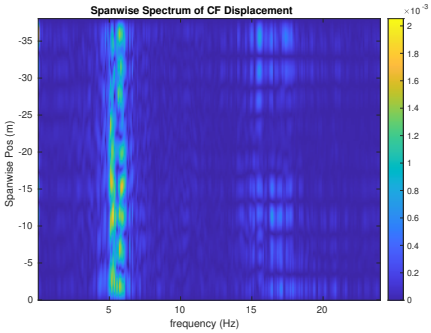

(e) Spanwise cross-flow spectrum of hydrodynamic displacement case 2230.

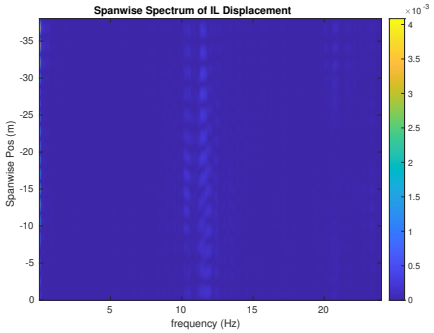

(f) Spanwise inline spectrum of hydrodynamic displacement case 2230.

Figure C-23: *Motion Analysis.* NDP Straight Riser ($L = 38m$) test case 2230.

NDP Straight Riser ($L = 38m$) test case 2240

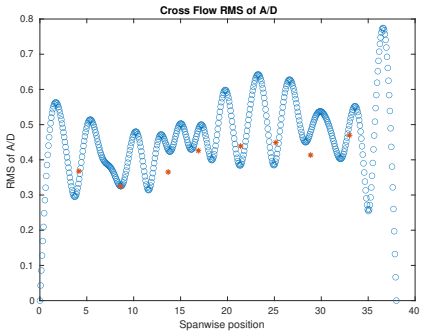

(a) Cross-flow RMS profile case 2240.

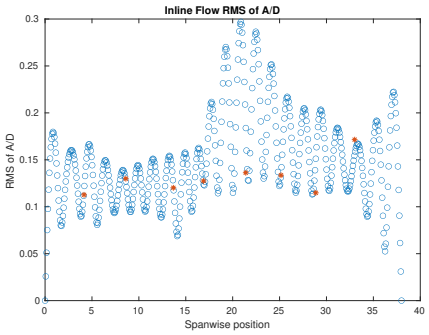

(b) Inline flow RMS profile case 2240.

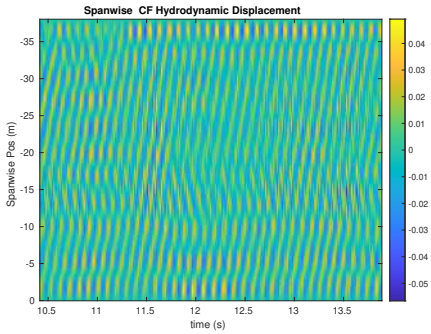

(c) Spanwise cross-flow hydrodynamic displacement case 2240.

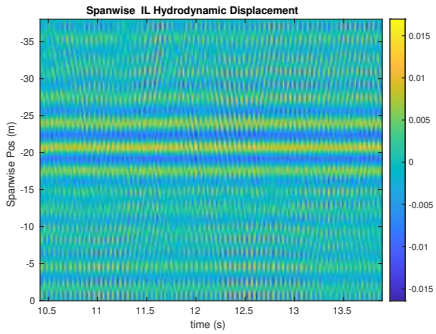

(d) Spanwise inline hydrodynamic displacement case 2240.

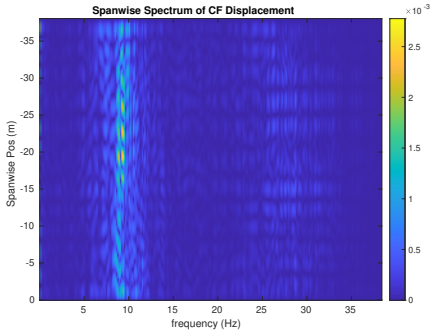

(e) Spanwise cross-flow spectrum of hydrodynamic displacement case 2240.

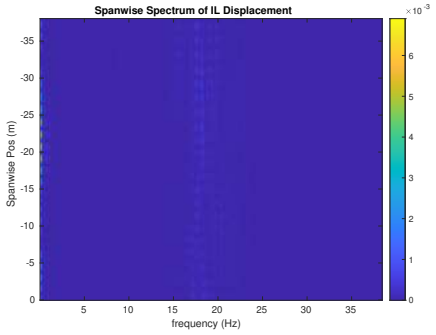

(f) Spanwise inline spectrum of hydrodynamic displacement case 2240.

Figure C-24: *Motion Analysis.* NDP Straight Riser ($L = 38m$) test case 2240.

NDP Straight Riser ($L = 38m$) test case 2310

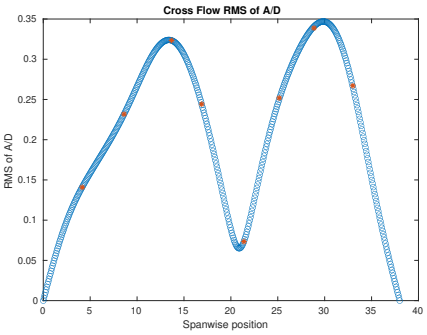

(a) Cross-flow RMS profile case 2310.

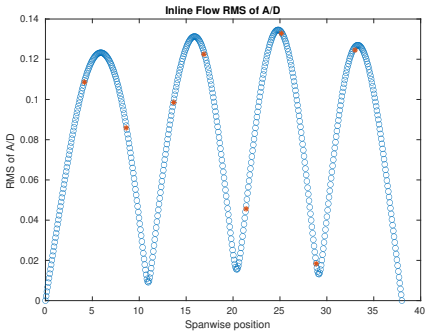

(b) Inline flow RMS profile case 2310.

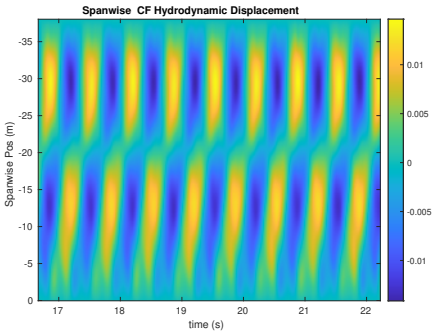

(c) Spanwise cross-flow hydrodynamic displacement case 2310.

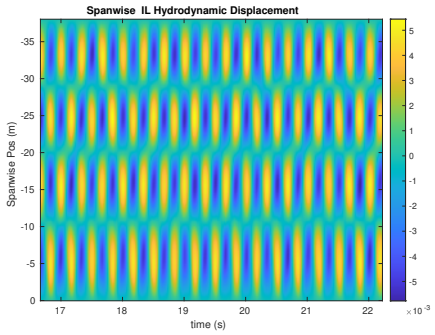

(d) Spanwise inline hydrodynamic displacement case 2310.

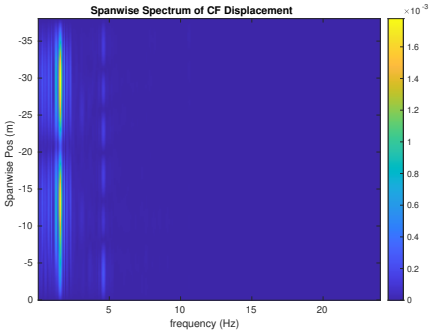

(e) Spanwise cross-flow spectrum of hydrodynamic displacement case 2310.

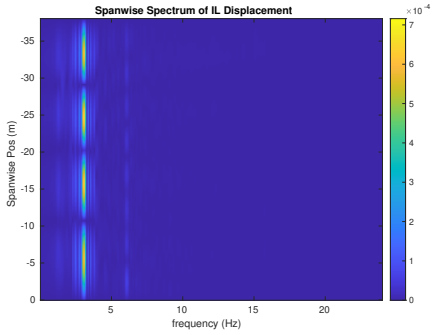

(f) Spanwise inline spectrum of hydrodynamic displacement case 2310.

Figure C-25: *Motion Analysis.* NDP Straight Riser ($L = 38m$) test case 2310.

NDP Straight Riser ($L = 38m$) test case 2320

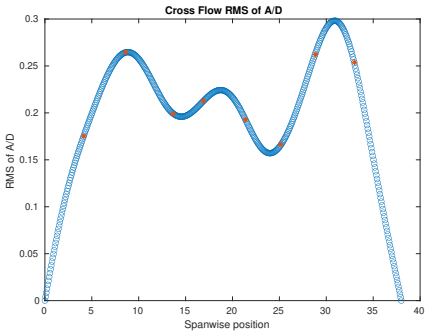

(a) Cross-flow RMS profile case 2320.

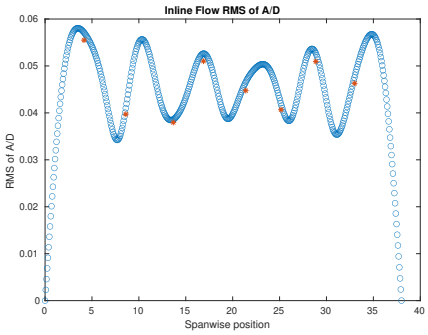

(b) Inline flow RMS profile case 2320.

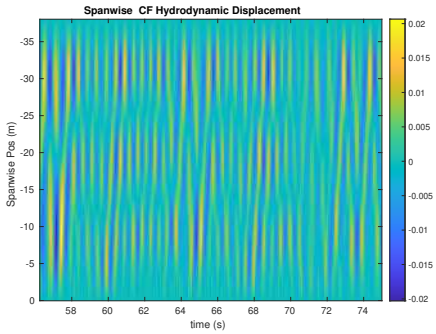

(c) Spanwise cross-flow hydrodynamic displacement case 2320.

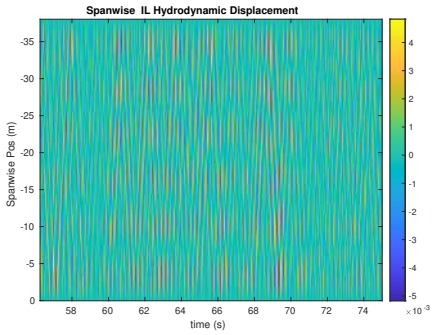

(d) Spanwise inline hydrodynamic displacement case 2320.

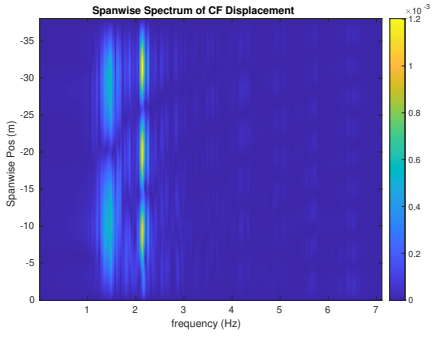

(e) Spanwise cross-flow spectrum of hydrodynamic displacement case 2320.

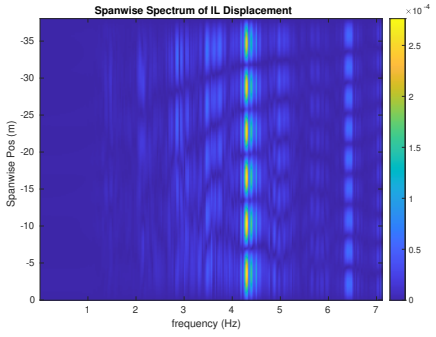

(f) Spanwise inline spectrum of hydrodynamic displacement case 2320.

Figure C-26: *Motion Analysis.* NDP Straight Riser ($L = 38m$) test case 2320.

NDP Straight Riser ($L = 38m$) test case 2330

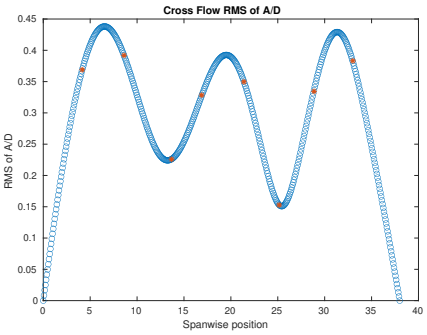

(a) Cross-flow RMS profile case 2330.

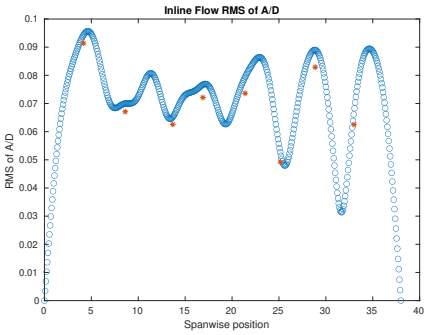

(b) Inline flow RMS profile case 2330.

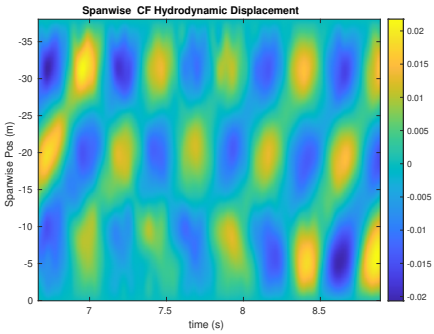

(c) Spanwise cross-flow hydrodynamic displacement case 2330.

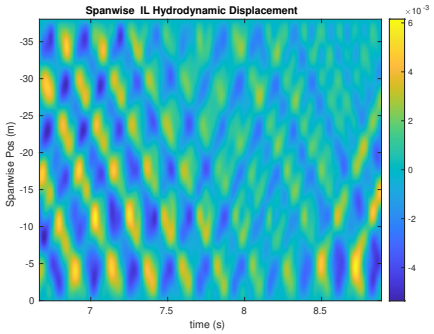

(d) Spanwise inline hydrodynamic displacement case 2330.

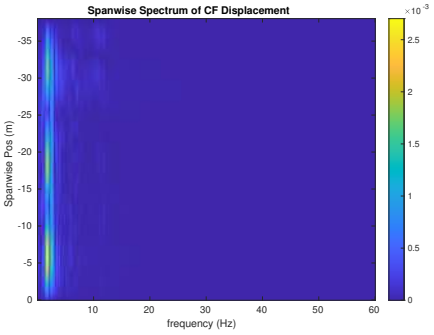

(e) Spanwise cross-flow spectrum of hydrodynamic displacement case 2330.

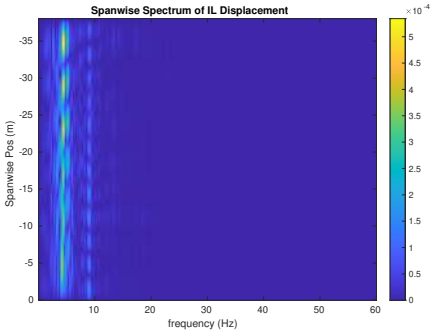

(f) Spanwise inline spectrum of hydrodynamic displacement case 2330.

Figure C-27: *Motion Analysis.* NDP Straight Riser ($L = 38m$) test case 2330.

NDP Straight Riser ($L = 38m$) test case 2340

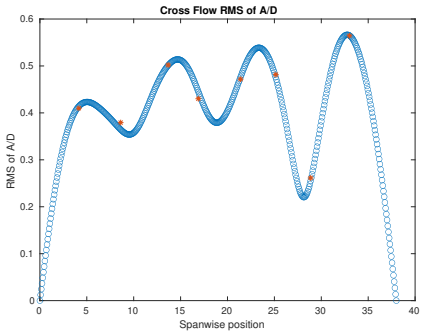

(a) Cross-flow RMS profile case 2340.

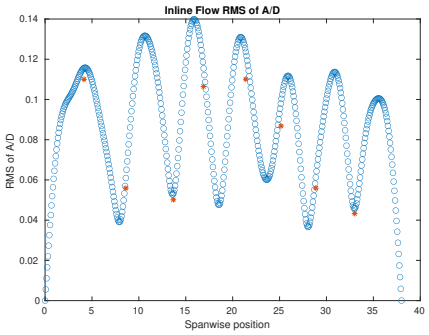

(b) Inline flow RMS profile case 2340.

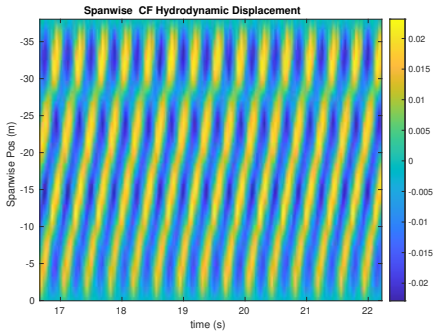

(c) Spanwise cross-flow hydrodynamic displacement case 2340.

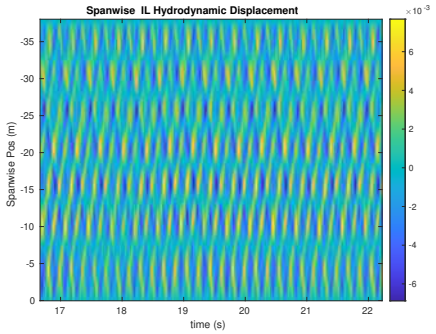

(d) Spanwise inline hydrodynamic displacement case 2340.

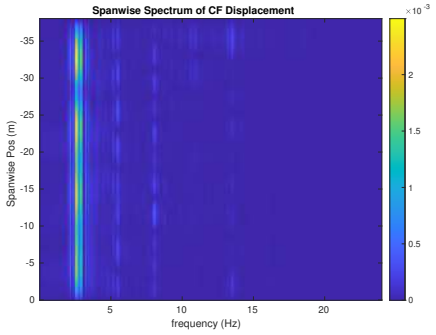

(e) Spanwise cross-flow spectrum of hydrodynamic displacement case 2340.

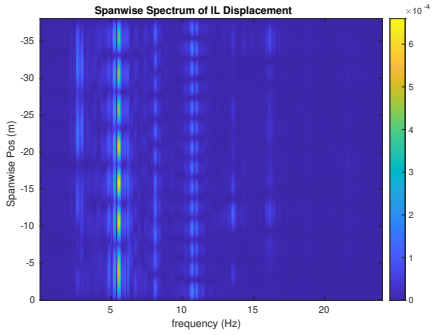

(f) Spanwise inline spectrum of hydrodynamic displacement case 2340.

Figure C-28: *Motion Analysis.* NDP Straight Riser ($L = 38m$) test case 2340.

NDP Straight Riser ($L = 38m$) test case 2350

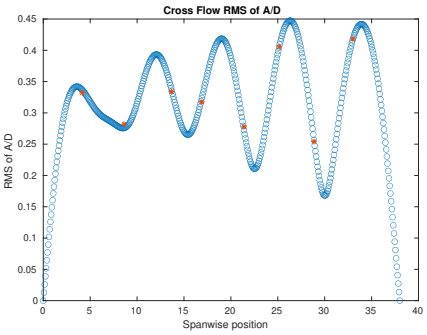

(a) Cross-flow RMS profile case 2350.

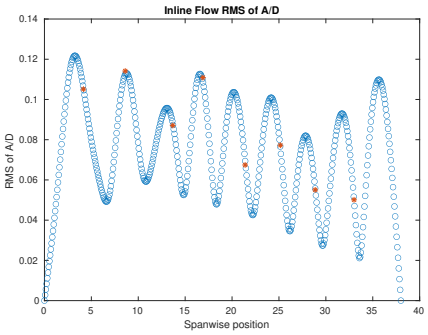

(b) Inline flow RMS profile case 2350.

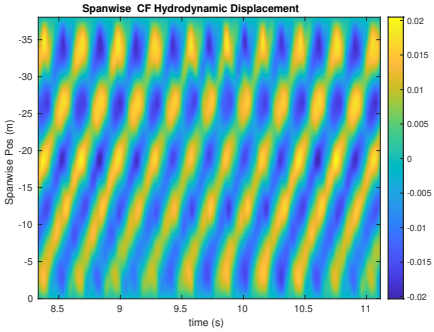

(c) Spanwise cross-flow hydrodynamic displacement case 2350.

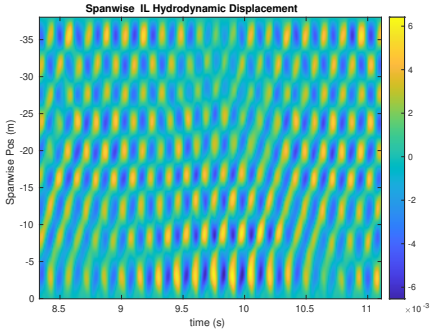

(d) Spanwise inline hydrodynamic displacement case 2350.

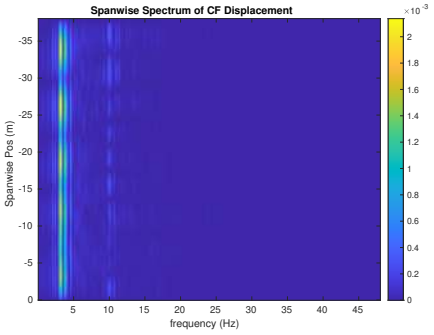

(e) Spanwise cross-flow spectrum of hydrodynamic displacement case 2350.

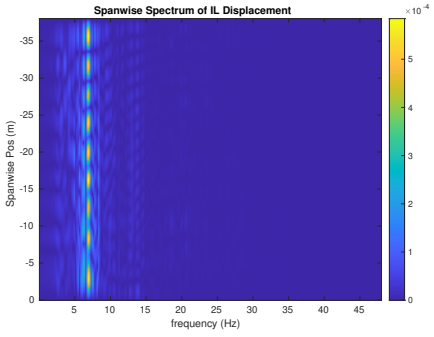

(f) Spanwise inline spectrum of hydrodynamic displacement case 2350.

Figure C-29: *Motion Analysis.* NDP Straight Riser ($L = 38m$) test case 2350.

NDP Straight Riser ($L = 38m$) test case 2360

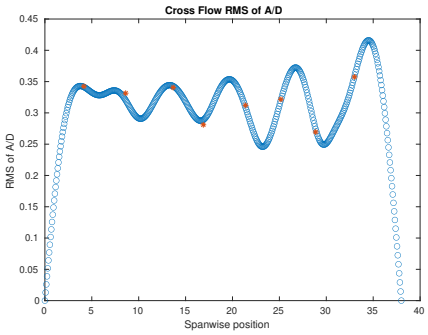

(a) Cross-flow RMS profile case 2360.

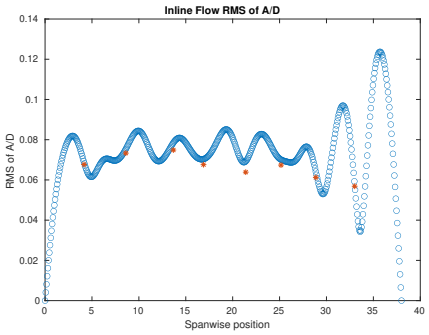

(b) Inline flow RMS profile case 2360.

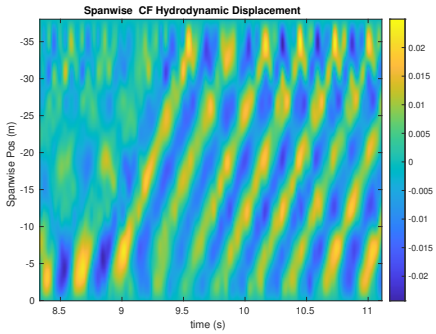

(c) Spanwise cross-flow hydrodynamic displacement case 2360.

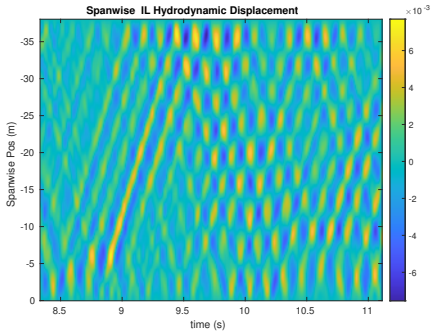

(d) Spanwise inline hydrodynamic displacement case 2360.

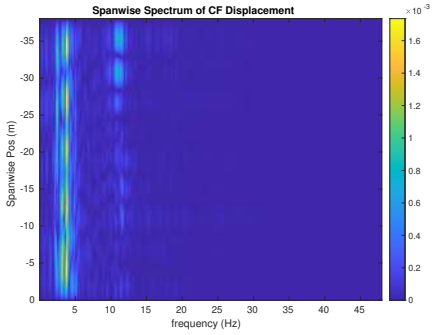

(e) Spanwise cross-flow spectrum of hydrodynamic displacement case 2360.

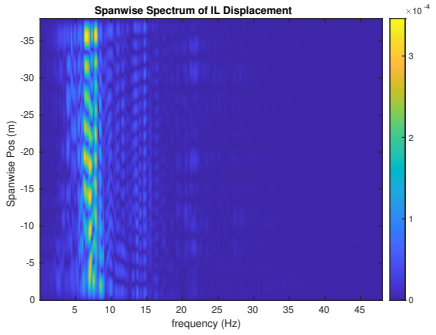

(f) Spanwise inline spectrum of hydrodynamic displacement case 2360.

Figure C-30: *Motion Analysis.* NDP Straight Riser ($L = 38m$) test case 2360.

NDP Straight Riser ($L = 38m$) test case 2370

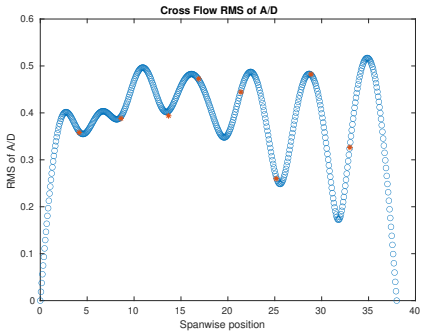

(a) Cross-flow RMS profile case 2370.

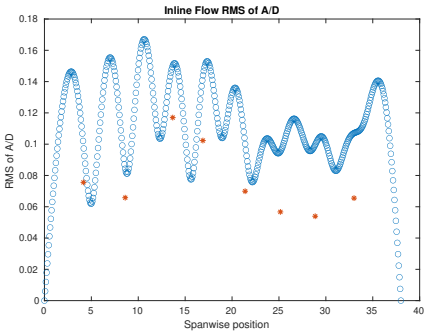

(b) Inline flow RMS profile case 2370.

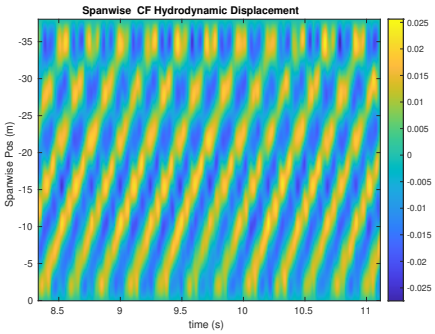

(c) Spanwise cross-flow hydrodynamic displacement case 2370.

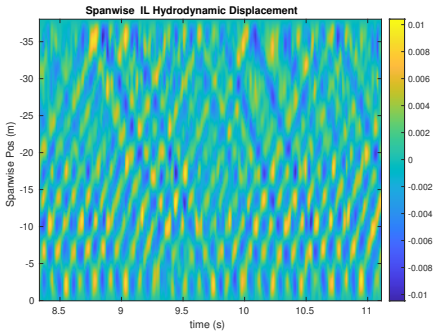

(d) Spanwise inline hydrodynamic displacement case 2370.

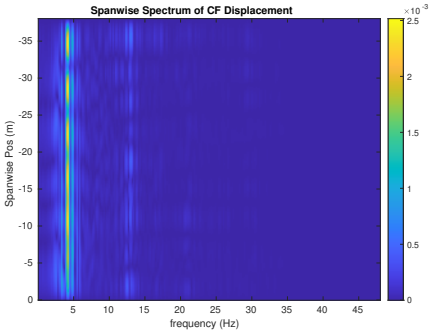

(e) Spanwise cross-flow spectrum of hydrodynamic displacement case 2370.

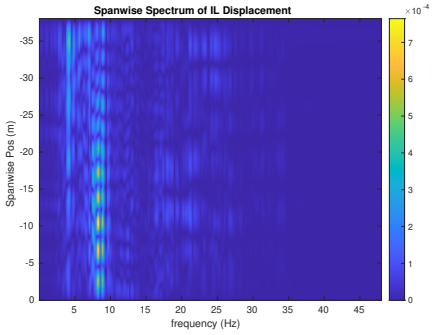

(f) Spanwise inline spectrum of hydrodynamic displacement case 2370.

Figure C-31: *Motion Analysis.* NDP Straight Riser ($L = 38m$) test case 2370.

NDP Straight Riser ($L = 38m$) test case 2380

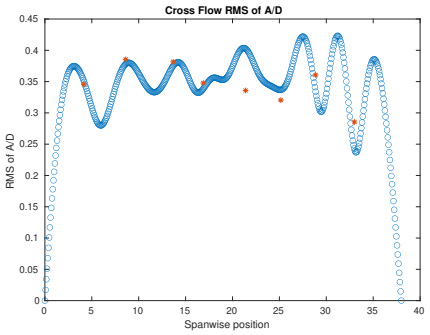

(a) Cross-flow RMS profile case 2380.

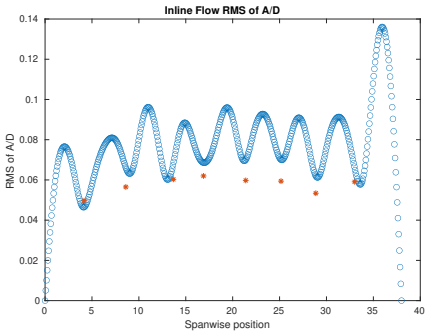

(b) Inline flow RMS profile case 2380.

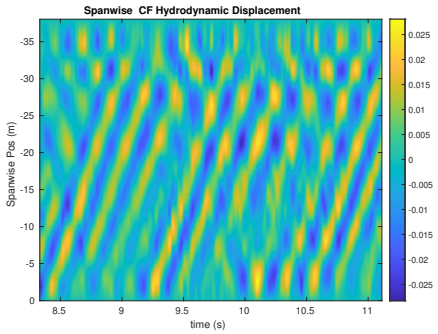

(c) Spanwise cross-flow hydrodynamic displacement case 2380.

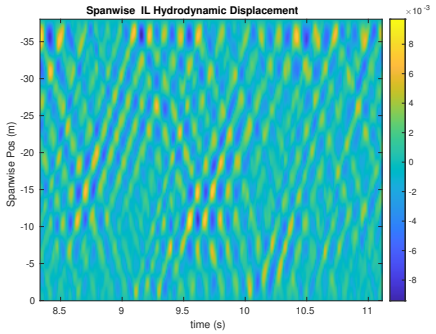

(d) Spanwise inline hydrodynamic displacement case 2380.

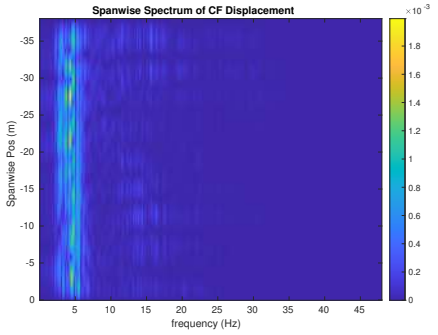

(e) Spanwise cross-flow spectrum of hydrodynamic displacement case 2380.

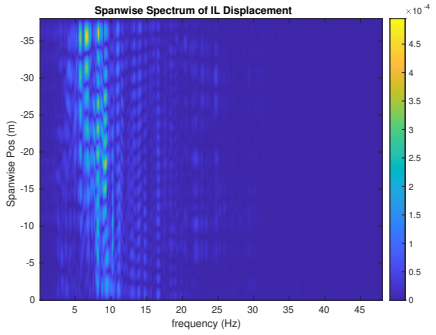

(f) Spanwise inline spectrum of hydrodynamic displacement case 2380.

Figure C-32: *Motion Analysis.* NDP Straight Riser ($L = 38m$) test case 2380.

NDP Straight Riser ($L = 38m$) test case 2390

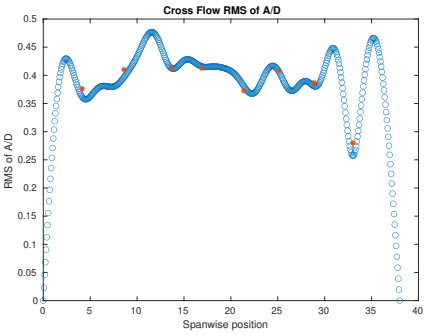

(a) Cross-flow RMS profile case 2390.

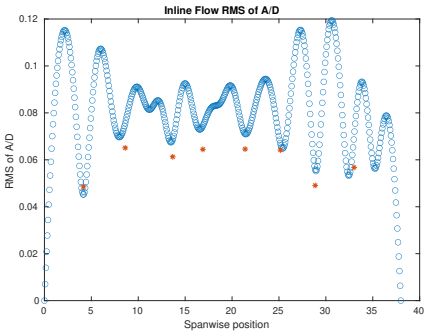

(b) Inline flow RMS profile case 2390.

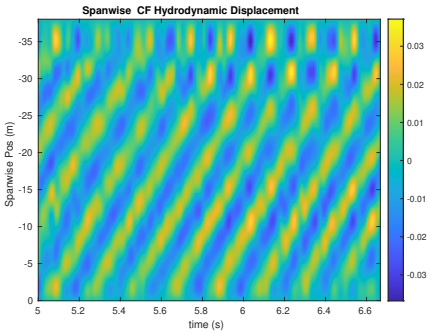

(c) Spanwise cross-flow hydrodynamic displacement case 2390.

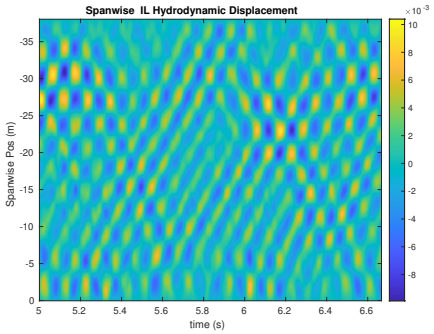

(d) Spanwise inline hydrodynamic displacement case 2390.

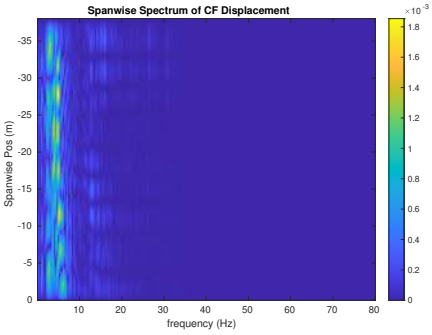

(e) Spanwise cross-flow spectrum of hydrodynamic displacement case 2390.

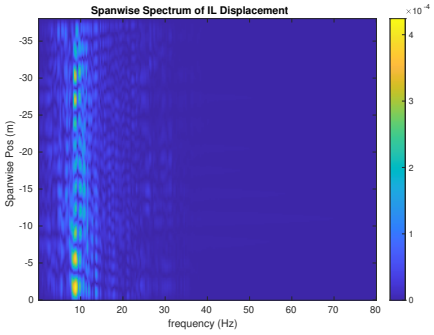

(f) Spanwise inline spectrum of hydrodynamic displacement case 2390.

Figure C-33: *Motion Analysis.* NDP Straight Riser ($L = 38m$) test case 2390.

NDP Straight Riser ($L = 38m$) test case 2400

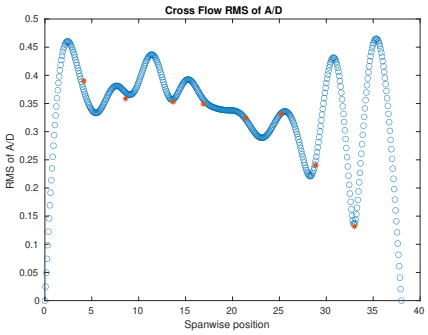

(a) Cross-flow RMS profile case 2400.

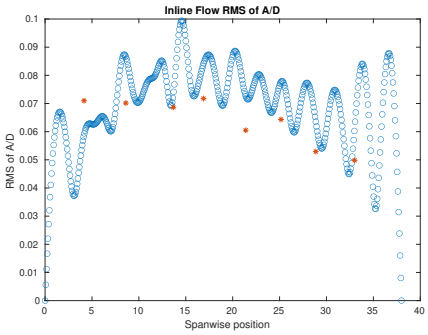

(b) Inline flow RMS profile case 2400.

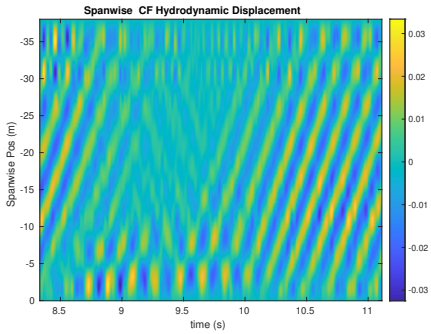

(c) Spanwise cross-flow hydrodynamic displacement case 2400.

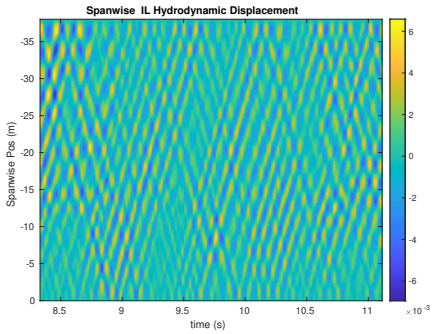

(d) Spanwise inline hydrodynamic displacement case 2400.

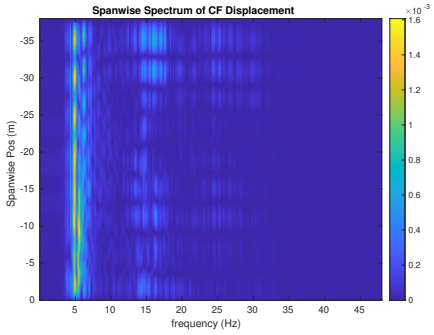

(e) Spanwise cross-flow spectrum of hydrodynamic displacement case 2400.

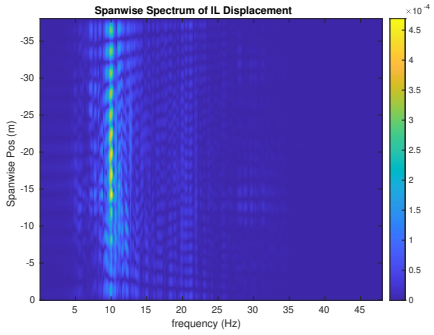

(f) Spanwise inline spectrum of hydrodynamic displacement case 2400.

Figure C-34: *Motion Analysis.* NDP Straight Riser ($L = 38m$) test case 2400.

NDP Straight Riser ($L = 38m$) test case 2410

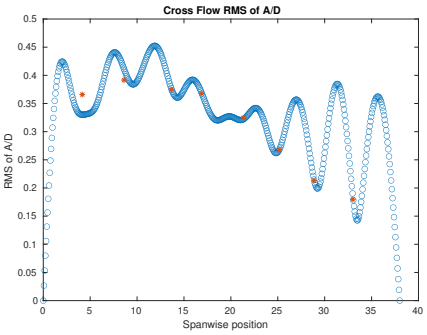

(a) Cross-flow RMS profile case 2410.

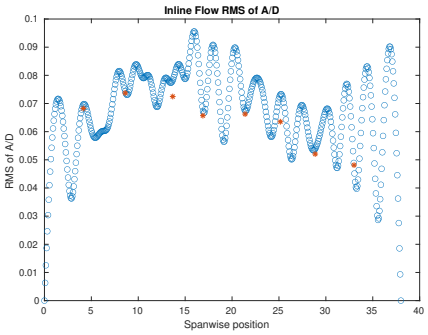

(b) Inline flow RMS profile case 2410.

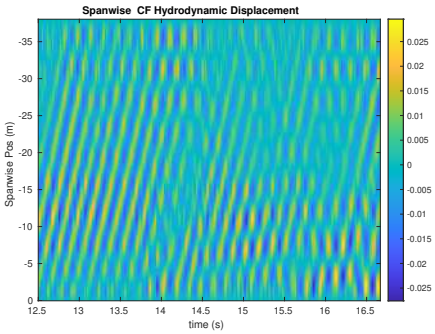

(c) Spanwise cross-flow hydrodynamic displacement case 2410.

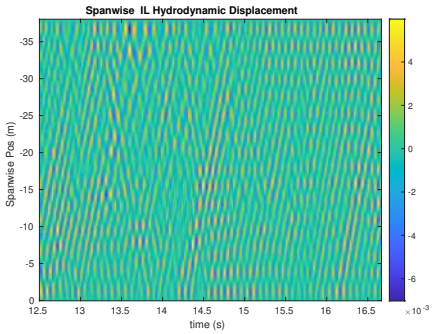

(d) Spanwise inline hydrodynamic displacement case 2410.

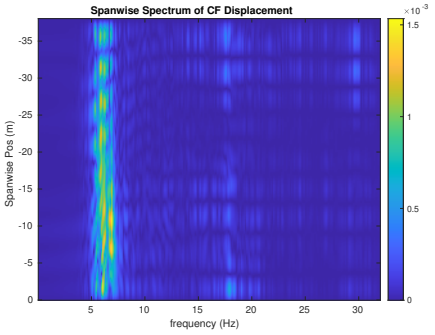

(e) Spanwise cross-flow spectrum of hydrodynamic displacement case 2410.

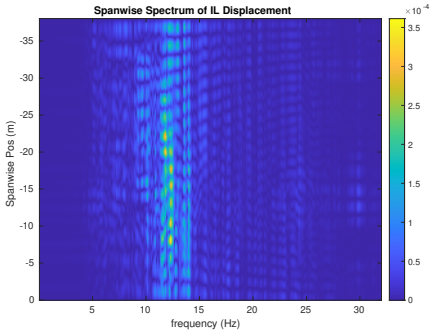

(f) Spanwise inline spectrum of hydrodynamic displacement case 2410.

Figure C-35: *Motion Analysis.* NDP Straight Riser ($L = 38m$) test case 2410.

NDP Straight Riser ($L = 38m$) test case 2420

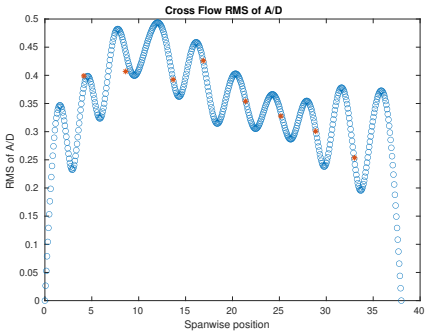

(a) Cross-flow RMS profile case 2420.

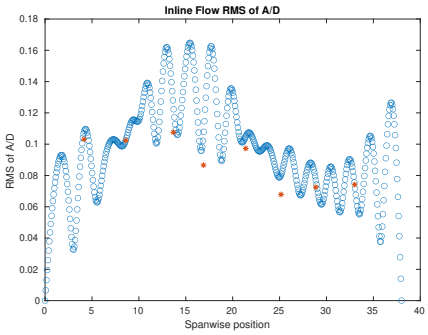

(b) Inline flow RMS profile case 2420.

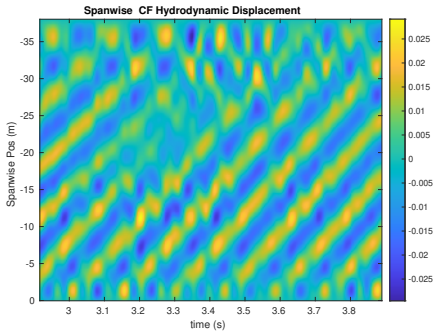

(c) Spanwise cross-flow hydrodynamic displacement case 2420.

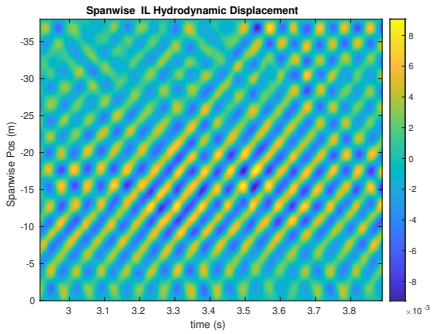

(d) Spanwise inline hydrodynamic displacement case 2420.

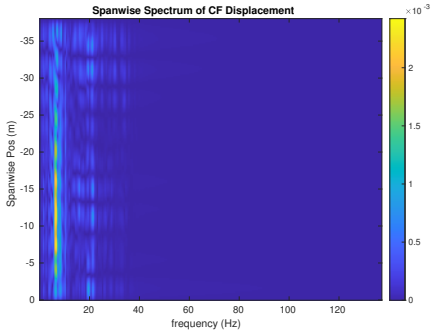

(e) Spanwise cross-flow spectrum of hydrodynamic displacement case 2420.

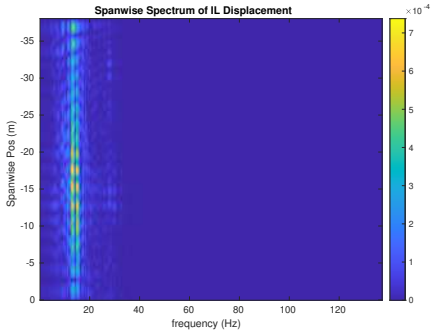

(f) Spanwise inline spectrum of hydrodynamic displacement case 2420.

Figure C-36: *Motion Analysis.* NDP Straight Riser ($L = 38m$) test case 2420.

NDP Straight Riser ($L = 38m$) test case 2430

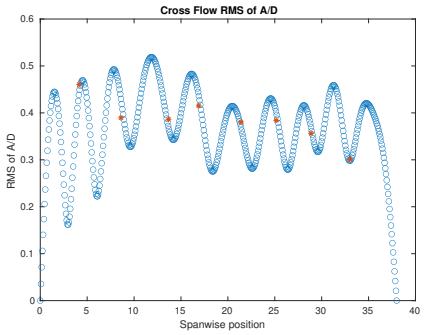

(a) Cross-flow RMS profile case 2430.

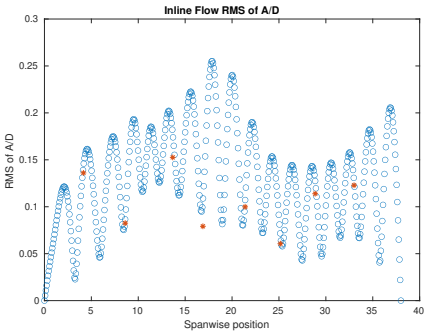

(b) Inline flow RMS profile case 2430.

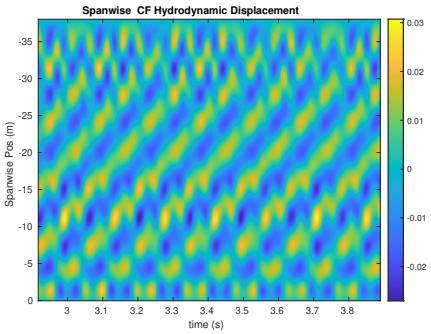

(c) Spanwise cross-flow hydrodynamic displacement case 2430.

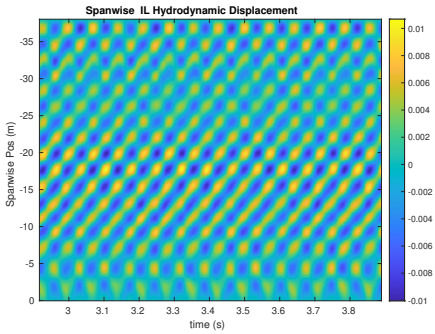

(d) Spanwise inline hydrodynamic displacement case 2430.

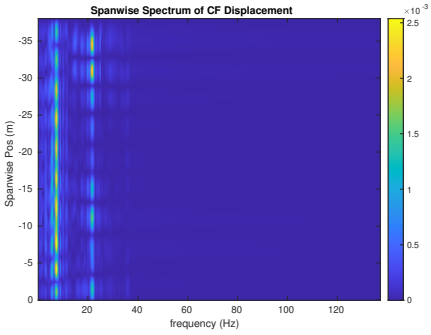

(e) Spanwise cross-flow spectrum of hydrodynamic displacement case 2430.

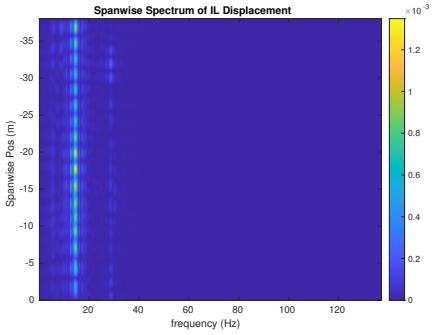

(f) Spanwise inline spectrum of hydrodynamic displacement case 2430.

Figure C-37: *Motion Analysis.* NDP Straight Riser ($L = 38m$) test case 2430.

NDP Straight Riser ($L = 38m$) test case 2440

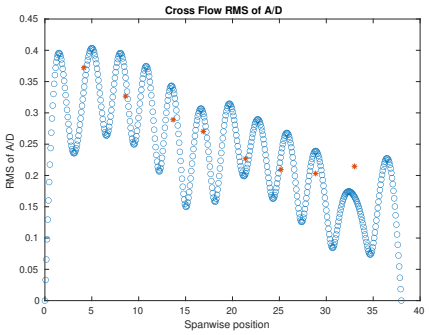

(a) Cross-flow RMS profile case 2440.

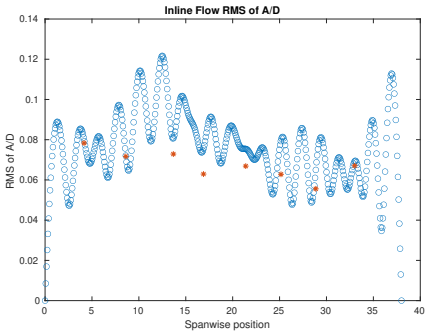

(b) Inline flow RMS profile case 2440.

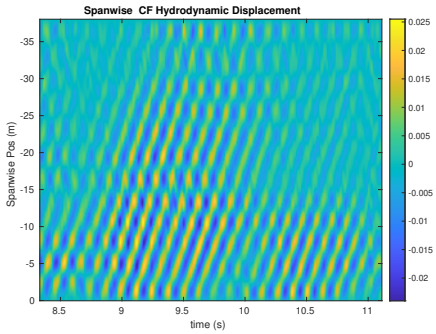

(c) Spanwise cross-flow hydrodynamic displacement case 2440.

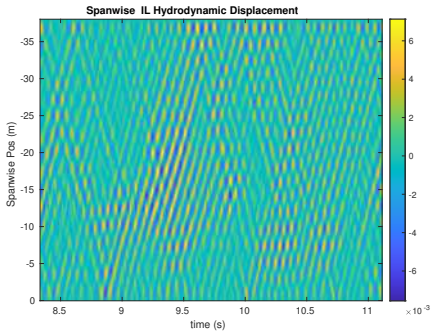

(d) Spanwise inline hydrodynamic displacement case 2440.

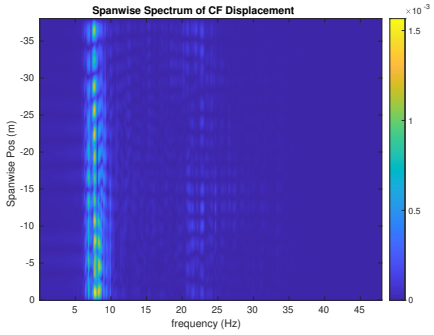

(e) Spanwise cross-flow spectrum of hydrodynamic displacement case 2440.

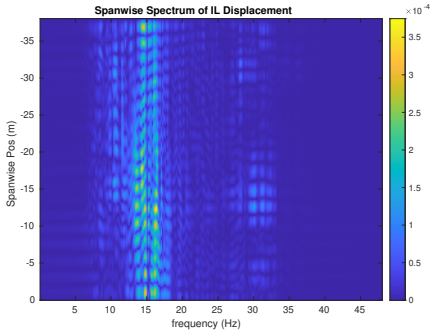

(f) Spanwise inline spectrum of hydrodynamic displacement case 2440.

Figure C-38: *Motion Analysis.* NDP Straight Riser ($L = 38m$) test case 2440.

NDP Straight Riser ($L = 38m$) test case 2450

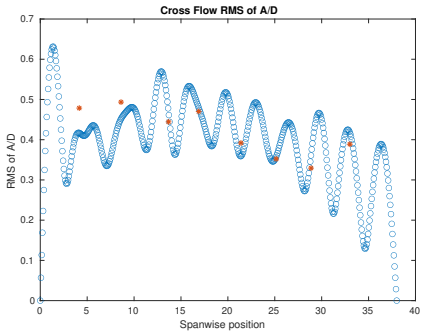

(a) Cross-flow RMS profile case 2450.

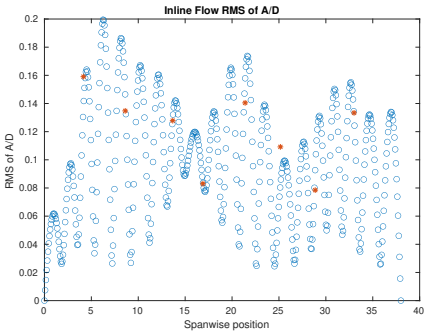

(b) Inline flow RMS profile case 2450.

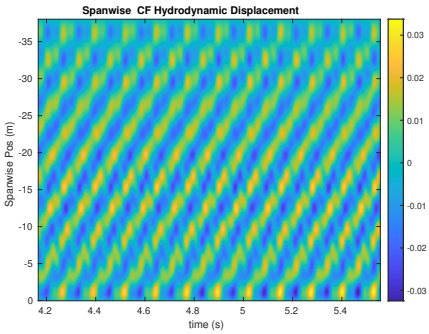

(c) Spanwise cross-flow hydrodynamic displacement case 2450.

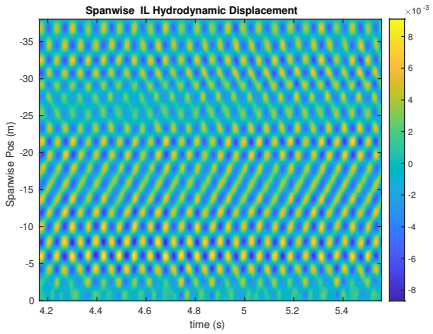

(d) Spanwise inline hydrodynamic displacement case 2450.

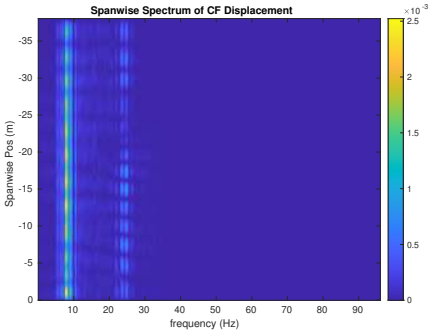

(e) Spanwise cross-flow spectrum of hydrodynamic displacement case 2450.

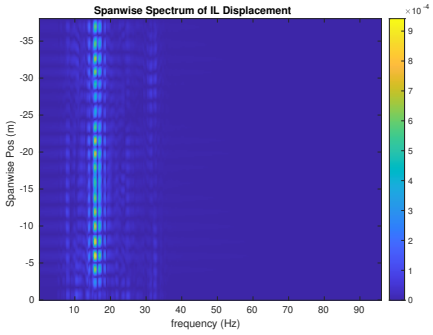

(f) Spanwise inline spectrum of hydrodynamic displacement case 2450.

Figure C-39: *Motion Analysis.* NDP Straight Riser ($L = 38m$) test case 2450.

NDP Straight Riser ($L = 38m$) test case 2460

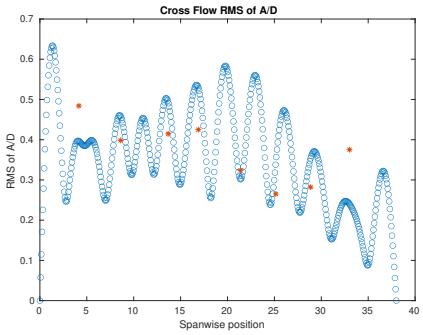

(a) Cross-flow RMS profile case 2460.

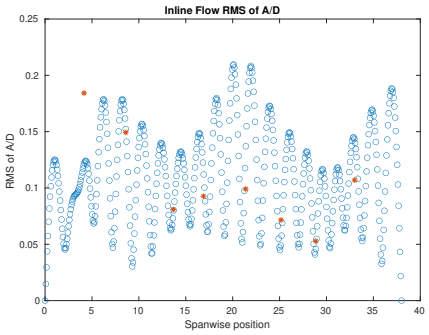

(b) Inline flow RMS profile case 2460.

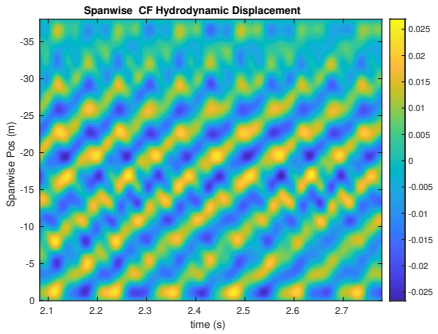

(c) Spanwise cross-flow hydrodynamic displacement case 2460.

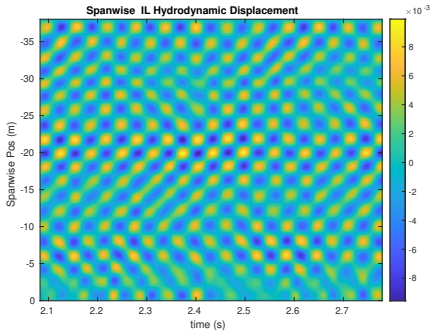

(d) Spanwise inline hydrodynamic displacement case 2460.

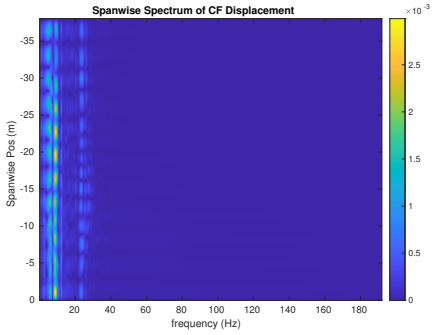

(e) Spanwise cross-flow spectrum of hydrodynamic displacement case 2460.

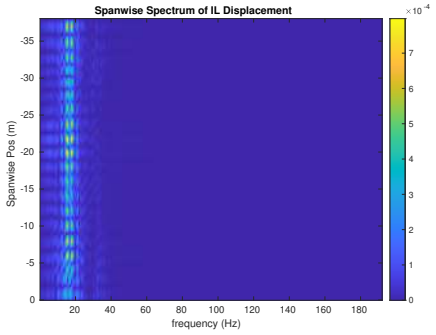

(f) Spanwise inline spectrum of hydrodynamic displacement case 2460.

Figure C-40: *Motion Analysis.* NDP Straight Riser ($L = 38m$) test case 2460.

NDP Straight Riser ($L = 38m$) test case 2470

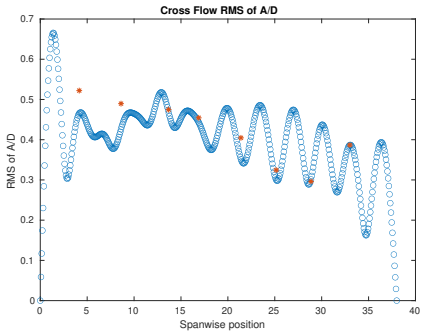

(a) Cross-flow RMS profile case 2470.

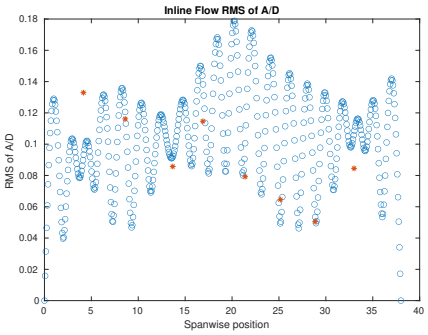

(b) Inline flow RMS profile case 2470.

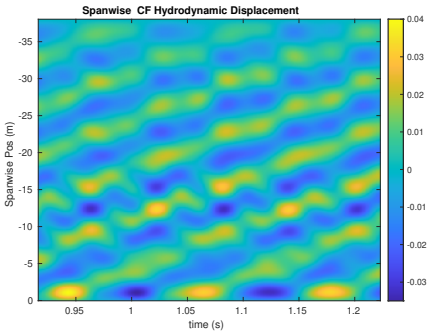

(c) Spanwise cross-flow hydrodynamic displacement case 2470.

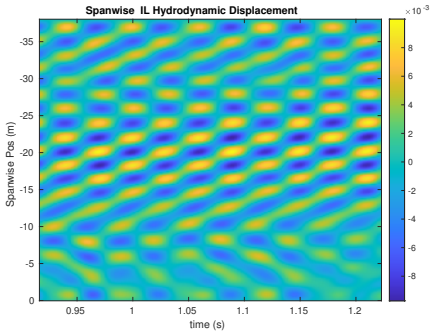

(d) Spanwise inline hydrodynamic displacement case 2470.

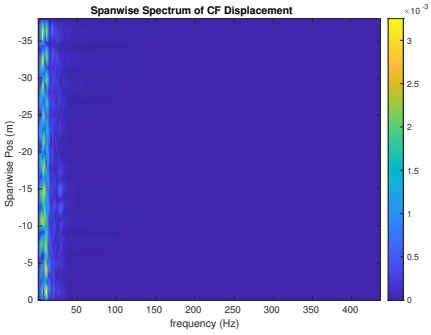

(e) Spanwise cross-flow spectrum of hydrodynamic displacement case 2470.

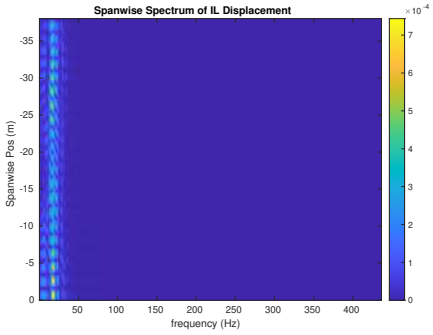

(f) Spanwise inline spectrum of hydrodynamic displacement case 2470.

Figure C-41: *Motion Analysis.* NDP Straight Riser ($L = 38m$) test case 2470.

NDP Straight Riser ($L = 38m$) test case 2480

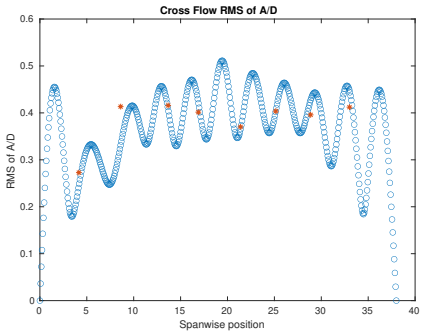

(a) Cross-flow RMS profile case 2480.

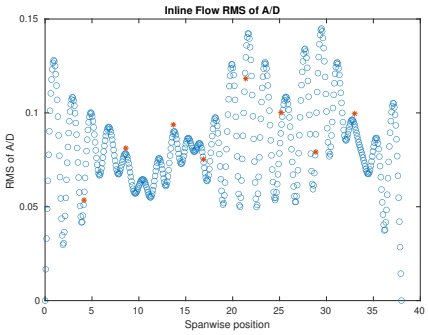

(b) Inline flow RMS profile case 2480.

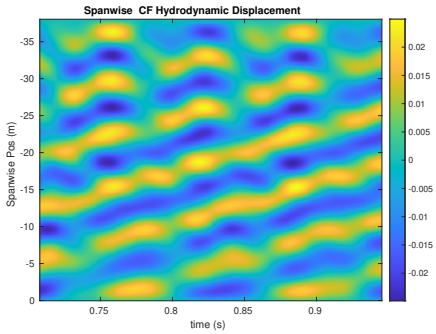

(c) Spanwise cross-flow hydrodynamic displacement case 2480.

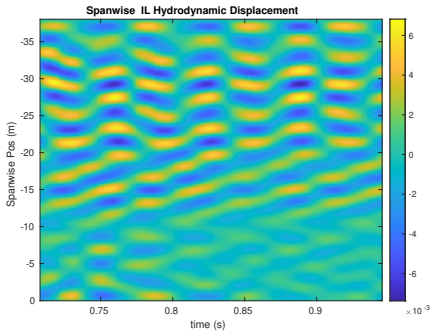

(d) Spanwise inline hydrodynamic displacement case 2480.

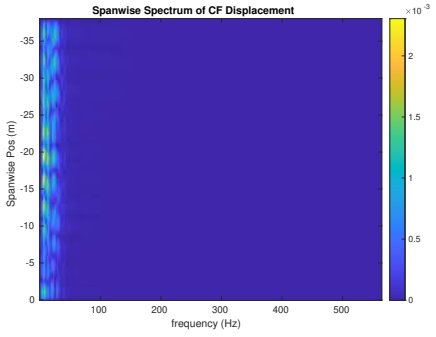

(e) Spanwise cross-flow spectrum of hydrodynamic displacement case 2480.

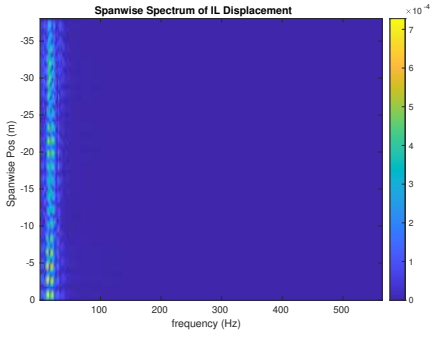

(f) Spanwise inline spectrum of hydrodynamic displacement case 2480.

Figure C-42: *Motion Analysis.* NDP Straight Riser ($L = 38m$) test case 2480.

NDP Straight Riser ($L = 38m$) test case 2490

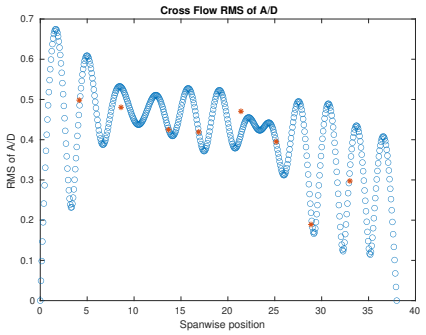

(a) Cross-flow RMS profile case 2490.

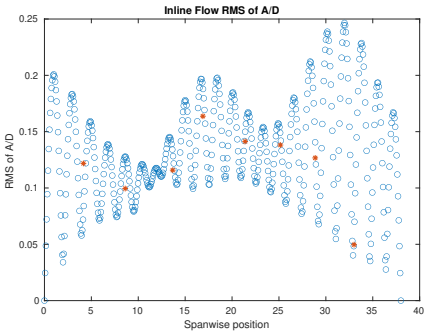

(b) Inline flow RMS profile case 2490.

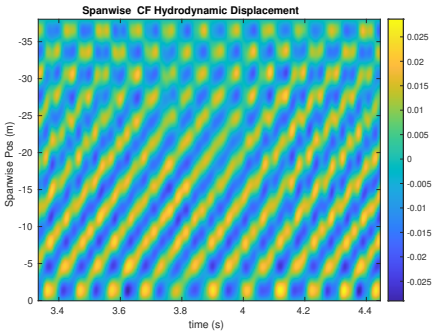

(c) Spanwise cross-flow hydrodynamic displacement case 2490.

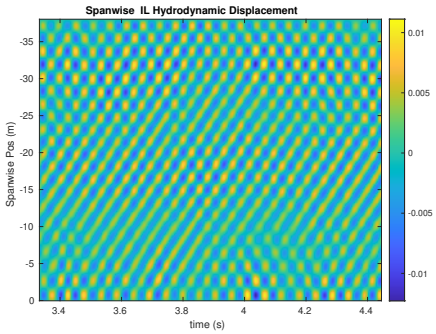

(d) Spanwise inline hydrodynamic displacement case 2490.

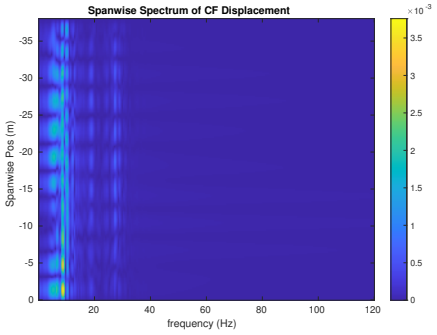

(e) Spanwise cross-flow spectrum of hydrodynamic displacement case 2490.

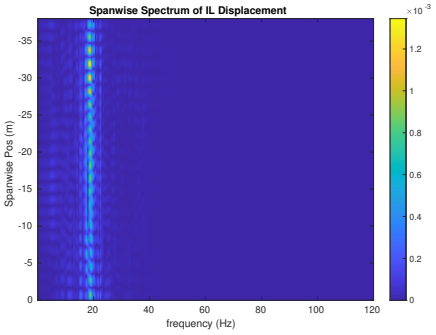

(f) Spanwise inline spectrum of hydrodynamic displacement case 2490.

Figure C-43: *Motion Analysis.* NDP Straight Riser ($L = 38m$) test case 2490.

NDP Straight Riser ($L = 38m$) test case 2500

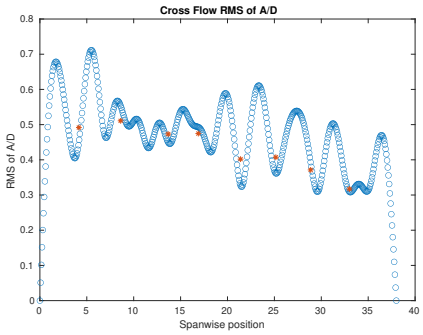

(a) Cross-flow RMS profile case 2500.

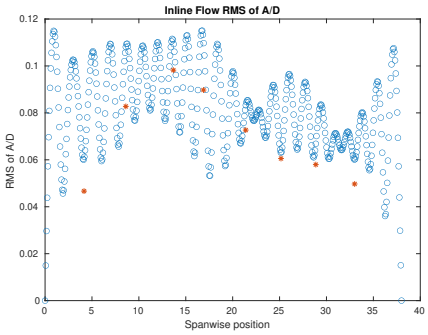

(b) Inline flow RMS profile case 2500.

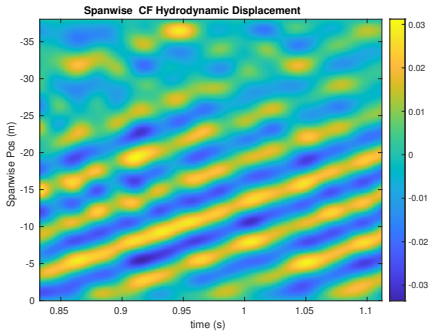

(c) Spanwise cross-flow hydrodynamic displacement case 2500.

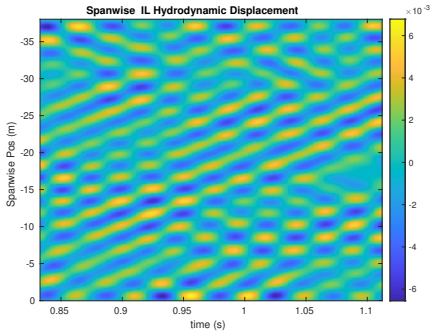

(d) Spanwise inline hydrodynamic displacement case 2500.

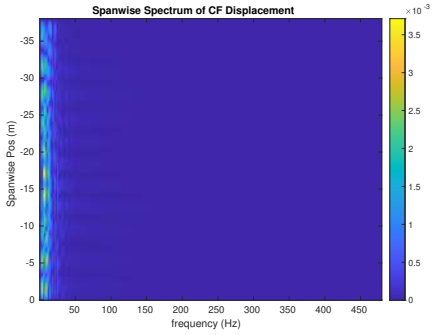

(e) Spanwise cross-flow spectrum of hydrodynamic displacement case 2500.

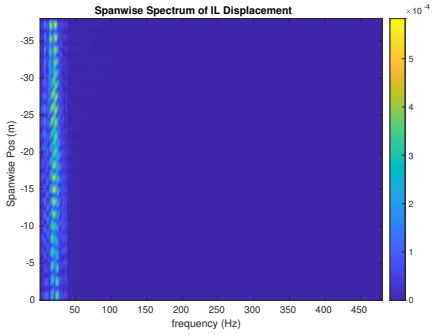

(f) Spanwise inline spectrum of hydrodynamic displacement case 2500.

Figure C-44: *Motion Analysis.* NDP Straight Riser ($L = 38m$) test case 2500.

NDP Straight Riser ($L = 38m$) test case 2510

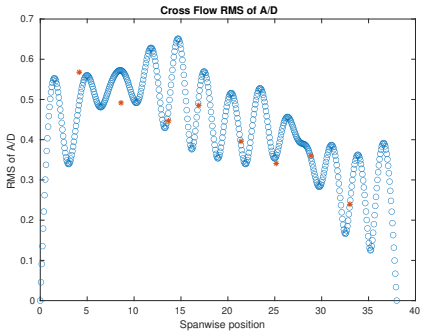

(a) Cross-flow RMS profile case 2510.

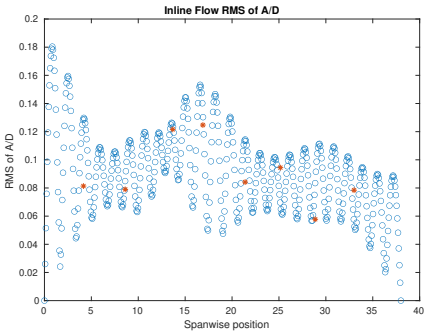

(b) Inline flow RMS profile case 2510.

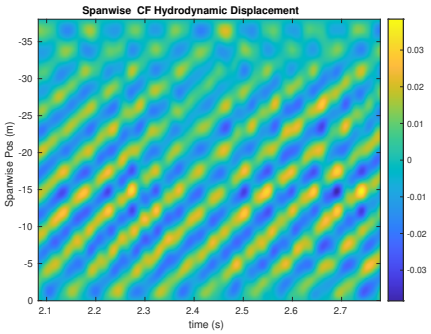

(c) Spanwise cross-flow hydrodynamic displacement case 2510.

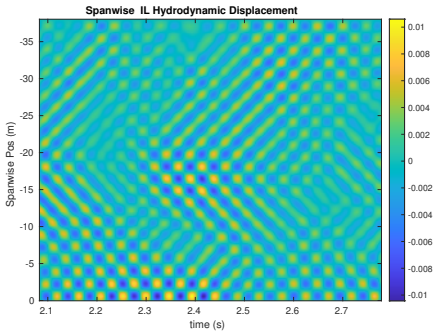

(d) Spanwise inline hydrodynamic displacement case 2510.

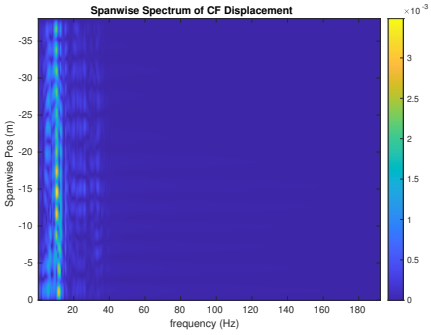

(e) Spanwise cross-flow spectrum of hydrodynamic displacement case 2510.

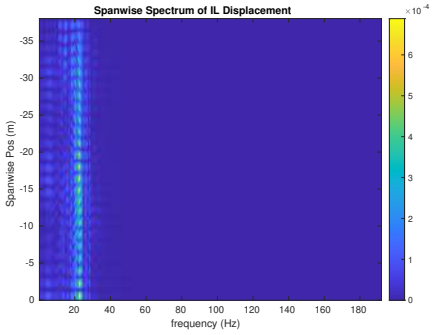

(f) Spanwise inline spectrum of hydrodynamic displacement case 2510.

Figure C-45: *Motion Analysis.* NDP Straight Riser ($L = 38m$) test case 2510.

NDP Straight Riser ($L = 38m$) test case 2520

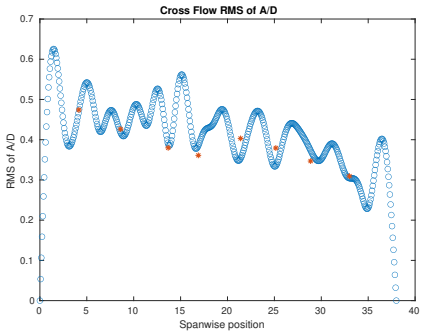

(a) Cross-flow RMS profile case 2520.

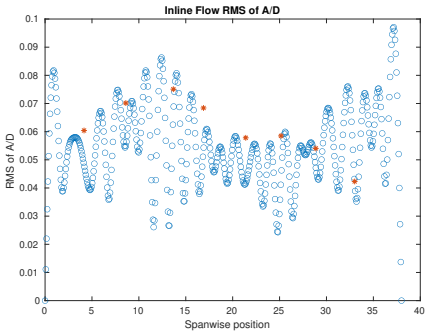

(b) Inline flow RMS profile case 2520.

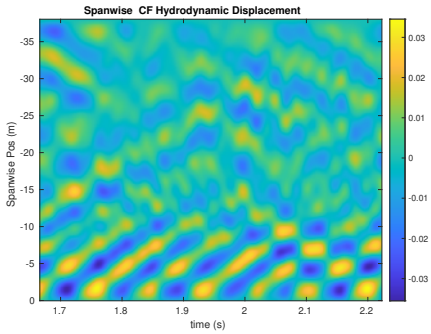

(c) Spanwise cross-flow hydrodynamic displacement case 2520.

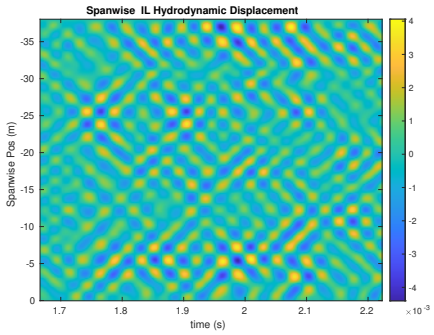

(d) Spanwise inline hydrodynamic displacement case 2520.

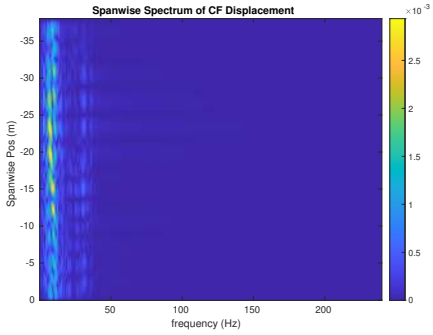

(e) Spanwise cross-flow spectrum of hydrodynamic displacement case 2520.

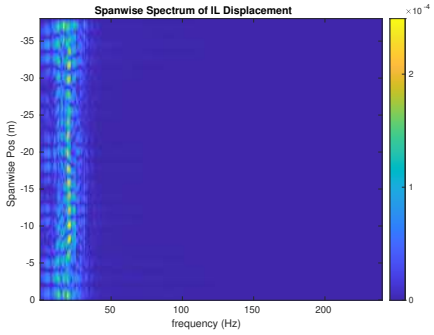

(f) Spanwise inline spectrum of hydrodynamic displacement case 2520.

Figure C-46: *Motion Analysis.* NDP Straight Riser ($L = 38m$) test case 2520.

NDP Straight Riser ($L = 38m$) test case 2530

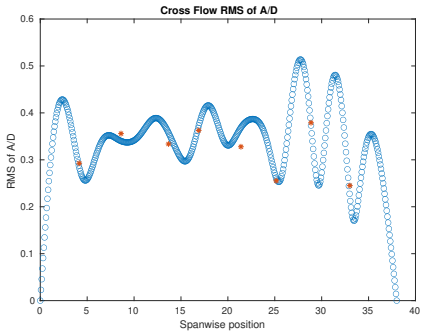

(a) Cross-flow RMS profile case 2530.

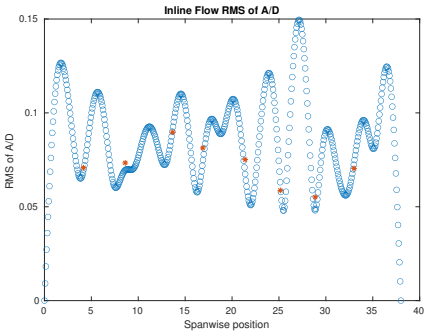

(b) Inline flow RMS profile case 2530.

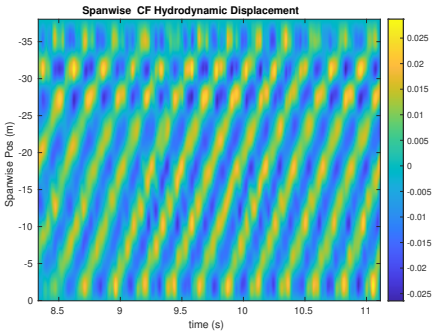

(c) Spanwise cross-flow hydrodynamic displacement case 2530.

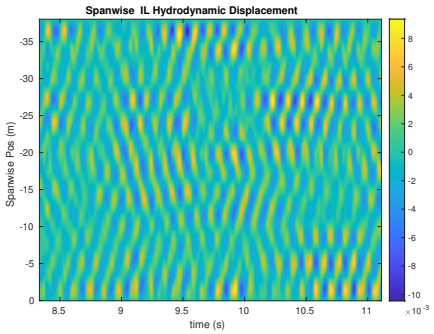

(d) Spanwise inline hydrodynamic displacement case 2530.

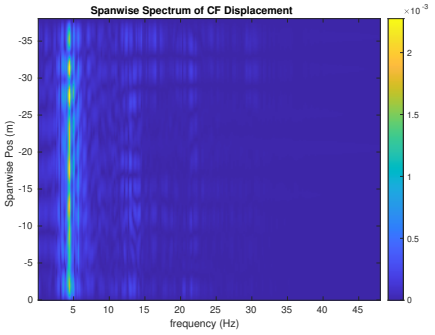

(e) Spanwise cross-flow spectrum of hydrodynamic displacement case 2530.

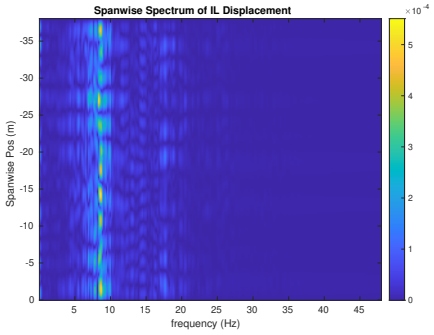

(f) Spanwise inline spectrum of hydrodynamic displacement case 2530.

Figure C-47: *Motion Analysis.* NDP Straight Riser ($L = 38m$) test case 2530.

NDP Straight Riser ($L = 38m$) test case 2540

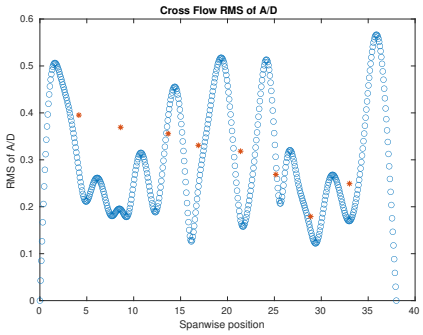

(a) Cross-flow RMS profile case 2540.

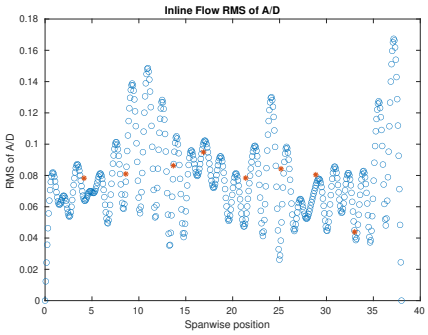

(b) Inline flow RMS profile case 2540.

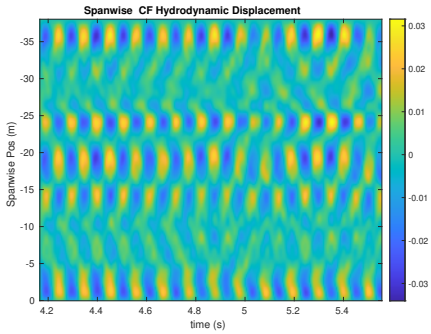

(c) Spanwise cross-flow hydrodynamic displacement case 2540.

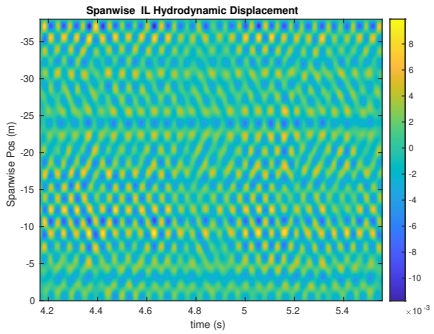

(d) Spanwise inline hydrodynamic displacement case 2540.

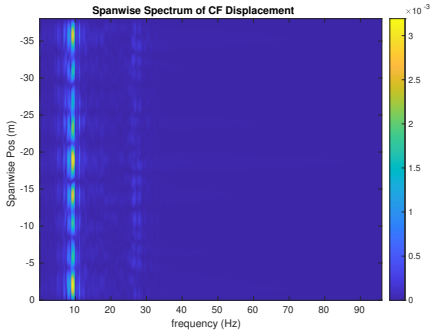

(e) Spanwise cross-flow spectrum of hydrodynamic displacement case 2540.

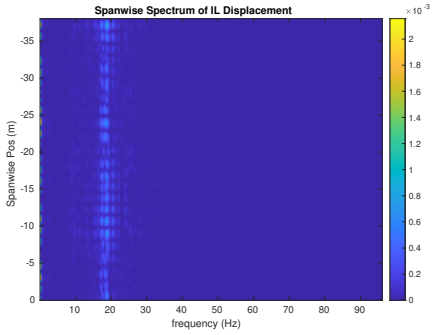

(f) Spanwise inline spectrum of hydrodynamic displacement case 2540.

Figure C-48: *Motion Analysis.* NDP Straight Riser ($L = 38m$) test case 2540.

NDP Straight Riser ($L = 38m$) test case 3010

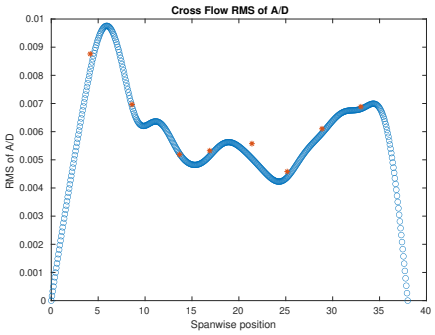

(a) Cross-flow RMS profile case 3010.

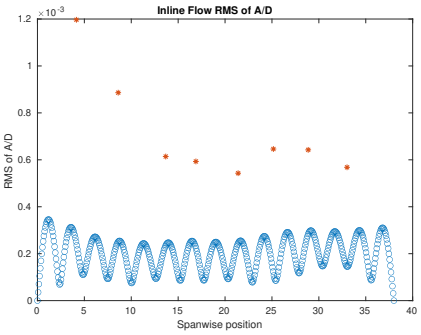

(b) Inline flow RMS profile case 3010.

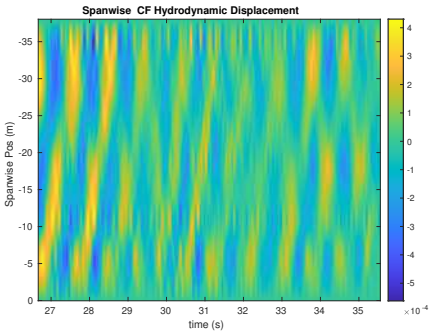

(c) Spanwise cross-flow hydrodynamic displacement case 3010.

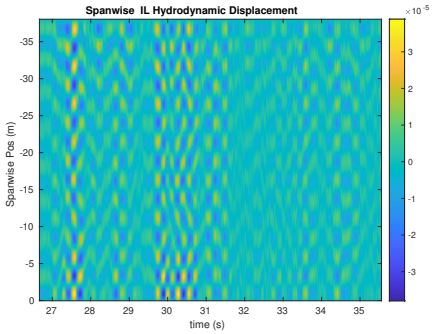

(d) Spanwise inline hydrodynamic displacement case 3010.

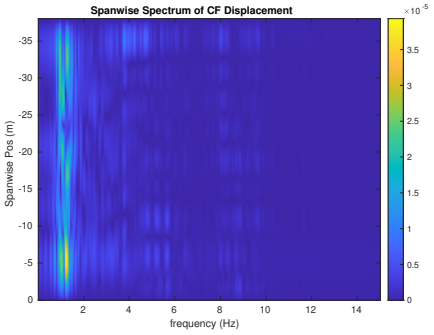

(e) Spanwise cross-flow spectrum of hydrodynamic displacement case 3010.

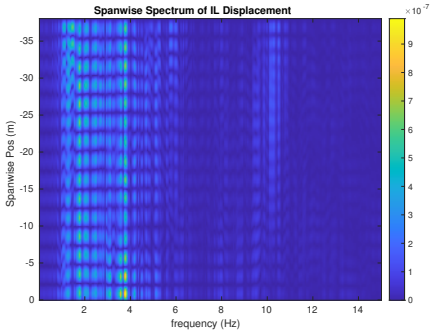

(f) Spanwise inline spectrum of hydrodynamic displacement case 3010.

Figure C-49: *Motion Analysis.* NDP Straight Riser ($L = 38m$) test case 3010.

NDP Straight Riser ($L = 38m$) test case 3020

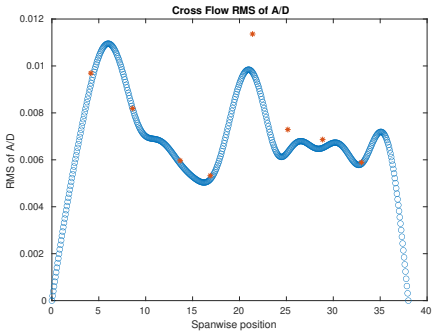

(a) Cross-flow RMS profile case 3020.

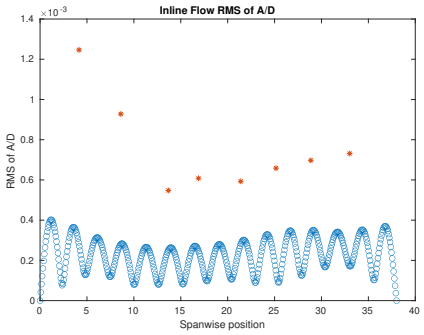

(b) Inline flow RMS profile case 3020.

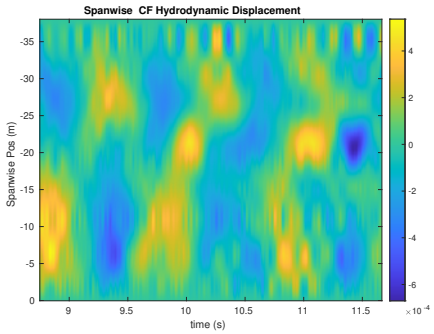

(c) Spanwise cross-flow hydrodynamic displacement case 3020.

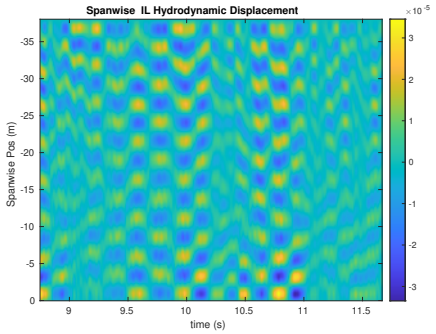

(d) Spanwise inline hydrodynamic displacement case 3020.

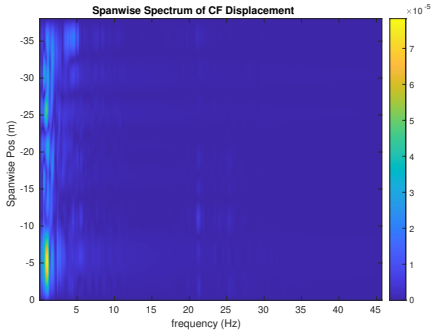

(e) Spanwise cross-flow spectrum of hydrodynamic displacement case 3020.

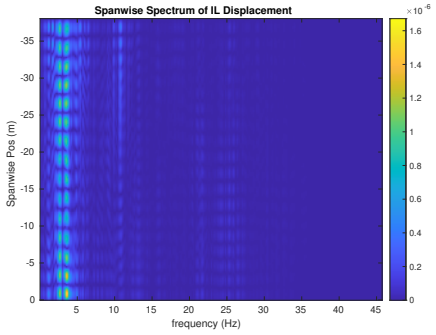

(f) Spanwise inline spectrum of hydrodynamic displacement case 3020.

Figure C-50: *Motion Analysis.* NDP Straight Riser ($L = 38m$) test case 3020.

NDP Straight Riser ($L = 38m$) test case 3030

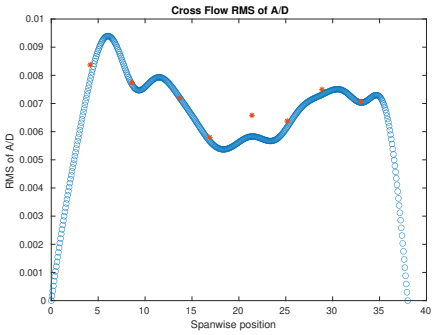

(a) Cross-flow RMS profile case 3030.

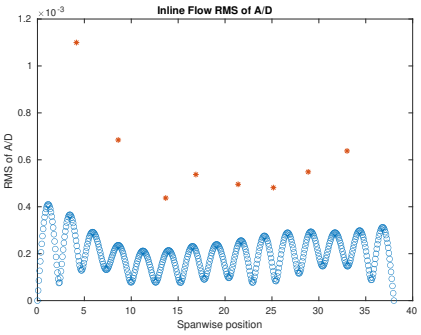

(b) Inline flow RMS profile case 3030.

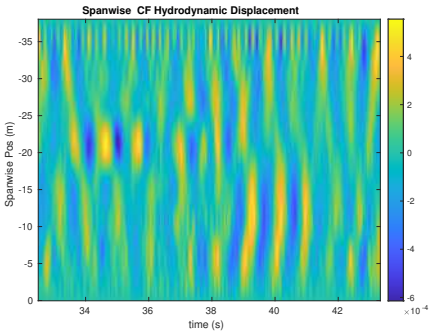

(c) Spanwise cross-flow hydrodynamic displacement case 3030.

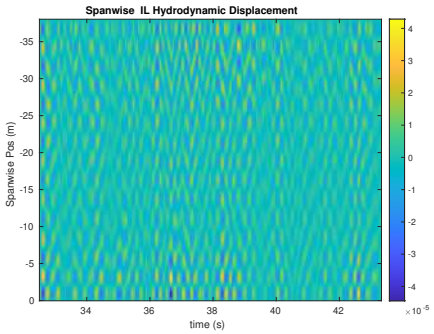

(d) Spanwise inline hydrodynamic displacement case 3030.

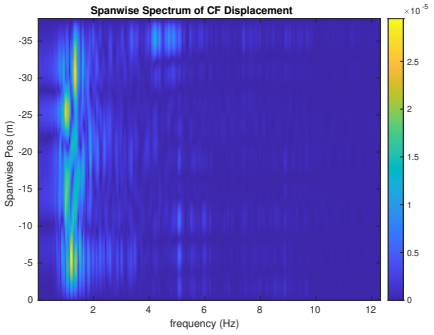

(e) Spanwise cross-flow spectrum of hydrodynamic displacement case 3030.

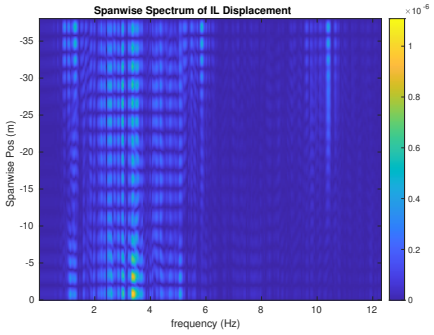

(f) Spanwise inline spectrum of hydrodynamic displacement case 3030.

Figure C-51: *Motion Analysis.* NDP Straight Riser ($L = 38m$) test case 3030.

NDP Straight Riser ($L = 38m$) test case 3040

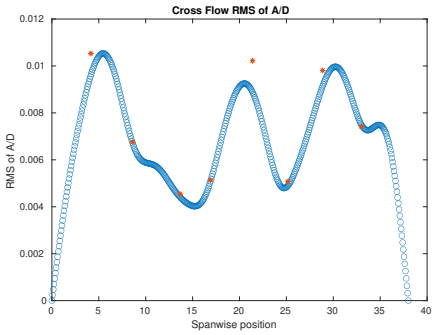

(a) Cross-flow RMS profile case 3040.

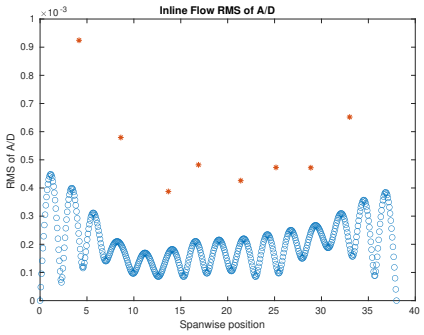

(b) Inline flow RMS profile case 3040.

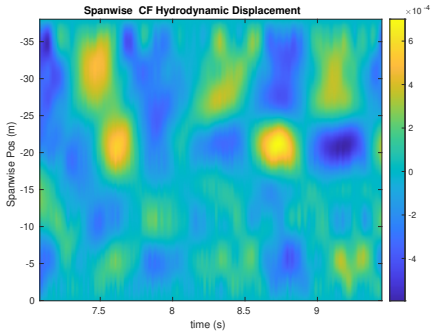

(c) Spanwise cross-flow hydrodynamic displacement case 3040.

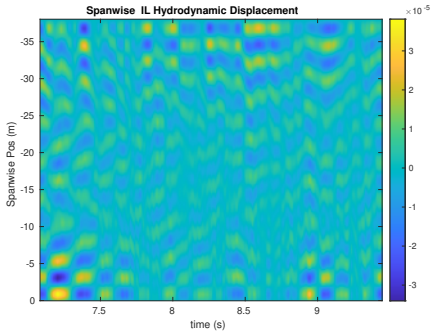

(d) Spanwise inline hydrodynamic displacement case 3040.

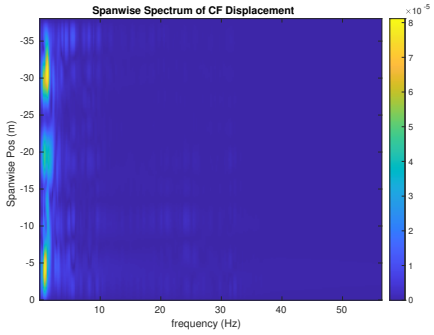

(e) Spanwise cross-flow spectrum of hydrodynamic displacement case 3040.

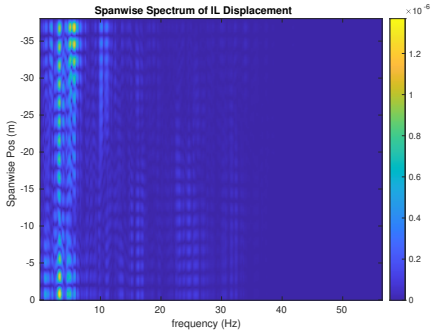

(f) Spanwise inline spectrum of hydrodynamic displacement case 3040.

Figure C-52: *Motion Analysis.* NDP Straight Riser ($L = 38m$) test case 3040.

NDP Straight Riser ($L = 38m$) test case 3050

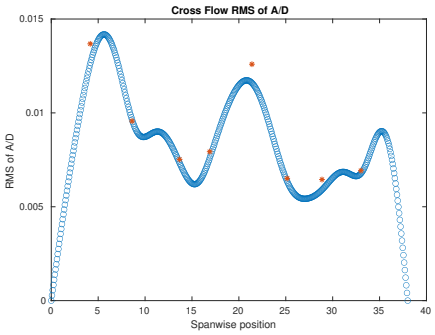

(a) Cross-flow RMS profile case 3050.

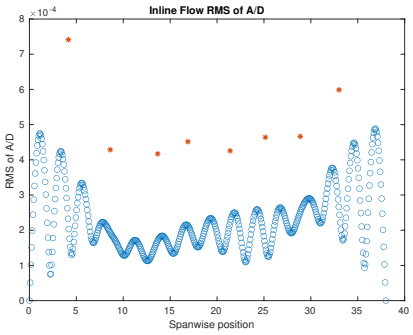

(b) Inline flow RMS profile case 3050.

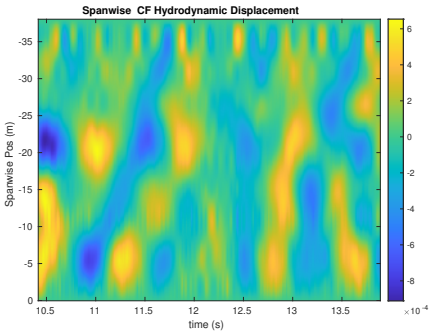

(c) Spanwise cross-flow hydrodynamic displacement case 3050.

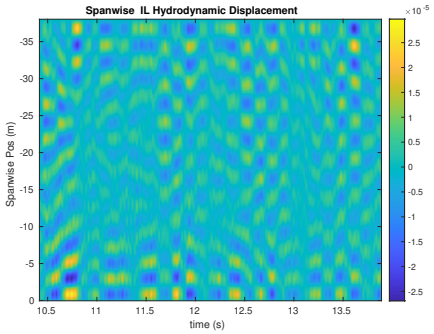

(d) Spanwise inline hydrodynamic displacement case 3050.

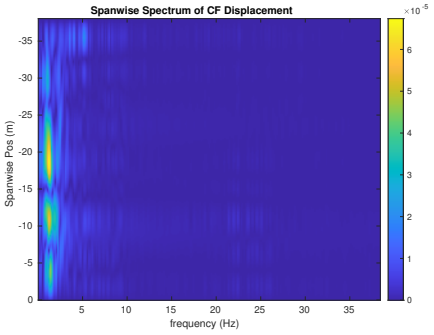

(e) Spanwise cross-flow spectrum of hydrodynamic displacement case 3050.

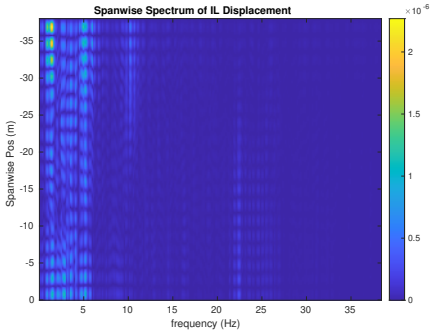

(f) Spanwise inline spectrum of hydrodynamic displacement case 3050.

Figure C-53: *Motion Analysis.* NDP Straight Riser ($L = 38m$) test case 3050.

NDP Straight Riser ($L = 38m$) test case 3060

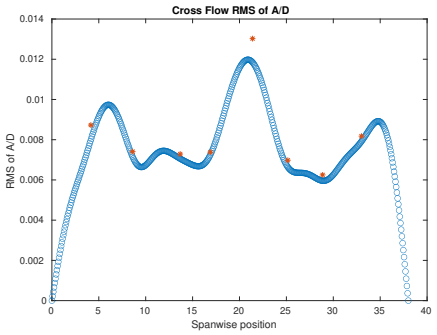

(a) Cross-flow RMS profile case 3060.

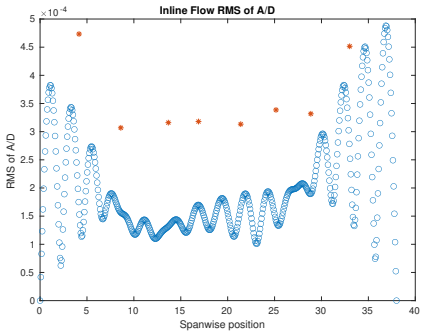

(b) Inline flow RMS profile case 3060.

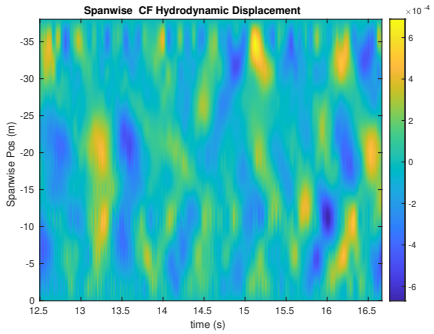

(c) Spanwise cross-flow hydrodynamic displacement case 3060.

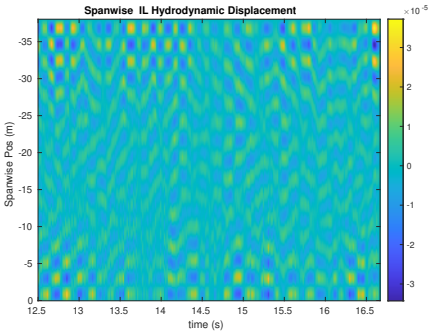

(d) Spanwise inline hydrodynamic displacement case 3060.

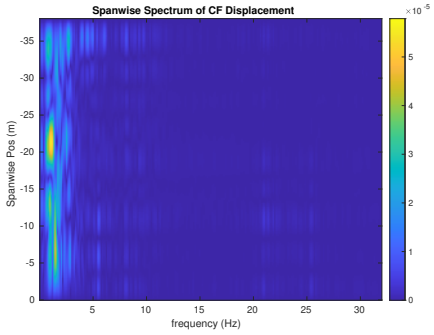

(e) Spanwise cross-flow spectrum of hydrodynamic displacement case 3060.

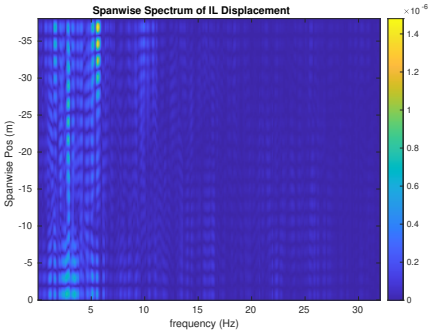

(f) Spanwise inline spectrum of hydrodynamic displacement case 3060.

Figure C-54: *Motion Analysis.* NDP Straight Riser ($L = 38m$) test case 3060.

NDP Straight Riser ($L = 38m$) test case 3070

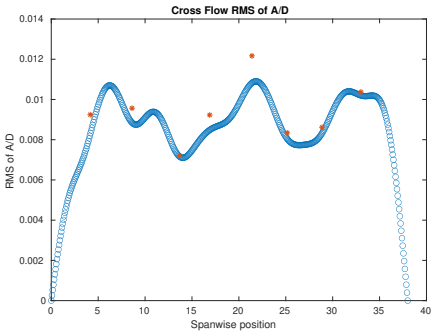

(a) Cross-flow RMS profile case 3070.

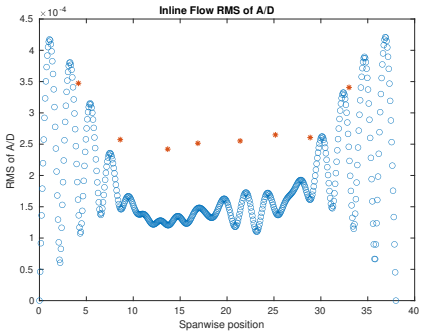

(b) Inline flow RMS profile case 3070.

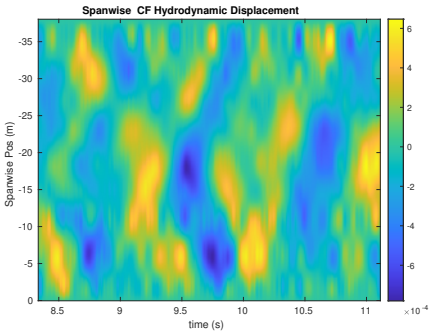

(c) Spanwise cross-flow hydrodynamic displacement case 3070.

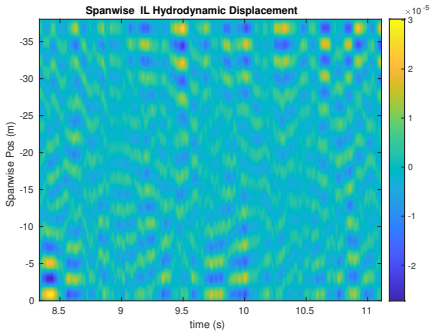

(d) Spanwise inline hydrodynamic displacement case 3070.

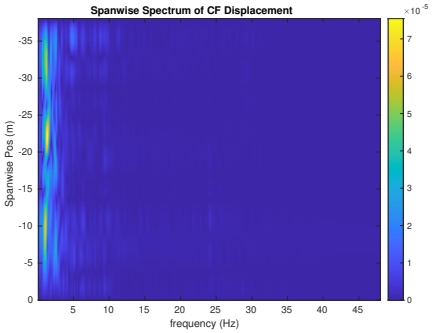

(e) Spanwise cross-flow spectrum of hydrodynamic displacement case 3070.

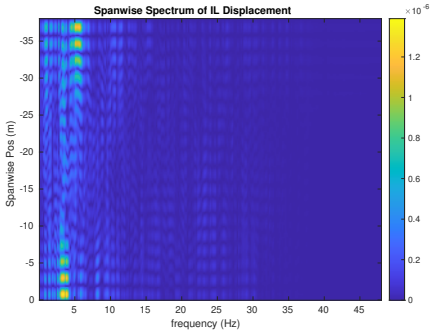

(f) Spanwise inline spectrum of hydrodynamic displacement case 3070.

Figure C-55: *Motion Analysis.* NDP Straight Riser ($L = 38m$) test case 3070.

NDP Straight Riser ($L = 38m$) test case 3081

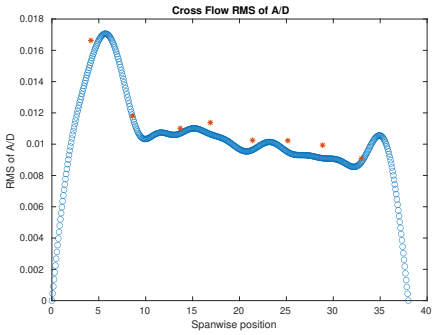

(a) Cross-flow RMS profile case 3081.

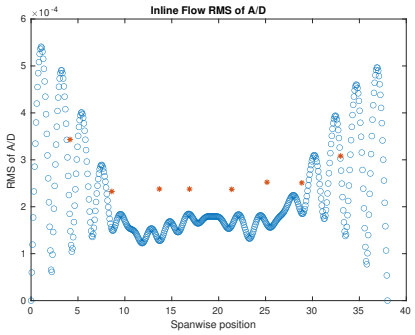

(b) Inline flow RMS profile case 3081.

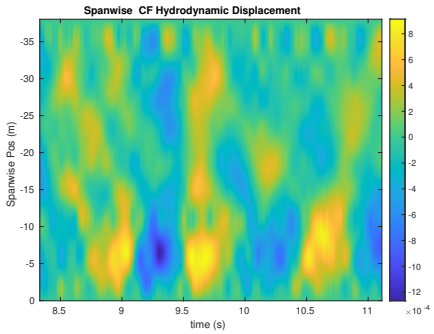

(c) Spanwise cross-flow hydrodynamic displacement case 3081.

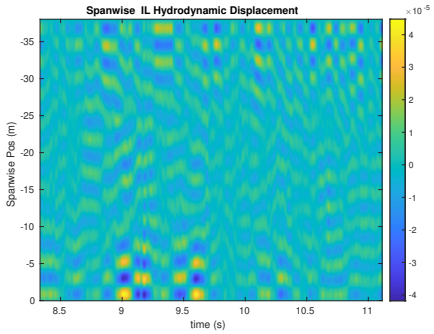

(d) Spanwise inline hydrodynamic displacement case 3081.

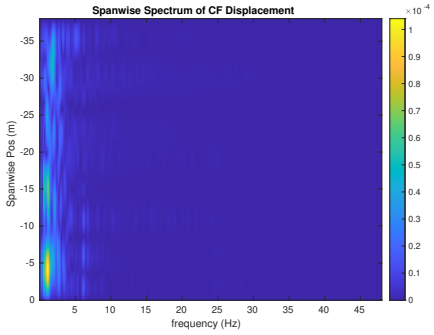

(e) Spanwise cross-flow spectrum of hydrodynamic displacement case 3081.

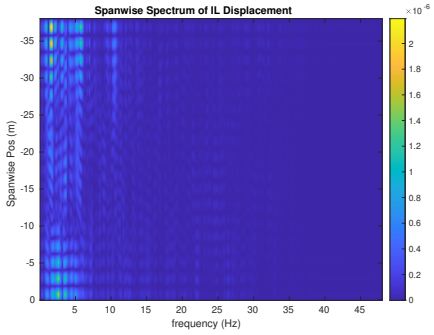

(f) Spanwise inline spectrum of hydrodynamic displacement case 3081.

Figure C-56: *Motion Analysis.* NDP Straight Riser ($L = 38m$) test case 3081.

NDP Straight Riser ($L = 38m$) test case 3090

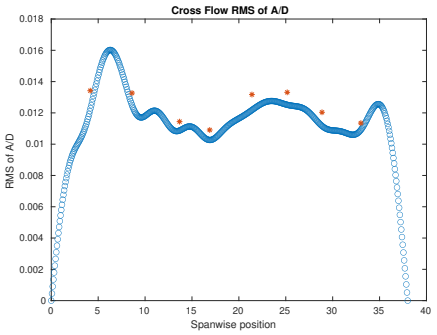

(a) Cross-flow RMS profile case 3090.

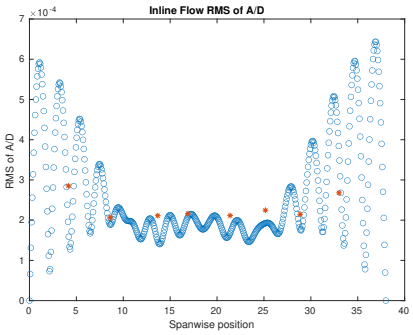

(b) Inline flow RMS profile case 3090.

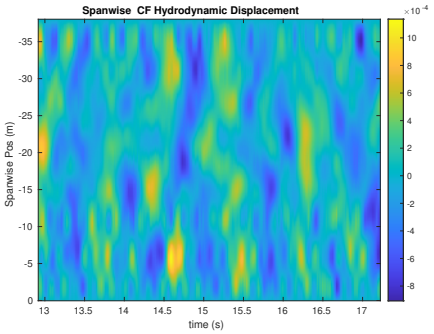

(c) Spanwise cross-flow hydrodynamic displacement case 3090.

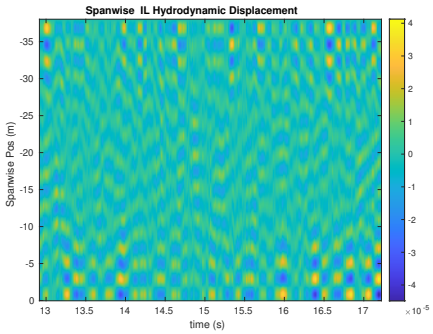

(d) Spanwise inline hydrodynamic displacement case 3090.

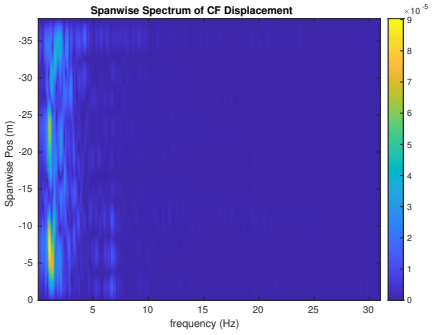

(e) Spanwise cross-flow spectrum of hydrodynamic displacement case 3090.

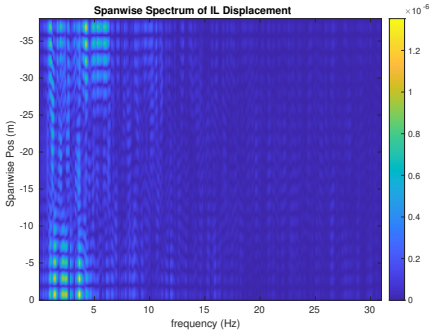

(f) Spanwise inline spectrum of hydrodynamic displacement case 3090.

Figure C-57: *Motion Analysis.* NDP Straight Riser ($L = 38m$) test case 3090.

NDP Straight Riser ($L = 38m$) test case 3100

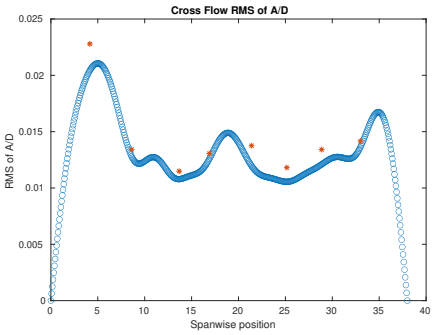

(a) Cross-flow RMS profile case 3100.

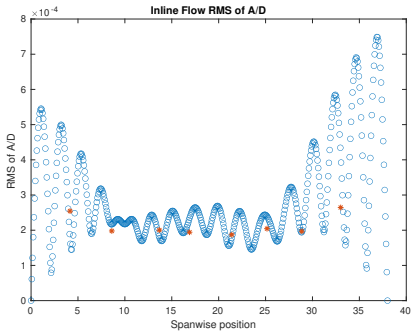

(b) Inline flow RMS profile case 3100.

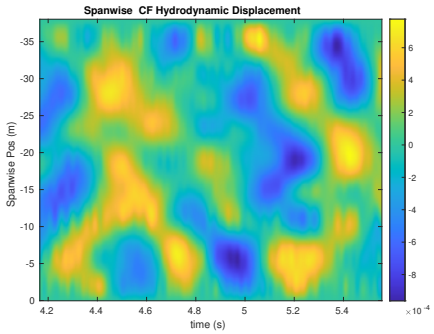

(c) Spanwise cross-flow hydrodynamic displacement case 3100.

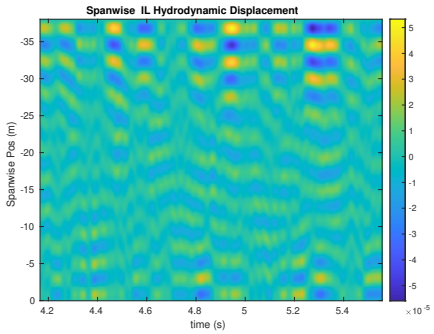

(d) Spanwise inline hydrodynamic displacement case 3100.

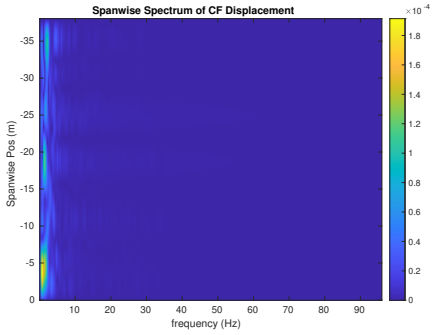

(e) Spanwise cross-flow spectrum of hydrodynamic displacement case 3100.

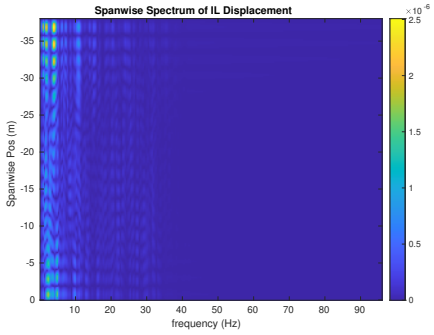

(f) Spanwise inline spectrum of hydrodynamic displacement case 3100.

Figure C-58: *Motion Analysis.* NDP Straight Riser ($L = 38m$) test case 3100.

NDP Straight Riser ($L = 38m$) test case 3110

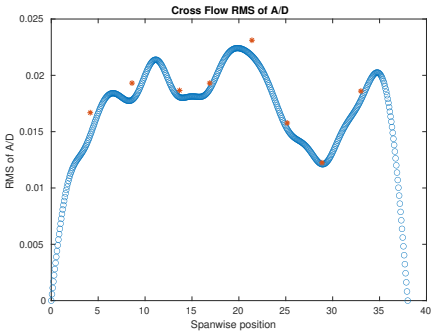

(a) Cross-flow RMS profile case 3110.

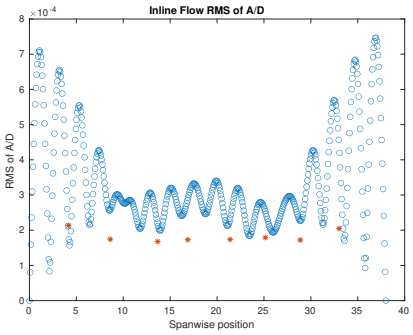

(b) Inline flow RMS profile case 3110.

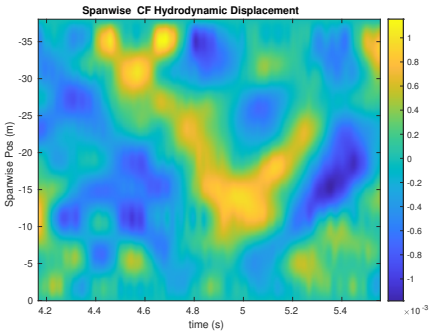

(c) Spanwise cross-flow hydrodynamic displacement case 3110.

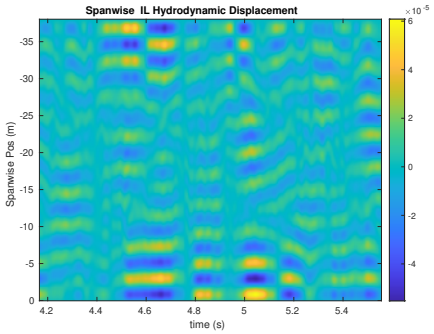

(d) Spanwise inline hydrodynamic displacement case 3110.

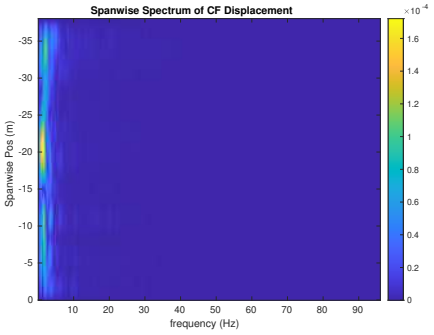

(e) Spanwise cross-flow spectrum of hydrodynamic displacement case 3110.

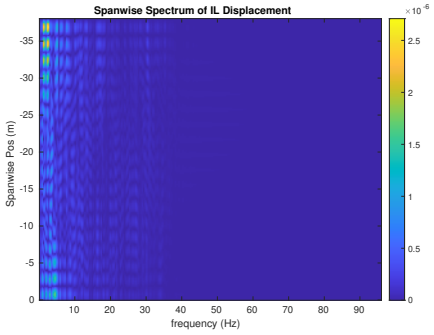

(f) Spanwise inline spectrum of hydrodynamic displacement case 3110.

Figure C-59: *Motion Analysis.* NDP Straight Riser ($L = 38m$) test case 3110.

NDP Straight Riser ($L = 38m$) test case 3120

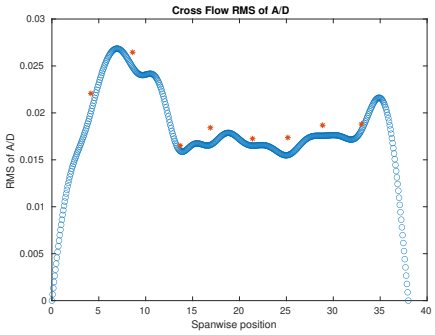

(a) Cross-flow RMS profile case 3120.

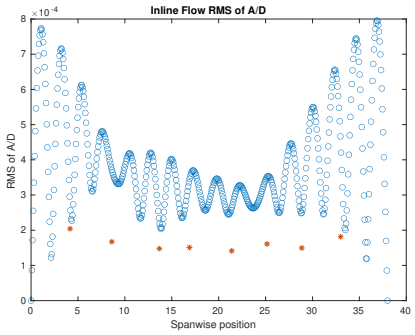

(b) Inline flow RMS profile case 3120.

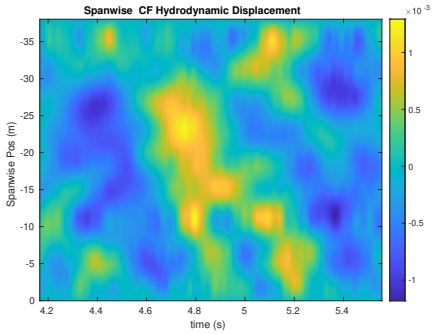

(c) Spanwise cross-flow hydrodynamic displacement case 3120.

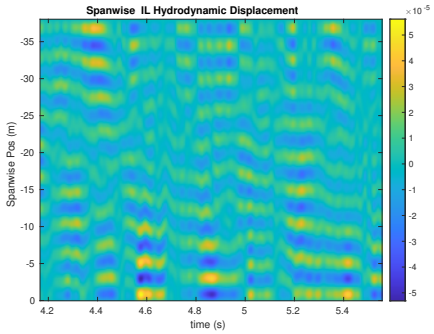

(d) Spanwise inline hydrodynamic displacement case 3120.

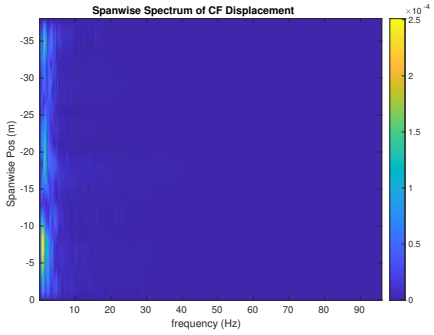

(e) Spanwise cross-flow spectrum of hydrodynamic displacement case 3120.

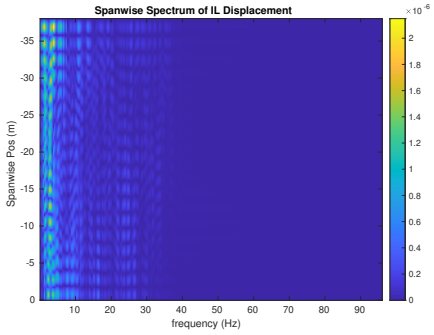

(f) Spanwise inline spectrum of hydrodynamic displacement case 3120.

Figure C-60: *Motion Analysis.* NDP Straight Riser ($L = 38m$) test case 3120.

NDP Straight Riser ($L = 38m$) test case 3130

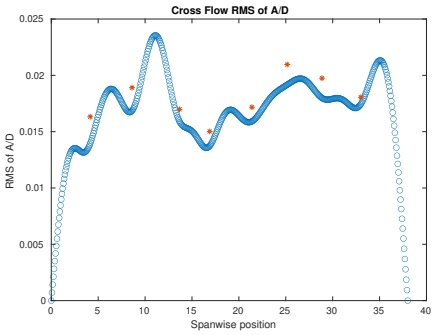

(a) Cross-flow RMS profile case 3130.

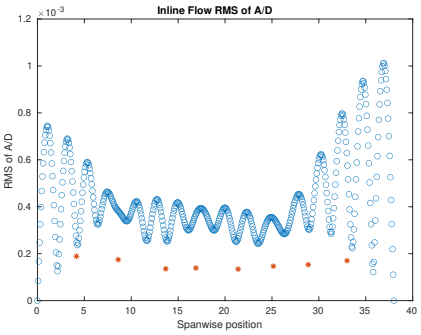

(b) Inline flow RMS profile case 3130.

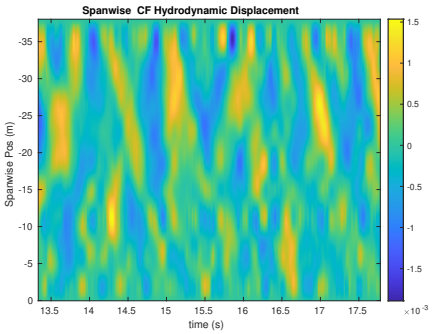

(c) Spanwise cross-flow hydrodynamic displacement case 3130.

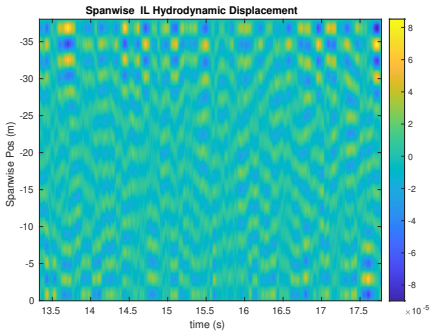

(d) Spanwise inline hydrodynamic displacement case 3130.

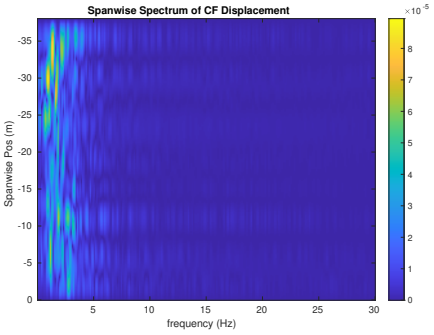

(e) Spanwise cross-flow spectrum of hydrodynamic displacement case 3130.

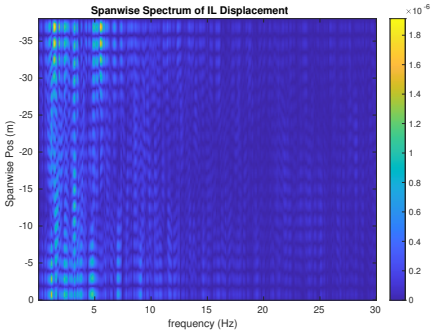

(f) Spanwise inline spectrum of hydrodynamic displacement case 3130.

Figure C-61: *Motion Analysis.* NDP Straight Riser ($L = 38m$) test case 3130.

NDP Straight Riser ($L = 38m$) test case 3140

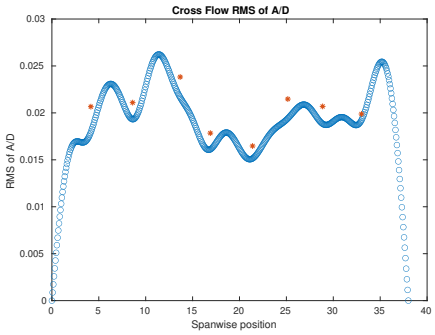

(a) Cross-flow RMS profile case 3140.

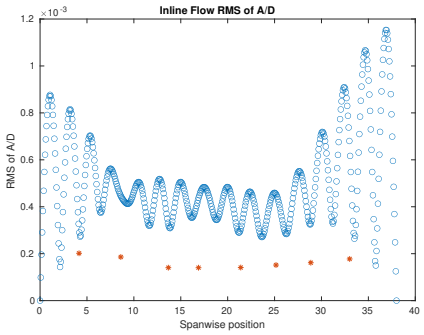

(b) Inline flow RMS profile case 3140.

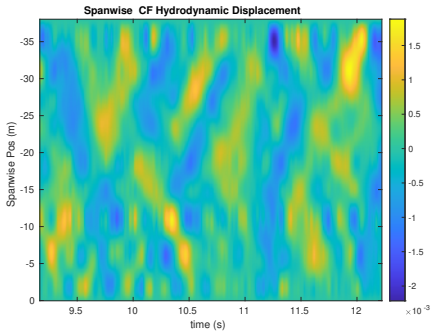

(c) Spanwise cross-flow hydrodynamic displacement case 3140.

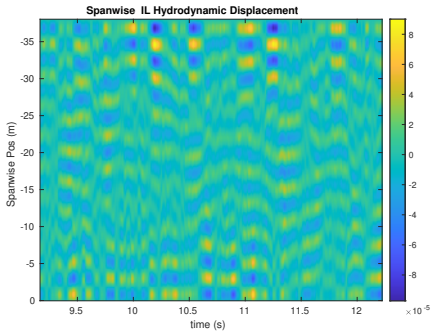

(d) Spanwise inline hydrodynamic displacement case 3140.

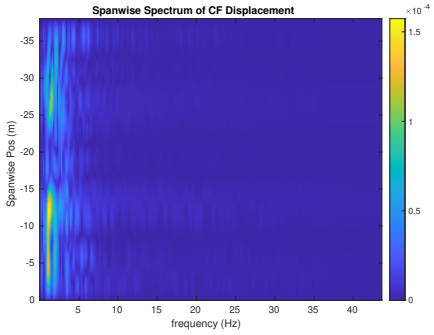

(e) Spanwise cross-flow spectrum of hydrodynamic displacement case 3140.

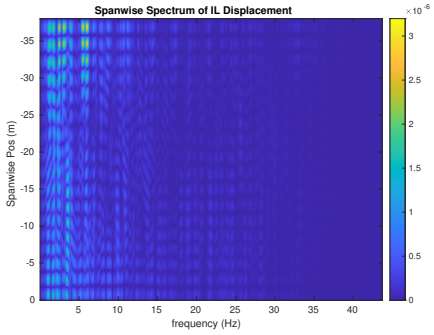

(f) Spanwise inline spectrum of hydrodynamic displacement case 3140.

Figure C-62: *Motion Analysis.* NDP Straight Riser ($L = 38m$) test case 3140.

NDP Straight Riser ($L = 38m$) test case 3150

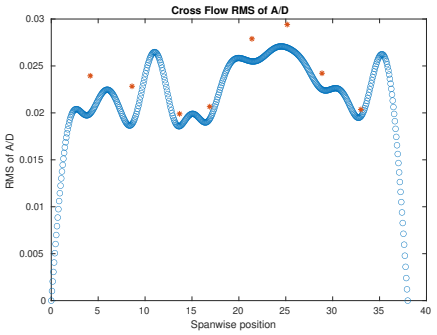

(a) Cross-flow RMS profile case 3150.

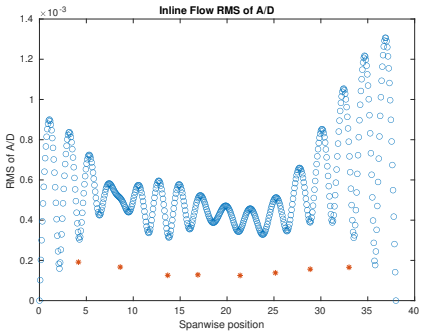

(b) Inline flow RMS profile case 3150.

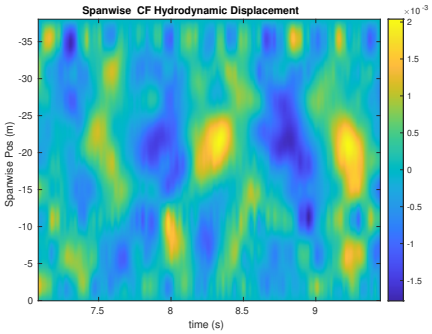

(c) Spanwise cross-flow hydrodynamic displacement case 3150.

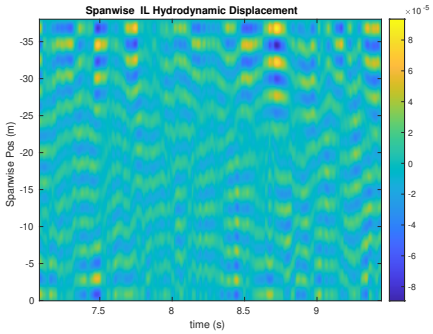

(d) Spanwise inline hydrodynamic displacement case 3150.

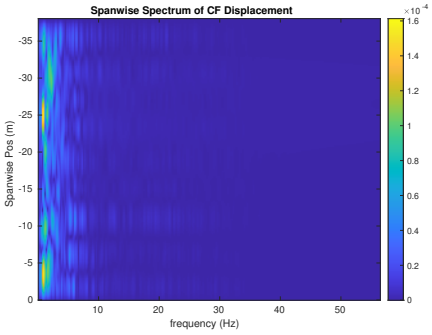

(e) Spanwise cross-flow spectrum of hydrodynamic displacement case 3150.

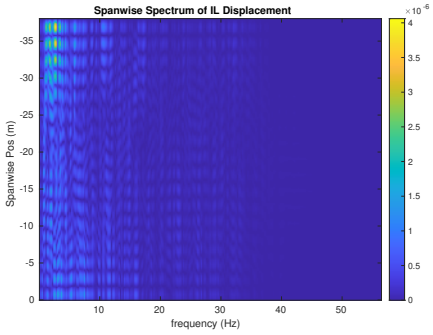

(f) Spanwise inline spectrum of hydrodynamic displacement case 3150.

Figure C-63: *Motion Analysis.* NDP Straight Riser ($L = 38m$) test case 3150.

NDP Straight Riser ($L = 38m$) test case 3160

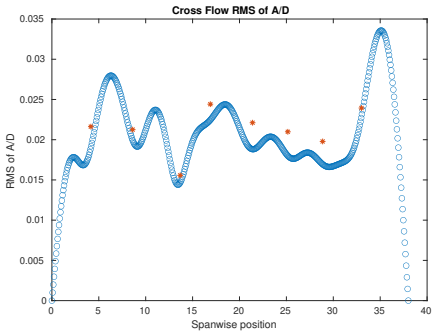

(a) Cross-flow RMS profile case 3160.

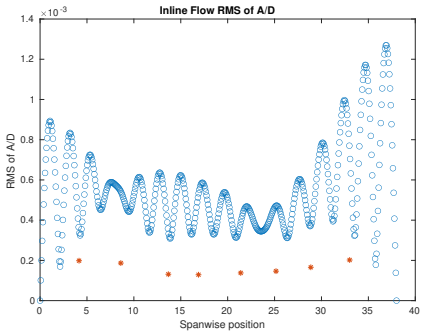

(b) Inline flow RMS profile case 3160.

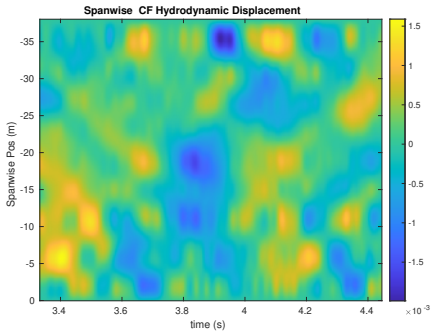

(c) Spanwise cross-flow hydrodynamic displacement case 3160.

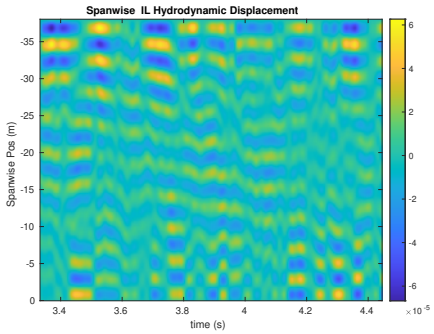

(d) Spanwise inline hydrodynamic displacement case 3160.

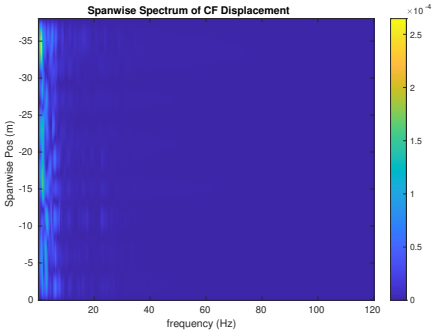

(e) Spanwise cross-flow spectrum of hydrodynamic displacement case 3160.

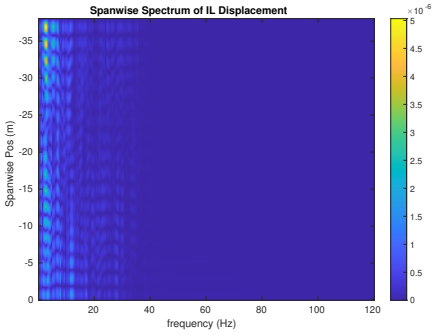

(f) Spanwise inline spectrum of hydrodynamic displacement case 3160.

Figure C-64: *Motion Analysis.* NDP Straight Riser ($L = 38m$) test case 3160.

NDP Straight Riser ($L = 38m$) test case 3170

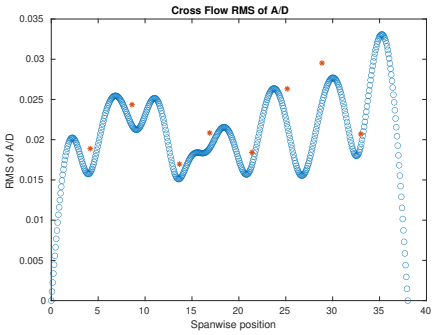

(a) Cross-flow RMS profile case 3170.

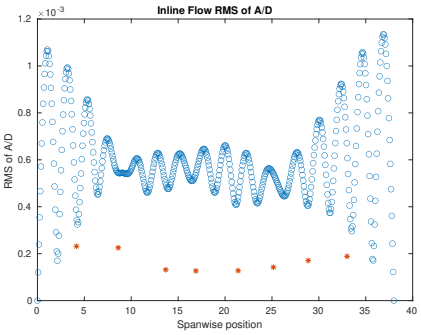

(b) Inline flow RMS profile case 3170.

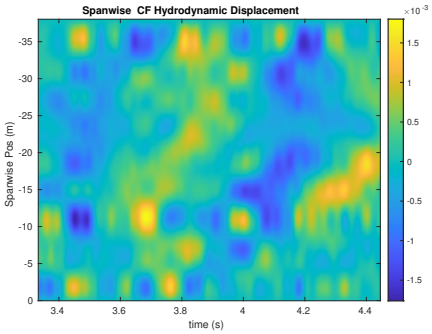

(c) Spanwise cross-flow hydrodynamic displacement case 3170.

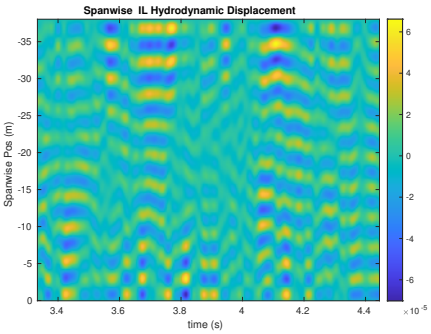

(d) Spanwise inline hydrodynamic displacement case 3170.

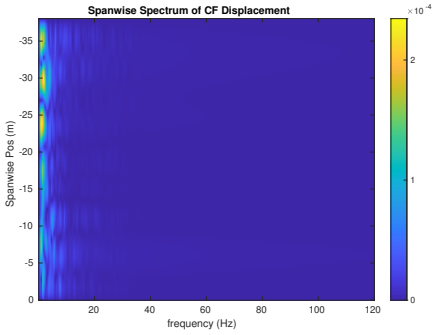

(e) Spanwise cross-flow spectrum of hydrodynamic displacement case 3170.

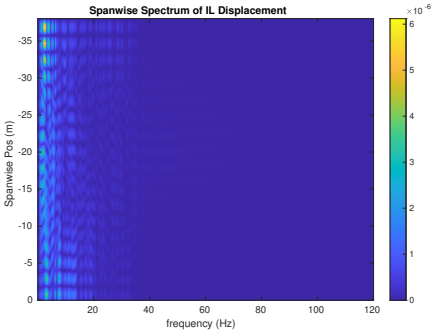

(f) Spanwise inline spectrum of hydrodynamic displacement case 3170.

Figure C-65: *Motion Analysis.* NDP Straight Riser ($L = 38m$) test case 3170.

NDP Straight Riser ($L = 38m$) test case 3180

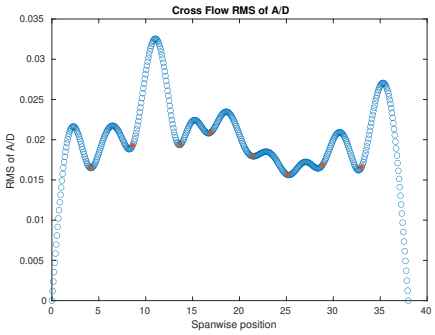

(a) Cross-flow RMS profile case 3180.

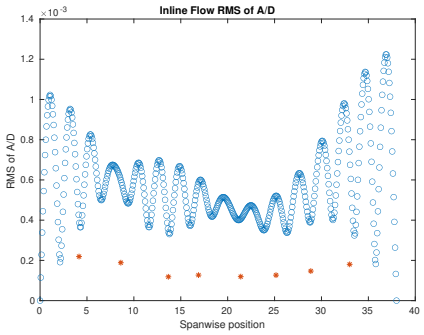

(b) Inline flow RMS profile case 3180.

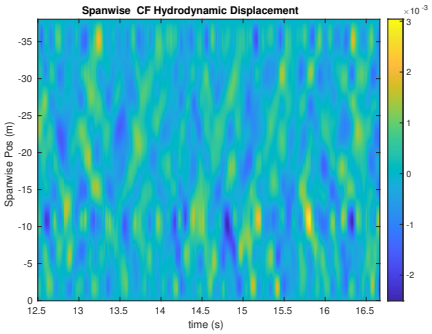

(c) Spanwise cross-flow hydrodynamic displacement case 3180.

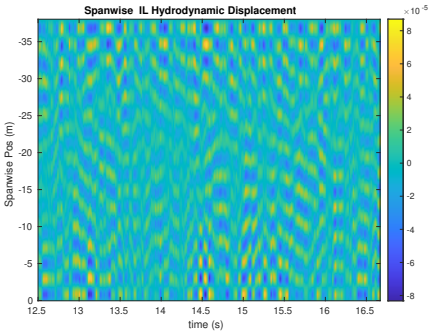

(d) Spanwise inline hydrodynamic displacement case 3180.

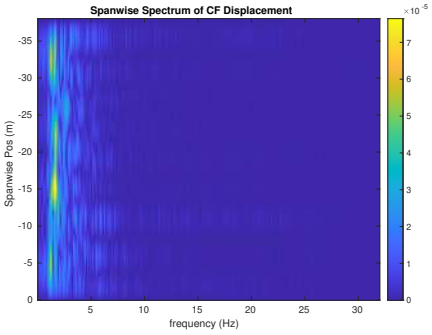

(e) Spanwise cross-flow spectrum of hydrodynamic displacement case 3180.

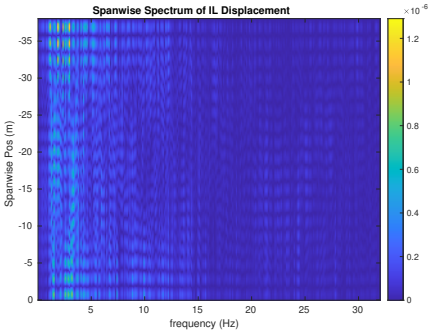

(f) Spanwise inline spectrum of hydrodynamic displacement case 3180.

Figure C-66: *Motion Analysis.* NDP Straight Riser ($L = 38m$) test case 3180.

NDP Straight Riser ($L = 38m$) test case 3190

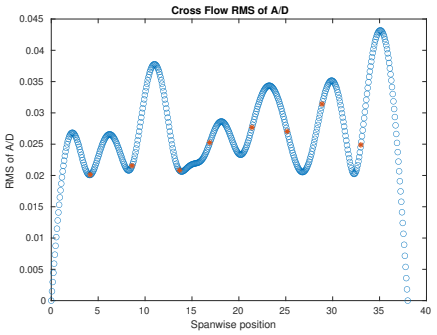

(a) Cross-flow RMS profile case 3190.

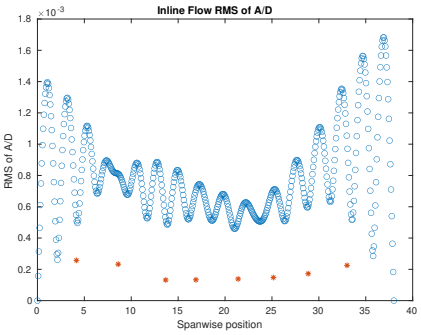

(b) Inline flow RMS profile case 3190.

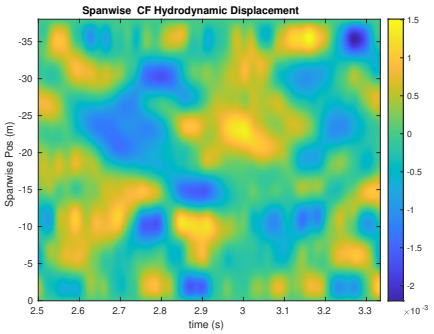

(c) Spanwise cross-flow hydrodynamic displacement case 3190.

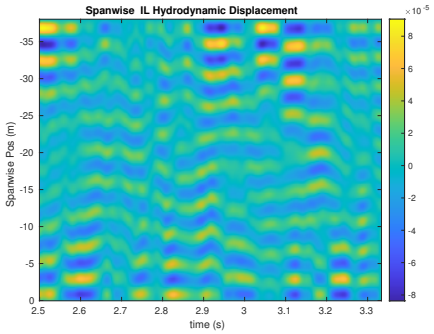

(d) Spanwise inline hydrodynamic displacement case 3190.

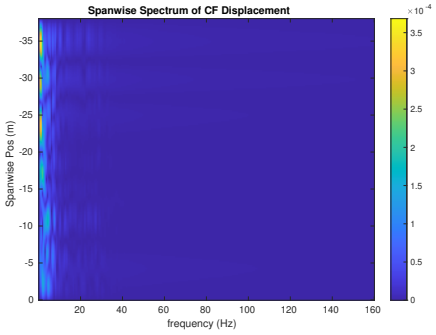

(e) Spanwise cross-flow spectrum of hydrodynamic displacement case 3190.

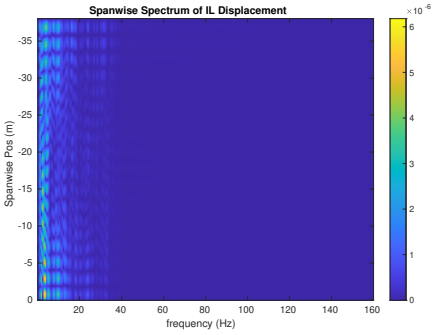

(f) Spanwise inline spectrum of hydrodynamic displacement case 3190.

Figure C-67: *Motion Analysis.* NDP Straight Riser ($L = 38m$) test case 3190.

NDP Straight Riser ($L = 38m$) test case 3200

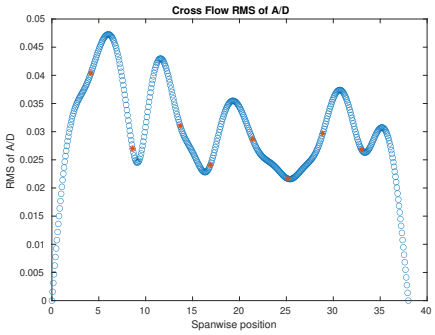

(a) Cross-flow RMS profile case 3200.

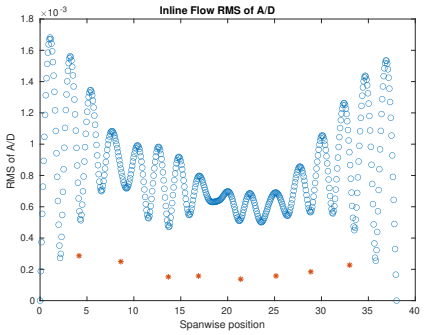

(b) Inline flow RMS profile case 3200.

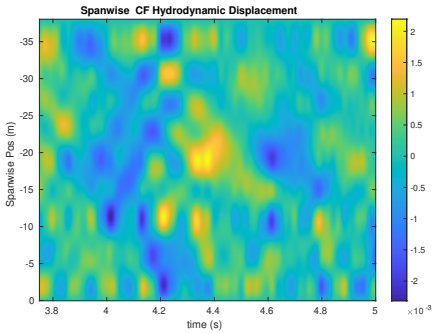

(c) Spanwise cross-flow hydrodynamic displacement case 3200.

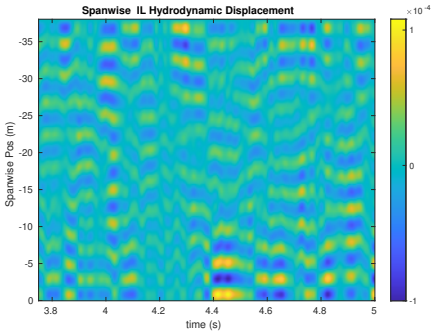

(d) Spanwise inline hydrodynamic displacement case 3200.

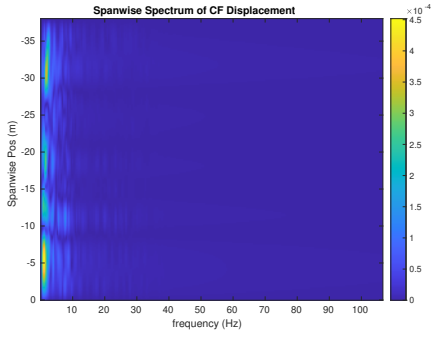

(e) Spanwise cross-flow spectrum of hydrodynamic displacement case 3200.

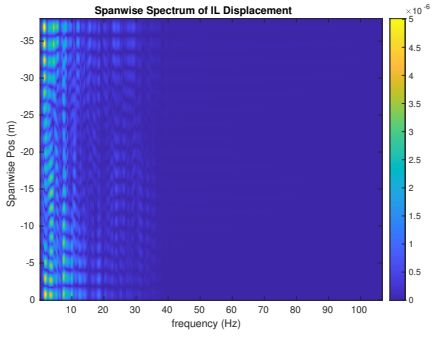

(f) Spanwise inline spectrum of hydrodynamic displacement case 3200.

Figure C-68: *Motion Analysis.* NDP Straight Riser ($L = 38m$) test case 3200.

NDP Straight Riser ($L = 38m$) test case 3210

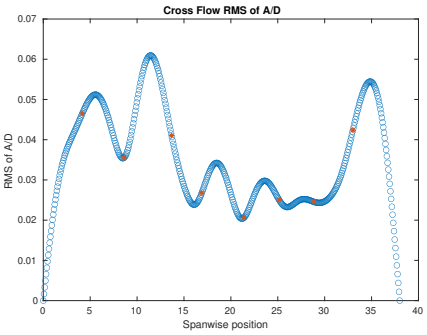

(a) Cross-flow RMS profile case 3210.

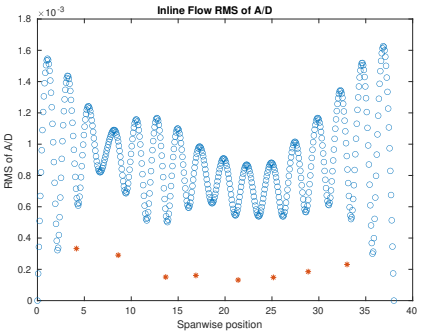

(b) Inline flow RMS profile case 3210.

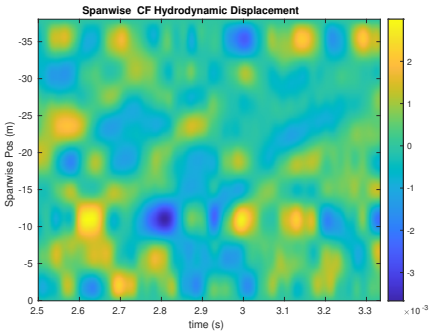

(c) Spanwise cross-flow hydrodynamic displacement case 3210.

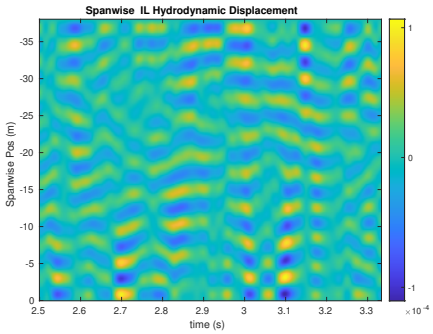

(d) Spanwise inline hydrodynamic displacement case 3210.

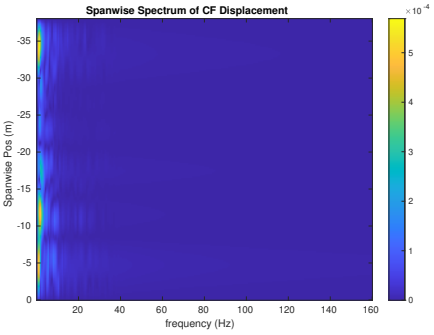

(e) Spanwise cross-flow spectrum of hydrodynamic displacement case 3210.

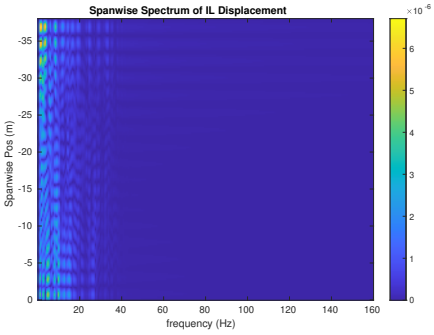

(f) Spanwise inline spectrum of hydrodynamic displacement case 3210.

Figure C-69: *Motion Analysis.* NDP Straight Riser ($L = 38m$) test case 3210.

NDP Straight Riser ($L = 38m$) test case 3220

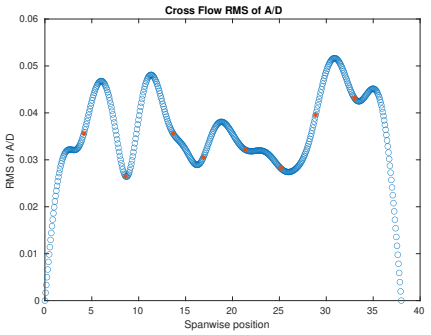

(a) Cross-flow RMS profile case 3220.

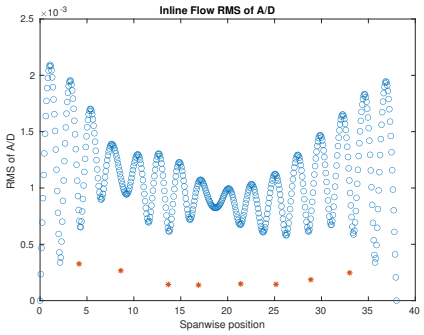

(b) Inline flow RMS profile case 3220.

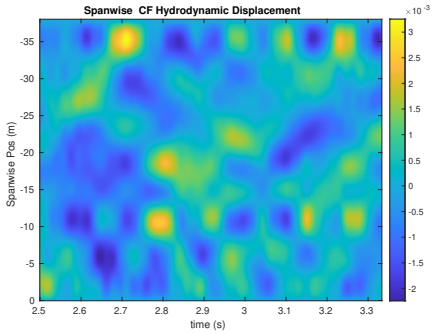

(c) Spanwise cross-flow hydrodynamic displacement case 3220.

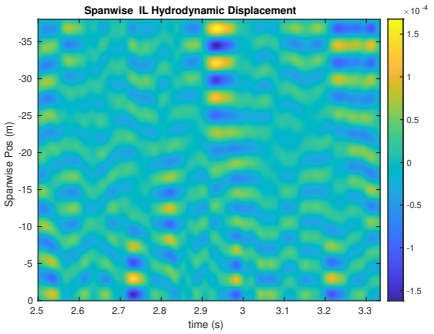

(d) Spanwise inline hydrodynamic displacement case 3220.

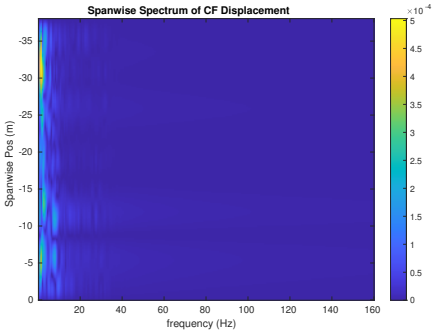

(e) Spanwise cross-flow spectrum of hydrodynamic displacement case 3220.

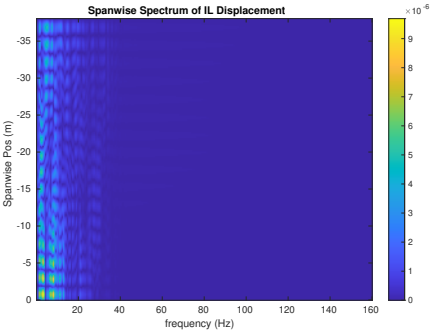

(f) Spanwise inline spectrum of hydrodynamic displacement case 3220.

Figure C-70: *Motion Analysis.* NDP Straight Riser ($L = 38m$) test case 3220.

NDP Straight Riser ($L = 38m$) test case 3320

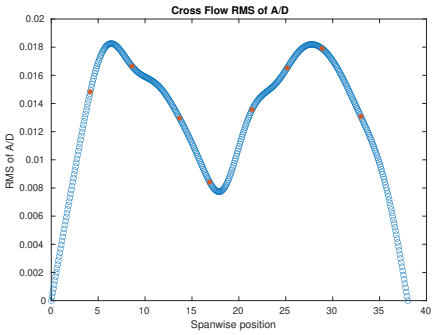

(a) Cross-flow RMS profile case 3320.

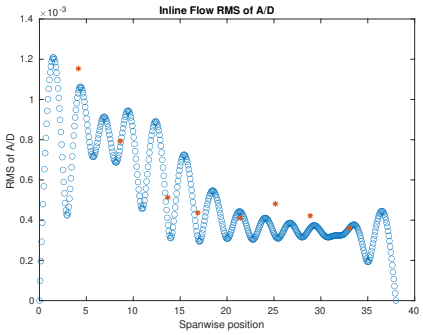

(b) Inline flow RMS profile case 3320.

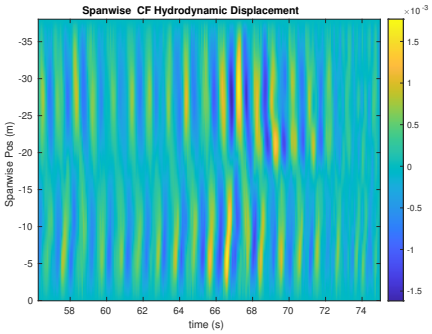

(c) Spanwise cross-flow hydrodynamic displacement case 3320.

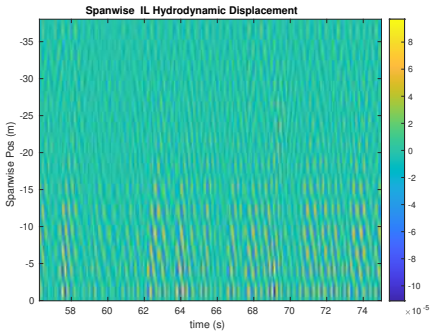

(d) Spanwise inline hydrodynamic displacement case 3320.

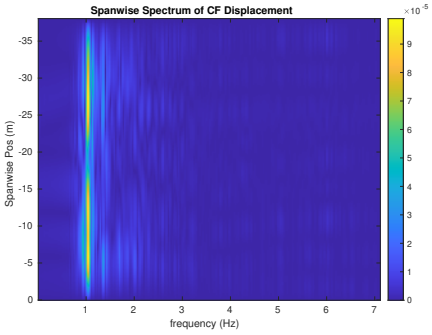

(e) Spanwise cross-flow spectrum of hydrodynamic displacement case 3320.

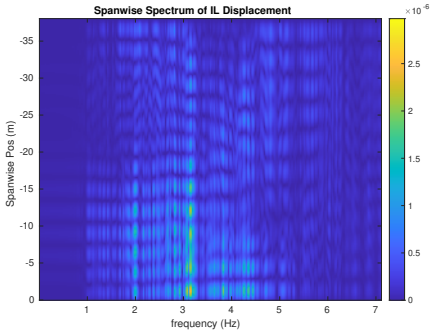

(f) Spanwise inline spectrum of hydrodynamic displacement case 3320.

Figure C-71: *Motion Analysis.* NDP Straight Riser ($L = 38m$) test case 3320.

NDP Straight Riser ($L = 38m$) test case 3340

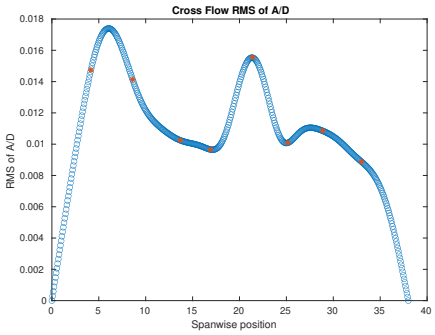

(a) Cross-flow RMS profile case 3340.

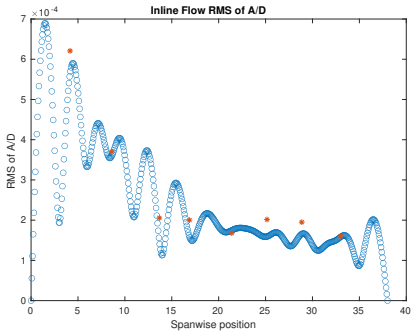

(b) Inline flow RMS profile case 3340.

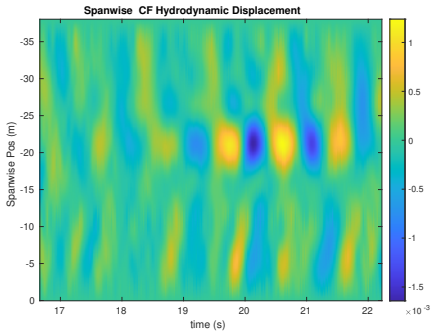

(c) Spanwise cross-flow hydrodynamic displacement case 3340.

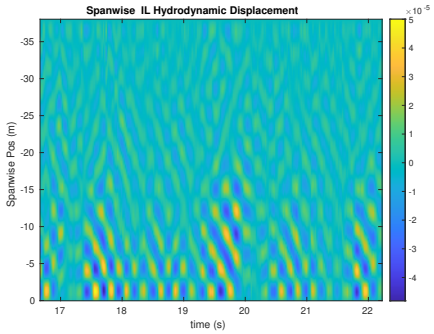

(d) Spanwise inline hydrodynamic displacement case 3340.

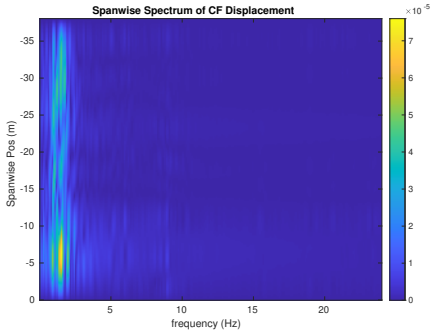

(e) Spanwise cross-flow spectrum of hydrodynamic displacement case 3340.

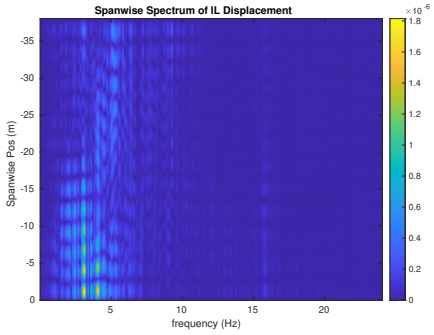

(f) Spanwise inline spectrum of hydrodynamic displacement case 3340.

Figure C-72: *Motion Analysis.* NDP Straight Riser ($L = 38m$) test case 3340.

NDP Straight Riser ($L = 38m$) test case 3360

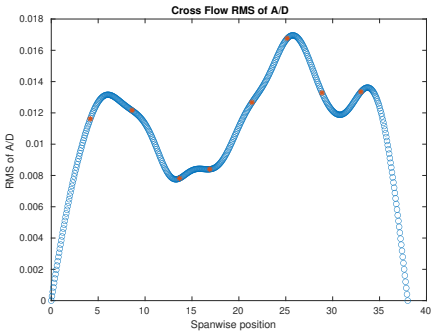

(a) Cross-flow RMS profile case 3360.

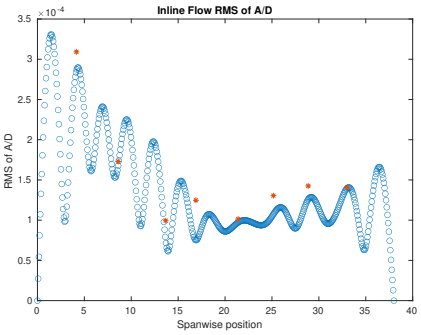

(b) Inline flow RMS profile case 3360.

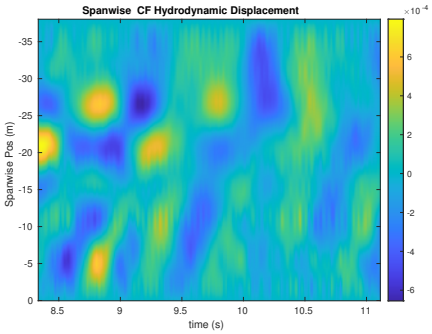

(c) Spanwise cross-flow hydrodynamic displacement case 3360.

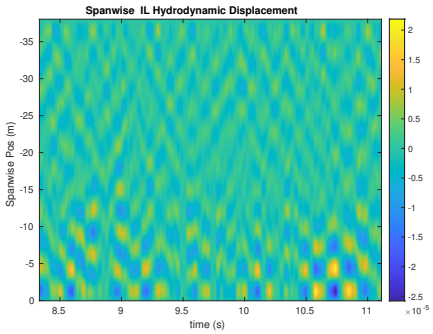

(d) Spanwise inline hydrodynamic displacement case 3360.

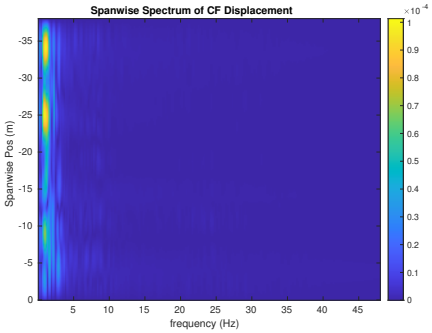

(e) Spanwise cross-flow spectrum of hydrodynamic displacement case 3360.

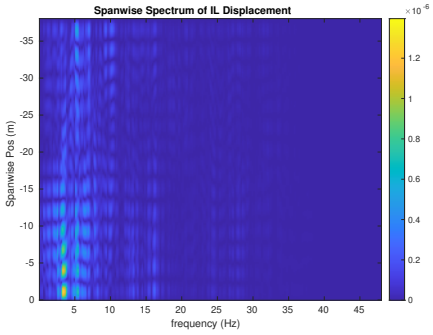

(f) Spanwise inline spectrum of hydrodynamic displacement case 3360.

Figure C-73: *Motion Analysis.* NDP Straight Riser ($L = 38m$) test case 3360.

NDP Straight Riser ($L = 38m$) test case 3380

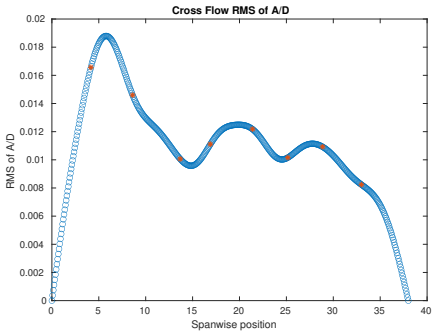

(a) Cross-flow RMS profile case 3380.

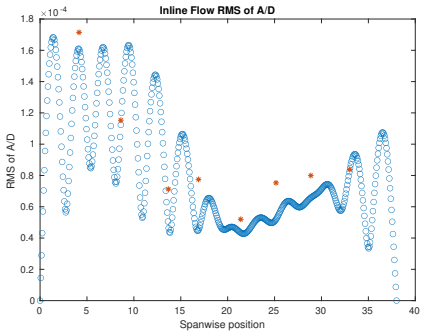

(b) Inline flow RMS profile case 3380.

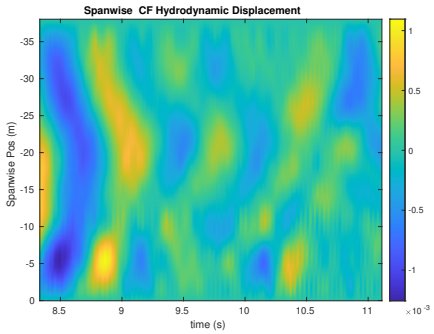

(c) Spanwise cross-flow hydrodynamic displacement case 3380.

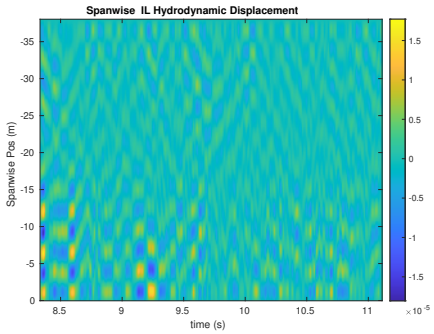

(d) Spanwise inline hydrodynamic displacement case 3380.

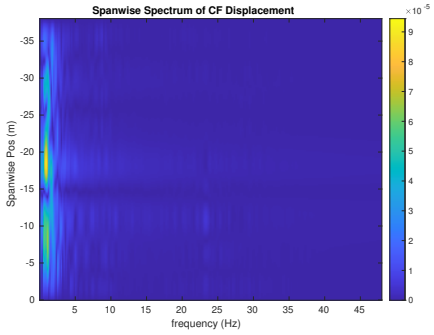

(e) Spanwise cross-flow spectrum of hydrodynamic displacement case 3380.

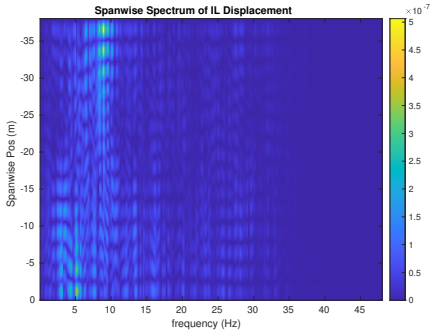

(f) Spanwise inline spectrum of hydrodynamic displacement case 3380.

Figure C-74: *Motion Analysis.* NDP Straight Riser ($L = 38m$) test case 3380.

NDP Straight Riser ($L = 38m$) test case 3400

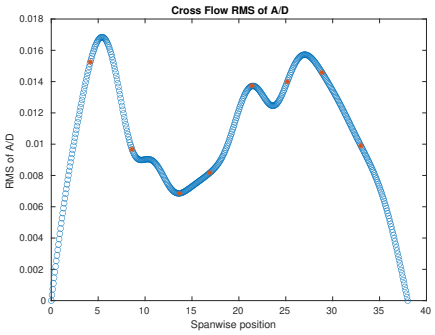

(a) Cross-flow RMS profile case 3400.

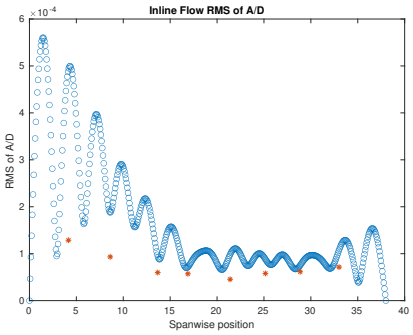

(b) Inline flow RMS profile case 3400.

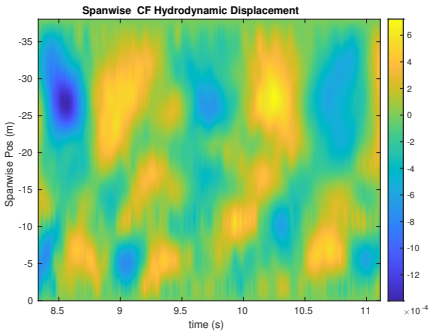

(c) Spanwise cross-flow hydrodynamic displacement case 3400.

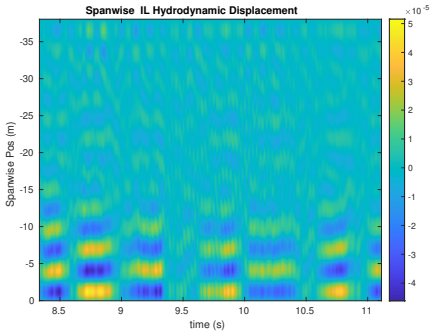

(d) Spanwise inline hydrodynamic displacement case 3400.

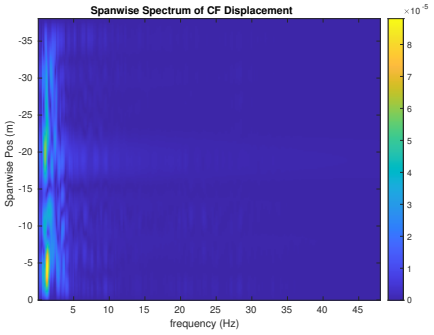

(e) Spanwise cross-flow spectrum of hydrodynamic displacement case 3400.

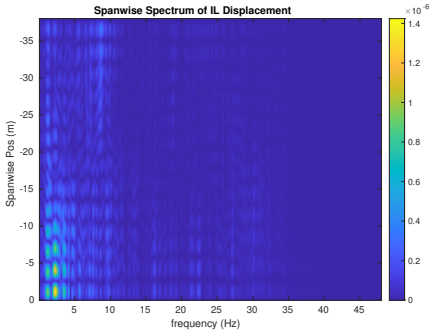

(f) Spanwise inline spectrum of hydrodynamic displacement case 3400.

Figure C-75: *Motion Analysis.* NDP Straight Riser ($L = 38m$) test case 3400.

NDP Straight Riser ($L = 38m$) test case 3420

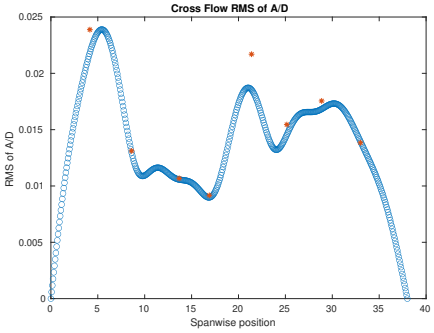

(a) Cross-flow RMS profile case 3420.

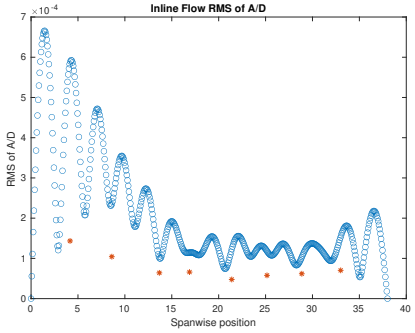

(b) Inline flow RMS profile case 3420.

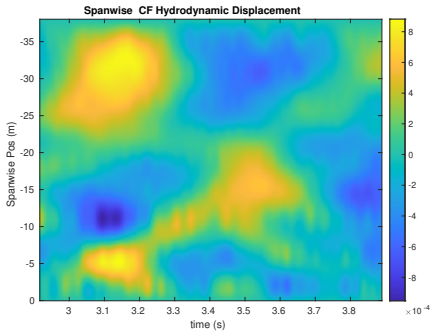

(c) Spanwise cross-flow hydrodynamic displacement case 3420.

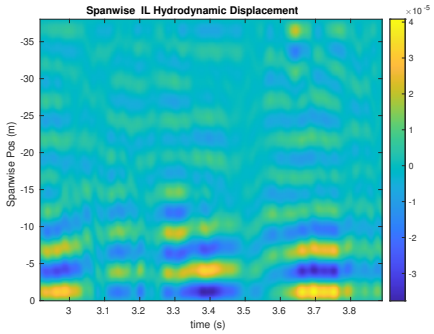

(d) Spanwise inline hydrodynamic displacement case 3420.

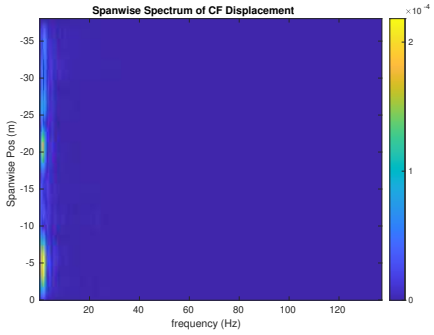

(e) Spanwise cross-flow spectrum of hydrodynamic displacement case 3420.

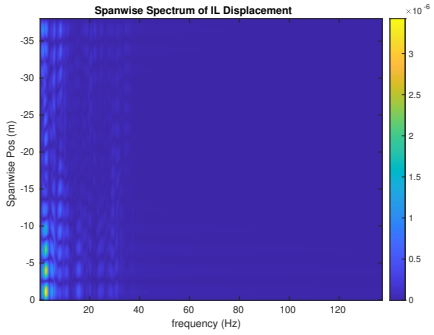

(f) Spanwise inline spectrum of hydrodynamic displacement case 3420.

Figure C-76: *Motion Analysis.* NDP Straight Riser ($L = 38m$) test case 3420.

NDP Straight Riser ($L = 38m$) test case 3440

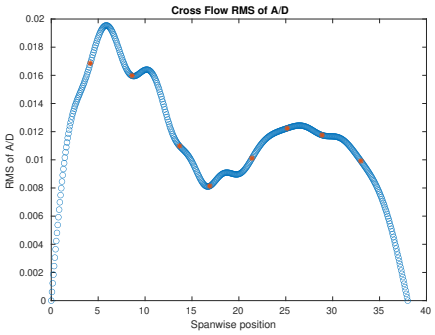

(a) Cross-flow RMS profile case 3440.

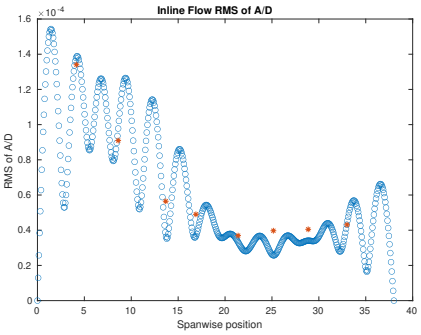

(b) Inline flow RMS profile case 3440.

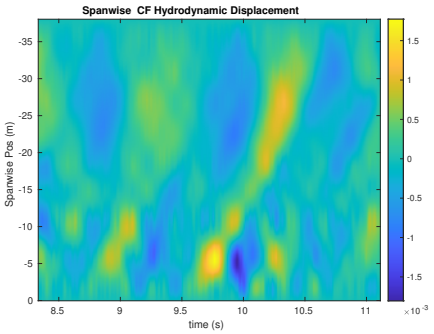

(c) Spanwise cross-flow hydrodynamic displacement case 3440.

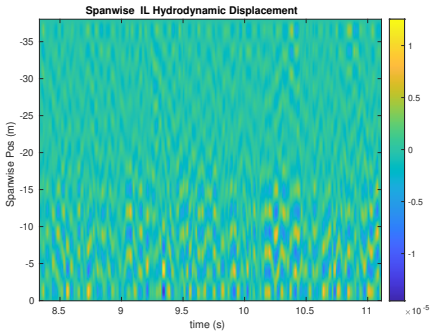

(d) Spanwise inline hydrodynamic displacement case 3440.

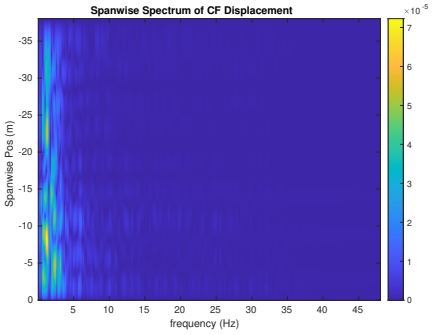

(e) Spanwise cross-flow spectrum of hydrodynamic displacement case 3440.

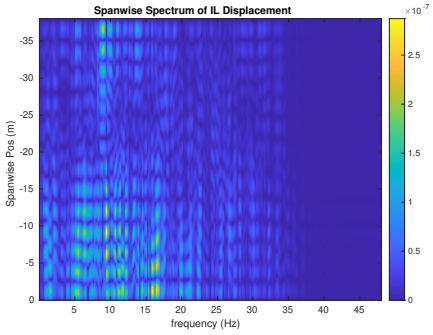

(f) Spanwise inline spectrum of hydrodynamic displacement case 3440.

Figure C-77: *Motion Analysis.* NDP Straight Riser ($L = 38m$) test case 3440.

NDP Straight Riser ($L = 38m$) test case 3460

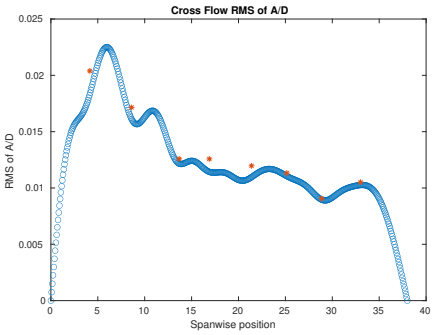

(a) Cross-flow RMS profile case 3460.

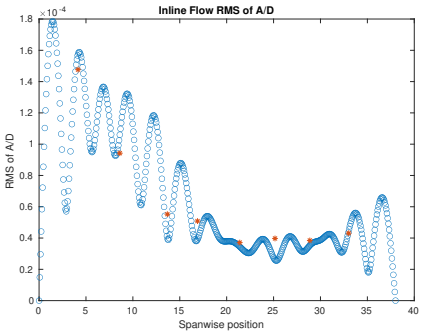

(b) Inline flow RMS profile case 3460.

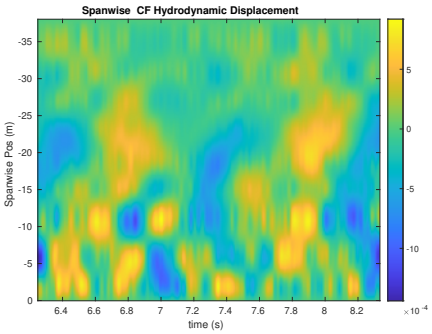

(c) Spanwise cross-flow hydrodynamic displacement case 3460.

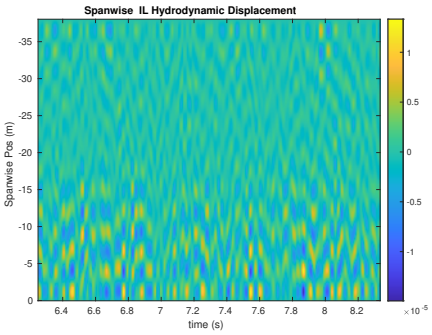

(d) Spanwise inline hydrodynamic displacement case 3460.

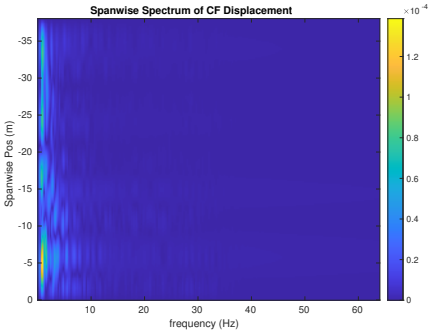

(e) Spanwise cross-flow spectrum of hydrodynamic displacement case 3460.

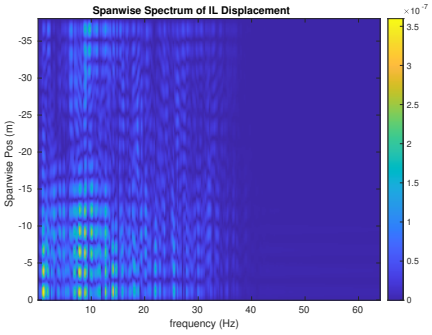

(f) Spanwise inline spectrum of hydrodynamic displacement case 3460.

Figure C-78: *Motion Analysis.* NDP Straight Riser ($L = 38m$) test case 3460.

NDP Straight Riser ($L = 38m$) test case 3481

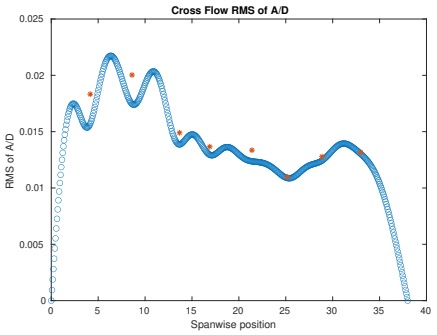

(a) Cross-flow RMS profile case 3481.

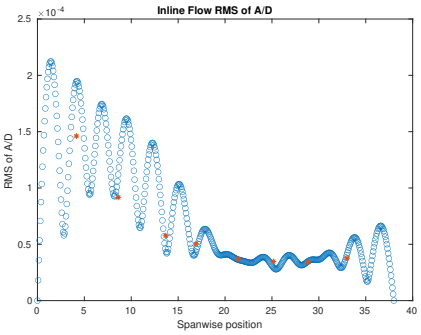

(b) Inline flow RMS profile case 3481.

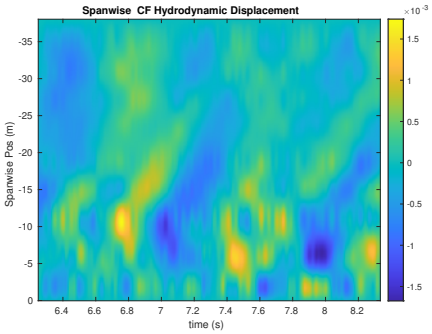

(c) Spanwise cross-flow hydrodynamic displacement case 3481.

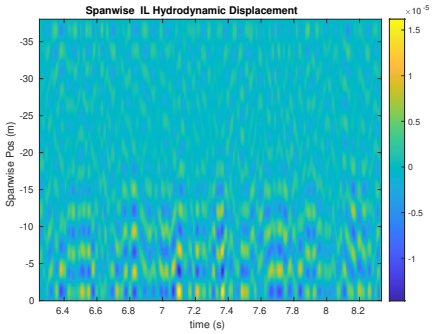

(d) Spanwise inline hydrodynamic displacement case 3481.

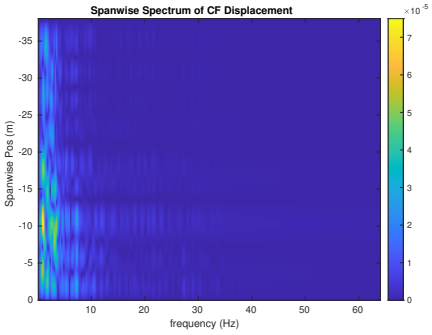

(e) Spanwise cross-flow spectrum of hydrodynamic displacement case 3481.

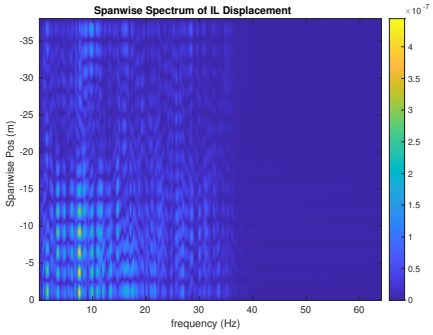

(f) Spanwise inline spectrum of hydrodynamic displacement case 3481.

Figure C-79: *Motion Analysis.* NDP Straight Riser ($L = 38m$) test case 3481.

NDP Straight Riser ($L = 38m$) test case 3500

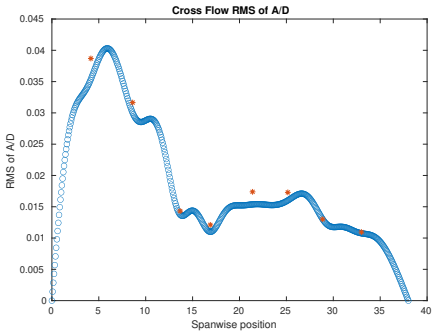

(a) Cross-flow RMS profile case 3500.

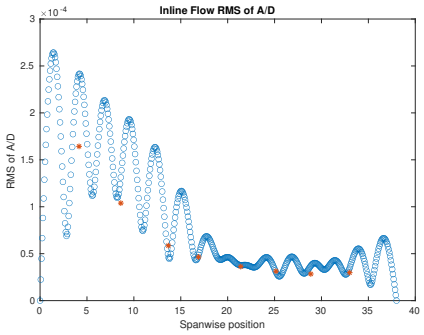

(b) Inline flow RMS profile case 3500.

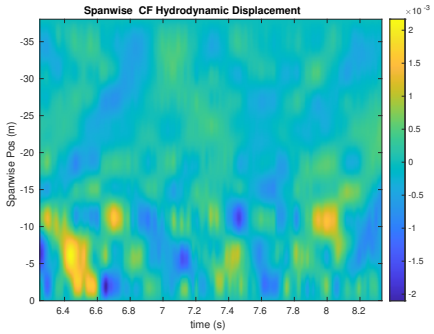

(c) Spanwise cross-flow hydrodynamic displacement case 3500.

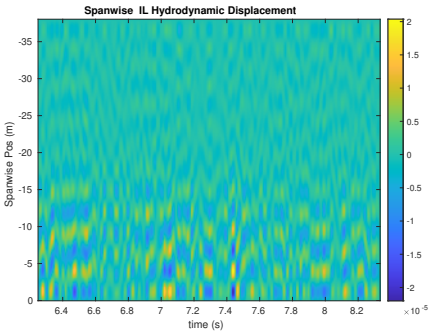

(d) Spanwise inline hydrodynamic displacement case 3500.

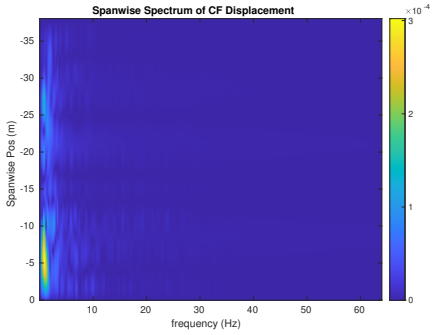

(e) Spanwise cross-flow spectrum of hydrodynamic displacement case 3500.

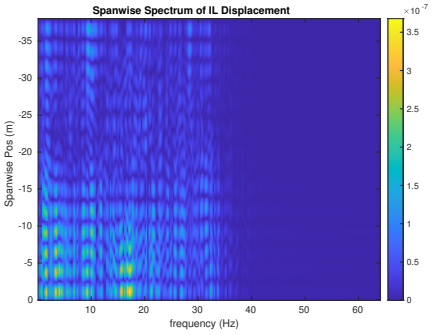

(f) Spanwise inline spectrum of hydrodynamic displacement case 3500.

Figure C-80: *Motion Analysis.* NDP Straight Riser ($L = 38m$) test case 3500.

NDP Straight Riser ($L = 38m$) test case 3520

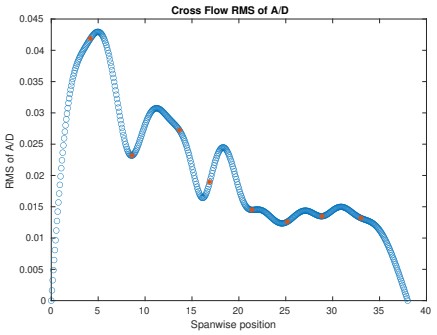

(a) Cross-flow RMS profile case 3520.

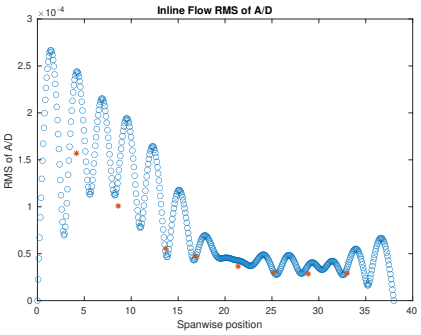

(b) Inline flow RMS profile case 3520.

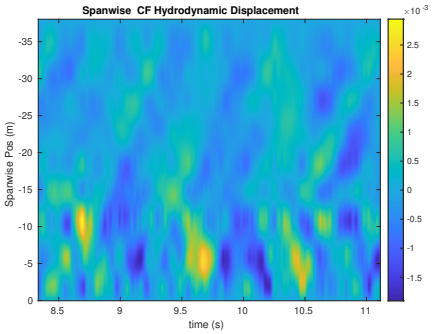

(c) Spanwise cross-flow hydrodynamic displacement case 3520.

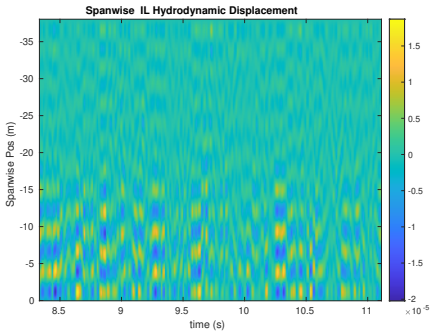

(d) Spanwise inline hydrodynamic displacement case 3520.

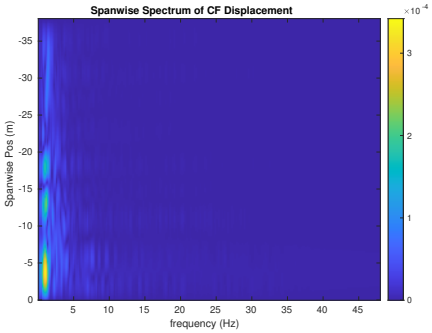

(e) Spanwise cross-flow spectrum of hydrodynamic displacement case 3520.

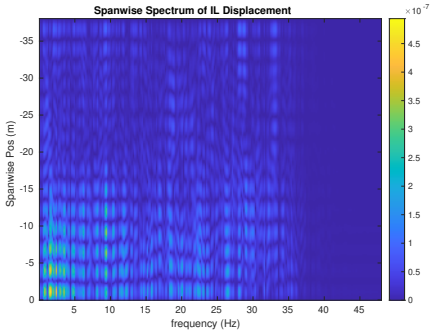

(f) Spanwise inline spectrum of hydrodynamic displacement case 3520.

Figure C-81: *Motion Analysis.* NDP Straight Riser ($L = 38m$) test case 3520.

NDP Straight Riser ($L = 38m$) test case 3530

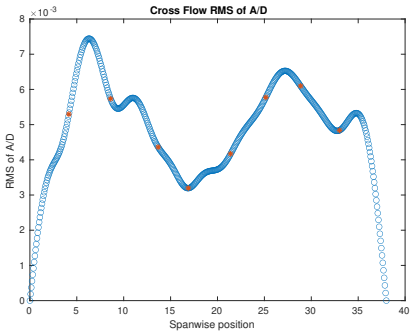

(a) Cross-flow RMS profile case 3530.

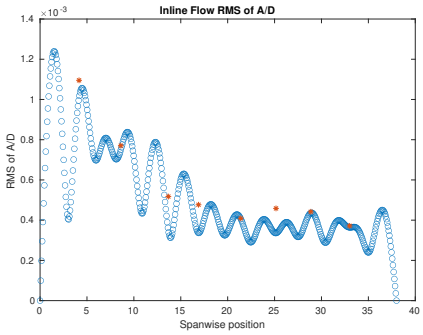

(b) Inline flow RMS profile case 3530.

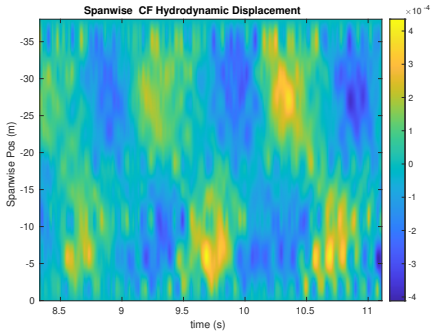

(c) Spanwise cross-flow hydrodynamic displacement case 3530.

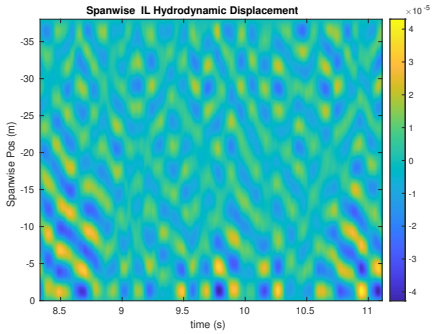

(d) Spanwise inline hydrodynamic displacement case 3530.

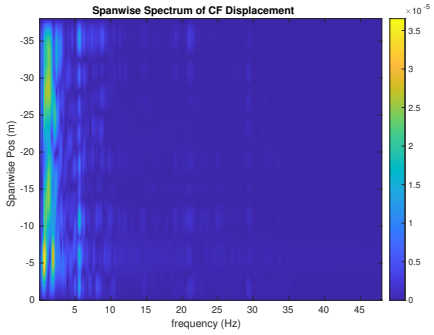

(e) Spanwise cross-flow spectrum of hydrodynamic displacement case 3530.

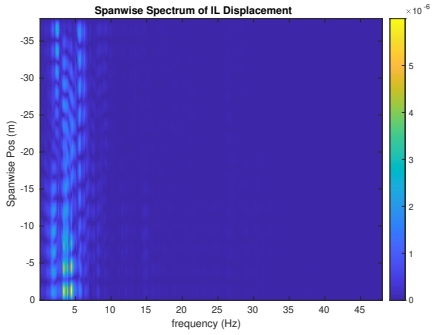

(f) Spanwise inline spectrum of hydrodynamic displacement case 3530.

Figure C-82: *Motion Analysis.* NDP Straight Riser ($L = 38m$) test case 3530.

NDP Straight Riser ($L = 38m$) test case 3540

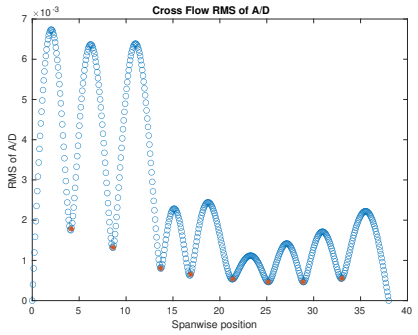

(a) Cross-flow RMS profile case 3540.

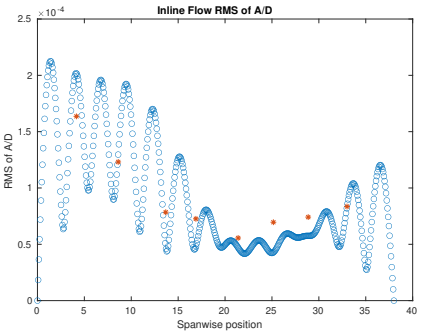

(b) Inline flow RMS profile case 3540.

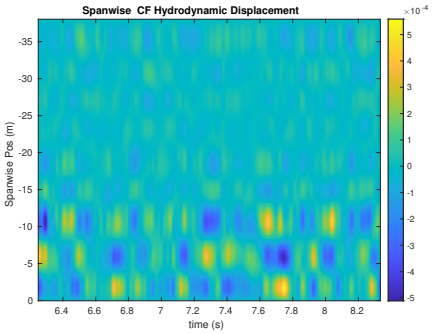

(c) Spanwise cross-flow hydrodynamic displacement case 3540.

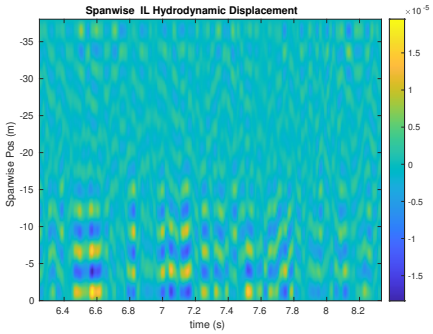

(d) Spanwise inline hydrodynamic displacement case 3540.

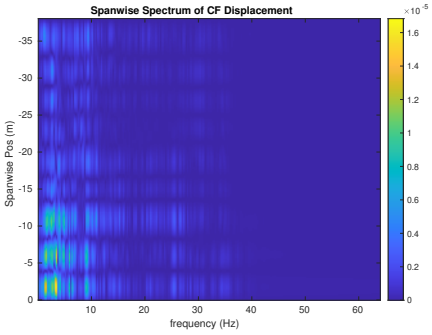

(e) Spanwise cross-flow spectrum of hydrodynamic displacement case 3540.

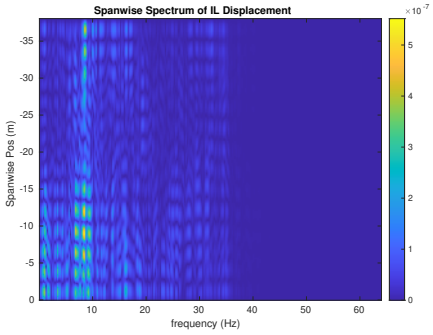

(f) Spanwise inline spectrum of hydrodynamic displacement case 3540.

Figure C-83: *Motion Analysis.* NDP Straight Riser ($L = 38m$) test case 3540.

NDP Straight Riser ($L = 38m$) test case 3610

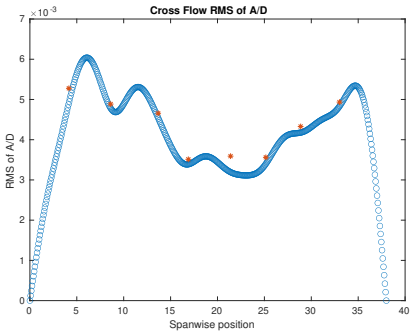

(a) Cross-flow RMS profile case 3610.

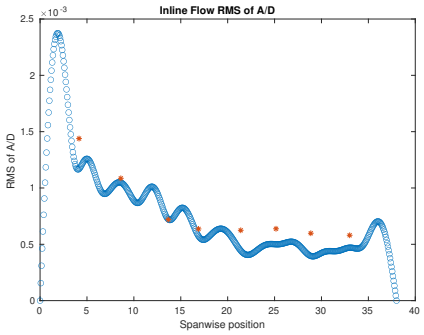

(b) Inline flow RMS profile case 3610.

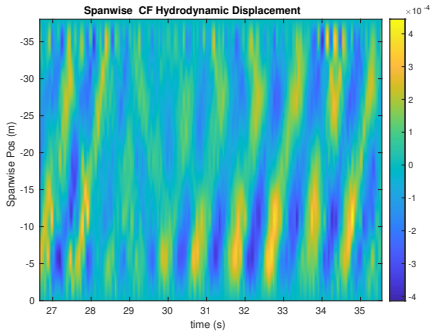

(c) Spanwise cross-flow hydrodynamic displacement case 3610.

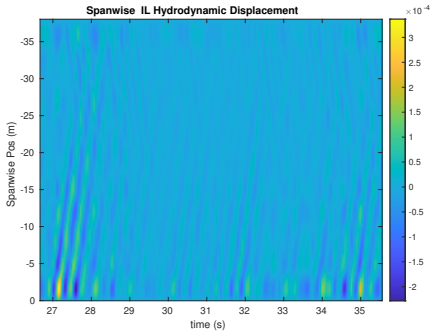

(d) Spanwise inline hydrodynamic displacement case 3610.

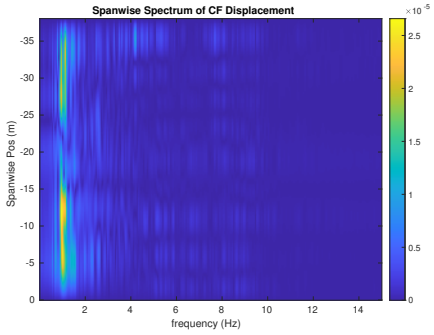

(e) Spanwise cross-flow spectrum of hydrodynamic displacement case 3610.

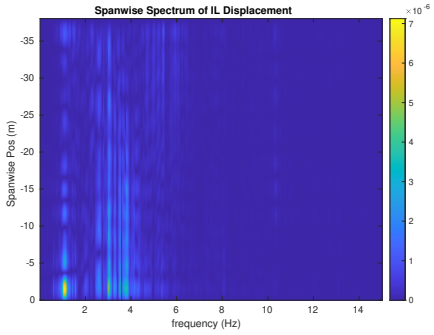

(f) Spanwise inline spectrum of hydrodynamic displacement case 3610.

Figure C-84: *Motion Analysis.* NDP Straight Riser ($L = 38m$) test case 3610.

NDP Straight Riser ($L = 38m$) test case 3620

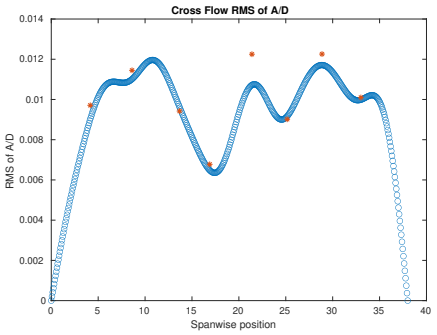

(a) Cross-flow RMS profile case 3620.

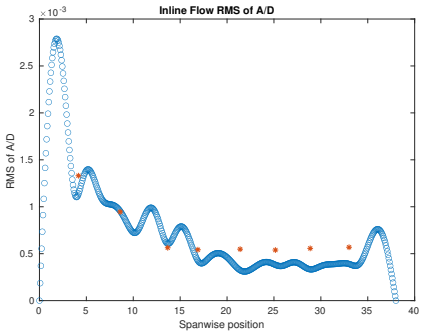

(b) Inline flow RMS profile case 3620.

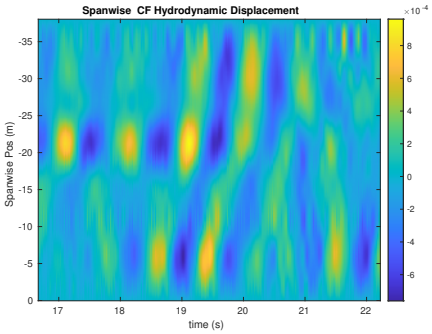

(c) Spanwise cross-flow hydrodynamic displacement case 3620.

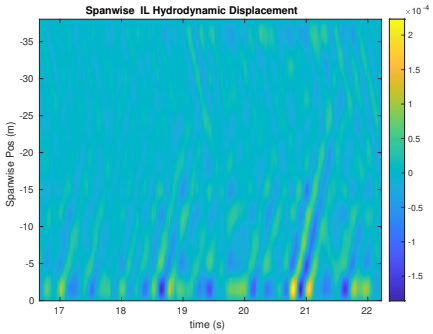

(d) Spanwise inline hydrodynamic displacement case 3620.

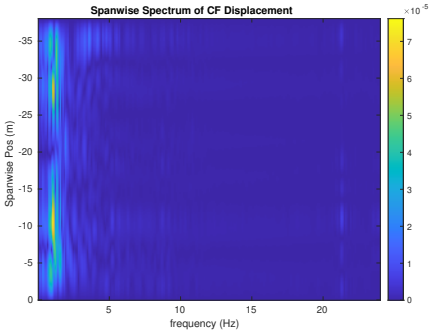

(e) Spanwise cross-flow spectrum of hydrodynamic displacement case 3620.

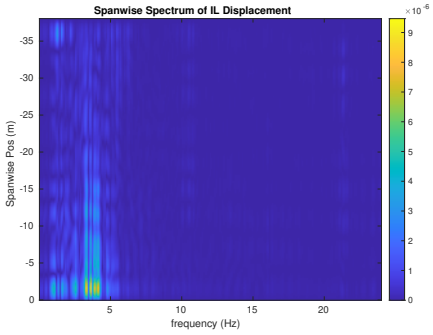

(f) Spanwise inline spectrum of hydrodynamic displacement case 3620.

Figure C-85: *Motion Analysis.* NDP Straight Riser ($L = 38m$) test case 3620.

NDP Straight Riser ($L = 38m$) test case 3630

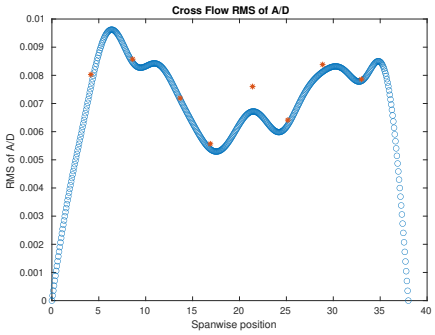

(a) Cross-flow RMS profile case 3630.

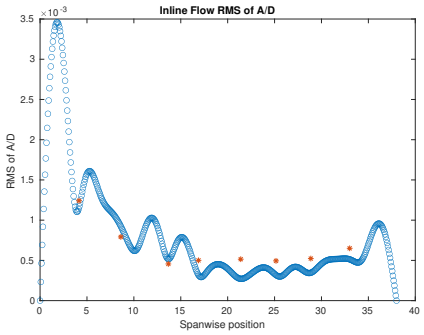

(b) Inline flow RMS profile case 3630.

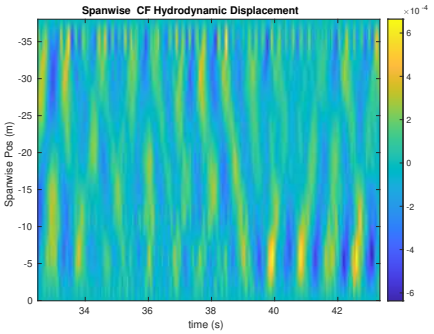

(c) Spanwise cross-flow hydrodynamic displacement case 3630.

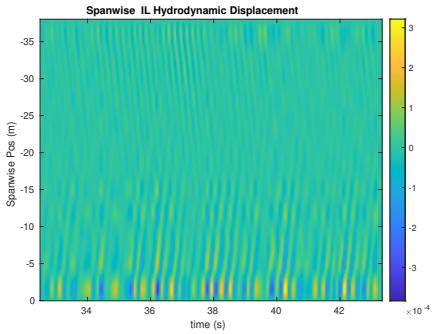

(d) Spanwise inline hydrodynamic displacement case 3630.

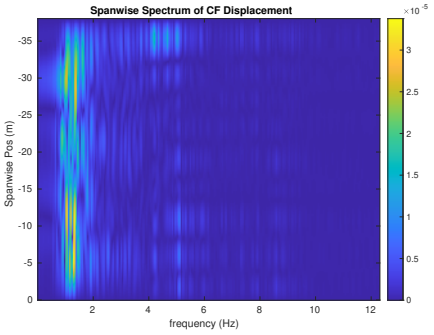

(e) Spanwise cross-flow spectrum of hydrodynamic displacement case 3630.

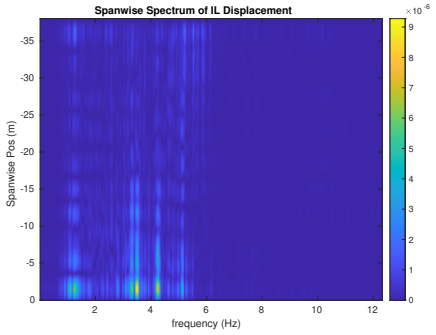

(f) Spanwise inline spectrum of hydrodynamic displacement case 3630.

Figure C-86: *Motion Analysis.* NDP Straight Riser ($L = 38m$) test case 3630.

NDP Straight Riser ($L = 38m$) test case 3640

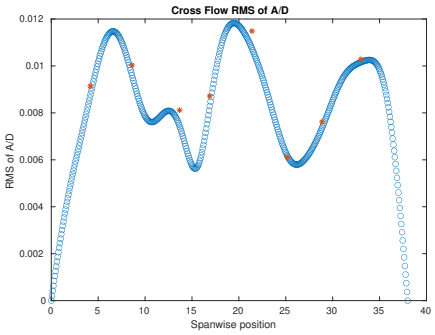

(a) Cross-flow RMS profile case 3640.

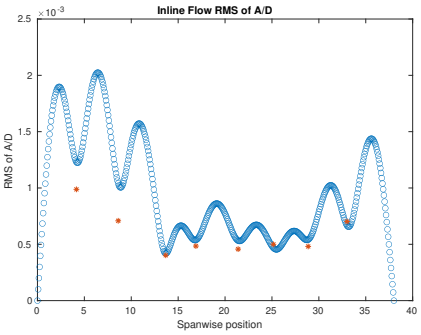

(b) Inline flow RMS profile case 3640.

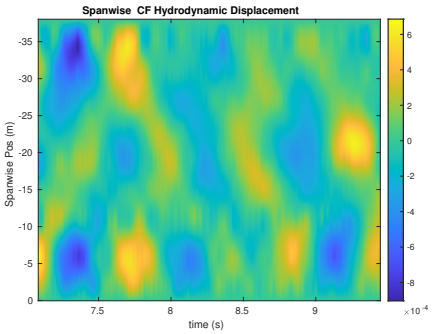

(c) Spanwise cross-flow hydrodynamic displacement case 3640.

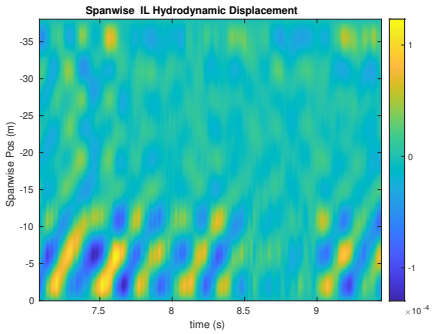

(d) Spanwise inline hydrodynamic displacement case 3640.

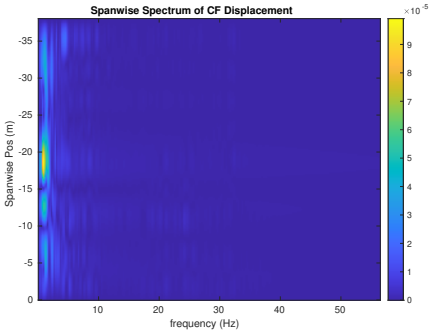

(e) Spanwise cross-flow spectrum of hydrodynamic displacement case 3640.

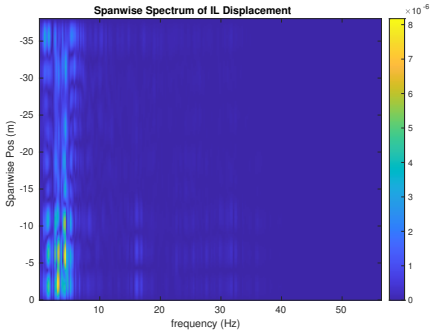

(f) Spanwise inline spectrum of hydrodynamic displacement case 3640.

Figure C-87: *Motion Analysis.* NDP Straight Riser ($L = 38m$) test case 3640.

NDP Straight Riser ($L = 38m$) test case 3650

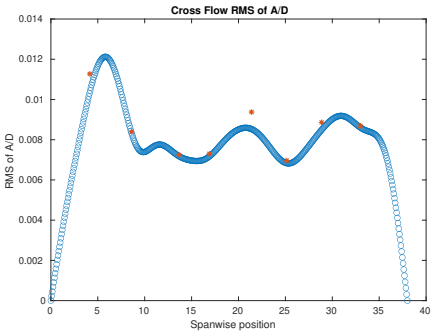

(a) Cross-flow RMS profile case 3650.

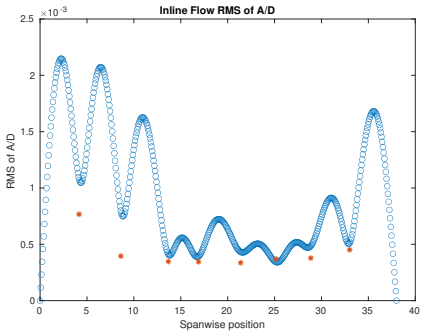

(b) Inline flow RMS profile case 3650.

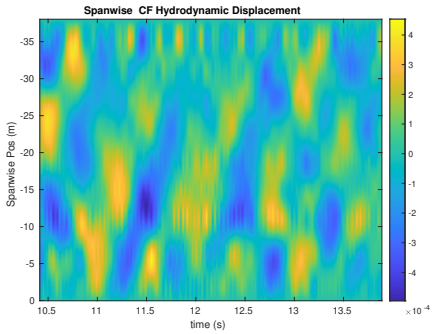

(c) Spanwise cross-flow hydrodynamic displacement case 3650.

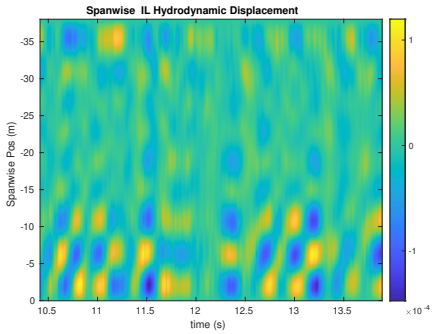

(d) Spanwise inline hydrodynamic displacement case 3650.

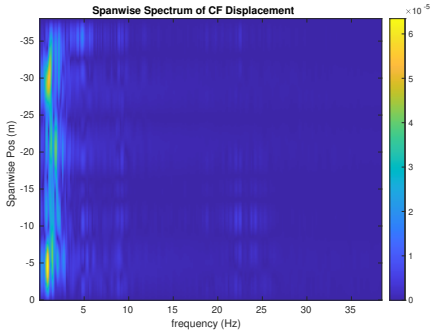

(e) Spanwise cross-flow spectrum of hydrodynamic displacement case 3650.

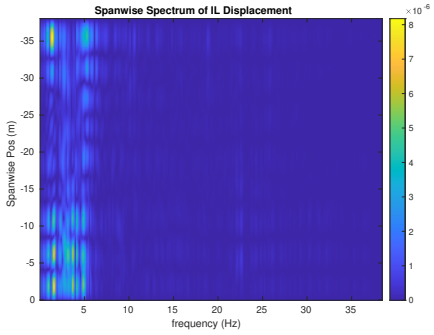

(f) Spanwise inline spectrum of hydrodynamic displacement case 3650.

Figure C-88: *Motion Analysis.* NDP Straight Riser ($L = 38m$) test case 3650.

NDP Straight Riser ($L = 38m$) test case 3660

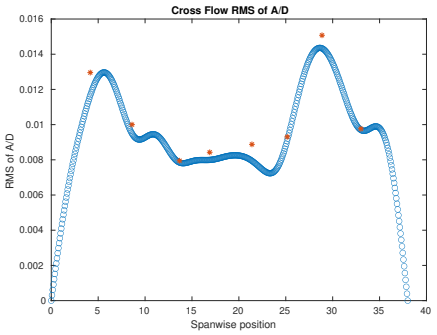

(a) Cross-flow RMS profile case 3660.

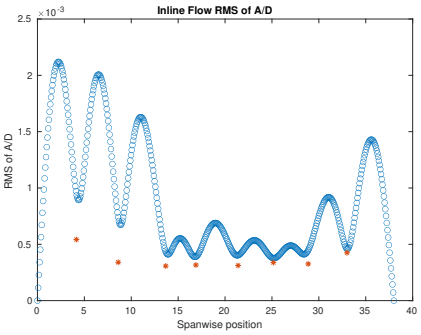

(b) Inline flow RMS profile case 3660.

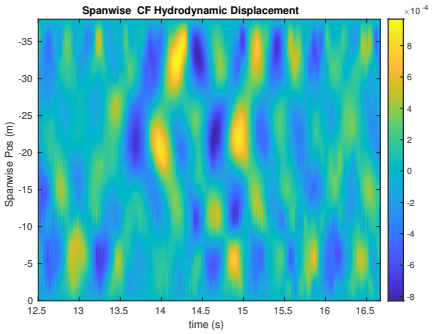

(c) Spanwise cross-flow hydrodynamic displacement case 3660.

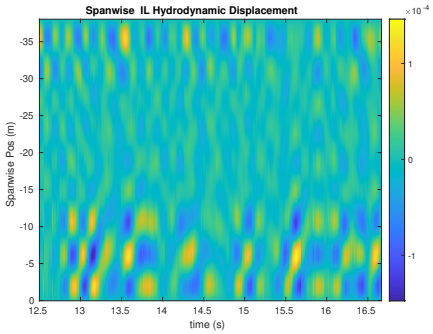

(d) Spanwise inline hydrodynamic displacement case 3660.

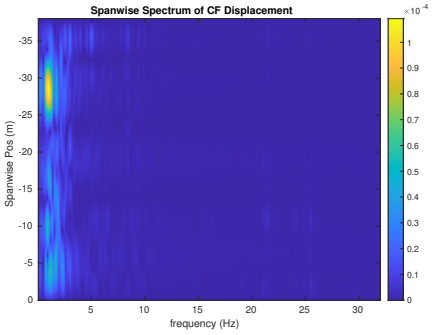

(e) Spanwise cross-flow spectrum of hydrodynamic displacement case 3660.

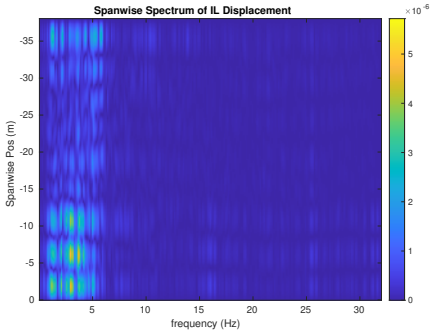

(f) Spanwise inline spectrum of hydrodynamic displacement case 3660.

Figure C-89: *Motion Analysis.* NDP Straight Riser ($L = 38m$) test case 3660.

NDP Straight Riser ($L = 38m$) test case 3670

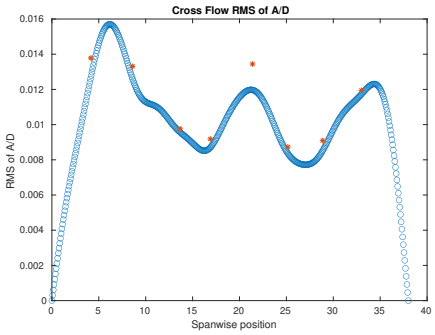

(a) Cross-flow RMS profile case 3670.

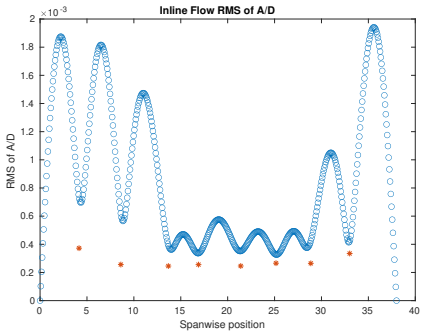

(b) Inline flow RMS profile case 3670.

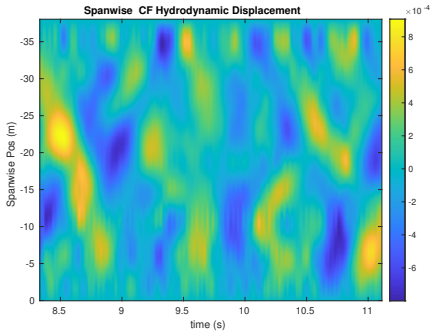

(c) Spanwise cross-flow hydrodynamic displacement case 3670.

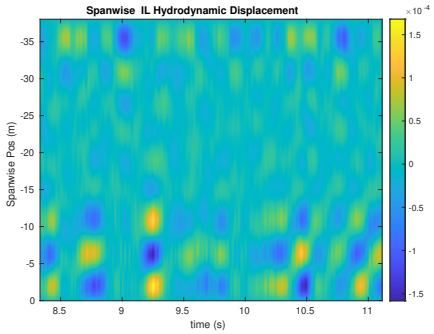

(d) Spanwise inline hydrodynamic displacement case 3670.

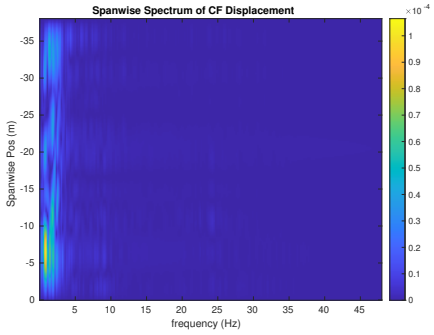

(e) Spanwise cross-flow spectrum of hydrodynamic displacement case 3670.

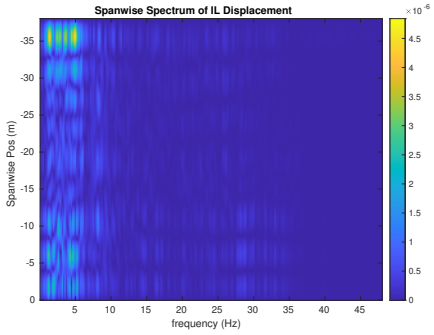

(f) Spanwise inline spectrum of hydrodynamic displacement case 3670.

Figure C-90: *Motion Analysis.* NDP Straight Riser ($L = 38m$) test case 3670.

NDP Straight Riser ($L = 38m$) test case 3680

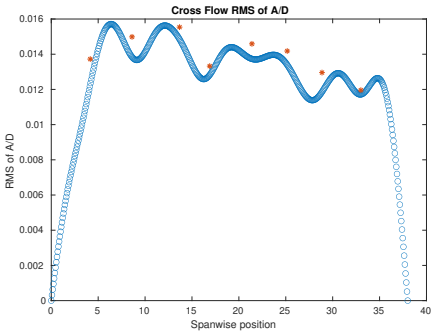

(a) Cross-flow RMS profile case 3680.

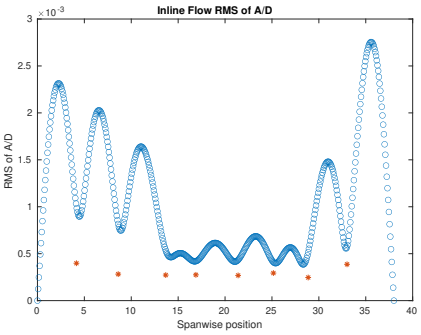

(b) Inline flow RMS profile case 3680.

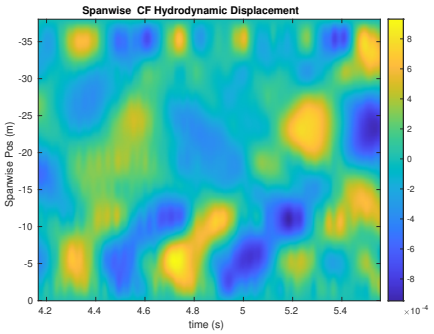

(c) Spanwise cross-flow hydrodynamic displacement case 3680.

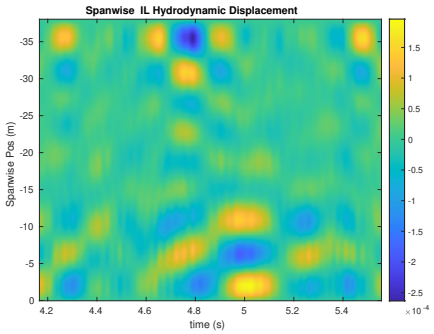

(d) Spanwise inline hydrodynamic displacement case 3680.

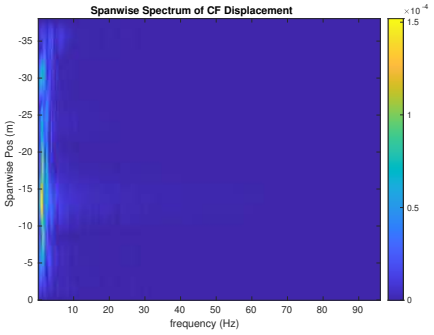

(e) Spanwise cross-flow spectrum of hydrodynamic displacement case 3680.

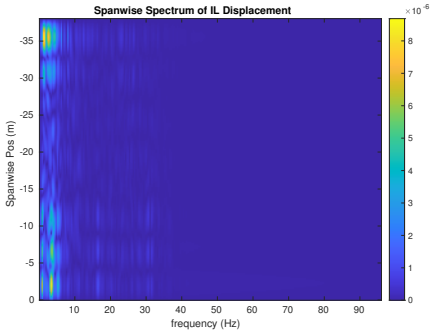

(f) Spanwise inline spectrum of hydrodynamic displacement case 3680.

Figure C-91: *Motion Analysis.* NDP Straight Riser ($L = 38m$) test case 3680.

NDP Straight Riser ($L = 38m$) test case 3690

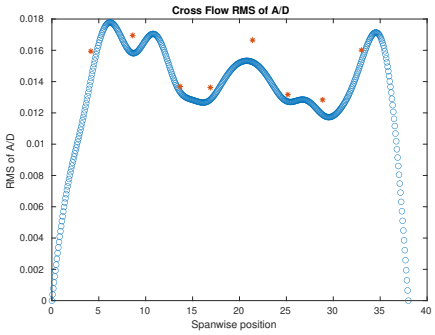

(a) Cross-flow RMS profile case 3690.

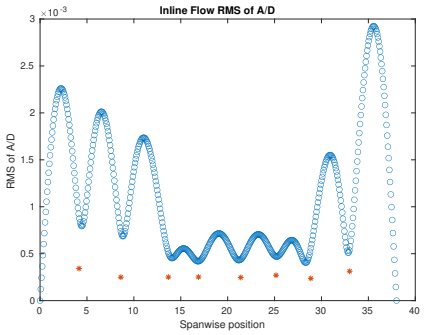

(b) Inline flow RMS profile case 3690.

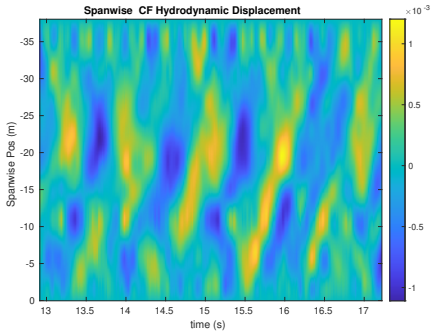

(c) Spanwise cross-flow hydrodynamic displacement case 3690.

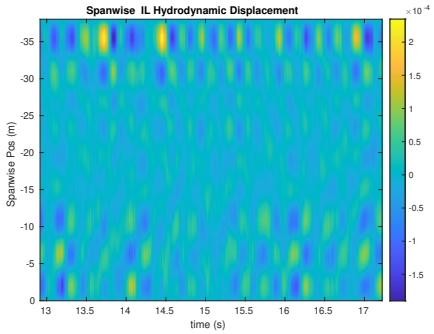

(d) Spanwise inline hydrodynamic displacement case 3690.

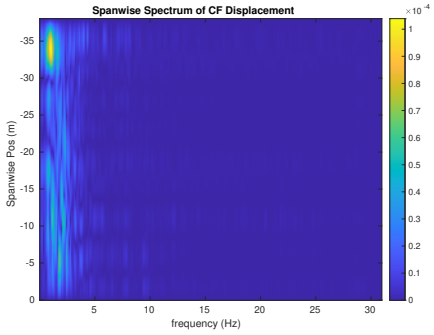

(e) Spanwise cross-flow spectrum of hydrodynamic displacement case 3690.

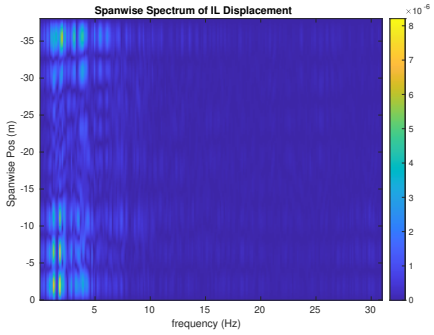

(f) Spanwise inline spectrum of hydrodynamic displacement case 3690.

Figure C-92: *Motion Analysis.* NDP Straight Riser ($L = 38m$) test case 3690.

NDP Straight Riser ($L = 38m$) test case 3700

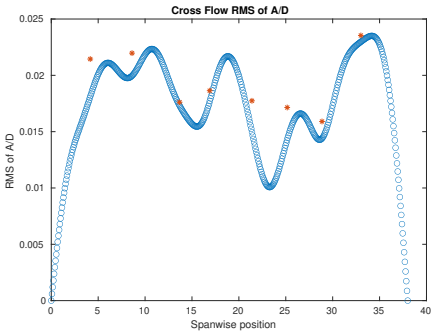

(a) Cross-flow RMS profile case 3700.

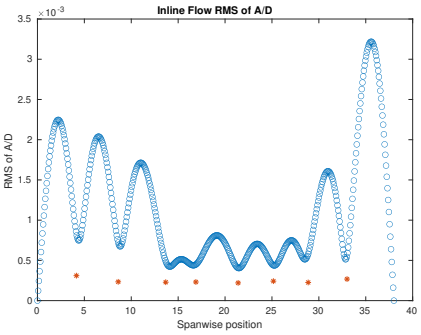

(b) Inline flow RMS profile case 3700.

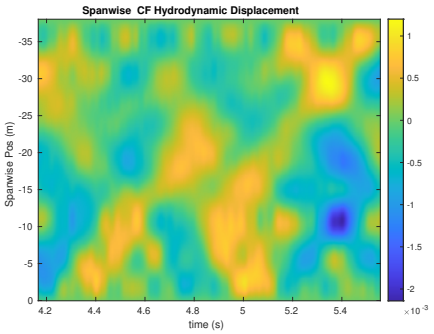

(c) Spanwise cross-flow hydrodynamic displacement case 3700.

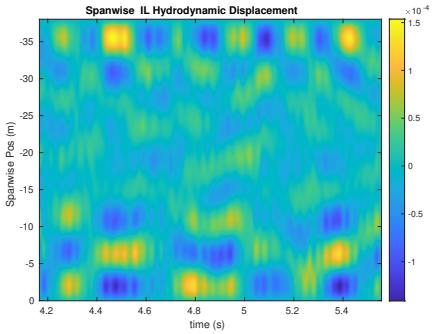

(d) Spanwise inline hydrodynamic displacement case 3700.

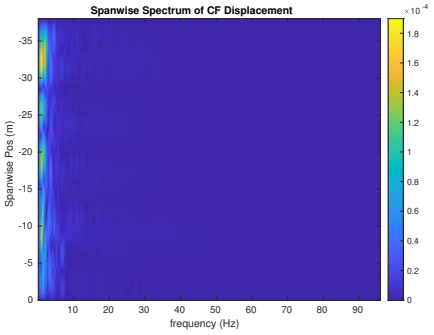

(e) Spanwise cross-flow spectrum of hydrodynamic displacement case 3700.

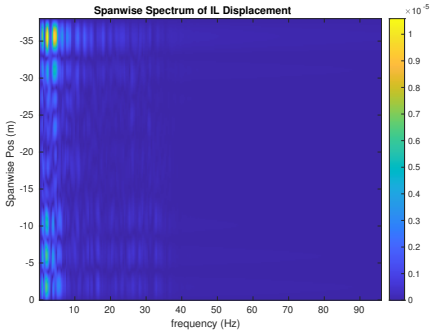

(f) Spanwise inline spectrum of hydrodynamic displacement case 3700.

Figure C-93: *Motion Analysis.* NDP Straight Riser ($L = 38m$) test case 3700.

NDP Straight Riser ($L = 38m$) test case 3710

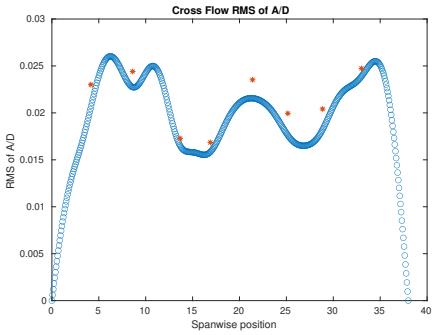

(a) Cross-flow RMS profile case 3710.

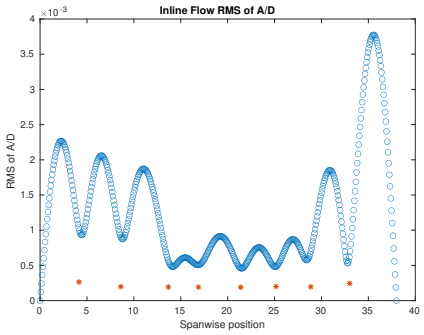

(b) Inline flow RMS profile case 3710.

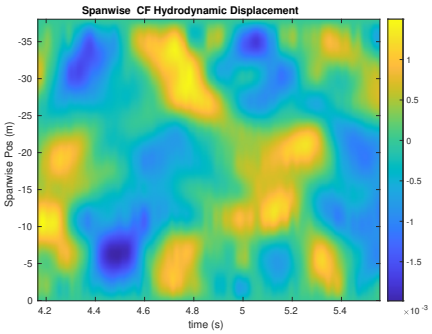

(c) Spanwise cross-flow hydrodynamic displacement case 3710.

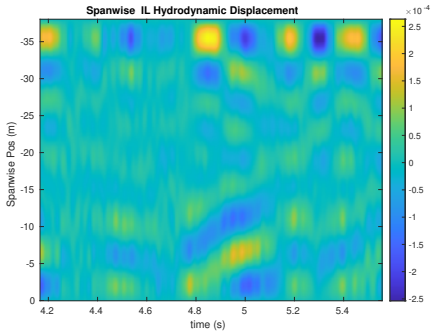

(d) Spanwise inline hydrodynamic displacement case 3710.

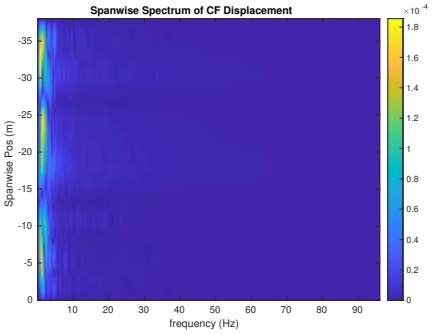

(e) Spanwise cross-flow spectrum of hydrodynamic displacement case 3710.

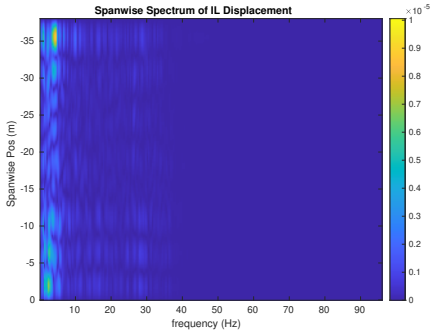

(f) Spanwise inline spectrum of hydrodynamic displacement case 3710.

Figure C-94: *Motion Analysis.* NDP Straight Riser ($L = 38m$) test case 3710.

NDP Straight Riser ($L = 38m$) test case 3720

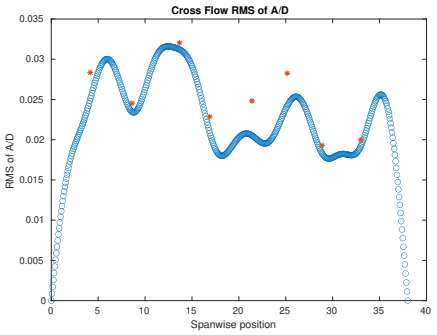

(a) Cross-flow RMS profile case 3720.

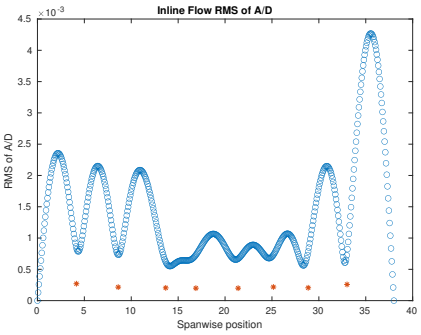

(b) Inline flow RMS profile case 3720.

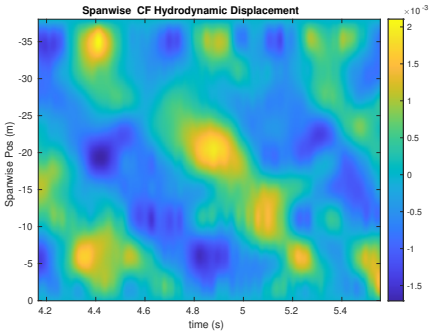

(c) Spanwise cross-flow hydrodynamic displacement case 3720.

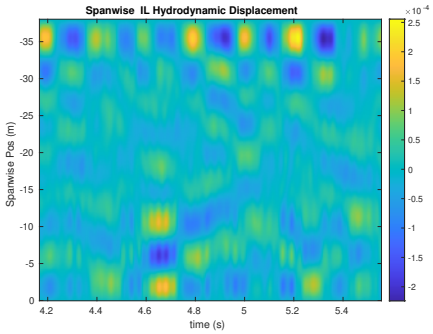

(d) Spanwise inline hydrodynamic displacement case 3720.

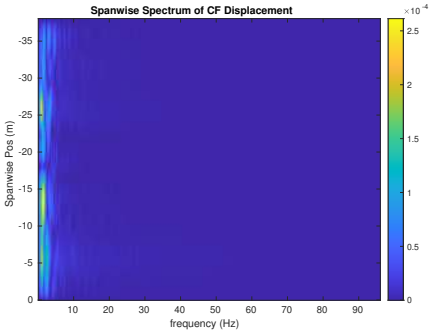

(e) Spanwise cross-flow spectrum of hydrodynamic displacement case 3720.

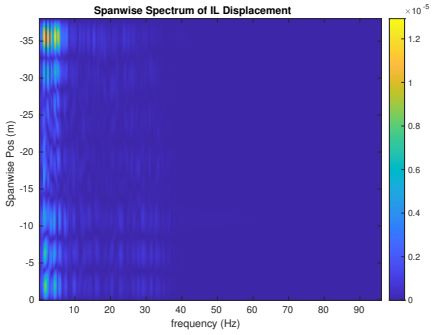

(f) Spanwise inline spectrum of hydrodynamic displacement case 3720.

Figure C-95: *Motion Analysis.* NDP Straight Riser ($L = 38m$) test case 3720.

NDP Straight Riser ($L = 38m$) test case 3730

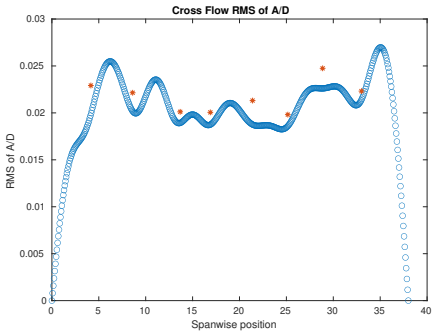

(a) Cross-flow RMS profile case 3730.

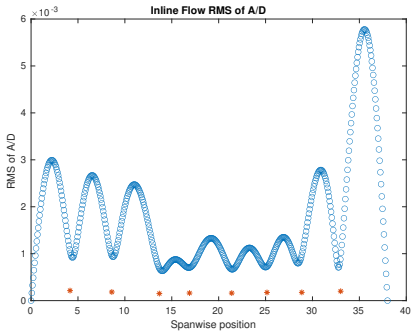

(b) Inline flow RMS profile case 3730.

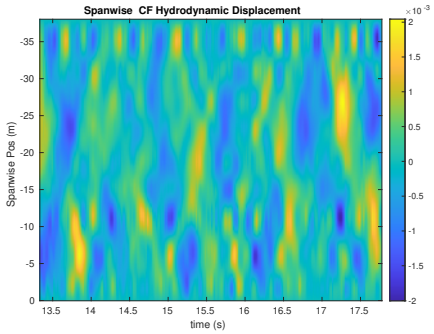

(c) Spanwise cross-flow hydrodynamic displacement case 3730.

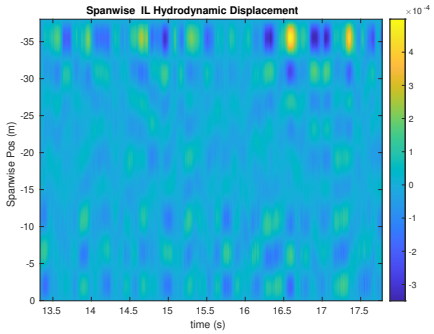

(d) Spanwise inline hydrodynamic displacement case 3730.

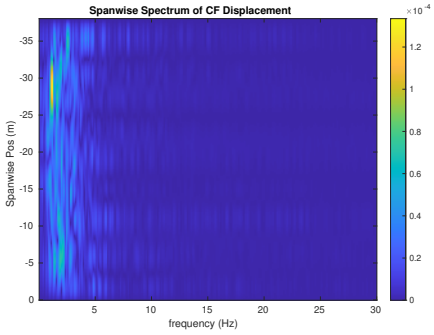

(e) Spanwise cross-flow spectrum of hydrodynamic displacement case 3730.

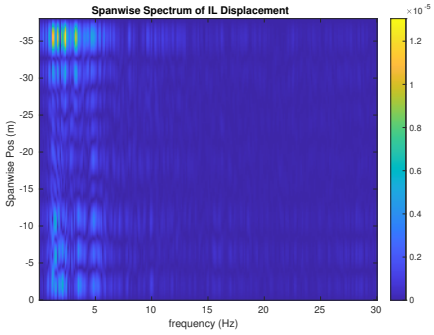

(f) Spanwise inline spectrum of hydrodynamic displacement case 3730.

Figure C-96: *Motion Analysis.* NDP Straight Riser ($L = 38m$) test case 3730.

NDP Straight Riser ($L = 38m$) test case 3740

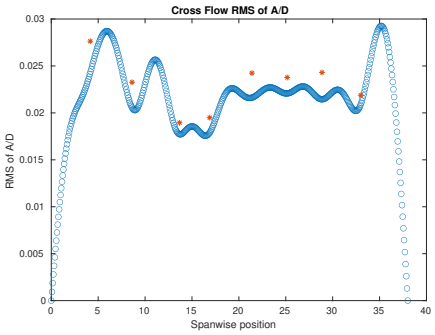

(a) Cross-flow RMS profile case 3740.

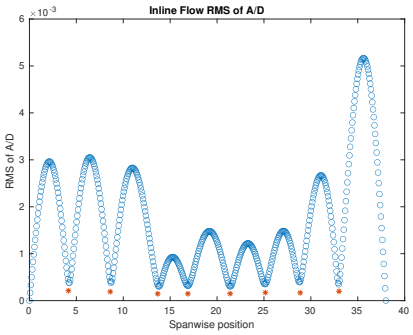

(b) Inline flow RMS profile case 3740.

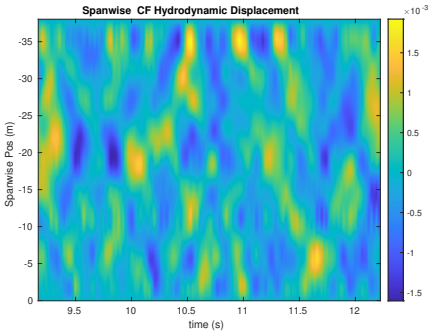

(c) Spanwise cross-flow hydrodynamic displacement case 3740.

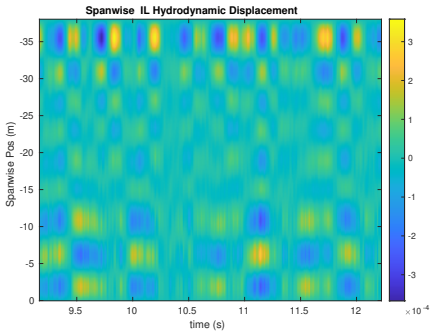

(d) Spanwise inline hydrodynamic displacement case 3740.

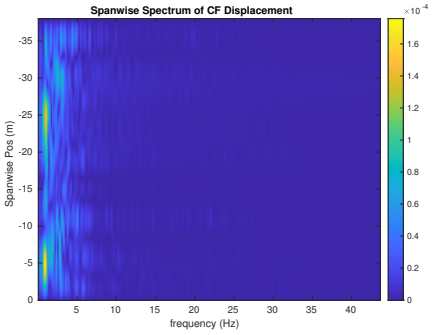

(e) Spanwise cross-flow spectrum of hydrodynamic displacement case 3740.

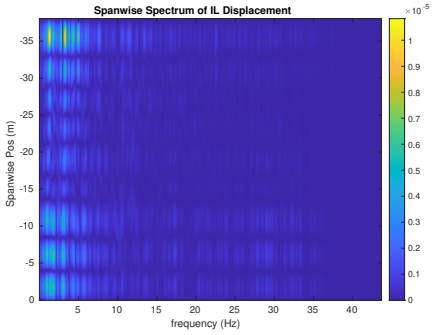

(f) Spanwise inline spectrum of hydrodynamic displacement case 3740.

Figure C-97: *Motion Analysis.* NDP Straight Riser ($L = 38m$) test case 3740.

NDP Straight Riser ($L = 38m$) test case 3750

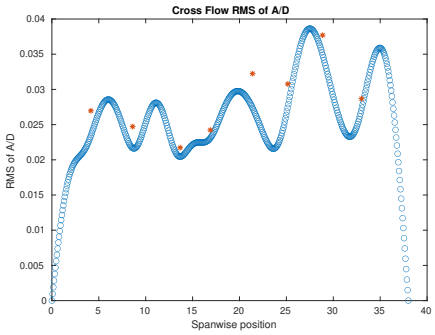

(a) Cross-flow RMS profile case 3750.

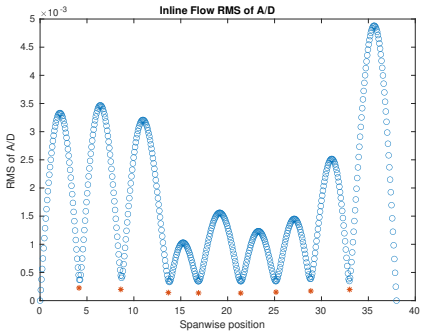

(b) Inline flow RMS profile case 3750.

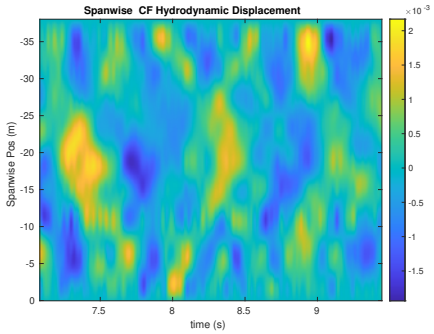

(c) Spanwise cross-flow hydrodynamic displacement case 3750.

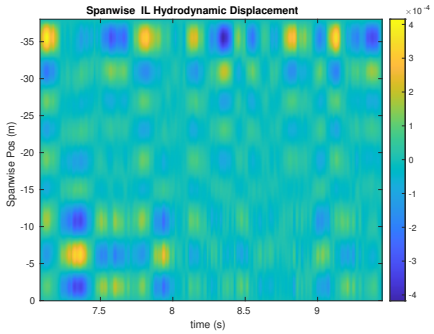

(d) Spanwise inline hydrodynamic displacement case 3750.

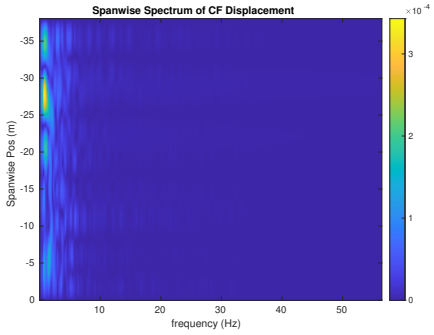

(e) Spanwise cross-flow spectrum of hydrodynamic displacement case 3750.

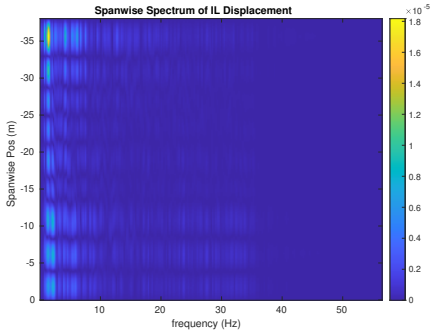

(f) Spanwise inline spectrum of hydrodynamic displacement case 3750.

Figure C-98: *Motion Analysis.* NDP Straight Riser ($L = 38m$) test case 3750.

NDP Straight Riser ($L = 38m$) test case 3760

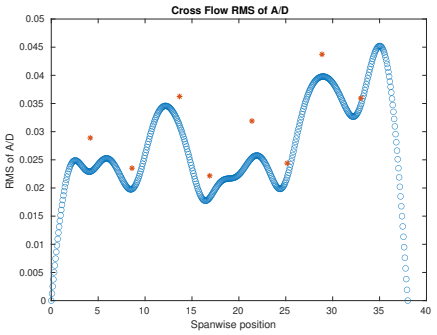

(a) Cross-flow RMS profile case 3760.

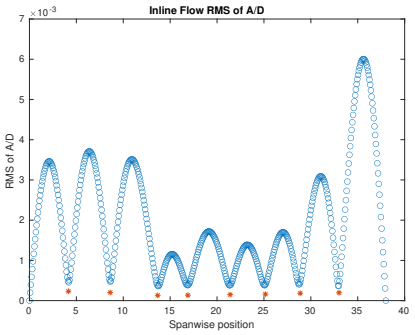

(b) Inline flow RMS profile case 3760.

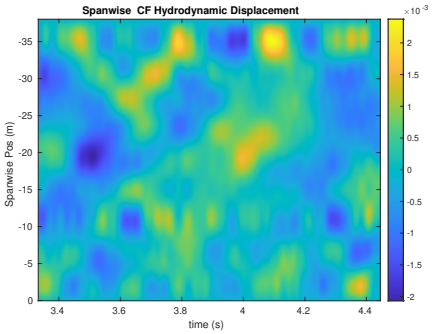

(c) Spanwise cross-flow hydrodynamic displacement case 3760.

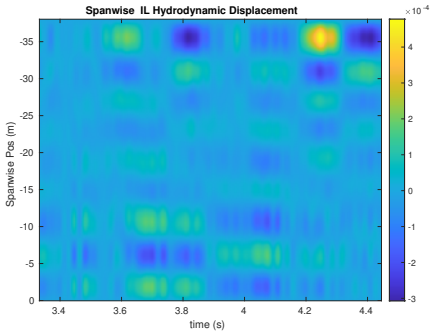

(d) Spanwise inline hydrodynamic displacement case 3760.

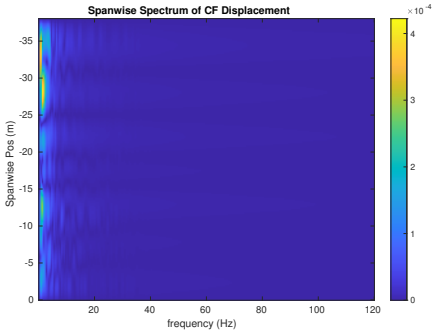

(e) Spanwise cross-flow spectrum of hydrodynamic displacement case 3760.

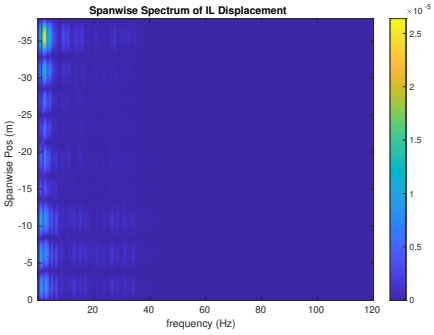

(f) Spanwise inline spectrum of hydrodynamic displacement case 3760.

Figure C-99: *Motion Analysis.* NDP Straight Riser ($L = 38m$) test case 3760.

NDP Straight Riser ($L = 38m$) test case 3770

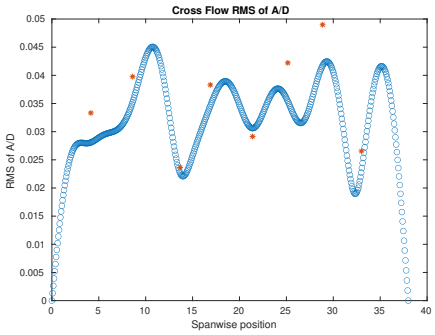

(a) Cross-flow RMS profile case 3770.

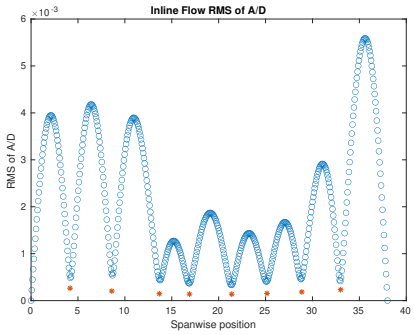

(b) Inline flow RMS profile case 3770.

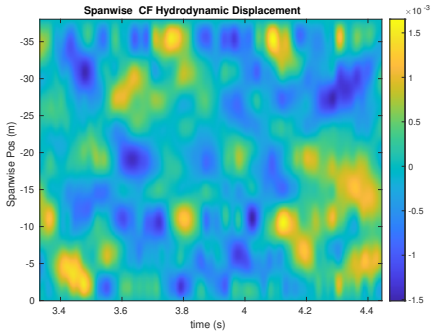

(c) Spanwise cross-flow hydrodynamic displacement case 3770.

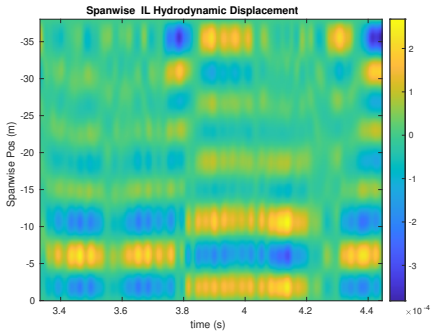

(d) Spanwise inline hydrodynamic displacement case 3770.

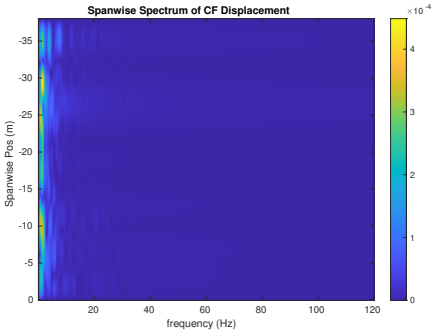

(e) Spanwise cross-flow spectrum of hydrodynamic displacement case 3770.

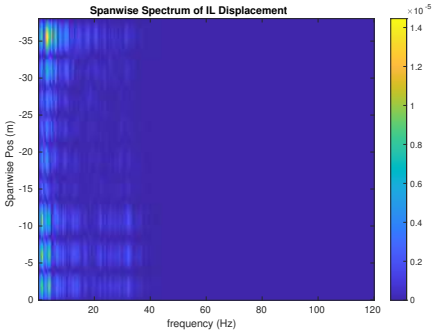

(f) Spanwise inline spectrum of hydrodynamic displacement case 3770.

Figure C-100: *Motion Analysis.* NDP Straight Riser ($L = 38m$) test case 3770.

NDP Straight Riser ($L = 38m$) test case 3780

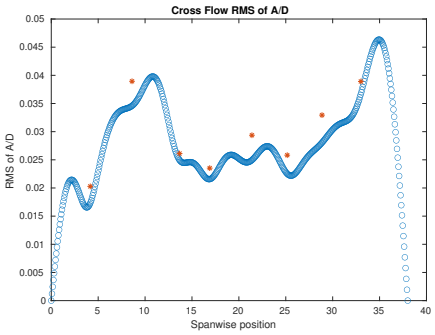

(a) Cross-flow RMS profile case 3780.

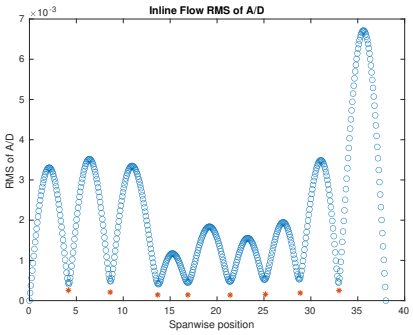

(b) Inline flow RMS profile case 3780.

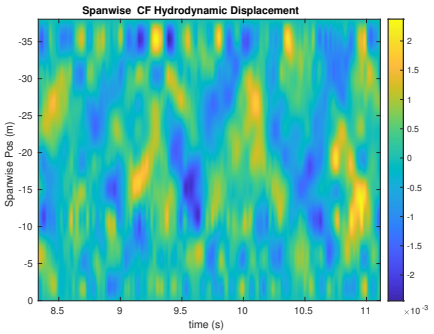

(c) Spanwise cross-flow hydrodynamic displacement case 3780.

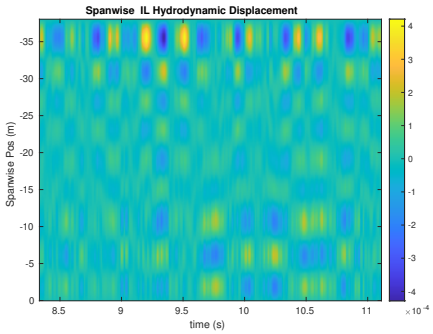

(d) Spanwise inline hydrodynamic displacement case 3780.

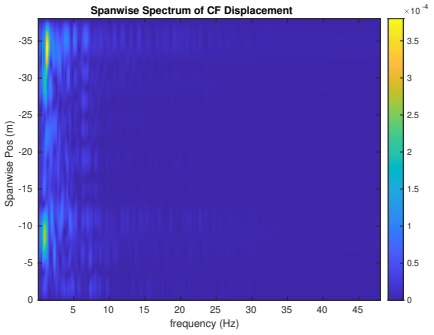

(e) Spanwise cross-flow spectrum of hydrodynamic displacement case 3780.

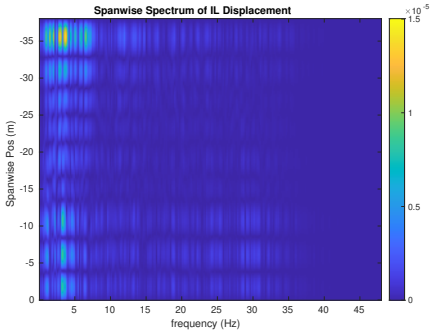

(f) Spanwise inline spectrum of hydrodynamic displacement case 3780.

Figure C-101: *Motion Analysis.* NDP Straight Riser ($L = 38m$) test case 3780.

NDP Straight Riser ($L = 38m$) test case 3790

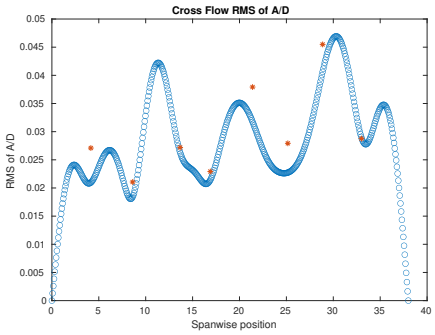

(a) Cross-flow RMS profile case 3790.

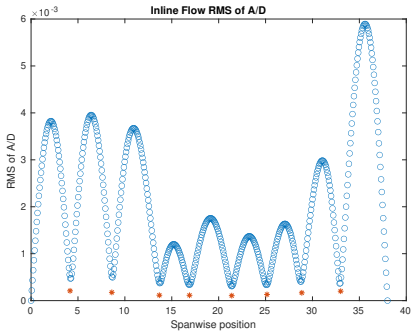

(b) Inline flow RMS profile case 3790.

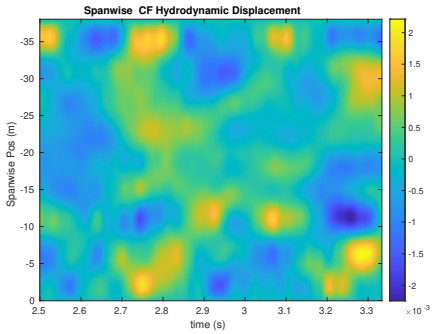

(c) Spanwise cross-flow hydrodynamic displacement case 3790.

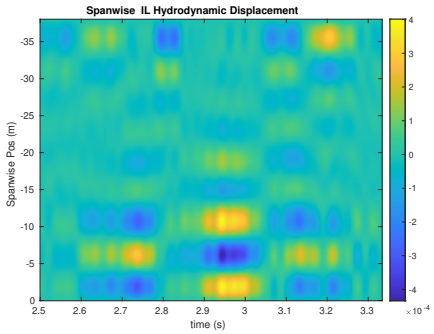

(d) Spanwise inline hydrodynamic displacement case 3790.

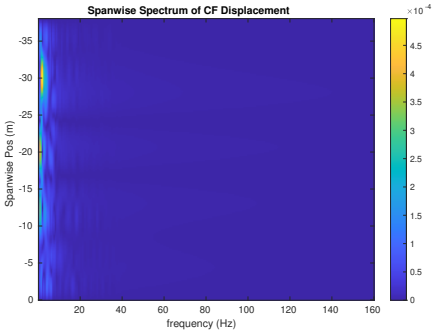

(e) Spanwise cross-flow spectrum of hydrodynamic displacement case 3790.

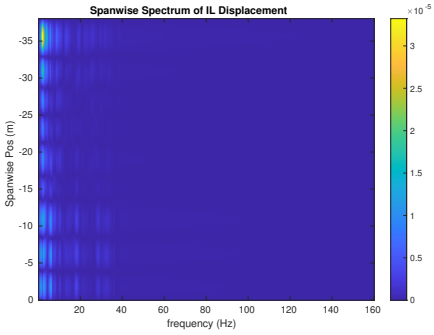

(f) Spanwise inline spectrum of hydrodynamic displacement case 3790.

Figure C-102: *Motion Analysis.* NDP Straight Riser ($L = 38m$) test case 3790.

NDP Straight Riser ($L = 38m$) test case 3800

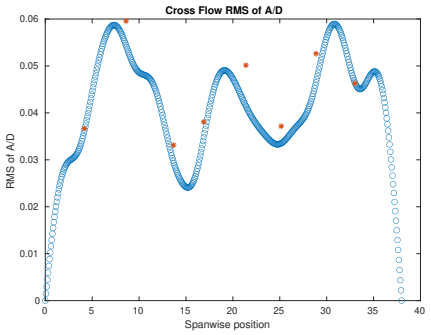

(a) Cross-flow RMS profile case 3800.

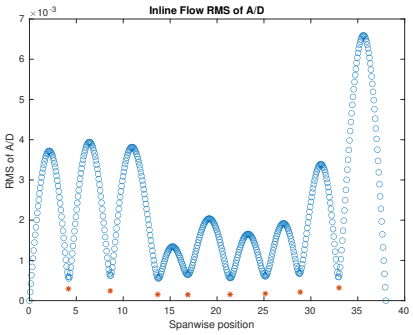

(b) Inline flow RMS profile case 3800.

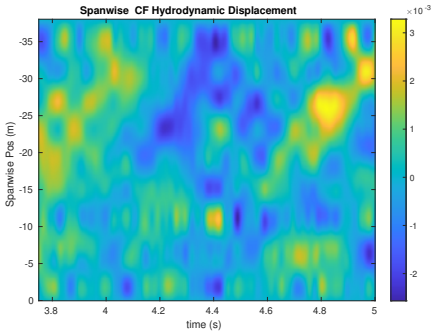

(c) Spanwise cross-flow hydrodynamic displacement case 3800.

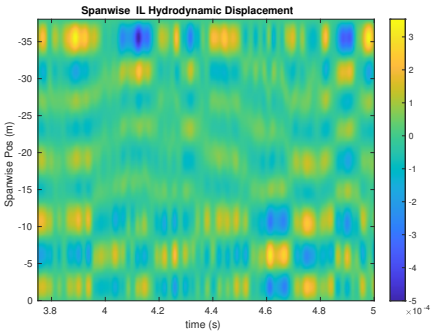

(d) Spanwise inline hydrodynamic displacement case 3800.

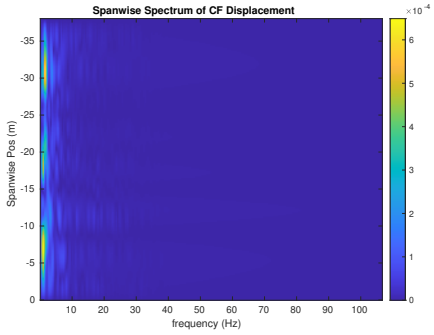

(e) Spanwise cross-flow spectrum of hydrodynamic displacement case 3800.

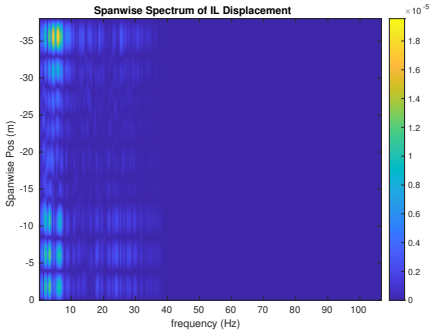

(f) Spanwise inline spectrum of hydrodynamic displacement case 3800.

Figure C-103: *Motion Analysis.* NDP Straight Riser ($L = 38m$) test case 3800.

NDP Straight Riser ($L = 38m$) test case 3810

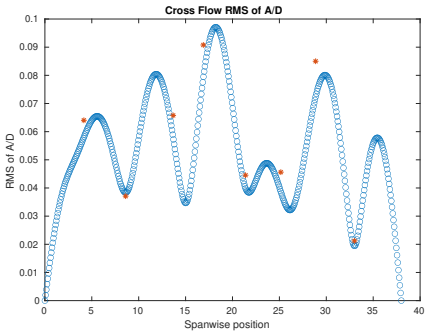

(a) Cross-flow RMS profile case 3810.

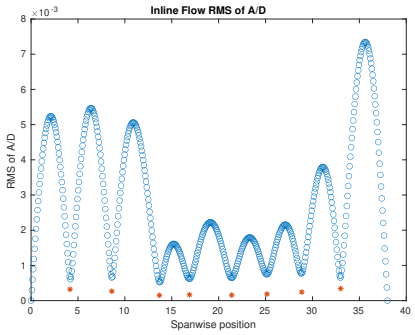

(b) Inline flow RMS profile case 3810.

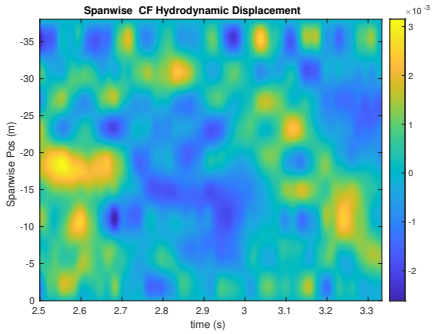

(c) Spanwise cross-flow hydrodynamic displacement case 3810.

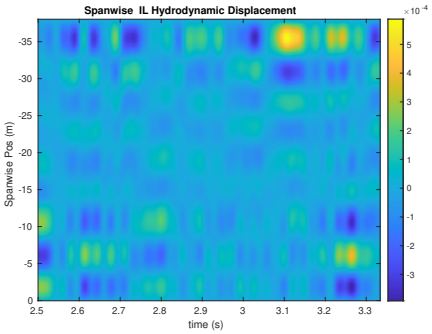

(d) Spanwise inline hydrodynamic displacement case 3810.

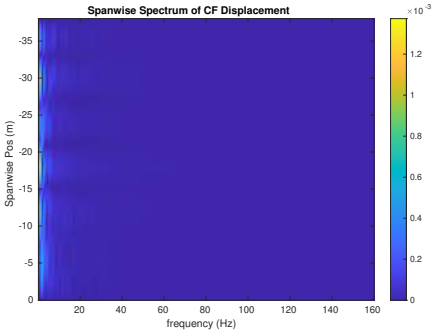

(e) Spanwise cross-flow spectrum of hydrodynamic displacement case 3810.

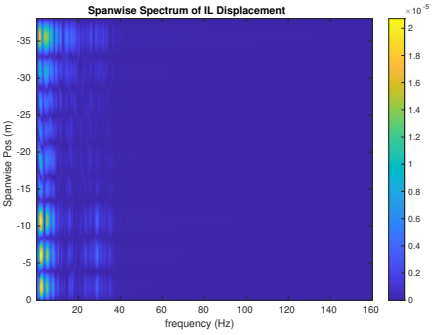

(f) Spanwise inline spectrum of hydrodynamic displacement case 3810.

Figure C-104: *Motion Analysis.* NDP Straight Riser ($L = 38m$) test case 3810.

NDP Straight Riser ($L = 38m$) test case 3820

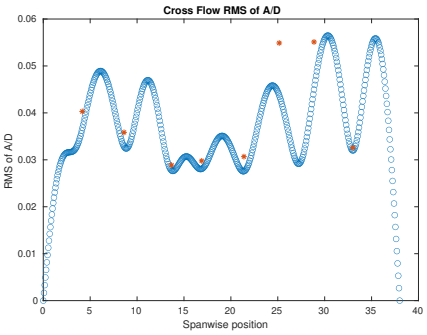

(a) Cross-flow RMS profile case 3820.

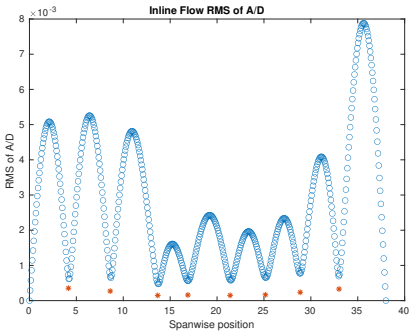

(b) Inline flow RMS profile case 3820.

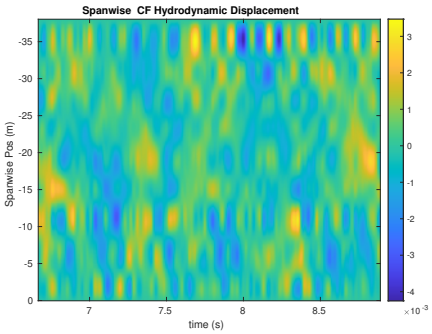

(c) Spanwise cross-flow hydrodynamic displacement case 3820.

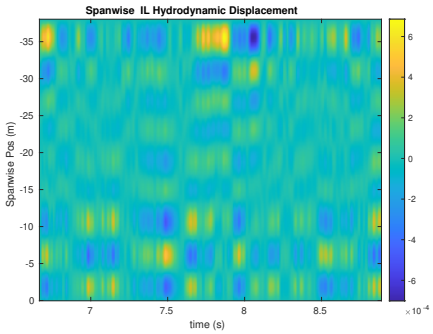

(d) Spanwise inline hydrodynamic displacement case 3820.

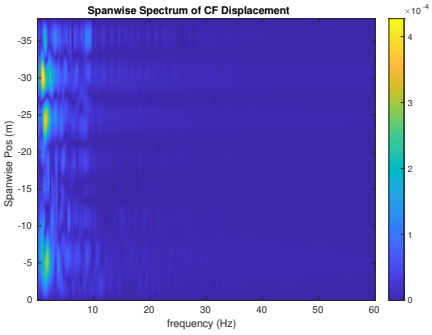

(e) Spanwise cross-flow spectrum of hydrodynamic displacement case 3820.

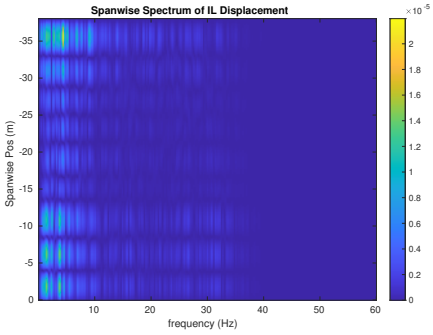

(f) Spanwise inline spectrum of hydrodynamic displacement case 3820.

Figure C-105: *Motion Analysis.* NDP Straight Riser ($L = 38m$) test case 3820.

NDP Straight Riser ($L = 38m$) test case 3830

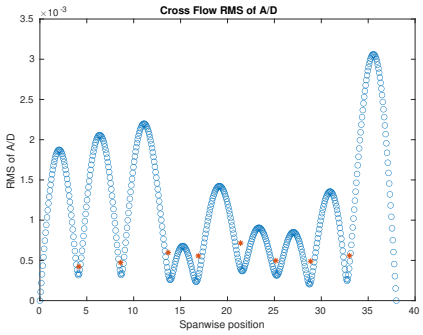

(a) Cross-flow RMS profile case 3830.

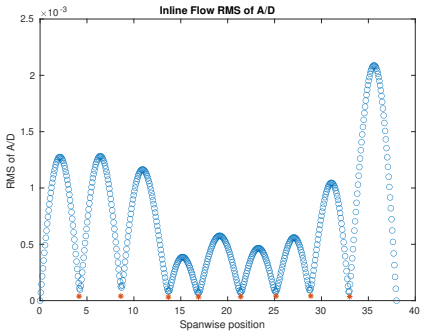

(b) Inline flow RMS profile case 3830.

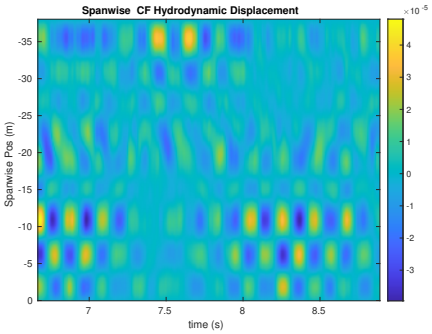

(c) Spanwise cross-flow hydrodynamic displacement case 3830.

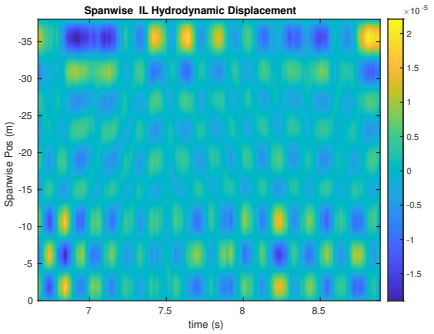

(d) Spanwise inline hydrodynamic displacement case 3830.

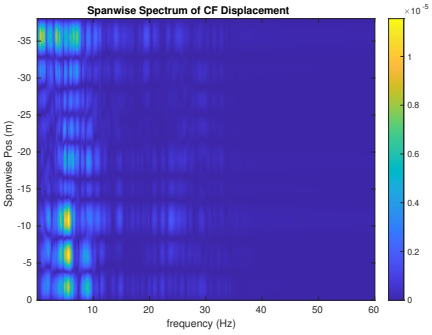

(e) Spanwise cross-flow spectrum of hydrodynamic displacement case 3830.

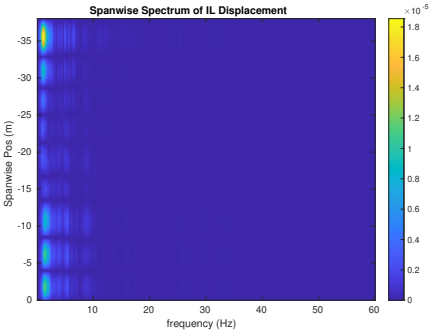

(f) Spanwise inline spectrum of hydrodynamic displacement case 3830.

Figure C-106: *Motion Analysis.* NDP Straight Riser ($L = 38m$) test case 3830.

NDP Straight Riser ($L = 38m$) test case 3910

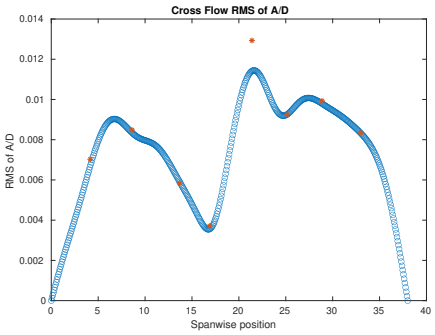

(a) Cross-flow RMS profile case 3910.

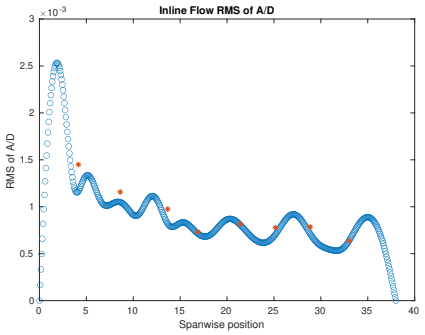

(b) Inline flow RMS profile case 3910.

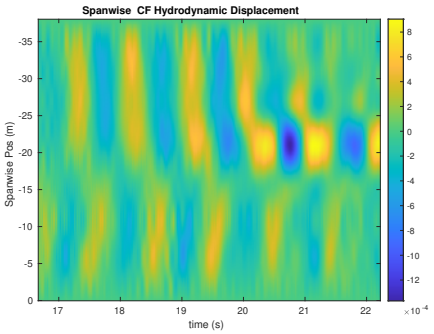

(c) Spanwise cross-flow hydrodynamic displacement case 3910.

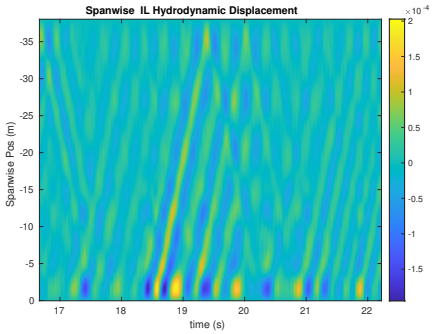

(d) Spanwise inline hydrodynamic displacement case 3910.

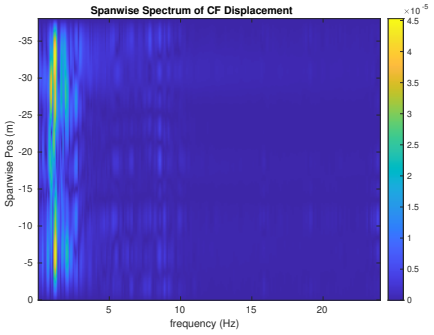

(e) Spanwise cross-flow spectrum of hydrodynamic displacement case 3910.

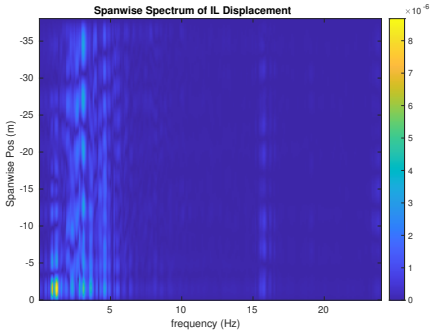

(f) Spanwise inline spectrum of hydrodynamic displacement case 3910.

Figure C-107: *Motion Analysis.* NDP Straight Riser ($L = 38m$) test case 3910.

NDP Straight Riser ($L = 38m$) test case 3920

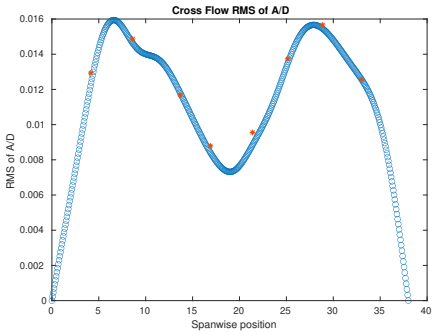

(a) Cross-flow RMS profile case 3920.

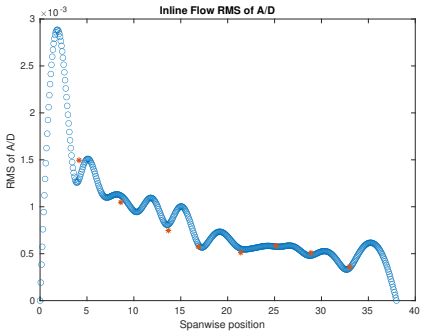

(b) Inline flow RMS profile case 3920.

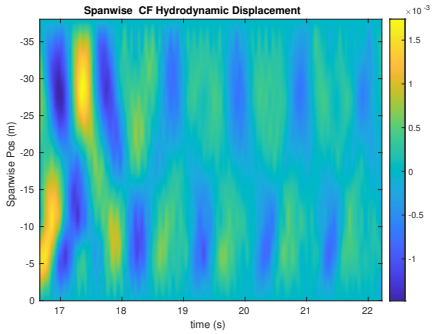

(c) Spanwise cross-flow hydrodynamic displacement case 3920.

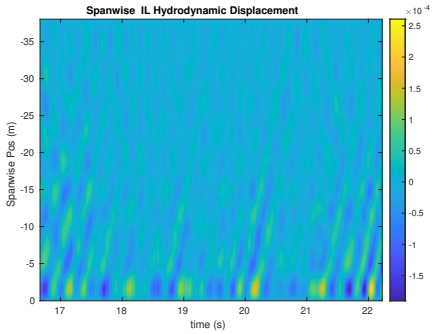

(d) Spanwise inline hydrodynamic displacement case 3920.

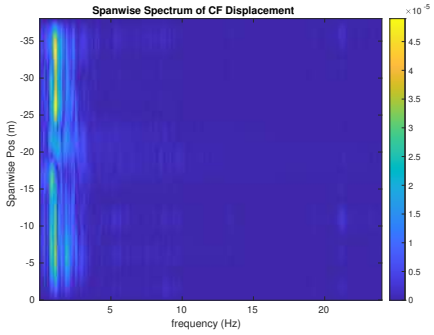

(e) Spanwise cross-flow spectrum of hydrodynamic displacement case 3920.

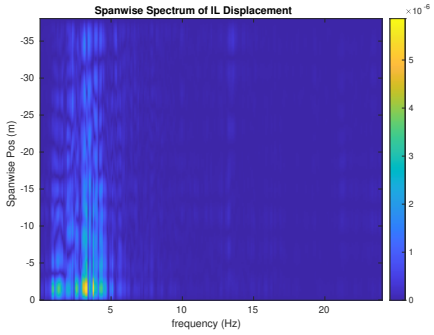

(f) Spanwise inline spectrum of hydrodynamic displacement case 3920.

Figure C-108: *Motion Analysis.* NDP Straight Riser ($L = 38m$) test case 3920.

NDP Straight Riser ($L = 38m$) test case 3930

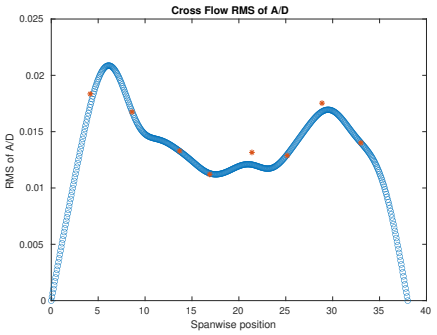

(a) Cross-flow RMS profile case 3930.

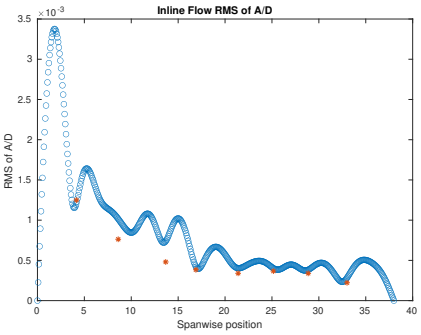

(b) Inline flow RMS profile case 3930.

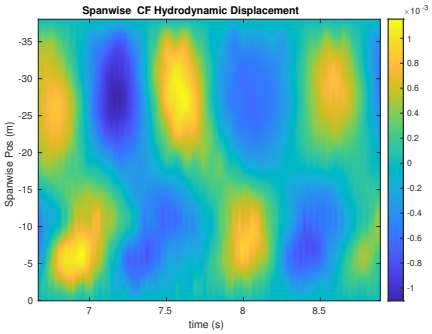

(c) Spanwise cross-flow hydrodynamic displacement case 3930.

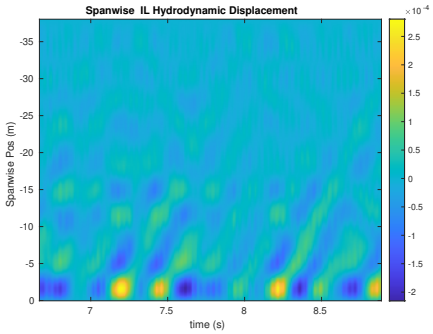

(d) Spanwise inline hydrodynamic displacement case 3930.

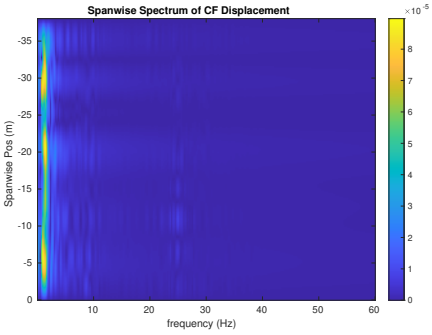

(e) Spanwise cross-flow spectrum of hydrodynamic displacement case 3930.

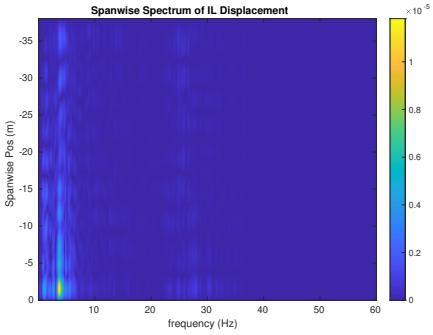

(f) Spanwise inline spectrum of hydrodynamic displacement case 3930.

Figure C-109: *Motion Analysis.* NDP Straight Riser ($L = 38m$) test case 3930.

NDP Straight Riser ($L = 38m$) test case 3940

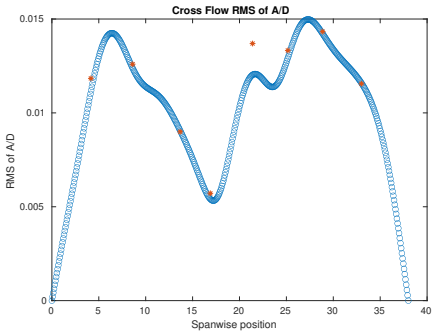

(a) Cross-flow RMS profile case 3940.

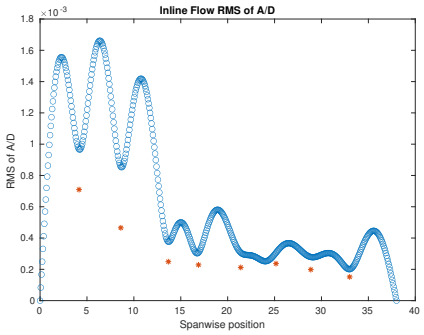

(b) Inline flow RMS profile case 3940.

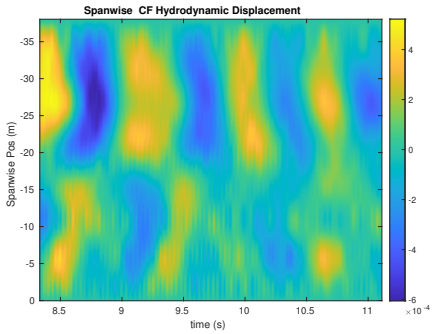

(c) Spanwise cross-flow hydrodynamic displacement case 3940.

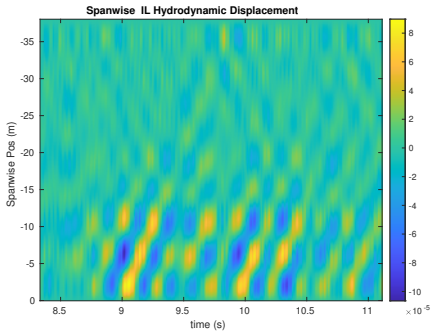

(d) Spanwise inline hydrodynamic displacement case 3940.

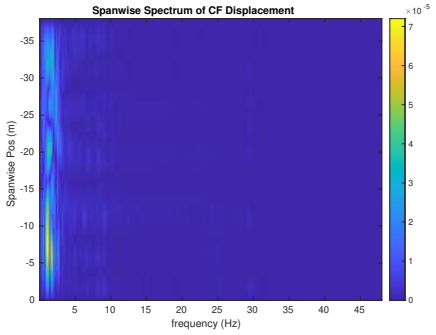

(e) Spanwise cross-flow spectrum of hydrodynamic displacement case 3940.

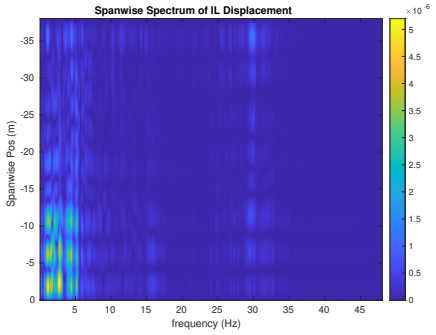

(f) Spanwise inline spectrum of hydrodynamic displacement case 3940.

Figure C-110: *Motion Analysis.* NDP Straight Riser ($L = 38m$) test case 3940.

NDP Straight Riser ($L = 38m$) test case 3950

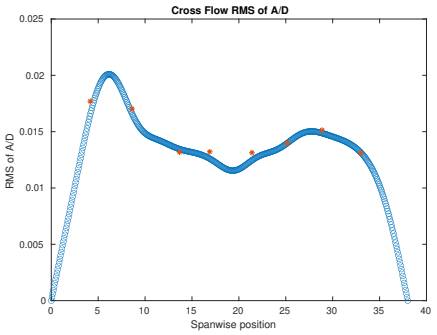

(a) Cross-flow RMS profile case 3950.

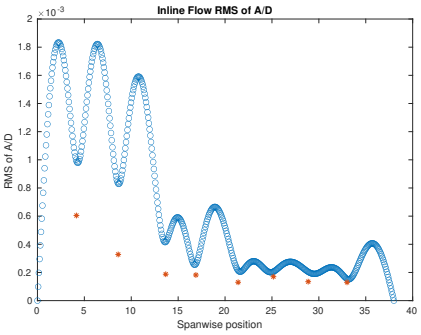

(b) Inline flow RMS profile case 3950.

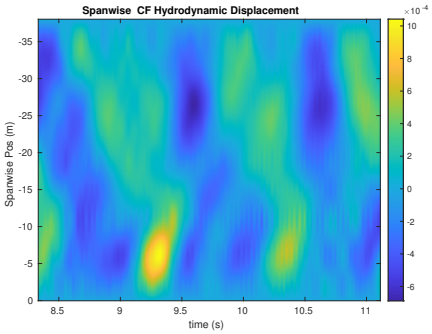

(c) Spanwise cross-flow hydrodynamic displacement case 3950.

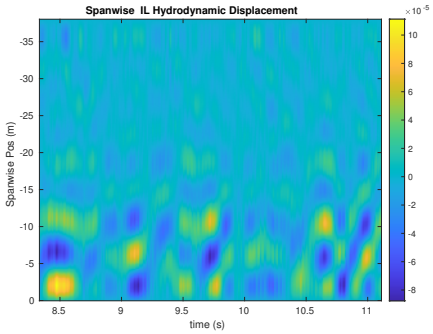

(d) Spanwise inline hydrodynamic displacement case 3950.

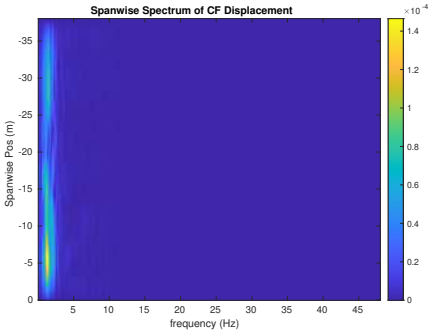

(e) Spanwise cross-flow spectrum of hydrodynamic displacement case 3950.

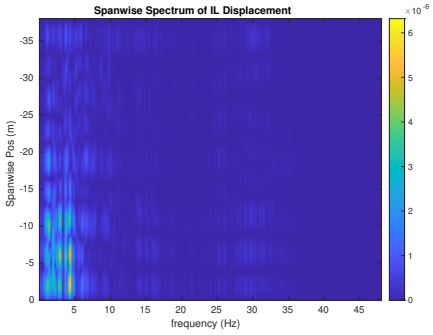

(f) Spanwise inline spectrum of hydrodynamic displacement case 3950.

Figure C-111: *Motion Analysis.* NDP Straight Riser ($L = 38m$) test case 3950.

NDP Straight Riser ($L = 38m$) test case 3960

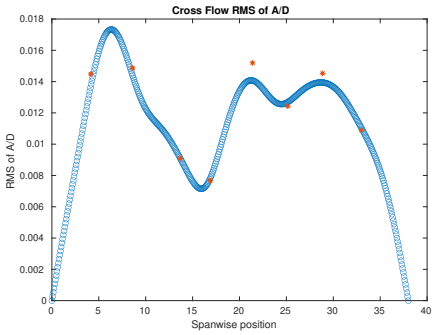

(a) Cross-flow RMS profile case 3960.

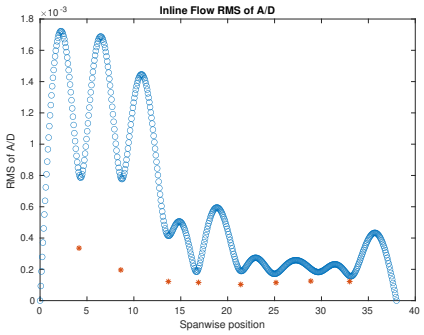

(b) Inline flow RMS profile case 3960.

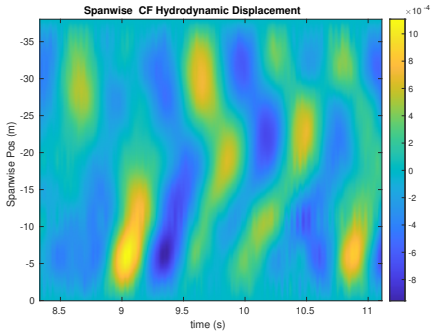

(c) Spanwise cross-flow hydrodynamic displacement case 3960.

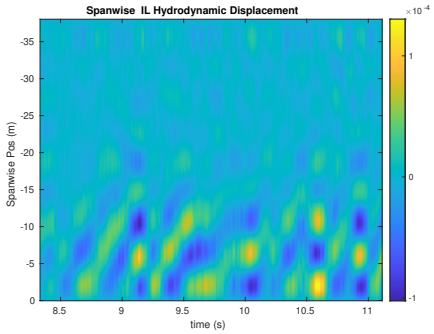

(d) Spanwise inline hydrodynamic displacement case 3960.

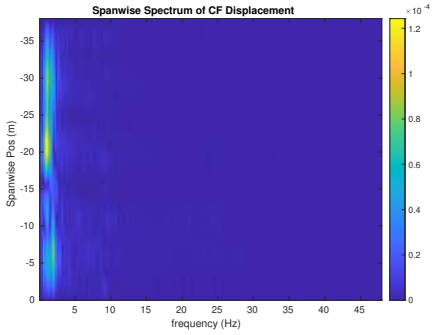

(e) Spanwise cross-flow spectrum of hydrodynamic displacement case 3960.

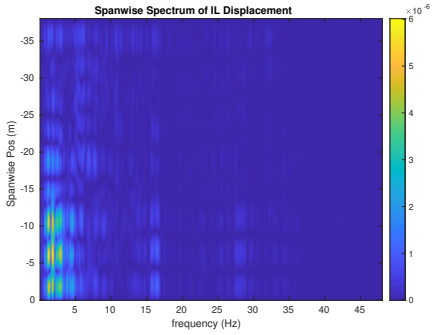

(f) Spanwise inline spectrum of hydrodynamic displacement case 3960.

Figure C-112: *Motion Analysis.* NDP Straight Riser ($L = 38m$) test case 3960.

NDP Straight Riser ($L = 38m$) test case 3970

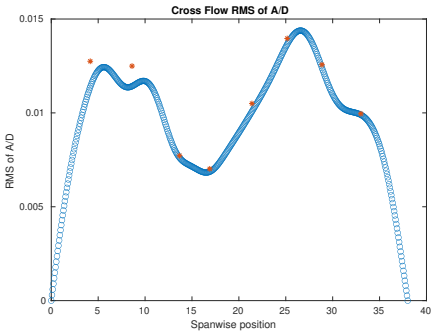

(a) Cross-flow RMS profile case 3970.

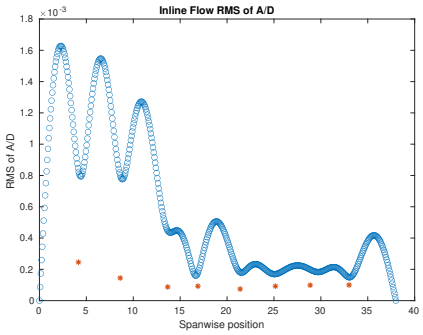

(b) Inline flow RMS profile case 3970.

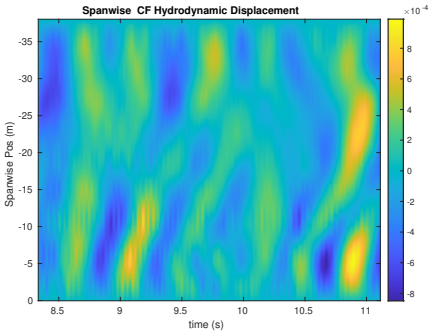

(c) Spanwise cross-flow hydrodynamic displacement case 3970.

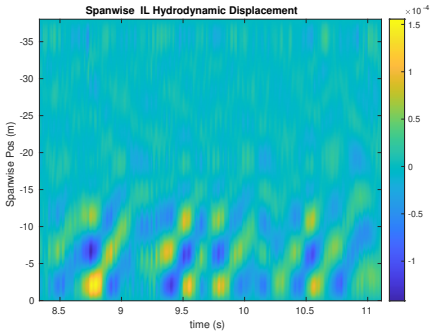

(d) Spanwise inline hydrodynamic displacement case 3970.

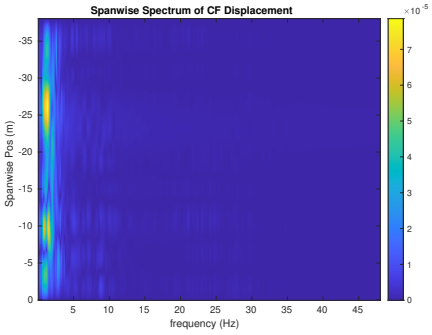

(e) Spanwise cross-flow spectrum of hydrodynamic displacement case 3970.

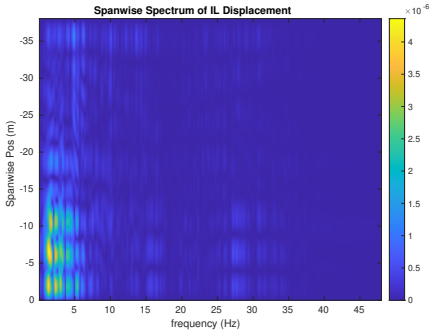

(f) Spanwise inline spectrum of hydrodynamic displacement case 3970.

Figure C-113: *Motion Analysis.* NDP Straight Riser ($L = 38m$) test case 3970.

NDP Straight Riser ($L = 38m$) test case 3980

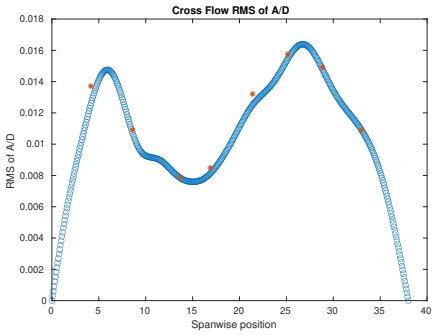

(a) Cross-flow RMS profile case 3980.

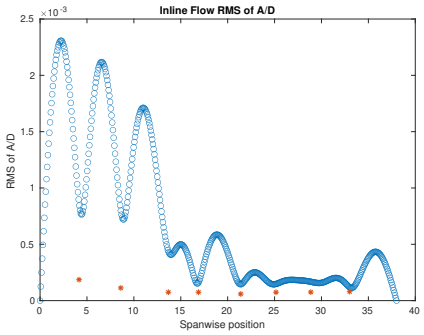

(b) Inline flow RMS profile case 3980.

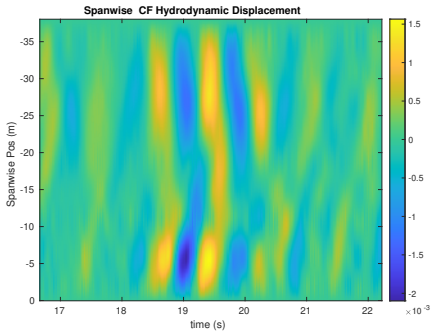

(c) Spanwise cross-flow hydrodynamic displacement case 3980.

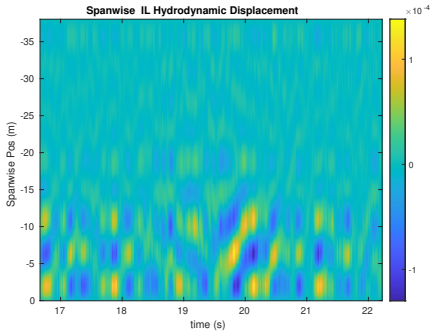

(d) Spanwise inline hydrodynamic displacement case 3980.

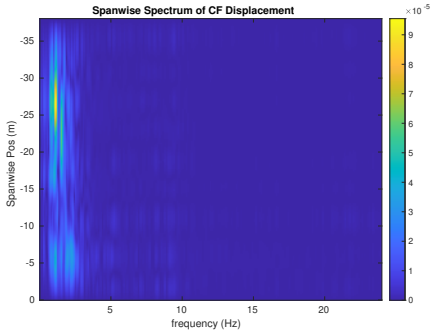

(e) Spanwise cross-flow spectrum of hydrodynamic displacement case 3980.

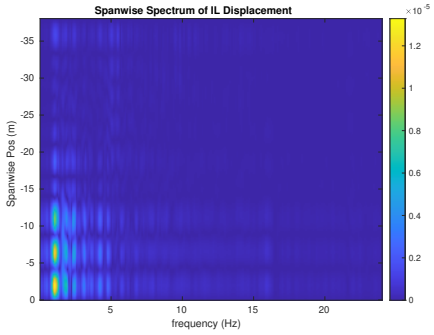

(f) Spanwise inline spectrum of hydrodynamic displacement case 3980.

Figure C-114: *Motion Analysis.* NDP Straight Riser ($L = 38m$) test case 3980.

NDP Straight Riser ($L = 38m$) test case 3990

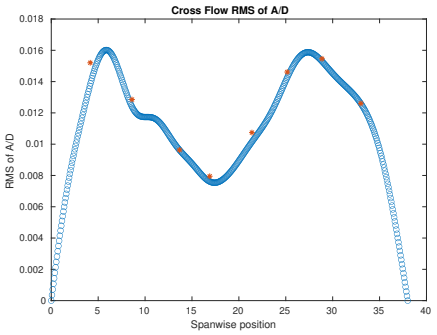

(a) Cross-flow RMS profile case 3990.

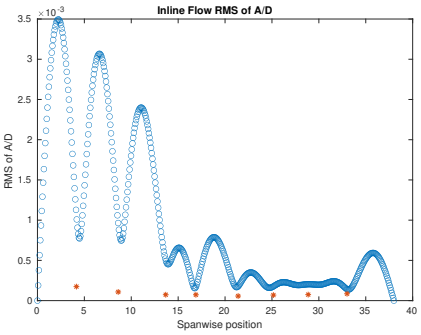

(b) Inline flow RMS profile case 3990.

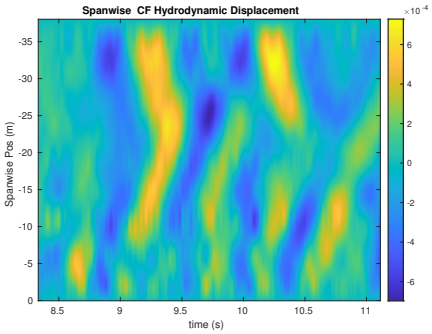

(c) Spanwise cross-flow hydrodynamic displacement case 3990.

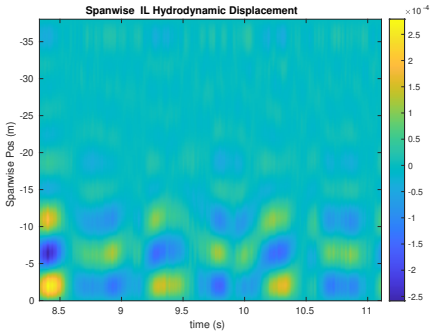

(d) Spanwise inline hydrodynamic displacement case 3990.

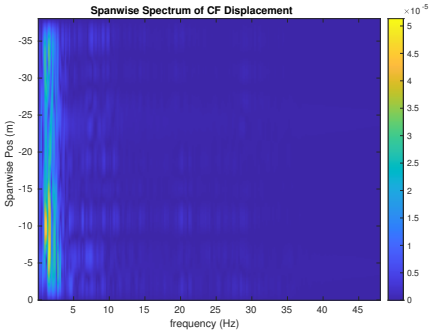

(e) Spanwise cross-flow spectrum of hydrodynamic displacement case 3990.

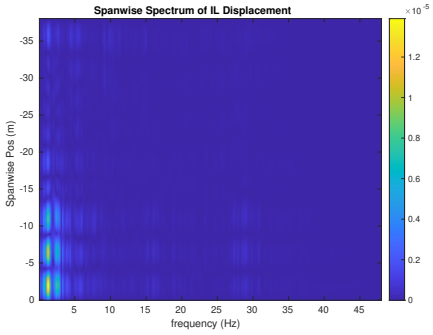

(f) Spanwise inline spectrum of hydrodynamic displacement case 3990.

Figure C-115: *Motion Analysis.* NDP Straight Riser ($L = 38m$) test case 3990.

NDP Straight Riser ($L = 38m$) test case 4000

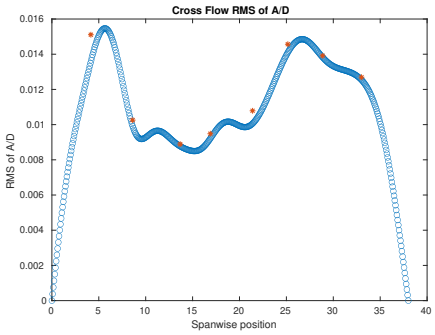

(a) Cross-flow RMS profile case 4000.

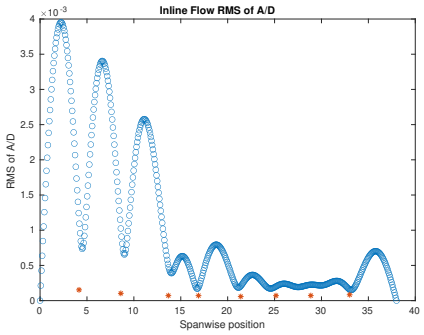

(b) Inline flow RMS profile case 4000.

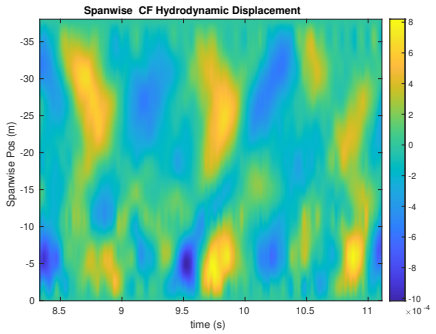

(c) Spanwise cross-flow hydrodynamic displacement case 4000.

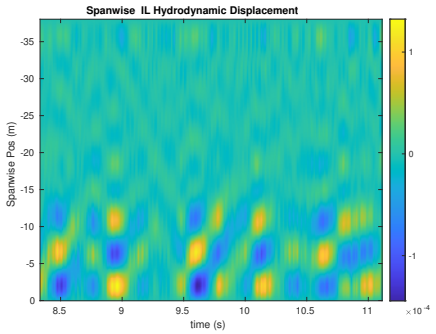

(d) Spanwise inline hydrodynamic displacement case 4000.

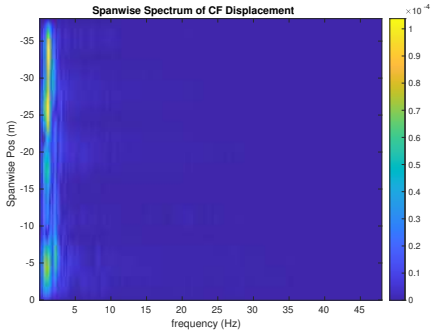

(e) Spanwise cross-flow spectrum of hydrodynamic displacement case 4000.

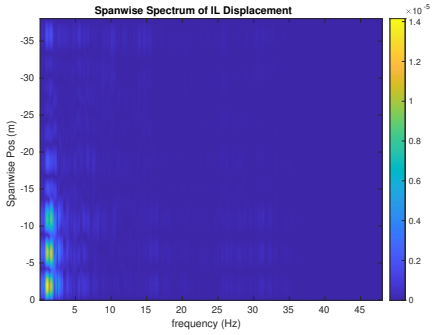

(f) Spanwise inline spectrum of hydrodynamic displacement case 4000.

Figure C-116: *Motion Analysis.* NDP Straight Riser ($L = 38m$) test case 4000.

NDP Straight Riser ($L = 38m$) test case 4010

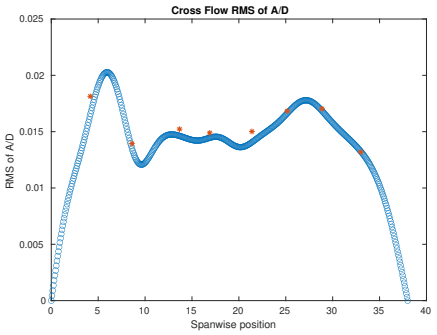

(a) Cross-flow RMS profile case 4010.

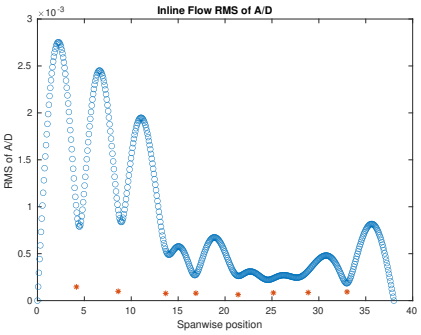

(b) Inline flow RMS profile case 4010.

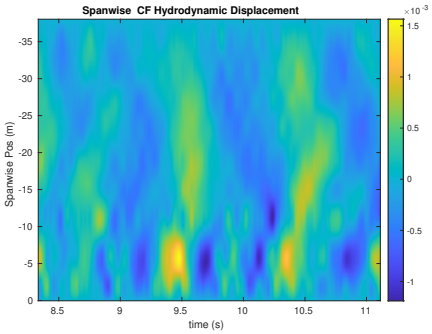

(c) Spanwise cross-flow hydrodynamic displacement case 4010.

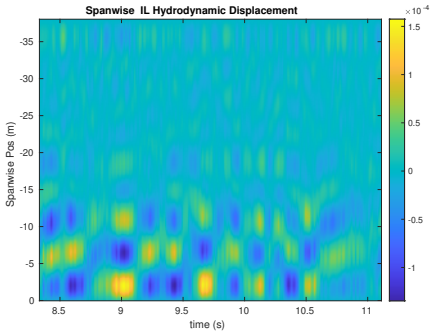

(d) Spanwise inline hydrodynamic displacement case 4010.

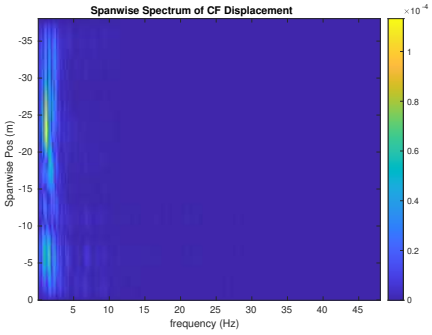

(e) Spanwise cross-flow spectrum of hydrodynamic displacement case 4010.

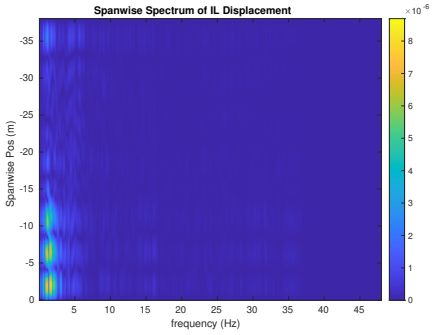

(f) Spanwise inline spectrum of hydrodynamic displacement case 4010.

Figure C-117: *Motion Analysis.* NDP Straight Riser ($L = 38m$) test case 4010.

NDP Straight Riser ($L = 38m$) test case 4020

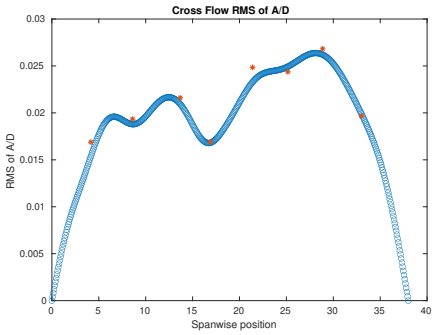

(a) Cross-flow RMS profile case 4020.

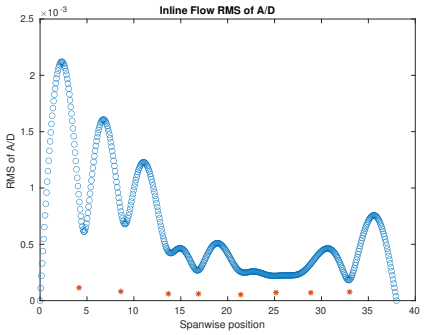

(b) Inline flow RMS profile case 4020.

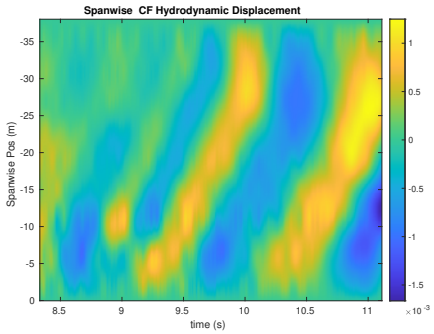

(c) Spanwise cross-flow hydrodynamic displacement case 4020.

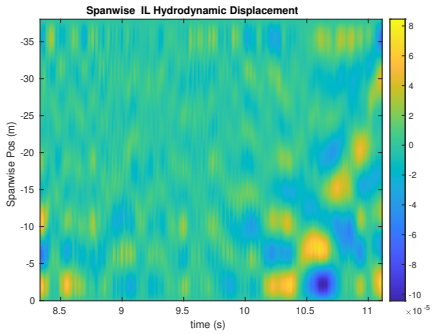

(d) Spanwise inline hydrodynamic displacement case 4020.

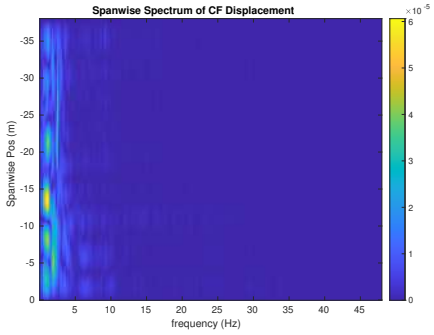

(e) Spanwise cross-flow spectrum of hydrodynamic displacement case 4020.

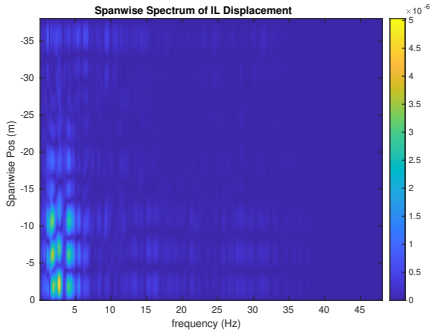

(f) Spanwise inline spectrum of hydrodynamic displacement case 4020.

Figure C-118: *Motion Analysis.* NDP Straight Riser ($L = 38m$) test case 4020.

NDP Straight Riser ($L = 38m$) test case 4030

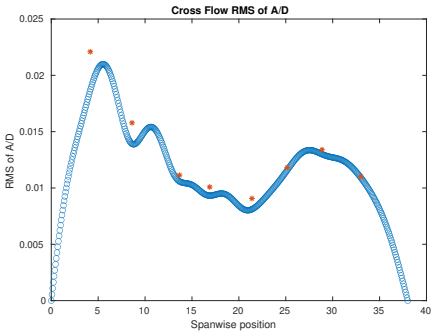

(a) Cross-flow RMS profile case 4030.

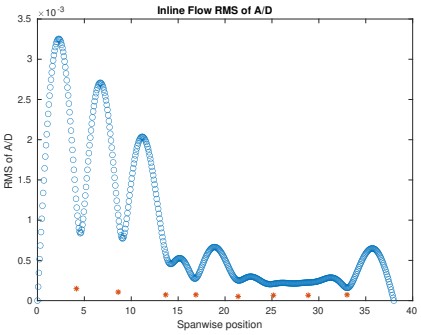

(b) Inline flow RMS profile case 4030.

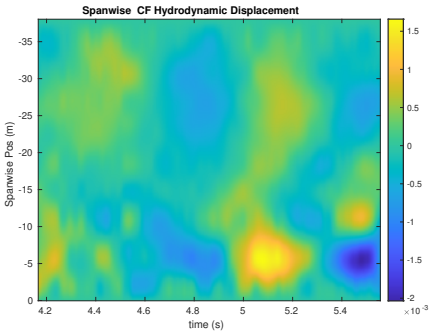

(c) Spanwise cross-flow hydrodynamic displacement case 4030.

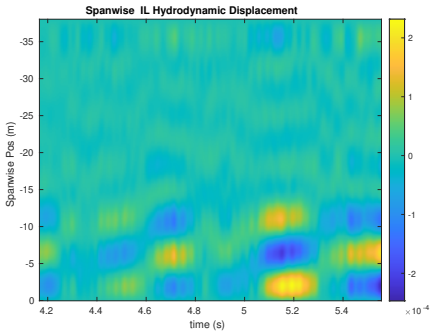

(d) Spanwise inline hydrodynamic displacement case 4030.

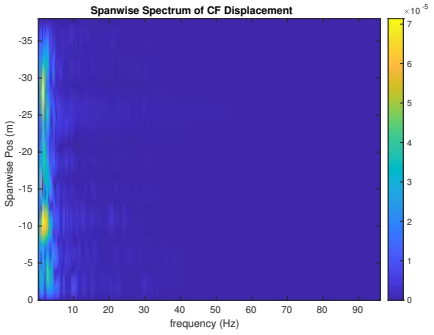

(e) Spanwise cross-flow spectrum of hydrodynamic displacement case 4030.

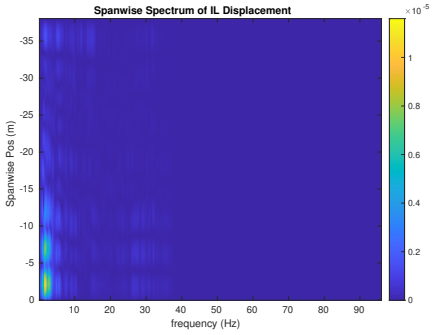

(f) Spanwise inline spectrum of hydrodynamic displacement case 4030.

Figure C-119: *Motion Analysis.* NDP Straight Riser ($L = 38m$) test case 4030.

NDP Straight Riser ($L = 38m$) test case 4040

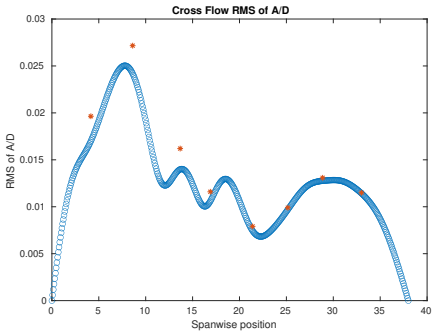

(a) Cross-flow RMS profile case 4040.

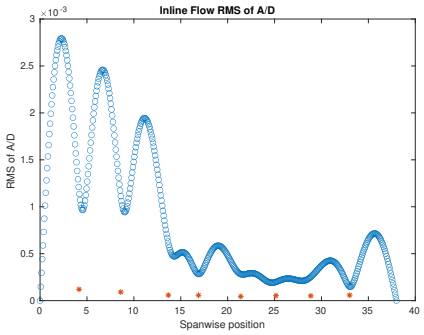

(b) Inline flow RMS profile case 4040.

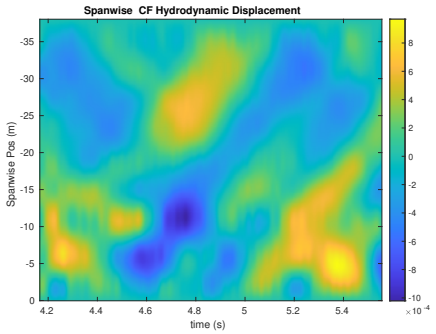

(c) Spanwise cross-flow hydrodynamic displacement case 4040.

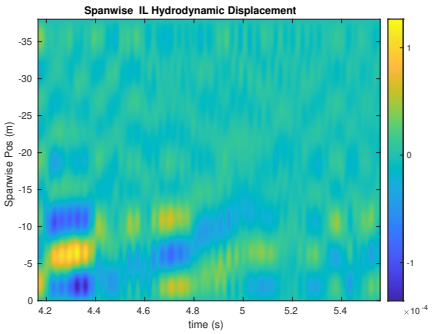

(d) Spanwise inline hydrodynamic displacement case 4040.

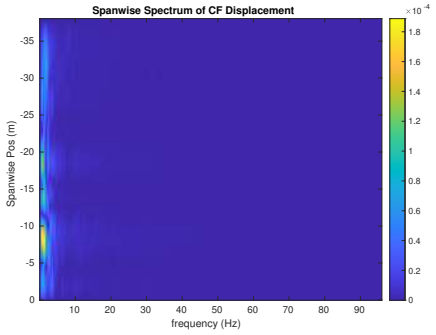

(e) Spanwise cross-flow spectrum of hydrodynamic displacement case 4040.

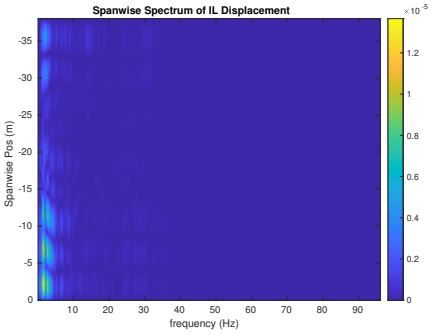

(f) Spanwise inline spectrum of hydrodynamic displacement case 4040.

Figure C-120: *Motion Analysis.* NDP Straight Riser ($L = 38m$) test case 4040.

NDP Straight Riser ($L = 38m$) test case 4050

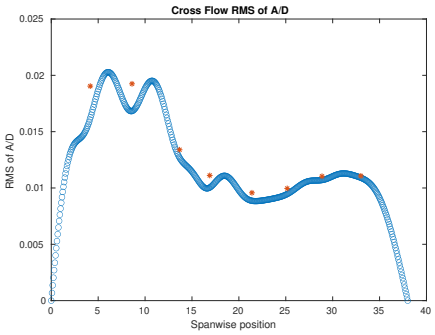

(a) Cross-flow RMS profile case 4050.

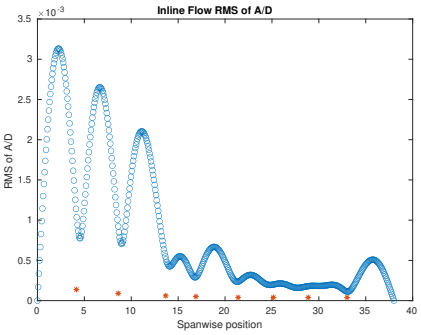

(b) Inline flow RMS profile case 4050.

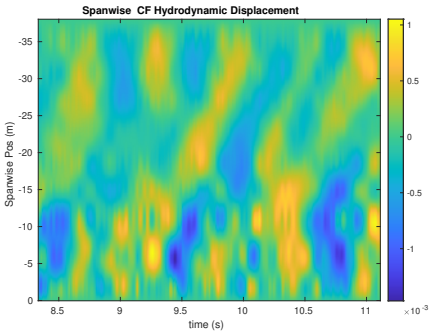

(c) Spanwise cross-flow hydrodynamic displacement case 4050.

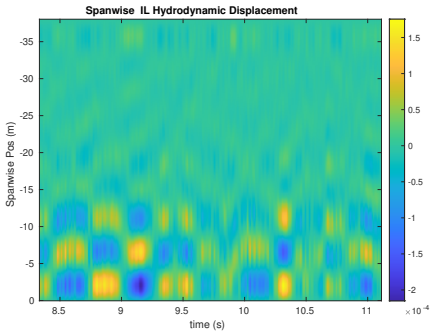

(d) Spanwise inline hydrodynamic displacement case 4050.

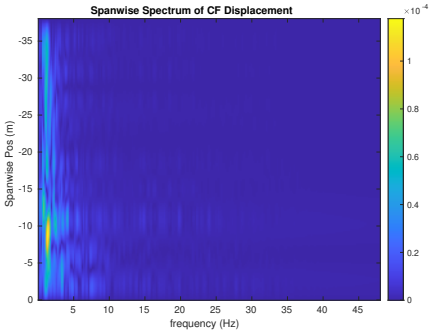

(e) Spanwise cross-flow spectrum of hydrodynamic displacement case 4050.

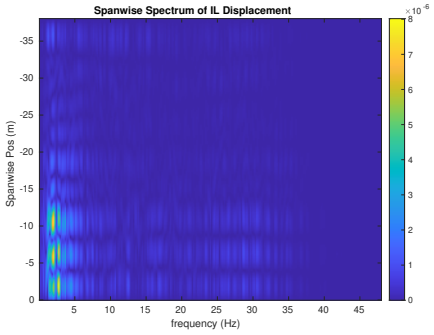

(f) Spanwise inline spectrum of hydrodynamic displacement case 4050.

Figure C-121: *Motion Analysis.* NDP Straight Riser ($L = 38m$) test case 4050.

NDP Straight Riser ($L = 38m$) test case 4060

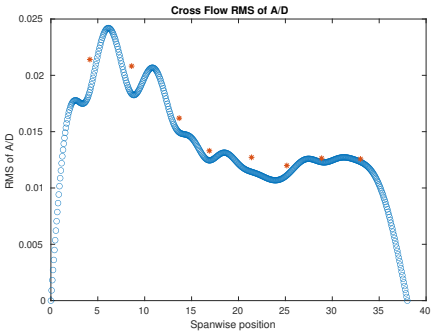

(a) Cross-flow RMS profile case 4060.

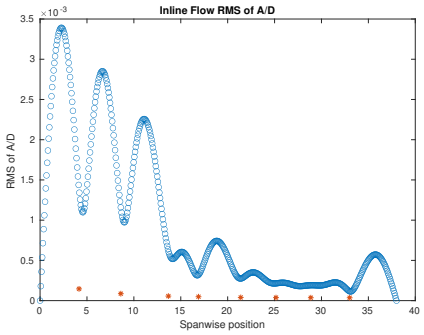

(b) Inline flow RMS profile case 4060.

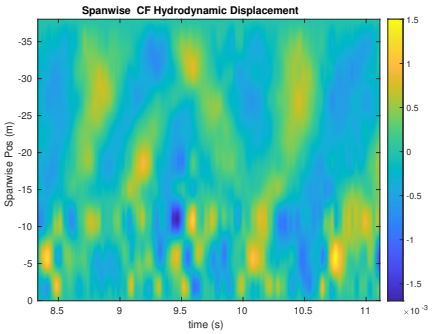

(c) Spanwise cross-flow hydrodynamic displacement case 4060.

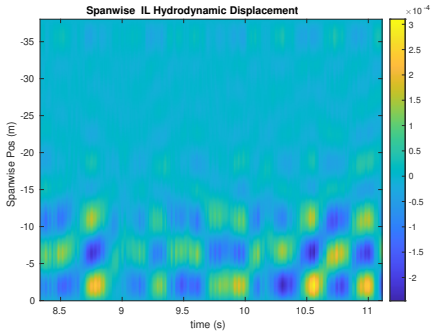

(d) Spanwise inline hydrodynamic displacement case 4060.

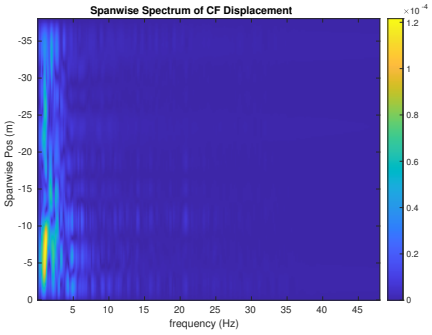

(e) Spanwise cross-flow spectrum of hydrodynamic displacement case 4060.

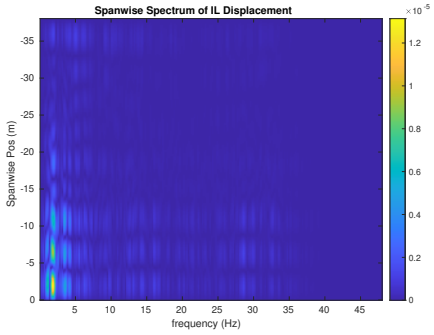

(f) Spanwise inline spectrum of hydrodynamic displacement case 4060.

Figure C-122: *Motion Analysis.* NDP Straight Riser ($L = 38m$) test case 4060.

NDP Straight Riser ($L = 38m$) test case 4070

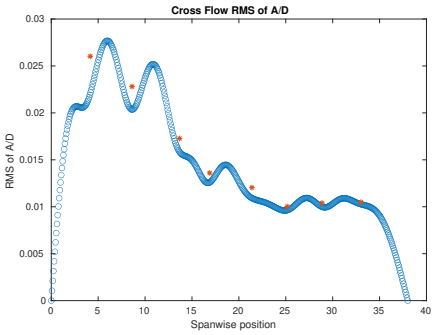

(a) Cross-flow RMS profile case 4070.

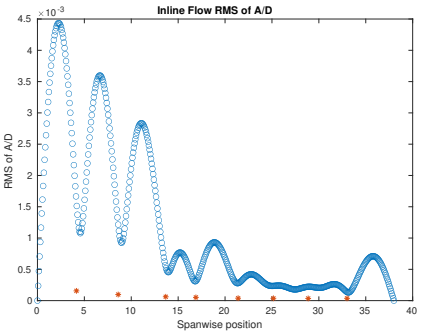

(b) Inline flow RMS profile case 4070.

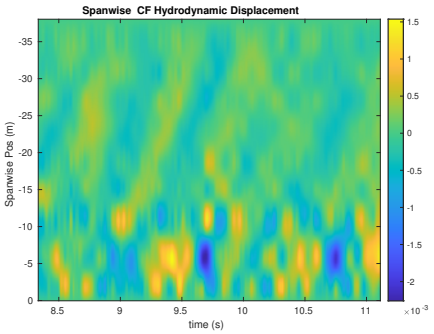

(c) Spanwise cross-flow hydrodynamic displacement case 4070.

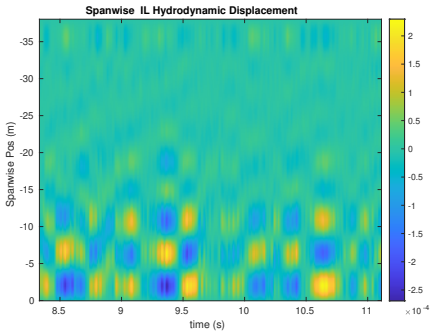

(d) Spanwise inline hydrodynamic displacement case 4070.

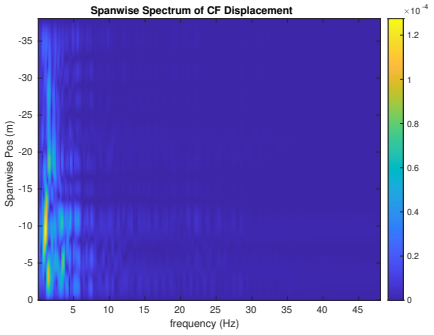

(e) Spanwise cross-flow spectrum of hydrodynamic displacement case 4070.

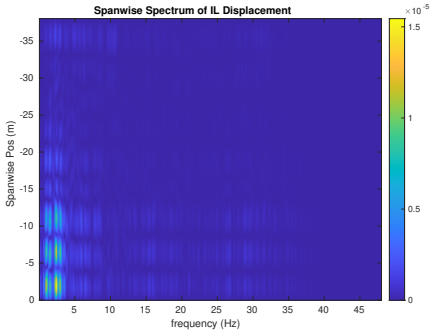

(f) Spanwise inline spectrum of hydrodynamic displacement case 4070.

Figure C-123: *Motion Analysis.* NDP Straight Riser ($L = 38m$) test case 4070.

NDP Straight Riser ($L = 38m$) test case 4080

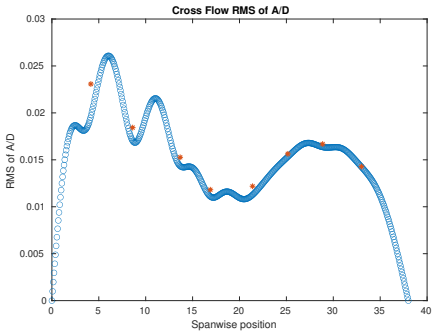

(a) Cross-flow RMS profile case 4080.

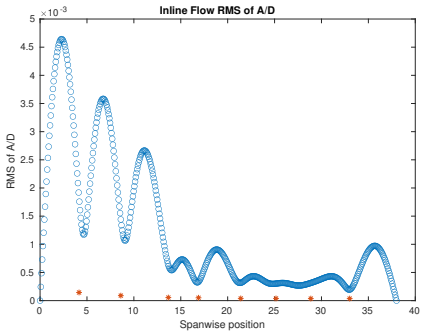

(b) Inline flow RMS profile case 4080.

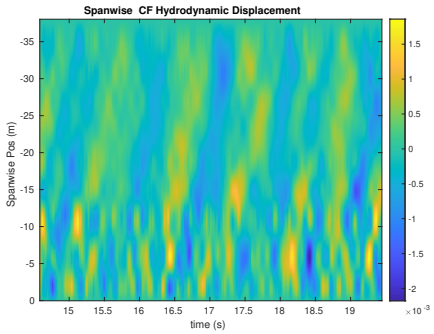

(c) Spanwise cross-flow hydrodynamic displacement case 4080.

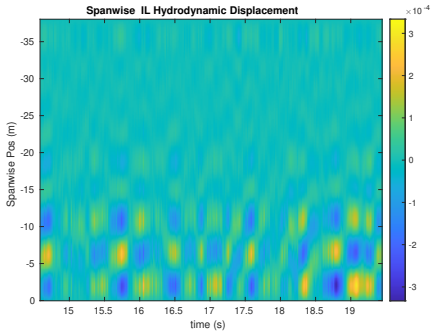

(d) Spanwise inline hydrodynamic displacement case 4080.

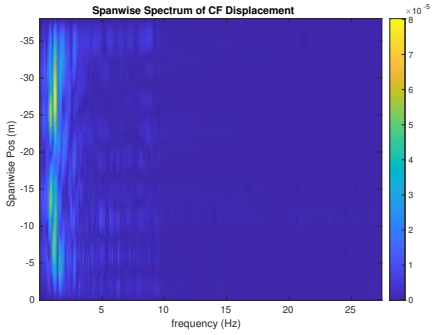

(e) Spanwise cross-flow spectrum of hydrodynamic displacement case 4080.

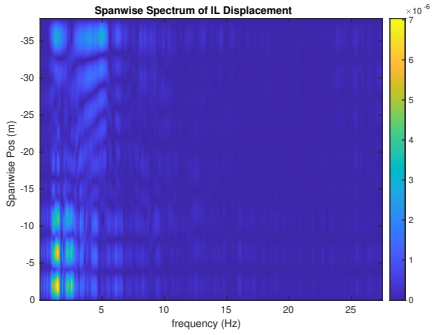

(f) Spanwise inline spectrum of hydrodynamic displacement case 4080.

Figure C-124: *Motion Analysis.* NDP Straight Riser ($L = 38m$) test case 4080.

NDP Straight Riser ($L = 38m$) test case 4090

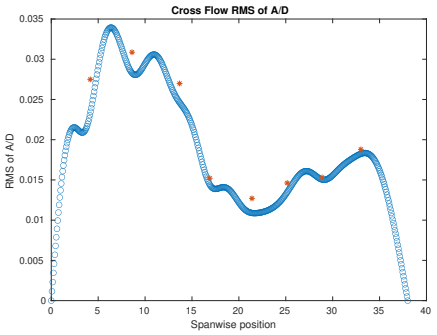

(a) Cross-flow RMS profile case 4090.

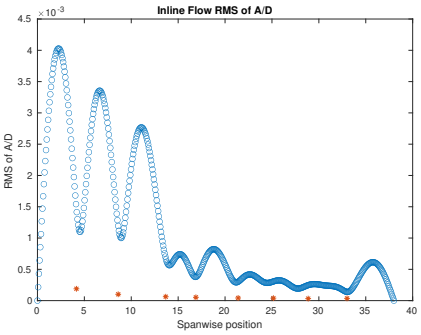

(b) Inline flow RMS profile case 4090.

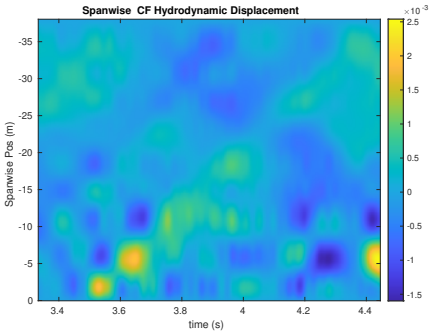

(c) Spanwise cross-flow hydrodynamic displacement case 4090.

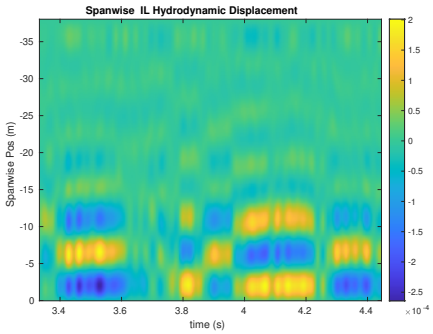

(d) Spanwise inline hydrodynamic displacement case 4090.

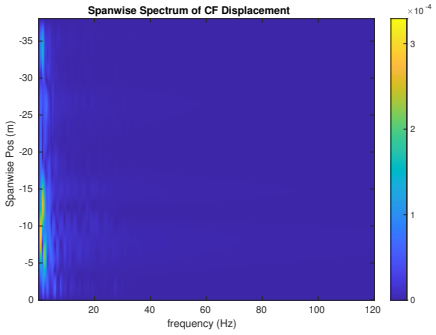

(e) Spanwise cross-flow spectrum of hydrodynamic displacement case 4090.

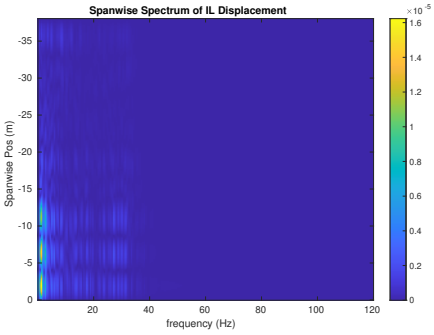

(f) Spanwise inline spectrum of hydrodynamic displacement case 4090.

Figure C-125: *Motion Analysis.* NDP Straight Riser ($L = 38m$) test case 4090.

NDP Straight Riser ($L = 38m$) test case 4100

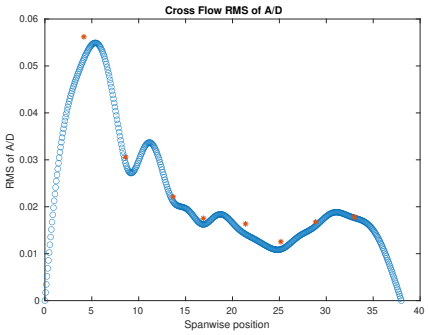

(a) Cross-flow RMS profile case 4100.

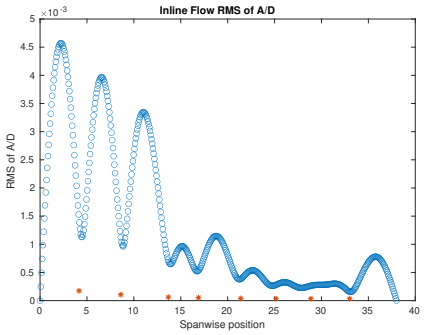

(b) Inline flow RMS profile case 4100.

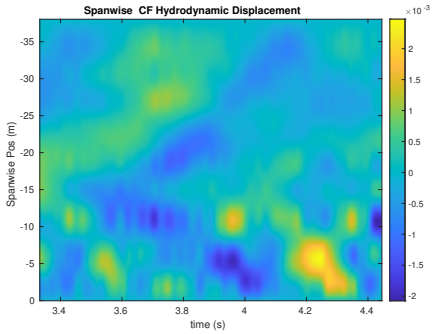

(c) Spanwise cross-flow hydrodynamic displacement case 4100.

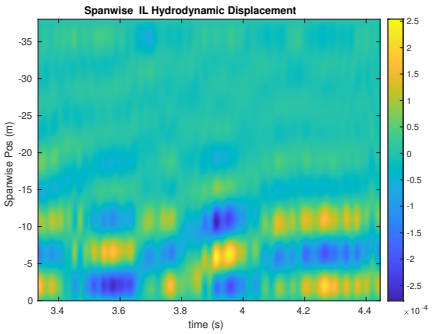

(d) Spanwise inline hydrodynamic displacement case 4100.

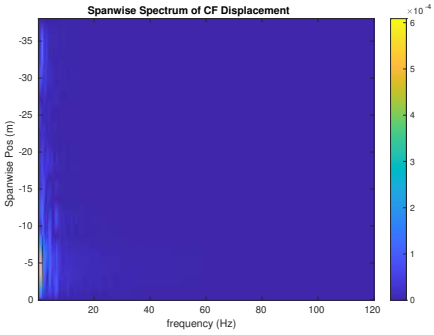

(e) Spanwise cross-flow spectrum of hydrodynamic displacement case 4100.

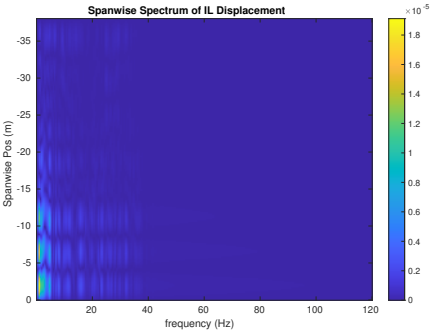

(f) Spanwise inline spectrum of hydrodynamic displacement case 4100.

Figure C-126: *Motion Analysis.* NDP Straight Riser ($L = 38m$) test case 4100.

NDP Straight Riser ($L = 38m$) test case 4110

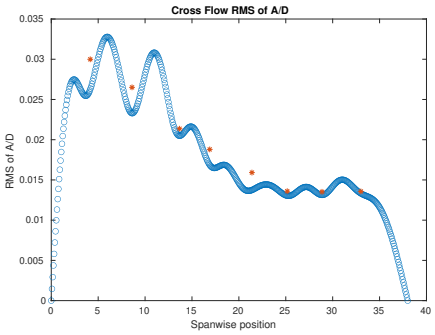

(a) Cross-flow RMS profile case 4110.

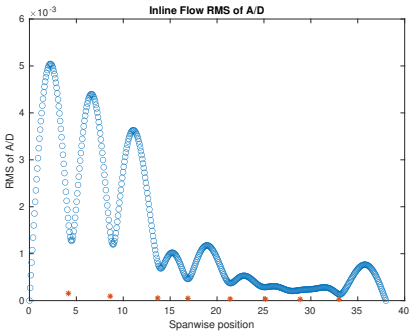

(b) Inline flow RMS profile case 4110.

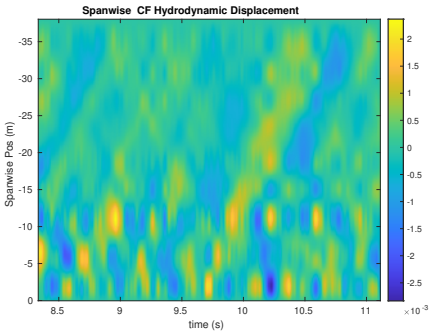

(c) Spanwise cross-flow hydrodynamic displacement case 4110.

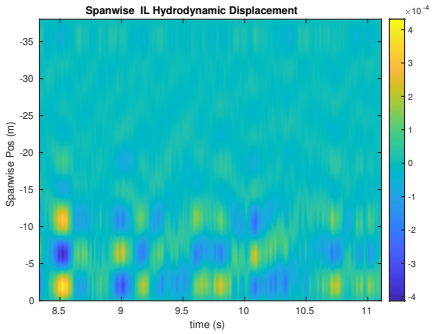

(d) Spanwise inline hydrodynamic displacement case 4110.

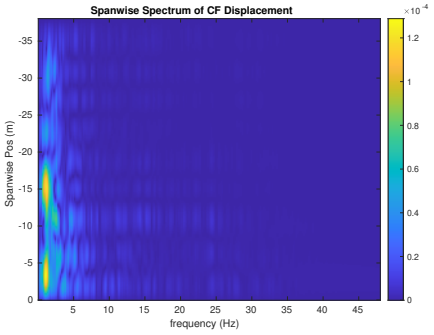

(e) Spanwise cross-flow spectrum of hydrodynamic displacement case 4110.

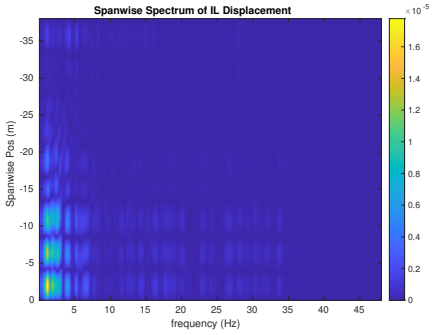

(f) Spanwise inline spectrum of hydrodynamic displacement case 4110.

Figure C-127: *Motion Analysis.* NDP Straight Riser ($L = 38m$) test case 4110.

NDP Straight Riser ($L = 38m$) test case 4120

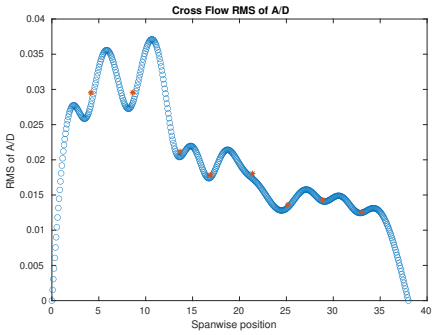

(a) Cross-flow RMS profile case 4120.

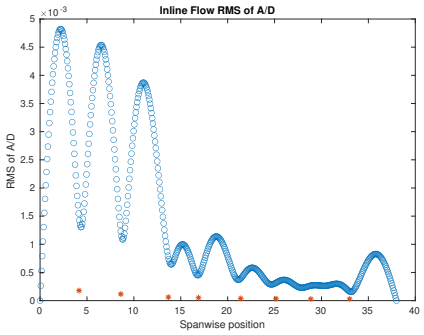

(b) Inline flow RMS profile case 4120.

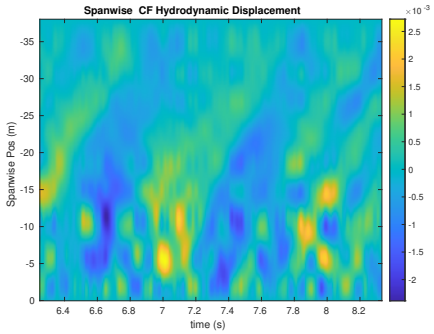

(c) Spanwise cross-flow hydrodynamic displacement case 4120.

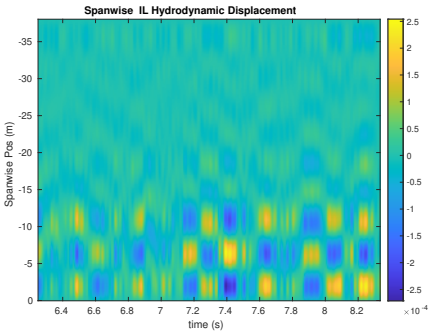

(d) Spanwise inline hydrodynamic displacement case 4120.

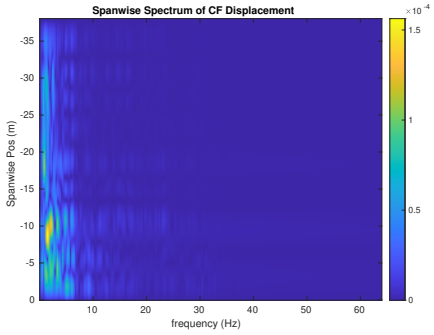

(e) Spanwise cross-flow spectrum of hydrodynamic displacement case 4120.

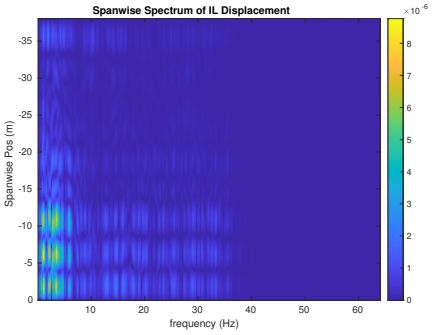

(f) Spanwise inline spectrum of hydrodynamic displacement case 4120.

Figure C-128: *Motion Analysis.* NDP Straight Riser ($L = 38m$) test case 4120.

NDP Straight Riser ($L = 38m$) test case 4130

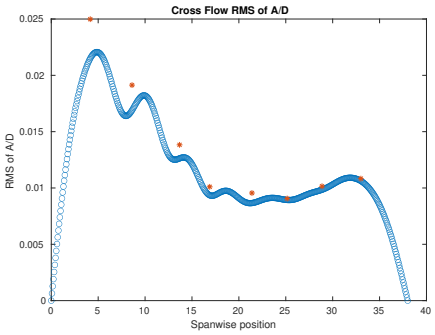

(a) Cross-flow RMS profile case 4130.

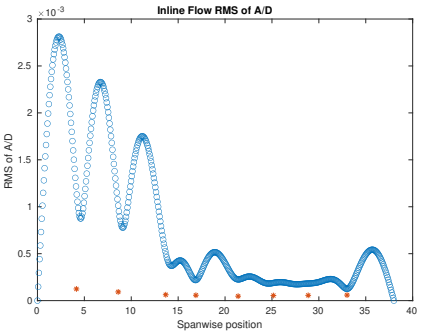

(b) Inline flow RMS profile case 4130.

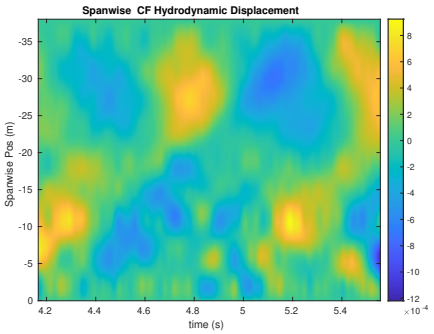

(c) Spanwise cross-flow hydrodynamic displacement case 4130.

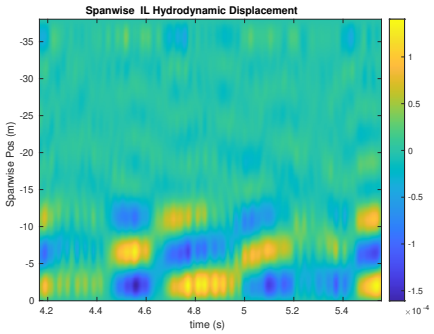

(d) Spanwise inline hydrodynamic displacement case 4130.

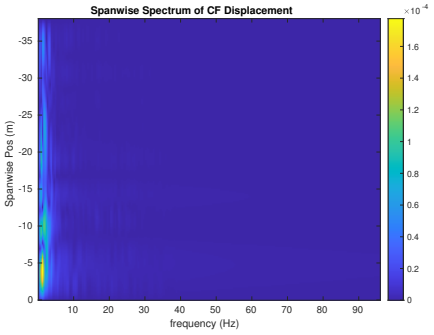

(e) Spanwise cross-flow spectrum of hydrodynamic displacement case 4130.

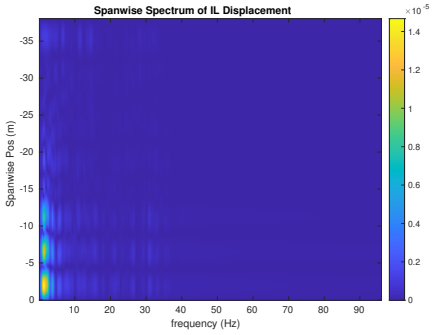

(f) Spanwise inline spectrum of hydrodynamic displacement case 4130.

Figure C-129: *Motion Analysis.* NDP Straight Riser ($L = 38m$) test case 4130.

NDP Straight Riser ($L = 38m$) test case 4220

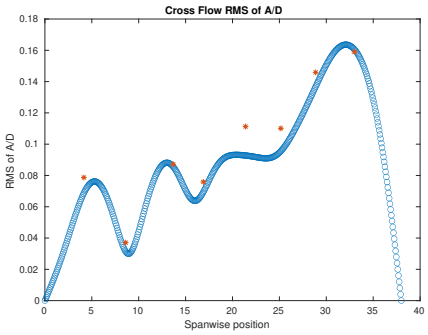

(a) Cross-flow RMS profile case 4220.

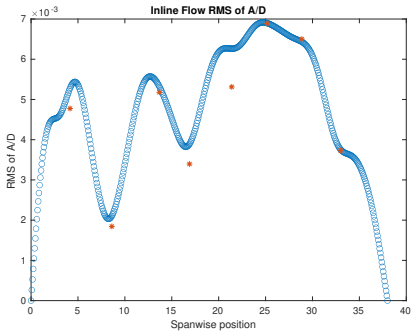

(b) Inline flow RMS profile case 4220.

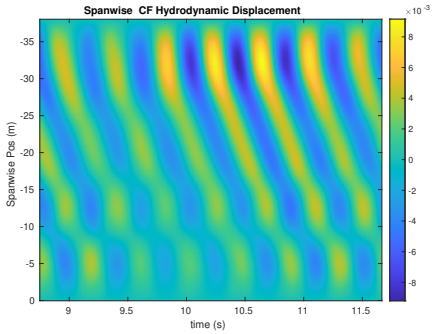

(c) Spanwise cross-flow hydrodynamic displacement case 4220.

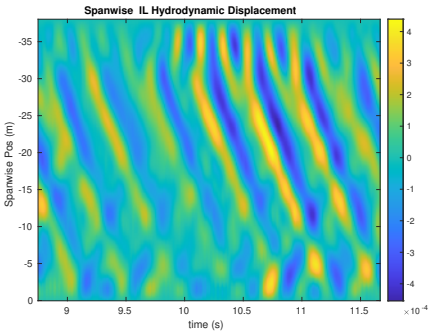

(d) Spanwise inline hydrodynamic displacement case 4220.

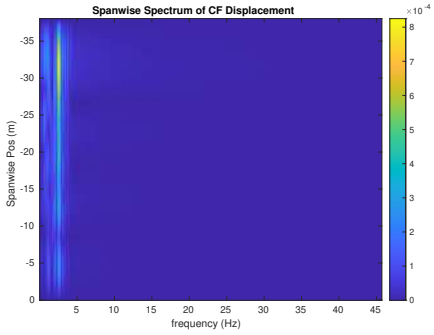

(e) Spanwise cross-flow spectrum of hydrodynamic displacement case 4220.

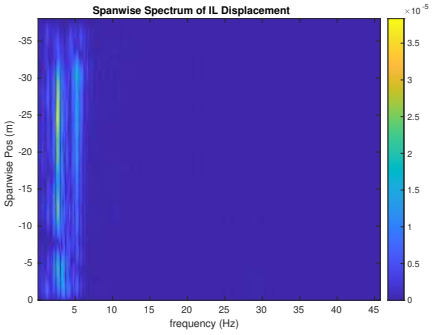

(f) Spanwise inline spectrum of hydrodynamic displacement case 4220.

Figure C-130: *Motion Analysis.* NDP Straight Riser ($L = 38m$) test case 4220.

NDP Straight Riser ($L = 38m$) test case 4240

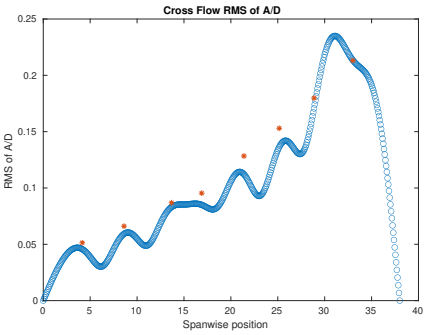

(a) Cross-flow RMS profile case 4240.

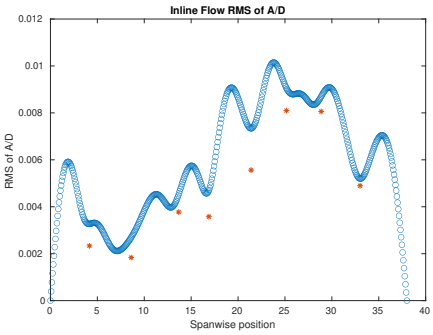

(b) Inline flow RMS profile case 4240.

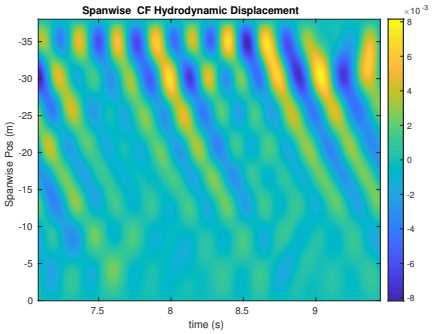

(c) Spanwise cross-flow hydrodynamic displacement case 4240.

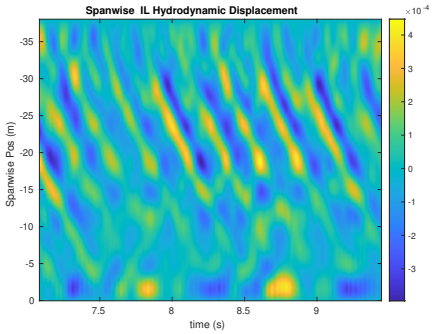

(d) Spanwise inline hydrodynamic displacement case 4240.

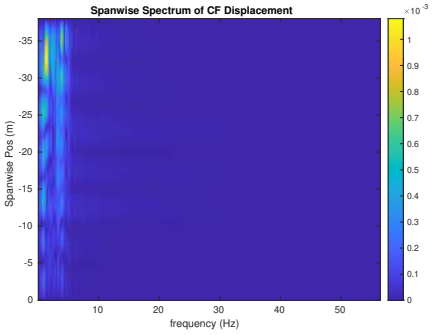

(e) Spanwise cross-flow spectrum of hydrodynamic displacement case 4240.

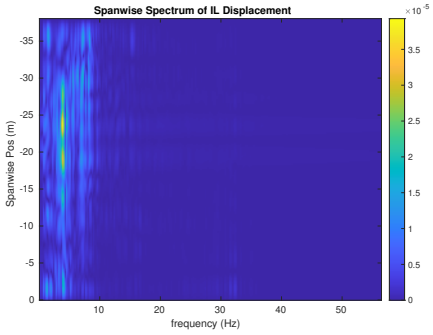

(f) Spanwise inline spectrum of hydrodynamic displacement case 4240.

Figure C-131: *Motion Analysis.* NDP Straight Riser ($L = 38m$) test case 4240.

NDP Straight Riser ($L = 38m$) test case 4260

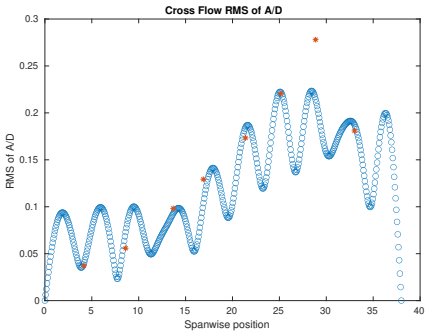

(a) Cross-flow RMS profile case 4260.

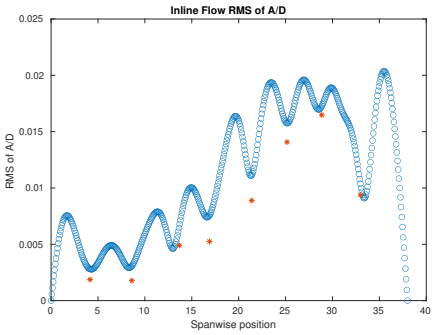

(b) Inline flow RMS profile case 4260.

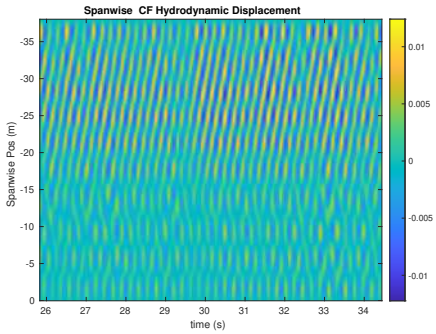

(c) Spanwise cross-flow hydrodynamic displacement case 4260.

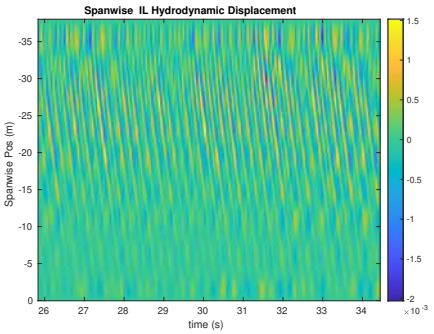

(d) Spanwise inline hydrodynamic displacement case 4260.

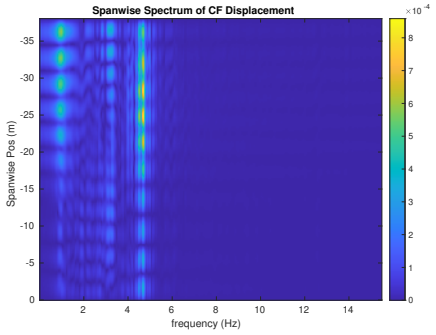

(e) Spanwise cross-flow spectrum of hydrodynamic displacement case 4260.

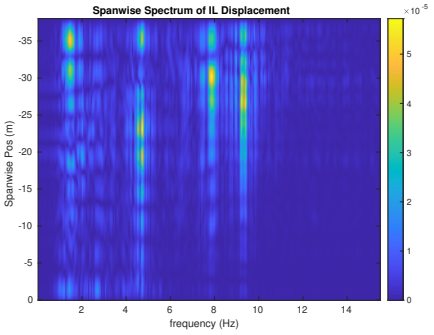

(f) Spanwise inline spectrum of hydrodynamic displacement case 4260.

Figure C-132: *Motion Analysis.* NDP Straight Riser ($L = 38m$) test case 4260.

NDP Straight Riser ($L = 38m$) test case 4280

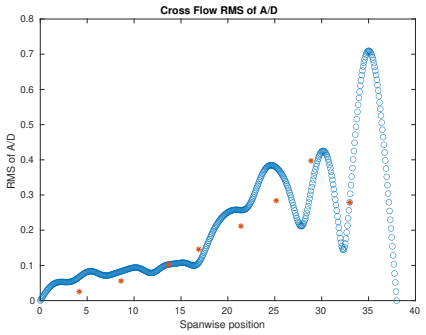

(a) Cross-flow RMS profile case 4280.

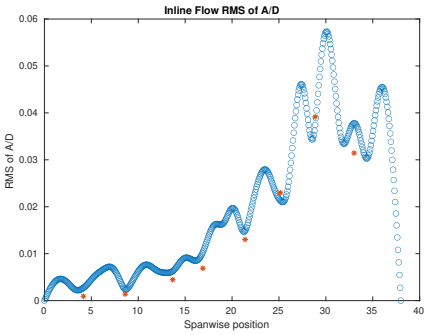

(b) Inline flow RMS profile case 4280.

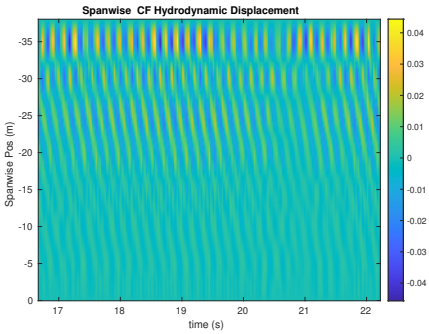

(c) Spanwise cross-flow hydrodynamic displacement case 4280.

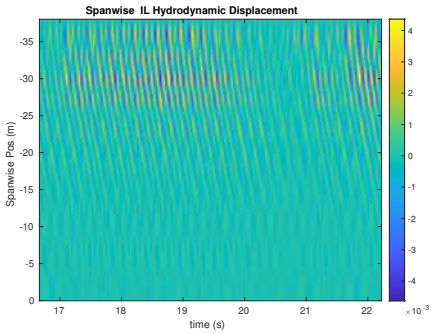

(d) Spanwise inline hydrodynamic displacement case 4280.

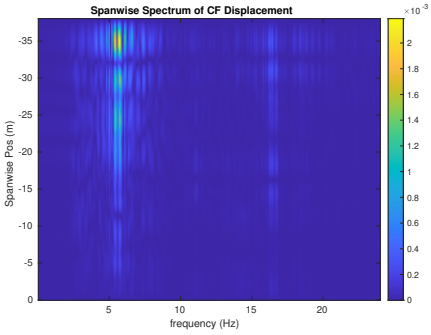

(e) Spanwise cross-flow spectrum of hydrodynamic displacement case 4280.

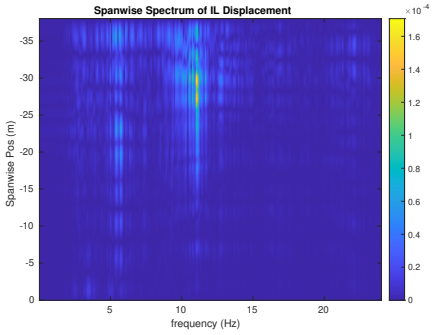

(f) Spanwise inline spectrum of hydrodynamic displacement case 4280.

Figure C-133: *Motion Analysis.* NDP Straight Riser ($L = 38m$) test case 4280.

NDP Straight Riser ($L = 38m$) test case 4300

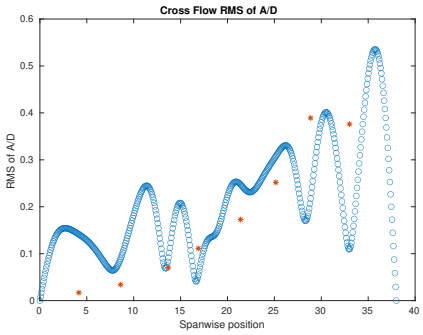

(a) Cross-flow RMS profile case 4300.

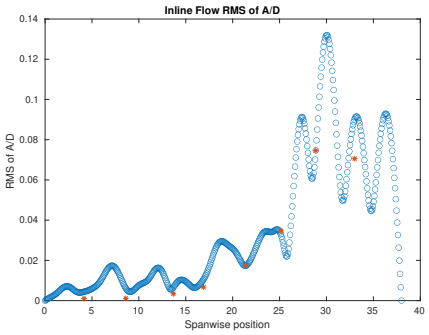

(b) Inline flow RMS profile case 4300.

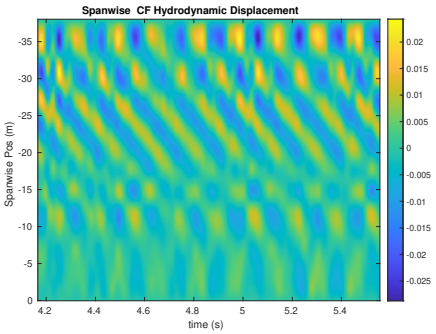

(c) Spanwise cross-flow hydrodynamic displacement case 4300.

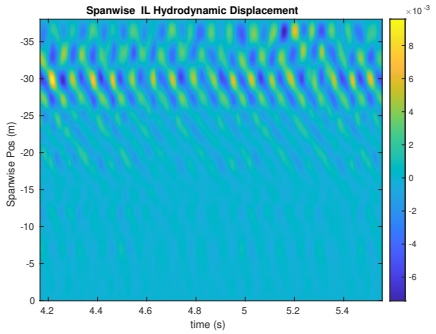

(d) Spanwise inline hydrodynamic displacement case 4300.

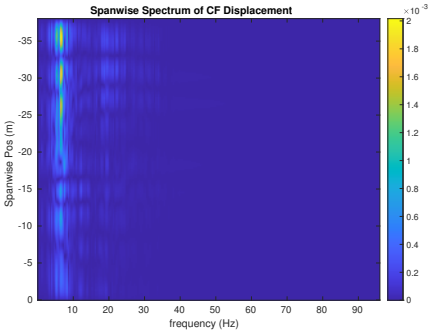

(e) Spanwise cross-flow spectrum of hydrodynamic displacement case 4300.

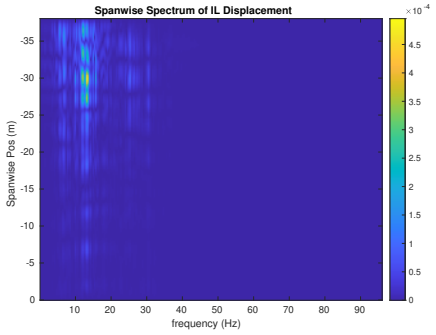

(f) Spanwise inline spectrum of hydrodynamic displacement case 4300.

Figure C-134: *Motion Analysis.* NDP Straight Riser ($L = 38m$) test case 4300.

NDP Straight Riser ($L = 38m$) test case 4320

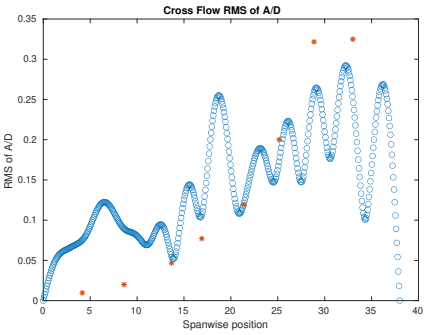

(a) Cross-flow RMS profile case 4320.

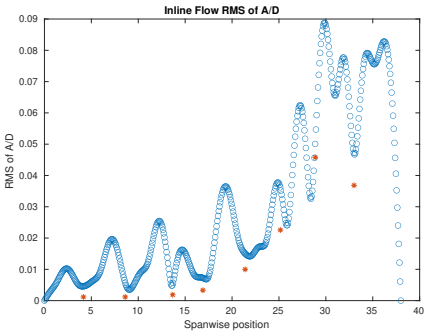

(b) Inline flow RMS profile case 4320.

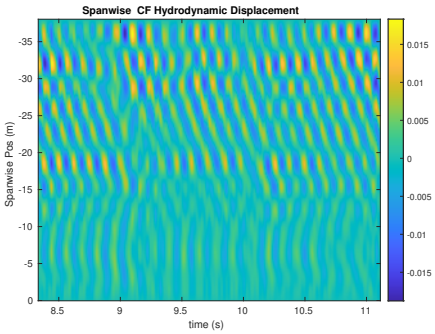

(c) Spanwise cross-flow hydrodynamic displacement case 4320.

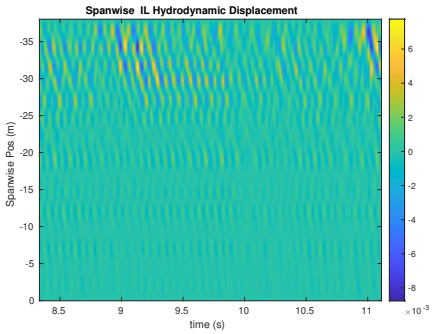

(d) Spanwise inline hydrodynamic displacement case 4320.

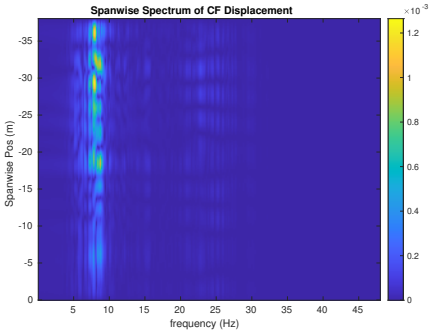

(e) Spanwise cross-flow spectrum of hydrodynamic displacement case 4320.

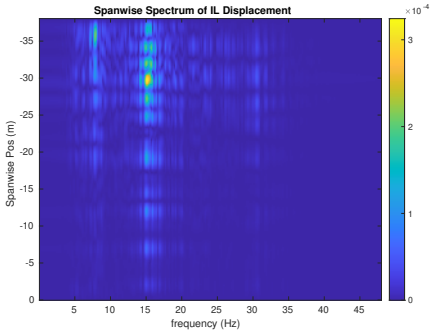

(f) Spanwise inline spectrum of hydrodynamic displacement case 4320.

Figure C-135: *Motion Analysis.* NDP Straight Riser ($L = 38m$) test case 4320.

NDP Straight Riser ($L = 38m$) test case 4340

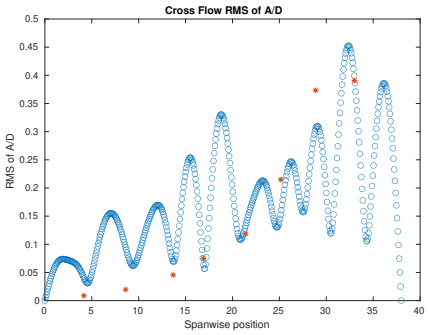

(a) Cross-flow RMS profile case 4340.

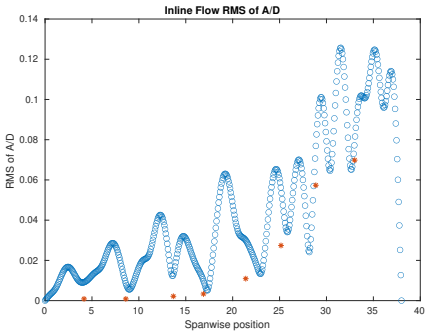

(b) Inline flow RMS profile case 4340.

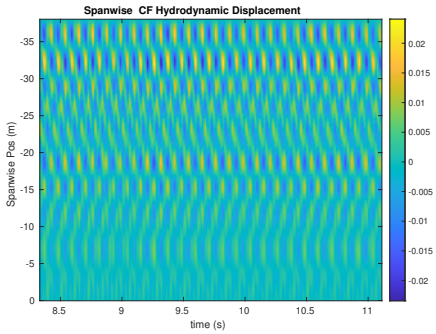

(c) Spanwise cross-flow hydrodynamic displacement case 4340.

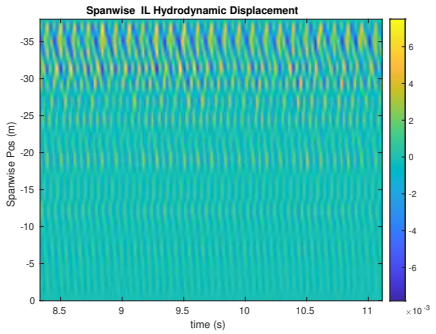

(d) Spanwise inline hydrodynamic displacement case 4340.

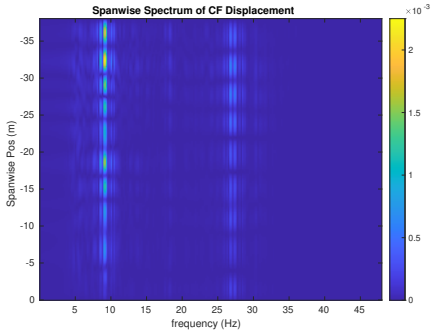

(e) Spanwise cross-flow spectrum of hydrodynamic displacement case 4340.

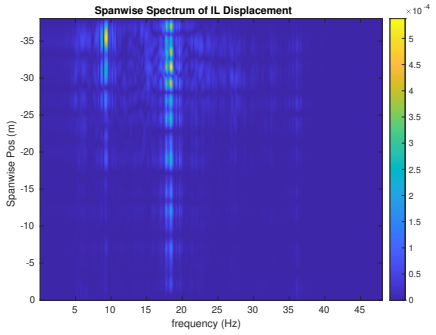

(f) Spanwise inline spectrum of hydrodynamic displacement case 4340.

Figure C-136: *Motion Analysis.* NDP Straight Riser ($L = 38m$) test case 4340.

NDP Straight Riser ($L = 38m$) test case 4360

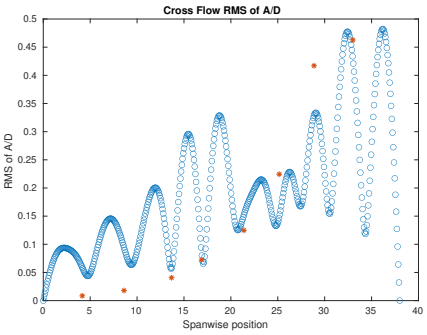

(a) Cross-flow RMS profile case 4360.

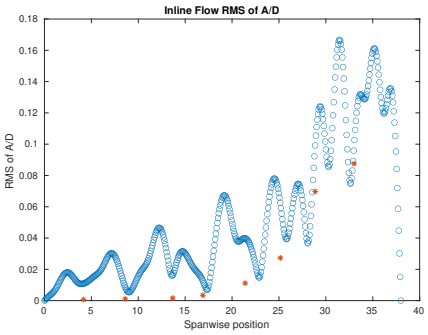

(b) Inline flow RMS profile case 4360.

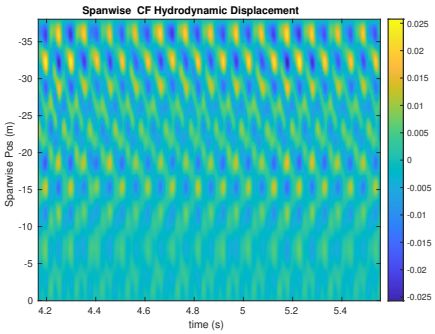

(c) Spanwise cross-flow hydrodynamic displacement case 4360.

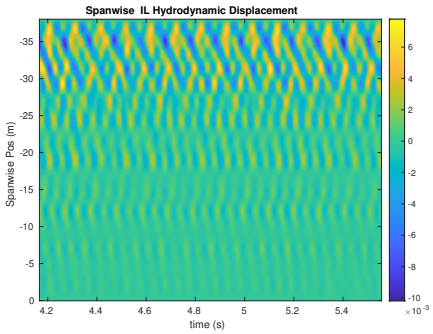

(d) Spanwise inline hydrodynamic displacement case 4360.

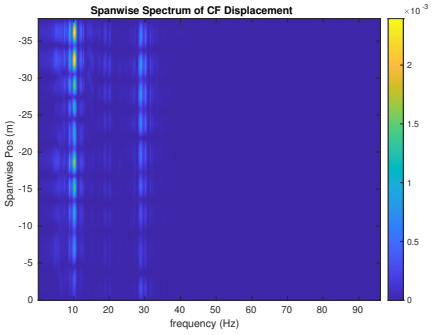

(e) Spanwise cross-flow spectrum of hydrodynamic displacement case 4360.

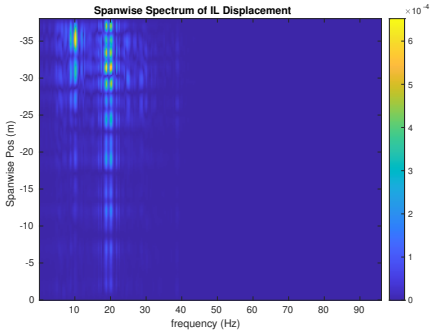

(f) Spanwise inline spectrum of hydrodynamic displacement case 4360.

Figure C-137: *Motion Analysis.* NDP Straight Riser ($L = 38m$) test case 4360.

NDP Straight Riser ($L = 38m$) test case 4380

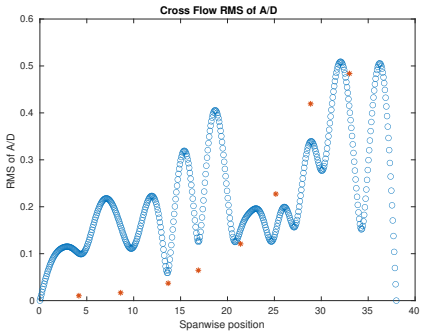

(a) Cross-flow RMS profile case 4380.

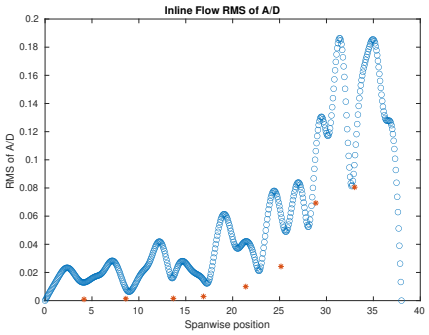

(b) Inline flow RMS profile case 4380.

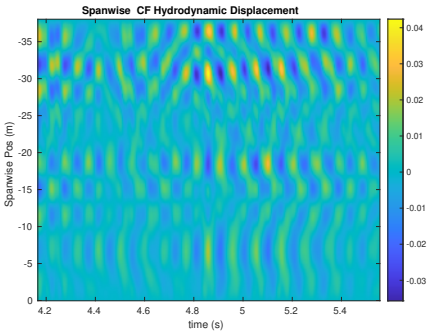

(c) Spanwise cross-flow hydrodynamic displacement case 4380.

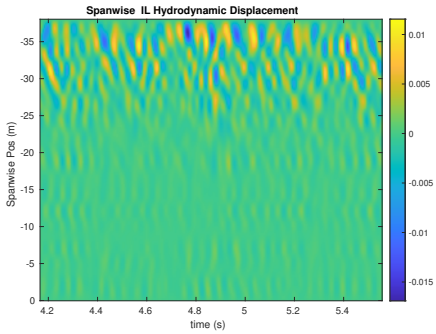

(d) Spanwise inline hydrodynamic displacement case 4380.

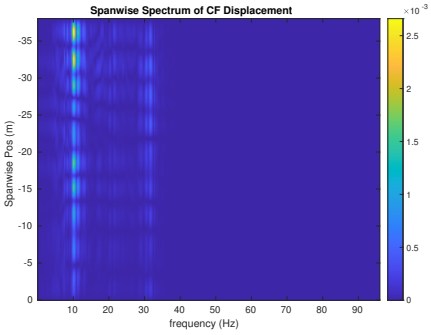

(e) Spanwise cross-flow spectrum of hydrodynamic displacement case 4380.

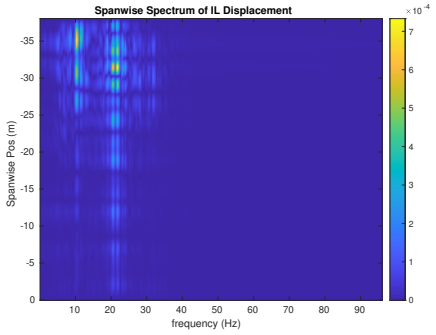

(f) Spanwise inline spectrum of hydrodynamic displacement case 4380.

Figure C-138: *Motion Analysis.* NDP Straight Riser ($L = 38m$) test case 4380.

NDP Straight Riser ($L = 38m$) test case 4400

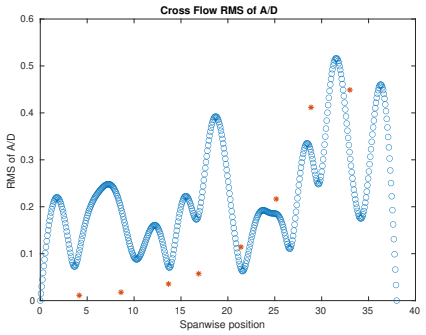

(a) Cross-flow RMS profile case 4400.

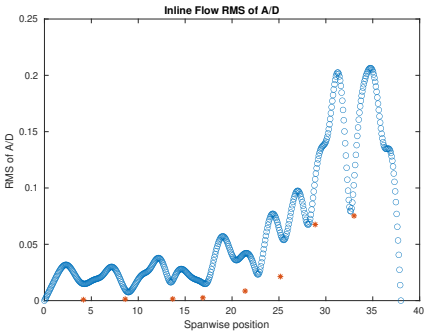

(b) Inline flow RMS profile case 4400.

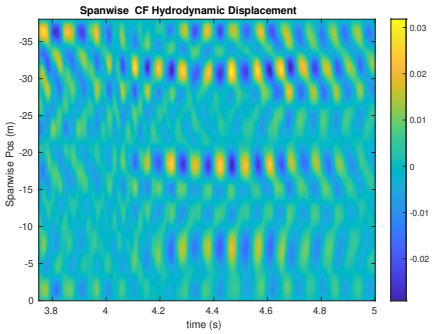

(c) Spanwise cross-flow hydrodynamic displacement case 4400.

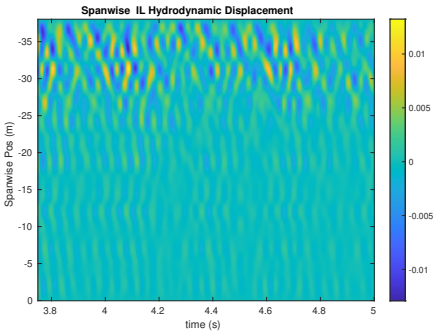

(d) Spanwise inline hydrodynamic displacement case 4400.

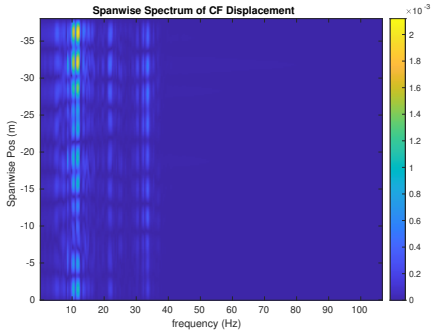

(e) Spanwise cross-flow spectrum of hydrodynamic displacement case 4400.

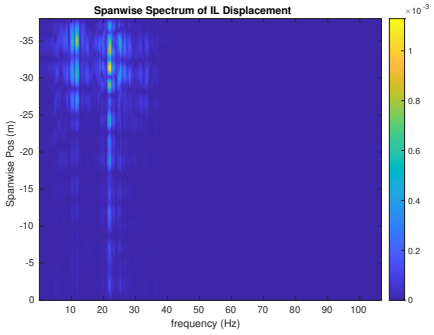

(f) Spanwise inline spectrum of hydrodynamic displacement case 4400.

Figure C-139: *Motion Analysis.* NDP Straight Riser ($L = 38m$) test case 4400.

NDP Straight Riser ($L = 38m$) test case 4420

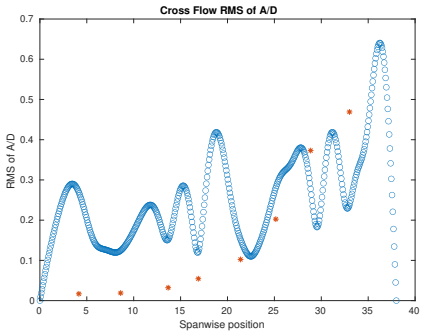

(a) Cross-flow RMS profile case 4420.

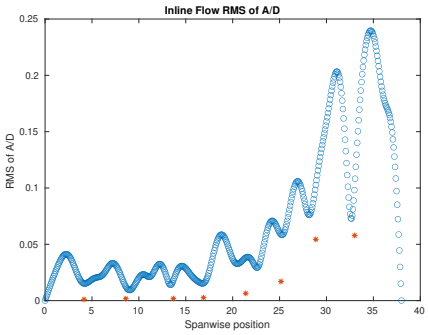

(b) Inline flow RMS profile case 4420.

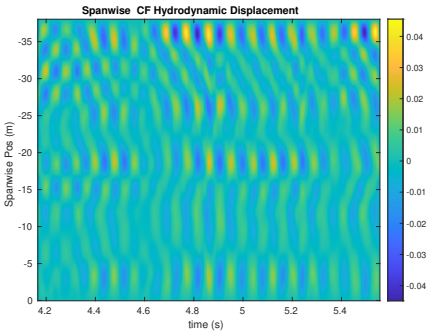

(c) Spanwise cross-flow hydrodynamic displacement case 4420.

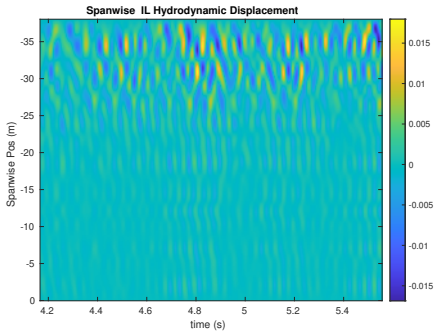

(d) Spanwise inline hydrodynamic displacement case 4420.

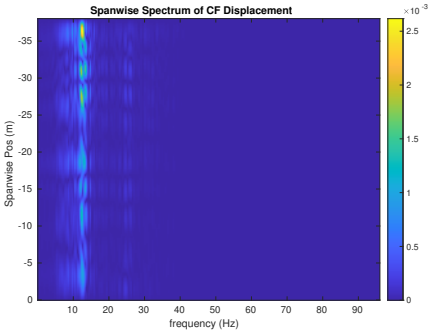

(e) Spanwise cross-flow spectrum of hydrodynamic displacement case 4420.

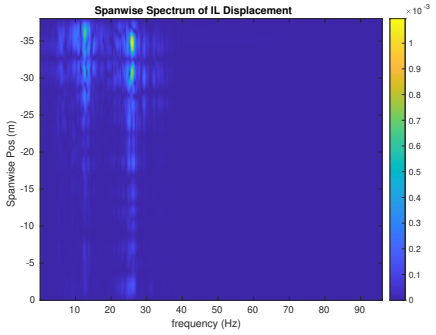

(f) Spanwise inline spectrum of hydrodynamic displacement case 4420.

Figure C-140: *Motion Analysis.* NDP Straight Riser ($L = 38m$) test case 4420.

NDP Straight Riser ($L = 38m$) test case 4430

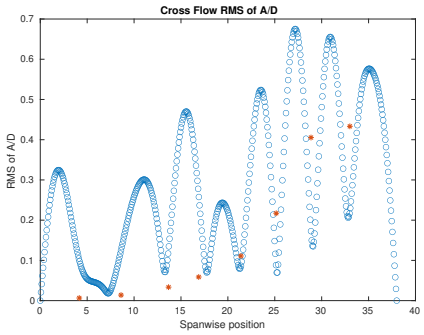

(a) Cross-flow RMS profile case 4430.

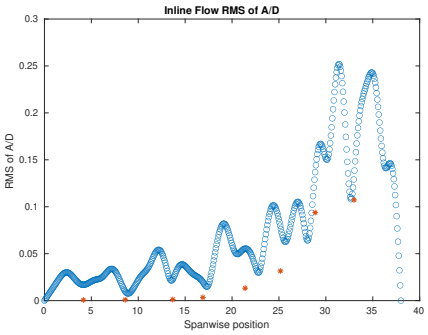

(b) Inline flow RMS profile case 4430.

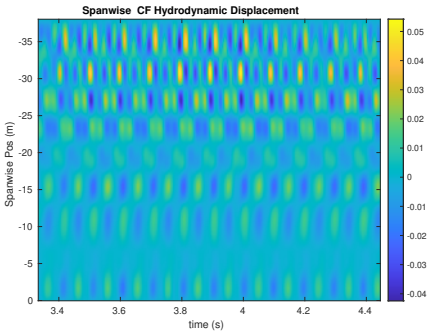

(c) Spanwise cross-flow hydrodynamic displacement case 4430.

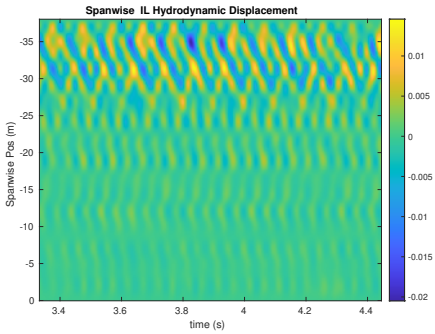

(d) Spanwise inline hydrodynamic displacement case 4430.

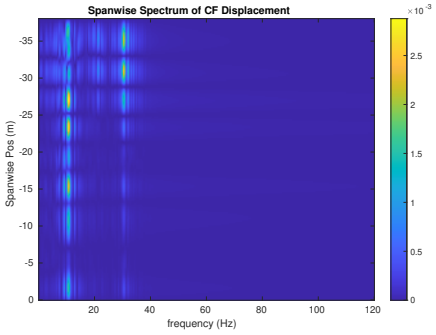

(e) Spanwise cross-flow spectrum of hydrodynamic displacement case 4430.

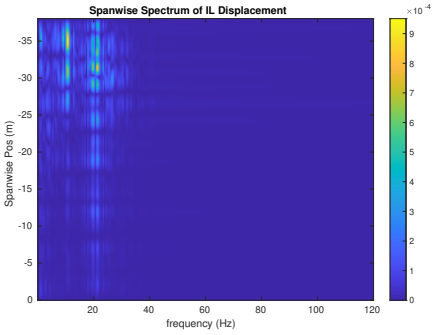

(f) Spanwise inline spectrum of hydrodynamic displacement case 4430.

Figure C-141: *Motion Analysis.* NDP Straight Riser ($L = 38m$) test case 4430.

NDP Straight Riser ($L = 38m$) test case 4520

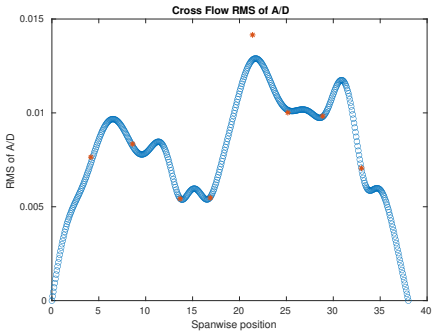

(a) Cross-flow RMS profile case 4520.

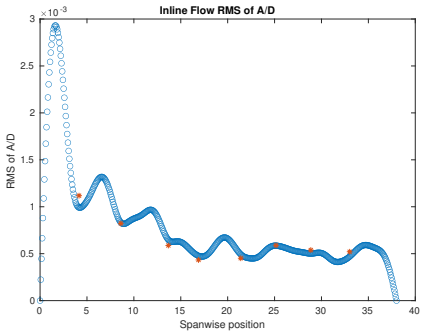

(b) Inline flow RMS profile case 4520.

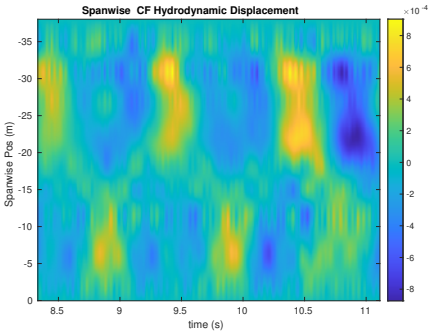

(c) Spanwise cross-flow hydrodynamic displacement case 4520.

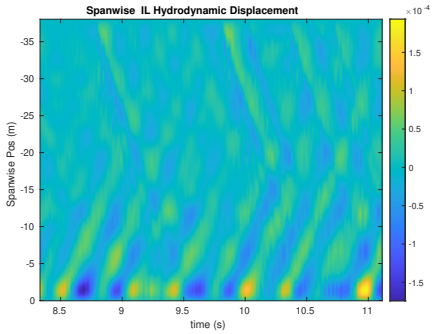

(d) Spanwise inline hydrodynamic displacement case 4520.

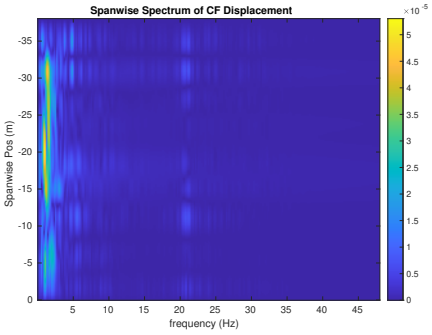

(e) Spanwise cross-flow spectrum of hydrodynamic displacement case 4520.

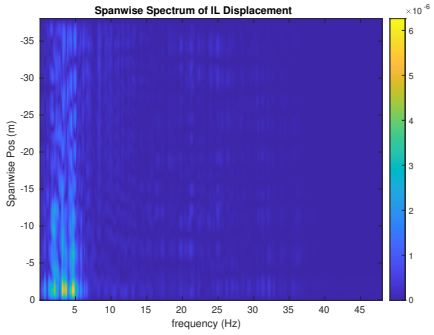

(f) Spanwise inline spectrum of hydrodynamic displacement case 4520.

Figure C-142: *Motion Analysis.* NDP Straight Riser ($L = 38m$) test case 4520.

NDP Straight Riser ($L = 38m$) test case 4540

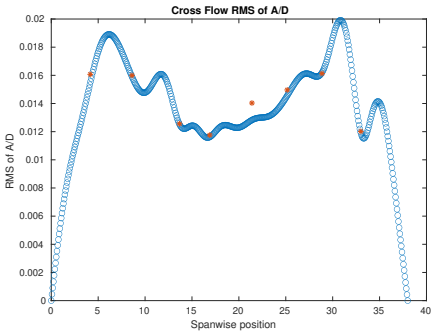

(a) Cross-flow RMS profile case 4540.

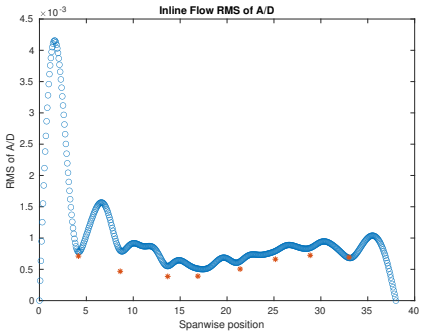

(b) Inline flow RMS profile case 4540.

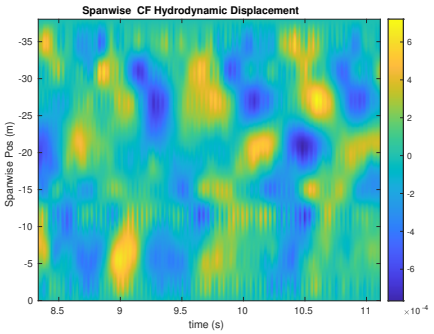

(c) Spanwise cross-flow hydrodynamic displacement case 4540.

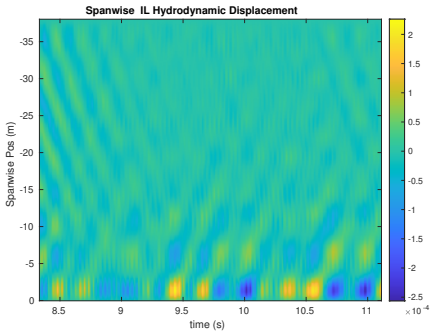

(d) Spanwise inline hydrodynamic displacement case 4540.

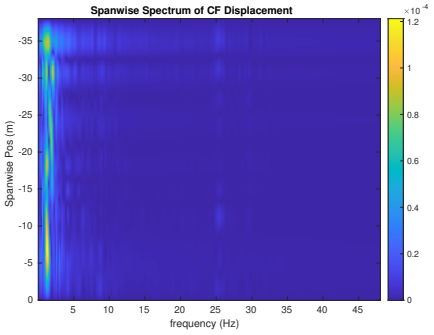

(e) Spanwise cross-flow spectrum of hydrodynamic displacement case 4540.

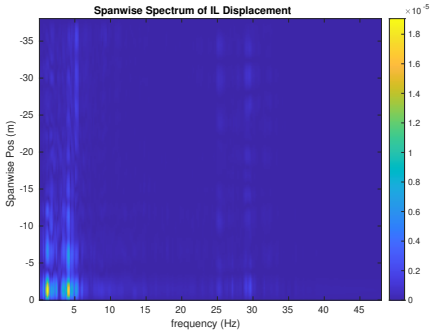

(f) Spanwise inline spectrum of hydrodynamic displacement case 4540.

Figure C-143: *Motion Analysis.* NDP Straight Riser ($L = 38m$) test case 4540.

NDP Straight Riser ($L = 38m$) test case 4560

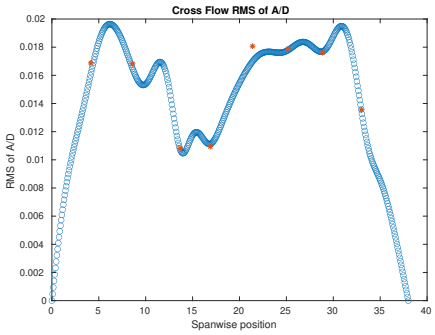

(a) Cross-flow RMS profile case 4560.

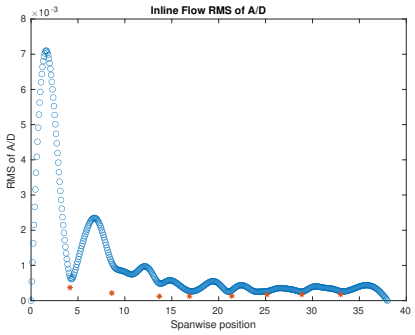

(b) Inline flow RMS profile case 4560.

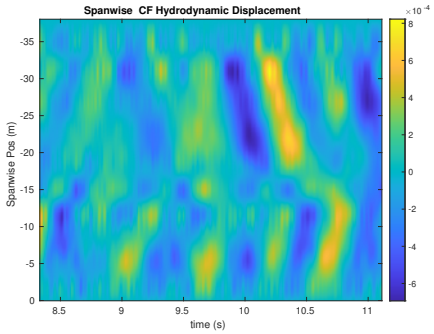

(c) Spanwise cross-flow hydrodynamic displacement case 4560.

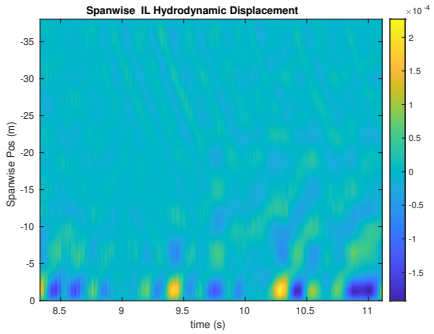

(d) Spanwise inline hydrodynamic displacement case 4560.

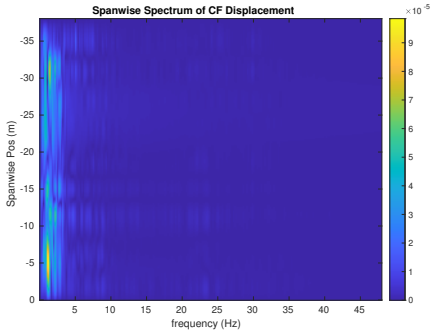

(e) Spanwise cross-flow spectrum of hydrodynamic displacement case 4560.

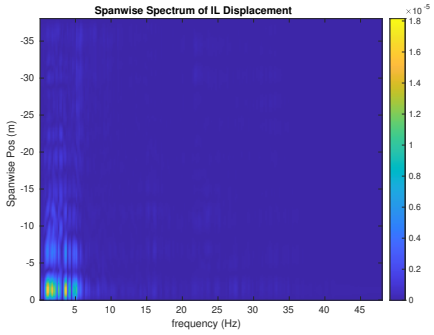

(f) Spanwise inline spectrum of hydrodynamic displacement case 4560.

Figure C-144: *Motion Analysis.* NDP Straight Riser ($L = 38m$) test case 4560.

NDP Straight Riser ($L = 38m$) test case 4580

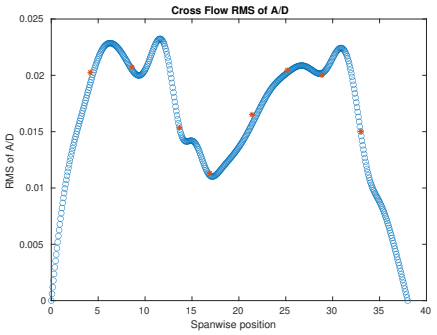

(a) Cross-flow RMS profile case 4580.

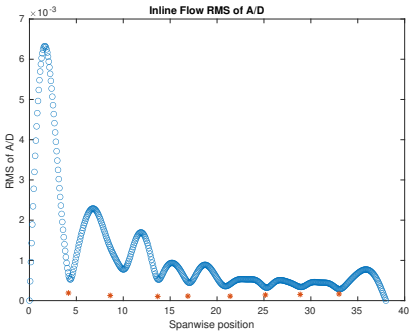

(b) Inline flow RMS profile case 4580.

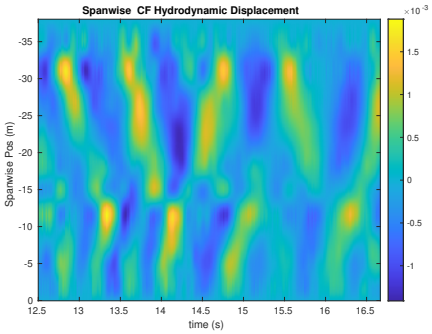

(c) Spanwise cross-flow hydrodynamic displacement case 4580.

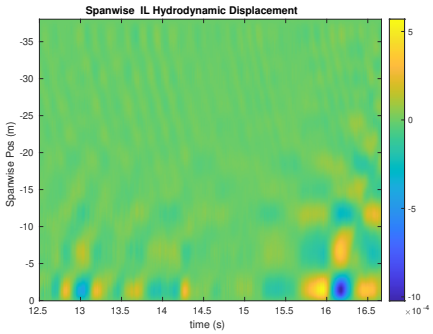

(d) Spanwise inline hydrodynamic displacement case 4580.

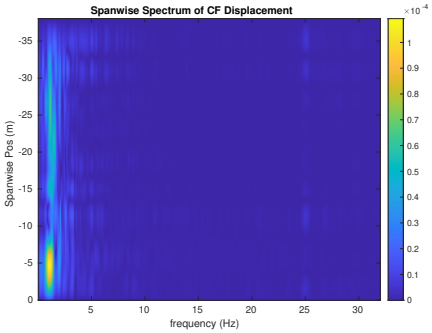

(e) Spanwise cross-flow spectrum of hydrodynamic displacement case 4580.

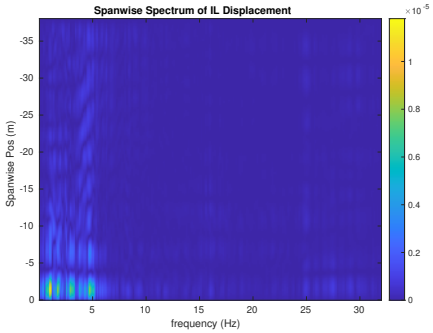

(f) Spanwise inline spectrum of hydrodynamic displacement case 4580.

Figure C-145: *Motion Analysis.* NDP Straight Riser ($L = 38m$) test case 4580.

NDP Straight Riser ($L = 38m$) test case 4600

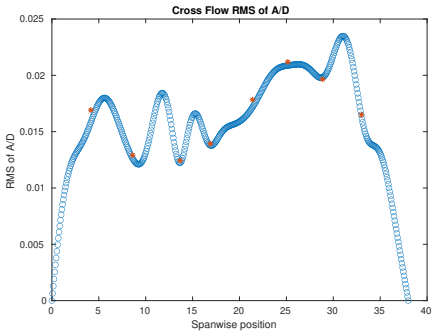

(a) Cross-flow RMS profile case 4600.

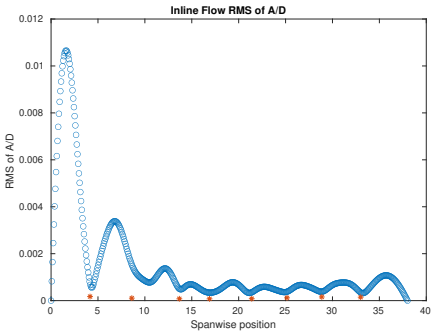

(b) Inline flow RMS profile case 4600.

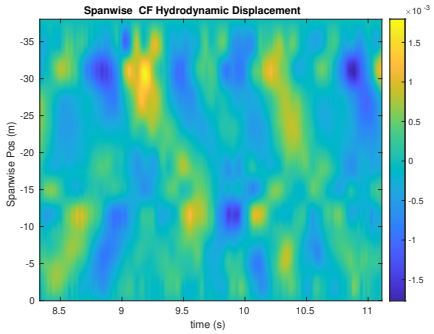

(c) Spanwise cross-flow hydrodynamic displacement case 4600.

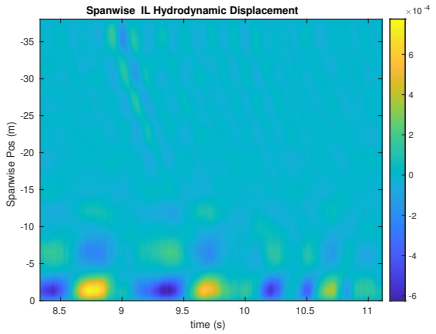

(d) Spanwise inline hydrodynamic displacement case 4600.

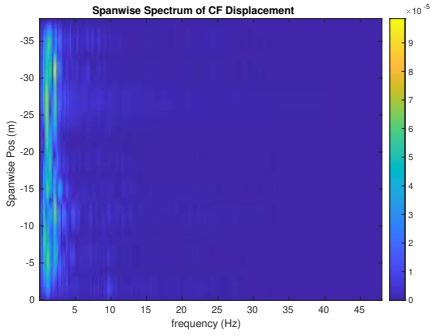

(e) Spanwise cross-flow spectrum of hydrodynamic displacement case 4600.

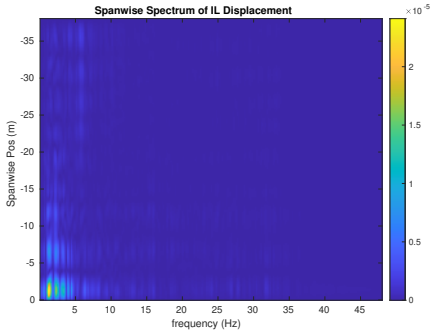

(f) Spanwise inline spectrum of hydrodynamic displacement case 4600.

Figure C-146: *Motion Analysis.* NDP Straight Riser ($L = 38m$) test case 4600.

NDP Straight Riser ($L = 38m$) test case 4620

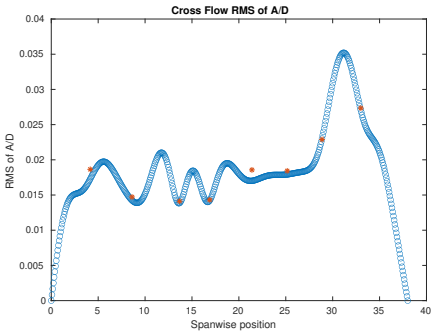

(a) Cross-flow RMS profile case 4620.

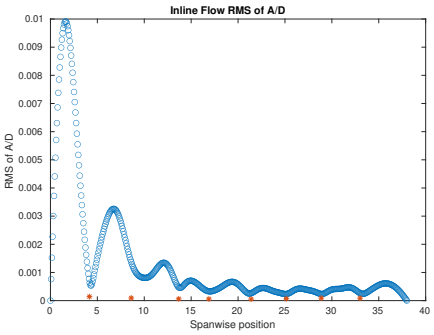

(b) Inline flow RMS profile case 4620.

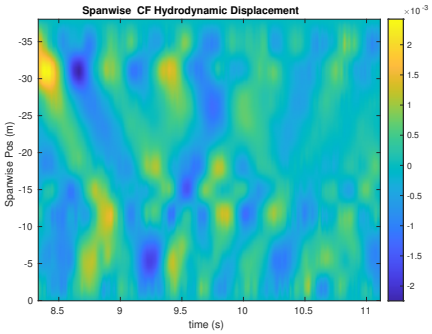

(c) Spanwise cross-flow hydrodynamic displacement case 4620.

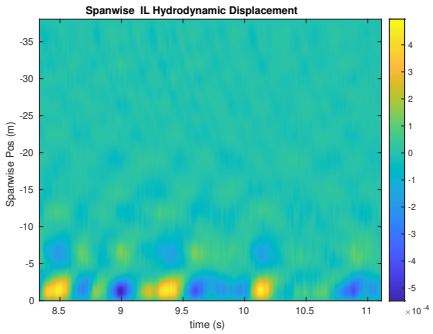

(d) Spanwise inline hydrodynamic displacement case 4620.

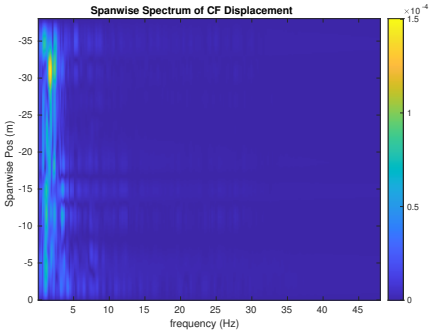

(e) Spanwise cross-flow spectrum of hydrodynamic displacement case 4620.

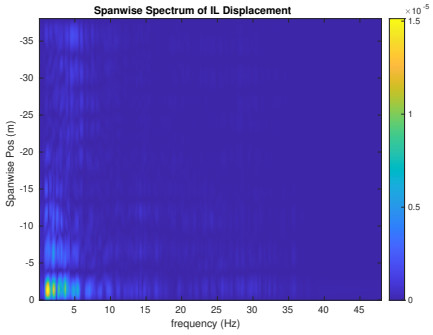

(f) Spanwise inline spectrum of hydrodynamic displacement case 4620.

Figure C-147: *Motion Analysis.* NDP Straight Riser ($L = 38m$) test case 4620.

NDP Straight Riser ($L = 38m$) test case 4640

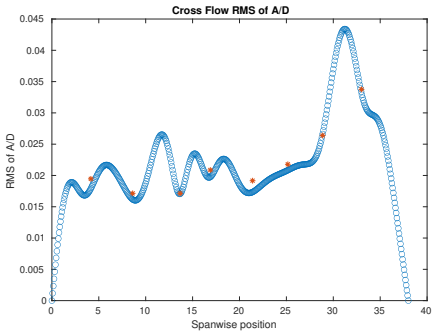

(a) Cross-flow RMS profile case 4640.

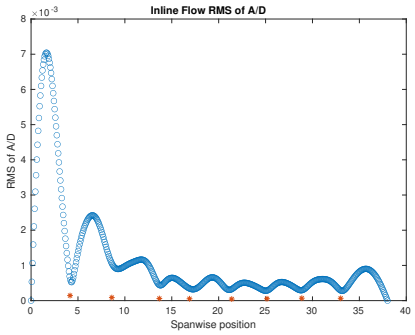

(b) Inline flow RMS profile case 4640.

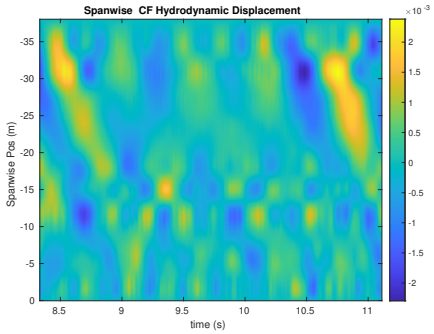

(c) Spanwise cross-flow hydrodynamic displacement case 4640.

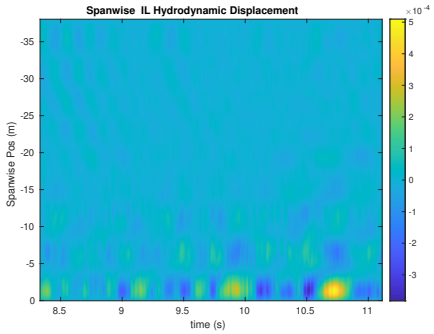

(d) Spanwise inline hydrodynamic displacement case 4640.

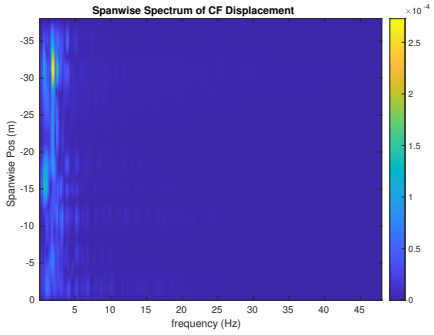

(e) Spanwise cross-flow spectrum of hydrodynamic displacement case 4640.

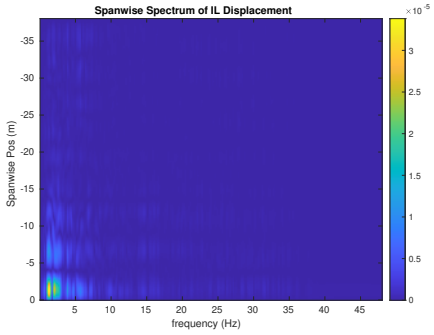

(f) Spanwise inline spectrum of hydrodynamic displacement case 4640.

Figure C-148: *Motion Analysis.* NDP Straight Riser ($L = 38m$) test case 4640.

NDP Straight Riser ($L = 38m$) test case 4660

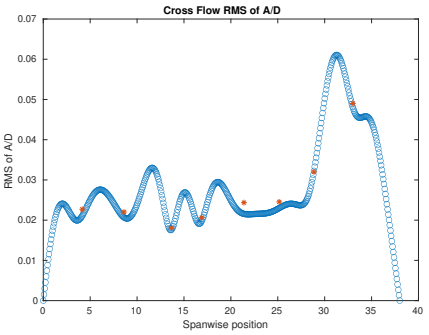

(a) Cross-flow RMS profile case 4660.

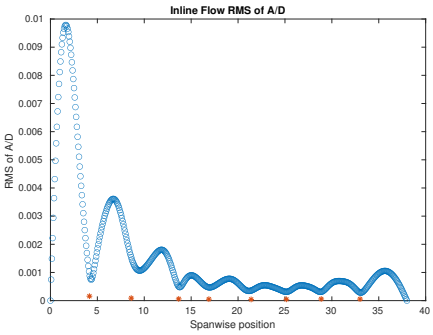

(b) Inline flow RMS profile case 4660.

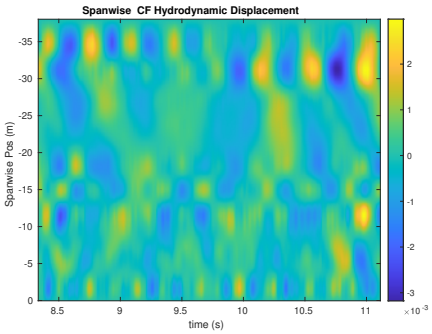

(c) Spanwise cross-flow hydrodynamic displacement case 4660.

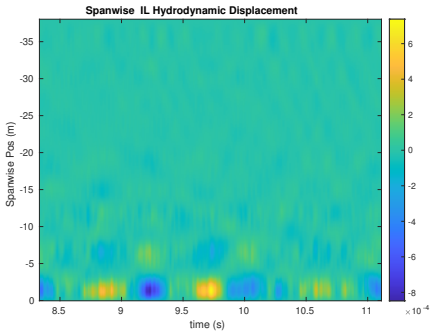

(d) Spanwise inline hydrodynamic displacement case 4660.

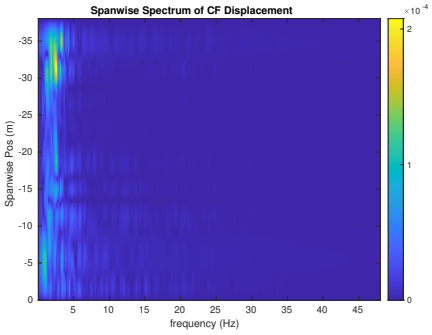

(e) Spanwise cross-flow spectrum of hydrodynamic displacement case 4660.

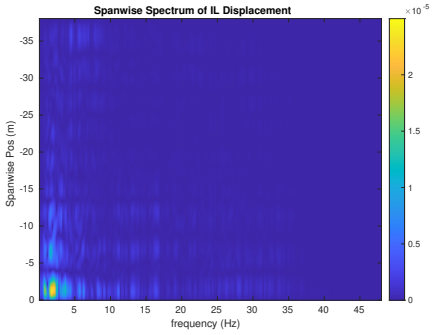

(f) Spanwise inline spectrum of hydrodynamic displacement case 4660.

Figure C-149: *Motion Analysis.* NDP Straight Riser ($L = 38m$) test case 4660.

NDP Straight Riser ($L = 38m$) test case 4680

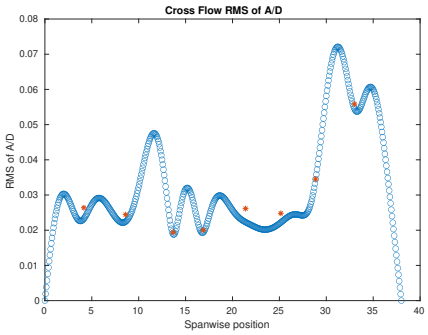

(a) Cross-flow RMS profile case 4680.

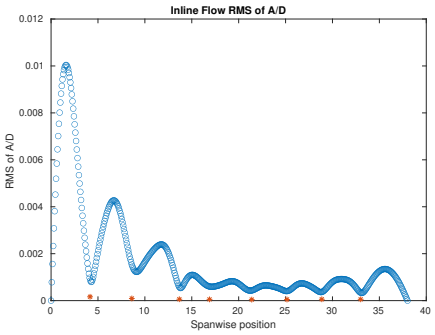

(b) Inline flow RMS profile case 4680.

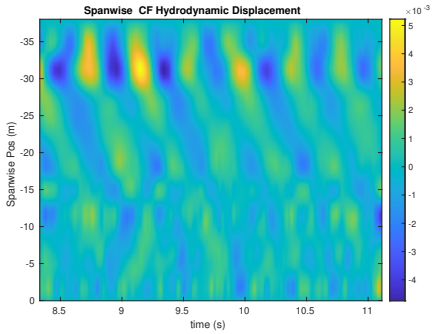

(c) Spanwise cross-flow hydrodynamic displacement case 4680.

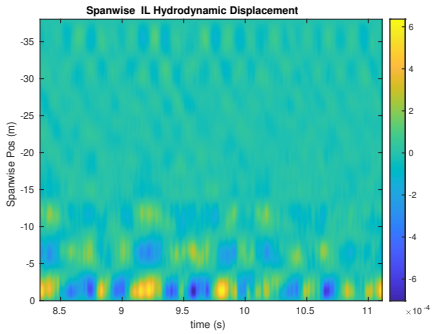

(d) Spanwise inline hydrodynamic displacement case 4680.

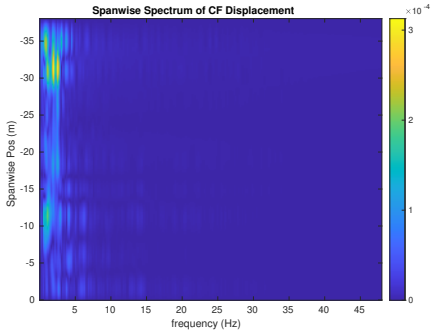

(e) Spanwise cross-flow spectrum of hydrodynamic displacement case 4680.

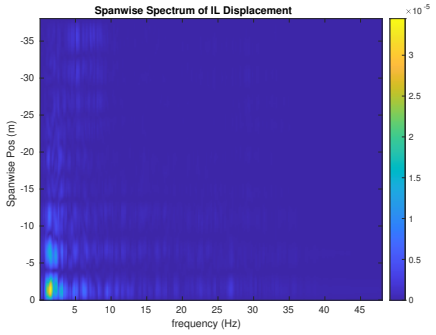

(f) Spanwise inline spectrum of hydrodynamic displacement case 4680.

Figure C-150: *Motion Analysis.* NDP Straight Riser ($L = 38m$) test case 4680.

NDP Straight Riser ($L = 38m$) test case 4700

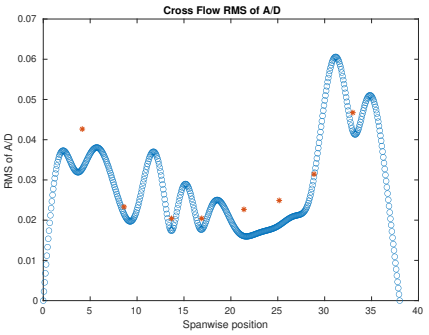

(a) Cross-flow RMS profile case 4700.

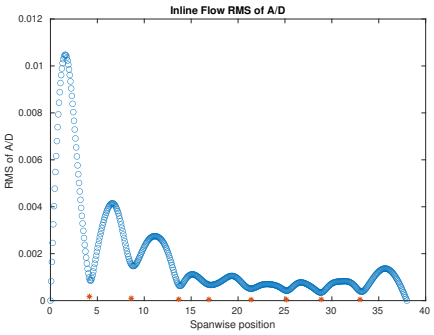

(b) Inline flow RMS profile case 4700.

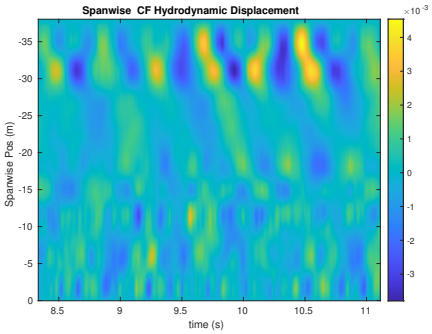

(c) Spanwise cross-flow hydrodynamic displacement case 4700.

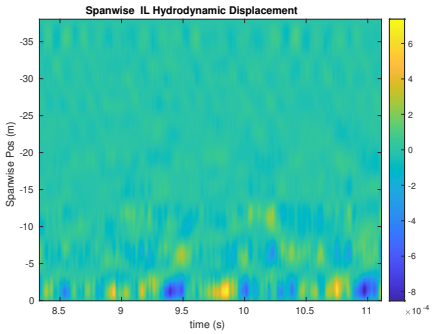

(d) Spanwise inline hydrodynamic displacement case 4700.

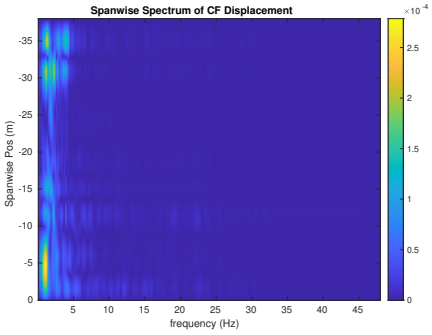

(e) Spanwise cross-flow spectrum of hydrodynamic displacement case 4700.

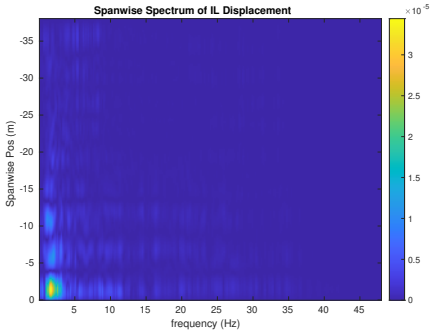

(f) Spanwise inline spectrum of hydrodynamic displacement case 4700.

Figure C-151: *Motion Analysis.* NDP Straight Riser ($L = 38m$) test case 4700.

NDP Straight Riser ($L = 38m$) test case 4720

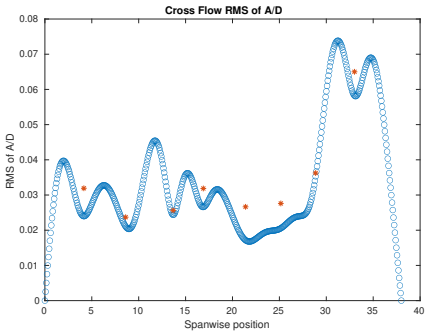

(a) Cross-flow RMS profile case 4720.

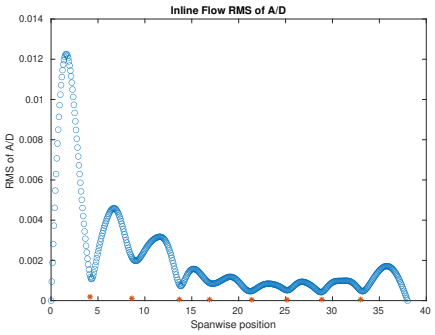

(b) Inline flow RMS profile case 4720.

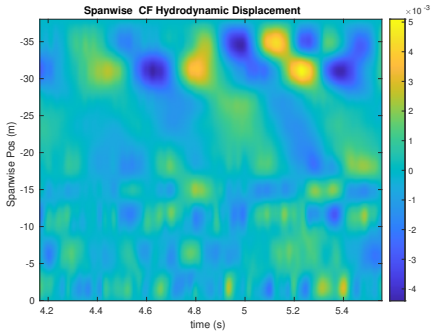

(c) Spanwise cross-flow hydrodynamic displacement case 4720.

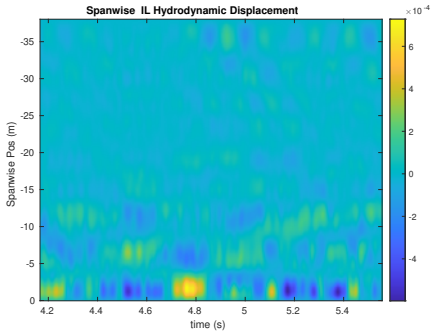

(d) Spanwise inline hydrodynamic displacement case 4720.

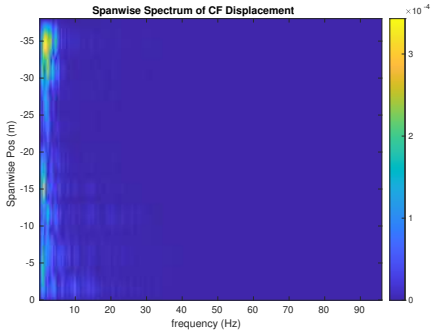

(e) Spanwise cross-flow spectrum of hydrodynamic displacement case 4720.

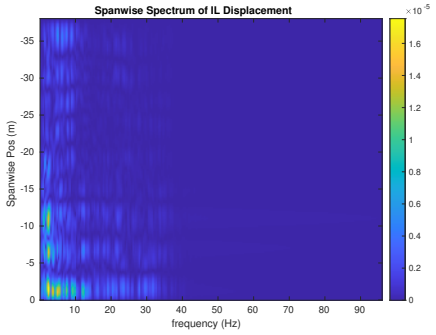

(f) Spanwise inline spectrum of hydrodynamic displacement case 4720.

Figure C-152: *Motion Analysis.* NDP Straight Riser ($L = 38m$) test case 4720.

NDP Straight Riser ($L = 38m$) test case 4730

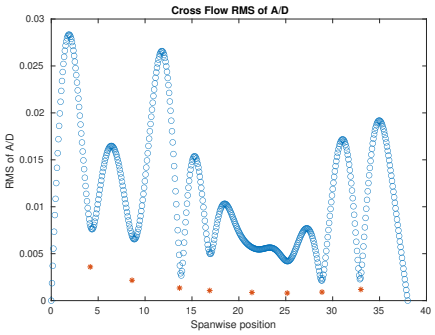

(a) Cross-flow RMS profile case 4730.

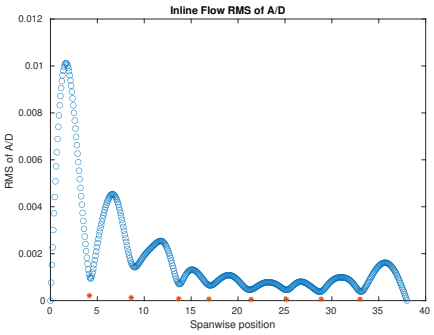

(b) Inline flow RMS profile case 4730.

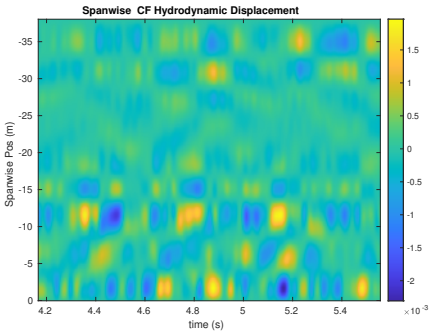

(c) Spanwise cross-flow hydrodynamic displacement case 4730.

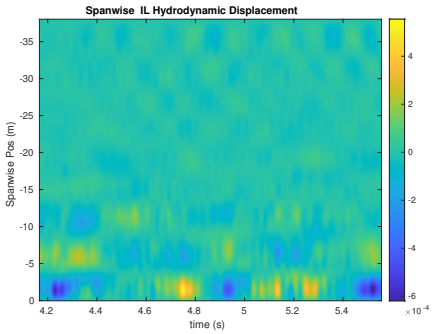

(d) Spanwise inline hydrodynamic displacement case 4730.

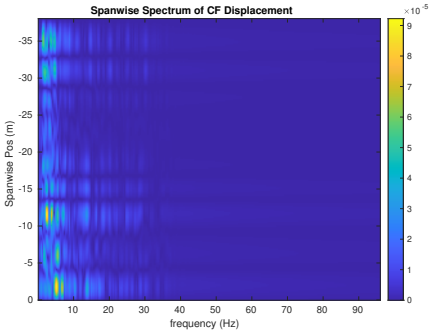

(e) Spanwise cross-flow spectrum of hydrodynamic displacement case 4730.

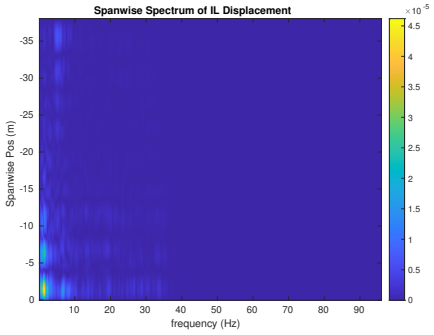

(f) Spanwise inline spectrum of hydrodynamic displacement case 4730.

Figure C-153: *Motion Analysis.* NDP Straight Riser ($L = 38m$) test case 4730.

NDP Straight Riser ($L = 38m$) test case 4811

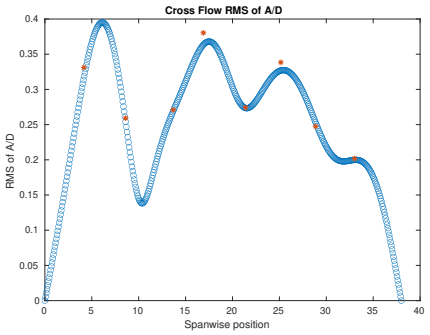

(a) Cross-flow RMS profile case 4811.

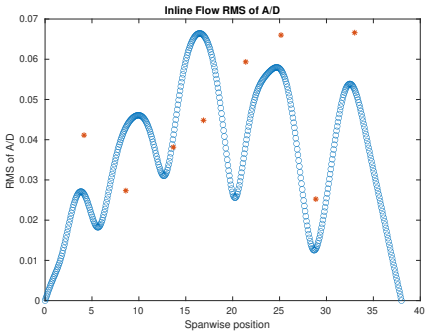

(b) Inline flow RMS profile case 4811.

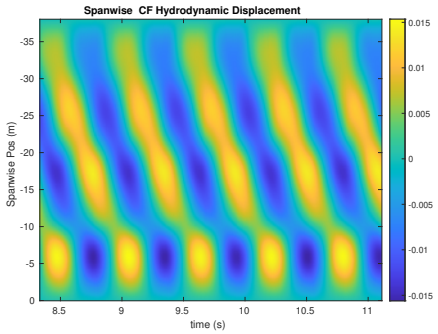

(c) Spanwise cross-flow hydrodynamic displacement case 4811.

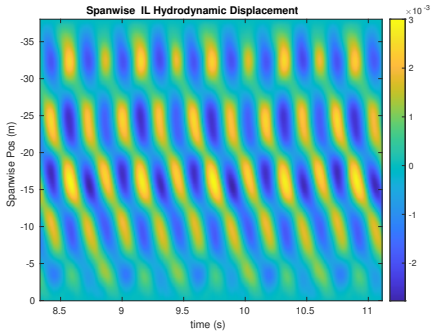

(d) Spanwise inline hydrodynamic displacement case 4811.

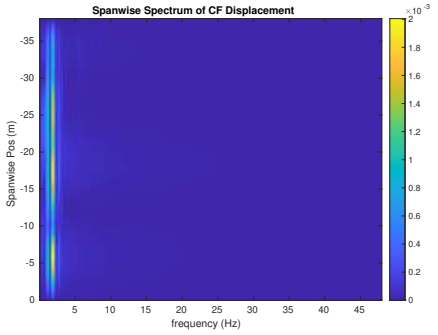

(e) Spanwise cross-flow spectrum of hydrodynamic displacement case 4811.

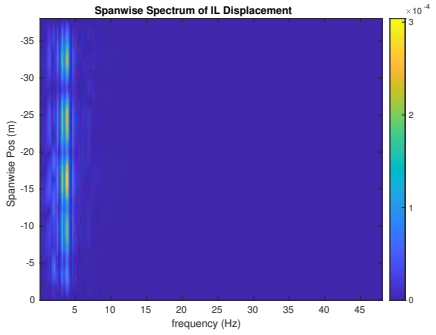

(f) Spanwise inline spectrum of hydrodynamic displacement case 4811.

Figure C-154: *Motion Analysis.* NDP Straight Riser ($L = 38m$) test case 4811.

NDP Straight Riser ($L = 38m$) test case 4820

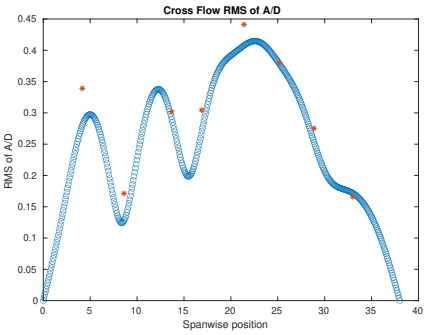

(a) Cross-flow RMS profile case 4820.

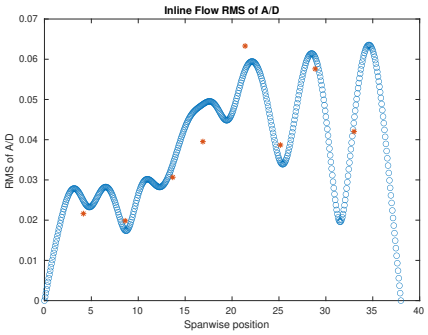

(b) Inline flow RMS profile case 4820.

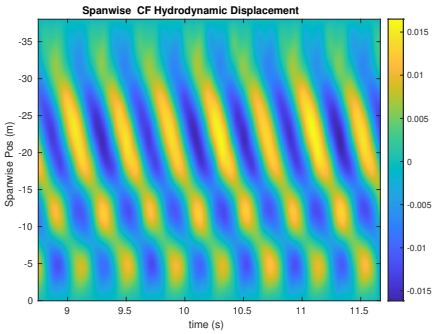

(c) Spanwise cross-flow hydrodynamic displacement case 4820.

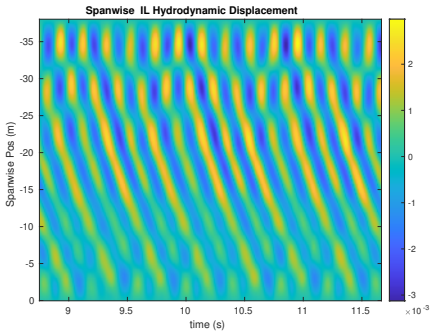

(d) Spanwise inline hydrodynamic displacement case 4820.

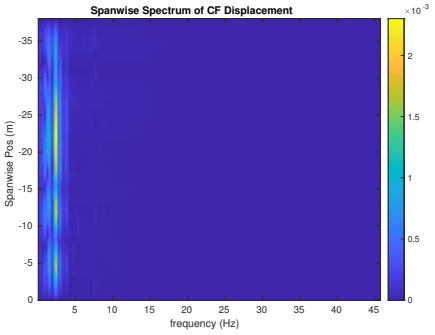

(e) Spanwise cross-flow spectrum of hydrodynamic displacement case 4820.

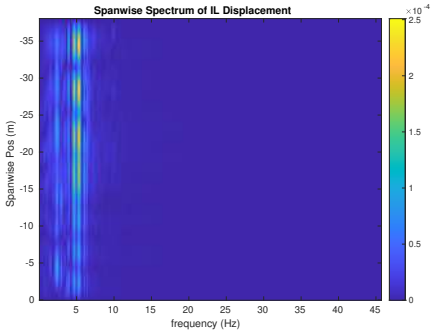

(f) Spanwise inline spectrum of hydrodynamic displacement case 4820.

Figure C-155: *Motion Analysis.* NDP Straight Riser ($L = 38m$) test case 4820.

NDP Straight Riser ($L = 38m$) test case 4830

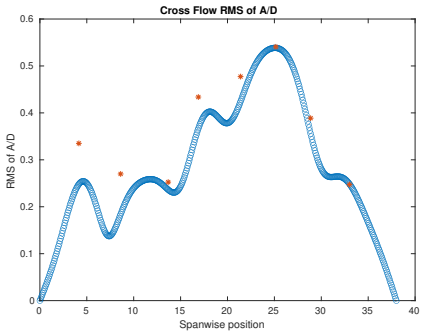

(a) Cross-flow RMS profile case 4830.

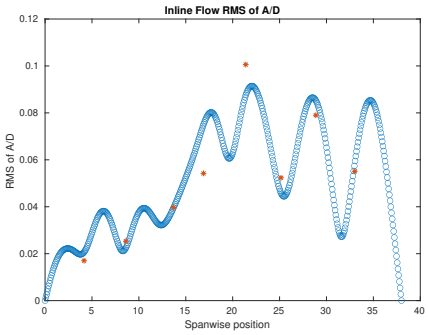

(b) Inline flow RMS profile case 4830.

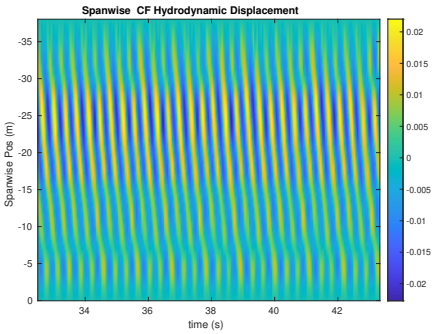

(c) Spanwise cross-flow hydrodynamic displacement case 4830.

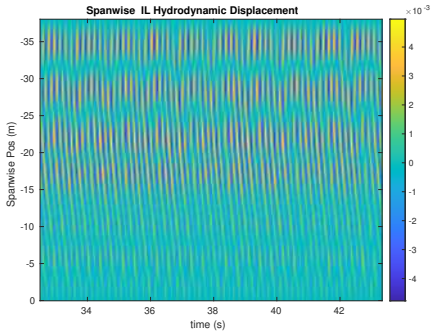

(d) Spanwise inline hydrodynamic displacement case 4830.

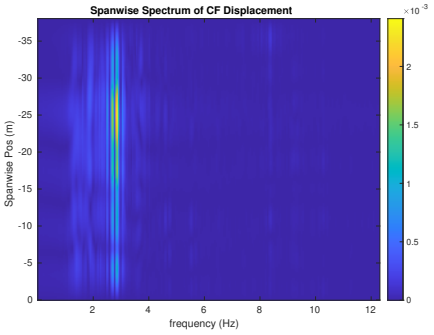

(e) Spanwise cross-flow spectrum of hydrodynamic displacement case 4830.

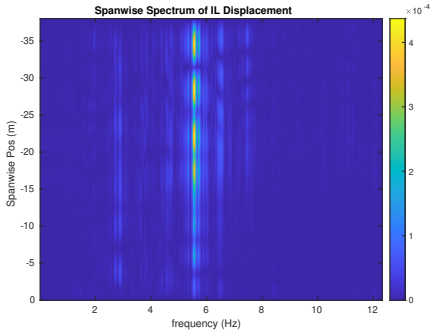

(f) Spanwise inline spectrum of hydrodynamic displacement case 4830.

Figure C-156: *Motion Analysis.* NDP Straight Riser ($L = 38m$) test case 4830.

NDP Straight Riser ($L = 38m$) test case 4840

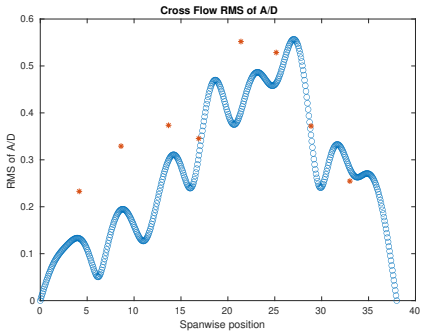

(a) Cross-flow RMS profile case 4840.

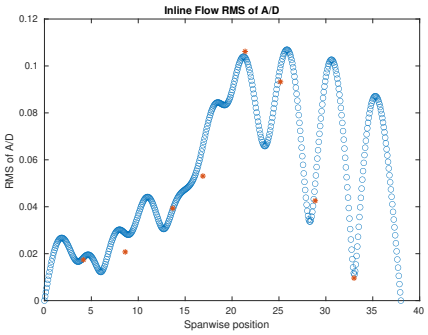

(b) Inline flow RMS profile case 4840.

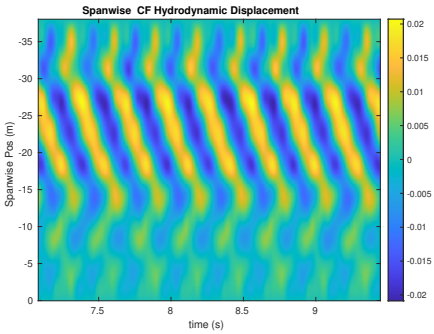

(c) Spanwise cross-flow hydrodynamic displacement case 4840.

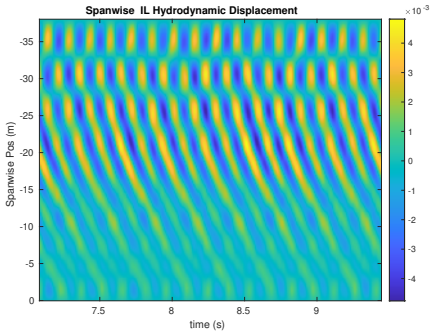

(d) Spanwise inline hydrodynamic displacement case 4840.

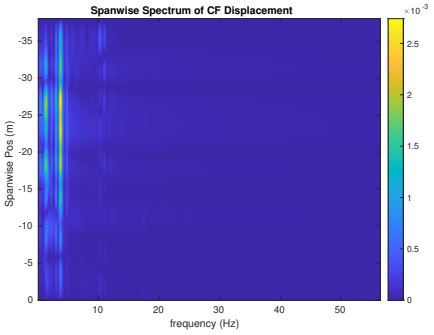

(e) Spanwise cross-flow spectrum of hydrodynamic displacement case 4840.

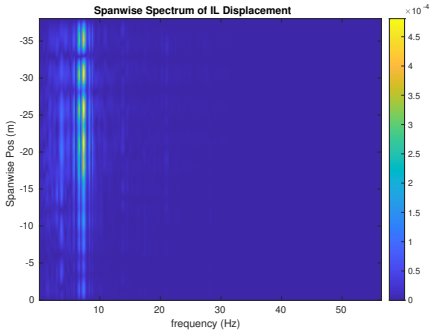

(f) Spanwise inline spectrum of hydrodynamic displacement case 4840.

Figure C-157: *Motion Analysis.* NDP Straight Riser ($L = 38m$) test case 4840.

NDP Straight Riser ($L = 38m$) test case 4850

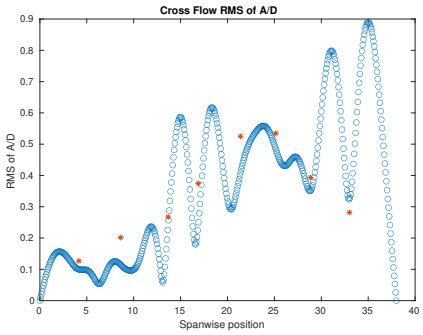

(a) Cross-flow RMS profile case 4850.

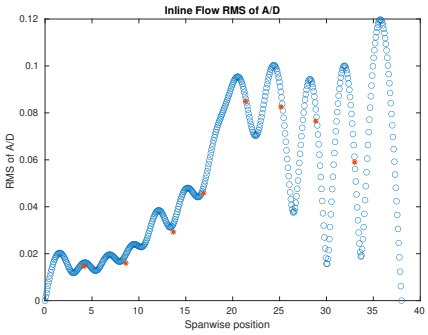

(b) Inline flow RMS profile case 4850.

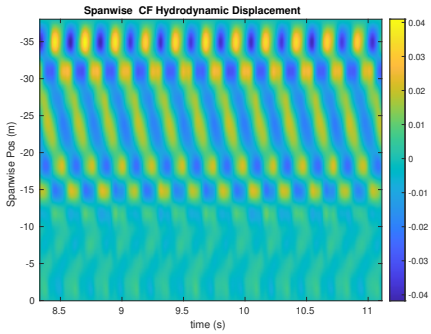

(c) Spanwise cross-flow hydrodynamic displacement case 4850.

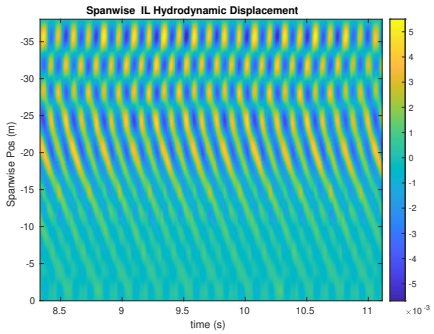

(d) Spanwise inline hydrodynamic displacement case 4850.

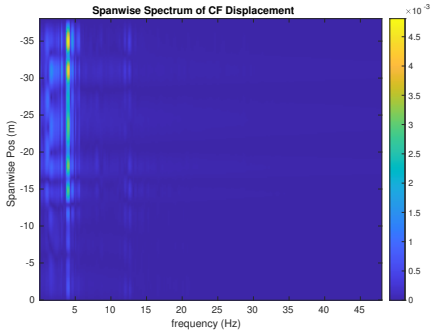

(e) Spanwise cross-flow spectrum of hydrodynamic displacement case 4850.

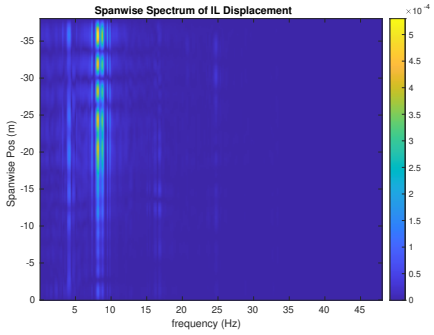

(f) Spanwise inline spectrum of hydrodynamic displacement case 4850.

Figure C-158: *Motion Analysis.* NDP Straight Riser ($L = 38m$) test case 4850.

NDP Straight Riser ($L = 38m$) test case 4860

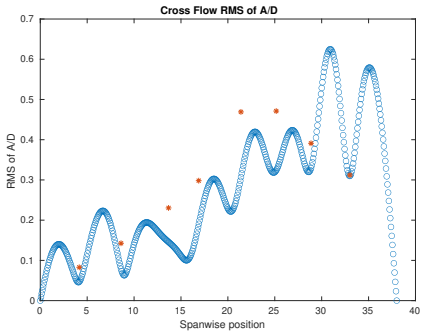

(a) Cross-flow RMS profile case 4860.

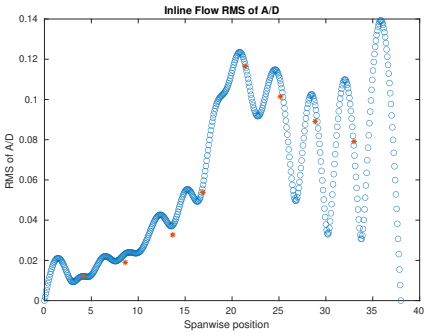

(b) Inline flow RMS profile case 4860.

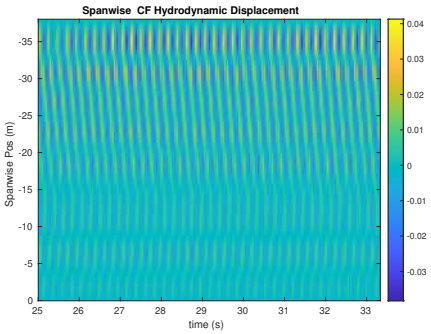

(c) Spanwise cross-flow hydrodynamic displacement case 4860.

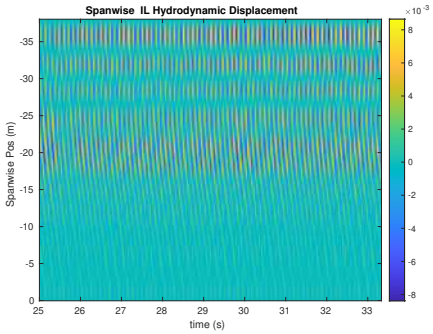

(d) Spanwise inline hydrodynamic displacement case 4860.

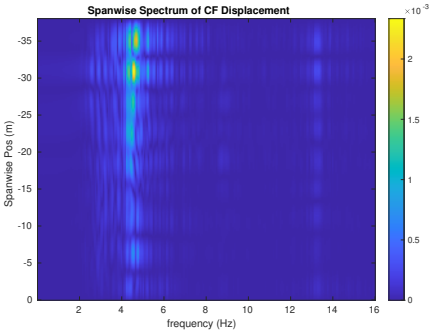

(e) Spanwise cross-flow spectrum of hydrodynamic displacement case 4860.

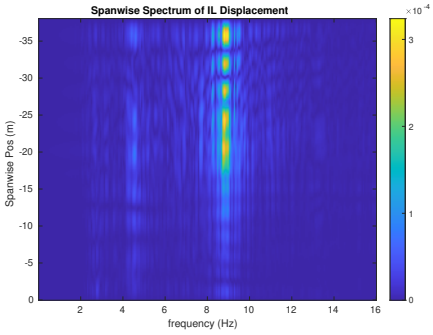

(f) Spanwise inline spectrum of hydrodynamic displacement case 4860.

Figure C-159: *Motion Analysis.* NDP Straight Riser ($L = 38m$) test case 4860.

NDP Straight Riser ($L = 38m$) test case 4870

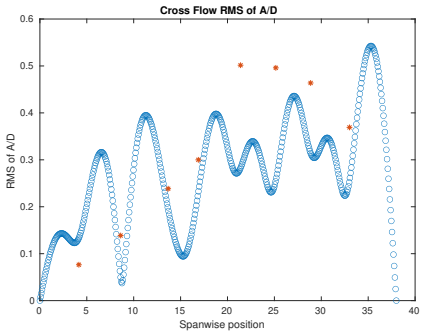

(a) Cross-flow RMS profile case 4870.

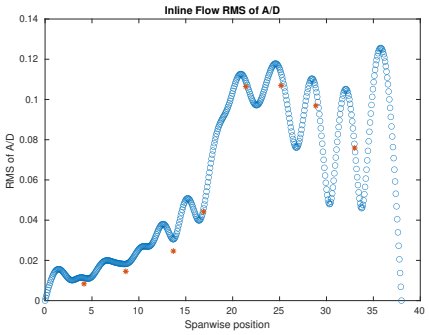

(b) Inline flow RMS profile case 4870.

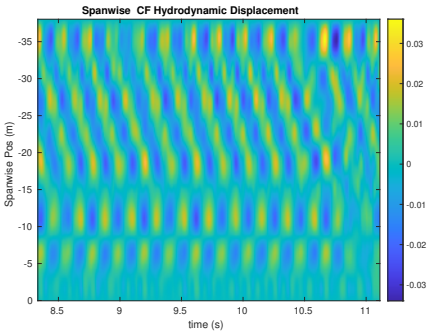

(c) Spanwise cross-flow hydrodynamic displacement case 4870.

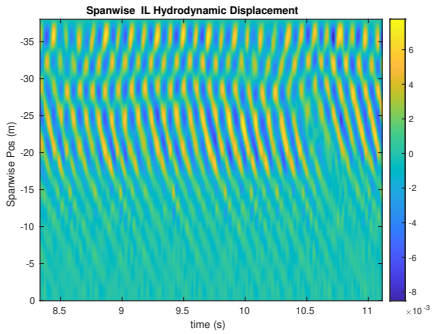

(d) Spanwise inline hydrodynamic displacement case 4870.

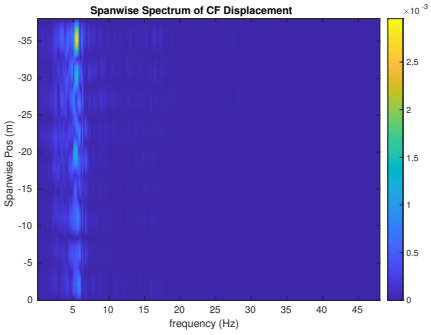

(e) Spanwise cross-flow spectrum of hydrodynamic displacement case 4870.

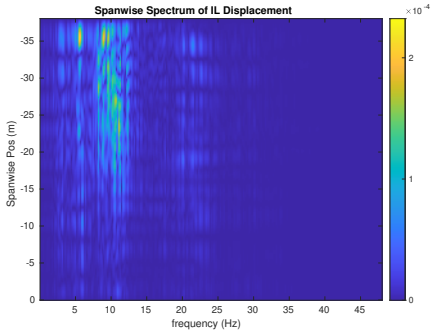

(f) Spanwise inline spectrum of hydrodynamic displacement case 4870.

Figure C-160: *Motion Analysis.* NDP Straight Riser ($L = 38m$) test case 4870.

NDP Straight Riser ($L = 38m$) test case 4880

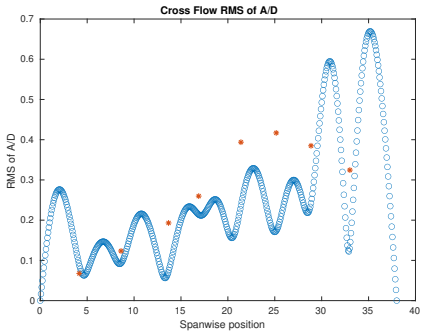

(a) Cross-flow RMS profile case 4880.

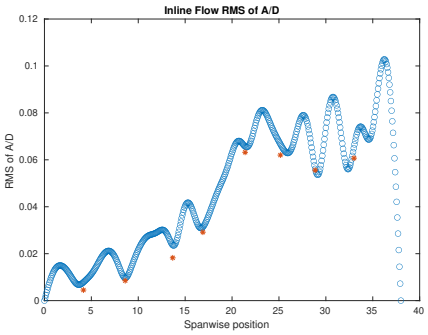

(b) Inline flow RMS profile case 4880.

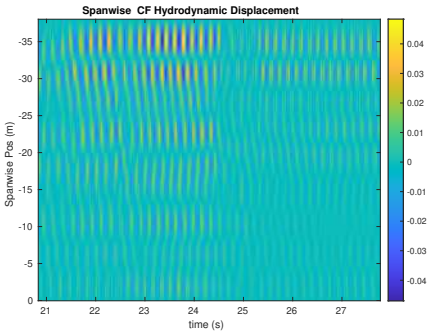

(c) Spanwise cross-flow hydrodynamic displacement case 4880.

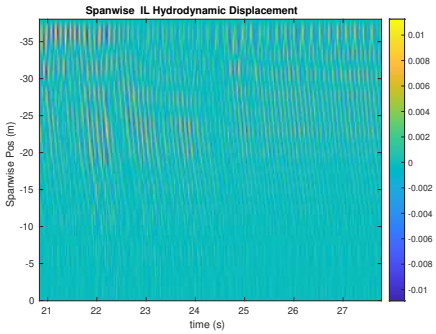

(d) Spanwise inline hydrodynamic displacement case 4880.

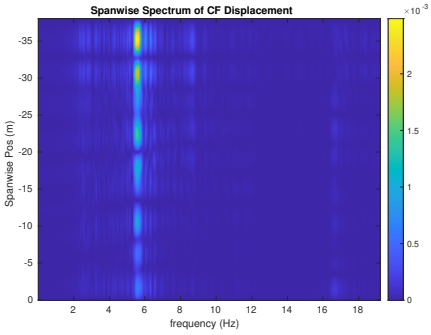

(e) Spanwise cross-flow spectrum of hydrodynamic displacement case 4880.

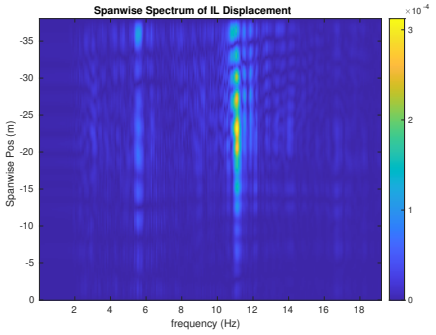

(f) Spanwise inline spectrum of hydrodynamic displacement case 4880.

Figure C-161: *Motion Analysis.* NDP Straight Riser ($L = 38m$) test case 4880.

NDP Straight Riser ($L = 38m$) test case 4890

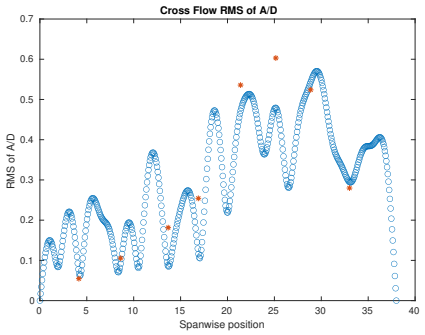

(a) Cross-flow RMS profile case 4890.

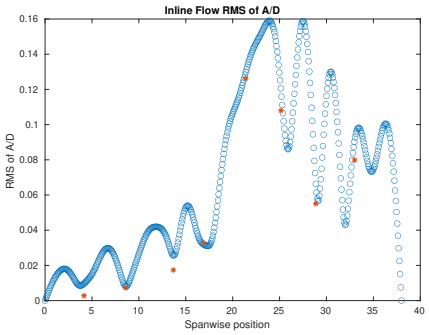

(b) Inline flow RMS profile case 4890.

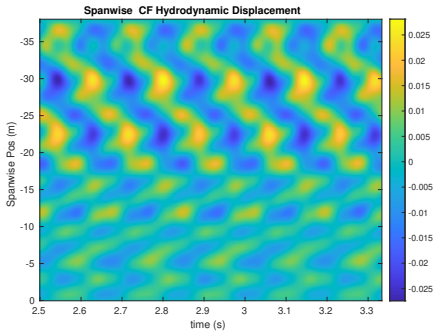

(c) Spanwise cross-flow hydrodynamic displacement case 4890.

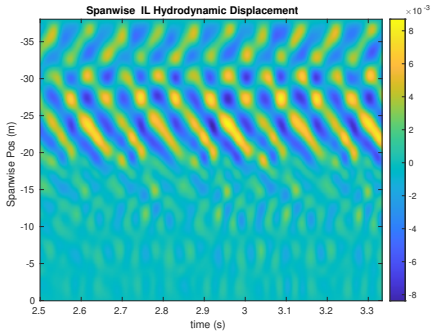

(d) Spanwise inline hydrodynamic displacement case 4890.

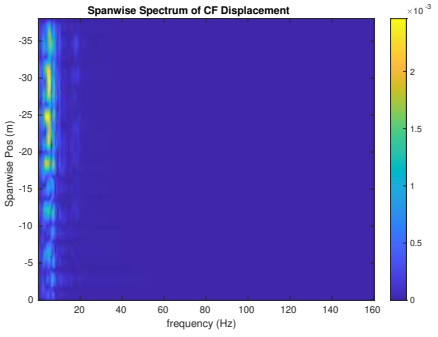

(e) Spanwise cross-flow spectrum of hydrodynamic displacement case 4890.

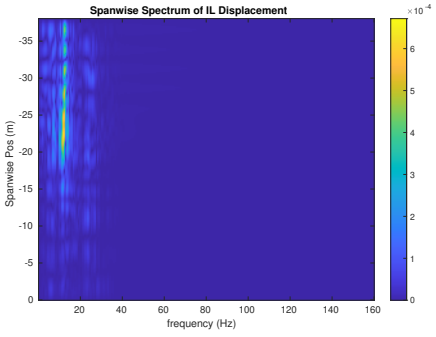

(f) Spanwise inline spectrum of hydrodynamic displacement case 4890.

Figure C-162: *Motion Analysis.* NDP Straight Riser ($L = 38m$) test case 4890.

NDP Straight Riser ($L = 38m$) test case 4900

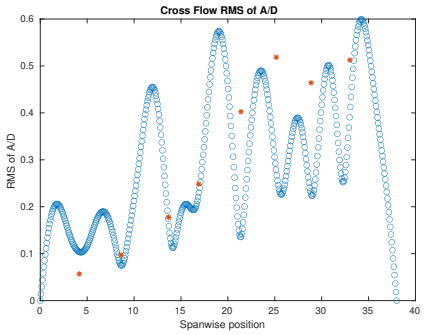

(a) Cross-flow RMS profile case 4900.

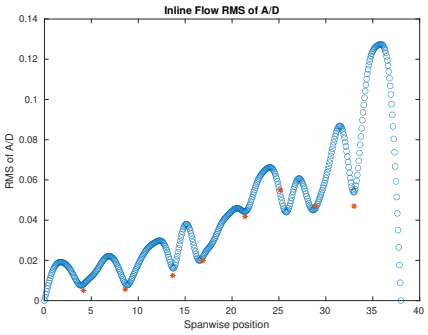

(b) Inline flow RMS profile case 4900.

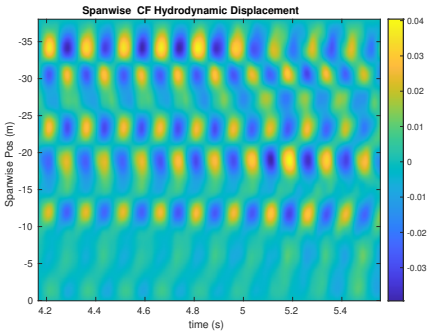

(c) Spanwise cross-flow hydrodynamic displacement case 4900.

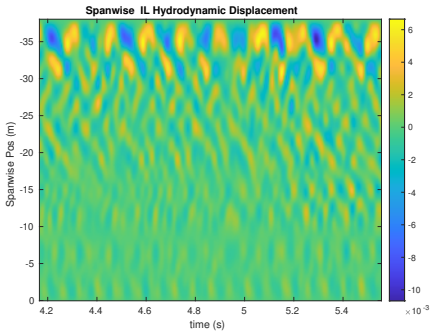

(d) Spanwise inline hydrodynamic displacement case 4900.

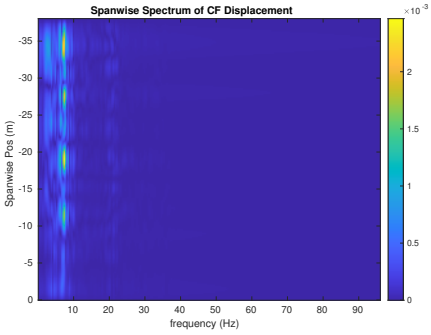

(e) Spanwise cross-flow spectrum of hydrodynamic displacement case 4900.

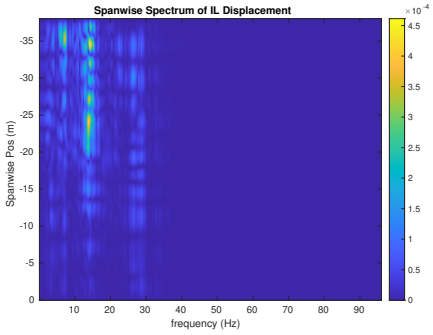

(f) Spanwise inline spectrum of hydrodynamic displacement case 4900.

Figure C-163: *Motion Analysis.* NDP Straight Riser ($L = 38m$) test case 4900.

NDP Straight Riser ($L = 38m$) test case 4910

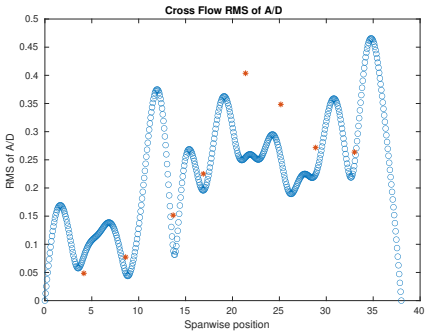

(a) Cross-flow RMS profile case 4910.

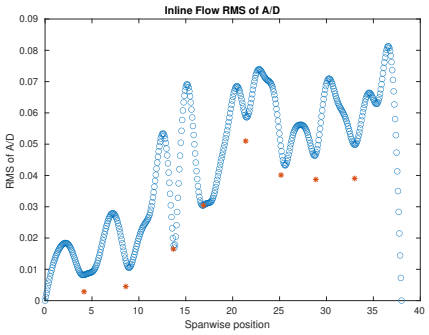

(b) Inline flow RMS profile case 4910.

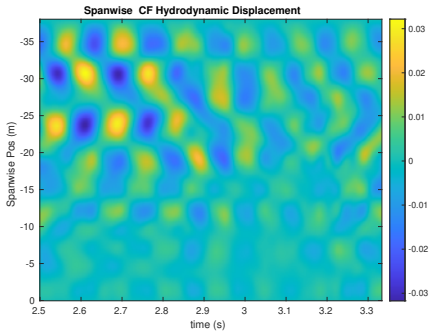

(c) Spanwise cross-flow hydrodynamic displacement case 4910.

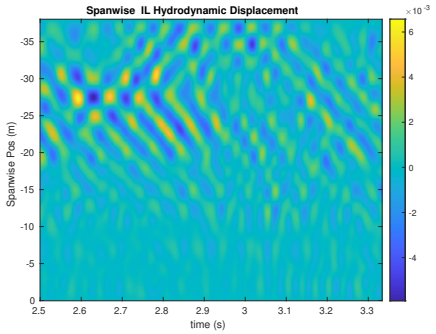

(d) Spanwise inline hydrodynamic displacement case 4910.

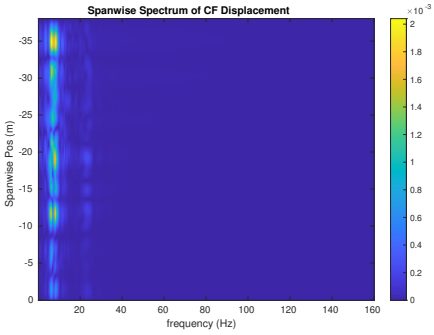

(e) Spanwise cross-flow spectrum of hydrodynamic displacement case 4910.

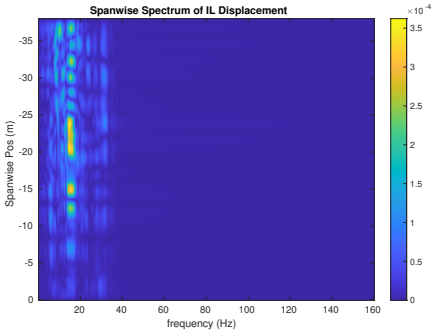

(f) Spanwise inline spectrum of hydrodynamic displacement case 4910.

Figure C-164: *Motion Analysis.* NDP Straight Riser ($L = 38m$) test case 4910.

NDP Straight Riser ($L = 38m$) test case 4920

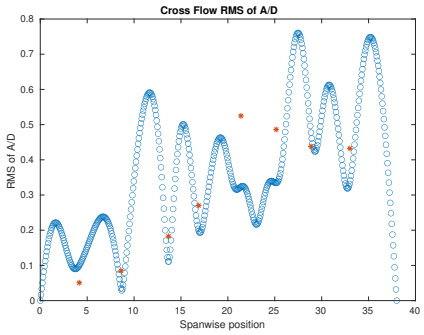

(a) Cross-flow RMS profile case 4920.

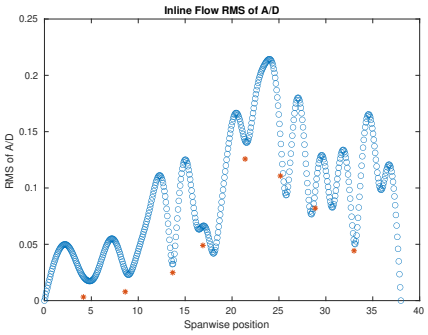

(b) Inline flow RMS profile case 4920.

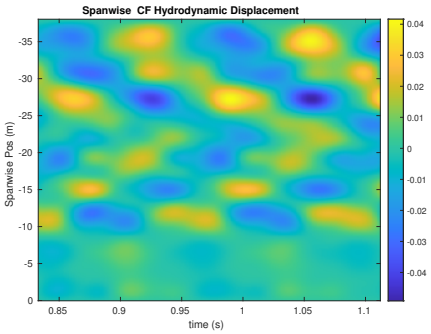

(c) Spanwise cross-flow hydrodynamic displacement case 4920.

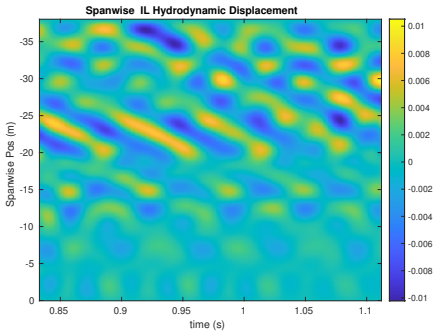

(d) Spanwise inline hydrodynamic displacement case 4920.

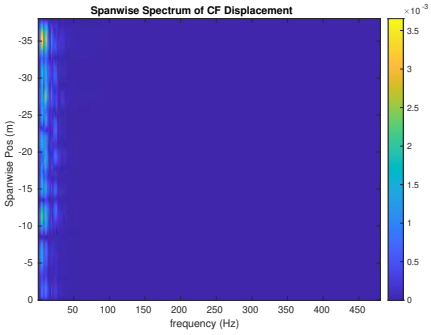

(e) Spanwise cross-flow spectrum of hydrodynamic displacement case 4920.

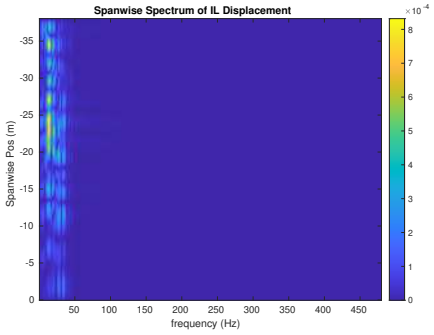

(f) Spanwise inline spectrum of hydrodynamic displacement case 4920.

Figure C-165: *Motion Analysis.* NDP Straight Riser ($L = 38m$) test case 4920.

NDP Straight Riser ($L = 38m$) test case 4930

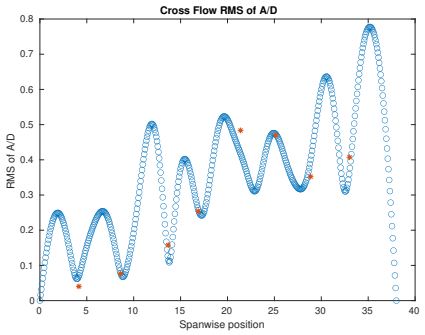

(a) Cross-flow RMS profile case 4930.

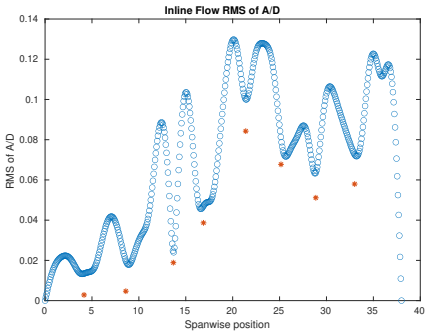

(b) Inline flow RMS profile case 4930.

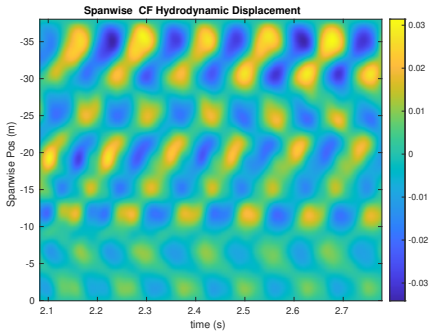

(c) Spanwise cross-flow hydrodynamic displacement case 4930.

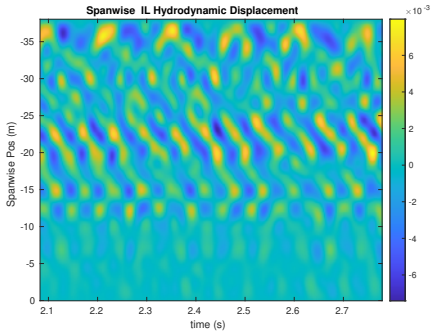

(d) Spanwise inline hydrodynamic displacement case 4930.

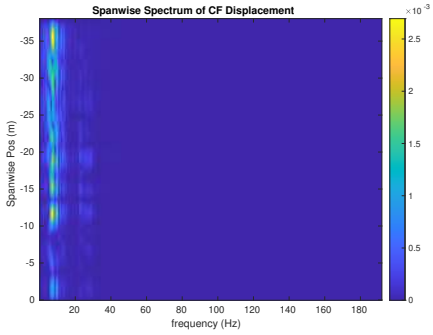

(e) Spanwise cross-flow spectrum of hydrodynamic displacement case 4930.

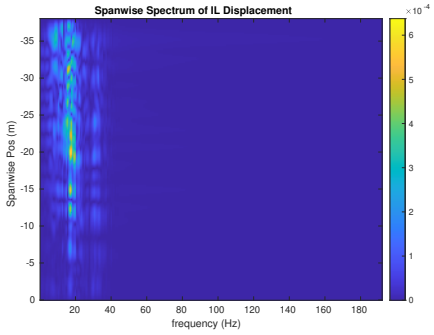

(f) Spanwise inline spectrum of hydrodynamic displacement case 4930.

Figure C-166: *Motion Analysis.* NDP Straight Riser ($L = 38m$) test case 4930.

NDP Straight Riser ($L = 38m$) test case 4940

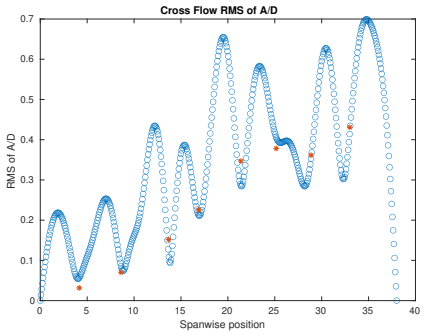

(a) Cross-flow RMS profile case 4940.

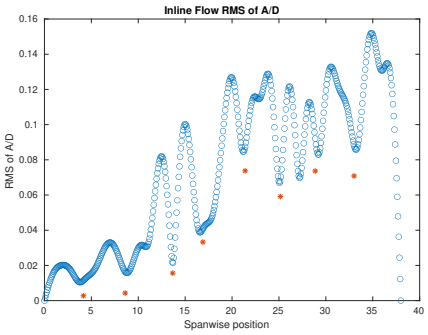

(b) Inline flow RMS profile case 4940.

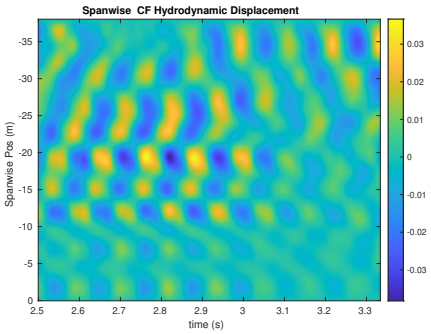

(c) Spanwise cross-flow hydrodynamic displacement case 4940.

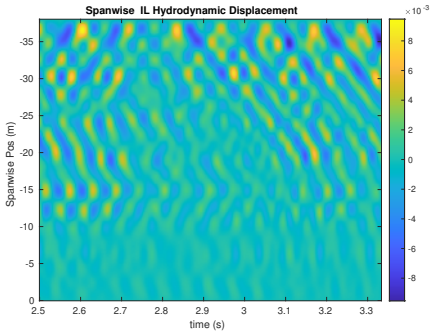

(d) Spanwise inline hydrodynamic displacement case 4940.

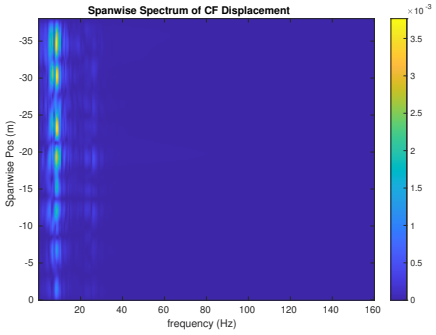

(e) Spanwise cross-flow spectrum of hydrodynamic displacement case 4940.

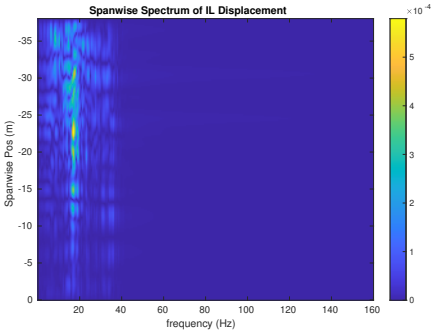

(f) Spanwise inline spectrum of hydrodynamic displacement case 4940.

Figure C-167: *Motion Analysis.* NDP Straight Riser ($L = 38m$) test case 4940.

NDP Straight Riser ($L = 38m$) test case 4950

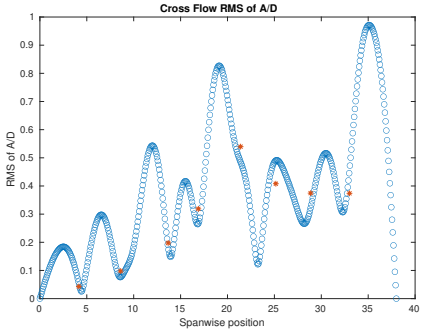

(a) Cross-flow RMS profile case 4950.

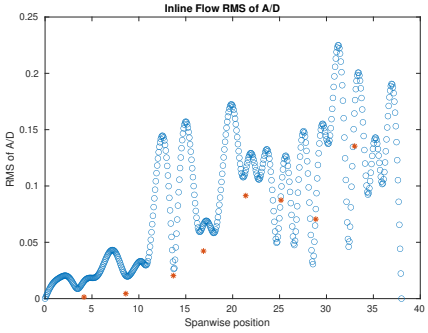

(b) Inline flow RMS profile case 4950.

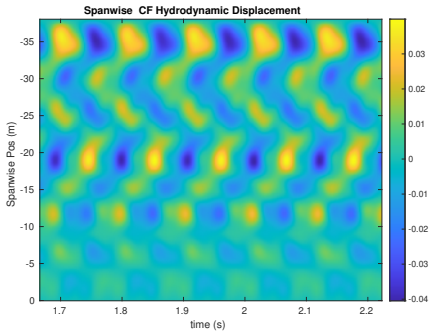

(c) Spanwise cross-flow hydrodynamic displacement case 4950.

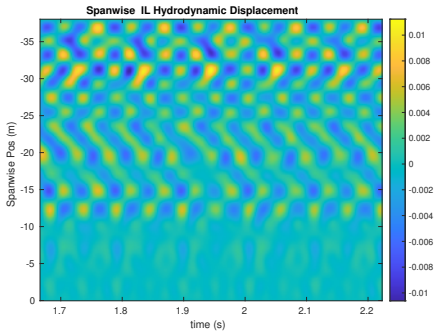

(d) Spanwise inline hydrodynamic displacement case 4950.

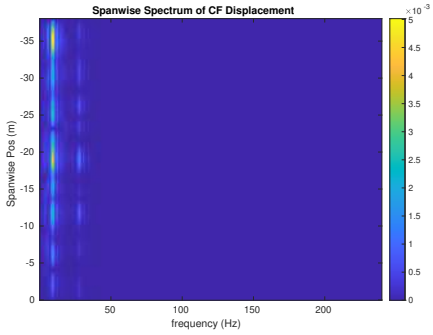

(e) Spanwise cross-flow spectrum of hydrodynamic displacement case 4950.

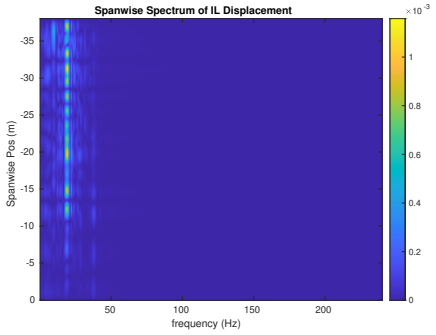

(f) Spanwise inline spectrum of hydrodynamic displacement case 4950.

Figure C-168: *Motion Analysis.* NDP Straight Riser ($L = 38m$) test case 4950.

NDP Straight Riser ($L = 38m$) test case 4960

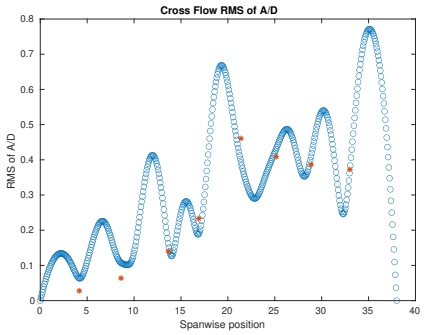

(a) Cross-flow RMS profile case 4960.

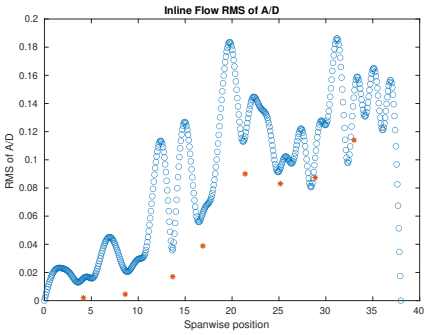

(b) Inline flow RMS profile case 4960.

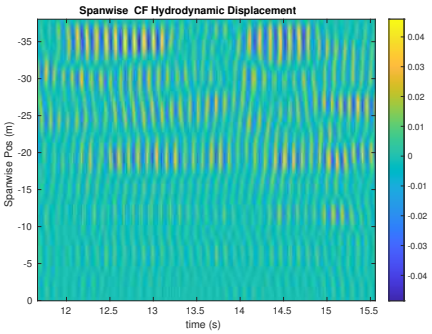

(c) Spanwise cross-flow hydrodynamic displacement case 4960.

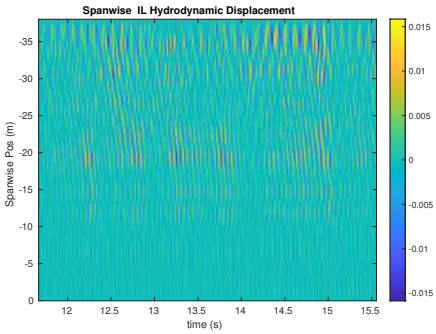

(d) Spanwise inline hydrodynamic displacement case 4960.

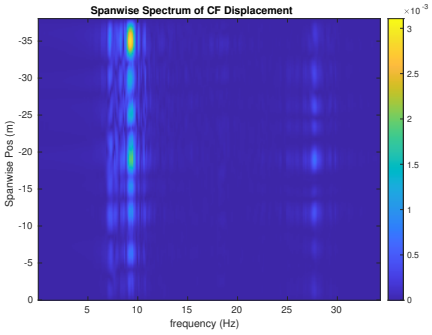

(e) Spanwise cross-flow spectrum of hydrodynamic displacement case 4960.

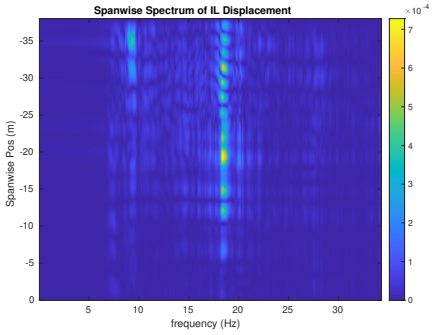

(f) Spanwise inline spectrum of hydrodynamic displacement case 4960.

Figure C-169: *Motion Analysis.* NDP Straight Riser ($L = 38m$) test case 4960.

NDP Straight Riser ($L = 38m$) test case 4970

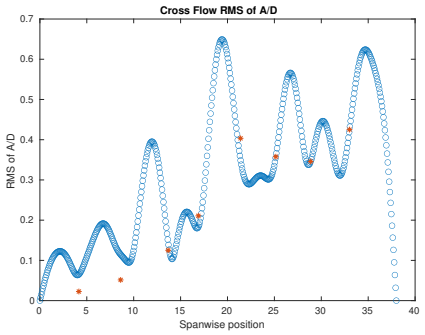

(a) Cross-flow RMS profile case 4970.

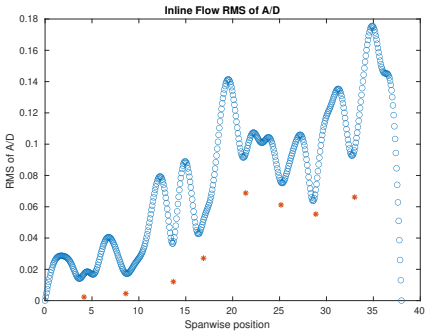

(b) Inline flow RMS profile case 4970.

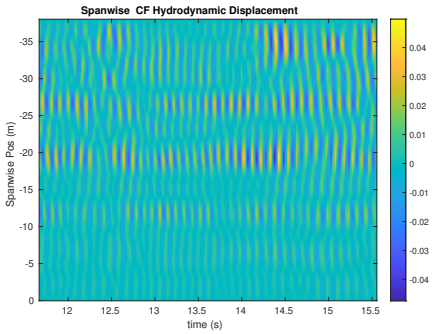

(c) Spanwise cross-flow hydrodynamic displacement case 4970.

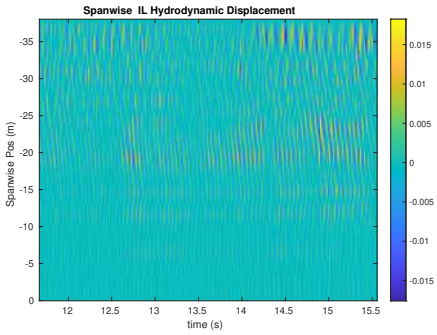

(d) Spanwise inline hydrodynamic displacement case 4970.

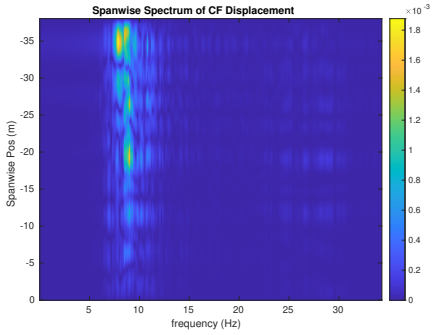

(e) Spanwise cross-flow spectrum of hydrodynamic displacement case 4970.

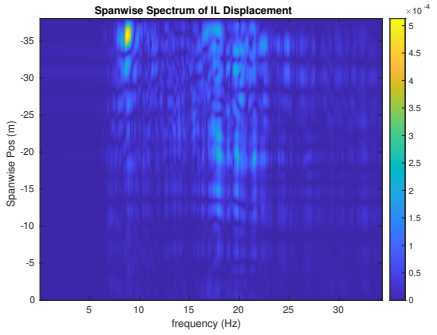

(f) Spanwise inline spectrum of hydrodynamic displacement case 4970.

Figure C-170: *Motion Analysis.* NDP Straight Riser ($L = 38m$) test case 4970.

NDP Straight Riser ($L = 38m$) test case 4980

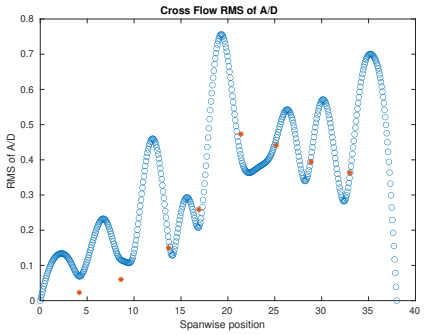

(a) Cross-flow RMS profile case 4980.

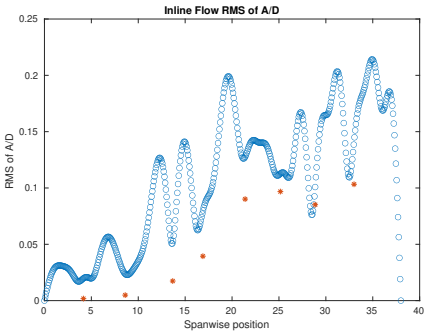

(b) Inline flow RMS profile case 4980.

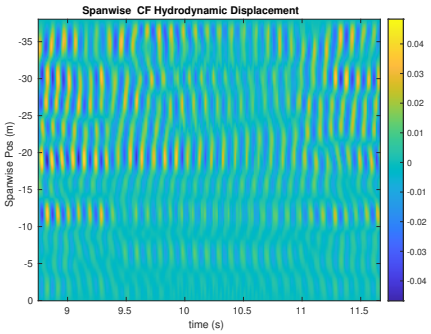

(c) Spanwise cross-flow hydrodynamic displacement case 4980.

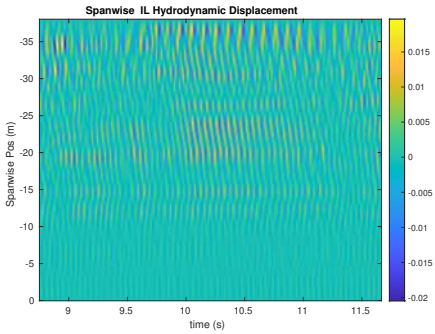

(d) Spanwise inline hydrodynamic displacement case 4980.

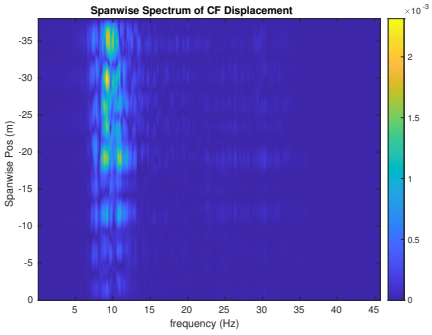

(e) Spanwise cross-flow spectrum of hydrodynamic displacement case 4980.

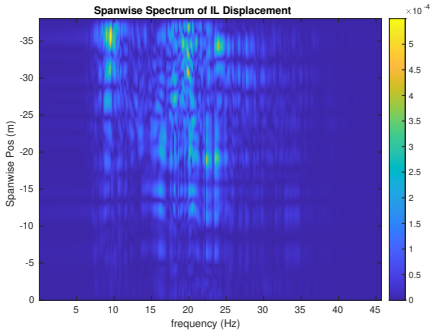

(f) Spanwise inline spectrum of hydrodynamic displacement case 4980.

Figure C-171: *Motion Analysis.* NDP Straight Riser ($L = 38m$) test case 4980.

NDP Straight Riser ($L = 38m$) test case 4990

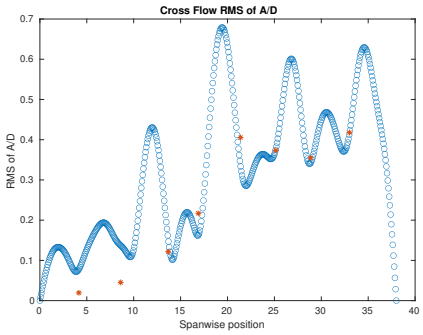

(a) Cross-flow RMS profile case 4990.

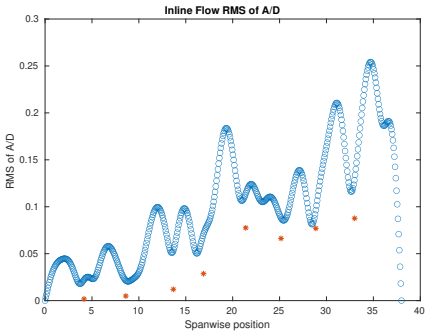

(b) Inline flow RMS profile case 4990.

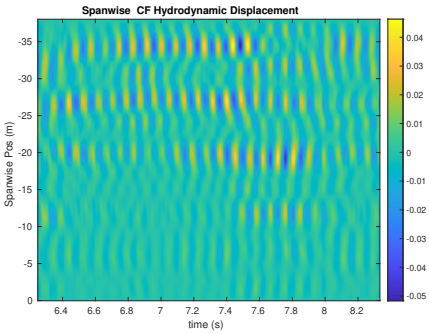

(c) Spanwise cross-flow hydrodynamic displacement case 4990.

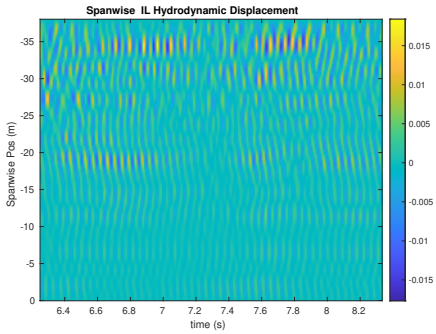

(d) Spanwise inline hydrodynamic displacement case 4990.

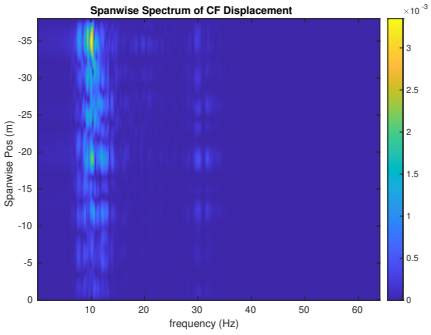

(e) Spanwise cross-flow spectrum of hydrodynamic displacement case 4990.

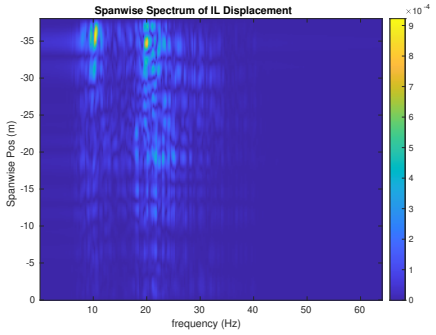

(f) Spanwise inline spectrum of hydrodynamic displacement case 4990.

Figure C-172: *Motion Analysis.* NDP Straight Riser ($L = 38m$) test case 4990.

NDP Straight Riser ($L = 38m$) test case 5000

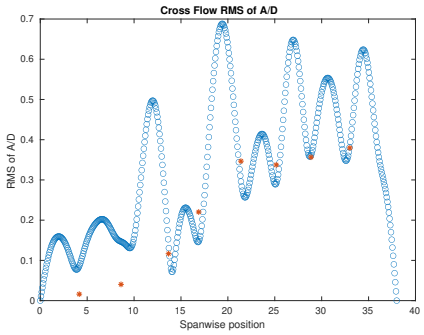

(a) Cross-flow RMS profile case 5000.

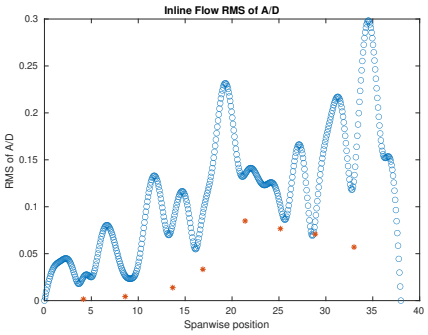

(b) Inline flow RMS profile case 5000.

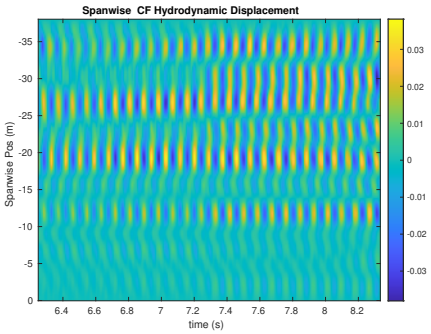

(c) Spanwise cross-flow hydrodynamic displacement case 5000.

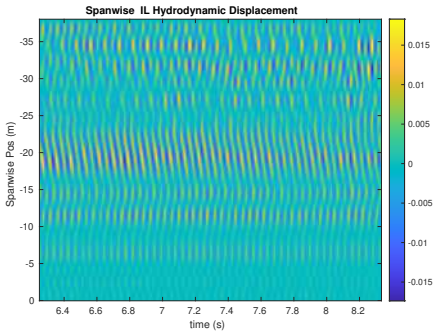

(d) Spanwise inline hydrodynamic displacement case 5000.

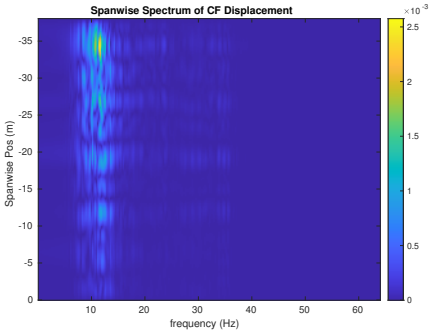

(e) Spanwise cross-flow spectrum of hydrodynamic displacement case 5000.

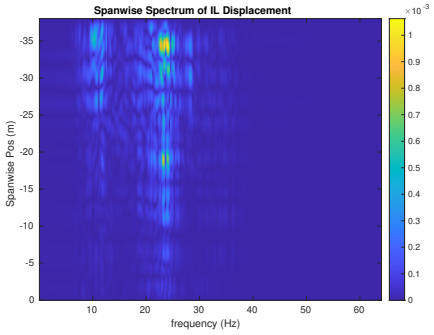

(f) Spanwise inline spectrum of hydrodynamic displacement case 5000.

Figure C-173: *Motion Analysis.* NDP Straight Riser ($L = 38m$) test case 5000.

NDP Straight Riser ($L = 38m$) test case 5010

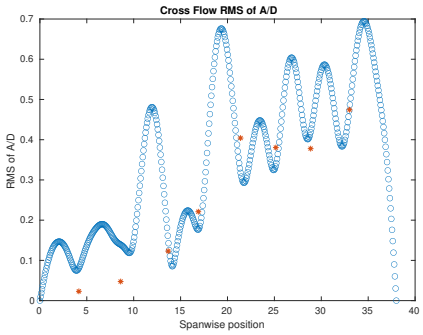

(a) Cross-flow RMS profile case 5010.

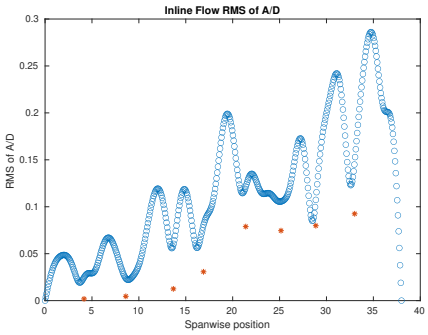

(b) Inline flow RMS profile case 5010.

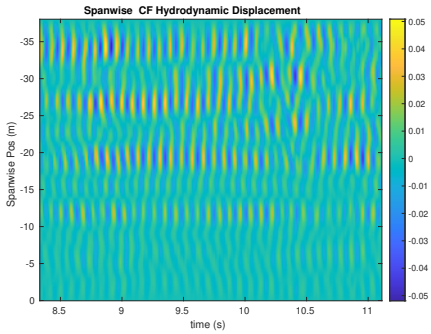

(c) Spanwise cross-flow hydrodynamic displacement case 5010.

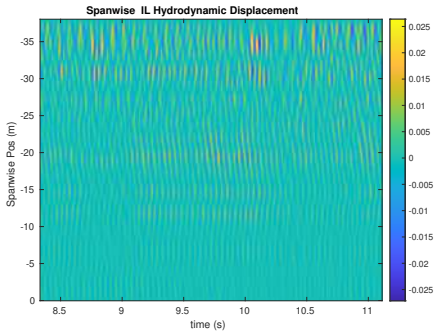

(d) Spanwise inline hydrodynamic displacement case 5010.

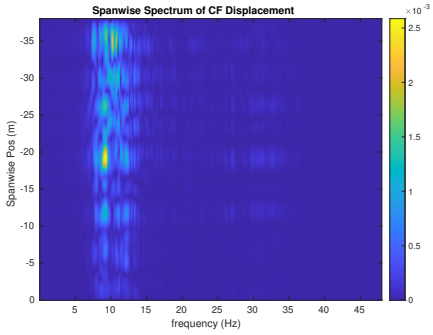

(e) Spanwise cross-flow spectrum of hydrodynamic displacement case 5010.

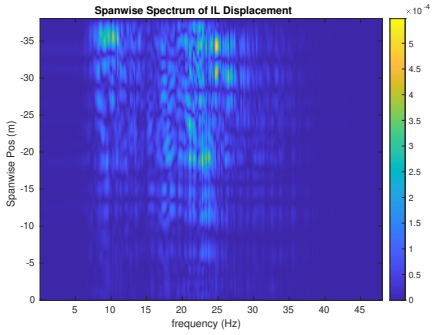

(f) Spanwise inline spectrum of hydrodynamic displacement case 5010.

Figure C-174: *Motion Analysis.* NDP Straight Riser ($L = 38m$) test case 5010.

NDP Straight Riser ($L = 38m$) test case 5020

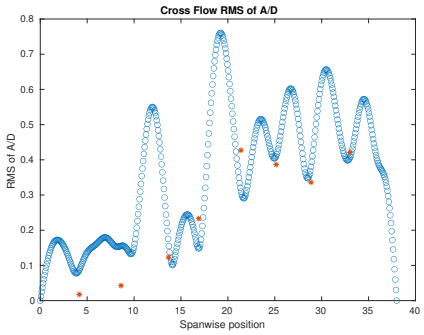

(a) Cross-flow RMS profile case 5020.

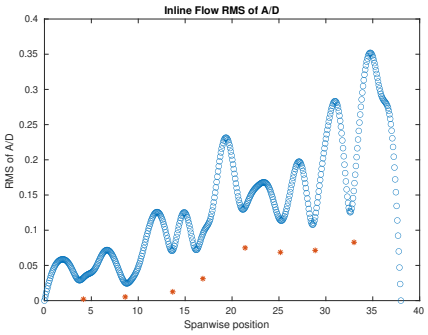

(b) Inline flow RMS profile case 5020.

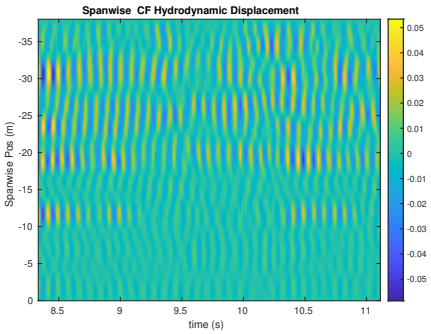

(c) Spanwise cross-flow hydrodynamic displacement case 5020.

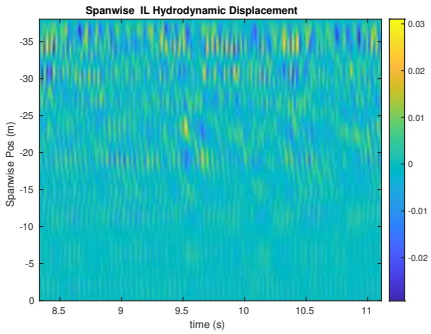

(d) Spanwise inline hydrodynamic displacement case 5020.

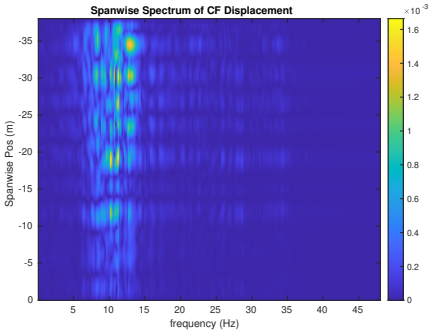

(e) Spanwise cross-flow spectrum of hydrodynamic displacement case 5020.

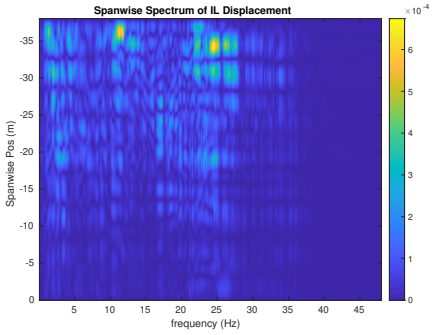

(f) Spanwise inline spectrum of hydrodynamic displacement case 5020.

Figure C-175: *Motion Analysis.* NDP Straight Riser ($L = 38m$) test case 5020.

NDP Straight Riser ($L = 38m$) test case 5110

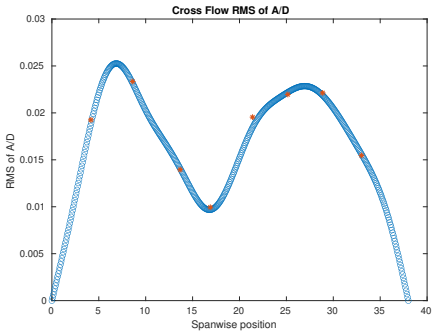

(a) Cross-flow RMS profile case 5110.

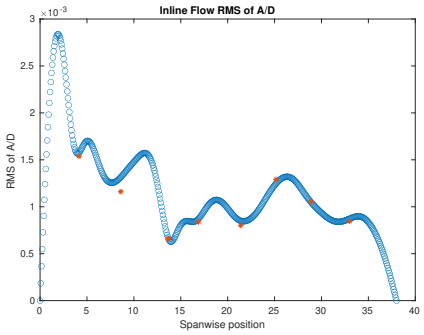

(b) Inline flow RMS profile case 5110.

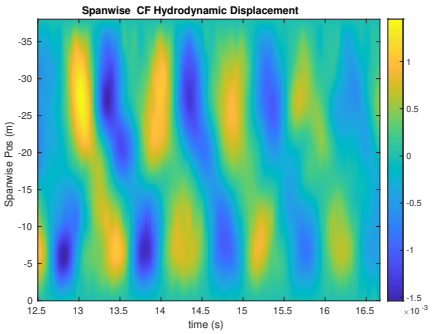

(c) Spanwise cross-flow hydrodynamic displacement case 5110.

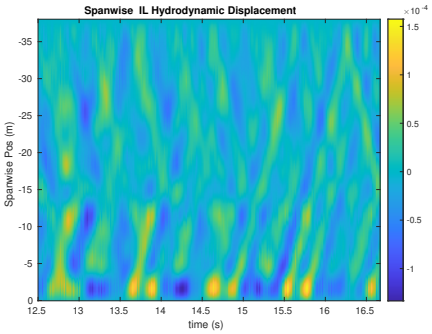

(d) Spanwise inline hydrodynamic displacement case 5110.

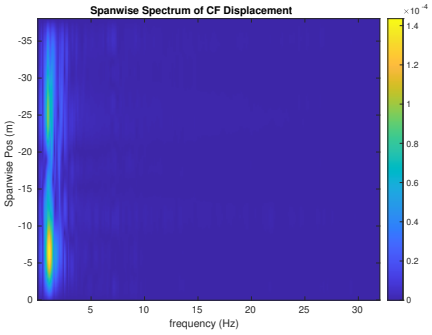

(e) Spanwise cross-flow spectrum of hydrodynamic displacement case 5110.

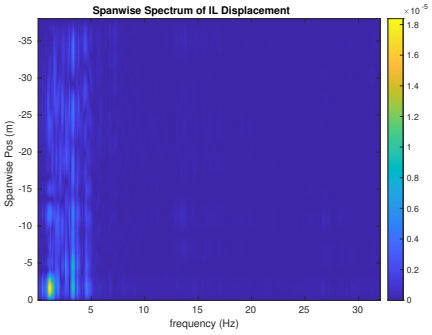

(f) Spanwise inline spectrum of hydrodynamic displacement case 5110.

Figure C-176: *Motion Analysis.* NDP Straight Riser ($L = 38m$) test case 5110.

NDP Straight Riser ($L = 38m$) test case 5120

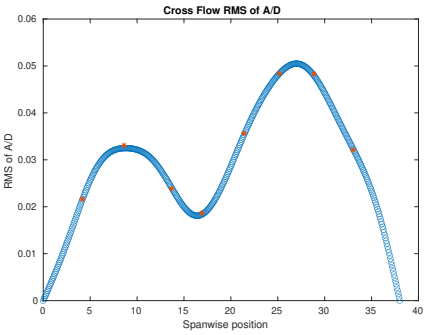

(a) Cross-flow RMS profile case 5120.

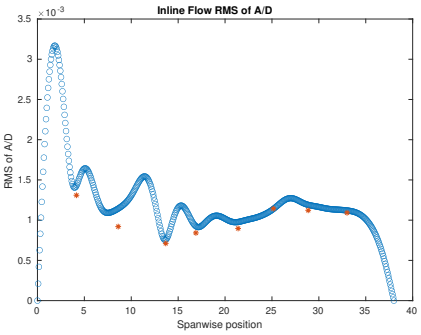

(b) Inline flow RMS profile case 5120.

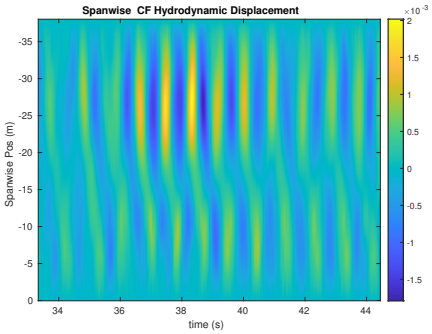

(c) Spanwise cross-flow hydrodynamic displacement case 5120.

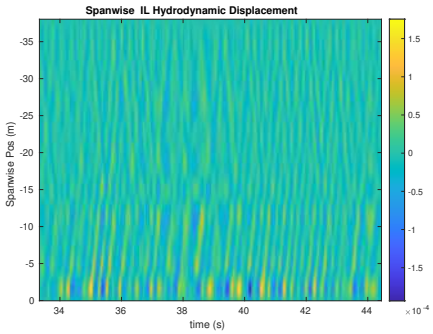

(d) Spanwise inline hydrodynamic displacement case 5120.

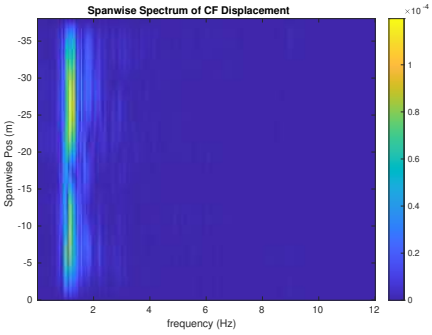

(e) Spanwise cross-flow spectrum of hydrodynamic displacement case 5120.

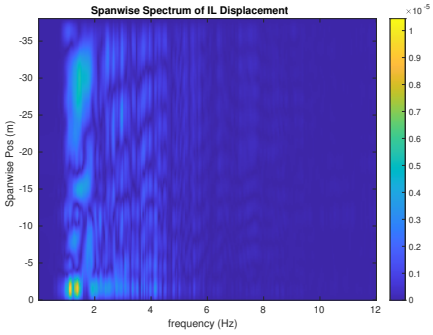

(f) Spanwise inline spectrum of hydrodynamic displacement case 5120.

Figure C-177: *Motion Analysis.* NDP Straight Riser ($L = 38m$) test case 5120.

NDP Straight Riser ($L = 38m$) test case 5130

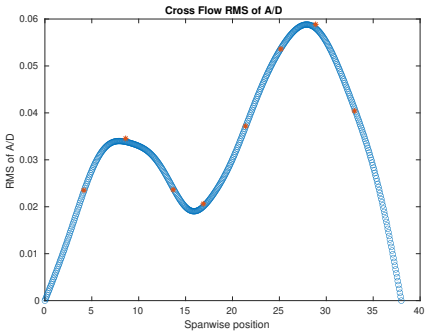

(a) Cross-flow RMS profile case 5130.

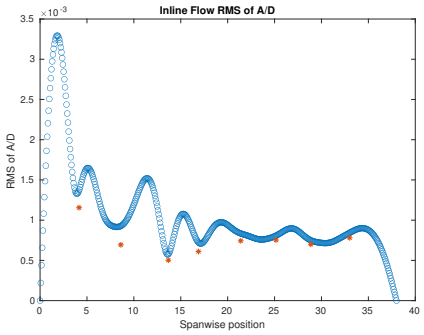

(b) Inline flow RMS profile case 5130.

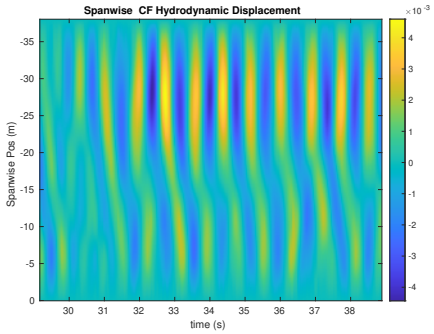

(c) Spanwise cross-flow hydrodynamic displacement case 5130.

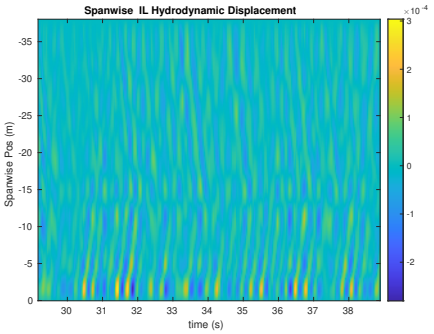

(d) Spanwise inline hydrodynamic displacement case 5130.

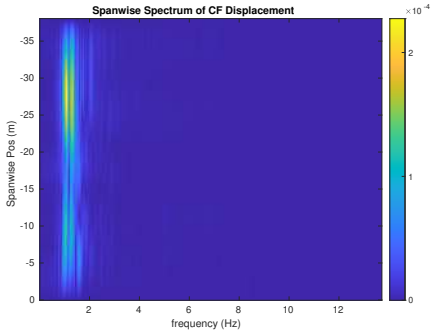

(e) Spanwise cross-flow spectrum of hydrodynamic displacement case 5130.

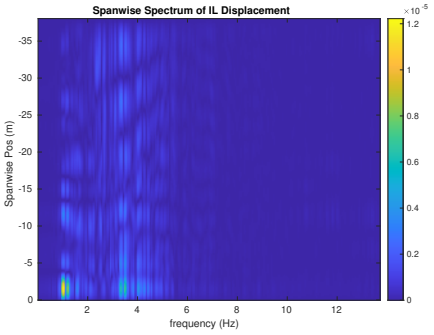

(f) Spanwise inline spectrum of hydrodynamic displacement case 5130.

Figure C-178: *Motion Analysis.* NDP Straight Riser ($L = 38m$) test case 5130.

NDP Straight Riser ($L = 38m$) test case 5140

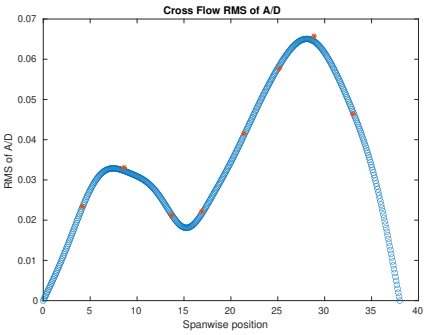

(a) Cross-flow RMS profile case 5140.

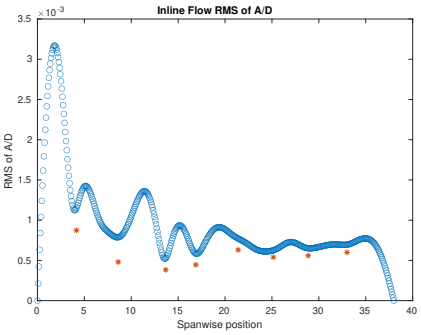

(b) Inline flow RMS profile case 5140.

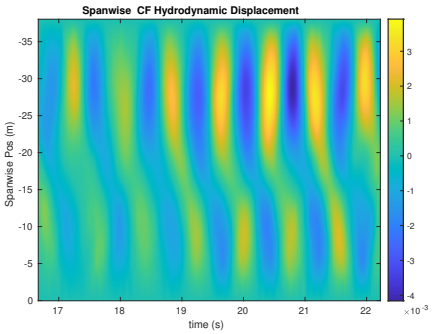

(c) Spanwise cross-flow hydrodynamic displacement case 5140.

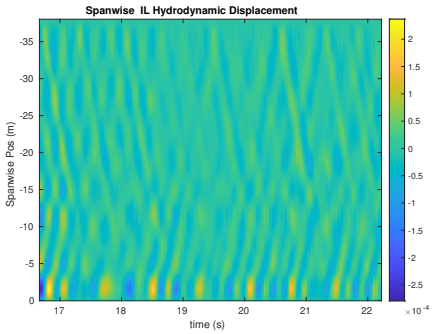

(d) Spanwise inline hydrodynamic displacement case 5140.

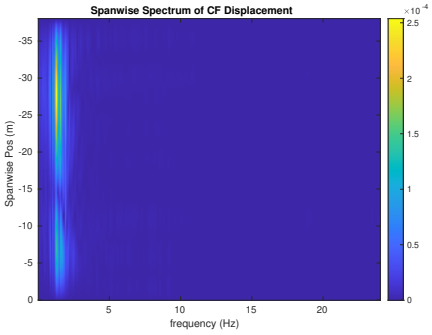

(e) Spanwise cross-flow spectrum of hydrodynamic displacement case 5140.

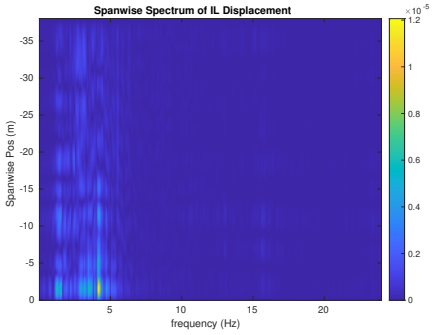

(f) Spanwise inline spectrum of hydrodynamic displacement case 5140.

Figure C-179: *Motion Analysis.* NDP Straight Riser ($L = 38m$) test case 5140.

NDP Straight Riser ($L = 38m$) test case 5150

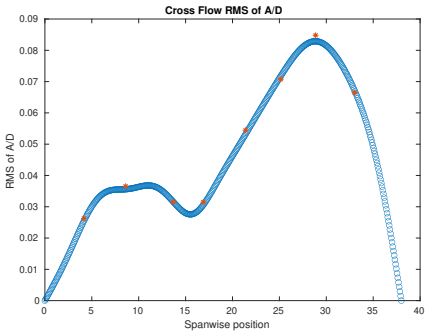

(a) Cross-flow RMS profile case 5150.

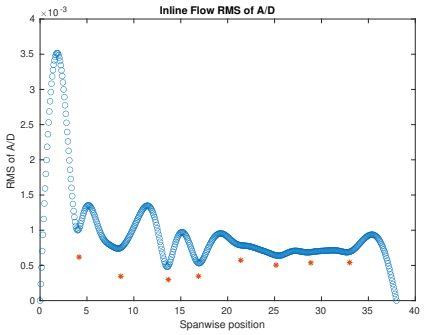

(b) Inline flow RMS profile case 5150.

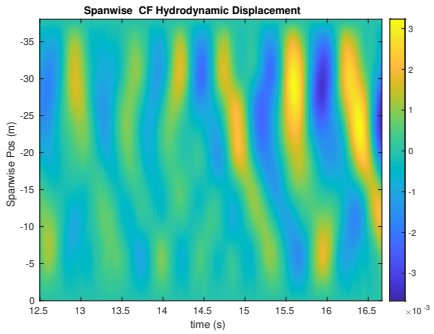

(c) Spanwise cross-flow hydrodynamic displacement case 5150.

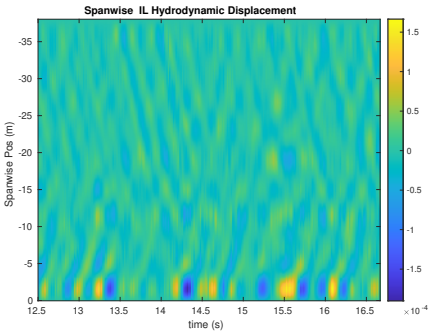

(d) Spanwise inline hydrodynamic displacement case 5150.

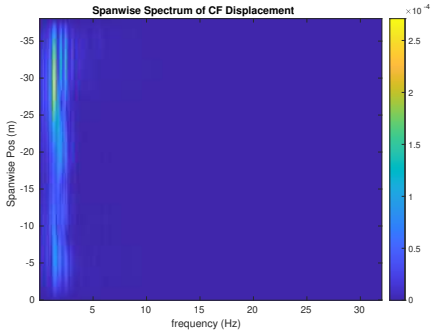

(e) Spanwise cross-flow spectrum of hydrodynamic displacement case 5150.

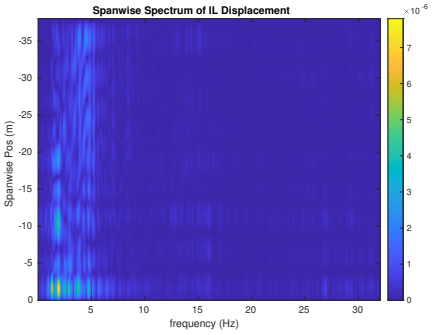

(f) Spanwise inline spectrum of hydrodynamic displacement case 5150.

Figure C-180: *Motion Analysis.* NDP Straight Riser ($L = 38m$) test case 5150.

NDP Straight Riser ($L = 38m$) test case 5160

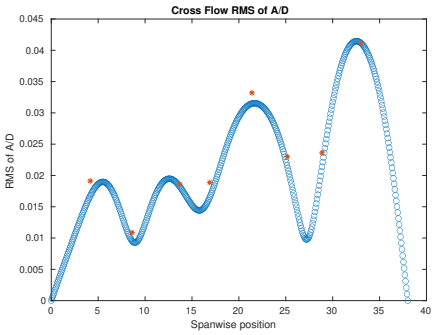

(a) Cross-flow RMS profile case 5160.

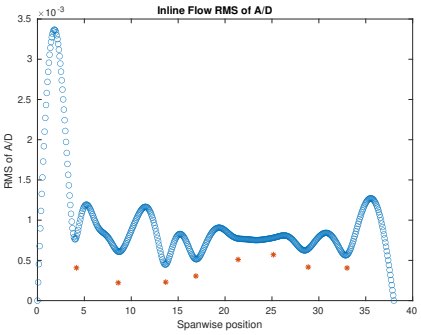

(b) Inline flow RMS profile case 5160.

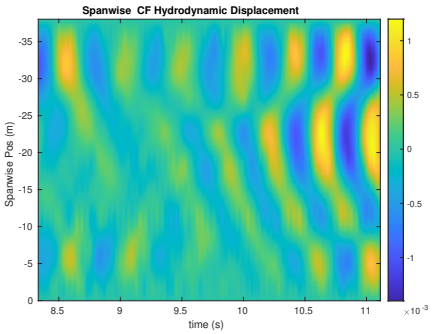

(c) Spanwise cross-flow hydrodynamic displacement case 5160.

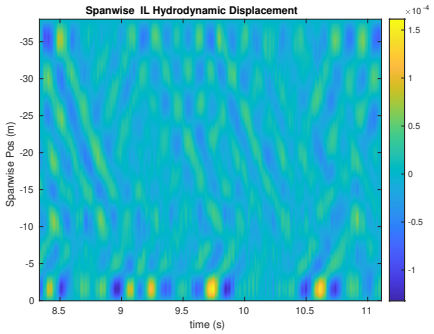

(d) Spanwise inline hydrodynamic displacement case 5160.

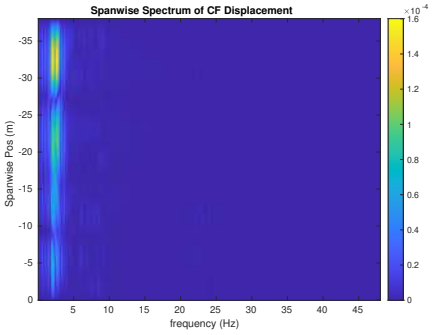

(e) Spanwise cross-flow spectrum of hydrodynamic displacement case 5160.

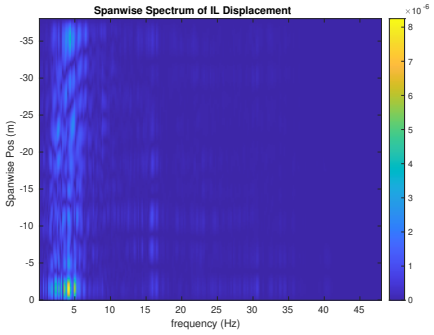

(f) Spanwise inline spectrum of hydrodynamic displacement case 5160.

Figure C-181: *Motion Analysis.* NDP Straight Riser ($L = 38m$) test case 5160.

NDP Straight Riser ($L = 38m$) test case 5170

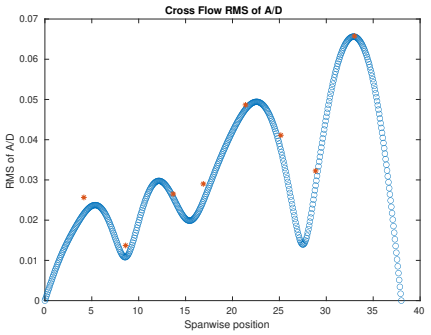

(a) Cross-flow RMS profile case 5170.

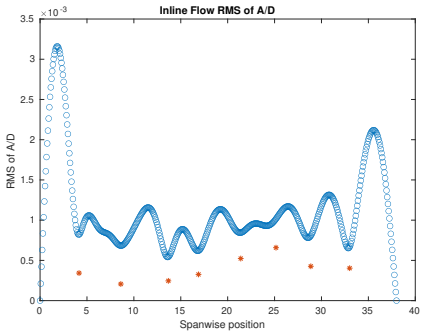

(b) Inline flow RMS profile case 5170.

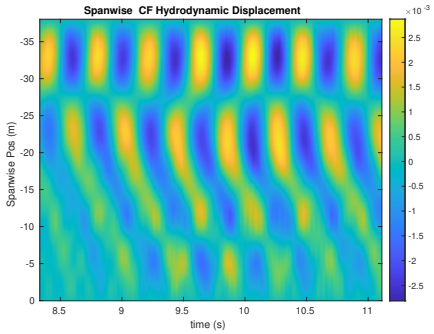

(c) Spanwise cross-flow hydrodynamic displacement case 5170.

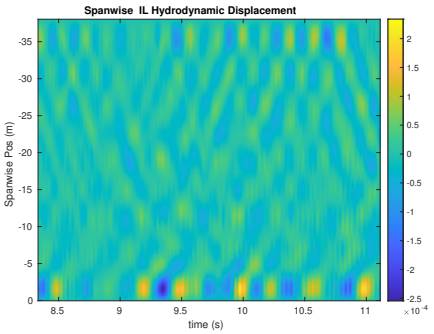

(d) Spanwise inline hydrodynamic displacement case 5170.

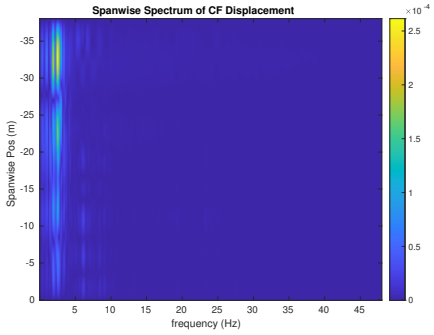

(e) Spanwise cross-flow spectrum of hydrodynamic displacement case 5170.

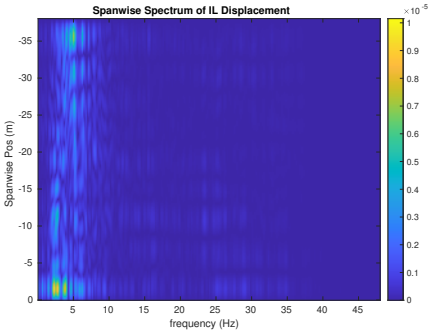

(f) Spanwise inline spectrum of hydrodynamic displacement case 5170.

Figure C-182: *Motion Analysis.* NDP Straight Riser ($L = 38m$) test case 5170.

NDP Straight Riser ($L = 38m$) test case 5180

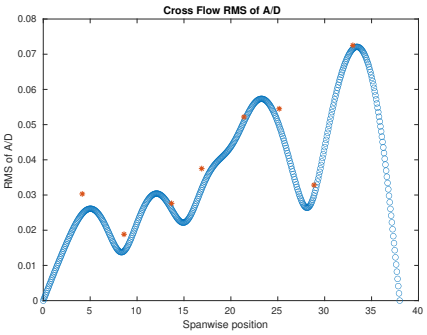

(a) Cross-flow RMS profile case 5180.

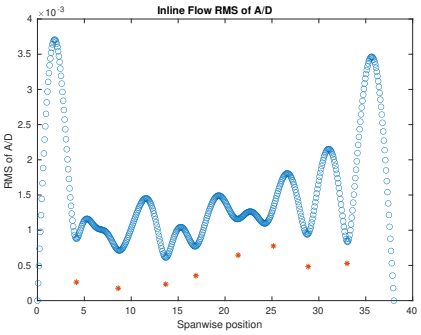

(b) Inline flow RMS profile case 5180.

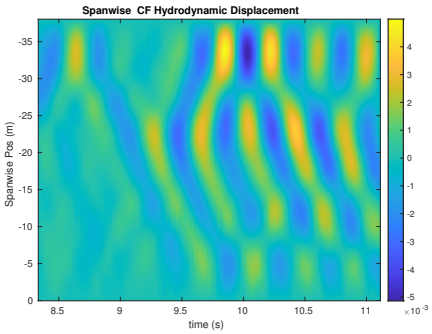

(c) Spanwise cross-flow hydrodynamic displacement case 5180.

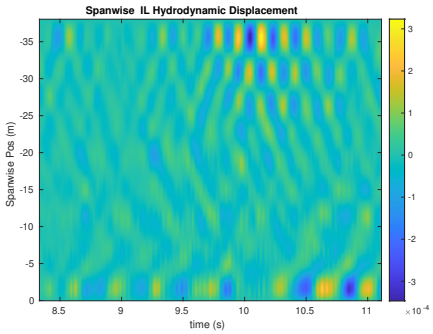

(d) Spanwise inline hydrodynamic displacement case 5180.

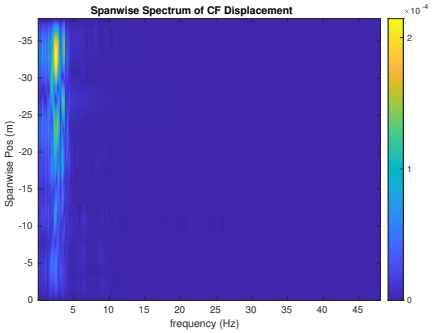

(e) Spanwise cross-flow spectrum of hydrodynamic displacement case 5180.

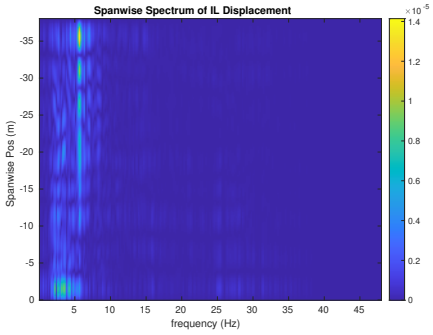

(f) Spanwise inline spectrum of hydrodynamic displacement case 5180.

Figure C-183: *Motion Analysis.* NDP Straight Riser ($L = 38m$) test case 5180.

NDP Straight Riser ($L = 38m$) test case 5190

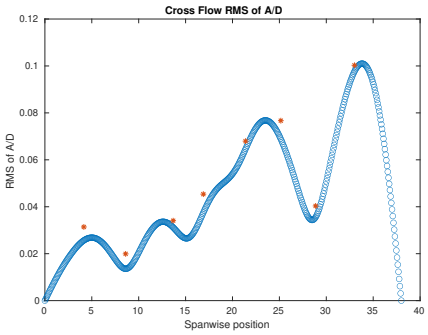

(a) Cross-flow RMS profile case 5190.

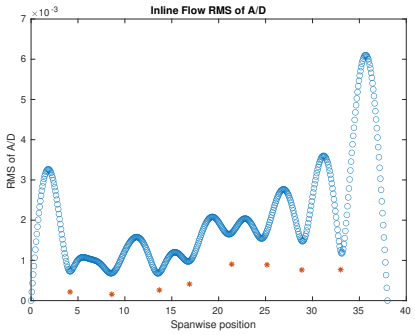

(b) Inline flow RMS profile case 5190.

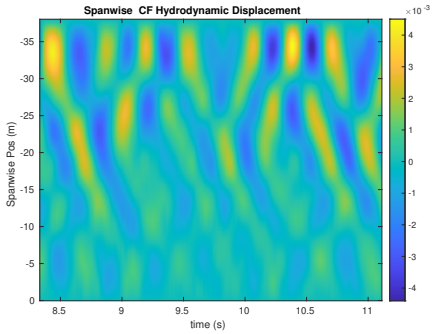

(c) Spanwise cross-flow hydrodynamic displacement case 5190.

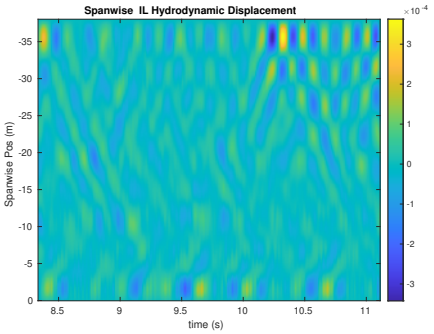

(d) Spanwise inline hydrodynamic displacement case 5190.

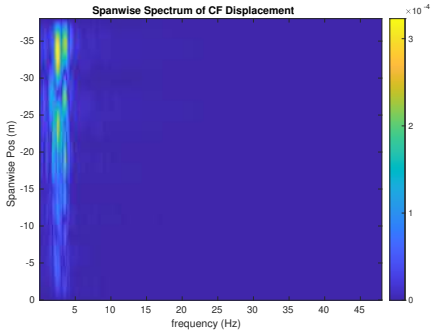

(e) Spanwise cross-flow spectrum of hydrodynamic displacement case 5190.

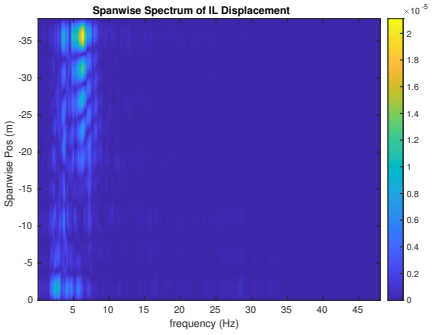

(f) Spanwise inline spectrum of hydrodynamic displacement case 5190.

Figure C-184: *Motion Analysis.* NDP Straight Riser ($L = 38m$) test case 5190.

NDP Straight Riser ($L = 38m$) test case 5200

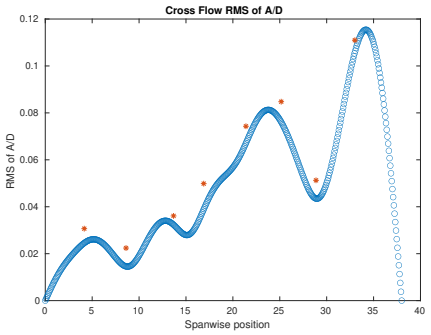

(a) Cross-flow RMS profile case 5200.

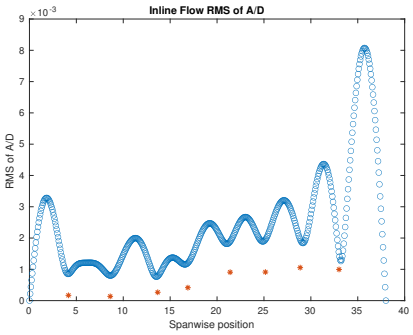

(b) Inline flow RMS profile case 5200.

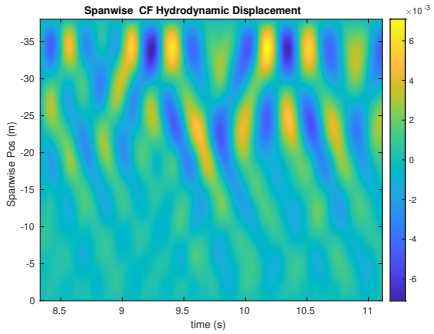

(c) Spanwise cross-flow hydrodynamic displacement case 5200.

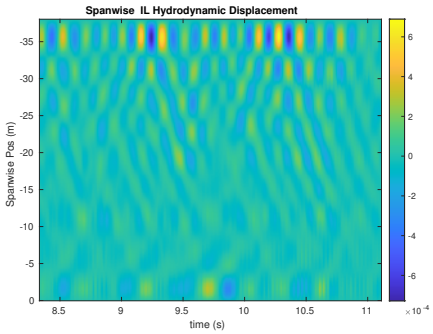

(d) Spanwise inline hydrodynamic displacement case 5200.

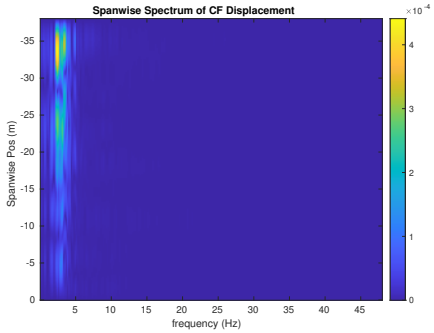

(e) Spanwise cross-flow spectrum of hydrodynamic displacement case 5200.

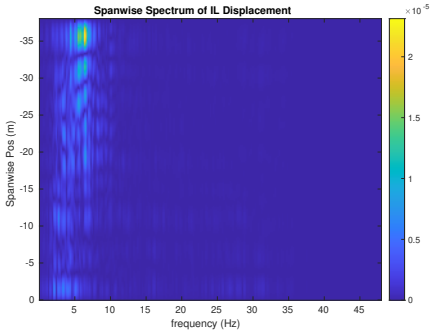

(f) Spanwise inline spectrum of hydrodynamic displacement case 5200.

Figure C-185: *Motion Analysis.* NDP Straight Riser ($L = 38m$) test case 5200.

NDP Straight Riser ($L = 38m$) test case 5210

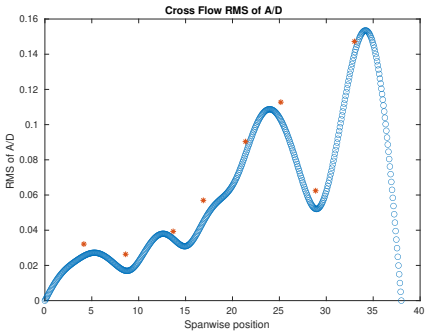

(a) Cross-flow RMS profile case 5210.

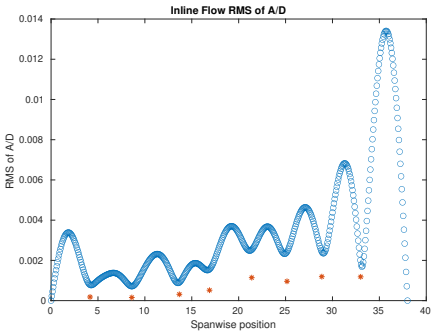

(b) Inline flow RMS profile case 5210.

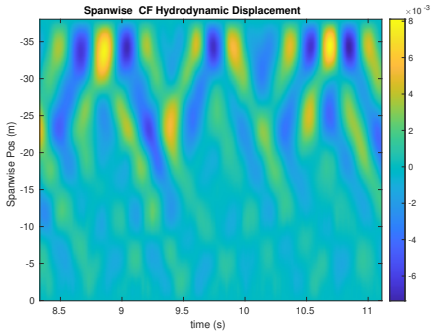

(c) Spanwise cross-flow hydrodynamic displacement case 5210.

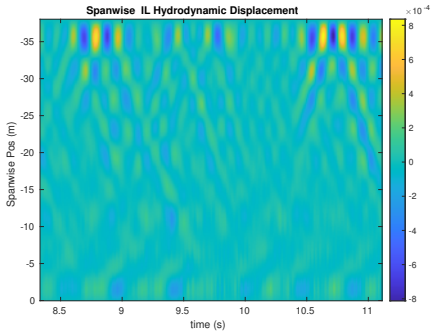

(d) Spanwise inline hydrodynamic displacement case 5210.

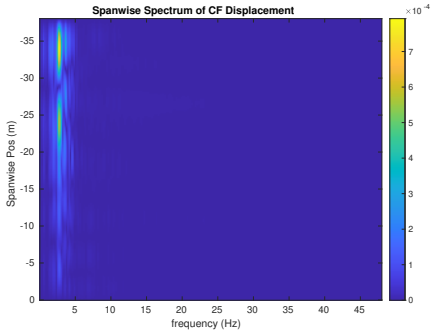

(e) Spanwise cross-flow spectrum of hydrodynamic displacement case 5210.

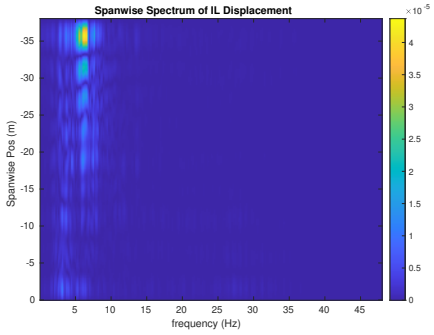

(f) Spanwise inline spectrum of hydrodynamic displacement case 5210.

Figure C-186: *Motion Analysis.* NDP Straight Riser ($L = 38m$) test case 5210.

NDP Straight Riser ($L = 38m$) test case 5220

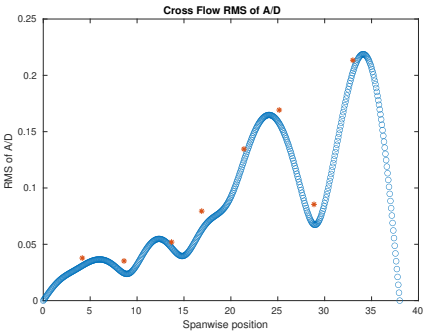

(a) Cross-flow RMS profile case 5220.

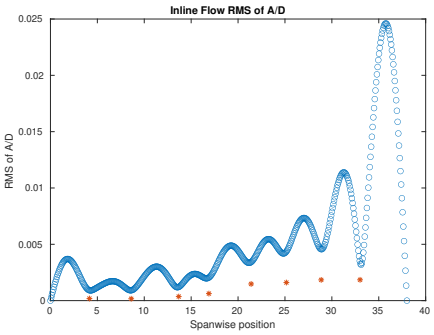

(b) Inline flow RMS profile case 5220.

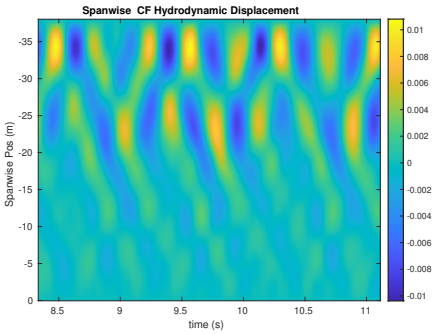

(c) Spanwise cross-flow hydrodynamic displacement case 5220.

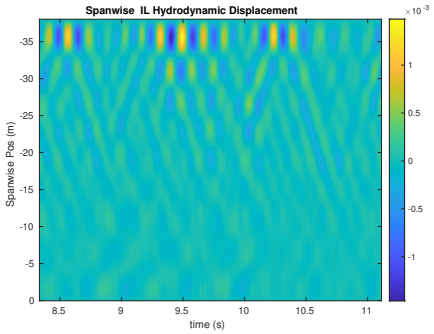

(d) Spanwise inline hydrodynamic displacement case 5220.

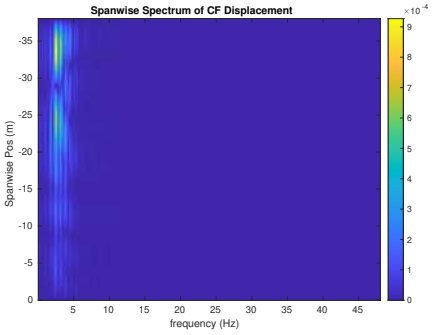

(e) Spanwise cross-flow spectrum of hydrodynamic displacement case 5220.

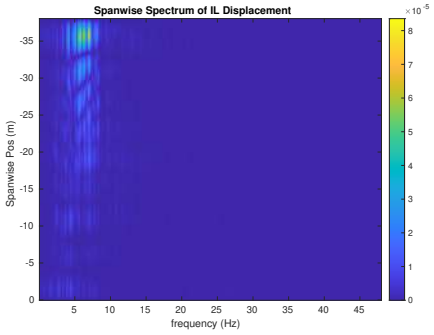

(f) Spanwise inline spectrum of hydrodynamic displacement case 5220.

Figure C-187: *Motion Analysis.* NDP Straight Riser ($L = 38m$) test case 5220.

NDP Straight Riser ($L = 38m$) test case 5230

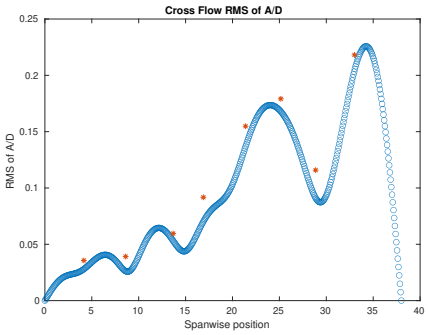

(a) Cross-flow RMS profile case 5230.

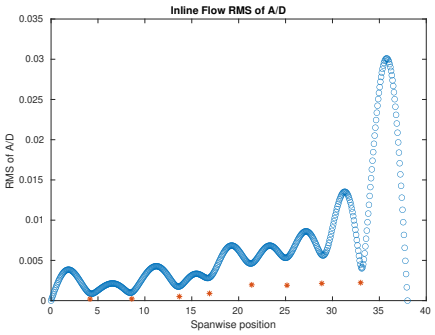

(b) Inline flow RMS profile case 5230.

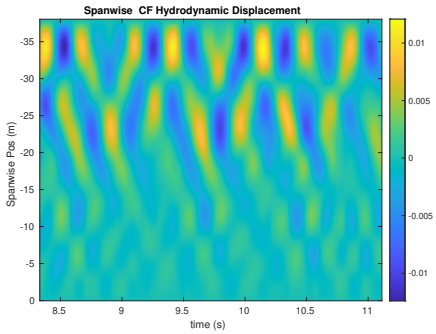

(c) Spanwise cross-flow hydrodynamic displacement case 5230.

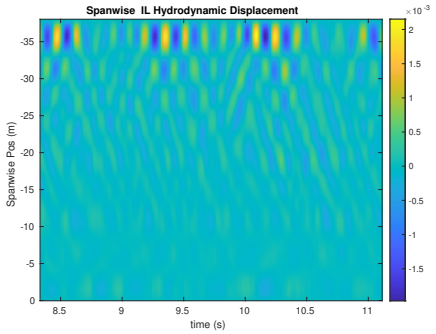

(d) Spanwise inline hydrodynamic displacement case 5230.

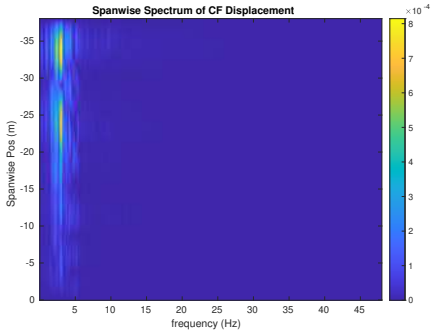

(e) Spanwise cross-flow spectrum of hydrodynamic displacement case 5230.

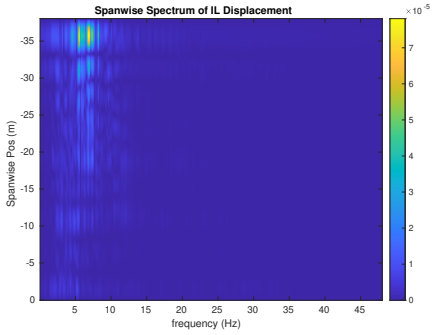

(f) Spanwise inline spectrum of hydrodynamic displacement case 5230.

Figure C-188: *Motion Analysis.* NDP Straight Riser ($L = 38m$) test case 5230.

NDP Straight Riser ($L = 38m$) test case 5240

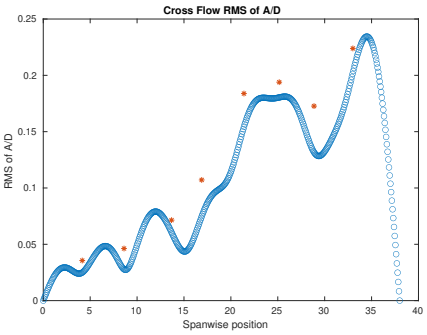

(a) Cross-flow RMS profile case 5240.

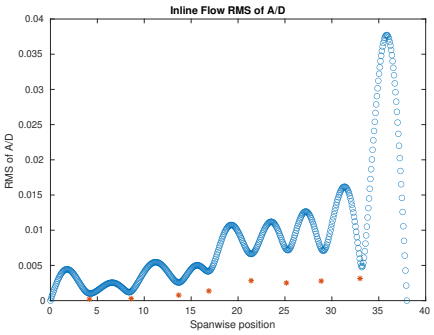

(b) Inline flow RMS profile case 5240.

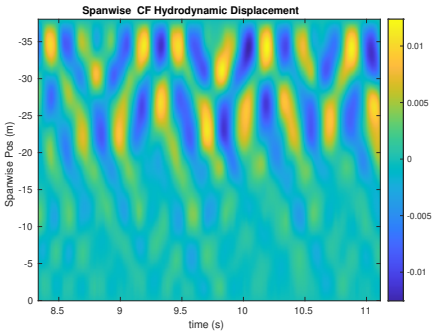

(c) Spanwise cross-flow hydrodynamic displacement case 5240.

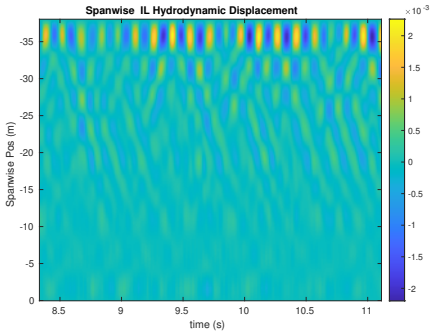

(d) Spanwise inline hydrodynamic displacement case 5240.

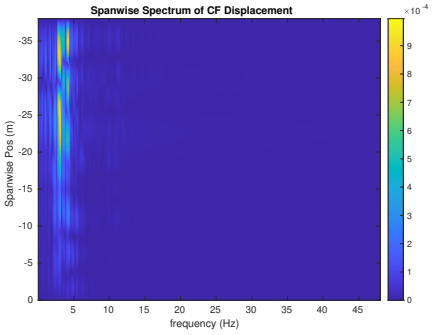

(e) Spanwise cross-flow spectrum of hydrodynamic displacement case 5240.

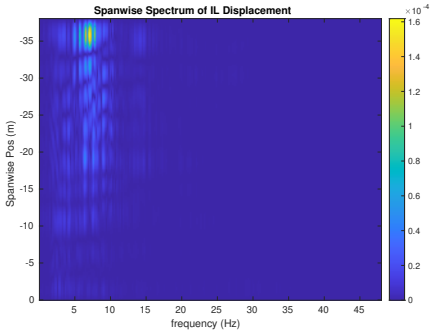

(f) Spanwise inline spectrum of hydrodynamic displacement case 5240.

Figure C-189: *Motion Analysis.* NDP Straight Riser ($L = 38m$) test case 5240.

NDP Straight Riser ($L = 38m$) test case 5250

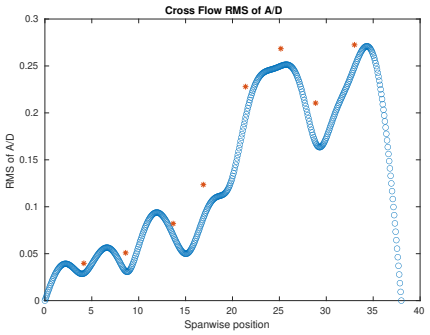

(a) Cross-flow RMS profile case 5250.

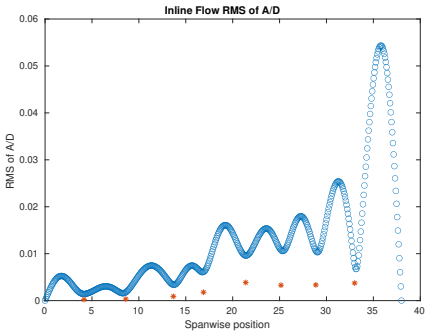

(b) Inline flow RMS profile case 5250.

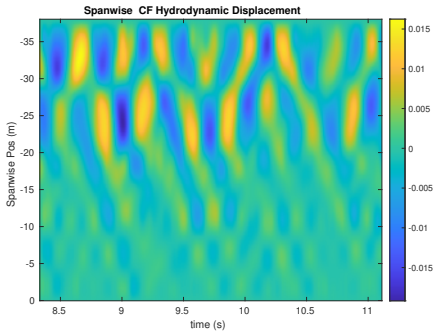

(c) Spanwise cross-flow hydrodynamic displacement case 5250.

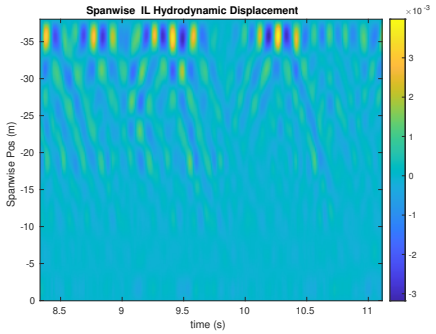

(d) Spanwise inline hydrodynamic displacement case 5250.

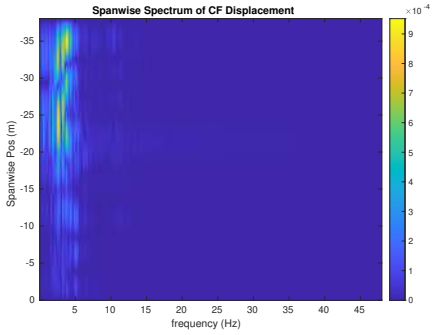

(e) Spanwise cross-flow spectrum of hydrodynamic displacement case 5250.

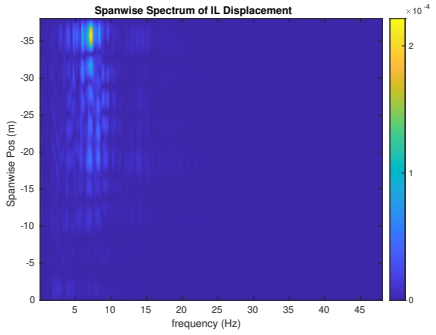

(f) Spanwise inline spectrum of hydrodynamic displacement case 5250.

Figure C-190: *Motion Analysis.* NDP Straight Riser ($L = 38m$) test case 5250.

NDP Straight Riser ($L = 38m$) test case 5260

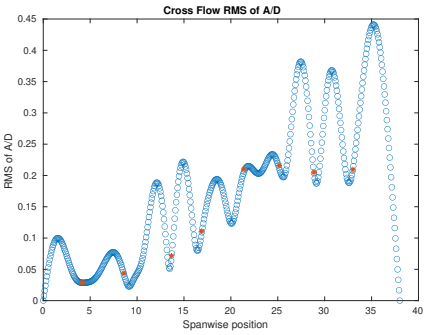

(a) Cross-flow RMS profile case 5260.

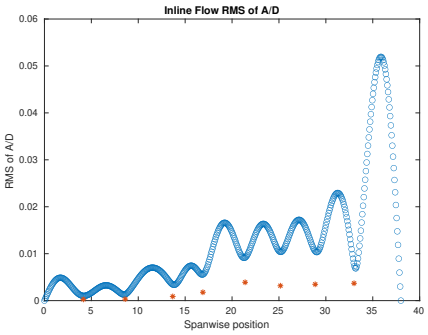

(b) Inline flow RMS profile case 5260.

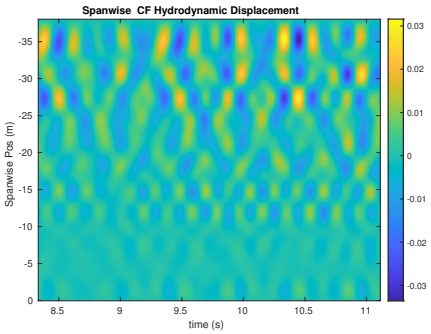

(c) Spanwise cross-flow hydrodynamic displacement case 5260.

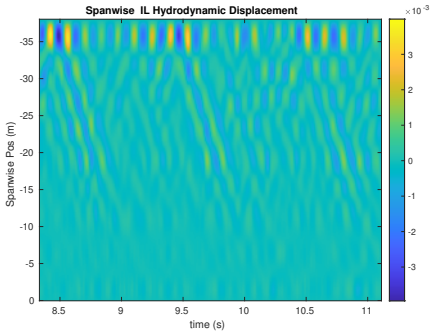

(d) Spanwise inline hydrodynamic displacement case 5260.

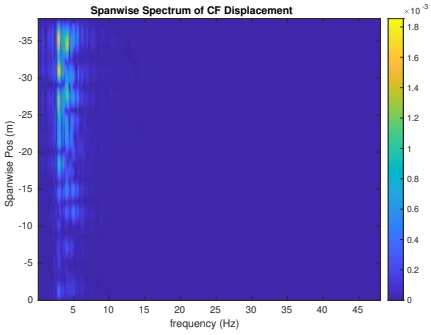

(e) Spanwise cross-flow spectrum of hydrodynamic displacement case 5260.

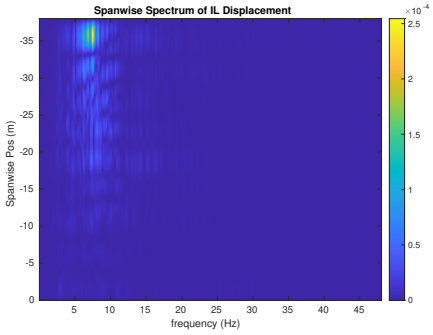

(f) Spanwise inline spectrum of hydrodynamic displacement case 5260.

Figure C-191: *Motion Analysis.* NDP Straight Riser ($L = 38m$) test case 5260.

NDP Straight Riser ($L = 38m$) test case 5270

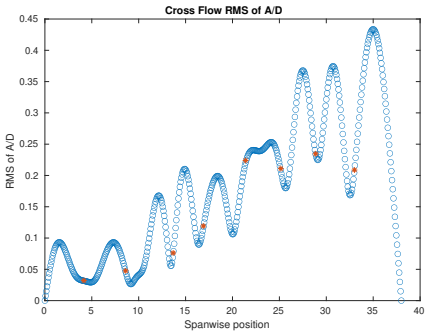

(a) Cross-flow RMS profile case 5270.

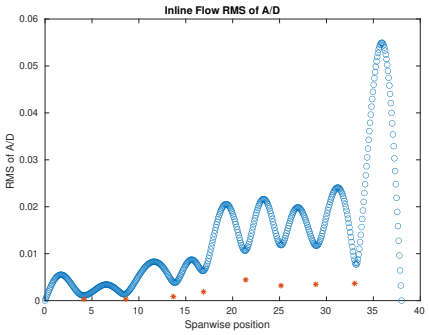

(b) Inline flow RMS profile case 5270.

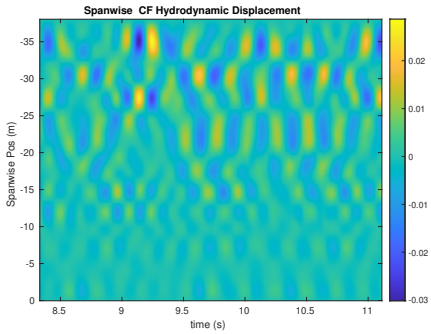

(c) Spanwise cross-flow hydrodynamic displacement case 5270.

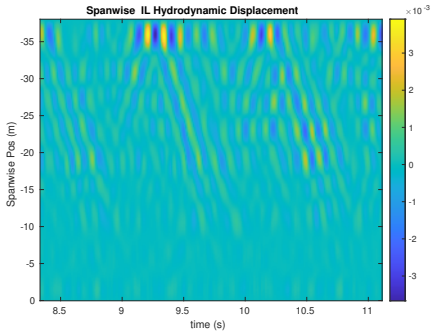

(d) Spanwise inline hydrodynamic displacement case 5270.

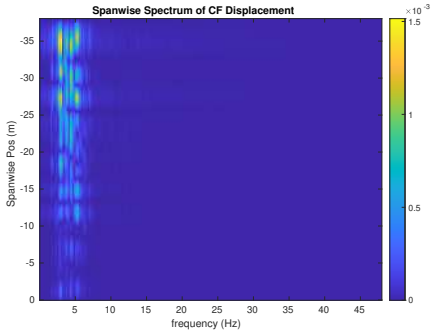

(e) Spanwise cross-flow spectrum of hydrodynamic displacement case 5270.

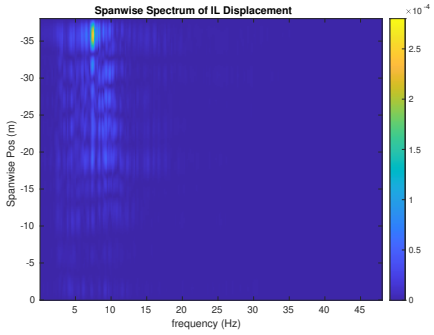

(f) Spanwise inline spectrum of hydrodynamic displacement case 5270.

Figure C-192: *Motion Analysis.* NDP Straight Riser ($L = 38m$) test case 5270.

NDP Straight Riser ($L = 38m$) test case 5280

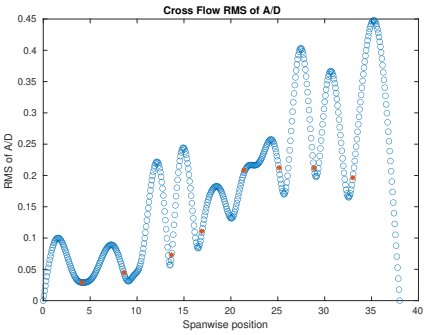

(a) Cross-flow RMS profile case 5280.

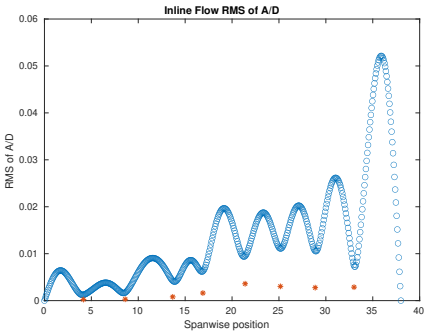

(b) Inline flow RMS profile case 5280.

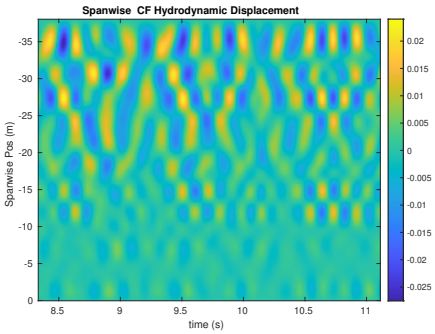

(c) Spanwise cross-flow hydrodynamic displacement case 5280.

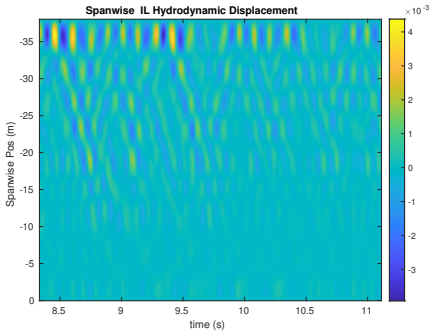

(d) Spanwise inline hydrodynamic displacement case 5280.

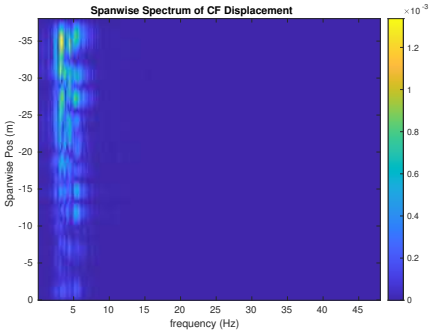

(e) Spanwise cross-flow spectrum of hydrodynamic displacement case 5280.

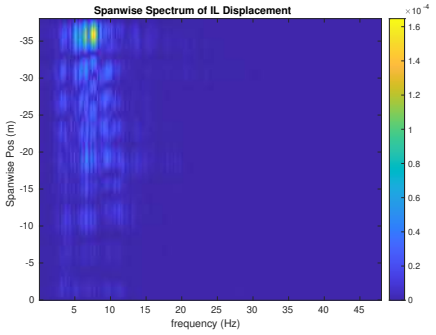

(f) Spanwise inline spectrum of hydrodynamic displacement case 5280.

Figure C-193: *Motion Analysis.* NDP Straight Riser ($L = 38m$) test case 5280.

NDP Straight Riser ($L = 38m$) test case 5290

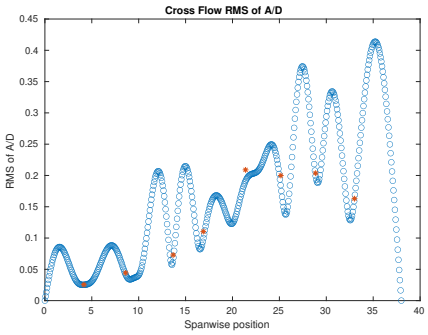

(a) Cross-flow RMS profile case 5290.

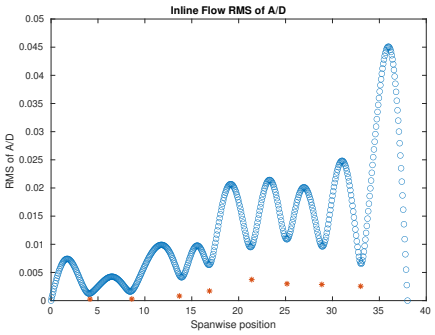

(b) Inline flow RMS profile case 5290.

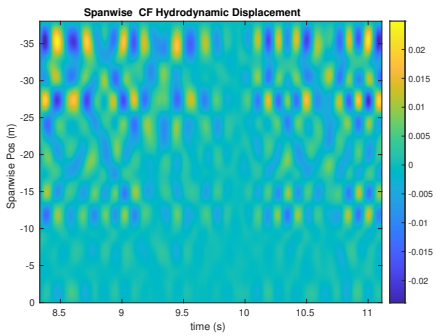

(c) Spanwise cross-flow hydrodynamic displacement case 5290.

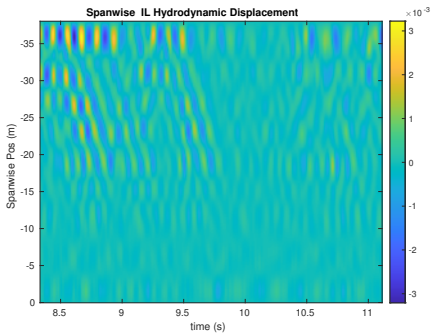

(d) Spanwise inline hydrodynamic displacement case 5290.

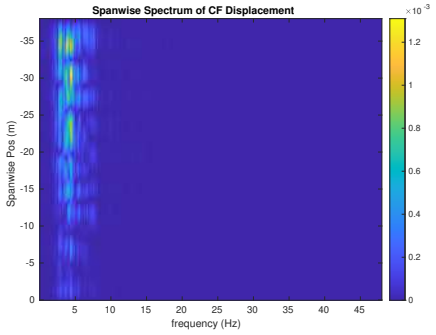

(e) Spanwise cross-flow spectrum of hydrodynamic displacement case 5290.

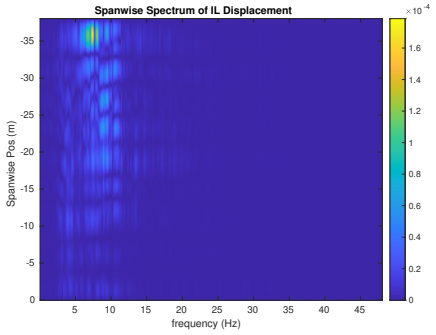

(f) Spanwise inline spectrum of hydrodynamic displacement case 5290.

Figure C-194: *Motion Analysis.* NDP Straight Riser ($L = 38m$) test case 5290.

NDP Straight Riser ($L = 38m$) test case 5300

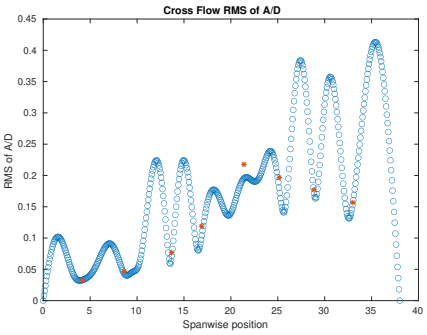

(a) Cross-flow RMS profile case 5300.

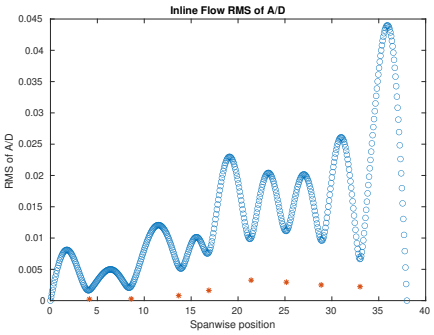

(b) Inline flow RMS profile case 5300.

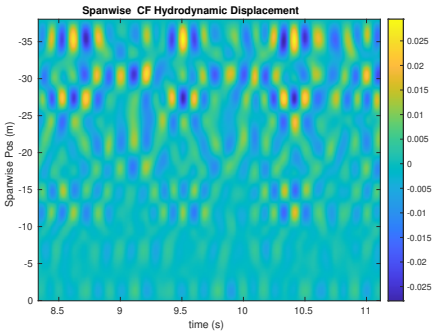

(c) Spanwise cross-flow hydrodynamic displacement case 5300.

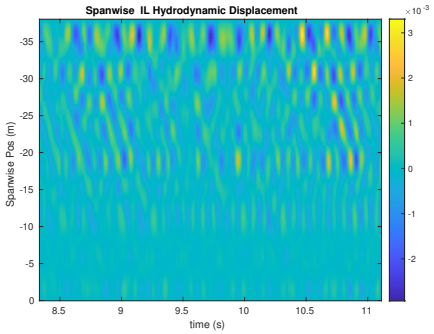

(d) Spanwise inline hydrodynamic displacement case 5300.

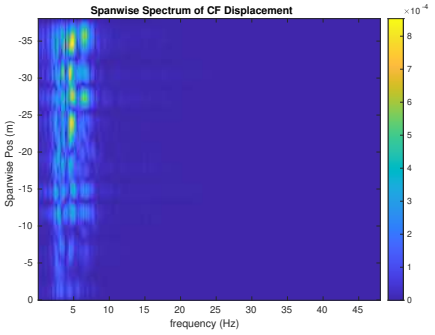

(e) Spanwise cross-flow spectrum of hydrodynamic displacement case 5300.

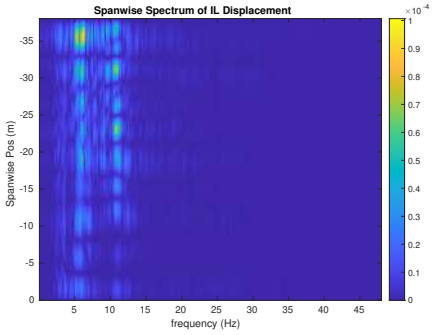

(f) Spanwise inline spectrum of hydrodynamic displacement case 5300.

Figure C-195: *Motion Analysis.* NDP Straight Riser ($L = 38m$) test case 5300.

NDP Straight Riser ($L = 38m$) test case 5310

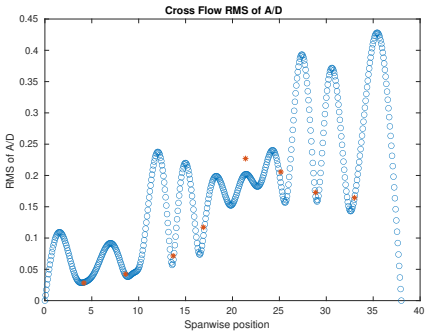

(a) Cross-flow RMS profile case 5310.

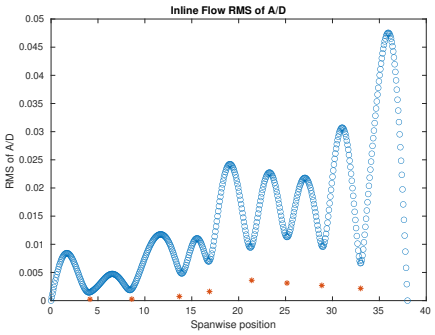

(b) Inline flow RMS profile case 5310.

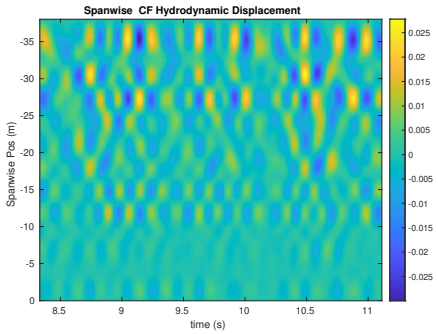

(c) Spanwise cross-flow hydrodynamic displacement case 5310.

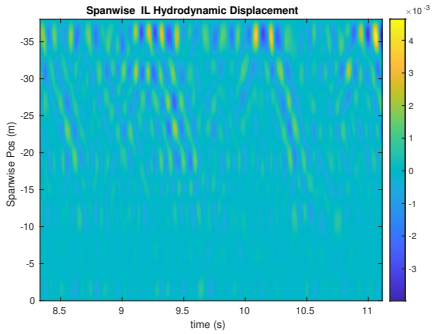

(d) Spanwise inline hydrodynamic displacement case 5310.

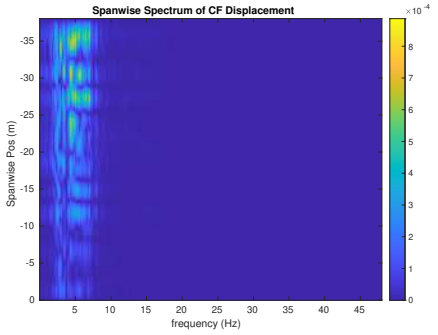

(e) Spanwise cross-flow spectrum of hydrodynamic displacement case 5310.

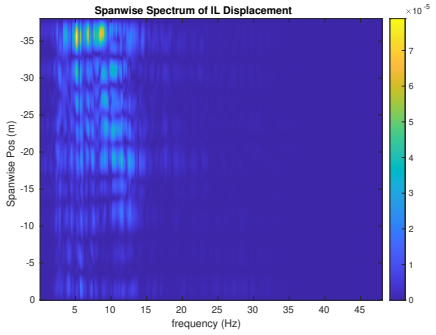

(f) Spanwise inline spectrum of hydrodynamic displacement case 5310.

Figure C-196: *Motion Analysis.* NDP Straight Riser ($L = 38m$) test case 5310.

NDP Straight Riser ($L = 38m$) test case 5320

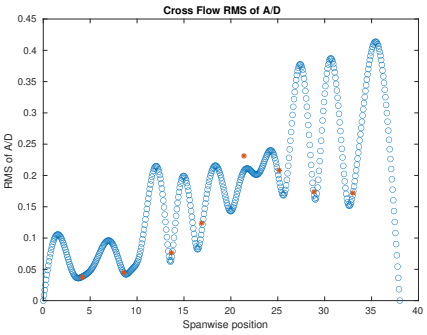

(a) Cross-flow RMS profile case 5320.

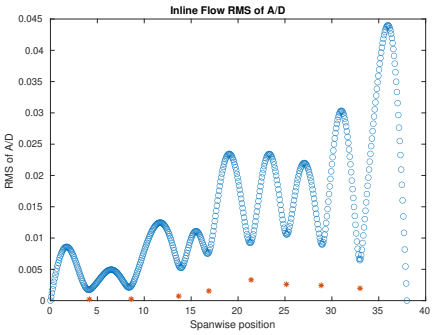

(b) Inline flow RMS profile case 5320.

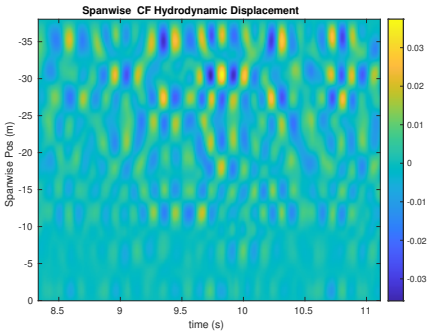

(c) Spanwise cross-flow hydrodynamic displacement case 5320.

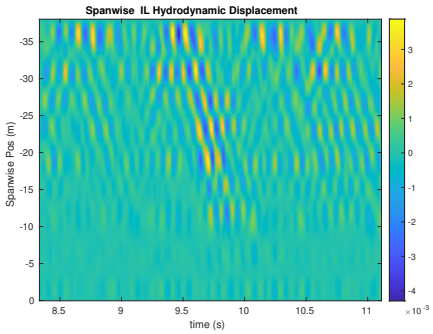

(d) Spanwise inline hydrodynamic displacement case 5320.

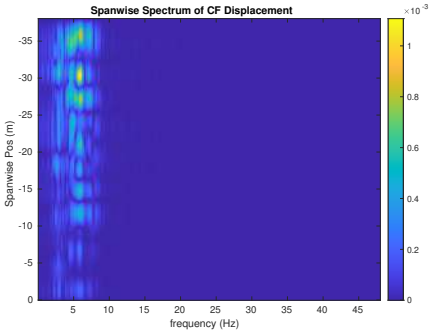

(e) Spanwise cross-flow spectrum of hydrodynamic displacement case 5320.

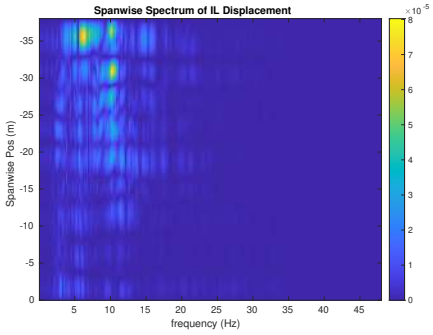

(f) Spanwise inline spectrum of hydrodynamic displacement case 5320.

Figure C-197: *Motion Analysis.* NDP Straight Riser ($L = 38m$) test case 5320.

NDP Straight Riser ($L = 38m$) test case 5330

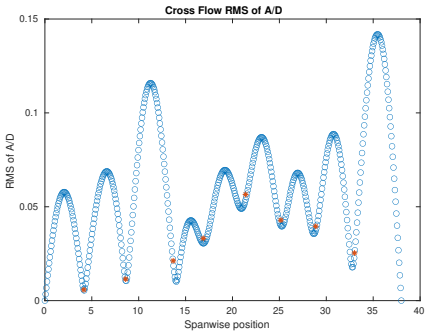

(a) Cross-flow RMS profile case 5330.

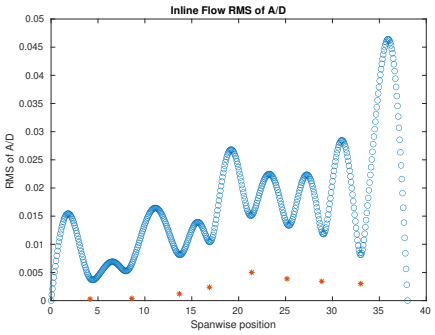

(b) Inline flow RMS profile case 5330.

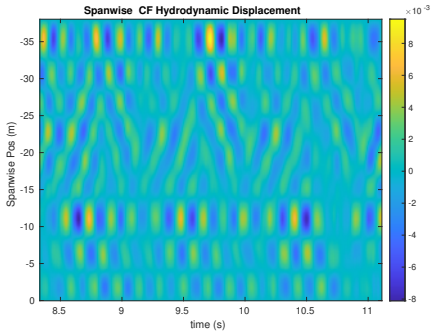

(c) Spanwise cross-flow hydrodynamic displacement case 5330.

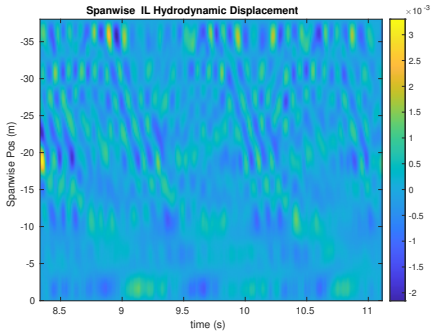

(d) Spanwise inline hydrodynamic displacement case 5330.

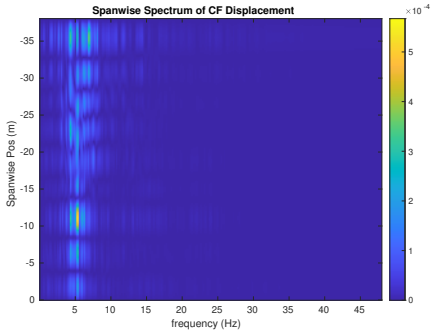

(e) Spanwise cross-flow spectrum of hydrodynamic displacement case 5330.

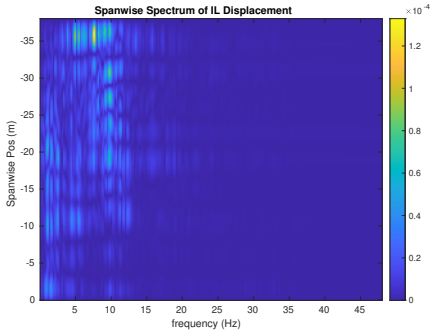

(f) Spanwise inline spectrum of hydrodynamic displacement case 5330.

Figure C-198: *Motion Analysis.* NDP Straight Riser ($L = 38m$) test case 5330.

NDP Straight Riser ($L = 38m$) test case 6010

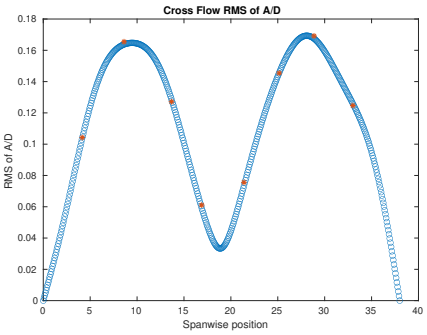

(a) Cross-flow RMS profile case 6010.

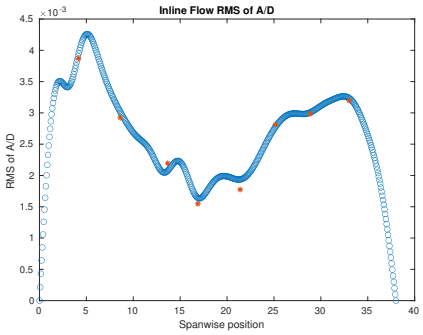

(b) Inline flow RMS profile case 6010.

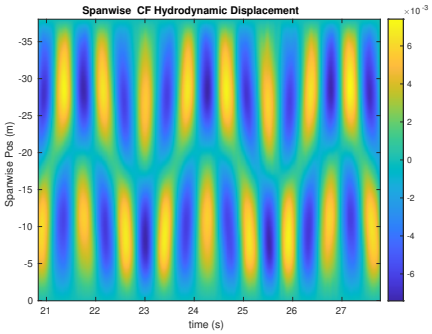

(c) Spanwise cross-flow hydrodynamic displacement case 6010.

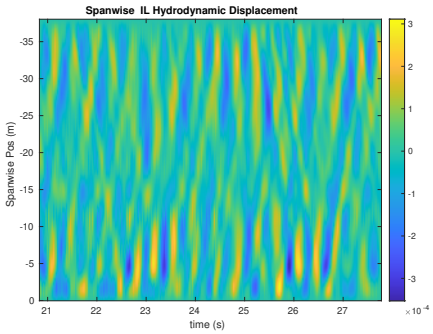

(d) Spanwise inline hydrodynamic displacement case 6010.

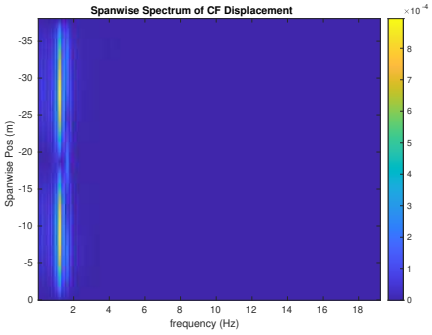

(e) Spanwise cross-flow spectrum of hydrodynamic displacement case 6010.

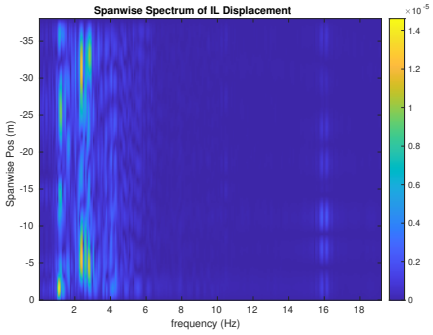

(f) Spanwise inline spectrum of hydrodynamic displacement case 6010.

Figure C-199: *Motion Analysis.* NDP Straight Riser ($L = 38m$) test case 6010.

NDP Straight Riser ($L = 38m$) test case 6020

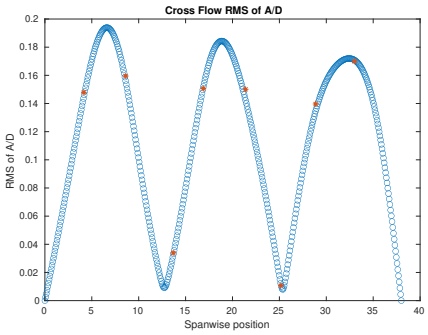

(a) Cross-flow RMS profile case 6020.

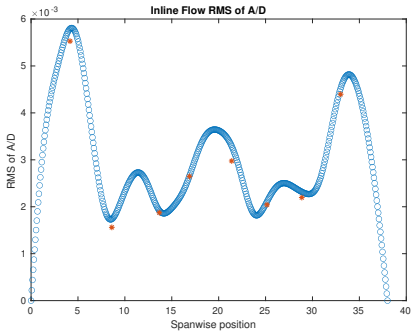

(b) Inline flow RMS profile case 6020.

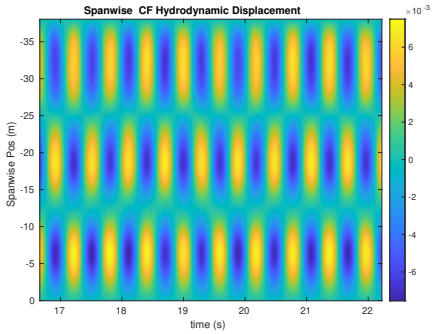

(c) Spanwise cross-flow hydrodynamic displacement case 6020.

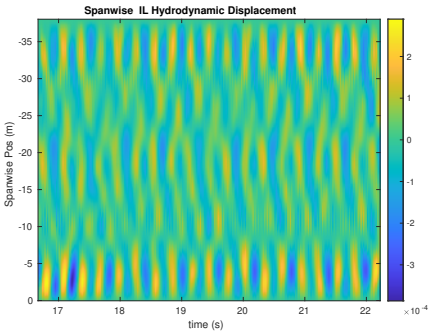

(d) Spanwise inline hydrodynamic displacement case 6020.

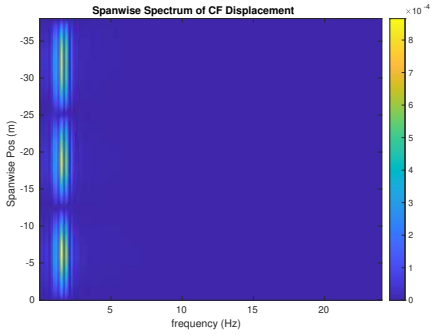

(e) Spanwise cross-flow spectrum of hydrodynamic displacement case 6020.

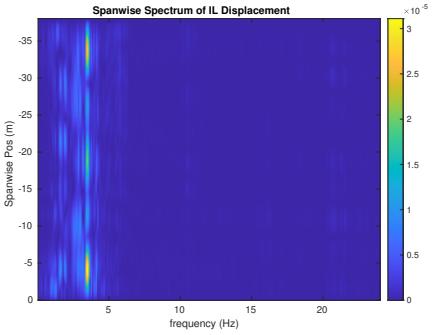

(f) Spanwise inline spectrum of hydrodynamic displacement case 6020.

Figure C-200: *Motion Analysis.* NDP Straight Riser ($L = 38m$) test case 6020.

NDP Straight Riser ($L = 38m$) test case 6030

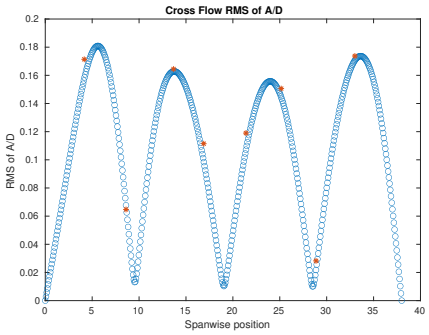

(a) Cross-flow RMS profile case 6030.

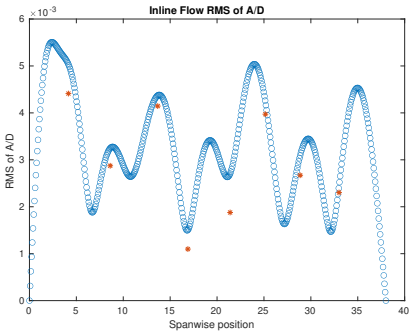

(b) Inline flow RMS profile case 6030.

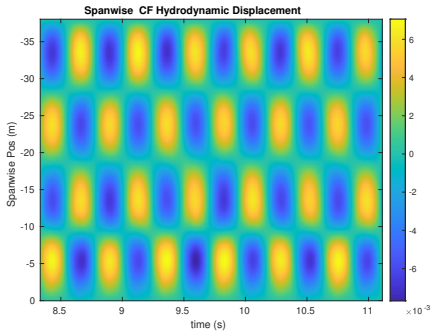

(c) Spanwise cross-flow hydrodynamic displacement case 6030.

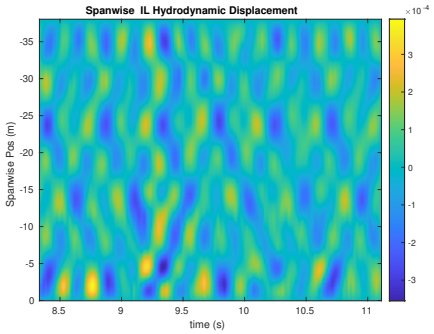

(d) Spanwise inline hydrodynamic displacement case 6030.

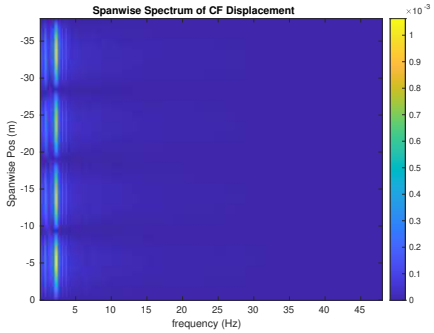

(e) Spanwise cross-flow spectrum of hydrodynamic displacement case 6030.

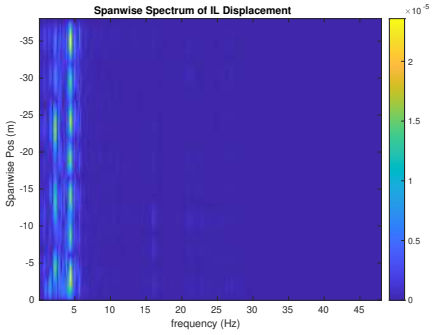

(f) Spanwise inline spectrum of hydrodynamic displacement case 6030.

Figure C-201: *Motion Analysis.* NDP Straight Riser ($L = 38m$) test case 6030.

NDP Straight Riser ($L = 38m$) test case 6040

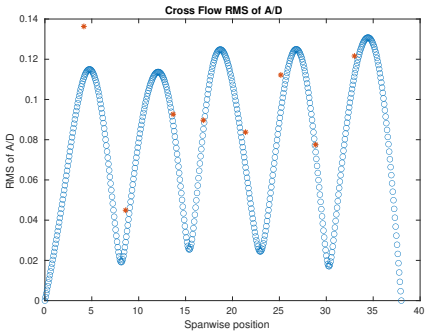

(a) Cross-flow RMS profile case 6040.

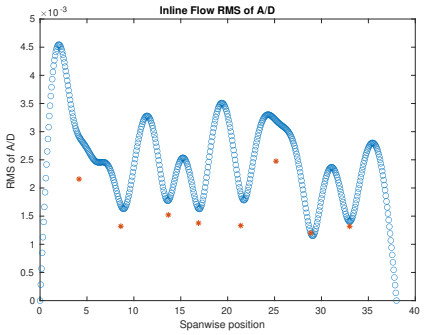

(b) Inline flow RMS profile case 6040.

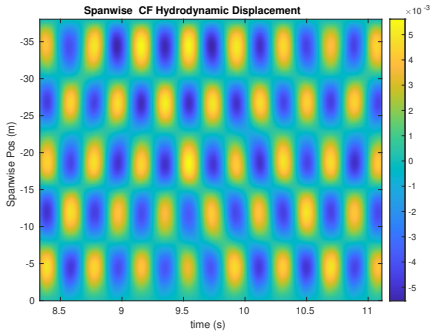

(c) Spanwise cross-flow hydrodynamic displacement case 6040.

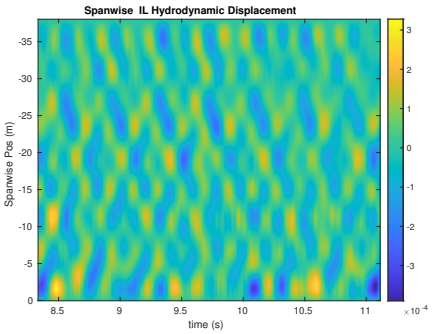

(d) Spanwise inline hydrodynamic displacement case 6040.

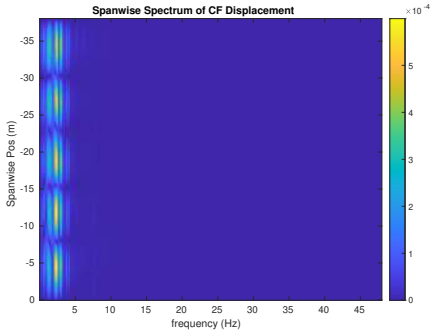

(e) Spanwise cross-flow spectrum of hydrodynamic displacement case 6040.

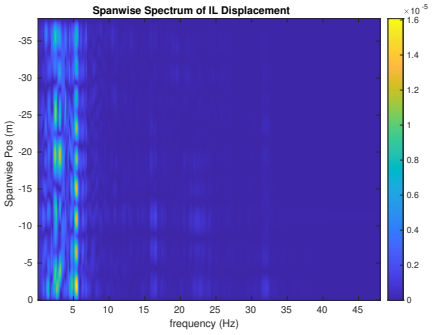

(f) Spanwise inline spectrum of hydrodynamic displacement case 6040.

Figure C-202: *Motion Analysis.* NDP Straight Riser ($L = 38m$) test case 6040.

NDP Straight Riser ($L = 38m$) test case 6050

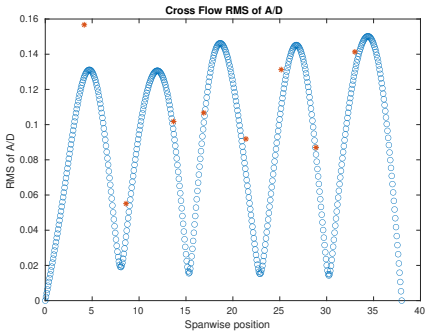

(a) Cross-flow RMS profile case 6050.

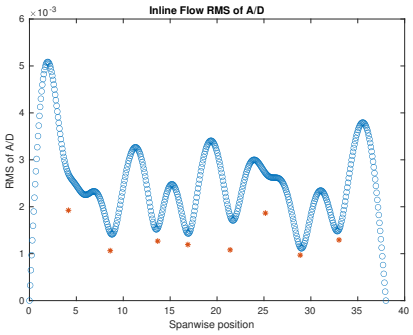

(b) Inline flow RMS profile case 6050.

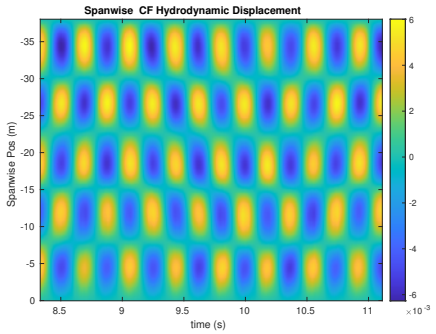

(c) Spanwise cross-flow hydrodynamic displacement case 6050.

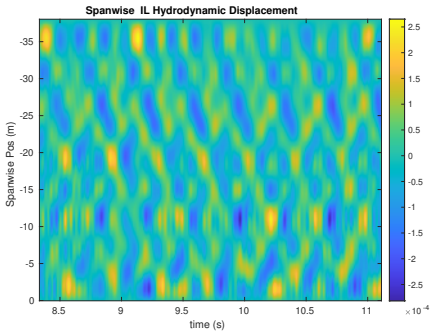

(d) Spanwise inline hydrodynamic displacement case 6050.

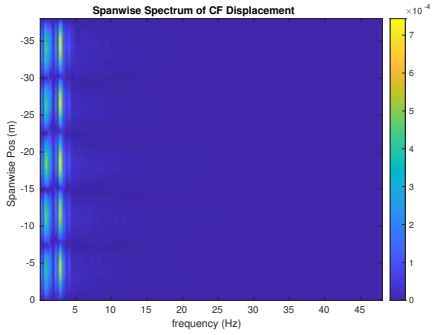

(e) Spanwise cross-flow spectrum of hydrodynamic displacement case 6050.

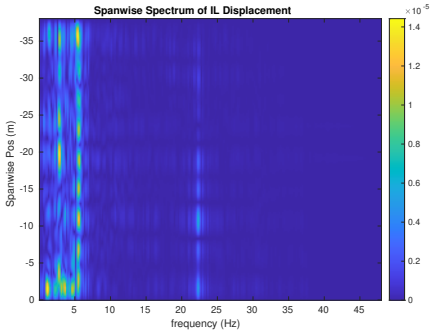

(f) Spanwise inline spectrum of hydrodynamic displacement case 6050.

Figure C-203: *Motion Analysis.* NDP Straight Riser ($L = 38m$) test case 6050.

NDP Straight Riser ($L = 38m$) test case 6060

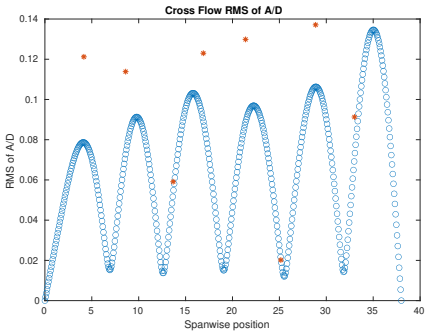

(a) Cross-flow RMS profile case 6060.

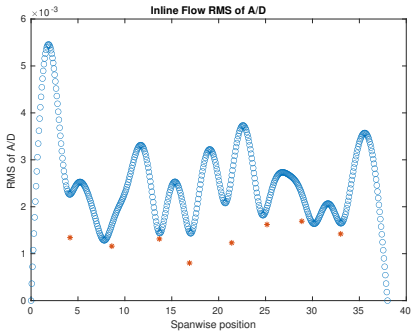

(b) Inline flow RMS profile case 6060.

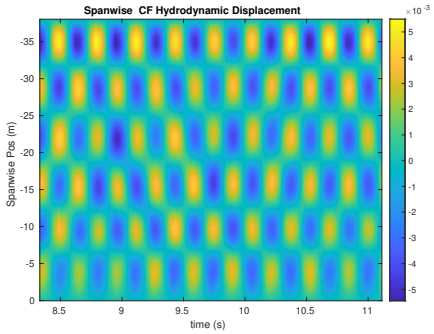

(c) Spanwise cross-flow hydrodynamic displacement case 6060.

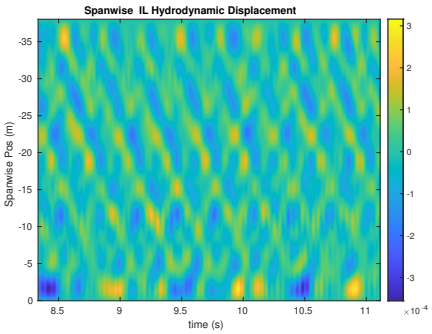

(d) Spanwise inline hydrodynamic displacement case 6060.

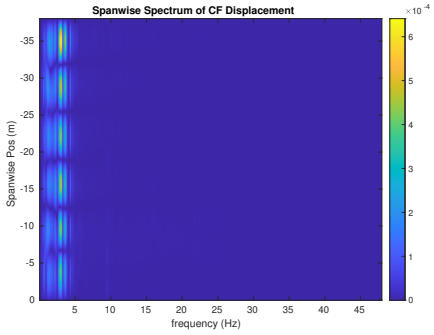

(e) Spanwise cross-flow spectrum of hydrodynamic displacement case 6060.

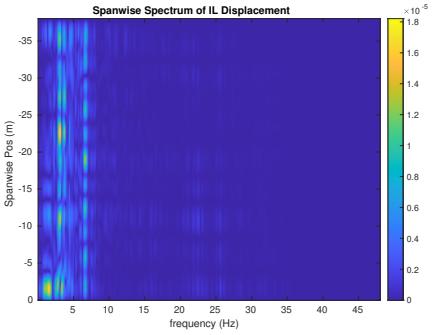

(f) Spanwise inline spectrum of hydrodynamic displacement case 6060.

Figure C-204: *Motion Analysis.* NDP Straight Riser ($L = 38m$) test case 6060.

NDP Straight Riser ($L = 38m$) test case 6070

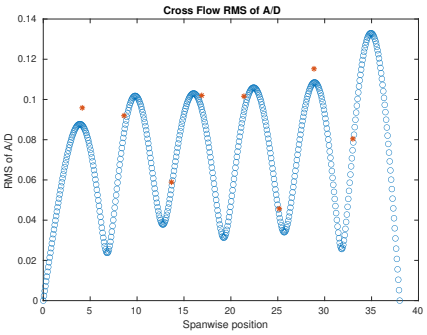

(a) Cross-flow RMS profile case 6070.

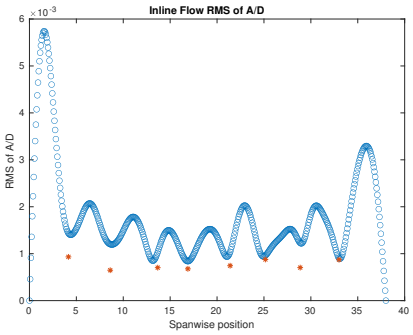

(b) Inline flow RMS profile case 6070.

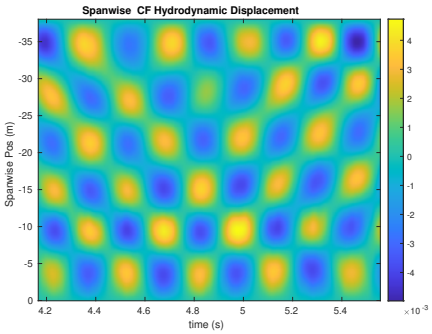

(c) Spanwise cross-flow hydrodynamic displacement case 6070.

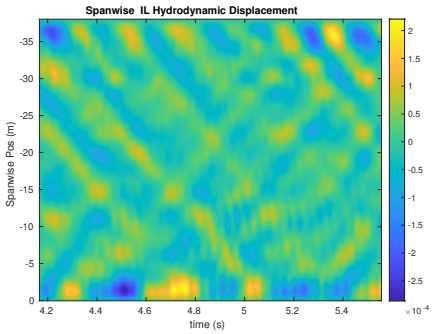

(d) Spanwise inline hydrodynamic displacement case 6070.

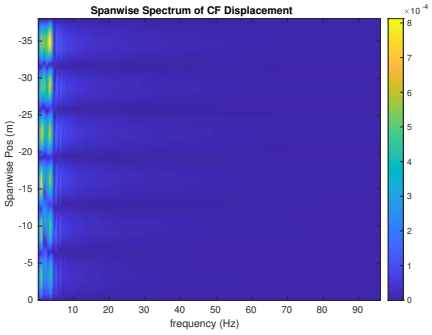

(e) Spanwise cross-flow spectrum of hydrodynamic displacement case 6070.

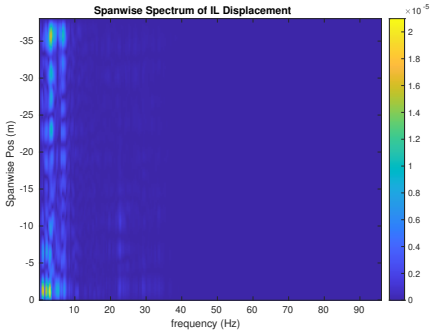

(f) Spanwise inline spectrum of hydrodynamic displacement case 6070.

Figure C-205: *Motion Analysis.* NDP Straight Riser ($L = 38m$) test case 6070.

NDP Straight Riser ($L = 38m$) test case 6080

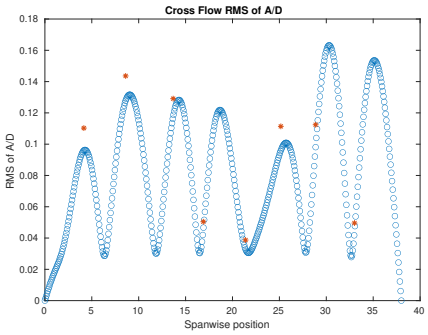

(a) Cross-flow RMS profile case 6080.

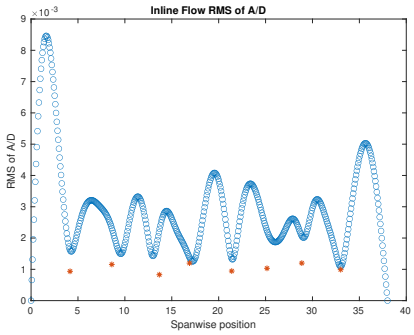

(b) Inline flow RMS profile case 6080.

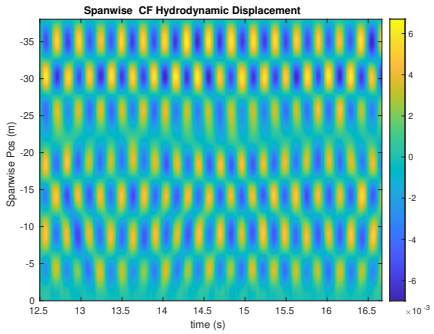

(c) Spanwise cross-flow hydrodynamic displacement case 6080.

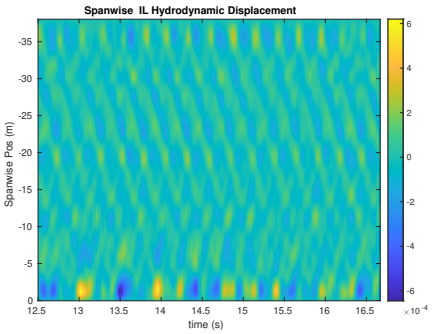

(d) Spanwise inline hydrodynamic displacement case 6080.

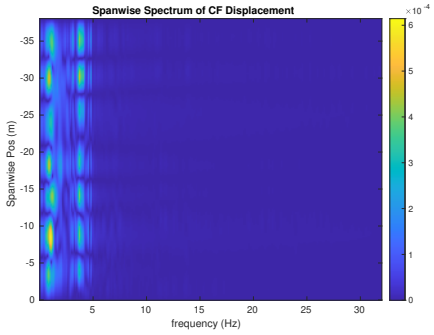

(e) Spanwise cross-flow spectrum of hydrodynamic displacement case 6080.

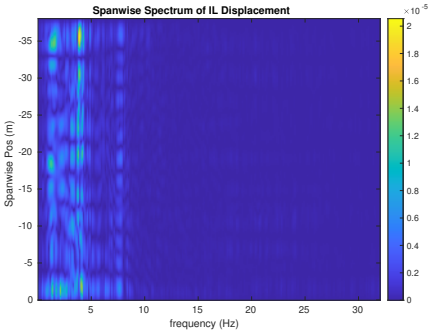

(f) Spanwise inline spectrum of hydrodynamic displacement case 6080.

Figure C-206: *Motion Analysis.* NDP Straight Riser ($L = 38m$) test case 6080.

NDP Straight Riser ($L = 38m$) test case 6090

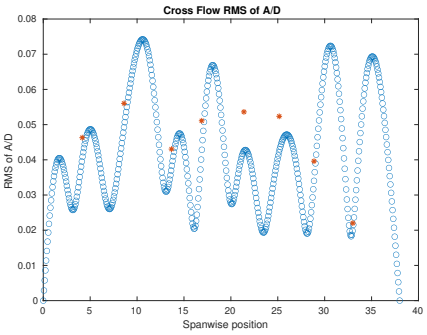

(a) Cross-flow RMS profile case 6090.

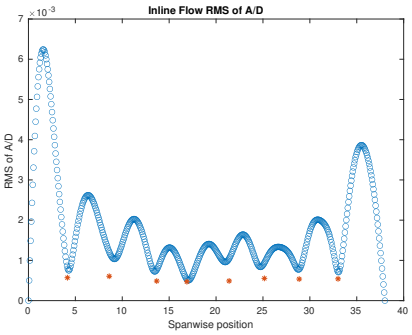

(b) Inline flow RMS profile case 6090.

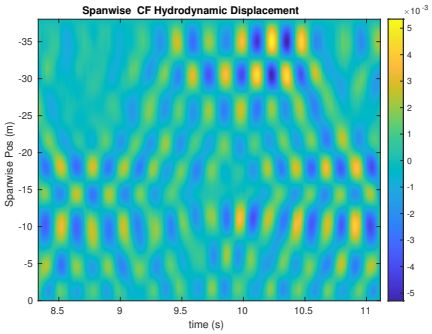

(c) Spanwise cross-flow hydrodynamic displacement case 6090.

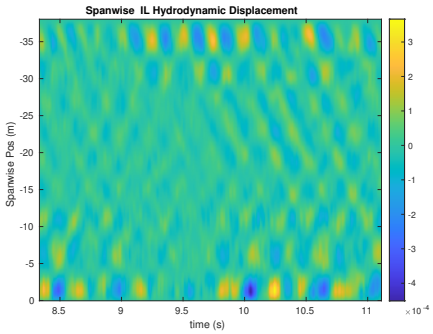

(d) Spanwise inline hydrodynamic displacement case 6090.

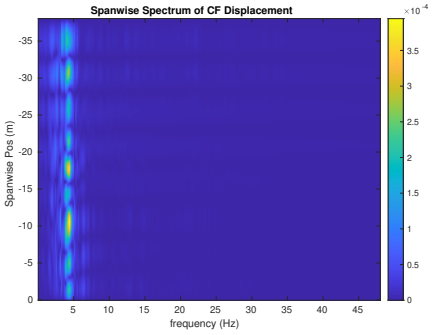

(e) Spanwise cross-flow spectrum of hydrodynamic displacement case 6090.

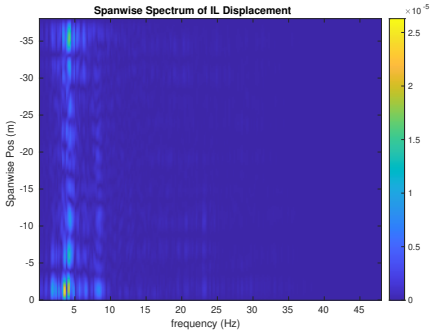

(f) Spanwise inline spectrum of hydrodynamic displacement case 6090.

Figure C-207: *Motion Analysis.* NDP Straight Riser ($L = 38m$) test case 6090.

NDP Straight Riser ($L = 38m$) test case 6100

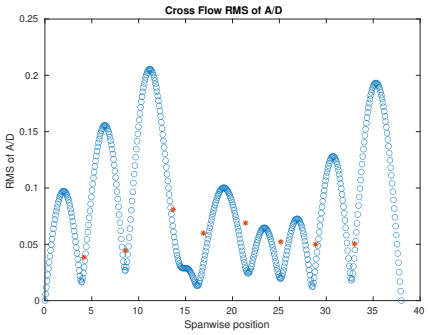

(a) Cross-flow RMS profile case 6100.

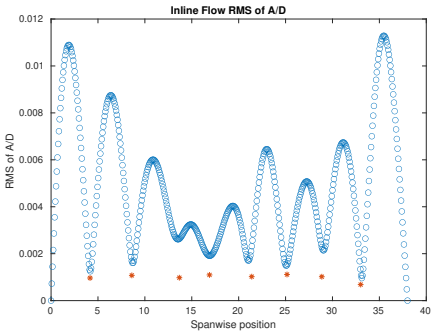

(b) Inline flow RMS profile case 6100.

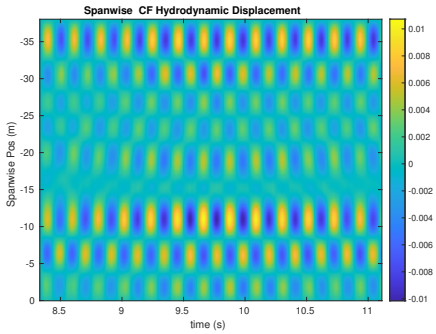

(c) Spanwise cross-flow hydrodynamic displacement case 6100.

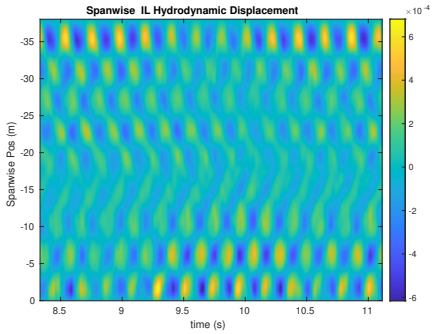

(d) Spanwise inline hydrodynamic displacement case 6100.

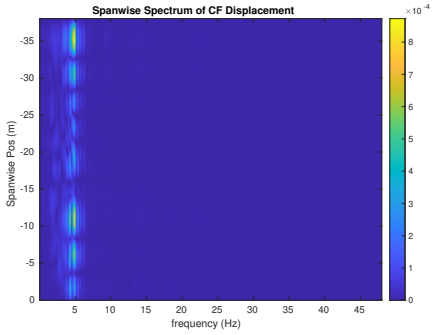

(e) Spanwise cross-flow spectrum of hydrodynamic displacement case 6100.

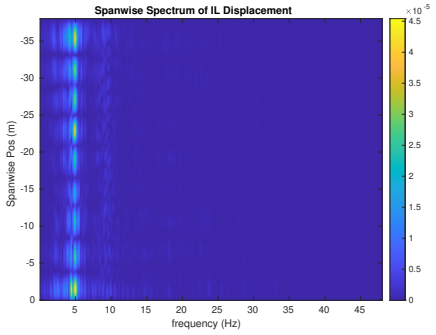

(f) Spanwise inline spectrum of hydrodynamic displacement case 6100.

Figure C-208: *Motion Analysis.* NDP Straight Riser ($L = 38m$) test case 6100.

NDP Straight Riser ($L = 38m$) test case 6110

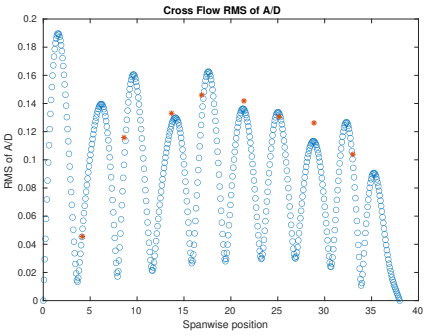

(a) Cross-flow RMS profile case 6110.

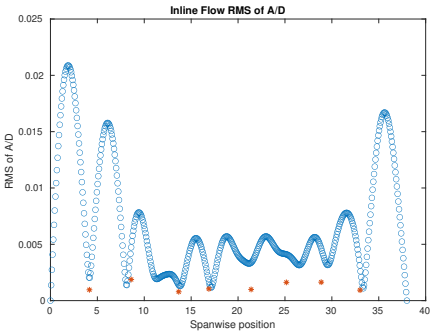

(b) Inline flow RMS profile case 6110.

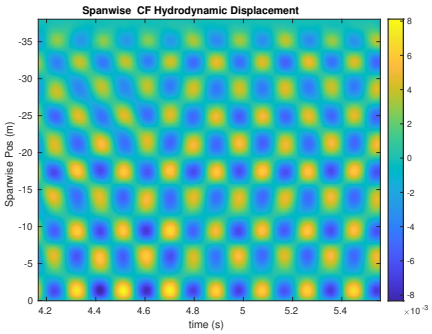

(c) Spanwise cross-flow hydrodynamic displacement case 6110.

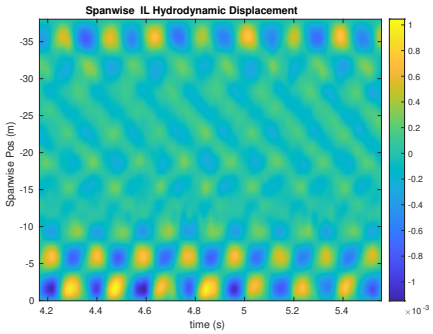

(d) Spanwise inline hydrodynamic displacement case 6110.

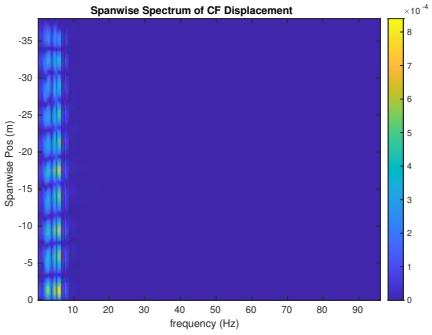

(e) Spanwise cross-flow spectrum of hydrodynamic displacement case 6110.

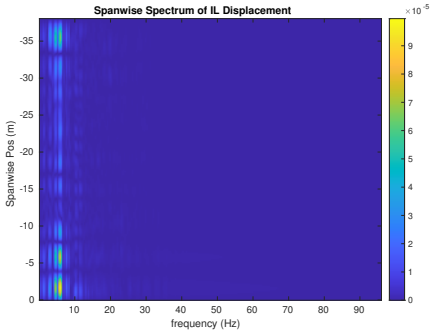

(f) Spanwise inline spectrum of hydrodynamic displacement case 6110.

Figure C-209: *Motion Analysis.* NDP Straight Riser ($L = 38m$) test case 6110.

NDP Straight Riser ($L = 38m$) test case 6120

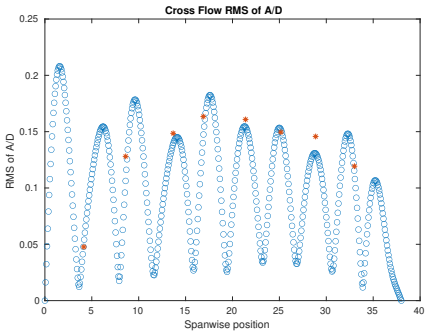

(a) Cross-flow RMS profile case 6120.

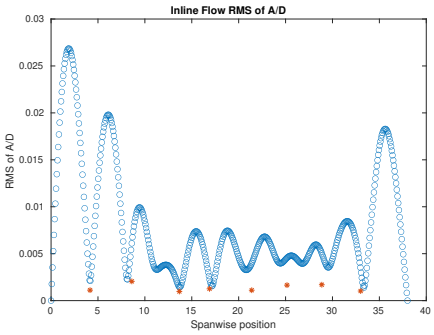

(b) Inline flow RMS profile case 6120.

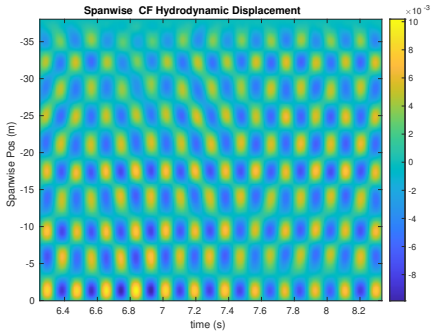

(c) Spanwise cross-flow hydrodynamic displacement case 6120.

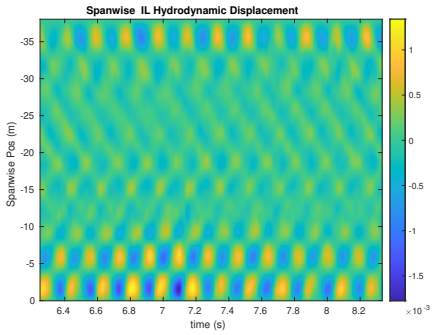

(d) Spanwise inline hydrodynamic displacement case 6120.

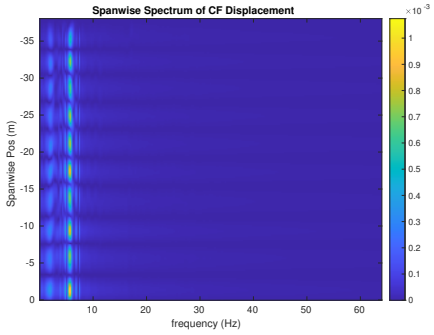

(e) Spanwise cross-flow spectrum of hydrodynamic displacement case 6120.

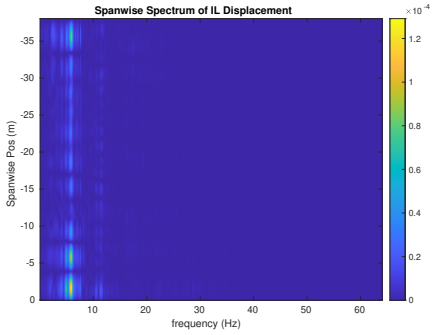

(f) Spanwise inline spectrum of hydrodynamic displacement case 6120.

Figure C-210: *Motion Analysis.* NDP Straight Riser ($L = 38m$) test case 6120.

NDP Straight Riser ($L = 38m$) test case 6130

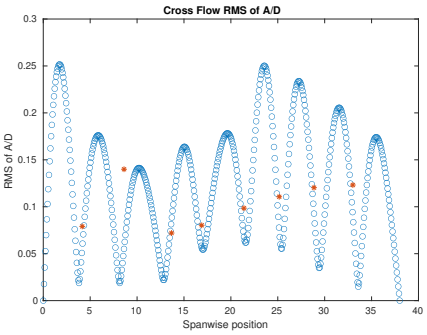

(a) Cross-flow RMS profile case 6130.

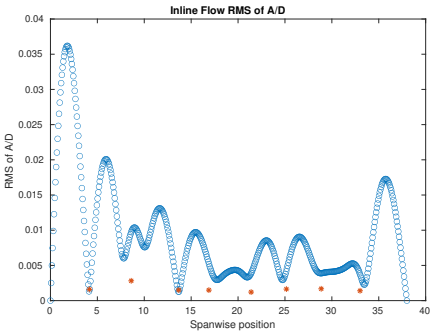

(b) Inline flow RMS profile case 6130.

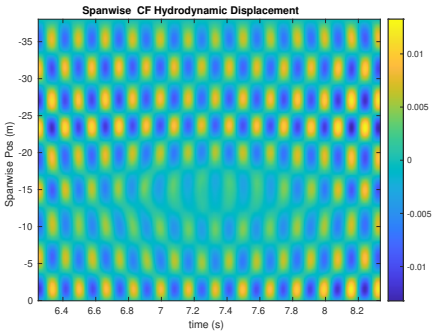

(c) Spanwise cross-flow hydrodynamic displacement case 6130.

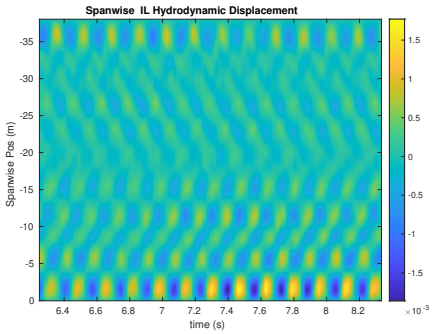

(d) Spanwise inline hydrodynamic displacement case 6130.

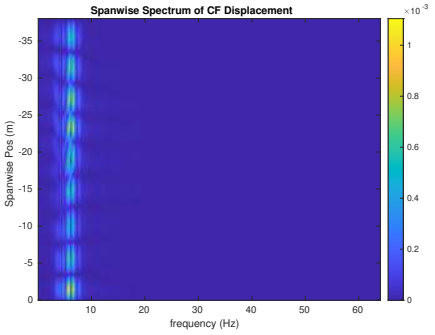

(e) Spanwise cross-flow spectrum of hydrodynamic displacement case 6130.

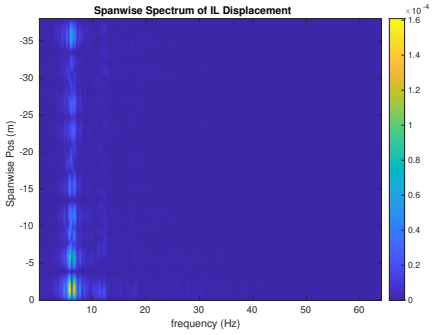

(f) Spanwise inline spectrum of hydrodynamic displacement case 6130.

Figure C-211: *Motion Analysis.* NDP Straight Riser ($L = 38m$) test case 6130.

NDP Straight Riser ($L = 38m$) test case 6140

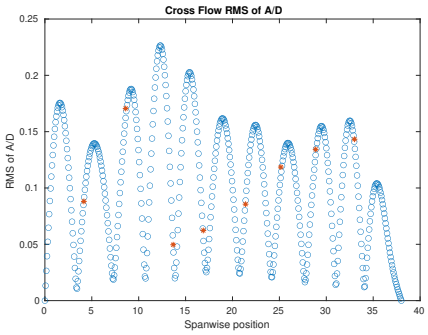

(a) Cross-flow RMS profile case 6140.

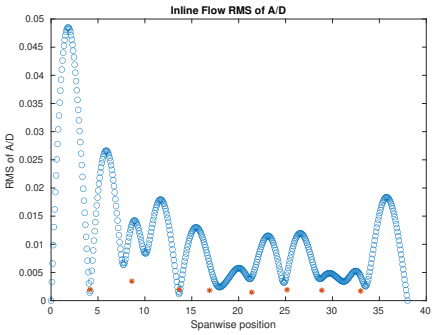

(b) Inline flow RMS profile case 6140.

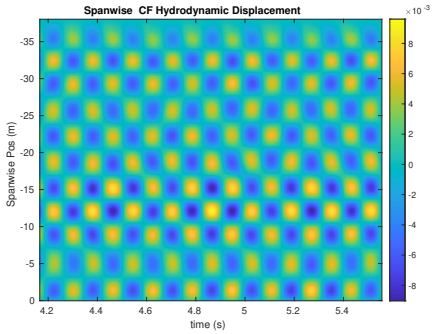

(c) Spanwise cross-flow hydrodynamic displacement case 6140.

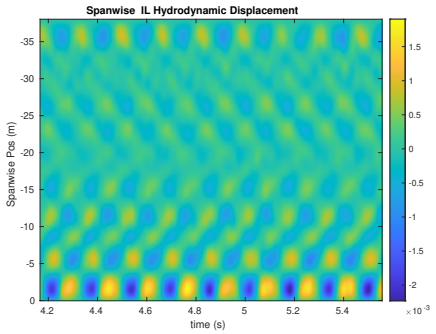

(d) Spanwise inline hydrodynamic displacement case 6140.

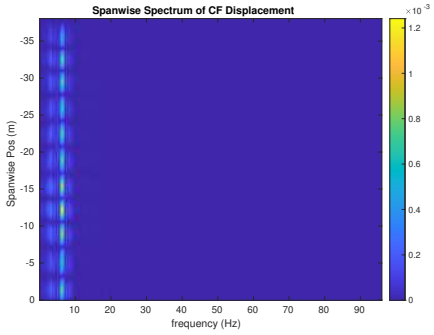

(e) Spanwise cross-flow spectrum of hydrodynamic displacement case 6140.

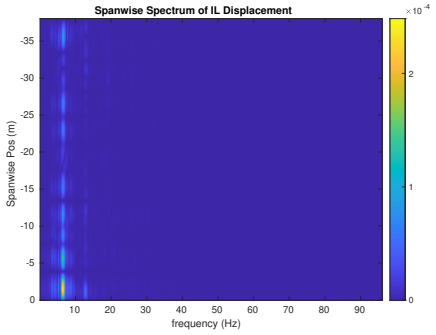

(f) Spanwise inline spectrum of hydrodynamic displacement case 6140.

Figure C-212: *Motion Analysis.* NDP Straight Riser ($L = 38m$) test case 6140.

NDP Straight Riser ($L = 38m$) test case 6150

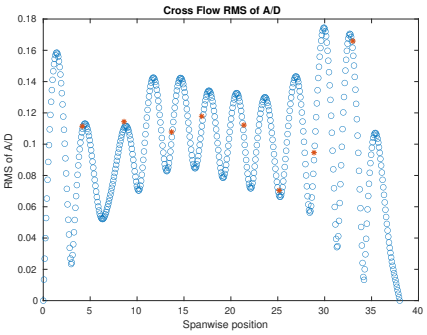

(a) Cross-flow RMS profile case 6150.

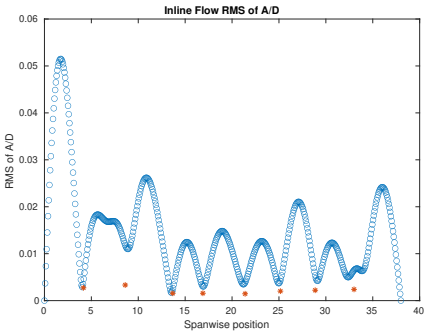

(b) Inline flow RMS profile case 6150.

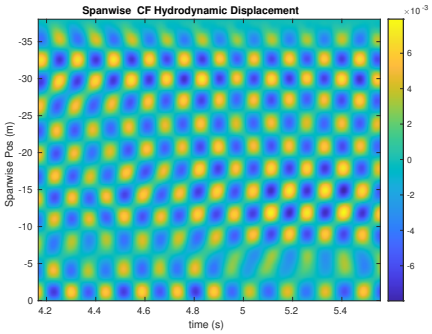

(c) Spanwise cross-flow hydrodynamic displacement case 6150.

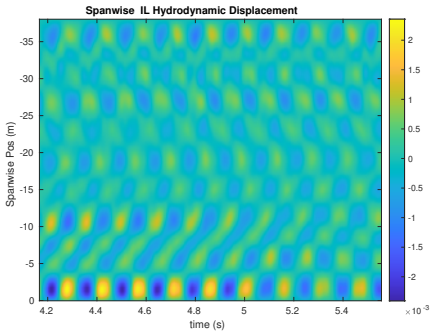

(d) Spanwise inline hydrodynamic displacement case 6150.

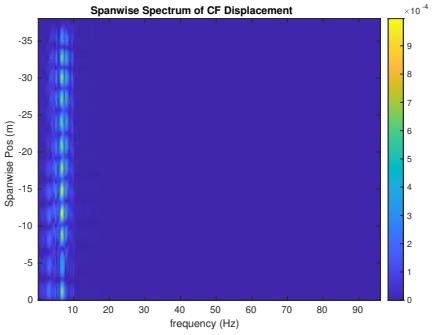

(e) Spanwise cross-flow spectrum of hydrodynamic displacement case 6150.

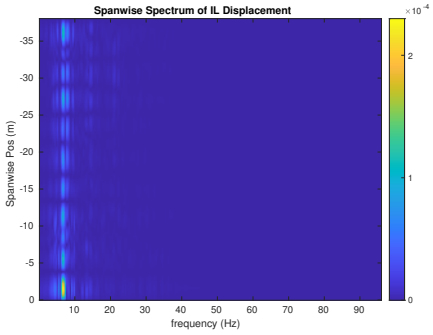

(f) Spanwise inline spectrum of hydrodynamic displacement case 6150.

Figure C-213: *Motion Analysis.* NDP Straight Riser ($L = 38m$) test case 6150.

NDP Straight Riser ($L = 38m$) test case 6160

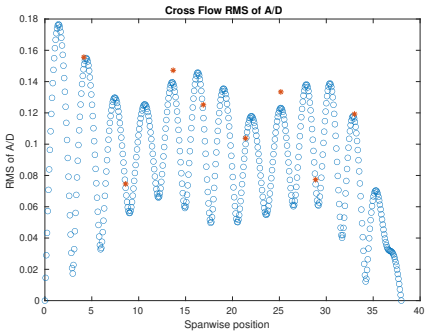

(a) Cross-flow RMS profile case 6160.

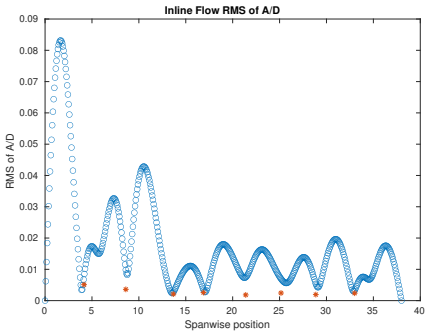

(b) Inline flow RMS profile case 6160.

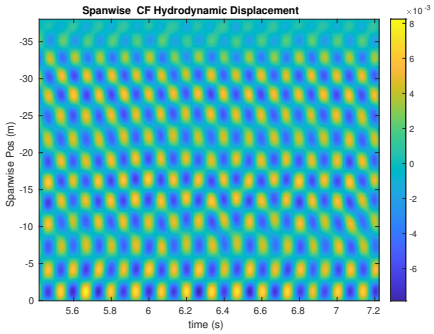

(c) Spanwise cross-flow hydrodynamic displacement case 6160.

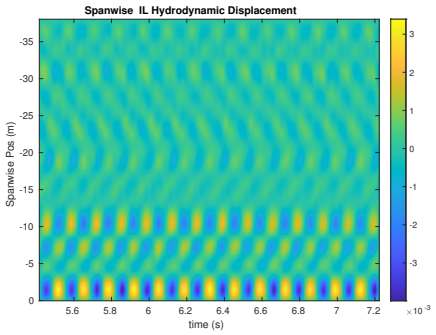

(d) Spanwise inline hydrodynamic displacement case 6160.

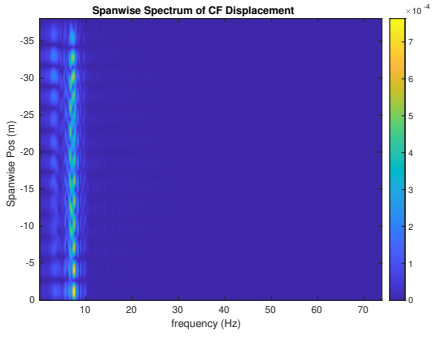

(e) Spanwise cross-flow spectrum of hydrodynamic displacement case 6160.

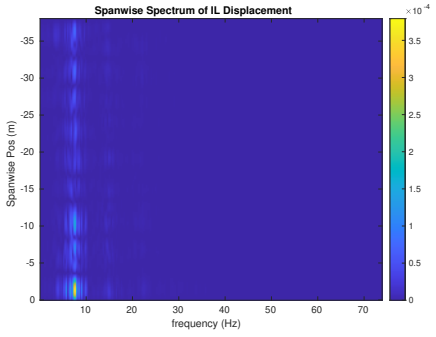

(f) Spanwise inline spectrum of hydrodynamic displacement case 6160.

Figure C-214: *Motion Analysis.* NDP Straight Riser ($L = 38m$) test case 6160.

NDP Straight Riser ($L = 38m$) test case 6170

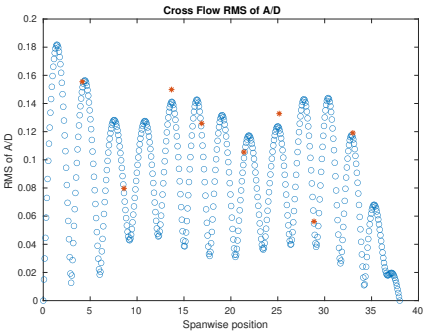

(a) Cross-flow RMS profile case 6170.

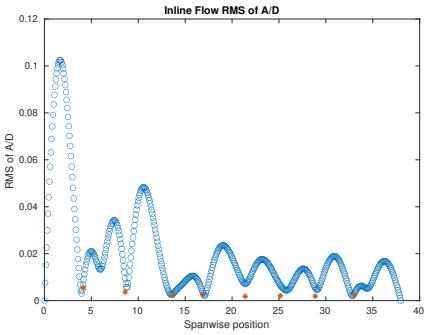

(b) Inline flow RMS profile case 6170.

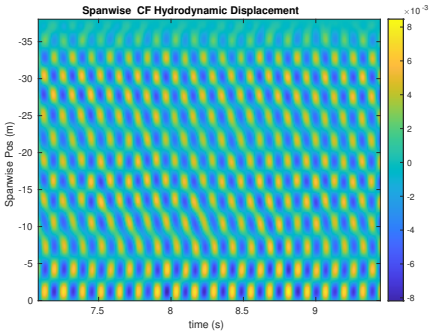

(c) Spanwise cross-flow hydrodynamic displacement case 6170.

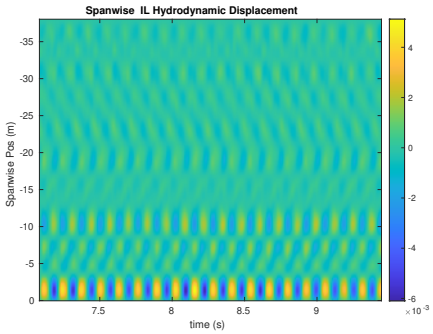

(d) Spanwise inline hydrodynamic displacement case 6170.

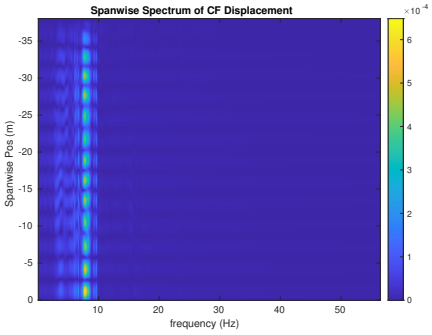

(e) Spanwise cross-flow spectrum of hydrodynamic displacement case 6170.

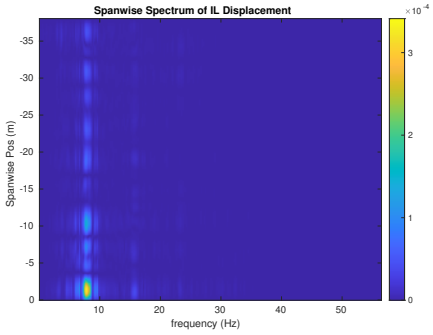

(f) Spanwise inline spectrum of hydrodynamic displacement case 6170.

Figure C-215: *Motion Analysis.* NDP Straight Riser ($L = 38m$) test case 6170.

NDP Straight Riser ($L = 38m$) test case 6180

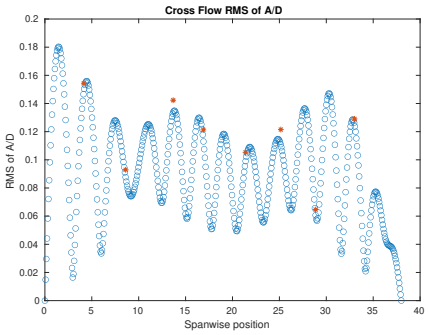

(a) Cross-flow RMS profile case 6180.

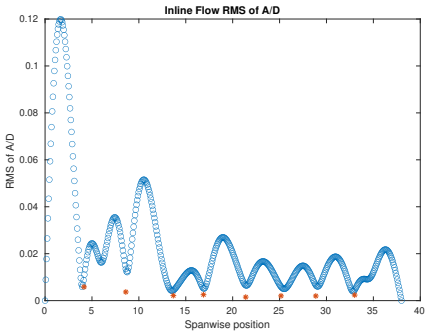

(b) Inline flow RMS profile case 6180.

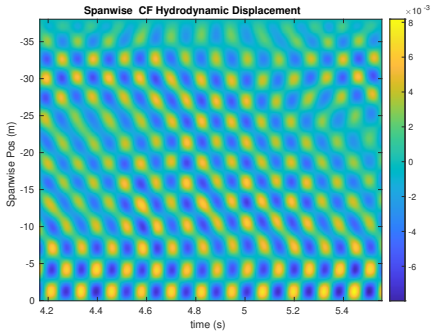

(c) Spanwise cross-flow hydrodynamic displacement case 6180.

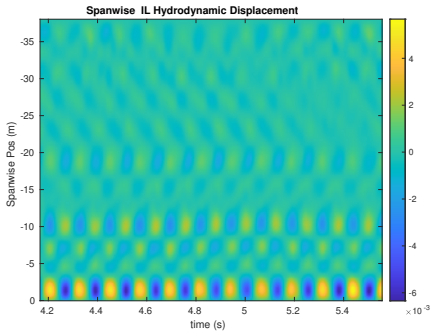

(d) Spanwise inline hydrodynamic displacement case 6180.

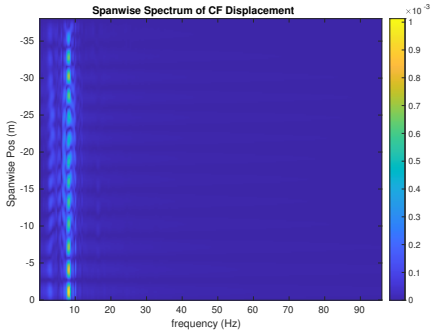

(e) Spanwise cross-flow spectrum of hydrodynamic displacement case 6180.

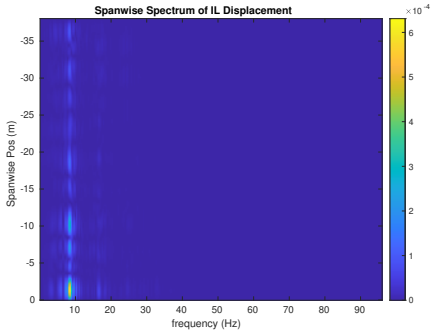

(f) Spanwise inline spectrum of hydrodynamic displacement case 6180.

Figure C-216: *Motion Analysis.* NDP Straight Riser ($L = 38m$) test case 6180.

NDP Straight Riser ($L = 38m$) test case 6190

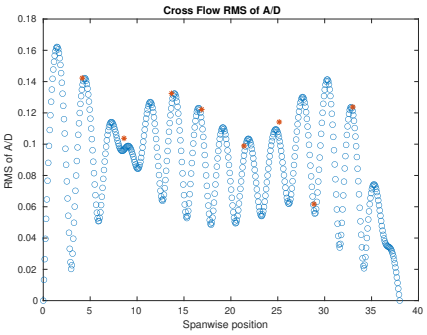

(a) Cross-flow RMS profile case 6190.

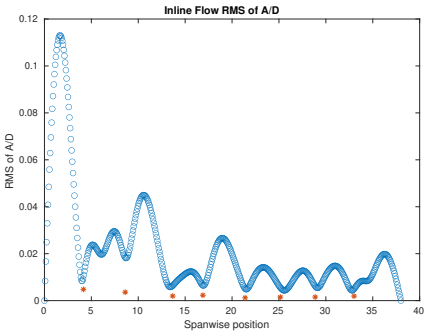

(b) Inline flow RMS profile case 6190.

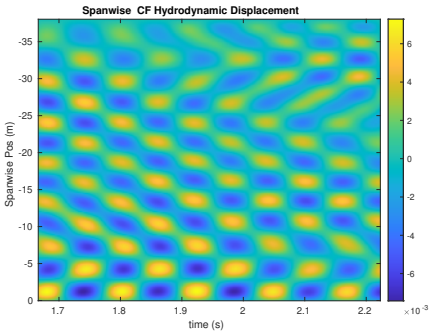

(c) Spanwise cross-flow hydrodynamic displacement case 6190.

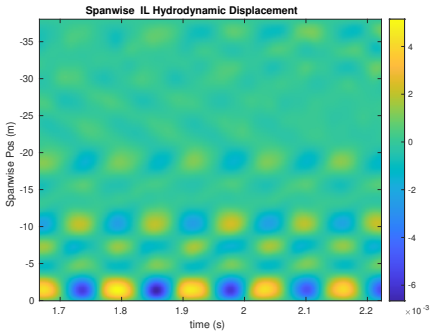

(d) Spanwise inline hydrodynamic displacement case 6190.

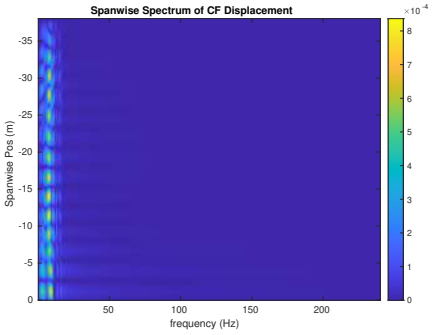

(e) Spanwise cross-flow spectrum of hydrodynamic displacement case 6190.

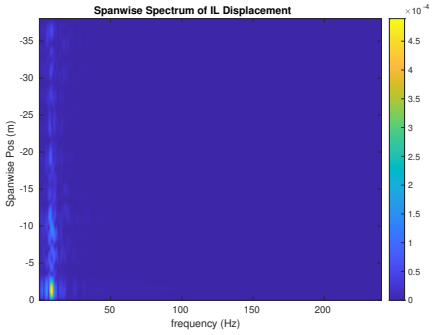

(f) Spanwise inline spectrum of hydrodynamic displacement case 6190.

Figure C-217: *Motion Analysis.* NDP Straight Riser ($L = 38m$) test case 6190.

NDP Straight Riser ($L = 38m$) test case 6200

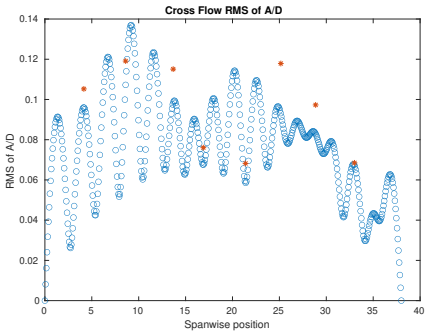

(a) Cross-flow RMS profile case 6200.

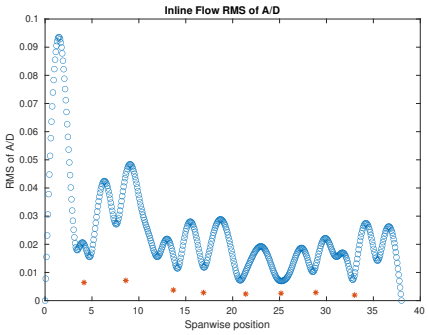

(b) Inline flow RMS profile case 6200.

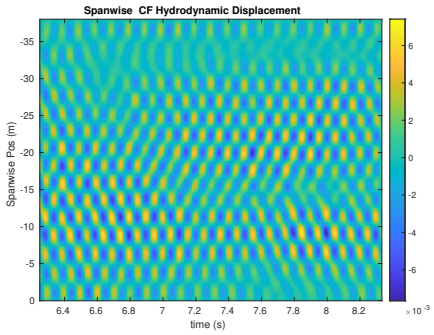

(c) Spanwise cross-flow hydrodynamic displacement case 6200.

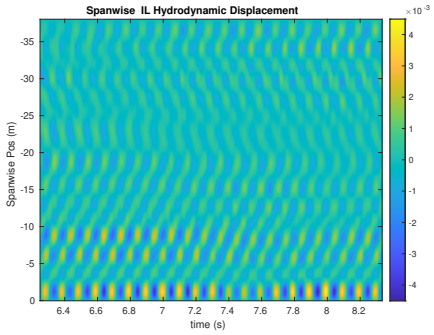

(d) Spanwise inline hydrodynamic displacement case 6200.

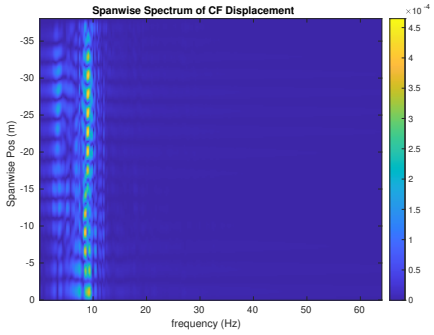

(e) Spanwise cross-flow spectrum of hydrodynamic displacement case 6200.

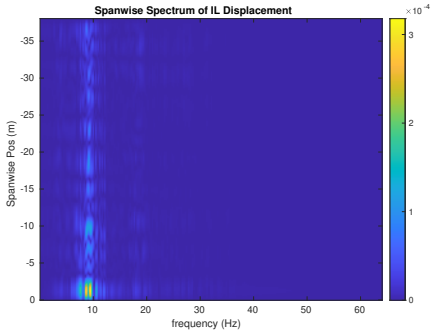

(f) Spanwise inline spectrum of hydrodynamic displacement case 6200.

Figure C-218: *Motion Analysis.* NDP Straight Riser ($L = 38m$) test case 6200.

NDP Straight Riser ($L = 38m$) test case 6210

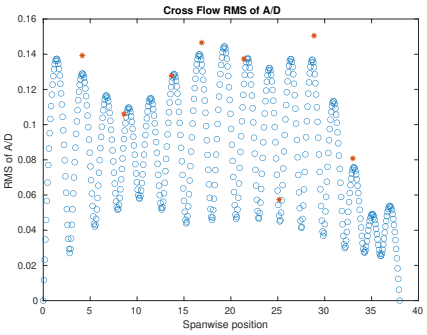

(a) Cross-flow RMS profile case 6210.

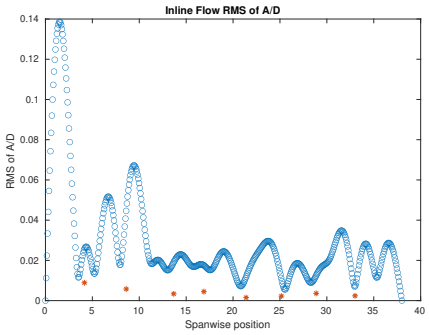

(b) Inline flow RMS profile case 6210.

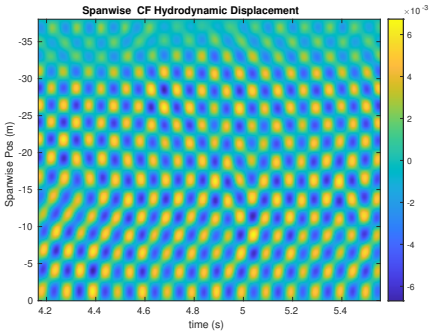

(c) Spanwise cross-flow hydrodynamic displacement case 6210.

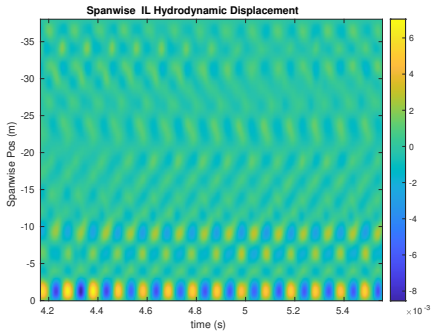

(d) Spanwise inline hydrodynamic displacement case 6210.

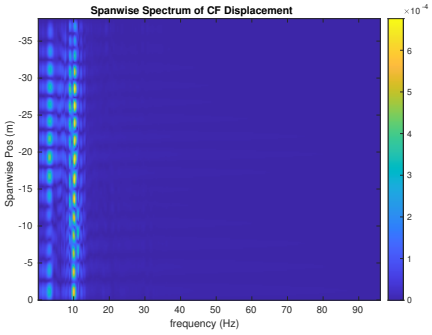

(e) Spanwise cross-flow spectrum of hydrodynamic displacement case 6210.

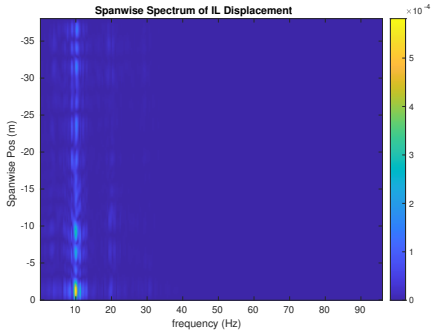

(f) Spanwise inline spectrum of hydrodynamic displacement case 6210.

Figure C-219: *Motion Analysis.* NDP Straight Riser ($L = 38m$) test case 6210.

NDP Straight Riser ($L = 38m$) test case 6220

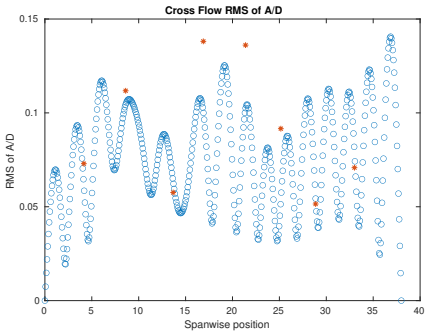

(a) Cross-flow RMS profile case 6220.

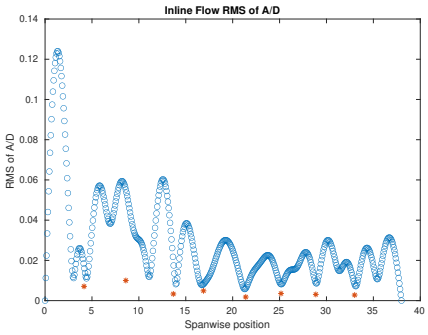

(b) Inline flow RMS profile case 6220.

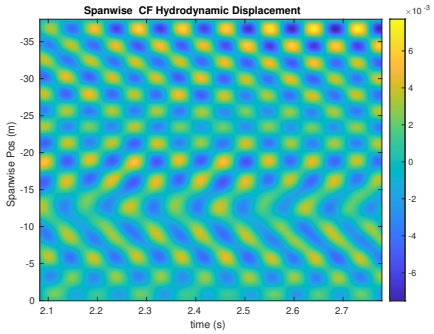

(c) Spanwise cross-flow hydrodynamic displacement case 6220.

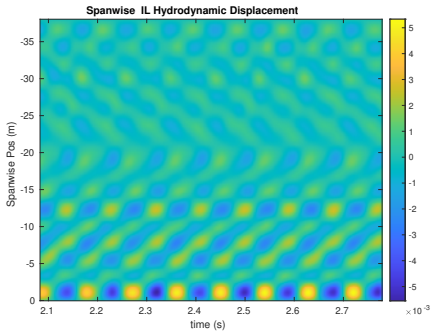

(d) Spanwise inline hydrodynamic displacement case 6220.

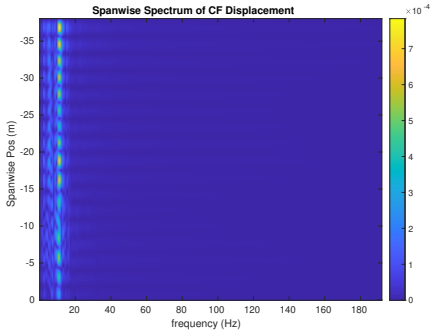

(e) Spanwise cross-flow spectrum of hydrodynamic displacement case 6220.

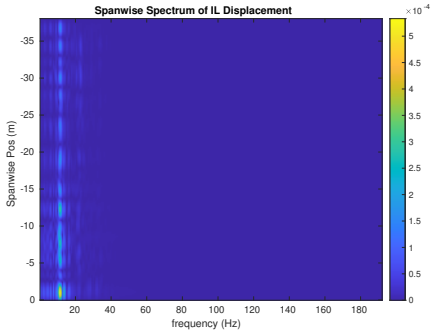

(f) Spanwise inline spectrum of hydrodynamic displacement case 6220.

Figure C-220: *Motion Analysis.* NDP Straight Riser ($L = 38m$) test case 6220.

NDP Straight Riser ($L = 38m$) test case 6230

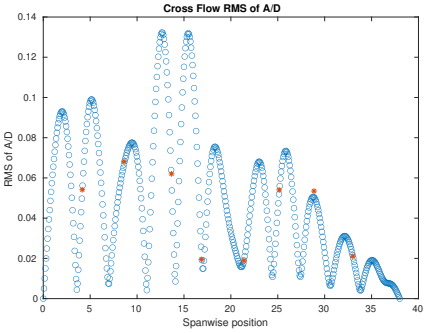

(a) Cross-flow RMS profile case 6230.

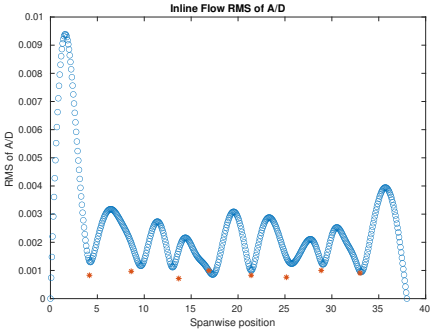

(b) Inline flow RMS profile case 6230.

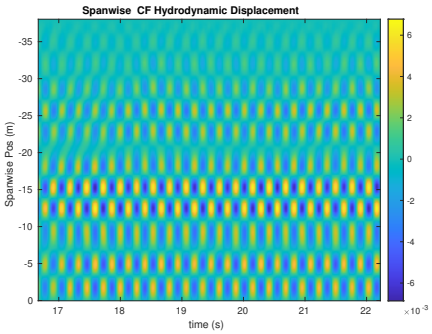

(c) Spanwise cross-flow hydrodynamic displacement case 6230.

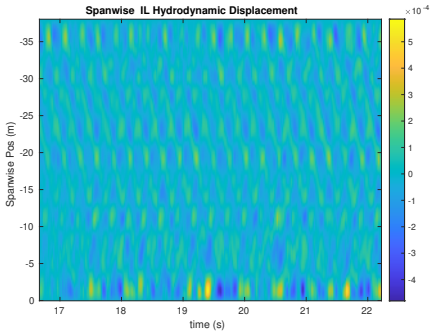

(d) Spanwise inline hydrodynamic displacement case 6230.

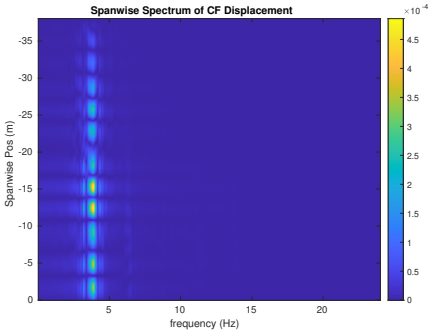

(e) Spanwise cross-flow spectrum of hydrodynamic displacement case 6230.

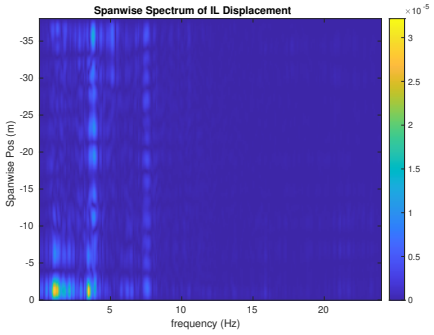

(f) Spanwise inline spectrum of hydrodynamic displacement case 6230.

Figure C-221: *Motion Analysis.* NDP Straight Riser ($L = 38m$) test case 6230.

NDP Straight Riser ($L = 38m$) test case 6240

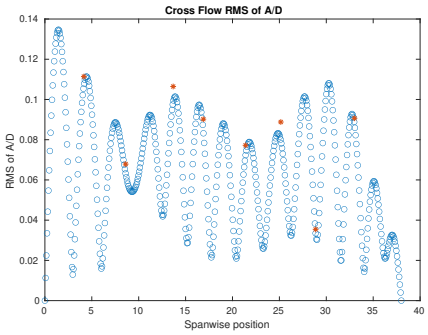

(a) Cross-flow RMS profile case 6240.

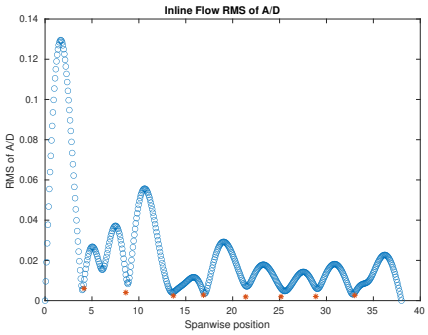

(b) Inline flow RMS profile case 6240.

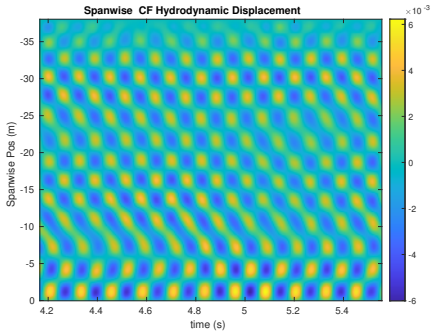

(c) Spanwise cross-flow hydrodynamic displacement case 6240.

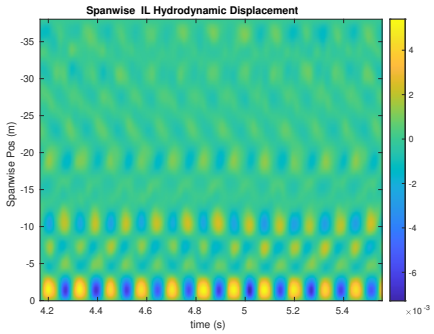

(d) Spanwise inline hydrodynamic displacement case 6240.

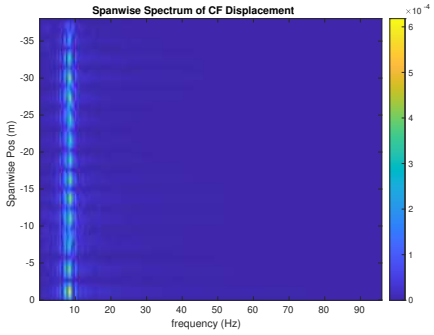

(e) Spanwise cross-flow spectrum of hydrodynamic displacement case 6240.

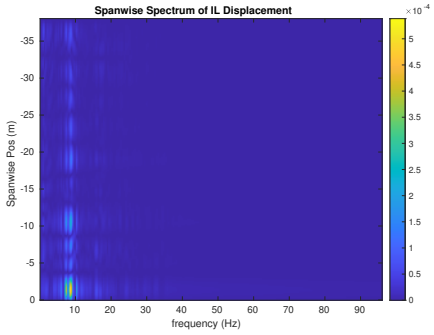

(f) Spanwise inline spectrum of hydrodynamic displacement case 6240.

Figure C-222: *Motion Analysis.* NDP Straight Riser ($L = 38m$) test case 6240.

NDP Straight Riser ($L = 38m$) test case 6310

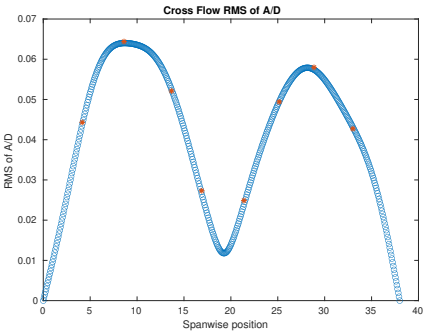

(a) Cross-flow RMS profile case 6310.

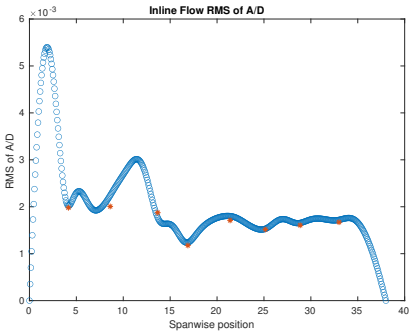

(b) Inline flow RMS profile case 6310.

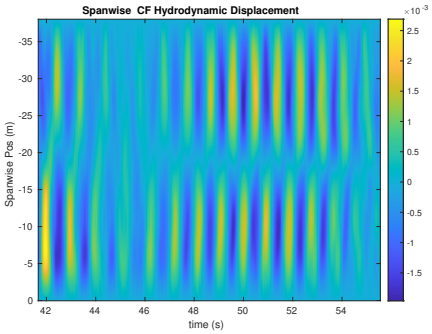

(c) Spanwise cross-flow hydrodynamic displacement case 6310.

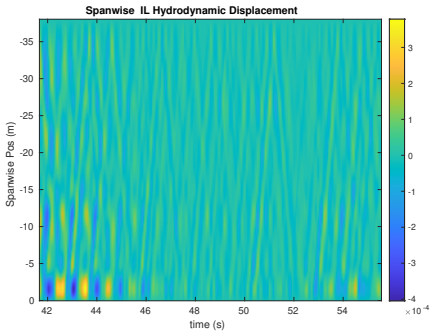

(d) Spanwise inline hydrodynamic displacement case 6310.

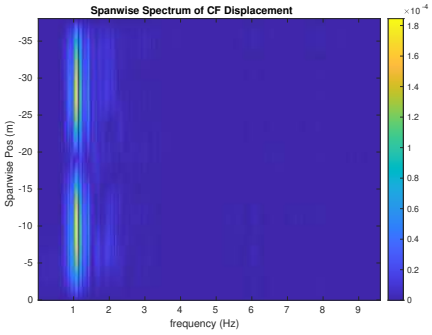

(e) Spanwise cross-flow spectrum of hydrodynamic displacement case 6310.

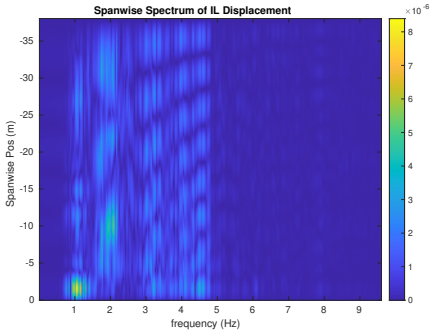

(f) Spanwise inline spectrum of hydrodynamic displacement case 6310.

Figure C-223: *Motion Analysis.* NDP Straight Riser ($L = 38m$) test case 6310.

NDP Straight Riser ($L = 38m$) test case 6320

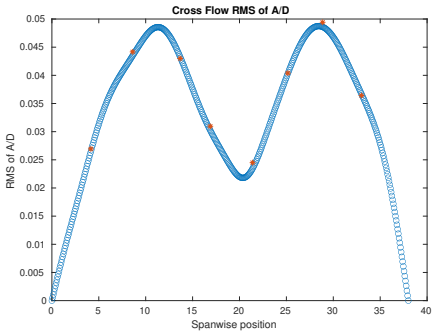

(a) Cross-flow RMS profile case 6320.

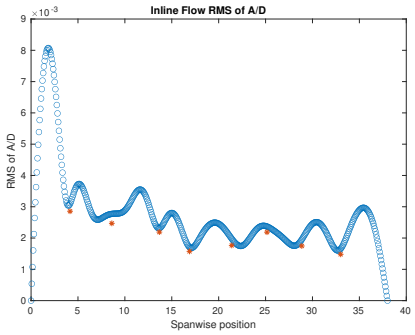

(b) Inline flow RMS profile case 6320.

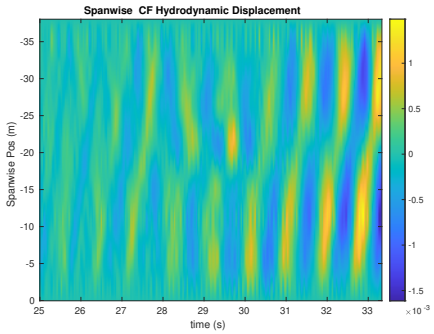

(c) Spanwise cross-flow hydrodynamic displacement case 6320.

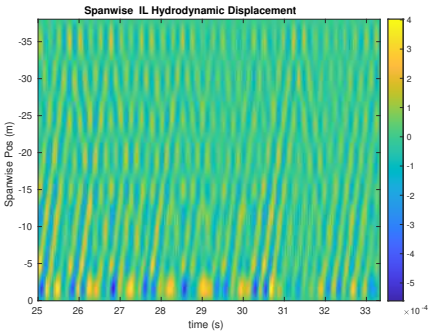

(d) Spanwise inline hydrodynamic displacement case 6320.

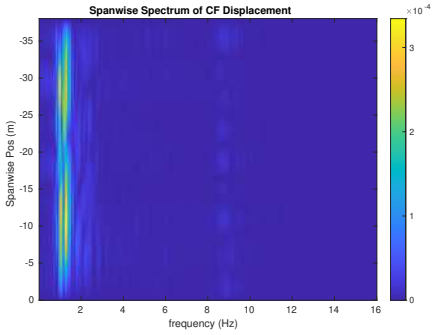

(e) Spanwise cross-flow spectrum of hydrodynamic displacement case 6320.

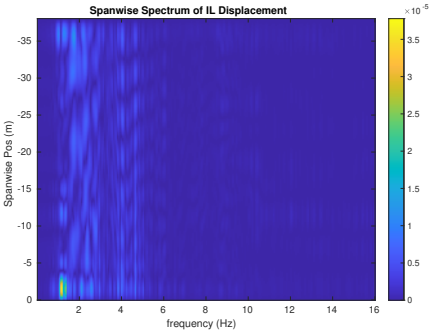

(f) Spanwise inline spectrum of hydrodynamic displacement case 6320.

Figure C-224: *Motion Analysis.* NDP Straight Riser ($L = 38m$) test case 6320.

NDP Straight Riser ($L = 38m$) test case 6330

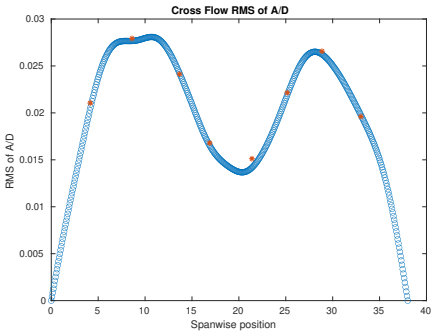

(a) Cross-flow RMS profile case 6330.

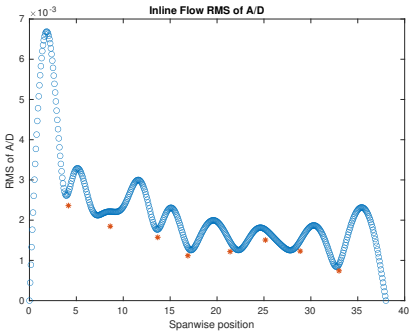

(b) Inline flow RMS profile case 6330.

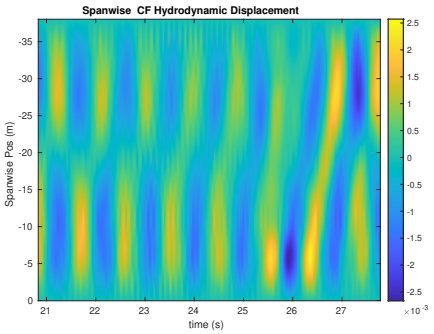

(c) Spanwise cross-flow hydrodynamic displacement case 6330.

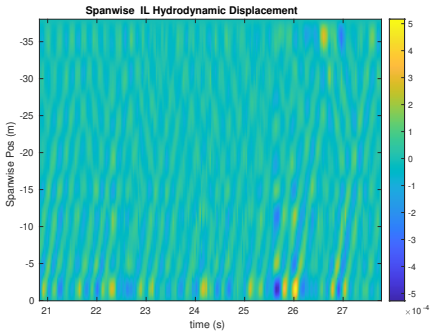

(d) Spanwise inline hydrodynamic displacement case 6330.

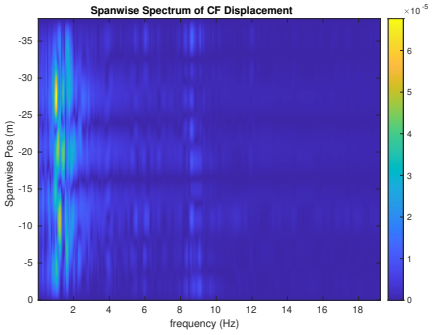

(e) Spanwise cross-flow spectrum of hydrodynamic displacement case 6330.

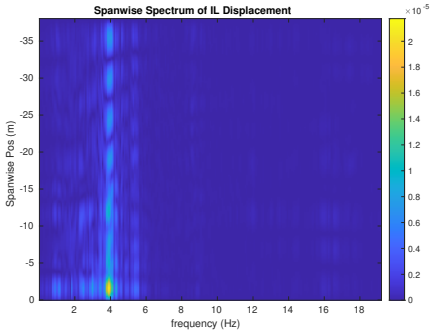

(f) Spanwise inline spectrum of hydrodynamic displacement case 6330.

Figure C-225: *Motion Analysis.* NDP Straight Riser ($L = 38m$) test case 6330.

NDP Straight Riser ($L = 38m$) test case 6340

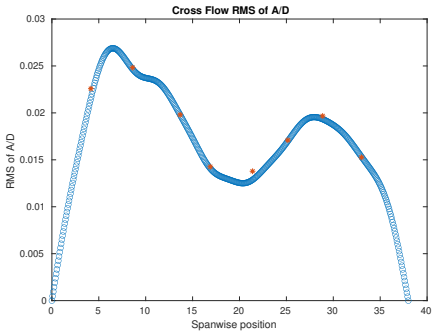

(a) Cross-flow RMS profile case 6340.

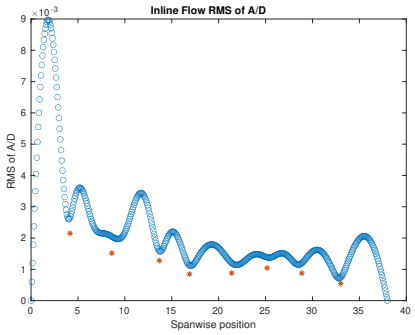

(b) Inline flow RMS profile case 6340.

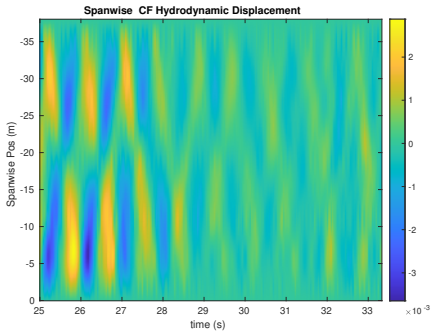

(c) Spanwise cross-flow hydrodynamic displacement case 6340.

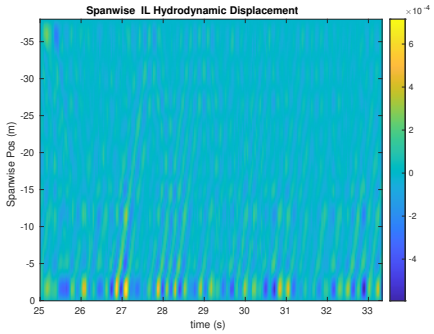

(d) Spanwise inline hydrodynamic displacement case 6340.

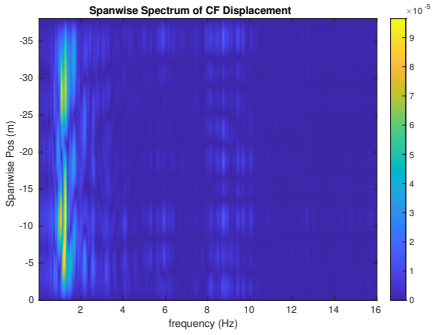

(e) Spanwise cross-flow spectrum of hydrodynamic displacement case 6340.

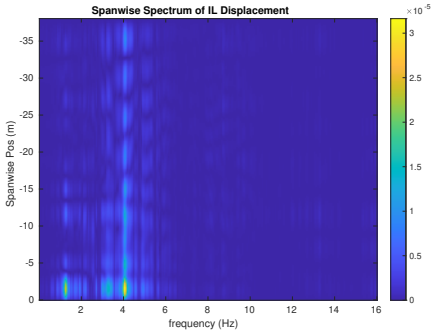

(f) Spanwise inline spectrum of hydrodynamic displacement case 6340.

Figure C-226: *Motion Analysis.* NDP Straight Riser ($L = 38m$) test case 6340.

NDP Straight Riser ($L = 38m$) test case 6350

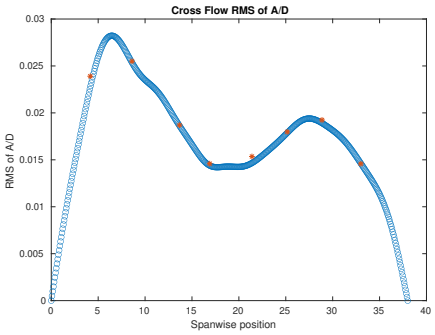

(a) Cross-flow RMS profile case 6350.

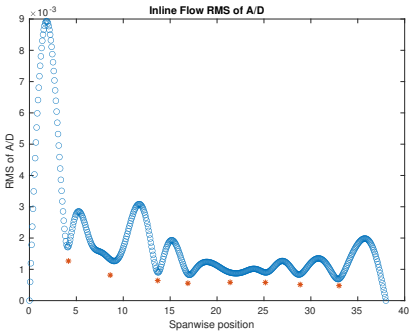

(b) Inline flow RMS profile case 6350.

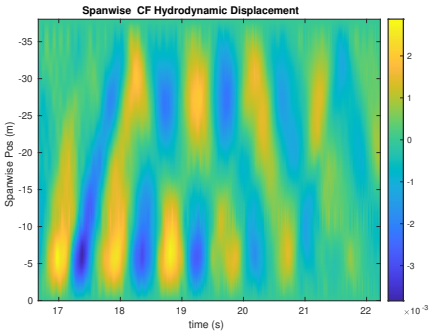

(c) Spanwise cross-flow hydrodynamic displacement case 6350.

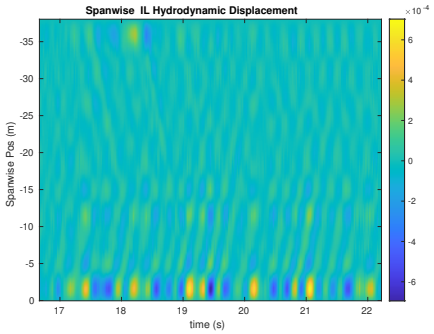

(d) Spanwise inline hydrodynamic displacement case 6350.

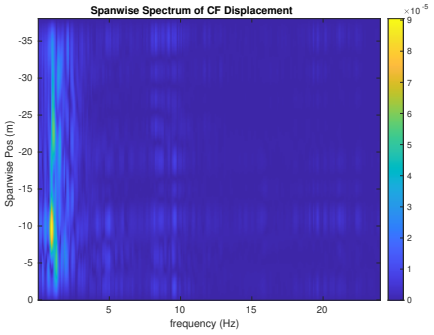

(e) Spanwise cross-flow spectrum of hydrodynamic displacement case 6350.

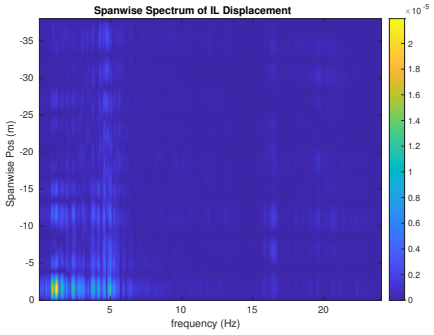

(f) Spanwise inline spectrum of hydrodynamic displacement case 6350.

Figure C-227: *Motion Analysis.* NDP Straight Riser ($L = 38m$) test case 6350.

NDP Straight Riser ($L = 38m$) test case 6360

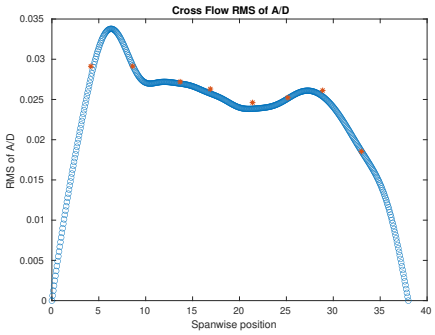

(a) Cross-flow RMS profile case 6360.

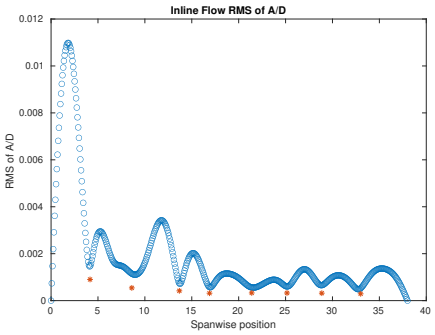

(b) Inline flow RMS profile case 6360.

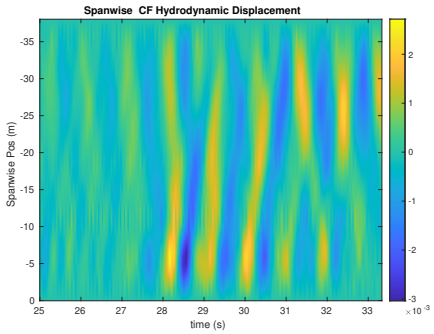

(c) Spanwise cross-flow hydrodynamic displacement case 6360.

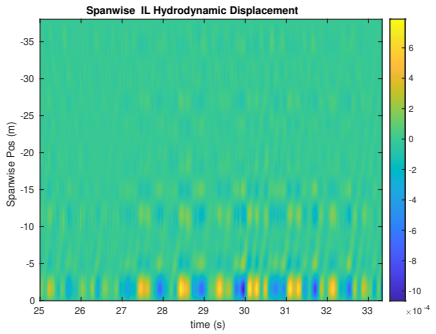

(d) Spanwise inline hydrodynamic displacement case 6360.

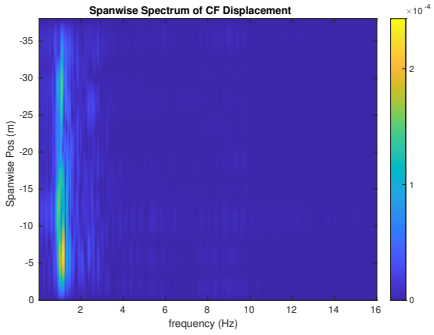

(e) Spanwise cross-flow spectrum of hydrodynamic displacement case 6360.

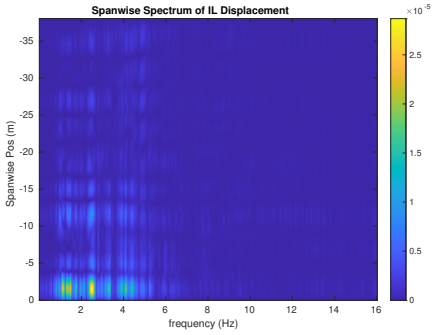

(f) Spanwise inline spectrum of hydrodynamic displacement case 6360.

Figure C-228: *Motion Analysis.* NDP Straight Riser ($L = 38m$) test case 6360.

NDP Straight Riser ($L = 38m$) test case 6370

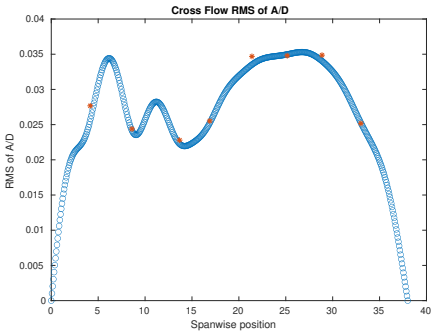

(a) Cross-flow RMS profile case 6370.

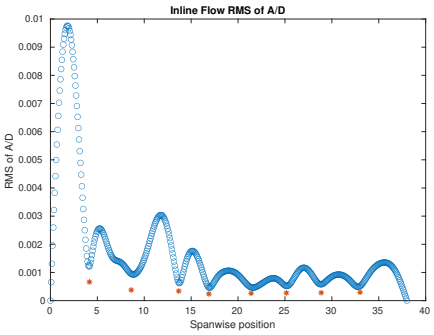

(b) Inline flow RMS profile case 6370.

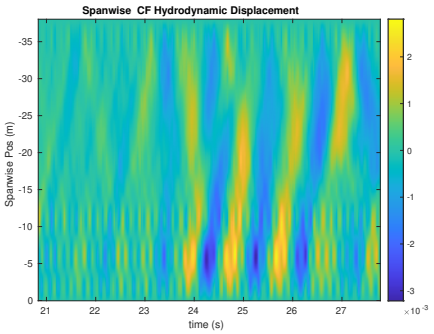

(c) Spanwise cross-flow hydrodynamic displacement case 6370.

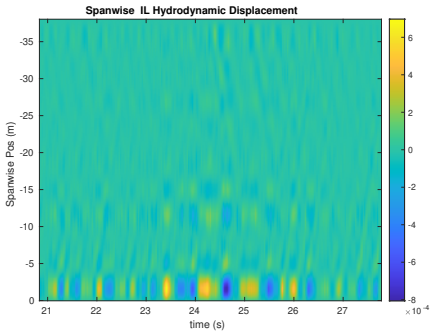

(d) Spanwise inline hydrodynamic displacement case 6370.

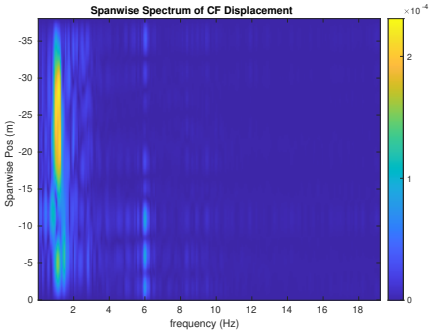

(e) Spanwise cross-flow spectrum of hydrodynamic displacement case 6370.

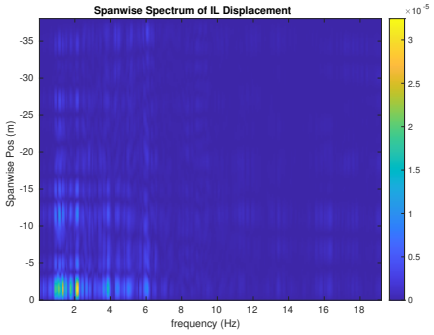

(f) Spanwise inline spectrum of hydrodynamic displacement case 6370.

Figure C-229: *Motion Analysis.* NDP Straight Riser ($L = 38m$) test case 6370.

NDP Straight Riser ($L = 38m$) test case 6380

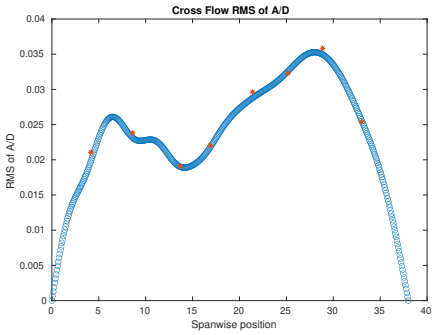

(a) Cross-flow RMS profile case 6380.

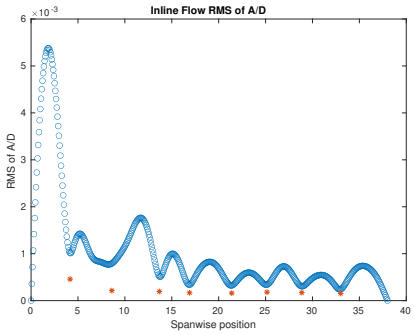

(b) Inline flow RMS profile case 6380.

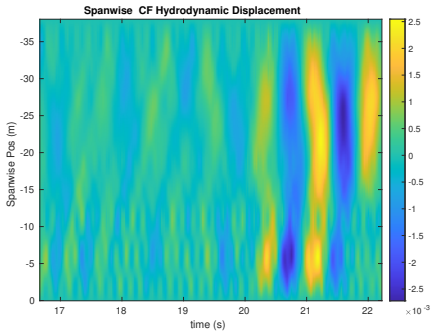

(c) Spanwise cross-flow hydrodynamic displacement case 6380.

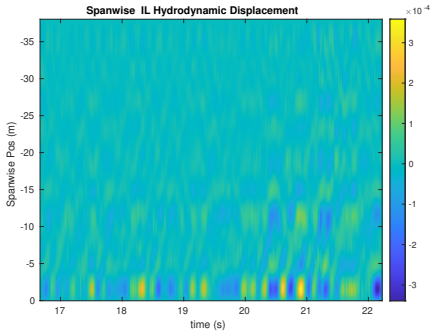

(d) Spanwise inline hydrodynamic displacement case 6380.

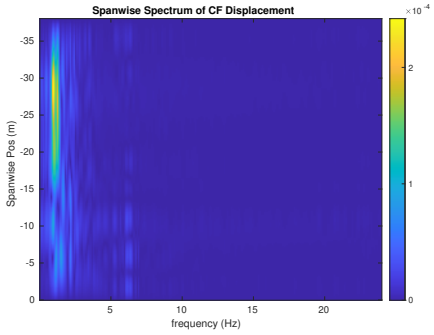

(e) Spanwise cross-flow spectrum of hydrodynamic displacement case 6380.

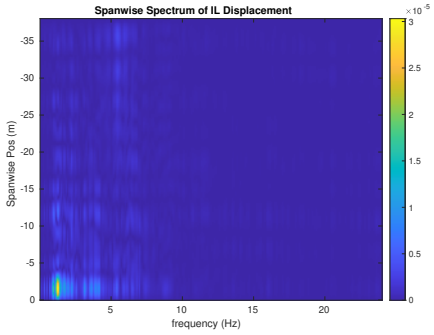

(f) Spanwise inline spectrum of hydrodynamic displacement case 6380.

Figure C-230: *Motion Analysis.* NDP Straight Riser ($L = 38m$) test case 6380.

NDP Straight Riser ($L = 38m$) test case 6391

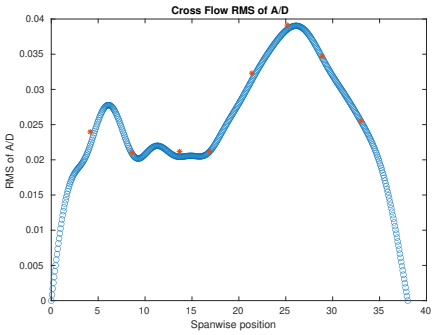

(a) Cross-flow RMS profile case 6391.

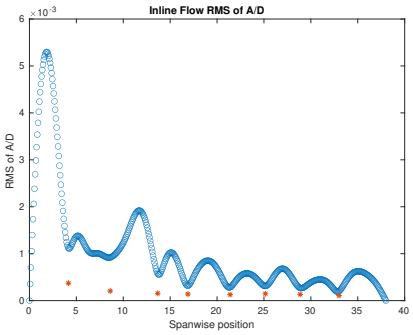

(b) Inline flow RMS profile case 6391.

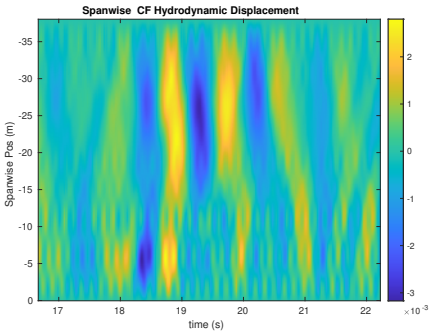

(c) Spanwise cross-flow hydrodynamic displacement case 6391.

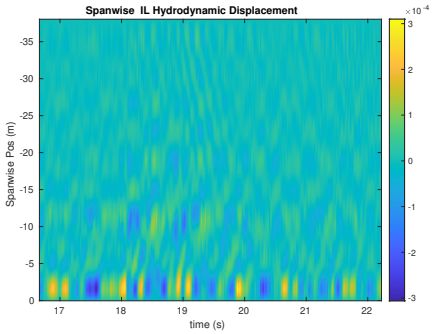

(d) Spanwise inline hydrodynamic displacement case 6391.

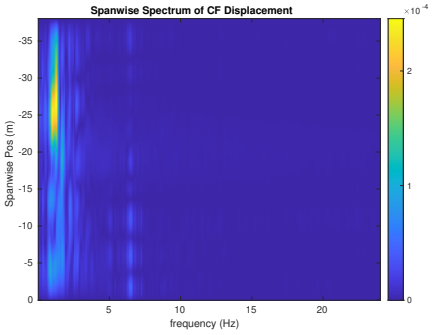

(e) Spanwise cross-flow spectrum of hydrodynamic displacement case 6391.

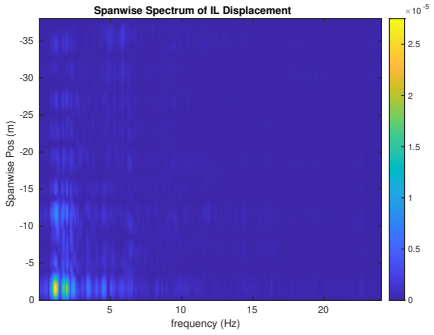

(f) Spanwise inline spectrum of hydrodynamic displacement case 6391.

Figure C-231: *Motion Analysis.* NDP Straight Riser ($L = 38m$) test case 6391.

NDP Straight Riser ($L = 38m$) test case 6400

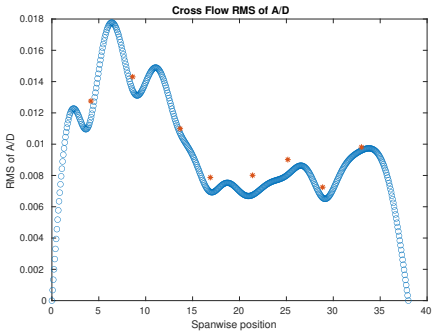

(a) Cross-flow RMS profile case 6400.

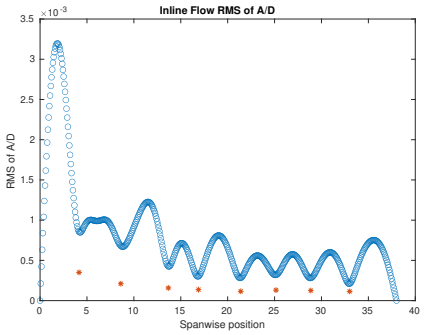

(b) Inline flow RMS profile case 6400.

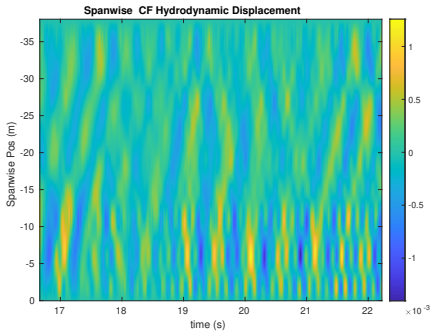

(c) Spanwise cross-flow hydrodynamic displacement case 6400.

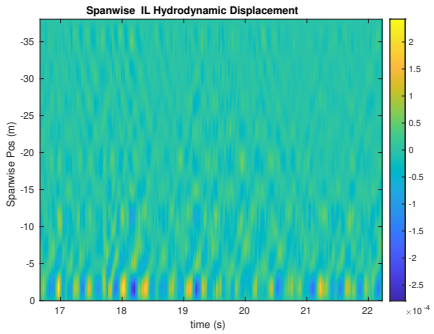

(d) Spanwise inline hydrodynamic displacement case 6400.

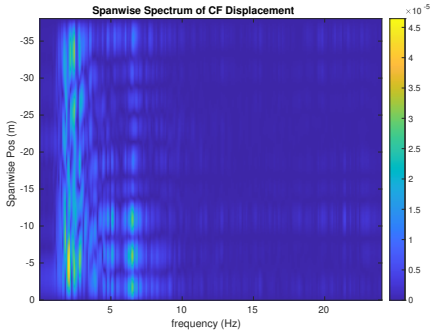

(e) Spanwise cross-flow spectrum of hydrodynamic displacement case 6400.

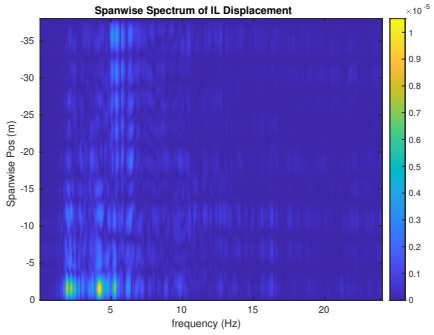

(f) Spanwise inline spectrum of hydrodynamic displacement case 6400.

Figure C-232: *Motion Analysis.* NDP Straight Riser ($L = 38m$) test case 6400.

NDP Straight Riser ($L = 38m$) test case 6410

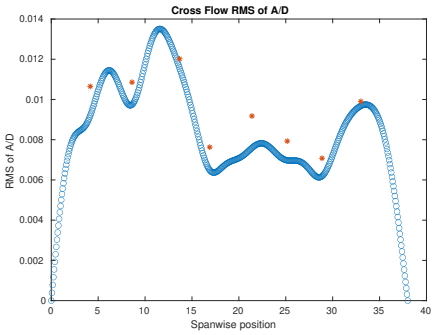

(a) Cross-flow RMS profile case 6410.

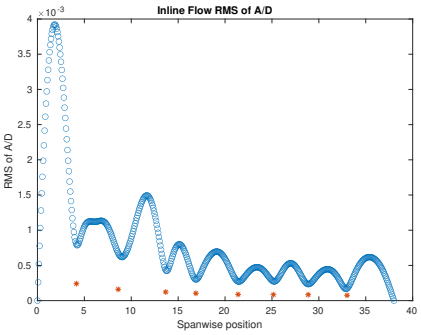

(b) Inline flow RMS profile case 6410.

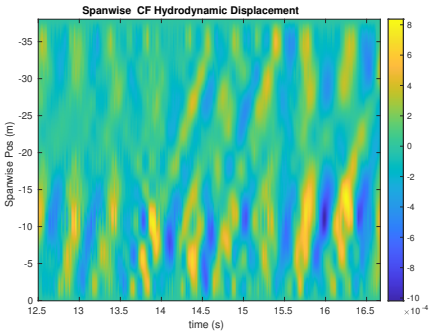

(c) Spanwise cross-flow hydrodynamic displacement case 6410.

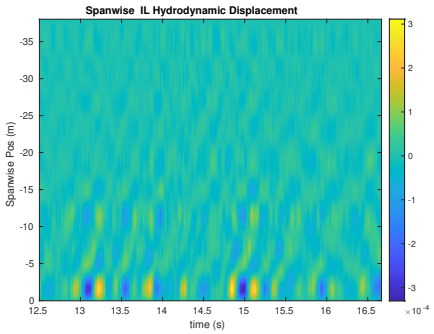

(d) Spanwise inline hydrodynamic displacement case 6410.

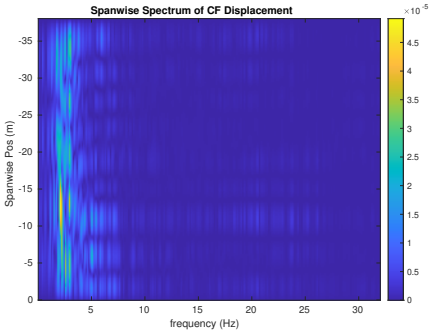

(e) Spanwise cross-flow spectrum of hydrodynamic displacement case 6410.

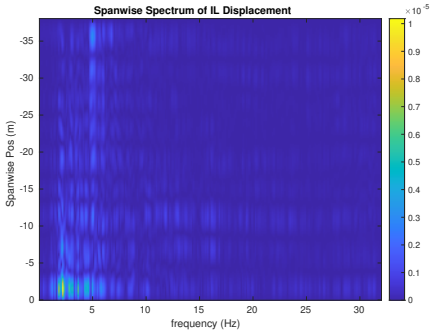

(f) Spanwise inline spectrum of hydrodynamic displacement case 6410.

Figure C-233: *Motion Analysis.* NDP Straight Riser ($L = 38m$) test case 6410.

NDP Straight Riser ($L = 38m$) test case 6420

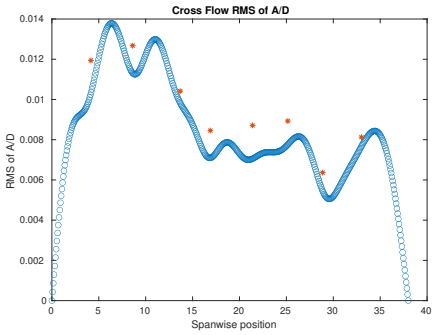

(a) Cross-flow RMS profile case 6420.

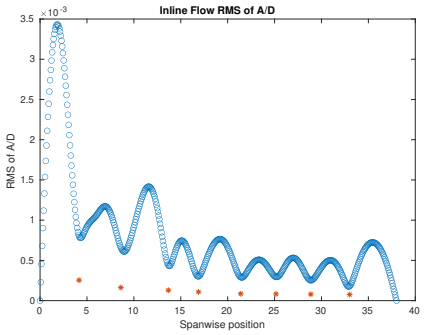

(b) Inline flow RMS profile case 6420.

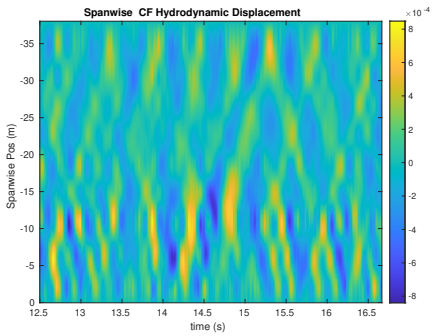

(c) Spanwise cross-flow hydrodynamic displacement case 6420.

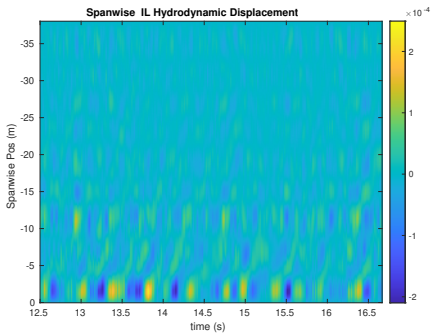

(d) Spanwise inline hydrodynamic displacement case 6420.

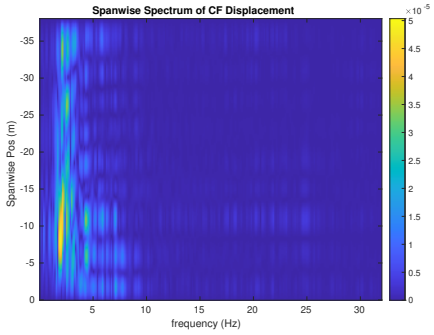

(e) Spanwise cross-flow spectrum of hydrodynamic displacement case 6420.

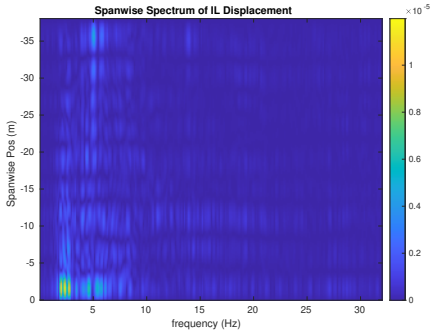

(f) Spanwise inline spectrum of hydrodynamic displacement case 6420.

Figure C-234: *Motion Analysis.* NDP Straight Riser ($L = 38m$) test case 6420.

NDP Straight Riser ($L = 38m$) test case 6430

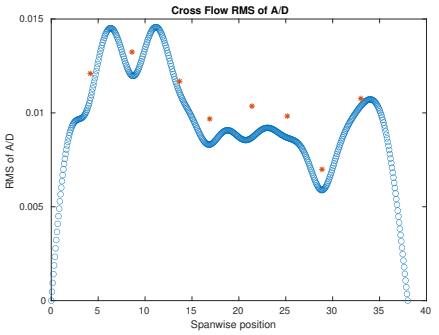

(a) Cross-flow RMS profile case 6430.

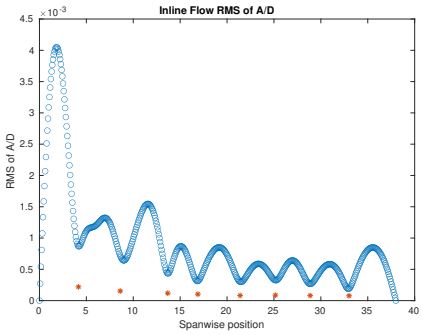

(b) Inline flow RMS profile case 6430.

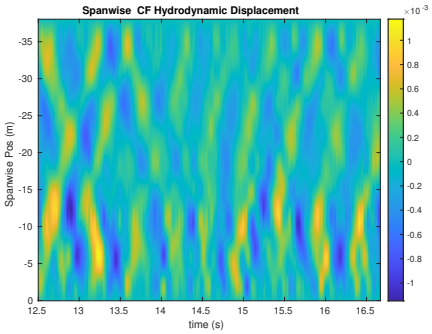

(c) Spanwise cross-flow hydrodynamic displacement case 6430.

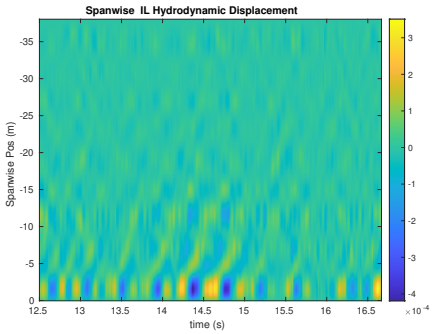

(d) Spanwise inline hydrodynamic displacement case 6430.

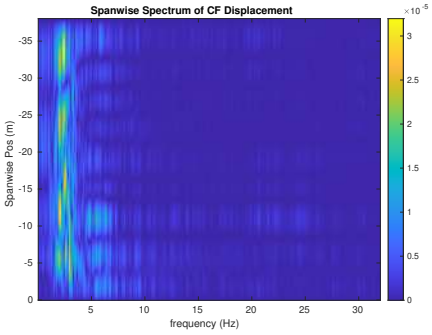

(e) Spanwise cross-flow spectrum of hydrodynamic displacement case 6430.

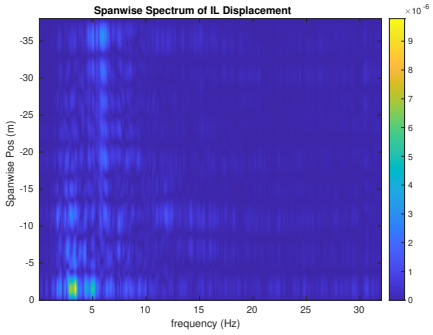

(f) Spanwise inline spectrum of hydrodynamic displacement case 6430.

Figure C-235: *Motion Analysis.* NDP Straight Riser ($L = 38m$) test case 6430.

NDP Straight Riser ($L = 38m$) test case 6440

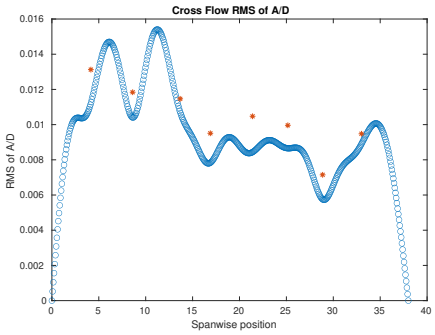

(a) Cross-flow RMS profile case 6440.

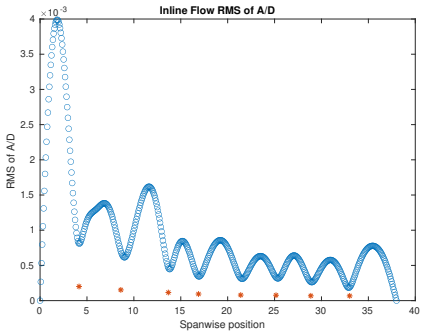

(b) Inline flow RMS profile case 6440.

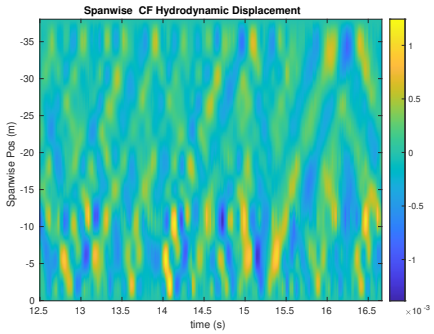

(c) Spanwise cross-flow hydrodynamic displacement case 6440.

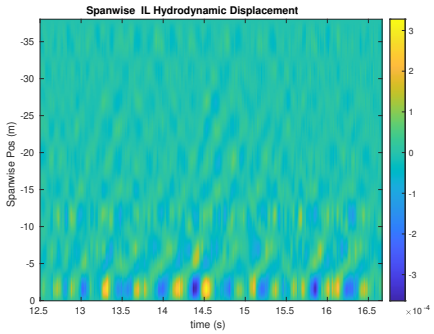

(d) Spanwise inline hydrodynamic displacement case 6440.

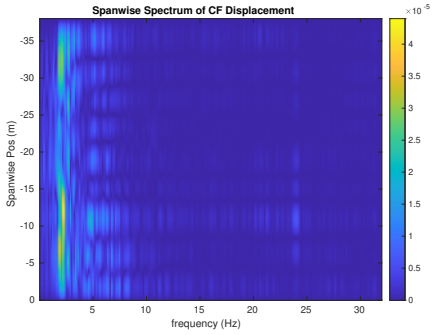

(e) Spanwise cross-flow spectrum of hydrodynamic displacement case 6440.

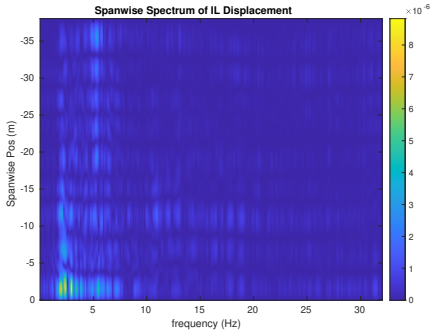

(f) Spanwise inline spectrum of hydrodynamic displacement case 6440.

Figure C-236: *Motion Analysis.* NDP Straight Riser ($L = 38m$) test case 6440.

NDP Straight Riser ($L = 38m$) test case 6450

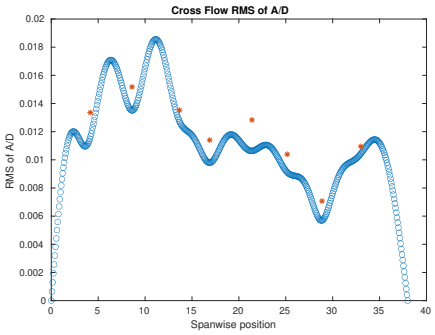

(a) Cross-flow RMS profile case 6450.

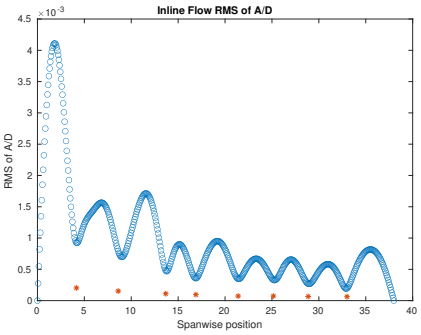

(b) Inline flow RMS profile case 6450.

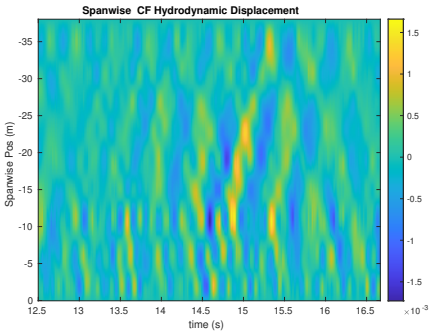

(c) Spanwise cross-flow hydrodynamic displacement case 6450.

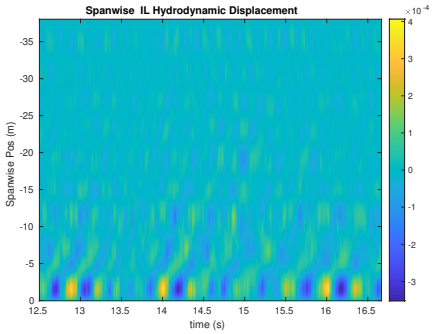

(d) Spanwise inline hydrodynamic displacement case 6450.

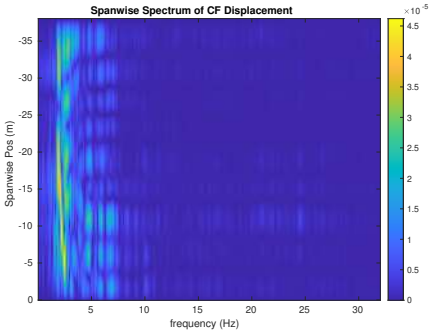

(e) Spanwise cross-flow spectrum of hydrodynamic displacement case 6450.

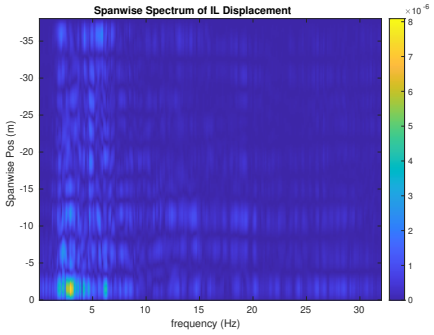

(f) Spanwise inline spectrum of hydrodynamic displacement case 6450.

Figure C-237: *Motion Analysis.* NDP Straight Riser ($L = 38m$) test case 6450.

NDP Straight Riser ($L = 38m$) test case 6460

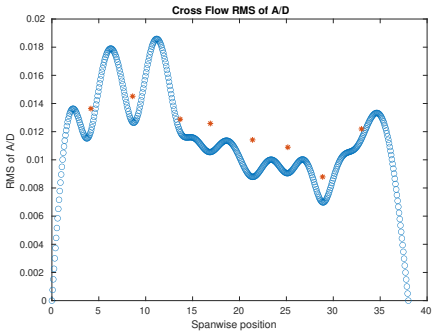

(a) Cross-flow RMS profile case 6460.

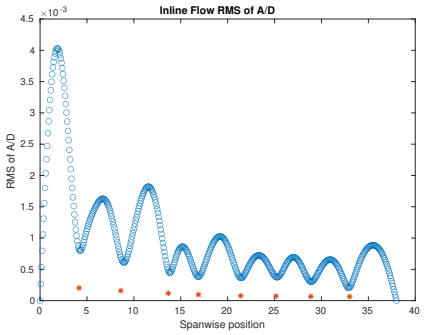

(b) Inline flow RMS profile case 6460.

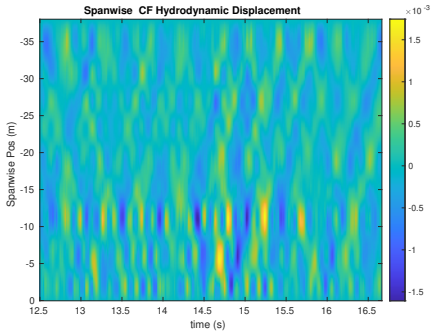

(c) Spanwise cross-flow hydrodynamic displacement case 6460.

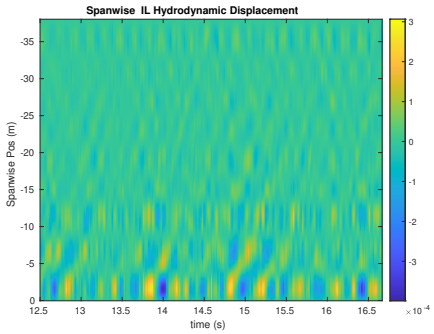

(d) Spanwise inline hydrodynamic displacement case 6460.

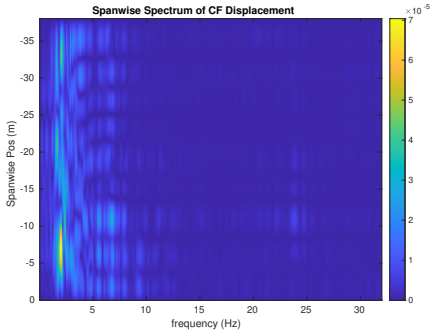

(e) Spanwise cross-flow spectrum of hydrodynamic displacement case 6460.

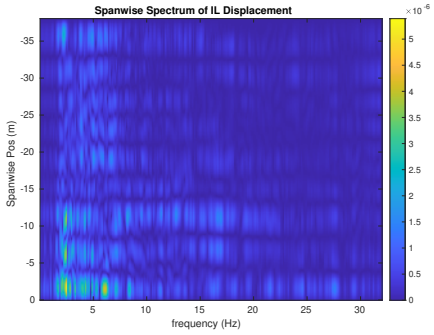

(f) Spanwise inline spectrum of hydrodynamic displacement case 6460.

Figure C-238: *Motion Analysis.* NDP Straight Riser ($L = 38m$) test case 6460.

NDP Straight Riser ($L = 38m$) test case 6470

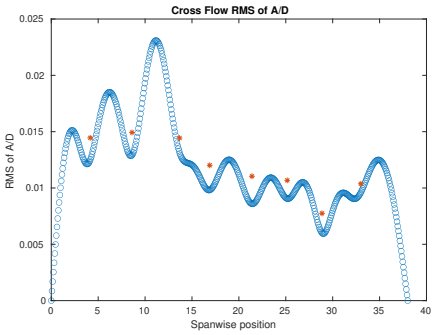

(a) Cross-flow RMS profile case 6470.

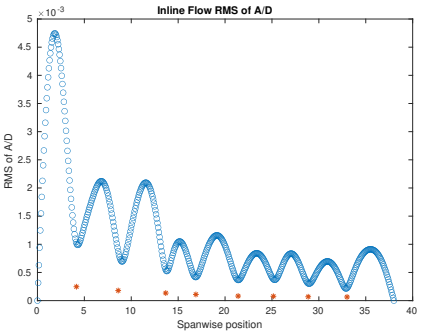

(b) Inline flow RMS profile case 6470.

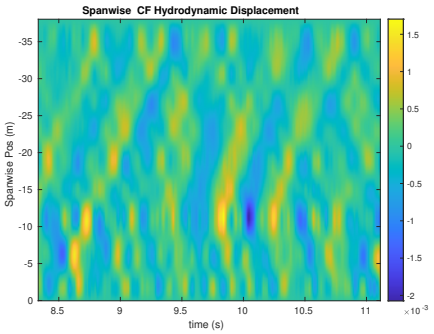

(c) Spanwise cross-flow hydrodynamic displacement case 6470.

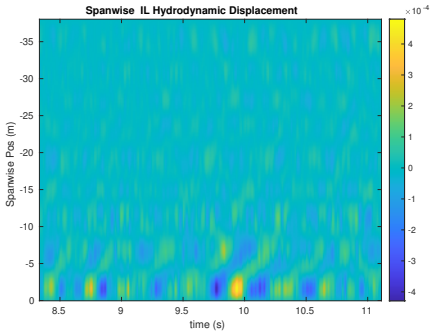

(d) Spanwise inline hydrodynamic displacement case 6470.

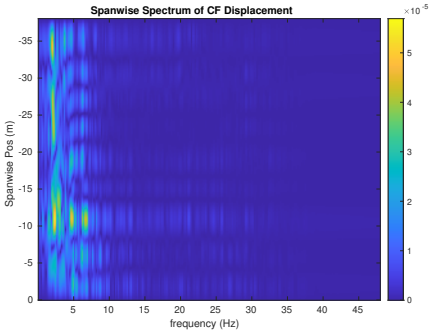

(e) Spanwise cross-flow spectrum of hydrodynamic displacement case 6470.

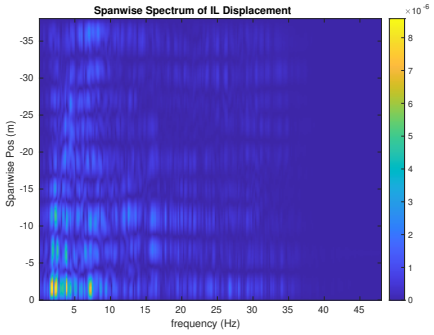

(f) Spanwise inline spectrum of hydrodynamic displacement case 6470.

Figure C-239: *Motion Analysis.* NDP Straight Riser ($L = 38m$) test case 6470.

NDP Straight Riser ($L = 38m$) test case 6480

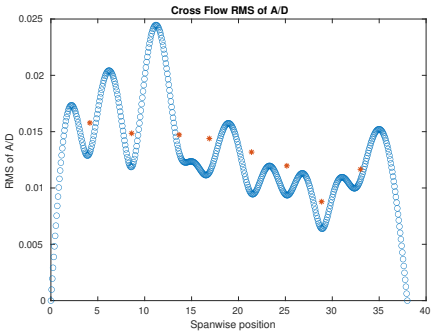

(a) Cross-flow RMS profile case 6480.

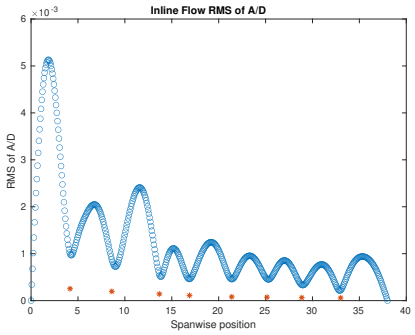

(b) Inline flow RMS profile case 6480.

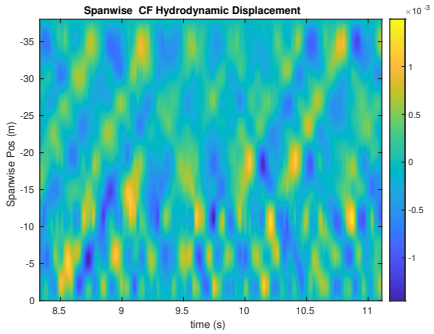

(c) Spanwise cross-flow hydrodynamic displacement case 6480.

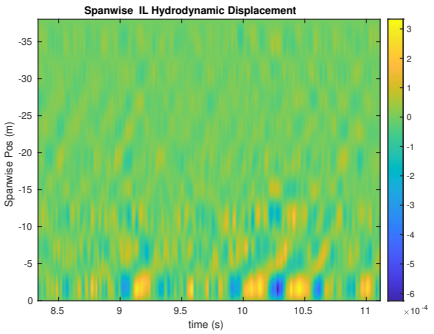

(d) Spanwise inline hydrodynamic displacement case 6480.

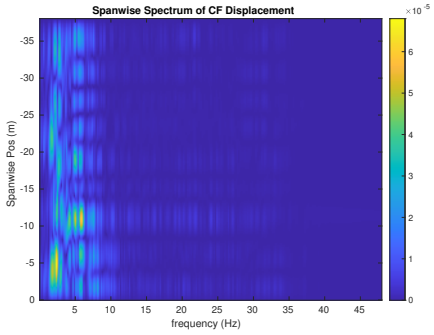

(e) Spanwise cross-flow spectrum of hydrodynamic displacement case 6480.

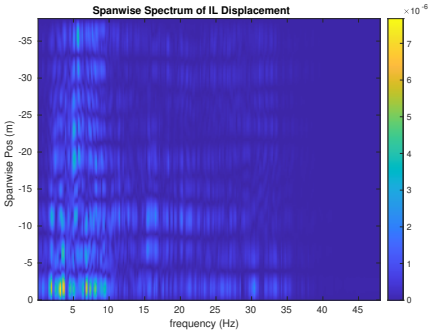

(f) Spanwise inline spectrum of hydrodynamic displacement case 6480.

Figure C-240: *Motion Analysis.* NDP Straight Riser ($L = 38m$) test case 6480.

NDP Straight Riser ($L = 38m$) test case 6490

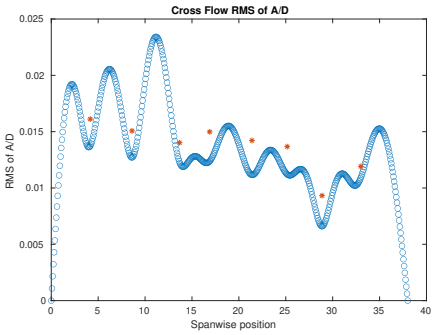

(a) Cross-flow RMS profile case 6490.

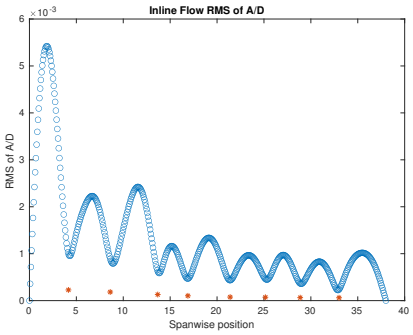

(b) Inline flow RMS profile case 6490.

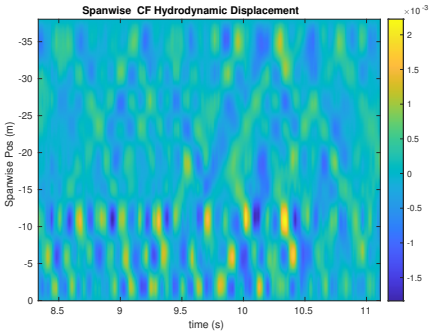

(c) Spanwise cross-flow hydrodynamic displacement case 6490.

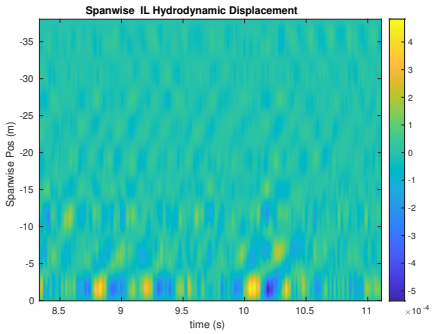

(d) Spanwise inline hydrodynamic displacement case 6490.

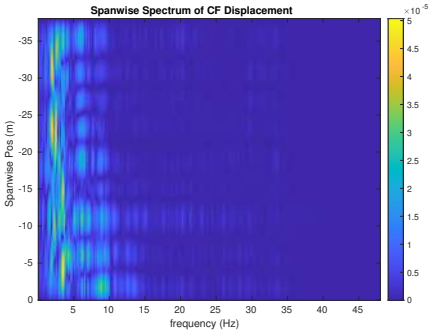

(e) Spanwise cross-flow spectrum of hydrodynamic displacement case 6490.

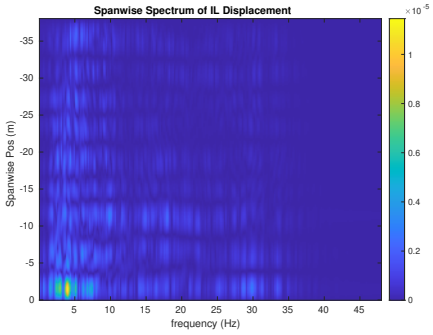

(f) Spanwise inline spectrum of hydrodynamic displacement case 6490.

Figure C-241: *Motion Analysis.* NDP Straight Riser ($L = 38m$) test case 6490.

NDP Straight Riser ($L = 38m$) test case 6500

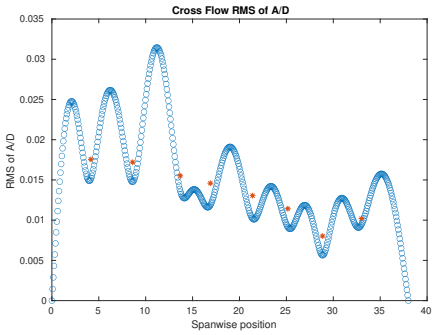

(a) Cross-flow RMS profile case 6500.

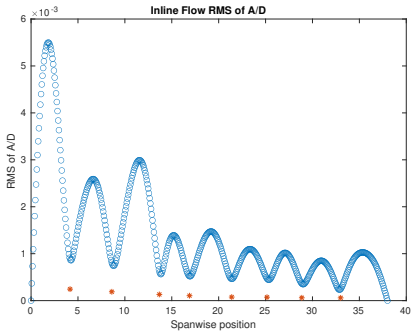

(b) Inline flow RMS profile case 6500.

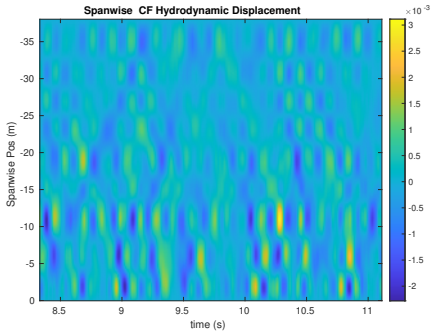

(c) Spanwise cross-flow hydrodynamic displacement case 6500.

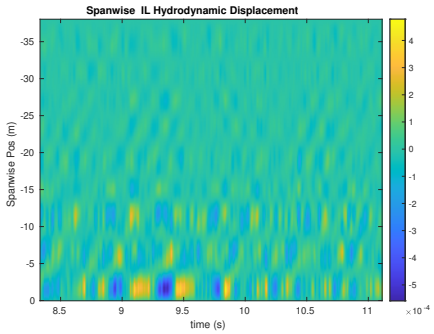

(d) Spanwise inline hydrodynamic displacement case 6500.

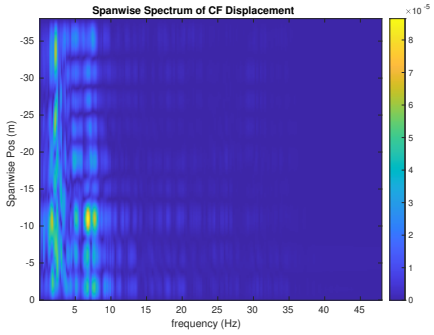

(e) Spanwise cross-flow spectrum of hydrodynamic displacement case 6500.

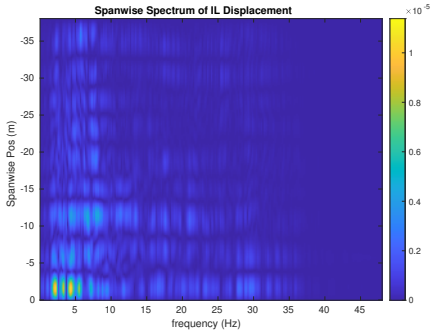

(f) Spanwise inline spectrum of hydrodynamic displacement case 6500.

Figure C-242: *Motion Analysis.* NDP Straight Riser ($L = 38m$) test case 6500.

NDP Straight Riser ($L = 38m$) test case 6510

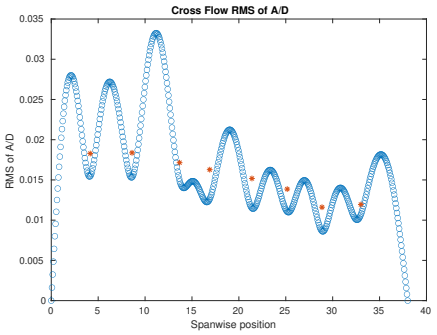

(a) Cross-flow RMS profile case 6510.

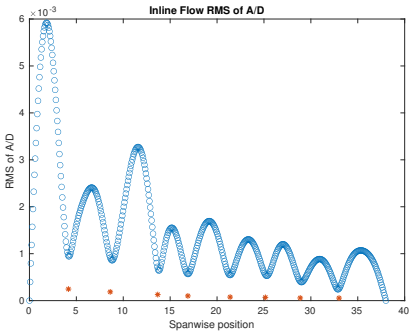

(b) Inline flow RMS profile case 6510.

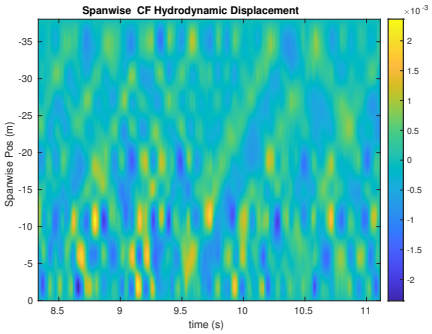

(c) Spanwise cross-flow hydrodynamic displacement case 6510.

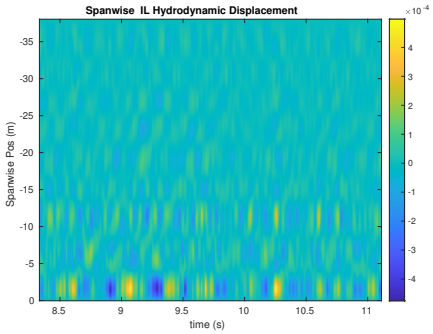

(d) Spanwise inline hydrodynamic displacement case 6510.

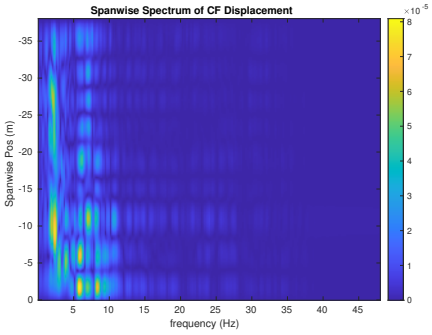

(e) Spanwise cross-flow spectrum of hydrodynamic displacement case 6510.

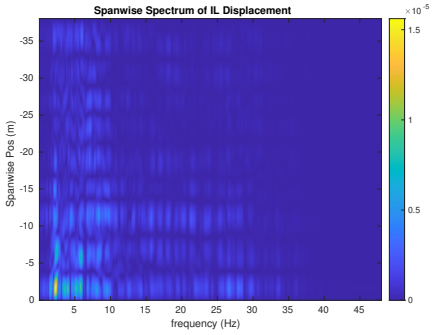

(f) Spanwise inline spectrum of hydrodynamic displacement case 6510.

Figure C-243: *Motion Analysis.* NDP Straight Riser ($L = 38m$) test case 6510.

NDP Straight Riser ($L = 38m$) test case 6520

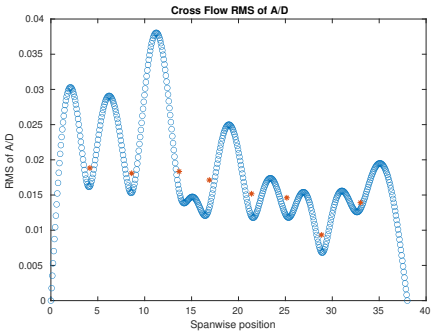

(a) Cross-flow RMS profile case 6520.

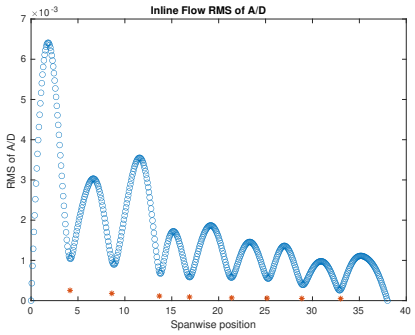

(b) Inline flow RMS profile case 6520.

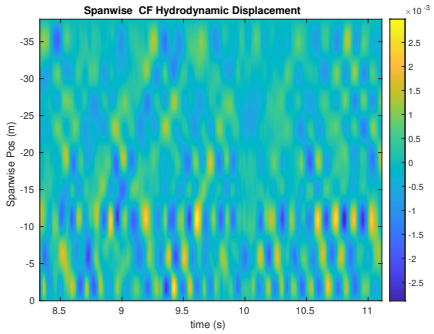

(c) Spanwise cross-flow hydrodynamic displacement case 6520.

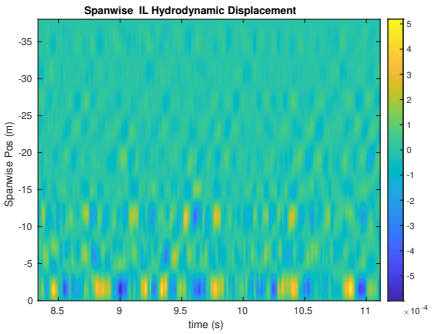

(d) Spanwise inline hydrodynamic displacement case 6520.

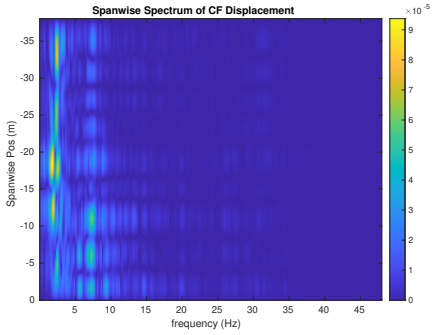

(e) Spanwise cross-flow spectrum of hydrodynamic displacement case 6520.

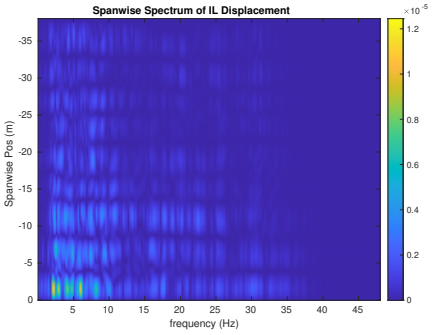

(f) Spanwise inline spectrum of hydrodynamic displacement case 6520.

Figure C-244: *Motion Analysis.* NDP Straight Riser ($L = 38m$) test case 6520.

NDP Straight Riser ($L = 38m$) test case 6530

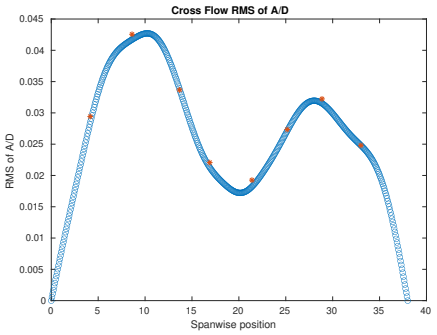

(a) Cross-flow RMS profile case 6530.

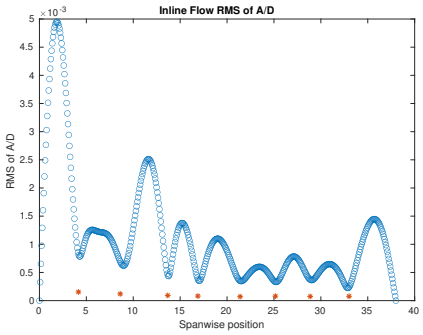

(b) Inline flow RMS profile case 6530.

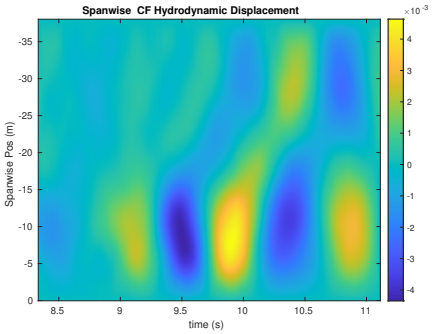

(c) Spanwise cross-flow hydrodynamic displacement case 6530.

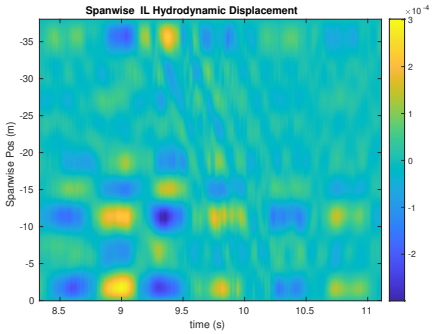

(d) Spanwise inline hydrodynamic displacement case 6530.

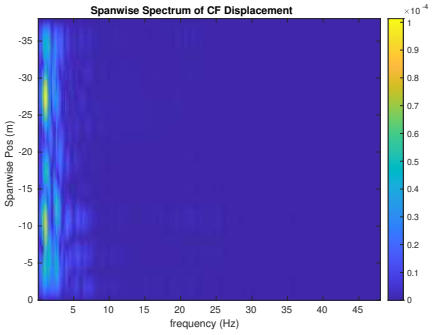

(e) Spanwise cross-flow spectrum of hydrodynamic displacement case 6530.

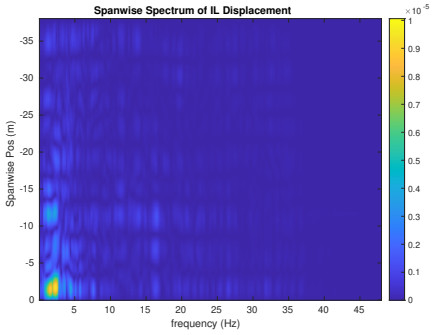

(f) Spanwise inline spectrum of hydrodynamic displacement case 6530.

Figure C-245: *Motion Analysis.* NDP Straight Riser ($L = 38m$) test case 6530.

NDP Straight Riser ($L = 38m$) test case 6610

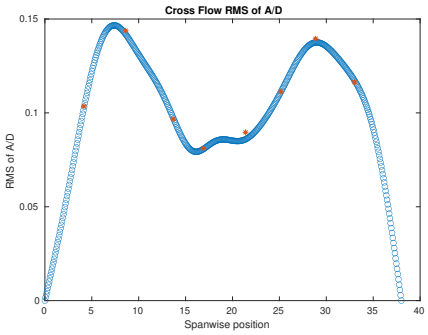

(a) Cross-flow RMS profile case 6610.

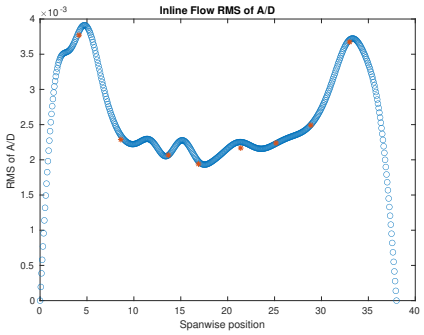

(b) Inline flow RMS profile case 6610.

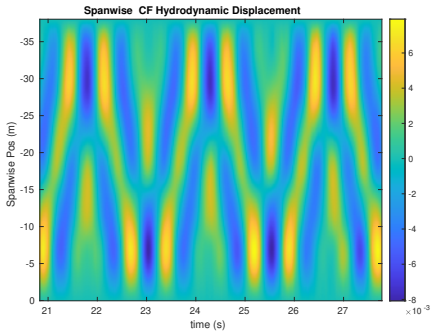

(c) Spanwise cross-flow hydrodynamic displacement case 6610.

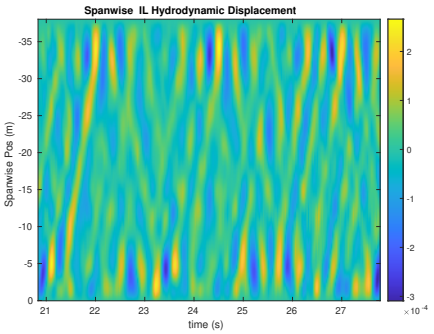

(d) Spanwise inline hydrodynamic displacement case 6610.

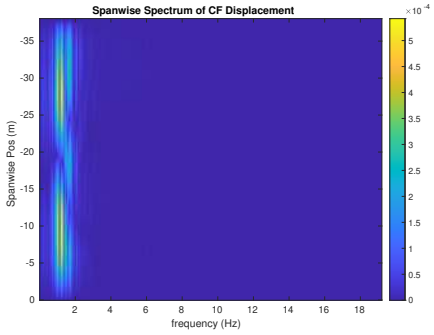

(e) Spanwise cross-flow spectrum of hydrodynamic displacement case 6610.

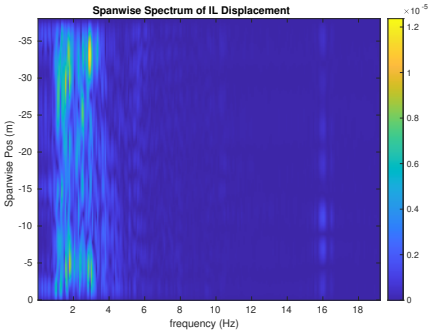

(f) Spanwise inline spectrum of hydrodynamic displacement case 6610.

Figure C-246: *Motion Analysis.* NDP Straight Riser ($L = 38m$) test case 6610.

NDP Straight Riser ($L = 38m$) test case 6620

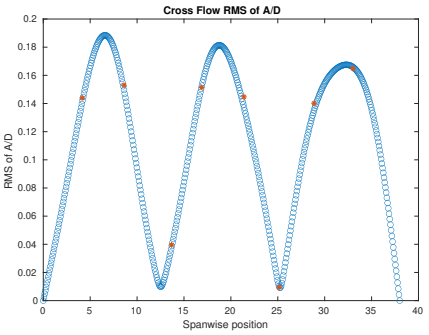

(a) Cross-flow RMS profile case 6620.

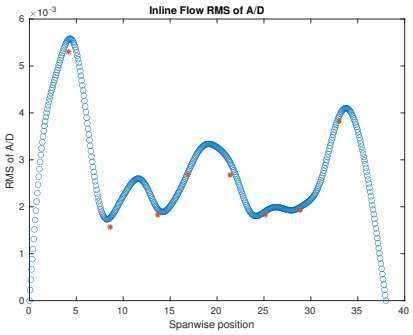

(b) Inline flow RMS profile case 6620.

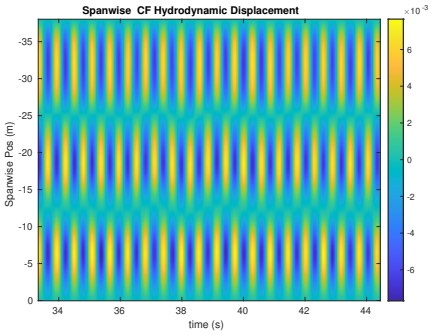

(c) Spanwise cross-flow hydrodynamic displacement case 6620.

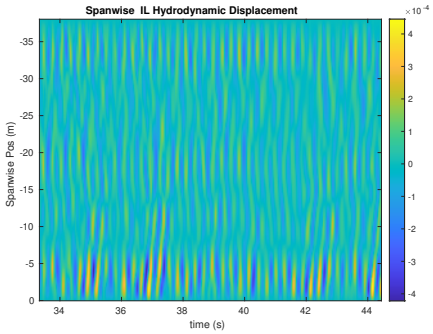

(d) Spanwise inline hydrodynamic displacement case 6620.

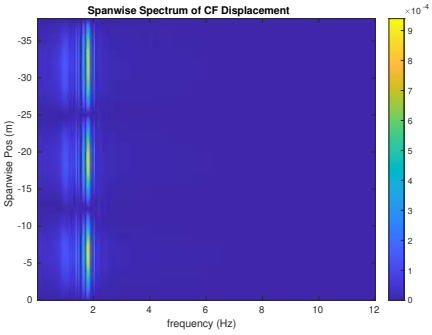

(e) Spanwise cross-flow spectrum of hydrodynamic displacement case 6620.

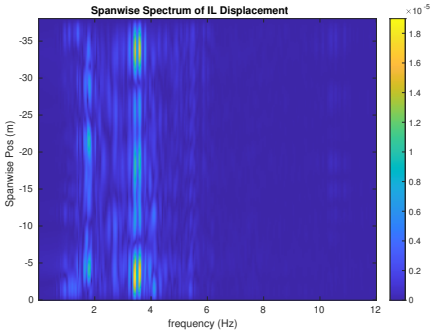

(f) Spanwise inline spectrum of hydrodynamic displacement case 6620.

Figure C-247: *Motion Analysis.* NDP Straight Riser ($L = 38m$) test case 6620.

NDP Straight Riser ($L = 38m$) test case 6630

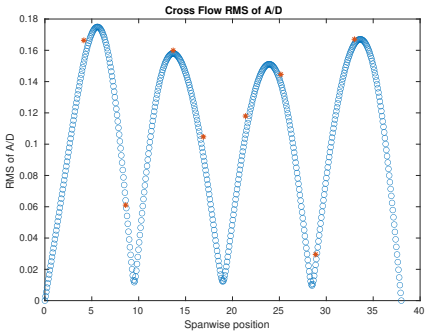

(a) Cross-flow RMS profile case 6630.

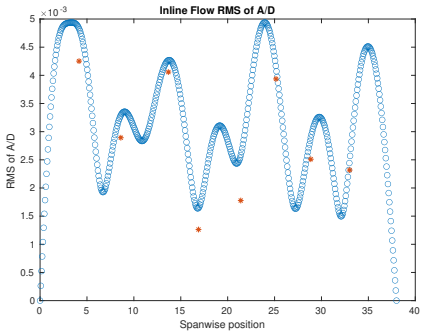

(b) Inline flow RMS profile case 6630.

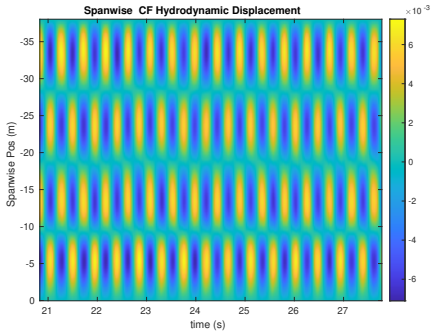

(c) Spanwise cross-flow hydrodynamic displacement case 6630.

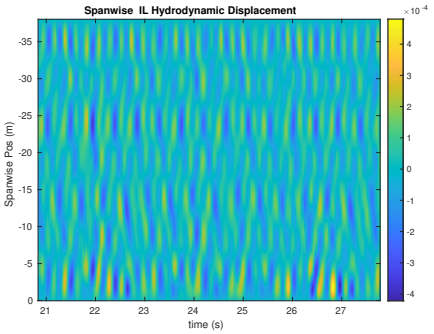

(d) Spanwise inline hydrodynamic displacement case 6630.

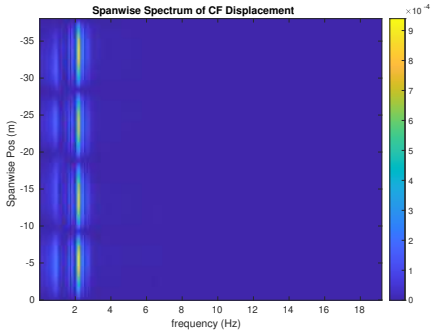

(e) Spanwise cross-flow spectrum of hydrodynamic displacement case 6630.

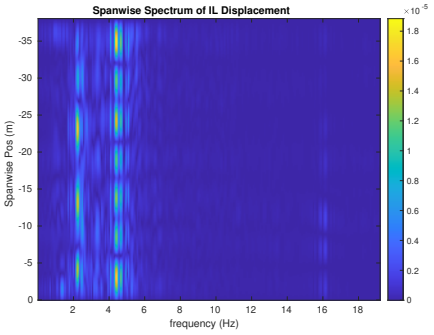

(f) Spanwise inline spectrum of hydrodynamic displacement case 6630.

Figure C-248: *Motion Analysis.* NDP Straight Riser ($L = 38m$) test case 6630.

NDP Straight Riser ($L = 38m$) test case 6640

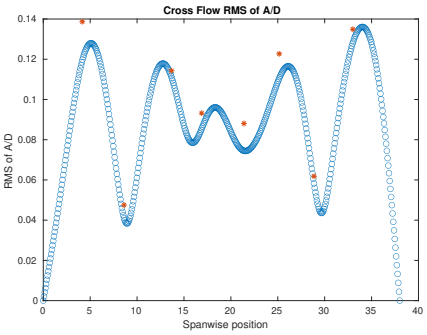

(a) Cross-flow RMS profile case 6640.

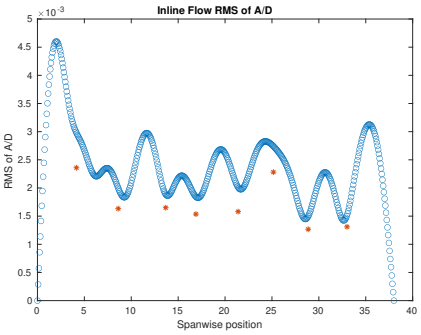

(b) Inline flow RMS profile case 6640.

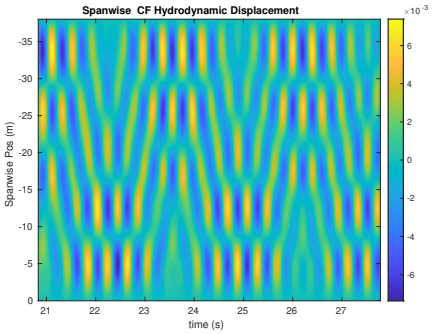

(c) Spanwise cross-flow hydrodynamic displacement case 6640.

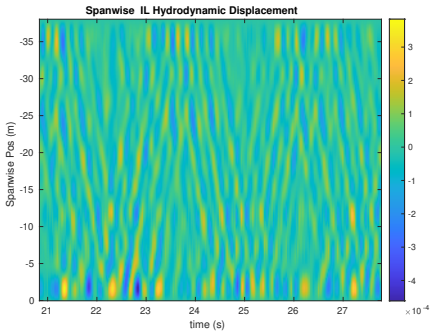

(d) Spanwise inline hydrodynamic displacement case 6640.

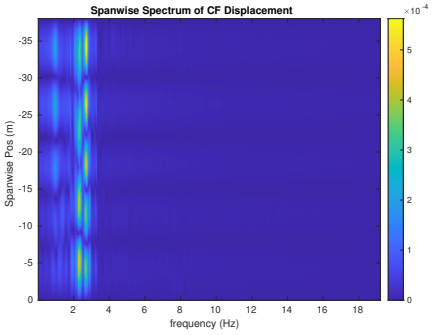

(e) Spanwise cross-flow spectrum of hydrodynamic displacement case 6640.

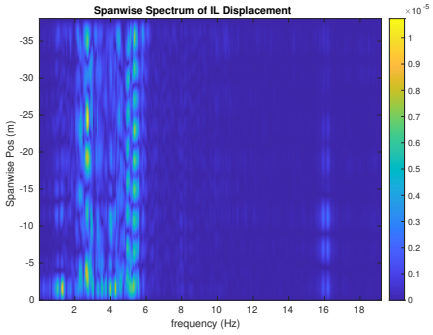

(f) Spanwise inline spectrum of hydrodynamic displacement case 6640.

Figure C-249: *Motion Analysis.* NDP Straight Riser ($L = 38m$) test case 6640.

NDP Straight Riser ($L = 38m$) test case 6650

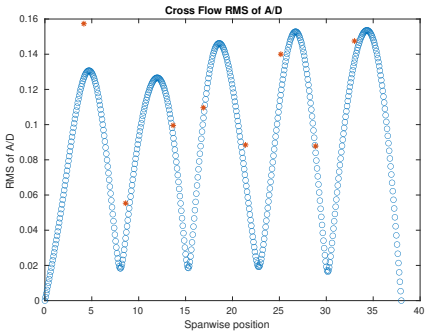

(a) Cross-flow RMS profile case 6650.

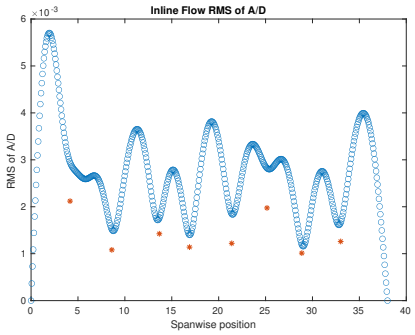

(b) Inline flow RMS profile case 6650.

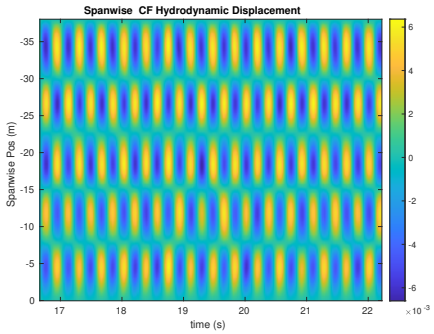

(c) Spanwise cross-flow hydrodynamic displacement case 6650.

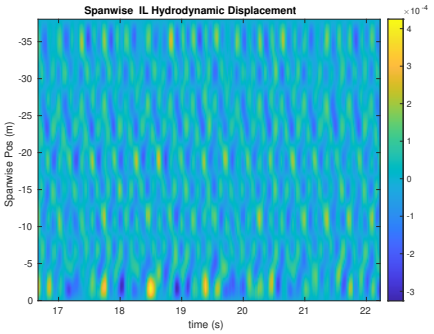

(d) Spanwise inline hydrodynamic displacement case 6650.

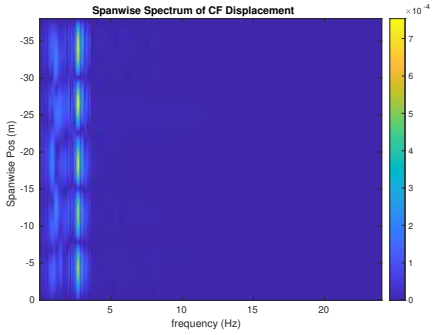

(e) Spanwise cross-flow spectrum of hydrodynamic displacement case 6650.

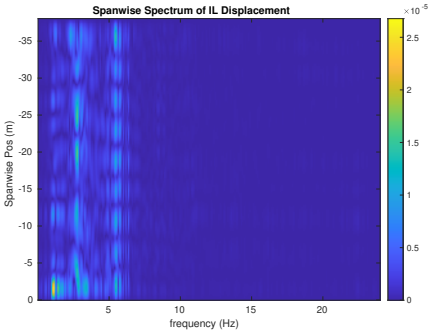

(f) Spanwise inline spectrum of hydrodynamic displacement case 6650.

Figure C-250: *Motion Analysis.* NDP Straight Riser ($L = 38m$) test case 6650.

NDP Straight Riser ($L = 38m$) test case 6660

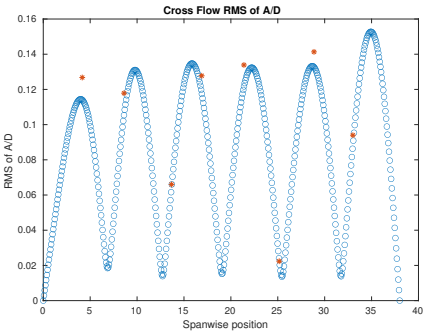

(a) Cross-flow RMS profile case 6660.

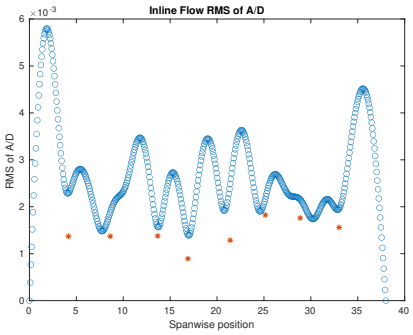

(b) Inline flow RMS profile case 6660.

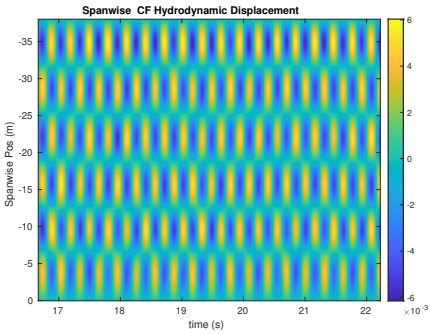

(c) Spanwise cross-flow hydrodynamic displacement case 6660.

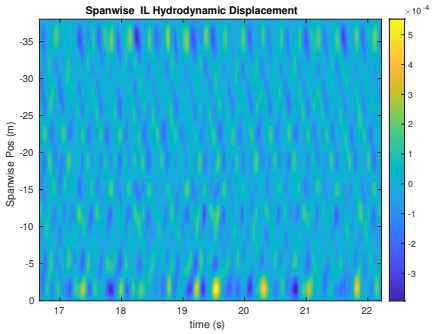

(d) Spanwise inline hydrodynamic displacement case 6660.

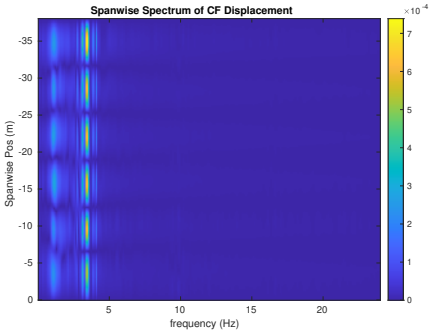

(e) Spanwise cross-flow spectrum of hydrodynamic displacement case 6660.

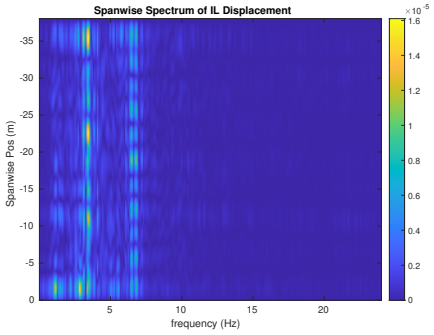

(f) Spanwise inline spectrum of hydrodynamic displacement case 6660.

Figure C-251: *Motion Analysis.* NDP Straight Riser ($L = 38m$) test case 6660.

NDP Straight Riser ($L = 38m$) test case 6670

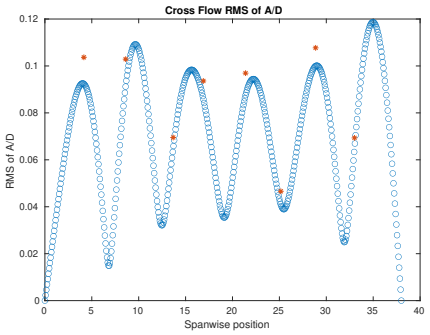

(a) Cross-flow RMS profile case 6670.

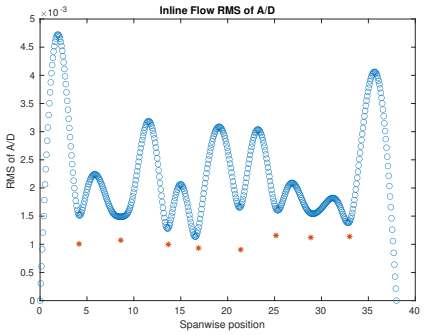

(b) Inline flow RMS profile case 6670.

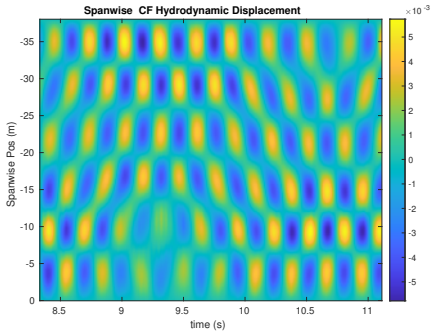

(c) Spanwise cross-flow hydrodynamic displacement case 6670.

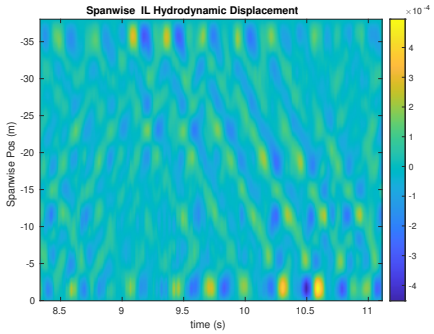

(d) Spanwise inline hydrodynamic displacement case 6670.

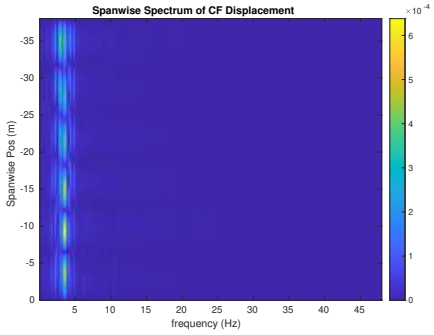

(e) Spanwise cross-flow spectrum of hydrodynamic displacement case 6670.

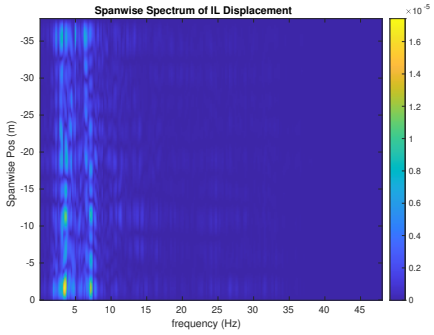

(f) Spanwise inline spectrum of hydrodynamic displacement case 6670.

Figure C-252: *Motion Analysis.* NDP Straight Riser ($L = 38m$) test case 6670.

NDP Straight Riser ($L = 38m$) test case 6680

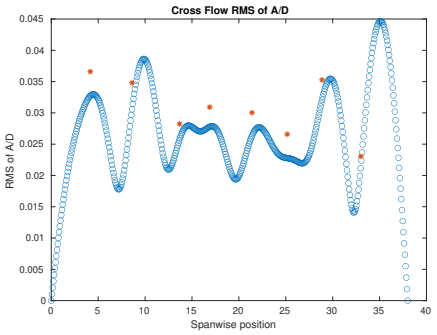

(a) Cross-flow RMS profile case 6680.

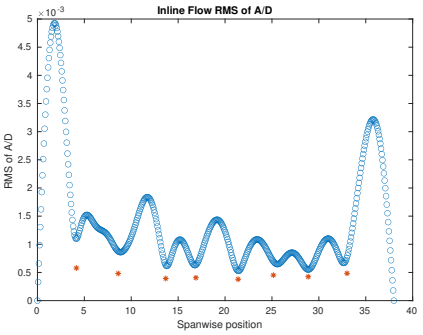

(b) Inline flow RMS profile case 6680.

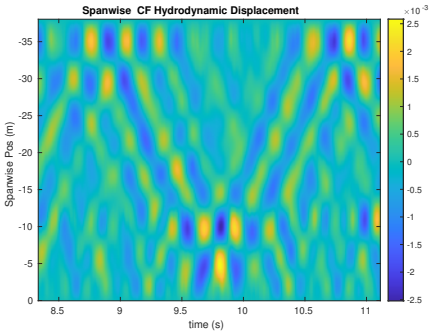

(c) Spanwise cross-flow hydrodynamic displacement case 6680.

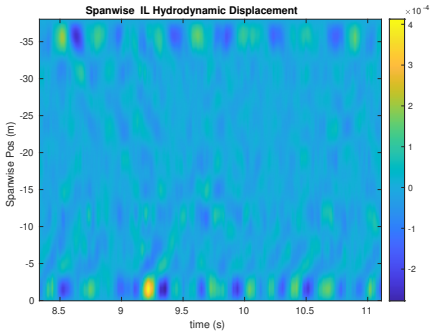

(d) Spanwise inline hydrodynamic displacement case 6680.

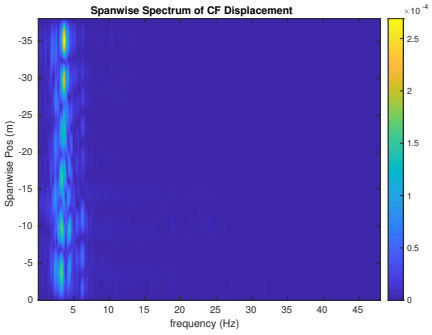

(e) Spanwise cross-flow spectrum of hydrodynamic displacement case 6680.

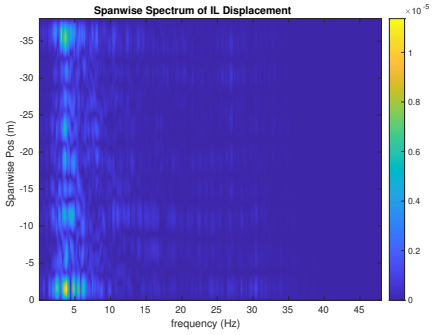

(f) Spanwise inline spectrum of hydrodynamic displacement case 6680.

Figure C-253: *Motion Analysis.* NDP Straight Riser ($L = 38m$) test case 6680.

NDP Straight Riser ($L = 38m$) test case 6690

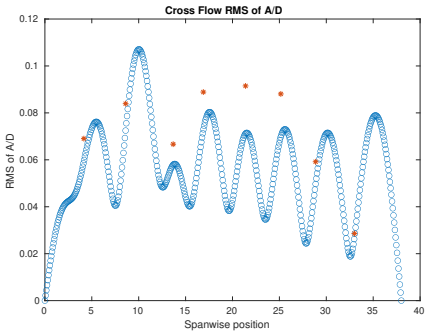

(a) Cross-flow RMS profile case 6690.

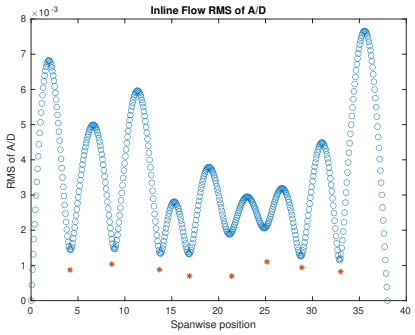

(b) Inline flow RMS profile case 6690.

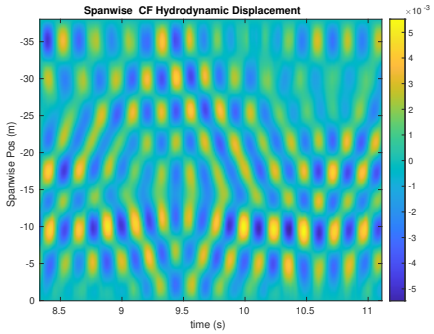

(c) Spanwise cross-flow hydrodynamic displacement case 6690.

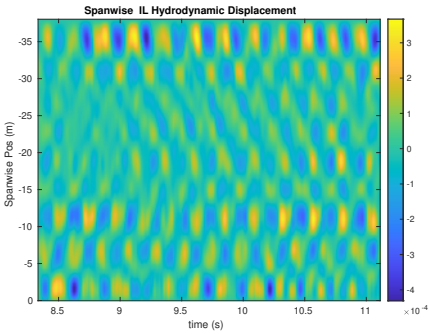

(d) Spanwise inline hydrodynamic displacement case 6690.

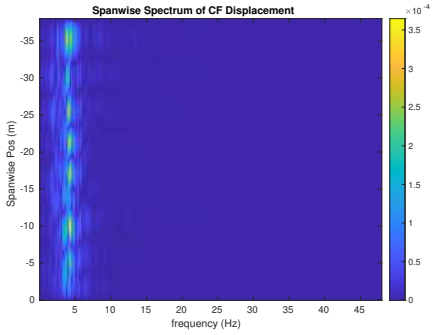

(e) Spanwise cross-flow spectrum of hydrodynamic displacement case 6690.

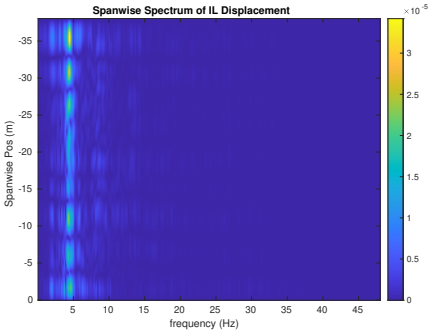

(f) Spanwise inline spectrum of hydrodynamic displacement case 6690.

Figure C-254: *Motion Analysis.* NDP Straight Riser ($L = 38m$) test case 6690.

NDP Straight Riser ($L = 38m$) test case 6700

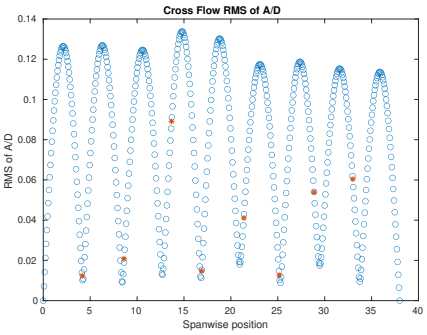

(a) Cross-flow RMS profile case 6700.

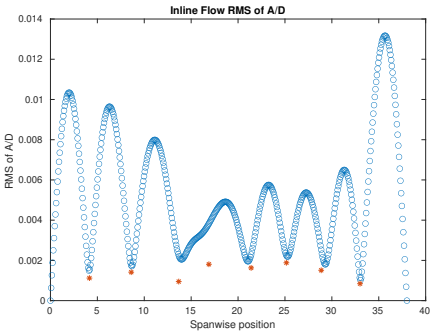

(b) Inline flow RMS profile case 6700.

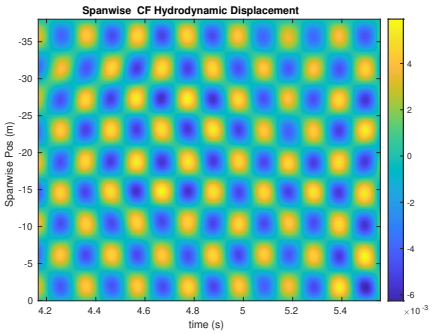

(c) Spanwise cross-flow hydrodynamic displacement case 6700.

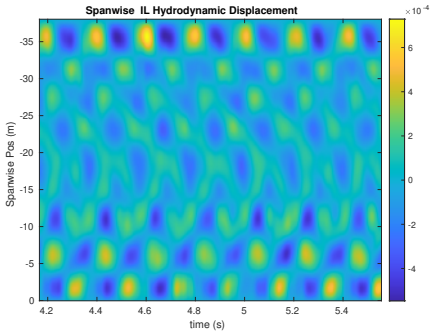

(d) Spanwise inline hydrodynamic displacement case 6700.

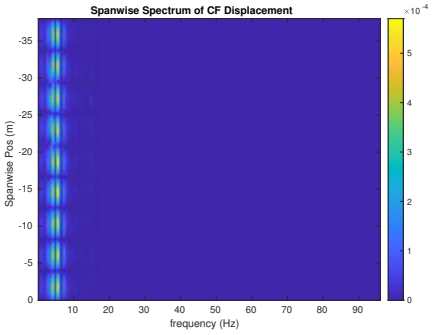

(e) Spanwise cross-flow spectrum of hydrodynamic displacement case 6700.

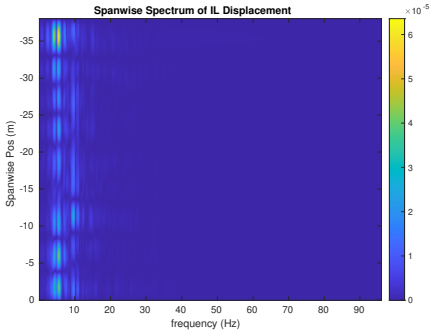

(f) Spanwise inline spectrum of hydrodynamic displacement case 6700.

Figure C-255: *Motion Analysis.* NDP Straight Riser ($L = 38m$) test case 6700.

NDP Straight Riser ($L = 38m$) test case 6710

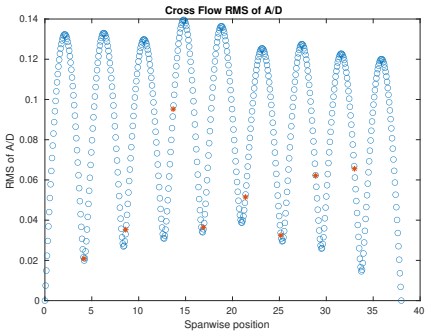

(a) Cross-flow RMS profile case 6710.

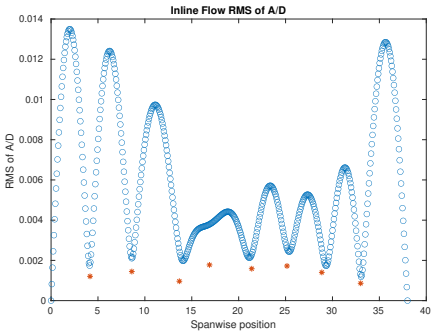

(b) Inline flow RMS profile case 6710.

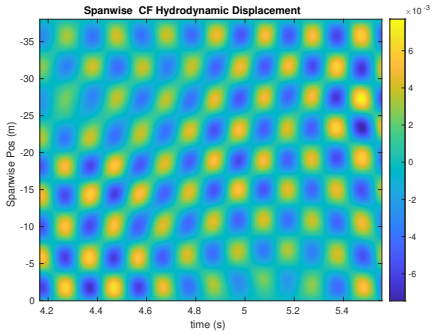

(c) Spanwise cross-flow hydrodynamic displacement case 6710.

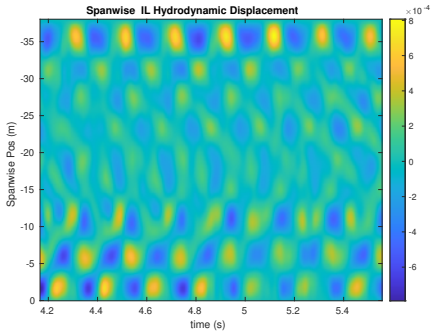

(d) Spanwise inline hydrodynamic displacement case 6710.

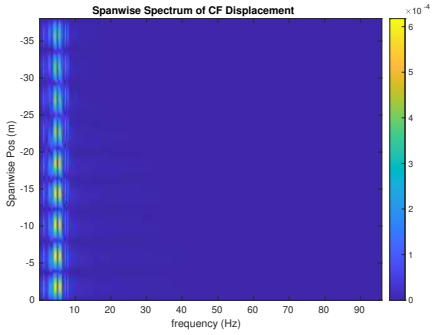

(e) Spanwise cross-flow spectrum of hydrodynamic displacement case 6710.

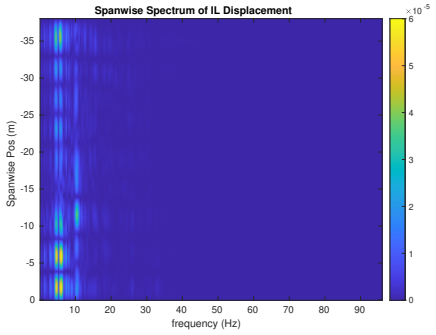

(f) Spanwise inline spectrum of hydrodynamic displacement case 6710.

Figure C-256: *Motion Analysis.* NDP Straight Riser ($L = 38m$) test case 6710.

NDP Straight Riser ($L = 38m$) test case 6720

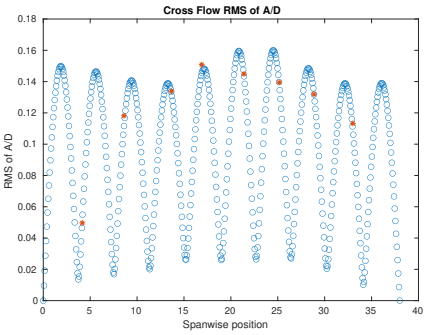

(a) Cross-flow RMS profile case 6720.

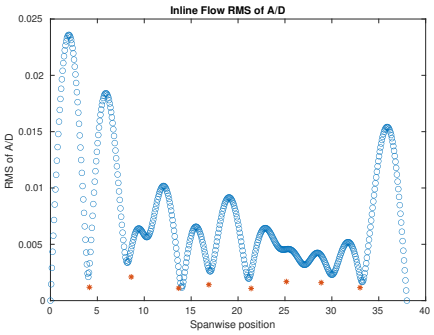

(b) Inline flow RMS profile case 6720.

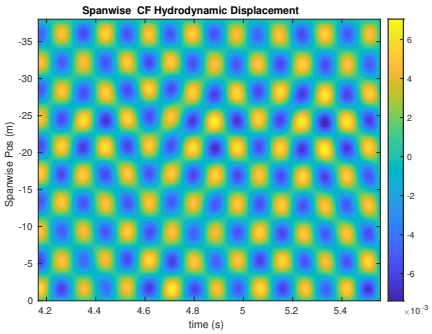

(c) Spanwise cross-flow hydrodynamic displacement case 6720.

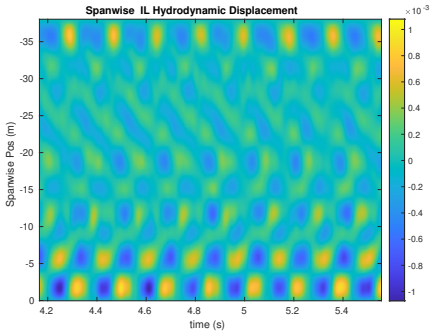

(d) Spanwise inline hydrodynamic displacement case 6720.

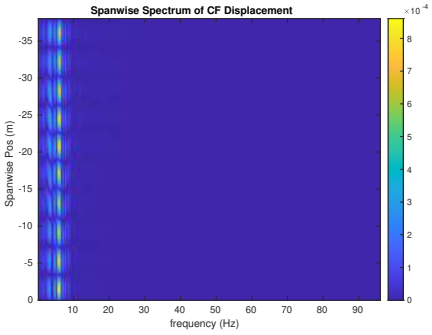

(e) Spanwise cross-flow spectrum of hydrodynamic displacement case 6720.

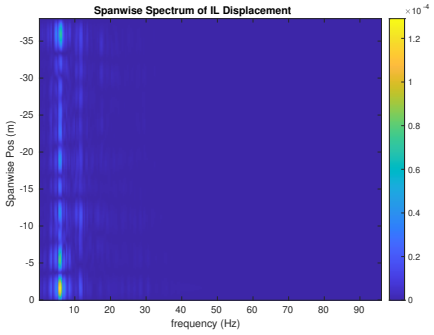

(f) Spanwise inline spectrum of hydrodynamic displacement case 6720.

Figure C-257: *Motion Analysis.* NDP Straight Riser ($L = 38m$) test case 6720.

NDP Straight Riser ($L = 38m$) test case 6730

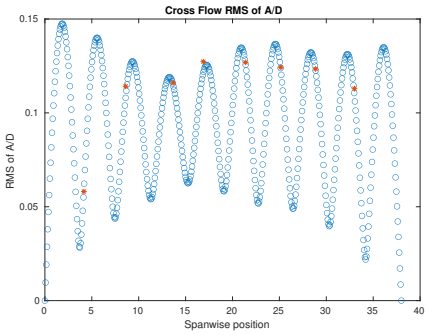

(a) Cross-flow RMS profile case 6730.

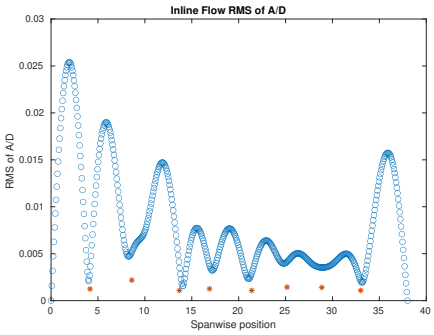

(b) Inline flow RMS profile case 6730.

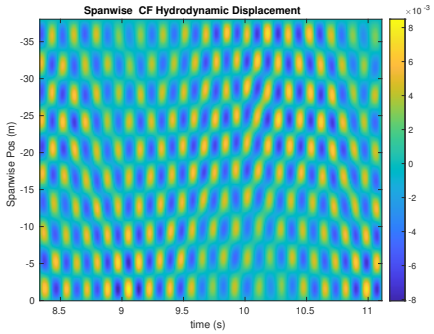

(c) Spanwise cross-flow hydrodynamic displacement case 6730.

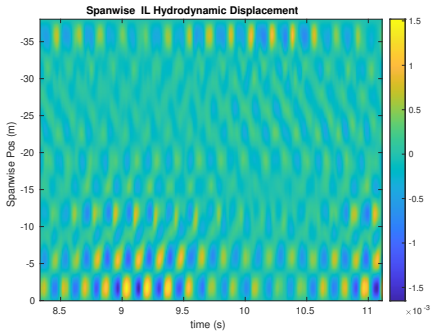

(d) Spanwise inline hydrodynamic displacement case 6730.

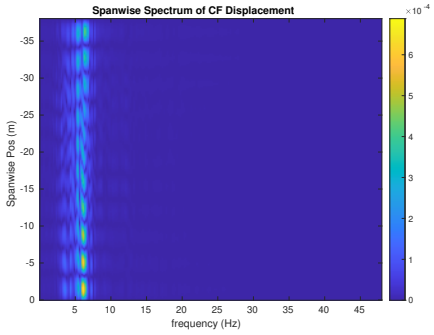

(e) Spanwise cross-flow spectrum of hydrodynamic displacement case 6730.

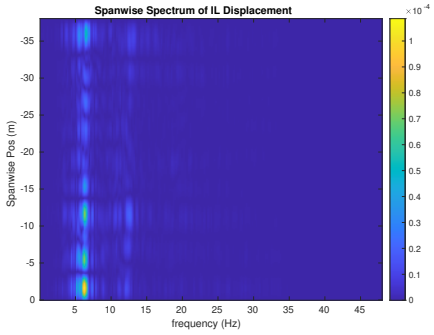

(f) Spanwise inline spectrum of hydrodynamic displacement case 6730.

Figure C-258: *Motion Analysis.* NDP Straight Riser ($L = 38m$) test case 6730.

NDP Straight Riser ($L = 38m$) test case 6740

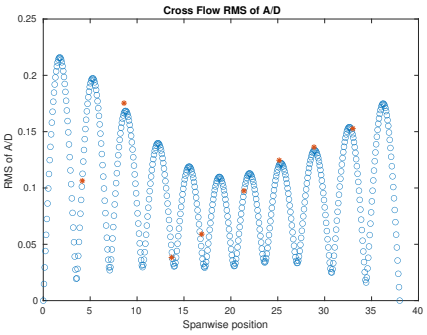

(a) Cross-flow RMS profile case 6740.

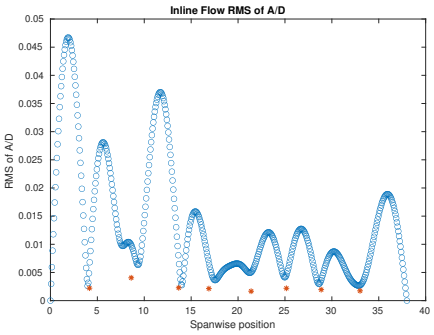

(b) Inline flow RMS profile case 6740.

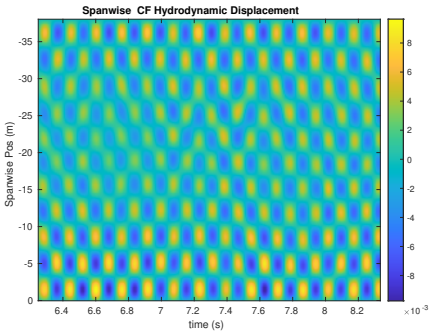

(c) Spanwise cross-flow hydrodynamic displacement case 6740.

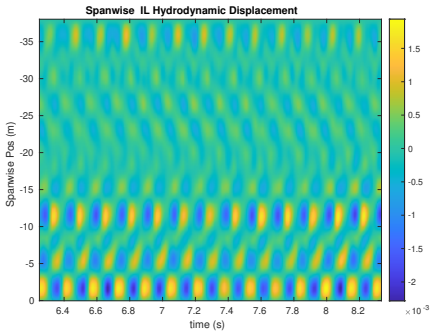

(d) Spanwise inline hydrodynamic displacement case 6740.

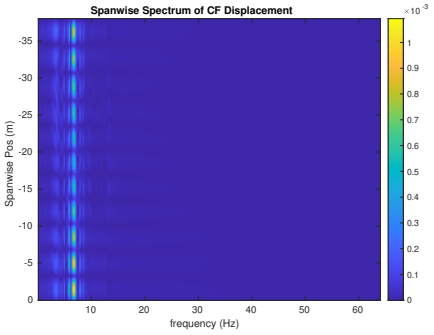

(e) Spanwise cross-flow spectrum of hydrodynamic displacement case 6740.

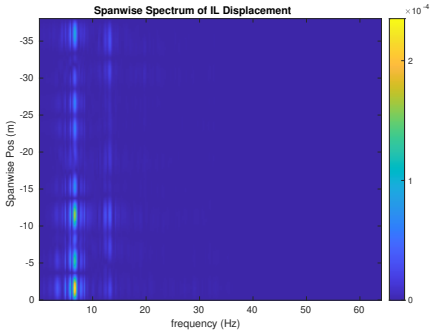

(f) Spanwise inline spectrum of hydrodynamic displacement case 6740.

Figure C-259: *Motion Analysis.* NDP Straight Riser ($L = 38m$) test case 6740.

NDP Straight Riser ($L = 38m$) test case 6750

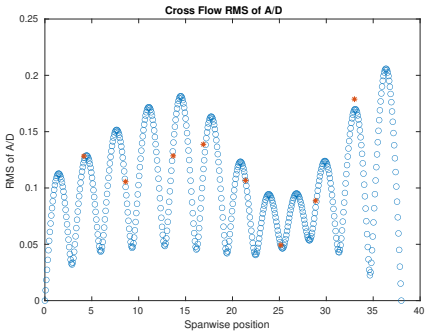

(a) Cross-flow RMS profile case 6750.

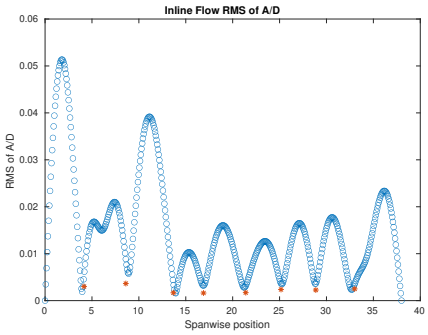

(b) Inline flow RMS profile case 6750.

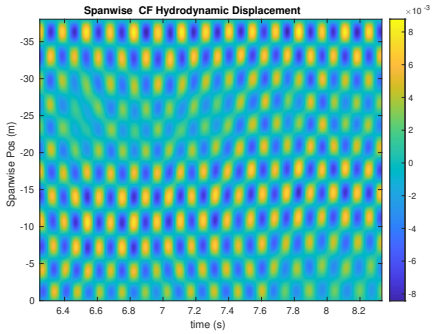

(c) Spanwise cross-flow hydrodynamic displacement case 6750.

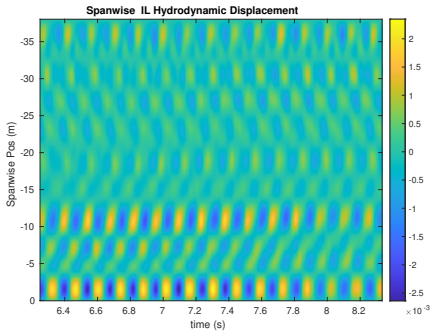

(d) Spanwise inline hydrodynamic displacement case 6750.

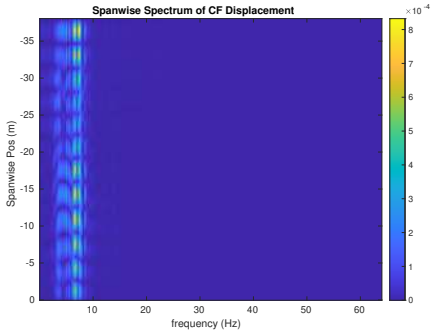

(e) Spanwise cross-flow spectrum of hydrodynamic displacement case 6750.

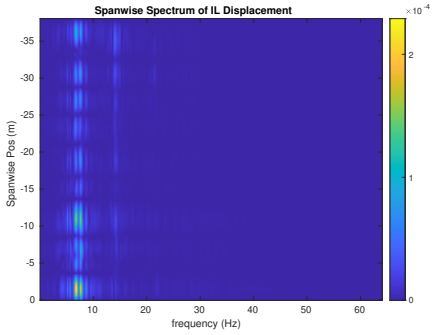

(f) Spanwise inline spectrum of hydrodynamic displacement case 6750.

Figure C-260: *Motion Analysis.* NDP Straight Riser ($L = 38m$) test case 6750.

NDP Straight Riser ($L = 38m$) test case 6760

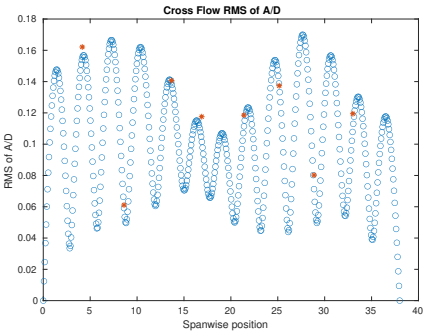

(a) Cross-flow RMS profile case 6760.

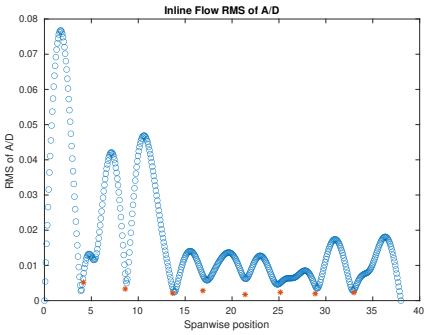

(b) Inline flow RMS profile case 6760.

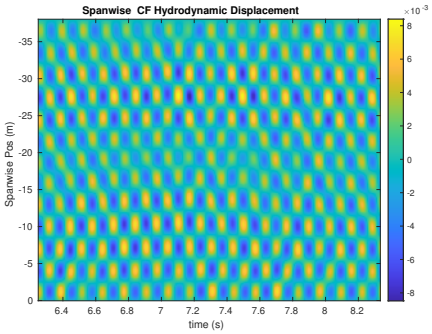

(c) Spanwise cross-flow hydrodynamic displacement case 6760.

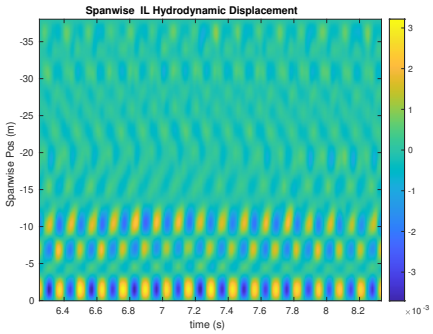

(d) Spanwise inline hydrodynamic displacement case 6760.

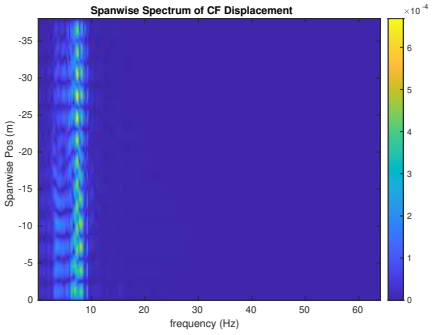

(e) Spanwise cross-flow spectrum of hydrodynamic displacement case 6760.

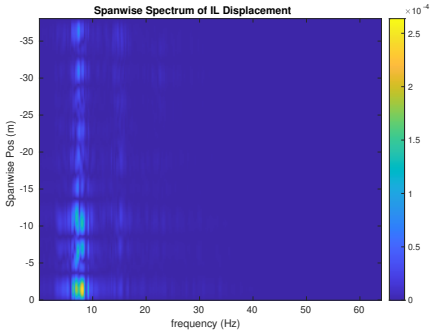

(f) Spanwise inline spectrum of hydrodynamic displacement case 6760.

Figure C-261: *Motion Analysis.* NDP Straight Riser ($L = 38m$) test case 6760.

NDP Straight Riser ($L = 38m$) test case 6770

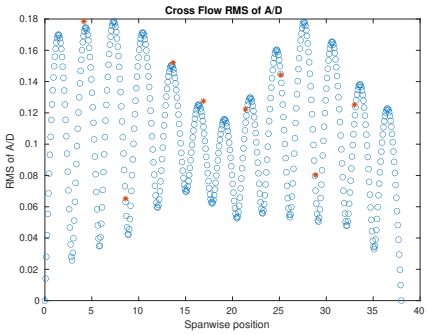

(a) Cross-flow RMS profile case 6770.

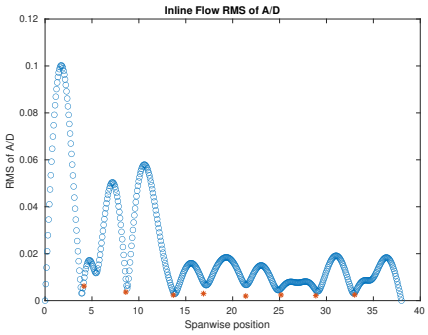

(b) Inline flow RMS profile case 6770.

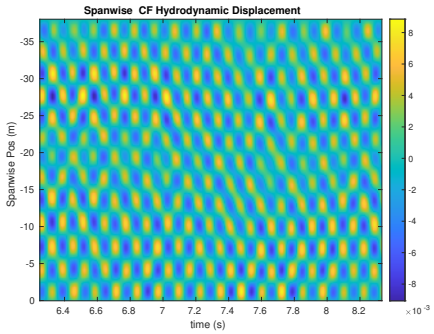

(c) Spanwise cross-flow hydrodynamic displacement case 6770.

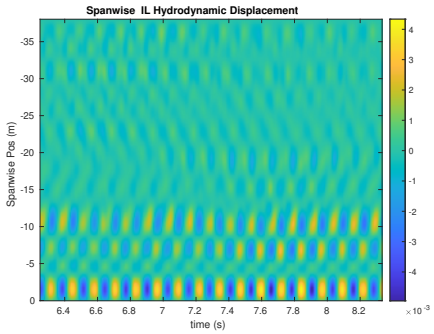

(d) Spanwise inline hydrodynamic displacement case 6770.

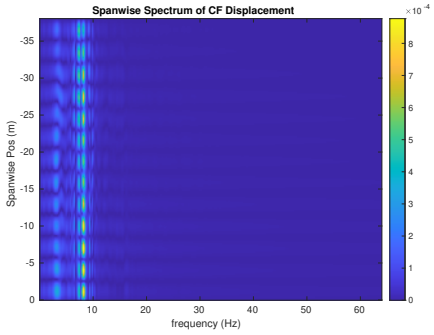

(e) Spanwise cross-flow spectrum of hydrodynamic displacement case 6770.

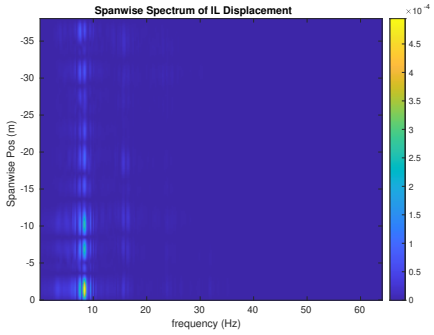

(f) Spanwise inline spectrum of hydrodynamic displacement case 6770.

Figure C-262: *Motion Analysis.* NDP Straight Riser ($L = 38m$) test case 6770.

NDP Straight Riser ($L = 38m$) test case 6780

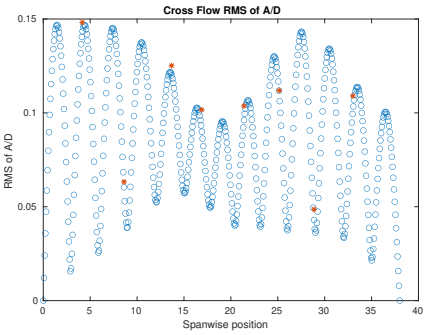

(a) Cross-flow RMS profile case 6780.

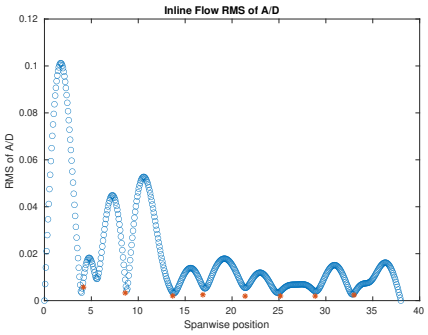

(b) Inline flow RMS profile case 6780.

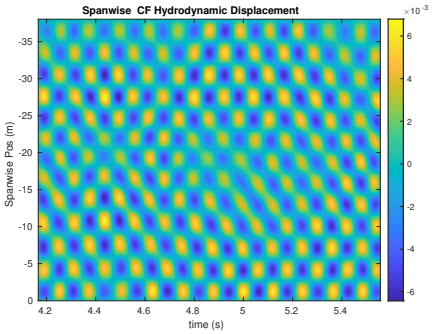

(c) Spanwise cross-flow hydrodynamic displacement case 6780.

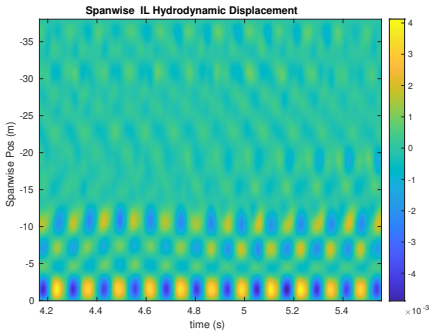

(d) Spanwise inline hydrodynamic displacement case 6780.

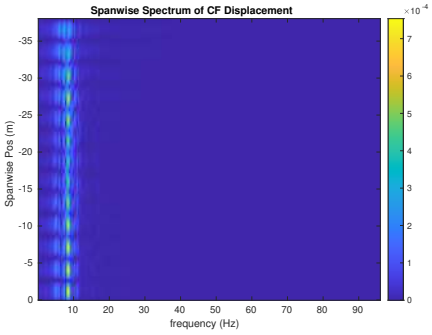

(e) Spanwise cross-flow spectrum of hydrodynamic displacement case 6780.

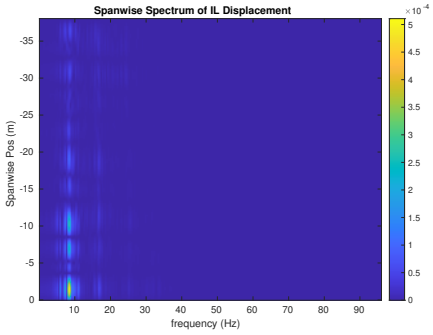

(f) Spanwise inline spectrum of hydrodynamic displacement case 6780.

Figure C-263: *Motion Analysis.* NDP Straight Riser ($L = 38m$) test case 6780.

NDP Straight Riser ($L = 38m$) test case 6790

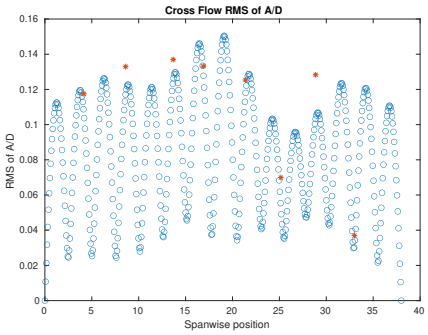

(a) Cross-flow RMS profile case 6790.

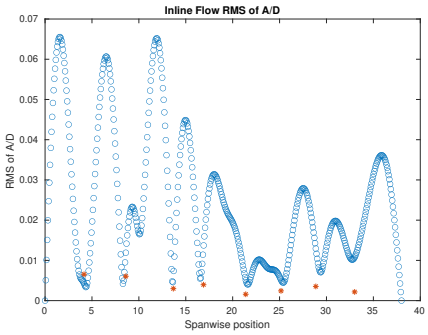

(b) Inline flow RMS profile case 6790.

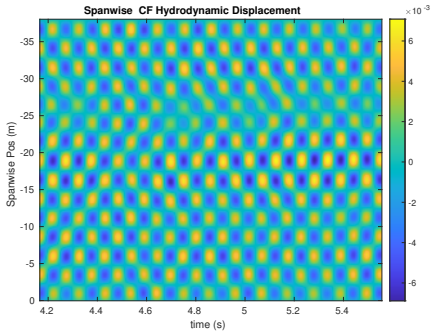

(c) Spanwise cross-flow hydrodynamic displacement case 6790.

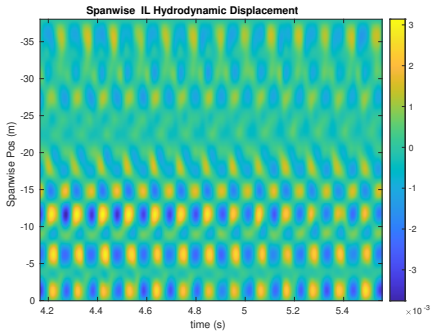

(d) Spanwise inline hydrodynamic displacement case 6790.

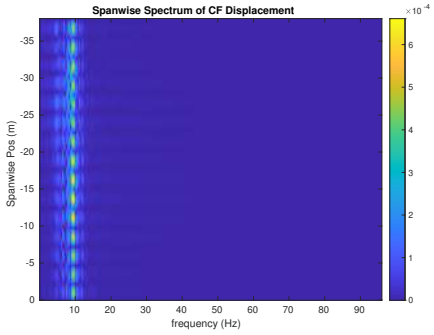

(e) Spanwise cross-flow spectrum of hydrodynamic displacement case 6790.

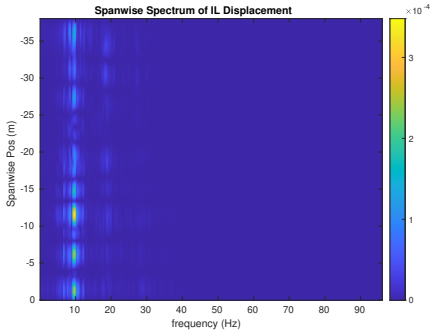

(f) Spanwise inline spectrum of hydrodynamic displacement case 6790.

Figure C-264: *Motion Analysis.* NDP Straight Riser ($L = 38m$) test case 6790.

NDP Straight Riser ($L = 38m$) test case 6800

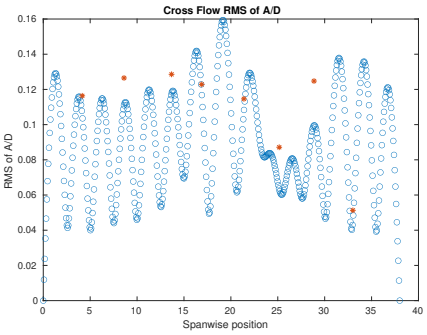

(a) Cross-flow RMS profile case 6800.

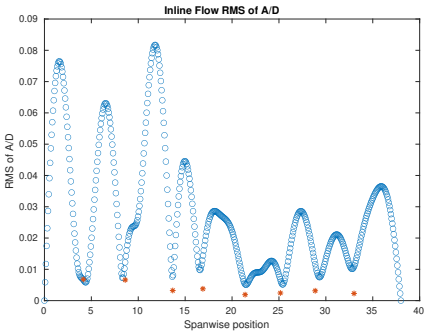

(b) Inline flow RMS profile case 6800.

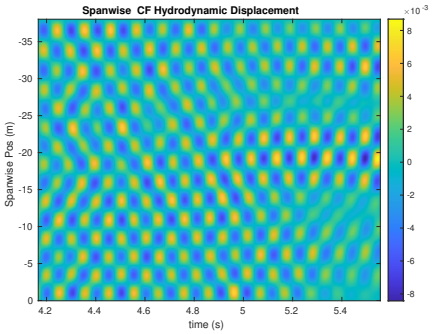

(c) Spanwise cross-flow hydrodynamic displacement case 6800.

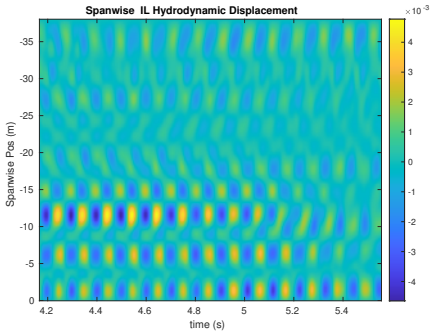

(d) Spanwise inline hydrodynamic displacement case 6800.

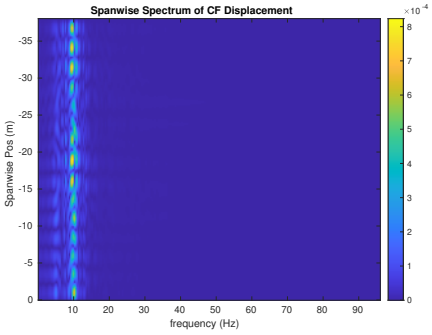

(e) Spanwise cross-flow spectrum of hydrodynamic displacement case 6800.

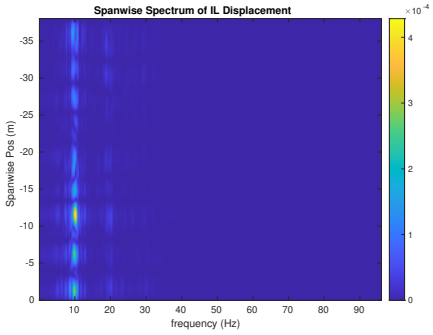

(f) Spanwise inline spectrum of hydrodynamic displacement case 6800.

Figure C-265: *Motion Analysis.* NDP Straight Riser ($L = 38m$) test case 6800.

NDP Straight Riser ($L = 38m$) test case 6810

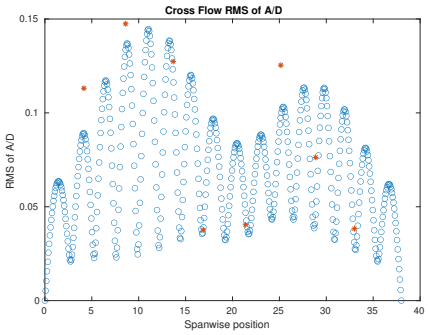

(a) Cross-flow RMS profile case 6810.

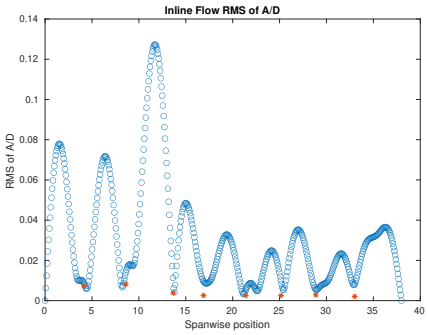

(b) Inline flow RMS profile case 6810.

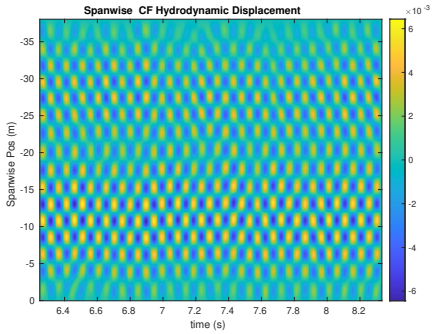

(c) Spanwise cross-flow hydrodynamic displacement case 6810.

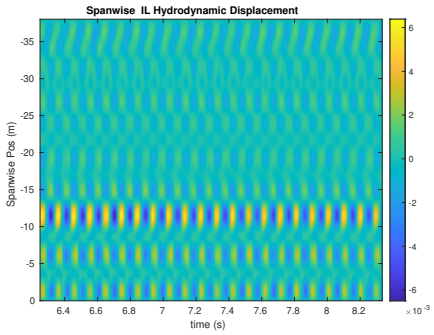

(d) Spanwise inline hydrodynamic displacement case 6810.

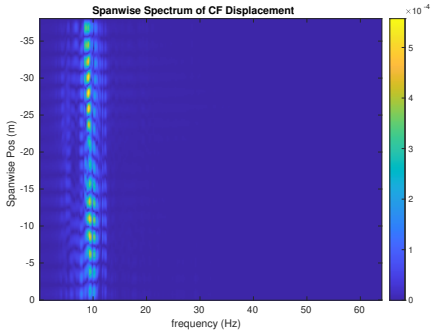

(e) Spanwise cross-flow spectrum of hydrodynamic displacement case 6810.

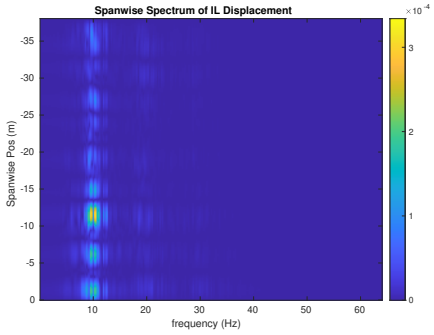

(f) Spanwise inline spectrum of hydrodynamic displacement case 6810.

Figure C-266: *Motion Analysis.* NDP Straight Riser ($L = 38m$) test case 6810.

NDP Straight Riser ($L = 38m$) test case 6820

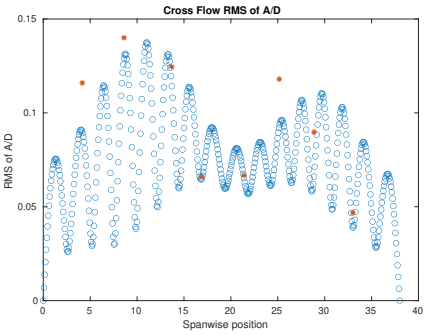

(a) Cross-flow RMS profile case 6820.

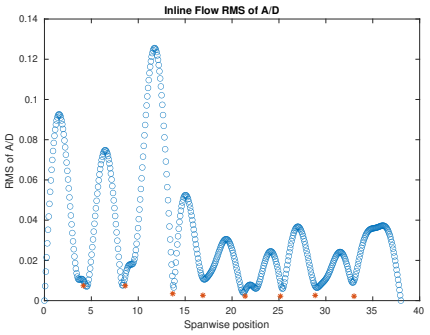

(b) Inline flow RMS profile case 6820.

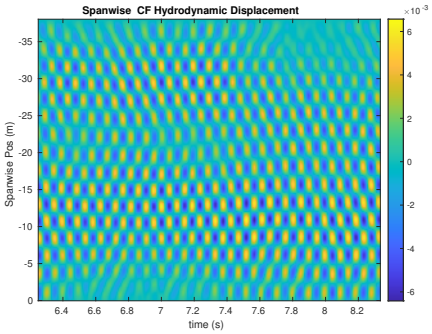

(c) Spanwise cross-flow hydrodynamic displacement case 6820.

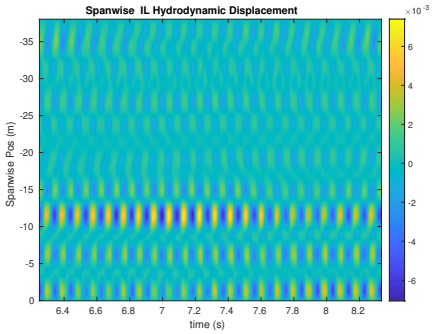

(d) Spanwise inline hydrodynamic displacement case 6820.

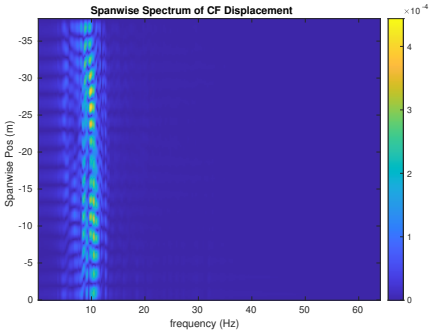

(e) Spanwise cross-flow spectrum of hydrodynamic displacement case 6820.

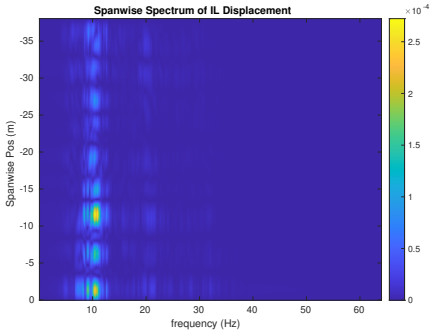

(f) Spanwise inline spectrum of hydrodynamic displacement case 6820.

Figure C-267: *Motion Analysis.* NDP Straight Riser ($L = 38m$) test case 6820.

NDP Straight Riser ($L = 38m$) test case 6830

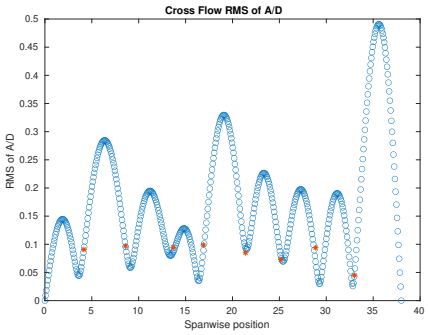

(a) Cross-flow RMS profile case 6830.

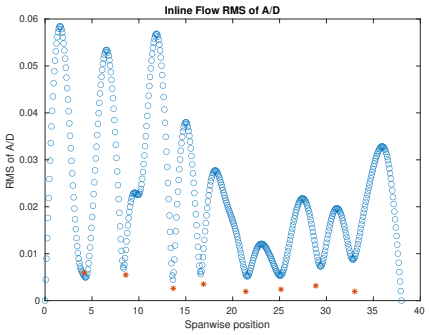

(b) Inline flow RMS profile case 6830.

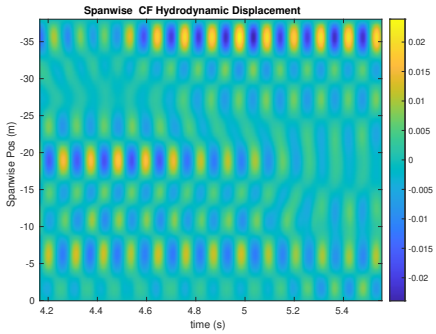

(c) Spanwise cross-flow hydrodynamic displacement case 6830.

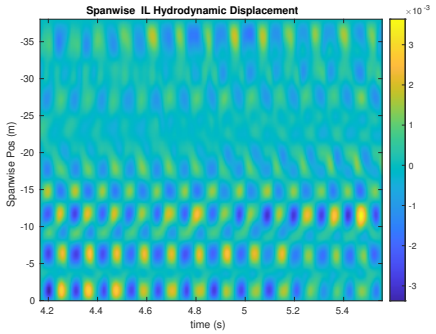

(d) Spanwise inline hydrodynamic displacement case 6830.

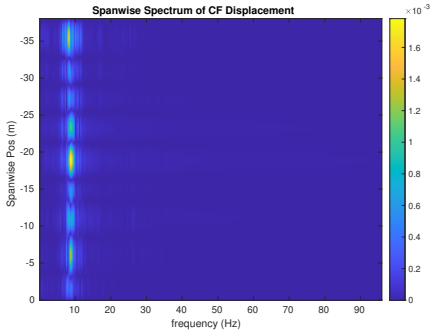

(e) Spanwise cross-flow spectrum of hydrodynamic displacement case 6830.

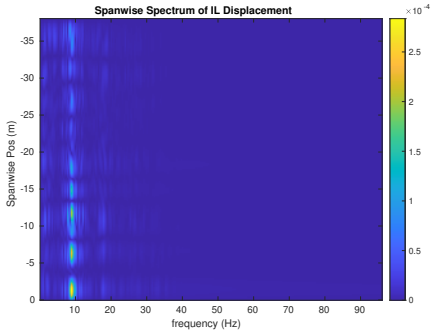

(f) Spanwise inline spectrum of hydrodynamic displacement case 6830.

Figure C-268: *Motion Analysis.* NDP Straight Riser ($L = 38m$) test case 6830.

NDP Straight Riser ($L = 38m$) test case 6910

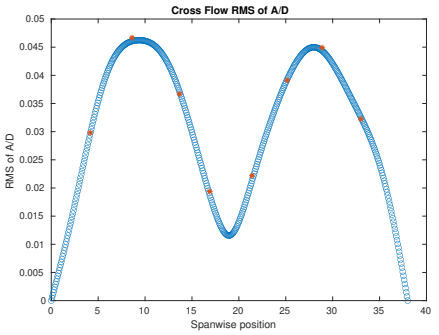

(a) Cross-flow RMS profile case 6910.

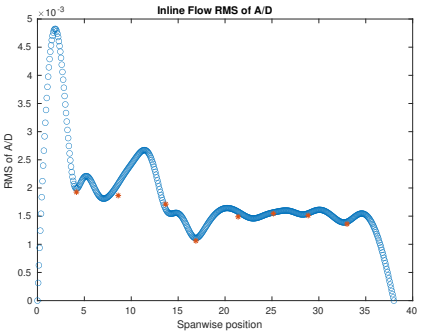

(b) Inline flow RMS profile case 6910.

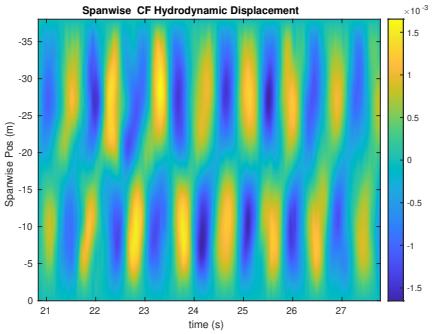

(c) Spanwise cross-flow hydrodynamic displacement case 6910.

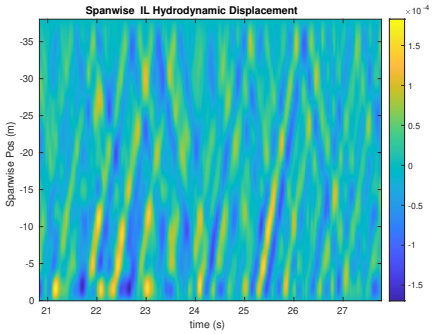

(d) Spanwise inline hydrodynamic displacement case 6910.

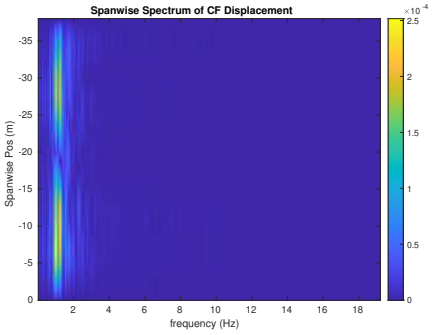

(e) Spanwise cross-flow spectrum of hydrodynamic displacement case 6910.

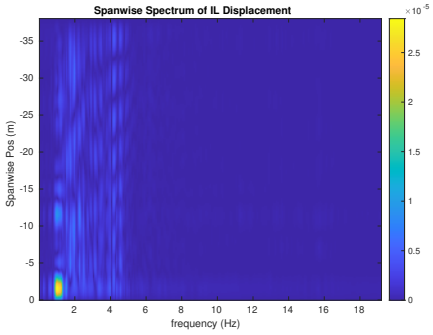

(f) Spanwise inline spectrum of hydrodynamic displacement case 6910.

Figure C-269: *Motion Analysis.* NDP Straight Riser ($L = 38m$) test case 6910.

NDP Straight Riser ($L = 38m$) test case 6920

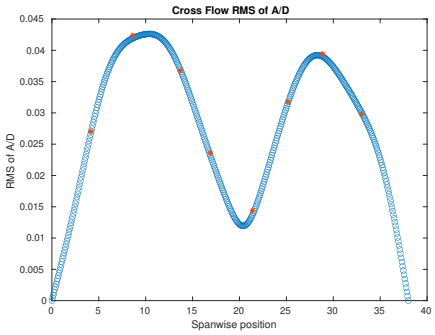

(a) Cross-flow RMS profile case 6920.

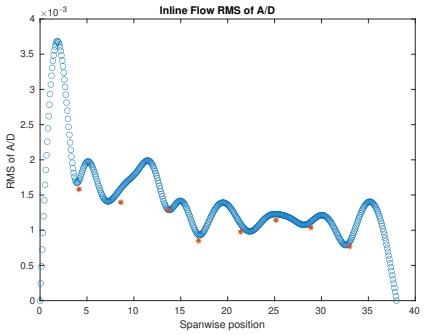

(b) Inline flow RMS profile case 6920.

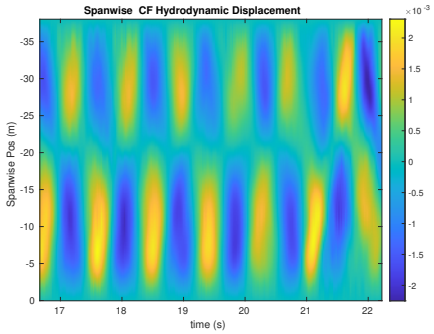

(c) Spanwise cross-flow hydrodynamic displacement case 6920.

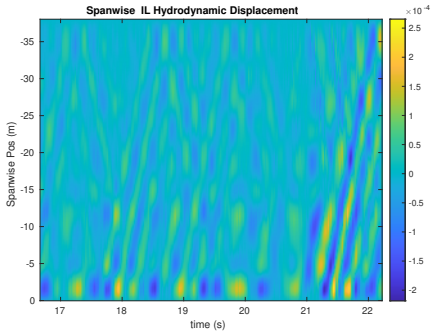

(d) Spanwise inline hydrodynamic displacement case 6920.

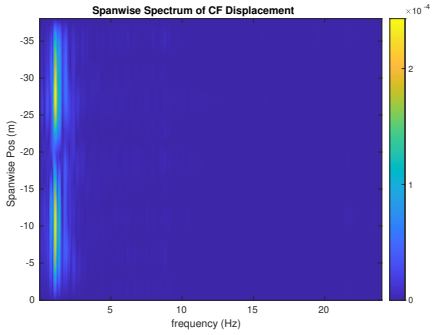

(e) Spanwise cross-flow spectrum of hydrodynamic displacement case 6920.

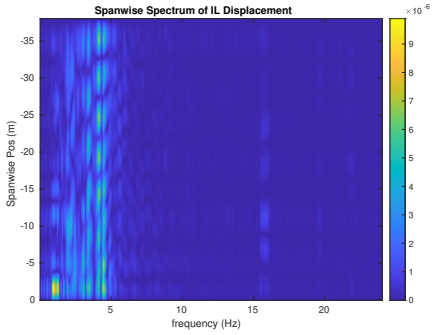

(f) Spanwise inline spectrum of hydrodynamic displacement case 6920.

Figure C-270: *Motion Analysis.* NDP Straight Riser ($L = 38m$) test case 6920.

NDP Straight Riser ($L = 38m$) test case 6930

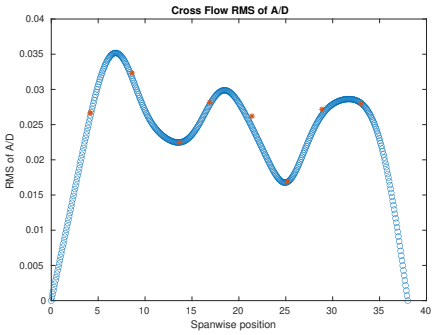

(a) Cross-flow RMS profile case 6930.

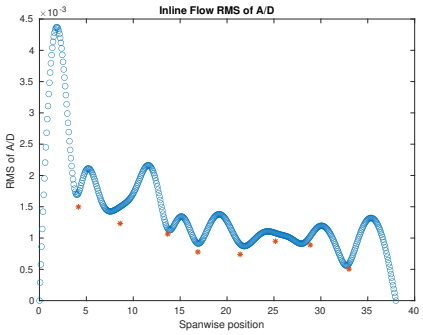

(b) Inline flow RMS profile case 6930.

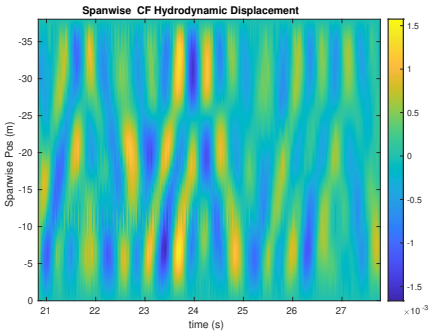

(c) Spanwise cross-flow hydrodynamic displacement case 6930.

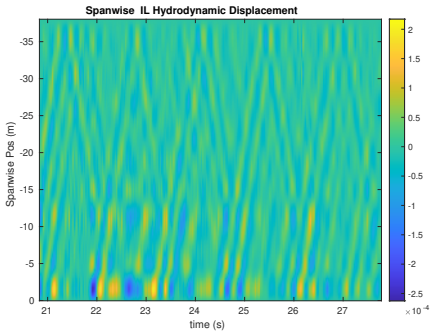

(d) Spanwise inline hydrodynamic displacement case 6930.

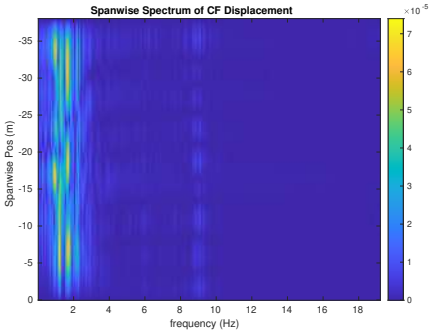

(e) Spanwise cross-flow spectrum of hydrodynamic displacement case 6930.

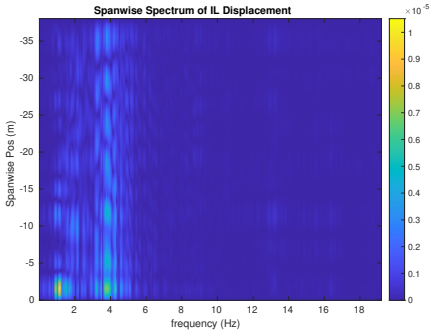

(f) Spanwise inline spectrum of hydrodynamic displacement case 6930.

Figure C-271: *Motion Analysis.* NDP Straight Riser ($L = 38m$) test case 6930.

NDP Straight Riser ($L = 38m$) test case 6940

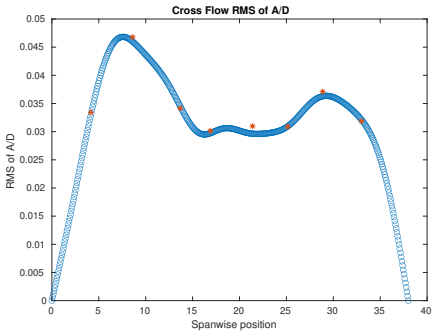

(a) Cross-flow RMS profile case 6940.

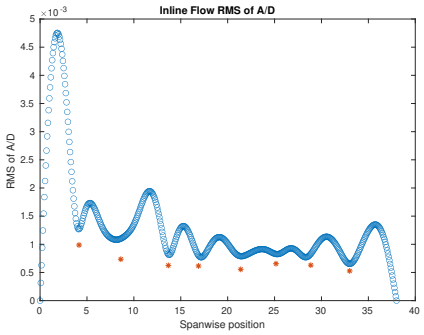

(b) Inline flow RMS profile case 6940.

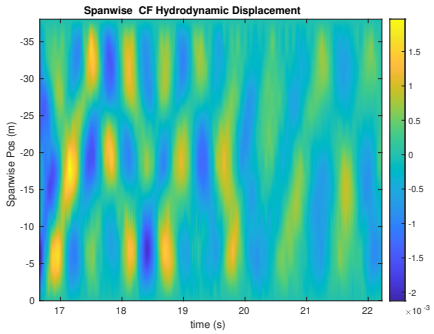

(c) Spanwise cross-flow hydrodynamic displacement case 6940.

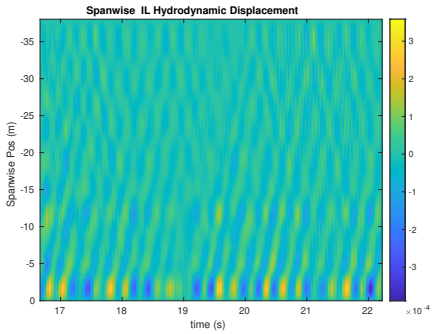

(d) Spanwise inline hydrodynamic displacement case 6940.

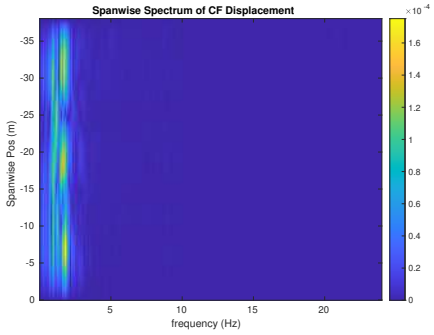

(e) Spanwise cross-flow spectrum of hydrodynamic displacement case 6940.

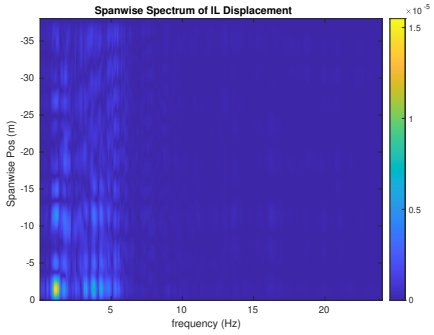

(f) Spanwise inline spectrum of hydrodynamic displacement case 6940.

Figure C-272: *Motion Analysis.* NDP Straight Riser ($L = 38m$) test case 6940.

NDP Straight Riser ($L = 38m$) test case 6950

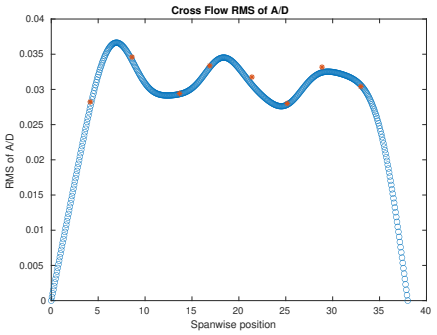

(a) Cross-flow RMS profile case 6950.

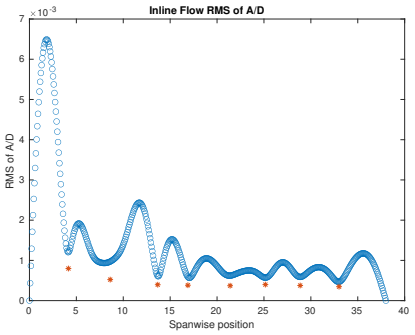

(b) Inline flow RMS profile case 6950.

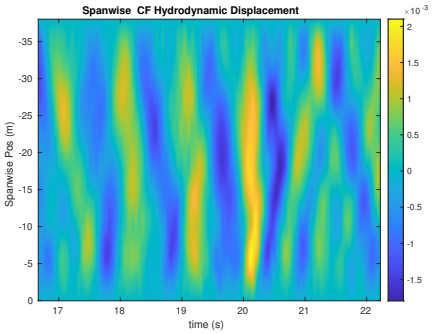

(c) Spanwise cross-flow hydrodynamic displacement case 6950.

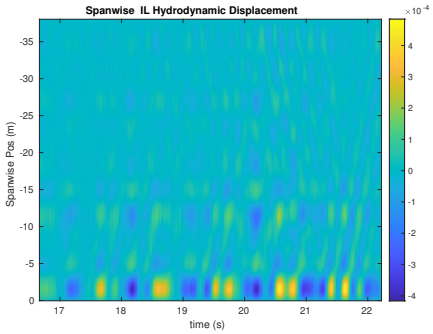

(d) Spanwise inline hydrodynamic displacement case 6950.

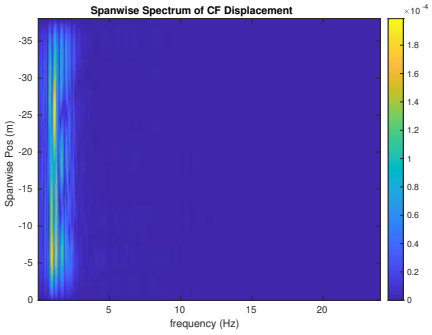

(e) Spanwise cross-flow spectrum of hydrodynamic displacement case 6950.

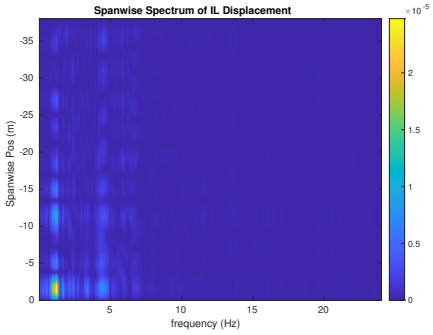

(f) Spanwise inline spectrum of hydrodynamic displacement case 6950.

Figure C-273: *Motion Analysis.* NDP Straight Riser ($L = 38m$) test case 6950.

NDP Straight Riser ($L = 38m$) test case 6960

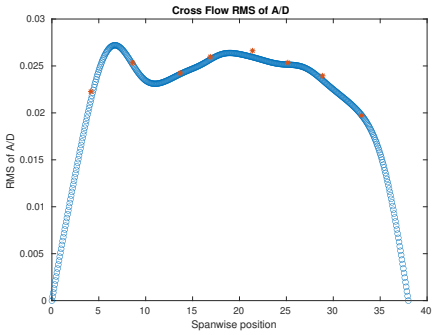

(a) Cross-flow RMS profile case 6960.

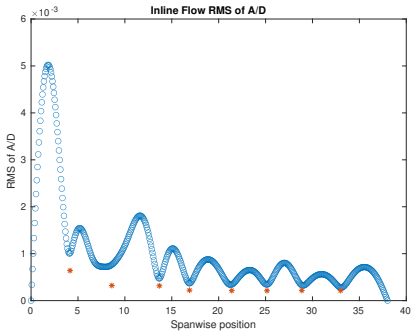

(b) Inline flow RMS profile case 6960.

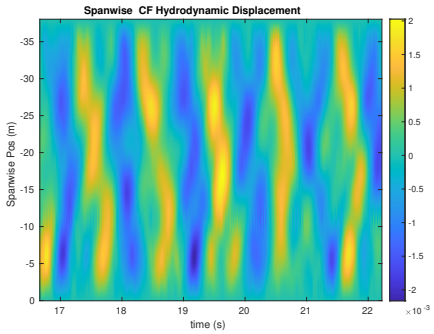

(c) Spanwise cross-flow hydrodynamic displacement case 6960.

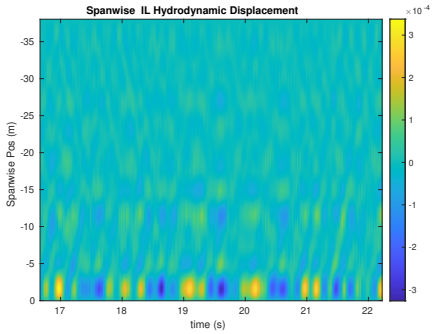

(d) Spanwise inline hydrodynamic displacement case 6960.

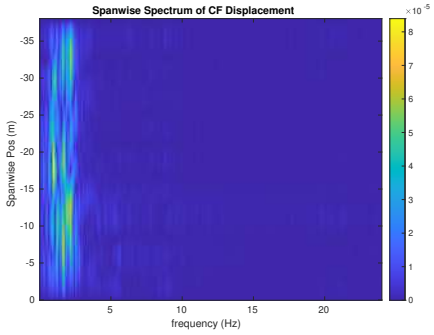

(e) Spanwise cross-flow spectrum of hydrodynamic displacement case 6960.

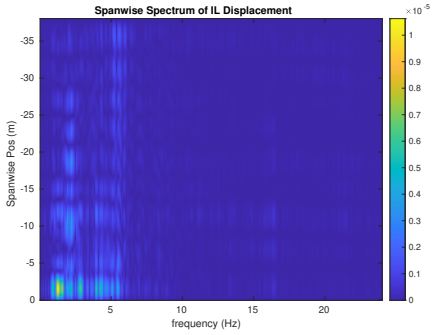

(f) Spanwise inline spectrum of hydrodynamic displacement case 6960.

Figure C-274: *Motion Analysis.* NDP Straight Riser ($L = 38m$) test case 6960.

NDP Straight Riser ($L = 38m$) test case 6970

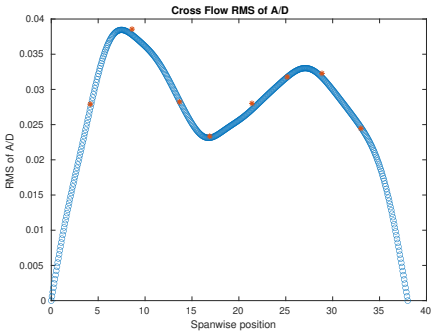

(a) Cross-flow RMS profile case 6970.

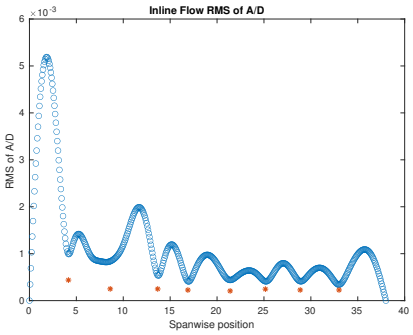

(b) Inline flow RMS profile case 6970.

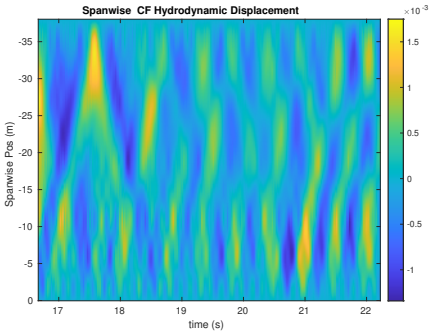

(c) Spanwise cross-flow hydrodynamic displacement case 6970.

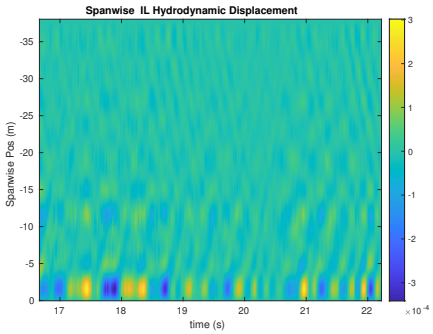

(d) Spanwise inline hydrodynamic displacement case 6970.

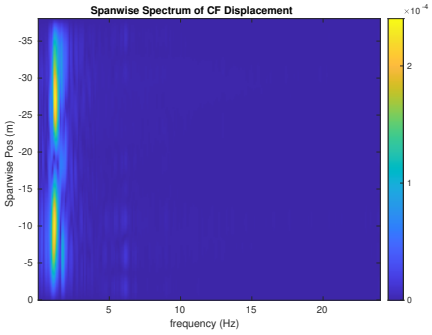

(e) Spanwise cross-flow spectrum of hydrodynamic displacement case 6970.

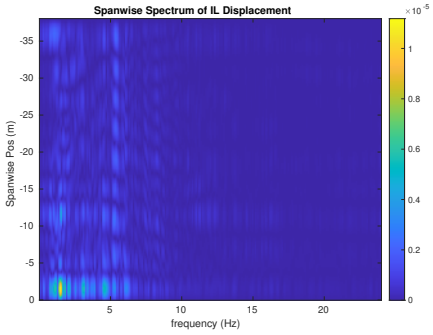

(f) Spanwise inline spectrum of hydrodynamic displacement case 6970.

Figure C-275: *Motion Analysis.* NDP Straight Riser ($L = 38m$) test case 6970.

NDP Straight Riser ($L = 38m$) test case 6980

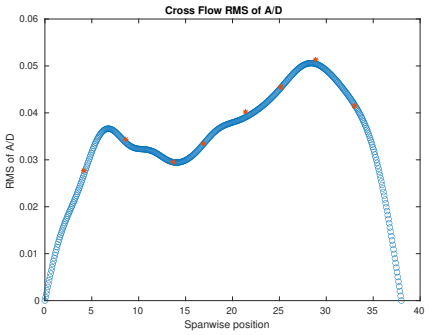

(a) Cross-flow RMS profile case 6980.

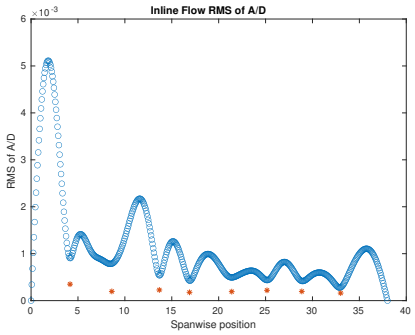

(b) Inline flow RMS profile case 6980.

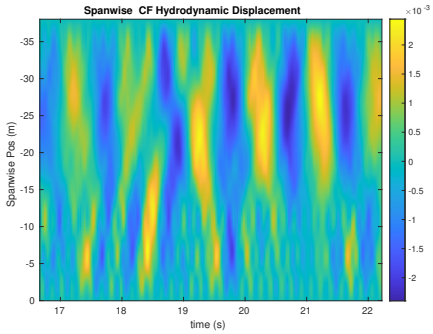

(c) Spanwise cross-flow hydrodynamic displacement case 6980.

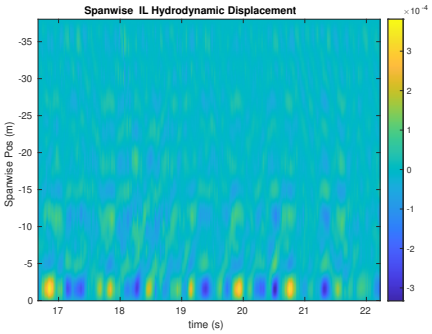

(d) Spanwise inline hydrodynamic displacement case 6980.

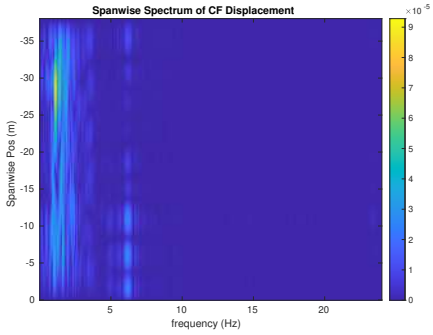

(e) Spanwise cross-flow spectrum of hydrodynamic displacement case 6980.

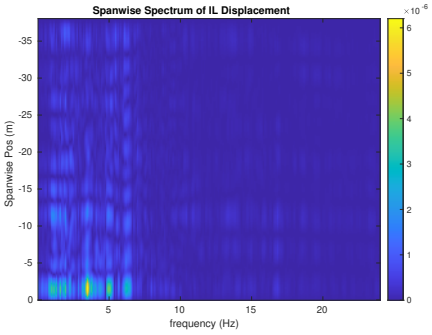

(f) Spanwise inline spectrum of hydrodynamic displacement case 6980.

Figure C-276: *Motion Analysis.* NDP Straight Riser ($L = 38m$) test case 6980.

NDP Straight Riser ($L = 38m$) test case 6990

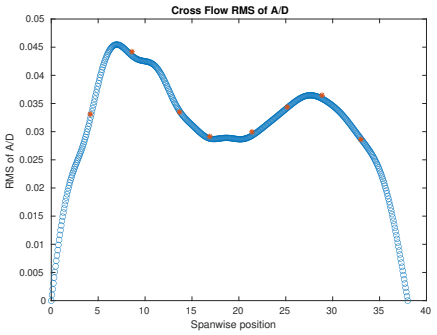

(a) Cross-flow RMS profile case 6990.

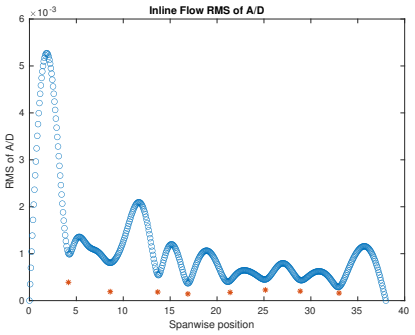

(b) Inline flow RMS profile case 6990.

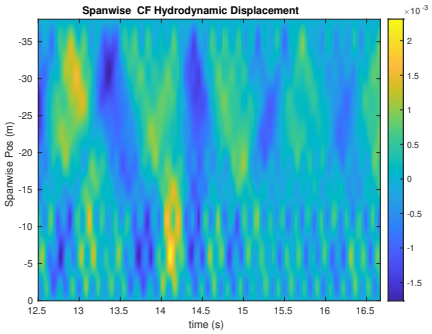

(c) Spanwise cross-flow hydrodynamic displacement case 6990.

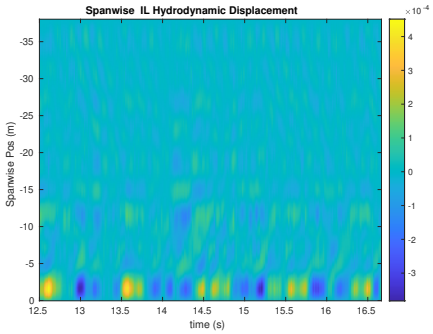

(d) Spanwise inline hydrodynamic displacement case 6990.

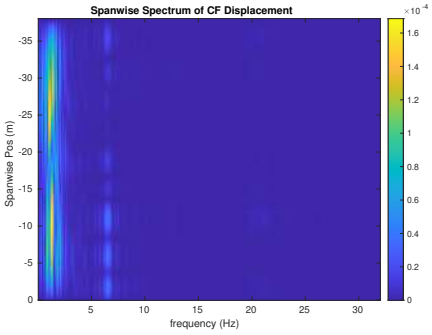

(e) Spanwise cross-flow spectrum of hydrodynamic displacement case 6990.

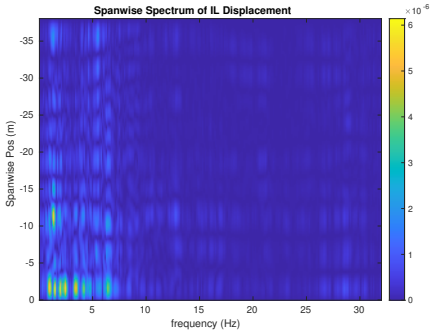

(f) Spanwise inline spectrum of hydrodynamic displacement case 6990.

Figure C-277: *Motion Analysis.* NDP Straight Riser ($L = 38m$) test case 6990.

NDP Straight Riser ($L = 38m$) test case 7000

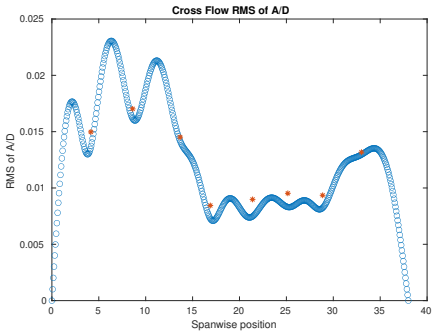

(a) Cross-flow RMS profile case 7000.

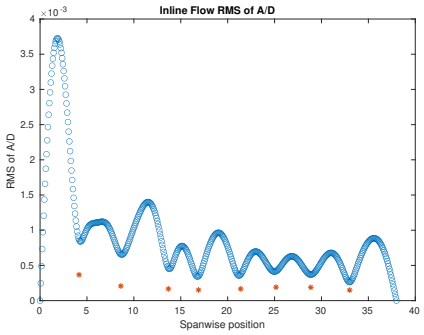

(b) Inline flow RMS profile case 7000.

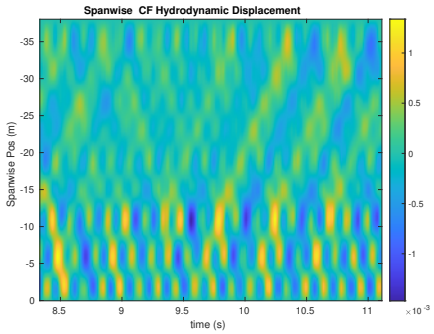

(c) Spanwise cross-flow hydrodynamic displacement case 7000.

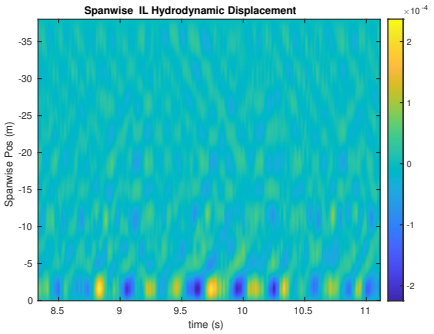

(d) Spanwise inline hydrodynamic displacement case 7000.

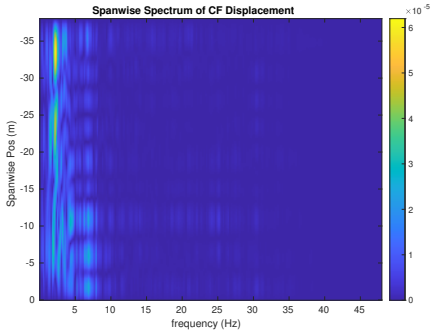

(e) Spanwise cross-flow spectrum of hydrodynamic displacement case 7000.

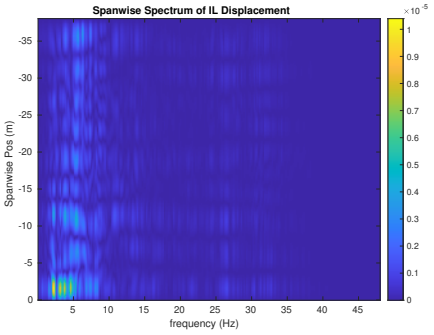

(f) Spanwise inline spectrum of hydrodynamic displacement case 7000.

Figure C-278: *Motion Analysis.* NDP Straight Riser ($L = 38m$) test case 7000.

NDP Straight Riser ($L = 38m$) test case 7010

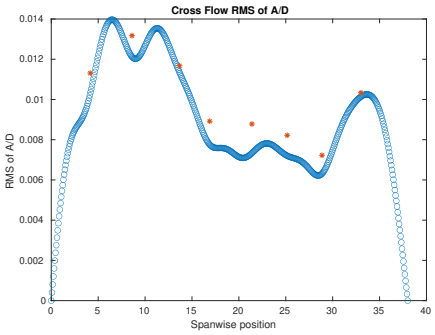

(a) Cross-flow RMS profile case 7010.

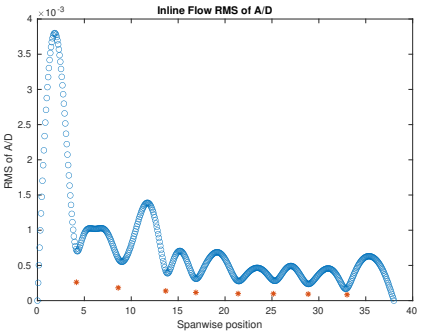

(b) Inline flow RMS profile case 7010.

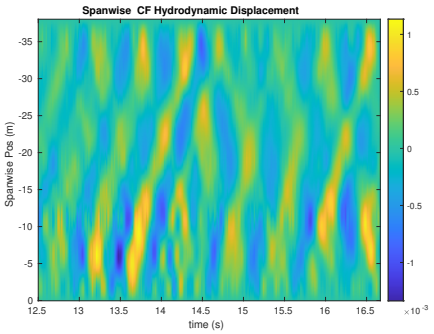

(c) Spanwise cross-flow hydrodynamic displacement case 7010.

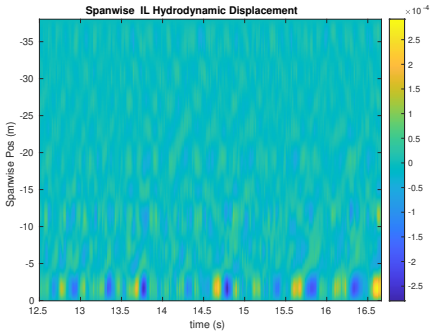

(d) Spanwise inline hydrodynamic displacement case 7010.

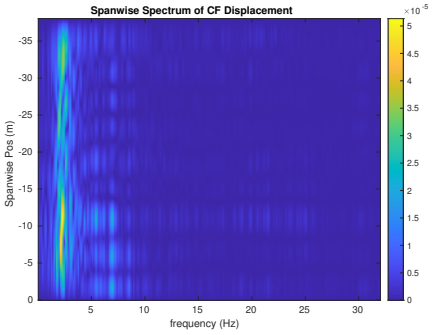

(e) Spanwise cross-flow spectrum of hydrodynamic displacement case 7010.

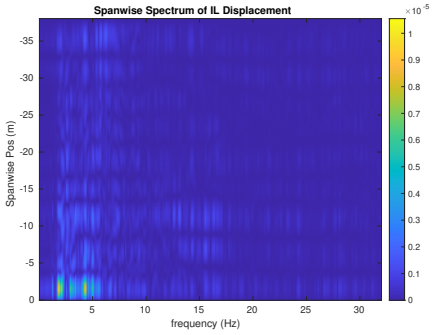

(f) Spanwise inline spectrum of hydrodynamic displacement case 7010.

Figure C-279: *Motion Analysis.* NDP Straight Riser ($L = 38m$) test case 7010.

NDP Straight Riser ($L = 38m$) test case 7020

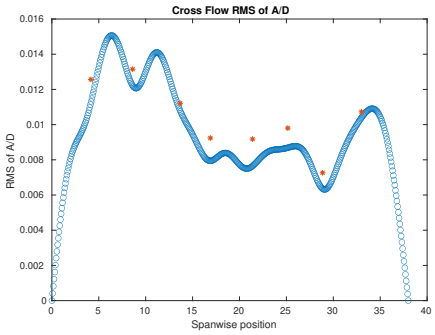

(a) Cross-flow RMS profile case 7020.

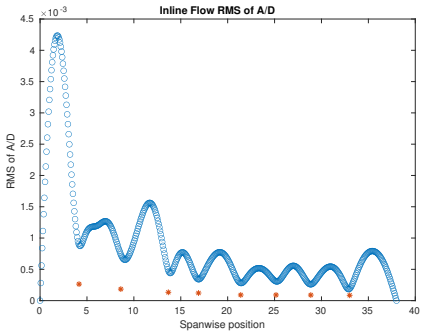

(b) Inline flow RMS profile case 7020.

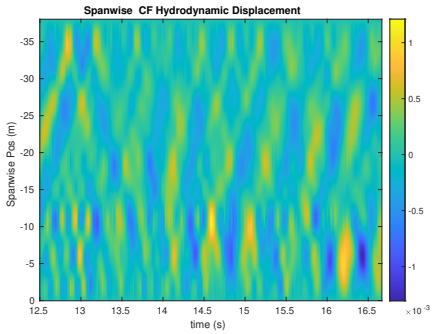

(c) Spanwise cross-flow hydrodynamic displacement case 7020.

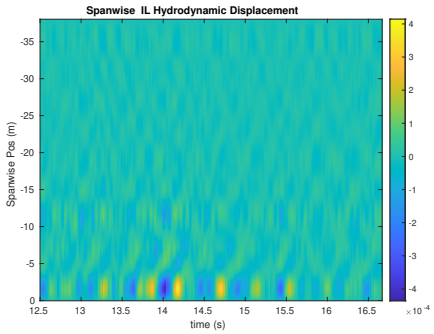

(d) Spanwise inline hydrodynamic displacement case 7020.

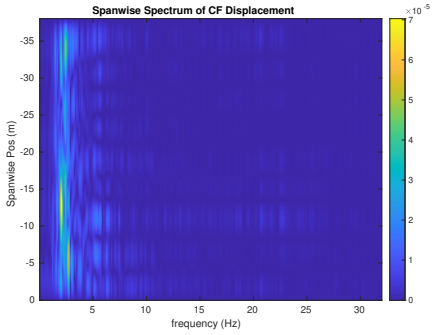

(e) Spanwise cross-flow spectrum of hydrodynamic displacement case 7020.

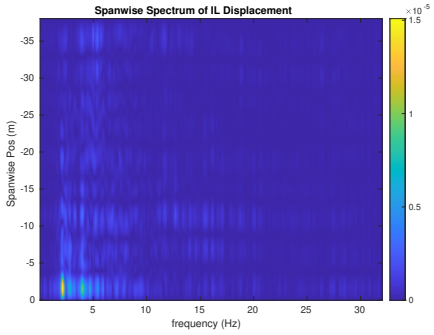

(f) Spanwise inline spectrum of hydrodynamic displacement case 7020.

Figure C-280: *Motion Analysis.* NDP Straight Riser ($L = 38m$) test case 7020.

NDP Straight Riser ($L = 38m$) test case 7030

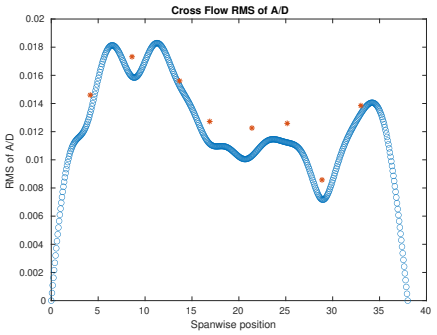

(a) Cross-flow RMS profile case 7030.

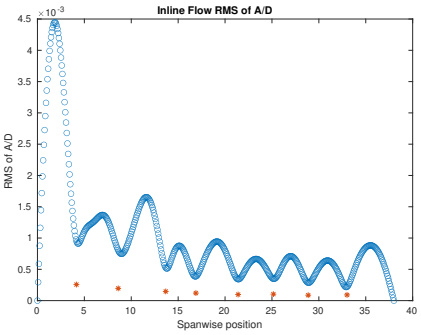

(b) Inline flow RMS profile case 7030.

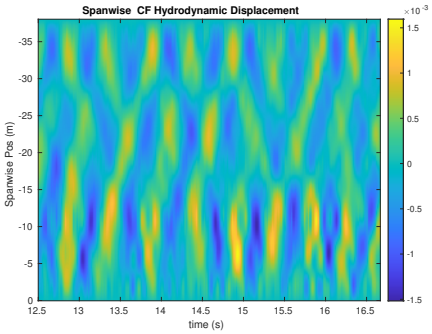

(c) Spanwise cross-flow hydrodynamic displacement case 7030.

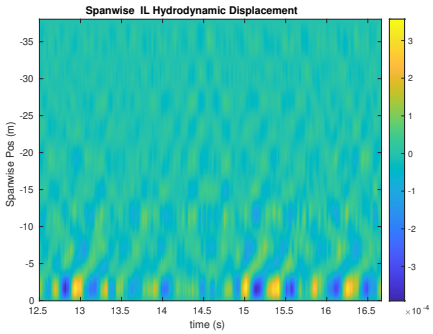

(d) Spanwise inline hydrodynamic displacement case 7030.

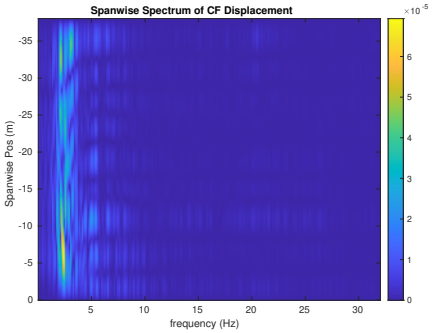

(e) Spanwise cross-flow spectrum of hydrodynamic displacement case 7030.

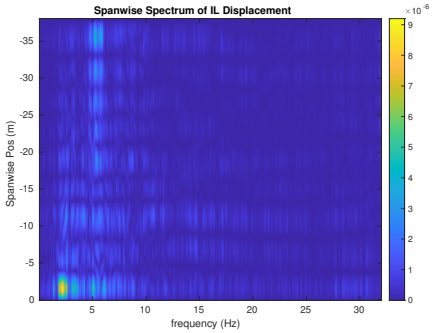

(f) Spanwise inline spectrum of hydrodynamic displacement case 7030.

Figure C-281: *Motion Analysis.* NDP Straight Riser ($L = 38m$) test case 7030.

NDP Straight Riser ($L = 38m$) test case 7040

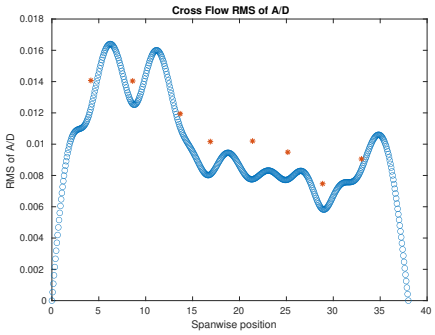

(a) Cross-flow RMS profile case 7040.

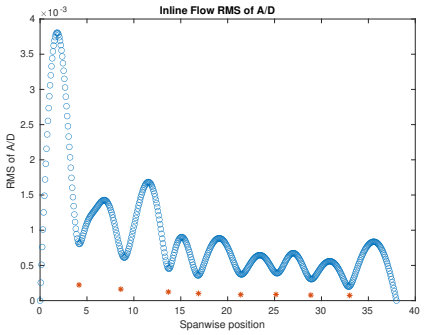

(b) Inline flow RMS profile case 7040.

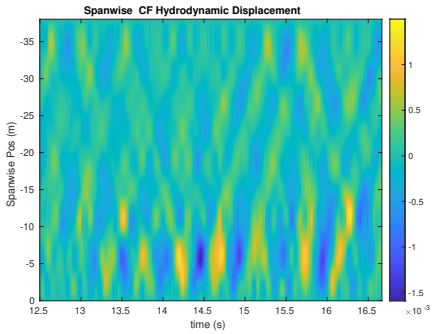

(c) Spanwise cross-flow hydrodynamic displacement case 7040.

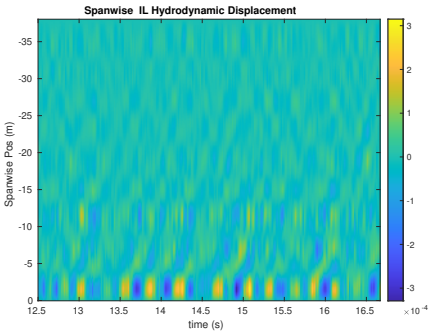

(d) Spanwise inline hydrodynamic displacement case 7040.

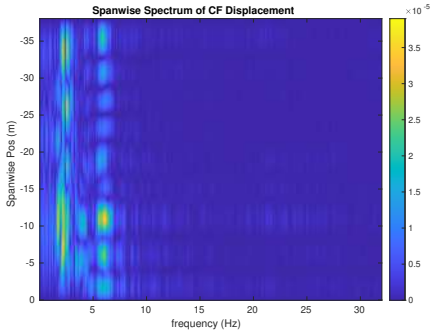

(e) Spanwise cross-flow spectrum of hydrodynamic displacement case 7040.

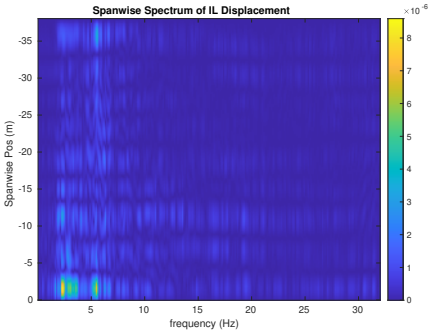

(f) Spanwise inline spectrum of hydrodynamic displacement case 7040.

Figure C-282: *Motion Analysis.* NDP Straight Riser ($L = 38m$) test case 7040.

NDP Straight Riser ($L = 38m$) test case 7050

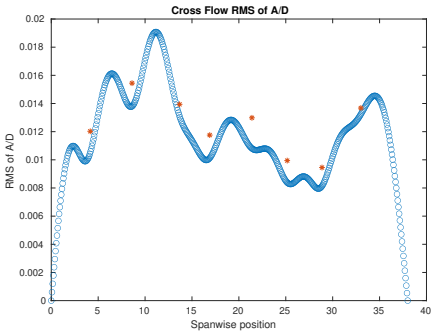

(a) Cross-flow RMS profile case 7050.

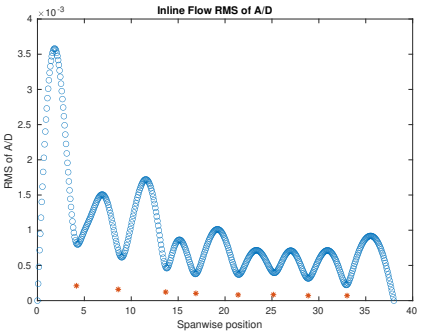

(b) Inline flow RMS profile case 7050.

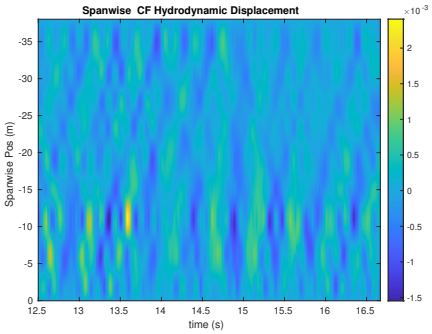

(c) Spanwise cross-flow hydrodynamic displacement case 7050.

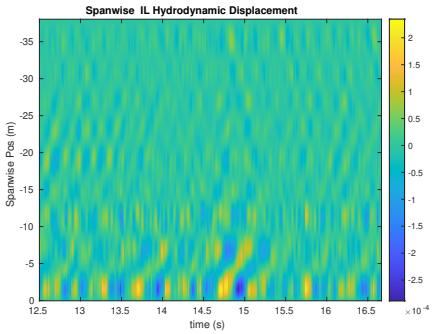

(d) Spanwise inline hydrodynamic displacement case 7050.

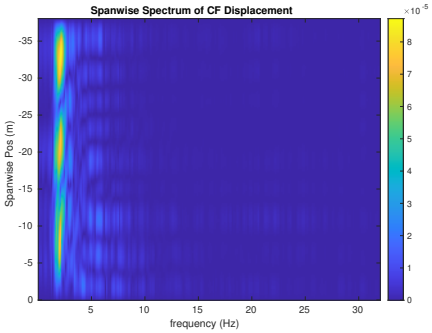

(e) Spanwise cross-flow spectrum of hydrodynamic displacement case 7050.

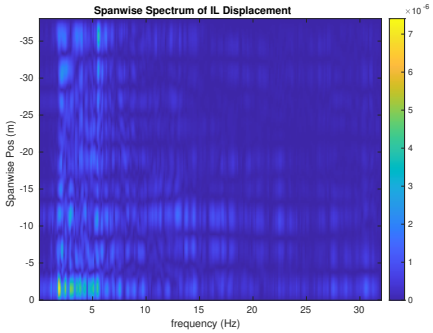

(f) Spanwise inline spectrum of hydrodynamic displacement case 7050.

Figure C-283: *Motion Analysis.* NDP Straight Riser ($L = 38m$) test case 7050.

NDP Straight Riser ($L = 38m$) test case 7060

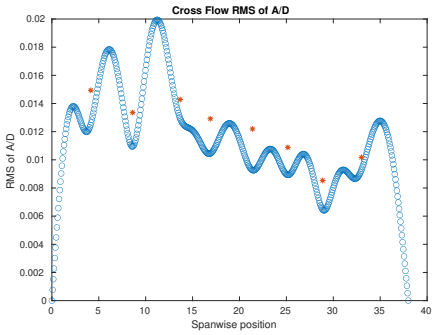

(a) Cross-flow RMS profile case 7060.

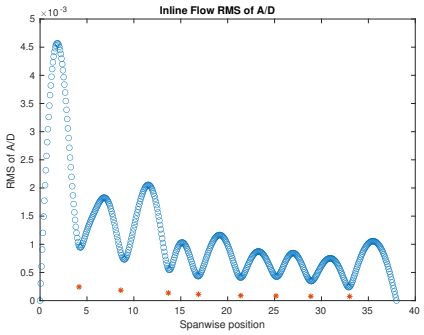

(b) Inline flow RMS profile case 7060.

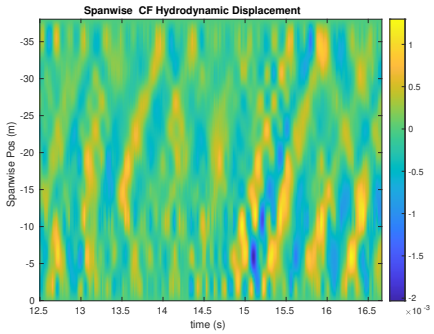

(c) Spanwise cross-flow hydrodynamic displacement case 7060.

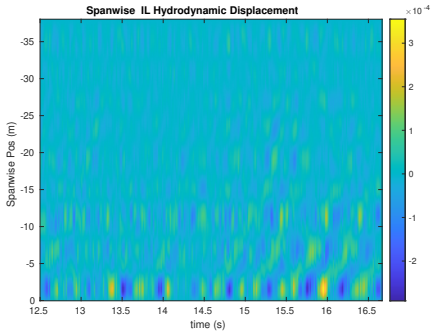

(d) Spanwise inline hydrodynamic displacement case 7060.

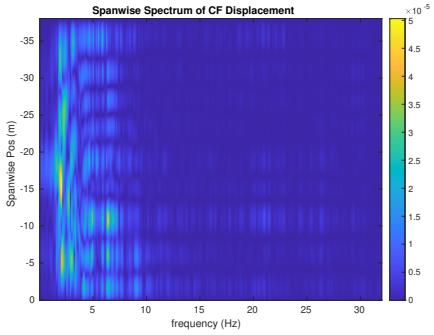

(e) Spanwise cross-flow spectrum of hydrodynamic displacement case 7060.

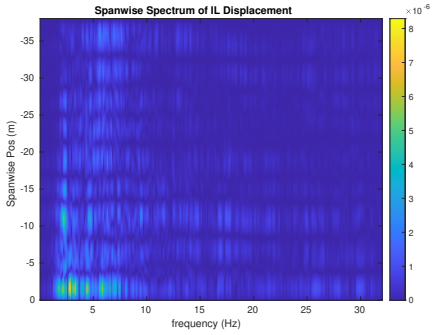

(f) Spanwise inline spectrum of hydrodynamic displacement case 7060.

Figure C-284: *Motion Analysis.* NDP Straight Riser ($L = 38m$) test case 7060.

NDP Straight Riser ($L = 38m$) test case 7070

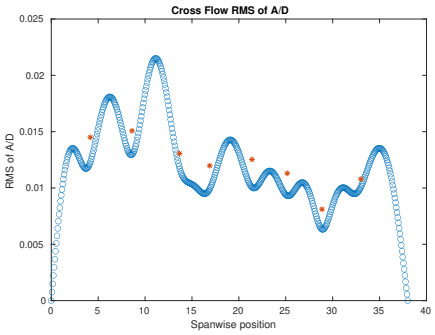

(a) Cross-flow RMS profile case 7070.

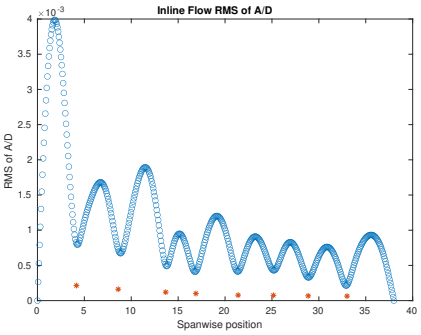

(b) Inline flow RMS profile case 7070.

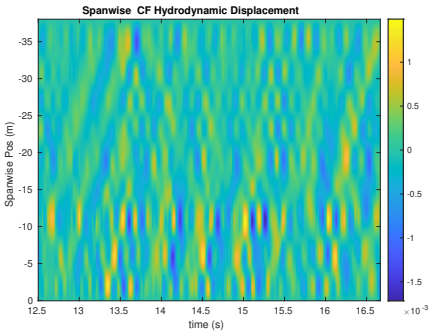

(c) Spanwise cross-flow hydrodynamic displacement case 7070.

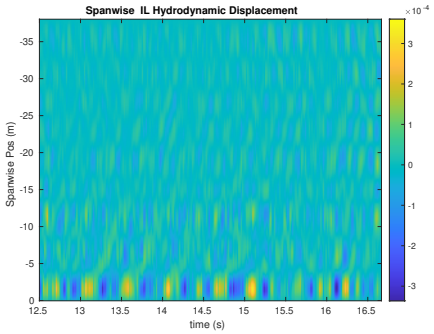

(d) Spanwise inline hydrodynamic displacement case 7070.

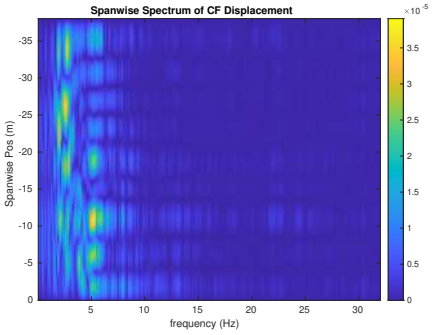

(e) Spanwise cross-flow spectrum of hydrodynamic displacement case 7070.

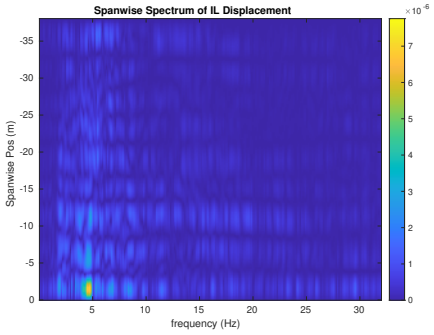

(f) Spanwise inline spectrum of hydrodynamic displacement case 7070.

Figure C-285: *Motion Analysis.* NDP Straight Riser ($L = 38m$) test case 7070.

NDP Straight Riser ($L = 38m$) test case 7080

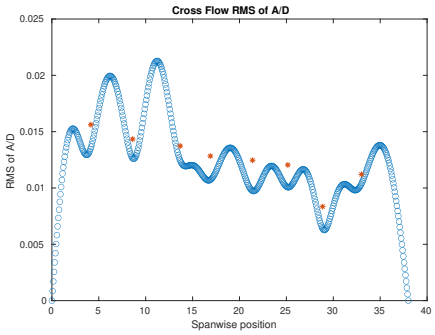

(a) Cross-flow RMS profile case 7080.

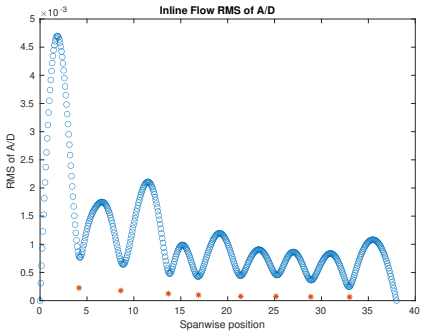

(b) Inline flow RMS profile case 7080.

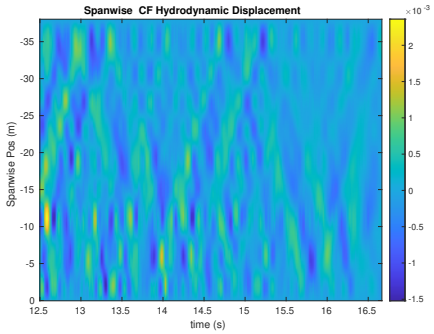

(c) Spanwise cross-flow hydrodynamic displacement case 7080.

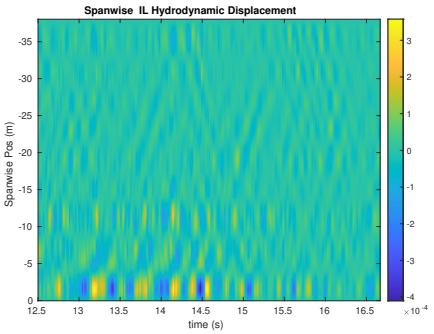

(d) Spanwise inline hydrodynamic displacement case 7080.

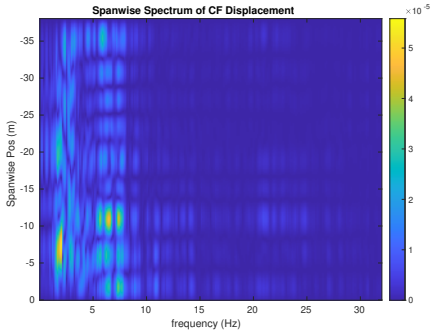

(e) Spanwise cross-flow spectrum of hydrodynamic displacement case 7080.

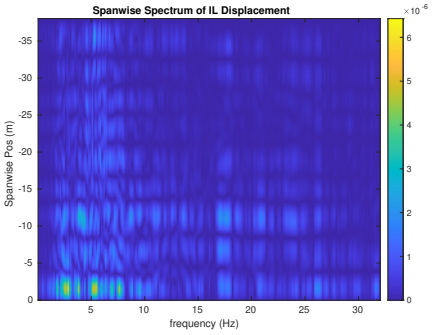

(f) Spanwise inline spectrum of hydrodynamic displacement case 7080.

Figure C-286: *Motion Analysis.* NDP Straight Riser ($L = 38m$) test case 7080.

NDP Straight Riser ($L = 38m$) test case 7090

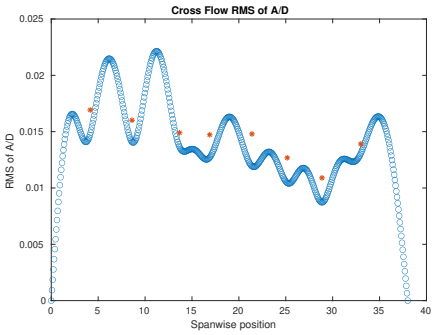

(a) Cross-flow RMS profile case 7090.

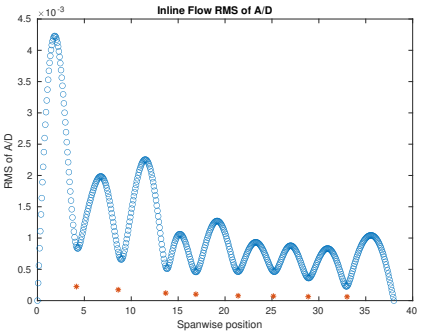

(b) Inline flow RMS profile case 7090.

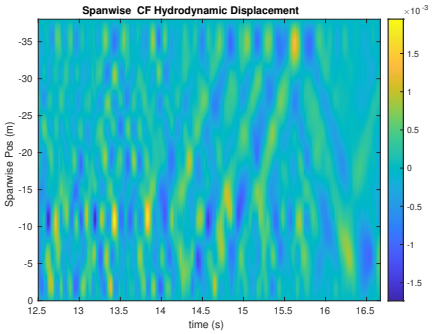

(c) Spanwise cross-flow hydrodynamic displacement case 7090.

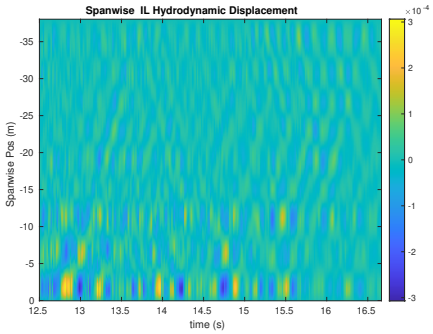

(d) Spanwise inline hydrodynamic displacement case 7090.

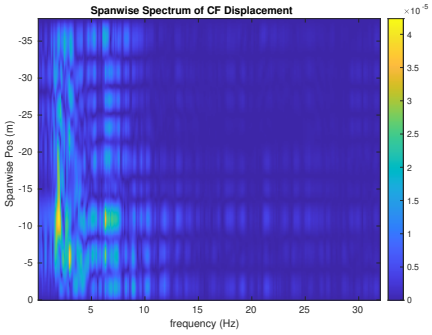

(e) Spanwise cross-flow spectrum of hydrodynamic displacement case 7090.

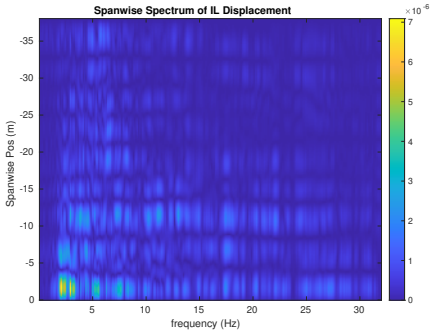

(f) Spanwise inline spectrum of hydrodynamic displacement case 7090.

Figure C-287: *Motion Analysis.* NDP Straight Riser ($L = 38m$) test case 7090.

NDP Straight Riser ($L = 38m$) test case 7100

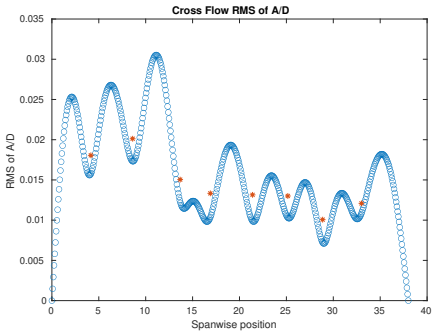

(a) Cross-flow RMS profile case 7100.

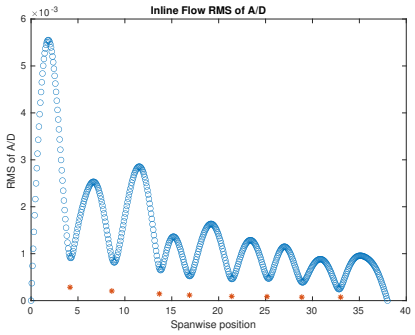

(b) Inline flow RMS profile case 7100.

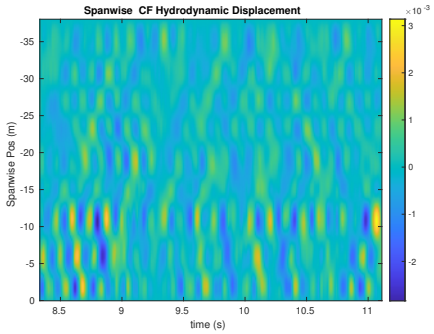

(c) Spanwise cross-flow hydrodynamic displacement case 7100.

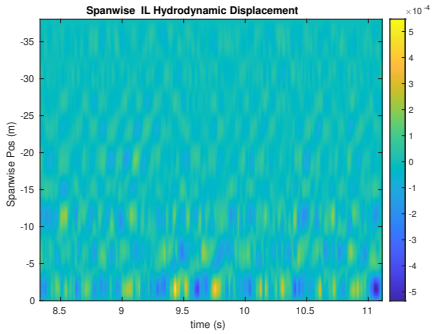

(d) Spanwise inline hydrodynamic displacement case 7100.

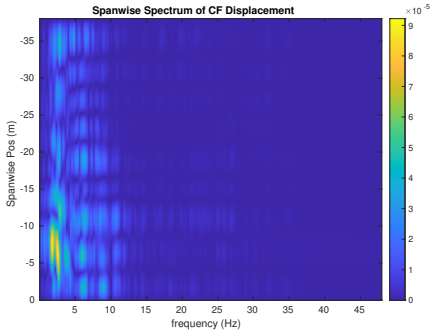

(e) Spanwise cross-flow spectrum of hydrodynamic displacement case 7100.

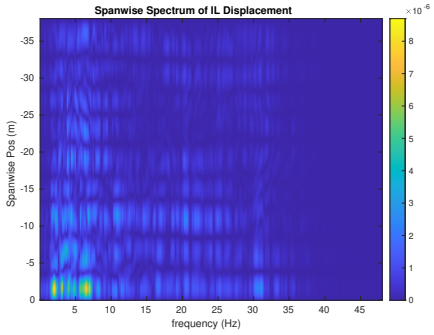

(f) Spanwise inline spectrum of hydrodynamic displacement case 7100.

Figure C-288: *Motion Analysis.* NDP Straight Riser ($L = 38m$) test case 7100.

NDP Straight Riser ($L = 38m$) test case 7110

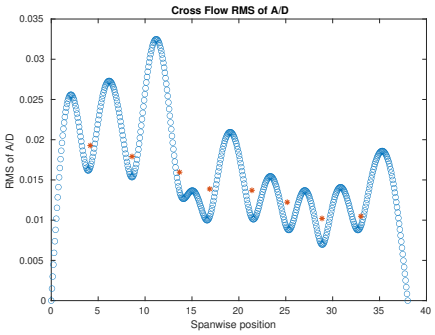

(a) Cross-flow RMS profile case 7110.

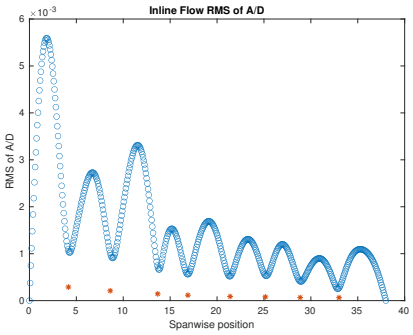

(b) Inline flow RMS profile case 7110.

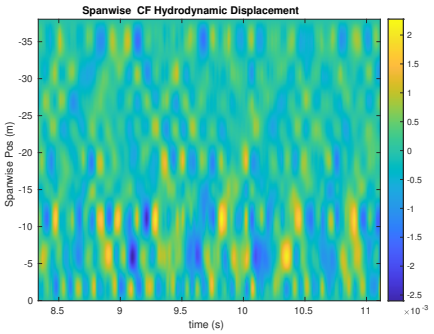

(c) Spanwise cross-flow hydrodynamic displacement case 7110.

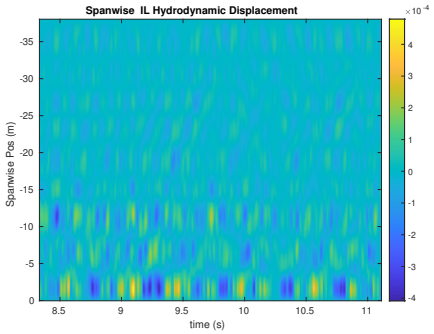

(d) Spanwise inline hydrodynamic displacement case 7110.

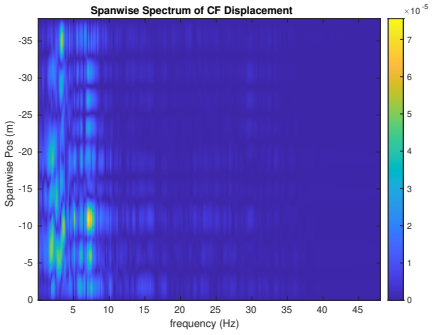

(e) Spanwise cross-flow spectrum of hydrodynamic displacement case 7110.

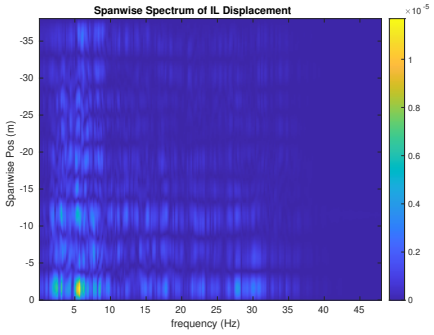

(f) Spanwise inline spectrum of hydrodynamic displacement case 7110.

Figure C-289: *Motion Analysis.* NDP Straight Riser ($L = 38m$) test case 7110.

NDP Straight Riser ($L = 38m$) test case 7120

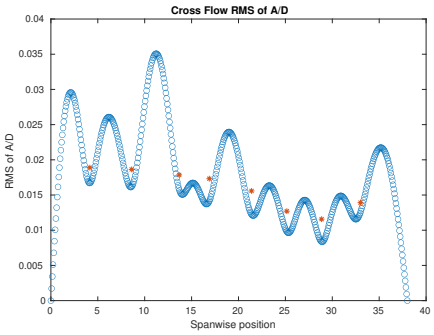

(a) Cross-flow RMS profile case 7120.

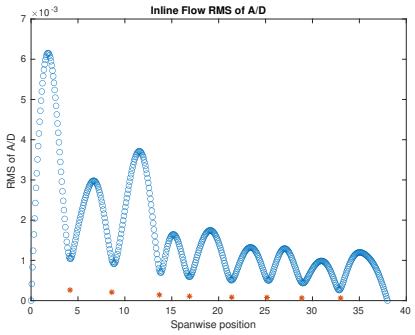

(b) Inline flow RMS profile case 7120.

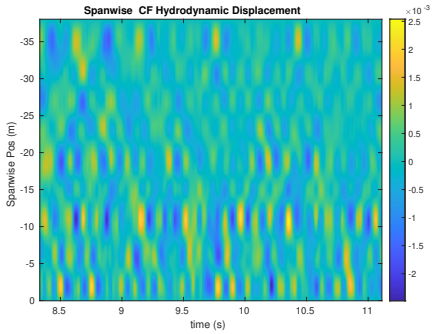

(c) Spanwise cross-flow hydrodynamic displacement case 7120.

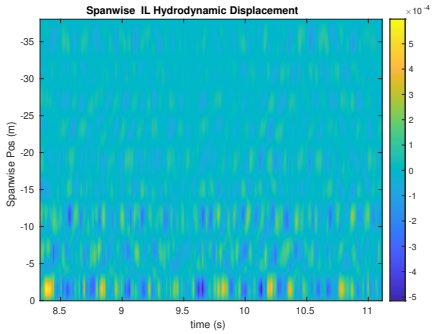

(d) Spanwise inline hydrodynamic displacement case 7120.

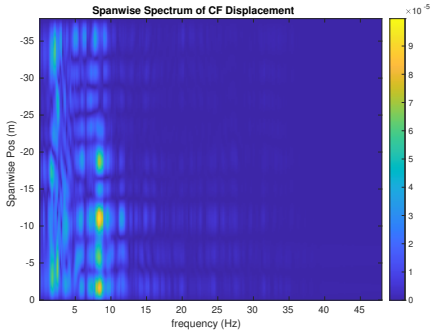

(e) Spanwise cross-flow spectrum of hydrodynamic displacement case 7120.

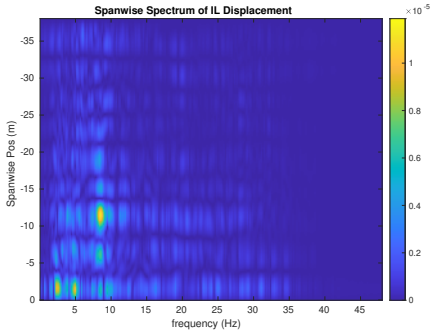

(f) Spanwise inline spectrum of hydrodynamic displacement case 7120.

Figure C-290: *Motion Analysis.* NDP Straight Riser ($L = 38m$) test case 7120.

NDP Straight Riser ($L = 38m$) test case 7130

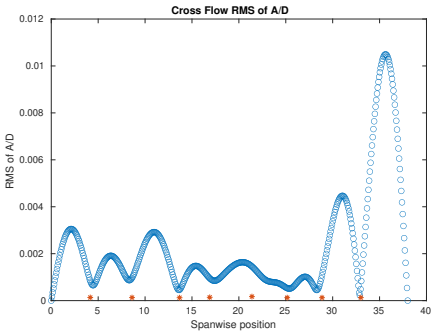

(a) Cross-flow RMS profile case 7130.

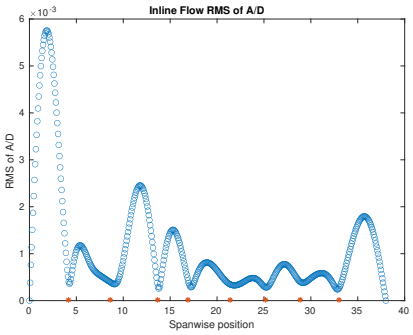

(b) Inline flow RMS profile case 7130.

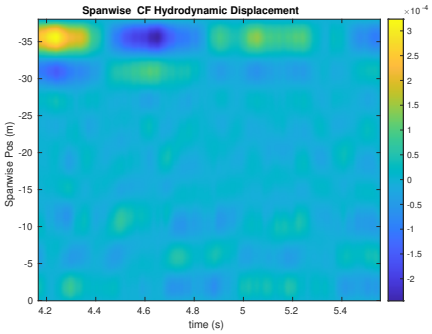

(c) Spanwise cross-flow hydrodynamic displacement case 7130.

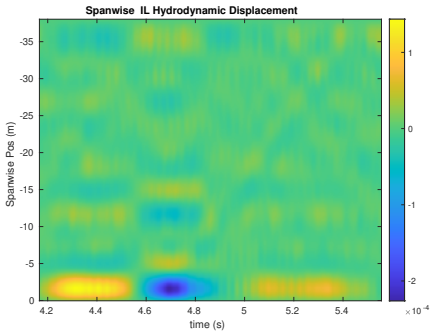

(d) Spanwise inline hydrodynamic displacement case 7130.

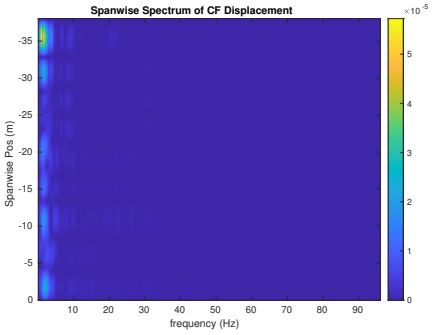

(e) Spanwise cross-flow spectrum of hydrodynamic displacement case 7130.

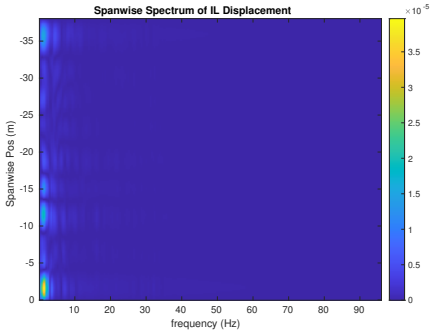

(f) Spanwise inline spectrum of hydrodynamic displacement case 7130.

Figure C-291: *Motion Analysis.* NDP Straight Riser ($L = 38m$) test case 7130.

NDP Straight Riser ($L = 38m$) test case 7140

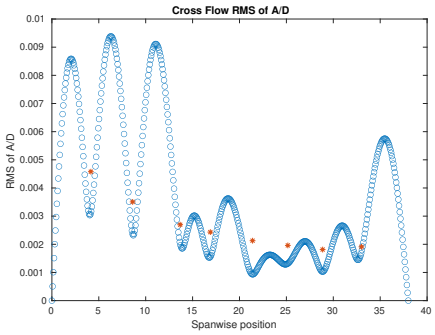

(a) Cross-flow RMS profile case 7140.

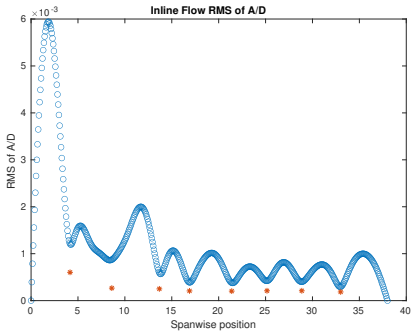

(b) Inline flow RMS profile case 7140.

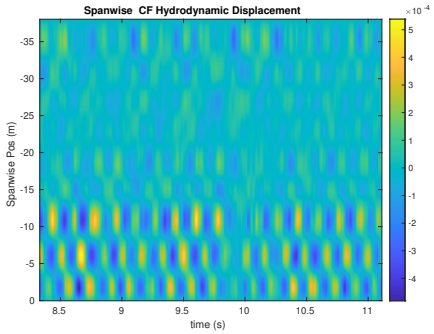

(c) Spanwise cross-flow hydrodynamic displacement case 7140.

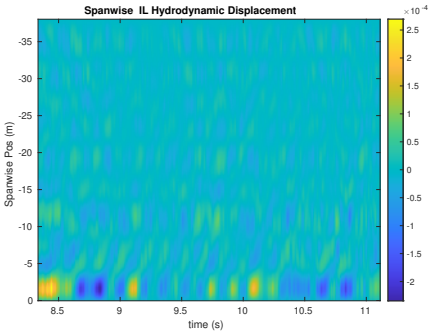

(d) Spanwise inline hydrodynamic displacement case 7140.

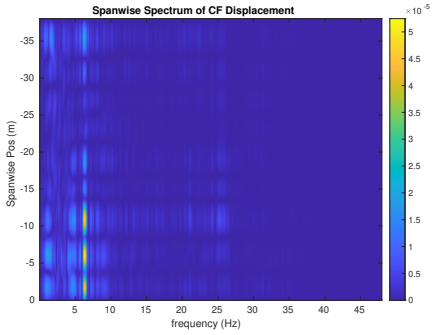

(e) Spanwise cross-flow spectrum of hydrodynamic displacement case 7140.

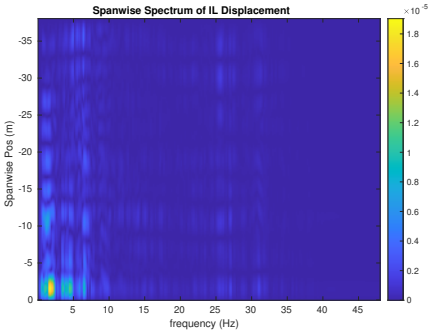

(f) Spanwise inline spectrum of hydrodynamic displacement case 7140.

Figure C-292: *Motion Analysis.* NDP Straight Riser ($L = 38m$) test case 7140.

NDP Straight Riser ($L = 38m$) test case 7210

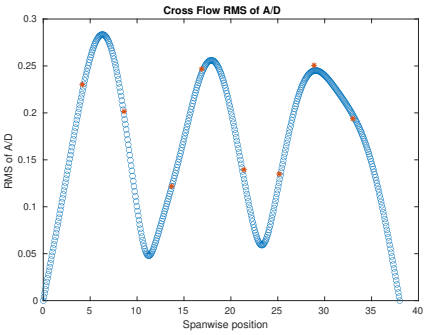

(a) Cross-flow RMS profile case 7210.

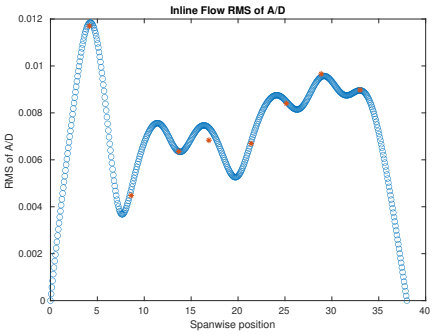

(b) Inline flow RMS profile case 7210.

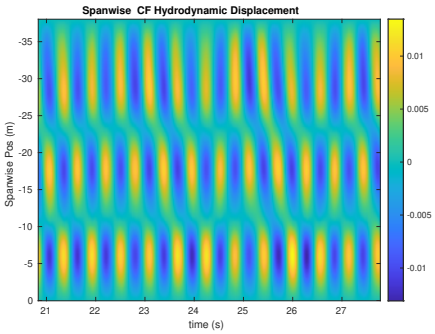

(c) Spanwise cross-flow hydrodynamic displacement case 7210.

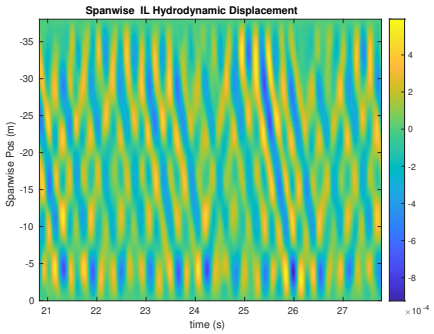

(d) Spanwise inline hydrodynamic displacement case 7210.

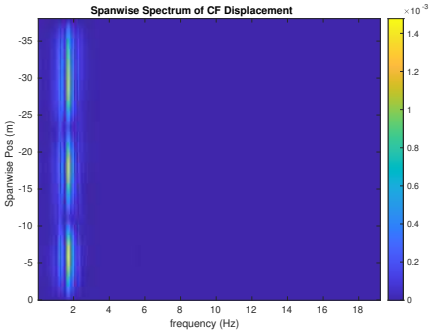

(e) Spanwise cross-flow spectrum of hydrodynamic displacement case 7210.

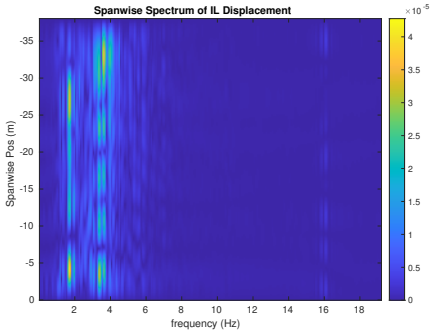

(f) Spanwise inline spectrum of hydrodynamic displacement case 7210.

Figure C-293: *Motion Analysis.* NDP Straight Riser ($L = 38m$) test case 7210.

NDP Straight Riser ($L = 38m$) test case 7220

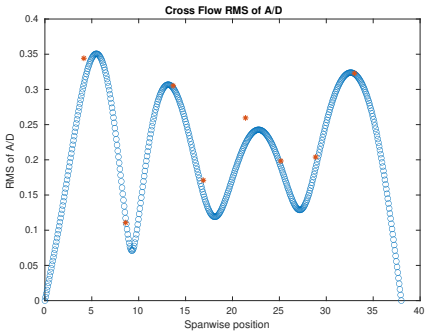

(a) Cross-flow RMS profile case 7220.

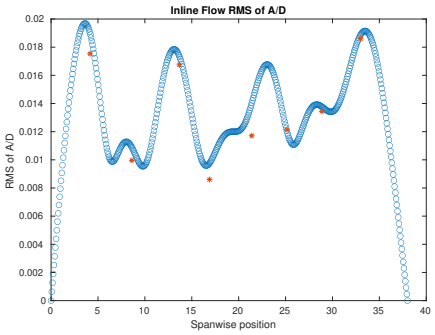

(b) Inline flow RMS profile case 7220.

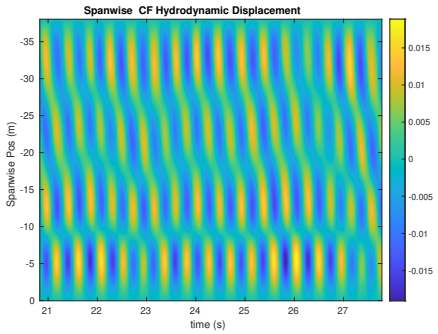

(c) Spanwise cross-flow hydrodynamic displacement case 7220.

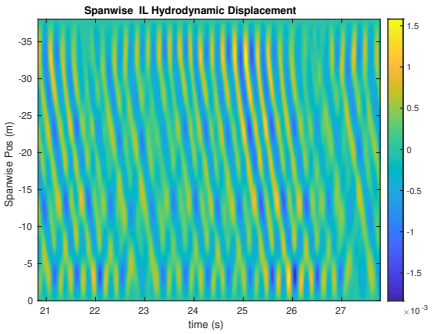

(d) Spanwise inline hydrodynamic displacement case 7220.

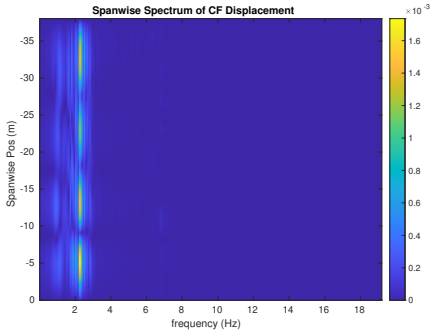

(e) Spanwise cross-flow spectrum of hydrodynamic displacement case 7220.

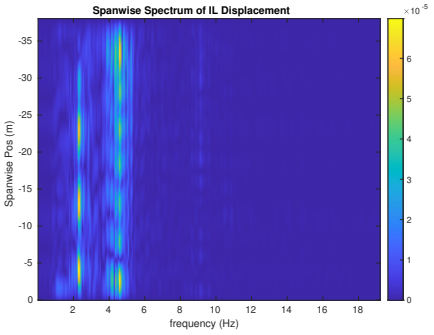

(f) Spanwise inline spectrum of hydrodynamic displacement case 7220.

Figure C-294: *Motion Analysis.* NDP Straight Riser ($L = 38m$) test case 7220.

NDP Straight Riser ($L = 38m$) test case 7230

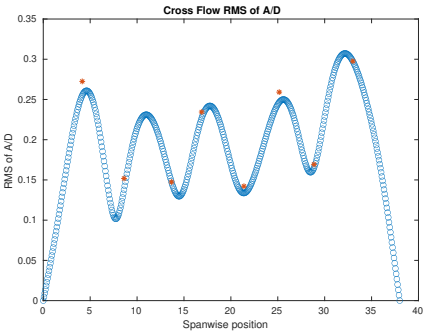

(a) Cross-flow RMS profile case 7230.

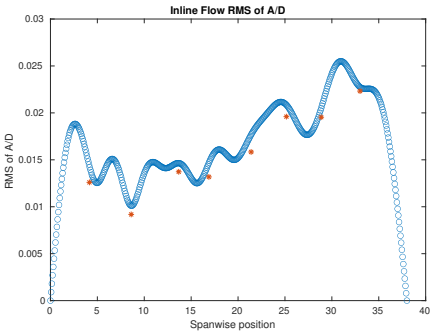

(b) Inline flow RMS profile case 7230.

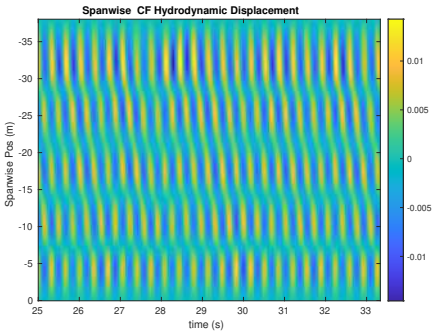

(c) Spanwise cross-flow hydrodynamic displacement case 7230.

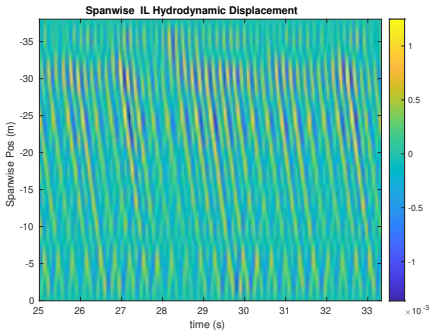

(d) Spanwise inline hydrodynamic displacement case 7230.

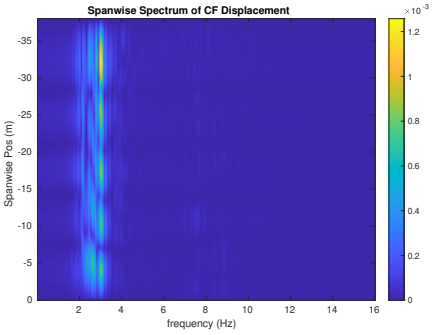

(e) Spanwise cross-flow spectrum of hydrodynamic displacement case 7230.

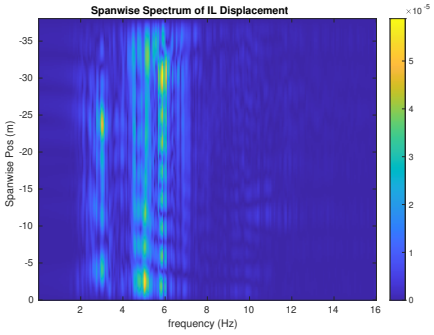

(f) Spanwise inline spectrum of hydrodynamic displacement case 7230.

Figure C-295: *Motion Analysis.* NDP Straight Riser ($L = 38m$) test case 7230.

NDP Straight Riser ($L = 38m$) test case 7240

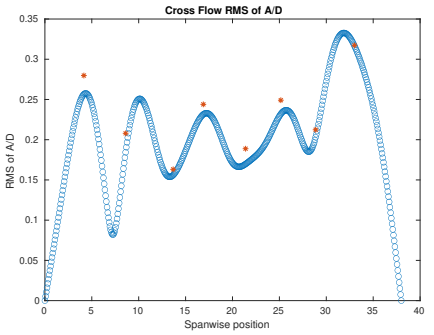

(a) Cross-flow RMS profile case 7240.

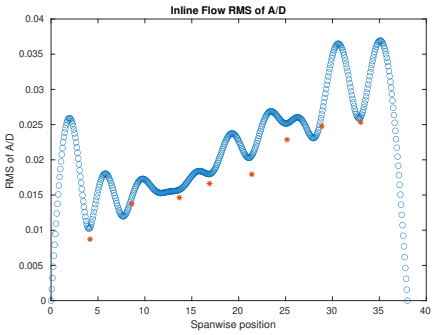

(b) Inline flow RMS profile case 7240.

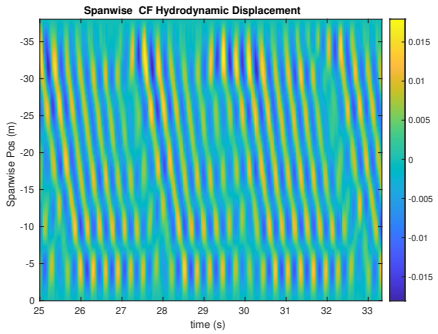

(c) Spanwise cross-flow hydrodynamic displacement case 7240.

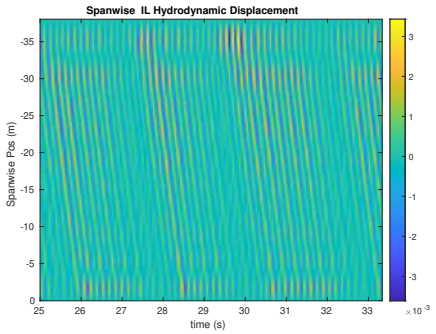

(d) Spanwise inline hydrodynamic displacement case 7240.

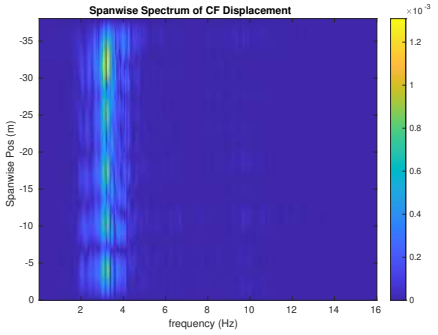

(e) Spanwise cross-flow spectrum of hydrodynamic displacement case 7240.

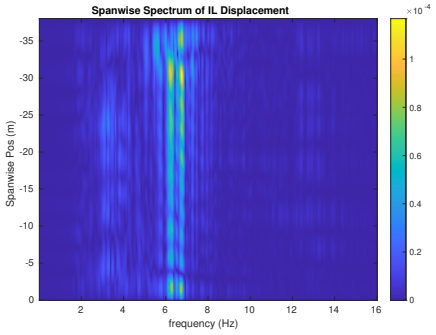

(f) Spanwise inline spectrum of hydrodynamic displacement case 7240.

Figure C-296: *Motion Analysis.* NDP Straight Riser ($L = 38m$) test case 7240.

NDP Straight Riser ($L = 38m$) test case 7250

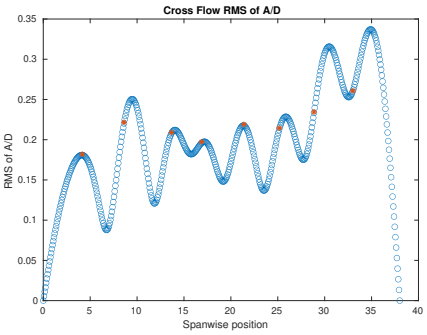

(a) Cross-flow RMS profile case 7250.

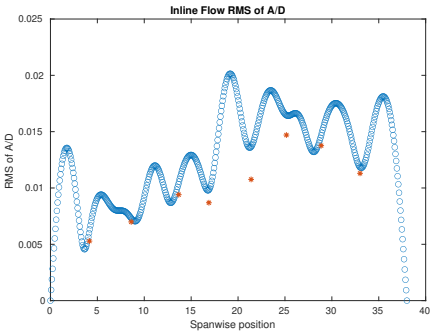

(b) Inline flow RMS profile case 7250.

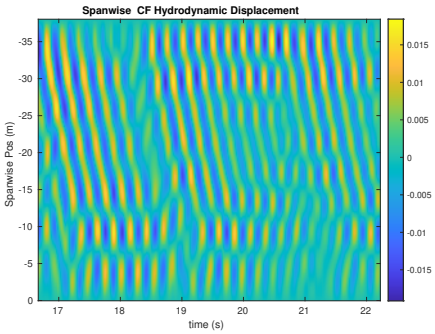

(c) Spanwise cross-flow hydrodynamic displacement case 7250.

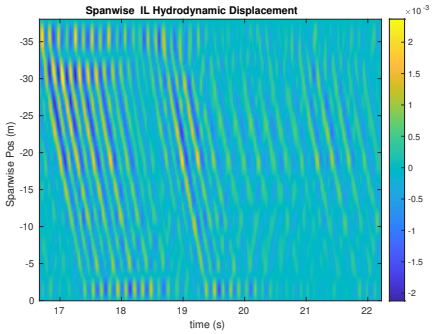

(d) Spanwise inline hydrodynamic displacement case 7250.

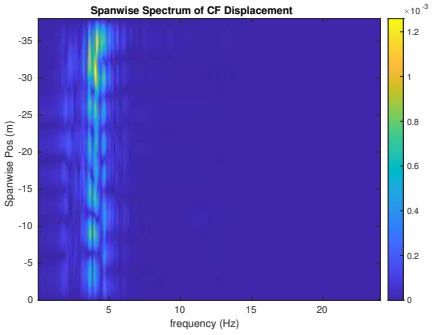

(e) Spanwise cross-flow spectrum of hydrodynamic displacement case 7250.

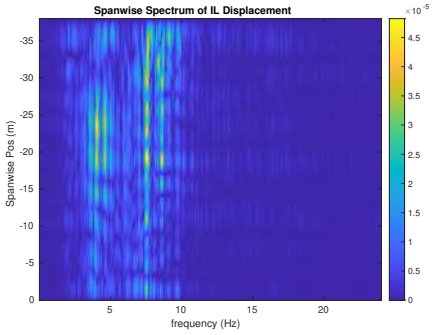

(f) Spanwise inline spectrum of hydrodynamic displacement case 7250.

Figure C-297: *Motion Analysis.* NDP Straight Riser ($L = 38m$) test case 7250.

NDP Straight Riser ($L = 38m$) test case 7260

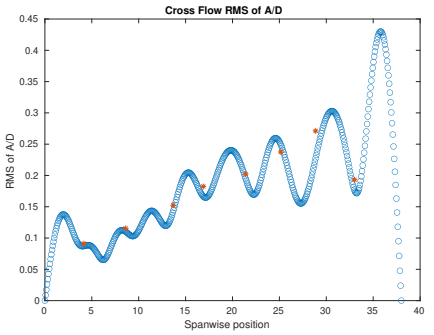

(a) Cross-flow RMS profile case 7260.

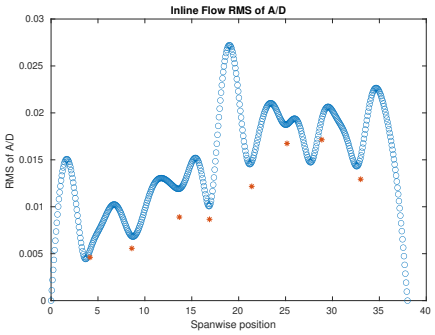

(b) Inline flow RMS profile case 7260.

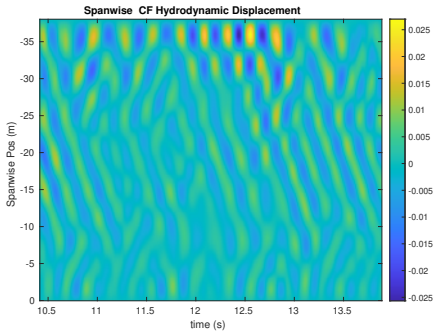

(c) Spanwise cross-flow hydrodynamic displacement case 7260.

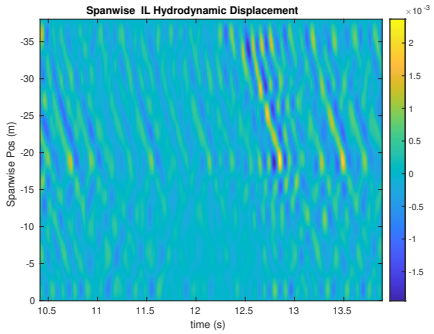

(d) Spanwise inline hydrodynamic displacement case 7260.

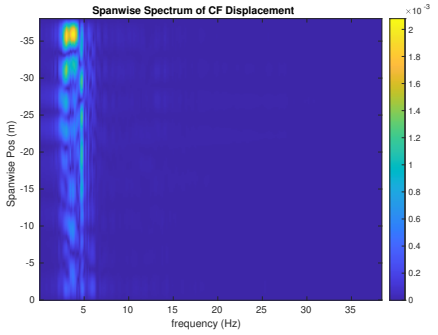

(e) Spanwise cross-flow spectrum of hydrodynamic displacement case 7260.

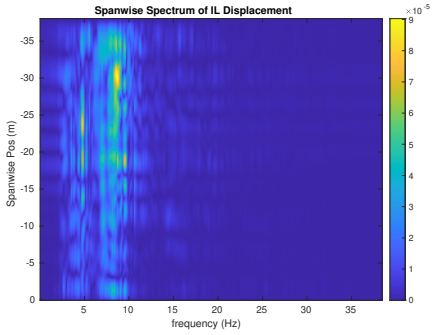

(f) Spanwise inline spectrum of hydrodynamic displacement case 7260.

Figure C-298: *Motion Analysis.* NDP Straight Riser ($L = 38m$) test case 7260.

NDP Straight Riser ($L = 38m$) test case 7270

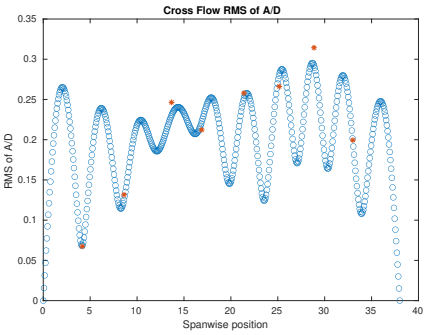

(a) Cross-flow RMS profile case 7270.

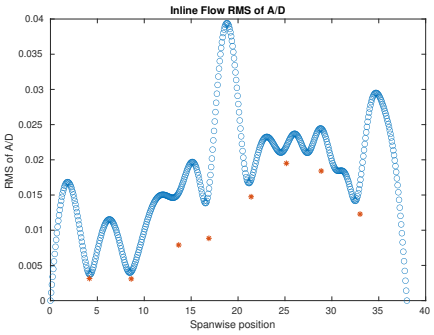

(b) Inline flow RMS profile case 7270.

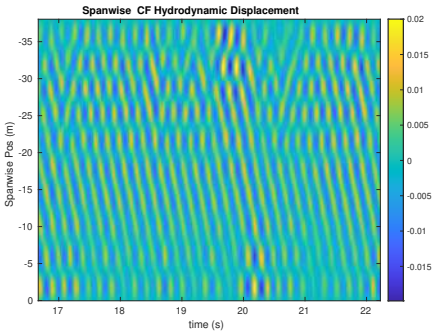

(c) Spanwise cross-flow hydrodynamic displacement case 7270.

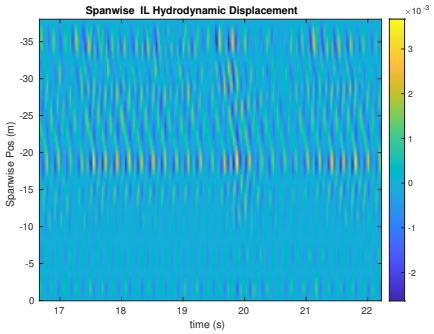

(d) Spanwise inline hydrodynamic displacement case 7270.

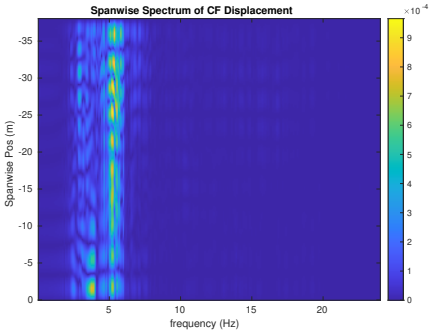

(e) Spanwise cross-flow spectrum of hydrodynamic displacement case 7270.

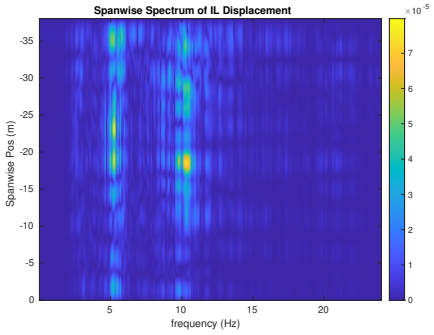

(f) Spanwise inline spectrum of hydrodynamic displacement case 7270.

Figure C-299: *Motion Analysis.* NDP Straight Riser ($L = 38m$) test case 7270.

NDP Straight Riser ($L = 38m$) test case 7280

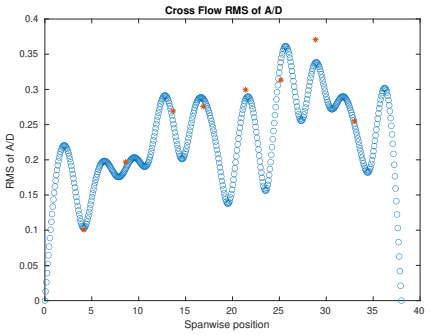

(a) Cross-flow RMS profile case 7280.

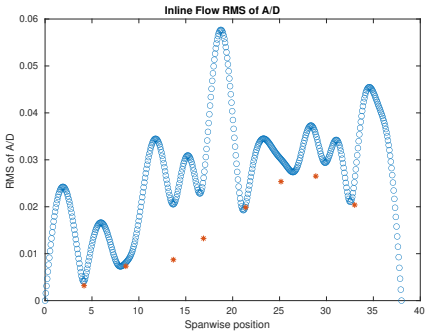

(b) Inline flow RMS profile case 7280.

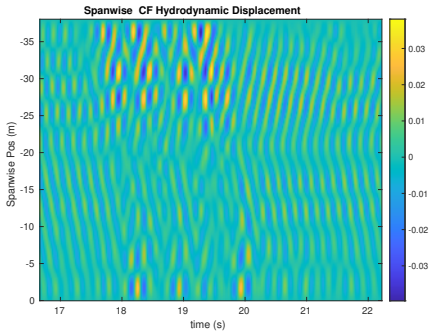

(c) Spanwise cross-flow hydrodynamic displacement case 7280.

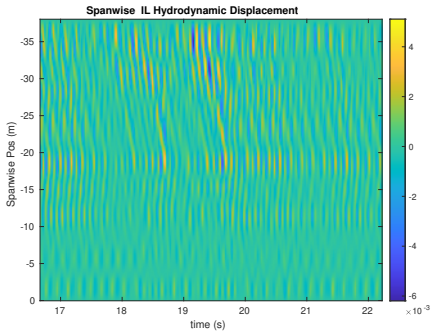

(d) Spanwise inline hydrodynamic displacement case 7280.

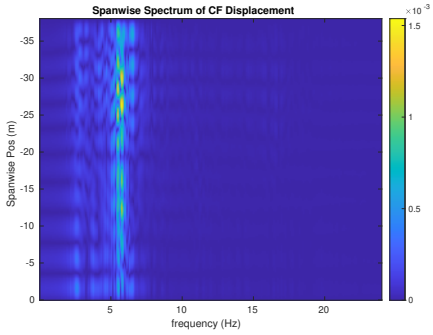

(e) Spanwise cross-flow spectrum of hydrodynamic displacement case 7280.

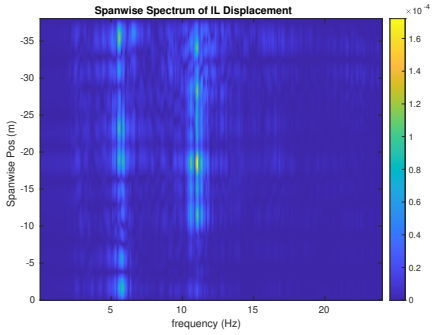

(f) Spanwise inline spectrum of hydrodynamic displacement case 7280.

Figure C-300: *Motion Analysis.* NDP Straight Riser ($L = 38m$) test case 7280.

NDP Straight Riser ($L = 38m$) test case 7290

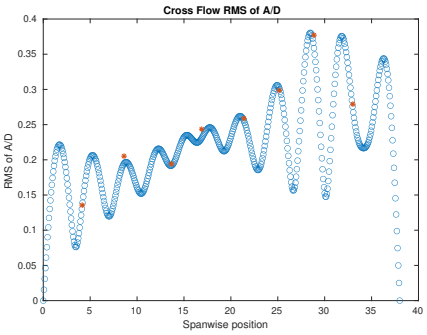

(a) Cross-flow RMS profile case 7290.

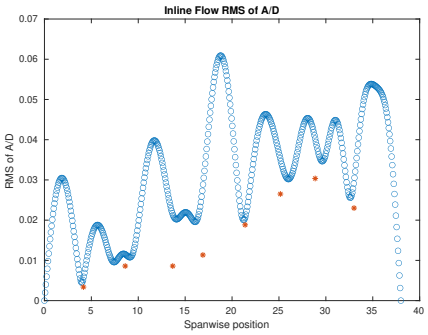

(b) Inline flow RMS profile case 7290.

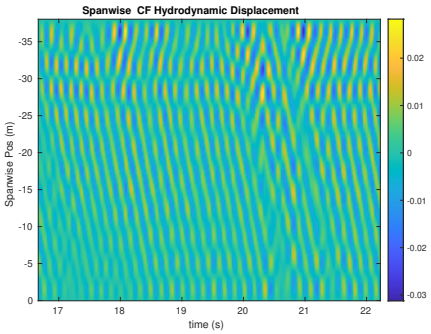

(c) Spanwise cross-flow hydrodynamic displacement case 7290.

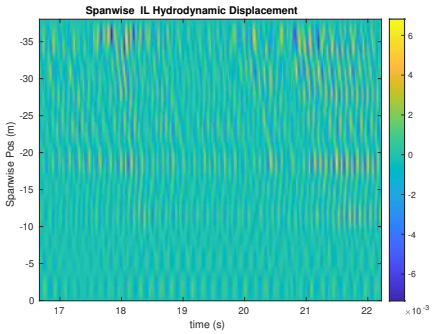

(d) Spanwise inline hydrodynamic displacement case 7290.

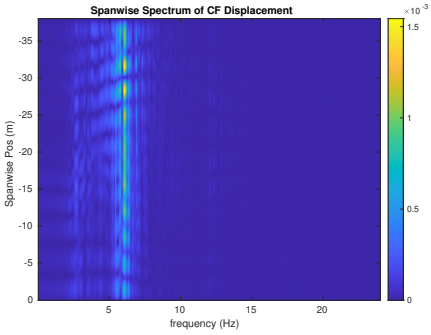

(e) Spanwise cross-flow spectrum of hydrodynamic displacement case 7290.

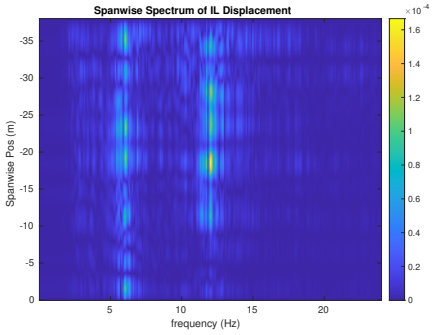

(f) Spanwise inline spectrum of hydrodynamic displacement case 7290.

Figure C-301: *Motion Analysis.* NDP Straight Riser ($L = 38m$) test case 7290.

NDP Straight Riser ($L = 38m$) test case 7300

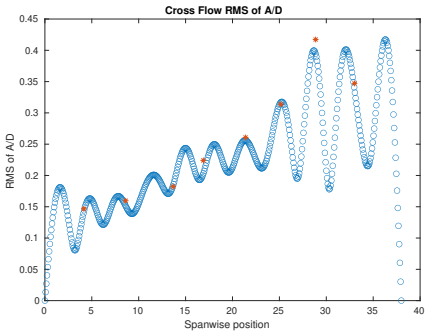

(a) Cross-flow RMS profile case 7300.

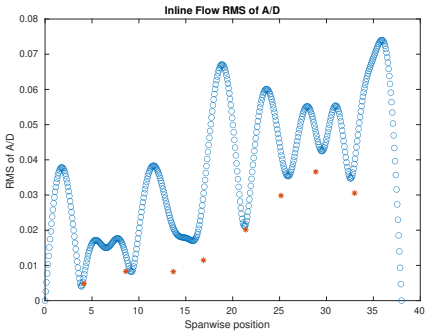

(b) Inline flow RMS profile case 7300.

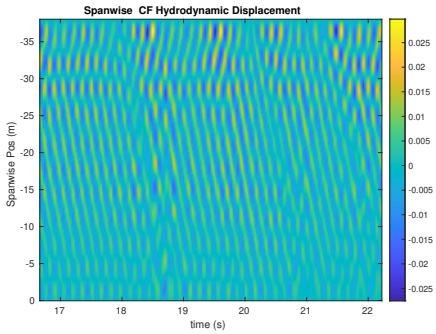

(c) Spanwise cross-flow hydrodynamic displacement case 7300.

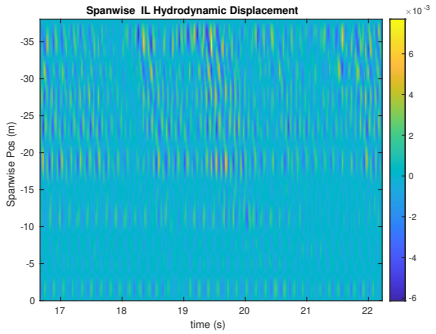

(d) Spanwise inline hydrodynamic displacement case 7300.

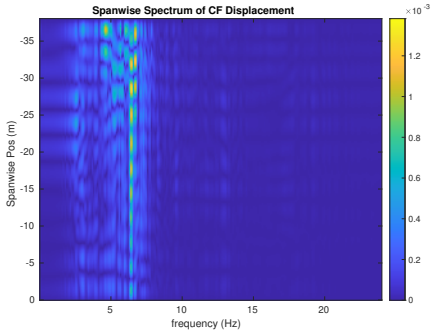

(e) Spanwise cross-flow spectrum of hydrodynamic displacement case 7300.

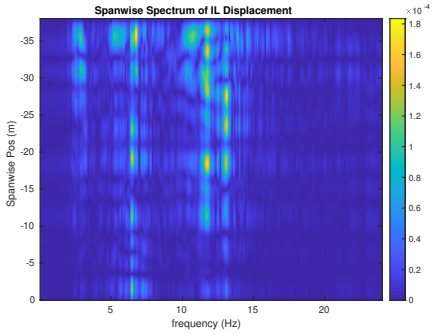

(f) Spanwise inline spectrum of hydrodynamic displacement case 7300.

Figure C-302: *Motion Analysis.* NDP Straight Riser ($L = 38m$) test case 7300.

NDP Straight Riser ($L = 38m$) test case 7310

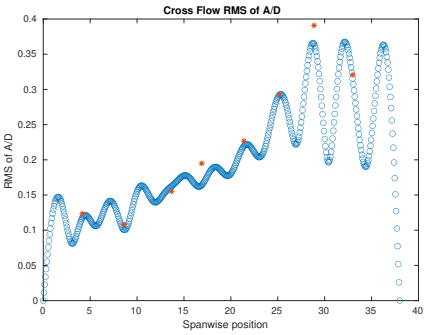

(a) Cross-flow RMS profile case 7310.

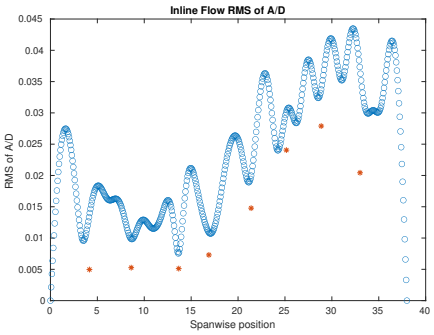

(b) Inline flow RMS profile case 7310.

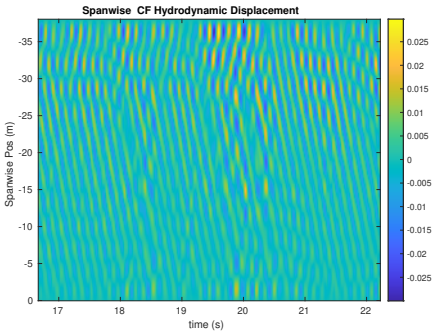

(c) Spanwise cross-flow hydrodynamic displacement case 7310.

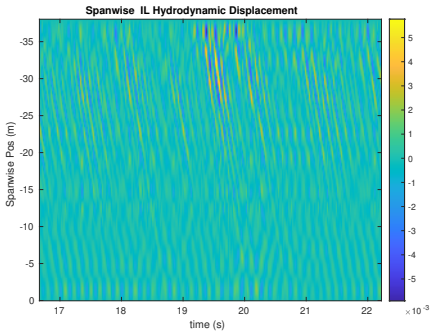

(d) Spanwise inline hydrodynamic displacement case 7310.

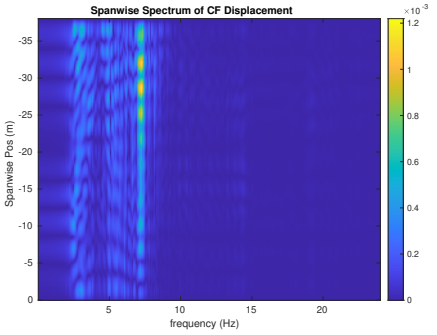

(e) Spanwise cross-flow spectrum of hydrodynamic displacement case 7310.

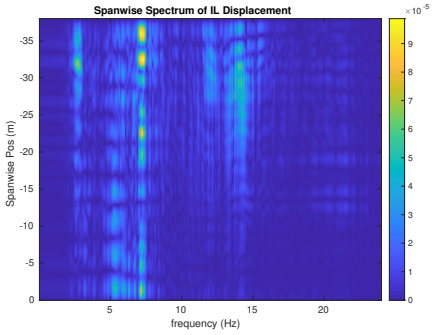

(f) Spanwise inline spectrum of hydrodynamic displacement case 7310.

Figure C-303: *Motion Analysis.* NDP Straight Riser ($L = 38m$) test case 7310.

NDP Straight Riser ($L = 38m$) test case 7320

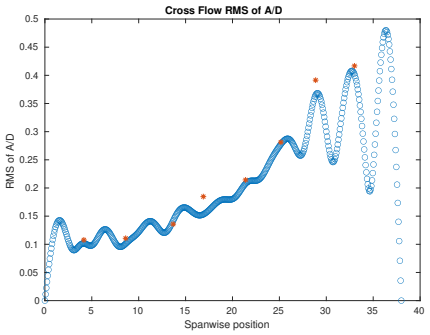

(a) Cross-flow RMS profile case 7320.

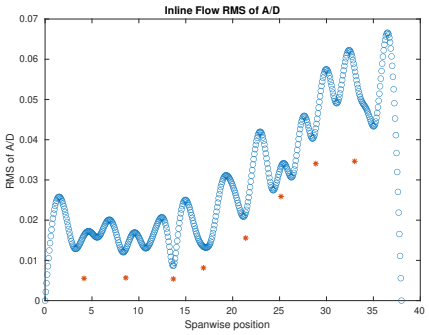

(b) Inline flow RMS profile case 7320.

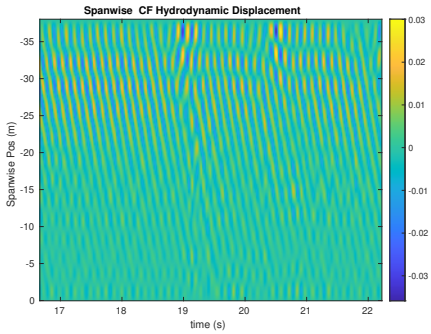

(c) Spanwise cross-flow hydrodynamic displacement case 7320.

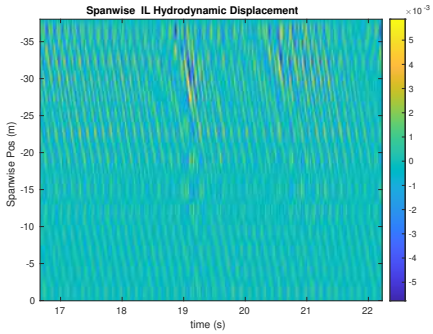

(d) Spanwise inline hydrodynamic displacement case 7320.

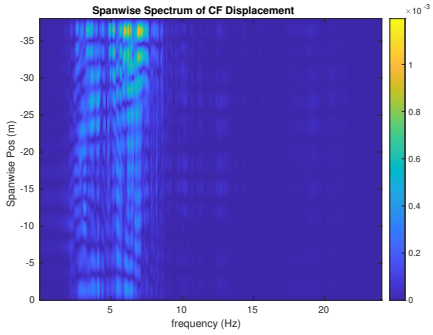

(e) Spanwise cross-flow spectrum of hydrodynamic displacement case 7320.

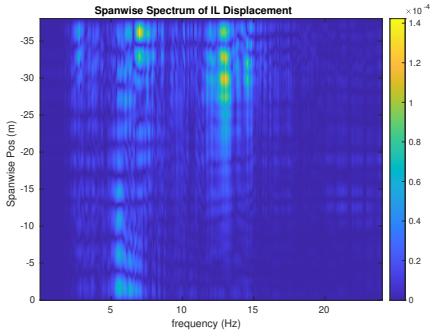

(f) Spanwise inline spectrum of hydrodynamic displacement case 7320.

Figure C-304: *Motion Analysis.* NDP Straight Riser ($L = 38m$) test case 7320.

NDP Straight Riser ($L = 38m$) test case 7330

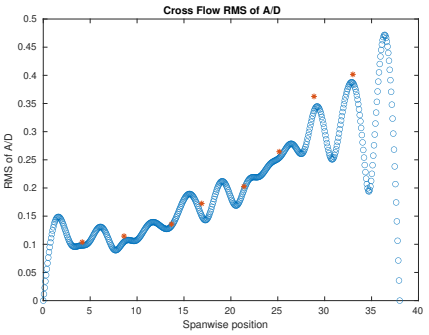

(a) Cross-flow RMS profile case 7330.

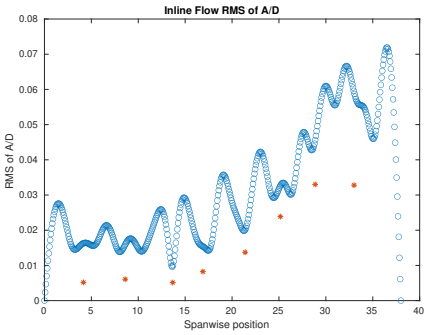

(b) Inline flow RMS profile case 7330.

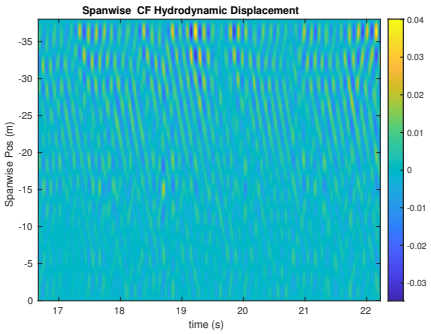

(c) Spanwise cross-flow hydrodynamic displacement case 7330.

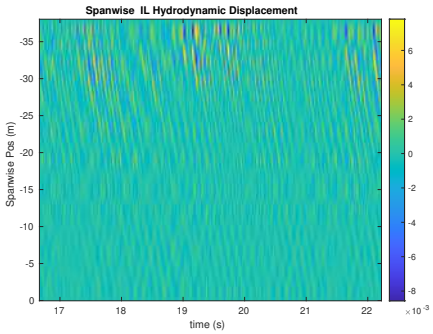

(d) Spanwise inline hydrodynamic displacement case 7330.

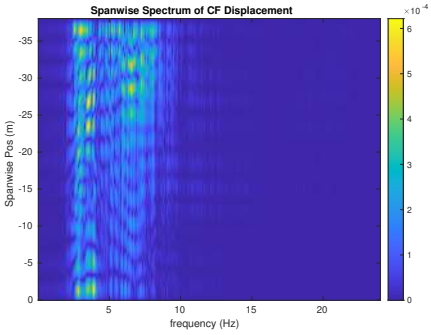

(e) Spanwise cross-flow spectrum of hydrodynamic displacement case 7330.

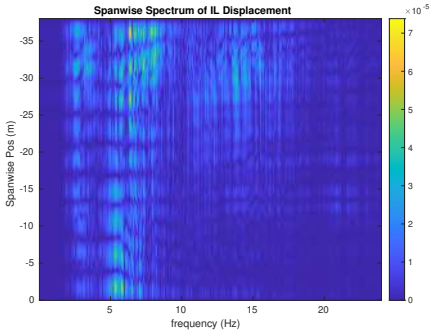

(f) Spanwise inline spectrum of hydrodynamic displacement case 7330.

Figure C-305: *Motion Analysis.* NDP Straight Riser ($L = 38m$) test case 7330.

NDP Straight Riser ($L = 38m$) test case 7340

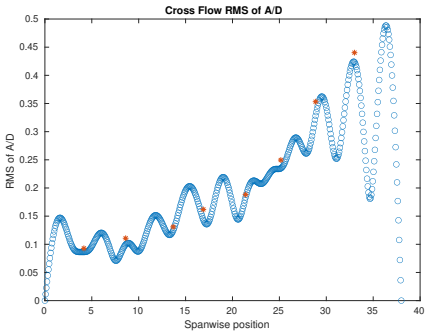

(a) Cross-flow RMS profile case 7340.

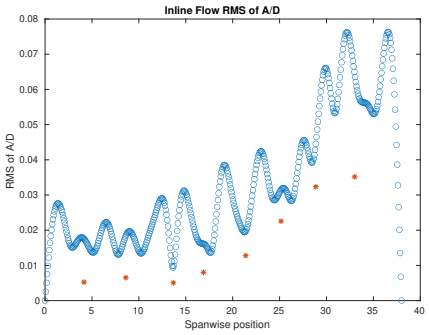

(b) Inline flow RMS profile case 7340.

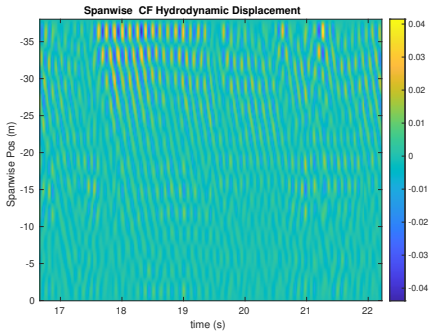

(c) Spanwise cross-flow hydrodynamic displacement case 7340.

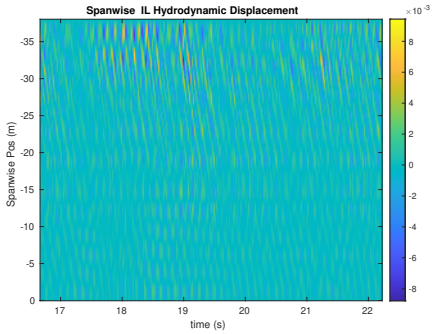

(d) Spanwise inline hydrodynamic displacement case 7340.

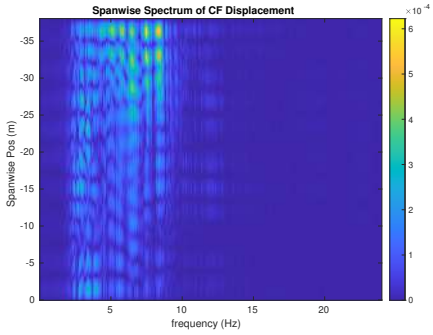

(e) Spanwise cross-flow spectrum of hydrodynamic displacement case 7340.

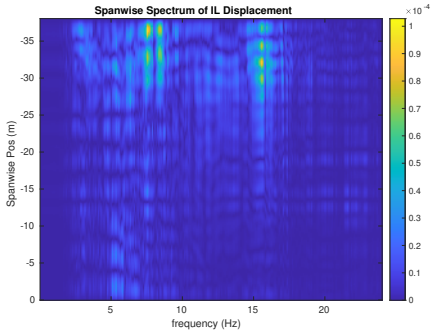

(f) Spanwise inline spectrum of hydrodynamic displacement case 7340.

Figure C-306: *Motion Analysis.* NDP Straight Riser ($L = 38m$) test case 7340.

NDP Straight Riser ($L = 38m$) test case 7350

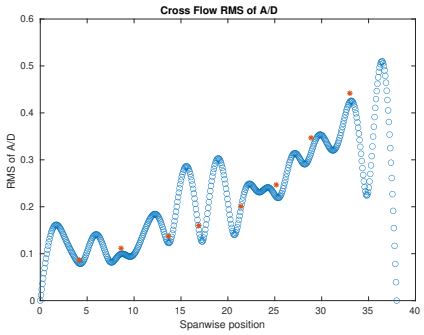

(a) Cross-flow RMS profile case 7350.

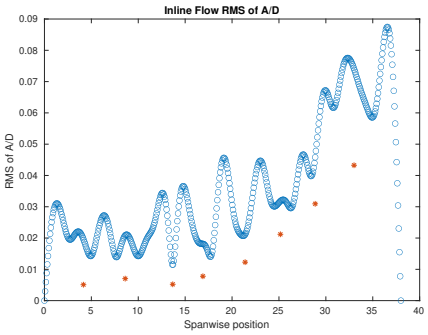

(b) Inline flow RMS profile case 7350.

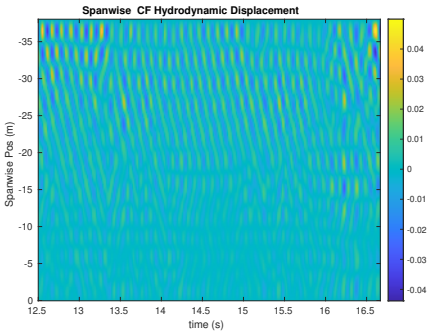

(c) Spanwise cross-flow hydrodynamic displacement case 7350.

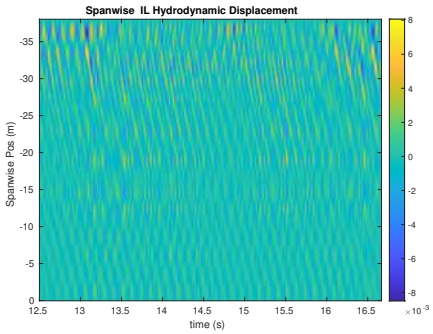

(d) Spanwise inline hydrodynamic displacement case 7350.

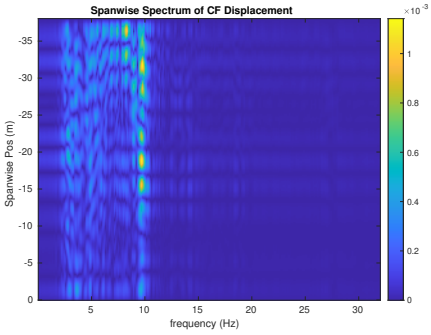

(e) Spanwise cross-flow spectrum of hydrodynamic displacement case 7350.

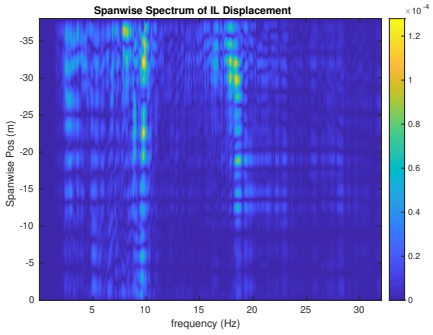

(f) Spanwise inline spectrum of hydrodynamic displacement case 7350.

Figure C-307: *Motion Analysis.* NDP Straight Riser ($L = 38m$) test case 7350.

NDP Straight Riser ($L = 38m$) test case 7360

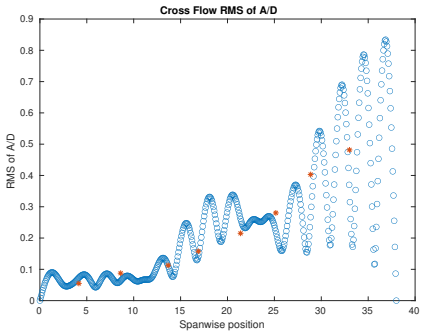

(a) Cross-flow RMS profile case 7360.

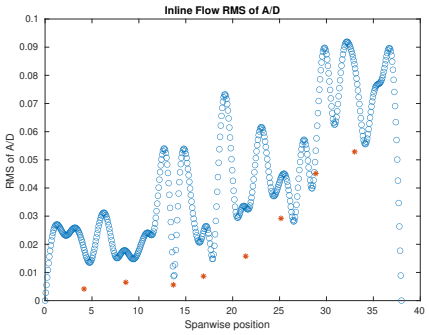

(b) Inline flow RMS profile case 7360.

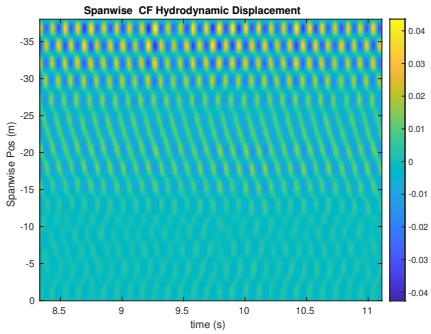

(c) Spanwise cross-flow hydrodynamic displacement case 7360.

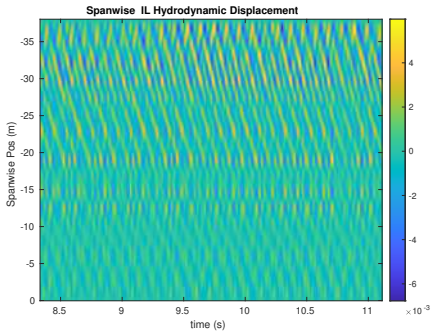

(d) Spanwise inline hydrodynamic displacement case 7360.

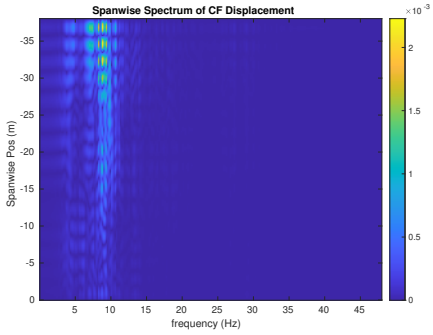

(e) Spanwise cross-flow spectrum of hydrodynamic displacement case 7360.

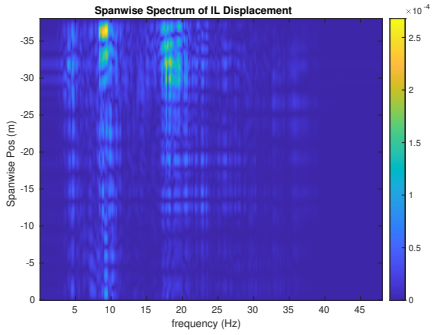

(f) Spanwise inline spectrum of hydrodynamic displacement case 7360.

Figure C-308: *Motion Analysis.* NDP Straight Riser ($L = 38m$) test case 7360.

NDP Straight Riser ($L = 38m$) test case 7370

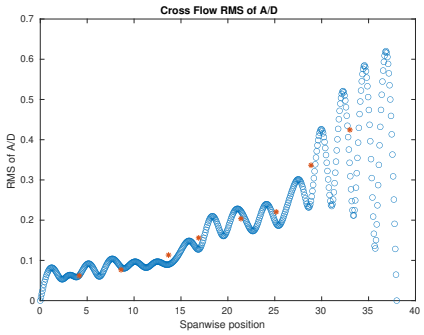

(a) Cross-flow RMS profile case 7370.

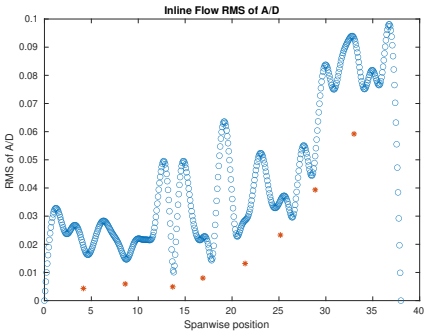

(b) Inline flow RMS profile case 7370.

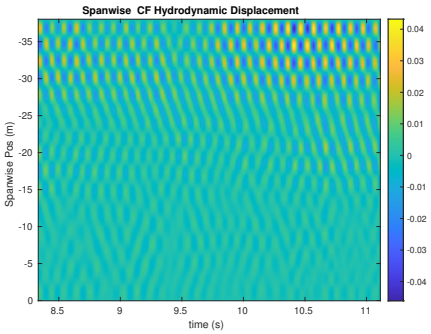

(c) Spanwise cross-flow hydrodynamic displacement case 7370.

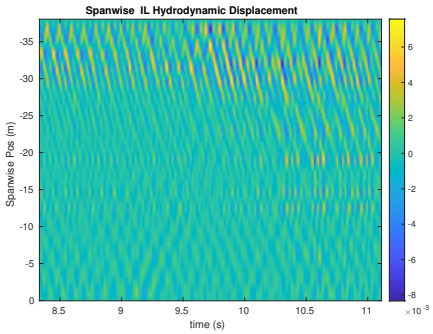

(d) Spanwise inline hydrodynamic displacement case 7370.

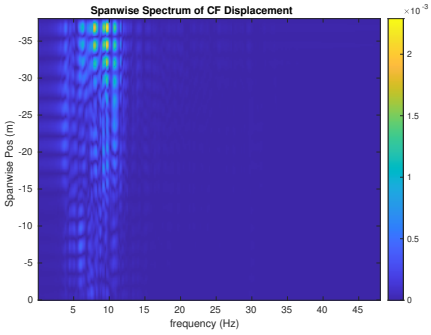

(e) Spanwise cross-flow spectrum of hydrodynamic displacement case 7370.

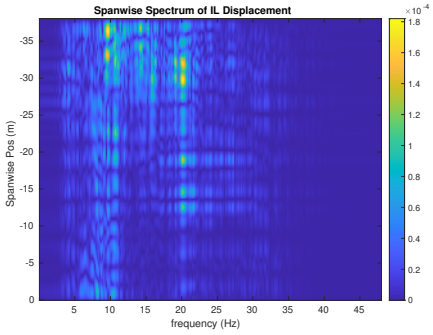

(f) Spanwise inline spectrum of hydrodynamic displacement case 7370.

Figure C-309: *Motion Analysis.* NDP Straight Riser ($L = 38m$) test case 7370.

NDP Straight Riser ($L = 38m$) test case 7380

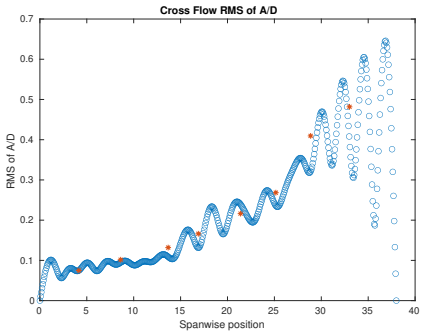

(a) Cross-flow RMS profile case 7380.

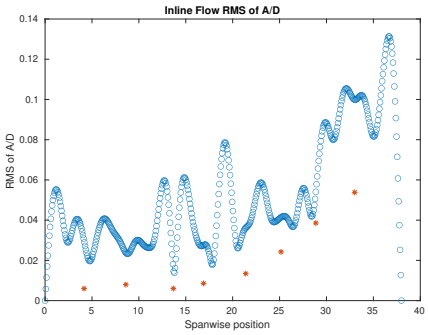

(b) Inline flow RMS profile case 7380.

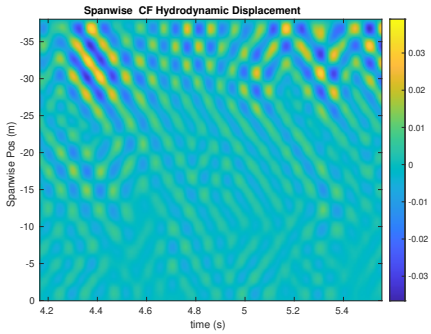

(c) Spanwise cross-flow hydrodynamic displacement case 7380.

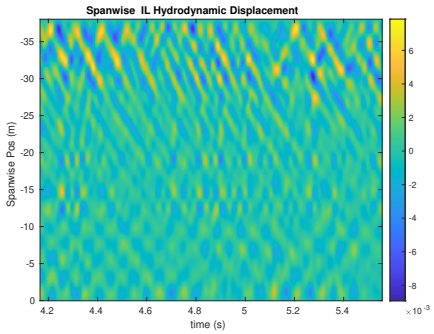

(d) Spanwise inline hydrodynamic displacement case 7380.

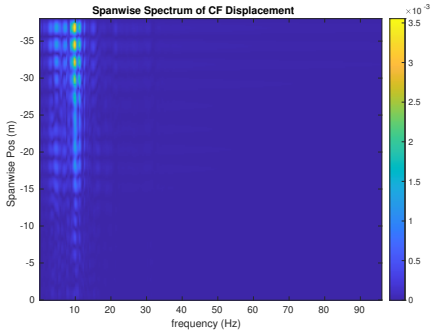

(e) Spanwise cross-flow spectrum of hydrodynamic displacement case 7380.

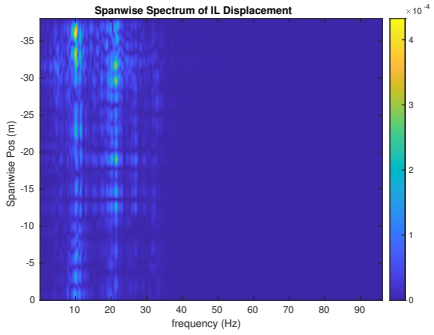

(f) Spanwise inline spectrum of hydrodynamic displacement case 7380.

Figure C-310: *Motion Analysis.* NDP Straight Riser ($L = 38m$) test case 7380.

NDP Straight Riser ($L = 38m$) test case 7390

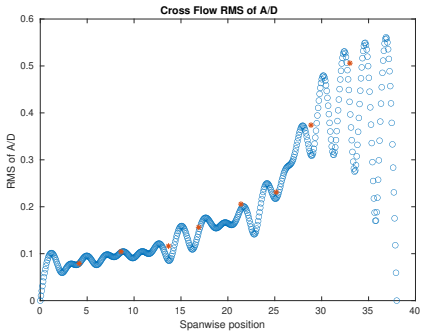

(a) Cross-flow RMS profile case 7390.

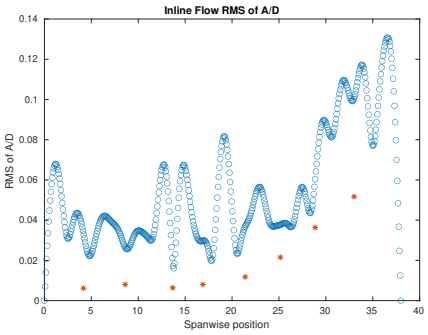

(b) Inline flow RMS profile case 7390.

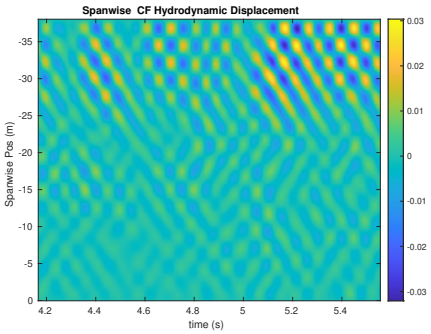

(c) Spanwise cross-flow hydrodynamic displacement case 7390.

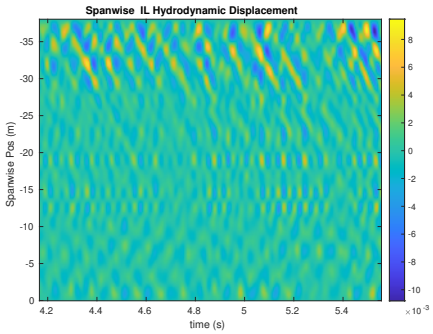

(d) Spanwise inline hydrodynamic displacement case 7390.

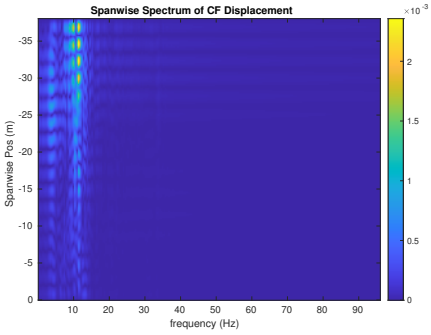

(e) Spanwise cross-flow spectrum of hydrodynamic displacement case 7390.

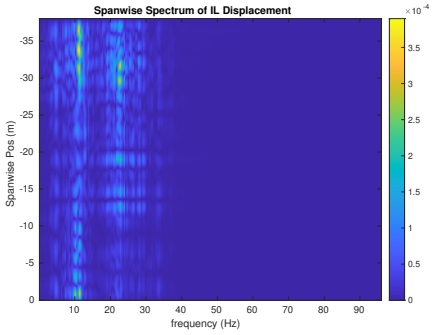

(f) Spanwise inline spectrum of hydrodynamic displacement case 7390.

Figure C-311: *Motion Analysis.* NDP Straight Riser ($L = 38m$) test case 7390.

NDP Straight Riser ($L = 38m$) test case 7400

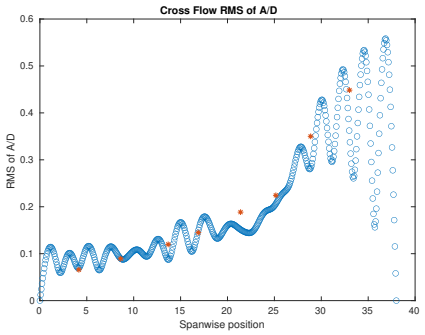

(a) Cross-flow RMS profile case 7400.

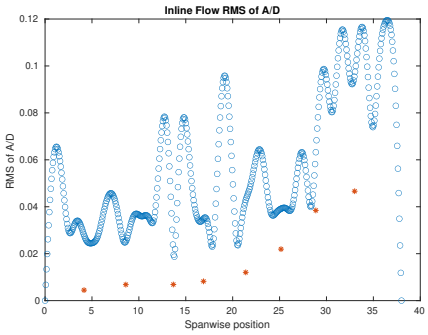

(b) Inline flow RMS profile case 7400.

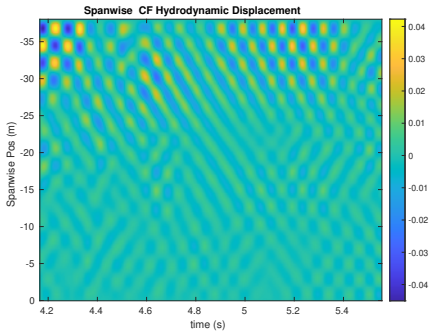

(c) Spanwise cross-flow hydrodynamic displacement case 7400.

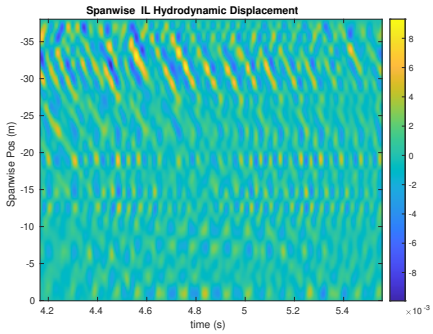

(d) Spanwise inline hydrodynamic displacement case 7400.

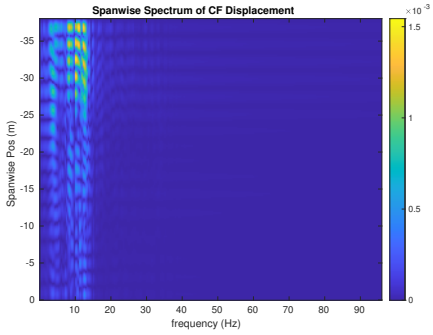

(e) Spanwise cross-flow spectrum of hydrodynamic displacement case 7400.

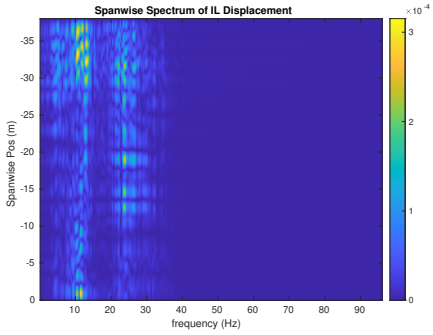

(f) Spanwise inline spectrum of hydrodynamic displacement case 7400.

Figure C-312: *Motion Analysis.* NDP Straight Riser ($L = 38m$) test case 7400.

NDP Straight Riser ($L = 38m$) test case 7410

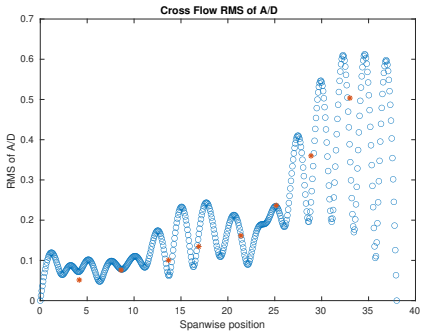

(a) Cross-flow RMS profile case 7410.

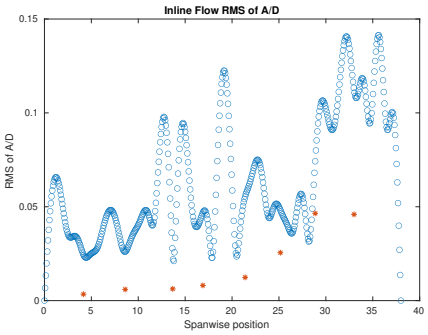

(b) Inline flow RMS profile case 7410.

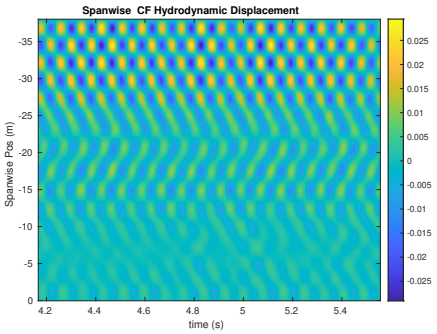

(c) Spanwise cross-flow hydrodynamic displacement case 7410.

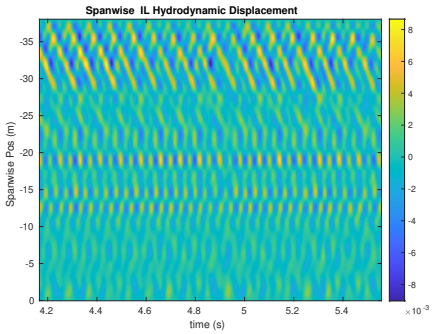

(d) Spanwise inline hydrodynamic displacement case 7410.

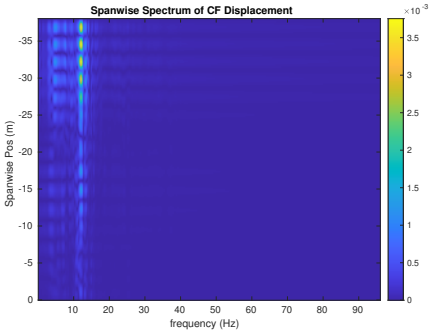

(e) Spanwise cross-flow spectrum of hydrodynamic displacement case 7410.

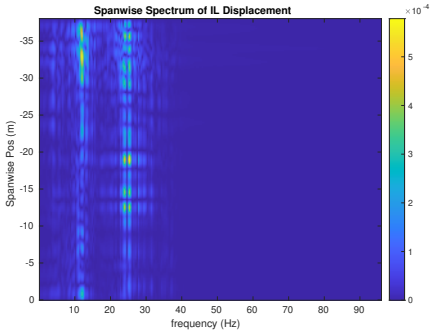

(f) Spanwise inline spectrum of hydrodynamic displacement case 7410.

Figure C-313: *Motion Analysis.* NDP Straight Riser ($L = 38m$) test case 7410.

NDP Straight Riser ($L = 38m$) test case 7420

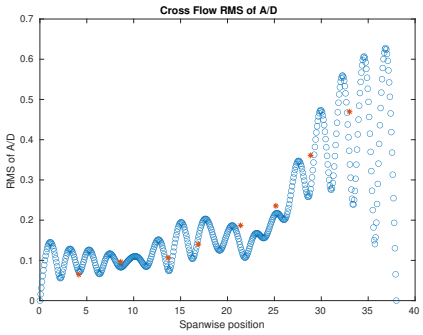

(a) Cross-flow RMS profile case 7420.

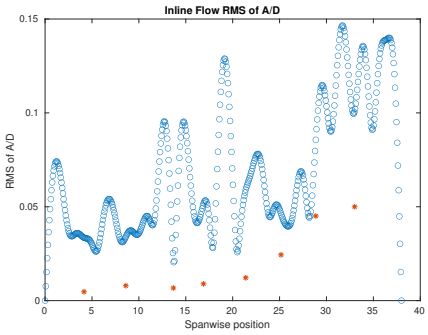

(b) Inline flow RMS profile case 7420.

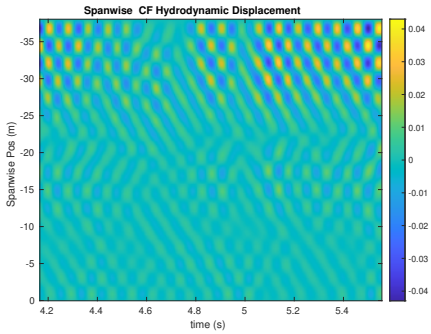

(c) Spanwise cross-flow hydrodynamic displacement case 7420.

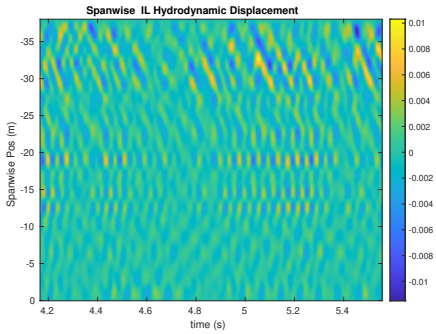

(d) Spanwise inline hydrodynamic displacement case 7420.

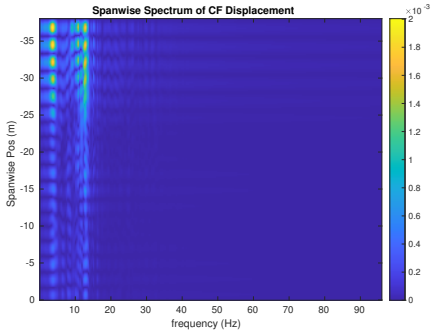

(e) Spanwise cross-flow spectrum of hydrodynamic displacement case 7420.

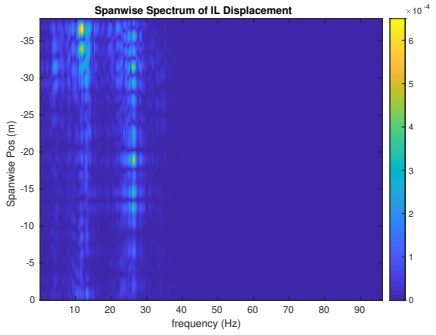

(f) Spanwise inline spectrum of hydrodynamic displacement case 7420.

Figure C-314: *Motion Analysis.* NDP Straight Riser ($L = 38m$) test case 7420.

NDP Straight Riser ($L = 38m$) test case 7430

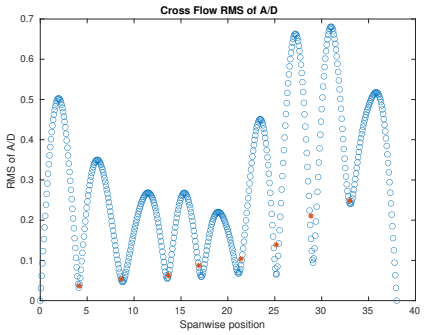

(a) Cross-flow RMS profile case 7430.

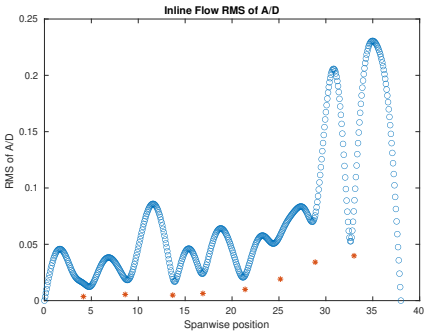

(b) Inline flow RMS profile case 7430.

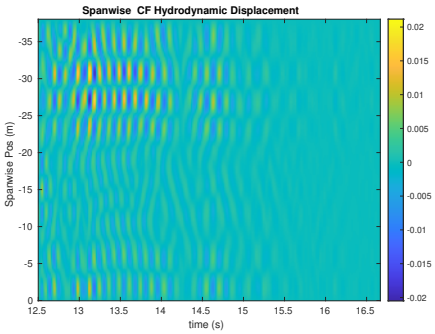

(c) Spanwise cross-flow hydrodynamic displacement case 7430.

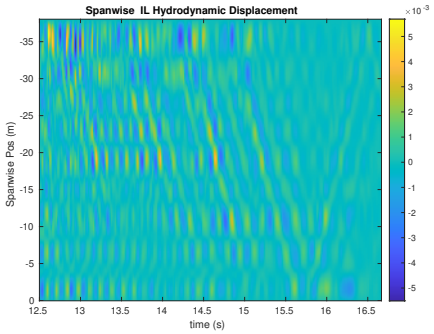

(d) Spanwise inline hydrodynamic displacement case 7430.

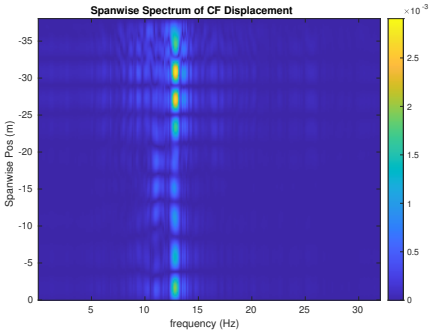

(e) Spanwise cross-flow spectrum of hydrodynamic displacement case 7430.

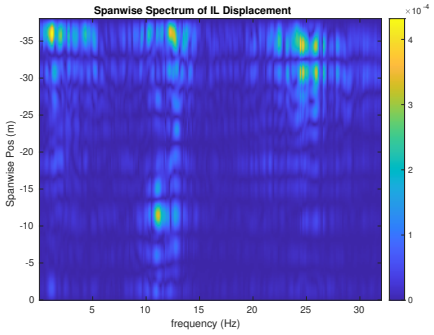

(f) Spanwise inline spectrum of hydrodynamic displacement case 7430.

Figure C-315: *Motion Analysis.* NDP Straight Riser ($L = 38m$) test case 7430.

NDP Straight Riser ($L = 38m$) test case 7810

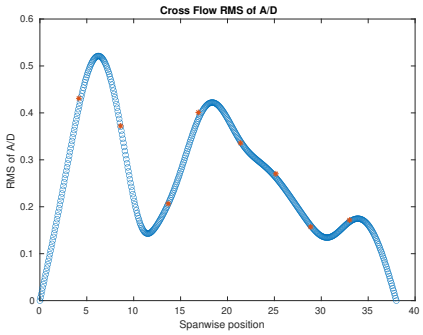

(a) Cross-flow RMS profile case 7810.

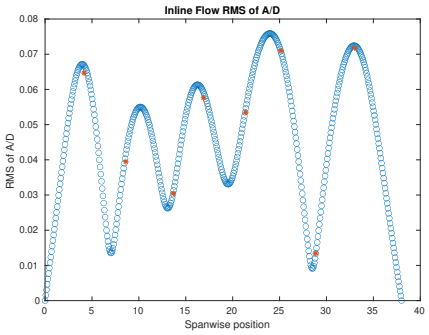

(b) Inline flow RMS profile case 7810.

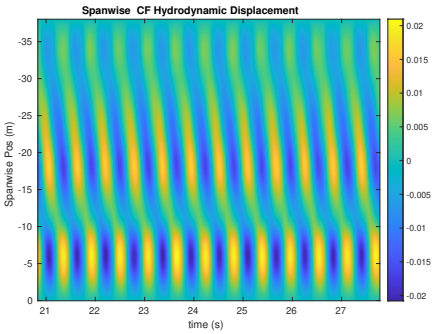

(c) Spanwise cross-flow hydrodynamic displacement case 7810.

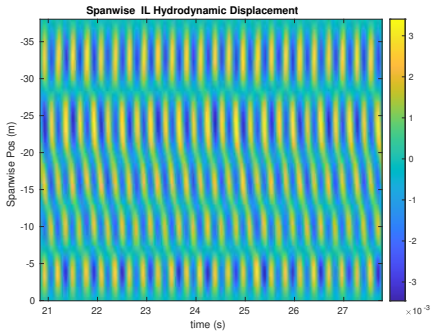

(d) Spanwise inline hydrodynamic displacement case 7810.

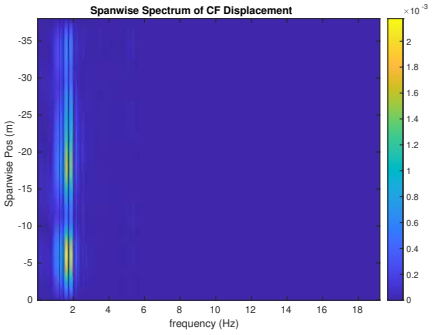

(e) Spanwise cross-flow spectrum of hydrodynamic displacement case 7810.

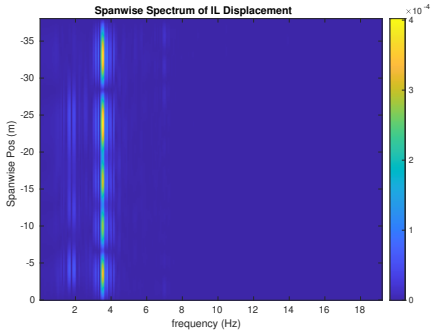

(f) Spanwise inline spectrum of hydrodynamic displacement case 7810.

Figure C-316: *Motion Analysis.* NDP Straight Riser ($L = 38m$) test case 7810.

NDP Straight Riser ($L = 38m$) test case 7820

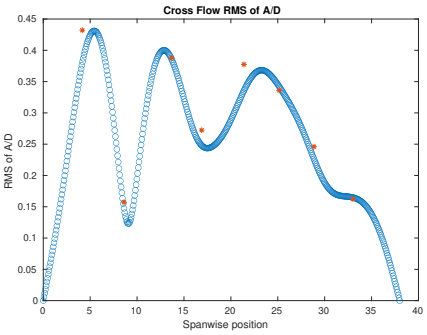

(a) Cross-flow RMS profile case 7820.

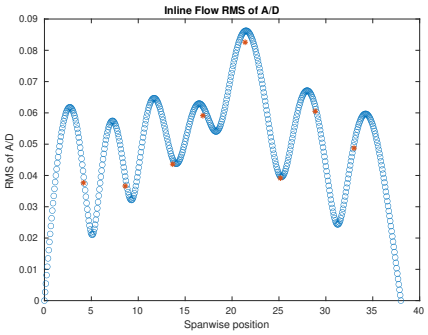

(b) Inline flow RMS profile case 7820.

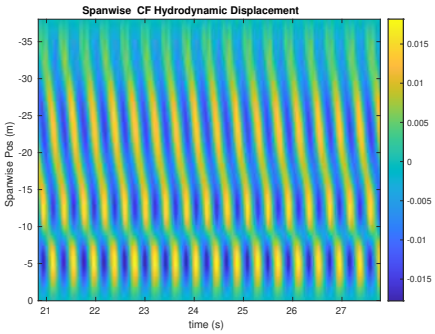

(c) Spanwise cross-flow hydrodynamic displacement case 7820.

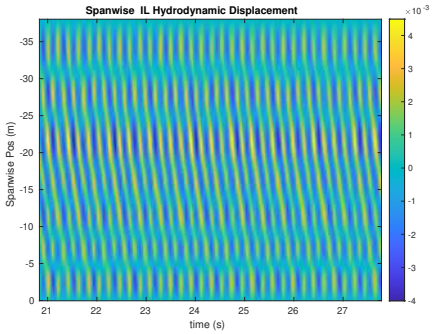

(d) Spanwise inline hydrodynamic displacement case 7820.

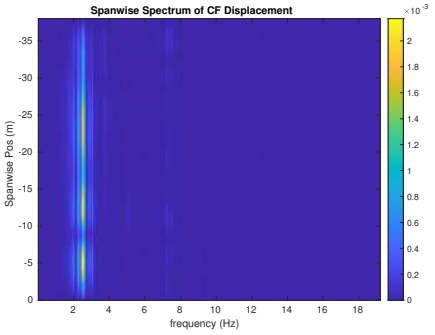

(e) Spanwise cross-flow spectrum of hydrodynamic displacement case 7820.

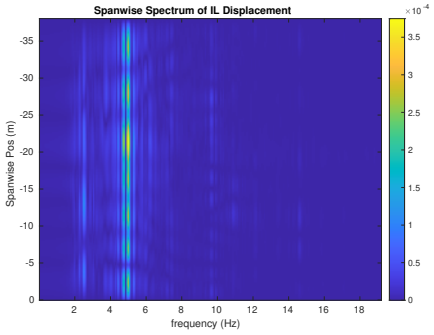

(f) Spanwise inline spectrum of hydrodynamic displacement case 7820.

Figure C-317: *Motion Analysis.* NDP Straight Riser ($L = 38m$) test case 7820.

NDP Straight Riser ($L = 38m$) test case 7830

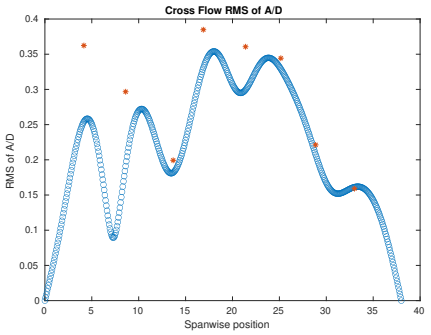

(a) Cross-flow RMS profile case 7830.

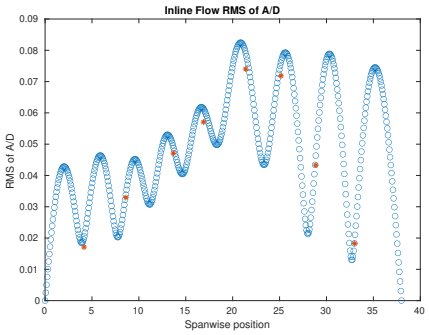

(b) Inline flow RMS profile case 7830.

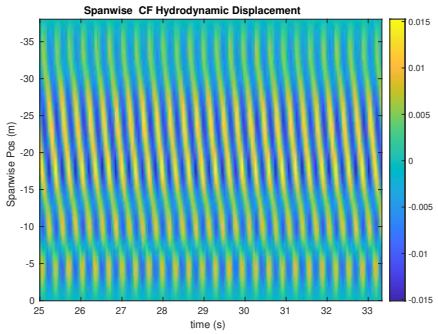

(c) Spanwise cross-flow hydrodynamic displacement case 7830.

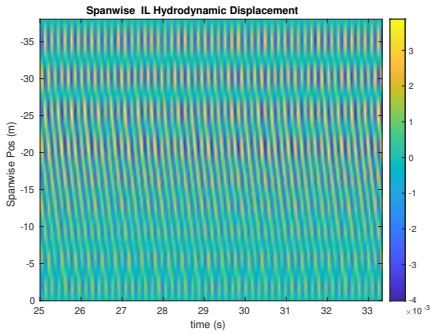

(d) Spanwise inline hydrodynamic displacement case 7830.

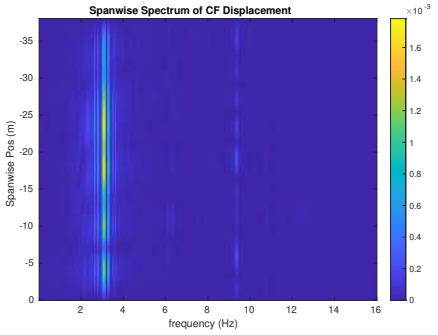

(e) Spanwise cross-flow spectrum of hydrodynamic displacement case 7830.

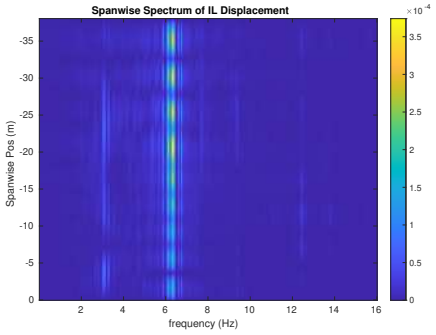

(f) Spanwise inline spectrum of hydrodynamic displacement case 7830.

Figure C-318: *Motion Analysis.* NDP Straight Riser ($L = 38m$) test case 7830.

NDP Straight Riser ($L = 38m$) test case 7840

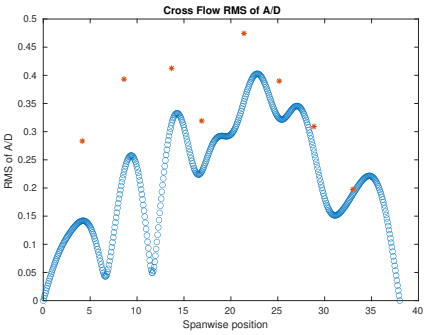

(a) Cross-flow RMS profile case 7840.

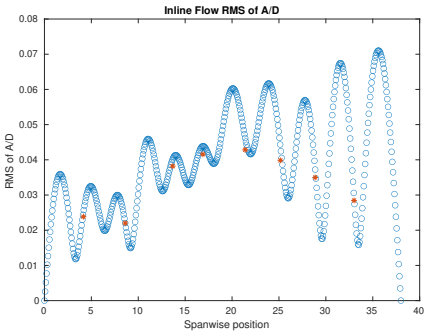

(b) Inline flow RMS profile case 7840.

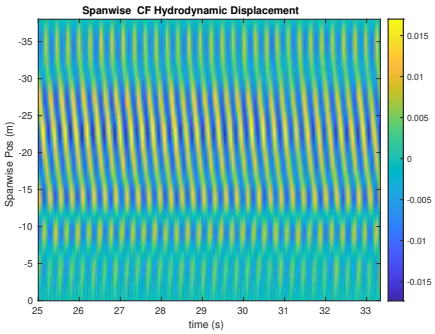

(c) Spanwise cross-flow hydrodynamic displacement case 7840.

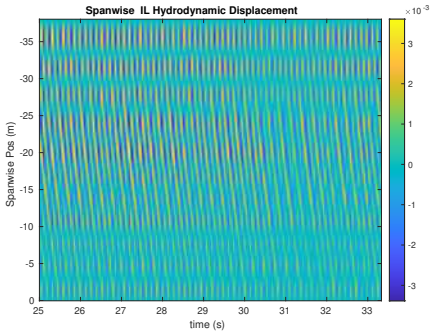

(d) Spanwise inline hydrodynamic displacement case 7840.

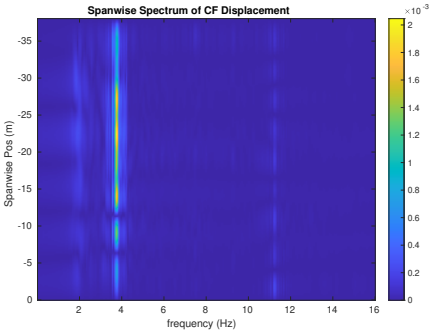

(e) Spanwise cross-flow spectrum of hydrodynamic displacement case 7840.

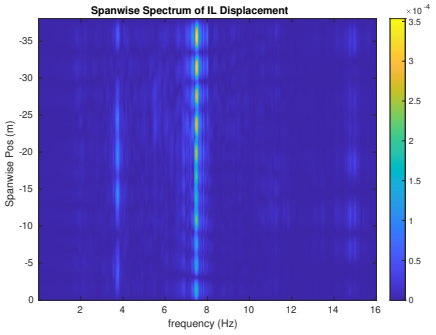

(f) Spanwise inline spectrum of hydrodynamic displacement case 7840.

Figure C-319: *Motion Analysis.* NDP Straight Riser ($L = 38m$) test case 7840.

NDP Straight Riser ($L = 38m$) test case 7850

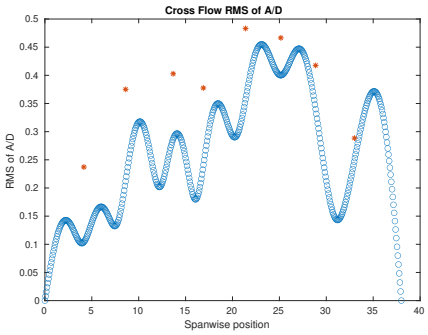

(a) Cross-flow RMS profile case 7850.

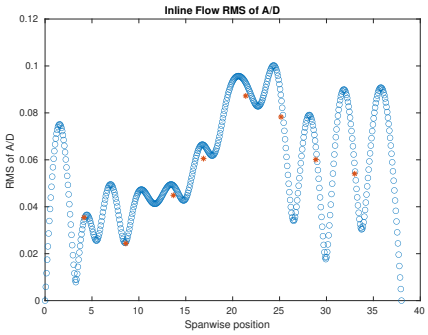

(b) Inline flow RMS profile case 7850.

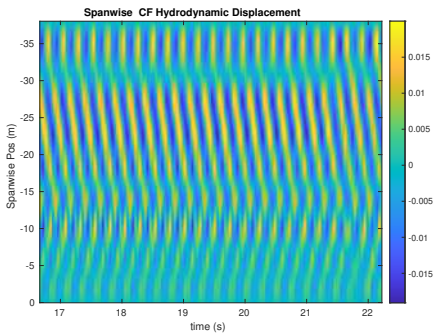

(c) Spanwise cross-flow hydrodynamic displacement case 7850.

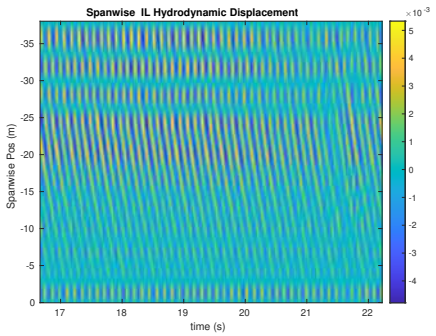

(d) Spanwise inline hydrodynamic displacement case 7850.

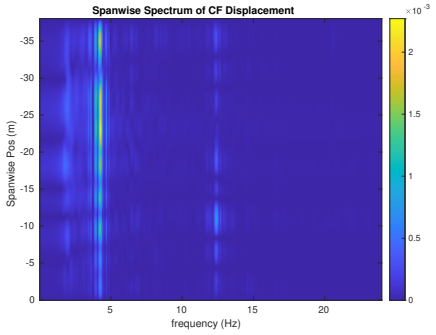

(e) Spanwise cross-flow spectrum of hydrodynamic displacement case 7850.

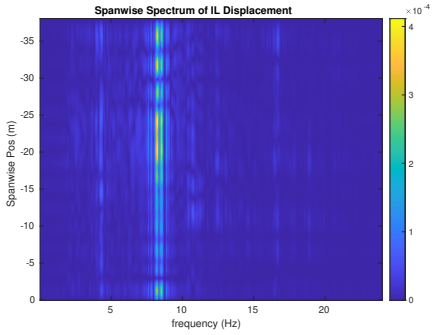

(f) Spanwise inline spectrum of hydrodynamic displacement case 7850.

Figure C-320: *Motion Analysis.* NDP Straight Riser ($L = 38m$) test case 7850.

NDP Straight Riser ($L = 38m$) test case 7860

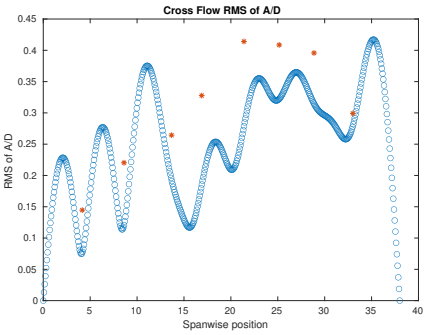

(a) Cross-flow RMS profile case 7860.

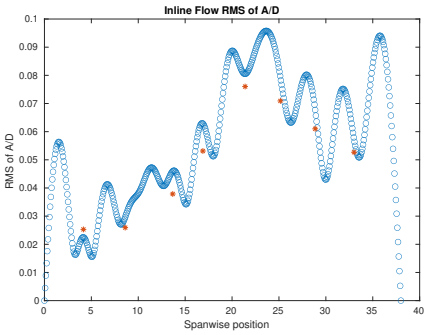

(b) Inline flow RMS profile case 7860.

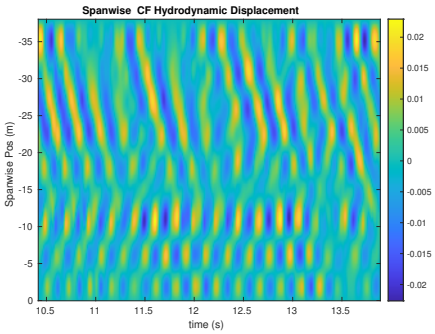

(c) Spanwise cross-flow hydrodynamic displacement case 7860.

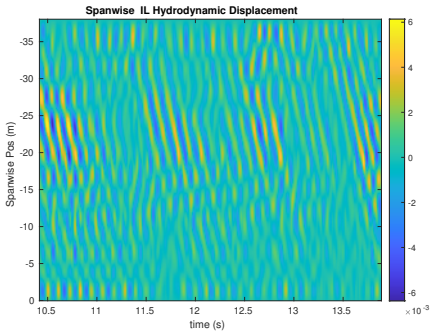

(d) Spanwise inline hydrodynamic displacement case 7860.

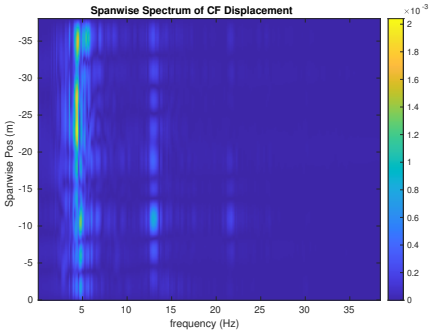

(e) Spanwise cross-flow spectrum of hydrodynamic displacement case 7860.

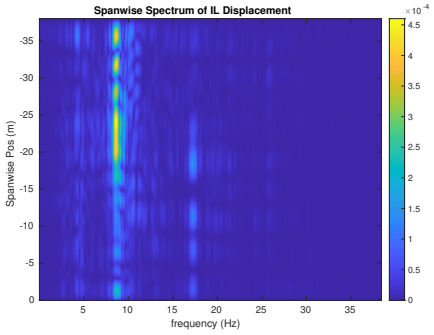

(f) Spanwise inline spectrum of hydrodynamic displacement case 7860.

Figure C-321: *Motion Analysis.* NDP Straight Riser ($L = 38m$) test case 7860.

NDP Straight Riser ($L = 38m$) test case 7870

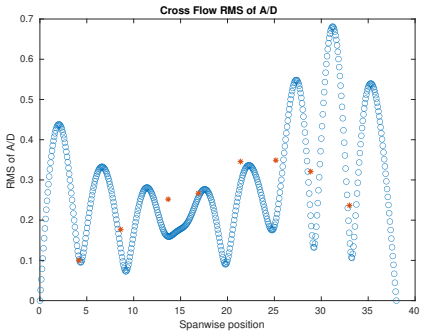

(a) Cross-flow RMS profile case 7870.

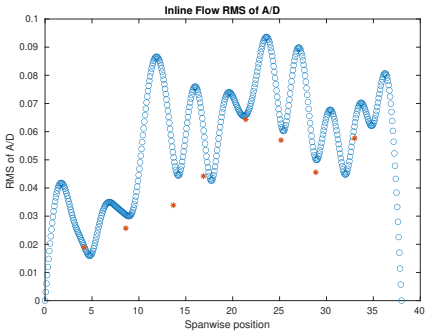

(b) Inline flow RMS profile case 7870.

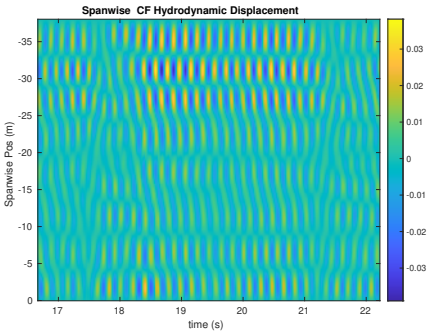

(c) Spanwise cross-flow hydrodynamic displacement case 7870.

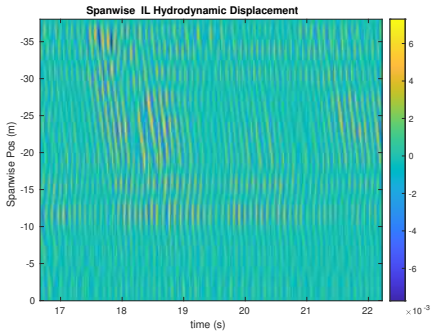

(d) Spanwise inline hydrodynamic displacement case 7870.

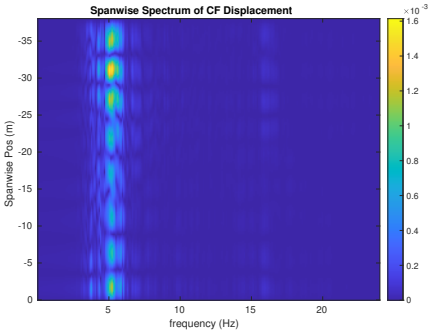

(e) Spanwise cross-flow spectrum of hydrodynamic displacement case 7870.

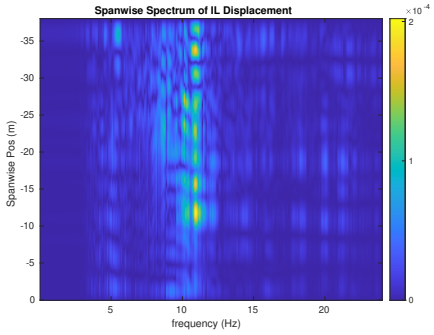

(f) Spanwise inline spectrum of hydrodynamic displacement case 7870.

Figure C-322: *Motion Analysis.* NDP Straight Riser ($L = 38m$) test case 7870.

NDP Straight Riser ($L = 38m$) test case 7880

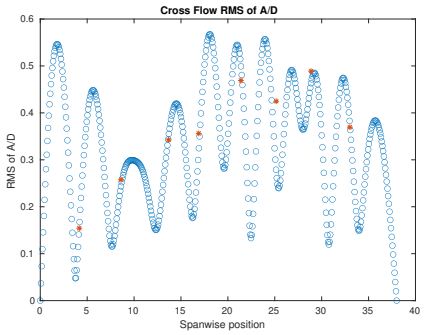

(a) Cross-flow RMS profile case 7880.

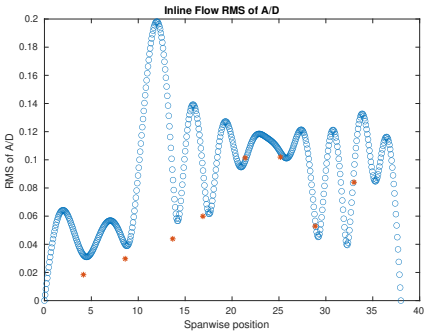

(b) Inline flow RMS profile case 7880.

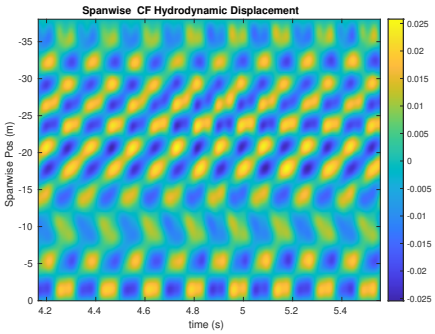

(c) Spanwise cross-flow hydrodynamic displacement case 7880.

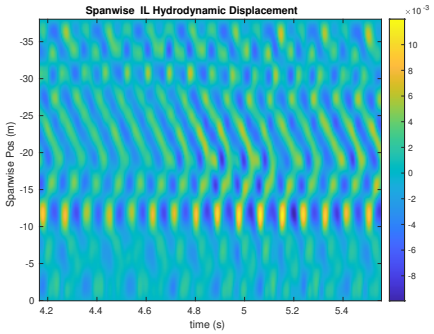

(d) Spanwise inline hydrodynamic displacement case 7880.

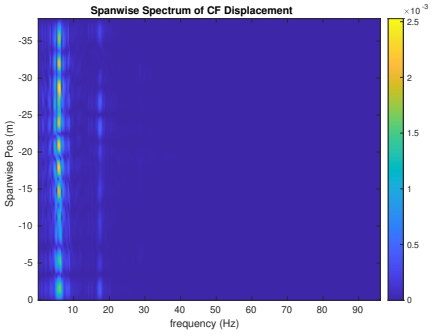

(e) Spanwise cross-flow spectrum of hydrodynamic displacement case 7880.

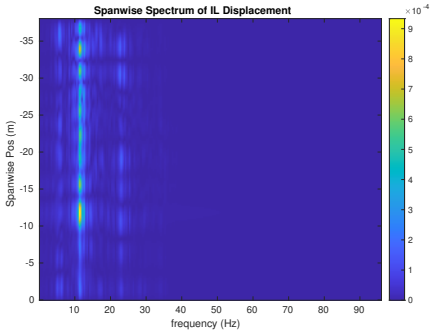

(f) Spanwise inline spectrum of hydrodynamic displacement case 7880.

Figure C-323: *Motion Analysis.* NDP Straight Riser ($L = 38m$) test case 7880.

NDP Straight Riser ($L = 38m$) test case 7890

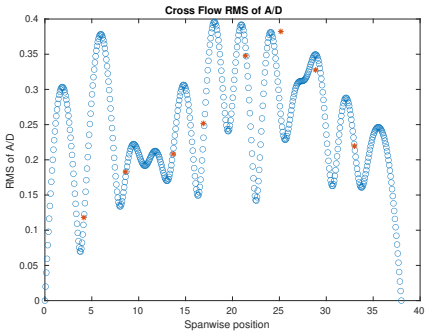

(a) Cross-flow RMS profile case 7890.

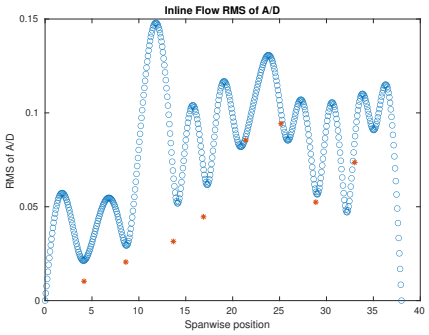

(b) Inline flow RMS profile case 7890.

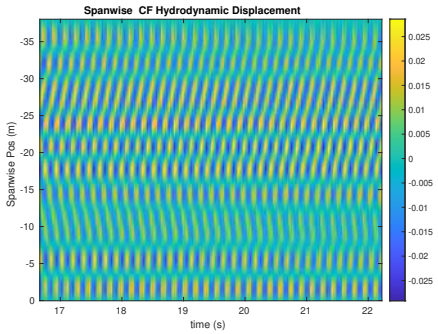

(c) Spanwise cross-flow hydrodynamic displacement case 7890.

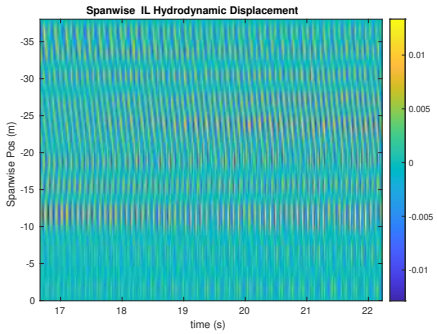

(d) Spanwise inline hydrodynamic displacement case 7890.

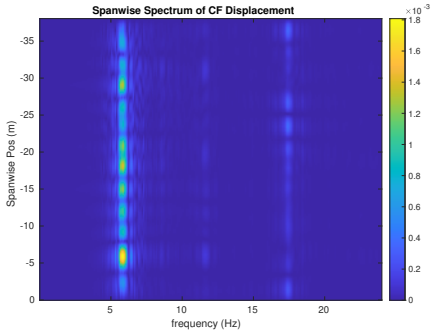

(e) Spanwise cross-flow spectrum of hydrodynamic displacement case 7890.

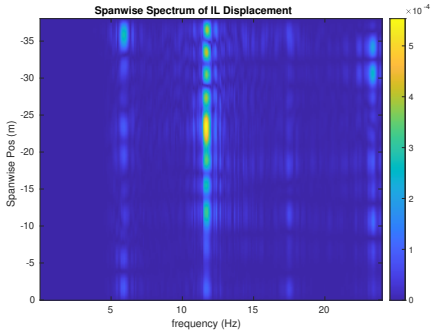

(f) Spanwise inline spectrum of hydrodynamic displacement case 7890.

Figure C-324: *Motion Analysis.* NDP Straight Riser ($L = 38m$) test case 7890.

NDP Straight Riser ($L = 38m$) test case 7900

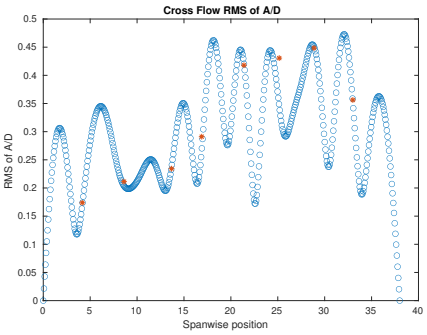

(a) Cross-flow RMS profile case 7900.

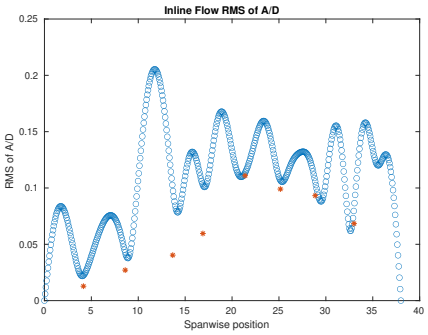

(b) Inline flow RMS profile case 7900.

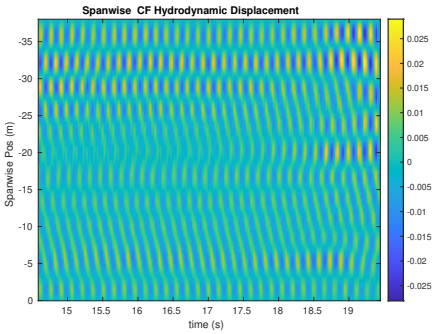

(c) Spanwise cross-flow hydrodynamic displacement case 7900.

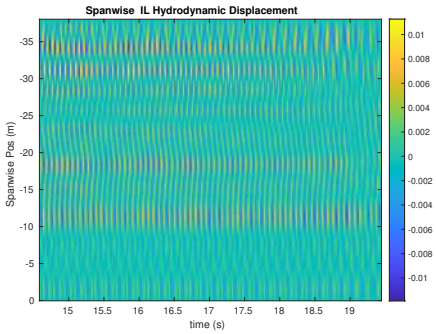

(d) Spanwise inline hydrodynamic displacement case 7900.

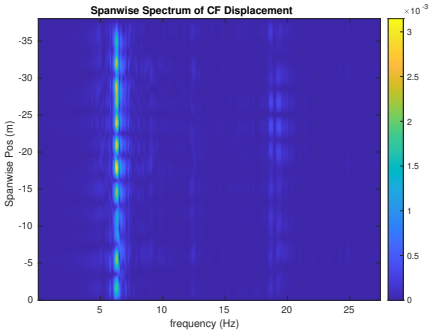

(e) Spanwise cross-flow spectrum of hydrodynamic displacement case 7900.

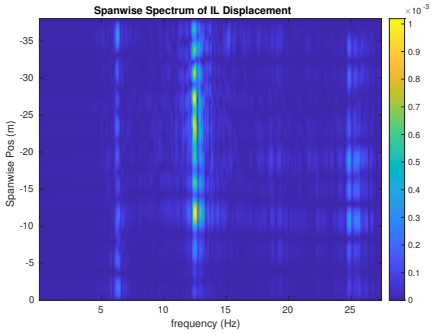

(f) Spanwise inline spectrum of hydrodynamic displacement case 7900.

Figure C-325: *Motion Analysis.* NDP Straight Riser ($L = 38m$) test case 7900.

NDP Straight Riser ($L = 38m$) test case 7910

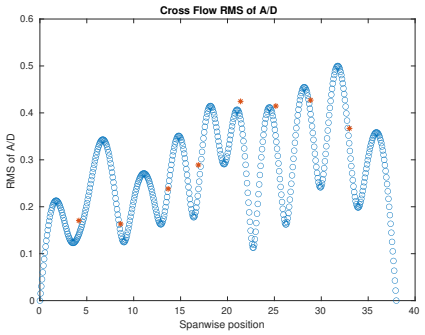

(a) Cross-flow RMS profile case 7910.

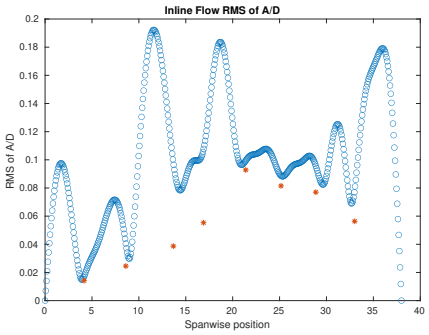

(b) Inline flow RMS profile case 7910.

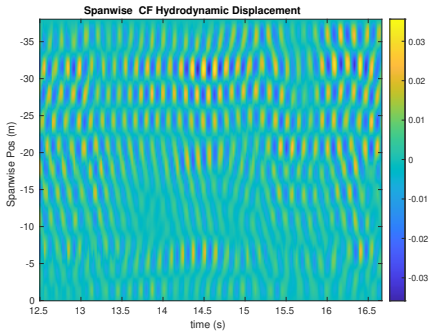

(c) Spanwise cross-flow hydrodynamic displacement case 7910.

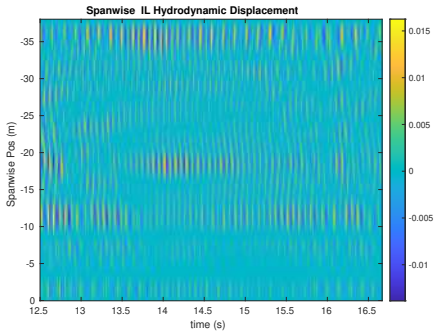

(d) Spanwise inline hydrodynamic displacement case 7910.

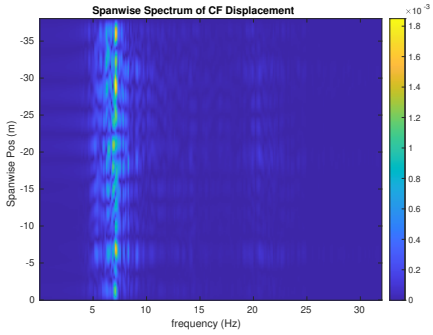

(e) Spanwise cross-flow spectrum of hydrodynamic displacement case 7910.

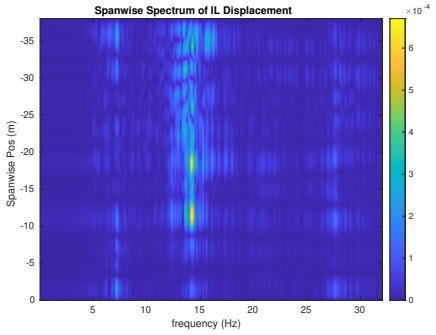

(f) Spanwise inline spectrum of hydrodynamic displacement case 7910.

Figure C-326: *Motion Analysis.* NDP Straight Riser ($L = 38m$) test case 7910.

NDP Straight Riser ($L = 38m$) test case 7920

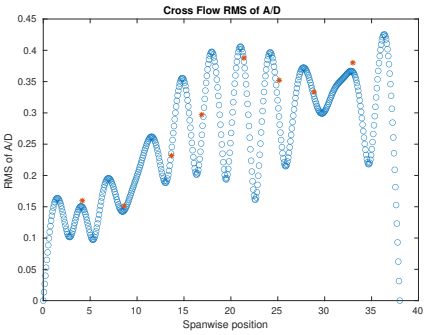

(a) Cross-flow RMS profile case 7920.

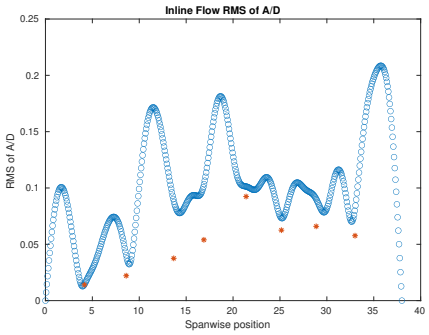

(b) Inline flow RMS profile case 7920.

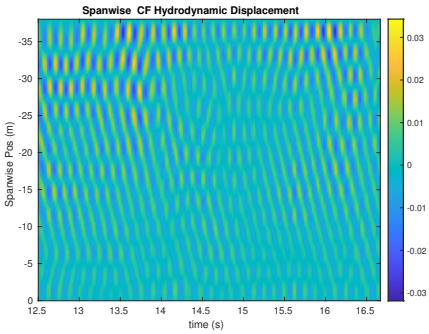

(c) Spanwise cross-flow hydrodynamic displacement case 7920.

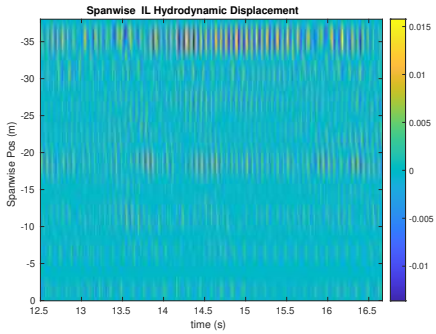

(d) Spanwise inline hydrodynamic displacement case 7920.

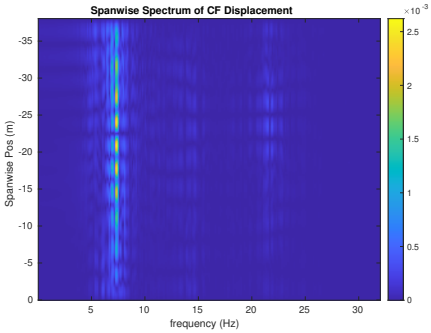

(e) Spanwise cross-flow spectrum of hydrodynamic displacement case 7920.

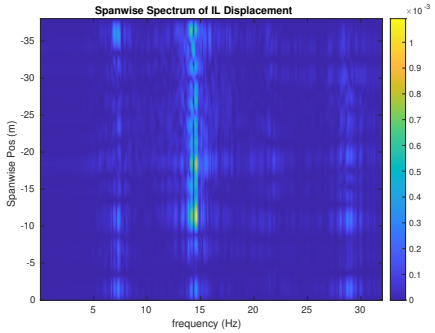

(f) Spanwise inline spectrum of hydrodynamic displacement case 7920.

Figure C-327: *Motion Analysis.* NDP Straight Riser ($L = 38m$) test case 7920.

NDP Straight Riser ($L = 38m$) test case 7930

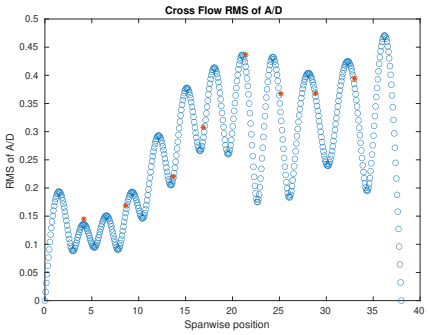

(a) Cross-flow RMS profile case 7930.

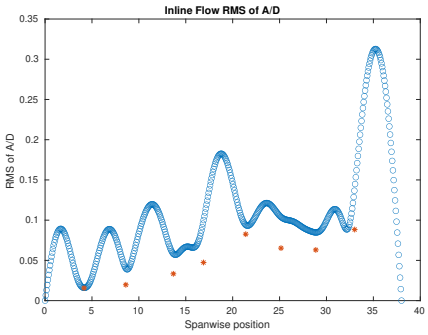

(b) Inline flow RMS profile case 7930.

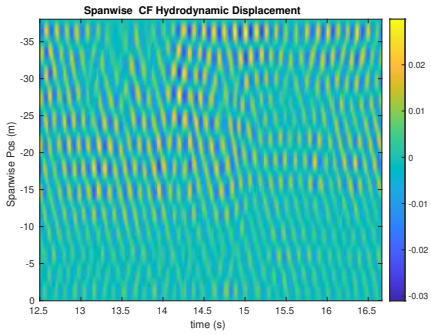

(c) Spanwise cross-flow hydrodynamic displacement case 7930.

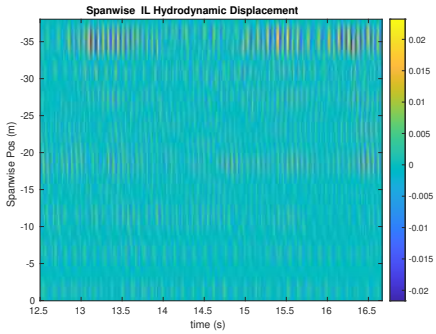

(d) Spanwise inline hydrodynamic displacement case 7930.

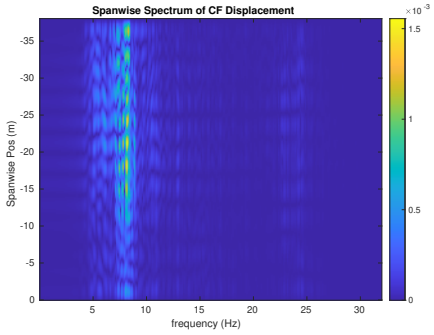

(e) Spanwise cross-flow spectrum of hydrodynamic displacement case 7930.

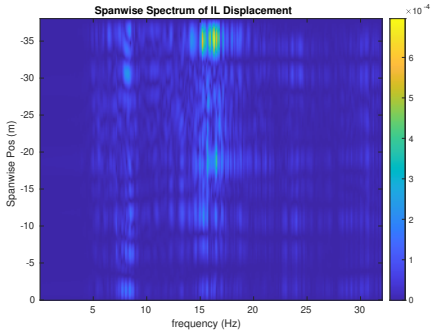

(f) Spanwise inline spectrum of hydrodynamic displacement case 7930.

Figure C-328: *Motion Analysis.* NDP Straight Riser ($L = 38m$) test case 7930.

NDP Straight Riser ($L = 38m$) test case 7940

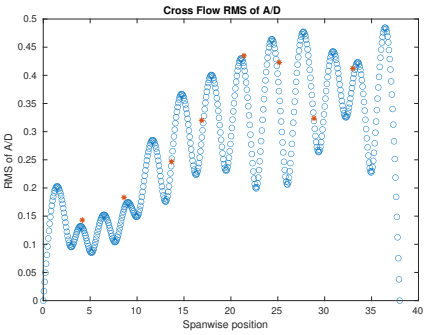

(a) Cross-flow RMS profile case 7940.

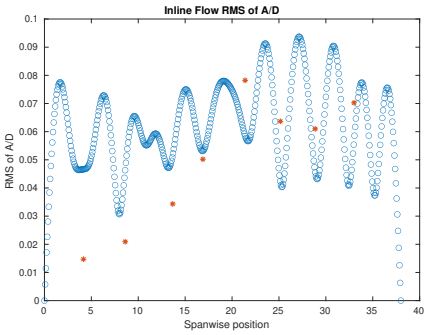

(b) Inline flow RMS profile case 7940.

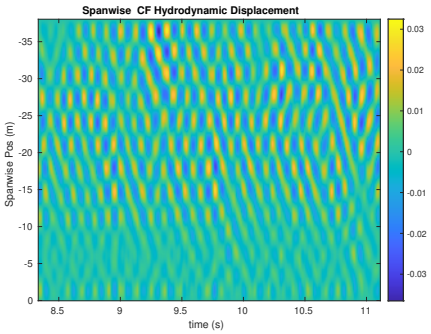

(c) Spanwise cross-flow hydrodynamic displacement case 7940.

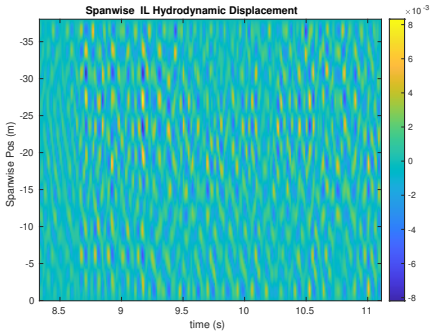

(d) Spanwise inline hydrodynamic displacement case 7940.

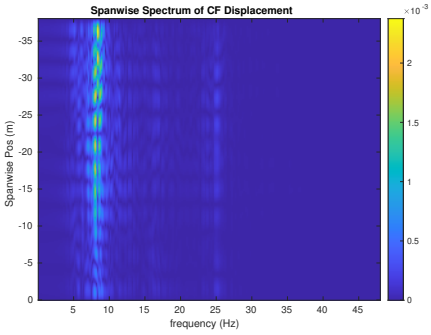

(e) Spanwise cross-flow spectrum of hydrodynamic displacement case 7940.

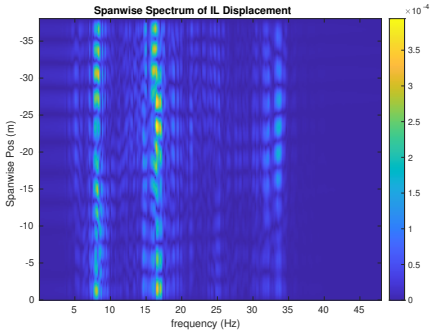

(f) Spanwise inline spectrum of hydrodynamic displacement case 7940.

Figure C-329: *Motion Analysis.* NDP Straight Riser ($L = 38m$) test case 7940.

NDP Straight Riser ($L = 38m$) test case 7950

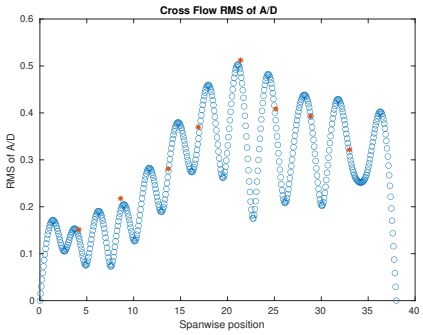

(a) Cross-flow RMS profile case 7950.

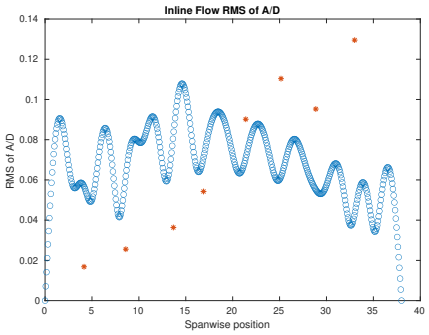

(b) Inline flow RMS profile case 7950.

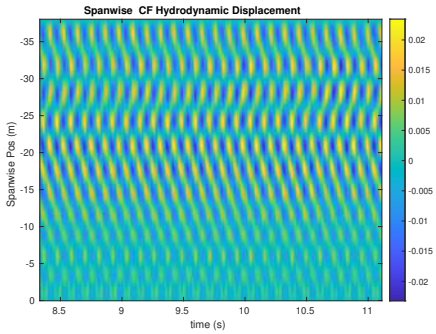

(c) Spanwise cross-flow hydrodynamic displacement case 7950.

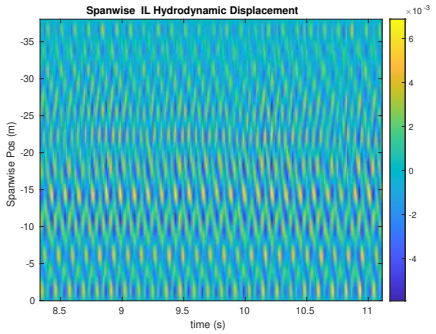

(d) Spanwise inline hydrodynamic displacement case 7950.

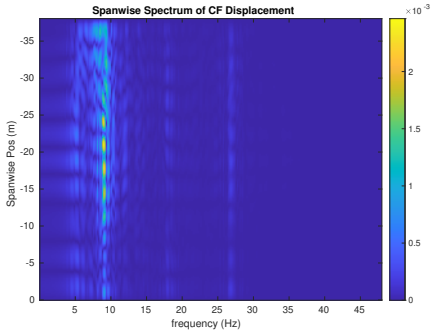

(e) Spanwise cross-flow spectrum of hydrodynamic displacement case 7950.

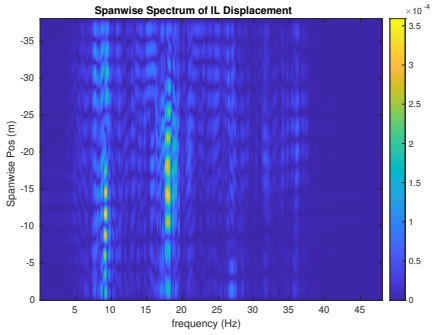

(f) Spanwise inline spectrum of hydrodynamic displacement case 7950.

Figure C-330: *Motion Analysis.* NDP Straight Riser ($L = 38m$) test case 7950.

NDP Straight Riser ($L = 38m$) test case 7960

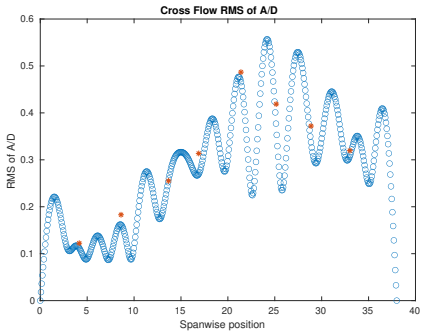

(a) Cross-flow RMS profile case 7960.

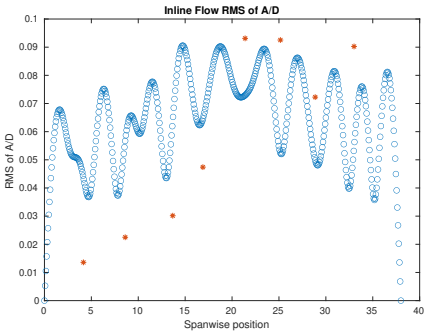

(b) Inline flow RMS profile case 7960.

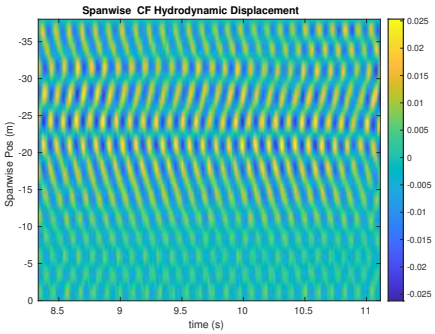

(c) Spanwise cross-flow hydrodynamic displacement case 7960.

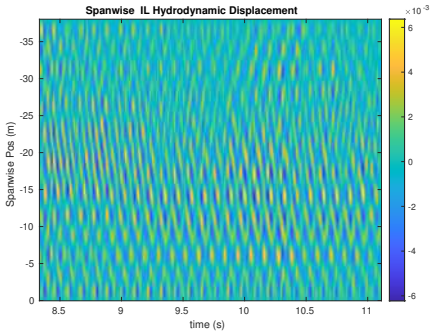

(d) Spanwise inline hydrodynamic displacement case 7960.

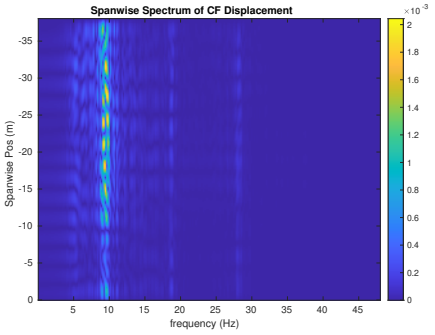

(e) Spanwise cross-flow spectrum of hydrodynamic displacement case 7960.

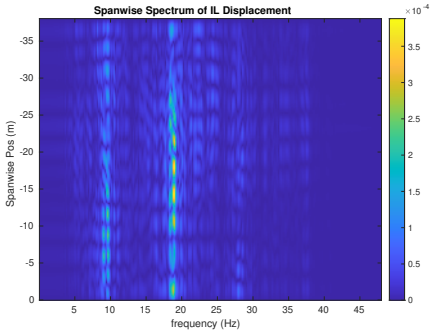

(f) Spanwise inline spectrum of hydrodynamic displacement case 7960.

Figure C-331: *Motion Analysis.* NDP Straight Riser ($L = 38m$) test case 7960.

NDP Straight Riser ($L = 38m$) test case 7970

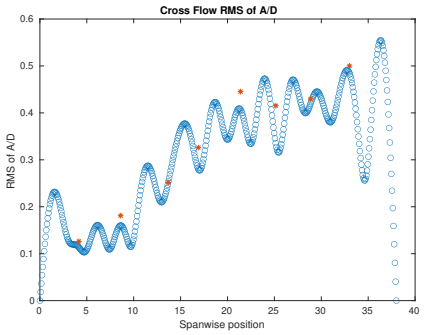

(a) Cross-flow RMS profile case 7970.

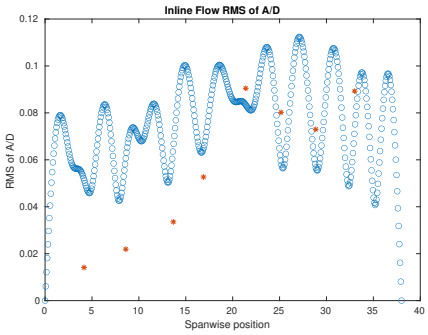

(b) Inline flow RMS profile case 7970.

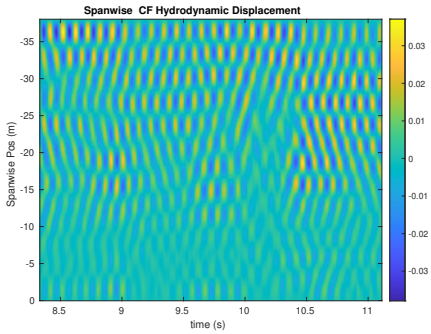

(c) Spanwise cross-flow hydrodynamic displacement case 7970.

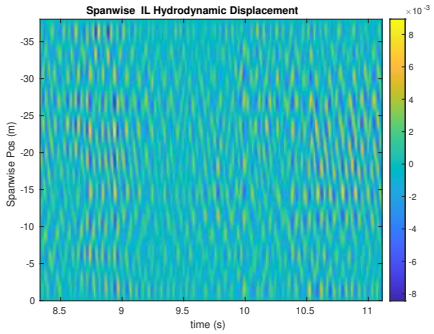

(d) Spanwise inline hydrodynamic displacement case 7970.

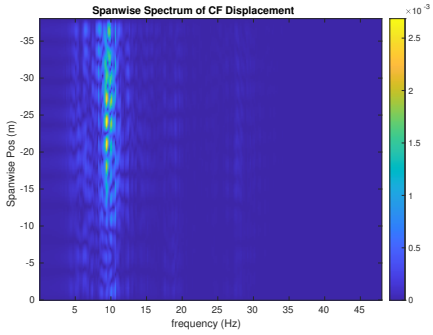

(e) Spanwise cross-flow spectrum of hydrodynamic displacement case 7970.

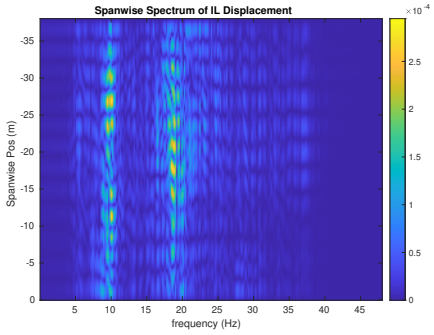

(f) Spanwise inline spectrum of hydrodynamic displacement case 7970.

Figure C-332: *Motion Analysis.* NDP Straight Riser ($L = 38m$) test case 7970.

NDP Straight Riser ($L = 38m$) test case 7980

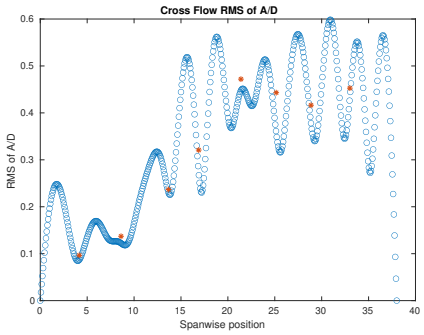

(a) Cross-flow RMS profile case 7980.

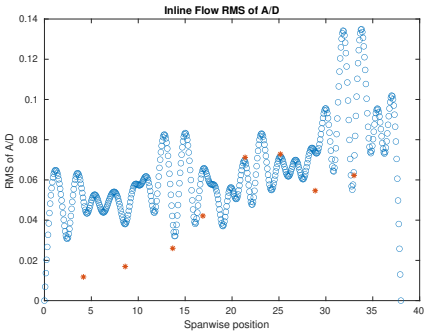

(b) Inline flow RMS profile case 7980.

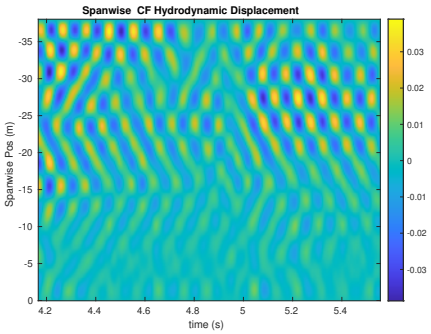

(c) Spanwise cross-flow hydrodynamic displacement case 7980.

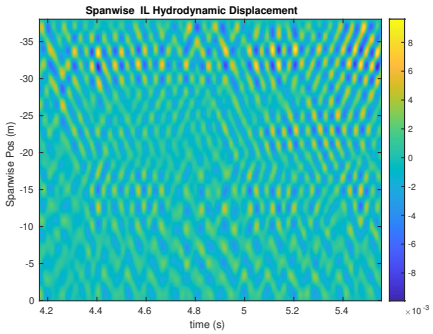

(d) Spanwise inline hydrodynamic displacement case 7980.

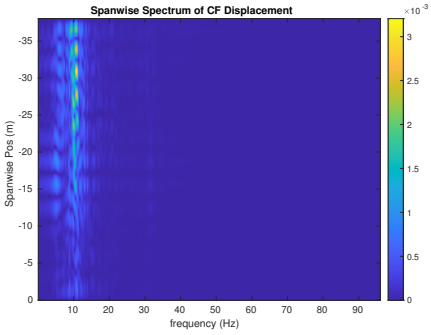

(e) Spanwise cross-flow spectrum of hydrodynamic displacement case 7980.

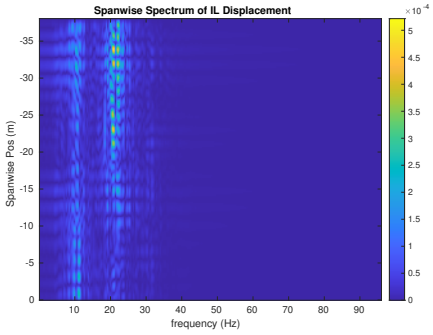

(f) Spanwise inline spectrum of hydrodynamic displacement case 7980.

Figure C-333: *Motion Analysis.* NDP Straight Riser ($L = 38m$) test case 7980.

NDP Straight Riser ($L = 38m$) test case 7990

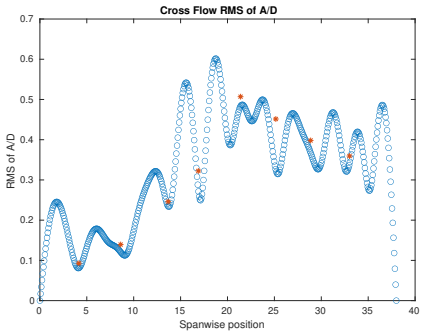

(a) Cross-flow RMS profile case 7990.

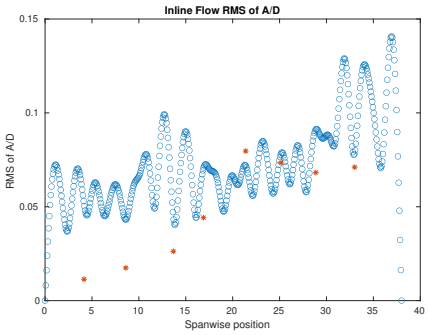

(b) Inline flow RMS profile case 7990.

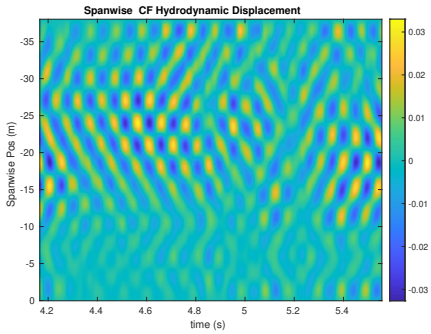

(c) Spanwise cross-flow hydrodynamic displacement case 7990.

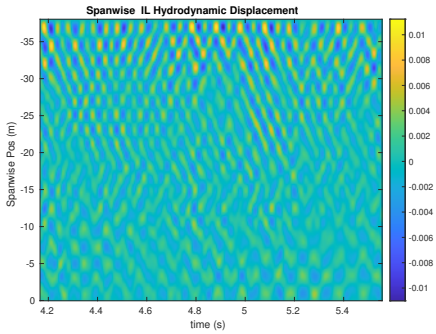

(d) Spanwise inline hydrodynamic displacement case 7990.

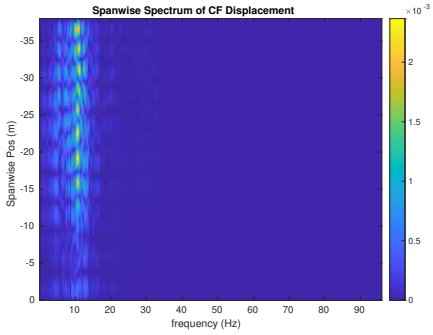

(e) Spanwise cross-flow spectrum of hydrodynamic displacement case 7990.

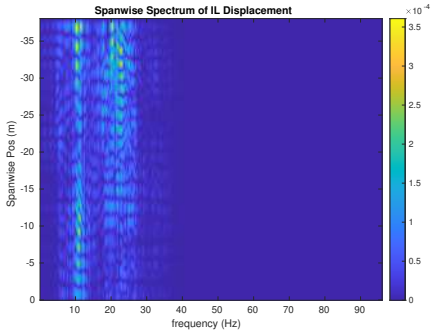

(f) Spanwise inline spectrum of hydrodynamic displacement case 7990.

Figure C-334: *Motion Analysis.* NDP Straight Riser ($L = 38m$) test case 7990.

NDP Straight Riser ($L = 38m$) test case 8000

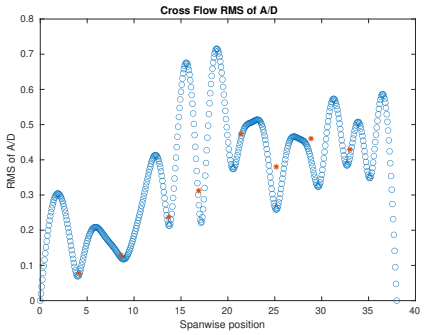

(a) Cross-flow RMS profile case 8000.

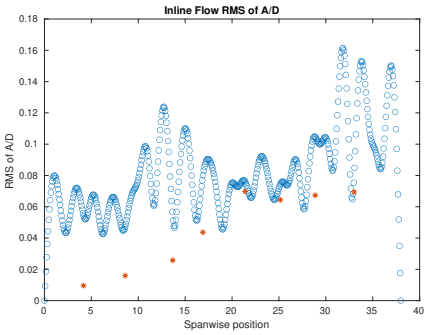

(b) Inline flow RMS profile case 8000.

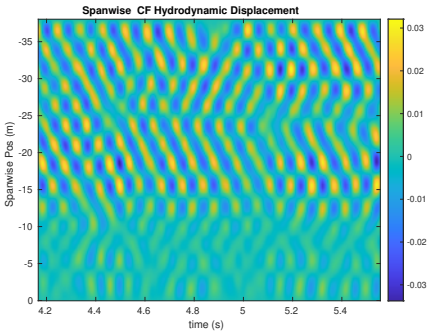

(c) Spanwise cross-flow hydrodynamic displacement case 8000.

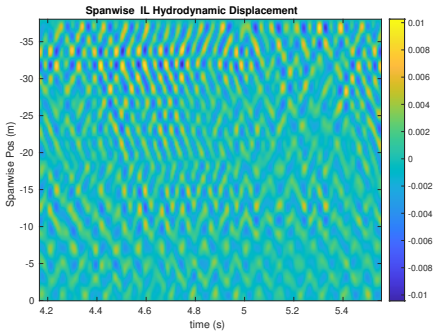

(d) Spanwise inline hydrodynamic displacement case 8000.

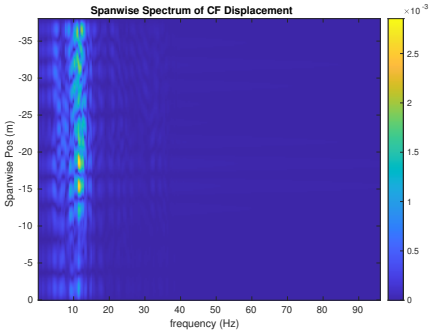

(e) Spanwise cross-flow spectrum of hydrodynamic displacement case 8000.

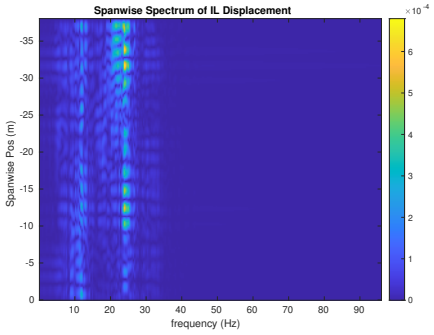

(f) Spanwise inline spectrum of hydrodynamic displacement case 8000.

Figure C-335: *Motion Analysis.* NDP Straight Riser ($L = 38m$) test case 8000.

NDP Straight Riser ($L = 38m$) test case 8010

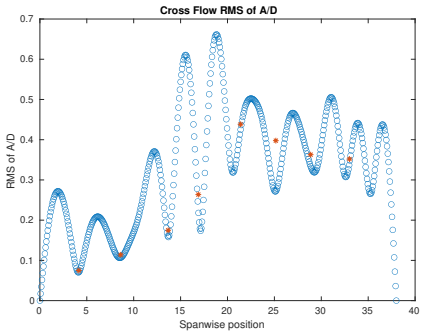

(a) Cross-flow RMS profile case 8010.

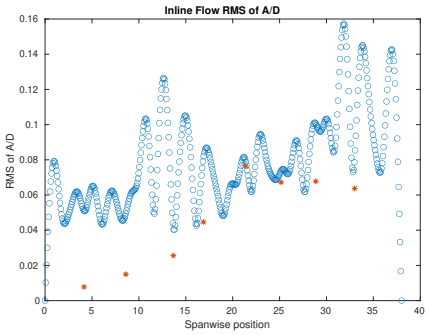

(b) Inline flow RMS profile case 8010.

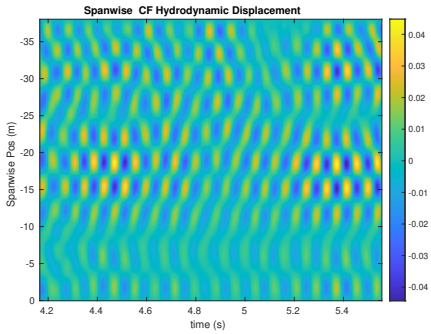

(c) Spanwise cross-flow hydrodynamic displacement case 8010.

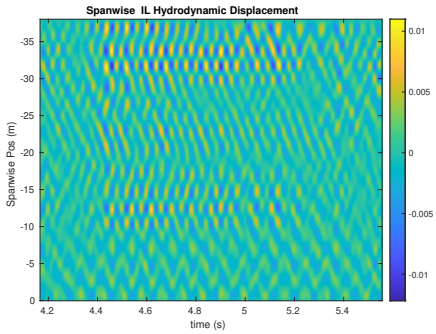

(d) Spanwise inline hydrodynamic displacement case 8010.

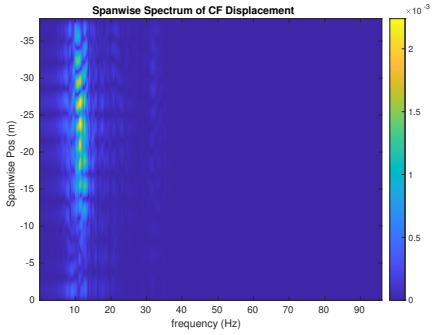

(e) Spanwise cross-flow spectrum of hydrodynamic displacement case 8010.

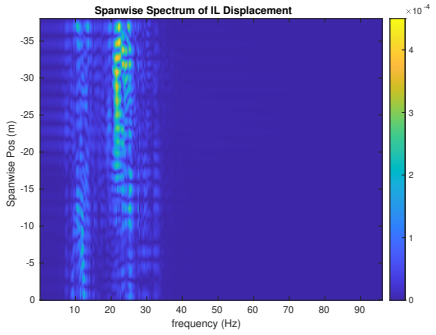

(f) Spanwise inline spectrum of hydrodynamic displacement case 8010.

Figure C-336: *Motion Analysis.* NDP Straight Riser ($L = 38m$) test case 8010.

NDP Straight Riser ($L = 38m$) test case 8020

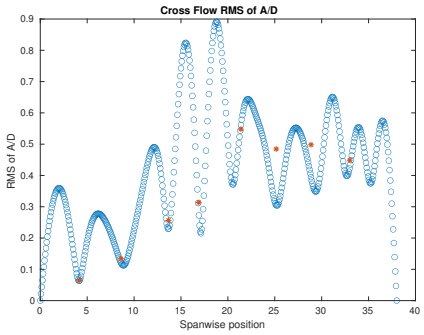

(a) Cross-flow RMS profile case 8020.

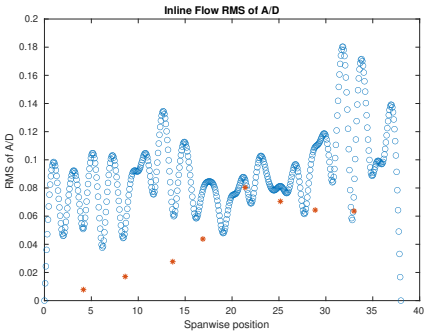

(b) Inline flow RMS profile case 8020.

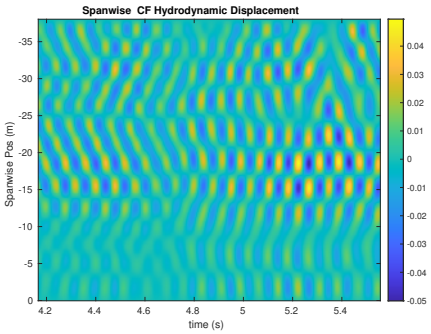

(c) Spanwise cross-flow hydrodynamic displacement case 8020.

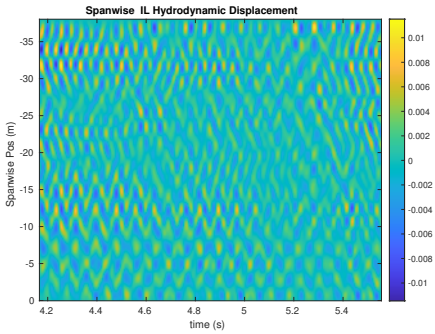

(d) Spanwise inline hydrodynamic displacement case 8020.

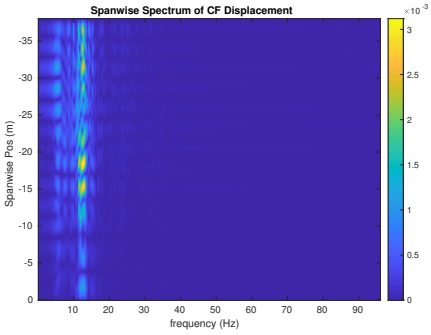

(e) Spanwise cross-flow spectrum of hydrodynamic displacement case 8020.

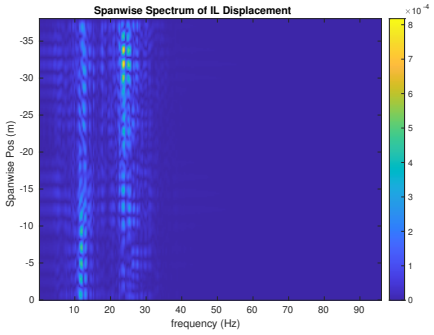

(f) Spanwise inline spectrum of hydrodynamic displacement case 8020.

Figure C-337: *Motion Analysis.* NDP Straight Riser ($L = 38m$) test case 8020.

NDP Straight Riser ($L = 38m$) test case 8030

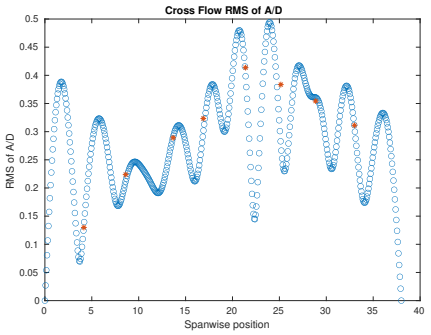

(a) Cross-flow RMS profile case 8030.

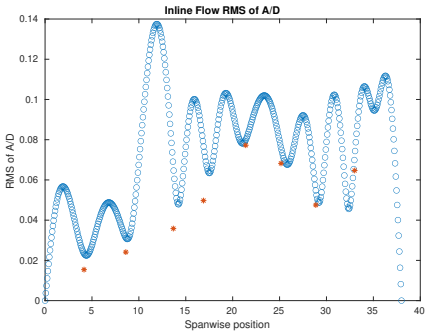

(b) Inline flow RMS profile case 8030.

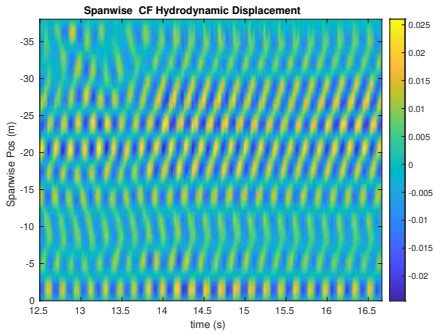

(c) Spanwise cross-flow hydrodynamic displacement case 8030.

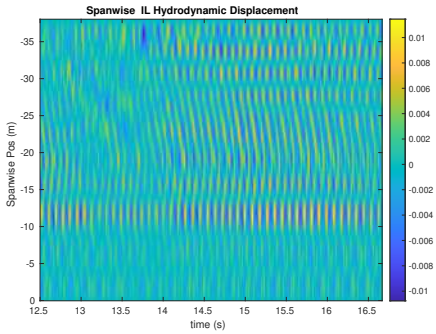

(d) Spanwise inline hydrodynamic displacement case 8030.

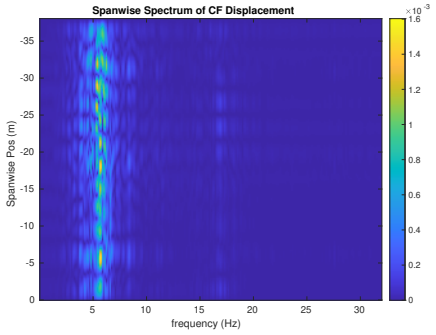

(e) Spanwise cross-flow spectrum of hydrodynamic displacement case 8030.

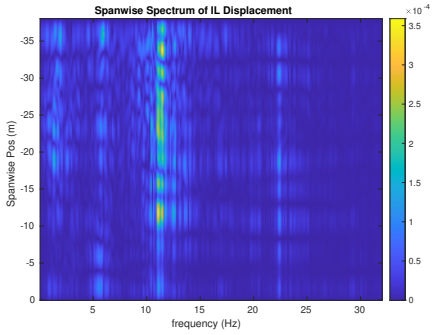

(f) Spanwise inline spectrum of hydrodynamic displacement case 8030.

Figure C-338: *Motion Analysis.* NDP Straight Riser ($L = 38m$) test case 8030.

NDP Straight Riser ($L = 38m$) test case 8040

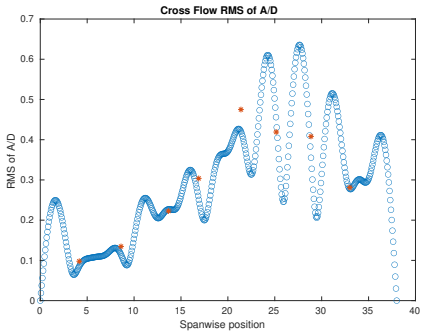

(a) Cross-flow RMS profile case 8040.

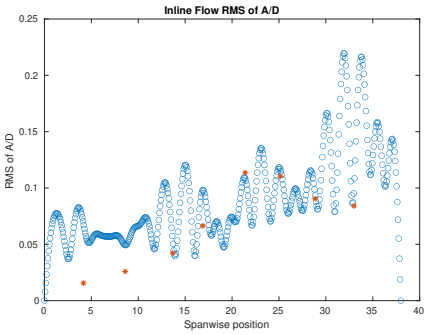

(b) Inline flow RMS profile case 8040.

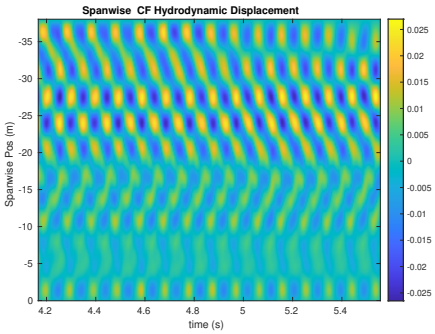

(c) Spanwise cross-flow hydrodynamic displacement case 8040.

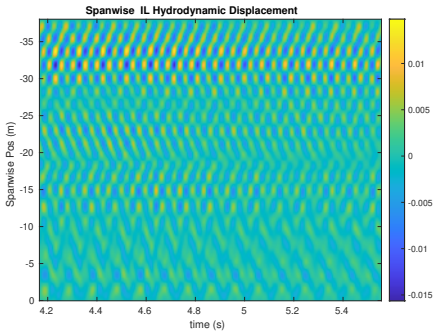

(d) Spanwise inline hydrodynamic displacement case 8040.

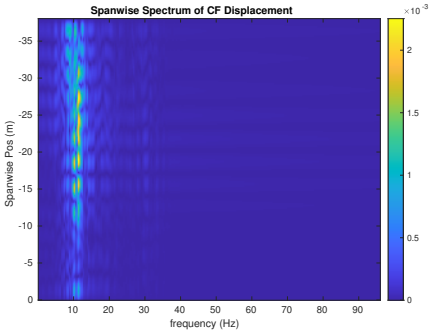

(e) Spanwise cross-flow spectrum of hydrodynamic displacement case 8040.

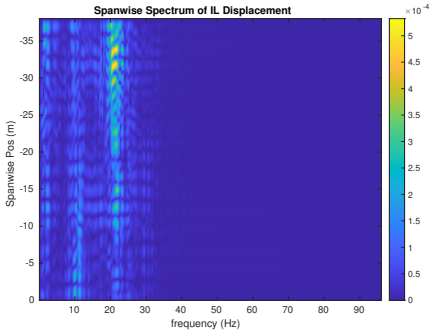

(f) Spanwise inline spectrum of hydrodynamic displacement case 8040.

Figure C-339: *Motion Analysis.* NDP Straight Riser ($L = 38m$) test case 8040.

Bibliography

[1] *Principles of Naval Architecture: Volume II - Resistance, Propulsion and Vibration.*

[2] *Vortex-Induced Vibration Analysis (VIVA) Based on Hydrodynamic Databases*, volume Volume 7: CFD and VIV; Offshore Geotechnics of *International Conference on Offshore Mechanics and Arctic Engineering*, 06 2011.

[3] Halil Hakan Açıkel, Melike Tosun, Mustafa Serdar Genç, and Kemal Koca. Numerical investigation on naca0012 airfoil with tubercular structure. In *EPJ Web of Conferences*, volume 269, page 01001. EDP Sciences, 2022.

[4] HE Ahmed, HA Mohammed, and Mohd Zamri Yusoff. An overview on heat transfer augmentation using vortex generators and nanofluids: approaches and applications. *Renewable and Sustainable Energy Reviews*, 16(8):5951–5993, 2012.

[5] Jose Henrique GM Alves, Michael L Banner, and Ian R Young. Revisiting the pierson–moskowitz asymptotic limits for fully developed wind waves. *Journal of physical oceanography*, 33(7):1301–1323, 2003.

[6] John Anderson. *EBOOK: Fundamentals of Aerodynamics (SI units)*. McGraw hill, 2011.

[7] Michael F Ashby, Hugh Shercliff, and David Cebon. *Materials: engineering, science, processing and design*. Butterworth-Heinemann, 2018.

[8] P Ashill, J Fulker, and K Hackett. Studies of flows induced by sub boundary layer vortex generators (sbvgs). In *40th AIAA aerospace sciences meeting & exhibit*, page 968, 2002.

[9] Bhanuprakash & Voonna Kiran Atreyapurapu, Krishna & Tallapragada. Simulation of a free surface flow over a container vessel using cfd. *Intl. Journal of Engineering Trends and Technology(IJETT)*, 2014.

[10] G.S. Baarholm, C.M. Larsen, and H. Lie. On fatigue damage accumulation from in-line and cross-flow vortex-induced vibrations on risers. *Journal of Fluids and Structures*, 22(1):109–127, 2006.

[11] Yong Bai and Qiang Bai. *Subsea pipelines and risers*, volume 3. Elsevier, 2005.

[12] Pierre Baldi and Peter J Sadowski. Understanding dropout. *Advances in neural information processing systems*, 26, 2013.

[13] ML Banner and DH Peregrine. Wave breaking in deep water. *Annual Review of Fluid Mechanics*, 25(1):373–397, 1993.

[14] Jewel B Barlow, William H Rae, and Alan Pope. *Low-speed wind tunnel testing*. John wiley & sons, 1999.

[15] Bryan Barrass and Capt DR Derrett. *Ship stability for masters and mates*. Elsevier, 2011.

[16] P W Bearman. Vortex shedding from oscillating bluff bodies. *Annual Review of Fluid Mechanics*, 16(1):195–222, 1984.

[17] DW Bechert, M Bruse, and W Hage. Experiments with three-dimensional riblets as an idealized model of shark skin. *Experiments in fluids*, 28(5):403–412, 2000.

[18] MJ Berger. Adaptive mesh refinement for hyperbolic conservation laws, 1995.

[19] V Bertram. Practical ship hydrodynamics. butterworthheinemann, 2000.

[20] Volker Bertram. *Practical ship hydrodynamics*. Elsevier, 2011.

[21] Adrian Biran and Rubén López-Pulido. *Ship hydrostatics and stability*. Butterworth-Heinemann, 2013.

[22] Christopher M Bishop and Nasser M Nasrabadi. *Pattern recognition and machine learning*, volume 4. Springer, 2006.

[23] Tuna Murat BODUR and Mustafa Serdar GENÇ. Numerical model and analysis of the application of tubercle structure to the nrel phase ii turbine blade.

[24] REMI BOURGUET, GEORGE E. KARNIADAKIS, and MICHAEL S. TRIANTAFYLLOU. Vortex-induced vibrations of a long flexible cylinder in shear flow. *Journal of Fluid Mechanics*, 677:342–382, 2011.

[25] Rémi Bourguet, George Em Karniadakis, and Michael S. Triantafyllou. Distributed lock-in drives broadband vortex-induced vibrations of a long flexible cylinder in shear flow. *Journal of Fluid Mechanics*, 717:361–375, 2013.

[26] Rémi Bourguet, Didier Lucor, and Michael S. Triantafyllou. Mono- and multi-frequency vortex-induced vibrations of a long tensioned beam in shear flow. *Journal of Fluids and Structures*, 32:52–64, 2012. The 7th International Symposium on Fluid-Structure Interactions, Flow-Sound Interactions, and Flow-Induced Vibrations Noise.

[27] Nathaniel Bowditch and Jonathan Ingersoll Bowditch. *New American Practical Navigator*. Number 9. US Government Printing Office, 1883.

[28] Henning Braaten and Halvor Lie. NDP riser high mode VIV tests. *Norwegian Marine Technology Research Institute, Technical Report*, (512394.00):01, 2004.

[29] Henning Braaten and Halvor Lie. Ndp riser high mode viv tests main report. *MARINTEK report, Trondheim, Norway*, 2005.

[30] Tobias Brandvik and Graham Pullan. Acceleration of a 3d euler solver using commodity graphics hardware. In *46th AIAA aerospace sciences meeting and exhibit*, page 607, 2008.

[31] Edgar Buckingham. On physically similar systems; illustrations of the use of dimensional equations. *Physical review*, 4(4):345, 1914.

[32] Richard L Burden. *Numerical analysis*. Brooks/Cole Cengage Learning, 2011.

[33] Lionel Casson. *Ships and seamanship in the ancient world*. JHU Press, 1995.

[34] Louis N Cattafesta III and Mark Sheplak. Actuators for active flow control. *Annual Review of Fluid Mechanics*, 43:247–272, 2011.

[35] L Cavaleri, J-HGM Alves, F Ardhuin, A Babanin, M Banner, K Belibassakis, M Benoit, M Donelan, J Groeneweg, THC Herbers, et al. Wave modelling–the state of the art. *Progress in oceanography*, 75(4):603–674, 2007.

[36] J.L. Cercos-Pita. Aquagpusph, a new free 3d sph solver accelerated with opencl. *Computer Physics Communications*, 192:295–312, 2015.

[37] Subrata Kumar Chakrabarti. *Hydrodynamics of offshore structures*. WIT press, 1987.

[38] J.R. Chaplin, P.W. Bearman, F.J. Huera Huarte, and R.J. Pattenden. Laboratory measurements of vortex-induced vibrations of a vertical tension riser in a stepped current. *Journal of Fluids and Structures*, 21(1):3–24, 2005. Fluid-Structure and Flow-Acoustic Interactions involving Bluff Bodies.

[39] J.R. Chaplin and R. King. Laboratory measurements of the vortex-induced vibrations of an untensioned catenary riser with high curvature. *Journal of Fluids and Structures*, 79:26–38, 2018.

[40] Steven C Chapra. *Numerical methods for engineers*. Mcgraw-hill, 2010.

[41] Ioannis K Chatjigeorgiou, Gilbert Damy, and Marc LeBoulluec. Numerical and experimental investigation on the dynamics of catenary risers and the riser-induced-damping phenomenon. In *International Conference on Offshore Mechanics and Arctic Engineering*, volume 48180, pages 671–680, 2008.

[42] Hongming Chen, Ola Engkvist, Yinhai Wang, Marcus Olivecrona, and Thomas Blaschke. The rise of deep learning in drug discovery. *Drug discovery today*, 23(6):1241–1250, 2018.

[43] T. Chen and H. Chen. Approximations of continuous functionals by neural networks with application to dynamic systems. *IEEE Transactions on Neural Networks*, 4(6):910–918, Nov 1993.

[44] Tianping Chen and Hong Chen. Universal approximation to nonlinear operators by neural networks with arbitrary activation functions and its application to dynamical systems. *IEEE Transactions on Neural Networks*, 6(4):911–917, 1995.

[45] L Chng, J Alber, D Ntouras, G Papadakis, N Kaufmann, P Ouro, and M Manolesos. On the combined use of vortex generators and gurney flaps for turbine airfoils. In *Journal of Physics: Conference Series*, volume 2265, page 032040. IOP Publishing, 2022.

[46] Kyunghyun Cho, Bart Van Merriënboer, Dzmitry Bahdanau, and Yoshua Bengio. On the properties of neural machine translation: Encoder-decoder approaches. *arXiv preprint arXiv:1409.1259*, 2014.

[47] Daniel Chung, Nicholas Hutchins, Michael P Schultz, and Karen A Flack. Predicting the drag of rough surfaces. *Annual Review of Fluid Mechanics*, 53:439–471, 2021.

[48] Luca Cortelezzi and Ann R Karagozian. On the formation of the counter-rotating vortex pair in transverse jets. *Journal of Fluid Mechanics*, 446:347–373, 2001.

[49] George Cybenko. Approximation by superpositions of a sigmoidal function. *Mathematics of control, signals and systems*, 2(4):303–314, 1989.

[50] J. M. DAHL, F. S. HOVER, M. S. TRIANTAFYLLOU, and O. H. OAKLEY. Dual resonance in vortex-induced vibrations at subcritical and supercritical reynolds numbers. *Journal of Fluid Mechanics*, 643:395–424, 2010.

[51] Thomas H Dawson. Offshore structural engineering. 1983.

[52] Robert G Dean and Robert A Dalrymple. *Water wave mechanics for engineers and scientists*, volume 2. world scientific publishing company, 1991.

[53] José del Águila Ferrandis, Stefano Brizzolara, and Chryssostomos Chryssostomidis. Influence of large hull deformations on the motion response of a fast catamaran craft with varying stiffness. *Ocean Engineering*, 163:207–222, 2018.

[54] José del Águila Ferrandis, Michael Triantafyllou, Chryssostomos Chryssostomidis, and George Karniadakis. Learning functionals via lstm neural networks for predicting vessel dynamics in extreme sea states. *arXiv preprint arXiv:1912.13382*, 2019.

[55] Samuel M Dollyhigh. Subsonic and supersonic longitudinal stability and control characteristics of an aft tail fighter configuration with cambered and uncambered wings and uncambered fuselage. Technical report, 1974.

[56] Pedro Domingos. A few useful things to know about machine learning. *Communications of the ACM*, 55(10):78–87, 2012.

[57] Jack Dongarra, Pete Beckman, Terry Moore, Patrick Aerts, Giovanni Aloisio, Jean-Claude Andre, David Barkai, Jean-Yves Berthou, Taisuke Boku, Bertrand Braunschweig, et al. The international exascale software project roadmap. *The international journal of high performance computing applications*, 25(1):3–60, 2011.

[58] James H Duncan. Spilling breakers. *Annual review of fluid mechanics*, 33(1):519–547, 2001.

[59] JH Duncan. An experimental investigation of breaking waves produced by a towed hydrofoil. *Proceedings of the Royal Society of London. A. Mathematical and Physical Sciences*, 377(1770):331–348, 1981.

[60] David Duvenaud. *Automatic model construction with Gaussian processes*. PhD thesis, University of Cambridge, 2014.

[61] First Edition, JMJ Journée, and WW Massie. Offshore hydromechanics. *Delft University of Technology*, 2001.

[62] Bradley Efron. Nonparametric standard errors and confidence intervals. *Canadian Journal of Statistics*, 9(2):139–158, 1981.

[63] Constantinos Evangelinos and George Em Karniadakis. Dynamics and flow structures in the turbulent wake of rigid and flexible cylinders subject to vortex-induced vibrations. *Journal of fluid mechanics*, 400:91–124, 1999.

[64] M.L. Facchinetti, E. de Langre, and F. Biolley. Coupling of structure and wake oscillators in vortex-induced vibrations. *Journal of Fluids and Structures*, 19(2):123–140, 2004.

[65] J. Falnes and A. Kurniawan. *Ocean Waves and Oscillating Systems: Linear Interactions Including Wave-Energy Extraction*. Cambridge Ocean Technology Series. Cambridge University Press, 2020.

[66] Odd Faltinsen. *Sea loads on ships and offshore structures*, volume 1. Cambridge university press, 1993.

[67] Dixia Fan, Zhicheng Wang, Michael Triantafyllou, et al. Mapping the properties of the vortex-induced vibrations of flexible cylinders in uniform oncoming flow. *Journal of Fluid Mechanics*, page to be appear, 2019.

[68] A. Farshidianfar and H. Zanganeh. A modified wake oscillator model for vortex-induced vibration of circular cylinders for a wide range of mass-damping ratio. *Journal of Fluids and Structures*, 26(3):430–441, 2010.

[69] CC Feng. *The measurement of vortex induced effects in flow past stationary and oscillating circular and D-section cylinders*. PhD thesis, University of British Columbia, 1968.

[70] John D Fenton. A fifth-order stokes theory for steady waves. *Journal of waterway, port, coastal, and ocean engineering*, 111(2):216–234, 1985.

[71] José del Águila Ferrandis, Luca Bonfiglio, Ricardo Zamora Rodríguez, Chryssostomos Chryssostomidis, Odd Magnus Faltinsen, and Michael Triantafyllou. Influence of Viscosity and Non-Linearities in Predicting Motions of a Wind Energy Offshore Platform in Regular Waves. *Journal of Offshore Mechanics and Arctic Engineering*, 142(6), 05 2020. 062003.

[72] Joel H Ferziger and Milovan Perić. *Computational methods for fluid dynamics*, volume 3. Springer, 2002.

[73] Alexander Forrester, Andras Sobester, and Andy Keane. *Engineering design via surrogate modelling: a practical guide*. John Wiley & Sons, 2008.

[74] George Z Forristall. Wave crest distributions: Observations and second-order theory. *Journal of physical oceanography*, 30(8):1931–1943, 2000.

[75] T.I. Fossen. *Marine Control Systems: Guidance, Navigation and Control of Ships, Rigs and Underwater Vehicles*. Marine Cybernetics, 2002.

[76] Willa France, Marc Levadou, Thomas Treakle, J.R. Paulling, R. Michel, and Colin Moore. An investigation of head-sea parametric rolling and its influence on container lashing systems. *Marine Technology*, 40:1–19, 01 2003.

[77] William N France, Marc Levadou, Thomas W Treakle, J Randolph Paulling, R Keith Michel, and Colin Moore. An investigation of head-sea parametric rolling and its influence on container lashing systems. *Marine Technology and SNAME news*, 40(01):1–19, 2003.

[78] Peter I Frazier. A tutorial on bayesian optimization. *arXiv preprint arXiv:1807.02811*, 2018.

[79] Robert Edmund Froude. On the part played in propulsion by differences of fluid pressure. *Trans. Inst. Naval Architects*, 30:390, 1889.

[80] William Froude. On the rolling of ships. *2nd Session of the Institution of Naval Architects, March 1861*, 1861.

[81] Mohamed Gad-el Hak. Flow control: The future. *Journal of aircraft*, 38(3):402–418, 2001.

[82] Yarin Gal and Zoubin Ghahramani. Dropout as a bayesian approximation: Representing model uncertainty in deep learning. In *international conference on machine learning*, pages 1050–1059. PMLR, 2016.

[83] Yun Gao, Shixiao Fu, Jungao Wang, Leijian Song, and Yifan Chen. Experimental study of the effects of surface roughness on the vortex-induced vibration response of a flexible cylinder. *Ocean Engineering*, 103:40–54, 2015.

[84] B Gaspar, AP Teixeira, and C Guedes Soares. Effect of the nonlinear vertical wave-induced bending moments on the ship hull girder reliability. *Ocean Engineering*, 119:193–207, 2016.

[85] Ersegun D. Gedikli, David Chelidze, and Jason M. Dahl. Observed mode shape effects on the vortex-induced vibration of bending dominated flexible cylinders simply supported at both ends. *Journal of Fluids and Structures*, 81:399–417, 2018.

[86] Ersegun D. Gedikli, Jason M. Dahl, and David Chelidze. Multivariate analysis of vortex-induced vibrations in a tensioned cylinder reveal nonlinear modal interactions. *Procedia Engineering*, 199:546–551, 2017. X International Conference on Structural Dynamics, EURODYN 2017.

[87] Aurélien Géron. *Hands-on machine learning with Scikit-Learn and TensorFlow: concepts, tools, and techniques to build intelligent systems.* " O'Reilly Media, Inc.", 2017.

[88] Thomas Gerz, Frank Holzäpfel, and Denis Darracq. Commercial aircraft wake vortices. *Progress in Aerospace Sciences*, 38(3):181–208, 2002.

[89] Laurent YM Gicquel, N Gourdain, J-F Boussuge, H Deniau, G Staffelbach, P Wolf, and Thierry Poinsot. High performance parallel computing of flows in complex geometries. *Comptes Rendus Mécanique*, 339(2-3):104–124, 2011.

[90] Gilles Godard and Michel Stanislas. Control of a decelerating boundary layer. part 1: Optimization of passive vortex generators. *Aerospace Science and Technology*, 10(3):181–191, 2006.

[91] Sergueï Konstantinovitch Godunov. A difference method for numerical calculation of discontinuous equations of hydrodynamics. *Math. Sb*, 47:217, 1959.

[92] Ian Goodfellow, Yoshua Bengio, and Aaron Courville. *Deep learning*. MIT press, 2016.

[93] David Greenblatt and Israel J Wygnanski. The control of flow separation by periodic excitation. *Progress in aerospace Sciences*, 36(7):487–545, 2000.

[94] Bingjie Guo, Elzbieta M Bitner-Gregersen, Hui Sun, and Jens Bloch Helmers. Statistics analysis of ship response in extreme seas. *Ocean Engineering*, 119:154–164, 2016.

[95] Hercules Haralambides. Globalization, public sector reform, and the role of ports in international supply chains, 2017.

[96] Klaus Hasselmann, Tim P Barnett, E Bouws, H Carlson, David E Cartwright, K Enke, JA Ewing, A Gienapp, DE Hasselmann, P Kruseman, et al. Measurements of wind-wave growth and swell decay during the joint north sea wave project (jonswap). *Ergaenzungsheft zur Deutschen Hydrographischen Zeitschrift, Reihe A*, 1973.

[97] Catherine Hetherington, Rhona Flin, and Kathryn Mearns. Safety in shipping: The human element. *Journal of safety research*, 37(4):401–411, 2006.

[98] SEandtemarel Hirdaris and P Temarel. Hydroelasticity of ships: recent advances and future trends. *Proceedings of the Institution of Mechanical Engineers, Part M: Journal of Engineering for the Maritime Environment*, 223(3):305–330, 2009.

[99] Cyril W Hirt and Billy D Nichols. Volume of fluid (vof) method for the dynamics of free boundaries. *Journal of computational physics*, 39(1):201–225, 1981.

[100] Sepp Hochreiter and Jürgen Schmidhuber. Long short-term memory. *Neural computation*, 9(8):1735–1780, 1997.

[101] Leo H Holthuijsen. *Waves in oceanic and coastal waters*. Cambridge university press, 2010.

[102] Kurt Hornik. Approximation capabilities of multilayer feedforward networks. *Neural networks*, 4(2):251–257, 1991.

[103] Kurt Hornik, Maxwell Stinchcombe, and Halbert White. Multilayer feedforward networks are universal approximators. *Neural networks*, 2(5):359–366, 1989.

[104] FS Hover and MS Triantafyllou. Linear dynamics of curved tensioned elastic beams. *Journal of sound and vibration*, 4(228):923–930, 1999.

[105] Hong-bo Huang, Yun Long, and Bin Ji. Experimental investigation of vortex generator influences on propeller cavitation and hull pressure fluctuations. *Journal of Hydrodynamics*, 32:82–92, 2020.

[106] Yifeng Huang and Paul D Sclavounos. Nonlinear ship motions. *Journal of Ship Research*, 42(02):120–130, 1998.

[107] F.J. Huera-Huarte and P.W. Bearman. Wake structures and vortex-induced vibrations of a long flexible cylinder—part 1: Dynamic response. *Journal of Fluids and Structures*, 25(6):969–990, 2009.

[108] Owen F Hughes. Ship structural design: a rationally-based, computer-aided, optimization approach. *(No Title)*, 1983.

[109] Thomas JR Hughes. *The finite element method: linear static and dynamic finite element analysis*. Courier Corporation, 2012.

[110] Kazuhiro Iijima, Tetsuya Yao, and Torgeir Moan. Structural response of a ship in severe seas considering global hydroelastic vibrations. *Marine structures*, 21(4):420–445, 2008.

[111] Sergey Ioffe and Christian Szegedy. Batch normalization: Accelerating deep network training by reducing internal covariate shift. In *International conference on machine learning*, pages 448–456. pmlr, 2015.

[112] ITTC ITTC. Recommended procedures and guidelines. *Resistance Test*, 2011.

[113] Anil Jain and Yahya Modarres-Sadeghi. Vortex-induced vibrations of a flexibly-mounted inclined cylinder. *Journal of Fluids and Structures*, 43:28–40, 2013.

[114] Adam Jirasek. Vortex-generator model and its application to flow control. *Journal of Aircraft*, 42(6):1486–1491, 2005.

[115] Gye-Wan Jo. The need for international policy regarding lost containers at sea for reducing marine plastic litter. *Journal of International Maritime Safety, Environmental Affairs, and Shipping*, 4(3):80–83, 2020.

[116] KD Jones, CM Dohring, and MF Platzer. Experimental and computational investigation of the knoller-betz effect. *AIAA journal*, 36(7):1240–1246, 1998.

[117] Yukio Kaneda and Takashi Ishihara. High-resolution direct numerical simulation of turbulence. *Journal of Turbulence*, (7):N20, 2006.

[118] Eirini Katsidoniotaki, Erik Nilsson, Anna Rutgersson, Jens Engström, and Malin Göteman. Response of point-absorbing wave energy conversion system in 50-years return period extreme focused waves. *Journal of Marine Science and Engineering*, 9(3), 2021.

[119] Nitish Shirish Keskar, Dheevatsa Mudigere, Jorge Nocedal, Mikhail Smelyanskiy, and Ping Tak Peter Tang. On large-batch training for deep learning: Generalization gap and sharp minima. *arXiv preprint arXiv:1609.04836*, 2016.

[120] Salman Khan, Muzammal Naseer, Munawar Hayat, Syed Waqas Zamir, Fahad Shahbaz Khan, and Mubarak Shah. Transformers in vision: A survey. *ACM computing surveys (CSUR)*, 54(10s):1–41, 2022.

[121] Christian Kharif and Efim Pelinovsky. Physical mechanisms of the rogue wave phenomenon. *European Journal of Mechanics-B/Fluids*, 22(6):603–634, 2003.

[122] Kyoung Kim, E Powers, C Ritz, R Miksad, and F Fischer. Modeling of the nonlinear drift oscillations of moored vessels subject to non-gaussian random sea-wave excitation. *IEEE journal of oceanic engineering*, 12(4):568–575, 1987.

[123] W-J Kim, JA Newlin, and JH Haws. Experimental and analytical investigation of soil/scr interaction under viv. In *The Sixteenth International Offshore and Polar Engineering Conference*. OnePetro, 2006.

[124] R. King. Vortex Excited Oscillations of Yawed Circular Cylinders. *Journal of Fluids Engineering*, 99(3):495–501, 09 1977.

[125] George Klir and Mark Wierman. *Uncertainty-based information: elements of generalized information theory*, volume 15. Springer Science & Business Media, 1999.

[126] Tamara G Kolda, Robert Michael Lewis, and Virginia Torczon. Optimization by direct search: New perspectives on some classical and modern methods. *SIAM review*, 45(3):385–482, 2003.

[127] J Zico Kolter and Gaurav Manek. Learning stable deep dynamics models. In *Advances in Neural Information Processing Systems*, pages 11128–11136, 2019.

[128] Gerbrand J Komen, Luigi Cavaleri, Mark Donelan, Klaus Hasselmann, S Hasselmann, and PAEM Janssen. *Dynamics and modelling of ocean waves*. 1996.

[129] Sotiris B Kotsiantis, Ioannis D Zaharakis, and Panayiotis E Pintelas. Machine learning: a review of classification and combining techniques. *Artificial Intelligence Review*, 26:159–190, 2006.

[130] Vladik Ya Kreinovich. Arbitrary nonlinearity is sufficient to represent all functions by neural networks: a theorem. *Neural networks*, 4(3):381–383, 1991.

[131] Ilan Kroo. Nonplanar wing concepts for increased aircraft efficiency. *VKI lecture series on innovative configurations and advanced concepts for future civil aircraft*, 2005.

[132] Solomon Kullback and Richard A Leibler. On information and sufficiency. *The annals of mathematical statistics*, 22(1):79–86, 1951.

[133] Pijush K Kundu, Ira M Cohen, and David R Dowling. *Fluid mechanics*. Academic press, 2015.

[134] Gustav Victor Lachmann. *Boundary layer and flow control: its principles and application*. Elsevier, 2014.

[135] Horace Lamb. *Hydrodynamics*. University Press, 1924.

[136] Carl M Larsen, Kyrre Vikestad, Rune Yttervik, Elizabeth Passano, and GS Baarholm. Vivana theory manual. *Marintek, Trondheim, Norway*, 2001.

[137] Lars Larsson. Ship resistance and flow. *Published by The Society of Naval Architects and Marine Engineers, SNAME, The Principles of Naval Architecture Series, ISBN: 978-0-939773-76-3*, 2010.

[138] Patrick Le Tallec and Jean Mouro. Fluid structure interaction with large structural displacements. *Computer methods in applied mechanics and engineering*, 190(24-25):3039–3067, 2001.

[139] Eun-Sug Lee, Damien Violeau, Réza Issa, and Stéphane Ploix. Application of weakly compressible and truly incompressible sph to 3-d water collapse in waterworks. *Journal of Hydraulic research*, 48(sup1):50–60, 2010.

[140] Randall J LeVeque. *Finite volume methods for hyperbolic problems*, volume 31. Cambridge university press, 2002.

[141] Edward M Lewandowski. Multi-vessel seakeeping computations with linear potential theory. *Ocean engineering*, 35(11-12):1121–1131, 2008.

[142] E.V. Lewis, Society of Naval Architects, Marine Engineers (U.S.), and Knovel (Firm). *Principles of Naval Architecture: Motions in waves and controllability*. Principles of Naval Architecture. Society of Naval Architects and Marine Engineers, 1988.

[143] Shuang Li, Lei Zhang, Jin Xu, Ke Yang, Juanjuan Song, and Guangxing Guo. Experimental investigation of a pitch-oscillating wind turbine airfoil with vortex generators. *Journal of Renewable and Sustainable Energy*, 12(6), 2020.

[144] Robert H Liebeck. Design of subsonic airfoils for high lift. *Journal of aircraft*, 15(9):547–561, 1978.

[145] MJ Lighthill. Physical interpretation of the mathematical theory of wave generation by wind. *Journal of Fluid Mechanics*, 14(3):385–398, 1962.

[146] John Lin, F Howard, and G Selby. Exploratory study of vortex-generating devices for turbulent flow separation control. In *29th aerospace sciences meeting*, page 42, 1991.

[147] John C Lin. Review of research on low-profile vortex generators to control boundary-layer separation. *Progress in aerospace sciences*, 38(4-5):389–420, 2002.

[148] Tianyang Lin, Yuxin Wang, Xiangyang Liu, and Xipeng Qiu. A survey of transformers. *AI Open*, 2022.

[149] Julia Ling, Andrew Kurzawski, and Jeremy Templeton. Reynolds averaged turbulence modelling using deep neural networks with embedded invariance. *Journal of Fluid Mechanics*, 807:155–166, 2016.

[150] MB Liu and GR2593940 Liu. Smoothed particle hydrodynamics (sph): an overview and recent developments. *Archives of computational methods in engineering*, 17:25–76, 2010.

[151] Tingting Liu, Hongfu Zhang, and Dabo Xin. Experimental study on mitigating extreme roof suctions by passive vortex generators. *Journal of Wind Engineering and Industrial Aerodynamics*, 219:104807, 2021.

[152] Rainald Löhner. An adaptive finite element solver for transient problems with moving bodies. In *Computational Structural Mechanics & Fluid Dynamics*, pages 303–317. Elsevier, 1988.

[153] Michael S Longuet-Higgins. The effect of non-linearities on statistical distributions in the theory of sea waves. *Journal of fluid mechanics*, 17(3):459–480, 1963.

[154] Michael S Longuet-Higgins and RW Stewart. Radiation stress and mass transport in gravity waves, with application to 'surf beats'. *Journal of Fluid Mechanics*, 13(4):481–504, 1962.

[155] Chung-Long Lu. *Three-dimensional flexural and torsional mechanics of low and high tension cables*. University of Michigan, 1994.

[156] Lu Lu, Pengzhan Jin, and George Em Karniadakis. Deeponet: Learning nonlinear operators for identifying differential equations based on the universal approximation theorem of operators. *arXiv preprint arXiv:1910.03193*, 2019.

[157] Kwan-Liu Ma and David M Camp. High performance visualization of time-varying volume data over a wide-area network. In *SC'00: Proceedings of the 2000 ACM/IEEE Conference on Supercomputing*, pages 29–29. IEEE, 2000.

[158] ZH Ma, DM Causon, L Qian, HB Gu, CG Mingham, and P Martinez Ferrer. A gpu based compressible multiphase hydrocode for modelling violent hydrodynamic impact problems. *Computers & Fluids*, 120:1–23, 2015.

[159] Fabricio Macia, Leo M González, Jose L Cercos-Pita, and Antonio Souto-Iglesias. A boundary integral sph formulation: consistency and applications to isph and wcsph. *Progress of Theoretical Physics*, 128(3):439–462, 2012.

[160] Alaa Mansour, Donald Liu, and J Randolph Paulling. The principles of naval architecture series. *Jersey City, NJ: The Society of Naval Architects and Marine Engineers*, 2008.

[161] Ricardo A Maronna, R Douglas Martin, Victor J Yohai, and Matías Salibián-Barrera. *Robust statistics: theory and methods (with R)*. John Wiley & Sons, 2019.

[162] Hajime Maruo. The excess resistance of a ship in rough seas. *International Shipbuilding Progress*, 4(35):337–345, 1957.

[163] Hajime Maruo. Calculation of the wave resistance of ships, the draught of which is as small as the beam. *Journal of Zosen Kiokai*, 1962(112):21–37, 1962.

[164] Hajime Maruo and Jun-ichi Matsumura. Ship waves and wave-resistance in a viscous fluid. *Journal of the Society of Naval Architects of Japan*, 1973(134):15–29, 1973.

[165] Barnes Warnock McCormick. *Aerodynamics of V/STOL flight*. Courier Corporation, 1999.

[166] Chiang C Mei. *The applied dynamics of ocean surface waves*, volume 1. World scientific, 1989.

[167] Xuhui Meng and George Em Karniadakis. A composite neural network that learns from multi-fidelity data: Application to function approximation and inverse pde problems. *Journal of Computational Physics*, 401:109020, 2020.

[168] Xuhui Meng, Liu Yang, Zhiping Mao, José del Águila Ferrandis, and George Em Karniadakis. Learning functional priors and posteriors from data and physics. *Journal of Computational Physics*, 457:111073, 2022.

[169] Florian R Menter. Two-equation eddy-viscosity turbulence models for engineering applications. *AIAA journal*, 32(8):1598–1605, 1994.

[170] John W Miles. On the generation of surface waves by shear flows. *Journal of Fluid Mechanics*, 3(2):185–204, 1957.

[171] A. MILIOU, A. DE VECCHI, S. J. SHERWIN, and J. M. R. GRAHAM. Wake dynamics of external flow past a curved circular cylinder with the free stream aligned with the plane of curvature. *Journal of Fluid Mechanics*, 592:89–115, 2007.

[172] Rajat Mittal and Parviz Moin. Suitability of upwind-biased finite difference schemes for large-eddy simulation of turbulent flows. *AIAA journal*, 35(8):1415–1417, 1997.

[173] Y Modarres-Sadeghi, F Chasparis, MS Triantafyllou, M Tognarelli, and P Beynet. Chaotic response is a generic feature of vortex-induced vibrations of flexible risers. *Journal of Sound and Vibration*, 330(11):2565–2579, 2011.

[174] Joe J Monaghan. Smoothed particle hydrodynamics. *Annual review of astronomy and astrophysics*, 30(1):543–574, 1992.

[175] Bittagopal Mondal, Carlos F Lopez, Ankit Verma, and Partha P Mukherjee. Vortex generators for active thermal management in lithium-ion battery systems. *International Journal of Heat and Mass Transfer*, 124:800–815, 2018.

[176] TL Morse and CHK Williamson. The effect of reynolds number on the critical mass phenomenon in vortex-induced vibration. *Physics of Fluids*, 21(4):045105, 2009.

[177] Hanns Mueller-Vahl, Georgios Pechlivanoglou, CN Nayeri, and CO Paschereit. Vortex generators for wind turbine blades: A combined wind tunnel and wind turbine parametric study. In *Turbo Expo: Power for Land, Sea, and Air*, volume 44724, pages 899–914. American Society of Mechanical Engineers, 2012.

[178] Harish Mukundan. *Vortex-induced vibration of marine risers: motion and force reconstruction from field and experimental data*. PhD thesis, Massachusetts Institute of Technology, 2008.

[179] Augustus Taber Murray et al. *The Odyssey*, volume 1. Harvard University Press, 1927.

[180] Radford M Neal. *Bayesian learning for neural networks*, volume 118. Springer Science & Business Media, 2012.

[181] Marcelo AS Neves and Claudio A Rodriguez. On unstable ship motions resulting from strong non-linear coupling. *Ocean Engineering*, 33(14-15):1853–1883, 2006.

[182] DAVID J. NEWMAN and GEORGE EM KARNIADAKIS. A direct numerical simulation study of flow past a freely vibrating cable. *Journal of Fluid Mechanics*, 344:95–136, 1997.

[183] John Nicholas Newman. *Marine hydrodynamics*. The MIT press, 2018.

[184] Andrew Y Ng. Feature selection, l 1 vs. l 2 regularization, and rotational invariance. In *Proceedings of the twenty-first international conference on Machine learning*, page 78, 2004.

[185] Ji ning Song, Lin Lu, Bin Teng, Han il Park, Guo qiang Tang, and Hao Wu. Laboratory tests of vortex-induced vibrations of a long flexible riser pipe subjected to uniform flow. *Ocean Engineering*, 38(11):1308–1322, 2011.

[186] Jorge Nocedal and Stephen J Wright. *Numerical optimization*. Springer, 1999.

[187] Michel K Ochi. Wave statistics for the design of ships and ocean structures. Technical report, 1978.

[188] Michel K Ochi. *Ocean waves*. 1998.

[189] Luca Oggiano, Fabio Pierella, Tor Anders Nygaard, Jacobus De Vaal, and Emile Arens. Comparison of experiments and cfd simulations of a braceless concrete semi-submersible platform. *Energy Procedia*, 94:278–289, 2016.

[190] T Francis Ogilvie. Recent progress toward the understanding and prediction of ship motions. In *David W. Taylor Model Basin, Washington DC, USA, Presented at: Proceedings of the 5th Symposium on Naval Hydrodynamics, Bergen, Norway, pp. 3-80*, 1964.

[191] M. Onorato, A. R. Osborne, M. Serio, L. Cavaleri, C. Brandini, and C. T. Stansberg. Observation of strongly non-gaussian statistics for random sea surface gravity waves in wave flume experiments. *Phys. Rev. E*, 70:067302, Dec 2004.

[192] Alfred R Osborne. Nonlinear ocean wave and the inverse scattering transform. In *Scattering*, pages 637–666. Elsevier, 2002.

[193] John D Owens, Mike Houston, David Luebke, Simon Green, John E Stone, and James C Phillips. Gpu computing. *Proceedings of the IEEE*, 96(5):879–899, 2008.

[194] Apostolos Papanikolaou. Holistic ship design optimization. *Computer-Aided Design*, 42(11):1028–1044, 2010.

[195] Apostolos Papanikolaou, Nikos Fournarakis, Dionysia Chroni, Shukui Liu, Timoleon Plessas, and Florian Sprenger. Simulation of the maneuvering behavior of ships in adverse weather conditions. In *Proceedings*, pages 11–16, 2016.

[196] Hector G Parra, Hernan D Ceron, William Gomez, and Elvis E Gaona. Experimental analysis of bio-inspired vortex generators on a blade with s822 airfoil. *Energies*, 16(12):4538, 2023.

[197] Jaideep Pathak, Zhixin Lu, Brian R Hunt, Michelle Girvan, and Edward Ott. Using machine learning to replicate chaotic attractors and calculate lyapunov exponents from data. *Chaos: An Interdisciplinary Journal of Nonlinear Science*, 27(12), 2017.

[198] J Randolph Paulling and RM Rosenberg. On unstable ship motions resulting from nonlinear coupling. *Journal of Ship Research*, 3(02):36–46, 1959.

[199] Paris Perdikaris, Maziar Raissi, Andreas Damianou, Neil D Lawrence, and George Em Karniadakis. Nonlinear information fusion algorithms for data-efficient multi-fidelity modelling. *Proceedings of the Royal Society A: Mathematical, Physical and Engineering Sciences*, 473(2198):20160751, 2017.

[200] FR Pereira, RT Gonçalves, CP Pesce, et al. A model scale experimental investigation on vortex-self induced vibrations (vsiv) of catenary risers, omae2013-10447. In *Proceedings of the ASME 32ndth International Conference on Ocean, Offshore and Arctic Engineering, June*, pages 9–14, 2013.

[201] Milovan Perić. Wave impact, body motion and overset grids in star-ccm. *STAR South East Asian Conference*, 2012.

[202] Moustafa Perić, R & Abdel-Maksoud. Reliable damping of free-surface waves in numerical simulations. *Ship Technology Research*, 63(8):1–13, 2016.

[203] Norbert Peters. Turbulent combustion. *Measurement Science and Technology*, 12(11):2022–2022, 2001.

[204] Willard J Pierson Jr and Lionel Moskowitz. A proposed spectral form for fully developed wind seas based on the similarity theory of sa kitaigorodskii. *Journal of geophysical research*, 69(24):5181–5190, 1964.

[205] Antonio Pigafetta. *Magellan's voyage: a narrative account of the first circumnavigation*. Courier Corporation, 2012.

[206] Paul R Pinet. *Invitation to oceanography*. Jones & Bartlett Learning, 2019.

[207] Johannes Albert Pinkster. Low frequency second order wave exciting forces on floating structures. 1980.

[208] Stephen B Pope. Turbulent flows. *Measurement Science and Technology*, 12(11):2020–2021, 2001.

[209] Martiqua L Post and Thomas C Corke. Separation control on high angle of attack airfoil using plasma actuators. *AIAA journal*, 42(11):2177–2184, 2004.

[210] L. Prandtl. Über flüssigkeitsbewegung bei sehr kleiner reibung. *Verhandlungen des dritten internationalen Mathematiker-Kongresses in Heidelberg*, 1904.

[211] Lutz Prechelt. Early stopping-but when? In *Neural Networks: Tricks of the trade*, pages 55–69. Springer, 2002.

[212] Harilaos N Psaraftis, Psaraftis Amboy, and Psaraftis. *Sustainable shipping*. Springer, 2019.

[213] Ali Punjani and Pieter Abbeel. Deep learning helicopter dynamics models. In *2015 IEEE International Conference on Robotics and Automation (ICRA)*, pages 3223–3230. IEEE, 2015.

[214] Di Qi and Andrew J. Majda. Using machine learning to predict extreme events in complex systems. *Proceedings of the National Academy of Sciences*, 117(1):52–59, 2020.

[215] Joaquin Quinonero-Candela and Carl Edward Rasmussen. A unifying view of sparse approximate gaussian process regression. *The Journal of Machine Learning Research*, 6:1939–1959, 2005.

[216] Maziar Raissi, Paris Perdikaris, and George Em Karniadakis. Physics informed deep learning (part i): Data-driven solutions of nonlinear partial differential equations. *arXiv preprint arXiv:1711.10561*, 2017.

[217] Rajendra K Raj, Carol J Romanowski, John Impagliazzo, Sherif G Aly, Brett A Becker, Juan Chen, Sheikh Ghafoor, Nasser Giacaman, Steven I Gordon, Cruz Izu, et al. High performance computing education: Current challenges and future directions. In *Proceedings of the Working Group Reports on Innovation and Technology in Computer Science Education*, pages 51–74. 2020.

[218] Steven E Ramberg. The effects of yaw and finite length upon the vortex wakes of stationary and vibrating circular cylinders. *Journal of Fluid Mechanics*, 128:81–107, 1983.

[219] JO Ramsay and BW Silvermann. Functional data analysis. springer series in statistics, 1998.

[220] Carl Edward Rasmussen. Gaussian processes in machine learning. In *Summer School on Machine Learning*, pages 63–71. Springer, 2003.

[221] Kenneth John Rawson and Eric Charles Tupper. *Basic Ship Theory Volume 1*, volume 1. Butterworth-Heinemann, 2001.

[222] Borja G Reguero, Iñigo J Losada, and Fernando J Méndez. A recent increase in global wave power as a consequence of oceanic warming. *Nature communications*, 10(1):205, 2019.

[223] Osborne Reynolds. Xxix. an experimental investigation of the circumstances which determine whether the motion of water shall be direct or sinuous, and of the law of resistance in parallel channels. *Philosophical Transactions of the Royal society of London*, (174):935–982, 1883.

[224] Patrick J Roache. *Verification and validation in computational science and engineering*, volume 895. Hermosa Albuquerque, NM, 1998.

[225] D Rockwell and Et Naudascher. Self-sustaining oscillations of flow past cavities. 1978.

[226] Ricardo Zamora Rodríguez. Olas: Notas de clase. *UPM*, 13 de febrero 2017.

[227] Susan Rose. Mathematics and the art of navigation: the advance of scientific seamanship in elizabethan england. *Transactions of the Royal Historical Society*, 14:175–184, 2004.

[228] Samuel Rudy, Dixia Fan, Jose del Aguila Ferrandis, Themistoklis Sapsis, and Michael S Triantafyllou. Learning optimal parametric hydrodynamic database for vortex-induced crossflow vibration prediction. *arXiv preprint arXiv:2104.05887*, 2021.

[229] Samuel H. Rudy and Themistoklis P. Sapsis. Output-weighted and relative entropy loss functions for deep learning precursors of extreme events. *Physica D: Nonlinear Phenomena*, 443:133570, 2023.

[230] Bjørn Ola & Borgen Henning Ruth, Eivind & Berge. Simulation of added resistance in high waves. American Society of Mechanical Engineers, 2015.

[231] Irwin W Sandberg. Approximation theorems for discrete-time systems. In *[1991] Proceedings of the 34th Midwest Symposium on Circuits and Systems*, pages 6–7. IEEE, 1992.

[232] Benjamin Sanderse, SP Van der Pijl, and Barry Koren. Review of computational fluid dynamics for wind turbine wake aerodynamics. *Wind energy*, 14(7):799–819, 2011.

[233] Thomas J Santner, Brian J Williams, William I Notz, and Brain J Williams. *The design and analysis of computer experiments*, volume 1. Springer, 2003.

[234] William S Saric, Helen L Reed, and Edward J Kerschen. Boundary-layer receptivity to freestream disturbances. *Annual review of fluid mechanics*, 34(1):291–319, 2002.

[235] T. Sarpkaya. Vortex-Induced Oscillations: A Selective Review. *Journal of Applied Mechanics*, 46(2):241–258, 06 1979.

[236] Hermann Schlichting and Joseph Kestin. *Boundary layer theory*, volume 121. Springer, 1961.

[237] Peter J Schmid. Dynamic mode decomposition of numerical and experimental data. *Journal of fluid mechanics*, 656:5–28, 2010.

[238] Galen B Schubauer and Harold K Skramstad. Laminar boundary-layer oscillations and transition on. *Journal of research of the National Bureau of Standards*, 38:251, 1947.

[239] Galen Brandt Schubauer and WG Spangenberg. Forced mixing in boundary layers. *Journal of Fluid Mechanics*, 8(1):10–32, 1960.

[240] Gerhart I Schuëller and Masanobu Shinozuka. *Stochastic methods in structural dynamics*, volume 10. Springer Science & Business Media, 2012.

[241] Matthias Seeger. Gaussian processes for machine learning. *International journal of neural systems*, 14(02):69–106, 2004.

[242] G Shankar and G Devaradjane. Experimental and computational analysis on aerodynamic behavior of a car model with vortex generators at different yaw angles. *Journal of Applied Fluid Mechanics*, 11(1):285–295, 2018.

[243] Songdong Shao and Edmond YM Lo. Incompressible sph method for simulating newtonian and non-newtonian flows with a free surface. *Advances in water resources*, 26(7):787–800, 2003.

[244] Masanobu Shinozuka, George Deodatis, and Takanori Harada. Digital simulation of seismic ground motion. In *Stochastic approaches in earthquake engineering*, pages 252–298. Springer, 1987.

[245] David Siegmund. Importance sampling in the monte carlo study of sequential tests. *The Annals of Statistics*, pages 673–684, 1976.

[246] S Silva, TA Santos, and C Guedes Soares. Parametrically excited roll in regular and irregular head seas. *International Shipbuilding Progress*, 52(1):29–56, 2005.

[247] Roger L Simpson. Turbulent boundary-layer separation. *Annual Review of Fluid Mechanics*, 21(1):205–232, 1989.

[248] Timothy W Simpson. Comparison of response surface and kriging models in the multidisciplinary design of an aerospike nozzle. Technical report, 1998.

[249] AK Slone, K Pericleous, Christopher Bailey, and M Cross. Dynamic fluid–structure interaction using finite volume unstructured mesh procedures. *Computers & structures*, 80(5-6):371–390, 2002.

[250] Edward Snelson and Zoubin Ghahramani. Sparse gaussian processes using pseudo-inputs. *Advances in neural information processing systems*, 18, 2005.

[251] Jasper Snoek, Hugo Larochelle, and Ryan P Adams. Practical bayesian optimization of machine learning algorithms. *Advances in neural information processing systems*, 25, 2012.

[252] Dan M Somers. Design and experimental results for the s809 airfoil. Technical report, National Renewable Energy Lab.(NREL), Golden, CO (United States), 1997.

[253] A Souto-Iglesias, L Delorme, L Pérez-Rojas, and S Abril-Pérez. Liquid moment amplitude assessment in sloshing type problems with smooth particle hydrodynamics. *Ocean Engineering*, 33(11-12):1462–1484, 2006.

[254] Antonio Souto-Iglesias, Fabricio Macià, Leo M. González, and Jose L. Cercos-Pita. On the consistency of mps. *Computer Physics Communications*, 184(3):732–745, 2013.

[255] KJ Spyrou. Dynamic instability in quartering seas: the behavior of a ship during broaching. *Journal of Ship Research*, 40(01):46–59, 1996.

[256] Nitish Srivastava, Geoffrey Hinton, Alex Krizhevsky, Ilya Sutskever, and Ruslan Salakhutdinov. Dropout: a simple way to prevent neural networks from overfitting. *The journal of machine learning research*, 15(1):1929–1958, 2014.

[257] Manley St Denis and Willard J Pierson. On the motions of ships in confused seas. *Trans. SnAMe*, 61:280–357, 1953.

[258] F Stern, HT Kim, VC Patel, and HC Chen. A viscous-flow approach to the computation of propeller-hull interaction. *Journal of Ship Research*, 32(04):246–262, 1988.

[259] Fred Stern, Robert V Wilson, Hugh W Coleman, and Eric G Paterson. Comprehensive approach to verification and validation of cfd simulations—part 1: methodology and procedures. *J. Fluids Eng.*, 123(4):793–802, 2001.

[260] Frederick Stern, Jianming Yang, Zhaoyuan Wang, Hamid Sadat-Hosseini, Maysam Mousaviraad, Shanti Bhushan, and Tao Xing. Computational ship hydrodynamics: Nowadays and way forward. *International Shipbuilding Progress*, 60(1-4):3–105, 2013.

[261] George Gabriel Stokes. On the theory of oscillatory waves. *Trans. Cam. Philos. Soc.*, 8:441–455, 1847.

[262] Martin Stopford. *Maritime economics 3e*. Routledge, 2008.

[263] Ilya Sutskever, Oriol Vinyals, and Quoc V Le. Sequence to sequence learning with neural networks. In *Advances in neural information processing systems*, pages 3104–3112, 2014.

[264] M Aziz Tayfun. Narrow-band nonlinear sea waves. *Journal of Geophysical Research: Oceans*, 85(C3):1548–1552, 1980.

[265] Eva Germaine Rimington Taylor. The heaven-finding art, a history of navigation from odysseus to captain cook. *The heaven-finding art*, 1971.

[266] Tahsin Tezdogan, Yigit Kemal Demirel, Paula Kellett, Mahdi Khorasanchi, Atilla Incecik, and Osman Turan. Full-scale unsteady rans cfd simulations of ship behaviour and performance in head seas due to slow steaming. *Ocean Engineering*, 97:186–206, 2015.

[267] Tahsin Tezdogan, Atilla Incecik, and Osman Turan. A numerical investigation of the squat and resistance of ships advancing through a canal using cfd. *Journal of marine science and technology*, 21:86–101, 2016.

[268] Martin Thomas and Peter Bruce. *Heavy Weather Sailing 8th Edition*. Bloomsbury Publishing, 2022.

[269] Joe F Thompson, Zahir UA Warsi, and C Wayne Mastin. *Numerical grid generation: foundations and applications*. Elsevier North-Holland, Inc., 1985.

[270] Geoffrey Till. *Seapower: A guide for the twenty-first century*, volume 51. Routledge Oxon, 2013.

[271] Neil Titchener and Holger Babinsky. A review of the use of vortex generators for mitigating shock-induced separation. *Shock Waves*, 25:473–494, 2015.

[272] Hendrik L Tolman et al. User manual and system documentation of wavewatch iii tm version 3.14. *Technical note, MMAB contribution*, 276(220), 2009.

[273] Lloyd N Trefethen and David Bau. *Numerical linear algebra*, volume 181. Siam, 2022.

[274] GS Triantafyllou. Vortex induced vibrations of long cylindrical structures. In *Summer Meeting ASME, Washington, DC*, 1998.

[275] Michael Triantafyllou, George Triantafyllou, YS Tein, et al. Pragmatic riser viv analysis. In *Offshore technology conference*. Offshore Technology Conference, 1999.

[276] A.D. Trim, H. Braaten, H. Lie, and M.A. Tognarelli. Experimental investigation of vortex-induced vibration of long marine risers. *Journal of Fluids and Structures*, 21(3):335–361, 2005. Marine and Aeronautical Fluid-Structure Interactions.

[277] Peter S Tromans, Ali R Anaturk, and Paul Hagemeijer. A new model for the kinematics of large ocean waves-application as a design wave. In *ISOPE International Ocean and Polar Engineering Conference*, pages ISOPE–I. ISOPE, 1991.

[278] Trebsijg van de Wijdeven and Joseph Katz. Automotive application of vortex generators in ground effect. *Journal of Fluids Engineering*, 136(2):021102, 2014.

[279] Edward R Van Driest. On turbulent flow near a wall. *Journal of the aeronautical sciences*, 23(11):1007–1011, 1956.

[280] J Kim Vandiver and Li Li. Shear7 v4. 4 program theoretical manual. *Massachusetts Institute of Technology*, 2005.

[281] Ashish Vaswani, Noam Shazeer, Niki Parmar, Jakob Uszkoreit, Llion Jones, Aidan N Gomez, Łukasz Kaiser, and Illia Polosukhin. Attention is all you need. *Advances in neural information processing systems*, 30, 2017.

[282] Roberto Vettor and C Guedes Soares. Development of a ship weather routing system. *Ocean Engineering*, 123:1–14, 2016.

[283] Jungao Wang, Shixiao Fu, Rolf Baarholm, Jie Wu, and Carl Martin Larsen. Fatigue damage of a steel catenary riser from vortex-induced vibration caused by vessel motions. *Marine Structures*, 39:131–156, 2014.

[284] Jungao Wang, Shixiao Fu, Rolf Baarholm, Jie Wu, and Carl Martin Larsen. Out-of-plane vortex-induced vibration of a steel catenary riser caused by vessel motions. *Ocean Engineering*, 109:389–400, 2015.

[285] Jungao Wang, Shixiao Fu, Carl Martin Larsen, Rolf Baarholm, Jie Wu, and Halvor Lie. Dominant parameters for vortex-induced vibration of a steel catenary riser under vessel motion. *Ocean Engineering*, 136:260–271, 2017.

[286] Kunpeng Wang, Wenyong Tang, and Hongxiang Xue. Time domain approach for coupled cross-flow and in-line viv induced fatigue damage of steel catenary riser at touchdown zone. *Marine Structures*, 41:267–287, 2015.

[287] Zi Wang and Stefanie Jegelka. Max-value entropy search for efficient bayesian optimization. In *International Conference on Machine Learning*, pages 3627–3635. PMLR, 2017.

[288] Frank M White and Joseph Majdalani. *Viscous fluid flow*, volume 3. McGraw-Hill New York, 2006.

[289] Bernard Widrow, Marcian E Hoff, et al. Adaptive switching circuits. In *IRE WESCON convention record*, volume 4, pages 96–104. New York, 1960.

[290] David C Wilcox et al. *Turbulence modeling for CFD*, volume 2. DCW industries La Canada, CA, 1998.

[291] Charles HK Williamson and R Govardhan. Vortex-induced vibrations. *Annu. Rev. Fluid Mech.*, 36:413–455, 2004.

[292] Christian Windt, Josh Davidson, and John V Ringwood. High-fidelity numerical modelling of ocean wave energy systems: A review of computational fluid dynamics-based numerical wave tanks. *Renewable and Sustainable Energy Reviews*, 93:610–630, 2018.

[293] GCOS WMO. Status of the global observing system for climate. 2015.

[294] Wanhai Xu, Yingsen Luan, Qinghua Han, Chunning Ji, and Ankang Cheng. The effect of yaw angle on viv suppression for an inclined flexible cylinder fitted with helical strakes. *Applied Ocean Research*, 67:263–276, 2017.

[295] Kyongmin Yeo and Igor Melnyk. Deep learning algorithm for data-driven simulation of noisy dynamical system. *Journal of Computational Physics*, 376:1212–1231, 2019.

[296] Decao Yin, Halvor Lie, and Jie Wu. Structural and Hydrodynamic Aspects of Steel Lazy Wave Riser in Deepwater. *Journal of Offshore Mechanics and Arctic Engineering*, 142(2), 12 2019. 020801.

[297] Decao Yin, Jie Wu, Halvor Lie, Elizabeth Passano, Svein Sævik, Guttorm Grytøyr, Michael Tognarelli, Torgrim Andersen, Ragnar Igland, Daniel Karunakaran, and Collin Gaskill. Wave effects on vortex-induced vibrations of a top-tensioned riser. *Journal of Offshore Mechanics and Arctic Engineering*, 145:1–9, 12 2022.

[298] Ian R Young. *Wind generated ocean waves*. Elsevier, 1999.

[299] Zhiqi Zhao, Lei Luo, Dandan Qiu, Songtao Wang, Zhongqi Wang, and Bengt Sundén. On the topology of vortex structures and heat transfer of a gas turbine blade internal tip with different arrangement of delta-winglet vortex generators. *International Journal of Thermal Sciences*, 160:106676, 2021.

[300] Xiaoyu Zhou, Hongxia Li, Yi Huang, and Yihua Liu. Deep learning machine based ship parametric rolling simulation and recognition algorithms. *Ocean Engineering*, 276:114137, 2023.

[301] Hongjun Zhu, Jie Hu, Yue Gao, Honglei Zhao, and Wanhai Xu. Spatial–temporal mode transition in vortex-induced vibration of catenary flexible riser. *Journal of Fluids and Structures*, 102:103234, 2021.

[302] Thalis PV Zis, Harilaos N Psaraftis, and Li Ding. Ship weather routing: A taxonomy and survey. *Ocean Engineering*, 213:107697, 2020.